The Provenance and thermal histories of the Carboniferous Midland Valley of Scotland

Eamon McKenna B.Sc. (Hons.)

Submitted in fulfilment for the requirements of the degree of Doctor of Philosophy (Ph.D.)

School of Geographical and Earth Sciences
College of Science and Engineering
University of Glasgow

April 2021

Supervisors:
Dr. Cristina Persano, Dr. Alison Monaghan MBE

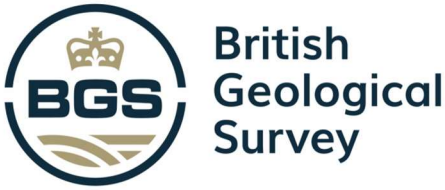

Abstract

Sedimentary basins are an important geological archive as they contain a wealth of information about the regions palaeogeographical setting, thermal evolution, and post depositional history, which are critical to many geological applications. However, establishing the source(s) of the sedimentary material stored within a basin, can be complicated by the refractory nature of some minerals often used as proxies for sediment provenance, meaning that a recycled component may be present and difficult to recognise. Thermal and burial history reconstructions based on the maturation of organic matter (vitrinite reflectance, VR) has been applied widely by the hydrocarbon industry to great success. However, due to the techniques inability to supply a quantification on time, its application in regions that lack post depositional constraints can lead to differing interpretations.

In this thesis two geochronometers (zircon and apatite U-Pb geochronology) and one thermochronometer (apatite fission track, AFT) have been applied to the Carboniferous sedimentary strata of the central and eastern regions of the Midland Valley of Scotland. The aim of which is to provide a better understanding of the evolution of post-Caledonian sediment source(s) and pathways and to better constrain the post-Carboniferous thermal histories of the Midland Valley. This will reduce the geological uncertainties associated with the region, which is vital for Scotland to meet its future low carbon geo-energy commitments.

A multi-proxy approach, applying U-Pb geochronology to detrital zircon and apatite has been utilised to investigate and constrain the provenance of the clastic material in Viséan to Westphalian B, Carboniferous sandstones of the Midland Valley of Scotland. The results of this provenance data clearly show three distinct sources for the sandstones: 1) Laurentian associated rocks (~900-2000 and ~2500-3100 Ma), 2) Caledonian orogeny associated rocks (395-475 Ma), and 3) Carboniferous volcanic associated rocks (~330-350 Ma). Applying U-Pb geochronology to both zircon and apatite from the same sandstone has allowed for the identification of recycled components, indicating that not all U-Pb age populations have been derived directly from their original source. Detrital zircon U-Pb age peaks that align with the Grenvillian (900-1200 Ma), Pinwarian (1450-1510 Ma), Labradorian (1600-1700 Ma), and Lewisian (2500-3100 Ma) orogenic events, lack equivalent apatite U-Pb counterparts. This suggests that Laurentian associated populations have been derived through the recycling of existing sedimentary and metasedimentary lithologies from the Devonian Old Red Sandstone, Grampian terrane, and Southern Uplands. Samples with complementary prominent

Caledonian orogeny associated zircon and apatite U-Pb age peaks, are likely to be derived from first cycle sources from north of the Midland Valley, while Carboniferous ages are most likely derived from volcanic sources within the region. Spatial and temporal variation in the sample detrital spectra, indicates the provenance source did not remain constant over time. Early-mid Viséan (Arundian-Asbian) U-Pb zircon samples are dominated by Proterozoic and Archean, Laurentian associated ages and lack a significant Caledonian peak, indicating recycling of Devonian Old Red Sandstone, Grampian terrane, and Southern Uplands dominated the sediment supply. U-Pb apatite samples from the same time are dominated by a Caledonian peak suggesting either a very minor Caledonian associated source was actively supplying a limited amount of sediment or recycling of apatite through existing sedimentary lithologies is possible, as previous investigations have shown late Devonian Old Red Sandstone to be lacking in Caledonian aged U-Pb zircon. Late Viséan (Brigantian) samples in the eastern Midland Valley of Scotland have a marked increase in Palaeozoic Caledonian associated zircon ages, indicating the source region now included first cycle Caledonian associate rocks, although Laurentian associated components still dominate the spectra. A Brigantian sample collected to the west of the Bathgate Hills Volcanic Formation, located towards the centre of the study area, still shows a paucity in Caledonian related zircon ages, suggesting the volcanic high was a barrier or at least hindered sediment from the northeast being deposited across the region. Carboniferous peaks present in Brigantian zircon and apatite samples indicate the volcanic highs were also local sediment sources. A major change in sediment provenance occurs during the early Namurian (Pendleian) evidenced by the reversal in the dominant source signal, with Laurentian associated ages now relatively insignificant compared to Palaeozoic peaks, indicating first cycle Caledonian associated rocks now dominated the source area. A similar signal is recorded in Carboniferous strata in the Millstone Grit Formation in the Pennine Basin, attributed to a regional source to the north supplied via the Pennine delta. This distal source was also likely supplying material into the Midland Valley as well as proximal sources from Scottish Caledonian rocks, which combined to drown out the recycled component. Caledonian ages continue to dominate the Midland Valley samples in the Westphalian, contrary to Carboniferous basins to the south, which experience a reduction in the influence from the northern source during the Westphalian. Sources that dominated basins to the south were most likely prevented from entering the Midland Valley of Scotland by the Southern Upland high, which allowed the Caledonian sources to prevail.

Undertaking detrital thermochronology is challenging due to the low yield of accessory minerals in some sedimentary rocks. However, results show AFT ages from the Midland Valley of Scotland reflect the geological structure of the region during the Carboniferous, with oldest ages located within the syncline cores and on structural highs. A complex series of forward and inverse modelling of individual and multi-sample profiles, combining outcrop and borehole samples, suggests the thermal histories can be sub-divided into three episodes: 1) Carboniferous-Permian heating, 2) Permian-Mesozoic Cooling, and 3) Cenozoic cooling. Inverse models also suggest initial heating was under the influence of an elevated geothermal gradient, supported by Carboniferous volcanic activity. These episodes are similar to those reported in other thermochronology investigations for onshore Scotland and show a contrast to those reported offshore, suggesting the onshore region was cooling as a coherent block from post-Carboniferous times. Though the general trend observed in profile models is one of cooling through the Mesozoic, indicating an absence of significant burial under continued successions, some individual samples display an element of late Mesozoic reheating, which may be attributable to the Late Cretaceous transgression. The final Cenozoic cooling pulse, evident across the region, has been recognised in numerous investigations and has been attributed to processes associated with the emplacement of the proto-Icelandic plume or far field stresses related to compressional forces associated with the opening of the North Atlantic Ocean and Alpine collision. However, the temperature sensitivity of AFT is not enough to resolve this part of the thermal history.

The results reported in this thesis reveal that the provenance of the Carboniferous sedimentary strata of the Midland Valley of Scotland did not remain constant through time and that post burial thermal maximum was attained following Carboniferous burial under an elevated geothermal gradient which was followed by episodes of cooling. These findings have important implications for assessing the future geo-energy potential within the Midland Valley of Scotland.

Table of Contents

The Provenance and thermal histories of the Carboniferous Midland Valley of Scotland i

Abstract.....i

Table of Contents.....iv

List of Figures x

List of Tables xvi

Acknowledgment xvii

Declaration.....xviii

Chapter 1 Introduction 1

1.1 Project rationale 1

1.1.1 Aims and objectives 3

1.2 Study area, methods, and sampling 4

1.2.1 Methods.....5

1.2.2 Sampling 6

1.2.3 Sample list and locations 10

1.3 Previous studies on the provenance and thermal hostory of the Midland Valley and nearby basins.....12

1.3.1 Provenance 13

1.3.2 Thermochronology studies in Scotland and northern England 16

1.3.3 Thermal studies in the Midland valley.....18

1.4 Thesis outline 22

Chapter 2 Geological context: Midland Valley of Scotland 23

2.1 Regional geological setting 24

2.2 The Midland Valley of Scotland.....29

2.2.1 Lower Palaeozoic tectonic setting.....29

2.2.2 Carboniferous tectonic framework 31

2.2.3 Structure.....35

2.3 Geology of the Midland Valley 37

2.3.1 Basement 39

2.3.2 Lower Palaeozoic evolution of the Midland Valley.....40

2.3.3 Upper Palaeozoic.....44

2.4 Carboniferous evolution of the Midland Valley.....46

2.4.1 Introduction.....46

2.4.2 Inverclyde Group 49
2.4.3 Strathclyde Group 51
2.4.4 Clackmannan Group 56
2.4.5 Scottish Coal Measures Group 61
2.4.6 Carboniferous-Permian Volcanic activity 63
2.5 Post-Carboniferous evolution of the Midland Valley 65
Chapter 3 Methodology 67
3.1 Introduction 67
3.1.1 Mass spectrometry for isotopic analysis 68
3.1.2 Laser Ablation Inductively Coupled Plasma Mass Spectrometry (LA-ICP-MS) 69
3.1.3 The age equation 71
3.2 Geochronology 73
3.2.1 Introduction 73
3.2.2 Geochronological equations 74
3.2.3 Graphical display of U-Pb data 75
3.2.4 U-Pb geochronology for provenance investigations 78
3.3 Thermochronology 82
3.3.1 Introduction 82
3.3.2 Fission track formation and revealing 85
3.3.3 General isotopic age equation 86
3.3.4 EDM uranium concentration and Fission Track age equation 88
3.3.5 EDM Zeta calibration 89
3.3.6 LA-ICP-MS AFT age determination 90
3.3.7 LA-ICP-MS Zeta approach 90
3.3.8 Absolute age equation 91
3.3.9 Pooled and central age and radial plots 92
3.3.10 Data quality assessment 94
3.3.11 Track Length Distribution (TLD) 101
3.3.12 Controls on annealing of fission tracks 104
3.4 Thermal history modelling 108
3.4.1 QTQt theoretical basis 108
3.5 Limitations and conclusions 111
Chapter 4 Provenance Results 113

4.1 Introduction....113
4.1.1 Zircon textures....116
4.1.2 Apatite textures....117
4.2 Results....118
4.2.1 LA ICP MS parameters table....120
4.3 Viséan samples....121
4.3.1 Fife Ness Formation (EM-014)....121
4.3.2 Anstruther Formation (EM-015)....123
4.3.3 Sandy Craig Formation (EM-010)....125
4.3.4 West Lothian Oil Shale Formation (EM-020)....126
4.3.5 West Lothian Oil Shale Formation (CHBH)....129
4.4 Namurian samples....131
4.4.1 Limestone Coal Formation (A6BH)....131
4.4.2 Limestone Coal Formation (THBH)....134
4.4.3 Upper Limestone Formation (DMG1)....137
4.5 Scottish Coal Measure sample....139
4.5.1 Middle Scottish Coal Measures (EM-017)....139
4.6 Carboniferous Midland Valley: Summary....142
4.6.1 Combined zircon KDE....144
4.6.2 Combined apatite KDE....145
4.6.3 Combined zircon and apatite KDE....146
4.6.4 Palaeozoic zircon KDE....147
4.6.5 Palaeozoic apatite KDE....148
4.6.6 Palaeozoic combined zircon and apatite KDE....149
Chapter 5 Provenance of the Carboniferous Midland Valley of Scotland....150
5.1 Potential source regions....150
5.2 Previous U-Pb geochronological studies....154
5.3 Provenance of the Midland Valley of Scotland....161
5.3.1 Proterozoic and Archean ages....162
5.3.2 Palaeozoic ages....164
5.3.3 Palaeogeographic reconstructions....169
5.4 Conclusions....173
Chapter 6 AFT Thermochronology....175

6.1 Results 176
6.2 AFT age data 177
6.2.1 AFT central age vs stratigraphic age 177
6.2.2 AFT central age vs depth 178
6.2.3 AFT data tables 179
6.2.4 Sample Dpar & ^{238}U concentration 183
6.2.5 Radial plots 186
6.3 Track lengths data 193
6.3.1 Track length distributions 195
6.3.2 AFT Central age vs Mean Track Length 195
6.4 Summary of AFT data 199
Chapter 7 AFT thermal histories 202
7.1 Forward thermal history modelling 202
7.1.1 Approach 202
7.1.2 Results 204
7.2 Inverse thermal history modelling 211
7.2.1 Approach 211
7.2.2 Pre-depositional history 211
7.3 Results 216
7.3.1 Central region 217
7.3.2 Leven 224
7.3.3 Fife (south) 228
7.3.4 Fife (north) 233
7.3.5 Lanarkshire 236
7.3.6 Lothians 238
7.4 Regional summary of individual samples 241
7.5 Multi-sample approach 242
7.5.1 Central region 243
7.5.2 Leven 244
7.5.3 Fife (south) 246
7.5.4 Fife (north) 247
7.5.5 Lanarkshire 248
7.5.6 Lothians 249

7.6 Regional summary of combined samples 250
7.7 Palaeogeothermal Gradient 251
Chapter 8 Burial and exhumation history of the Midland Valley 253
8.1 Combining forward and inverse modelling 253
8.2 Main thermal history episodes 255
8.2.1 Carboniferous-Permian heating 257
8.2.2 Permian-Mesozoic cooling 262
8.2.3 Cenozoic cooling 271
8.3 Conclusions 275
8.3.1 Burial and exhumation history of the Midland Valley 275
8.3.2 Implication for petroleum prospectivity 278
Chapter 9 Conclusions and future work 282
9.1 Provenance 283
9.1.1 Future work 287
9.2 Thermochronology 287
9.2.1 Carboniferous-Permian heating 288
9.2.2 Permian-Mesozoic cooling 288
9.2.3 Cenozoic cooling 289
9.2.4 Implication for petroleum prospectivity 289
9.2.5 Future work 290
9.3 Concluding remarks .... **Error! Bookmark not defined.**
Chapter 10 Appendices 292
10.1 Appendix A - Sample details 292
10.2 Appendix B - Sample preparation 295
10.2.1 Mineral separation 295
10.2.2 Mounting 296
10.2.3 Polishing 296
10.2.4 Etching 296
10.2.5 Microscope Methodology for AFT analysis 296
10.2.6 The University of Glasgow 297
10.2.7 The University of Melbourne 297
10.3 Appendix C - U-Pb data tables 298
10.4 Appendix D - AFT sample data sheets - Outcrop 354

10.5 Appendix E - AFT sample data sheets - Borehole.....369

List of References.....388

List of Figures

Figure 1-1: Simplified geological map of the Midland Valley of Scotland. 4
Figure 1-2: Sample location map. 9
Figure 1-3: Samples and lithostratigraphical framework modified from Browne *et al.* (1999). 11
Figure 1-4: Locations of previous provenance and thermal history investigations of the Midland Valley and nearby basins. 12
Figure 1-5: Compilation of AFT central ages from previous investigations across northern England and Scotland. 16
Figure 1-6: AFT ages UK. 17
Figure 1-7: VR data for the Milton of Balgonie borehole (see Figure 1-4 for borehole location). 18
Figure 1-8: Burial history model for the Milton of Balgonie borehole. 19
Figure 1-9: Schematic burial history plot for the West Lothian Oil Shale Formation. 20
Figure 1-10: Estimated petroleum generation zones and common thermochronometers. 21
Figure 2-1: Digital Elevation Model (DEM) of Scotland. 23
Figure 2-2: Map of the geological terranes of Ireland and Britain. 24
Figure 2-3: Simplified geological map of Scotland. 25
Figure 2-4: Offshore 250K geology map. 27
Figure 2-5: Regional tectonic model. 30
Figure 2-6: Regional tectonic model of Coward (1993). 32
Figure 2-7: Summary of the timing and events of the tectonic histories highlighted above. 34
Figure 2-8: Traces of main structural features of MVS. 35
Figure 2-9: Simplified geological map of the Midland Valley of Scotland. 37
Figure 2-10: Midland Valley of Scotland basement. 39
Figure 2-11: Two models for the interpretation of the Midland Valley during the Ordovician. 41
Figure 2-12: Simplified map of Ordovician and Silurian outcrops of the Midland Valley. 42
Figure 2-13: Simplified geological map of Devonian outcrop in the Midland Valley. 44
Figure 2-14: Lithostratigraphical framework classification for the Carboniferous Midland Valley of Scotland. 48
Figure 2-15: Simplified geological map of the Inverclyde Group locations. 49
Figure 2-16: Simplified geological map of the Strathclyde Group outcrop locations. 51
Figure 2-17: Strathclyde Group isopach map. 52
Figure 2-18: Interpretation of the palaeogeographical setting of the Midland Valley during the Strathclyde Group deposition. 54
Figure 2-19: Simplified geological map of the Clackmannan Group outcrop locations. 56
Figure 2-20: Lower Limestone Formation isopach map and palaeocurrent indicators. 57
Figure 2-21: Limestone Coal Formation isopach map and palaeocurrent indicators. 58
Figure 2-22: Upper Limestone Formation isopach map and palaeocurrent indicators. 59
Figure 2-23: Simplified geological map of Scottish Coal Measures Group outcrop locations. 61
Figure 2-24: Lower-Middle Scottish Coal Measures isopach map and palaeocurrent indicators. Isopachs in meters, also showing direction of transport of coarse grained siliciclastic material (black arrows) and locations of semi-isolated basins (blue arrows) adapted from (Read *et al.* 2002). 62

Figure 2-25: Carboniferous-Permian volcanism across the Midland Valley. 63
Figure 2-26: Carboniferous and Permian volcanic outcrop locations across the Midland Valley. 64
Figure 2-27: Carboniferous and Permian intrusions locations across the Midland Valley. 65
Figure 2-28: Simplified geological map of Permian outcrop location (Mauchline Basin) across the Midland Valley and offshore extent of Permian and younger units. 66
Figure 3-1: Isotopes of lithium. 67
Figure 3-2: Typical laser ablation setup and ablation pit examples. 69
Figure 3-3:Typical Inductively Coupled Plasma (ICP). 70
Figure 3-4: U-(Th)-Pb decay series for ^{238}U, ^{235}U, and ^{232}Th. 73
Figure 3-5: Wetherill Concordia curve displaying concordant data. 76
Figure 3-6: Wetherill Concordia diagram displaying discordant data. 77
Figure 3-7: Tera-Wasserburg space plot for sample EM-17 collected for this thesis. 78
Figure 3-8: PDP and histogram (left) and KDE (right) examples for a detrital zircon sample EM-20 from this thesis. 81
Figure 3-9: Apatite KDE produced from data from sample EM-17. 81
Figure 3-10: Thermochronometers and their Partial Retention/Partial Annealing Zones. 83
Figure 3-11: Ion-spike model for fission track formation. 85
Figure 3-12: Apatite crystal before and after etching. 86
Figure 3-13: Reflected light image of a c-axis parallel Durango apatite. 87
Figure 3-14: AFT analysis by EDM vs LA-ICP-MS. 88
Figure 3-15: Example of radial plot. 93
Figure 3-16: ^{238}U ppm values for reference material from this investigation. 95
Figure 3-17: Durango apatite chards. 96
Figure 3-18: Mount Dromedary crystals. 97
Figure 3-19: Glasgow AFT age reference apatite A. 98
Figure 3-20: Glasgow AFT age reference apatite B. 98
Figure 3-21: Radial plot and TLD example. 101
Figure 3-22: Confined track length. 102
Figure 3-23: Track length measurements for annealed and unannealed induced tracks in Durango apatite at the University of Glasgow. 103
Figure 3-24: Hypothetical cooling histories and their corresponding Track Length Distributions. ..104
Figure 3-25: Kinetic parameter Dpar. 105
Figure 3-26: Dpar calibration. 106
Figure 3-27: Confined track length angle to the crystals c-axis. 107
Figure 3-28: QTQt thermal history model. 110
Figure 4-1: U-Pb analysis sample locations. 113
Figure 4-2: Approximate sample locations on the lithostratigraphic column. 115
Figure 4-3. Zircon textures. 116
Figure 4-4: Apatite textures. 117
Figure 4-5: Selection of CL images from sample from the Fife Ness Formation, EM-014. 121
Figure 4-6: Zircon results for EM-014. 122
Figure 4-7: Apatite results for EM-014. 123
Figure 4-8: Selection of CL images from sample from the Anstruther Formation, EM-015. 124

Figure 4-9: Zircon results for EM-015. 124
Figure 4-10: Apatite results for EM-015. 125
Figure 4-11: Zircon results for EM-010. 126
Figure 4-12: Selection of CL images from sample from the West Lothian Oil Shale Fm, EM-020. 127
Figure 4-13: Zircon results for EM-020. 128
Figure 4-14: Apatite results for EM-020. 129
Figure 4-15: Selection of CL images from sample from the West Lothian Oil Shale Fm, CHBH. ..130
Figure 4-16: Zircon results for CHBH. 130
Figure 4-17: Apatite results for CHBH. 131
Figure 4-18: Selection of CL images from sample from the Limestone Coal Fm, A6BH. 132
Figure 4-19: Zircon results for A6BH. 133
Figure 4-20: Apatite results for A6BH. 134
Figure 4-21: Selection of CL images from sample from the Limestone Coal Formation, THBH. ...135
Figure 4-22: Zircon results for THBH. 135
Figure 4-23: Apatite results for THBH. 136
Figure 4-24: Selection of CL images from sample from the Upper Limestone Formation, DMBH. 137
Figure 4-25: Zircon results for DMBH. 138
Figure 4-26: Apatite results for DMBH. 139
Figure 4-27: Selection of CL images from sample from the Middle Scottish Coal Measures EM-017. 140
Figure 4-28: Zircon results for EM-017. 140
Figure 4-29: Apatite results for EM-017. 141
Figure 4-30: Combined zircon KDE for all samples. 144
Figure 4-31: Combined apatite KDE for all samples. 145
Figure 4-32: Combined zircon and apatite KDE for all samples. 146
Figure 4-33: Palaeozoic zircon KDE. 147
Figure 4-34: Palaeozoic apatite KDE. 148
Figure 4-35: Combined Palaeozoic zircon (green) and apatite (orange) KDE. 149
Figure 5-1: Overview of post-Caledonian North Sea region. 151
Figure 5-2: Caledonian related intrusions and associated volcanic rocks in Scotland. 152
Figure 5-3: Caledonian and Laurentian related orogenic events. 153
Figure 5-4: Timing of volcanism in the Midland Valley during the Carboniferous. 153
Figure 5-5: Location map of previous U-Pb zircon geochronological studies connected to the Midland Valley. 154
Figure 5-6: Probability density plots redrawn from Phillips *et al.* (2009) and McKellar (2017). 155
Figure 5-7: Palaeogeographical map for provenance sources during the late Devonian-early Carboniferous. 156
Figure 5-8: Palaeogeographical map for provenance sources during the Namurian. 157
Figure 5-9: Palaeogeographical map for provenance sources during the Westphalian. 158
Figure 5-10: Combined probability density diagrams from previous publications. 159
Figure 5-11: Detrital zircon age spectra from ORS 1 and ORS 2. 160
Figure 5-12: Combined apatite and zircon KDE with potential Laurentian sources. 161
Figure 5-13: Probability density diagrams for Grampian terrane and Southern Uplands terrane. .164

Figure 5-14: Palaeozoic zircon and apatite KDE plot. 165
Figure 5-15: Palaeogeographic reconstruction model for Arundian-Asbian samples....169
Figure 5-16: Palaeogeographic reconstruction model for Brigantian samples. 170
Figure 5-17: Palaeogeographic reconstruction model for Pendleian-Arnsbergian samples. 171
Figure 5-18: Palaeogeographic reconstruction model for Westphalian sample. 172
Figure 6-1: Sample locations used for AFT investigation plotted on geological map from Chapter 2. 175
Figure 6-2: Individual sample AFT central age vs Stratigraphic age. 177
Figure 6-3: Sample AFT central ages and 1σ errors plotted against sample depth. 178
Figure 6-4:Offshore borehole locations. 182
Figure 6-5: Midland Valley and Geotrack offshore well data. 183
Figure 6-6: Average Dpar (μm) and standard deviation (1SD) for each sample. 184
Figure 6-7: AFT central age (±1σ) vs Dpar (±1SD). 184
Figure 6-8: Average ^{238}U concentration and 1SD for samples from the Midland Valley. 185
Figure 6-9: AFT central age (±1σ) plotted against ^{238}U (±1SD) concentration in parts per million (ppm). 186
Figure 6-10: Outcrop radial plots (Dpar). 188
Figure 6-11: Borehole radial plots (Dpar). 189
Figure 6-12: Outcrop radial plots (^{238}U). 190
Figure 6-13: Borehole radial plots (^{238}U). 191
Figure 6-14: Measured mean track length (MTL) (orange) and projected MTL (green). 193
Figure 6-15: Outcrop measured (orange) and projected (green) MTL (±1SD). 194
Figure 6-16: MTL(±1SD) vs Depth. 194
Figure 6-17: Track length distributions for outcrop samples. 196
Figure 6-18: Track length distributions for borehole samples. 197
Figure 6-19: AFT age vs MTL's for data in this investigation. 198
Figure 6-20: AFT central ages vs MTL's for data collected across all of Scotland. 198
Figure 6-21: AFT data across the Midland Valley. 199
Figure 7-1: Existing burial history models for the Midland Valley. 203
Figure 7-2: Forward model, synthetic data, and inversion of Duddy et al. (1992) scenario. 207
Figure 7-3: Forward model, synthetic data, and inversion including VR of Duddy et al. (1992) scenario. 208
Figure 7-4: Forward model, synthetic data, and inversion of Vincent et al (2010) data. 209
Figure 7-5: Forward model, synthetic data, and inversion including VR of Vincent et al (2010) data. 210
Figure 7-6: No pre-deposition vs pre-deposition point. 214
Figure 7-7: Rapid cooled vs slow cooled pre-depositional history. 215
Figure 7-8: Map showing AFT sample locations and samples grouped into regions for modelling reporting. 216
Figure 7-9: Key for all thermal history models, track length distribution (TLDs), and summary plots for multi-sample models. 217
Figure 7-10: Thermal history modelling results from BDBH and DMBH samples from the Central (west) region. 219

Figure 7-11: Thermal history modelling results from A6BH samples from the Central (west) region. 220
Figure 7-12: Thermal history modelling results from the GLBH and KEBH samples from the Central (east) region. 221
Figure 7-13: Thermal history modelling results from MHBH samples from the Central (east) region. 222
Figure 7-14: Thermal history modelling results from LGBH samples from the Central (east) region. 223
Figure 7-15: Thermal history modelling results from samples EM-04 and EM-05 from the Leven region. 226
Figure 7-16: Thermal history modelling results from sample EM-17 from the Leven region. 227
Figure 7-17: Thermal history modelling results from THBH samples from the Leven region. 228
Figure 7-18: Thermal history modelling results from samples EM-14 and EM-18 from the Fife (south) region. 231
Figure 7-19: Thermal history modelling results from sample EM-07 from the Fife (south) region. 232
Figure 7-20: Thermal history modelling results from samples EM-10 and EM-15 from the Fife (north) region. 234
Figure 7-21: Thermal history modelling results from samples EM-09 and EM-08 from the Fife (north) region. 235
Figure 7-22: Thermal history modelling results from samples EM-13 and CHBH from the Lanarkshire region. 237
Figure 7-23: Thermal history modelling results from samples EM-02 and EM-12 from the Lothians region. 239
Figure 7-24: Thermal history modelling results from samples EM-21 and C6BH from the Lothians region. 240
Figure 7-25: Regional summary of heating and cooling of Midland Valley samples. 241
Figure 7-26: A multi-sample thermal history model for the Central region of the Midland Valley...243
Figure 7-27: A multi-sample thermal history model for the Leven region. 244
Figure 7-28: A multi-sample thermal model for the Leven region including Thornton-1 borehole samples. 245
Figure 7-29: A multi-sample thermal history model for the Fife (south) region of the Midland Valley. 246
Figure 7-30: A multi-sample thermal history model for the Fife (north) region of the Midland Valley. 247
Figure 7-31: A multi-sample thermal history model for the Lanarkshire region of the Midland Valley. 248
Figure 7-32: A multi-sample thermal history model for the Lothians region of the Midland Valley.249
Figure 7-33: Regional summary of heating and cooling of combined Midland Valley samples (multi-samples approach). 250
Figure 7-34: Geothermal gradients from multi-sample thermal models. 252
Figure 8-1: Multi-sample profile thermal history models and their regional location (next page). ..255
Figure 8-2: Summary for Carboniferous volcanic activity across the Midland Valley. 258

Figure 8-3: Multi-sample profile thermal model of the Central region combined with local igneous activity. 259
Figure 8-4: Multi-sample profile thermal model of the Leven region combined with local igneous activity. 260
Figure 8-5: Multi-sample profile thermal model of the Fife (south) region combined with local igneous activity. 260
Figure 8-6: Multi-sample profile thermal model of the Fife (north) region combined with local igneous activity. 261
Figure 8-7: Multi-sample profile thermal model of the Lanarkshire region combined with local igneous activity. 261
Figure 8-8: Multi-sample profile thermal model of the Lothians region combined with local igneous activity. 262
Figure 8-9: Thermal history models produced from Scotland. 263
Figure 8-10: Thermal history models produced from samples from the Grampian terrane. 264
Figure 8-11: Tectonic model of Late Caledonian and Variscan continental escape tectonics. 265
Figure 8-12: Palaeogeographical reconstruction for the Late Cretaceous. 267
Figure 8-13: Estimated denudation in km for the regions of the Midland Valley. 269
Figure 8-14: Scenarios of exhumation and movement of isotherms in relation to exhumation. 270
Figure 8-15: Digital elevation model of western Europe. 271
Figure 8-16: All Expected multi-sample profile thermal histories combined. 273
Figure 8-17: Map of Cenozoic exhumation across Britain and Ireland including new Midland Valley estimates. 274
Figure 8-18: Cubic spline interpolation of AFT central ages across the Midland Valley. 275
Figure 8-19: Relationship between the onshore and offshore geology of Scotland. 277
Figure 8-20: Petroleum elements table from the Midland Valley. 279
Figure 8-21: Modified petroleum elements table from the Midland Valley. 280
Figure 9-1: Palaeogeographical reconstruction indicating the suggested sediment provenance and pathways for previous studies during the late Devonian-Namurian. 283
Figure 9-2: Palaeogeographical reconstruction indicating the suggested sediment provenance and pathways from previous studies during the Westphalian. 284
Figure 9-3: Palaeogeographical reconstruction indicating the suggested sediment provenance and pathways from this thesis during the Carboniferous. 286
Figure 10-1: Sample locations and geology 292

List of Tables

Table 1-1: Sample list and locations. 10
Table 3-1: Half-lives and decay constants of some radioactive isotopes used in this thesis. 73
Table 3-2: Analytical protocol table for LA-ICP-MS analysis acquired at both the University of Melbourne and the University of Glasgow. 100
Table 4-1: LA-ICP-MS parameter table. 120
Table 6-1: Midland Valley outcrop AFT summary table. 179
Table 6-2: Midland Valley AFT borehole summary table. 180
Table 6-3: Geotrack Forth Approaches Basin borehole AFT summary table. 181
Table 8-1: Permian-Mesozoic denudation estimate input values. 268
Table 10-1:Sample details. 293

Acknowledgment

My sincerest gratitude goes to my supervisors Dr. Cristina Persano and Dr. Alison Monaghan, as without their help, the successful completion of this thesis would not have been possible. To them I will be eternally grateful.

My deepest thanks also go to all who I have shared the University of Glasgow Apatite Fission Track and mineral processing facilities with, both past and present especially Dr. Katarzyna Luszczak, Dr. Mark Wildman and Dr. Awara Amin. Special thanks go to lab technicians Robert MacDonald and John Gilleece for their help during sample preparation and Peter Chung for his assistance when using the ISSAC facilities. Andy Gleadow, Barry Kohn, and Ling Chung are thanked for their assistance during my visit to the University of Melbourne. Matthew Horstwood is thanked for his assistance at BGS Keyworth and the numerous discussions on geochronology.

My fellow PhD students in GES, especially Pamela Rattigan and Allan Hollinsworth, with whom I have shared a room with for almost the entirety of my PhD are thanked for all the discussions, laughs, and forced coffee breaks. All staff in GES at the University of Glasgow at thanked especially those who I have taught undergraduate courses with, as I most likely railroaded the class to revolve around apatite and/or zircon regardless of the intended subject matter.

The NERC CDT in Oil and Gas including Prof. John Underhill, Anna Clark and Lorna Munro are thanked especially for their role in coordinating the CDT that this project benefited from (Grant number NE/M00278X/1).

Finally, to my family and close friends, for their support and which has been vital in continuing with this ridiculous endeavour. To my mother Mary, sister Joanne, and brothers Philip, Anthony, and Peter who sadly passed away during this project, this work is dedicated to you.

Declaration

I declare that, except where explicit reference is made to the contribution of others, that this dissertation is the result of my own work and has not been submitted for any other degree at the University of Glasgow or any other institution.

Eamon McKenna

Chapter 1 Introduction

1.1 Project rationale

Sedimentary basins can provide an invaluable insight into paleogeographic and paleotectonic settings through geological time, as they contain an archive of the detrital material sourced from these ancient settings that may have now been eroded away (Hurst and Morton 2014). The study of this detrital material is therefore fundamental in determining the geological history of a region, and for constraining and understanding the functioning of sediment routing systems through time. Defining these sedimentary, source-to-sink pathways throughout the geologic past is often problematic, particularly because the source and transfer zones are often poorly preserved, making the interpretation of ancient sediment routing systems one of the major challenges for sedimentary geoscientists (Allen 2009). Framework grain (Naing *et al.* 2014), heavy mineral analysis (Morton and Hallsworth 1999), geochemistry (Lancaster *et al.* 2017), and geochronology (Bue and Andresen 2014) have been successfully applied to sedimentary basins to determine the source of the detrital material contained within them. However, the nature of the sediment deposited and preserved within these basins is heavily influenced by the lithology of the source area (mineral fertility, recycling of detrital material), climatic forces acting on the sediment prior to final burial (mineral susceptibility to weathering) and post burial processes (diagenesis); all these factors produce biases that may hamper our ability to decipher the source, sediment pathways and post-depositional history. Recent improvements in the precision and accuracy of isotopic analysis using in situ techniques have led to an increase in single mineral investigations; hundreds of determinations can be performed in a short time frame and at a reasonable cost, as to accurately fingerprint the provenance of the single grains. For example, U-Pb ages of single detrital zircon grains are commonly used in sedimentary provenance analysis, providing a reliable guide to the ages of basement source rocks (Moecher and Samson 2006; Dickinson 2008; Thomas 2011; Gehrels 2012) However, the interpretation of these data is often complicated by the refractory nature of zircon and its ability to be recycled over geological time (Andersen *et al.* 2016). Therefore, analysis of multiple species of minerals, with a variety of chemical and isotopic signatures, can greatly strengthen the sediment provenance investigation and remove potential bias in the rock record.

Once deposited and buried, detrital material can also provide a wealth of information about the post-depositional thermal evolution of sedimentary basins. Thermal maturation of organic material,

through vitrinite reflectance (VR) determinations, can be used to provide an estimate of the maximum paleotemperature attained, while low temperature thermochronology can give quantitative and qualitative insights into the magnitude, duration, and rates of the time-temperature history of the rocks (t-T pathway) (Gleadow *et al.* 1986). Together, sediment provenance and basin thermal history provide key information about the paleogeography of the source and sink areas, their geomorphological and tectonic evolution through time, changes in basal heat flow, indicative of large-scale plate movements, and the causes, magnitude, and rates of basin exhumation. These insights can be used to define reservoir characteristics, the timing and duration of hydrocarbon source rock maturation, estimates of the temporal and spatial variations of paleo-geothermal gradients, time of diagenesis and erosion of the overburden, all invaluable information not only for oil and gas exploration, but also for shallow and deep geothermal energy and Hydrogen storage solutions.

In the past, the Midland Valley has been the centre of Scotland's economic development, hosting most of the country's population, wealth, and once economically extractable coal deposits. Recently its geology has returned to the centre of a series of studies aimed at meeting the Scottish energy transition goal, to be carbon neutral by 2040 (Heinemann *et al.* 2019). The sedimentary rocks of the Carboniferous Midland Valley of Scotland have been investigated for their potential for both conventional and unconventional oil and gas exploration (Hallett *et al.* 1985; Underhill *et al.* 2008; Monaghan 2014). While the possibility of producing renewable geothermal energy from both shallow, abandoned mines and deep geological formations (Gillespie *et al.* 2013; Comerford *et al.* 2018; Monaghan *et al.* 2018), storing hydrogen gas in geological reservoirs (Heinemann *et al.* 2018), and capturing and storing carbon (Carbon Capture Storage; CCS) (Jin *et al.* 2012) have also received recent attention. Despite this attention, the geological thermal history and provenance of the sedimentary basin fill of the region is still poorly constrained and many uncertainties remain. This thesis represents an opportunity to reduce these uncertainties by constraining the provenance of the Carboniferous detrital material and the post depositional thermal history of the region. The understanding of the latter, in particular, is key to establishing the reservoir potentials, regardless of the stored medium (hydrocarbons, hydrogen, geothermal water), constraining the magnitude and timing of post-Carboniferous heating, vital for generation and migration of hydrocarbons from their source rock, and estimating the magnitude of burial and exhumation, essential for de-risking potential geo-energy options.

1.1.1 Aims and objectives

The main aims of this thesis are to provide a better understanding of the evolution of post-Caledonian sediment source(s) and pathways and to better constrain the post-Carboniferous thermal histories of the Midland Valley. This will reduce the geological uncertainties associated with the region, which is vital for Scotland to meet its future low carbon geo-energy commitments. To meet these aims, the objectives of this study are to:

- Quantify the provenance of Carboniferous detrital material. To attain this objective, a novel combination of multi-mineral, single-grain (U-Pb) determinations has been used to discriminate between possible polycyclic and first cycle sources within the Midland Valley. This technique has the potential to be applied to any basin the provenance of which may be complicated by the re-working of material through the erosion of sedimentary rocks.

- Construct, using the provenance data, palaeogeographical maps to identify sediment transport pathways and pinpoint the tectonic setting of the Midland Valley within the wider Carboniferous tectonic framework of the North Atlantic region.

- Quantify the timing, duration, and rate of the post-burial heating and cooling in the central and eastern Midland Valley using Apatite Fission Track Analysis, combining outcrop and borehole sample data.

- Use these results to investigate the potential for hydrocarbon prospectivity in terms of timing of source rock maturity and generation.

- Highlight the wider implications of this thesis in relation to de-risking geo-energy resource potential.

1.2 Study area, methods, and sampling

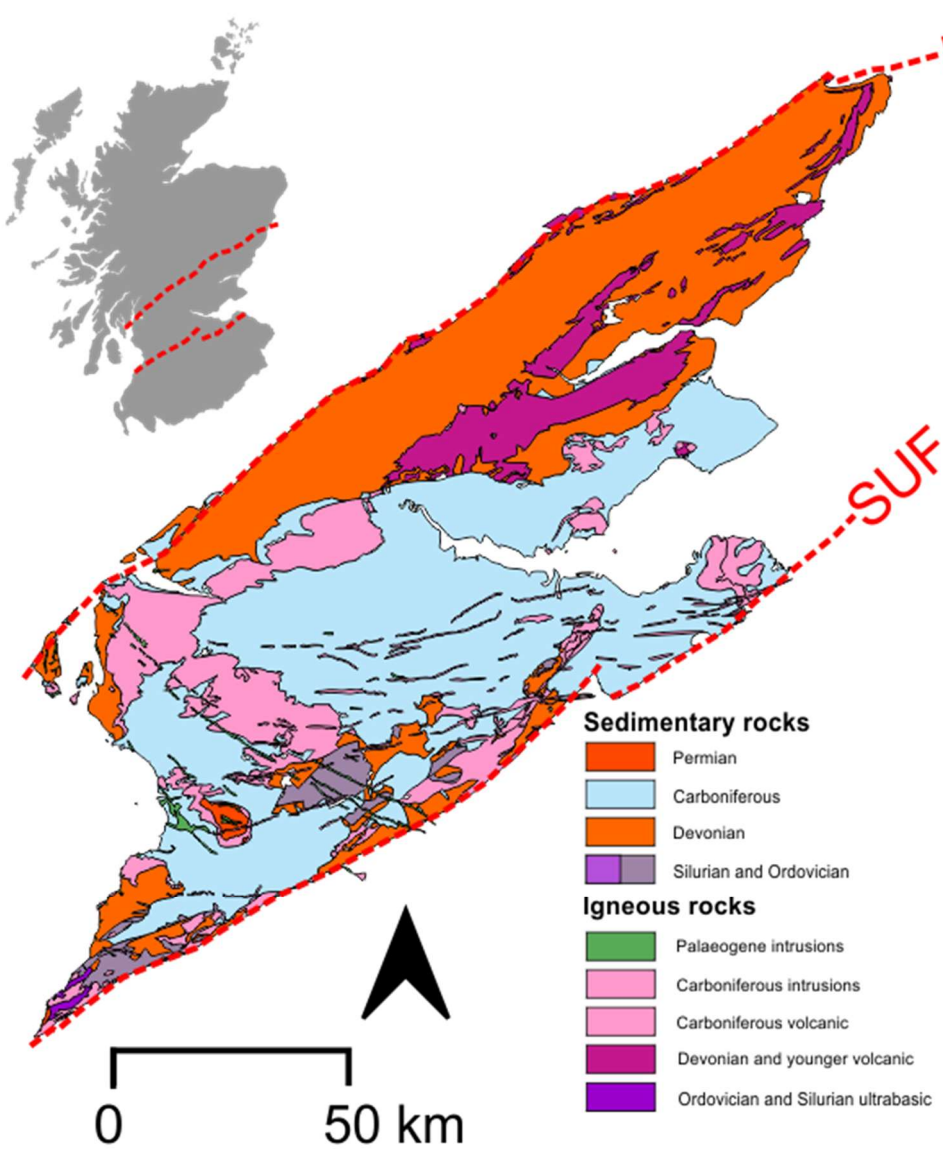

Figure 1-1: Simplified geological map of the Midland Valley of Scotland. Modified from Trewin (2002) showing the extent of the Carboniferous lithologies, sedimentary (blue), igneous (pink). HBF: Highland Boundary Fault; SUF: Southern Uplands Fault

The Midland Valley of Scotland is bound to the north and south by the Highland Boundary (HBF) and Southern Upland Faults (SUF), respectively (Figure 1-1). It is dominated by an internally complex arrangement of Carboniferous sedimentary rocks and contemporaneous intrusive and extrusive volcanic lithologies; the entire sequence is locally, up to 5 km thick and was deposited conformably above fluvial Devonian Old Red Sandstone (Monaghan *et al.* 2014). Without surface exposure, the pre-Palaeozoic basement of the Midland Valley of Scotland has been interpreted indirectly through seismic profiles, clast provenance studies and xenoliths found within volcanic vents; all these observations suggest high-grade Granulite facies lithologies form the basement of the Midland Valley

(Bamford 1979; Bluck 1984; Upton *et al.* 1984; Dentith and Hall 1989). Lower Palaeozoic rocks occur as discrete Ordovician and Silurian inliers, located predominantly along the southern margin of the region (Figure 1-1). These outcrops display a shallowing upwards, trend from a marine to a terrestrial environment during the mid-Silurian, suggesting increasing aridity of the region as it moved towards the equator (Cocks and Toghill 1973; Cameron and Stephenson 1985). Semi-arid conditions persisted into the Early Devonian, where thick deposits of coarse fluvial sediments and contemporaneous volcanic material were deposited in what are considered to be intracontinental basins (Bluck 2000). Separated by the Middle Devonian Acadian unconformity (Wilson 1980), Upper Devonian deposits, are generally fine grained and lack the evidence for volcanic activity seen in the Early Devonian (Browne 1980). They pass conformably into cyclical fluvial-deltaic Carboniferous sedimentary lithologies punctuated by widespread, contemporaneous, intrusive and extrusive volcanism; thin limestones also were deposited, as a result of periodic marine incursions which flooded the region (Read 1988; Ritchie *et al.* 2003). Permian aeolian sandstones are the youngest sedimentary units found in the onshore Midland Valley, and they occur only in the southwest, Mauchline basin (Cameron and Stephenson 1985). Offshore, however, Permian and younger deposits are present in the Forth Approaches, Firth of Clyde, Arran and Northern Ireland; it has been suggested that the Mesozoic cover also encroached onshore and it has been subsequently removed by erosion (Vincent *et al.* 2010). Igneous intrusions associated with Paleogene volcanic activity and the opening of the North Atlantic are the youngest igneous rocks found in the Midland Valley (Cameron and Stephenson 1985). Quaternary glaciations have deposited glacial till, often tens of metres thick across the region, overlying most of the Palaeozoic strata; the present landscape is considered to be the result of this glacial activity (Boulton *et al.* 1991). A more detailed description of the complex geological history of the Midland Valley is found in Chapter 2.

1.2.1 Methods

Despite some in-depth studies of the lower Paleozoic basin fill of the Midland Valley (Phillips *et al.* 2004; Phillips *et al.* 2009; McKellar 2017) the provenance of the Carboniferous sedimentary rocks and their source-to-sink pathways are poorly constrained; this lack of information makes understanding the tectonic framework within which the sedimentary basin formed and developed particularly difficult. In this study, U-Pb geochronology of detrital zircon has been used, as in many other sedimentary basins, to elucidate the paleogeographic and paleotectonic evolution of the source area and the pathways through which the material was transported to the basin. However, the

interpretation of these data in terms of constraining the catchment areas and drainage patterns of the rivers transporting the sediments from their source to their sink, can be complicated, as zircon may not be present in some lithologies and/or derived from recycling existing sedimentary rocks (Andersen *et al.* 2016). For these reasons, detrital apatite U-Pb geochronology was also applied to this investigation. Unlike the robust, potentially polycyclic zircon, apatite is known to crystalise in a wide compositional range of rock types, can be physically broken-down during transportation, and chemically dissolved by both weathering and post-depositional dissolution (Morton and Hallsworth 1999; Kirkland *et al.* 2018). Due to this susceptibility, apatite is often considered to be a strong indicator of first cycle sediment only (Gillespie *et al.* 2018), although the possibility of apatite deriving from proximal, relatively apatite-rich sedimentary sources cannot be discarded. Recycled zircon populations can therefore potentially be identified by the absence of any corresponding first cycle apatite populations, providing a robust constraint to differentiate between first and polycyclic material to accurately define the sediment sources of the Carboniferous Midland Valley.

Although present offshore, the extent of any post-Carboniferous sediments deposited in the onshore portion of the Midland Valley is poorly constrained, as Permian-Mesozoic sediments are absent, except for the isolated Permian Mauchline Basin in the southwest (Chapter 2). Thus, details about the post Carboniferous thermal history including the timing and duration of heating and cooling events, evolution of the geothermal gradient, and magnitude of denudation in the exhumed sedimentary basin are poorly constrained. Apatite fission track is a well-established low temperature thermochronology technique used to determine the post burial thermal history and denudation in exhumed sedimentary basins (Powell *et al.* 2018; Schneider and Issler 2019) In this thesis, a regional sampling approach of both borehole and outcrop locations has provided a strong apatite fission track dataset that has been used to characterise the time-temperature history of the central and eastern portion of the basin since Carboniferous times.

1.2.2 Sampling

Due to sample availability, this thesis focusses on the central and east regions of the Midland Valley, with sample locations shown in Figure 1-2. Samples were collected from outcrops and boreholes to provide the best spatial and temporal insight into the provenance and thermal history of the region. Outcrop samples were collected from sandstones that were not in the vicinity of any intrusive or extrusive igneous rocks, or major faults, to avoid the potential thermal disruptions caused by

conducive heating and the circulation of hot fluids (Malusà and Fitzgerald 2019b; Tagami 2019). When possible, samples were collected as close as possible to localities of already existing VR data (Raymond 1991). Outcrop exposure is largely limited to coastal areas in the Midland Valley, due to recent glacial deposits covering much of the inland region. Due to the nature of some of the outcrops, apatite yield was often poor to none, particularly in mature, fluvio-deltaic, Viséan samples, located in the eastern region of the Midland Valley (Figure 1-2, Figure 1-3). To counteract the scarcity of apatite grains in these sedimentary rocks, samples in excess of 10 kg were collected from these locations and processed. Of the twenty-one outcrop samples collected, fourteen successfully yielded both apatite and zircon crystals.

The BGS holds over 200,000 borehole records for the Midland Valley of Scotland (Monaghan 2014). These were examined, using the BGS Geoindex interactive web application (BGS-Geoindex 2020), and those that contain included sandstones, either in archived core or cuttings, were singled-out, as this is the sedimentary rock that most probably contains apatite in crystals large enough for the analyses (usually >60 microns in diameter (Kohn *et al.* 2019)). After processing the available data, c.50 boreholes were selected and further investigated at the BGS Lyell Centre, Edinburgh. Here, drilling logs, thin sections, and core scans were made available for scrutiny, prior to requesting access to borehole material, stored at the BGS core repository, Keyworth (BGS-Geoindex 2020).

The sampling strategy was based, alongside lithological suitability, on providing the best constraints for reconstructing the spatial and temporal evolution of the Midland Valley. To this avail, the ideal scenario is the availability of widespread boreholes, with apatite-bearing samples covering a range of depths; in this way, the boreholes single-sample derived data can be modelled together, to retrieve the spatial variation of sediment sources and the thermal history of basin. Failing this, samples were collected from outcrops and at different depths from close-by boreholes, to create pseudo profiles; the apatite fission track data were modelled both as single-samples and, those from the same region, together, as if they were collected on one profile; this strategy and the results from the thermal modelling are described in great details in Chapter 3 and Chapter 7. A total of thirteen boreholes were selected to be reviewed, which took place over four weeks in Keyworth. Selected drill core samples were shipped to Glasgow University where they were processed (Appendix B). Of the nineteen samples selected for processing, fourteen yielded both apatite and zircon (Table 1-1).

Of the forty samples processed for this thesis, nine were selected for provenance to determine sediments provenance and twenty-eight for thermal history investigation. Sample selection for the former was based on; 1) the presence of at least 100 datable grains of both apatite and zircon, in agreement with the most recent recommendations for provenance studies (Vermeesch 2004; Vermeesch 2012) and 2) sample location and stratigraphic age, to be able to retrieve information of sediment sources and their temporal evolution, across as much as possible of the Midland Valley. In the case of the AFT analysis, sample selection was simply based on apatite availability, working on the principle that the more data were available, the more precise and accurate the thermal histories would have been.

The stratigraphy of the Carboniferous Midland Valley of Scotland has been studied extensively over time and various criteria have been used to differentiate between units (George 1960; Neves *et al.* 1973; Paterson and Hall 1986; Browne *et al.* 1999). This thesis uses the lithostratigraphical framework of Browne *et al.* (1999). Figure 1-3 shows the positions of the samples collected, relative to this complex framework.

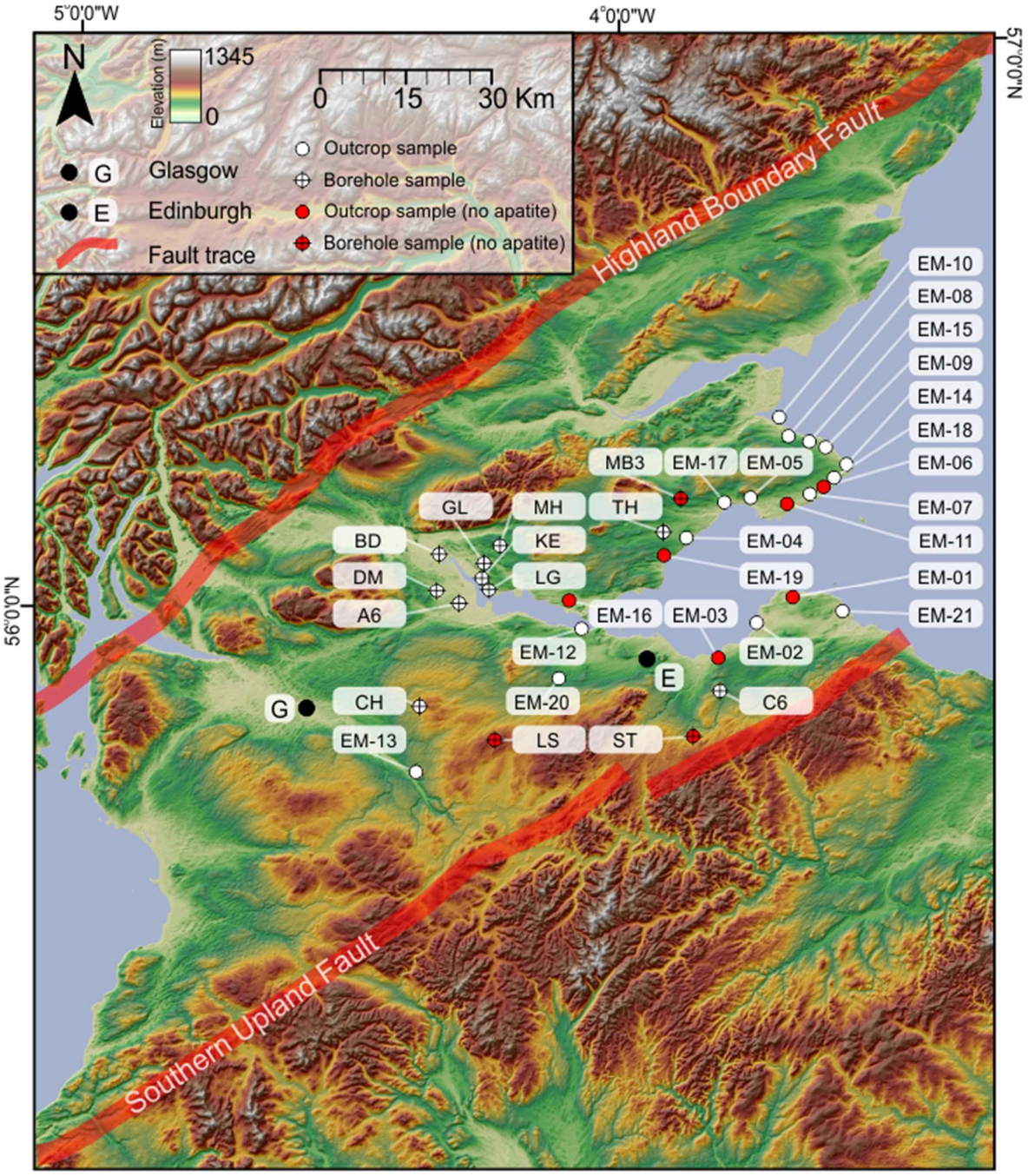

Figure 1-2: Sample location map. Samples collected from boreholes and outcrop across the Midland Valley of Scotland. Trace of bounding faults and location of Glasgow (G) and Edinburgh (E) also shown on map. Details of samples can be found in Table 1-1. DEM produced using downloaded SRTM data (USGS 2021).

1.2.3 Sample list and locations

Sample I.D.	Lat. (°)	Long. (°)	Depth (m)	Series	Formation	Analysis	VR Est.
Outcrop							
EM-001	56.0625	-2.8120	Outcrop	Viséan	Gullane Fm	No apatite	N/A
EM-002	56.0390	-2.8480	Outcrop	Viséan	Gullane Fm	AFT	0.5-0.6*
EM-003	55.9730	-2.9400	Outcrop	Namurian	ULGS	No apatite	N/A
EM-004	56.1420	-3.0810	Outcrop	Westphalian	MCMS	AFT	0.6-1.0*
EM-005	56.2110	-2.9450	Outcrop	Westphalian	MCMS	AFT	0.6-1.0*
EM-006	56.2863	-2.6000	Outcrop	Viséan	Clyde Sst Fm	No apatite	N/A
EM-007	56.2100	-2.7390	Outcrop	Viséan	Pathhead Fm	AFT	0.5-0.6*
EM-008	56.3277	-2.7327	Outcrop	Viséan	Pittenweem Fm	AFT	0.5-0.6*
EM-009	56.2930	-2.6259	Outcrop	Viséan	Anstruther Fm	AFT	0.5-0.6*
EM-010	56.3320	-2.7750	Outcrop	Viséan	Sandy Craig Fm	AFT & U-Pb	0.5-0.6*
EM-011	56.2130	-2.7240	Outcrop	Viséan	Pittenween Fm	No apatite	N/A
EM-012	55.9906	-3.3882	Outcrop	Viséan	WLOS (H)	AFT	0.5-0.6*
EM-013	55.7136	-3.8224	Outcrop	Viséan	Lawmuir Fm	AFT	N/A
EM-014	56.2800	-2.5880	Outcrop	Viséan	Fife Ness Fm	AFT & U-Pb	0.5-0.6*
EM-015	56.3095	-2.6544	Outcrop	Viséan	Anstrusther Fm	AFT & U-Pb	0.5-0.6*
EM-016	56.0294	-3.4690	Outcrop	Viséan	Pathhead Fm	No apatite	N/A
EM-017	56.2099	-2.9582	Outcrop	Westphalian	MCMS	AFT & U-Pb	0.6-1.0*
EM-018	56.2610	-2.6180	Outcrop	Viséan	Anstruther Fm	AFT	0.5-0.6*
EM-019	56.1210	-3.1300	Outcrop	Namurian	Passage Fm	No apatite	N/A
EM-020	55.8915	-3.4749	Outcrop	Viséan	WLOS (H)	U-Pb	N/A
EM-021	56.0236	-2.5900	Outcrop	Tournasian	Ballagan Fm	AFT	N/A
Borehole							
A6-G1	56.0490	-3.7880	-745	Namurian	LCF	AFT	0.8-0.9*
A6-G2	56.0490	-3.7880	-817	Namurian	LCF	AFT	0.8-0.9*
A6-G3	56.0490	-3.7880	-873	Namurian	LCF	AFT & U-Pb	0.94**
BD-G1	56.1160	-3.8420	-471	Namurian	LCF	AFT	>1.0*
LG-G1	56.0570	-3.7040	-810	Namurian	LCF	No apatite	N/A
LG-G2	56.0570	-3.7040	-941	Namurian	LCF	AFT	>1.0*
MH-G1	56.1271	-3.6722	-686	Namurian	LCF	AFT	>1.0*
MH-G2	56.1271	-3.6722	-815	Namurian	LCF	AFT	>1.0*
TH-G1	56.1590	-3.1360	-611	Namurian	LCF	AFT	0.6-1.0*
TH-G2	56.1590	-3.1360	-734	Namurian	LCF	AFT	0.6-1.0*
TH-G3	56.1590	-3.1360	-798	Namurian	LCF	AFT & U-Pb	0.6-1.0*
CH-G1	55.8370	-3.8750	-620	Viséan	WLOS (H)	AFT & U-Pb	0.8-0.9**
C6-G2	55.9010	-2.9870	-460	Viséan	WLOS (C)	AFT	0.6-0.8**
DM-G1	56.0790	-3.8110	-340	Namurian	ULGS	AFT & U-Pb	>1.0*
KE-G1	56.0580	-3.7050	-280	Namurian	ULGS	AFT	>1.0*
GL-G1	56.1140	-3.7050	-568	Namurian	ULGS	AFT & U-Pb	0.6-0.7*
MB3-G1	56.1790	-3.1070	-1141	Namurian	LLGS	No apatite	N/A
ST-G1	55.8710	-3.0190	-626	Viséan	Gullane Fm	No apatite	N/A
LS-G1	55.8020	-3.6510	-428	Viséan	WLOS (H)	No apatite	N/A

Table 1-1: Sample list and locations. Borehole full name can be identified from first two letters of sample I.D.: A6, Airth 6; BD, Bandeath; LG, Longannet 1; MH, Meadowhill 1z; TH, Thornton 1; CH, Craighead 1; C6, Cousland 6; DM, Dunmore Moss; KE, Kincardine East Longannet Coillery; GL, Gartlove; MB, Milton of Balgonie 3; ST, Stewart 1; LS, Leven Seat 1. All outcrop samples were collected from coastal areas or from <10 m elevation, sample depths from boreholes were provided from drill log records. The formation column refers to the nomenclature explained in Figure xx. The 'Analysis' column indicates whether sample was selected for U-Pb (apatite and zircon) and/or apatite fission track analysis (AFT), or whether no apatite was found in sample separate (No apatite). VR Est. indicates VR estimation for each sample. *Estimated from organic maturity maps (Raymond 1991). **Estimated from Monaghan (2014) using Tmax values converted to VR using formula from Jarvie *et al.* (2001), (VR=0.0180*Tmax–7.16).

(Ma)		Series	Stage	Group	Ayrshire	Central Coalfields	Fife	West Lothian	East Lothian	Bathgate	Sample details
298.9	Permian			Mauchline	Sandstone / Volcanic	Alkaline basicsills 298.3 ±1.3 - 292.0 ±2.7 Ma $^{40}Ar/^{39}Ar$	East Fife vents				
308.0						Midland Valley Sill Complex and tholeiitic dykes 307.6 ±4.8 Ma U-Pb					
	Pennsylvanian / Silesian	Westphalian C	Bolsovian	Coal Measures: Cyclical sedimentary units with coal. Alluvial and lacustrine environments of deposition. Forest,flood plain,river delta and lake.	Upper Coal Measures (>1200 m): Fluviodeltaic. Cyclical sandstone, siltstone, mudstone. Coal rare. *Aegiranum Marine Band*						Coal Measures: EM-004: Westphalian-MCMS; EM-005: Westphalian-MCMS; EM-017: Westphalian-MCMS
		Westphalian B	Duckmantian		Middle Coal Measures (350 m): Fluviodeltaic. Cyclical sandstone, siltstone, mudstone, with seatearth and coal. *Vanderbeckei Marine Band*						
		Westphalian A	Langsettian		Lower Coal Measures (240 m): Fluviodeltaic. Cyclical sandstone, siltstone, mudstone, with seatearth and coal. *Lowstone Marine Band*						
316.5		Namurian	Yeadonian - Chokierian	Clackmannan Group: Comprised of cyclical sedimentary units. Lower and Upper Fm. contains the highest proportion of marine deposits, while Passage Fm. is dominated by alluvial deposits.	Passage Formation (380 m): Fluvial, mostly braided rivers. Fine to coarse sandstones with occasional conglomerates. *Castlecary Limestone* *Netherwood marine band*						Clackmannan Group: EM-019: Namurian-Passage Fm; DM-G1: Namurian-ULGS; KE-G1: Namurian-ULGS; GL-G1: Namurian-ULGS; EM-003: Namurian-ULGS; A6-G1: Namurian-LCF; A6-G2: Namurian-LCF; A6-G3: Namurian-LCF; BD-G1: Namurian-LCF; LG-G1: Namurian-LCF; LG-G2: Namurian-LCF; MH-G1: Namurian-LCF; MH-G2: Namurian-LCF; TH-G1: Namurian-LCF; TH-G2: Namurian-LCF; TH-G3: Namurian-LCF; MB3-G1: Namurian-LLGS
			Arnsbergian		Upper Limestone Formation (>600 m): Upward coarsening cycles of marine limestone overlain by mudstone, siltstone and sandstone. Capped with seatearth and coals. *Index Limestone* *Orchard Lst*					Bathgate Group (1000 m): **Salsburgh Volcanic Formation**, highly altered basaltic lavas interbedded with strata from the West Lothian Oil Shale Fm. **Bathgate Hills Volcanic Formation**, Lavas, tuffs and volcaniclastic sedimentary rocks. Long lived volcanic event, mainly terrestrial but occasionally into water. **Kinghorn Volcanic Formation** mainly subaerial but occasionally subaqueous, Fife coast between Kinghorn and Kircaldy.	
			Pendleian		Limestone Coal Formation (550 m): Cycles of fine to medium sandstone, siltstone and mudstone usually capped with seatearth and coal. *Top Hosie Limestone* *Black metals marine band*						
323.2					Lower Limestone Formation (240 m): Repeated upward coarsening cycles of limestone, mudstone, siltstone and sandstone. Yoredale type marine to fluviodeltaic cycles. *Hurlet Limestone* *Blackhall Lst*						
	Mississippian / Dinantian	Visean	Brigantian	Strathclyde Group: Lithologies change from the cornstone and cementstone bearing Inverclyde Group to seatearths and coal bearing strata with volcanics.	Lawmuir Formation (300 m): Mudstone, siltstone, sandstone with seatearths and coals. Base is transitional with the loss of volcaniclastic material. Fluvial sandstones dominate.		Pathhead Formation (220m): Predominantly mudstone and siltstone with thin coal and ironstone. Marine bands with abundant fauna.	West Lothian Oil Shale (>1120 m): Seams of oil shale in cyclical sandstone, siltstone and mudstone, with common coals. Also contains volcanic derived detrital. Oil shales deposited in large freshwater lagoons rich in algae and organic matter. **Hopetoun Member** *Burdiehouse limestone* **Calders Member**	Aberlady Formation (140 m): Cyclical sedimentary rocks with subordinate but common coals. Fluviodeltaic environments deposited into lakes and marine embayments. Lateral transitional boundary with the West Lothian Oil Fm. distinguished by the lack of oil shales. *Macgregor Marine Band* Alkaline basic sills 331.8 ±1.3 - 323 ±1.5 Ma $^{40}Ar/^{39}Ar$		Strathclyde Group: EM-007: Viséan-Pathhead Fm; EM-016: Viséan-Pathhead Fm; EM-010: Viséan-Sandy Craig Fm; EM-008: Viséan-Pittenweem Fm; EM-011: Viséan-Pittenweem Fm; EM-009: Viséan-Anstruther Fm; EM-015: Viséan-Anstruther Fm; EM-018: Viséan-Anstruther Fm; EM-014: Viséan-Fife Ness Fm; EM-006: Viséan-Clyde Sandstone Fm; EM-020: Viséan-WLOS (Hopetoun Member); EM-012: Viséan-WLOS (Hopetoun Member); CH-G1: Viséan-WLOS (Hopetoun Member); C6-G1: Viséan-WLOS (Calders Member); LS-G1: Viséan-WLOS (Hopetoun Member); EM-001: Viséan-Gullane Fm; EM-002: Viséan-Gullane Fm; ST-G1: Viséan-Gullane Fm; EM-013: Viséan-Lawmuir Fm
			Asbian		Kirkwood Formation (36 m): Tuffs and tuffaceous mudstones overlying the CPLF. Largely derived from the underlying volcanic rock.		Sandy Craig Formation (670 m): Upward coarsening deltaic cycles. Various sedimentary unit with non-marine limestone.				
					Clyde Plateau Volcanic Formation (900 m): Lavas, tuffs and volcaniclastic sedimentary rocks, produced by a major episode of subaerial volcanic activity. Lavas are mildly alkaline but show a wide range of compositions. Locations: Campsie Fells, Renfrew Hills, Kilpatrick Hills etc. 335.2 ±2 Ma U-Pb		Pittenweem Formation (>260 m): Mudstone and siltstone with thin coal with locally thick sandstones. Contains organic shale beds. Upward coarsening deltain cycles.				
			Holkerian				Anstruther Formation (>810 m): Dominated by fine-grained sedimentary units but thick beds of sandstone are present. Minor oil-shale beds.	Gullane Formation (560 m): Cyclical sequences of sandstone interbedded with mudstone and siltstone. Contains seatearths, coals and rare limestone. Interpreted as fluviodeltaic environments into lakes that occasionally became marine. Top is Macgregor Marine Band.			
							Fife Ness Formation (>230 m): Fluvial and lacustrine, upward fining cycles of sandstone. Marine strata and seatearths are present but coals are absent.	Arthur's Seat Volcanic Formation (560 m): Lavas and tuffs produced by a short lived episode. 341.2 ±0.8 Ma $^{40}Ar/^{39}Ar$	Garleton Hills Volcanic Formation (560 m): Lavas and tuffs produced by a short lived episode. 343.4 ±1.0 Ma U-Pb		
			Arundian								
346.7		Tournaisian	Chadian	Inverclyde Group: Sandstone with carbonates and dolomite. Base is where sandstone dominated Devonian is succeeded by carbonate bearing strata.	Clyde Sandstone Formation (>300 m): Fine to coarse grained sandstone with local conglomerate, deposited in fluviatile environments from braided stream to flood p lain.						Inverclyde Group: EM-021: Tournasian-Ballagan Fm
					Ballagan Formation (900 m): Grey mudstone and siltstone with nodules and beds of ferroan dolomite (cementstones). Contains thin and locally thick sandstone units.						
			Courceyan		Kinnesswood Formation (640 m): Fine to coarse, cross bedded sandstones with pedogenic carbonates (Cornstones). River channel with finer grained over bank deposits.						
358.9											

Figure 1-3: Samples and lithostratigraphical framework modified from Browne *et al.* (1999). This table is placed here to be used throughout this thesis. Maximum thicknesses and facies associated with each formation is provided as guidance. Published geochronology ages from investigations targeting the intrusive and extrusive igneous lithologies are provided in red (Monaghan and Pringle 2004; Monaghan and Parrish 2006; Monaghan *et al.* 2014).

1.3 Previous studies on the provenance and thermal hostory of the Midland Valley and nearby basins

The following section provides a review of the existing provenance and thermal history investigations connected to the Midland Valley with their locations shown in Figure 1-4 below.

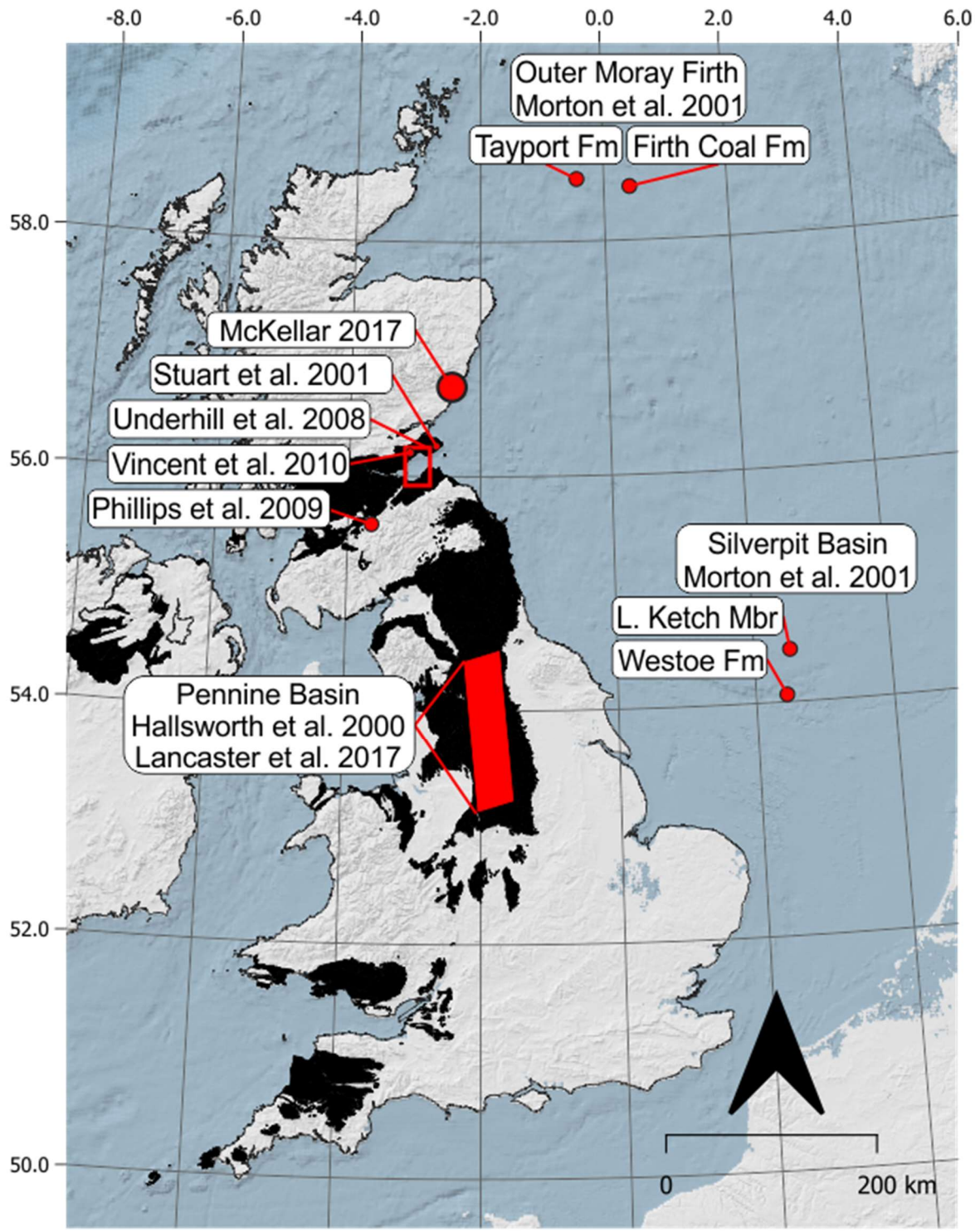

Figure 1-4: Locations of previous provenance and thermal history investigations of the Midland Valley and nearby basins. Locations of onshore Carboniferous outcrops are highlighted in black and studies discussed in text below.

1.3.1 Provenance

Although the provenance of the Lower Palaeozoic to Devonian sedimentary sequences has been studied in detail (Phillips *et al.* 1997; Phillips *et al.* 2004; Phillips *et al.* 2009; McKellar 2017), the source(s) of the Carboniferous clastic material in Scotland has not been fully quantified (Stuart *et al.* 2001). Zircon age constraints on Silurian inliers (Phillips *et al.* 2009) revealed bi-modal spectra, dominated by Lower Palaeozoic (c.475 Ma) and Mesoproterozoic components (c.1000 Ma). The lower Palaeozoic component was interpreted as being derived from a volcanic-plutonic source from within the Midland Valley terrane, whereas the Mesoproterozoic age peak was interpreted as being derived from either a first or recycled Grenvillian source. The scarcity of Palaeoproterozoic and Archean ages, which are present in the Grampian terrane to the North (Cawood *et al.* 2003), was used to exclude the former as a source for the Ordovician-Silurian sediments. Petrographic and compositional similarities between Silurian to Devonian sedimentary rocks were taken to indicate a derivation from the same source terrane, with variations attributed to the influence of Silurian sub-basin architecture (Phillips *et al.* 2004). These sub-basins were unified by the Lower Devonian with the formation of the larger Lanark Basin, at the same time as calc-alkaline volcanism (Phillips *et al.* 1997). The absence of Dalradian detrital material in the south of the Midland Valley suggested a barrier preventing transport across the terrane (Trewin and Thirlwall 2002) or a Dalradian peneplain, with little or no relief and, thus, very limited erosion (Haughton and Bluck 1988). The provenance of Lower Devonian sediments in the southern Midland Valley was, therefore, attributed to the erosion of a volcanic or igneous complex located either within the Midland Valley or introduced by sinistral strike-slip faulting (Phillips *et al.* 2004). Recent zircon U-Pb ages from the Lower Old Red Sandstone in the north of the Midland Valley (McKellar 2017) however reveal strong similarities with zircon U-Pb ages from the Dalradian (Cawood *et al.* 2003), contradicting previous work. McKellar's (2017) age spectra also pinpoint a Palaeozoic component, interpreted as representing first cycle Caledonian material.

Detrital muscovite $^{40}Ar/^{39}Ar$ ages derived from Carboniferous Midland Valley also revealed Lower Palaeozoic ages (415 Ma with minor peaks at 440 and 390 Ma), which were interpreted as related to the cooling of the Scandinavian-Greenland Caledonian orogeny (Stuart *et al.* (2001). However, more recent work by Small *et al.* (2013) on rutile, found Palaeozoic cooling ages from the Moine and the Dalradian, opening the possibility of a Scottish source for at least part of the Carboniferous sediments in the Midland Valley.

Though no further work has been undertaken to investigate the Carboniferous sediment provenance in the Midland Valley, similar age units have been analysed in the North Sea and the Pennine Basin (Hallsworth *et al.* 2000; Morton *et al.* 2001; Morton and Whitham 2002; Lancaster *et al.* 2017). Heavy mineral and detrital zircon U-Pb analysis in the Pennine Basin indicated that Carboniferous sediment was supplied from the north by the Pennine delta, via the proto-Viking graben during the Namurian (Hallsworth *et al.* 2000). The source terrane was high grade metasediments and granitic intrusions affected by the Caledonian orogeny, though Scotland was discounted as a source due to contrasting garnet content (low grossular-high pyrope garnets are found in the Pennine Basin are not recorded in Scottish samples) (Hallsworth *et al.* 2000) in favour of a more northern sourceland, however the extensive dissolution of garnets in Carboniferous North Sea samples, have excluded them from other provenance investigations (Morton *et al.* 2001). Sediment supply from the north declined during the Westphalian, when a westerly source of recycled (largely Devonian) sediment and ultra-mafic (spinel rich) rocks and a supply from the uplifting Variscan orogeny to the south became increasingly important (Hallsworth *et al.* 2000).

Latest Devonian sandstones from the Outer Moray Firth (Buchan Fm) indicated that this sediment was largely derived from the Scottish land mass. Minor amounts of Scottish input was also recognised in the Carboniferous Firth Coal Fm, however a source north of Britain is believed to dominate during this time (Morton *et al.* 2001). Viséan samples from the Outer Moray Firth (Tayport and Firth Coal Fm) contain a high peak of Caledonian zircon U-Pb ages, very few Archean ages, and a poorly defined range of Meso-Palaeoproterozoic ages, which closely resembles the Namurian Ashover Grit and Rough Rock of the Pennine basin; this similarity has brought to the conclusions that these two basins share a provenance, located somewhere to the north, although Archean ages are slightly more common in the Pennine Basin (Hallsworth *et al.* 2000; Morton *et al.* 2001). As with the Pennine Basin, the influence and importance of the northern source diminished in the Westphalian, when a new influx from the west and south appeared.

The Westoe Fm (Westphalian B) from the Silverpit Basin in southern North Sea was derived from the European central Variscides to the southeast (Morton *et al.* 2001). Carboniferous sedimentary rocks in East Greenland were deposited by a northward flowing fluvial system; they are separated by a major unconformity that spans the Viséan to the Westphalian, corresponding to the formation of the southward flowing Namurian Pennine fluvial delta system (Morton and Whitham 2002). Westphalian A in Greenland and Namurian in the Pennine basin are similar in terms of heavy mineral

concentrations (Morton and Whitham 2002), which suggests that, during the Namurian, uplift of the Norwegian-Greenland Sea region may have diverted the northward flowing fluvial system southward, to the Pennine basin. Sediment supply from the north diminished when rifting during the Westphalian allowed the northward fluvial system to be re-established (Morton and Whitham 2002), and the Variscan orogeny became the main source for Westphalian sediments.

Lancaster *et al.* (2017) revisited the Namurian samples in the Pennine Basin previously studied by Hallsworth *et al.* (2000) with a multi-proxy approach to unravel the complexities of potentially recycled sediment. Here U-Pb zircon data revealed Caledonian (c.430 Ma) and Archean (c.2700 Ma) populations, and a range of Meso-Palaeoproterozoic ages (1000-2000 Ma). Pb isotopes in K-feldspars indicated that the Archean and Caledonian were first cycle input, with the 1000-2000 Ma ages derived from recycling. Heavy mineral analysis indicated a granulitic or charnockitic source, along with metapelitic input. Greenland Caledonides was suggested as the primary source, due to the abundance of the Archean signal; however a Scottish contribution could not be ruled out, as the Lewisian is of similar age and composition. The broad distribution of ages between 1000-2000 Ma, with increased Palaeoproterozoic ages, has been observed in the Torridonian of Scotland (Lancaster *et al.* 2011), Krummedal sequences of East Greenland (Kalsbeek *et al.* 2000) and the Svaerholt in Western Norway (Kirkland *et al.* 2007); however, the opposite trend of Mesoproterozoic dominated samples are observed in the Scottish Southern Uplands (Waldron *et al.* 2008). Multi-proxy evidence from Lancaster *et al.* (2017) and the presence of a major discontinuity (Morton and Whitham 2002) suggest that East Greenland was the dominant source for first cycle Namurian sediment in the Pennine Basin; however the Authors could not rule out contribution from both Scotland and Norway. The relative stability of the provenance data was also used to suggest that the detrital input was driven by tectonic influences, rather than climate or glacio-eustatic changes (Cliff *et al.* 1991).

1.3.2 Thermochronology studies in Scotland and northern England

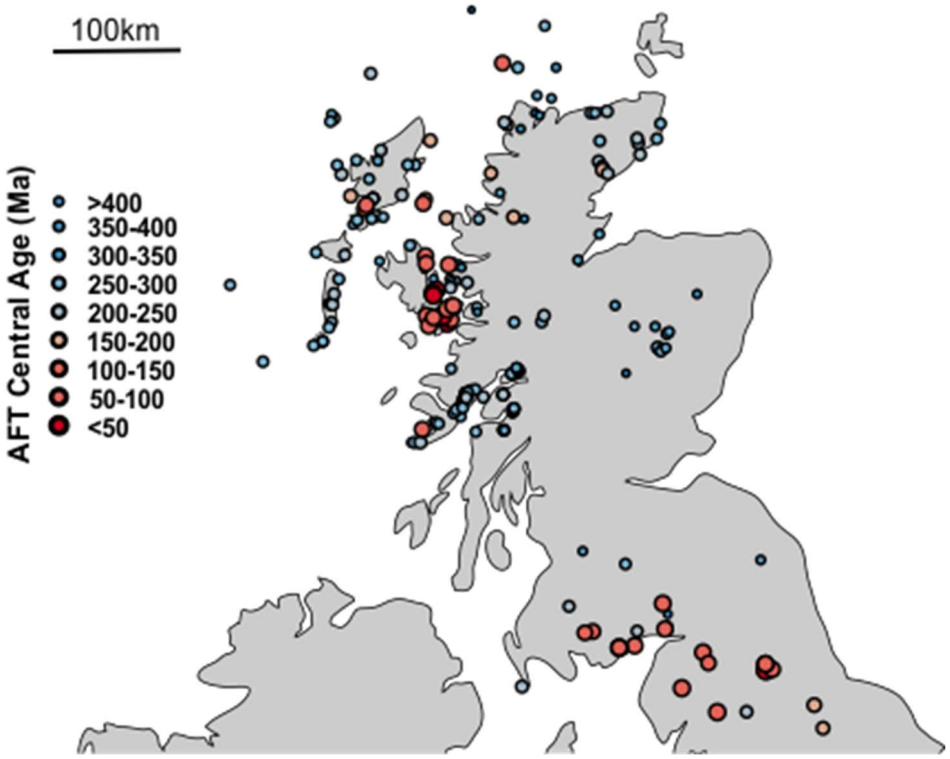

Figure 1-5: Compilation of AFT central ages from previous investigations across northern England and Scotland. Data collected from (Lewis *et al.* 1992; Thomson *et al.* 1999; Jolivet 2007; Persano *et al.* 2007; Holford *et al.* 2010; Cogné *et al.* 2016; Łuszczak 2016; Döpke 2017; Amin 2020).

Low temperature thermochronology has been applied to a range of geological settings and locations across Scotland (Hurford 1977; Lewis *et al.* 1992; Thomson *et al.* 1999) and its surrounding basins (Green 1986; Holford *et al.* 2005; Holford *et al.* 2010), primarily to unravel the post-Caledonian exhumation of the region. Many of these earlier studies have taken place prior to recent advancement on methodological practices, data modelling, and interpretation (Chapter 3) and thus some areas have been recently revisited to gain a deeper understanding of their thermal histories (Łuszczak 2016; Webster 2018; Amin 2020). Broadly speaking, the resulting Mesozoic thermal histories for the region can be divided into two groups i.e., those which identify repeated cycles of burial and exhumation (Hillis *et al.* 2008; Holford *et al.* 2009; Holford *et al.* 2010) and those that do not (Hurford 1977; Thomson *et al.* 1999; Persano *et al.* 2007; Amin 2020). While these latter studies do not identify periodical exhumation and reburial events in their thermal histories, variations in cooling rates through the Mesozoic are identified associated with Caledonian cooling and unroofing. Building on previous work from Persano et al (2007), who used the strategy of 'vertical profiles' to reconstruct the palaeogeothermal gradient, Amin (2020) used a multi-thermochronometric approach to constrain

thermal histories of western Scotland and attributed variations in cooling rates to the consecutive effects of the Variscan orogeny, Pangaea related Permo-Triassic rifting, and Early Palaeogene impinging of the proto-Icelandic plume. Studies that identify multiple phases of reburial during the Mesozoic, have done so by compiling offshore stratigraphy, including the presence of unconformities, and extrapolating these conclusions onshore (Hillis *et al.* 2008; Holford *et al.* 2009; Holford *et al.* 2010). While all investigations indicate increased cooling rates during the early Cenozoic, the driving forces, timings, and number of events differ; again, two end-member hypotheses can be identified, one supporting far-field stress associated with North Atlantic spreading and Alpine orogeny (Holford *et al.* 2005; Japsen *et al.* 2007; Hillis *et al.* 2008; Holford *et al.* 2009; Holford *et al.* 2010) and one supporting mantle driven processes associated with proto-Icelandic plume development (White 1988; White 1997; Jones *et al.* 2002; Al-Kindi *et al.* 2003; Jones and White 2003; Persano *et al.* 2007). This subject received considerable attention from Döpke (2017) and Cogné *et al.* (2014), who concluded that Cenozoic exhumation in Ireland and Britain was driven by mantle processes associated with the proto-Icelandic plume and the emplacement of the NAIP (North Atlantic Igneous Province).

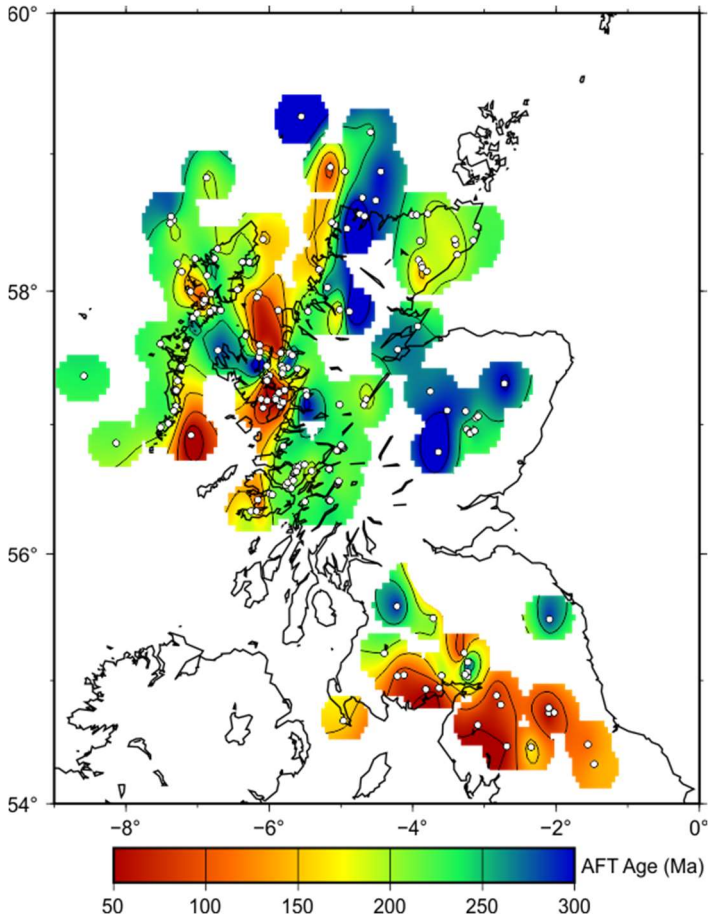

Figure 1-6: AFT ages UK. Compiled AFT age data from Figure 1-5 were used to create an AFT age contour map using GMT (Wessel *et al.* 2019). Note the lack of data from the Midland Valley.

1.3.3 Thermal studies in the Midland valley

Prior to the research presented in this thesis, limited quantitative analyses had been undertaken to quantify the thermal history of the Midland Valley basin. These mainly focused on the use of vitrinite reflectance (VR) and the maturation of organic matter to identify maximum burial temperatures (Raymond and Murchison 1988a; Raymond and Murchison 1988b; Murchison and Raymond 1989; Raymond 1991). While investigating the effect of igneous activity on the petrology and geochemistry of the organic material contained in the Carboniferous rocks of the Midland Valley, Raymond (1991) concluded that the maturation of organic matter was generally due to burial, and not magmatic intrusions (Raymond and Murchison 1988b), localised thermal effects of sill and dyke emplacement were evident in the Midland Valley succession, as spikes in VR within the thermal aureole of an intrusion (Figure 1-7) (Raymond and Murchison 1988a).

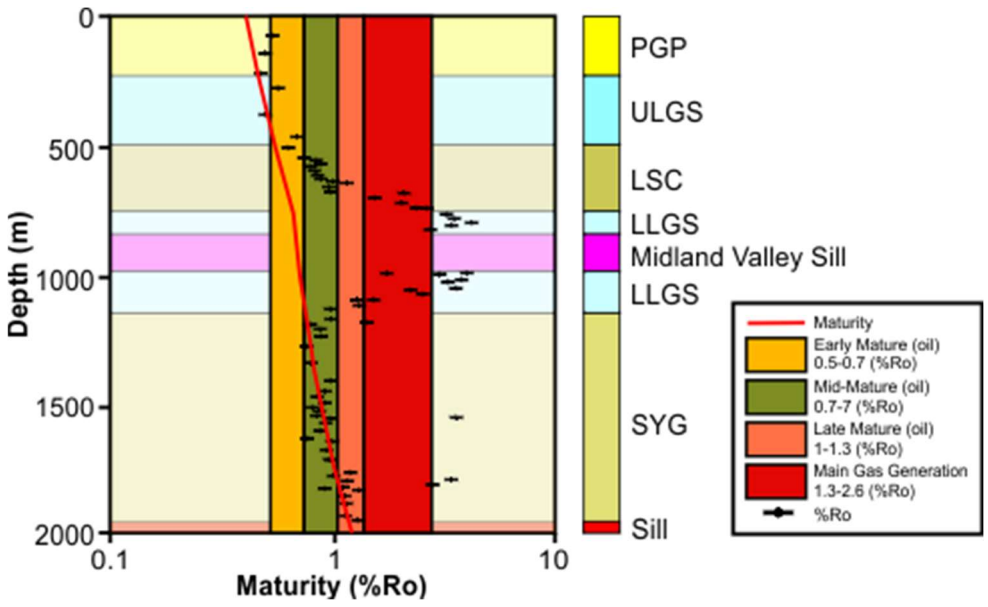

Figure 1-7: VR data for the Milton of Balgonie borehole (see Figure 1-4 for borehole location). Figure shows the effect of the intrusion of the Midland Valley Sill Complex on the VR data. Localised heating caused by the quartz-dolerite-tholeiitic intrusion has increased the maturity of the organic matter, changing its 'ranking', from mid-mature to main gas generation. PGP, Passage Formation; ULGS, Upper Limestone Formation; LSC, Limestone Coal Formation; LLGS, Lower Limestone Formation; SYG, Strathclyde Group. Note, data points of high value in the Strathclyde Group were also collected near minor intrusions. From Raymond and Murchison 1988b.

Sediment consolidation state at the time of the intrusion emplacement was also found to affect organic maturation, with the earlier alkaline basic suite intruding unconsolidated wet sediments having a lesser effect than the later quartz-tholeiitic suite intruding into more consolidated packages (Raymond and Murchison 1988a). Regional variations in VR rank across the basin, with, for the same stratigraphic level, higher values in the Clackmannan-Central coalfield basins than further east in the

Fife-Midlothian Basin , suggest that a greater regional palaeo-heat flow existed in the centre and west Midland Valley compared to the east, possibly due to the increased thickness of volcanic material there (Raymond and Murchison 1988b; Raymond 1991). However, the VR data may have been supressed in some of the samples in that study by the presence of liptinitic and exinitic matter, as comparisons with coal rank to this data show a separation of 0.2-0.3% (Raymond 1991).

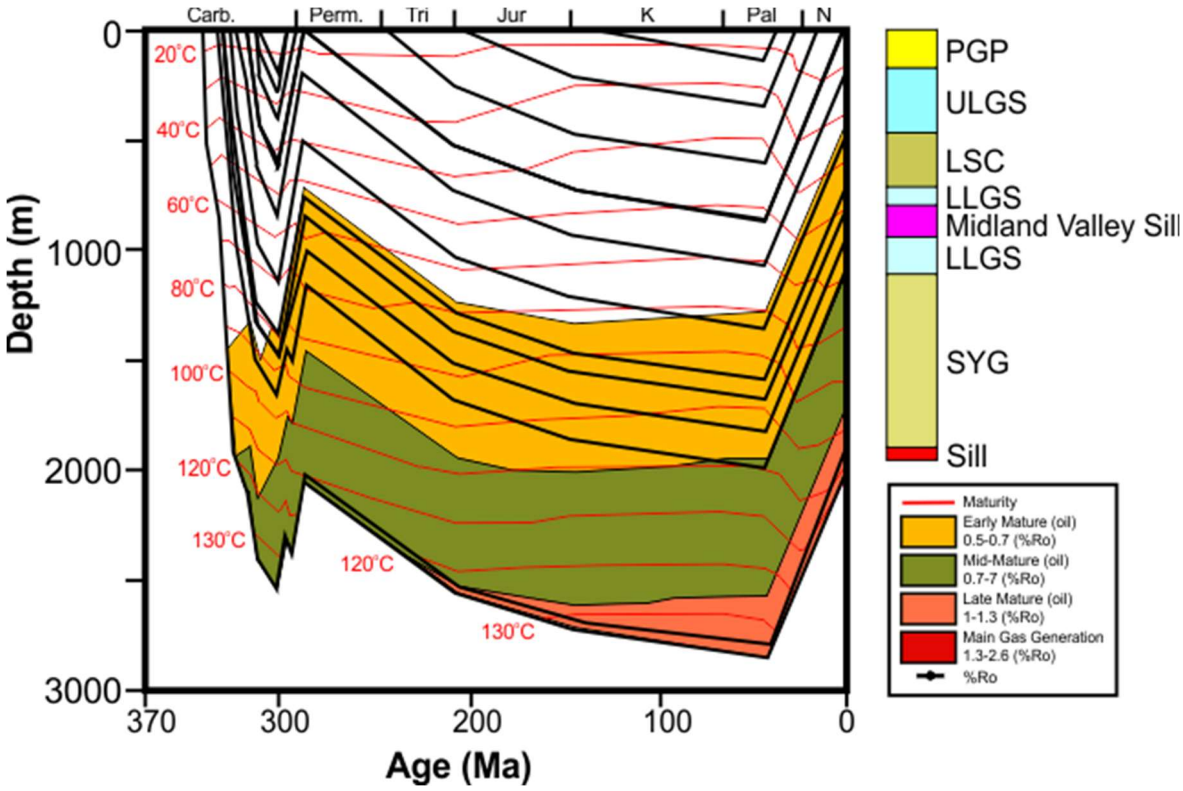

Figure 1-8: Burial history model for the Milton of Balgonie borehole. Vincent *et al* (2010) used the VR data, plotted in Figure 1-7 above, to create this burial history model for the borehole. Model suggests late Carboniferous uplift caused by the Variscan orogeny, followed by Mesozoic sedimentation leading to maximum burial at the onset of Cenozoic, prior to Paleogene uplift.

In an investigation into the thermal and burial history modelling in the Midlothian-Leven syncline, Vincent *et al*. (2010) used VR data from Raymond (1991) on selected Midland Valley boreholes (and the Platte River software BasinMod) along with a sediment decompaction model (HotPot (Rowley *et al.* 1993)) to reconstruct the subsidence and thermal history of the basin (Figure 1-8). These models suggest that a thickness of 420-660 m of late Carboniferous sediment has been eroded due to uplift by the Variscan orogeny. A subsequent 1300-1800 m of Permian-early Palaeogene sediments were then deposited on the unconformity (Vincent *et al.* 2010), and then removed following recent uplift, due to far-field stress associated with North Atlantic spreading and Alpine orogeny (Hillis *et al.* 2008; Holford *et al.* 2010) or emplacement of the proto-Icelandic plume (White 1988; Persano *et al.* 2007). Estimates of overburden were taken from surrounding offshore boreholes where the Mesozoic

deposits are still present and best fit curves on VR data; the extensional setting heat flow model of Jarvis and McKenzie (1980) was employed. The model uses an initially high heat flow associated with basin extension, until the mid-Namurian where extension gives way to thermal subsidence and cessation of volcanism, resulting in a decline in heat flow which continues to reach the present-day value (Hurter and Schellschmidt 2003). Vincent et al (2010) estimated that maximum paleo-temperature was achieved in the basin via continuous burial during the Mesozoic, prior to Cenozoic uplift and exhumation.

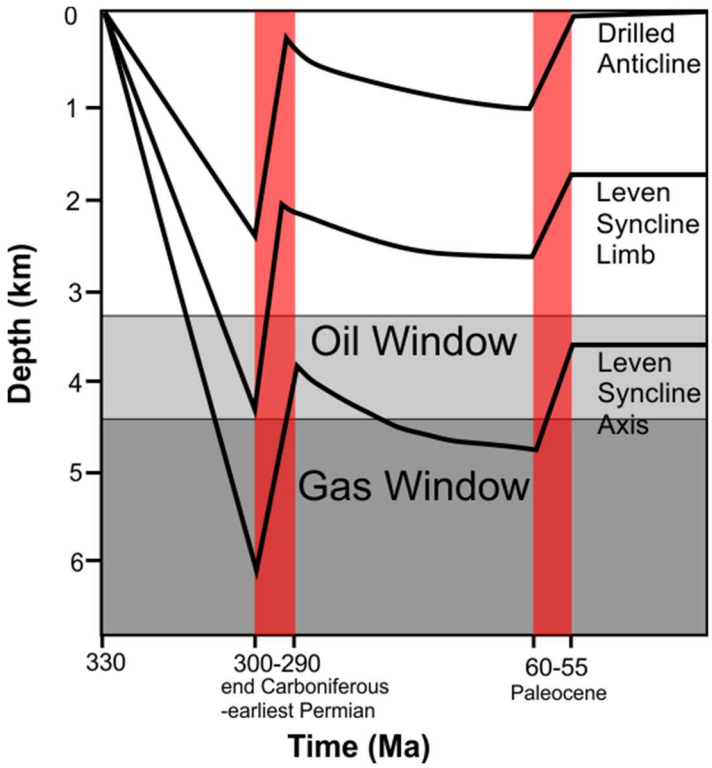

Figure 1-9: Schematic burial history plot for the West Lothian Oil Shale Formation. In this plot Underhill *et al.* (2008) show schematic burial curves for different areas of the Midlothian-Leven Syncline. This burial history suggests that maximum burial was achieved towards the end Carboniferous, followed by Variscan uplift and Mesozoic burial. Depths attained during Mesozoic burial were not of those reached during the Carboniferous, but possibly enough to keep the syncline axis in the hydrocarbon production window.

Underhill *et al* (2008) produced a schematic burial and uplift history to explain the generation of hydrocarbons in the Midlothian-Leven Syncline, suggesting that organic maturation was due exclusively to burial (Figure 1-9). Burial curves suggest end-Carboniferous to early Permian uplift was on a greater scale than the estimates of Vincent *et al.* (2010), c. 2 km, arresting petroleum generation, followed by c.1 km of Mesozoic burial and Paleogene uplift (White 1988; Hillis *et al.* 1994; Persano *et al.* 2007). Alternatively to Vincent *et al.* (2010), this investigation suggests that maximum temperatures were achieved prior to Variscan uplift and intrusion of the Midland Valley Sill Complex. When Mesozoic sedimentation resumed, it was only enough to bury the syncline axis to depths of oil

and gas generation. The VR data highlighted above was also used by Monaghan (2014) in a shale resource estimation and by Underhill *et al.* (2008) to investigate petroleum prospectivity in the Midland Valley. Although VR is extremely useful in providing an estimate for maximum temperature attained, it cannot provide any insight into the timing and duration of the burial, or indeed on the exhumation history of the basin. This information, which is critical to constrain the evolution of sedimentary basins and their potential as oil and gas reservoirs, can be retrieved from the application of low temperature thermochronology. Figure 1-10 shows the estimated relationship between increasing depth, temperature, organic matter maturity (Ro % & Tmax °C), crystallinity, and conodont alteration index (CAI) have with commonly used thermochronometers, including AFT which is utilised in this investigation.

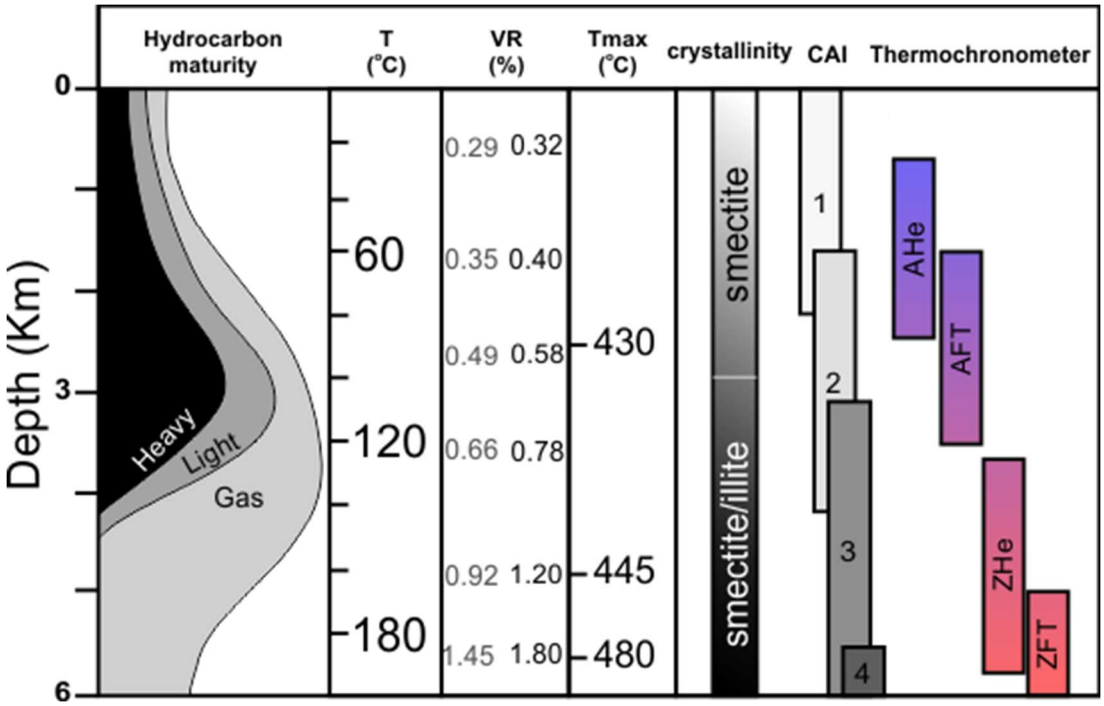

Figure 1-10: Estimated petroleum generation zones and common thermochronometers. Values are approximate as they vary with organic matter type, heating rate and duration, mineral chemistry, and other geological factors. Ro (%) represent values of vitrinite reflectance after models by (grey) and Nielsen *et al.* (2017) (black). CAI, conodont alteration index. Thermochronometers, AHe, (U-Th)He in apatite; AFT, apatite fission track; ZHe, (U-Th)/He in zircon; ZFT, zircon fission track. Modified from Gleadow *et al.* (1983) and Schneider and Issler (2019).

1.4 Thesis outline

This thesis presents new detrital apatite and zircon U-Pb ages, apatite fission track data, and thermal history models from samples collected across the Carboniferous Midland Valley of Scotland with the aim of providing a better understanding of the evolution of post-Caledonian sediment source/s and pathways and to better constrain the post-Carboniferous thermal histories of the Midland Valley. The thesis outline is presented below:

Chapter 2: An overview of the geological history of the Midland Valley including the regional setting, tectonic framework, and geological evolution through time. Particular focus is placed on the Carboniferous period.

Chapter 3: Detailed description of the methods applied in this thesis including U-Pb geochronology, apatite fission track thermochronology, and modelling of low temperature thermochronology data.

Chapter 4 and 5: The results and interpretation of the U-Pb apatite and zircon geochronology from the Midland Valley. The analytical setting and results are described in Chapter 4, discussed, and compared with existing models in Chapter 5. The data are then used to produce palaeogeographical maps presenting the evolution of the sources and sediment pathways through the Carboniferous.

Chapter 6 and 7: Results from apatite fission track analysis and thermal histories produced from QTQt. The novel combination of forward and inverse modelling is further described and the advantages of this new approach highlighted. Finally, the AFT data from this thesis are used as input for the inverse models to investigate the post-burial history of the basin.

Chapter 8: Discussion on the burial and exhumation history of the Carboniferous Midland Valley of Scotland as based on the apatite fission track analysis results and the inverse model-derived thermal histories. In this chapter, the post-Carboniferous evolution of the basin in summarized in three episodes, the Carboniferous-Permian, the Permian-Mesozoic, and the Cenozoic to recent, discussing the possible tectonic and/or climatic forces that acted on the basin and estimates of denudation.

Chapter 9: Presents the conclusions and wider implication for this work and suggests further work that could be carried out to help resolve remaining issues.

Chapter 2 Geological context: Midland Valley of Scotland

This chapter provides a review of the tectonic and geological history of the Midland Valley of Scotland. This literature review is important because it places the new geochronological and thermochronological results in succeeding chapters into context. Due to the vast amount of research undertaken in the Midland Valley of Scotland this review is an updated synthesis of more detailed reviews available in (Cameron and Stephenson 1985; Browne *et al.* 1999; Read *et al.* 2002; Woodcock *et al.* 2012a).

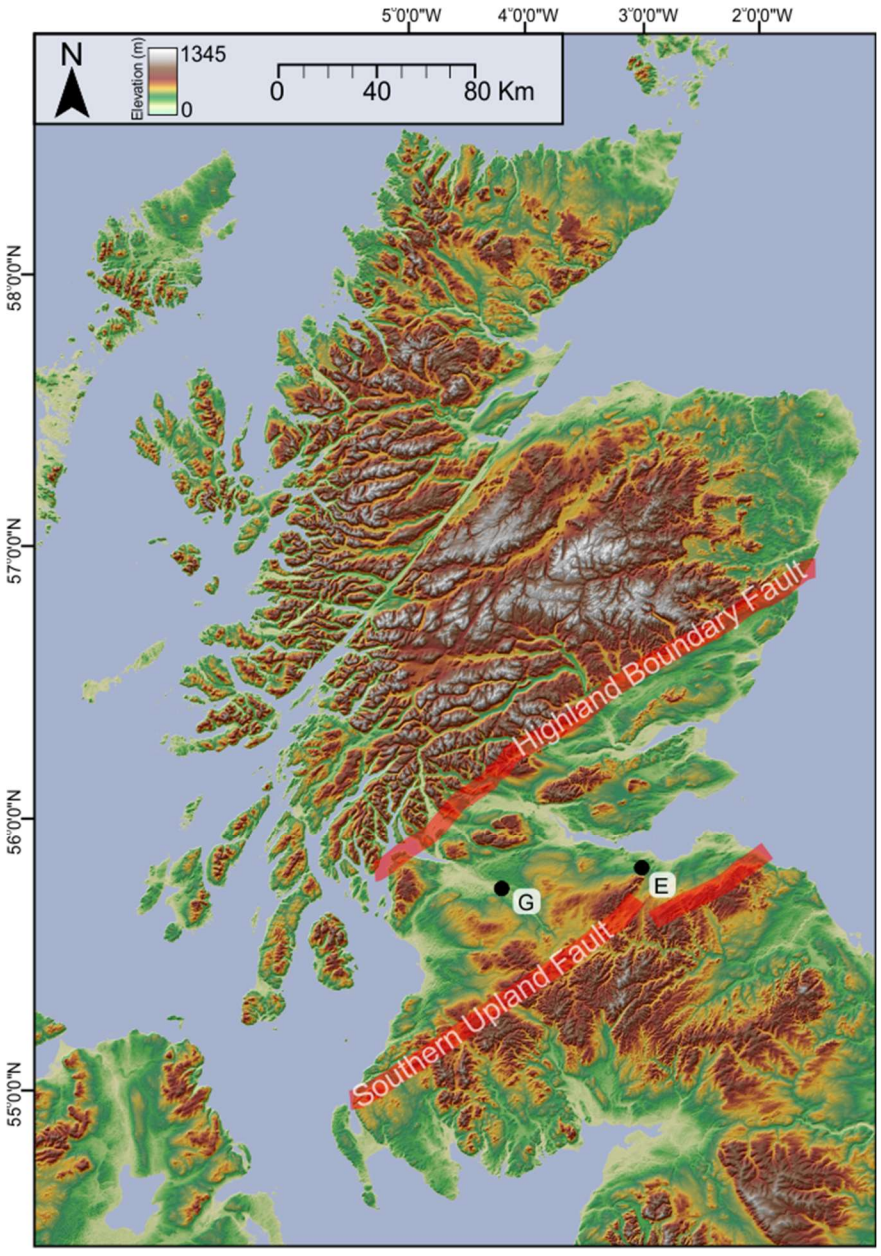

Figure 2-1: Digital Elevation Model (DEM) of Scotland. Approximate trace of bounding faults in red, along with locations of Glasgow (G) and Edinburgh (E). DEM produced using downloaded SRTM data (USGS 2021).

2.1 Regional geological setting

The region of Ireland and Britain can be divided into a series of fault bounded blocks, each with a distinct geological history, known as terranes (Woodcock *et al.* 2012b). These terranes can be sub-divided into two groups, those north of the Iapetus suture, known as the Laurentian terranes and those south of the suture, known as the Gondwanan terranes. The names of the individual terranes, their bounding faults and approximate fault trace are shown in Figure 2-2 below. Located entirely north of the Iapetus suture, Scotland is comprised of five Laurentian terranes and has a protracted geological history that spans as far back as the Archean (Trewin 2002).

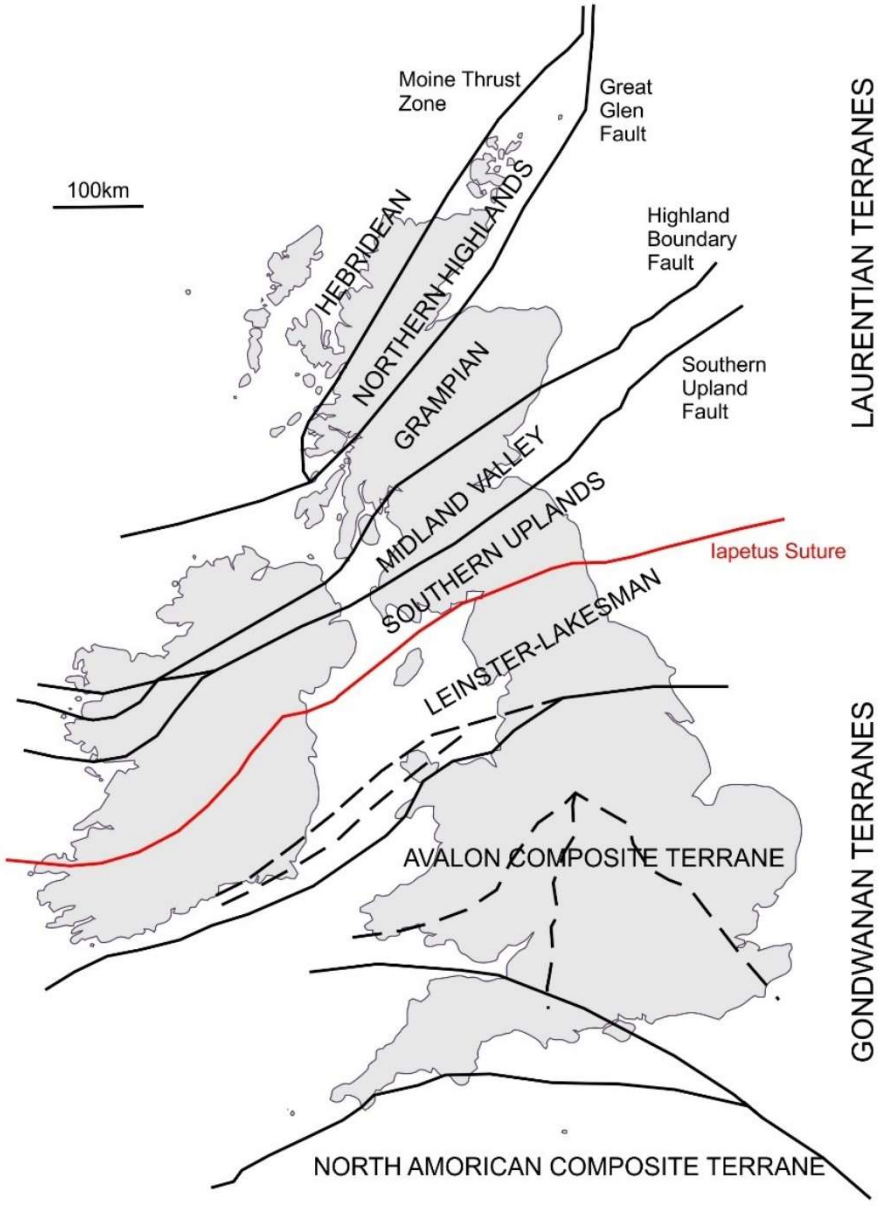

Figure 2-2: Map of the geological terranes of Ireland and Britain. Terranes are divided by the Iapetus suture (red) into the Gondwanan terranes (south of the suture) and Laurentian terranes (north of the suture). Bounding faults north of the Iapetus suture are named. Modified from Woodcock (2003).

A regional summary and geological map of Scotland (Figure 2-3), extensively modified for simplicity, is given here to help place the Midland Valley in context of its surrounding terranes. The figure shows the age and main lithologies found within the terranes, which were sutured together during the Caledonian orogeny as a result of the closure of the Iapetus ocean (Chew and Strachan 2014).

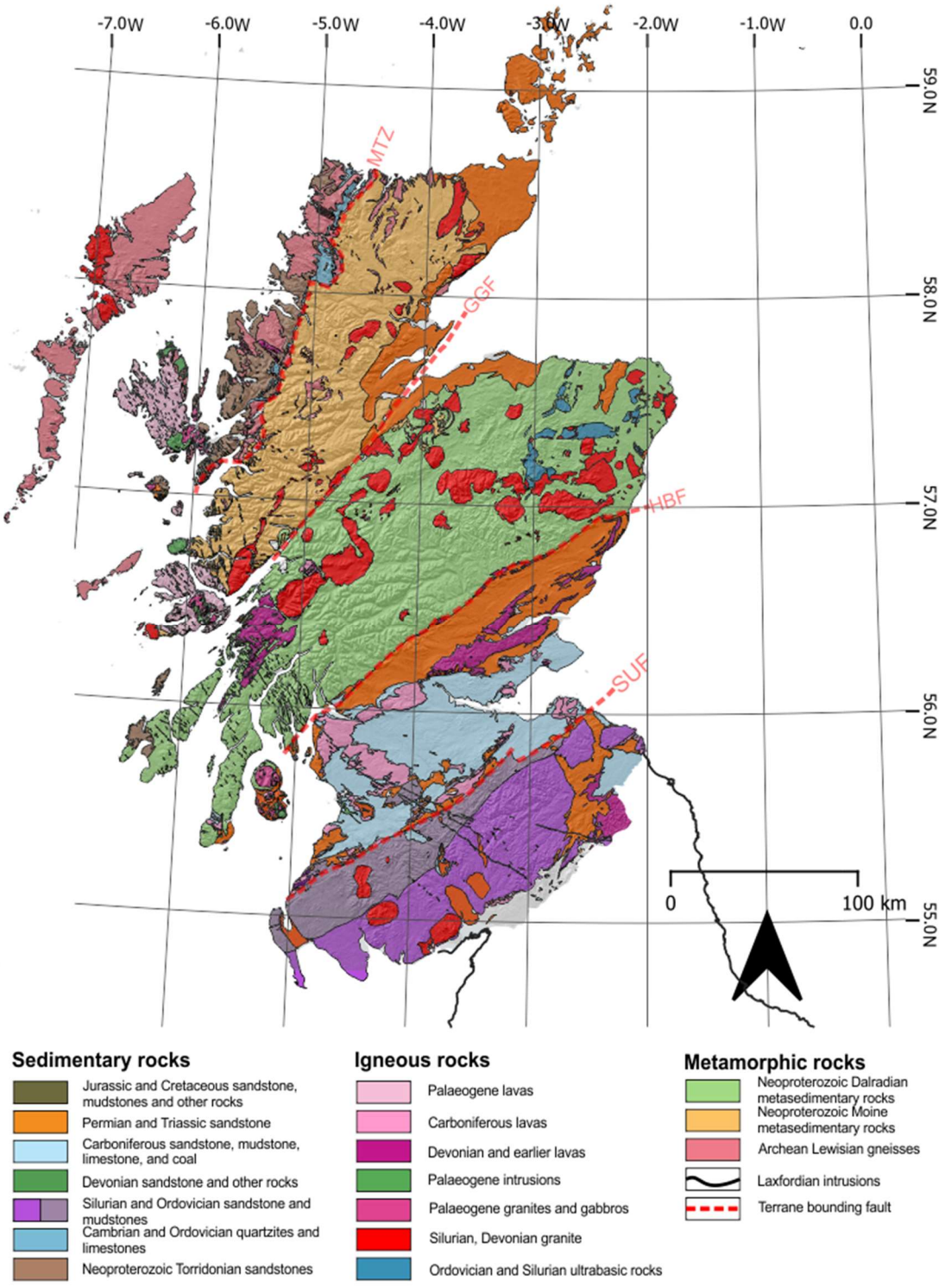

Figure 2-3: Simplified geological map of Scotland. This map has been extensively simplified from data downloaded from BGS Digimap (DiGRock250k 2013).

The oldest rocks in Scotland, located in the most northerly Hebridean terrane (Figure 2-3) are comprised of Archean to Paleoproterozoic gneissose basement, the Lewisian Complex (Park *et al.* 2002). Attempts to unravel the Lewisian Complex have subdivided the lithologies and structures into a series of events, the finer details of which are not essential to this summary. The dates, derived from zircons within the various events, however, are noteworthy given the aims of this investigation; they generally fall into three age groups, the oldest at c.2.5-3.1 Ga (Whitehouse *et al.* 1997) is associated with the protolith and metamorphism, the next at c.1.7 Ga is attributed to the Laxfordian event, and the youngest at c.1.1 Ga is believed to be with the result of the Grenvillian orogeny (Friend and Kinny 2001; Park *et al.* 2002). The Lewisian Gneiss basement is unconformably overlain by the thick Torridonian sandstones, deposited prior to the opening of the Iapetus, near the Grenvillian orogenic belt, which dominates the detrital zircon population of this succession (Rainbird *et al.* 2001). The Cambrian and Ordovician quartzites and limestones rest unconformably on the older lithologies; they formed on the northern Laurentian passive margin of the Iapetus Ocean (McKerrow *et al.* 1991). These rocks are in tectonic contact with the Moine Thrust Zone (MTZ), with the Neoproterozoic Moine metasedimentary rocks providing a minimum age for the thrust fault movement that brought the Moine into position. Detrital zircon within the Moine give a range of ages between 1.0-1.9 Ga, thus excluding the Lewisian as their source (Friend *et al.* 2003). Instead, the Grenvillian orogenic belt, formed during the assembly of the Rodinia supercontinent, is considered the most likely source for the Moine Supergroup (Friend *et al.* 2003). Polyphase regional metamorphism in the Knoydartian (820-870 Ma) and during the Caledonian orogeny (McKerrow *et al.* 2000) altered the Moine sedimentary sequences to psammites and pelites which now extend throughout the Northern Highland terrane, from the Moine Thrust to its southern boundary, at the Great Glen Fault (Strachan *et al.* 2002). Neoproterozoic Dalradian metasediments dominate the area between the Great Glen and Highland Boundary Faults, known as the Grampian terrane. Younger than the Moine, Dalradian sediments accumulated in the Iapetus Ocean, following the Rodinia supercontinent breakup (Strachan *et al.* 2002). The range of sedimentary and igneous rocks are testament to the complexity of the geological history of the terrane, which is much debated (Dempster *et al.* 2002). Faulting, folding, and metamorphism took place during the Caledonian orogeny, along with the intrusion of suites of plutonic rocks with a range of compositions, and contemporaneous volcanism. Basic intrusions and a suite of granites known as the “Older Granites” intruded during peak Caledonian metamorphism at c.470 Ma, while a younger suite termed the “Newer Granites” intruded around c.400-425 Ma (Read 1961) followed by uplift and unroofing of the granites, prior to Devonian

sedimentation. The Southern Uplands are the most southerly of the Scottish terranes and are dominated by Ordovician and Silurian sedimentary rocks. These accumulated within the Iapetus Ocean and have been subsequently deformed into an imbricate thrust belt during its closure (Oliver *et al.* 2002). The terranes southerly extent is bound by the Iapetus Suture, which marks the collisional suture between Laurentia and Avalonia and final closure of the Iapetus Ocean during the Caledonian orogeny (McKerrow and Soper 1989).

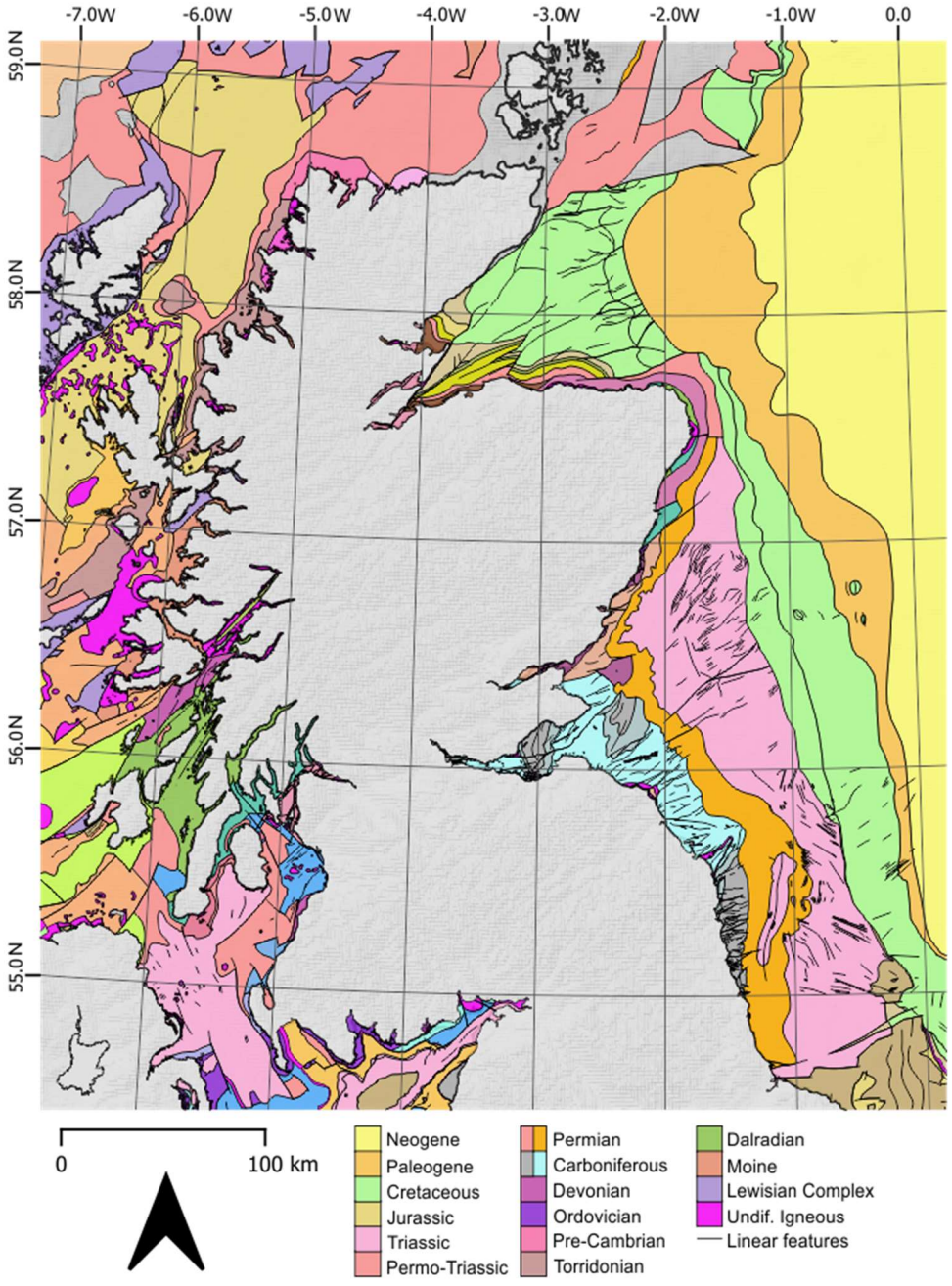

Figure 2-4: Offshore 250K geology map. Map adapted from offshore geology data downloaded from BGS Digimap (DiGRock250k 2013).

The immediate post-Caledonian history of Scotland comprised of Devonian and Carboniferous lithologies have been expanded upon in detail on below, as they represent the focus of this study.

Here it suffices to say that, Permian, Mesozoic, and Cenozoic lithologies are rare onshore, but present in Scotland's offshore regions (Figure 2-4). The Variscan orogeny and Pangea supercontinent formation led to uplift and erosion, creating the sub-Permian unconformity in Scotland and basin inversion in the Midland Valley terrane (Underhill *et al.* 2008), although in the Mauchline Basin, in the southwestern portion of the Midland Valley, Permian deposits are potentially conformable with the underlying Carboniferous lithologies (Glennie 1995). Permo-Triassic deposits are typically aeolian dune facies (Clemmensen and Abrahamsen 1983) and have been preserved in small fault bound basins (Minch Basin) or in marginal to larger subsidence depositional basins offshore (Moray Firth Basin) (Glennie 1995). Terrestrial facies with a Scottish provenance also dominate the offshore Permo-Triassic deposits around Scotland (Figure 2-4), although marine transgression with evaporites are present in the North Sea, associated with Pangea breakup and North Sea rifting (Ziegler and Dèzes 2006). Active rifting continued into the Jurassic when deposition was focused in offshore basins, with rare onshore deposits preserved (e.g. Skye), suggesting that Scotland was most likely emergent at this time (Hudson and Trewin 2002). These offshore deposits have been extensively studied due to hydrocarbon exploration and reflect a wetter climate as Scotland continued to move, from the tropics in the Carboniferous, to more northerly latitudes. Deposition continued in the offshore basins during the Cretaceous, although the tectonic regime switched from the east-west extension of the Jurassic to compression driven by the Austrian orogeny to the south (Harker 2002). Onshore Scotland was still an emergent landmass during the Early Cretaceous, though remnants of shallow marine deposits fringe the present coastline (Lowden *et al.* 1992). Global sea-level rise in the Late Cretaceous with offshore carbonates being present in the Hebrides (Hancock 1989) a reduction of clastic deposits suggests that Scotland may have experienced marine flooding at this time (Harker 2002). Rifting continued, with initiation of the opening of the North Atlantic, which proceeded at the same time as the Alpine orogeny as Africa and India migrated north towards Europe and Asia. First oceanic crust was produced in the North Atlantic at c.55 Ma (White 1988; Saunders *et al.* 1997) and Scotland became part of the NE Atlantic passive margin. Uplift associated with the opening would be expected; however, it has also been identified prior to the ocean crust formation (Mackay *et al.* 2005). The North Atlantic Igneous Province (NAIP) represented by volcanic centres and lava sheets extends through Greenland, Ireland, west coast Scotland and the Faroe Isles, emplacement of which pre-dates ocean crust formation (Dobson *et al.* 2010) has been attributed to initiation of the proto-Icelandic plume (White 1997). This earlier plume emplacement has been suggested as the driver for earlier uplift initiation, which then proceeded with

sea floor spreading (White 1997). NAIP activity ended c.55 Ma (Bell *et al.* 2002; Ganerød *et al.* 2010) as the plume remained at the ocean spreading ridge that proceeded to move Scotland eastwards, thus waning the uplift affecting the region. North Sea basins continued to receive material during this time derived from the uplifting Scotland landmass, though this is generally dominated by muds with marginal clastic material, suggesting that the source may have been dominated by carbonates (Parker 1993). Scotland's present-day landscape has been sculpted by repeated glaciation, creating the dramatic excavated highlands, while the lowlands have been covered with thick glacial and surficial deposits.

2.2 The Midland Valley of Scotland

Situated between the metamorphic Grampian Highlands and the trench sequence Southern Uplands terrane, the Midland Valley terrane of Scotland (MVS) is a fault bounded, Late Palaeozoic, WSW-ENE trending sedimentary basin (Figure 2-2) (Cameron and Stephenson 1985; Trewin 2002). The MVS is bound to the north and south by the Highland Boundary Fault (HBF) and the Southern Upland Fault (SUF), respectively; they are major NE-SW bounding faults, believed to have originated during the Palaeozoic Caledonian Orogeny (Bluck 1987). Onshore Scotland, the basin extends from Girvan to Dunbar in the south and from Greenock to Stonehaven in the north, forming a c.90km wide, c.150km long, relatively low-lying crustal block (Figure 2-1). The MVS also extends offshore, to the east, to the Forth Approaches, and to west, across the Firth of Clyde, towards Arran and Ireland (Waters *et al.* 2011). Numerous tectonic models have been proposed to account for the complex structures and lithologies present within the terrane. The MVS formed as a fore-arc (Leggett 1980; Leeder 1982) or inter-arc basin (Bluck 1983) between the Caledonian mountains and the Southern Uplands, in response to the northward subduction of the Iapetus oceanic crust driven by the collision between Laurentia, Baltica, and Avalonia (Figure 2-5). The following section provides a brief overview of the regional and local tectonic models proposed to explain the Palaeozoic evolution of the region.

2.2.1 Lower Palaeozoic tectonic setting

During the closure of the Iapetus ocean, leading to the Caledonian Orogenic Cycle, the continents of Avalonia, Baltica, and the southern margin of Laurentia, lay south of the equator (Chew and Strachan 2014). As the oceanic crust subducted, it initiated a series of arc-arc, arc-continent, and

continent-continent collisions (Chew and Strachan 2014). At this time, Scotland lay on the southern margin of the Laurentian continent, and experienced three main phases in the orogenic cycle: the Grampian Orogeny (c.475-465 Ma), the Scandian Orogeny (c.435-425 Ma), and the Arcadian Orogeny (c.405 Ma) (McKerrow *et al.* 2000). Figure 2-5 shows how the progressive ocean closure led to the collision of these continents, with the Laurussian continent forming by the end of the Caledonian Orogenic cycle in the mid-Devonian, followed by the collision of Laurussia and Gondwana forming the Variscan orogeny during the Late Devonian and continuing to the Early Permian (Woodcock *et al.* 2012a).

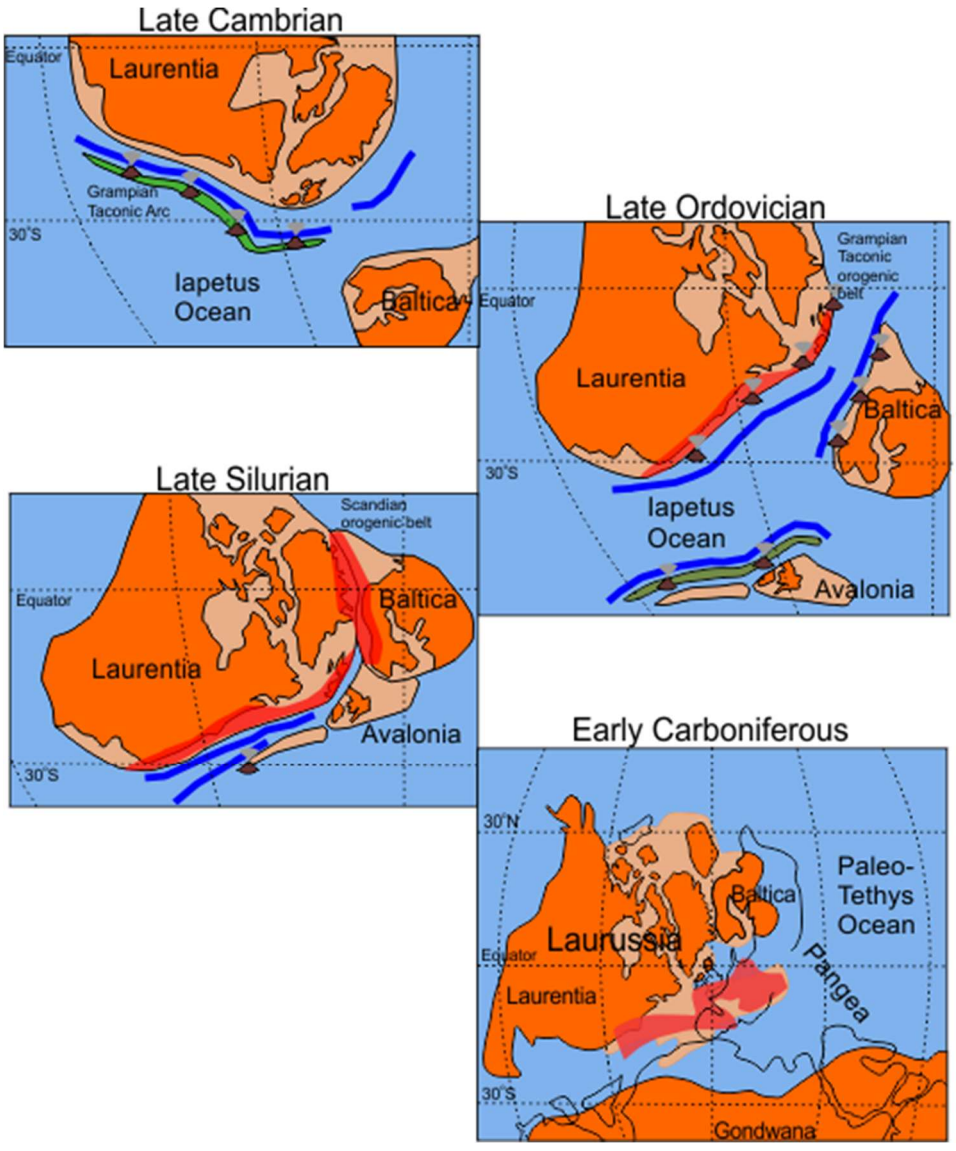

Figure 2-5: Regional tectonic model. Subduction zones show in blue, volcanic arcs in green and orogens in red. Late Cambrian, Scotland lay on the southern margin of the Laurentian continent; the Iapetus oceanic began to subduct. Ordovician: An island arc created by this subduction collides with Laurentia forming the Grampian orogeny. Silurian collision between Baltica and Laurentia formed the Scandian orogeny (Thigpen *et al.* 2013). By the beginning of the Carboniferous, the final Caledonian event (Arcadian) had been completed, forming the Laurussian continent and the Variscan orogeny initiated. Adapted from Chew and Strachan (2014).

2.2.2 Carboniferous tectonic framework

Several contrasting models have been proposed to explain Late Palaeozoic basin development in Northern Britain and in particular, the Carboniferous evolution of the Midland Valley. These have been detailed in the section below and summarised in Figure 2-7. The variety of models is due to the internal structural complexity, which includes sigmoidal NNE-SSW striking folds, reactivated NE-SW Caledonian faults, ENE-WSW orientated faults, and NW-SE oriented structures (Figure 2-8). Regional and local tectonic syntheses are often conflicting, a testament to the complex nature of the polyphase tectonic history and evolving stress field of the Midland Valley.

In an early interpretation of the Midland Valley Paleozoic basin, George (1960) described the region as adhering to a classic rift valley model. Subsequent models however, realised the necessity to invoke a more complex formation. Building upon work done by McKenzie (1978) in northwest Europe, Leeder (1982) explained Midland Valley formation with a North-South Extension model. In this model, Leeder suggests that the Midland Valley basin formed due to N-S extension followed by thermal subsidence. Subduction of the Iapetus oceanic plate during the late Devonian was interpreted to drive fore-arc crustal stretching in the Midland Valley with thermal subsidence in the Westphalian (Leeder and McMahon 1988).

This model was opposed by Haszeldine (1988) and Stedman (1988), who postulated that east-west tension associated with early rifting of the proto-Atlantic, independent of any Variscan Orogeny influence, formed north-south orientated sub-basins across the Midland Valley. These models suggested strike-slip movement played only a minor role, if any, in basin formation. In contrast, other workers (Arthaud and Matte 1977; Dewey 1982; Coward 1993) suggested there is convincing evidence that major strike-slip movement played a dominant role in Midland Valley tectonic development.

Dewey (1982) suggested that a subduction zone to the south of Britain would have caused dextral strike slip (mega-shear) to dominate tectonic movements across northern Britain. Working on structural patterns within the central parts of the Midland Valley, Read's (1988) observations agreed with Dewey's model (1982), documenting pull-apart basins formed due to late Carboniferous (Silesian) dextral strike-slip movement on existing NE-SW trending faults, such as the Southern

Upland and Highland Boundary Faults. This followed Early Devonian lithosphere stretching and rifting with Late Devonian-Carboniferous regional thermal subsidence.

Coward's (1993) regional tectonic model suggests 'lateral expulsion' of the triangular UK-North Sea-Baltic block, as it was squeezed out by the North American-Greenland and West Europe Variscan Block Figure 2-6. The Midland Valley initially experienced sinistral strike-slip movement on NE-SW trending faults, with the formation of pull-apart basins during the late Devonian-early Carboniferous. Inversion, growth folding, and erosion then occurred during the late Carboniferous due to a reversal in stress field and associated dextral strike-slip movement, caused by the re-insertion of the triangular block in association with the closure of the Ural Ocean (Figure 2-6).

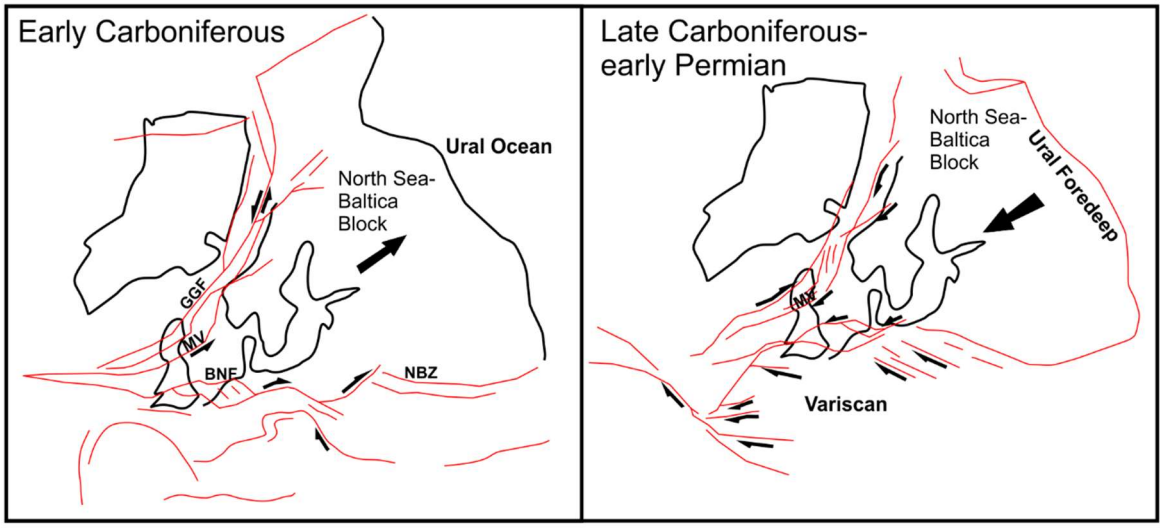

Figure 2-6: Regional tectonic model of Coward (1993). The model suggests 'lateral expulsion' of the triangular UK-North Sea-Baltic block, as it was squeezed out by the North American-Greenland and West Europe Variscan Block, followed by its re-insertion in association with the closure of the Ural Ocean.

On examining the Ochil fault bounding the Central Coalfield, Rippon et al (1996) also concluded that a phase of sinistral strike-slip movement controlled basin subsidence in the early Carboniferous. A rotation in stress orientation was then interpreted to have caused reversal on reactivated faults during the late Carboniferous. Analysis of folding and faulting around the Firth of Clyde (Caldwell and Young 2013) suggest that faulting was the primary control on stratigraphy, structure and geomorphology since the Late Devonian termination of the Caledonian Orogeny. These faults were either initiated or reactivated by Variscan stresses leading to sinistral strike-slip faulting from Late Devonian to early Carboniferous times, followed by dextral movements in the late Carboniferous.

Ritchie et al (2003) identify 3 main phases of tectonic activity: 1) Late Devonian to Dinantian (early Carboniferous) fault-controlled subsidence; 2) basin-wide Silesian (late Carboniferous) subsidence with local structural inversion and growth folding; 3) Late Silesian dextral transtensional and transpressional strike-slip faulting and inversion. Their findings also concur with the Late Devonian to Dinantian sinistral strike-slip faulting followed by Silesian dextral motions on Caledonian faults mentioned above (Coward 1993; Rippon *et al.* 1996).

Interpretation of seismic data from the Firth of Forth (Underhill *et al.* 2008) supported a longer lived, late Viséan-Westphalian onset of progressive dextral strike-slip on basin-bounding faults, as a mechanism for basin formation in the eastern Midland Valley. This was followed by late Carboniferous uplift, inversion, and fold tightening before late Carboniferous-early Permian extensional faulting and magmatism.

The more recently published tectonic models summarised above, contain differences in timing depending on the location of the studied area and dataset utilised but commonalties exist, such as; Late Devonian and earliest Carboniferous basin formation with extensional and/or sinistral strike-slip control; recognition of strike-slip transtensional/transpressional movements upon an inherited Caledonian basement fabric; early or late Carboniferous thermal subsidence and dextral strike-slip, with latest Carboniferous fold tightening/transpression followed by latest Carboniferous-early Permian extension and magmatism.

The datasets provided by this research will allow testing of the rates of burial, subsidence and subsequent uplift in several locations across the Midland Valley, any spatial and temporal variations across the basin and have the potential to contribute to future models of basin evolution.

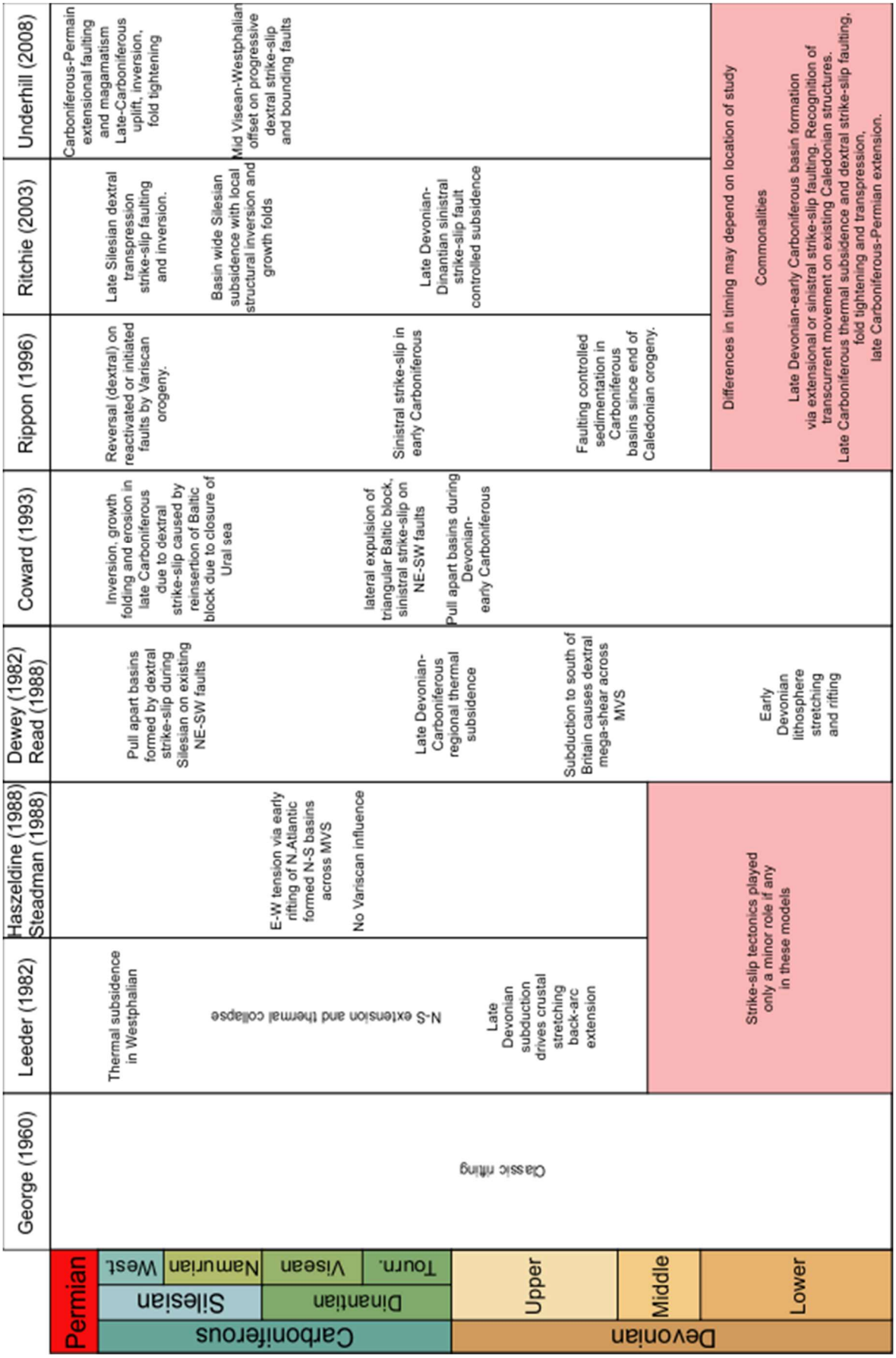

Figure 2-7: Summary of the timing and events of the tectonic histories highlighted above.

2.2.3 Structure

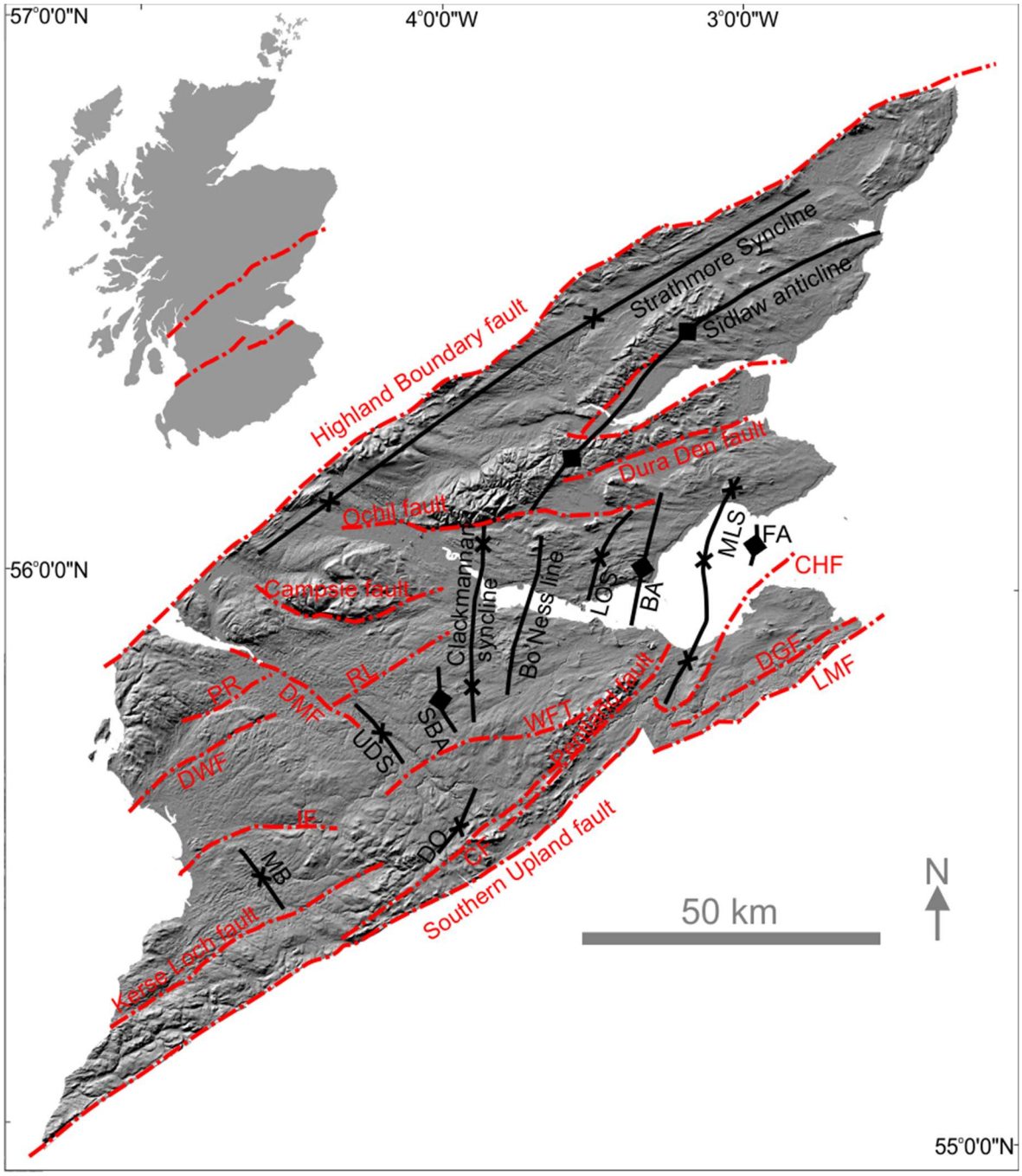

Figure 2-8: Traces of main structural features of MVS. Adapted from Read *et al.* (2002) BA, Burntisland Anticline; FA, Forth Anticline; CF, Carmichael Fault; CHF, Crossgatehall Fault; DGR Dunbar-Gifford Fault; DMF Dechmont Fault; DWF, Dusk Water Fault; IF, Inchgotrick Fault; LMF, Lammermuir Fault; LOS Lochore Syncline; MB, Mauchline Basin; MLS, Midlothian-Leven Syncline; PR, Pasley Ruck; RL, Richey Line; SBA, Salsburgh Anticline; UDS Uddingston Syncline; WFT, Wilsontown Fault.

Evidenced by the tectonic framework outlined above, the stress field of the Midland Valley did not remain constant but changed over time before and during the Carboniferous. Deep Caledonian terrane bounding lineaments, the Highland Boundary Fault (HBF) and the Southern Upland Fault (SUF) (Figure 2-8), were reactivated numerous times over their history (Cameron and Stephenson 1985). Lower Paleozoic rocks show evidence of folding prior to Lower Devonian sedimentation in

some locations, while elsewhere the boundary is transitional (Smith 1995). Lower Devonian rocks have been folded with a NE-SW trending fold axis. These folds tighten and are locally overturned towards the bounding faults (Bluck 2000). Carboniferous folding, faulting and volcanic activity formed four major depocenters across the Midland Valley, the Fife-Midlothian Basin, Stirling-Clackmannan-Central Coalfield Basin, Ayrshire Basin and the Douglas Coalfield Basin (Read *et al.* 2002). Structural features across the terrane can be divided into four groups based on orientation and are displayed in Figure 2-8 (Read *et al.* 2002).

- N-S trending folds with sigmoidal axis which curve towards the northeast in the north and southwest in the south (e.g., the Midlothian-Leven Syncline and the Burntisland Anticline). The synclines contain the Central and Midlothian Coalfields and developed throughout the Carboniferous with formation completed by the end of the Carboniferous. Offset between the present-day fold axis from the depositional fold axis is believed to be an indication of strike-slip faulting (Stedman *et al.* 1988).
- NE-SW structures that run approximately parallel to the HBF and SUF. These possibly represent reactivated Caledonian basement structures (e.g., Dusk Water Fault, Kerse Loch Fault and the Pentland Fault (Read *et al.* 2002). Many of these faults have throws in excess of 500 m, were active during the Carboniferous and controlled sedimentation into the basins (Cameron and Stephenson 1985).
- ENE-WSW and E-W structures, oblique to the bounding faults. Examples are the Ochil and Campsie Faults and those associated with the intrusion of the Midland Valley Sill-Complex and dykes during the late Carboniferous-early Permian (Read *et al.* 2002). Carboniferous sedimentary rocks terminate against the normal-offset Ochil Fault, with a down throw of about 3000m (Cameron and Stephenson 1985) is a significant fracture through the Midland Valley, and, although it was active during the Carboniferous, most of its movement is believed to have occurred later (Rippon *et al.* 1996).
- NW-SE and WNW-ESE structures, predominantly located in the Ayrshire Basin and believed to post-date E-W faulting; they influenced Permian sedimentation in Mauchline Basin (Mykura *et al.* 1967).

2.3 Geology of the Midland Valley

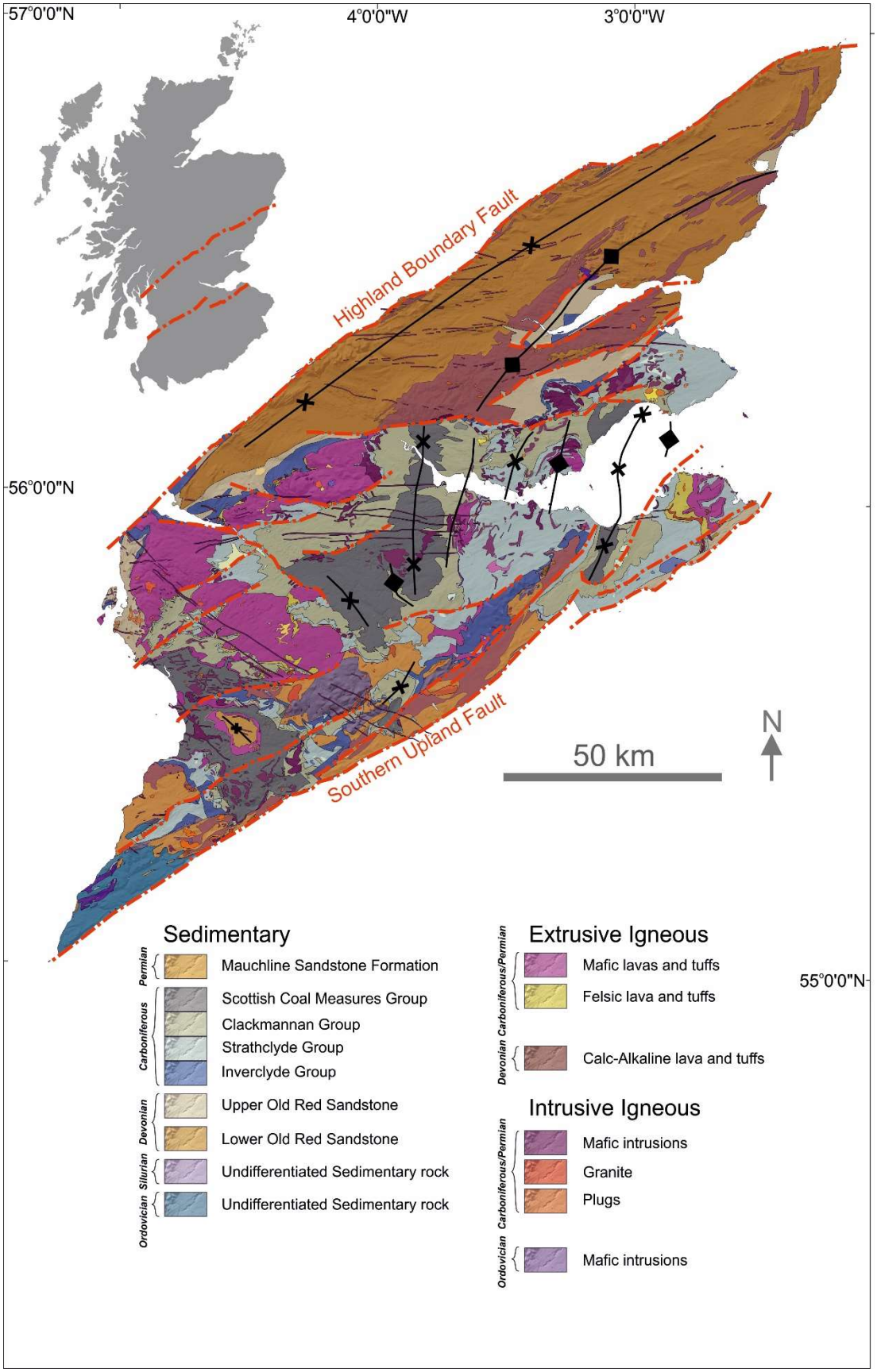

Figure 2-9: Simplified geological map of the Midland Valley of Scotland. Modified from map downloaded from BGS Digimap (DiGRock250k 2013). For structural identification see Figure 2-8.

A scale map showing the 1:250,000 bedrock geology of the Midland Valley was created from geological maps downloaded from Edina Digimap (DiGRock250k 2013) (Figure 2-9). Upper Palaeozoic sedimentary and volcanic rocks dominate the lithological exposure of the Midland Valley, leaving the Early Palaeozoic history of the region challenging to unravel (Bluck 1984). Lower Palaeozoic rocks occur in the form of discrete Ordovician and Silurian inliers, located predominantly along the southern margin of the MVS, with the exception at Stonehaven (Cameron and Stephenson 1985) display a shallowing upwards trend from a marine to a terrestrial environment, which was reached during the mid-Silurian (Cocks and Toghill 1973) indicate increasing aridity of the region, as it moved, from the southern tropics, toward the equator. Semi-arid conditions persisted into the Early Devonian, where thick deposits of coarse fluvial sediments and contemporaneous volcanic material were deposited in intracontinental basins (Bluck 2000). A period of deformation and erosion in the Middle Devonian created the Acadian unconformity, which separates the Lower and Upper Devonian deposits (Wilson 1980). When sedimentation returned, in the Upper Devonian, the deposits were generally finer grained and lack the evidence for volcanic activity seen in the Early Devonian (Browne 1980). These units pass conformably into cyclical fluvial-deltaic Carboniferous sedimentary lithologies punctuated by widespread, contemporaneous, intrusive and extrusive volcanic activity (Read 1988; Ritchie *et al.* 2003). The MVS was now positioned in an equatorial region (Read *et al.* 2002), where climatic conditions favoured the growth of vast forests (Read and Forsyth 1991) however, thin limestones also developed, as a result of periodic marine incursions which flooded the region (Bluck 1987). Syn-depositional folding created the major NNE-SSW trending structures seen across the MVS (Figure 2-8 & Figure 2-9), which were fully formed by the end of the Carboniferous (Read 1988). These were subsequently cut and intruded by late Carboniferous-early Permian faults and intrusions (Upton *et al.* 2004; Monaghan and Parrish 2006). Following a hiatus at the end of the Carboniferous, Permian sedimentary units were deposited, the oxidation of which indicate that the arid conditions had returned to the Midland Valley. Onshore, Permian aeolian sandstone deposits are the youngest sedimentary units found on the MVS (Cameron and Stephenson 1985), occurring only in the Mauchline basin to the west. Offshore however, Permian and younger deposits are present in the Forth Approaches, Firth of Clyde, Arran and Northern Ireland (Read *et al.* 2002), and possibly Mesozoic sediments could once have encroached onshore (Figure 2-4). Igneous intrusions associated with Paleogene volcanic activity and the opening of the North Atlantic (Cameron and Stephenson 1985) are the youngest igneous rocks found in the Midland Valley. Quaternary

glaciations have sculpted the present-day landscape and deposited the glacial till, often tens of metres thick, that overlies most of the Palaeozoic strata (Boulton *et al.* 1991).

2.3.1 Basement

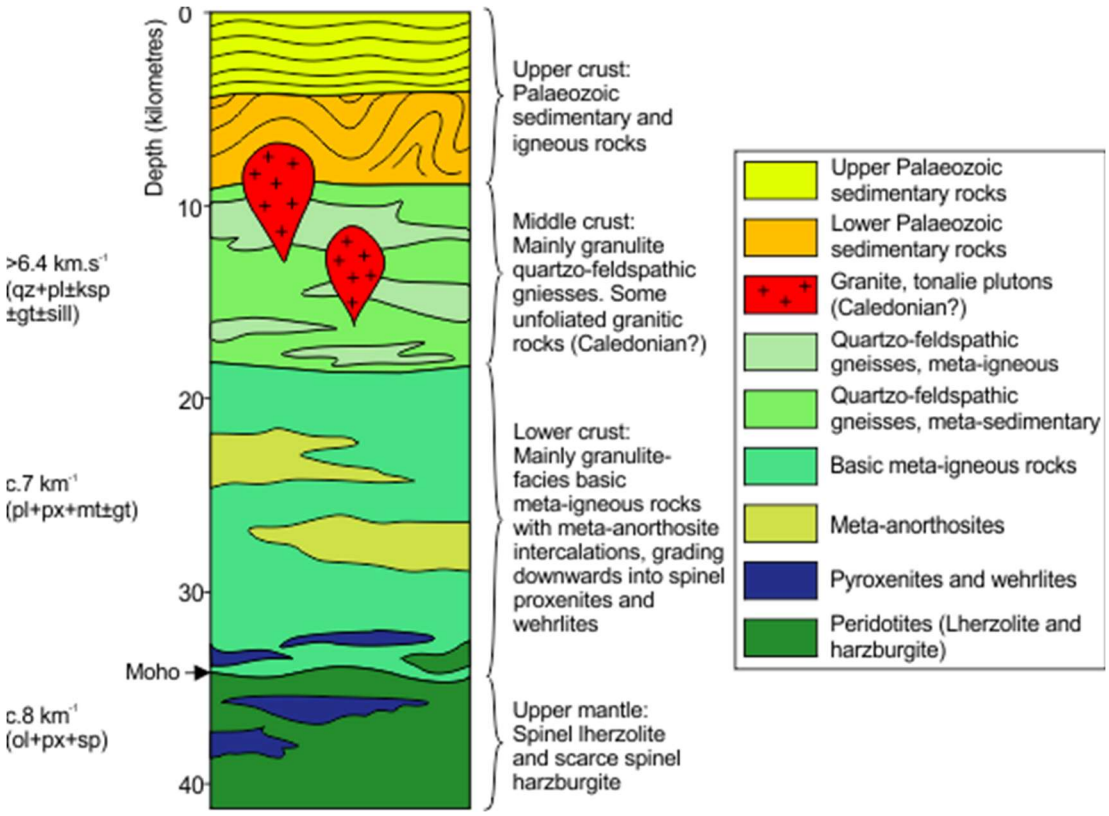

Figure 2-10: Midland Valley of Scotland basement. Generalised section through the upper lithosphere beneath the Midland Valley; redrawn from (Upton *et al.* 2004) with seismic velocities from (Bamford 1979) and lithological details from (Upton *et al.* 1984) (qt, quartz; pl, plagioclase feldspar; ksp, potassium feldspar; gt, garnet; sill, sillimanite; mt, magnetite; px, pyroxene; ol, olivine; sp, spinel).

Due to the lack of surface exposure the basement of the Midland Valley of Scotland, it has been interpreted indirectly through seismic profiles, clast provenance studies and xenoliths found within volcanic vents (Bamford 1979; Bluck 1984; Upton *et al.* 1984; Dentith and Hall 1989). These information have been summarised in Figure 2-10 that a high-grade Granulite facies basement lies beneath the Midland Valley, at shallower depths (7-9 km) than in the neighbouring Southern Uplands and Grampian terranes, where it is found at depths of 14-16 Km (Bamford 1979). The basement has an estimated thickness of 25 km and can be subdivided into Upper and Lower units. These are present beneath the Midland Valley and Grampian terrane to the north, however they are not recognised beneath the Southern Uplands, suggesting a major crustal discontinuity between the two terranes (Bamford 1979). Further evidence as to what forms the MVS basement was obtained from gneissic xenoliths which occur in Carboniferous and Permian volcanic vents in the Midland Valley

(Upton *et al.* 1976; Graham and Upton 1978). The xenoliths are categorised into two groups, a quartzo-feldspathic granulite that is sometimes garnet bearing (garnet granulite), and a pyroxene-granulite. It is believed that these two categories correspond to the Upper and Lower unit reported by Bamford (1979), as the petrological results indicate Granulite facies metamorphism (Cameron and Stephenson 1985).

2.3.2 Lower Palaeozoic evolution of the Midland Valley

2.3.2.1 Ordovician

Ordovician rocks occur in the southwest around Girvan and rest unconformably above the obducted ophiolite of the Ballantrae Complex (Williams 1962). This ultramafic, gabbroic and volcanic assemblage was emplaced onto the southern margin of the Midland Valley following either a switch in subduction polarity or arc-continent collision (Smellie and Stone 2000) on the southern margin of Laurentia (Hamilton *et al.* 1984). Active faulting controlled sedimentation into three basins, which young in a northwest direction (Williams 1962; Bluck 1983; Bluck 1984). Continental conglomerates, which terminate against these active basin faults, mature into turbiditic sandstone to the southeast (Williams 1962). The basins contain limestones with shallow water assemblages; however, deep water assemblages are also present and they indicate times where the tectonic driven subsidence outpaced sedimentation (Bluck *et al.* 1992). Shallow water shelf and storm deposits are found in the youngest and most northerly basin, which has been interpreted as having developed on the southern margin of a widespread shelf, that continued to the north into the Midland Valley. Interpretation of the conglomerate clasts and radiometric dating led some (Longman 1980; Bluck 1984) to suggest that a volcanic-plutonic arc complex was present within the Midland Valley at this time, which shed debris to its southern margin, supplying material into the fore-arc basin (Figure 2-11). It has also been suggested that the Palaeozoic sediments of the Midland Valley were deposited in a fore-arc basin that divided the Southern Uplands accretionary complex from a basement terrane further to the north (Figure 2-11) (Leggett 1980). In contrast, Hutchison and Oliver (1998) and Oliver et al (2000) suggest the sediment was derived from uplift of the Grampian terrane and deposited in the southern Midland Valley terrane.

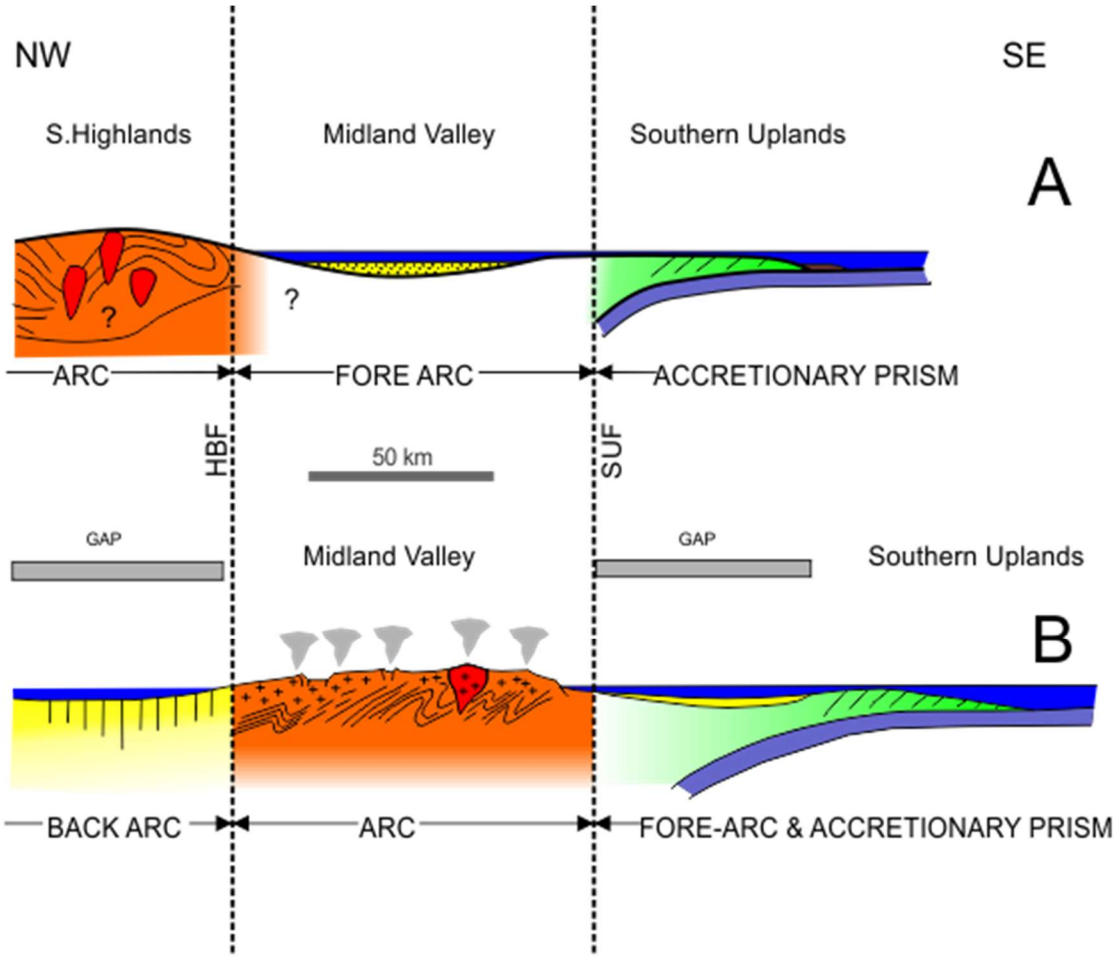

Figure 2-11: Two models for the interpretation of the Midland Valley during the Ordovician. A, Midland Valley as a fore-arc with the arc within the Dalradian block (Leggett 1980). B, Midland Valley as an arc complex (Bluck 1983) GAP indicates regions that existed during the Ordovician but are not preserved in the rock record.

2.3.2.2 Silurian

Silurian outcrops are more abundant and widespread than the Ordovician, and, where the boundary is exposed, lie unconformably above Ordovician deposits along the southern margin of the Midland Valley (Smith 1995). The five main inliers known as Lesmahagow, Hagshaw Hills, Carmichael, Eastfield and the Pentland Hills (Bavelaw Castle, North Esk, and Loganlee) (Figure 2-12) record a shallowing upward transition from marine to terrestrial sedimentation (Bluck 1984). This Mid-Silurian (LIndovery-Wenlock) transition has also been identified in areas of Laurentia, Baltica and Avalonia (Clarkson *et al.* 1998) which may suggest that the regression was driven by global scale sea-level changes, with only minor local tectonic influence (Williams and Harper 1988; Williams and Harper 1991).

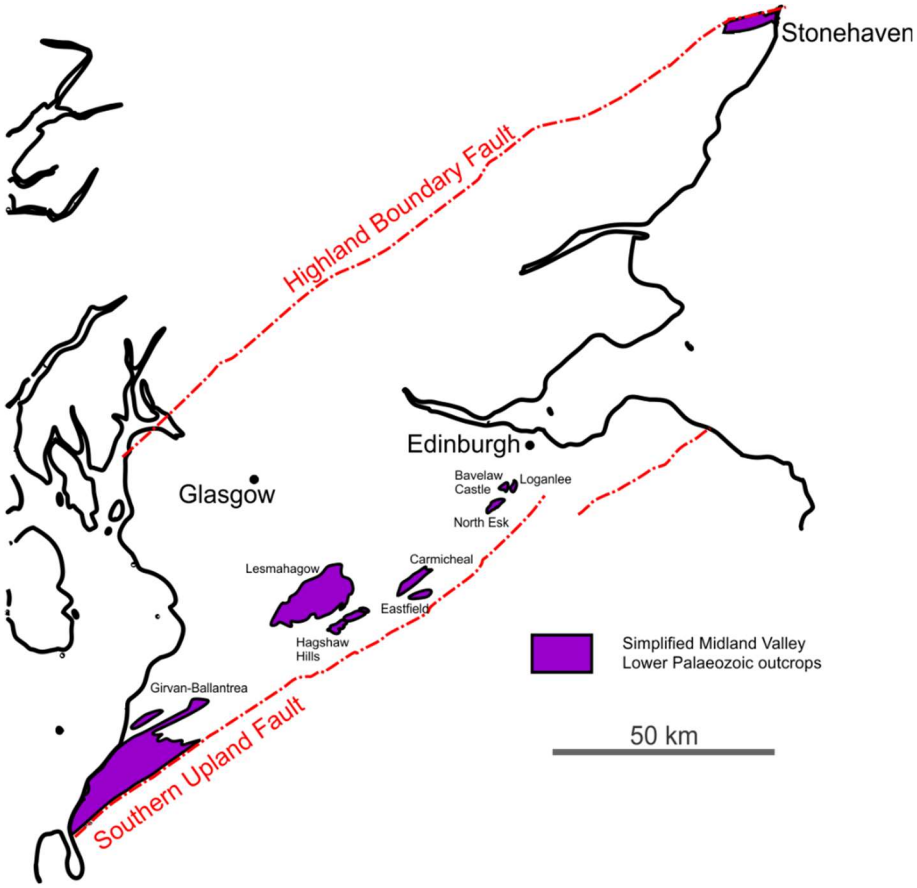

Figure 2-12: Simplified map of Ordovician and Silurian outcrops of the Midland Valley.Adapted after Cameron and Stephenson (1985).

Llandovery to Early Wenlock outcrops have a dominantly marine signature including deep water turbidites that shallow into transgressive deposits (Cocks and Toghill 1973). Although these rocks seem to broadly share the same history, attempted correlations (Cocks and Toghill 1973) highlight variations within them, suggesting that their deposition was within isolated, strike slip controlled sub-basins (Smith 1995; Phillips *et al.* 1997). Approaching the Wenlock, the rocks develop a shallow marine signature, with storm deposits, pro-delta facies and the appearance of freshwater fauna and thin conglomerates (Cocks and Toghill 1973). The transition from marine to terrestrial deposits occurred during the mid-Silurian, at the Llandovery-Wenlock boundary, with the deposition of sandstones and alluvial fan conglomerates, except around Girvan where marine conditions persisted a little longer (Ince 1984).

Among these terrestrial deposits, the lithological characteristics of three conglomerate layers have been used to inform the geological structure of the Silurian Midland Valley. The first of these, known as the Parishholm or Igneous Conglomerate, is the thinnest (max thickness of 40 m (Bluck 2013)) and lowest in the succession. This conglomerate contains abundant igneous clasts of various lithologies including granite, acidic and basic lavas, gabbro and dolerite (Smith 1995). The unit thins

to the northwest and palaeocurrent indicators suggest transport in the same direction. The igneous clasts within the conglomerate cannot be matched to any rocks present in the Southern Uplands, suggesting to McGiven (1968) and Bluck (1983) that the source is Ordovician volcanic and plutonic rocks on a quartzite basement to the south, which is no longer exposed. The second of these conglomerates, known as the Hareshaw or Quartzite Conglomerate, has a maximum thickness of 100 m (Bluck 2013), is dominated by quartzite clasts but also contains abundant igneous and vein quartz clasts. Interpreted as an alluvial fan radiating from the east-southeast (Bluck 1983), it thins to the northwest is also believed to have been sourced from a uplifted block to the south. The third and final conglomerate, the Greywacke Conglomerate, is up to 300m thick (Bluck 2013), displays a combination of palaeoflow directions both towards the northwest and southwest. The geochemical signature of clasts within this conglomerate differs from the signature of those present Southern Upland terrane greywacke (McGiven 1968; Syba 1989; Stone and Evans 2000), indicating the source of these clasts has since been removed through either erosion of faulting.

Palaeocurrent indicators from all three conglomerates suggest that the provenance of the sediment was to the south. However, compositionally matching this material to the Southern Uplands terrane has proven problematical (Syba 1989). This had led to the suggestion that the Silurian sedimentary rocks accumulated in a back-arc or inter-arc (Haughton 1988) strike-slip basins (Phillips *et al.* 1997) ,when the Midland Valley extended further to the south than at present (Bluck 1983; Phillips *et al.* 1997). An alternative to the arc setting of the Midland Valley has been offered by Armstrong and Owen (2001) who suggest that the source may have been a micro-continent that has since been displaced by faulting.

In summary, the sedimentological evidence suggests that these Silurian basins infilled as Laurentia and Avalonia collided following the oblique closure of the Iapetus Ocean, driven by the north-westly subduction under the Laurentian margin (Figure 2-5) (Bluck 2013). While the continents of Avalonia and Laurentia merged in the southwest, Baltica and Laurentia collided synchronously in the west, ending subduction and forming the Laurussian supercontinent (Figure 2-5). The position of the Dalradian block is uncertain during the Silurian; although it would have been experiencing uplift (Dempster 1985) no detrital evidence of the Dalradian is found within the Silurian Midland Valley basins (Bluck 1984).

2.3.3 Upper Palaeozoic

2.3.3.1 Lower Devonian

By the beginning of the Devonian, the Iapetus Ocean had closed and Laurentia, Avalonia and Baltica had collided to form the Laurussian supercontinent; the Midland Valley sat c.30° south of the equator (Witzke and Heckel 1988). Climatic indicators suggest a dominantly arid climate at this time however, periods of semi-arid and cool wet conditions existed in Devonian basins, possibly reflecting Milankovitch-Kroll cyclicity (Kelly 1992). With the exception of the Lesmahagow and Stonehaven inliers (Figure 2-12), Lower Devonian deposits rest unconformably on Silurian rocks (Bluck 2000) and were deposited within intracontinental basins, which lay between the Caledonian Orogeny and the Southern Uplands accretionary prism. The continental facies, also known as the 'Old Red Sandstone', were deposited predominantly in the northeast-southwest striking, non-contemporaneous Strathmore and Lanark Basins (Figure 2-13) (Trewin and Thirlwall 2002), which were separated from each other by a line of volcanoes, the Ayr-Ochil-Sidlaw axis (Trewin and Thirlwall 2002).

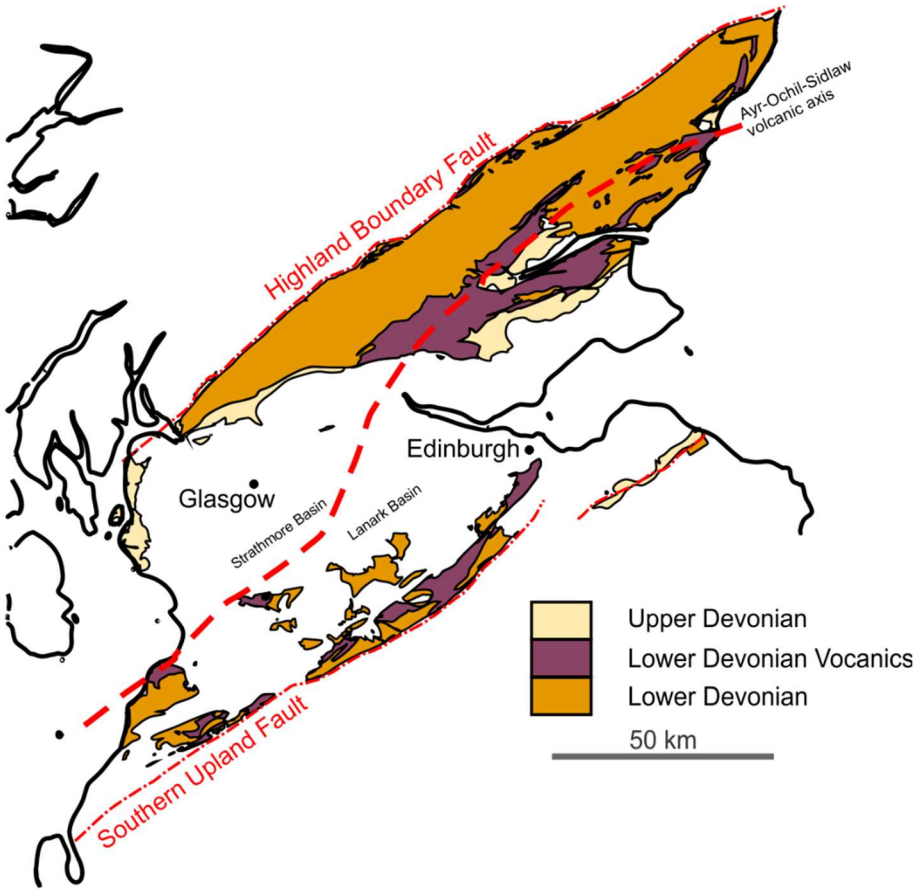

Figure 2-13: Simplified geological map of Devonian outcrop in the Midland Valley. Approximate position of the Ayr-Ochil-Sidlaw axis, which separated the Strathmore and Lanark basins, marked by the red dashed line, adapter after Trewin and Thirlwall (2002).

Both basins display an upward fining and maturing sequence of sediments, with initial locally sourced conglomeritic material feeding basins laterally influenced by strike-slip faulting (Phillips *et al.* 1997). The sediment then fines and matures upward, as it is deposited from major distal fluvial systems sourced from the coeval Scandian Orogeny, resulting from the collision between the Laurentian and Baltic plates to the northeast (Haughton and Bluck 1988). Reworking of the contemporaneous basaltic and andesitic volcanic material also provided a major source of sediment to the basins (Bluck 2000). Geochemical analysis of the volcanic material indicates that it was of calc-alkaline composition (Thirlwall 1983), commonly associated with active continental margins (Upton *et al.* 2004). Cessation of this volcanism at the end of the Lower Devonian suggests the end of subduction of the Iapetus slab, final suturing of the Laurussian landmass and final stage of the Caledonian Orogeny.

Dalradian clasts are absent in the Lower Devonian Strathmore basin, indicating that the source of this coarse material lies elsewhere (Bluck 1983; Bluck *et al.* 1984). With the main phase of Dalradian uplift over prior to Devonian sedimentation, the Southern Highlands during this time may have not been an area of great relief (Dempster *et al.* 1995) and locally was receiving sediment rather than shedding it, like the Glen Turret and Lintrathen outliers suggest (Bluck 2000). The existence of well-rounded polycyclic quartzite clasts led Bluck (1984) to suggest the existence of a metamorphic terrane, subsequently removed by faulting and erosion, between the Dalradian block and the Midland Valley. As the Dalradian block moved southward during the deposition of Lower Devonian sediment, it generated the steep northern limb of the asymmetrical Strathmore syncline (Bluck 2000). The encroaching of the Dalradian block allowed it to shed sediment into the basin in the later stage of the Early Devonian and removed the northern margin of the basin which extended some distance to the NW into ground now occupied by the Dalradian block.

In the south, the Lanark basin also has palaeocurrent indicators for longitudinal fill from the NE, however, coarser material was laterally fed from the SE (Bluck 2000) and NW (Syba 1989). The deposits are thinner, contain more sandstone and finer grain conglomerates, compared to the Strathmore Basin. As in the north, locating the provenance of the coarser clastic material is problematic, as the clast composition does not match the material presently found in the Southern Uplands (McGiven 1968; Syba 1989; Smith 1995). An allochthonous greywacke sheet of unknown provenance that covered the Southern Uplands has been suggested. It is also possible that the

Lanark basin once occupied a much wider area than at present and subsequent strike-slip movements along faults have shortened the region (Bluck 2000; Phillips *et al.* 2004).

2.3.3.2 Upper Devonian

During the Upper Devonian, volcanic activity ended and the Acadian unconformity formed, as sinistral strike-slip movement (Smith 1995) along Caledonian lineaments caused folding (e.g., the Strathmore syncline and the Sidlaw anticline), uplift and erosion of the early Devonian sedimentary basins (Bluck 2000; Trewin and Thirlwall 2002). When sedimentation returned during the Upper Devonian, the material was of increased maturity, finer grained and lacking in volcanic detrital material compared to the earlier deposits (Bluck 2000). Paleocurrent indicators show that the flow was towards the east and northeast, contrary to the early Devonian trend (Woodcock *et al.* 2012a) possibly due to fault-controlled subsidence (Ritchie *et al.* 2003). The sequence forms a broadly upward fining cycle with braided streams passing up into aeolian deposits. This maturation of the landscape continues into the Carboniferous where the conformable boundary is indicated by the first appearance of carbonate bearing horizons, which formed on alluvial plains (Paterson and Hall 1986) indicating tectonic stability.

2.4 Carboniferous evolution of the Midland Valley

2.4.1 Introduction

The stratigraphy of the Carboniferous Midland Valley of Scotland has been studied extensively over time and various criteria have been used to differentiate between units (George 1960; Neves *et al.* 1973; Paterson and Hall 1986; Browne *et al.* 1999). This thesis uses the lithostratigraphical framework of Browne *et al.* (1999), which has been summarised in Figure 2-14 below.

By the beginning of the Carboniferous, the Midland Valley sat c.10-20° south of the equator (Read 1988; Witzke and Heckel 1988) on the southwest coast of the Laurussian continent. Laurussia continued a northerly migration throughout the Carboniferous, with the Midland Valley crossing the equator during the Namurian and reaching c.10° north of the equator by the end of the Westphalian (Browne *et al.* 1999). This plate migration meant that the stress field changed dramatically throughout this time (Coward 1993; Rippon *et al.* 1996), and the changes in latitude and climate are reflected in the depositional environments recorded in the Carboniferous lithologies (Figure 2-14) (Browne *et al.*

1999). To add to this, the chemical composition of the Carboniferous atmosphere experienced an increase in oxygen and a decrease in carbon dioxide levels (Beerling *et al.* 2002). These atmospheric conditions were biologically beneficial to flora and fauna, allowing the development of giant insects and vast tropical rainforests (Scott 2001) which mark the proliferation of land plants. The preservation of these forests and their diagenesis created the economical coal deposits, which have been mined since the 12th Century (Monaghan 2014).

During the Viséan, clastic sediments, suspected to originate from the Caledonian mountains to the north (Stuart *et al.* 2001; Morton and Whitham 2002) are intercalated with thin marine deposits predominantly from easterly derived incursions, often used for cross basin correlation. The deposits are typically cyclical, beginning with marine limestones or mudstones, followed by non-marine mudstones, sandstones, seat-earths, and finally coals. Although often incomplete, average cycles are c.10 m thick, but can be up to 30 m. The deposits are consistently typical of a shallow water, indicating that the depositional surface was never far from base level and sedimentation kept pace with subsidence. By the end of the Carboniferous, parts of the Midland Valley basin are believed to have contained up to 5 km of sedimentary deposits (Leeder 1982; Monaghan and Parrish 2006).

Volcanism returned to the Midland Valley having been relatively absent since Early Devonian times, with peak activity taking place during Viséan (Upton *et al.* 2004), with the eruptions of the Garleton Hills, Arthur's Seat and Clyde Plateau Volcanic Formations. This volcanic activity continued into the mid-Permian although on a more subdued and localised scale (Stephenson 2003), allowing thermal subsidence of the crust. Dating of this igneous activity has given valuable insight into the timing of the tectonic structure of the Midland Valley (Monaghan and Pringle 2004; Monaghan and Parrish 2006; Monaghan *et al.* 2014).

Correlation of the Carboniferous sedimentary succession of the Midland Valley is largely based on lithostratigraphy and palynology (Figure 2-14), due to the lack of zonal goniatite bands that exist elsewhere. Thus, difficulties arise while attempting to correlate Scottish Carboniferous deposits to those found in Europe. Non-marine bivalves and miospores have been used to give some temporal constraints (Neves *et al.* 1973; Owens *et al.* 2005), with the greatest success found in the Westphalian where the Scottish Coal Measures have been correlated to the Coal Measures found throughout Europe. The following section summarises the geology of the Carboniferous Midland

Valley, divided into the Inverclyde, Strathclyde, Clackmannan, and Scottish Coal Measures Groups (Figure 2-14).

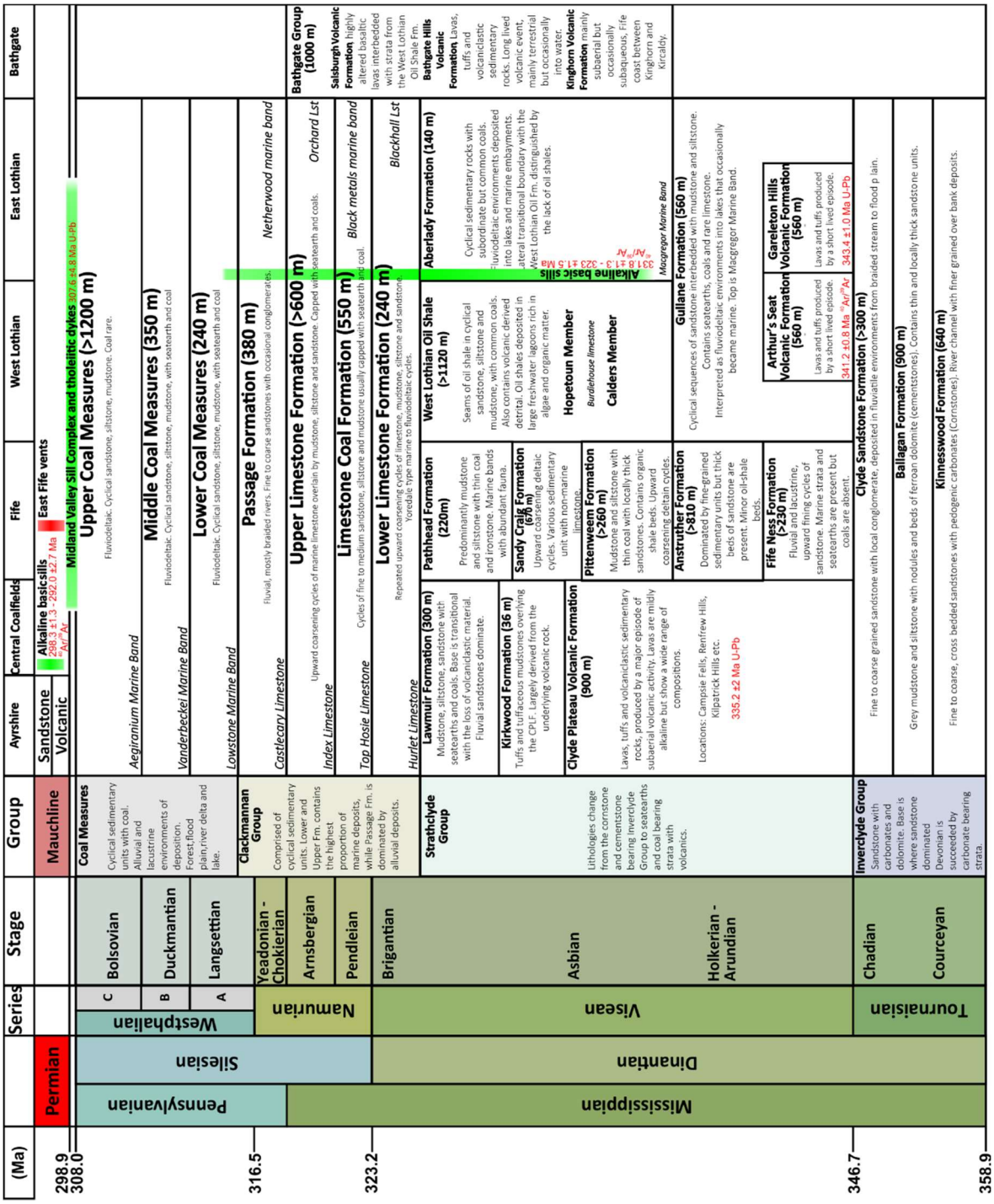

Figure 2-14: Lithostratigraphical framework classification for the Carboniferous Midland Valley of Scotland. Classification of the Carboniferous rocks of the Midland Valley is commonly based on lithostratigraphy and palynology due to the lack of diagnostic zone fossils. Modified from Browne *et al.* (1999). Geochronological ages from Monaghan *et al.* (2014) and (Monaghan and Parrish 2006).

2.4.2 Inverclyde Group

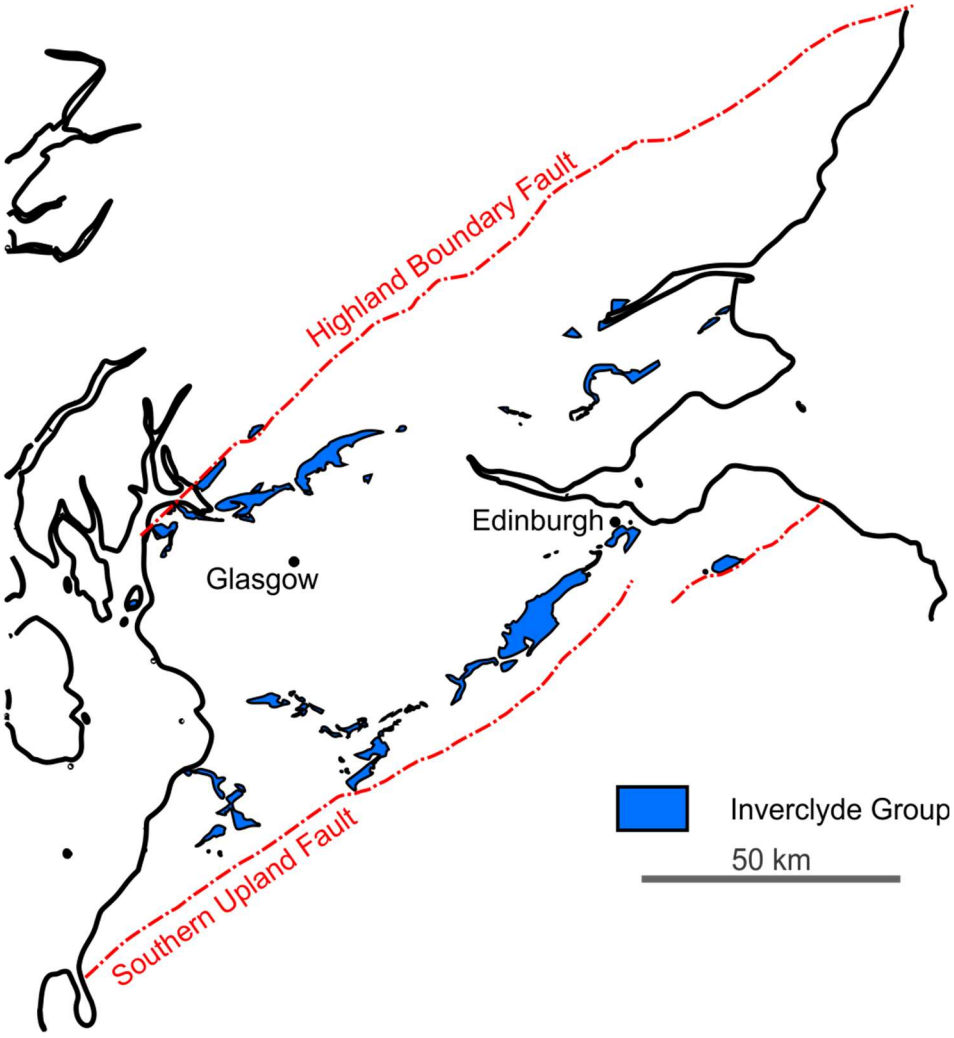

Figure 2-15: Simplified geological map of the Inverclyde Group locations. Adapted from Cameron and Stephenson (1985).

The boundary between the Devonian and the Carboniferous rocks in the Midland Valley is transitional and marked by the first appearance of calcareous horizons (cornstones) (Browne et al. 1999). These Inverclyde Group pedogenic calcretes, formed while the Midland Valley lay at low latitudes, south of the equator (Witzke and Heckel 1988) and had a semi-arid, seasonally wet climate (Read *et al.* 2002). The Inverclyde Group (Paterson and Hall 1986), comprised of the Kinnesswood, Ballagan and Clyde Sandstone Formations (Figure 2-15), is characterised by these calcareous horizons interbedded with siliciclastic fluvio-lacustrine and lagoonal deposits, with rare marine beds and evaporites, coal seams and oil-shales are absent (Browne et al. 1999). The Kinnesswood Formation (Chisholm and Dean 1974) consists of upward fining fluvial cycles of sandstone deposited in meandering and braided streams. Carbonate cornstones developed in soil profiles of the overbank deposits on stable alluvial plains under the influence of a fluctuating water table (Browne *et al.* 1999). Locally, the formation exceeds 300 m thick and, although unfossiliferous, it has been assigned to the

base of the Tournaisian by palynology (Smith 1996). Typically finer grained, the Ballagan Formation is dominated by mudstone, siltstone and dolostone (cementstone) (Browne 1980). Thin sandstone beds probably derived from alluvial fans sourced in the Southern Uplands are also frequent. Evidence for a lowering of the water table such as desiccation cracks and evaporites of gypsum and anhydrite are common (Browne *et al.* 1999). Periodic desiccation with exposure to fluctuating salinity has been interpreted as result of seawater introduction by storm flooding events. Andrews (1991) interpreted the formation as being laid down in coastal alluvial plains and marginal marine flats, subjected to marine incursions from the open sea, which lay initially to the east, but more to the south in later stages (Cope *et al.* 1992). Deposited by braided streams and meandering river flood plains during the Late Tournaisian, the Clyde Sandstone Formation (Paterson and Hall 1986) is characterised by white and pale grey fluvial channel and overbank deposits (Browne *et al.* 1999). Similar to earlier formations, calcareous horizons formed on stable alluvial plains. Towards the north of the Midland Valley, Dalradian pebbles occur in conglomeritic deposits, however elsewhere the coarse material is comprised of locally sourced calcareous and mud clasts (Browne *et al.* 1999).

2.4.3 Strathclyde Group

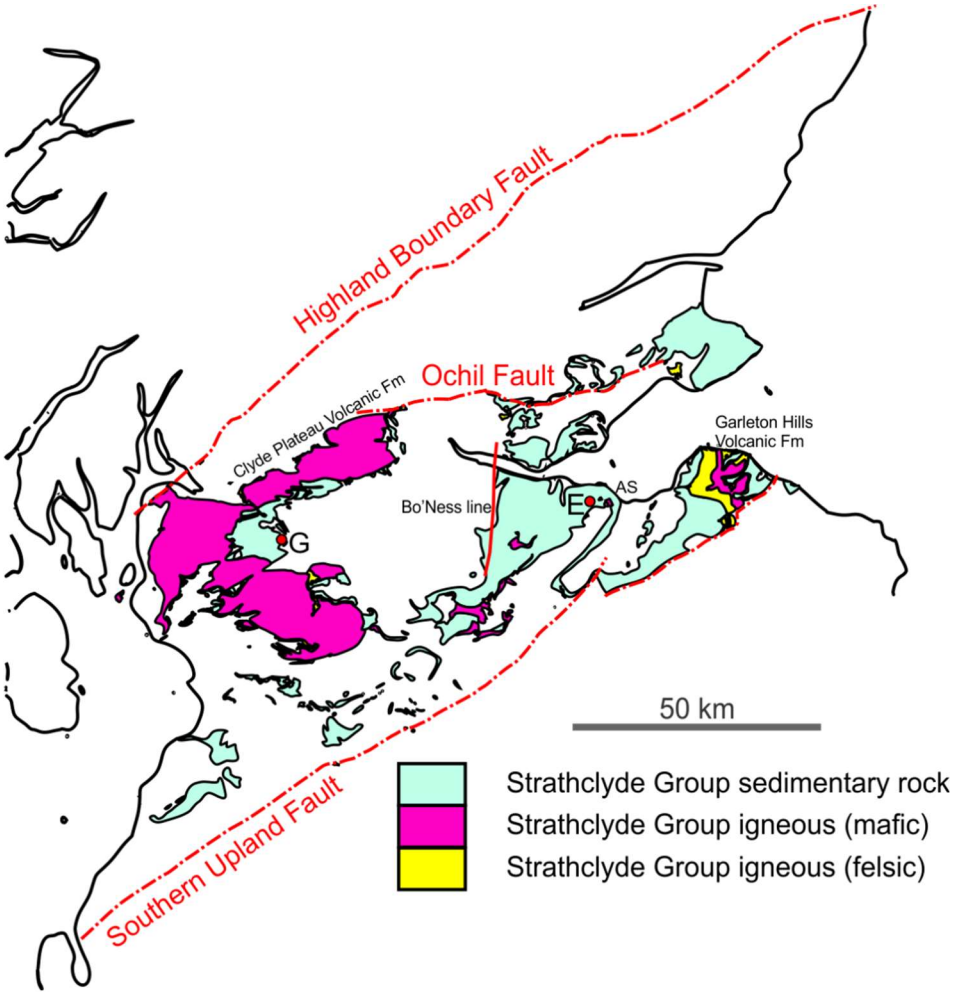

Figure 2-16: Simplified geological map of the Strathclyde Group outcrop locations. Clyde Plateau Volcanic Formation; semi-circular volcanic block forming the Campsie Fells, Kilpatrick Hills, and the Renfrewshire Hills underlies the Central Coalfield sedimentary deposits; AS, Arthurs Seat.G= Glasgow, E=Edinburgh

The Strathclyde Group (Paterson and Hall 1986) consists of a varied sedimentary and volcanic succession, characterised by the presence of carbonaceous beds of coal and oil shale which differentiates the Strathclyde Group from Early Carboniferous deposits (Browne *et al.* 1999). Increased floral and faunal diversity suggests that rainfall increased, as the Midland Valley approached the equator (Trewin 2002). Transitional to alkaline, basaltic to rhyolitic volcanic activity was intense and widespread throughout the Midland Valley during the Viséan (Upton *et al.* 2004) with the Garleton Hills and Arthur's Seat Volcanic Formations in the eastern Midland Valley (Monaghan and Pringle 2004; Monaghan *et al.* 2014) while slightly later, a major episode of volcanic activity produced the Clyde Plateau Volcanic Formation in the west (Monaghan and Parrish 2006) (Figure 2-14). The Bathgate Hills Volcanic Formation of central and west Lothian and Kinghorn Volcanic Formation in Fife (Figure 2-14), initiated during the late Viséan and persisted into the

Namurian, suggesting a high heat flow across the Midland Valley (Upton *et al.* 2004). The volcanic piles and tectonic highs divided the area into a series of N-S trending semi-isolated basins indicated in the Strathclyde Group isopach map (Figure 2-17); these basins developed in response to tectonic stresses and were infilled with volcanic, fluvio-deltaic, lagoonal and lacustrine facies deposits, derived from the northeast (Browne *et al.* 1999).

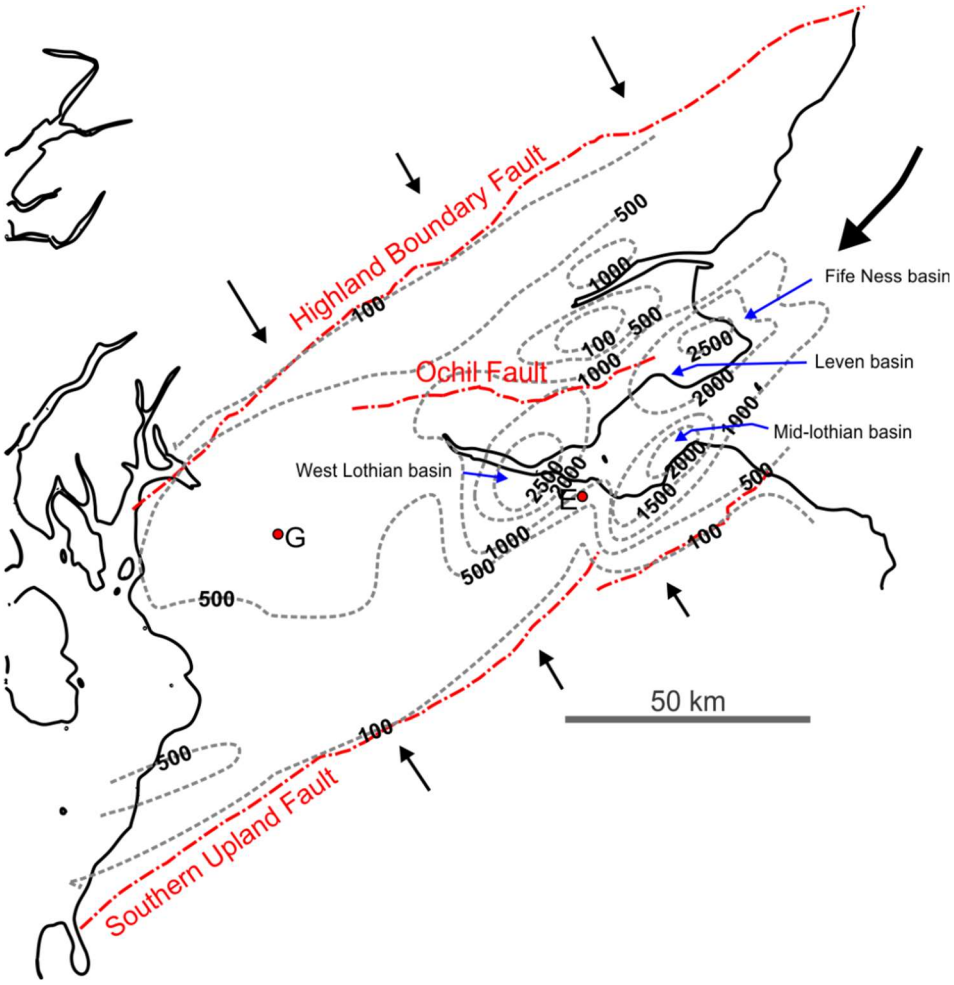

Figure 2-17: Strathclyde Group isopach map. Isopachs in meters, also showing direction of transport of coarse-grained siliciclastic material (black arrows) and locations of semi-isolated basins (blue arrows) adapted from (Read *et al.* 2002).

2.4.3.1 Western Midland Valley

The Clyde Plateau Volcanic Formation (Figure 2-16), an intense but short-lived event, formed a c.900 m thick volcanic pile (Monro 1982). The thick subaerial exposure dominated the western Midland Valley and remained a topographic high until mid-Brigantian, constituting a major barrier to sedimentation flux between eastern and western Midland Valley. A NNE-trending topographical volcanic high known as the Bo'ness line (Figure 2-16), is proposed to have acted as a barrier to easterly derived marine incursions and divided the lithostratigraphical and sedimentologically

different eastern and western basins (Rippon *et al.* 1996). Although most of the volcanic block remained above sea-level until the Lower Limestone Formation deposition, some areas were covered by thick reworked volcano-sedimentary sequences reflecting its uneven topography (Browne *et al.* 1999). The Kirkwood Formation (Monro 1982) consists of volcanic detritus and mudstones which unconformably overlies part of the Clyde Plateau Volcanic Formation. The Kirkwood Formation varies in thickness from 0-30 m and displays evidence of intense subaerial tropical weathering and lateritisation (Browne *et al.* 1999). Above this lie the sedimentary sequences of the Lawmuir Formation (Paterson and Hall 1986). The lower part of this succession is fluviatile with channel, floodplain and coal deposits, some of which are locally thickened by strike slip faulting or slumping. The upper part is cyclic, with laterally persistent marine and non-marine limestone horizons (Browne *et al.* 1999).

2.4.3.2 Eastern Midland Valley

The east of the Midland Valley shows more sedimentary variability than the west, and the contrasting deposits found in Fife, West Lothian and East Lothian provide more evidence for semi-isolated basins separated by intrabasinal highs (Figure 2-17). In West Lothian, the base of the Strathclyde Group is marked by the Arthur's Seat Volcanic Formation which contains c.300m of lavas, tuffs and volcanoclastic sedimentary rocks (Monaghan *et al.* 2014). Exposed in Holyrood Park in Edinburgh, the Formation was produced by a short-lived volcanic episode which erupted on a coastal plain (Mitchell and Mykura 1962). This is overlain by the fluvial, deltaic and lacustrine sedimentary deposits of the Gullane Formation which also contains coals and limestones and persists laterally into East Lothian (Browne *et al.* 1999). To the west, lies the rhythmic West Lothian Oil Shale Formation, which was once extensively mined, particularly in the upper part of the sequence for the seams of oil-shale it contains (Monaghan 2014). The Formation was deposited in a large, restricted, shallow water lacustrine environment termed Lake Cadell (Figure 2-18) (Loftus and Greensmith 1988; Raymond 1991). The presence of marine limestones indicates periodic marine incursions from the east, while freshwater limestones and rhythmic deposits reflect the development of a substantial lake with a humid climate in a slowly subsiding basin. Abundant accumulation of benthonic cyanobacteria with minor planktonic input interbedded with siliciclastic detritus developed during periods of tectonic quiescence in hydrologically open, stratified, deep lakes with stable shorelines and water levels. Regionally dolostones (Maddox and Andrews 1987), markers of basin wide regression, were formed

in hydrologically closed, shallow playa lakes (Guirdham 1998). Switches between the two was driven by climate change, increased aridity, seasonality and local tectonism with volcanic activity.

In East Lothian, the base of the Strathclyde Group is marked by the mildly alkaline lavas and tuffs of the Garleton Hills Volcanic Formation (Read *et al.* 2002). The formation has been proven in boreholes further west suggesting it may correlate with to the Arthurs Seat Volcanic Formation (Browne *et al.* 1999). However, recent dating (Monaghan *et al.* 2014) indicates that its formation predates Arthur's Seat, casting doubt on the previous suggestion. The Gullane Formation rests above this volcanic formation and, in turn, is overlain by the Aberlady Formation. This is a lateral equivalent to the West Lothian Oil Shale Formation with a similar depositional environment but has notably more marine bands and limestone with diverse faunas and fewer oil-shale beds than in West Lothian (Browne *et al.* 1999).

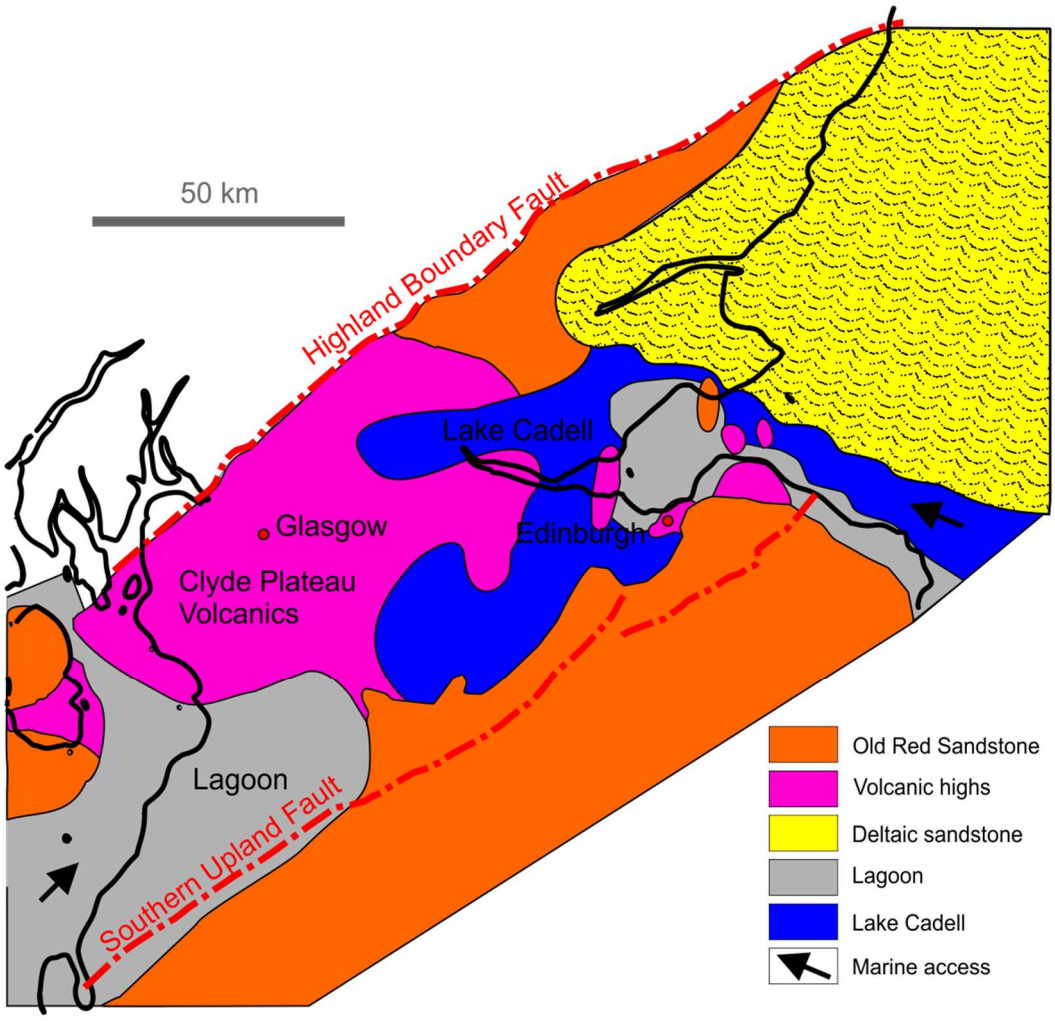

Figure 2-18: Interpretation of the palaeogeographical setting of the Midland Valley during the Strathclyde Group deposition. Volcanic centres divided the region into sub-basins and a major lake, named Lake Cadell provided the environment for the rhythmic deposits of the West Lothian Oil Shale. Modified from Loftus and Greensmith (1988).

2.4.3.3 Fife

Exposed along the coast but lacking inland exposure, equivalent-age facies in Fife are arenaceous cyclical alternation of sandstone, limestone, shale, coals and dolomite that are over 2000 m thick (Browne *et al.* 1999). Rhythmic sedimentation was formed by the advance and retreat of a large fluvio-deltaic complex from the NE (Figure 2-18), which helped to block sea entry into Lake Cadell (Loftus and Greensmith 1988). Deposited in fluvial, lacustrine and deltaic environments with rare marine influences, the Fife deposits have been separated into five lithostratigraghical formations (Browne *et al.* 1999), (Fife Ness, Anstruther, Pittenweem, Sandy Craig, and Pathhead Formations) based on their lithological content and palynology (Browne *et al.* 1999) (Figure 2-14). The Fife Ness Formation (c.230 m thick) is found only in east Fife and contains fluvial and lacustrine upward-fining sandstone and mudstone; coal seams and marine beds are absent (Browne *et al.* 1999). The Anstruther Formation (c.810 m thick) contains thin upward-coarsening deltaic cycles capped with erosive upward-fining fluvial channel sandstones and locally thick multi-storey sandstones. Thin non-marine limestones and locally mined oil-shales occur with thin marine beds that contain restricted fauna. The Pittenween Formation (c.260 m thick) is similar to the underlying Anstruther Formation, although it contains less non-marine limestone. Marine units occur with more abundant and diverse fauna especially those found in the Macgregor Marine Bands (Wilson 1974), the first fully marine incursions to the Midland Valley during Carboniferous times (Wilson 1989). The Sandy Craig Formation (c.670 m thick) is also characterised by upward-coarsening deltaic cycles capped with erosive upward fining fluvial sandstones with non-marine limestones and oil shales. Marine units with restricted fauna occur but are rare. The Pathhead Formation (c.220 m thick) is more argillaceous than the underlying formations and it contains upward-coarsening deltaic sandstones, capped with fluvial sandstones. Marine bands and limestones, indicating periodic inundation of the delta by the sea from the NE (Stuart *et al.* 2001), become more prominent and contain more diverse fauna.

2.4.4 Clackmannan Group

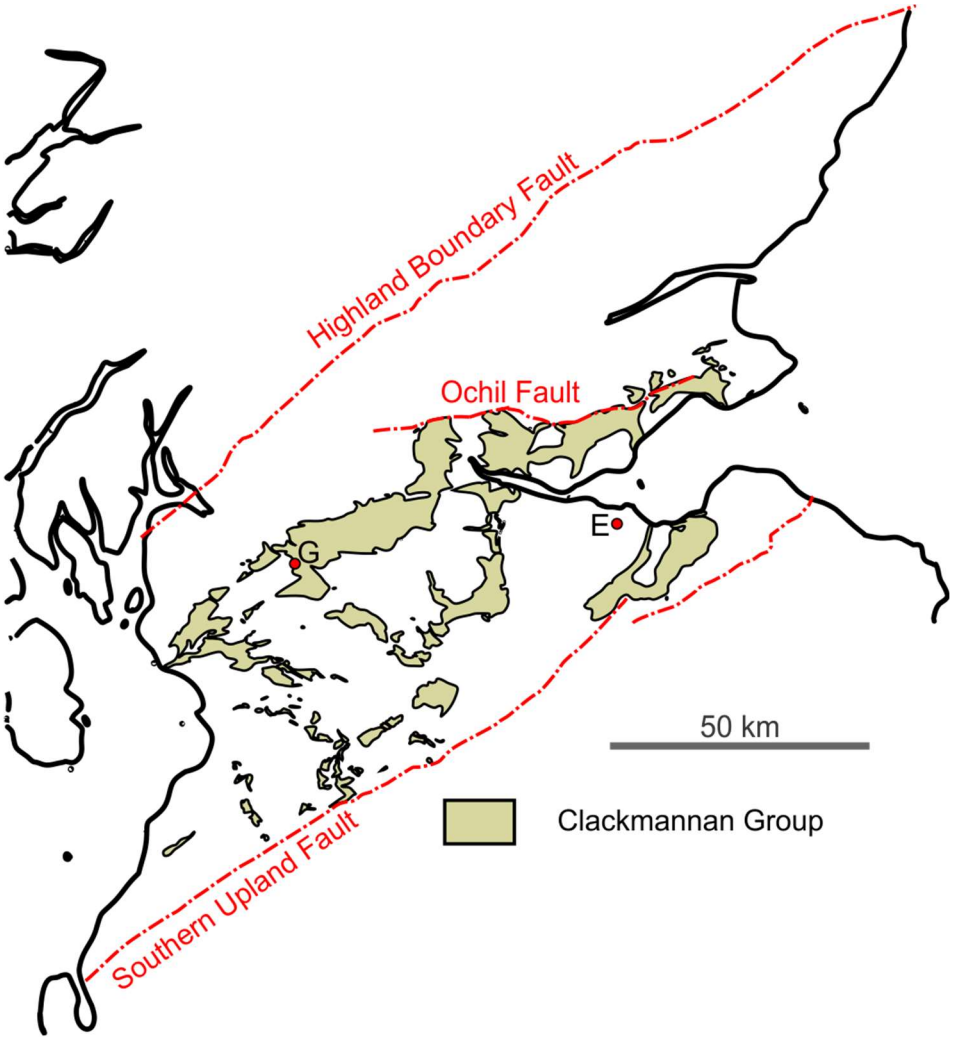

Figure 2-19: Simplified geological map of the Clackmannan Group outcrop locations. Adapted after Cameron and Stephenson (1985).

Comprised of the late Viséan Lower Limestone Fm (LLGS) and the Namurian Limestone Coal (LSC), Upper Limestone (ULGS), and Passage Group Formations (PGP) (Figure 2-14), the Clackmannan Group deposits of the Midland Valley (Figure 2-19) represent a time when the region crossed the equator and lay in an ever-wet, coal belt region dominated by Lycopod trees, forming vast primitive rainforests (Trewin 2002). The broadly similar, cyclical marine and fluvio-deltaic deposits of the Lower Limestone, Limestone Coal and Upper Limestone Formations which has yielded vast quantities of coal in the past (Underhill *et al.* 2008), are capped by the proximal, fluvial sandstone, Passage Formation (Forsyth *et al.* 1996). The volcanic activity that was prominent in the Strathclyde Group had now waned, with heat flow in the upper crust reducing, giving way to thermal subsidence and submergence of Devonian and Strathclyde volcanic highs. The Clyde Plateau, Bathgate Hills and Kinghorn Volcanic Formations persisted as topographic highs and areas of minimum subsidence, helping to divide the region into three major depocenters, the Ayrshire, Central Coalfield and Fife-

Midlothian basins (Figure 2-20). Widespread laterally persistent, transgressional marine limestones, e.g. the Hurlet Limestone, indicate that there were periodic marine influences on the depositional environment. Sediment laid down at this time displays a strong cyclicity, possibly reflecting glacio-eustatic sea-level changes (Read *et al.* 2002), with transgressive marine limestones marking interglacial maximum flooding stages and erosive based multi-storey fluvial sandstones defining lowstands.

2.4.4.1 Lower Limestone Formation

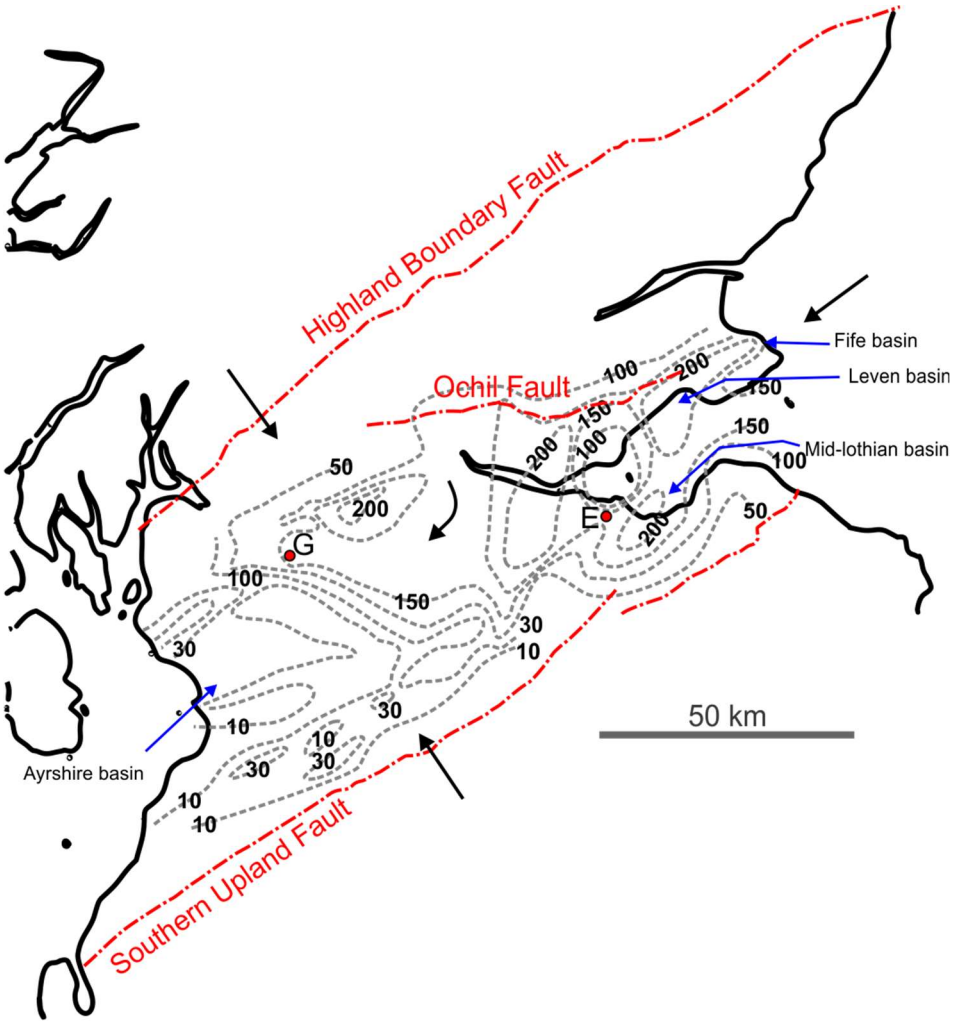

Figure 2-20: Lower Limestone Formation isopach map and palaeocurrent indicators. Isopachs in meters, also showing direction of transport of coarse grained siliciclastic material (black arrows) and locations of semi-isolated basins (blue arrows) adapted from (Read *et al.* 2002).

The base of the formation is the Hurlet Limestone (Figure 2-14), which marks the first basin wide marine transgression, where sea level covered almost the whole of the basin, leaving only a few isolated highs that escaped flooding (Read *et al.* 2002). The formation also includes six other major marine transgressions (Inchinnan, Blackhall, Main, Mid, Second, and Top Hosie limestones), all of which can be traced across the Midland Valley (Wilson 1989). The basin wide correlation indicates

the breakdown of barriers and a unification of the once semi-isolated sub-basins, though volcanic highs like the Clyde Plateau and Bathgate Hills would have persisted as topographic highs, indicated by the isopach map (Figure 2-20) (Read *et al.* 2002). Compared to the underlying Strathclyde Group, the deposits are more rhythmic cycles of shallow water marine shelf sediments with minor fluvio-deltaic influences. The presence of coals, particularly in the east, indicates periods of low water levels, enabling the colonisation of plants, though the coals are not laterally persistent nor abundant. Active faults were still a control on sedimentation, as the variations on unit thickness around faults indicate, with differential subsidence controlled by the lava piles.

2.4.4.2 Limestone Coal Formation

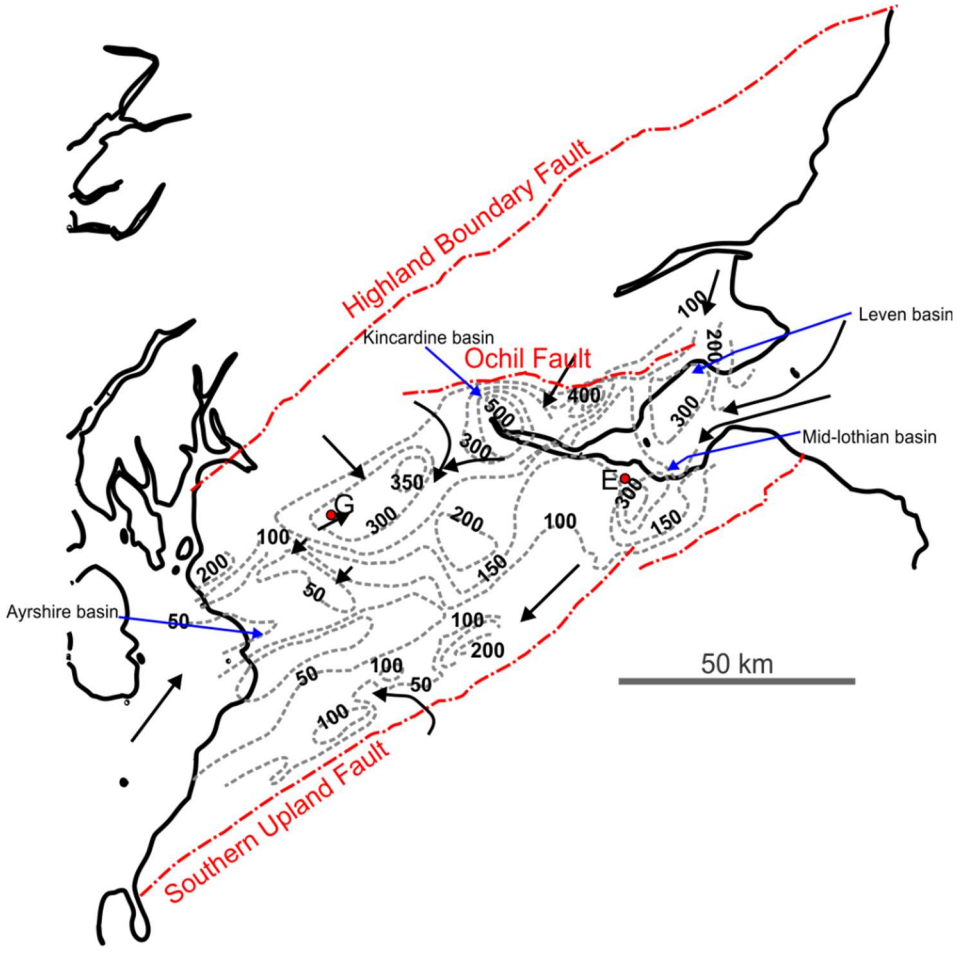

Figure 2-21: Limestone Coal Formation isopach map and palaeocurrent indicators. Isopachs in meters, also showing direction of transport of coarse grained siliciclastic material (black arrows) and locations of semi-isolated basins (blue arrows) adapted from (Read *et al.* 2002).

The Top Hosie Limestone marks the base of this formation (Figure 2-14), which is the lowermost of the Namurian deposits recognised in the Midland Valley and renowned for the numerous coal seams and ironstones, many of which have been mined in the past. Sedimentation was predominantly fluvio-deltaic and non-marine high frequency cycles (Read 1994) however, there is evidence of two major

marine incursions, the Johnston Shell Bed and the Black Metals Marine Band (Read 1994). These were derived from the west, opposed to Lower Limestone marine incursions from the east (Read *et al.* 2002). Though little quantitative provenance analysis has been completed, it has been suggested that early Namurian uplift of the 'Highland High', may have provided proximal sediment supply to Midland Valley, along with more distal supply from Scandinavia (Read *et al.* 2002). Faults continued to dominate sedimentary patterns, although differential subsidence of older volcanic piles and minor volcanic activity on the Bathgate Hills, along the Bo'ness Line, and in north Ayrshire (Cameron and Stephenson 1985) had an influence, clearly indicated by the isopach map (Figure 2-21). Lateral changes in thickness and sedimentary style exist across the basin at this time with regularly spaced high frequency cycles linked to Milankovitch cyclicity (Weedon and Read 1995) in the west. In the centre of the basin, rapid subsidence in the asymmetrical Kincardine Basin, allowed thickness of 550 m to be reached (Figure 2-21), while the east was dominated by fluvial deposition.

2.4.4.3 Upper Limestone Formation

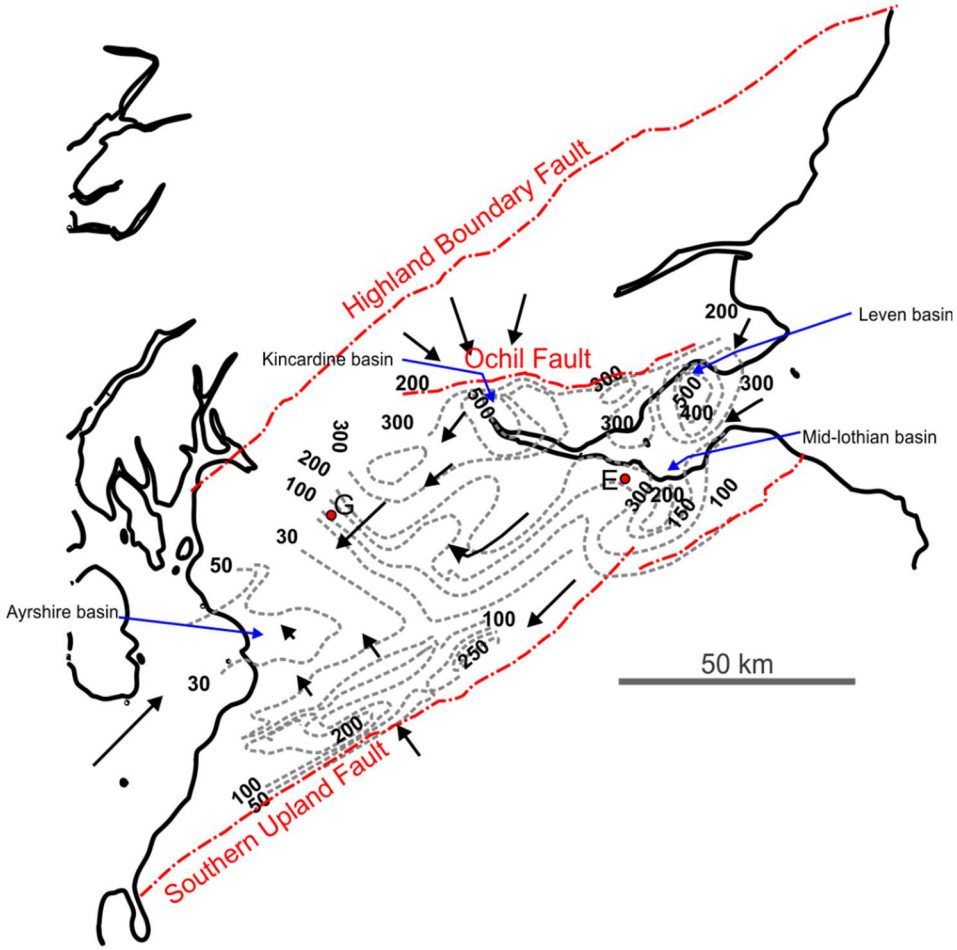

Figure 2-22: Upper Limestone Formation isopach map and palaeocurrent indicators. Isopachs in meters, also showing direction of transport of coarse grained siliciclastic material (black arrows) and locations of semi-isolated basins adapted from (Read *et al.* 2002).

The base of the formation is taken from the Index Limestone, while the upper limit is the Castlecary Limestone (Figure 2-14). The same structural controls continued to influence sedimentation, with the maximum onshore thickness still being found in the central Kincardine Basin with deposits reaching over 600 m thick (Browne *et al.* 1985). Volcanism and tectonism waned, but there was still activity in Ayrshire, Bo'ness Line, Bathgate hills, and Largo Law with movements on E-W faults (Rippon 1998). Cyclical sedimentation persisted but with an increase of marine influence compared to the Limestone Coal Formation. Marine transgression came from both the east and west allowing for the development of multiple laterally persistent marine limestones and muds which can be correlated across the basin (Read *et al.* 2002). Siliciclastic sediments still dominate basin fill with thick multi-storey and upward-fining fluvial sandstones and channel deposits, numerous thin coals are also present.

2.4.4.4 Passage Formation

The Passage Formation is the uppermost formation of the Namurian in the Midland Valley, the base is taken at the Castlecary Limestone or the unconformity that has removed it, with the top taken at the base of the Lowstone Marine Band (Figure 2-14). Rhythmic sedimentation was still taking place however, this has been somewhat obscured as the arenaceous deposits, with a maximum thickness of 380 m in the central Midland Valley, contain multiple erosively-based alluvial sandstones (Read *et al.* 2002). Thin marine shales and impersistent thin coal seams are present, indicating rapidly alternating uplift and subsidence. Extensive volcanism returned to Ayrshire and Fife but died out in the Bathgate Hills (Upton *et al.* 2004) along with local structural and basin inversion (Brand *et al.* 1980). As with other Clackmannan Group deposits, quantitative provenance analysis is lacking, but it has been suggested that the proximal source of the siliciclastic sediments was the uplifted 'Highlands High' (Muir 1963) with a limited input from the Southern Uplands High, while distal material would have been sourced from Scandinavia (Read *et al.* 2002).

2.4.5 Scottish Coal Measures Group

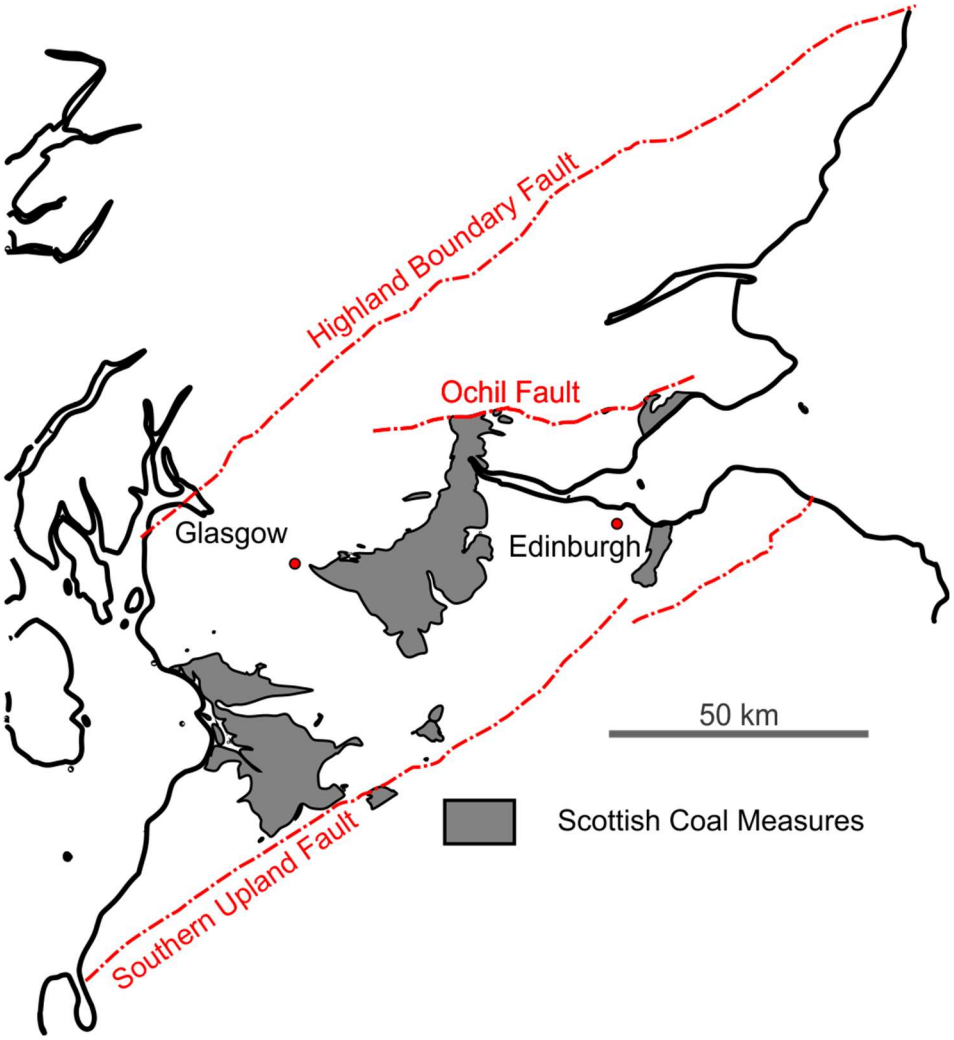

Figure 2-23: Simplified geological map of Scottish Coal Measures Group outcrop locations. Outcrops are eroded remnants at thickest locations of a once more extensive formation adapted from Cameron and Stephenson (1985).

The Scottish Coal Measures are entirely Westphalian in age and divided into the Lower, Middle and Upper Coal Measures formations by the Vanderbeckei and Aegiranum Marine Bands (Figure 2-14), which are traceable across northern Europe (Read *et al.* 2002). The correlatable Westphalian base is absent in the Midland Valley, instead the Coal Measures base is taken at the Lowstone Marine Band or its lateral equivalent and extends up to the Sub-Permian unconformity (Browne *et al.* 1999). The proposed provenance and sedimentation style of the upper Carboniferous deposits is similar to that of the Limestone Coal Formation, with cyclical fluvio-deltaic sediments with erosive channel deposits, numerous coals, and rare marine incursions (Read *et al.* 2002). Replacing the sandy braided river deposits of the upper Passage Formation, coal forming conditions were re-established and thick coal seams developed as the Midland Valley lay within the Euramerican floral province, where prolonged coal swamps conditions dominated by Lycopods thrived (Cameron and Stephenson

1985). As the Midland Valley moved north of the equator, out of the ever-wet belt of the Namurian, through a seasonally wet region, by the end Carboniferous, a semi-arid climate was established due to the rain shadow created by the Variscan Orogen to the south (Stephenson 2003), replacing the Lycopods with tree and seed ferns, and, later, conifers (Read *et al.* 2002). Following the tectonic instability of the Passage Formation, the Midland Valley reverted back to a region of subsidence with diminished fault activity; however, continued N-S compression from the Variscan orogeny to the south along with dextral strike-slip and associated E-W compression resulted in syn-sedimentary folding with anticline and syncline growth structures (Coward 1993; S.M. Corfield *et al.* 1996; Underhill *et al.* 2008). Subsidence slowed in the Kincardine Basin and Westfield basin (Brand *et al.* 1980) though increased in the Midlothian-Leven Basins (Read 1988). Oxidation and reddening of the Upper Coal Measures sediments, mainly alluvial and braided river deposits, was caused by the alteration, replacement and destruction of coal seams (Cameron and Stephenson 1985). In the latest Carboniferous and early Permian, a major change in tectonic style occurred when N-S extension caused by the gravitational collapse of the Variscan Orogen, created or rejuvenated existing E-W faults with associated dyke and sill intrusion (Upton *et al.* 2004; Monaghan and Parrish 2006) along with post-depositional basin inversion (Underhill *et al.* 2008).

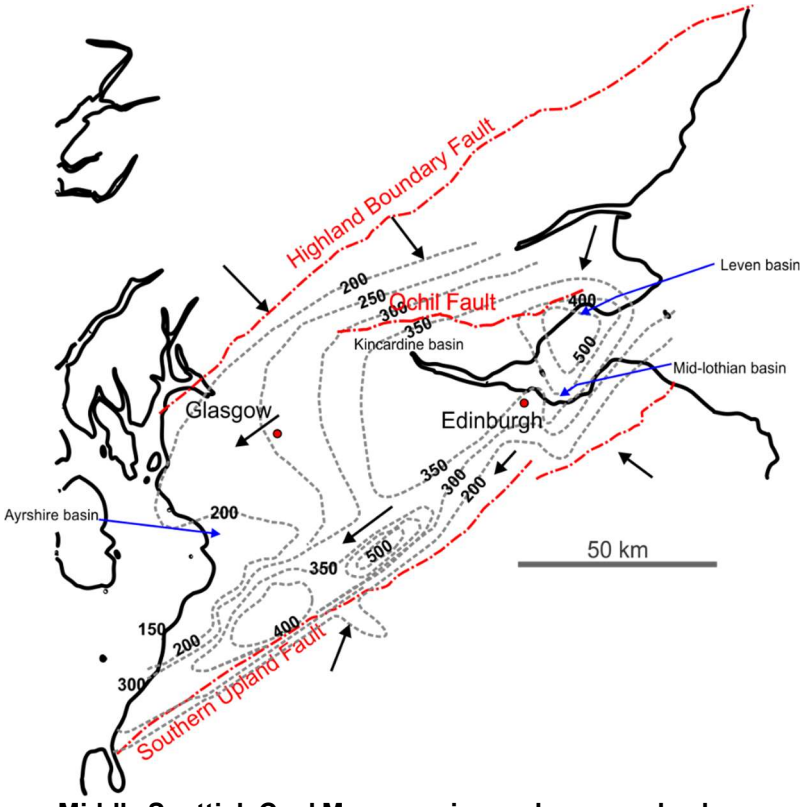

Figure 2-24: Lower-Middle Scottish Coal Measures isopach map and palaeocurrent indicators. Isopachs in meters, also showing direction of transport of coarse grained siliciclastic material (black arrows) and locations of semi-isolated basins (blue arrows) adapted from (Read *et al.* 2002).

2.4.6 Carboniferous-Permian Volcanic activity

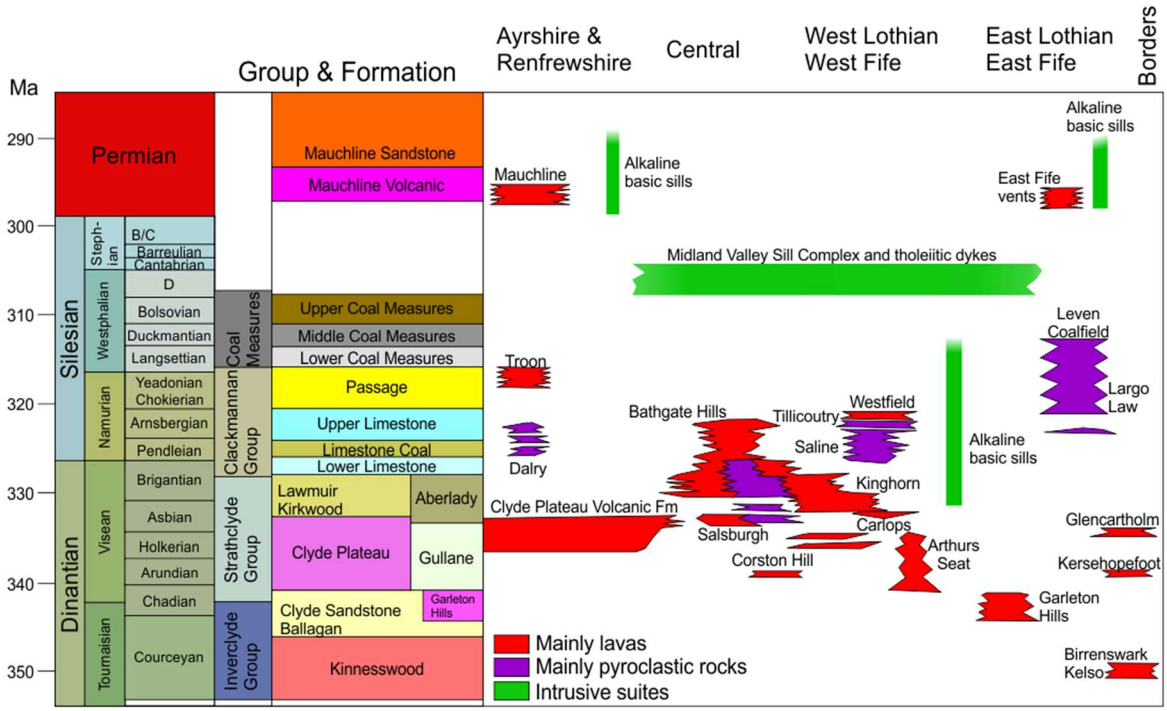

Figure 2-25: Carboniferous-Permian volcanism across the Midland Valley. Extrusive and intrusive igneous activity in the Midland Valley has been divided by location and eruption style. Modified from Monaghan *et al.* (2014).

The timing and region of Carboniferous-Permian volcanic activity has been summarised in Figure 2-25 above, while the geographical locations of the outcrops are shown in Figure 2-26 below. Following its absence since the Early Devonian, magmatic activity returned to the Midland Valley in the early Viséan (Figure 2-25) (Cameron and Stephenson 1985) initially in the east with the Garleton Hills Volcanic Formation, followed by Arthur's Seat Volcanic Formation (Monaghan *et al.* 2014). In the west and partly coeval with the latest stage of the Arthur's Seat Volcanic Formation, was the Clyde Plateau Volcanic Formation (Monaghan and Parrish 2006; Monaghan *et al.* 2014). Lavas erupted through fissures with a Caledonian NE-SW alignment, reached a thickness of c.900 m in places and extended some 3000 km^2 (Read *et al.* 2002). Following this effusive activity, there was an increase in pyroclastic style eruptions and the focus of the volcanic activity shifted towards the central Midland Valley, in the Lothians, and Fife areas (Figure 2-25). Significant and persistent eruptions occurred from the late Viséan through the Namurian, forming the Kinghorn and Bathgate Hills Volcanic Formations. Eruptions then became smaller with more localised centres at Largo Law, Troon, and Elie (Upton *et al.* 2004). Early Permian activity in the Mauchline Basin erupted lavas with a thickness of over 200 m with multiple coeval volcanic vents occurring in Fife (Read *et al.* 2002).

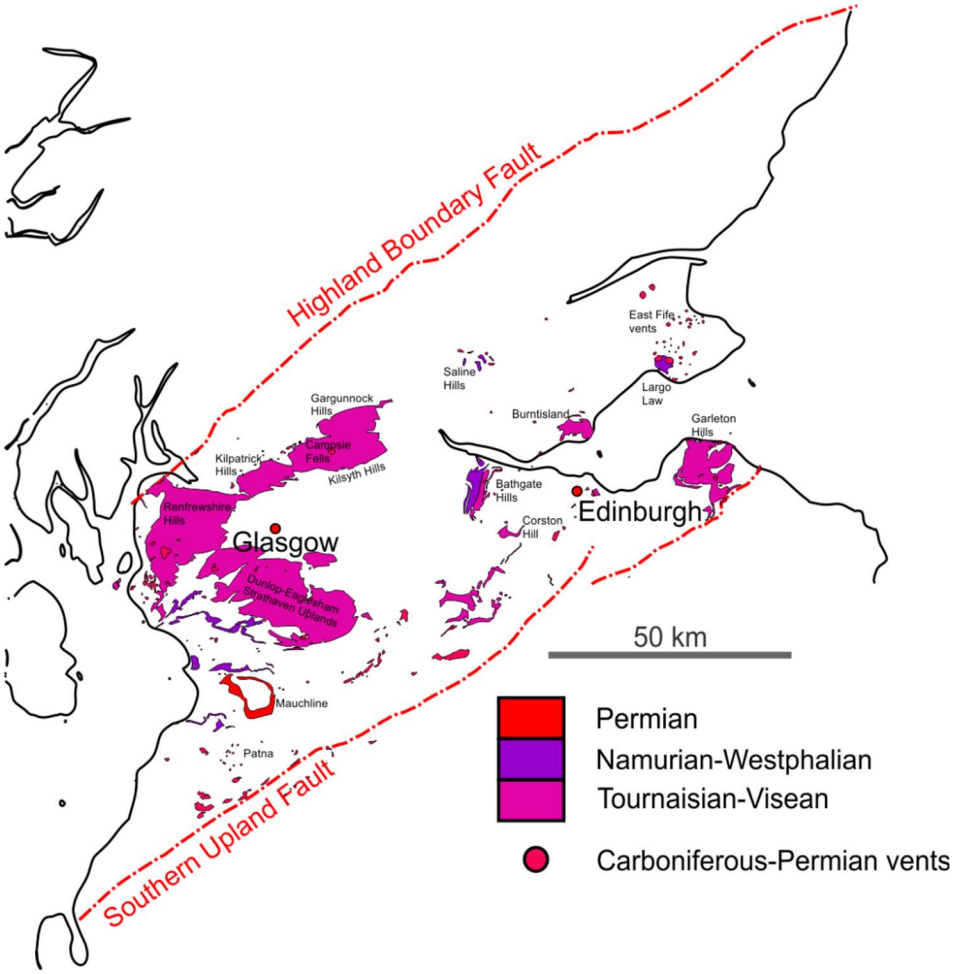

Figure 2-26: Carboniferous and Permian volcanic outcrop locations across the Midland Valley. Modified from Cameron and Stephenson (1985).

There were also multiple episodes of intrusive activity across the Midland Valley during the Carboniferous and Permian (Ayrshire), which can be divided into alkaline basic and quartz dolerite-tholeiitic intrusions (Figure 2-27) (Cameron and Stephenson 1985). Timing and regions of the widespread alkaline basic intrusions, which can be further sub-divided on the bases of their chemical signature, have been summarised in Figure 2-25 above, along with their geographical extent (Figure 2-27a) (Cameron and Stephenson 1985; Upton *et al.* 2004). The quartz-dolerite-tholeiitic intrusions (Figure 2-25) have a widespread distribution across the Midland Valley (Figure 2-27b) but intruded during a short-lived event. The suite consists of generally E-W trending tholeiitic dykes and associated quartz dolerite sills collectively known as the Midland Valley Sill-Complex, where extensional faulting provided conduits for pulses of magma to exploit (Stephenson 2003). Doleritic dykes located in the SW of the Midland Valley with a NW-SE trend and associated sills, have been attributed to the Paleogene dyke swarm related to the Mull Central Complex (Macdonald *et al.* 2015).

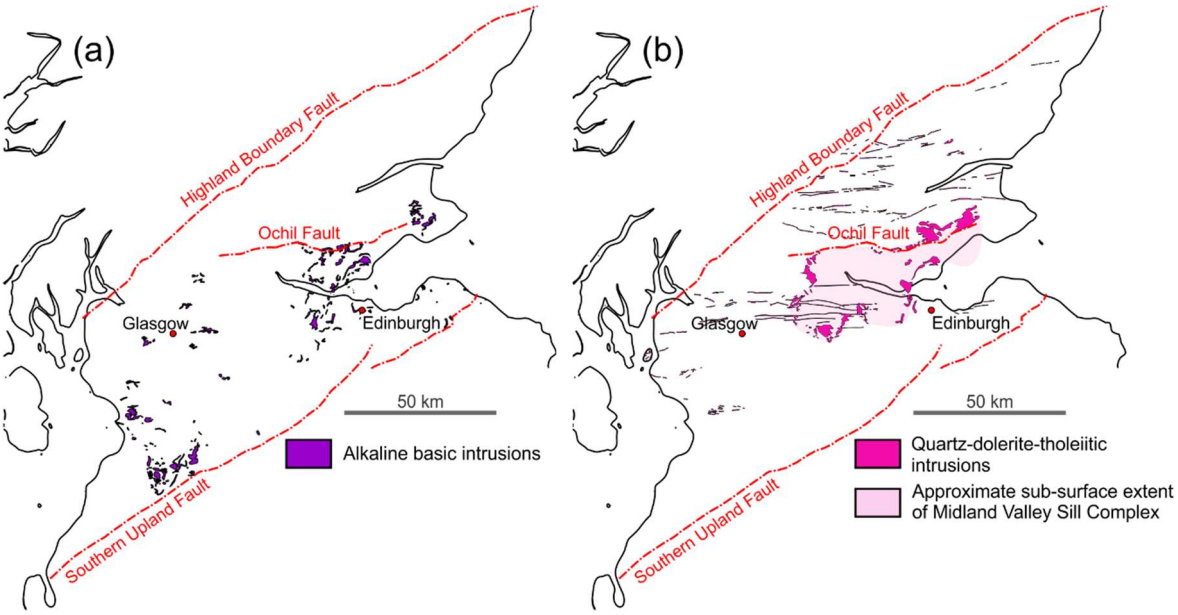

Figure 2-27: Carboniferous and Permian intrusions locations across the Midland Valley. (a) Extent of the Alkaline basic suite. (b) Extent of the quartz-dolerite-tholeiitic intrusions. Adapted from Upton *et al.* (2004).

2.5 Post-Carboniferous evolution of the Midland Valley

Onshore post-Carboniferous sediments in the Midland Valley are found only in Ayrshire's Mauchline Basin (Figure 2-28). The Mauchline Sandstone Formation consists of approximately 450 m of Permian, red aeolian sandstones that were deposited in an arid, desertic environment (Cameron and Stephenson 1985). The quartz rich sandstones display large scale dune cross bedding with windblown quartz grains and flash flood deposits (Mykura *et al.* 1967). This gives further evidence to the change in climate that was indicated by the reddening of the Upper Coal Measure deposits, as the Midland Valley now approached c.10° north of the equator and entered an arid to semi-arid climate region (Cameron and Stephenson 1985). Evidence for Permian volcanic activity exists in Ayrshire, with Mauchline lavas outcrop around the overlying sandstones along with numerous alkaline intrusions, which are also present in Fife and East Lothian (Figure 2-26) (Stephenson 2003; Upton *et al.* 2004).

Mesozoic sediments are present in the areas surrounding the Midland Valley of Scotland e.g. in the Firth of Clyde, Forth Approaches (Cartwright *et al.* 2001), Arran, and Northern Ireland (Penn *et al.* 1983) (Figure 2-4) and a more regional overview of their occurrence onshore Scotland and in offshore basins is given in Section 2.1 above. The presence of these Mesozoic deposits, being of substantial thicknesses in some localities offshore has led to the hypothesis that sediments of a similar age once encroached onto what is now the onshore Midland Valley (Vincent *et al.* 2010). If so, regional uplift

of Scotland since the opening of the North Atlantic (Hillis *et al.* 1994) and/or underplating of the proto-Icelandic plume in the Cenozoic (White 1988; Persano *et al.* 2007), may provide a mechanism for the removal of the younger successions, exposing the underlying Carboniferous-Permian rocks.

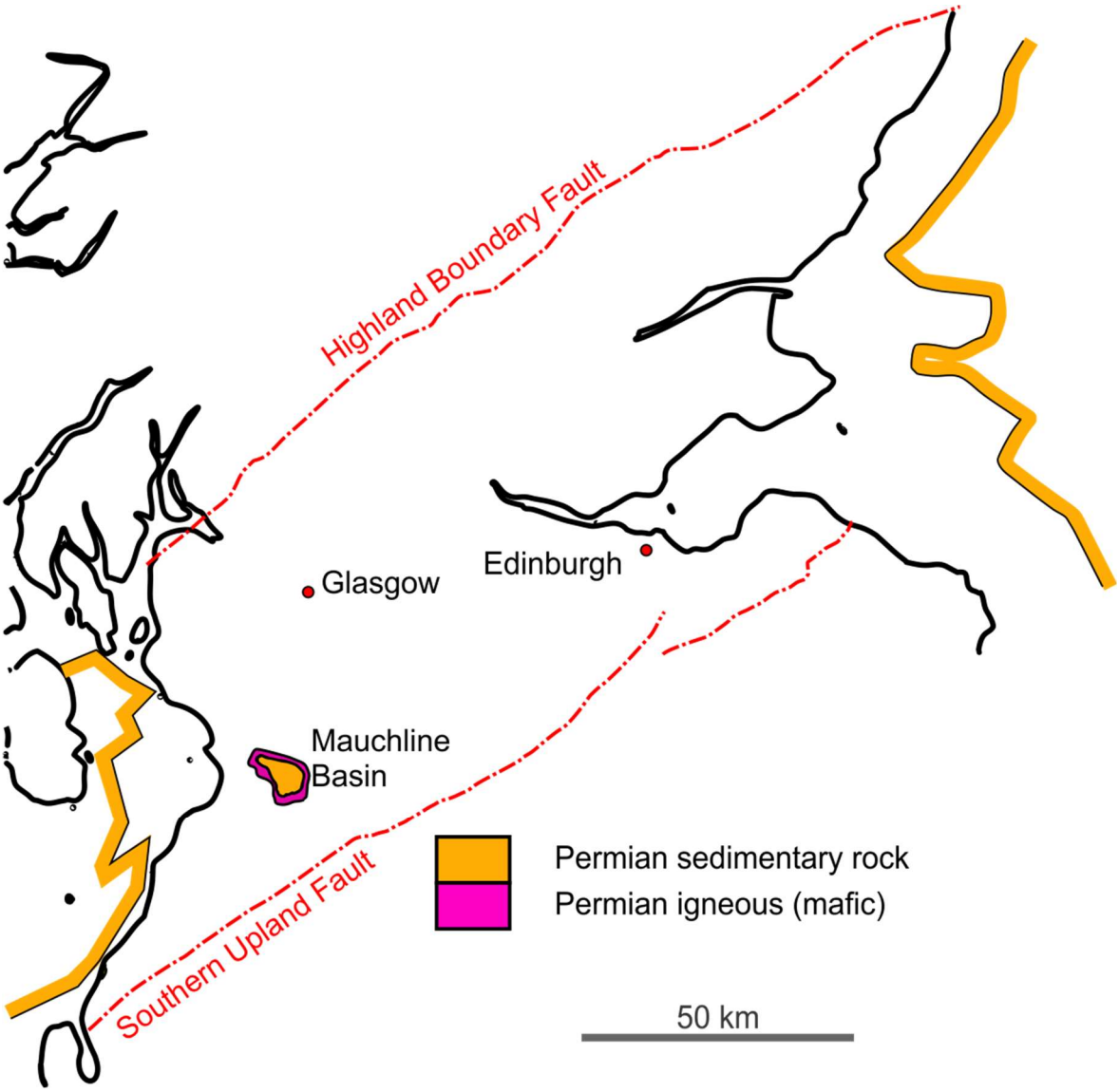

Figure 2-28: Simplified geological map of Permian outcrop location (Mauchline Basin) across the Midland Valley and offshore extent of Permian and younger units. Adapted after Cameron and Stephenson (1985).

Chapter 3 Methodology

This chapter presents the principles of the analytical techniques utilised in this thesis, along with the uncertainties associated with the data. It also describes the modelling procedures applied and d the graphical methods adopted for a clear representation of the data, which are interpreted later in the thesis.

3.1 Introduction

The universe and all its contents are comprised of naturally occurring chemical elements (X). These primary constituents of all matter are distinguished by the number of protons (Z) and neutrons (N) held within the atomic nucleus, the combined mass of which defines an elements mass number (A) (Figure 3-1) (Rutherford 1920; Masson 1921). The number of protons define the chemical properties of each element and is therefore responsible for the elements position in the periodic table (Dickin 2018). Elements with the same number of protons (Z) but a different number of neutrons (N), have the same chemical properties but different physical characteristics, i.e., they have a different mass; these nuclides are called isotopes (Figure 3-1) (A=N+Z) (Soddy 1913).

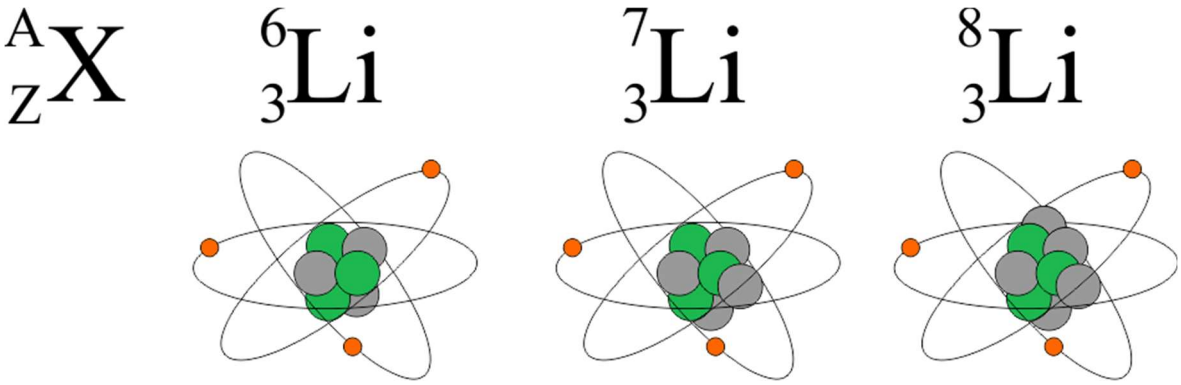

Figure 3-1: Isotopes of lithium. Figure shows an example of isotopes for the element lithium. Though the element remains the same due to the fixed number of protons (Z-green), the mass of the element (A), is increased by the addition of neutrons (N-grey).

Atomic nuclei may be stable or unstable, in the latter case they decay radioactively from the initial parent isotope (N_p) to subsequent daughter isotope(s) (N_d). This decay may occur via one or more steps producing various daughter products, proceeding until eventually a stable isotope is formed. The mechanisms for decay towards stable isotope production are alpha decay, beta decay, gamma decay, electron capture and nuclear fission (Faure 1977). Unstable isotopes may survive from milli-seconds to millions of years, depending on their decay constant (λ). As daughter production proceeds at a known rate, a measurement of parent and daughter concentration can be used to calculate the

time that has elapsed since accumulation began, providing clocks that operate on a geological timescale.

3.1.1 Mass spectrometry for isotopic analysis

Discrimination between isotopes and quantification of their abundance is achieved using a mass spectrometer (Dempster 1918). There are three principal mass spectrometry techniques applied to U-Pb geochronology: one of these is the Isotope Dilution–Thermal Ionisation Mass Spectrometry (ID-TIMS), which requires the dissolution and heating of the sample to high temperature (thermal ionisation) to measure the isotopes once held within the crystal lattice (Parrish *et al.* 2003). While the precision of this technique is much greater than alternative in-situ methods, its expense and time-consuming methodology usually exclude it from being used to investigate large sample quantities, such as those needed for provenance studies. When the Secondary Ionisation Mass Spectrometry (SIMS) is adopted, the sample is introduced into the mass spectrometer having been ablated in-situ, by a small diameter high energy ion beam (Andersen and Hinthorne 1972); however, laboratories with SIMS capabilities are rare as the equipment and the analyses are very costly. When the Laser Ablation Inductively Coupled Mass Spectrometry (LA-ICP-MS) is used (Fedo *et al.* 2003), a small volume (usually a cylinder with diameter of 20-50 microns and a depth of ~10 microns) of the sample is introduced to the mass spectrometer following ablation and ionisation of the ablated material in an argon (Ar) plasma. While in the traditional AFT thermochronology a mas-spectrometer is not used, recently AFT ages have been produced by a few laboratories using LA-ICP-MS (Chew and Donelick 2012). In this thesis, both the zircon and apatite (U-Pb) and apatite fission track ages were produced using a LA-ICP-MS; the protocol used is described in the following sections. Detrital apatite and zircon U-Pb determinations were performed at the NERC Isotope Geosciences Laboratory-Geochronology and Tracers Facility (NIGL-GTF) at BGS, Keyworth. The LA-ICP-MS facilities at the University of Glasgow and the University of Melbourne were used for the determination of isotopes used in AFT thermochronology (section 3.3). The textural control on the analysis sites was done at the University of Glasgow using optical microscopes and the Scanning Electron Microscope (SEM) at the imaging spectroscopy and analysis centre (ISAAC) (Chapter 4).

3.1.2 Laser Ablation Inductively Coupled Plasma Mass Spectrometry (LA-ICP-MS)

In an Inductively Coupled Plasma Mass-Spectrometer (ICP-MS) the sample is introduced following either dissolution or ablation and is ionised in a plasma. The ionic particles, under high vacuum conditions, pass through a collision cell to remove interferences that can hamper the signal and are focused into a beam by the ion optics, which guide the sample into the mass-spectrometer, discarding any particles with no charge (Košler 2007). The mass-spectrometer acts as a filter, sorting the ions according to their mass to charge ratio. The separated ions then impact with a series of detectors which measure the count rates (counts per second, cps) on each measured mass, which are then transformed, using internal and external calibration protocols into isotopic concentrations (Sylvester 2001). Like SIMS, LA-ICP-MS has the capabilities of *in-situ* analysis, however LA-ICP-MS is faster, more cost effective, capable of a greater throughput and to accurate (~±1 %) determinations at ppm level (Košler and Sylvester 2003). Due to the high precision, fast throughput and relatively low costs, the LA-ICPMS is used for a vast range of isotopic determinations, including geo- and thermo-chronology (Chew and Spikings 2015).

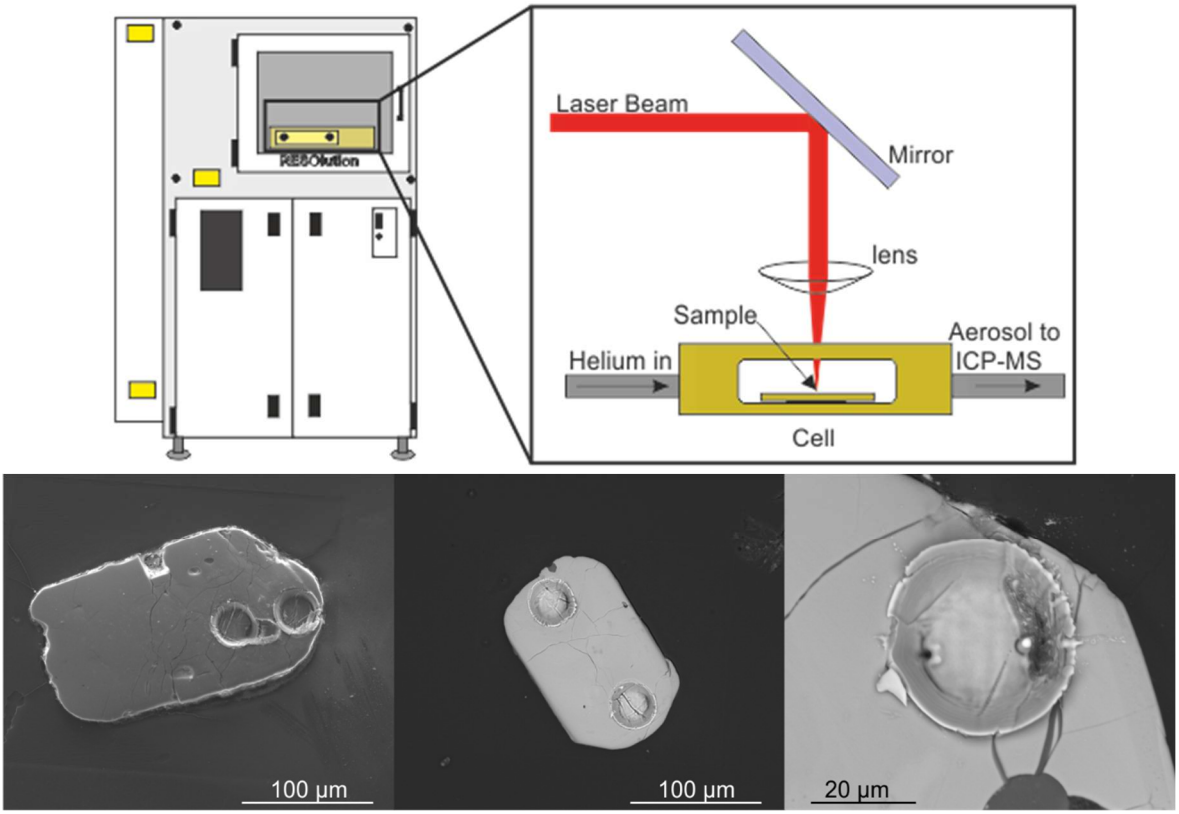

Figure 3-2: Typical laser ablation setup and ablation pit examples. Modified from the laser ablation unit at the University of Glasgow, ASI Resolution 193 ArF excimer laser and Lauren Technic S-155 ablation cell. Ablation pit examples on zircon from sample EM-14, as an example.

The LA-ICP-MS technique is partially destructive, as a laser focussed on the material surface ablates the sample (Figure 3-2). The ablated material is transported as an aerosol via a carrier gas, usually helium, towards the mass spectrometer, which could be a quadrupole single or multi-collector, or magnetic sector field mass spectrometer, depending on the accuracy, precision, and type of data required. In this thesis, a quadrupole single collector has been used when acquiring data for AFT thermochronology (Universities of Glasgow and Melbourne) while a multi-collector was used when acquiring data for U-Pb geochronology (NIGL-GTF at BGS, Keyworth); the main features of this kind of equipment are described below. The sample aerosol passes through the inductively coupled plasma (ICP), where it is ionised (Figure 3-3). Inter element fractionation may occur during ablation, however short wavelength lasers (i.e., 193nm ArF excimer, Figure 3-2) were used to gather the data in this investigation meaning this fractionation has been greatly reduced (Chew and Donelick 2012). Fractionation may also occur during the transportation of the aerosol towards the ICP and in the ICP itself. This fractionation is limited by shortening the space the aerosol needs to travel, by positioning the laser as close as possible to the ICP, and it is corrected for by bracketing the unknown samples with a standard reference material of known elemental abundances and isotopic ratios. The correction derived from the reference material is applied to the unknown samples increasing the accuracy of the data, however the full extent of the external uncertainty may not be fully captured and therefore the analytical errors may be underestimated (Paton *et al.* 2011).

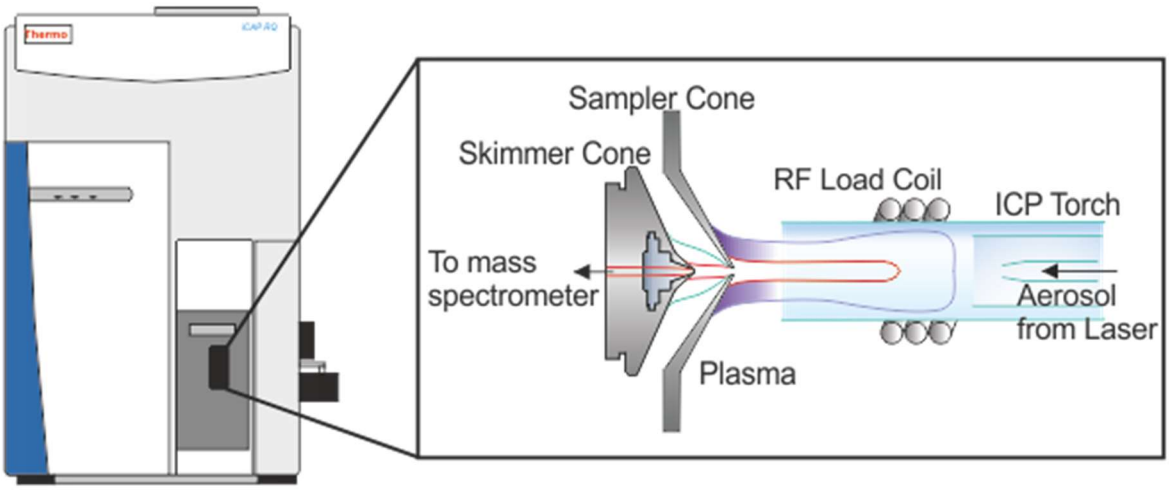

Figure 3-3:Typical Inductively Coupled Plasma (ICP). Modified from the ICP MS unit at the University of Glasgow. Radio frequency (RF) load coil, encircles the ICP torch and generates the magnetic field to stabilise the plasma. Sampler cone, outer cone interface with the plasma, allows for a pressure reduction before the sample interacts with the skimmer cone where the ion beams can expand. The ion-beam representative of the analyte-rich portion of the plasma then passes through the skimmer cone to the mass spectrometer.

3.1.3 The age equation

Isotopic dating techniques are based on the natural radioactive decay of the unstable parent isotope (N_p) producing a daughter product (N_d) at a rate defined by the decay constant (λ). The decay constant, the probability that a nucleus will decay within a given period of time, has a specific value for each radionuclide and is expressed in units of inverse time (time^{-1}). The rate of decay is proportional to the amount of unstable parent isotope remaining after any time (t) (Rutherford and Soddy 1902):

$$\mathrm{d}N_p/\mathrm{dt} = -\lambda N_p \tag{3.1}$$

The change in the abundance of the parent isotope over time is calculated by measuring the initial number of parent isotope present $(N_p)_0$ and assuming that at $t = 0$ none of the parent isotopes have yet decayed:

$$N_p = (N_p)_0 e^{-\lambda t} \tag{3.2}$$

However, the initial parent isotope abundance is usually unknown. To calculate this, both the present amounts of parent and daughter isotopes are necessary. Equation (3.2) can be written as:

$$(N_p)_0 = N_p\, e^{\lambda t} \tag{3.3}$$

Given that the abundance of the daughter at any time is:

$$N_d = \left(N_p\right)_0 - N_p \tag{3.4}$$

Equation (3.3) can be substituted into equation (3.4) to give:

$$N_d = N_p\,(e^{\lambda t} - 1) \tag{3.5}$$

Or, if an initial daughter (N_{d_0}) needs to be considered:

$$N_d = N_{d_0} + N_p\,(e^{\lambda t} - 1) \tag{3.6}$$

Equation 1.6 can be rearranged for t, to give the general form of the isotopic age equation (3.7). Thus, by measuring the parent and daughter isotope abundances, time (t) since the beginning of daughter accumulation can be calculated (Parrish *et al.* 2003):

$$t = \frac{1}{\lambda} \ln \left(\frac{N_d}{N_p} + 1 \right) \tag{3.7}$$

The rate of decay of a radionuclide is often referred to as the 'half-life' ($t_{1/2}$) of the isotope (Rutherford and Soddy 1902). This is defined by the amount of time that is required for half the parent isotopes to decay into daughter isotopes:

$$t_{1/2} = \frac{\ln 2}{\lambda} \tag{3.8}$$

These equations form the fundamental basis of many geochronological and thermochronological dating techniques such as, ^{40}K-^{40}Ar, ^{40}Ar-^{39}Ar, ^{87}Sr-^{86}Sr, ^{176}Lu-^{176}Hf, ^{187}Re-^{187}Os, AFT, and U-Pb series dating (Dickin 2018). Each system utilises radioactive decay and can be applied to a specific geological setting depending on the question that is being addressed. This thesis will utilise U-Pb geochronology on detrital apatite and zircon and AFT thermochronology on detrital apatite from the Midland Valley of Scotland in attempt to: trace the provenance of clastic sediments found in the sedimentary basin; elucidate palaeogeographic and palaeotectonic evolution; highlight sediment transport pathways; discriminate potential source regions of the sedimentary material; and provide insight into the post burial thermal history of basin.

3.2 Geochronology

3.2.1 Introduction

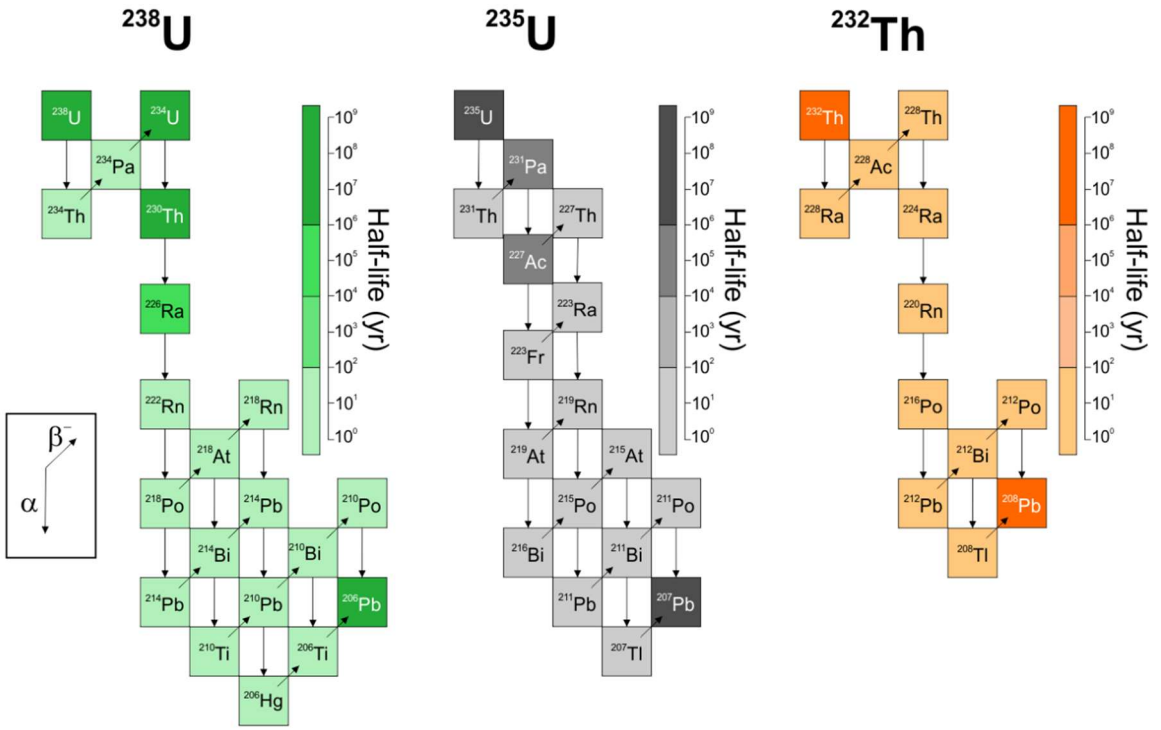

Figure 3-4: U-(Th)-Pb decay series for ^{238}U, ^{235}U, and ^{232}Th. Colour bars give an indication of the relative stability of the intermediate daughter products, while the arrow directions indicate the decay process i.e. alpha or beta decay, image redrawn from Dickin (2018).

U-Pb dating is one of the most widely used dating techniques in geoscience (Hanchar 2013), as the lengthy half-lives of the isotopic series means they are ideally suited for analysis investigating processes acting over geological time (Table 3-1).

Decay route			Half-life ($t_{1/2}$)	Decay constant (λ) years^{-1}
^{238}U	→	^{206}Pb	4.47×10^{9}	1.55125×10^{-10}
^{235}U	→	^{207}Pb	0.704×10^{9}	9.8485×10^{-10}
^{232}Th	→	^{208}Pb	14.01×10^{9}	0.49475×10^{-10}

Table 3-1: Half-lives and decay constants of some radioactive isotopes used in this thesis. Modified from Jaffey et al. (1971).

The decay of the parent, ^{238}U, ^{235}U, ^{232}Th isotopes to their respective daughters, ^{206}Pb, ^{207}Pb and ^{208}Pb, proceeds through a complex series of decay chains (Figure 3-4). The relatively short-lived intermediate members of each series can be generally ignored when timescales of millions of years are involved as secular equilibrium can be assumed (Faure 1977). In geochronology, the parent-

daughter ratio is measured in naturally occurring minerals e.g., zircon, apatite, and monazite, to calculate the amount of time that has passed since accumulation of daughter isotope began.

3.2.2 Geochronological equations

The equations for these radiogenic systems can be derived from the general equation (3.6):

$$^{206}Pb^{*} = {}^{206}Pb_{i} + {}^{238}U\,(e^{\lambda_{238}t} - 1) \quad (3.9)$$

$$^{207}Pb^{*} = {}^{207}Pb_{i} + {}^{235}U\,(e^{\lambda_{235}t} - 1) \quad (3.10)$$

$$^{208}Pb^{*} = {}^{208}Pb_{i} + {}^{232}Th\,(e^{\lambda_{232}t} - 1) \quad (3.11)$$

Where (*) indicates radiogenic Pb and (i) indicates initial abundance of isotope in the crystal before decay of the parent isotopes commences. These equations can be simplified if the minerals being dated do not incorporate Pb into their crystal lattice during crystallisation, as this reduced Pb_i to 0; one of such minerals is zircon. As mass spectrometers measure ratios of elements more accurately and precisely compared to absolute concentrations, measuring the parent-daughter ratio produces a more accurate age. Thus equations (3.9), (3.10), and (3.11) can be rearranged to provide the time that has passes since the accumulation of the daughter product began i.e., the isotopic "age":

$$t_{206} = \frac{1}{\lambda_{238}}\ln\left(\frac{^{206}Pb^{*}}{^{238}U} + 1\right) \quad (3.12)$$

$$t_{207} = \frac{1}{\lambda_{235}}\ln\left(\frac{^{207}Pb^{*}}{^{235}U} + 1\right) \quad (3.13)$$

$$t_{208} = \frac{1}{\lambda_{232}}\ln\left(\frac{^{208}Pb^{*}}{^{232}Th} + 1\right) \quad (3.14)$$

The isotopic "age" is a function of the parent-daughter ratio ($\frac{N_d}{N_p}$), the decay constant (λ), and the initial Pb content (Pb_i), if present. A great strength of using U-Pb for geological dating is that the paired ^{238}U and ^{235}U isotopic system provides an internal quality assessment and disagreement in the resultant ages may indicate open system behaviour, such as Pb loss or inheritance (Dickin 2018).

Another age can be calculated using the Pb isotopic ratio ($\frac{^{207}Pb^{*}}{^{206}Pb^{*}}$), which does not require the measurement of uranium (3.15); this equation is transcendental and is solved iteratively, changing the value of t until the two members of the equations are equal to each other (Dickin 2018). Combining these isotopic age equations provides a robust qualitative assessment for the isotopic age, even if Pb loss is suspected. Equation 1.15 can be applied to any U-bearing mineral, but is necessary in minerals, such as apatite, where Pb can be incorporated in the mineral lattice at the time of crystallization ($Pb_i \neq 0$). In this case, the determination of the non-radiogenic component ^{204}Pb provides a more robust age estimate for the grain being analysed.

$$\frac{^{207}Pb^{*}}{^{206}Pb^{*}} = \frac{\left(\frac{^{207}Pb}{^{204}Pb}\right) - \left(\frac{^{207}Pb}{^{204}Pb}\right)_i}{\left(\frac{^{206}Pb}{^{204}Pb}\right) - \left(\frac{^{206}Pb}{^{204}Pb}\right)_i} = \frac{1}{137.818}\frac{e^{\lambda 235t} - 1}{e^{\lambda 238} - 1} \quad (3.15)$$

3.2.3 Graphical display of U-Pb data

The results of the parent-daughter isotopic equations outlined above can be plotted graphically, providing a rapid data quality assessment. On a $\frac{^{206}Pb^{*}}{^{238}U}$ versus $\frac{^{207}Pb^{*}}{^{235}U}$ ratios plot, equations (3.16), (3.17), any U-Pb age should lie on a curve termed the 'Concordia' (Wetherill 1956) (Figure 3-5); if this is the case, the two ages calculated using equations (1.16) and (1.17) are the same, there has not been any loss or inheritance of U and/or Pb, and the crystal is deemed to have behaved as a closed system since the time of crystallisation.

$$\frac{^{206}Pb^{*}}{^{238}U} = (e^{\lambda 238t} - 1) \quad (3.16)$$

$$\frac{^{207}Pb^{*}}{^{235}U} = (e^{\lambda 235t} - 1) \quad (3.17)$$

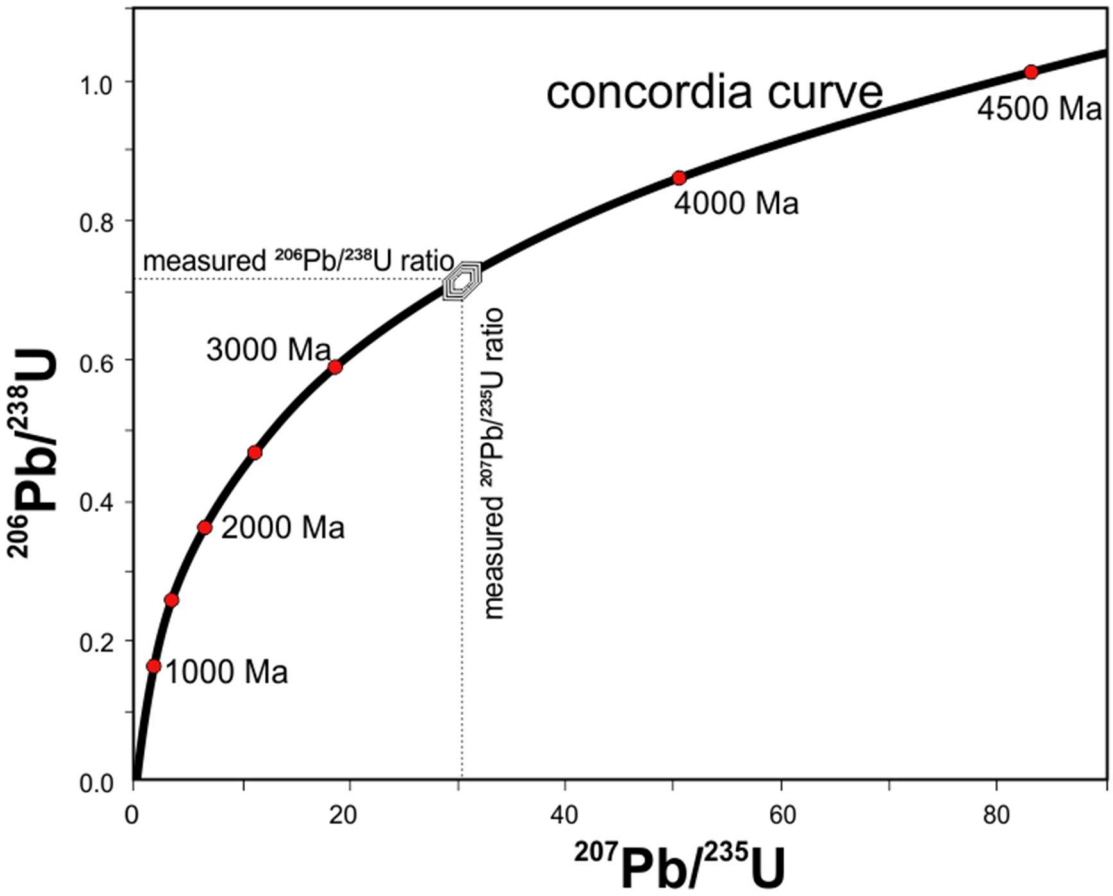

Figure 3-5: Wetherill Concordia curve displaying concordant data. Thick black line defines the Concordia curve with red spots showing geological time markers. $^{206}Pb/^{238}U$ and $^{207}Pb/^{235}U$ ratios of the same age, will plot along the Concordia curve (Wetherill 1956). Figure shows a zircon that has been analysed yielding concordant $^{206}Pb/^{238}U$ and $^{207}Pb/^{235}U$ ratios, giving it an age of c.3500 Ma.

However, physical processes may complicate the accurate determination of U/Pb ratios. The radioactive decay process that generates radiogenic Pb, also causes damage to the host minerals crystals lattice through recoil of the isotope undergoing decay. The decay of every ^{238}U, ^{235}U, and ^{232}Th parent isotope to their radiogenic daughter Pb, involves the expulsion of 8, 7, and 6 alpha particles (α-particles), respectively. Over time the α-recoil events form a percolating network of damage zones, causing the deterioration of the crystal lattice integrity and metamictisation (Chakoumakos *et al.* 1987). The metamict state may lead to the diffusion of radiogenic Pb out of the host mineral, decreasing the Pb/U ratio resulting in an erroneously young age, when analysed. As ^{206}Pb and ^{207}Pb accumulate at different rates, defined by their parental λ, their loss from the host crystal is not fractionated. Thus, a U/Pb ratio of a mineral that has experienced Pb loss, will plot along a discordant line ('discordia') Figure 3-6. This line will intercept the Concordia curve with the upper intercept indicating the initial accumulation/crystallisation age and the lower intercept indicating the time of Pb loss. Other possibilities for discordant data include, and mixed-age analysis of multiple

age zones i.e. a xenocrystic core and younger rim and Pb loss through diffusion due to a heating (metamorphic) event or weathering (Parrish *et al.* 2003).

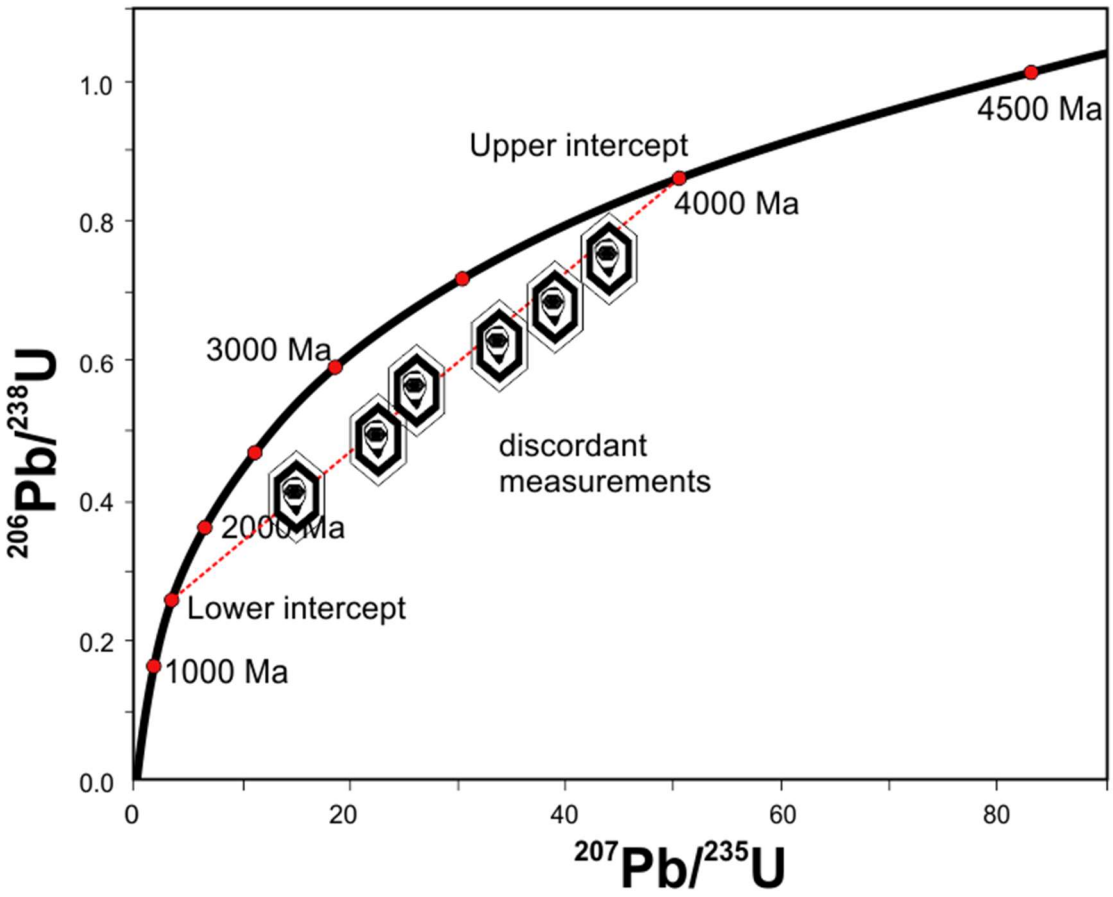

Figure 3-6: Wetherill Concordia diagram displaying discordant data. The figure shows a Wetherhill Concordia (1956) plot as above, however the plotted data are discordant, and they may have experienced Pb loss by diffusion. The analysis has formed an array, through which a discordia chord can be drawn. The upper intercept of this line gives an estimation of the crystallisation age while the lower intercept can be interpreted as an estimation of the (metamorphic) event that caused Pb loss.

An alternative to the Wetherill Concordia diagram outlined above is the Tera-Wasserburg (T-W) Concordia diagram (Tera and Wasserburg 1972) which plots $^{238}U/^{206}Pb$ and $^{207}Pb/^{206}Pb$ on the x-axis and y-axis respectively, and is preferred when visualizing younger ages or minerals with a potential common Pb component. As with the Wetherill diagrams above, analysed samples that have not experienced Pb loss will be concordant, while discordant data are an indication of open system behaviour or the presence of common (Pb_i). As variable amounts of non-radiogenic Pb would be expected in detrital apatite, such as the ones analysed in this thesis, with unknown initial Pb_i component, a common Pb correction needs to be applied to produce meaningful results. This was achieved by plotting uncorrected U/Pb results in Tera-Wasserburg space (Figure 3-7), cogenetic apatite populations would typically form linear arrays; a linear regression through the data determines

the y-axis interception, which represents the initial $^{207}Pb/^{206}Pb$ ratio that, in turn, can be used to calculate the unanchored ^{207}Pb based correction (Mark *et al.* 2016). Multiple populations of apatite may be present within each sample, each representing an age population with its own initial $^{207}Pb/^{206}Pb$ ratio, if this is the case then a linear regression is fitted to each cogenetic population to produce population specific ^{207}Pb corrected U-Pb ages.

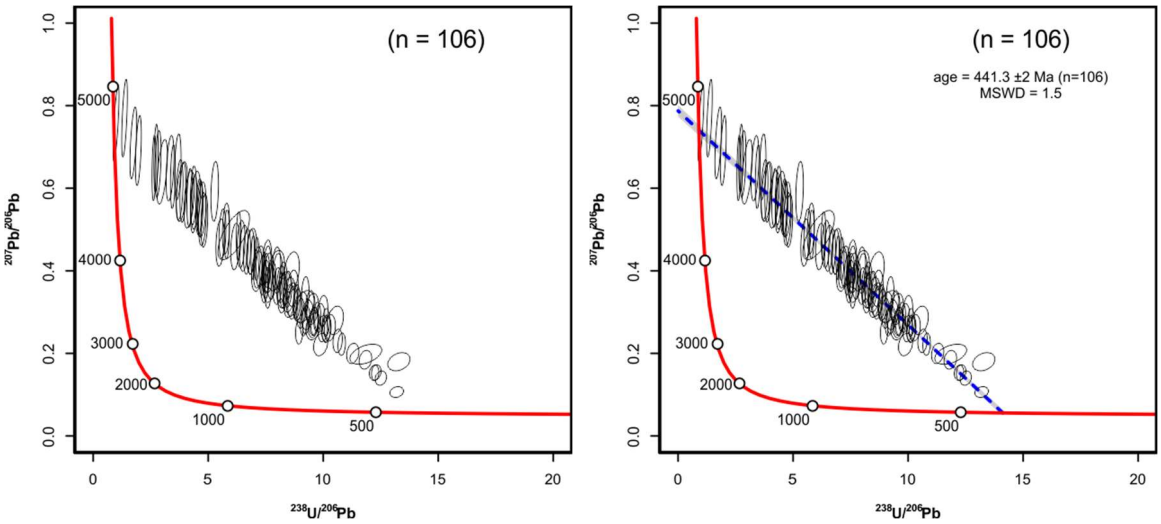

Figure 3-7: Tera-Wasserburg space plot for sample EM-17 collected for this thesis. The figure shows the data points (2σ error ellipses) form a linear array in T-W space indicating that the apatite grains are cogenetic (left). A linear regression line can then be fitted to this data (right) to provide an estimate of the initial $^{207}Pb/^{206}Pb$ ratio necessary to calculate meaningful ages of the population and relevant single grain ages. This example indicates an initial $^{207}Pb/^{206}Pb$ ratio of 0.81 for the population. N = number of analysis, age = population age and 1σ uncertainty.

3.2.4 U-Pb geochronology for provenance investigations

U-Pb geochronology can be applied to gain a deeper understanding of a wide range of geological processes such as timing and duration of magmatic and volcanic events, geochemical fingerprinting of geological units, and the evolution of prospective deposits (Corfu *et al.* 2003). The focus of the geochronological analysis in this thesis will be to investigate the provenance of the detrital sedimentary material into the Midland Valley of Scotland. In order to do this, a spectrum of ages from detrital zircon and apatite, present within sedimentary units of Carboniferous age, will be used to investigate the spatial and temporal diversity of clastic input into the basin. The LA-ICP-MS method (section 3.1.2) will be utilised, as it is particularly well suited to this type of investigation due to the large throughput and rapid data acquisition that is required.

3.2.4.1 Zircon geochronology

Zircon is a robust, relatively abundant accessory mineral found in igneous, metamorphic, and sedimentary rocks. During crystallisation the mineral will incorporate uranium into its lattice but will rarely incorporate lead (Finch and Hanchar 2003). Resistant to chemical and physical weathering, the mineral is often targeted as a means to date the Earth's oldest rocks (Cavosie *et al.* 2007). Detrital zircon preserves isotopic information about the properties of its source rock; thus, zircon crystals are often used as a representative of clastic sedimentary material, from its original crystalline bedrock source to deposition in a sedimentary basin sink often referred to as 'source-to-sink investigation' (Hallsworth *et al.* 2000; Morton *et al.* 2001). The preference to incorporate uranium but not lead allows the equations (3.12), (3.13), and (3.14) above, to be applied when dating the mineral. Diffusion of U, Th, and Pb at temperatures <900°C (zircon U-Pb closure temperature) is so incredibly slow, that the U-Pb ratio displays closed system behaviour, even over geological time (Cherniak and Watson 2001). This effectively means that U-Pb dating in zircon indicates the crystallisation age or very high temperature metamorphism of the mineral (Cherniak and Watson 2001).

There is a limited range of magmatic compositions from which zircon will crystallise (Gillespie *et al.* 2018), which may potentially bias the results of a provenance study and under or over represent an age population (Andersen *et al.* 2016). To address this potential bias, this thesis will combine U-Pb zircon and U-Pb apatite analysis, to characterise the potential source rocks and highlight the complementary nature of the geochemical data.

3.2.4.2 Apatite geochronology

Like zircon, apatite is present in many igneous, metamorphic, and sedimentary rock types and will incorporate uranium into its crystal lattice (Donelick 2005), though at much lower quantities than those often found in zircon (Kirkland *et al.* 2018). However, apatite will also incorporate moderate to significant quantities of non-radiogenic Pb (common Pb, Pb_i) into its lattice (Kirkland *et al.* 2018). The presence of high common to radiogenic Pb ratio, provides a challenge when attempting U-Pb geochronology dating of the mineral. The non-radiogenic Pb content can be accounted for by measuring ^{204}Pb, the only non-radiogenic isotope of Pb, and applying the 'common Pb correction' (Andersen 2002). Due to the necessity of this correction and the uncertainty associated with in situ analysis of ^{204}Pb, U-Pb apatite dating rarely reaches the precision and accuracy of U-Pb zircon dating (Chew and Donelick 2012; Glorie *et al.* 2017). Temperature dependent diffusion of Pb from apatite

occurs at a much lower temperature than in zircon, with a closure temperature of 375-600°C (Schoene and Bowring 2007; Cochrane *et al.* 2014). As well as uranium, apatite can incorporate high concentrations of Rare Earth Elements (REE), and other trace elements, reflecting the geochemical signature of the parent rock (Henrichs *et al.* 2018), meaning it can be a valuable provenance indicator (Jennings *et al.* 2011; Gillespie *et al.* 2018).

Contrary to the robust, potentially polycyclic behaviour of zircon, apatite is physically vulnerable during sediment transport and chemically susceptible to dissolution in slightly acidic conditions (Morton and Hallsworth 1999). This fragility means apatite is most likely derived from the first cycle of sediment only. This allows for the two geochronometers to complement provenance investigation and discriminate between first and polycyclic sediment.

3.2.4.3 Detrital age spectra display

Detrital provenance investigation requires a large number of analysis, typically >100 grains per sample (Vermeesch 2004). Displaying these data on a Concordia diagram (section 3.2.3) can become visually confusing and difficult to interpret. Probability distribution diagrams and frequency histograms (Figure 3-8) are an alternative way to visually display the provenance data. These plots allow for the discrimination of multiple populations within a single sample but also the direct comparison between multiple samples. This thesis utilised the probability density plotter software of Vermeesch (2018). These Probability Density Plots (PDP) incorporate individual grain ages and their associated analytical uncertainties, to produce a probability distribution of the sample ages; each peak has a normal (Gaussian) distribution, of which the mean is the age of the population represented by the peak, and the standard deviation is determined by the analytical uncertainties (Figure 3-8). The Kernel Density Estimate (KDE) is also a frequency plot, but each peak is approximated to a normal distribution the standard deviation of which depends on the probability density of the ages close to the peak, rather than their analytical precision (Figure 3-8), The result is a smooth, continuous curve, which has been suggested to better suit geochronological analysis aimed at detrital provenance investigations (Vermeesch 2012). In KDE, the standard deviation of the peaks better reflects the true variation in ages within the population, rather than the analytical precision used in PDP, which is usually high, giving an erroneous perception of the data quality, both in terms of number of populations and their precise determination (Vermeesch 2012). Analysis of

>100 grains reduces the probability of missing a provenance component to 5% (Vermeesch 2004), therefore in this investigation a target of 150 grains per sample was set.

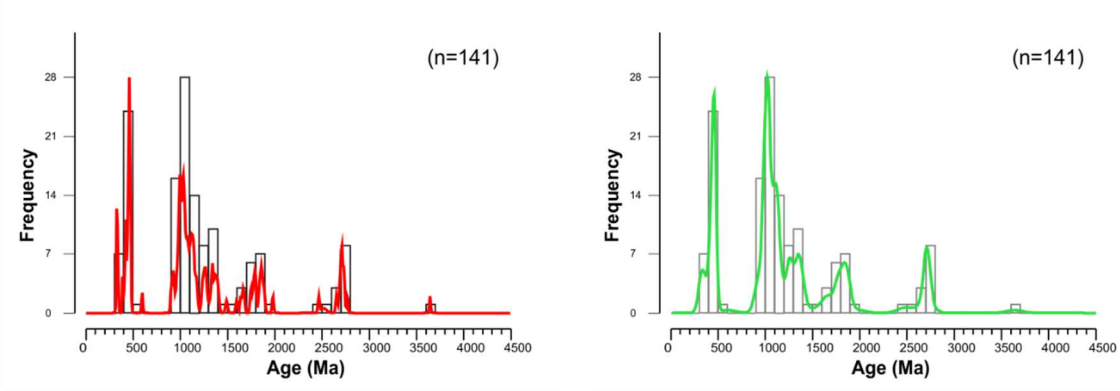

Figure 3-8: PDP and histogram (left) and KDE (right) examples for a detrital zircon sample EM-20 from this thesis. More peaks are generated by the data in the PDP (left) which are also narrow in width. If each of these peaks are interpreted as an individual population then the sample is indicating c.15 populations. The KDE from the same data (right) produces much fewer peaks, c.7, that are wider and not normally distributed.

Similar plots can be produced for apatite U-Pb geochronology; Figure 3-9 shows the resulting KDE for sample EM-17 from Figure 3-7following correcting the raw data for its Pb_i content. The U-Pb geochronology data acquired in this thesis is presented in Chapter 5, which also includes the analytical procedures and data reduction. For each zircon sample, the Wetherill concordia, PDP, and KDE plots are presented, while each apatite sample has its associated T-W and KDE plots.

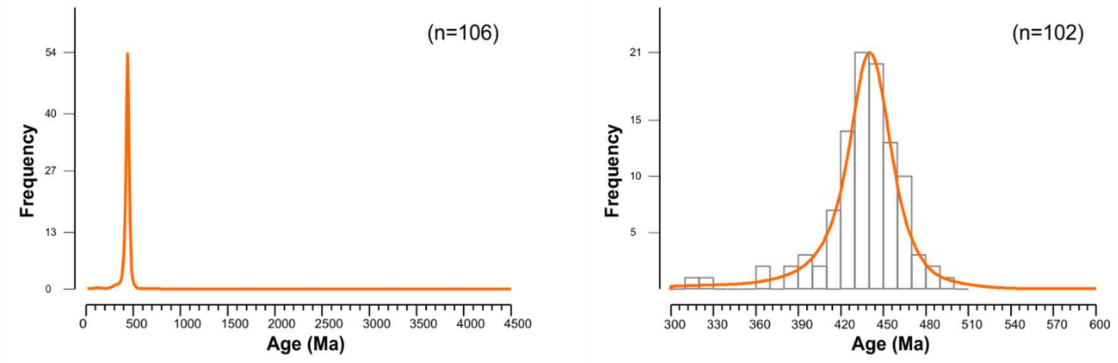

Figure 3-9: Apatite KDE produced from data from sample EM-17. After being plotted in T-W space the sample initial $^{207}Pb/^{206}Pb$ ratio was calculated from the regression line to be 0.81. This was used to calculate the ^{207}Pb corrected single grain ages which have then been plotted in a KDE using the software of Vermeesch (2018). Left plot shows the entire sample while the plot on the right has focussed in on the Palaeozoic component.

3.3 Thermochronology

3.3.1 Introduction

Thermochronology is the quantitative study of the time-Temperature (t-T) or thermal history of rocks and minerals using radiometric systems that are sensitive to temperature changes over geological time (Gallagher *et al.* 1998). Accessory minerals, such as apatite and zircon, often incorporate radioactive elements, such as uranium, into their crystal lattice during crystallization (see Geochronology 3.2, above). Thermochronology utilises the decay of these radioactive isotopes (parent) to produce daughter products (radiogenic isotopes or damage trails) that accumulate at a constant rate (λ) within the crystal lattice. Radioactive decay proceeds via either α-decay, producing ^{4}He atoms, β-decay, producing an electron or positron, or spontaneous fission, producing a damage trail (fission track) (Dickin 2018). Radioactive decay will proceed at a constant rate irrespective of host mineral phase or physical influence upon it; however the retention of the daughter products is primarily controlled by temperature (Fleischer *et al.* 1965a; Braun *et al.* 2006).

Retention of the daughter product occurs only below a critical temperature, known as 'closure temperature' (T_c) (Dodson 1973), where the rates of diffusion and annealing are so low that all daughter product is retained within the crystal lattice, even over geological time. In thermochronology, diffusion kinetics and track annealing cannot be defined by a discrete 'closure temperature' as proposed by Dodson (1973) but rather these phenomena occur over a temperature range (Figure 3-10), which separates the 'open system', where all daughter product is lost via diffusion or fission track annealing (zero retention), and the 'closed system' where all daughter product is retained (total retention). This range of temperatures between the open and closed system where there is partial loss of the daughter product, is known as the Partial Retention Zone, PRZ (for example, the retention of helium produced by the alpha-decay of uranium) or Partial Annealing Zone, PAZ (fission track daughter), and is specific to each mineral and decay series (Figure 3-10). The temperature control on daughter diffusion (or annealing) is at the base of a multi-thermochronometric approach, whereby several thermochronometers can be applied to different minerals in the same rock to decipher the thermal history of the target area.

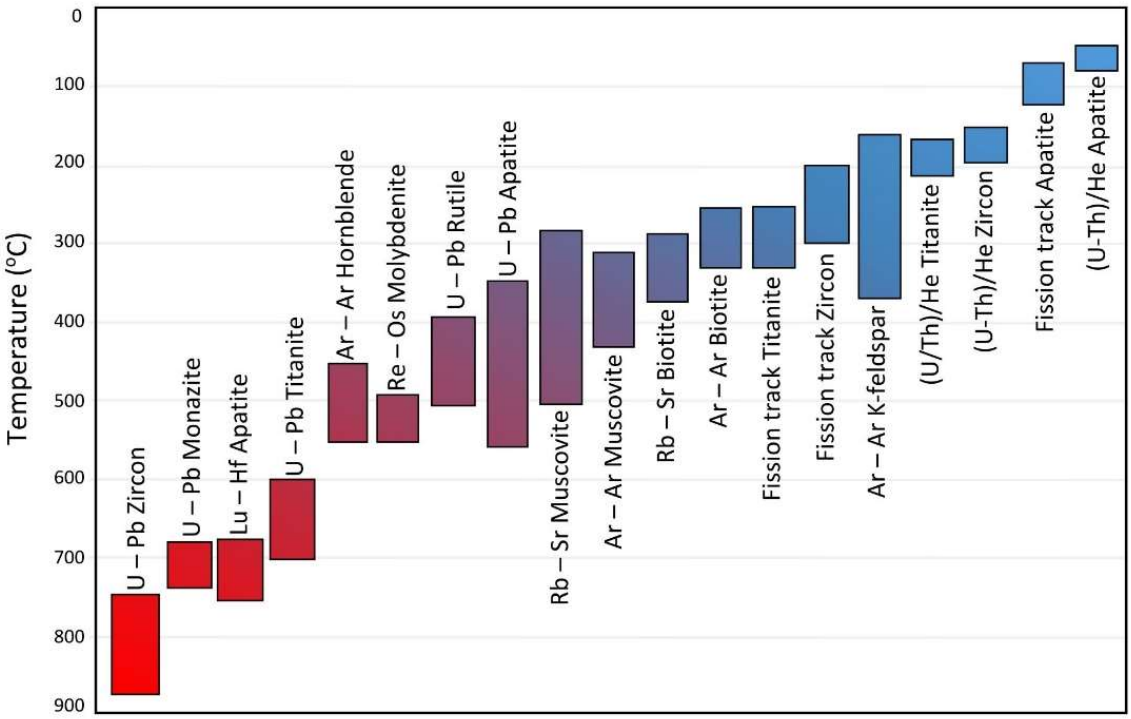

Figure 3-10: Thermochronometers and their Partial Retention/Partial Annealing Zones. Redrawn from Chew and Spikings (2015), the figure shows the parent-daughter radio-isotopic decay system used in thermochronology and the range of temperature sensitivity for each specific mineral.

The parent-daughter ratio is dependent upon decay rate, time elapsed, cooling rate, and thermally activated diffusion/annealing. Therefore, measurement of this ratio and application of the specific decay rate constant, allows the time since daughter accumulation began to be calculated and facilitates the extraction of the thermal history of the sample. Diffusion rates are so slow in some systems even at high temperatures, their 'closure temperature' can often be interpreted as a crystallisation age or timing of a high-grade metamorphic event i.e. zircon U-Pb (section 3.2 above) (Horstwood *et al.* 1999; Sláma *et al.* 2008). Mid-range temperature thermochronometers (c.300-500°C) are often used to investigate lower grade metamorphic events and the cooling of rocks through the middle-crust (c.15-5 km depth) (Warren *et al.* 2012). Thermochronometers sensitive to temperatures <c.300°C are collectively known as Low Temperature Thermochronometers (LTT) and are often used to access the cooling history of rocks at a shallow crustal level (<c.5 km), investigating landscape evolution and shallow tectonic processes (Reiners *et al.* 2005; Persano *et al.* 2007; Wildman *et al.* 2017). Apatite fission track thermochronology (AFT) has a temperature sensitivity range between ~60 and ~120°C (Figure 3-10) and is the LTT technique that will be applied in this study. The following section highlights the theoretical principles, uncertainties, and modelling procedures used, while details on the practical approach can be found in Appendix B.

The AFT technique is based on the accumulation of damage trails (fission tracks) caused by the spontaneous fission of 238-uranium atoms (^{238}U) within the crystal lattice of a mineral, over geological time (Price and Walker 1963). Although other naturally occurring radioactive elements may exist within the mineral (^{235}U and ^{232}Th) their half-life is too long or natural abundance too low, to produce a significant number of tracks (Gallagher *et al.* 1998). The technique aims at providing two sets of data, the AFT age, which is calculated using the density of fission tracks intersecting a polished surface of a crystal and the U concentration within the crystal, and the track length distribution (TLD), which is produced by measuring horizontal, confined tracks, intersected by surface features. Combining these two components provides the "when" and "how" a rock has cooled over geological time, between ~60 and ~120°C. Fission tracks are sub-microscopic but can be revealed by chemical etching (Price and Walker 1962), enabling them to be seen, counted, and measured with an optical microscope. Spontaneous fission tracks are not a permanent feature but are susceptible to thermally-activated shortening, a process known as annealing (Fleischer *et al.* 1975; Gleadow *et al.* 1986; Green *et al.* 1989). This feature is a great asset when attempting to constrain the thermal history of the sample as, once formed, each fission track records the thermal history the host mineral subsequently undergoes; their length, therefore, is strongly dependent on the amount of time the rock has spent in the PAZ. When the AFT age is combined with the TLD and known geological constraints, a detailed thermal history of the rock and, therefore, of the target area, can be reconstructed.

Latent tracks were first observed using a transmission electron microscope (Silk and Barnes 1959) and the technique has been applied to geological settings since the late 1960's (Wagner 1968). Since then, the fission track method has seen considerable refinement in methodology and greater understanding in track formation and annealing, which are fully discussed elsewhere (Gallagher *et al.* 1998; Donelick 2005; Lisker *et al.* 2009; Malusà and Fitzgerald 2019a). There are, however, still aspects of the technique that require further investigation; the role that the physical and chemical properties of the host mineral play in controlling the process of annealing, in particular for slowly cooled rocks, is still unresolved, producing over dispersion in the data and uncertainties in the derived thermal histories that may hamper our ability to confidently reconstruct the geological evolution of the study area (Hendriks and Redfield 2005; Larson *et al.* 2006; Vermeesch and Tian 2014; Gallagher and Ketcham 2018; McDannell *et al.* 2019).

3.3.2 Fission track formation and revealing

Chemically unetched fission tracks, known as latent tracks (Gallagher *et al.* 1998) are formed when a heavy, unstable radioactive nucleus e.g. ^{238}U, either spontaneously or artificially (induced by the bombardment of high energy particles within a nuclear reactor) decays and splits into two positively charged fragments that repel away from each other in opposite directions (Tagami and O'Sullivan 2005). The fission fragments are accompanied with ~160meV (milli-electron volt) of kinetic energy and have a stopping distance in the range of 8-11 μm, depending on the density of the mineral lattice (Jonckheere 2003). Several models have been suggested to describe track formation, including the ion spike (Fleischer *et al.* 1965b), thermal spike (Seitz 1949; Bonfiglioli *et al.* 1961; Chadderton and Montagu-Pollock 1963) and compound spike models (Chadderton 2003) (Figure 3-11).

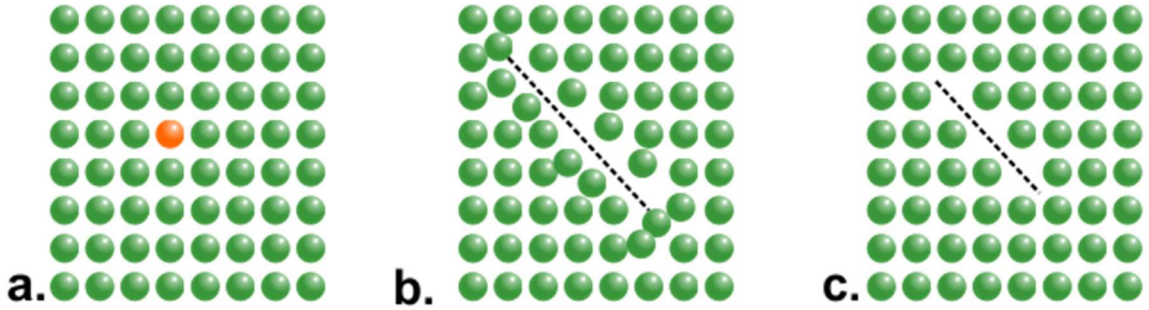

Figure 3-11: Ion-spike model for fission track formation. (a) Atom of ^{238}U (orange) is contained in the lattice of a mineral. (b) Spontaneous decay of ^{238}U releases predominantly kinetic energy, as the two fragments recoil from the reaction site in opposite directions. The highly charged ions, recoil through the mineral lattice at high velocity, interacting with other atoms by electron stripping and ionisation (Fleischer *et al.* 1975). This ionisation results in an array of positively charged ions that repel from each other and move from their original position within the crystals lattice, due to Coulomb repulsion. As the atomic interactions continue, energy is transferred away from the decay fragments until they slow and eventually come to a stop, leaving a damage trail in their wake (Chadderton 2003). (c) Thermally activated annealing of the latent fission track allows for the restoration of the lattice structure and shortening of the track length.

The thermal spike model has been offered as an alternative to explain the formation of fission tracks (Vineyard 1976). This model suggests that, following a fission event, there is a rapid dispersion of energy in the form of heat along the trajectory of the fission fragments. The heating and atomic collisions creates a plasma which is cooled via conduction of heat into the surrounding lattice. Once quenched, the lattice remains in a disordered state, forming a damage trail. Chadderton (2003) does not see the ion- and thermal spike models as exclusive and thus combines them to form the compound spike model, suggesting that nuclear tracks in solids, produced by swift heavy ions, are a result of both thermal and ionisation phenomena, to different degrees.

Latent fission tracks are sub-microscopic features but can be revealed by chemical, etching as minerals used in fission track analysis are soluble in acidic conditions (Fleischer *et al.* 1975). The disordered region of the lattice forming the track core (Figure 3-11) is more susceptible to etching than the undamaged lattice, enabling tracks to be enlarged to a point where they can be viewed under an optical microscope (Fleischer *et al.* 1975; Durrani and Bull 1987). The procedure for the chemical etching process has been refined by experimentation and must be strictly adhered to, as the algorithms that describe the annealing process and are used in software to extract thermal histories are strongly dependant on etching conditions (Tagami and O'Sullivan 2005). In this investigation, the apatite etching protocols of 5.5 M HNO_3 for 20.0s (± 0.5s) at 20°C (± 1.0°C) was used (Carlson *et al.* 1999); the thermal histories derived from the AFT data are based on the algorithms that used this same protocol (Ketcham *et al.* 2007b; Ketcham *et al.* 2007a).

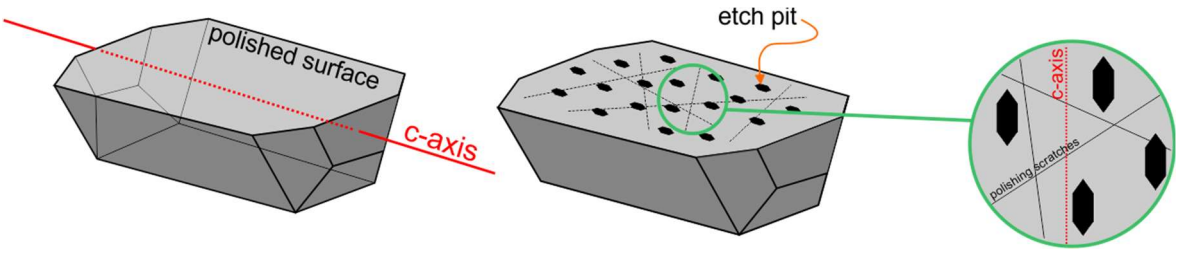

Figure 3-12: Apatite crystal before and after etching. Apatite crystals are mounted in epoxy resin and polished to reveal an internal surface. After etching, fission tracks intersecting the polished surface will be revealed and an etch pit will become visible when viewed under a microscope. Polished surfaces with sharp polishing scratches and etch pits with aligned long axis, indicate the polished surface is parallel to the crystals c-axis and can be used for AFT age determination.

3.3.3 General isotopic age equation

As mentioned above, AFT thermochronology relies on two pieces of information, the AFT age and the TLD. The following section deals with the derivation of the AFT age. As with other isotopic dating techniques, the fission track 'age' is based on the natural radioactive decay of the unstable parent isotope (N_p) producing a daughter product (N_d) at a rate defined by the decay constant (λ) (3.1). In fission track analysis, the parent isotope (N_p, ^{238}U) spontaneously decays to form daughter fission tracks ($N_{fission}$) within the crystal lattice at a decay rate of λ_f. Where λ_D is the total decay constant:

$$N_{fission} = \frac{\lambda_f}{\lambda_D} N_p (e^{\lambda_D t} - 1) \tag{3.18}$$

This equation can be solved for time (t), where N_s is the number of spontaneous tracks and ^{238}U is the number of 238-uranium atoms in the same crystal:

$$t = \frac{1}{\lambda_D} \ln \left(\frac{\lambda_D}{\lambda_f} \frac{N_s}{^{238}U} + 1 \right) \quad (3.19)$$

It is not possible to measure the total number of parent (^{238}U) and daughter (fission tracks) contained within an entire crystal. Instead, the number of fission tracks intersecting a polished crystal surface, revealed by etching (etch pits, Figure 3-12), are counted over an area; this is known as the spontaneous track density (ρ_s) (Figure 3-13).

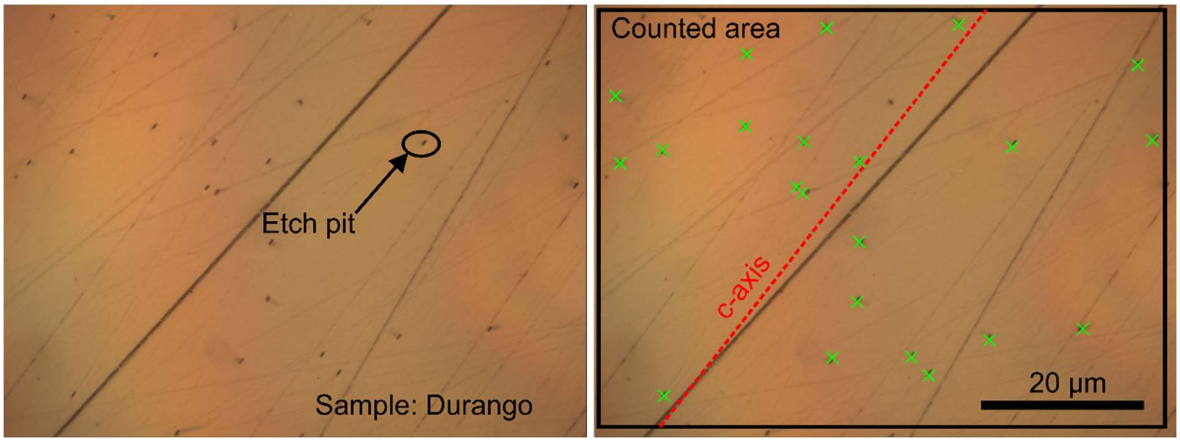

Figure 3-13: Reflected light image of a c-axis parallel Durango apatite. Black square on the right panel indicates the area over within which tracks have been counted, dashed red line shows the direction of the crystallographic c-axis as indicated by the aligned etch pits, green crosses indicate counted etch pits for AFT age calculation. Straight dark lines are polishing scratches revealed after etching.

The spontaneous track density (ρ_s) is proportional to the concentration of ^{238}U on this counted area and the time that has elapsed since the beginning of track accumulation (t), and hence, the time since the apatite crystal cooled to temperatures less than ~120°C. The concentration of ^{238}U can be determined by using either the external detector method (EDM) (Hurford and Green 1982) or Laser Ablation Inductively Coupled Plasma Mass Spectrometry (LA-ICP-MS) (Figure 3-14) (Hasebe et al. 2004; Chew and Donelick 2012; Chew and Spikings 2015; Gleadow et al. 2019). The AFT ages produced in this thesis were derived from the latter method; the EDM approach, however, is briefly described below because is it the more traditional protocol used in AFT analyses and it constitutes the conceptual base from which the LA-ICP-MS technique applied to the fission track method was derived.

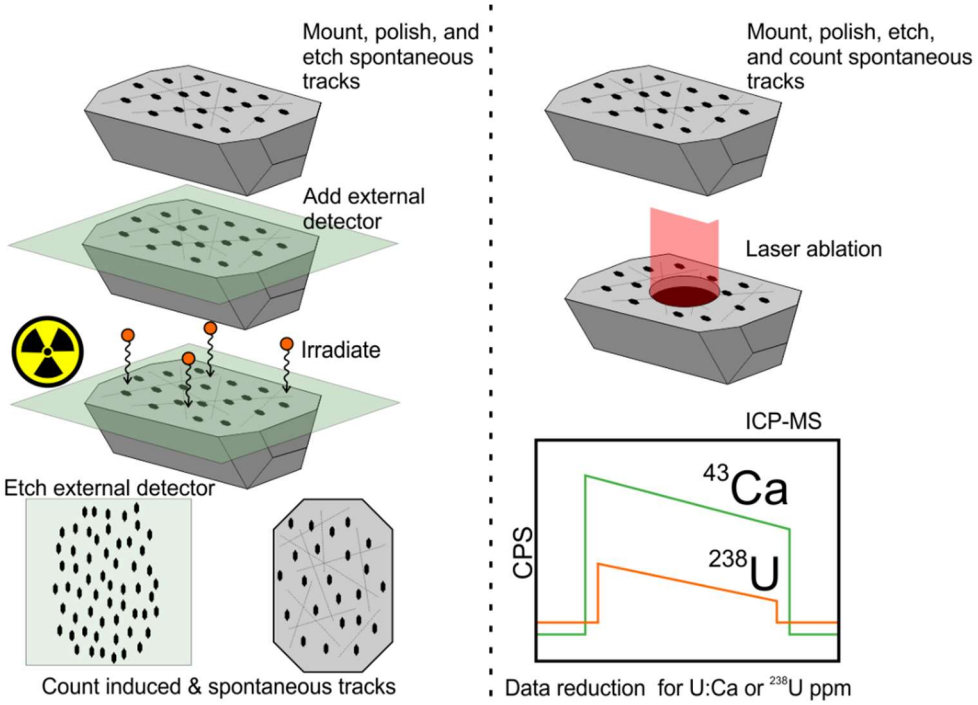

Figure 3-14: AFT analysis by EDM vs LA-ICP-MS. Figure shows the steps necessary to produce an AFT age for a single grain in both EDM and LA-ICP-MS methods. This figure shows that, although the technique is still being refined and the implications of the analytical uncertainties still discussed, the LA-ICP-MS method requires much fewer steps compared to EDM and avoids sample irradiation. CPS, counts per second measured on the mass spectrometer. For details on the two methods, see text.

3.3.4 EDM uranium concentration and Fission Track age equation

EDM (Hurford and Green 1983) involves attaching a thin sheet of low uranium, fission track free mica (the external detector – ED) to the mineral grain mount. The grain mount and external detector are then packed together with at least two dosimeters, artificial glasses of known U concentration, to which a sheet of mica is also attached. Pairs of samples-micas, bounded at each end by a pair dosimeter-mica are then irradiated in a nuclear reactor core, where a constant flux of thermal neutrons induces a proportion of ^{235}U contained in both the dosimeter and in the apatite crystals to fission. The tracks formed by the fission of the ^{235}U atoms at or very near the polished surface of the grain mount are registered on the mica detector sheet as ‘induced’ tracks. Once their areal density is counted, it is converted into the apatite ^{235}U concentration by referring to the track areal density of the dosimeters. The ^{235}U concentration is then converted into ^{238}U concentration using the natural value of the ^{238}U:^{235}U ratio of 137.818 (Hiess *et al.* 2012).

The fission track age (t_{EDM}), can then be determined using the formula:

$$t_{\mathrm{EDM}} = \frac{1}{\lambda_D} \ln\left(1 + \frac{\lambda_D\, \phi\sigma GI}{\lambda_f}\, \frac{\rho_s}{\rho_I}\right) \tag{3.20}$$

Where: λ_D is the total decay constant (1.55125x10^{-10} year^{-1}), λ_f is the fission decay constant (7.9-8.7x10^{-17}year^{-1}), ϕ is the thermal-neutron fluence (cm^2.s^{-1}), σ is the thermal neutron fission cross section for ^{235}U (580.2 x10^{-24} cm^{-2}), G is the geometry factor to account for the fact that part of the grain has been lost in the polishing process and therefore tracks intersecting the surface of the apatite have the same probability to have been created by an atoms of ^{238}U in the volume of the crystal still in the mount or the portion polished away (G= 0.5), I is the ^{235}U/^{238}U isotopic ratio (7.253 x 10^{-3}), ρ_s is the spontaneous track density, ρ_I is the areal induced track density (Tagami and O'Sullivan 2005).

Some of the parameters in equation (3.20) have been determined with a low accuracy, may vary from one irradiation to the other, or if the neutron flux is not constant, within the same stack of samples (e.g. ϕ). To combat these uncertainties that hamper the accuracy of the AFT ages and to systematically treat discrepancies between analysts, a zeta (ζ) calibration factor is applied. Prior counting tracks in unknown samples, each fission track analyst needs to compile their own zeta value, counting tracks on apatite AFT standards, i.e., Durango, Mt Dromedary and Fish Canyon Tuff. The zeta value is considered acceptable when this value become stable.

3.3.5 EDM Zeta calibration

EDM zeta calibration (ζ) (Hurford and Green 1983) involves irradiating standard apatite along with unknown samples. This removes some of the uncertainties associated with the method and is defined as:

$$\zeta = \frac{(e^{\lambda_D t_{std}} - 1)}{\lambda_D\, (\rho_s/\rho_I) std\; G\; \rho_d} \tag{3.21}$$

Where (t_{std}) is the age of the standard apatite and $(\rho_s/\rho_I)std$ is the ratio of spontaneous to induced tracks in the standard apatite. The fission track age equation including the zeta calibration becomes:

$$t_{\mathrm{EDM}} = \frac{1}{\lambda_D}\ln\ [1 + G\lambda_D\zeta\rho_d\ (\rho_s/\rho_I)] \tag{3.22}$$

The associated error is given by:

$$\sigma_{(t_{EDM})} \approx t_{EDM}\sqrt{\left(\frac{s(\zeta)}{\zeta}\right)^2 + \frac{1}{N_s} + \frac{1}{N_i} + \frac{1}{N_d}} \tag{3.23}$$

3.3.6 LA-ICP-MS AFT age determination

Improved accuracy and precision of mass spectrometry used for in situ analysis coupled to a short wavelength laser, has made it possible for labs to acquire direct ^{238}U measurements without the need for irradiation of samples and the additional steps that follow (Figure 3-14) (Chew and Donelick 2012) described in section 3.1.2 above. Two approaches have been proposed, a modified zeta (stoichiometric ratio) approach (Donelick 2005; Chew and Donelick 2012), and an absolute approach (Hasebe *et al.* 2004). Background corrected signals from the mass spectrometer are normalised to the ^{43}Ca signal, as calcium is stoichiometric in apatite. Using ^{43}Ca as an internal standard, allows the ablations to be monitored for single grain zonation (changes in ^{238}U:^{43}Ca) and session wide drift of the analytical equipment (variations in signal intensities). Single grain (i) fission track ages can be calculated using the equations described below, depending on the approach used.

3.3.7 LA-ICP-MS Zeta approach

With the removal of the irradiation, the fission track age formula using laser ablation is simpler than the EDM method. Using the stoichiometric ratio approach, the spontaneous track density for grain *i* ($\rho_{s,i}$) is calculated and divided by the stoichiometric ratio (P_i,) i.e., ^{238}U:^{43}Ca in grain *i*. A mass spectrometer zeta factor, (ζ_{ms}) is included in the formula, which removes some uncertainty (analyst and $\lambda_{fission}$) in the calculation and is calibrated to an age reference apatite (Donelick 2005).

$$\mathrm{t}_i = \frac{1}{\lambda_\mathrm{D}}\ln\left(\ 1 + \frac{1}{2}\lambda_\mathrm{D}\ \zeta_{ms}\left(\rho_{s,i}/P_i\right)\right) \tag{3.24}$$

Where ζ_{ms} is given by (3.25), where t_{std} is the age of the apatite standard, P_{std} is the stoichiometric ratio i.e., ^{238}U: ^{43}Ca of the apatite standard and Ω is the counted area in cm^2 of the apatite standard:

$$\zeta_{ms} = \frac{(e^{\lambda_D t_{std}} - 1)}{\frac{1}{2}\lambda_D(\rho_s/P_{std}\,\Omega)} \tag{3.25}$$

The associated error is given by:

$$\sigma_i = \sqrt{\frac{1}{N_{s,i}} + \left[\frac{\sigma(^{238}U/^{43}Ca)_i}{(^{238}U/^{43}Ca)_i}\right]^2 + \left[\frac{\sigma\zeta_{ms}}{\zeta_{ms}}\right]^2} \tag{3.26}$$

3.3.8 Absolute age equation

Calculating fission track age using absolute uranium concentrations obtained via laser ablation requires more parameters, compared to the stoichiometric ratio equation outlined above. However, many of the formula inputs are knowns or at least fairly well constrained (Hasebe *et al.* 2004; Gleadow *et al.* 2015), it is therefore only necessary to count the fission tracks ($\rho_{s,i}$), and measure the uranium concentration (^{238}U) on the sample to be dated:

$$\mathrm{t}_i = \frac{1}{\lambda_D}\left(1 + \ln\lambda_D\,\epsilon\,\frac{\rho_{s,i}}{^{238}U}\right) \tag{3.27}$$

Where ϵ is:

$$\epsilon = \left(\frac{M}{\lambda f\, N_A\, d\, R\, \alpha}\right) \tag{3.28}$$

Where, M is the atomic mass of ^{238}U (238.0508); N_A is Avogadro's number (6.022x10^{23} mol^{-1}); ^{238}U is the uranium concentration measured by LA-ICP-MS (ppm); d is the mineral density (apatite 3.19 ± 0.04 g.cm^{-3}); R is half of the mean etchable spontaneous fission track length (7.5 ±0.25 x 10^{-4} cm); α is an experimental factor based on etching and observation conditions (usually 0.9-1.0) (Gleadow *et al.* 2015).

The associated error is given by:

$$\sigma_i = t_i \sqrt{\frac{1}{N_{s,i}} + \left[\frac{\sigma_{(^{238}U)_i}}{^{238}U_i}\right]^2 + \left[\frac{\sigma_{\zeta_{MS}}}{\zeta_{MS}}\right]^2} \quad (3.29)$$

3.3.9 Pooled and central age and radial plots

The equations outlined above are applied when calculating single grain ages, which are subsequently subjected to a chi-squared test (χ^2) to determine if they belong to the same statistical population. The resulting p-value is reported to indicate the probability that the sample grain age distribution has failed the χ^2 test (the null hypothesis is that the grains belong to the same population), a p-value less than the cut-off taken at 0.05 (5%), indicates that the grains are not consistent with a common age population (Galbraith 2005). The pooled age can be used only when all the single grain ages belong to the same discrete population (consistent with a common age), i.e. χ^2 value >0.05. In practise, the pooled age treats the sample data as if they were all derived from a single crystal (3.30) (Galbraith 2005; Vermeesch 2017):

$$t_{pooled} = \frac{1}{\lambda_d} ln\left(1 + \lambda_d \zeta g \frac{\sum_1^j N_{s,j}}{\sum_1^j P_j \, \Omega_j}\right) \quad (3.30)$$

Failing of the χ^2 test supplies enough evidence to reject the common age model, this is usually due to either the apatite in the sample not being from the same source (detrital samples) and/or have spent time cooling through the PAZ, where differences in annealing behaviour (variable apatite chemistry) between grains has caused the single grain ages to become dispersed. In such cases, the central age, which is a weighted mean of the log-normal distribution of single grain ages is computed, through a multistage iterative approach (Galbraith and Laslett 1993; Galbraith 2005):

$$t_{central} = \frac{1}{\lambda_d} ln\left(1 + \lambda_d \zeta g \left(\frac{\eta}{1-\eta}\right)\right) \quad (3.31)$$

Where η is the weighted average of single grain variance.

Another important parameter, usually provided by the software used to statistically treat the single grain AFT ages, is dispersion; this value, often in %, represents the dispersion that cannot be

explained by the uncertainties related to the Poissonian distribution of the ages and it suggest the presence of inter-crystal chemical heterogeneities and/or a complex geological history with a detrital component being present.

3.3.9.1 Radial Plots

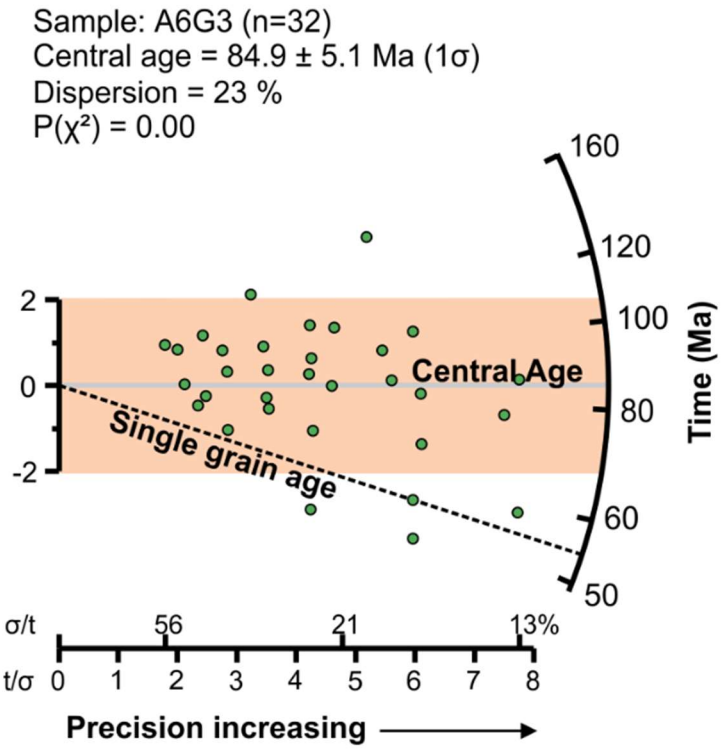

Figure 3-15: Example of radial plot. The figure shows an example of a radial plot produced for sample A6G3 from the Midland Valley. The features of the plot are explained in the text. Once single AFT ages for a sample have been calculated, they are traditionally plotted on radial plots; this allows for the sample, its single grain ages and their associated errors to be plotted together and can be evaluated graphically. The radial plot above indicates how single grain AFT ages as well as the sample central age and error can be read. In this case, sample A6G3 did not pass the chi-square test and the data are over-dispersed (23%), which means that there is a mixture of different age components that need to be explained.

The Radial Plot software version 9.5 (Vermeesch 2009) was used to calculate the χ^2 test, central age and its uncertainty, and sample dispersion, in this thesis. Single grain apatite fission track age data are also represented on radial plot diagrams (Galbraith 1988; Galbraith 1990). These plots display single grain age dispersion while also having the ability to display the precision of each measurement. The plots display individual grain ages in a single sample in x, y space.

$$x_j = \frac{1}{\sigma(z_j)} \tag{3.32}$$

$$y_j = \frac{(z_j - z_0)}{\sigma(z_j)} \quad (3.33)$$

Where $z_j$is a transformation of the fission track age of grain j and $\sigma(z_j)$ is its age uncertainty and z_0 is a reference age, usually the central age of the sample (Figure 3-15). A straight-line projection from the origin through a single point will define the age of the point, which is displayed radially on the right of the plot, with age in Ma. The x value will define the precision of that point; less precise data will plot nearer the origin. The plot is accompanied by other information, such as t/sigma and a vertical bar representing the two sigma variation (2σ) of the central age (Figure 3-15). As this investigation examines sedimentary data with known stratigraphic age, radial plots have been produced in several ways which is explained in the text in Chapter 6 section 6.2.5.

3.3.10 Data quality assessment

As mentioned above AFT age data were acquired in this investigation using the LA-ICP-MS method. Prior to undertaking analysis of unknown Midland Valley samples, the quality of the data produced by the LA-ICP-MS methods was assessed. This consisted of multiple analysis of AFT age reference calibrators, Durango and Mount Dromedary Complex apatite, as well as two University of Glasgow in-house age reference apatite. At the University of Glasgow, single grain ages were calculated using the LA-ICP-MS modified zeta and absolute approach. The University of Melbourne favours the use of the absolute approach (Gleadow *et al.* 2015), so for consistency throughout the data, this method was adopted for all AFT age calculations. Details of the practical approach to the analytical protocol can be found in Appendix B and analytical parameters are summarised in Table 3-2 and below.

At the University of Melbourne, images of selected areas for fission track counting were captured by TrackWorks™ using a 3.2MP AVT Oscar F-320C camera mounted on a Zeiss AxioImager microscope with a 1000x total magnification and a 100x dry objective (calibration = 0.07µm by 0.07µm per pixel). Spontaneous track densities were determined on prismatic (110) internal apatite surfaces after etching with 5.5M HNO_3 for 20 sec at 20ºC. Track counts were obtained by automated counting in FastTracks™ using the 'coincidence mapping' technique of Gleadow et al. (2009) followed by manual inspection. Uranium concentrations of each grain were determined by LA-ICP-MS single spot analysis using a New Wave Nd:YAG Laser (λ=213nm with 5Hz @ ~50% power, spot size=30µm) connected to an Agilent 7700 mass spectrometer.

Raw data were reduced offline using the TraceElements_IS data reduction scheme in the Iolite™ 3.4 software package (Paton *et al.* 2011). Isotopic analysis in all apatite were normalised using ^{43}Ca as the internal standard, using in-house matrix matched standards of Durango (12.20 ±0.6 ppm ^{238}U) and Mud Tank (2.95 ±0.125 ppm ^{238}U) apatite (Figure 3-16). An average apatite Ca concentration of 39.85 wt.% was used for unknown samples, which assumes Ca content in all apatite measured is stoichiometric. The procedure employed standard-sample bracketing, with repeat analysis of the matrix matched reference material every c.10 unknown analysis. During data reduction, the Mud Tank apatite was used as the primary reference material due to its low ^{238}U ppm 1σ standard error, however the Durango reference material was also swapped in as the primary reference material to investigate any variation in results due to using a higher ^{238}U ppm concentration reference material. Results for the matrix matched reference material set as the secondary standard can be seen in Figure 3-16, displaying highly reproducible data. Periodical analysis of the NIST 612 glass (Pearce *et al.* 1997) was also undertaken in order to monitor LA-ICP-MS stability and assess session wide sensitivity and drift.

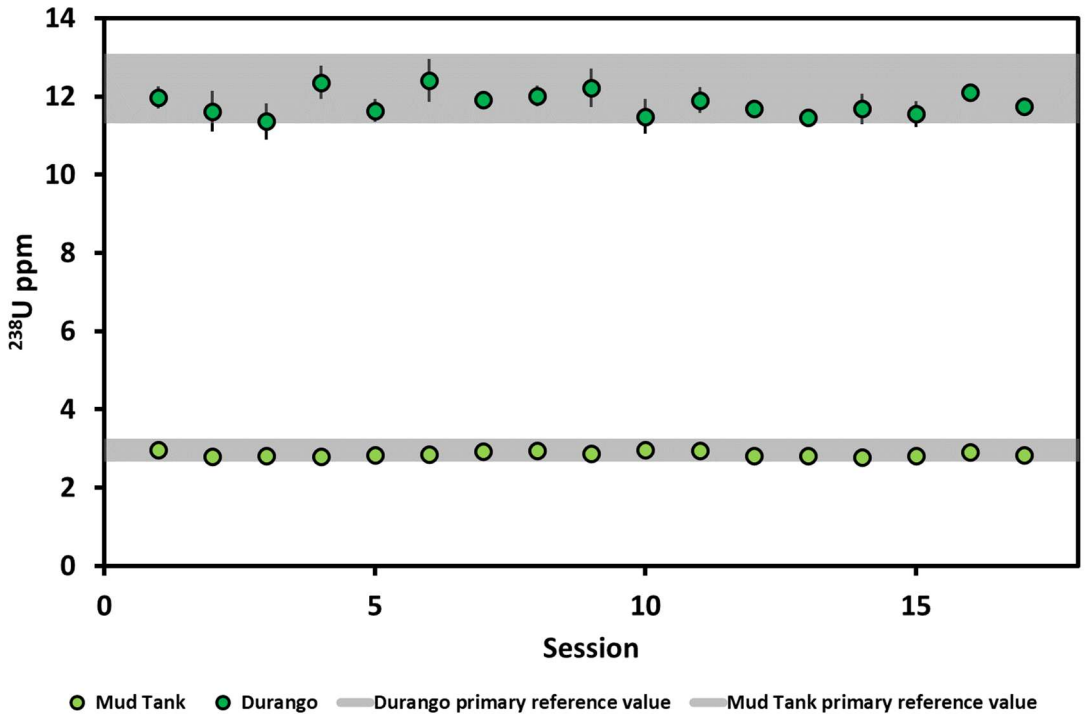

Figure 3-16: ^{238}U ppm values for reference material from this investigation. Grey bars indicate recommended value of ^{238}U content of reference material, green marker indicate values attained during various sessions of this investigation. Mud Tank errors smaller than markers.

Single grain and pooled AFT ages and 1σ standard errors for Durango (31.44 ±0.18 (McDowell *et al.* 2005)) chards from several crystals, along with Mount Dromedary Complex (99.12 ±0.14 Ma (Renne *et al.* 1998)), and Glasgow in-house age reference apatite A (75.0 ±3.1 Ma (Łuszczak 2016))

and B (63.4 ±2.8 Ma (Łuszczak 2016)), were calculated using the IsoplotR package (Vermeesch 2018). AFT ages were obtained using single spot analysis with a diameter of 30μm, drilled to a depth of c.8μm beneath the surface. The resulting AFT ages from the data assessment (Figure 3-17, Figure 3-18, Figure 3-19, & Figure 3-20) were, Durango, 32.40 ±1.44 Ma; Mount Dromedary, 107.00 ±3.76 Ma; Glasgow apatite A, 80.07 ±5.1 Ma; Glasgow apatite B, 58.97 ±7.57 Ma.

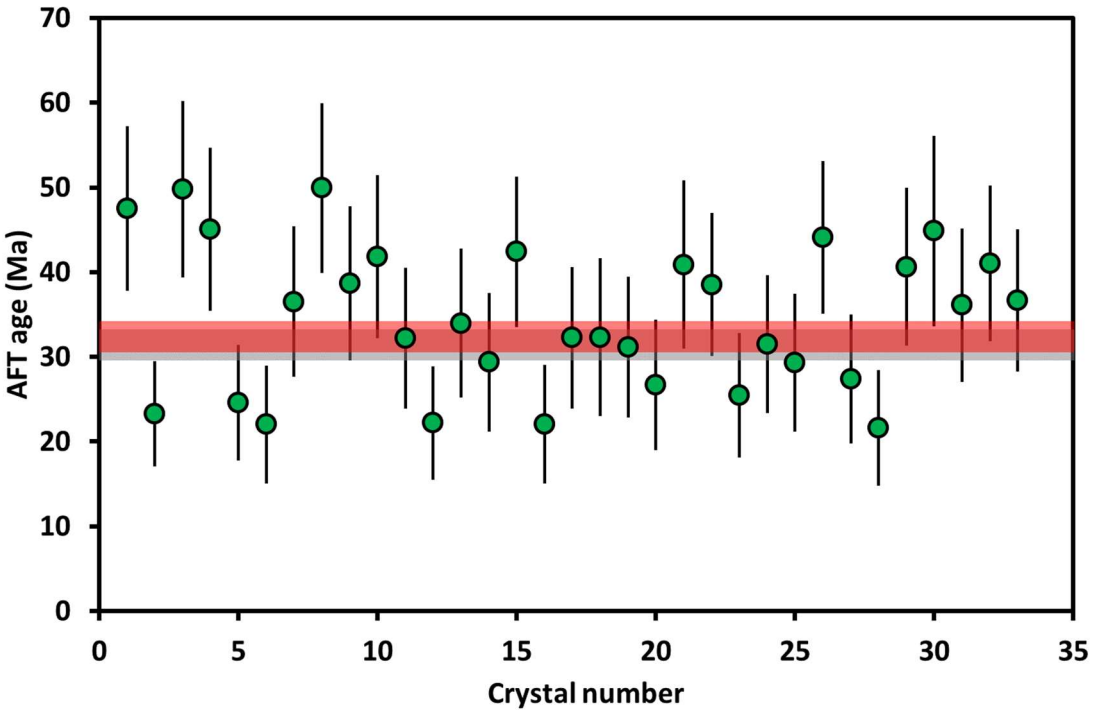

Figure 3-17: Durango apatite chards. Durango reference AFT age 31.44 ±1.5 Ma, grey bar, plotted along with individual single grain AFT ages and 1σ errors from this study. Pooled age 32.40 ±1.44 Ma, red bar.

All AFT ages fall within the accepted 1σ error of the apatites, except for the Mount Dromedary Complex sample, which is slightly older but falls within 2σ error of the accepted AFT age; this slight inaccuracy may be a result of the large number of dislocations defects noted in the sample at the time of counting. The data from the standard apatites indicate that that the AFT dating method utilised in this investigation is directly comparable to the conventional External Detector Method (EDM). Central ages and 1σ standard errors were estimated from single grain ages and 1σ standard errors according to the formulas given by Galbraith (2005) using the Newton-Raphson method.

At the University of Glasgow, track densities were obtained manually at x1250 magnification on a Zeiss Axioplan microscope attached to a Trevor Dumitru stage system and the FT Stage 4.04 software programme (Dumitru 1993), following the same polishing and etching protocol as employed at the University of Melbourne. Uranium concentrations were determined by LA-ICP-MS single spot

analysis using an ASI RESOlution eximer laser (λ=193nm with 5Hz @ 3.0J/cm^2, spot size 30μm) connected to a Thermo Scientific iCAP mass spectrometer. The subsequent data was processed in the same manner as highlighted above for the data acquired at the University of Melbourne.

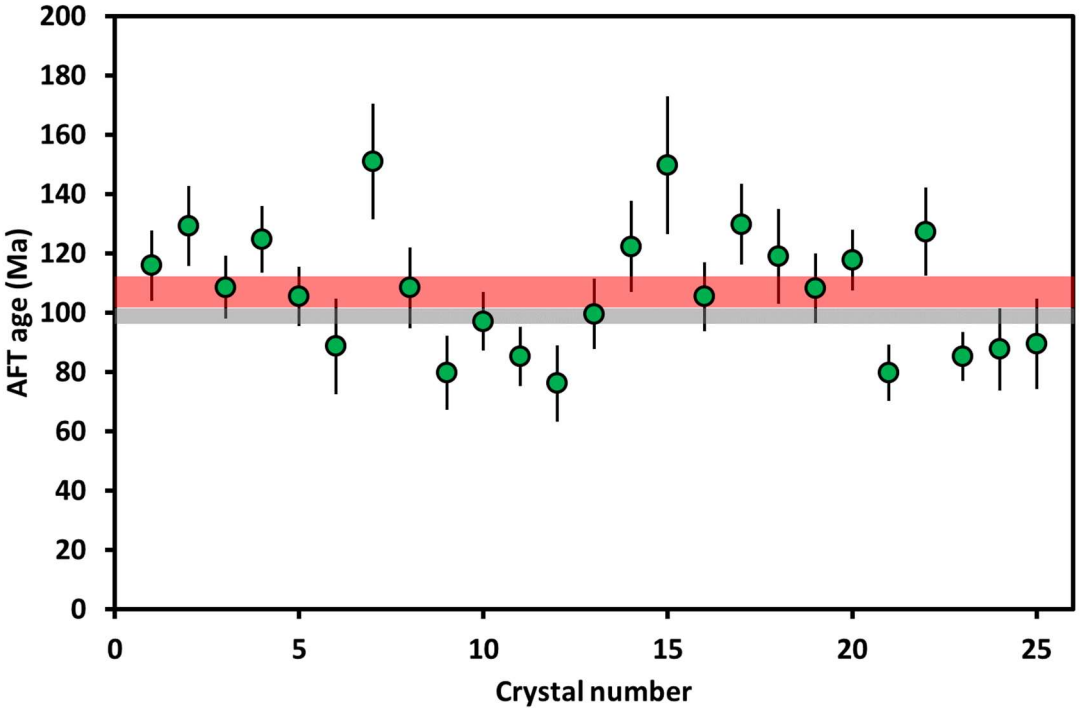

Figure 3-18: Mount Dromedary crystals. Mount Dromedary reference AFT age 99.1 ±0.14 Ma, grey bar, plotted with individual single grain AFT ages and 1σ errors from this study. Pooled age 107.00 ±3.76 Ma, red bar.

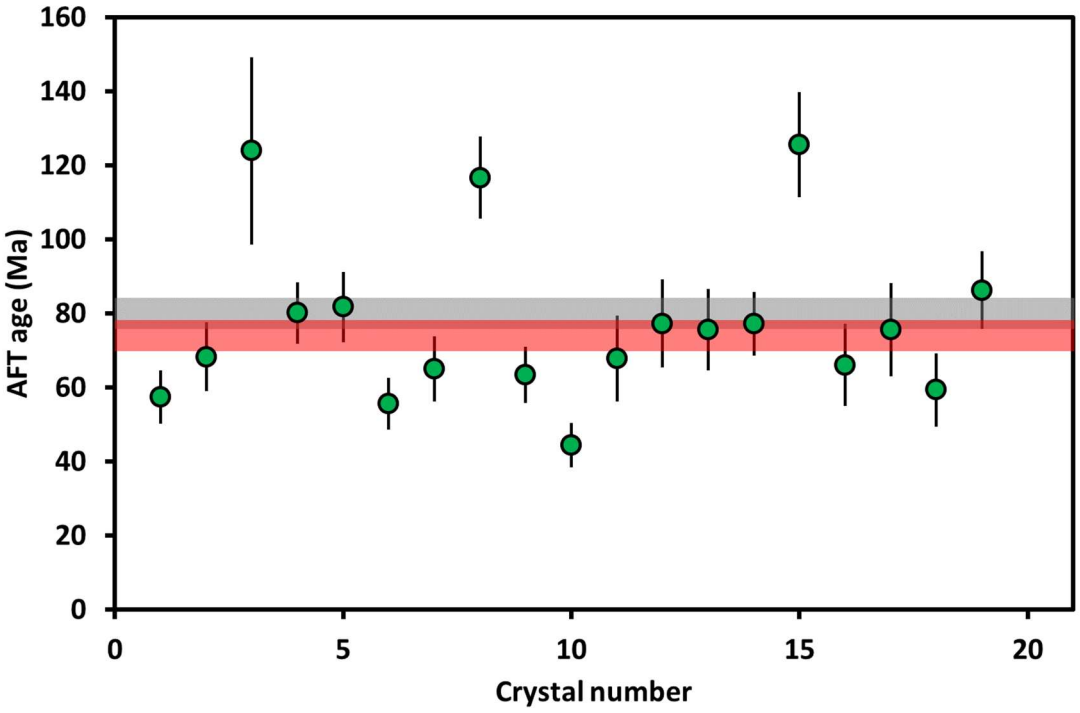

Figure 3-19: Glasgow AFT age reference apatite A. Apatite A reference AFT age 75.0 ±3.1 Ma, grey bar, plotted with individual single grain AFT ages from this study. Pooled age 80.07 ±5.1 Ma, red bar.

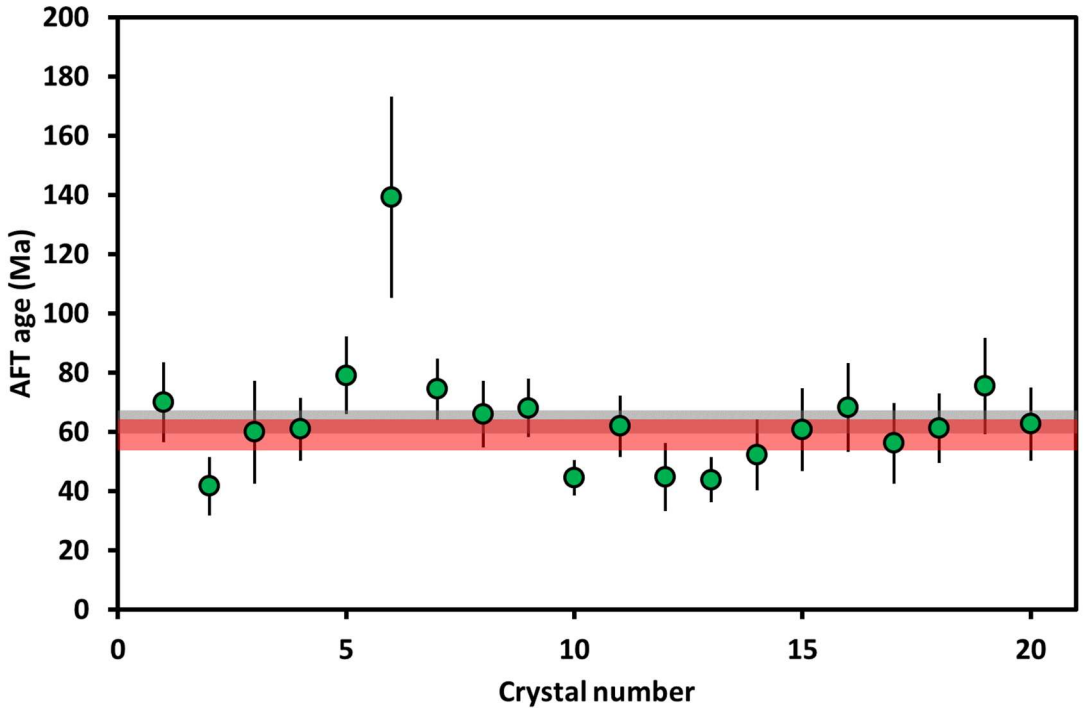

Figure 3-20: Glasgow AFT age reference apatite B. Apatite B reference AFT age 63.4 ±2.8Ma, grey bar, plotted with individual single grain AFT ages from this study. Pooled age 58.97 ±7.57 Ma, red bar.

The results of the data quality assessment into the LA-ICP-MS methodology above, indicate that it provides an alternative to the more traditional EDM methodology for acquiring uranium concentrations in apatite grains for fission track analysis. The technique has many advantages over the traditional EDM approach, including removal of the neutron irradiation step, direct measurement of the ^{238}U parent isotope instead of ^{235}U, high precision and accuracy of ^{238}U measurements, high spatial resolution, and the possibility to include more isotopic measurements when acquiring data, such as U-Pb determinations and REE fingerprinting. However, the method is also relatively new and as yet has not been rigorously tested in a multi-lab comparison investigation nor have the approaches i.e., modified zeta and absolute, been standardised. The method also only requires single track density measurements on the sample (ρs) compared to the induced and dosimeter densities required from EDM. Although this is an advantage in that it reduces the amount of time required to analyse samples, screening for potential uranium zonation that is evident in the EDM induced track mount, is lost, while the age equations may need revaluating to assess whether they are capturing all of the uncertainties of the methodology. The process is also destructive and once ablated, all record of the counted track area is lost.

Despite these limitations, the LA-ICP-MS method was still applied to this thesis as the advantages outpace the issue; attempts to limit the effect of these setbacks were considered. Images of counted areas were taken prior to ablation for permanent record, digital coordinate system were setup to ensure the ablation pit was located on the counted area, zonation was monitored during the data reduction process and any grains indicating uranium zonation were discounted. Matrix matched reference apatite were used in the data reduction stage to account for the ablation behaviour of the unknowns apatite instead of using NIST glasses, though these were also included for monitoring sensitivity drift during analytical sessions.

3.3.10.1 Analytical protocol table

Laboratory and sample preparation		
Laboratory	University of Glasgow	University of Melbourne
Mineral type	Apatite	Apatite
Sample preparation	Conventional	Conventional
Imaging	Optical microscope	Optical microscope
Laser ablation parameters		
Laser model	ASI RESOlution	New Wave Research
Ablation cell	Lauren Technic S-155	SuperCell
Wavelength	193 nm (eximer ArF)	213 (Nd:YAG)
Pulse width	4 ns	4 ns
Fluence	2.5 J/cm^2	3.3 J/cm^2 (50-55%)
Repetition rate	5 Hz	5 Hz
Spot diameter	30µm	30µm
Ablation duration	30 s	25 s
Sampling mode	Static spot	Static spot
Carrier gas	100% He in cell, Ar make-up	100% He in cell, Ar make-up
Flow rate	~0.35 l min^{-1}	~0.4 l min^{-1}
ICP-MS parameters		
Instrument model/type	iCAP Qc	Agilent Tec.7700
Sample introduction	Ablated aerosol	Ablated aerosol
RF (Forward power)	1300 W	1350 W
Carrier gas & flow rate	He ~0.35 L/min	He ~0.4 L/min
Make-up gas & flow rate	Ar ~0.8 L/min	Ar ~1L/min
Plasma gas & flow rate	Ar ~14 L/min	Ar ~14L/min
Detection system	Single collector quadrupole	Single collector quadrupole
Data acquisition parameters		
Operation mode	Standard mode	Standard mode
Sampling scheme	Sample bracketing	Sample bracketing
Background scanning	25 s	25 s
Data acquisition time	25 s	25 s
Washout time	30 s	30 s
Integration time per peak/dwell time	200 ms	200 ms
Isotopes measured	^{43}Ca,^{35}Cl, ^{26}Mg, ^{55}Mn, ^{88}Sr, ^{89}Y, ^{139}La, ^{140}Ce, ^{141}Pr, ^{146}Nd, ^{147}Sm, ^{153}Eu, ^{157}Gd, ^{159}Tb, ^{163}Dy, ^{165}Ho, ^{166}Er, ^{169}Tm, ^{172}Yb, ^{175}Lu, ^{232}Th, ^{238}U	^{43}Ca, ^{139}La, ^{238}U
Data processing		
Gas blank	25 s	25 s
Calibration strategy	**Primary** – NIST 612, Durango apatite	**Primary** – NIST 612, Mud Tank apatite, Durango apatite
	Secondary - Mount Dromedary Complex apatite, Glasgow age reference A & B	**Secondary** - Mount Dromedary Complex apatite, Glasgow age reference A & B
Data processing package	Iolite–Trace elements DRS	Iolite–Trace elements DRS
Common Pb correction applied	No	No
Quality control/Validation	Mount Dromedary Complex apatite , Glasgow age reference A & B	Mount Dromedary Complex apatite, Glasgow age reference A & B

Table 3-2: Analytical protocol table for LA-ICP-MS analysis acquired at both the University of Melbourne and the University of Glasgow.

3.3.11 Track Length Distribution (TLD)

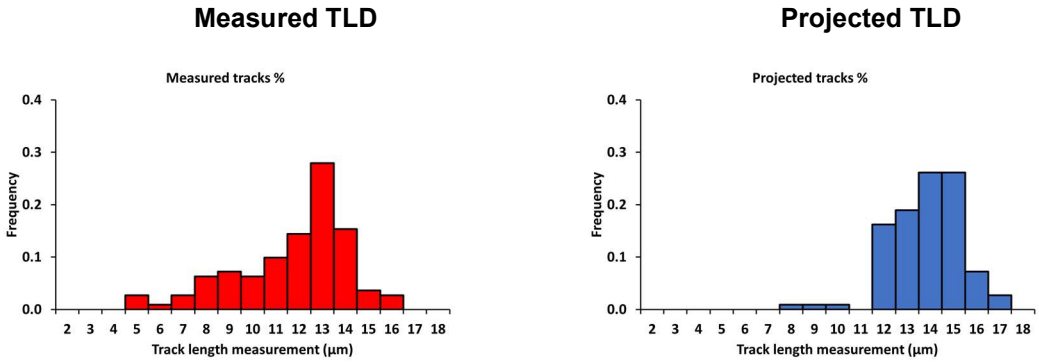

Figure 3-21: Radial plot and TLD example. The TLD of horizontal confined tracks for the same sample (A6G3) both before (left) and after (right) c-axis projection correction has been applied.

Details of the thermal history the sample has undergone is not solely contained within the fission track density but also with the horizontal confined track length distribution (TLD) (Figure 3-21) (Bertagnolli *et al.* 1983; Gleadow *et al.* 1986). Initial track length is controlled by the host mineral and the energy released during spontaneous decay; therefore, for a given mineral, initial track lengths are the same; in apatite, under standard etching conditions, when a track forms, it is 16.0 ±1µm (Gleadow *et al.* 1986; Donelick *et al.* 1999; Ketcham *et al.* 2007a). Any reduction in length is the function of the time during which the apatite was subjected to elevated temperatures (Fleischer et al. 1975). Annealing is the gradual restoration of the minerals ordered lattice from the amorphous state (Figure 3-11) and proceeds via initial track length shortening, followed by segmentation of the track (Green et al. 1986). As new tracks form continuously, each track experiences a different fraction of the total thermal history; if many confined tracks (~100) are measured, they provide an insight into the samples cooling history.

Confined tracks are contained completely beneath the polished surface and have been revealed due to their intersection with a track that intersects the polished surface of the crystal (Track In Track, TINT) (Figure 3-22) or with a defect (Track In Cleavage, TINCLE) providing a pathway for the acid. In this investigation, only TINT's were measured and included in the TLD due to uncertainties associated around TINCLE measurements (Reiners and Ehlers 2005). Where possible, at least 100 lengths were measured, per sample. Due to the low amount of measurable confined track lengths present in some of the samples, ^{252}Cf irradiation was used to enhance the number of recordable lengths for TLD. This irradiation took place on a second grain mount, not used for track density (fission track age) determinations. The pathways created by the ^{252}Cf irradiation increase the

potential for the acid to intersect a confined track for TLD measurements (Donelick and Miller 1991). ^{252}Cf irradiation was performed at the University of Melbourne (Australia).

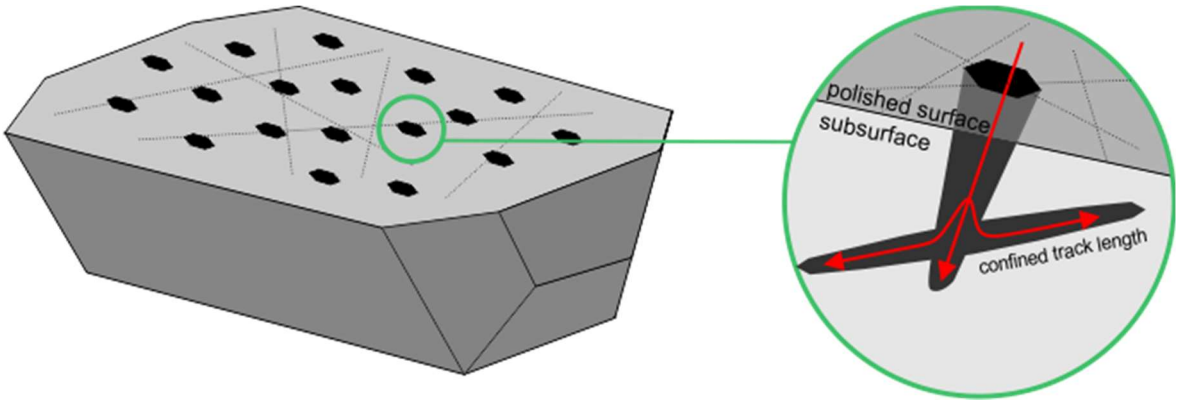

Figure 3-22: Confined track length. Fission tracks intersecting the polished surface are revealed by etching. Sometimes, this fission track intersects another that is confined beneath the polished surface, creating a pathway for the acid (red arrows). When both ends of the track can be seen clearly and it does not dip more the 10° from horizontal, the length of the track can be measured and recorded as TINT (Track IN Track). Horizontal, confined tracks that are revealed because the intersect a plane of cleavage through which the acid has penetrated inside the crystal can also be measured; they are called TINCLE (Track IN CLEavage).

3.3.11.1 Length calibration

Discrepancies between track length measurements both within and between labs, potentially due to etching technique, microscope settings, or the protocol used for taking the measurements have been highlighted in several studies (Miller et al., 1993; Barbarend et al., 2003; Ketcham et al., 2009; Ketcham et al., 2015). Consistency has been improved by introducing the c-axis projection (3.3.12.4), which adjust for the anisotropic annealing behaviour of fission tracks, but the issue has not been completely resolved (Ketcham 2005; Ketcham *et al.* 2007b). As the amount of annealing provides constraints on the maximum temperature experienced by the rock, the initial track length (unannealed, L_0) is an important parameter when modelling fission track data to retrieve thermal histories. L_0 however, rarely observable as most samples have experienced an element of annealing. It has been suggested that the initial track length correlates to Dpar measurements, and thus Dpar can be used as kinematic indicator to identify the samples initial track length (L_0) (Ketcham *et al.* 2007b).

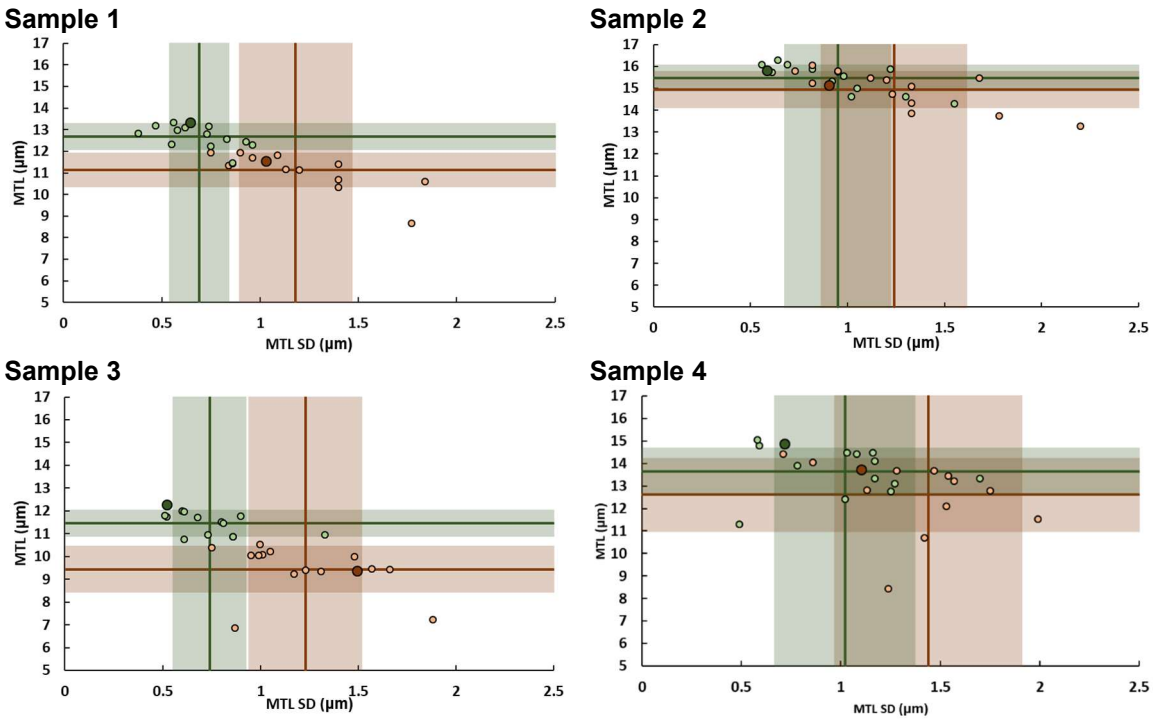

Figure 3-23: Track length measurements for annealed and unannealed induced tracks in Durango apatite at the University of Glasgow. Brown colour boxes encompass the variation of the raw track length measurements, while the green boxes represent the projected data. Light brown and green circles are the raw and projected results of individual analysts, dark brown and green spots measured by E.McKenna. Vertical and horizontal line represent lab average with ±1SD in shaded area.

Prior to undertaking confined track length measurements in unknown samples, horizontal confined track lengths were measured in a series of variably annealed and one unannealed Durango apatite crystals (Ketcham *et al.* 2015) by E McKenna in order to mitigate measurement bias. The results for the measured and projected track length for 15 analysts at the University of Glasgow, trained by Dr. Cristina Persano can be seen in Figure 3-23. The figure shows how track lengths are more reproducible once the c-axis projection has been applied. There is also good agreement between analysts within the lab with most measurements falling with 1 SD of the mean average. Track lengths recorded in this study are therefore suggested to be comparable to other fission track analysts and any measurement bias should be of a minimum.

3.3.12 Controls on annealing of fission tracks

3.3.12.1 Temperature

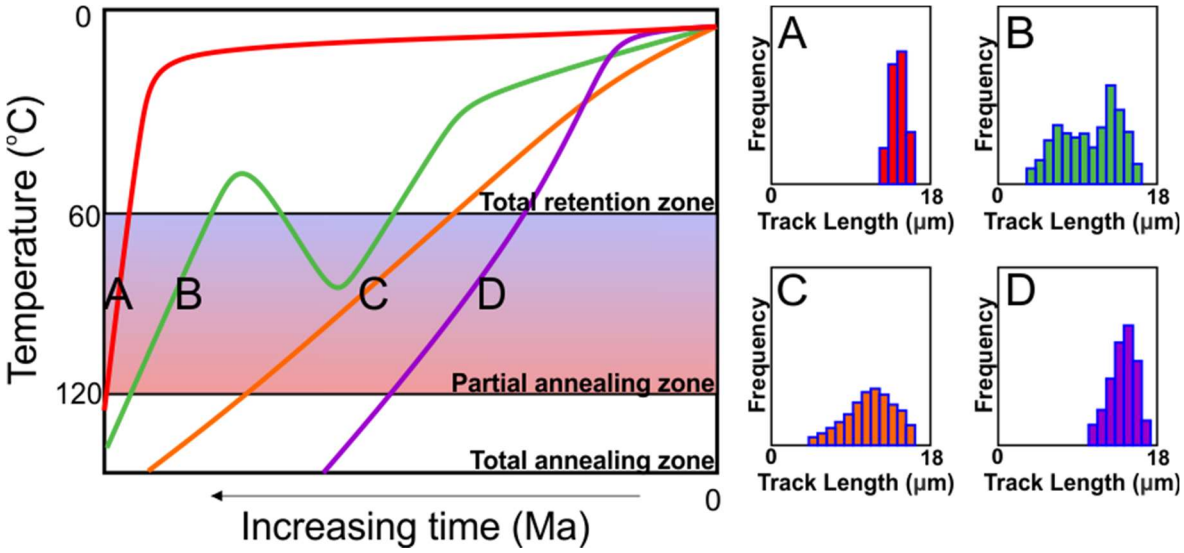

Figure 3-24: Hypothetical cooling histories and their corresponding Track Length Distributions. (A) Rapid cooling through the PAZ producing a narrow TLD, potentially a volcanic source. (B) A wide bimodal TLD indicating sample reheating into the PAZ temperature range, having cooled through it at an earlier time. (C) Slow protracted cooling through the PAZ, potentially from an undisturbed basement sample. (D) Moderate cooling through the PAZ creating a right skewed TLD

As temperature and time exhibit such a strong control over annealing, considerable research has been done in both laboratory (Green *et al.* 1986; G.M. Laslett *et al.* 1987) and natural settings such as deep boreholes (Gleadow and Duddy 1981; Naeser 1981) have proven that, over geological time (>~10,000 years) temperatures between ~60°C and ~120°C exhibit the strongest controls on annealing rate. At temperatures greater than ~120°C, fission tracks are totally annealed, whereas at temperatures colder than ~60°C (Spiegel *et al.* 2007), it proceeds at such a reduced rate that the tracks remain virtually unannealed, even over geological time. Different styles of thermal histories will produce variations of track length distributions, allowing the thermal history to be deduced Figure 3-24 (Gallagher 2012).

3.3.12.2 Chemical composition

Although temperature exhibits the dominant influence on annealing, the chemical composition of apatite $Ca_5(PO_4)_3(OH,F,Cl)$, the crystallographic orientation of the polished surface, uranium concentration, and pressure have also been suggested to influence annealing rate. Though the range of apatite chemistries are numerous due to both anion and cation substitutions, they typically fall into one of three end members; fluorapatite $Ca_5(PO_4)_3F$, chlorapatite $Ca_5(PO_4)_3Cl$, hydroxylapatite

$Ca_5(PO_4)_3(OH)$; in rocks, apatites have a composition that range between F- and Cl-rich; hydroxylapatite are typically found in organisms, for example in bones and teeth (Carlson *et al.* 1999). Early research into the influence of chemistry on annealing indicated that chlorapatite will anneal at a slower rate than fluorapatite and hydroxylapatite (Green *et al.* 1986; Carlson *et al.* 1999). Other element substitutions may also have an influence on annealing rate (Mn, Sr, Fe and REE), yet the extent of their influence is less understood (Barbarand *et al.* 2003; Ketcham *et al.* 2007b). Measuring the chlorine content (Cl wt%) to quantify annealing behaviour is traditionally done by either direct measurement by electron microprobe analysis (EPMA) or LA-ICP-MS, where apatites with a range of known chlorine content are analysed synchronously with unknown samples, creating a calibration curve (Chew *et al.* 2014). Alternatively, the kinetic parameter Dpar can be used as a proxy for annealing behaviour.

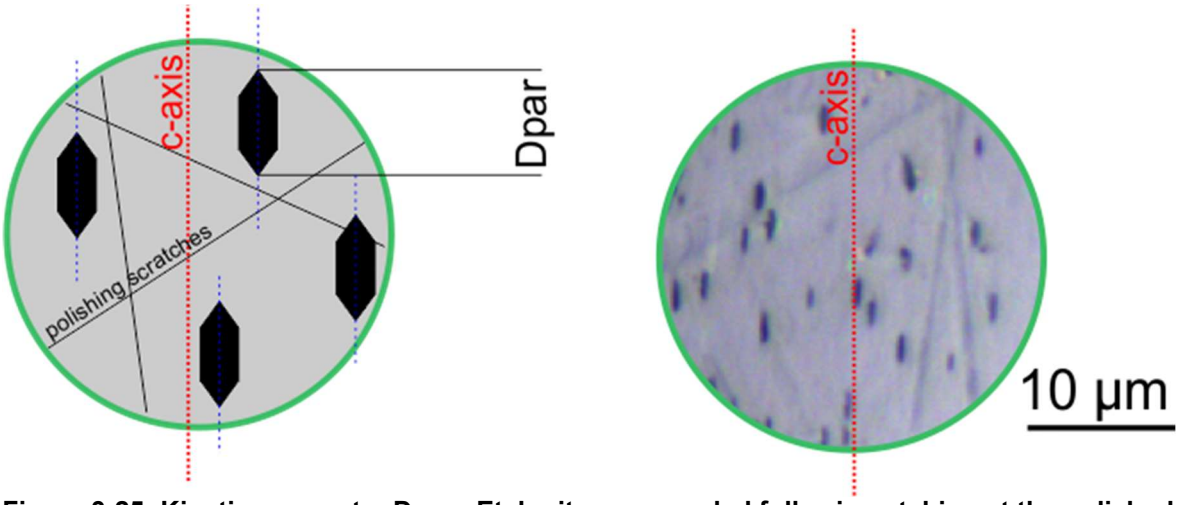

Figure 3-25: Kinetic parameter Dpar. Etch pits are revealed following etching at the polished surface and fission track interface. When the polished surface is parallel to the crystals c-axis the etch pits will be aligned with their long axis parallel to the crystals c-axis. Sample A6G2.

Etch pits form where the polished surface intersects an etched fission track. In apatite, polished surfaces aligning with the crystallographic c-axis tend to have etch figures with an elongate hexagonal form with the long axis parallel to the c-axis (Figure 3-25) (Donelick 2005). The measurement of the maximum diameter of an etch figure is known as the Dpar (Diameter parallel to c-axis). Dpar measurements are used as an independent parameter to constrain annealing behaviour in apatites and are often incorporated into the annealing algorithms used by the thermal history models. Grains with relatively low Dpar values anneal similarly to crystals of fluorapatite composition, while grains with a high Dpar value indicate compositional complexity and potentially increased annealing resistance (Carlson *et al.* 1999). Although the parameter has been positively correlated with chlorine (Cl) and hydroxyl (OH) content and negatively correlated with fluorine (F)

content, it is not a proxy for Cl content and the length of Dpars seem to be affected also by other factors, including the concentration of trace elements such as Sr, Mn and REE (Sobel and Seward 2010).

3.3.12.3 Dpar assessment

In this thesis Dpar length measurements were recorded for all analysed apatite, in order to investigate the accuracy and consistency of these measurements, more than 200 Dpars were measured on the unannealed Dur-2 sample of Ketcham (2015). This yielded a mean Dpar length of 1.75 ±0.17µm (Figure 3-26); Dpar values in Durango are rarely quoted in the literature and, given the difficulty of measuring such a short distance, it is expected to be slightly variable from analyst to analyst; the value that appears in the software HeFTy as default is 1.80 microns, very similar to the one obtained here. Dpar measurements from another Durango mount are also shown in Figure 3-26, yielding an average of 1.71 ±0.19µm. The two mean values overlap, indicating that Dpar are measured accurately and consistently.

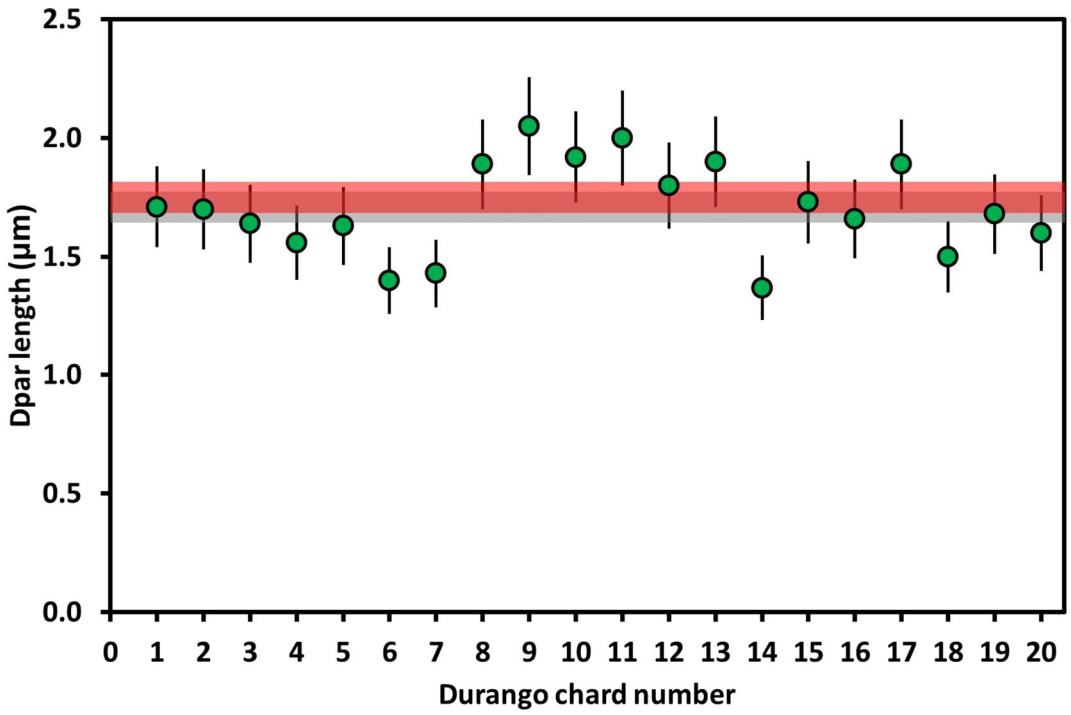

Figure 3-26: Dpar calibration. Mean average Dpar measurements for unannealed Dur-2 sample 1.75 ±0.17µm, grey bar (n = 200), plotted with individual Dpar measurements from another unannealed Durango apatite crystal, with a mean average of 1.71 ±0.19µm, red bar.

In this thesis, kinetic parameter Dpar was measured in all grains selected for AFT age calculations and in all grains where horizontal, confined fission tracks were measured. The thermal histories were derived using the multi-kinetic model of Ketcham that constrains annealing using Dpar values

(Ketcham *et al.* 2007a; Ketcham *et al.* 2007b). Single grain ages and Dpar values have been plotted using Radial Plotter (Vermeesch 2009) for each sample (Chapter 6 section 6.2.5); no correlation between Dpar and single grain age is apparent, suggesting that, in this case, either the chemical composition of the analysed grains is roughly constant or that it does not play a major role in controlling annealing.

3.3.12.4 Crystallographic orientation

Annealing and etching rates in apatite are anisotropic in relation to crystallographic orientation; tracks perpendicular to the c-axis anneal at a faster rate compared to those parallel (Green *et al.* 1985; Green *et al.* 1986; Donelick 1991), while tracks parallel to c-axis will etch faster than those perpendicular (Gallagher *et al.* 1998). This indicates that the angle of a confined track length and the c-axis (on the 110) plane should be measured and used in modelling thermal histories. In this thesis, only confined track lengths in grains with the polished surface parallel to crystallographic c-axis were measured, along with the lengths angle to the c-axis. Length orientation in relation to the crystals c-axis can be used to project the lengths, removing the effect of anisotropic annealing (Ketcham *et al.* 2007a). Only c-axis projected lengths were used in thermal history modelling in this thesis, however both non-projected and projected confined track lengths are reported in Chapter 6 and Appendix D & E.

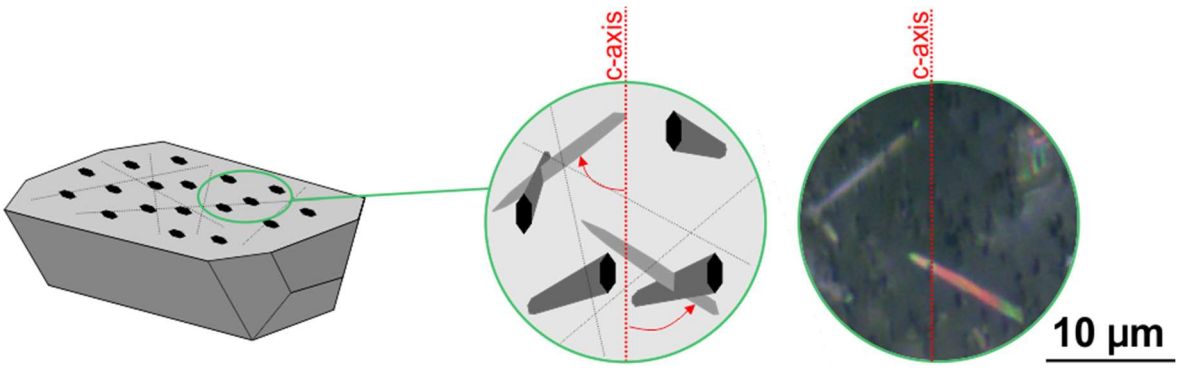

Figure 3-27: Confined track length angle to the crystals c-axis. Confined track lengths at a high angle to the crystals c-axis will anneal at a faster rate than those at a low angle, thus both confined track length, angle to the crystals c-axis (red arrow) and Dpar must be recorded for every track length measurement used in the TLD. Sample A6G2.

3.3.12.5 Radiation enhanced annealing

AFT analysis undertaken in areas that have been geologically stable for >100Ma have produced results that may indicate that enhanced annealing has taken place at low temperatures (Hendriks

and Redfield 2005; McDannell *et al.* 2019). Hendriks and Redfield (2005) attribute this enhanced annealing to the high radioactive element content within the samples (U & Th) and suggest that Radiation Enhanced Annealing (REA) due to alpha emission could be driving this low temperature recovery. However, this has been the subject of much debate (Larson *et al.* 2006; Kohn *et al.* 2009). In order to explore this in this thesis, the ^{238}U concentration for each single grain age has been plotted on a radial plot to investigate whether a radiation enhanced annealing becomes evident. This is discussed further in Chapters 6 and 9.

3.4 Thermal history modelling

Examining the AFT age and track length distribution outlined above allows for some direct interpretation of the data to be made. However, as there are complex mechanisms at play, such as annealing properties, variations in apatite chemistry, and track c-axis orientation (Green *et al.* 1986; G. Laslett *et al.* 1987; Ketcham *et al.* 2007b), numerical modelling of these observed data is often required. There are two widely available, user-friendly software programmes used to extract cooling histories of AFT data, Hefty or QTQt (Ketcham 2005; Gallagher 2012). These software programmes can be used to model the observed data through either forward or inverse modelling. Forward modelling allows the user to define a thermal history in the time-Temperature space; the software predicts, using defined annealing algorithms, the fission track dataset (AFT age and TLD) that would be consistent with the defined thermal history; these data can be directly compared to the observed for interrogation. Inverse modelling finds, within the given time-Temperature space, the thermal histories that are consistent with the observed data. If available, additional data such as (U-Th)/He ages, vitrinite reflectance, and U-Pb ages can be added to provide tighter constraints and potentially more robust thermal histories. Geological constraints, such as sedimentary stratigraphic ages or unconformities must also be added as constraints for the thermal history model.

3.4.1 QTQt theoretical basis

This thesis utilises the inverse and forward thermal history modelling of the observed thermochronological data detailed in Chapter 6, using the Bayesian trans-dimensional modelling software QTQt version 5.7 (Gallagher 2012), with the multi-kinetic fission track annealing model of Ketcham (2007b). The software utilises the observed AFT data to derive thermal history models using a Reversible Jump Markov Chain Monte Carlo (RJ-MCMC) iterative approach (Sambridge *et*

al. 2006; Gallagher *et al.* 2009; Gallagher 2012). A general range on time and temperature is provided as prior information model space. This model space is then randomly sampled (MCMC approach), producing a proposed model that is either accepted or rejected, based on the fit with the observed data. The trans-dimensional aspect to the approach means that the number of time-temperature points that define each thermal history is not predefined and can therefore be treated as an unknown parameter that can be optimised as the modelling progresses, allowing the data to determine the model complexity, not the user. The Bayesian aspect to the approach is a statistical method based on conditional probabilities, utilising a log likelihood algorithm to quantify the fit of the observed data to the model predicted data. The software penalises overly complex models proposed during the MCMC sampling, in favour of models with fewer T-t points that adequately fit the observed data. This is done by calculating the posterior probability of the model:

$$P(M \mid D) = P(M).P(D \mid M) \tag{3.34}$$

Where P(M|D) is the posterior probability of obtaining the proposed model given the data; P(D|M) is the likelihood probability function of obtaining the data given the model and P(M) is the prior probability density function given to the model (Gallagher 2012). The general prior model space is searched iteratively with creations of multiple thermal histories that are tested against the observed data creating an expected thermal history weighted for its posterior probability distribution (i.e., the probability of obtaining the proposed model, given the data). New thermal models are proposed from the initial thermal model by changing a time (t), temperature (T), both t and T, adding a new t-T point (birth), removing a t-T point (death), offset value in multiple sample modelling, resampling kinetic parameters (Dpar, chemical composition), or resampling observed data. The outcome is a range of credible models which fit the data and excludes unjustified, overly complex models. A great strength of this approach is that the user is not required to add constraints prior to modelling; however, these constraints can be added in successive iterations, if required to test hypothesis on the thermal history. The software also allows for multiple samples in a profile i.e. a borehole or samples from a specific region to be modelled together to provide a more robust interpretation of the thermal history; these strengths were utilised in Chapter 7.

The MCMC approach can be separated into two parts, the *burn-in* and the *post-burn-in*. The burn-in represents the initial search of the model space, which helps to define credible thermal histories; these models are a ‘starting point’ and will be successively discarded. The post-burn-in is used to

estimate the posterior probability distribution by keeping accepted thermal histories. Initially, short c.10,000 burn in, 10,000 post burn-in iteration runs are performed to optimise the MCMC search parameters. Once adequate acceptance rates have been achieved, longer runs with a minimum of 200,000 iterations (*burn-in* and *post-burn-in*) are performed. This approach provides an output of accepted thermal history models and their associated posterior probability of fitting the observed data, such as the maximum likelihood model, maximum posterior model, and maximum mode model. The Maximum Likelihood model statistically fits the observed data the best; however, to do so, it contains more t-T points than other output models, often creating an overly complicated and potentially geologically unjustified thermal history, potentially leading to over interpretation of the data (Gallagher 2012). The Maximum Posterior model typically contains fewer t-T points than the Maximum Likelihood, while the maximum mode model is produced by dividing the model space into squares with the dimensions of 1°C by 1 million years and plotting the mode value that passes through each 1 million year step. The software also produces a mean thermal history, weighted for its posterior probability, known as the Expected model, which is the preferred model in Bayesian formulations; the model is accompanied by its 95% credible intervals. Debate still exists on which model should be used to explain the data, in particular if the maximum likelihood model or a weighted mean expected model should be used. In this thesis the expected model, along with its 95% credible intervals, Max. Likelihood, and Max. Posterior models were produced for all thermal histories. This was done to provide a more robust assessment of how each of the models fit the observed data and provide a critical insight on the validity of the derived thermal histories (Figure 3-28).

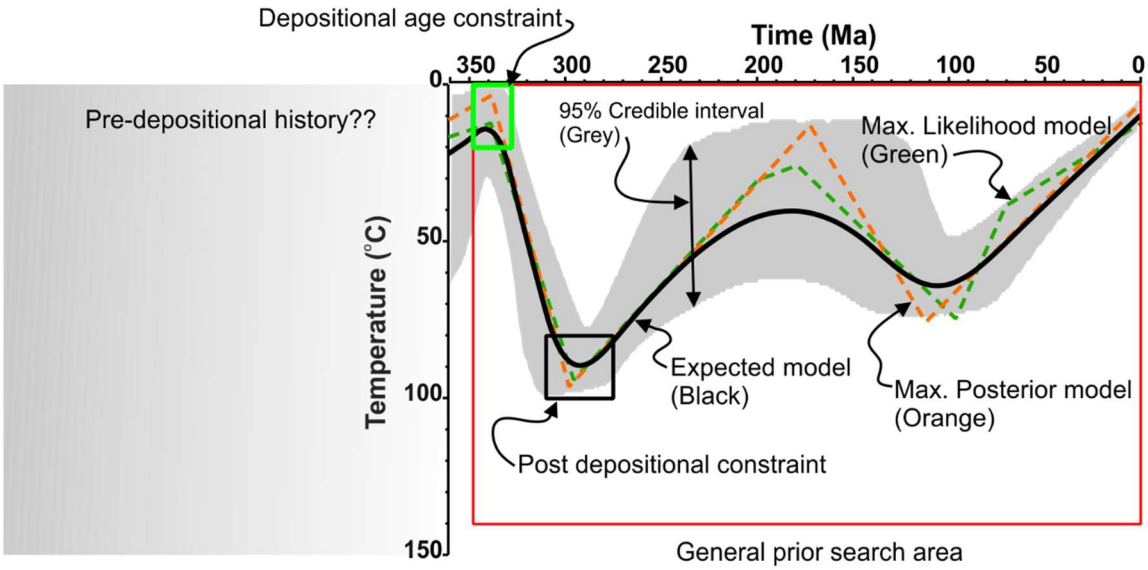

Figure 3-28: QTQt thermal history model. Figure shows the thermal history model for sample EM-12 from the Midland Valley. See text for definition of components and model types.

3.5 Limitations and conclusions

AFT thermochronology has had a long and successful history as an extremely useful tool to investigate the thermal evolution of the upper crust, with applications in a wide range of geological settings. Despite this success, the technique is not without its limitations, some of which are highlighted below along with how they were addressed in this thesis:

- Accessory minerals like apatite are usually only present in small quantities or not at all in sedimentary rocks. Apatite is susceptible to physical and chemical weathering and alteration by acidic solutions, hampering the quantity and quality of the data that can be extracted.

Large samples were collected when possible and all apatite were screened for cracks, inclusions, and dissolution textures prior to analysis to ensure the quality of the data.

- The technique is very time consuming; samples need to be crushed, separated, mounted, polished, and etched prior to any analysis.

Robust workflows were setup to ensure the samples were processed thoroughly and methodically.

- When the EDM is used, samples are required to be irradiated in nuclear reactors where the thermal flux is extremely constant and stored safely for several weeks following irradiation.

LA-ICP-MS method was used for AFT age determination which continues to see refinement; however, the most current published methodologies at the time of analysis were adhered to (Gleadow *et al.* 2015).

- The etching preparation stage is vital, samples that have been over or under etched will produce inaccurate data; etching conditions are particularly important for Dpar and confined track length measurements.

Samples of Durango apatite with a well constrained Dpar value were etched alongside unknown samples as a quality assurance check for etching protocol.

- The lack of an external detector for age determination by LA-ICP-MS makes uranium zonation, common in apatites (Jolivet *et al.* 2003) difficult to detect. This is problematic for apatites where U concentration is variable within the crystal or low, or for grains with zero tracks (Vermeesch 2019).

All analysis were monitored at the data reduction stage in iolite where uranium zonation can easily be spotted due to the changing signal in the $^{43}Ca/^{238}U$ ratio. Analysis displaying zonation were discounted. No zero track apatites were found in this study.

- The location of the ablated spot needs to be monitored with care to ensure correlation with the counted area.

Counted area coordinates were imported into the LA-ICP-MS system from the FT microscope and examined prior to ablation. Excellent agreement between the counted area and ablation spot were observed.

The results from AFT thermochronology and thermal history modelling are presented in Chapter 6 and 7, followed by the discussion of their implications on the burial and exhumation history of the Midland Valley of Scotland in Chapter 8.

Chapter 4 Provenance Results

4.1 Introduction

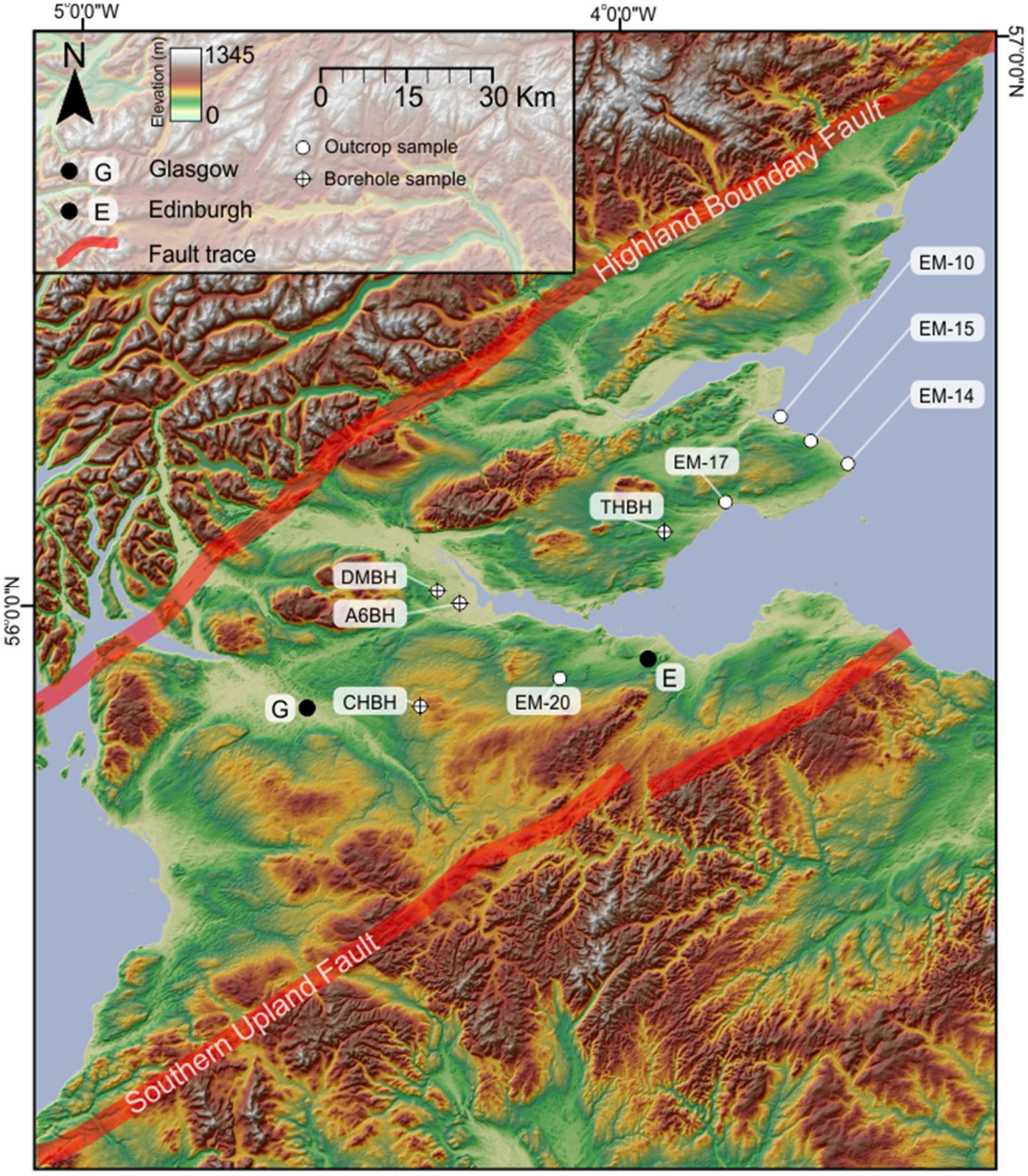

Figure 4-1: U-Pb analysis sample locations. Apatite and zircon sample locations for detrital U-Pb analysis collected for this investigation.

This chapter presents the detrital zircon and apatite U-Pb analytical results from Carboniferous sandstones collected from outcrops and boreholes (BGS core repository, Keyworth) located across the central and eastern Midland Valley of Scotland (Figure 4-1). Samples were selected on the bases of giving the best spatial and temporal insight into the provenance evolution of the Carboniferous sedimentary rock, providing the samples yielded both detrital apatite and zircon (Figure 4-2). Apatite

and zircon grains from the same samples were separated and mounted using the methods outline in Appendix B at the University of Glasgow, mineral processing facility. Sample CHBH yielded a small amounts of apatite grains, so the conclusions derived from these data need to be taken with caution and interpreted with the caveat of the small number of analysis. EM-010 only yielded zircon crystals, and so U-Pb apatite ages are not available. The mineral mounts were inspected and imaged under cathodoluminescence (CL) and back scattered electron (BSE) at the Imaging spectroscopy and analysis centre (ISAAC) at the University of Glasgow, using the FEI Quanta 200F Scanning Electron Microscope (SEM) and the Carl Zeiss SIGMA VP SEM. The observation was performed to identify micro-textures, growth zonation, cracks and inclusions that had gone under-detected under the optical microscope; crystals with such features were excluded from analysis, as they would hamper the accuracy of the U-Pb determinations. Zircon grain sizes were typically <300 μm on their longest axis, with morphologies ranging from euhedral to well-rounded, and colour range from purple to colourless. CL microscopy revealed a range of textures (Figure 4-3), from unzoned, sector zoned, and oscillatory zoned crystals. Zircon populations were dominated by single growth crystals; however, crystals containing xenocrystic cores and recrystalised or new growth domain rims were present, while others appeared to be fragments of former megacrystic zircon. Apatite grain sizes were typically <200 μm on their longest axis, morphologies range from euhedral to rounded, and were always colourless and clear, except when discoloured by inclusions. CL microscopy also revealed growth zonation, while ^{238}U zonation was revealed by chemical etching (Figure 4-4).

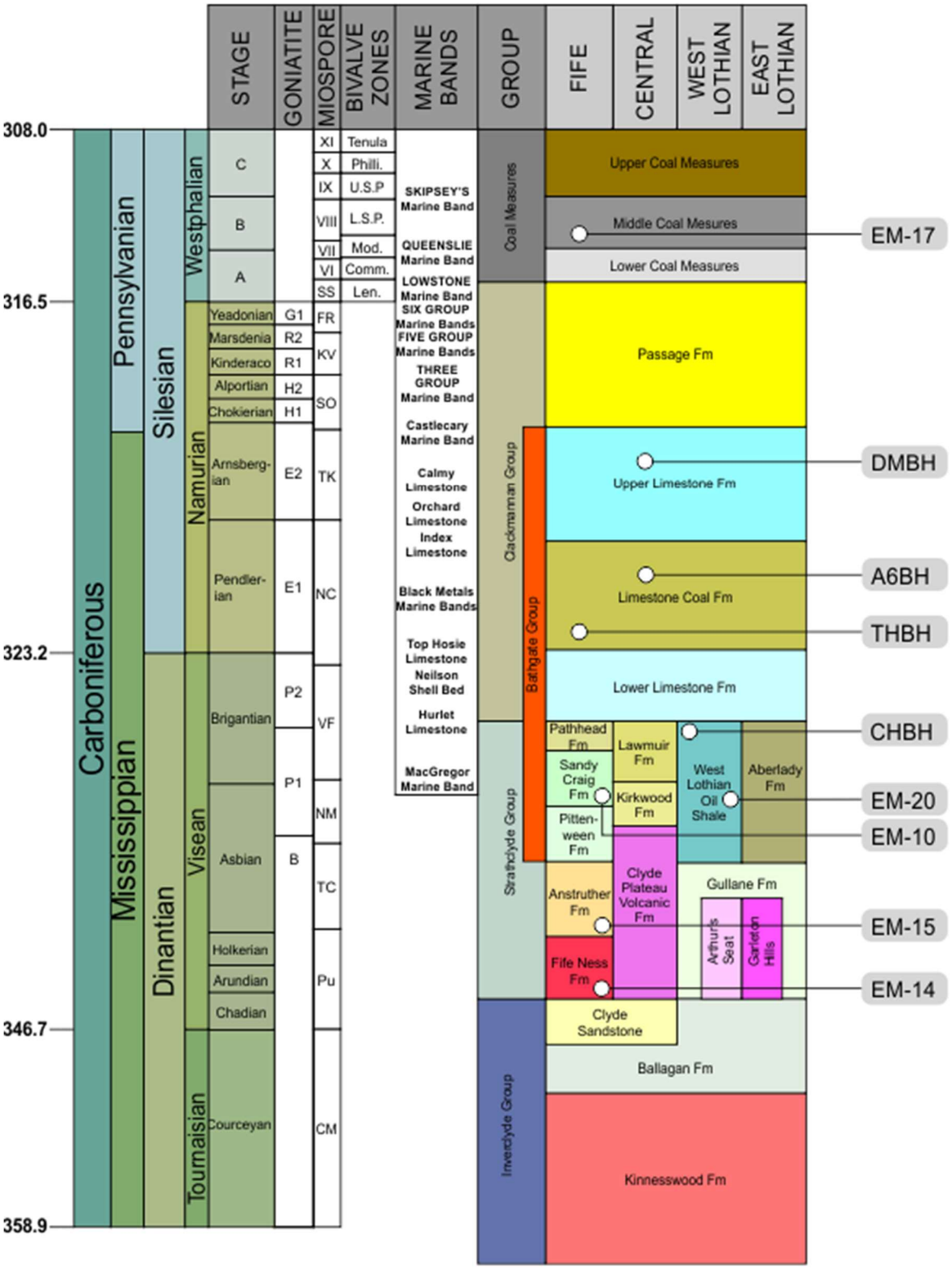

Figure 4-2: Approximate sample locations on the lithostratigraphic column. Column adapted from lithostratigraphical chart Chapter 2.

4.1.1 Zircon textures

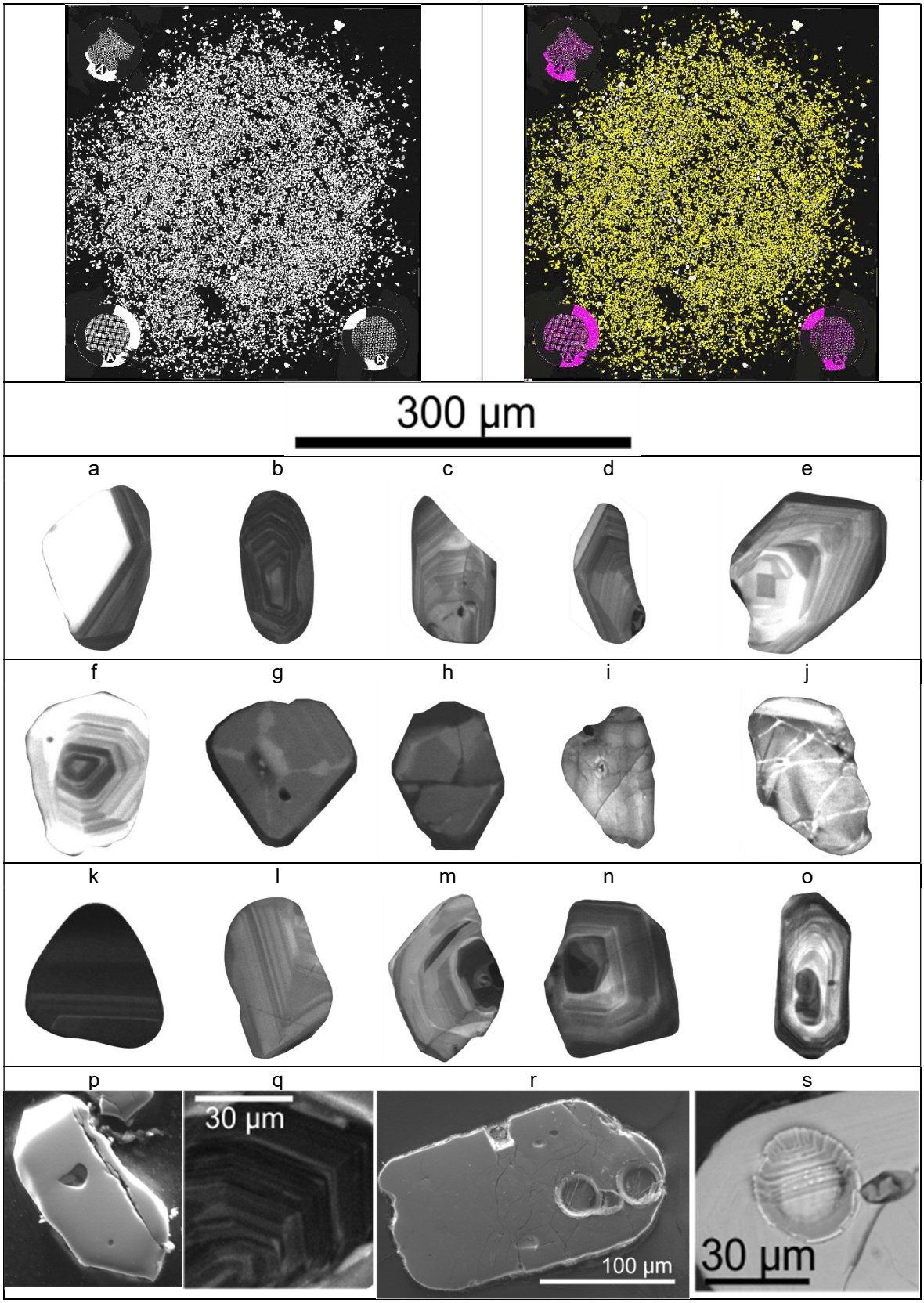

Figure 4-3. Zircon textures. Top row: Sample THBH (left) BSE scan of a typical 25mm zircon mount from this thesis, (right) EDX compositional map for zirconium (yellow) on the same mount. (a) Bimodal zoning, (b-f) oscillatory growth zoning, (g) Sector zoned, (h) discrete fracture, (i) complex network of fractures, (j) complex network of infilled fractures, (k-l) megacrystic zircon, (m-o) xenocrystic cores, (p) polished surface, (q) high frequency oscillatory zoning, (r-s) laser ablation pits.

4.1.2 Apatite textures

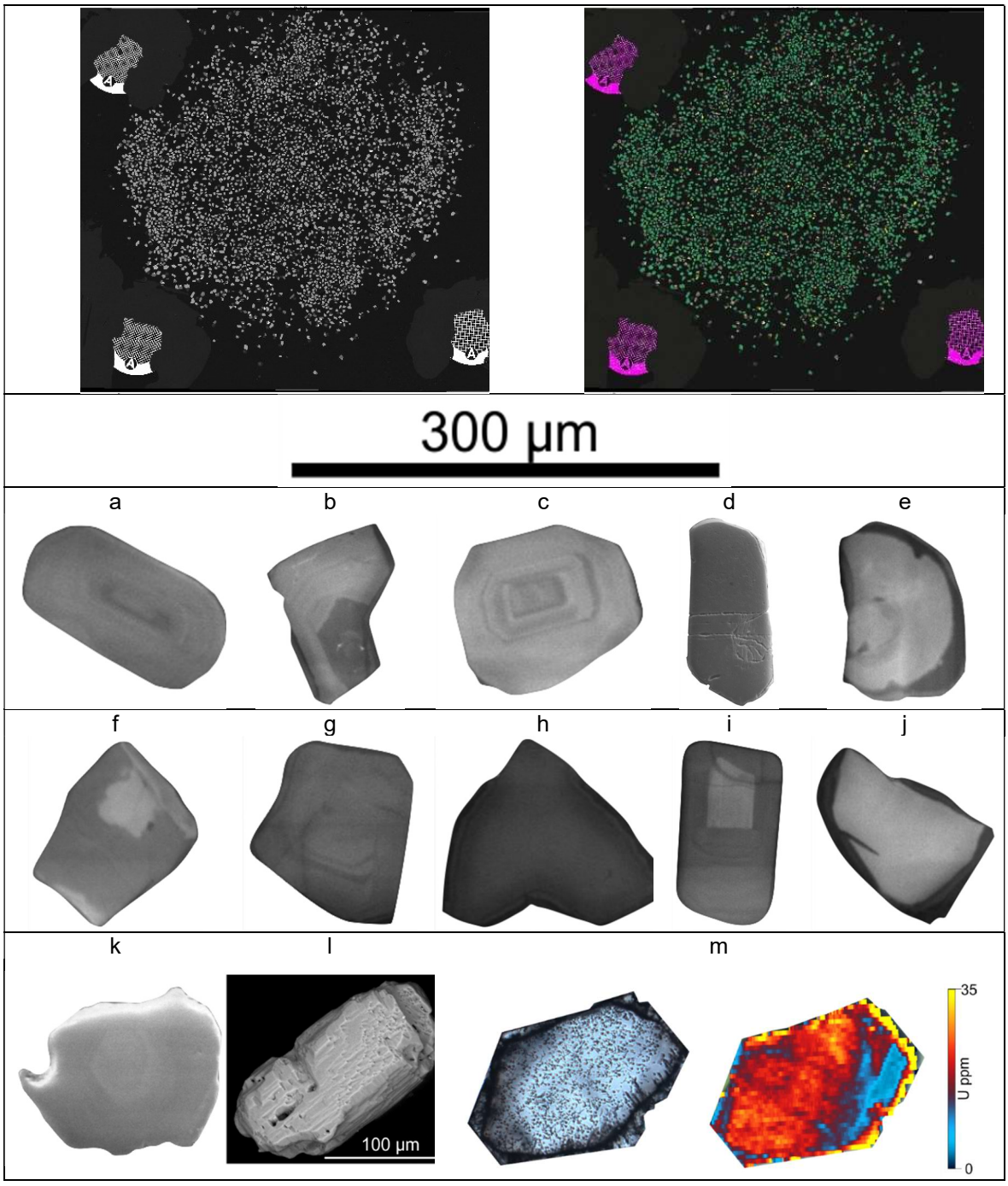

Figure 4-4: Apatite textures. . Top row sample THBH (left) BSE scan of a typical 25mm apatite mount from this thesis, (right) EDX compositional map for phosphorous (green) on the same mount. (a-c) CL images pf apatite, (d) Secondary Electron image of polished surface, (e) dark CL rim surrounding apatite, (f) bright CL cored apatite, (g-h) dark featureless apatite, (i) bright CL cored apatite, (j) dark CL rim apatite,(k) BSE image of apatite, (l) BSE image of apatite not in resin, showing dissolved exterior, (m) LA-ICP-MS image of an apatite, (left) etched apatite polished across the basal section shows authigenic rim. (right) laser ablation image showing U concentration is enriched n the authigenic rim compared to the interior, bottom left shows low uranium concentration which corresponds to area of lower track density of the left.

4.2 Results

U-Pb data was obtained by laser ablation inductively coupled plasma mass spectrometry (LA-ICP-MS) using a New Wave 193 nm ArF Excimer laser coupled to a Nu Instruments, Nu Plasma HR, MC-ICP-MS at the National Environmental Research Council Geochronology and Tracers Facility (NERC-GTF) based in BGS, Keyworth, England; the analytical parameters are summarised in Table 4-1. Eight isotopes were acquired for each grain (^{91}Zr, ^{202}Hg, ^{204,206,207,208}Pb, ^{232}Th, ^{238}U), using a 25 µm laser spot, 10 Hz repetition rate, and a fluence of 2.3 J/cm^{-2} for zircon, and a 32 µm laser spot with a fluence of 2.0 J/cm^{-2} for apatite. The analytical procedure utilised repeated analysis of a primary standard reference material dispersed throughout each analytical session, to correct for instrumental drift and downhole fractionation; each session also contained secondary reference materials for accuracy checks and quality control measures. The iolite™ software package (Paton *et al.* 2011) was used to reduce all raw data in this investigation. This software applies a user defined baseline correction for each isotope and analytical session. Time-resolved fractionation response is characterised using a user defined downhole fractionation correction model, which is applied by the data reduction scheme (DRS) to the analytical session. Sample-standard bracketing is used to account for the session wide drift of the isotopic ratios, by normalising the ratios to those of the primary standard reference material. For zircon analysis, the 91500 zircon (^{206}Pb/^{238}U TIMS age of 1065.4 ±0.6 Ma (Wiedenbeck *et al.* 1995)) was used as the primary reference material, followed by Pleisovice (^{206}Pb/^{238}U TIMS age of 337.13 ±0.37 Ma (Sláma *et al.* 2008)), GJ-1 (^{206}Pb/^{238}U 0.097877 ± 0.07% in-house TIMS standard) and Mud Tank zircon (^{206}Pb/^{238}U LA-ICP-MS age of 731.0 ±0.2 Ma (Gain *et al.* 2019)) as secondary reference materials. Raw data were reduced using the Geochronology Data Reduction Scheme (DRS) (Paton *et al.* 2011); IsoplotR (Vermeesch 2018) and BGS in-house software (GTF Visualisation) were used for U-Pb age calculations and data display. Results for all analyses have been tabulated and can be found in Appendix C, ages are quoted at 2σ absolute level after propagation by quadratic addition. Reference material used as quality control for the analysis yielded a ^{206}Pb/^{238}U age of 338.0 ±3 Ma (2σ), MSWD (Mean Square Weighted Deviation) 0.9 for the Pleisovice; ^{206}Pb/^{238}U age 602.0 ±5 (2σ), MSWD 1.1 for the GL-1, and a ^{206}Pb/^{238}U age of 733.0 ±3 Ma (2σ), MSWD 4 for the Mud Tank zircon, which are in good agreement with the published data highlighted above. Concordia plots have been produced with >±10% discordant grains excluded. Probability density plots (PDP's) and Kernel density estimates (KDE's) have been produced for all samples (sections 4.3-4.5); however, only KDE's are used for

interpretation of data due to the preferred statistical approach of this method, as discussed in Chapter 3 (Vermeesch 2012).

For apatite analysis, the Madagascar apatite ($^{206}Pb/^{238}U$ ID-TIMS age of 473.5 ±0.17 (Thomson *et al.* 2012)) was used as the primary reference material, followed by Mount McClure apatite ($^{207}Pb/^{235}U$ ID-TIMS age of 523.51 ±1.47 Ma (Schoene and Bowring 2006)) and Durango apatite ($^{40}Ar/^{39}Ar$ age of 31.44 ±0.18 Ma (McDowell *et al.* 2005)) as secondary reference materials. Raw data were reduced using the VizualAge DRS in iolite™ (Paton *et al.* 2011; Petrus and Kamber 2012), which allows for the correction of non-radiogenic Pb (aka common Pb or initial Pb), often found in apatite. Here a ^{207}Pb based correction was applied to the reference materials, based on assumed initial $^{207}Pb/^{206}Pb$ ratio from the publications outlined above. As variable amounts of non-radiogenic Pb would be expected in detrital apatite with unknown initial $^{207}Pb/^{206}Pb$ ratio, a common Pb correction needs to be applied, in order to produce meaningful results. This was achieved by plotting uncorrected U-Pb results in Tera-Wasserburg space (Chapter 3 section 3.2.3). In this plot the $^{238}U/^{206}Pb$ and $^{207}Pb/^{206}Pb$ values of cogenetic apatite populations would typically form linear arrays; a linear regression through the data determines the y-axis interception, which represents the initial $^{207}Pb/^{206}Pb$ ratio that, in turn, can be used to calculate the unanchored ^{207}Pb based correction (Mark *et al.* 2016). In detrital samples, multiple populations of apatite may be present within each sample, each representing an age population with its own initial $^{207}Pb/^{206}Pb$ ratio, which was used to produce population specific ^{207}Pb corrected U-Pb ages. Results for all analyses have been tabulated and can be found in Appendix C. Reference material used as quality control for the analysis yielded age of 519 ±4 Ma (2σ), MSWD 2.4 for the Mount McClure, and 32.2 ± 1.5 Ma (2σ) MSWD 1.5 for Durango, which are in good agreement with the published data highlighted above. Tera-Wasserburg plots for each sample excluding those with large analytical uncertainties (typically >c.25%) have been produced, along with ^{207}Pb corrected age KDE's plots and are presented in the sections below.

4.2.1 LA ICP MS parameters table

Laboratory and sample preparation		
Laboratory	NIGL-GTF	NIGL-GTF
Mineral type	Zircon	Apatite
Sample preparation	Conventional	Conventional
Imaging	BSE, CL, Optical	BSE, CL, Optical
Laser ablation parameters		
Laser model	New Wave Research	New Wave Research
Ablation cell	TV2	TV2
Wavelength	193 nm (eximer ArF)	193 nm (eximer ArF)
Pulse width	4 ns	4 ns
Fluence	2.3 J/cm^2	2.0 J/cm^2
Repetition rate	10 Hz	10 Hz
Spot diameter	25 µm	32 µm
Ablation duration	30 s	20 s
Sampling mode	Static spot	Static spot
Carrier gas	100% He in cell, Ar make-up	100% He in cell, Ar make-up
Flow rate	~0.8 l min^{-1}	~0.8 l min^{-1}
ICP-MS parameters		
Instrument model/type	Nu Instruments, Nu Plasma HR, MC-ICP-MS	Nu Instruments, Nu Plasma HR, MC-ICP-MS
Sample introduction	Air aspiration/ablated aerosol	Air aspiration/ablated aerosol
RF (Forward power)	1300 W	1300 W
Make-up gas flow rate	Sourced from Nu Instruments DSN-100 desolvating nebulizer. Neb pressure 24psi (estimated at 0.7l/min) Ar.	Sourced from Nu Instruments DSN-100 desolvating nebulizer. Neb pressure 24psi (estimated at 0.7l/min) Ar.
Detection system	Mixed Faraday-multiple ion counting array	Mixed Faraday-multiple ion counting array
Data acquisition parameters		
Operation mode	Standard mode	Standard mode
Sampling scheme	Sample bracketing	Sample bracketing
Background scanning	25 Sec	25 Sec
Data acquisition time	25 Sec	25 Sec
Washout time	30 Sec	30 Sec
Integration time per peak/dwell time	200 ms	200 ms
Masses measured	202-207, 235, 238	202-207, 235, 238
Data processing		
Gas blank	25 s	30 s
Calibration strategy	**Primary** - 91500	**Primary** - Madagascar
	Secondaries/Validation - GJ-1, Mud Tanks, Pleisovice	**Secondaries/Validation** – Mount McClure, Durango
Data processing package	Iolite & GTF visualisation	Iolite & GTF visualisation
Common Pb correction applied	No	See text for details
Quality control/Validation	Pleisovice $^{206}Pb/^{238}U$ age 338.0 ±3 (2σ), MSWD 0.9 GJ-1 $^{206}Pb/^{238}U$ age 602.0 ±5 (2σ) MSWD 1.1 Mud Tank $^{206}Pb/^{238}U$ age 733.0 ±3 Ma (2σ) MSWD 4	Mount McClure $^{206}Pb/^{238}U$ age 519 ±4 Ma (2σ) MSWD 2.4 Durango $^{206}Pb/^{238}U$ age 32.2 ±1.5 Ma (2σ) MSWD 1.5

Table 4-1: LA-ICP-MS parameter table. NIGL-GTF (NERC Isotope Geosciences Laboratory – Geochronology and Tracers Facility)

4.3 Viséan samples

4.3.1 Fife Ness Formation (EM-014)

4.3.1.1 Zircon

A total of 150 zircon grains were analysed with 139 yielding ages within the concordance level outlined above (±10%) (Figure 4-6). Ages ranged from c.400 Ma to c.3000 Ma, with KDE plots showing populations occurring in the Phanerozoic, Proterozoic, and Archean; Phanerozoic ages (c.10% of the entire population) all fall between c.400-500 Ma; Proterozoic ages (c.80%) dominate the sample; There is a general lack of ages between c.500-900 Ma, except for one grain yielding a $^{206}Pb/^{238}U$ age of 568 ±5 Ma. Predominant peaks are present at c.1100 Ma, c.1400 Ma, 1650 Ma, and c.1750 Ma followed by another absence of ages between c.1850 Ma and c.2500 Ma. Archean ages (c.10%) form a small broad bi-modal distribution with one peak at c. 2500 Ma and another slightly larger peak at 2750 Ma.

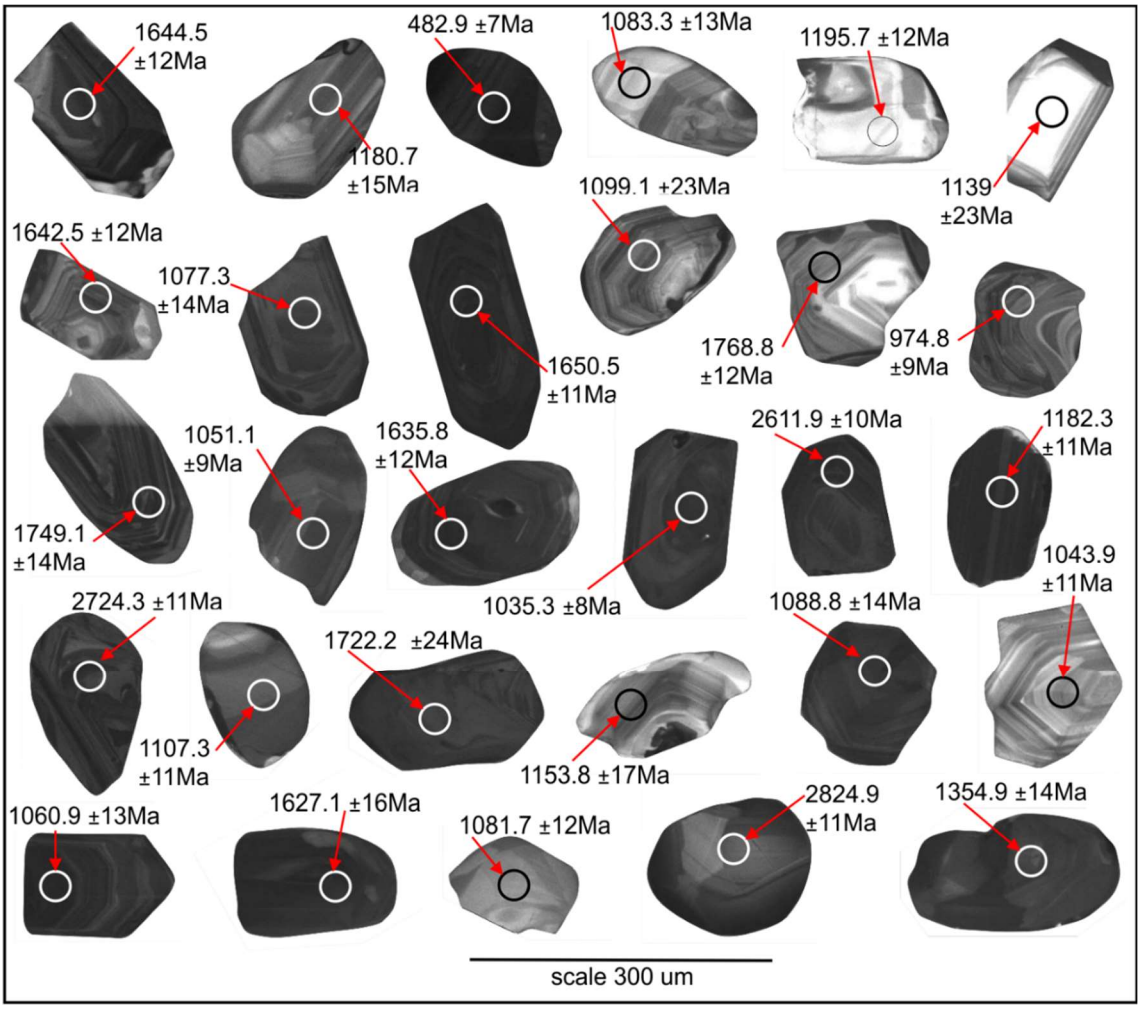

Figure 4-5: Selection of CL images from sample from the Fife Ness Formation, EM-014. Circle within grain indicates the location of the laser ablation with corresponding age and 2σ error.

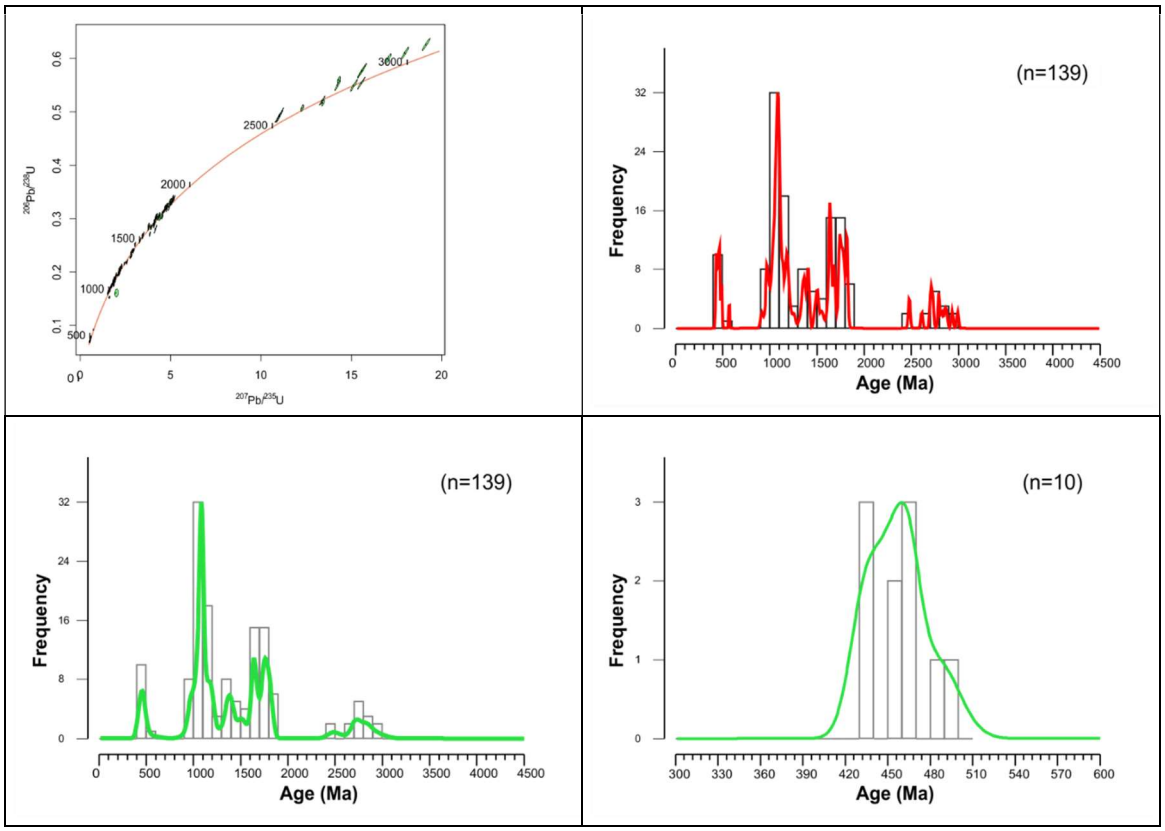

Figure 4-6: Zircon results for EM-014. Top left, concordia diagram; top right probability density plot (PDP); bottom left kernel density estimate (KDE); bottom right kernel density estimate (KDE) for Palaeozoic ages only. n = number of analysis. All plots produced using IsoplotR (Vermeesch 2018).

4.3.1.2 Apatite

A total of 150 apatite grains were analysed with 131 yielding ages within the concordance and uncertainty level outlined above. The raw data are shown in T-W space (Figure 4-7) form three linear arrays, which allows for the calculation of the unanchored common Pb regression lines (Figure 4-7), providing population ages of 421.5 ±2 Ma, 1536.7 ±6 Ma, and 2498.0 ±60 Ma. 131 individual apatite U-Pb ages were calculated following a ^{207}Pb correction based on the upper intercept (^{207}Pb/^{206}Pb) of the relevant common Pb regression line. The ^{207}Pb corrected single grain ages are displayed on a KDE plot, with the dominant Palaeozoic peak also shown in more detail.

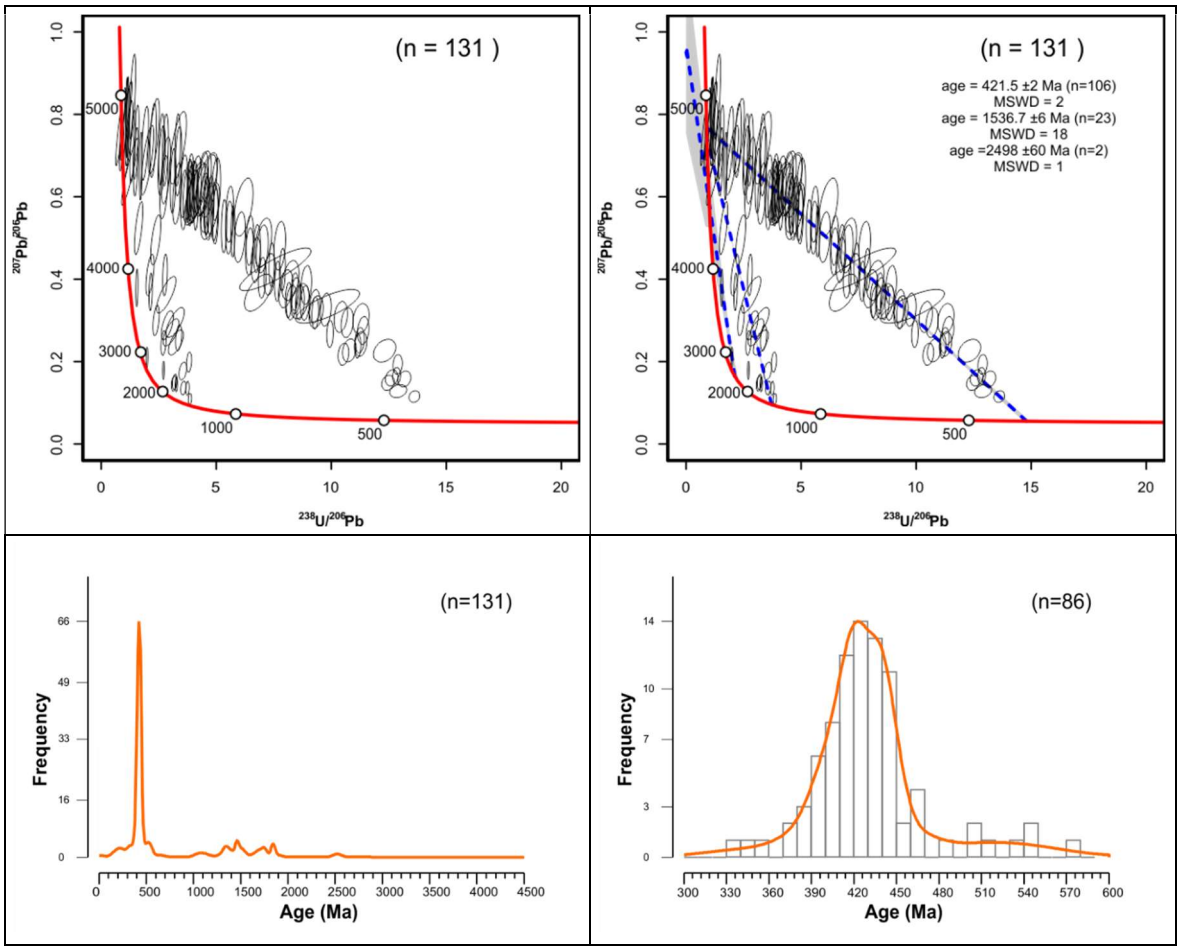

Figure 4-7: Apatite results for EM-014. Top left, 2σ ellipse Tera-Wasserburg (T-W) plot without regression lines; top right T-W plot with regression lines through suggested populations; bottom left kernel density estimate (KDE) for ^{207}Pb corrected single grain ages; bottom right kernel density estimate (KDE) for Palaeozoic ages. n = number of analysis. MSWD-mean square of weighted deviations. T-W and KDE plots produced using IsoplotR (Vermeesch 2018).

4.3.2 Anstruther Formation (EM-015)

4.3.2.1 Zircon

A total of 214 zircons were analysed with 189 yielding ages within the concordance cut-off level. Ages range from c.400 to c.3200 Ma, with KDE plots showing populations occurring in the Phanerozoic, Proterozoic, and Archean. Phanerozoic ages (5%) fall between 400-500 Ma, Proterozoic ages (75%) dominate the sample with predominant peaks at c.1100 Ma, c.1350 Ma, and 1700 Ma, with the Palaeoproterozoic peak having subordinate peaks at 1800 Ma and 1900 Ma. There is a general lack of ages between 500 and 900 Ma and 2000 and 2500 Ma. The Archean peak (c.20%) has a subordinate peak at 2500 Ma, but is dominated by a peak at c.2700 Ma. The oldest zircon in this sample returned a $^{207}Pb/^{206}Pb$ age of 3197 ±14 Ma.

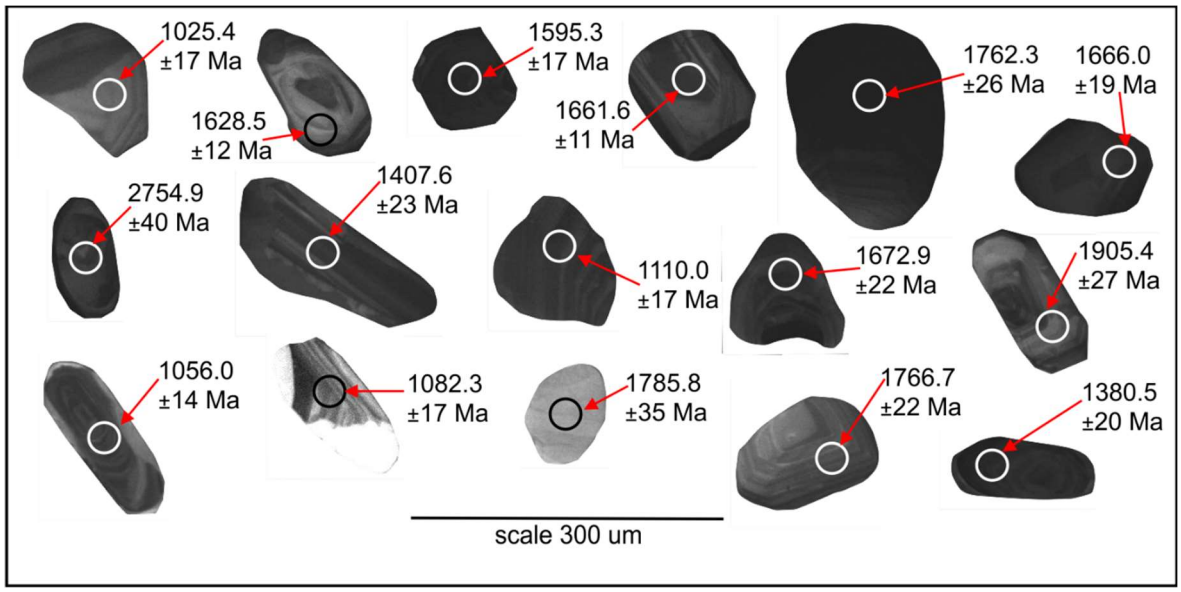

Figure 4-8: Selection of CL images from sample from the Anstruther Formation, EM-015. Circle within grain indicates the location of the laser ablation with corresponding age and 2σ error.

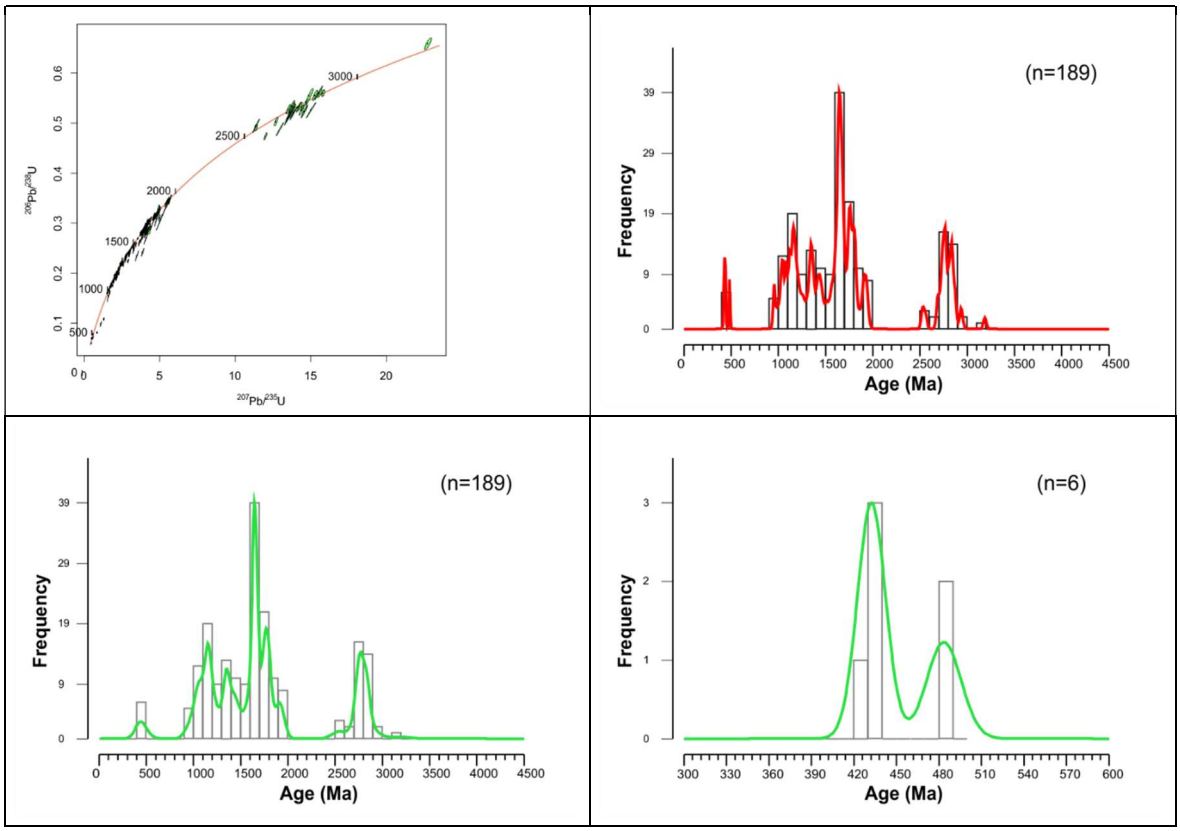

Figure 4-9: Zircon results for EM-015. Top left, concordia diagram; top right probability density plot (PDP); bottom left kernel density estimate (KDE); bottom right kernel density estimate (KDE) for Palaeozoic ages. n = number of analysis. All plots produced using IsoplotR (Vermeesch 2018).

4.3.2.2 Apatite

A total of 150 apatite grains were analysed, with 103 yielding ages within the concordance and uncertainty level outlined above. Raw data are shown in T-W space (Figure 4-10); the data form

three linear arrays allowing for the calculation of the unanchored common Pb regression lines (Figure 4-10) providing population ages of 428.4 ±4 Ma, 1839.9 ±9 Ma, and 2521.3 ±11 Ma. 103 individual apatite U-Pb ages were calculated following a ^{207}Pb correction based on the upper intercept ($^{207}Pb/^{206}Pb$) of the relevant common Pb regression line. Corrected single grain ages are displayed on a KDE plot with the dominant Palaeozoic peak also shown in more detail.

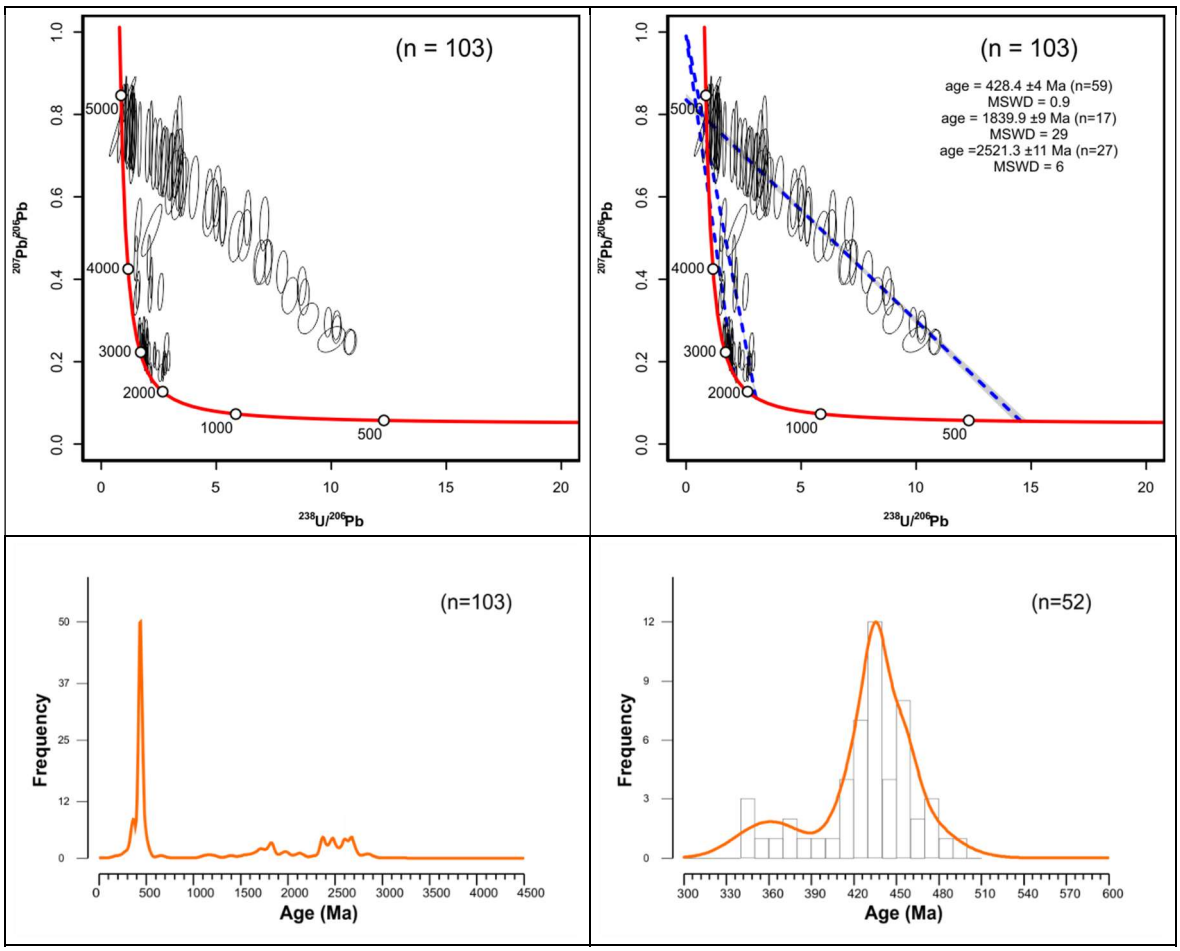

Figure 4-10: Apatite results for EM-015. Top left, 2σ ellipse Tera-Wasserburg (T-W) plot without regression lines; top right T-W plot with regression lines through suggested population; bottom left kernel density estimate (KDE) for ^{207}Pb corrected single grain ages; bottom right kernel density estimate (KDE) for Palaeozoic ages. n = number of analysis. MSWD-mean square of weighted deviations. T-W and KDE plots produced using IsoplotR (Vermeesch 2018).

4.3.3 Sandy Craig Formation (EM-010)

4.3.3.1 Zircon

A total of 150 zircons were analysed, with 132 yielding ages within the concordance cut-off level. Ages range from c.400 to c.2700 Ma; the KDE plots show Phanerozoic, Proterozoic, and Archean populations. Phanerozoic ages (25%) fall between 330-500 Ma, Proterozoic ages (65%) dominate the sample with predominant peaks at c.1100 Ma, c.1500 Ma, and 1700 Ma. There is a general lack

of ages between 500 and 900 Ma and 2000 and 2500 Ma. The Archean peak (c.10%) is dominated by a peak at c.2700 Ma. The oldest zircon in this sample returned a $^{207}Pb/^{206}Pb$ age of 2805 ±33 Ma. No apatite grains were found in this sample.

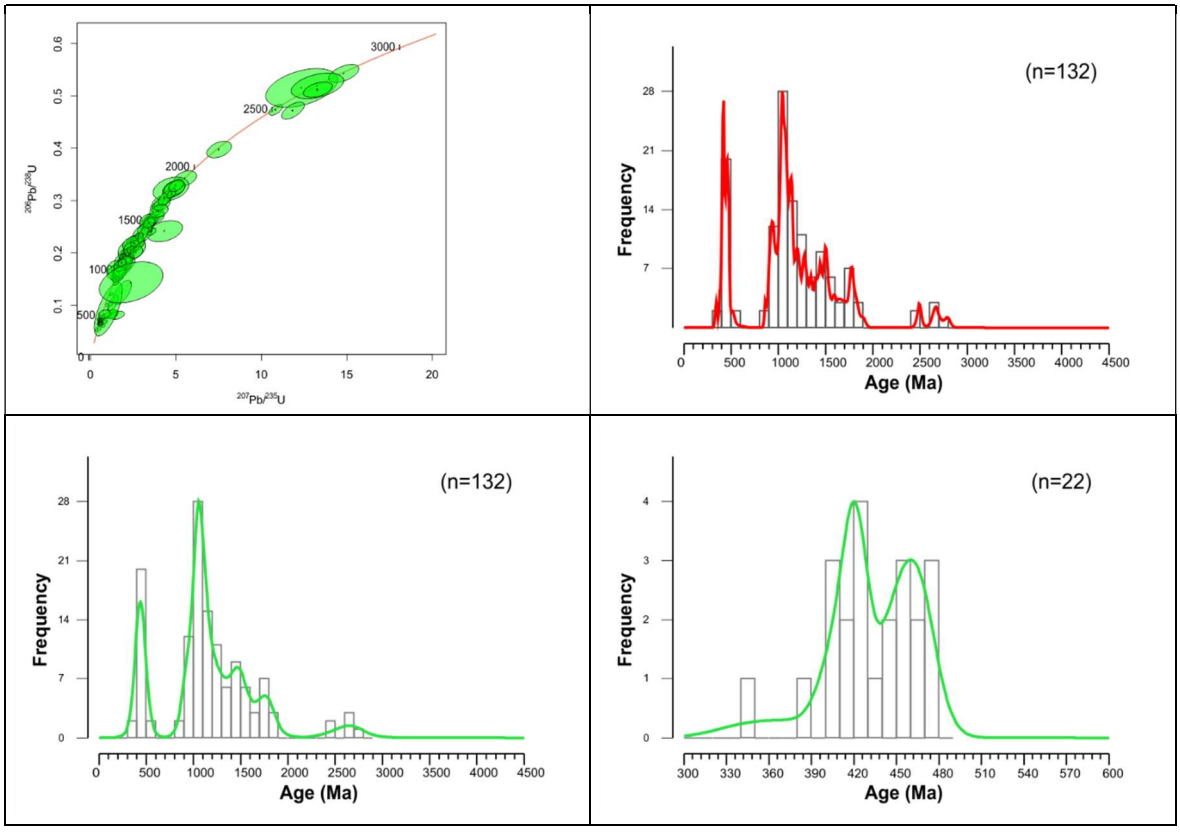

Figure 4-11: Zircon results for EM-010. Top left, concordia diagram; top right probability density plot (PDP); bottom left kernel density estimate (KDE); bottom right kernel density estimate (KDE) for Palaeozoic ages. n = number of analysis. All plots produced using IsoplotR (Vermeesch 2018).

4.3.4 West Lothian Oil Shale Formation (EM-020)

4.3.4.1 Zircon

A total of 150 zircons were analysed, with 141 yielding age within the concordance cut-off level. Ages range from c.330 to c.3600 Ma with KDE plots showing populations occurring in the Phanerozoic, Proterozoic and Archean. Phanerozoic ages (c.20%) fall between 300-500 Ma, and can be subdivided into two peaks, one at c.330 Ma and a second, more prominent, at 400-500 Ma. Proterozoic ages (c.60%) dominate the sample with main peaks at c.1100 Ma, c.1300 Ma, and 1800 Ma. Like for the older samples, there is a general lack of ages between 500 and 900 Ma and 2000 and 2500 Ma. The Archean peak (c.20%) has a subordinate peak at 2500 Ma, but is dominated by a peak at c.2700 Ma. The youngest zircon in this sample was dated at 327 ±5 Ma ($^{206}Pb/^{238}U$) while oldest zircon returned a $^{207}Pb/^{206}Pb$ age of 3643 ±11 Ma.

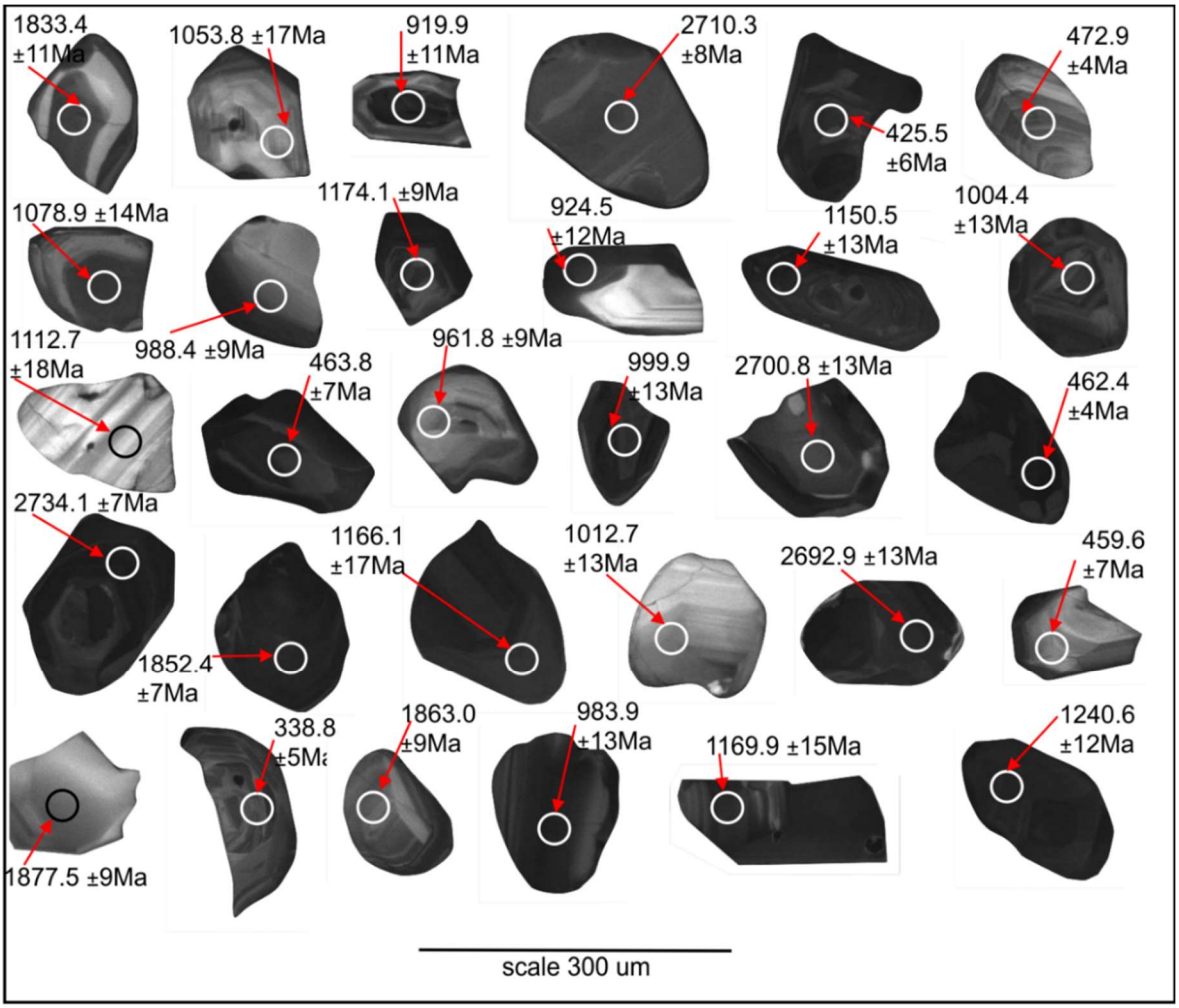

Figure 4-12: Selection of CL images from sample from the West Lothian Oil Shale Fm, EM-020. Circle within grain indicates the location of the laser ablation with corresponding age and 2σ error.

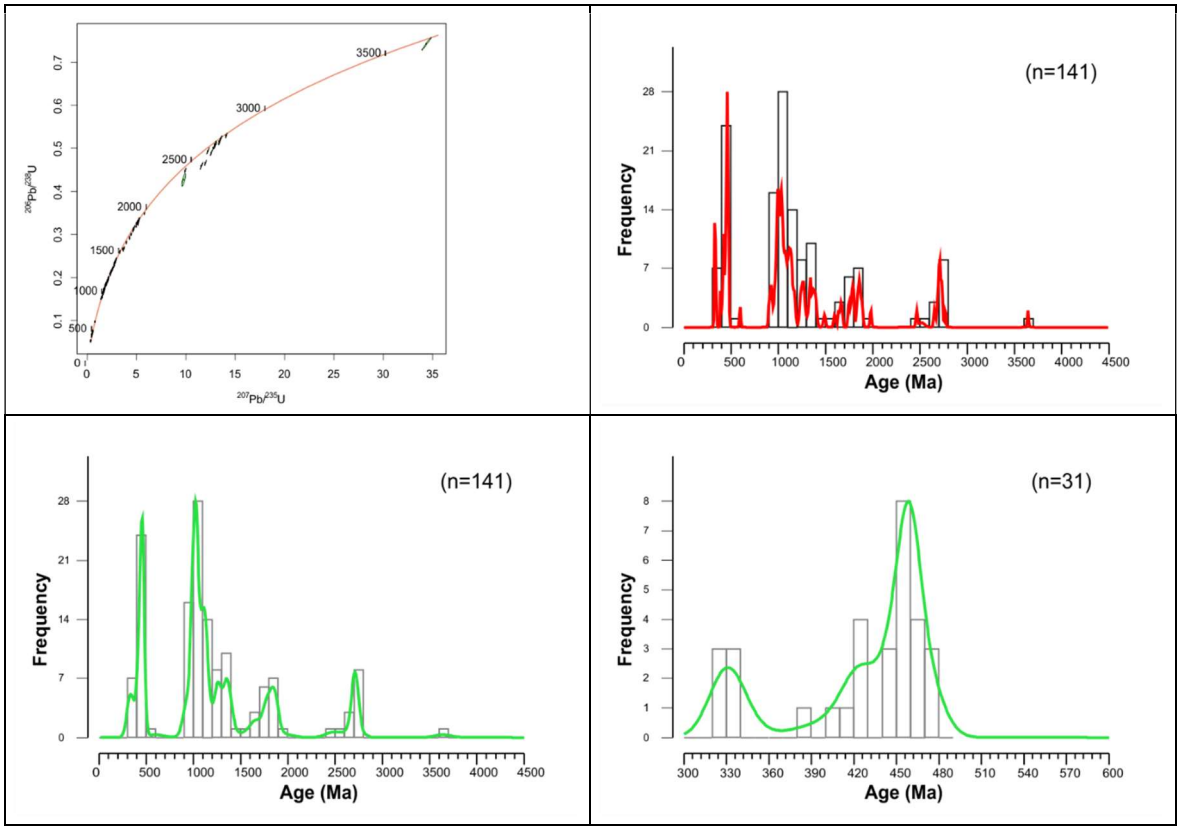

Figure 4-13: Zircon results for EM-020. Top left, concordia diagram; top right probability density plot (PDP); bottom left kernel density estimate (KDE); bottom right kernel density estimate (KDE) for Palaeozoic ages. n = number of analysis. All plots produced using IsoplotR (Vermeesch 2018).

4.3.4.2 Apatite

A total of 150 apatite grains were analysed, with 122 yielding ages within the concordance and uncertainty level outlined above. Raw data are shown in T-W space (Figure 4-14); the data form four linear arrays which allows for the calculation of the unanchored common Pb regression lines (Figure 4-14), providing population ages of 341.2 ±2 Ma, 461.1 ±2 Ma, 1566 ±8 Ma, and 2270.0 ±37 Ma. 122 individual apatite U-Pb ages were calculated following a ^{207}Pb correction based on the upper intercept ($^{207}Pb/^{206}Pb$) of the relevant common Pb regression line. Corrected single grain ages are displayed on a KDE plot with the dominant Palaeozoic peak also shown in more detail.

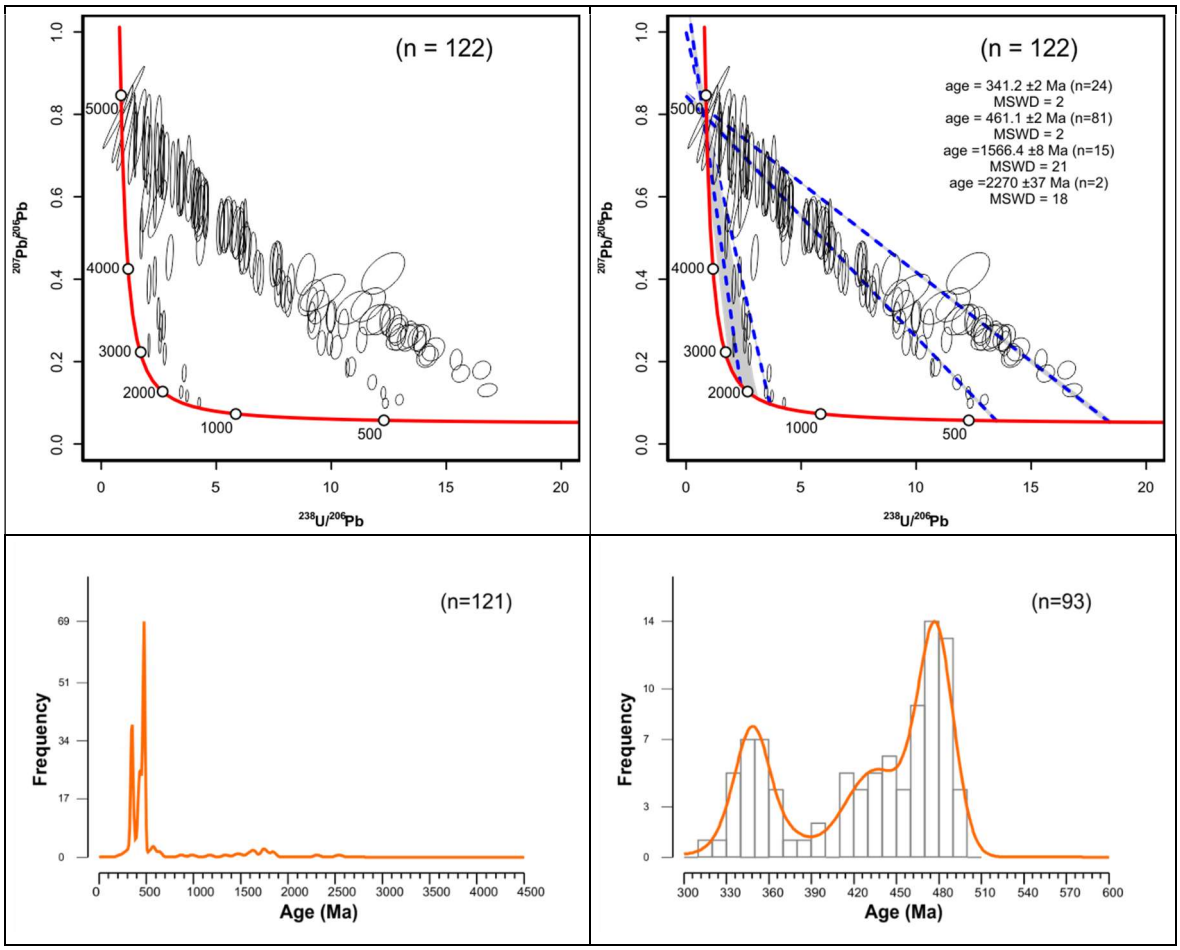

Figure 4-14: Apatite results for EM-020. Top left, 2σ ellipse Tera-Wasserburg (T-W) plot without regression lines; top right T-W plot with regression lines through suggested population; bottom left kernel density estimate (KDE) for ^{207}Pb corrected single grain ages; bottom right kernel density estimate (KDE) for Palaeozoic ages. n = number of analysis. MSWD-mean square of weighted deviations. T-W and KDE plots produced using IsoplotR (Vermeesch 2018).

4.3.5 West Lothian Oil Shale Formation (CHBH)

4.3.5.1 Zircon

A total of 150 zircons were analysed with 133 yielding age within the concordance cut-off level. Ages range from c.340 to c.3500 Ma with KDE plots showing populations occurring in the Phanerozoic, Proterozoic and Archean. Phanerozoic ages (c.5%) fall between 340-450 Ma and only consist of 4 grains. Proterozoic ages (c.85%) dominate the sample with main peaks at c.1100 Ma, 1700 Ma, and 1800 Ma. Subordinate peaks also occur at 1200 Ma and 1500 Ma. There is a general lack of ages between 500 and 900 Ma and 2000 and 2500 Ma. The Archean ages (c.10%) are dominated by c.2700 Ma ages though a subordinate peak at 2500 Ma is also present. The youngest zircon in this sample was dated at 339 ±11 Ma ($^{206}Pb/^{238}U$) while oldest zircon returned a $^{207}Pb/^{206}Pb$ age of 3549 ±19 Ma.

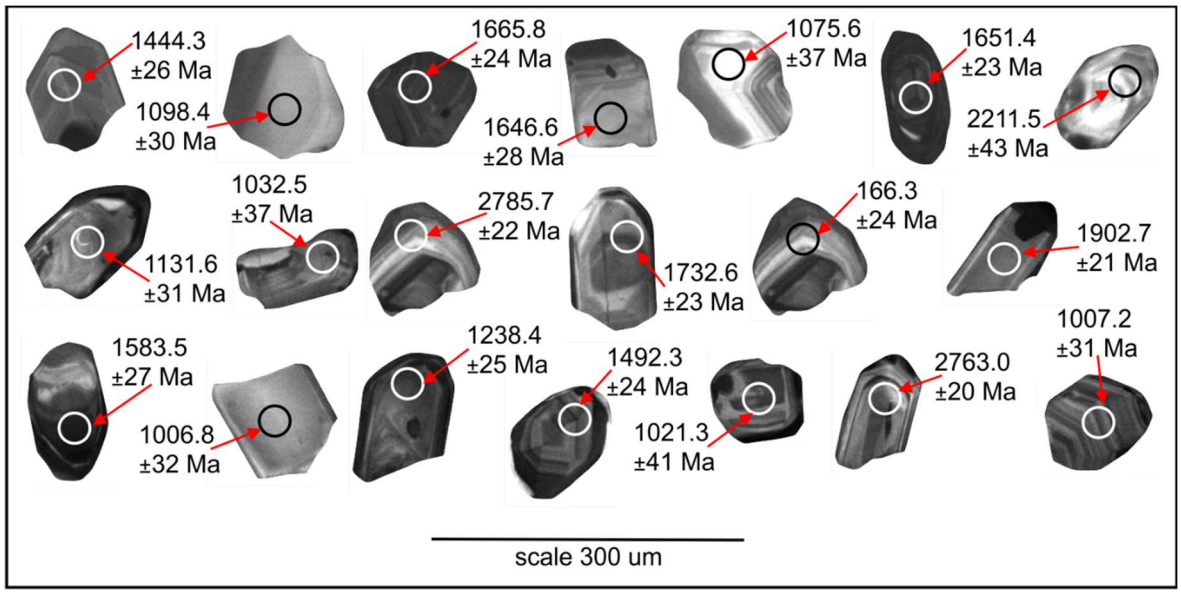

Figure 4-15: Selection of CL images from sample from the West Lothian Oil Shale Fm, CHBH. Circle within grain indicates the location of the laser ablation with corresponding age and 2σ error.

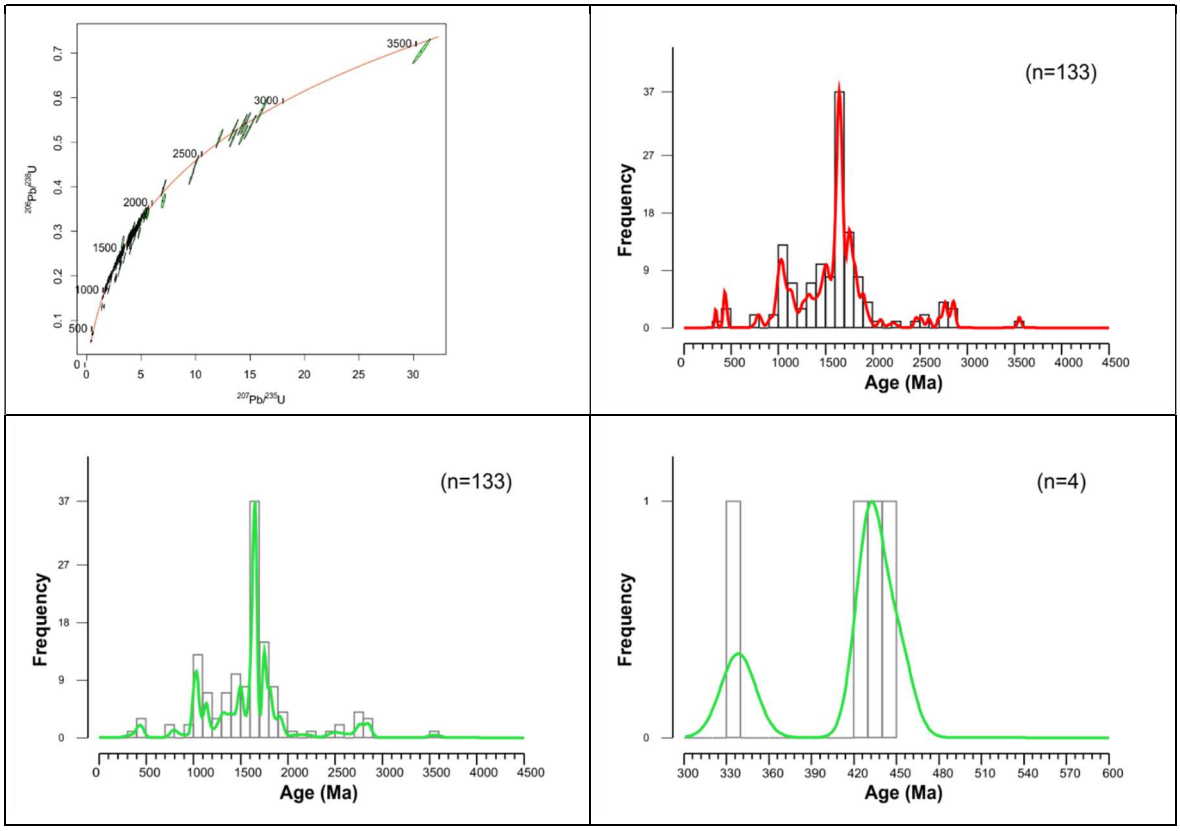

Figure 4-16: Zircon results for CHBH. Top left, concordia diagram; top right probability density plot (PDP); bottom left kernel density estimate (KDE); bottom right kernel density estimate (KDE) for Palaeozoic ages. n = number of analysis. All plots produced using IsoplotR (Vermeesch 2018).

4.3.5.2 Apatite

A total of 30 apatite grains were analysed with 22 yielding ages within the concordance and uncertainty level outlined above. Raw data are shown in T-W space (Figure 4-17) with the data

forming two linear arrays which allows for the calculation of the unanchored common Pb regression lines (Figure 4-17) providing population ages of 434.8 ±9 Ma and 2295.1 ±40 Ma. 22 individual apatite U-Pb ages were calculated following a ^{207}Pb correction based on the upper intercept ($^{207}Pb/^{206}Pb$) of the relevant common Pb regression line. Corrected single grain ages are displayed on a KDE plot with the dominant Palaeozoic peak also shown in more detail.

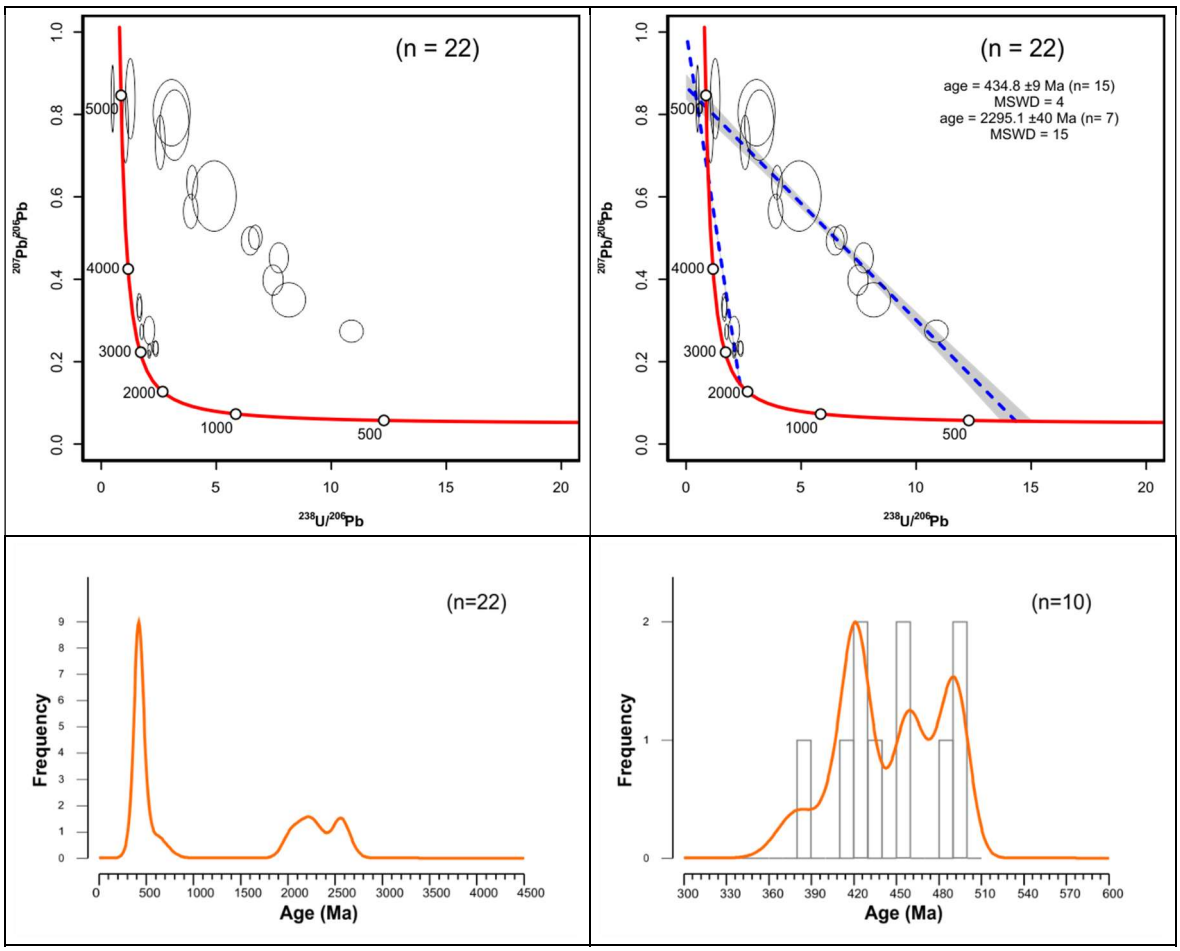

Figure 4-17: Apatite results for CHBH. Top left, 2σ ellipse Tera-Wasserburg (T-W) plot without regression lines; top right T-W plot with regression lines through suggested population; bottom left kernel density estimate (KDE) for ^{207}Pb corrected single grain ages; bottom right kernel density estimate (KDE) for Palaeozoic ages. n = number of analysis. MSWD-mean square of weighted deviations. T-W and KDE plots produced using IsoplotR (Vermeesch 2018).

4.4 Namurian samples

4.4.1 Limestone Coal Formation (A6BH)

4.4.1.1 Zircon

A total of 150 zircons were analysed with 133 yielding age within the concordance cut-off level. Ages range from c.400 to c.3000 Ma with KDE plots showing populations occurring in the Phanerozoic,

Proterozoic and Archean. Phanerozoic ages (c.60%) dominate the sample with ages falling between 400-500 Ma. Proterozoic ages (c.20%) are poorly defined, though peaks at 1100 Ma and 1700 Ma are still visible. Again, there is a general lack of ages between 500 and 900 Ma and 1800 and 2500 Ma. The Archean peak (c.20%) has a subordinate peak at 2500 Ma composed of only two grains and a dominant peak at c.2700-2900 Ma. The youngest zircon in this sample was dated at 392 ±5 Ma ($^{206}Pb/^{238}U$) while oldest zircon returned a $^{207}Pb/^{206}Pb$ age of 2978 ±11 Ma.

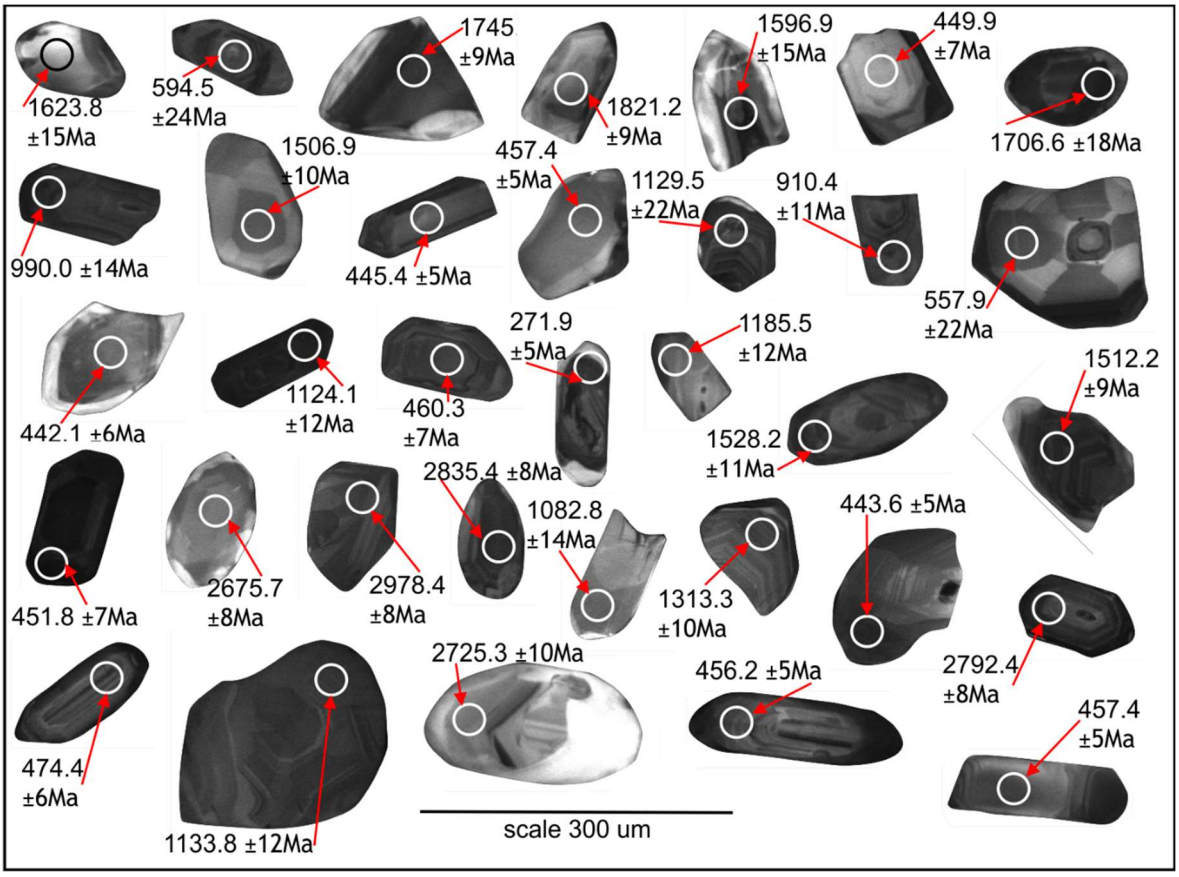

Figure 4-18: Selection of CL images from sample from the Limestone Coal Fm, A6BH. Circle within grain indicates the location of the laser ablation with corresponding age and 2σ error.

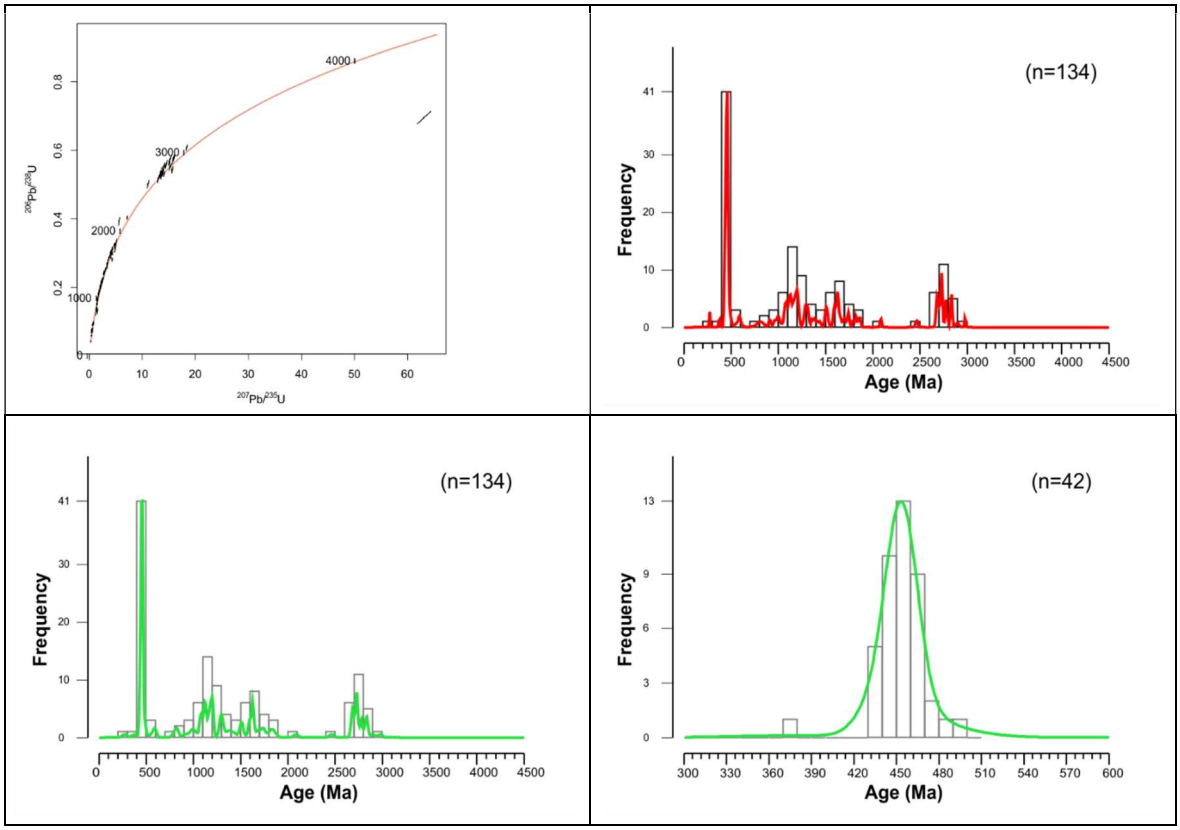

Figure 4-19: Zircon results for A6BH. Top left, concordia diagram; top right probability density plot (PDP); bottom left kernel density estimate (KDE); bottom right kernel density estimate (KDE) for Palaeozoic ages. n = number of analysis. All plots produced using IsoplotR (Vermeesch 2018).

4.4.1.2 Apatite

A total of 150 apatite grains were analysed with 146 yielding ages within the concordance and uncertainty level outlined above. Raw data are shown in T-W space (Figure 4-20) with the data forming one linear array which allows for the calculation of the unanchored common Pb regression line (Figure 4-20), providing an age population of 405.8 ±2 Ma. 146 individual apatite U-Pb ages were calculated following a ^{207}Pb correction based on the upper intercept ($^{207}Pb/^{206}Pb$) of the relevant common Pb regression line. Corrected single grain ages are displayed on a KDE plot with the dominant Palaeozoic peak also shown in more detail.

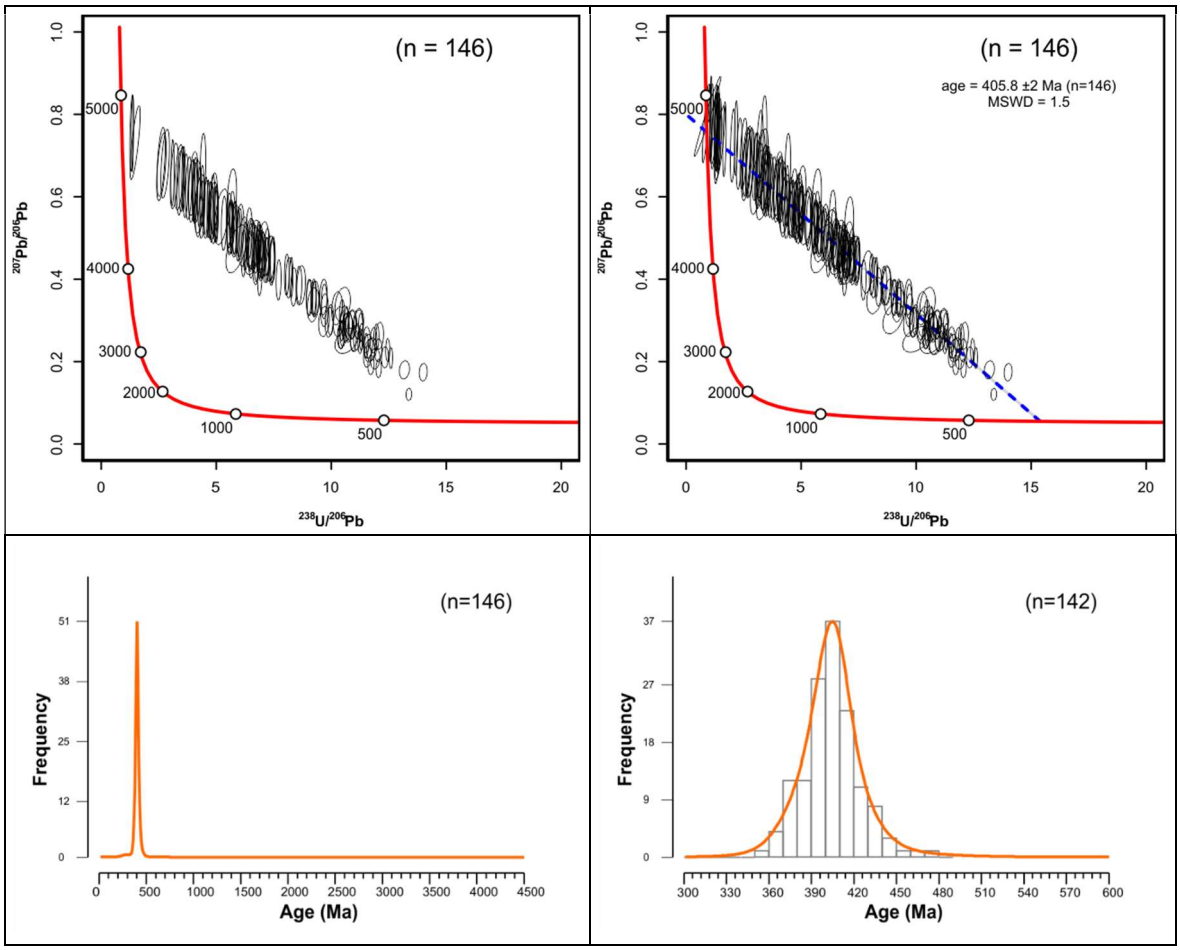

Figure 4-20: Apatite results for A6BH. Top left, 2σ ellipse Tera-Wasserburg (T-W) plot without regression lines; top right T-W plot with regression lines through suggested population; bottom left kernel density estimate (KDE) for ^{207}Pb corrected single grain ages; bottom right kernel density estimate (KDE) for Palaeozoic ages. n = number of analysis. MSWD-mean square of weighted deviations. T-W and KDE plots produced using IsoplotR (Vermeesch 2018).

4.4.2 Limestone Coal Formation (THBH)

4.4.2.1 Zircon

A total of 175 zircons were analysed, with 159 yielding age within the concordance cut-off level. Ages range from c.400 to c.3700 Ma with KDE plots showing populations occurring in the Phanerozoic, Proterozoic and Archean. Phanerozoic ages (c.50%) dominate the sample, with ages falling between 400-500 Ma. Proterozoic ages (c.30%) have defined peaks at 1100 Ma and 1700 Ma, however small peaks are visible at 1500 Ma and 1900 Ma with a general lack of ages between 500 and 900 Ma and 1900 and 2400 Ma. Archean ages (c.20%) fall into two clearly separated peaks, one at 2400 Ma and another at 2700-2800 Ma. The youngest zircon in this sample was dated at 412 ±13 Ma ($^{206}Pb/^{238}U$) while oldest zircon returned a $^{207}Pb/^{206}Pb$ age of 3745 ±21 Ma.

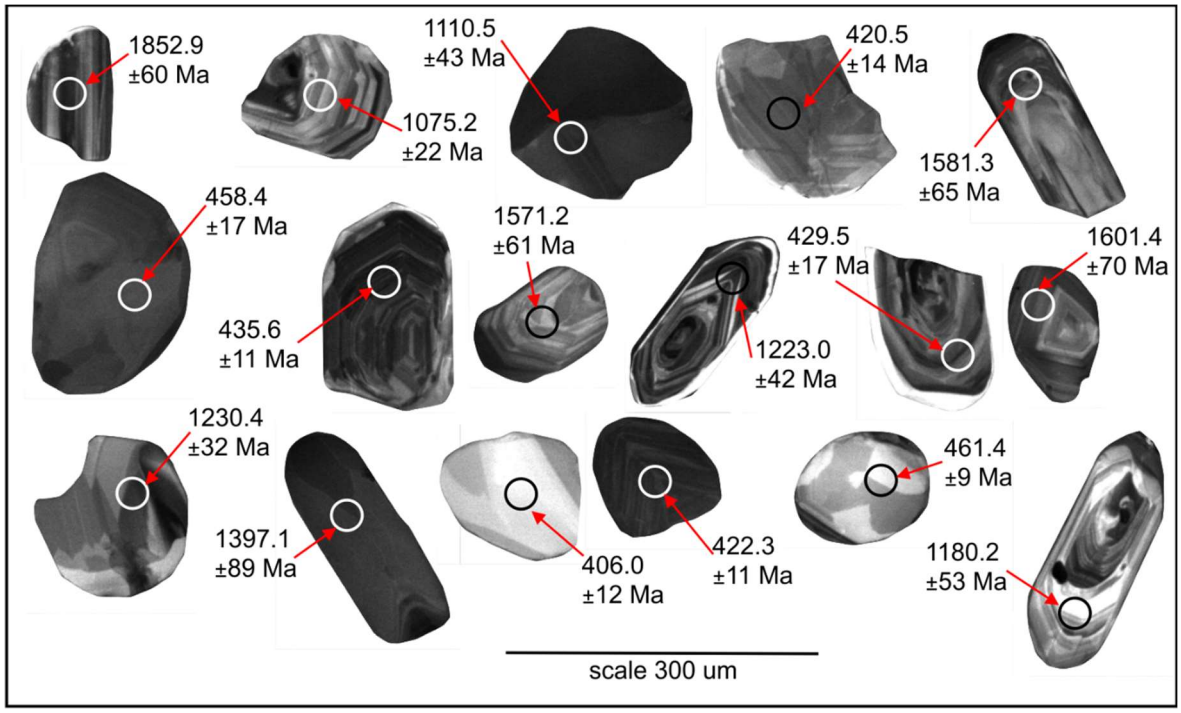

Figure 4-21: Selection of CL images from sample from the Limestone Coal Formation, THBH. Circle within grain indicates the location of the laser ablation with corresponding age and 2σ error.

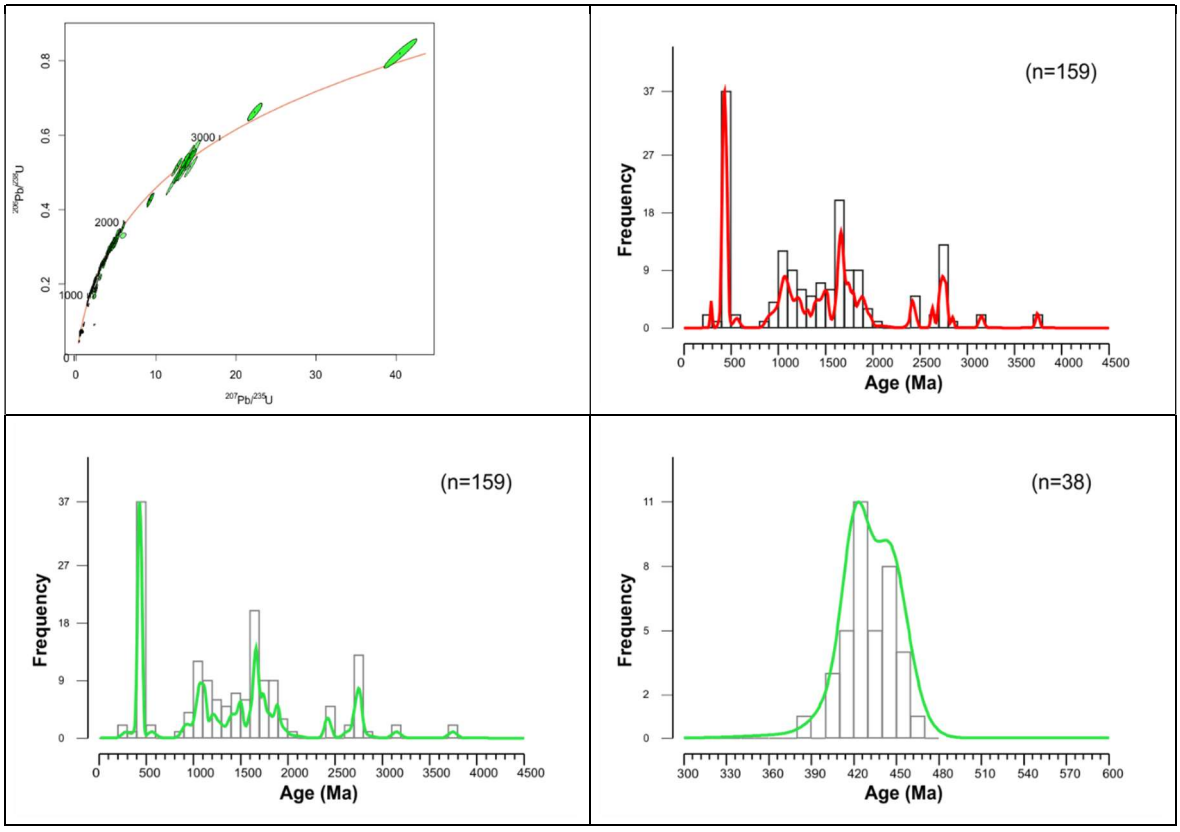

Figure 4-22: Zircon results for THBH. Top left, concordia diagram; top right probability density plot (PDP); bottom left kernel density estimate (KDE); bottom right kernel density estimate (KDE) for Palaeozoic ages. n = number of analysis. All plots produced using IsoplotR (Vermeesch 2018).

4.4.2.2 Apatite

A total of 175 apatite grains were analysed with 170 yielding ages within the concordance and uncertainty level outlined above. Raw data are shown in T-W space (Figure 4-23) with the data forming one linear array which allows for the calculation of the unanchored common Pb regression line (Figure 4-23), providing an age population of 405.5 ±2 Ma. 170 individual apatite U-Pb ages were calculated following a ^{207}Pb correction based on the upper intercept (^{207}Pb/^{206}Pb) of the relevant common Pb regression line. Corrected single grain ages are displayed on a KDE plot with the dominant Palaeozoic peak also shown in more detail.

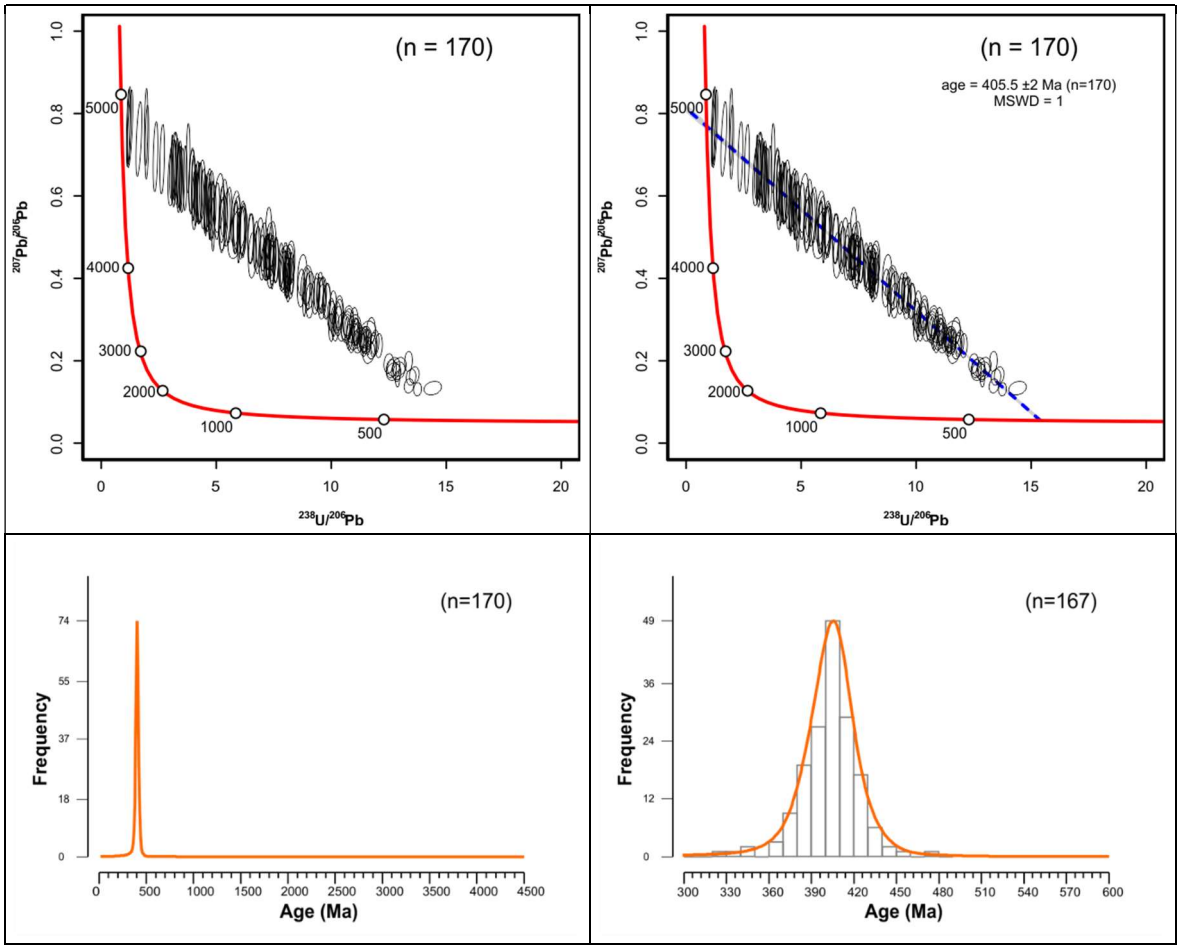

Figure 4-23: Apatite results for THBH. Top left, 2σ ellipse Tera-Wasserburg (T-W) plot without regression lines; top right T-W plot with regression lines through suggested population; bottom left kernel density estimate (KDE) for ^{207}Pb corrected single grain ages; bottom right kernel density estimate (KDE) for Palaeozoic ages. n = number of analysis. MSWD-mean square of weighted deviations. T-W and KDE plots produced using IsoplotR (Vermeesch 2018).

4.4.3 Upper Limestone Formation (DMG1)

4.4.3.1 Zircon

A total of 175 zircons were analysed, with 159 yielding age within the concordance cut-off level. Ages range from c.390 to c.3000 Ma with KDE plots showing populations occurring in the Phanerozoic, Proterozoic and Archean. Phanerozoic ages (c.30%) fall between 400-500 Ma. Proterozoic ages (c.60%) dominate the sample and are defined by peaks at 1100 Ma, 1400 Ma and 1700 Ma. Subordinate peaks are visible at 900 Ma, 1500 Ma, and 1900 Ma with a general lack of ages between 500 and 900 Ma and 2000 and 2500 Ma. Archean ages (c.10%) form a small, poorly defined peak at c. 2800 Ma that is comprised of only 8 grains. The youngest zircon in this sample was dated at 385 ±13 Ma ($^{206}Pb/^{238}U$) while oldest zircon returned a $^{207}Pb/^{206}Pb$ age of 2991 ±15 Ma.

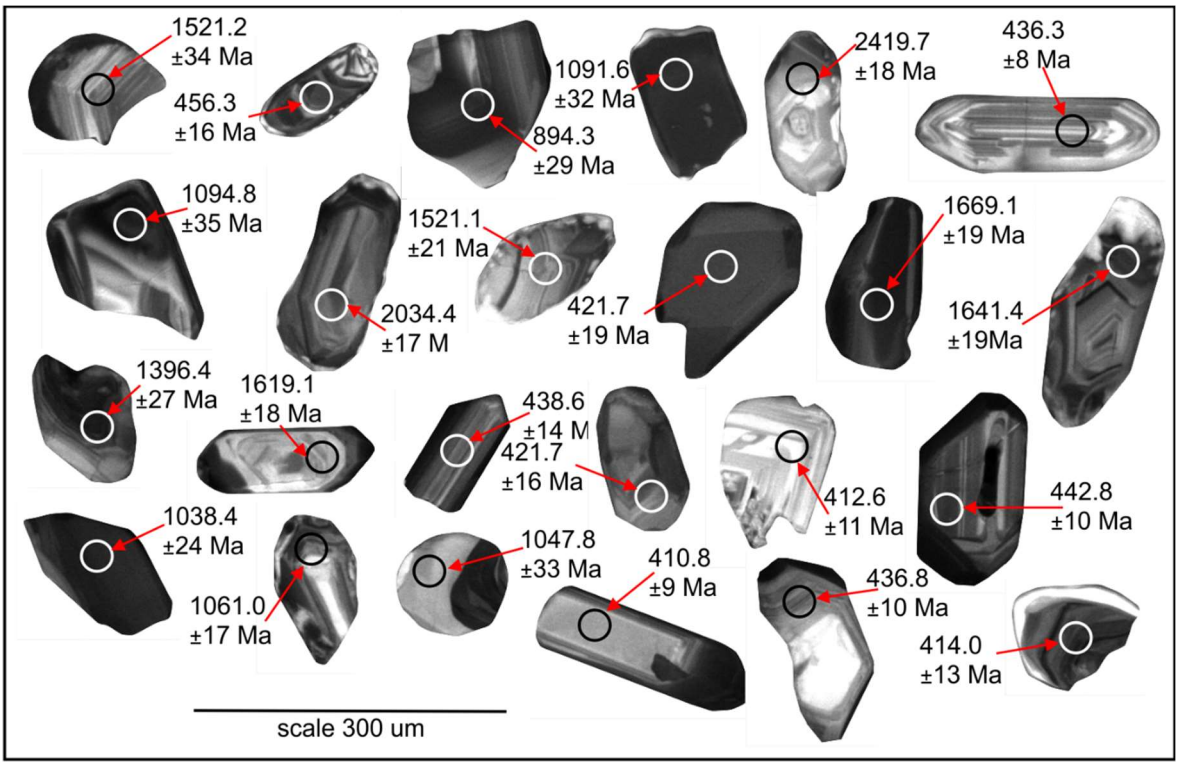

Figure 4-24: Selection of CL images from sample from the Upper Limestone Formation, DMBH. Circle within grain indicates the location of the laser ablation with corresponding age and 2σ error.

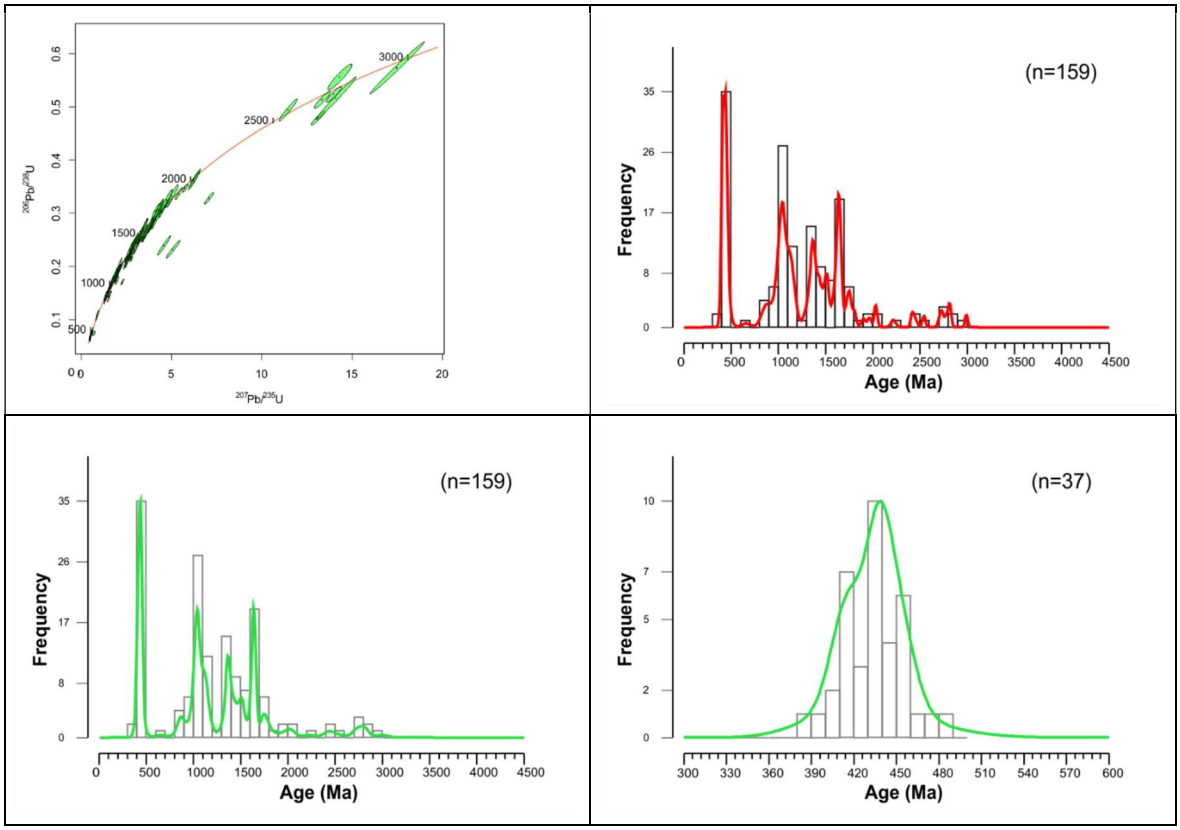

Figure 4-25: Zircon results for DMBH. Top left, concordia diagram; top right probability density plot (PDP); bottom left kernel density estimate (KDE); bottom right kernel density estimate (KDE) for Palaeozoic ages. n = number of analysis. All plots produced using IsoplotR (Vermeesch 2018).

4.4.3.2 Apatite

A total of 175 apatite grains were analysed with 160 yielding ages within the concordance and uncertainty level outlined above. Raw data are shown in T-W space (Figure 4-26) with the data forming two linear arrays which allows for the calculation of the unanchored common Pb regression lines (Figure 4-26), providing age populations of 430.8 ±2 Ma and 2508.1 ±23 Ma. 160 individual apatite U-Pb ages were calculated following a ^{207}Pb correction based on the upper intercept ($^{207}Pb/^{206}Pb$) of the relevant common Pb regression line. Corrected single grain ages are displayed on a KDE plot with the dominant Palaeozoic peak also shown in more detail.

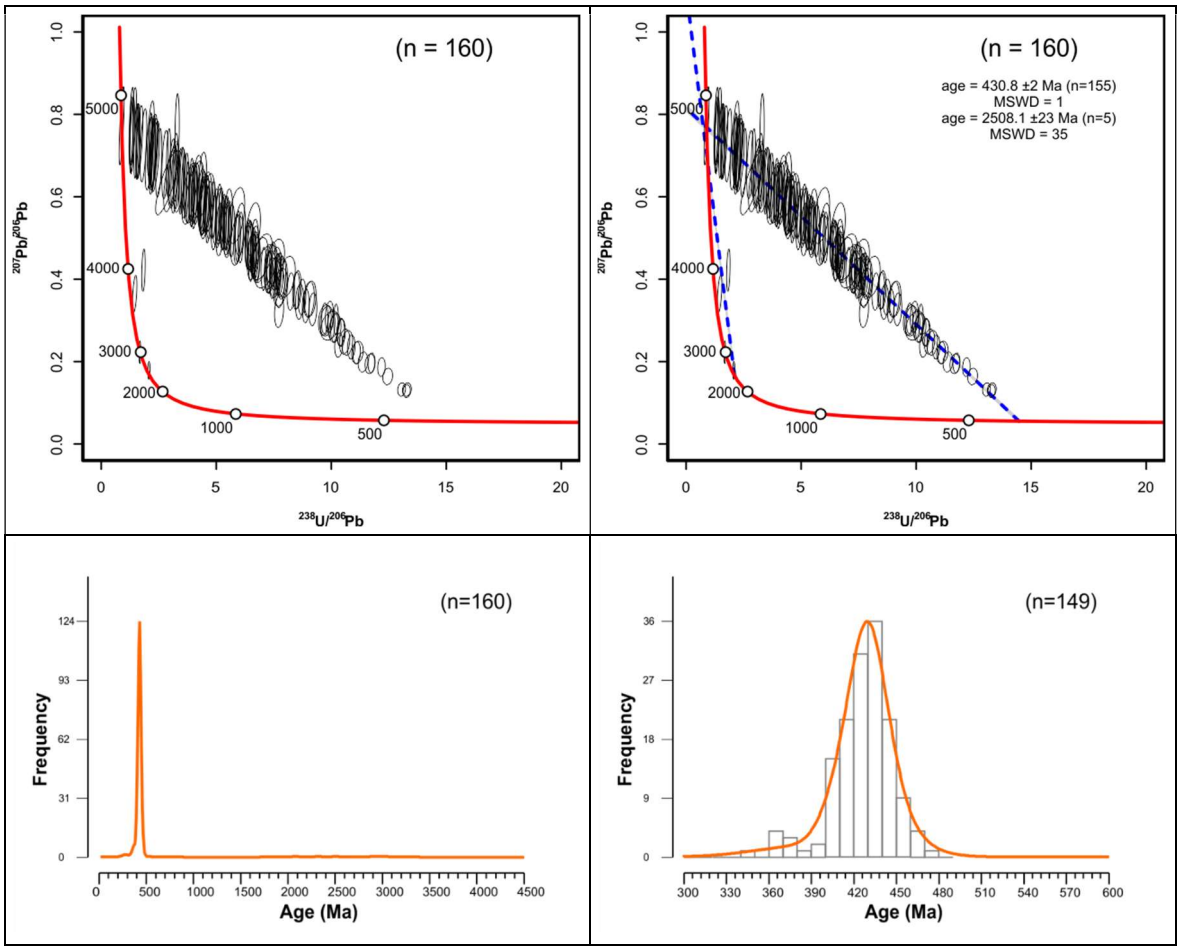

Figure 4-26: Apatite results for DMBH. Top left, 2σ ellipse Tera-Wasserburg (T-W) plot without regression lines; top right T-W plot with regression lines through suggested population; bottom left kernel density estimate (KDE) for ^{207}Pb corrected single grain ages; bottom right kernel density estimate (KDE) for Palaeozoic ages. n = number of analysis. MSWD-mean square of weighted deviations. T-W and KDE plots produced using IsoplotR (Vermeesch 2018).

4.5 Scottish Coal Measure sample

4.5.1 Middle Scottish Coal Measures (EM-017)

4.5.1.1 Zircon

A total of 125 zircons were analysed with 120 yielding age within the concordance cut-off level. Ages range from c.380 to c.2800 Ma with KDE plots being dominated by Phanerozoic ages; however Proterozoic and Archean age are present. Phanerozoic ages (c.80%) dominate the sample with ages falling between 380-470 Ma. Proterozoic ages (c.10%) are spread between c.900 to 2000 Ma; however no distinguishable populations peaks are present, with a general lack of ages between 500 and 900 Ma and 2000 and 2500 Ma. Archean ages (c.10%) fall into two separated peaks, one at 2700 Ma and another at 2800 Ma. The youngest zircon in this sample was dated at 386 ±7 Ma ($^{206}Pb/^{238}U$) while oldest zircon returned a $^{207}Pb/^{206}Pb$ age of 2859 ±10 Ma.

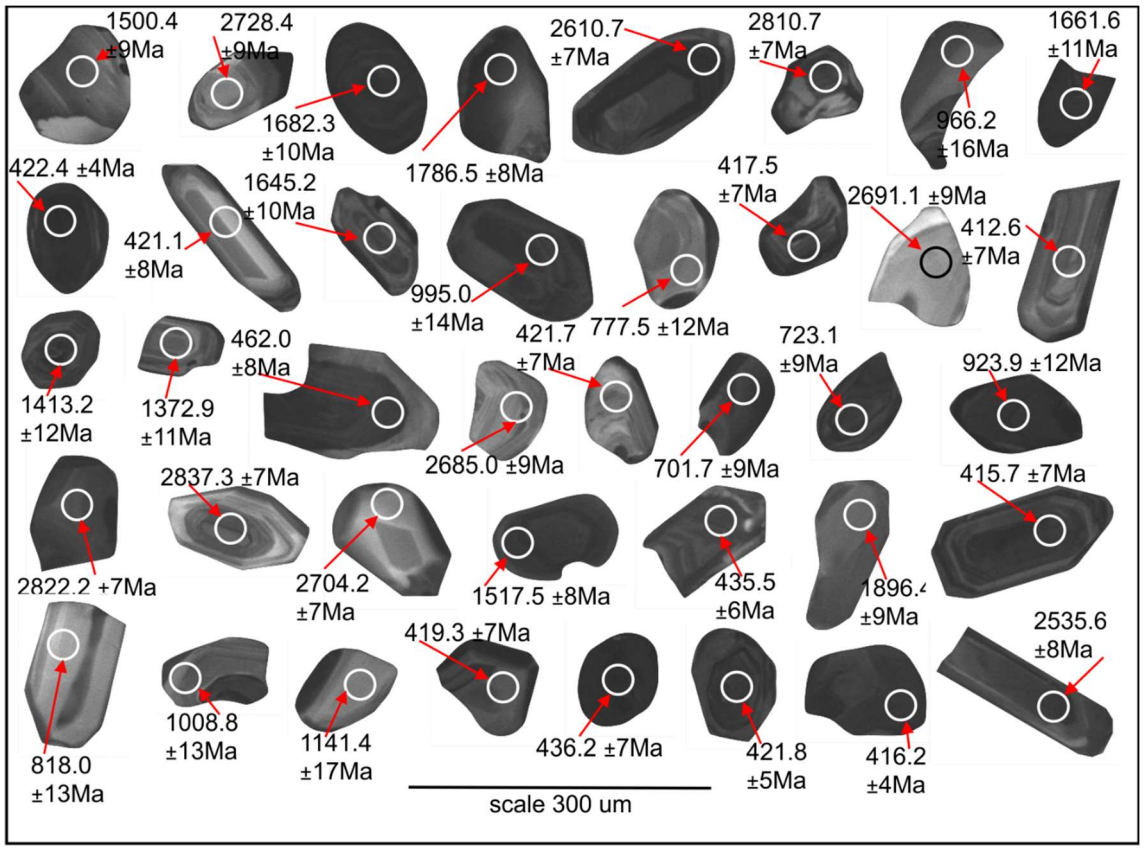

Figure 4-27: Selection of CL images from sample from the Middle Scottish Coal Measures EM-017. Circle within grain indicates the location of the laser ablation with corresponding age and 2σ error.

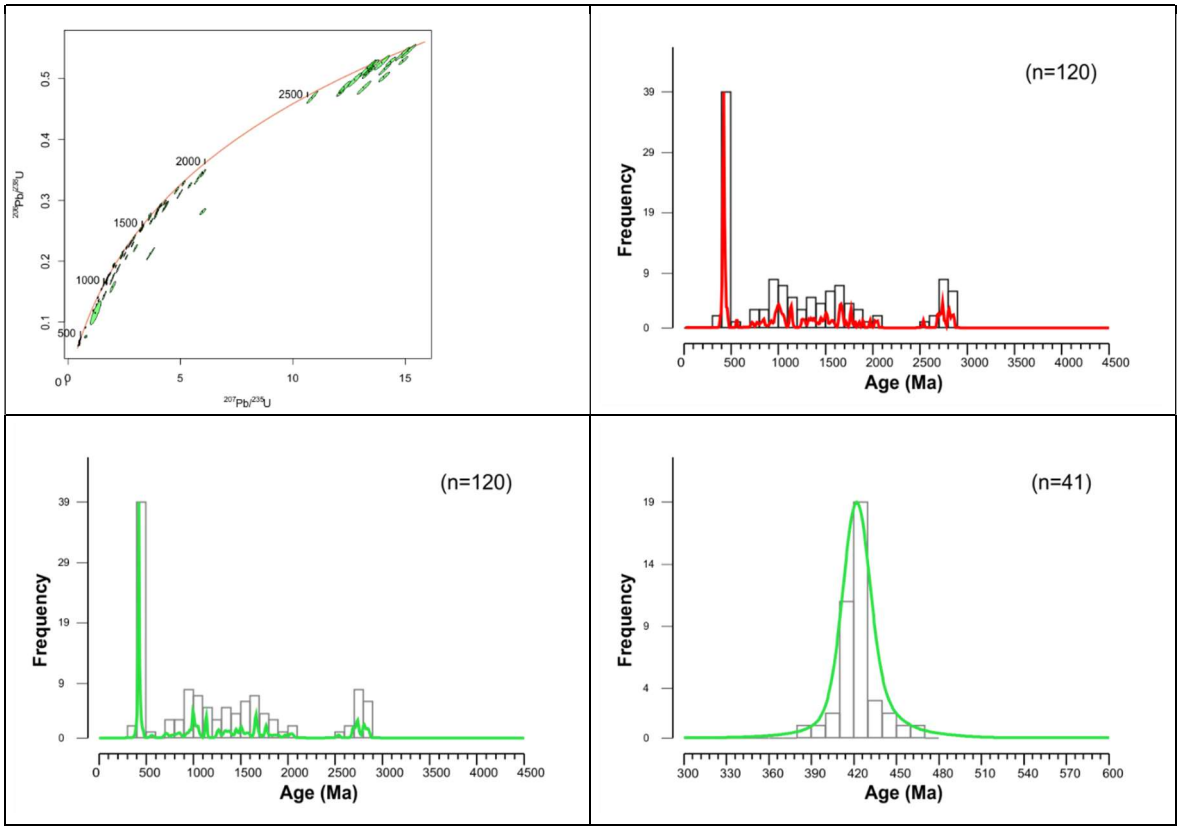

Figure 4-28: Zircon results for EM-017. Top left, concordia diagram; top right probability density plot (PDP); bottom left kernel density estimate (KDE); bottom right kernel density estimate (KDE) for Palaeozoic ages. n = number of analysis. All plots produced using IsoplotR (Vermeesch 2018).

4.5.1.2 Apatite

A total of 120 apatite grains were analysed with 106 yielding ages within the concordance and uncertainty level outlined above. Raw data are shown in T-W space (Figure 4-29) with the data forming one linear array which allows for the calculation of the unanchored common Pb regression line (Figure 4-29), providing an age population of 441.3 ±2 Ma. 106 individual apatite U-Pb ages were calculated following a ^{207}Pb correction based on the upper intercept (^{207}Pb/^{206}Pb) of the relevant common Pb regression line. Corrected single grain ages are displayed on a KDE plot with the dominant Palaeozoic peak also shown in more detail.

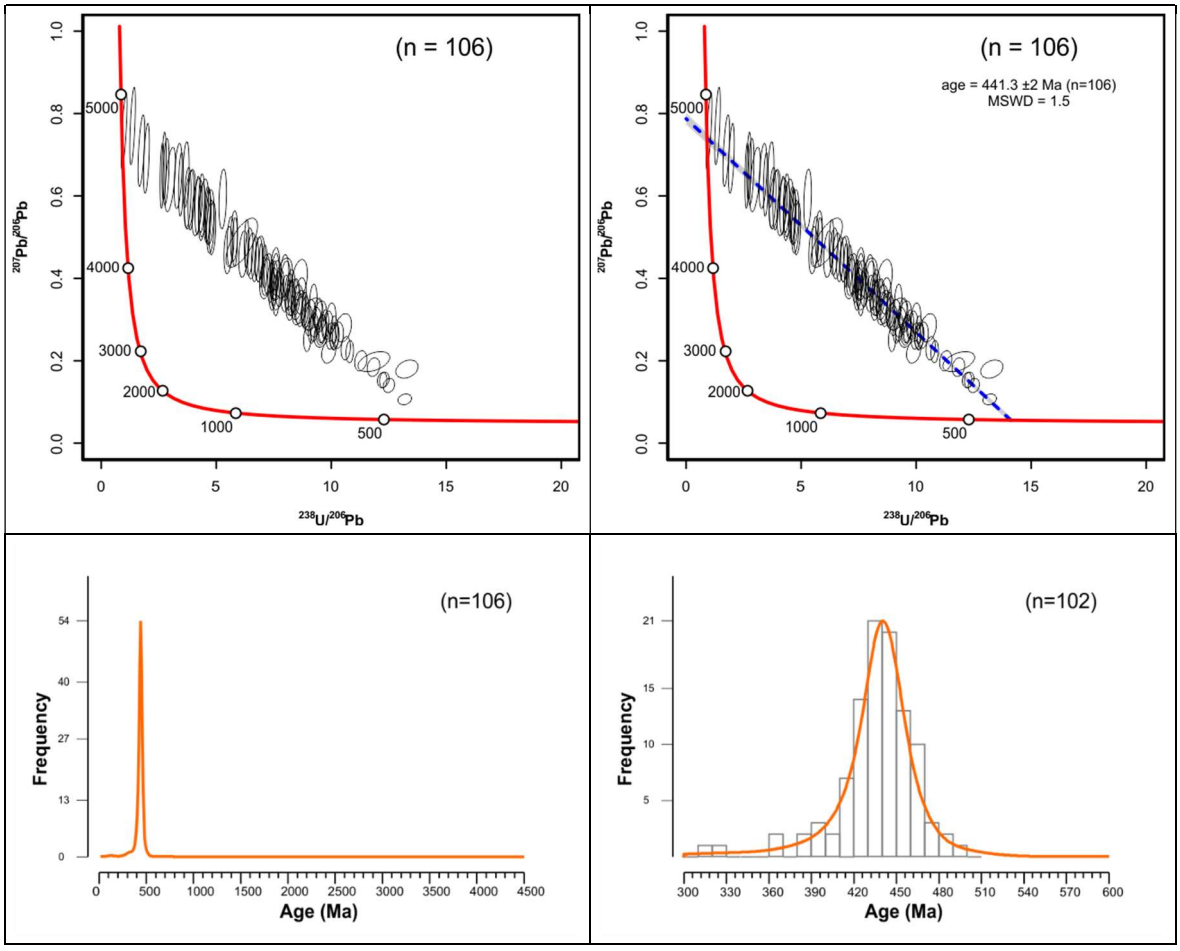

Figure 4-29: Apatite results for EM-017. Top left, 2σ ellipse Tera-Wasserburg (T-W) plot without regression lines; top right T-W plot with regression lines through suggested population; bottom left kernel density estimate (KDE) for ^{207}Pb corrected single grain ages; bottom right kernel density estimate (KDE) for Palaeozoic ages. n = number of analysis. MSWD-mean square of weighted deviations. T-W and KDE plots produced using IsoplotR (Vermeesch 2018).

4.6 Carboniferous Midland Valley: Summary

Detrital zircon populations from the Carboniferous Midland Valley sandstones can be compared by examining their Palaeozoic, Proterozoic and Archean content (Figure 4-30). All samples display a general absence of ages between c.500 - 900 Ma and 2000 - 2500 Ma. Although zircons older than c.3000 Ma have been dated, they are rare (four in total, one grain each from samples EM-15, EM-20, CHBH, and THBH) and do not represent a statistically significant population; they are potentially the result of analysing an inherited core, rather than representing the age of the source rock. Combining the samples into a stacked KDE plot provides a way to compare the results for each sample, highlighting similarities and showing the evolution of the source area (Figure 4-30). Major changes between the age spectra can be seen to occur between the Viséan, Namurian, and Westphalian samples, however variations between formations from the same time Series also exist, which will be discussed in Chapter 5.

Viséan samples (Figure 4-30) differ from Namurian and Westphalian samples by the dominance of their Proterozoic content, though variations exist with either Meso or Palaeoproterozoic dominant peaks. EM-014 from the Fife Ness Formation is the stratigraphically oldest sample analysed in this investigation and has a notable lack of Palaeozoic grains and a prominent early Mesoproterozoic peak. Subordinate peaks occur in the early Palaeoproterozoic, with a very minor Archean peak. EM-015 also displays a lack of Palaeozoic ages; however, the sample has the largest Archean peak of all the samples analysed in this investigation; the dominant peak is in the early Palaeoproterozoic, with subordinate Mesoproterozoic peaks. EM-010 is the youngest sample from the fluvio-deltaic Viséan sequence from Fife and it is the first to record a significant Palaeozoic peak, though early Mesoproterozoic ages still dominate the age distribution; there is also an absence of Archean ages as in EM-014. EM-020 from the West Lothian Oil Shale Fm displays a similar trend to the Sandy Craig Fm sample (EM-010), the Mesoproterozoic peaks are still predominant, with subordinate, but important, Palaeozoic and Neoproterozoic peaks, and a return of the Archean peak that is not present in EM-010. The Craighead borehole sample (CHBH) is the western-most sample and bares a strong similarity to EM-015, with a lack of Palaeozoic ages and a dominance of early Palaeoproterozoic ages, however it has a much smaller Archean peak than seen in EM-015.

In contrast to the Viséan samples, the Namurian A6BH and THBH from the Limestone Coal Formation are dominated by Palaeozoic ages, with poorly defined Proterozoic peaks and rare

Archean ages. DMBH from the younger Upper Limestone Formation is also dominated by Palaeozoic ages, however subordinate Mesoproterozoic and early Palaeoproterozoic peaks are present. The youngest sample, EM-017 from the Westphalian is defined by a very narrow Palaeozoic peak and a general absence of any older grains.

Apatite results have been combined into a stacked KDE plot (Figure 4-31) that shows substantial differences from the stacked zircon spectra KDE plot (Figure 4-30) described above. Spectra produced for all apatite samples are dominated by a single Palaeozoic age population, except EM-015 and EM-020, with a subordinated but well-defined Palaeozoic peak (in particular, in EM-020). The apatite KDEs from EM-014, EM-015, EM-020, and CHBH indicate the presence of some ages older than the Palaeozoic; however, these are composed of relatively few grains and are best viewed and interpreted from the T-W plot above (section 4.2 above). As mentioned above, CHBH contains very few analyses (n=22), lower than the required amount to allow for a statistically valid interpretation (Vermeesch 2004) however, the sample displays a similar trend to others and, for this reason, it has been included in the stacked plots, for comparison.

The stacked zircon and apatite KDE plots have been combined (Figure 4-32) for ease of intra sample and across samples comparison between the multi-proxy approaches. Palaeozoic zircon and apatite KDE plots (Figure 4-33 and Figure 4-34) and a combined zircon and apatite Palaeozoic KDE plot (Figure 4-35) have also been produced for higher resolution of this time, to be discussed in Chapter 5.

4.6.1 Combined zircon KDE

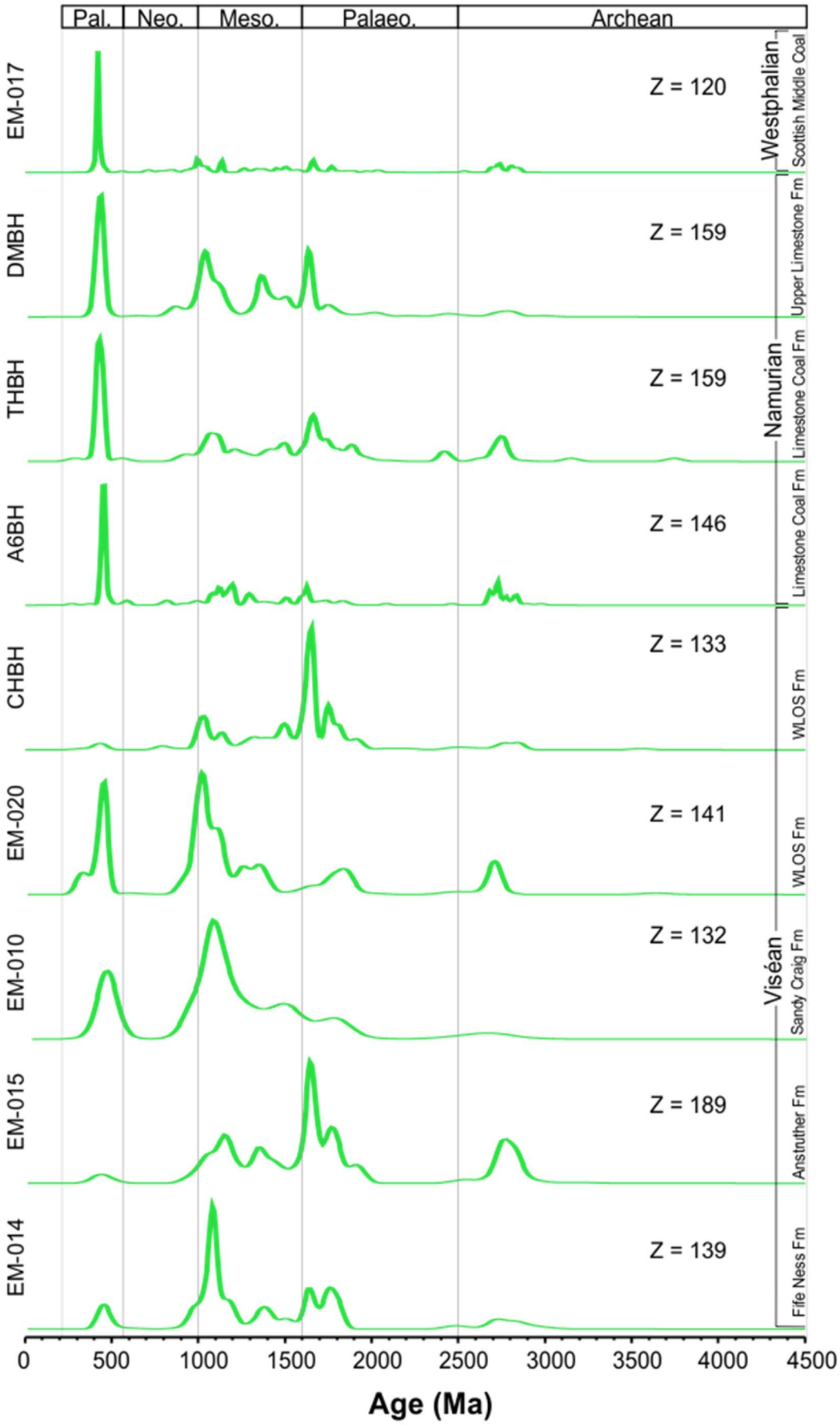

Figure 4-30: Combined zircon KDE for all samples. KDE produced using IsoplotR (Vermeesch 2018).

4.6.2 Combined apatite KDE

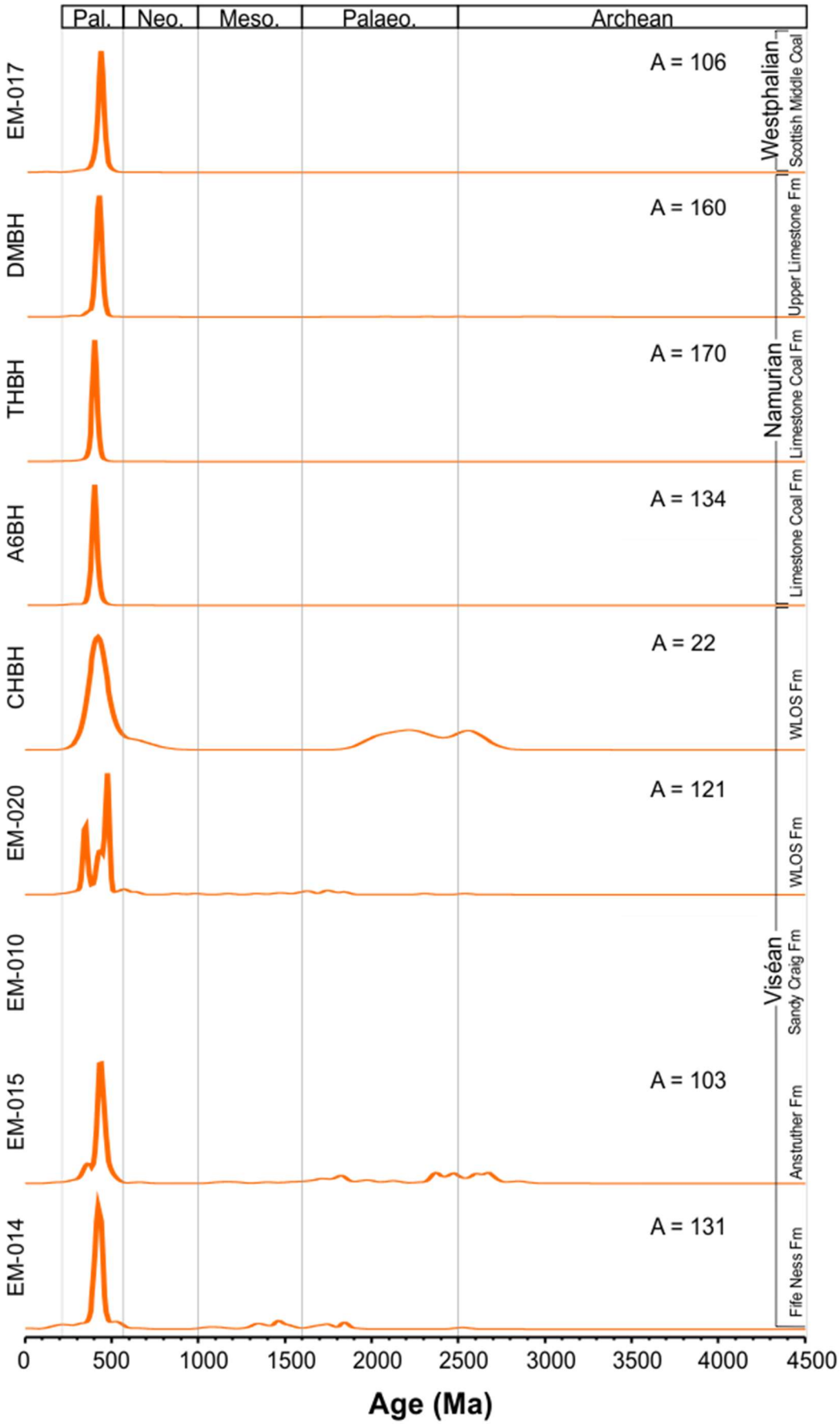

Figure 4-31: Combined apatite KDE for all samples. KDE produced using IsoplotR (Vermeesch 2018).

4.6.3 Combined zircon and apatite KDE

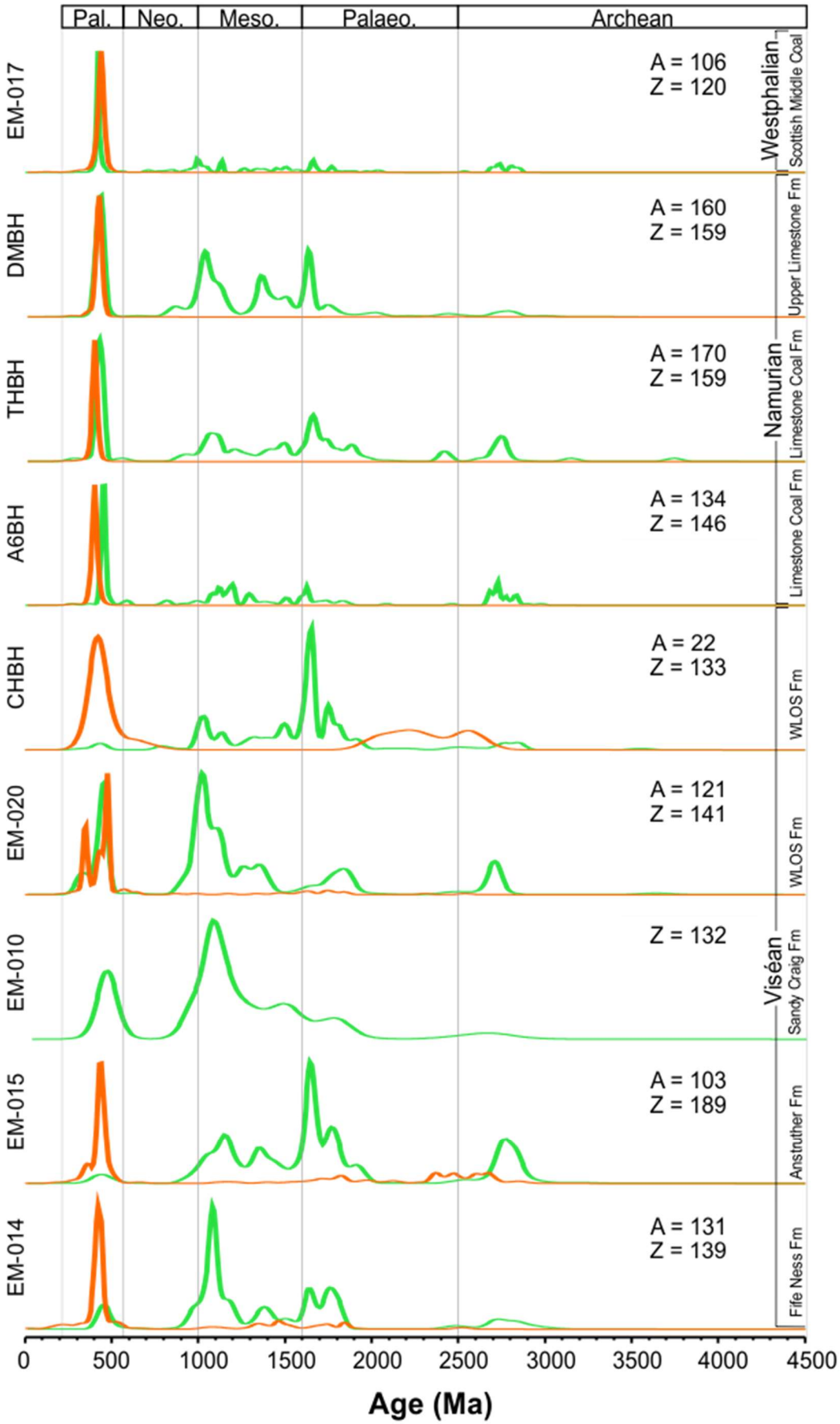

Figure 4-32: Combined zircon and apatite KDE for all samples. KDE produced using IsoplotR (Vermeesch 2018). Zircon; green, apatite; orange.

4.6.4 Palaeozoic zircon KDE

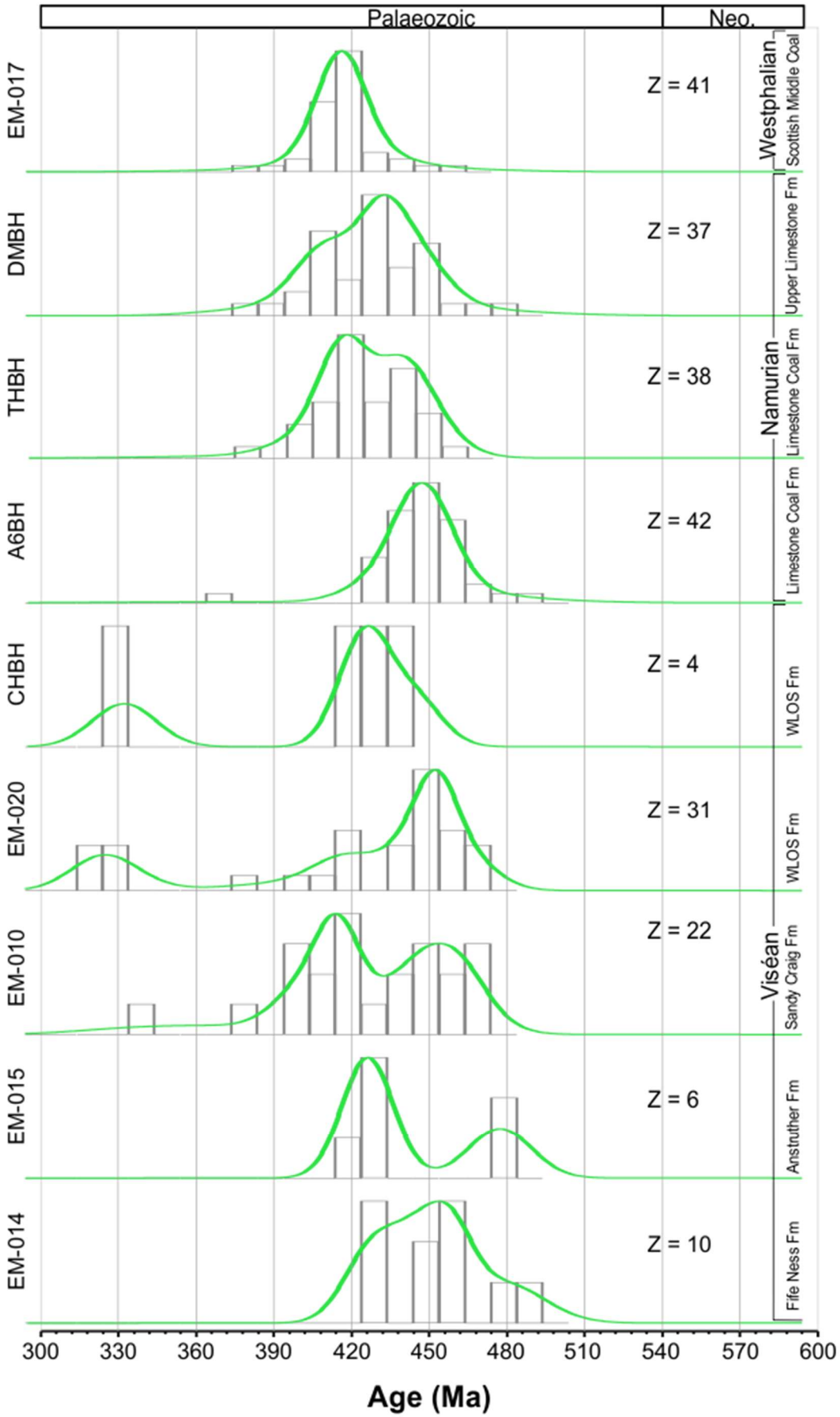

Figure 4-33: Palaeozoic zircon KDE. KDE produced using IsoplotR (Vermeesch 2018).

4.6.5 Palaeozoic apatite KDE

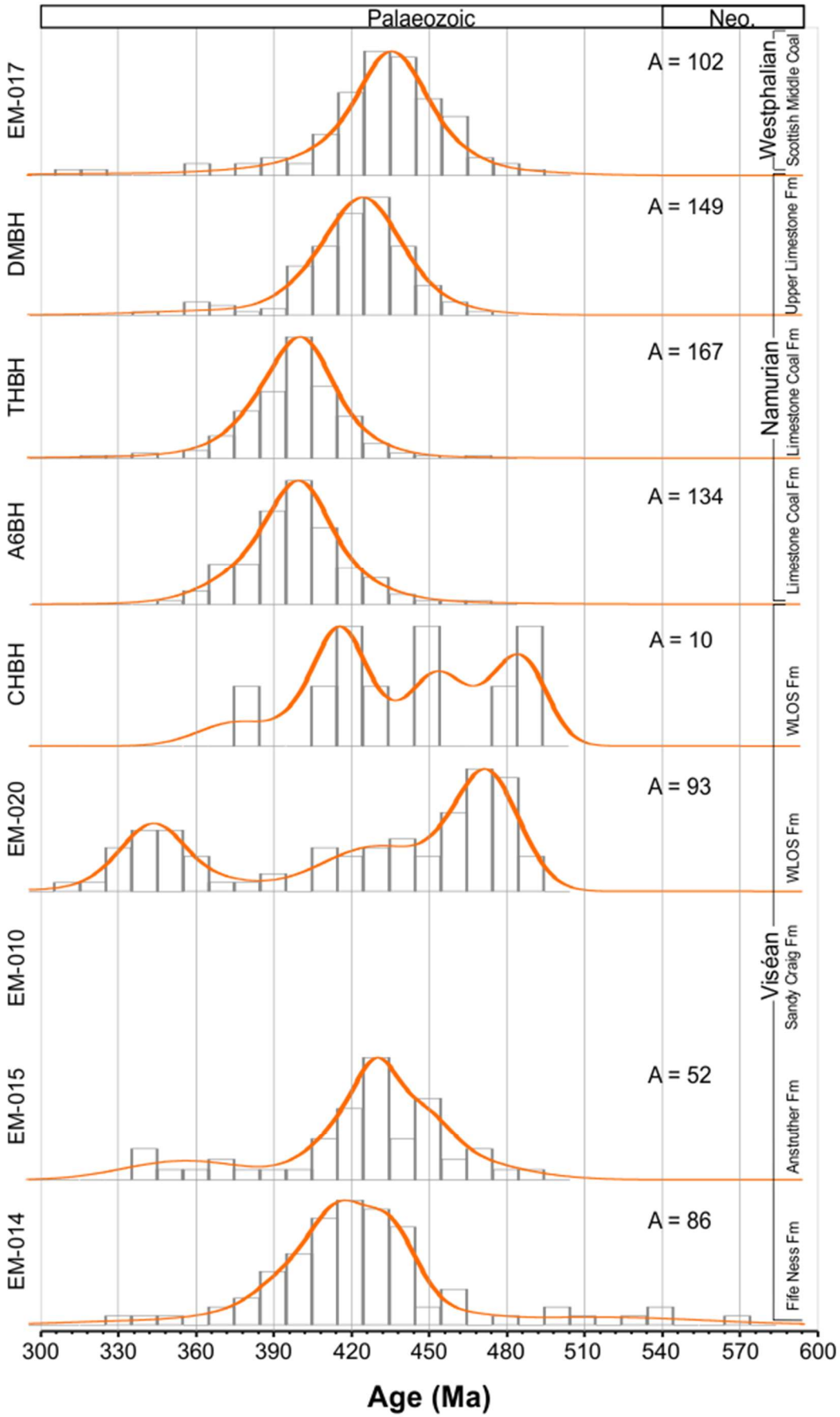

Figure 4-34: Palaeozoic apatite KDE. KDE produced using IsoplotR (Vermeesch 2018).

4.6.6 Palaeozoic combined zircon and apatite KDE

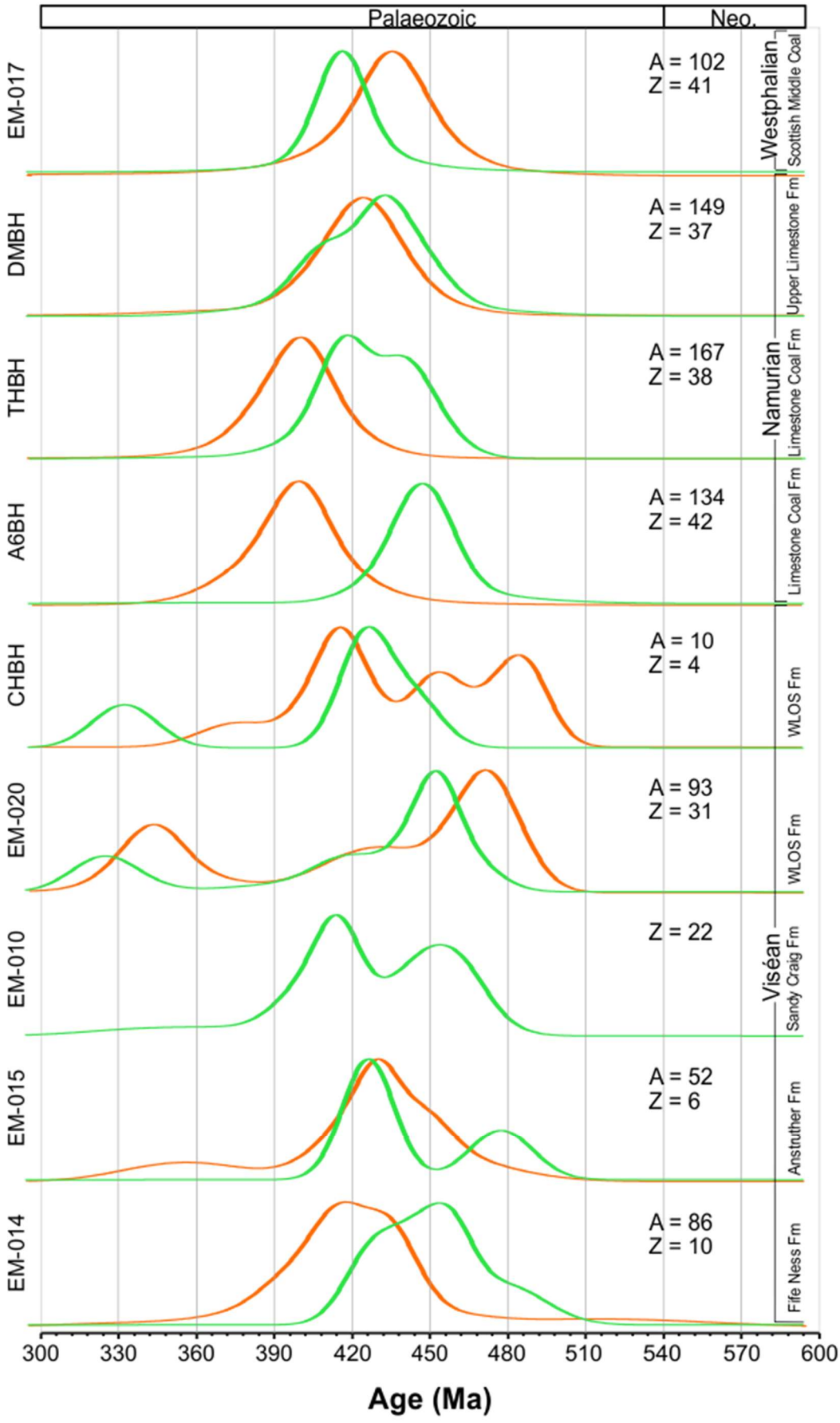

Figure 4-35: Combined Palaeozoic zircon (green) and apatite (orange) KDE. KDE produced using IsoplotR (Vermeesch 2018).

Chapter 5 Provenance of the Carboniferous Midland Valley of Scotland

This chapter summarises the potential source region surrounding the Midland Valley during the Carboniferous and the findings of previous geochronological investigations obtained from within the Midland Valley and the contemporaneous Pennine and Outer Moray Firth Basins. The results reported in Chapter 4 are then discussed and compared to these previous findings to highlight potential source regions and sediment pathways with the aim of improving the current understanding and palaeogeographical reconstructions for what is now the north Atlantic region during the Carboniferous.

5.1 Potential source regions

The region surrounding the Midland Valley was tectonically active during the Palaeozoic with plate collisions occurring between Avalonia, Baltica, and Laurentia, leading to the closure of the Iapetus Ocean and the onset of the Caledonian Orogeny (Chew and Strachan 2014). The palaeogeography suggests that all three continents could be potential sediment suppliers to the Midland Valley. Figure 5-1 shows the positions of these continents during the Carboniferous and the ages of basement rocks within their terranes, based on previous work adapted from Lundmark *et al.* (2014) and Lancaster *et al.* (2017). In summary, to the south, the Avalonian continent (570-665 Ma) is also associated with the Meguma (550-650 Ma), Cadomia (540-625 Ma) and Iberian (540-600 Ma) terranes. These terranes were regrouped by Nance *et al.* (2008) as the peri-Gondwanan terranes and have a collective age range of 525-690 Ma. To the east and northeast, the Baltica continent is comprised of Meso-Neoarchean cratons to the north, with Palaeoproterozoic basement to the south (2000-1500 Ma). The west coast of Baltica is formed of Mesoproterozoic (1500-1000 Ma) and Caledonian (460-420 Ma) metamorphic belts. The Laurentian related terranes to the north and northwest are comprised of the submerged Palaeoproterozoic Rockall High (2100-1700 Ma), Eoarchean (>3500 Ma) and Paleoproterozoic (2000-1800 Ma) basement in southwest Greenland, and Caledonian metamorphic and igneous rocks (~430 Ma) intruded into Neoproterozoic metasedimentary (950-920 Ma) and Archean basement in northeast Greenland. The Archean Lewisian complex (3100-2500 Ma) is located to the northwest of Scotland, which also records Laxfordian zircon U-Pb ages (~1700 Ma).

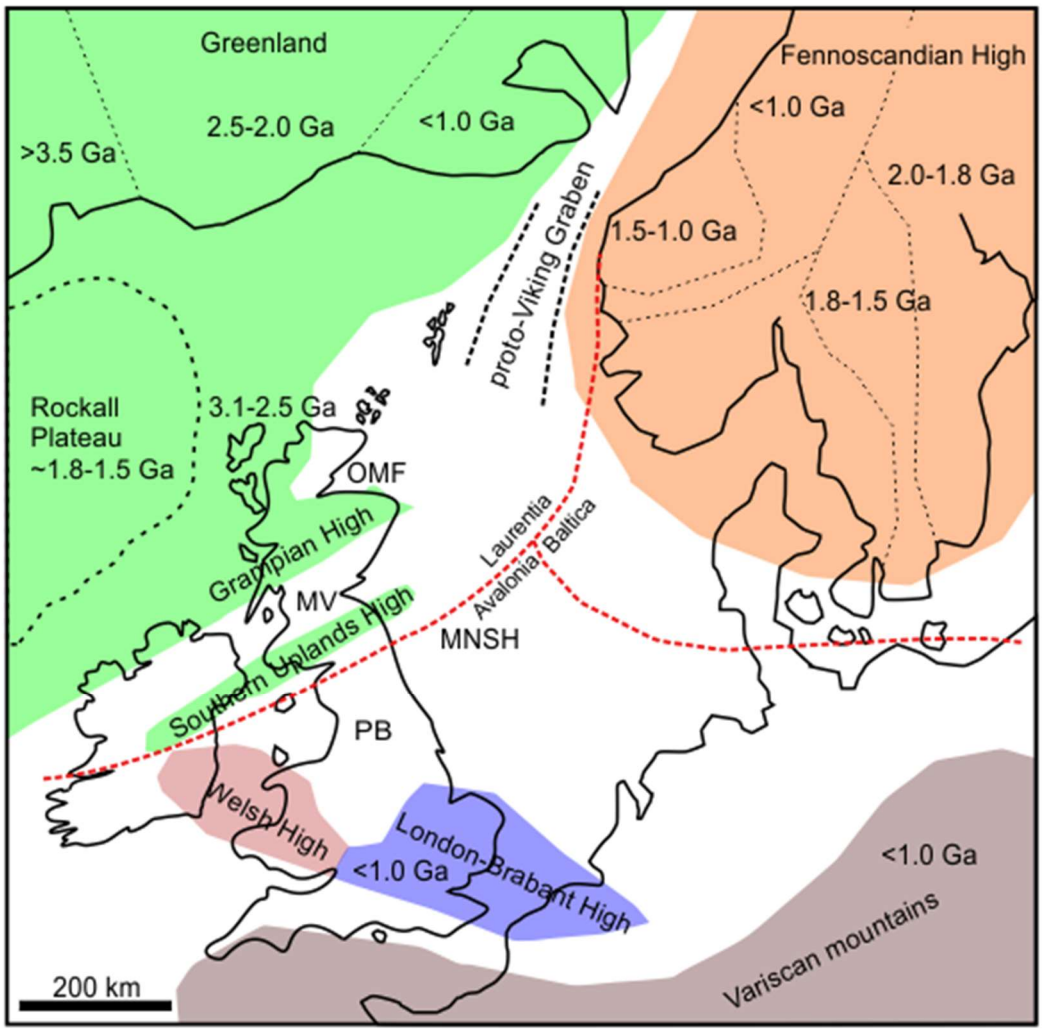

Figure 5-1: Overview of post-Caledonian North Sea region. Adapted from Lundmark *et al.* (2014) the figure shows palaeo-highs surrounding the Midland Valley during the Carboniferous with basement rock ages; adapted from Lancaster *et al.* (2017). Approximate location of the proto-Viking Graben and plate boundaries surrounding the Midland Valley (MV). PB; Pennine Basin, OMF; Outer Moray Firth Basin, MNSH; Mid North Sea High.

The Laurentian supercontinent was impacted by several orogenies i.e., the Grenvillian (900-1200 Ma), the Pinwarian (1450-1510 Ma), and the Labradorian (1600-1710 Ma) (Gower 1996; Spencer *et al.* 2015) prior to the closure of the Iapetus. The Caledonian Orogenic cycle (390-475 Ma), which occurred as a result of the closure of the Iapetus Ocean, impacted both Laurentia and Baltica, the two northern major source areas (Chew and Strachan 2014). The distribution of Caledonian related intrusions and associated volcanic rocks located in Scotland are shown in Figure 5-2 along with the reported geochronology ages (U-Pb zircon unless stated otherwise) of some of the igneous bodies (see figure caption for dates and references).

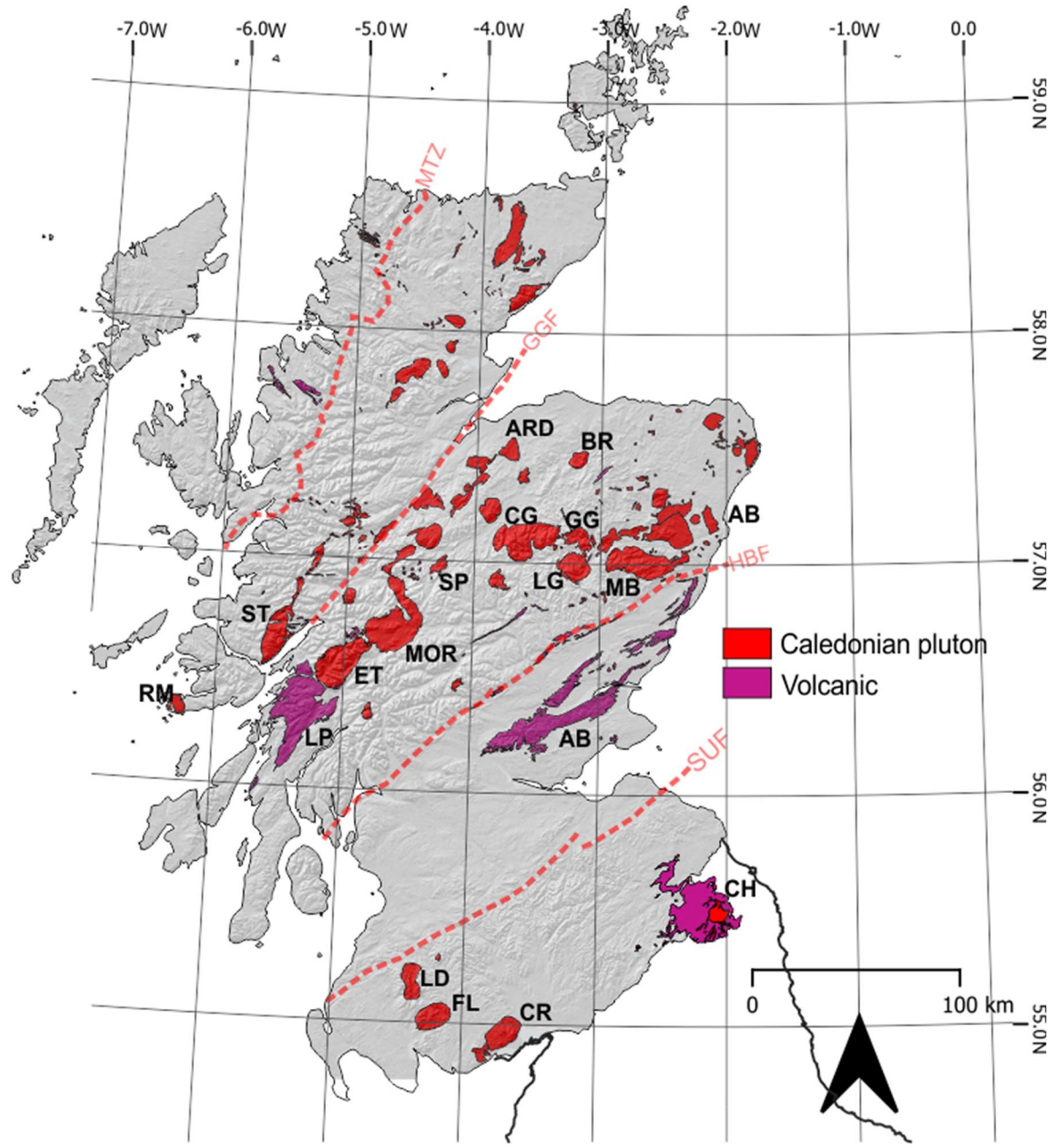

Figure 5-2: Caledonian related intrusions and associated volcanic rocks in Scotland. Southern Uplands: LD, Loch Doon, 408 Ma, FL, Fleet, 392 Ma, CR, Criffel, 397 Ma (Stephens and Halliday 1979). Grampian terrane: AB, Aberdeen 470 Ma (monazite) (Kneller and Aftalion 1987), ARD, Auldearn Granite, 470 Ma, BR, Ben Rinnes, 411 Ma, CG, Cairngorns, 404 Ma, ET, Etive, 415 Ma, GG, Glen Gairn, 415 Ma, LG, Lochnagar, 420 Ma, MB, Mount Battock, 406 Ma, MOR, Moor of Rannoch, 409 Ma, SP, Strathspey, 449 Ma, LP. Northern Highlands terrane: RM, Ross of Mull, 418 Ma, (Oliver *et al.* 2008). ST, Strontian, 418 Ma (Paterson and Fowler Jr 1993). Volcanic: CH, Cheviot Hills Lava, 395 Ma (Rb-Sr) (Thirlwall 1988) . Lorne Plateau, 400 Ma (Rb-Sr) (Clayburn *et al.* 1983), , AB, Arbuthnott Group, (undated Devonian Lava) (Thirlwall 1988). SUF, Southern Uplands Fault, HBF, Highland Boundary Fault, GGF, Great Glan Fault, MTZ, Moine Thrust Zone. Figure adapted from Oliver *et al.* (2008).

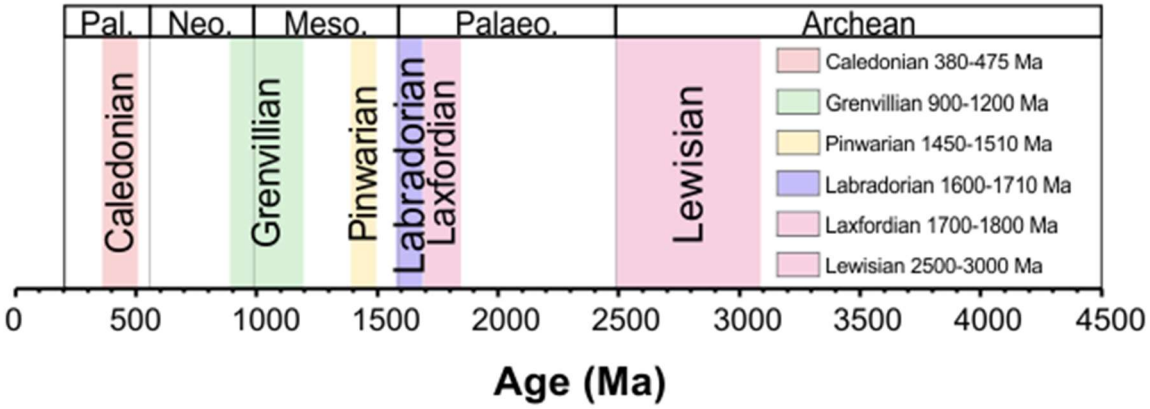

Figure 5-3: Caledonian and Laurentian related orogenic events. Caledonian orogeny stages, Grampian (465-475 Ma) Scandian (425-436 Ma) and Acadian (395 Ma) (Chew and Strachan 2014). Grenvillian (Spencer *et al.* 2015), Pinwarian and Labradorian (Gower 1996), Laxfordian and Lewisian (Whitehouse *et al.* 1997).

Figure 5-3 summarises the timing of the Laurentian related orogenic events, including the Caledonian orogeny. For simplicity, the three major events of the Caledonian orogeny, the Grampian (465-475 Ma), Scandian (425-436 Ma) and the Acadian (395 Ma), have been combined and represented as the general 'Caledonian orogeny'. As well as the regional potential sources of sediment into the Midland Valley, the volcanism occurring during the deposition of the sediments may have provided an internal sediment source. The timing, locations, and names of these igneous rocks are summarised in Figure 5-4.

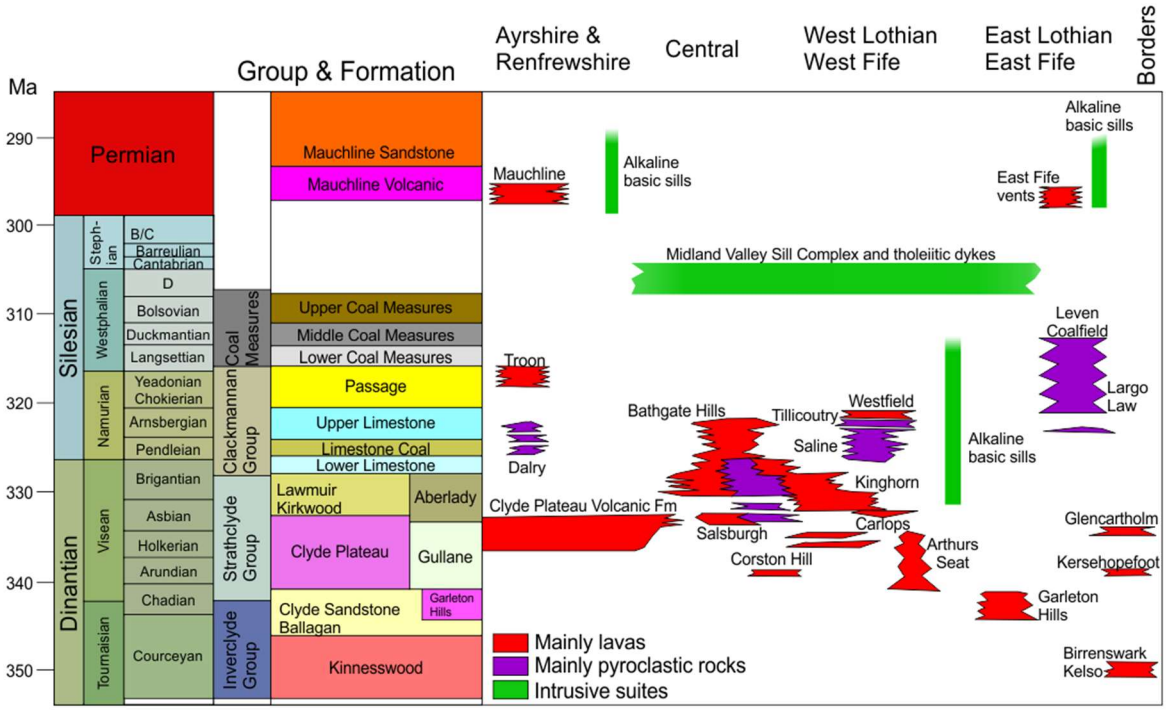

Figure 5-4: Timing of volcanism in the Midland Valley during the Carboniferous. Adapted from Monaghan and Parrish (2006).

5.2 Previous U-Pb geochronological studies

Previous studies investigating the provenance of detrital material connected to this thesis either directly from within the Midland Valley or from contemporaneous onshore and offshore basins, were highlighted in Chapter 1. The following section provides an in-depth review of existing provenance studies, with particular focus on zircon U-Pb geochronology, as this allows for a direct comparison to the new U-Pb data presented in Chapter 4. See Figure 4-2 for details on Carboniferous stage names and timings.

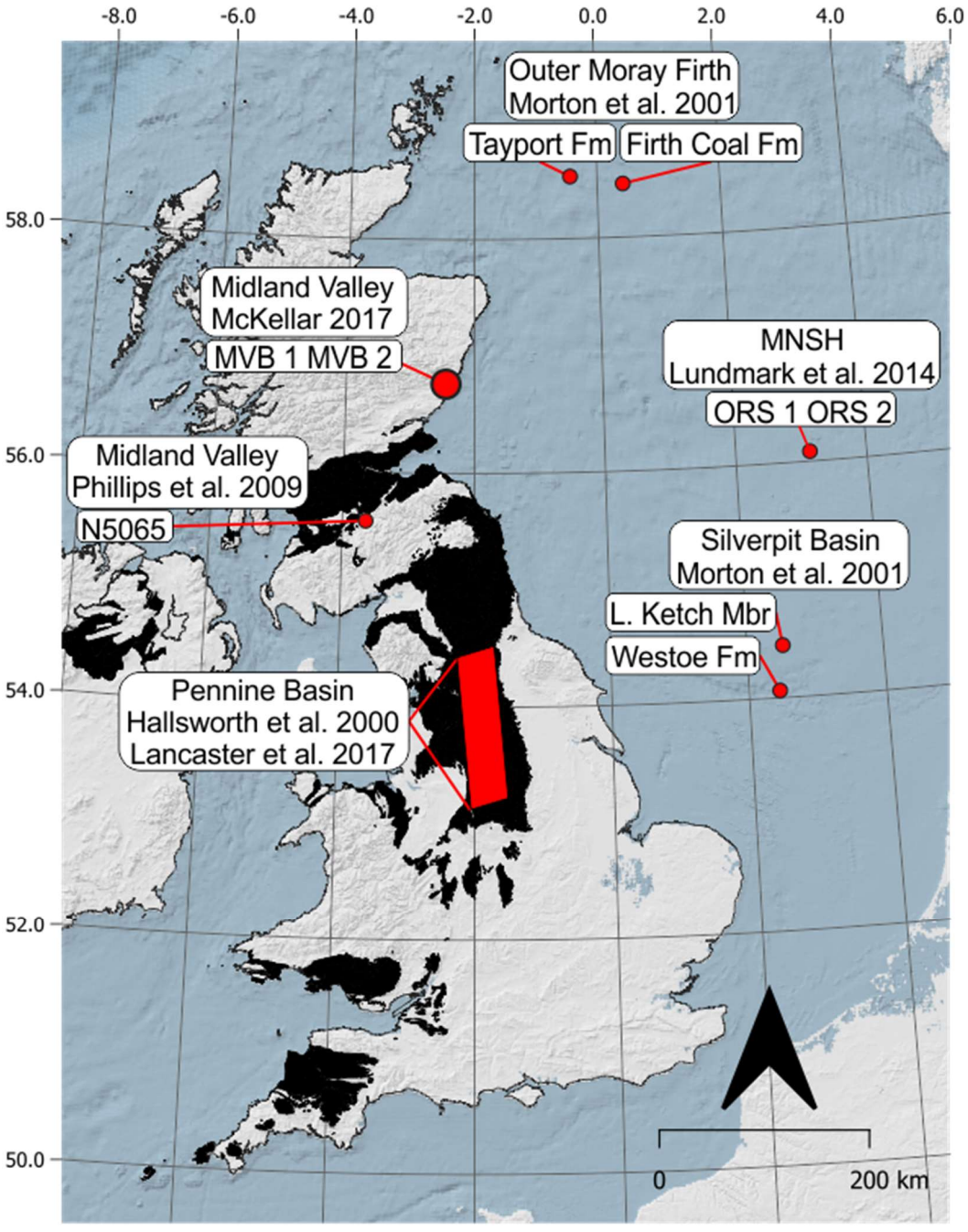

Figure 5-5: Location map of previous U-Pb zircon geochronological studies connected to the Midland Valley. Onshore Carboniferous outcrops are highlighted in Black. MNSH, Mid North Sea high.

As highlighted in Chapter 1, detrital zircon U-Pb geochronology has previously been performed on Silurian and Devonian samples within the Midland Valley (Phillips *et al.* 2009; McKellar 2017) and coeval Carboniferous samples from the Pennine and Outer Moray Firth Basins (Figure 5-5) (Hallsworth *et al.* 2000; Morton *et al.* 2001; Lancaster *et al.* 2017). Probability density plots from these publications have been adapted and redrawn in Figure 5-6 and Figure 5-10.

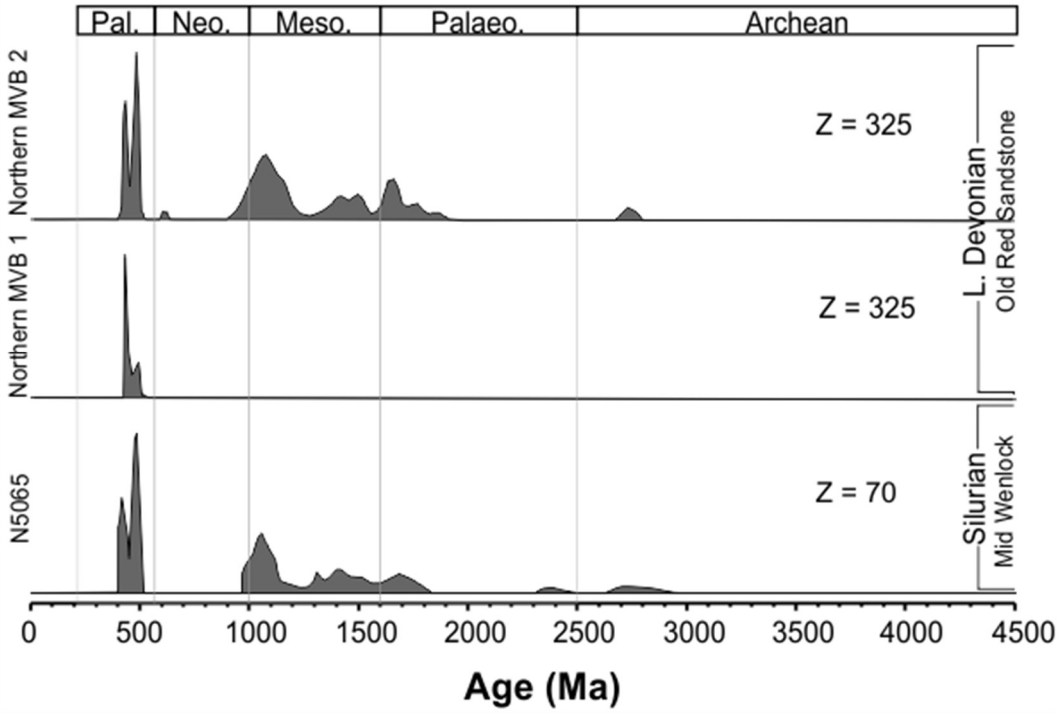

Figure 5-6: Probability density plots redrawn from Phillips *et al.* (2009) and McKellar (2017). Sample N5065 is from the Silurian March Wood Fm (Phillips *et al.* 2009) while northern MVB 1 and northern MVB 2 are redrawn from Figure 6.26 representing the two populations found in the Lower Devonian Old Red Sandstone from McKellar (2017). Z = number of zircons analysed in each sample.

Silurian and Lower Devonian detrital zircon and compositional analysis from the south of the Midland Valley display bi-modal age spectra with Palaeozoic and early Mesoproterozoic peaks e.g., N5065, Figure 5-6 (Phillips *et al.* 2004; Phillips *et al.* 2009). The Palaeozoic component, dominated by c.475 Ma ages was interpreted by Phillips *et al.* (2009) to be derived from a volcanic or plutonic source within the Midland Valley, whereas, the Mesoproterozoic component was interpreted to be derived from Grenvillian basement, either from first cycle, or recycled from existing sedimentary rocks (Phillips *et al.* 2009). The scarcity of Palaeoproterozoic and Archean ages present in the Grampian terrane (Cawood *et al.* 2003) excluded it from being seen as a source for the Lower Palaeozoic southern Midland Valley (Phillips *et al.* 2004; Phillips *et al.* 2009). Detrital zircon from Lower Devonian sedimentary rocks in the north of the Midland Valley (McKellar 2017) display a bi-modal Palaeozoic component, with peaks at c.430 and c.475 Ma (Figure 5-6); however, these were not attributed to a

source within the Midland Valley, but from uplift and tectonic rejuvenation of the Caledonian foreland and penecontemporaneous volcanism. These samples also contain a wide range of Proterozoic ages, though these were subordinate to the Palaeozoic peaks. The similarity between Lower Devonian spectra from the Midland Valley and the Grampian terrane spectra (Cawood *et al.* 2003), was used by McKellar (2017) to suggest that, at this time, the Grampian terrane was supplying sedimentary material, at least in the northern portion of the Midland Valley, contrary to previous models (Haughton and Bluck 1988). The relative stability of the provenance signal through the Lower Devonian indicates that the source region remained constant (McKellar 2017). The samples from northern Midland Valley were divided into two groups by McKellar (2017), one dominated by Phanerozoic ages, between 400-500 Ma, representing a completely Caledonian influence, sourced from Scottish Caledonian plutons and associated volcanic material (Figure 5-2) The other group containing both Phanerozoic and Proterozoic ages, represents a combination of both Caledonian and Grampian influence (Northern MVB 1 and Northern MVB 2 respectively in Figure 5-6).

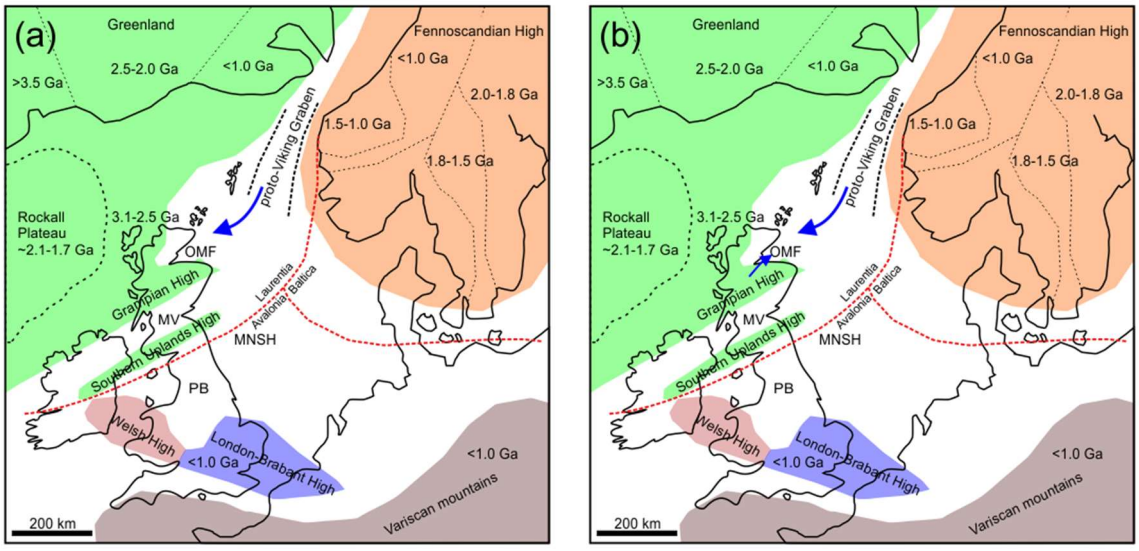

Figure 5-7: Palaeogeographical map for provenance sources during the late Devonian-early Carboniferous. (a) Fammenian-Chadian Tayport Fm, derived from a region north of the British Isles via the proto-Viking graben. (b) Brigantian Firth Coal Fm, northern source is supplemented by material from the Scottish landmass. Figure adapted from Figure 5-1 above with arrows interpreted from text description of Morton *et al.* (2001).

Detrital zircon age spectra from the late Devonian to early Carboniferous, Tayport Fm (Fammenian-Chadian) and Brigantian (late Viséan) Firth Coal Fm from the Outer Moray Firth (Figure 5-5 & Figure 5-10) (Morton *et al.* 2001) resemble those from the Lower Devonian northern MVB 2 (Figure 5-6). They are dominated by Palaeozoic ages, with a range of subordinate Proterozoic and rare Archean ages. However, the source of the material in the Tayport Fm was attributed to an area north of the British Isles, with material transported via the proto-Viking Graben, as the lack of Proterozoic material

excluded Scotland from being a dominant source region (Figure 5-7a) (Morton *et al.* 2001). The increased number of Proterozoic ages in the Firth Coal Fm (Figure 5-10) suggests that the northerly source was being supplemented by material derived from the Scottish landmass, either directly or recycled through Devonian Old Red Sandstone (Figure 5-7b) (Morton *et al.* 2001).

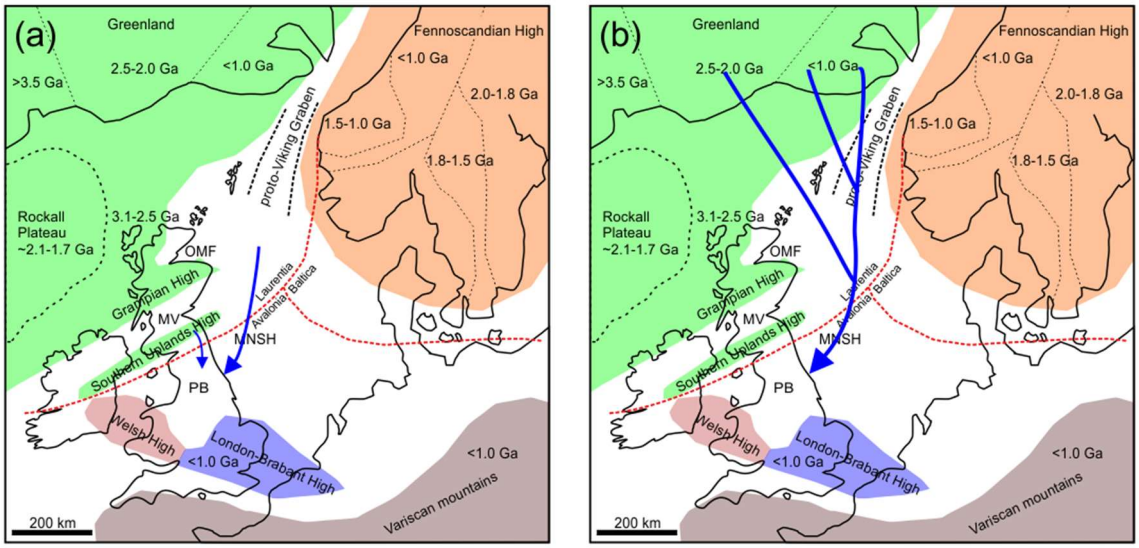

Figure 5-8: Palaeogeographical map for provenance sources during the Namurian. (a) Early Namurian, Pendleian (sample 11LYK05), provenance interpreted as being derived from a northern source with Mesoproterozoic ages, similar to that recorded for the Southern Uplands of Scotland, suggesting it was supplementing material. (b) Millstone Grit samples are dominate by Caledonian zircon U-Pb ages and interpreted to be largely derived from East Greenland (Hallsworth *et al.* 2000; Lancaster *et al.* 2017).

Detrital zircon ages from the Namurian Pennine Basin to the south of the Midland Valley record sharp peaks at c.430 and c.2700 Ma, with a broad range of ages between 1000-2000 Ma (Figure 5-10) (Hallsworth *et al.* 2000; Lancaster *et al.* 2017). Lancaster *et al.* (2017) revisited the samples of Hallsworth *et al.* (2000) and found a much greater Archean component than originally recorded, with the older peaks equalling or exceeding the Palaeozoic population. However, it is worth noting that the number of analysis per sample in Lancaster *et al.* (2017) (n= <c.40 analysis) would still be deemed lower than that required for a statistically valid interpretation (Vermeesch 2004). The Palaeozoic peak was attributed to first cycle material sourced from Caledonian igneous intrusions, whereas the Archean peaks were from basement located in East Greenland (Lancaster *et al.* 2017). Although zircon ages derived from the Lewisian complex in Scotland closely match those recorded in the study, it was ruled out as a source area by the greater availability of material from East Greenland (Figure 5-1). The Proterozoic ages were interpreted as representing recycled material, with early Namurian (Pendleian) sedimentary samples in the Pennine Basin being dominated by Mesoproterozoic ages, similar to that recorded for the Southern Uplands of Scotland (Figure 5-13)

(Waldron *et al.* 2008), which may represent the direct source of these sediments or recycling through the Devonian Old Red Sandstone (Figure 5-8a). Broad distributions of Proterozoic ages have also been found in Torridonian, East Greenland, and western Norway (Kalsbeek *et al.* 2000; Kirkland *et al.* 2007; Lancaster *et al.* 2011) although Palaeoproterozoic ages are more abundant. In the Pennine Basin, samples from the Chokierian-Yeadonian, Millstone Grit (Ashover Grit and Rough Rock, Figure 5-10) also display a dominant Palaeozoic peak indicating the continued supply of sediment from the northern source (Figure 5-8b).

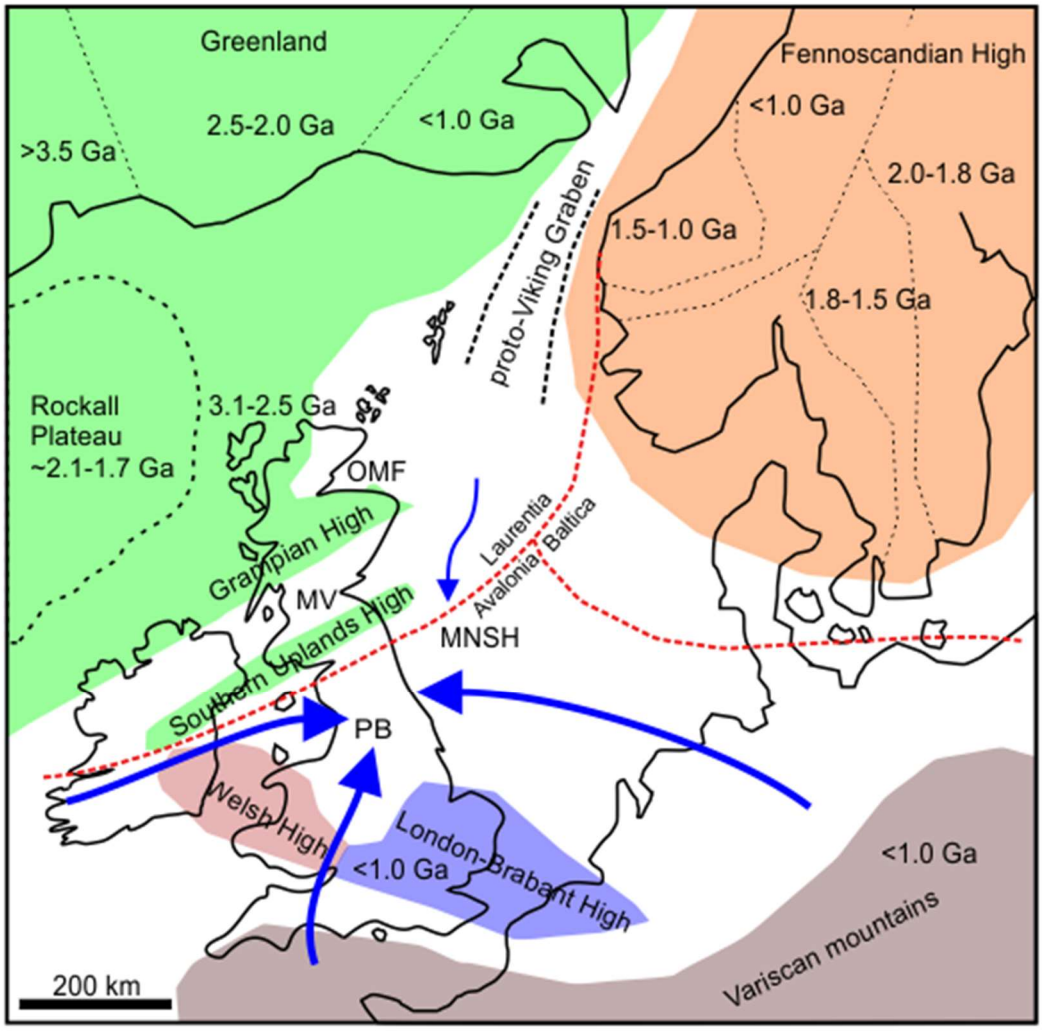

Figure 5-9: Palaeogeographical map for provenance sources during the Westphalian. Decline in northerly sourced material during the Westphalian. The dominant source was now from the east, west, and south attributed to Variscan and Cadomian sources. Adapted from Figure 5-1 with arrows from figure 10 of Hallsworth *et al.* (2000).

Detrital zircons from Westphalian samples from the Southern North Sea (Westoe Coal Fm, Silverpit Basin Figure 5-5 and Figure 5-10) and onshore in the Pennine Basin (Dalton Rock & Halesowen Fm Figure 5-10) are different to the Namurian samples (Morton *et al.* 2001). Palaeocurrent indicators suggest that the dominant source was now from the east, west, and south, with a decline in northerly

sourced material (Figure 5-9). This is reflected in the zircon age spectra with the appearance of a younger Palaeozoic (c.330 Ma) and a 500-650 Ma populations, which are attributed to Variscan and Cadomian sources to the south (Figure 5-10) (Morton *et al.* 2001). This change in provenance and paleocurrents suggests that the northern source that was prominent during the Namurian in supplying material to the Pennine Basin and the Southern North Sea basins was relatively insignificant by the beginning of the Westphalian.

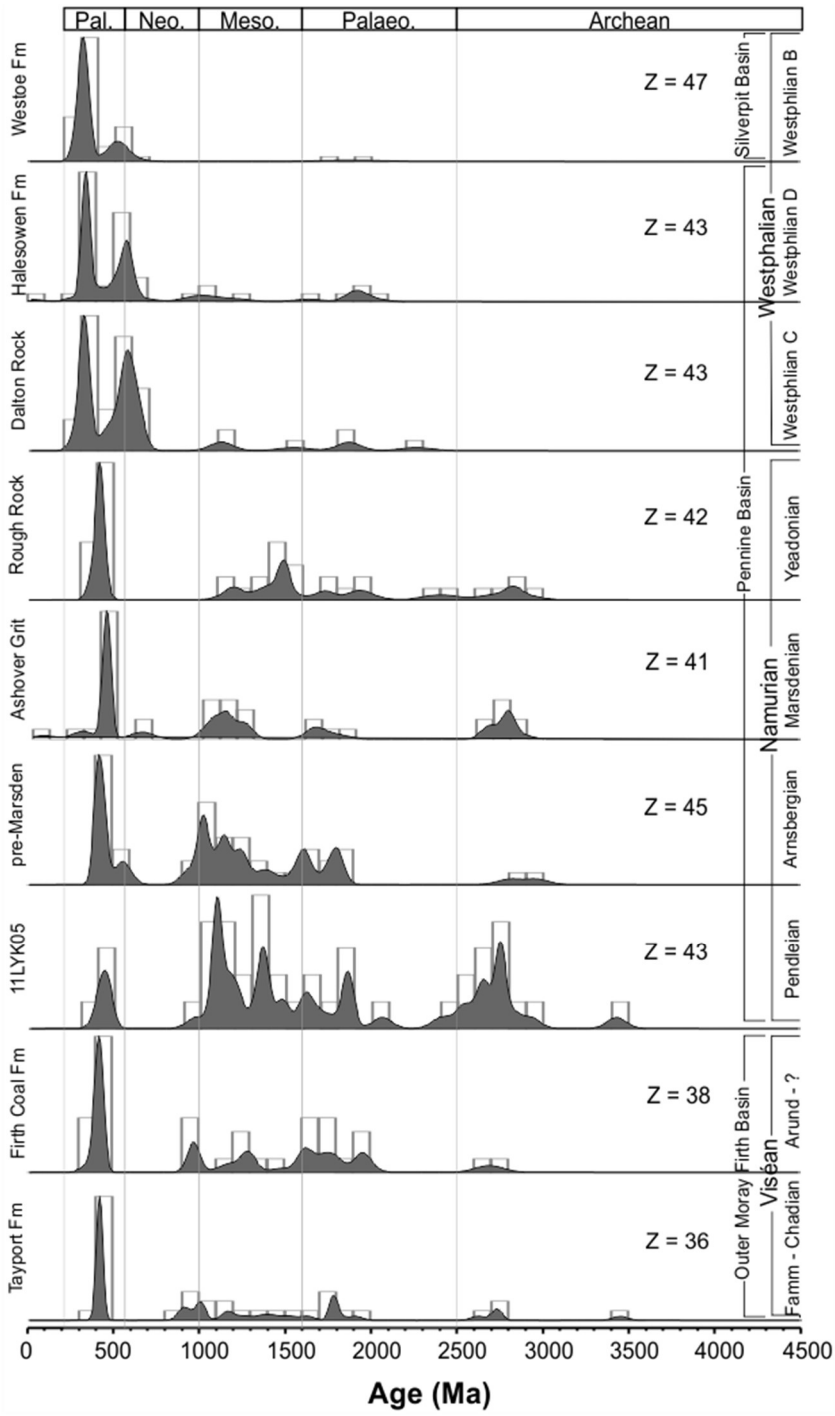

Figure 5-10: Combined probability density diagrams from previous publications. Outer Moray Firth Basin and Westoe Fm samples from Morton *et al.* (2001), Pennine Basin sample 11LYK05 from Lancaster *et al.* (2017), remaining Pennine Basin samples from Hallsworth *et al.* (2000). Z = number of analysis in each sample. For sample location, please see Figure 5-5.

Although located some distance offshore from the Midland Valley, the results from Late Devonian to early Permian terrestrial sandstone from the northern flank of the Mid North Sea High (MNSH) (Figure 5-5) reported by Lundmark *et al.* (2014) are also discussed here. Lundmark *et al.* (2014) subdivided their samples into two groups, ORS 1 and ORS 2 (Figure 5-11). ORS 1 were dominated by low-medium grade rutile and Proterozoic zircon ages but contained few Palaeozoic or Archean grains. ORS 2 were dominated by high-grade rutile and Palaeozoic zircon ages, these samples also contained Proterozoic populations, but Archean ages were rare. ORS 1 samples were interpreted as having originated from recycled metasediment from the Scottish Caledonides, while ORS 2 were suggested to have been sourced from East Greenland, reflecting a change in sediment source from the northwest to the northeast, at some point between the Late Devonian-early Carboniferous (Lundmark *et al.* 2014).

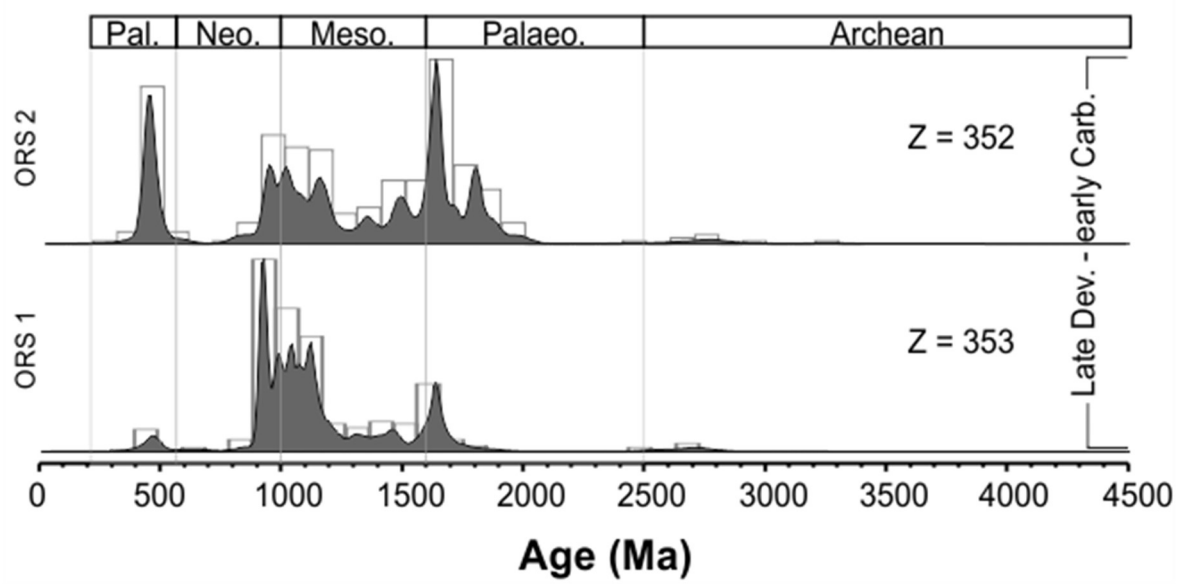

Figure 5-11: Detrital zircon age spectra from ORS 1 and ORS 2. Relative probability plots are redrawn from Fig. 3 Lundmark *et al.* (2014).

In summary, the review of this previous published literature allows for several key conclusions to be made. 1) The presence of Palaeozoic zircon ages in OMF and Pennine Basin sandstones has been attributed to a source north of Scotland, with Scotland contributing relatively little in terms of sediment. 2) Palaeozoic material been interpreted to be derived from first cycle Caledonian related material, 3) The Proterozoic and Archean component in previous Carboniferous detrital zircon age spectra is always subordinate to the Caledonian component, 4) A major change occurs during the Westphalian, when the northern source becomes less influential and provenance is dominated by material derived from the east, west, and south.

5.3 Provenance of the Midland Valley of Scotland

The following section discusses the zircon and apatite U-Pb geochronology data from Chapter 4 and the previous studies highlighted above, to place the Midland Valley in the wider Carboniferous tectonic framework and pinpoint the sources for the detrital material.

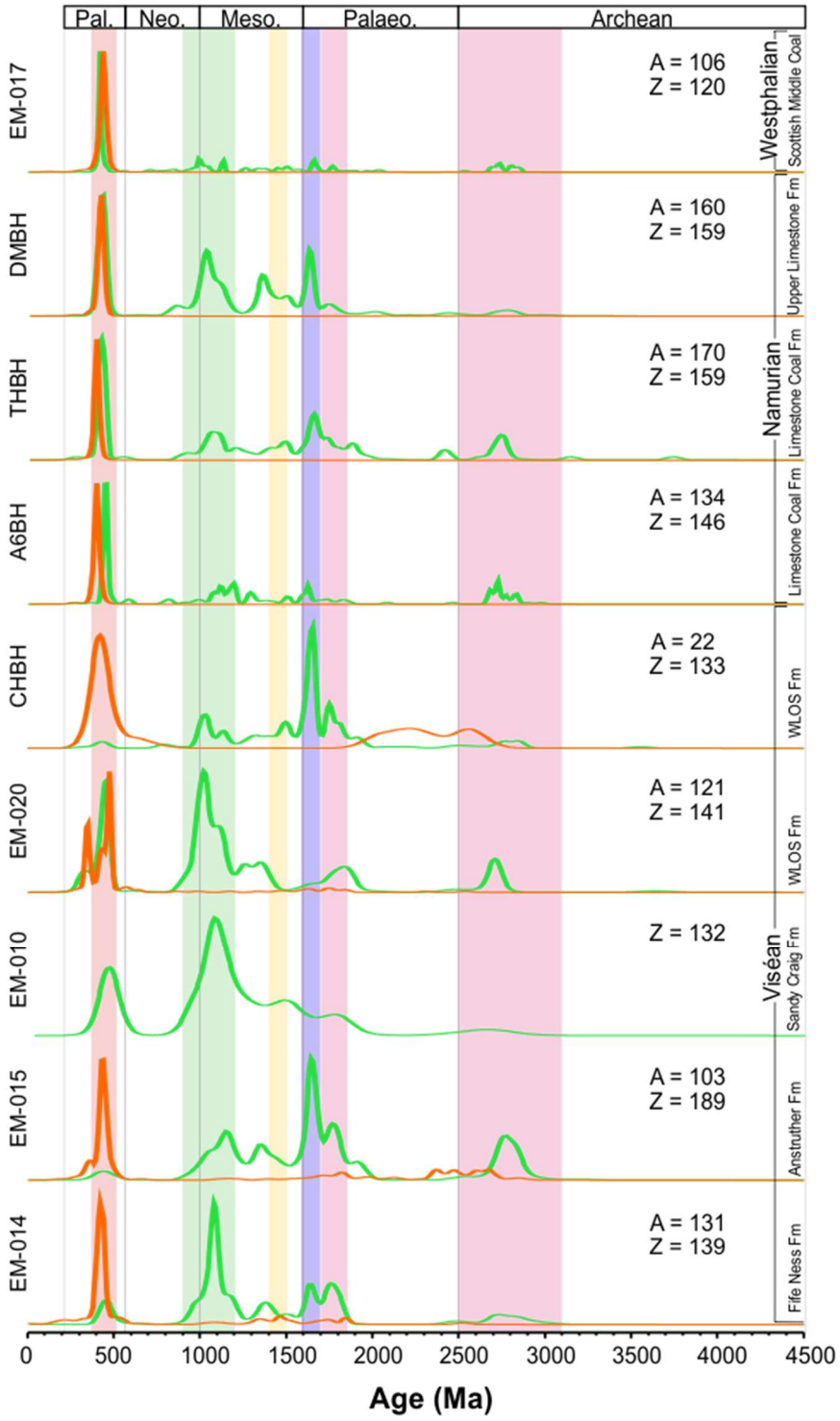

Figure 5-12: Combined apatite and zircon KDE with potential Laurentian sources. See Figure 5-3 for Laurentian events timings and related references. Individual sample zircon KDE (Green line); Individual sample apatite KDE (orange line). KDE produced using IsoplotR (Vermeesch 2018).

The zircon and apatite KDEs (Figure 4-32) have been combined with Figure 5-3 showing the timing of the Caledonian and Laurentian related orogenic events to produce Figure 5-12. This figure shows that there is a strong correlation between Laurentian and Caledonian orogenic events and the U-Pb peaks from detrital material in the Midland Valley. This observation agrees with results from previous provenance analysis, that the dominant source of Carboniferous sedimentary material came from Laurentian related terranes (Hallsworth *et al.* 2000; Morton *et al.* 2001; Lancaster *et al.* 2017), and palaeocurrent indicators, which show that the dominant sediment routing system into the Midland Valley came from the northeast, via fluvio-deltaic progradation and marine incursions (Chapter 2) (Read *et al.* 2002). The absence of Variscan and 525-690 Ma U-Pb ages suggests that peri-Gondwanan terranes and associated orogenic events (Nance *et al.* 2008) to the south were not contributing sediment into the Carboniferous Midland Valley, even during the Westphalian, when they were the dominant source for the Pennine Basin. Despite all samples suggesting a Laurentian source, variation between samples of different ages and the two provenance proxies used in this investigation (zircon and apatite U-Pb) are evident. This allows for provenance refinement between the differing age peaks between samples and the source(s) of recycled and first cycle material. This information has been depicted in a series of palaeogeographic reconstructions (section 5.3.3) which are referenced in the following text.

5.3.1 Proterozoic and Archean ages

When combined, the apatite and zircon KDE from a single sample indicate Caledonian and Laurentian associations (Figure 5-12). Individually however, it is only the zircon that fingerprints provenance from both these sources. Apatite KDEs are dominated by Palaeozoic ages only, with the exception of EM-14, EM-15, and CHBH which have subordinate Proterozoic and Archean populations, which will be discussed later. This ability to differentiate between mineral populations is the greatest strength of using a multi-proxy approach, and had it not been applied here, it would not be possible to distinguish between first cycle and polycyclic sources.

Zircon is a robust mineral, known to survive sedimentary recycling (Andersen *et al.* 2016) while apatite less robust and is more likely to be derived from first cycle material (Morton and Hallsworth 1999). The difference in mineral hardness, the refractory nature of zircon and the lack of associate Proterozoic and/or Archean apatite peaks gives a strong indication that the Laurentian related Proterozoic and Archean zircon peaks are derived from recycled sources, where any associated

apatite grains have failed to survive recycling. Although source rock fertility and post burial dissolution could also be a factor with respect to the lack of apatite. Laurentian associated rocks capable of producing Proterozoic and Archean aged zircon grains that have been recycled from existing sedimentary and/or metasedimentary rocks are located to the north, east, and south of the Midland Valley in Devonian sedimentary rocks (McKellar 2017) the Dalradian Supergroup metasediments (Cawood *et al.* 2003), and the Ordovician-Silurian Southern Uplands (Waldron *et al.* 2008). The U-Pb zircon spectra from Devonian Old Red Sandstone samples are shown in Figure 5-6 while examples from the Grampian terrane and Southern Uplands are shown in Figure 5-13. An apparent similarity can be seen when comparing the Proterozoic and Archean components from the Carboniferous samples from this investigation, particularly in Viséan aged samples (Figure 5-12) to those in Figure 5-6 and Figure 5-13, suggesting that these sources were suppling the Proterozoic and Archean age components into the Midland Valley during the Carboniferous. The dominant Proterozoic component in Viséan samples from the Midland Valley is contrary to what has been recorded in Carboniferous sandstones discussed above (Figure 5-10). Although samples from these previous studies are from the late Devonian-early Carboniferous (Morton *et al.* 2001) and Namurian Millstone Grit (Hallsworth *et al.* 2000), the subsequent interpretation was that the Pennine delta system was the dominant sediment supplier throughout this time, including the Viséan. This interpretation was largely based on the lack of Proterozoic peaks and the occurrence of a large Paleozoic peak, suggested to represent first cycle material derived from the Caledonian orogeny north of Scotland, with Morton and Whitham (2002) and Lancaster *et al.* (2017) suggesting Greenland as the most likely source.

Therefore, the strong similarity between the Proterozoic and Archean ages recoded in samples from the Midland Valley and those shown in Figure 5-13, suggests that this age component has been derived from the recycling of Devonian Old Red Sandstone, Grampian terrane metasediments, and Ordovician-Silurian sediments from the Southern Uplands. As this age components dominate the Viséan samples of the Midland Valley at a time when first cycle Palaeozoic sediments were believed to be entering other Carboniferous basins to the north and south of the Midland Valley indicating the Caledonian source was not yet established in the Midland Valley. Importantly, the Proterozoic and Archean zircon spectra vary significantly through the stratigraphy and with sample location. This indicates that the sediments were not well homogenised prior to being deposited and that the source region evolved through the Carboniferous. This evolution led to an increasing amount of relative

Palaeozoic material entering the Midland Valley and a reduction of the Proterozoic and Archean content.

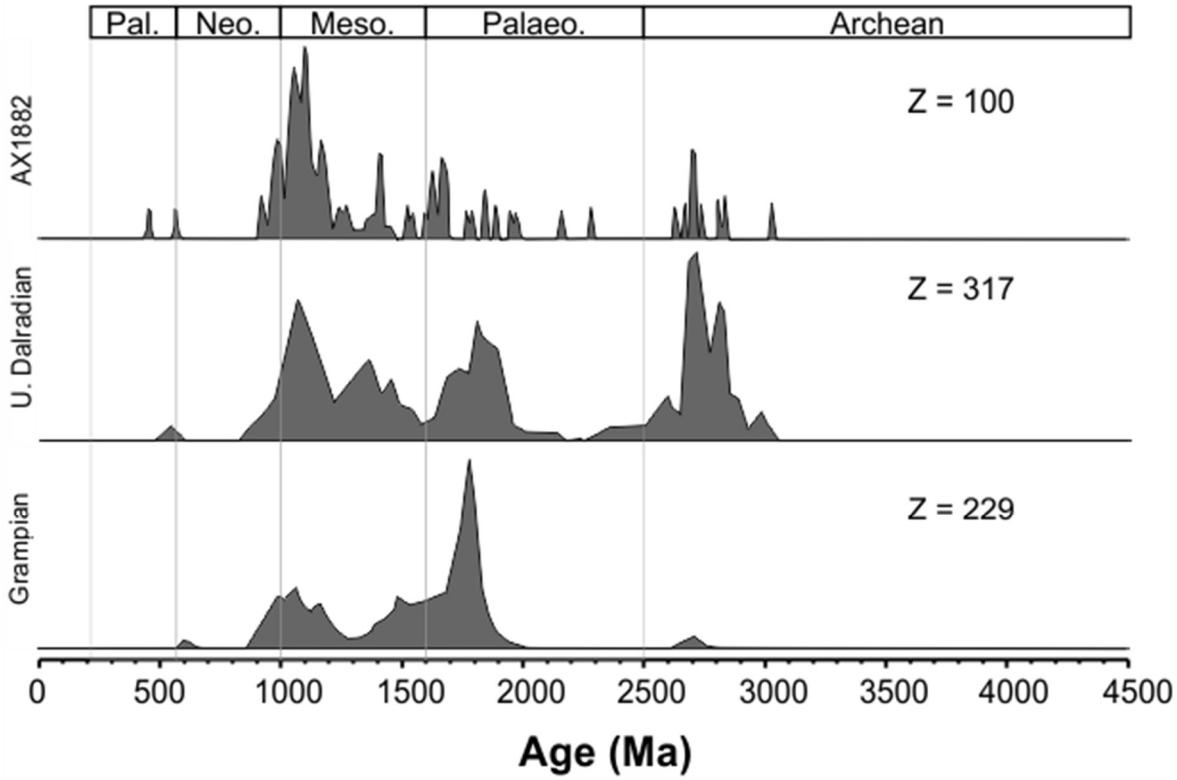

Figure 5-13: Probability density diagrams for Grampian terrane and Southern Uplands terrane. Grampian and Upper Dalradian samples redrawn from Figure 7 of Cawood *et al.* (2007), sample AX1882 from Glenwargen, Southern Uplands terrane, redrawn from Figure 2 of Waldron *et al.* (2008). Zircon age spectra derived from the Grampian Highlands and Southern Uplands terranes notably lack a significant Palaeozoic age component, are dominated by Proterozoic ages and have variable Archean content.

5.3.2 Palaeozoic ages

Apatite U-Pb KDEs produced in this thesis are all dominated by Palaeozoic ages, however significant Palaeozoic zircon U-Pb ages with peaks defined by at least 20 grains, do not appear until the Brigantian (late Viséan), (EM-010 and EM-020), although Proterozoic aged zircons still dominate these samples. Later Pendleian (A6BH and THBH), Arnsbergian (DMBH), and Westphalian B (EM-17) samples are all dominated by Palaeozoic U-Pb zircon ages (Figure 5-12). KDE plots for each sample spanning 300-600 Ma for zircon and apatite are shown in Figure 4-33, Figure 4-34 respectively, while a combined zircon and apatite Palaeozoic KDE is shown in Figure 5-14.

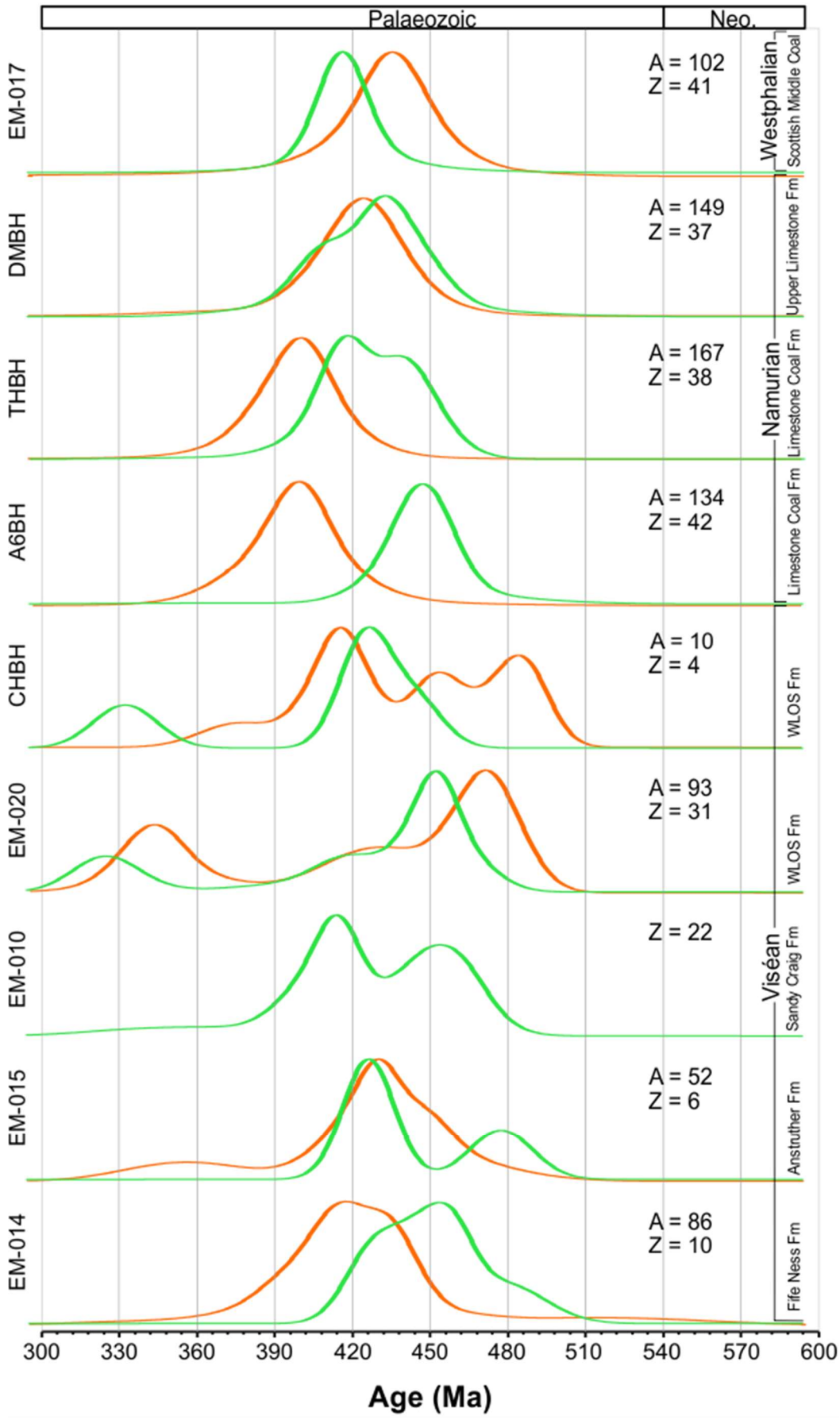

Figure 5-14: Palaeozoic zircon and apatite KDE plot. Individual sample zircon KDE (Green line); Individual sample apatite KDE (orange line). KDE produced using IsoplotR (Vermeesch 2018). Note scales on KDE plots are relative probability, for histograms see Figure 4-33 and Figure 4-34.

Palaeozoic peaks occur between 330-500 Ma (Figure 5-14) indicating a Caledonian orogeny and/or Carboniferous volcanic association (Figure 5-3, Figure 5-4), are present in all zircon and apatite samples, but in contrasting relative amounts. Arundian-Asbian (early-mid Viséan) samples EM-14 and EM-15, contain relatively few Palaeozoic zircon (10 and 6 respectively, Figure 5-14) and although apatite U-Pb KDEs are dominated by a Palaeozoic peak, subordinate populations of Proterozoic and Archean populations are present (Figure 4-7and Figure 4-10). These samples are from mineralogically mature quartz arenites which suggest that recycling of sediment has occurred, although extensive chemical weathering is a possibility in deriving such mature sandstones, it is unlikely due the presence of apatite in both EM-14 and EM-15, which is known to be extremely vulnerable to chemical weathering (Morton and Hallsworth 1999). Although it was highlighted earlier that the presence of apatite was an indicator of first cycle sediment only, the lack of a Palaeozoic zircon population, the presence of Proterozoic and Archean aged apatite, and the mineralogical maturity of these samples, suggests that recycled material dominates the source of these samples, potentially even the apatite. Devonian Old Red Sandstone are found offshore to the north and east of the Midland Valley. Late Devonian Old Red Sandstone samples from boreholes located north of the Mid North Sea High ORS 1 (Lundmark *et al.* 2014) have detrital U-Pb zircon age spectra that are similar to EM-14 and EM-15 (Figure 5-11). Lundmark *et al.* (2014) interpreted these samples as being derived from the Grampian and Southern Uplands Highs, which is in agreement with palaeocurrent interpretations during this time (Leeder 1988). A heavy mineral assemblage investigation has also shown that Devonian Old Red Sandstone are rich in apatite (McKellar *et al.* 2020). Thus, given their location to the north and east, the absence of Palaeozoic zircon, and the proven apatite content, the recycling of Devonian Old Red Sandstone strata located offshore are considered here to be the most likely source of Arundian-Asbian (early-mid Viséan) samples EM-14 and EM-15 (Figure 5-15).

Brigantian sample EM-10 lacks an apatite population (Figure 5-12), however the Palaeozoic zircon population shows a marked increase compared to Arundian-Asbian samples (EM-14 and EM-15). Although palaeocurrent indicators still suggest a dominant source from the northeast, the increased Palaeozoic zircon population suggests that this material was being supplemented by first cycle Caledonian material (Figure 5-16). EM-20, which is also Brigantian, but located more internally within the Midland Valley (Figure 5-16), also displays a Caledonian population along with a Carboniferous peak also present in CHBH (Figure 5-12). These younger Palaeozoic peaks are found in both apatite

and zircon KDEs in sample EM-020 and in the zircon KDE of sample CHBH (Figure 5-14). Based on relatively few data points (6 zircon and c.20 apatite in EM20 and 1 zircon in CHBH), it is difficult to pin point the exact source of these populations however, at c.330 Ma (Figure 5-14), these apatite and zircon U-Pb ages coincide with volcanic activity occurring within the Midland Valley at this time, highlighted in Figure 5-4 above, and most likely represent first cycle material derived from this activity.

While both Brigantian EM-10 and EM-20 have more prominent Caledonian peaks compared to Arundian-Asbian samples (EM-14 and EM-15), they are still dominated by recycled Laurentian related Proterozoic populations as discussed above. The CHBH sample is also Brigantian, however it contains limited Palaeozoic zircon and apatite grains (4 and 10 grains respectively). This lack of Palaeozoic component is most likely caused by the samples position within the Midland Valley. The sample is located to the west of the Bathgate Hills volcanic centre (BH, Figure 5-16), which acted as a barrier to north-easterly derived material that is recorded in the Asbian-Brigatian samples (EM-14, EM-15, EM-10, and EM-20). The lack of Caledonian ages in CHBH, indicates that the source of this material is dominated by sediment recycling as discussed above, which may lie to the south in the Southern Uplands (Figure 5-16).

A significant change occurs between the Palaeozoic component of Asbian-Brigantian samples (EM-14, EM-15, EM-10, EM-20, and CHBH) and Pendleian-Arnsbergian (early-Namurian) samples A6BH, THBH, and DMBH in the Midland Valley. The recycled Proterozoic component which dominated all earlier samples becomes much more subdued in the Pendleian-Arnsbergian and the Palaeozoic component now dominates (Figure 5-12). These samples strongly resemble Fammenian-Chadian (Tayport Fm) and Brigantian (Firth Coal Fm) samples from the Outer Moray Firth Basin (Morton *et al.* 2001) and Chokierian-Yeadonian (Millstone Grit) samples from the Pennine Basin (Figure 5-10) (Hallsworth *et al.* 2000; Lancaster *et al.* 2017). The Outer Moray Firth and Pennine Basin samples were interpreted as being derived from a northern source, potentially East Greenland, which dominated the source of Caledonian first cycle material into Carboniferous basins of the British Isles via the Pennine Delta system (Hallsworth *et al.* 2000; Morton *et al.* 2001; Morton and Whitham 2002; Lundmark *et al.* 2014; Lancaster *et al.* 2017). It is worth noting that the earliest sample from Lancaster *et al.* (2017) from the Pennine Basin is from the Pendleian (11LYK05, Figure 5-10) and has a similar spectra to the Brigantian EM-010 of the Midland Valley. Although the Caledonian population was interpreted as being derived from East Greenland, the important Proterozoic

population was interpreted as indicating a local supply from the Southern Uplands and/or recycling of Devonian Old Red Sandstone (Figure 5-8a).

Though earlier studies excluded Scotland as being a source for the Palaeozoic component of their detrital U-Pb spectra (Hallsworth *et al.* 2000; Morton *et al.* 2001; Morton and Whitham 2002; Lancaster *et al.* 2017), paleocurrent indicators from within the Midland Valley suggest that the source of the sediment lay to the north (Chapter 2). This information, along with the findings of McKellar (2017) that show Scottish Caledonian intrusions and associated volcanic material (Figure 5-2) were supplying sediment into Lower Devonian Midland Valley Basins, suggests that a Palaeozoic, Scottish Caledonian source cannot be excluded for the provenance of detrital material in the Carboniferous Midland Valley (Figure 5-17), along with the long range distal source to the north of Scotland that was the regional sediment supplier, as suggested by previous work (Hallsworth *et al.* 2000; Morton *et al.* 2001; Morton and Whitham 2002; Lancaster *et al.* 2017).

The Millstone Grit equivalent in the Midland Valley (Chokierian-Yeadonian, Passage Fm) was not sampled in this investigation due to the lack of exposure, therefore it is not possible to directly compare the basins at this time. However, the Westphalian B sample EM-17 does allow for time equivalent comparison. In the Midland Valley, EM-17, both zircon and apatite U-Pb spectra continue to be dominated by Palaeozoic ages (Figure 5-12 and Figure 5-14). Suggesting that the Caledonian source of the Pendleian-Arnsbergian samples (A6BH, THBH, and DMBH) continued to dominate the source region. The same is not true for the Westphalian samples to the south in the Pennine and Southern North Sea basins (Dalton Rock, Halesowen Fm, and Westoe Fm, Figure 5-10). The influence of the northern source that dominated the Caledonian, Palaeozoic population during the Chokierian-Yeadonian in the southern basins, appears to have waned during the Westphalian and is replaced by Variscan and Cadomian age populations with palaeocurrent indicators now suggesting sediment supply was dominantly from the east, south, and west (Figure 5-9) (Morton *et al.* 2001) as sedimentation returns to East Greenland (Morton and Whitham 2002).The Westphalian B, EM-17, in the Midland Valley does not contain these Variscan or Cadomian populations, indicating that the Southern Uplands was a structural high at this time, acting as a barrier to the southerly derived material. As well as the continued first cycle source from Caledonian intrusions and volcanic material the Westphalian samples in the Midland Valley are interpreted in this study as being recycled from Carboniferous material previously deposited offshore and within the Midland Valley terrane itself

(Figure 5-18) as suggested by palaeocurrent indicators (Chapter 2) and the lack of Proterozoic peaks, implying long range sediment transport had switched off.

5.3.3 Palaeogeographic reconstructions

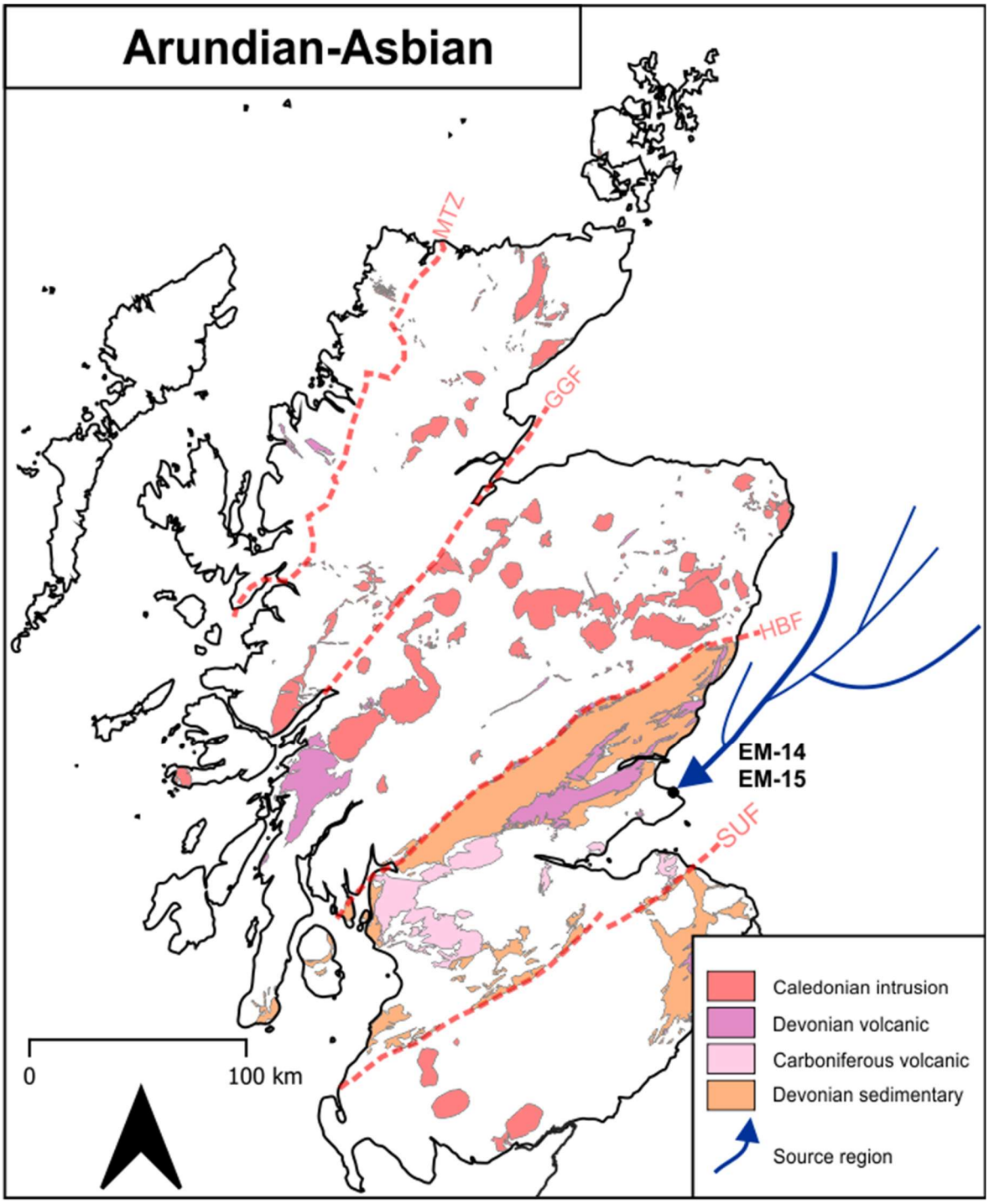

Figure 5-15: Palaeogeographic reconstruction model for Arundian-Asbian samples. Samples EM-14 and EM-15 from the mid-Viséan are interpreted to be derived from recycled material with palaeocurrent indicators showing transport from the northeast. Variations in the Proterozoic and Archean peaks suggest sediment was not well-homogenised prior to deposition and was sourced directly from the Grampian terrane and/or recycled from the Devonian Old Red Sandstone strata which was located to the northeast. The lack of Palaeozoic zircons indicated limited Caledonian first cycle input.

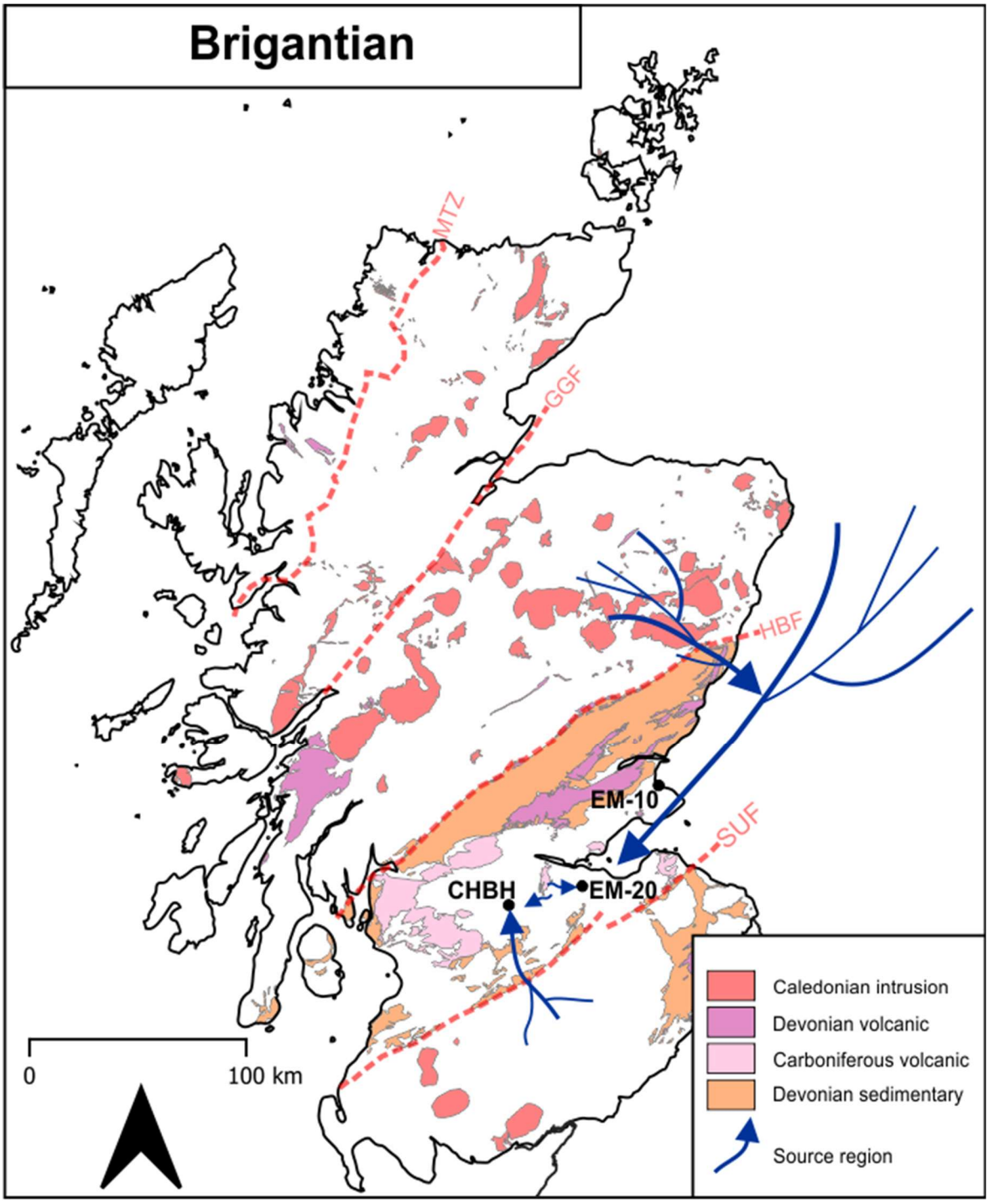

Figure 5-16: Palaeogeographic reconstruction model for Brigantian samples. BH, Bathgate Hills. Sample EM-10 and EM-20 now have defined Palaeozoic peaks suggesting that first cycle Caledonian material was now entering the Midland Valley, potentially derived from Scottish intrusions and associated volcanic material. Proterozoic ages still dominate these spectra so the recycled components form the Arundian-Asbian are still the major sediment source in the east. EM-20 and CHBH contain Carboniferous age components where were derived from the contemporaneous volcanism. CHBH in the west of the Midland Valley contains only minor amounts of Palaeozoic material due to the volcanic highs acting as barriers to the first cycle Palaeozoic components arriving from the northeast. The source of this material most likely originates to the south in the Southern Uplands due to the Volcanic highs to the north.

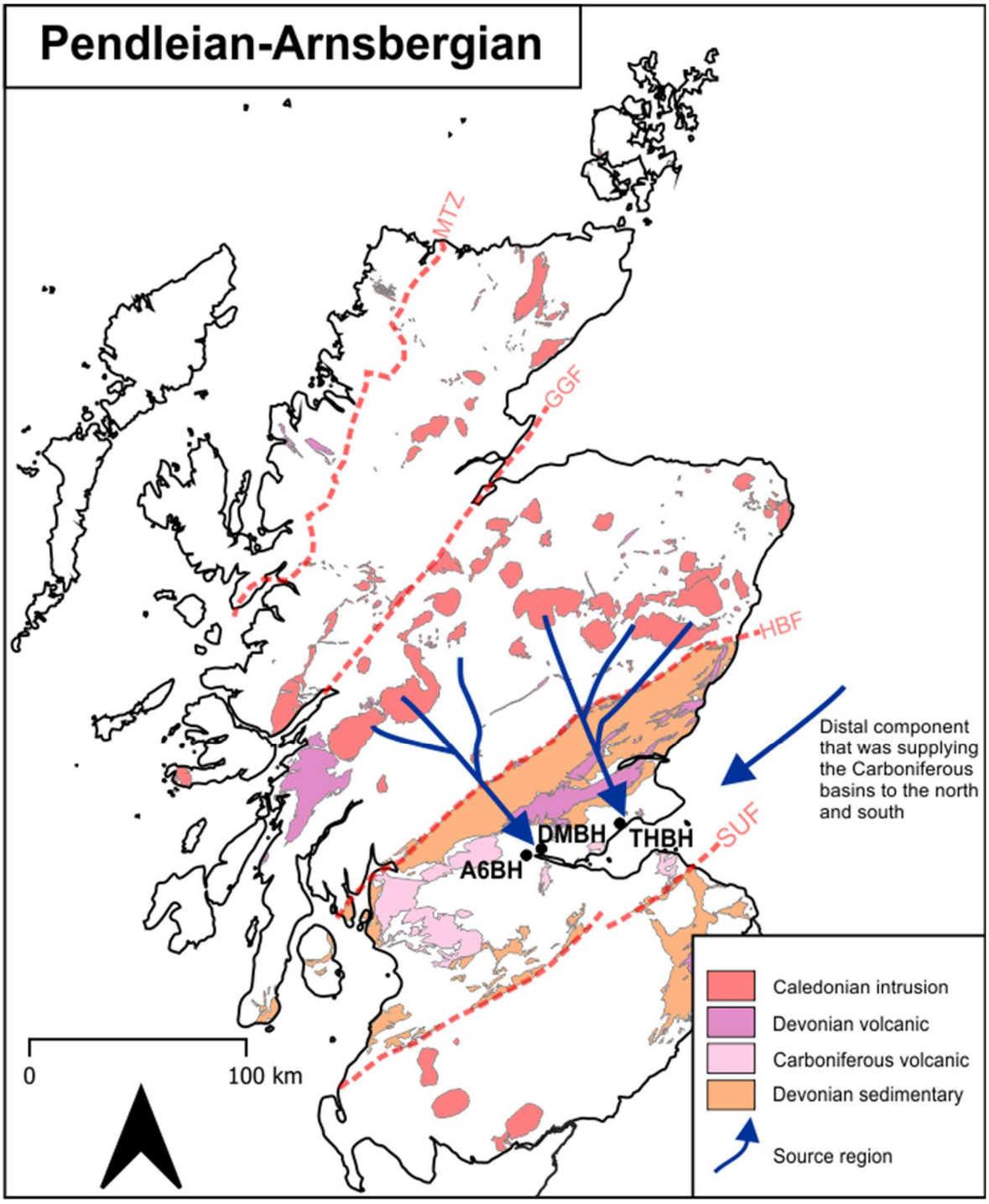

Figure 5-17: Palaeogeographic reconstruction model for Pendleian-Arnsbergian samples. A6BH, THBH, and DMBH are now dominated by Palaeozoic peaks with only minor Proterozoic and Archean peaks. The dominance of Palaeozoic ages indicates that first cycle Caledonian material sourced from the proximal Scottish Caledonian and distal Caledonian sources (Greenland) was diluting the recycled components. This is similar to what is seen in the Outer Moray Firth and Pennine Basins, however Scotland was excluded as a major source to these coeval basins. Recycled sediment from the Grampian and Southern Uplands terranes was still actively contributing material into the Midland Valley during the Pendleian-Arnsbergian.

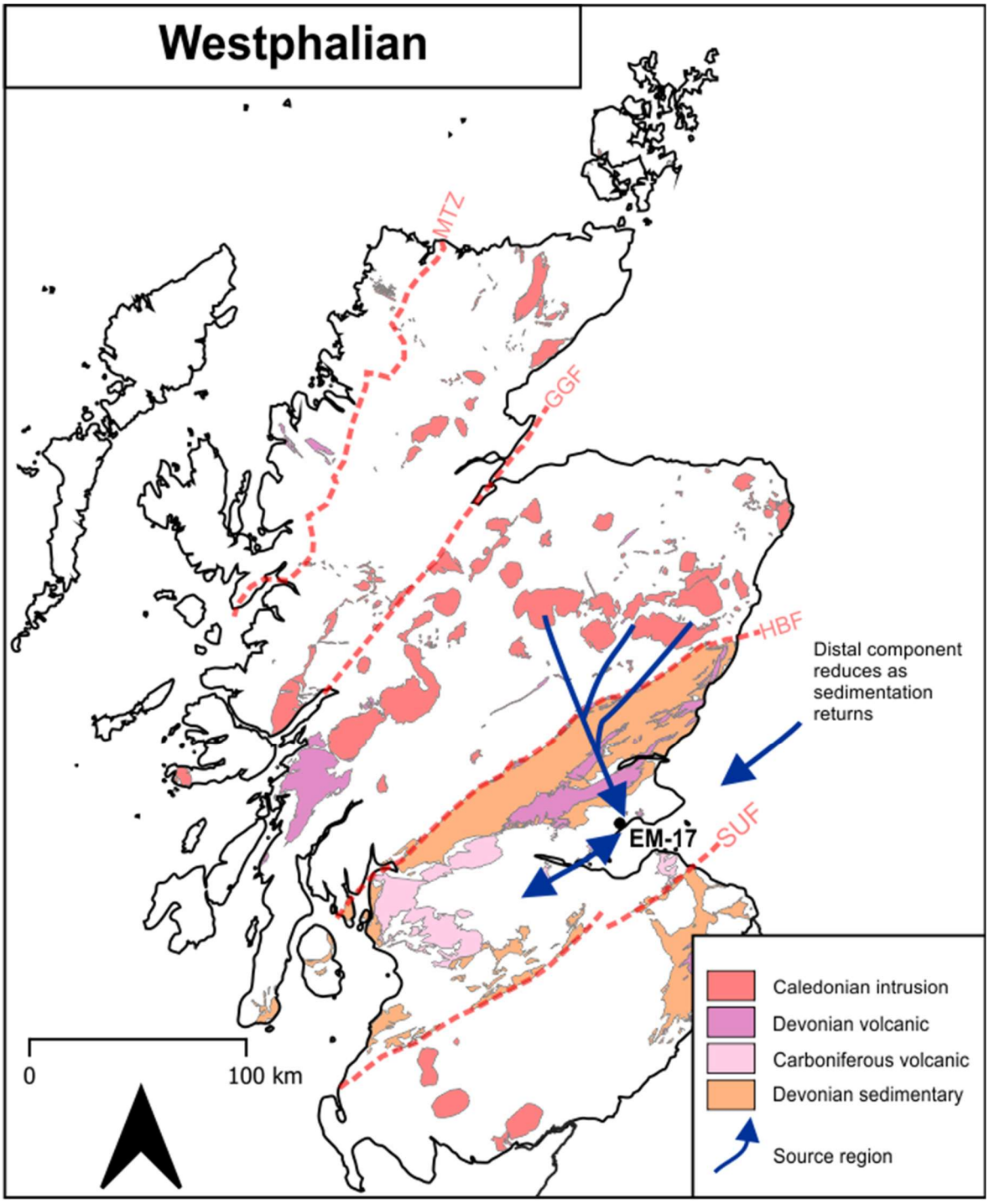

Figure 5-18: Palaeogeographic reconstruction model for Westphalian sample. While Westphalian samples to the south record a change in sediment provenance with the appearance of peri-Gondwanan related ages, the Palaeozoic Caledonian ages persist in the Midland Valley. The regional Caledonian source from north of the region reduces as sedimentation returns to East Greenland. First cycle material into the Midland Valley derived from the Scottish Caledonian sources continues, however a recycling of early deposits is also likely due to the basin structure and tectonic activity at this time.

5.4 Conclusions

For the U-Pb apatite and zircon provenance work carried out here the following conclusions can be made:

- A multi-proxy approach to provenance investigations allows for the discrimination between first cycle and polycyclic material. Without the complementary zircon and apatite U-Pb spectra, it would not have been possible to differentiate between which zircon populations were first cycle and which were derived from sediment recycling.
- Sediment deposited in the Midland Valley during the Arundian-Asbian was 'Scotland' derived from recycled material from the Devonian Old Red Sandstone, Grampian High (onshore and offshore north-east Scotland), and Southern Uplands terrane.
- This Arundian-Asbian material was dominated by recycled material with little or no first cycle input suggesting that in the right conditions (limited exposure to acidic weathering, abundant in host sedimentary rock, relatively short residence time) apatite can be recycled from pre-existing sedimentary basins.
- Evidence of first cycle material beginning to enter the Midland Valley occurs during the Brigantian evidenced by the appearance of the Caledonian aged zircon peak in EM-010 and EM-020.
- Local volcanism within the Midland Valley was supplying sediment during the Brigantian, with volcanic highs acting as barriers, largely preventing north easterly derived material being deposited across the basin, with sediment supply from the Southern Uplands.
- Caledonian aged material became the dominant source of sediment into the Midland Valley during the Pendleian-Arnsbergian (early Namurian). This was derived from Scottish Caledonian intrusions and volcanic material along with distant east Greenland Caledonian sources typical to samples from the Pennine Basin and Outer Moray Firth.
- Locally sourced recycled material from the Scottish landmass continued to supply sediment to the Midland Valley, though it was diluted by first cycle Caledonian aged material.
- The Southern Uplands was a structural high preventing southerly sourced material from entering the Midland Valley during the Westphalian.

- While Caledonian aged material remained prominent during the Westphalian, it may have been sourced from recycling previously deposited Carboniferous material from within and offshore to the Midland Valley.
- Overall, compared to some previous interpretations (Hallsworth *et al.* 2000; Morton *et al.* 2001; Morton and Whitham 2002; Lancaster *et al.* 2017), the new Carboniferous Midland Valley provenance work shows a great dominance of Scotland-derived material, either through recycling of Grampian High metamorphic rocks, the Southern Uplands terrane and Devonian Old Red Sandstone strata or first cycle Caledonian intrusions and associated volcanic material.
- Palaeozoic zircon and apatite KDEs (Figure 5-14) display an interesting and complex relationship particularly in relation to their Namurian and Westphalian trends with zircon displaying a broad trend towards younger zircon populations up sequence while apatite samples display the opposite trend. This relationship is not yet understood and requires further work to unravel, for example by using analysing the chemistry of the grains to fingerprint specific sources.
- This in-depth work of the individual grain chemistry may help differentiate the Palaeozoic components into sub-populations which may help tie the detrital material to specific plutons.

Chapter 6 AFT Thermochronology

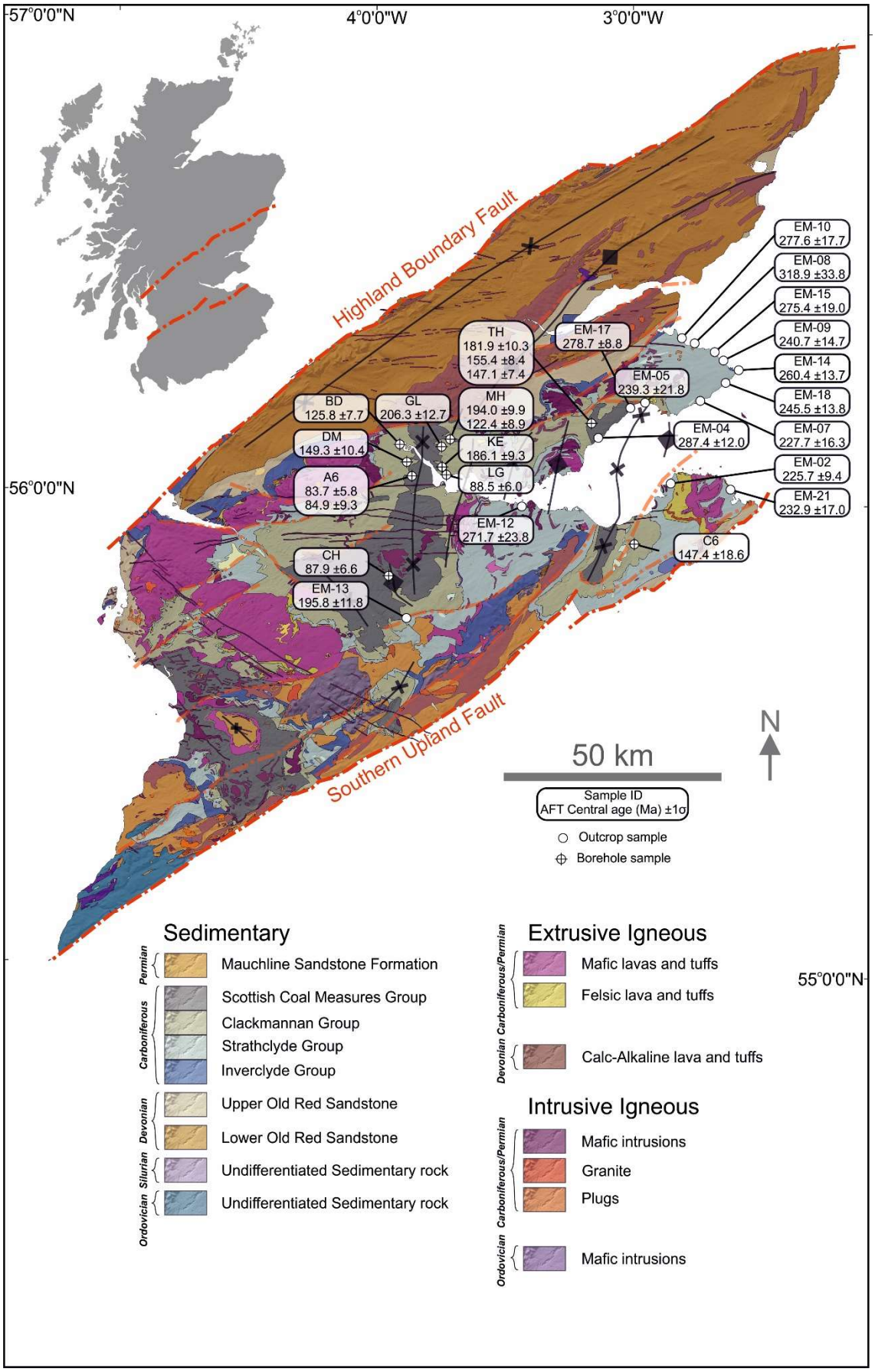

Figure 6-1: Sample locations used for AFT investigation plotted on geological map from Chapter 2. Also shown are the AFT central ages and their ±1σ uncertainty.

6.1 Results

Apatite fission track (AFT) analysis was performed on detrital apatite from Carboniferous sandstones located across the Midland Valley of Scotland, using the laser ablation–inductively coupled plasma-mass spectrometer (LA-ICP-MS) method outlined in Chapter 3. From the twenty-one outcrop and nineteen borehole samples collected and processed, fourteen outcrop and fourteen borehole samples yielded sufficient apatite to perform AFT analysis. The sample locations and AFT central ages (±1σ) are shown in Figure 6-1, while full sample details can be found in Table 6-1 and Table 6-2. In addition to the onshore Midland Valley AFT data, offshore wells investigated by Geotracks (Duddy *et al.* 1992) have been presented in Table 6-3 and further discussed in Chapter 8. AFT central ages and 1σ errors obtained in this study were calculated using the formula outlined in Chapter 3 using the IsoplotR software of Vermeesch (2018). A target of counting a minimum of 20 grains per sample for fission track age determination was set; however, due to the low yield of apatite from outcrop samples, this value was rarely exceeded, with the exception of EM-17 for which 60 grains were counted; 30-40 grains were counted in all borehole samples with the exception of C6-G1 (Table 6-2). All samples central ages are younger than their respective stratigraphic age (Figure 6-2) and range from 318.9 ±33.8 Ma (EM-08) to 83.7 ±5.8 Ma (A6G2), however EM-08 1σ uncertainty does overlap with its stratigraphical age. Samples have been collected from coastal outcrop exposures, all of which had an elevation of less than 10 meters (Table 6-1) and borehole core samples, with depths up to -941 meters below ground level (Longannet-1 borehole, LGG2) (Table 6-2.). Resulting AFT central ages displaying a strong negative correlation with depth i.e., younger ages are found with increasing depth (Figure 6-3). Kinetic parameter Dpar was measured as a proxy for annealing resistance (Chapter 3 section 3.3.12.3) (Carlson *et al.* 1999), sample average values (±1 SD) are shown on Figure 6-6 and range between 1.50µm ±0.15 and 1.92 ±0.49µm. ^{238}U concentration is a vital component in AFT age determination and has been suggested to influence annealing behaviour in apatite (Hendriks and Redfield 2005; McDannell *et al.* 2019). Due to the detrital nature of these samples, the ^{238}U concentration (±1 SD) displays a large variation, ranging between 9.64 ±1.5 and 51.8 ±7.9 ppm (Figure 6-8). Radial plots (Chapter 3 section 3.3.9.1) (Galbraith 1990) have been produced in two ways using the software of Vermeesch (2009): 1) The traditional approach whereby the sample single grains ages are plotted with their respective kinetic parameter Dpar (Figure 6-10 and Figure 6-11). 2) The single grains ages are plotted indicating their ^{238}U concentration. A Kernel Density Estimate (KDE, Chapter 3 section 3.2.4.3) is aligned with the time axis on the radial plot and

the stratigraphic age for each sample has been adjusted to the horizontal position, for convenience (Figure 6-12 and Figure 6-13). All plots and individual sample details can be viewed in the sample data sheets section (Appendix D & E). Horizontal confined tracks (HCT) were measured to investigate the thermal history of the samples (Chapter 3); a target of one hundred HCT was set per sample, which was often achieved or exceeded due to exposing the samples to ^{252}Cf irradiation at the University of Melbourne. Unprojected mean track length and standard deviation ranged between 9.13 ±2.50 and 12.58 ±1.57 µm, c-axis projected mean track length (Ketcham *et al.* 2007a) ranged between 12.27 ±1.32 and 14.10 ±1.01 µm (section 6.3). AFT central ages and MTL data from the Midland Valley have been plotted in isolation (Figure 6-19) and along with existing published data from Scotland (Figure 6-20) to investigate if a 'boomerang' style relationship exists (Green 1986; Gallagher *et al.* 1998; Ketcham 2019).

6.2 AFT age data

6.2.1 AFT central age vs stratigraphic age

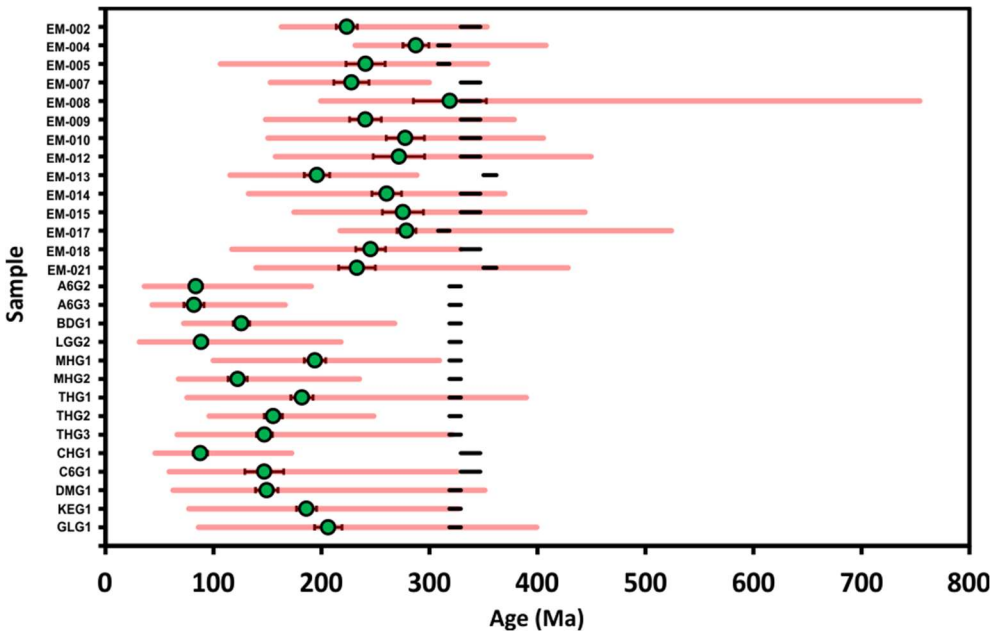

Figure 6-2: Individual sample AFT central age vs Stratigraphic age. Sample central age and 1σ standard error (green markers) are plotted with spread of sample single grain ages (pink bar) and stratigraphic age for each sample (black bar). Plotted in same order as Table 6-1 & Table 6-2.

AFT central ages, from both outcrop and borehole samples have been plotted against their respective stratigraphic age (Figure 6-2). The AFT central age of the outcrop samples range between 318.9 ±33.8 and 195.8 ±11.8 Ma (Table 6-1), while boreholes range between 206.3 ±12.7 Ma and 83.7 ±5.8 (Table 6-2). All sample AFT central ages are younger than stratigraphic age, though there

is overlap of the 1σ standard error of sample EM-008. The spread of AFT single grain ages for each sample, represented by the pink bar, is highly variable, as expected in detrital apatites (Figure 6-5). All outcrop samples except for EM-007 and EM-013, and three of the borehole samples (THG1, DMG1, & GLG1) show an overlap between single grain ages and sample stratigraphic age. Whether the spread of single grain ages takes the form of a continuous mixture or multiple discrete age populations is investigated using radial plots in section 6.2.5. Samples with youngest AFT central age have the smallest 1σ uncertainty and the relationship between AFT central age and depth will be investigated next.

6.2.2 AFT central age vs depth

Samples that have experienced greater temperature more recently should have an apparent AFT age that is younger that samples that have been at a cooler temperature (Reiners and Ehlers 2005). This is a basic principle of AFT analysis and Age vs elevation plots (depth in boreholes) are commonly used to investigate this relationship. As borehole samples have been collected from greater depth than outcrop samples their AFT central age should be younger. This relationship is clear in Figure 6-3, where the range of outcrop samples (green) have older AFT central ages than the borehole sample (see key and Table 6-2 for borehole details).

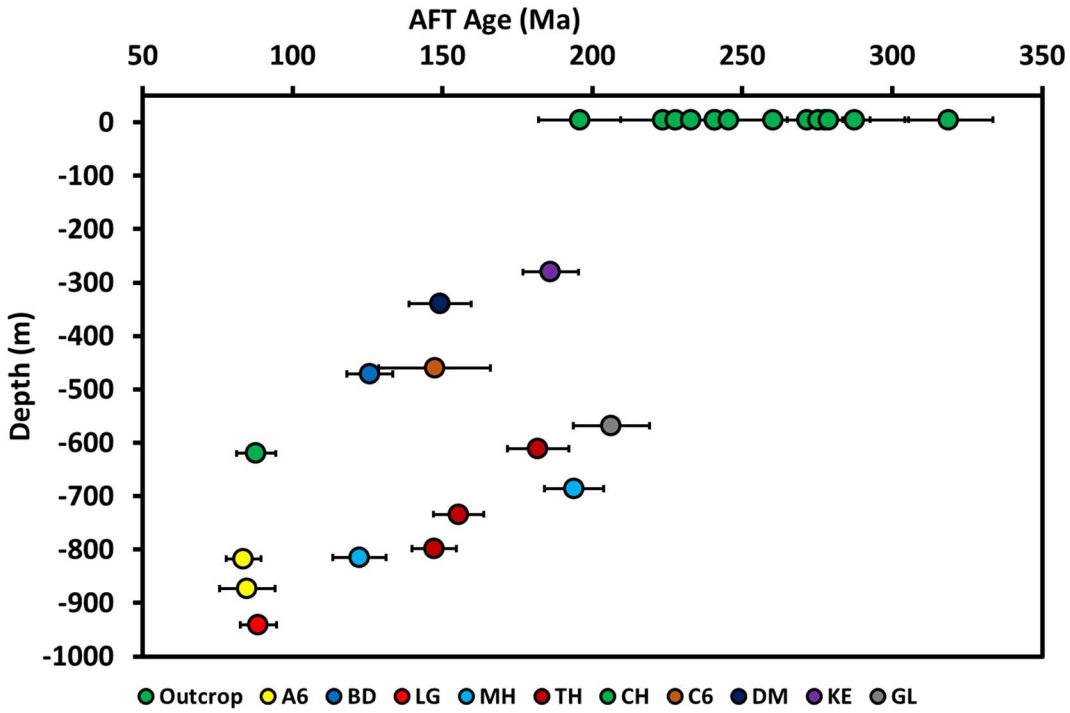

Figure 6-3: Sample AFT central ages and 1σ errors plotted against sample depth. AFT central ages for samples from the Midland Valley generally decrease with increasing depth.

6.2.3 AFT data tables

6.2.3.1 Outcrop samples

Sample	Stratigraphic age	Lat. (°)	Long. (°)	Elevation /depth (m)	# of crystals	Ns[a]	Ps[b] (x10^6)	Dpar[c]	Diss.[d] (%)	X^2 [e]	^{238}U[f]	Central age [g]	±1σ	# of lengths	M MTL[h] (µm) (±1σ)	SD[i]	P MTL[j] (µm) (±1σ)	SD[k]
EM-001	Viséan	56.0625	-2.8120	<10	No Ap.													
EM-002	Viséan	56.0390	-2.8480	<10	20	1549	1.37	1.66	9.6	0.12	34.63	225.7	9.4	101	11.28 (0.25)	2.56	13.67 (0.18)	1.47
EM-003	Viséan	55.9730	-2.9400	<10	No Ap.													
EM-004	Westphalian	56.1420	-3.0810	<10	20	3057	4.02	1.60	10	0.00	30.92	287.4	12.0	103	11.82 (0.21)	2.18	13.46 (0.15)	1.23
EM-005	Westphalian	56.2110	-2.9450	<10	20	578	1.49	1.58	19	0.19	16.24	239.3	21.8	102	11.90 (0.19)	1.89	13.55 (0.15)	1.19
EM-006	Viséan	56.2863	-2.6000	<10	No Ap.													
EM-007	Viséan	56.2100	-2.7390	<10	20	614	1.62	1.67	0	0.93	22.25	227.7	16.3	82	12.06 (0.23)	2.05	13.95 (0.18)	1.42
EM-008	Viséan	56.3277	-2.7327	<10	20	996	1.46	1.68	38	0.00	9.64	318.9	33.8	108	9.13 (0.24)	2.50	12.27 (0.13)	1.32
EM-009	Viséan	56.2930	-2.6259	<10	20	949	1.98	1.89	9.3	0.47	20.43	240.7	14.7	100	11.56 (0.19)	1.91	13.81 (0.15)	1.21
EM-010	Viséan	56.3320	-2.7750	<10	20	2100	2.78	1.92	16	0.00	25.57	277.6	17.7	106	11.89 (0.16)	1.69	14.01 (0.15)	1.17
EM-011	Viséan	56.2130	-2.7240	<10	No Ap.													
EM-012	Viséan	55.9906	-3.3882	<10	20	1576	2.65	1.72	27	0.00	21.70	271.7	23.8	121	12.06 (0.16)	1.73	14.06 (0.15)	1.16
EM-013	Tournasian	55.7136	-3.8224	<10	20	2039	2.07	1.66	17	0.00	24.50	195.8	11.8	105	12.36 (0.20)	2.03	13.85 (0.14)	1.42
EM-014	Viséan	56.2800	-2.5880	<10	23	1808	2.27	1.66	15	0.00	17.78	260.4	13.7	120	10.78 (0.16)	1.79	13.00 (0.11)	1.17
EM-015	Viséan	56.3095	-2.6544	<10	18	1545	3.17	1.70	23	0.00	27.15	275.4	19.0	112	11.18 (0.16)	1.66	13.17 (0.11)	1.45
EM-016	Viséan	56.0294	-3.4690	<10	No Ap.													
EM-017	Westphalian	56.2099	-2.9582	<10	60	5538	2.79	1.60	17	0.00	20.78	278.7	8.8	120	11.50(0.15)	1.64	13.46 (0.14)	1.11
EM-018	Viséan	56.2610	-2.6180	<10	20	1209	1.46	1.68	3	0.48	15.09	245.5	13.8	122	11.74 (0.18)	1.95	13.79 (0.16)	1.27
EM-019	Namurian	56.1210	-3.1300	<10	No Ap.													
EM-020	Viséan	55.8915	-3.4749	<10	Not Analysed													
EM-021	Tournasian	56.0236	-2.5900	<10	20	633	1.71	1.77	21	0.02	16.90	232.9	17.0	122	11.98 (0.17)	2.28	13.69 (0.15)	1.34

Table 6-1: Midland Valley outcrop AFT summary table. For superscript explanation see Table 6-3 figure caption.

6.2.3.2 Midland Valley borehole samples

Sample	Stratigraphic age	Lat. (°)	Long. (°)	Elevation (m)	T (°C)	# of crystals	Ns[a]	Ps[b] (x10^6)	Dpar[c]	Diss.[d]	X^2_e	^{238}U[f]	Central age [g]	±1σ	# of lengths	M MTL[h] (µm) (±1σ)	SD[i]	P MTL[j] (µm) (±1σ)	SD[k]
A6-G1	Namurian	56.0490	-3.7880	-745	26±2	No Ap.													
A6-G2	Namurian	56.0490	-3.7880	-817	27±2	32	901	1.04	1.51	31	0.0	27.45	83.7	5.8	89	12.58 (0.17)	1.57	14.10 (0.17)	1.01
A6-G3	Namurian	56.0490	-3.7880	-873	30±2	36	3014	4.36	1.58	24	0.0	34.08	84.9	9.3	111	11.20 (0.23)	2.41	13.35 (0.19)	1.47
BD-G1	Namurian	56.1160	-3.8420	-471	23±2	42	2467	1.61	1.50	26	0.0	30.95	125.8	7.7	120	11.01 (0.20)	2.21	13.02 (0.19)	1.51
LG-G1	Namurian	56.0570	-3.7040	-810	27±2	No Ap.													
LG-G2	Namurian	56.0570	-3.7040	-941	31±2	48	1337	0.84	1.80	23	0.0	19.42	88.5	6.0	120	11.57 (0.19)	2.10	13.56 (0.16)	1.30
MH-G1	Namurian	56.1271	-3.6722	-686	28±2	35	4411	2.72	1.50	25	0.0	30.64	194.0	9.9	120	11.10 (0.17)	1.88	13.22 (0.15)	1.21
MH-G2	Namurian	56.1271	-3.6722	-815	30±2	40	1423	1.09	1.51	25	0.0	17.57	122.4	8.9	120	12.05 (0.15)	1.62	13.77 (0.14)	1.08
TH-G1	Namurian	56.1590	-3.1360	-611	18±2	40	3147	2.37	1.78	29	0.0	28.79	181.9	10.3	120	10.65 (0.20)	2.18	12.98 (0.16)	1.28
TH-G2	Namurian	56.1590	-3.1360	-734	23±2	35	2206	2.37	1.47	23	0.0	32.55	155.4	8.4	120	10.92 (0.17)	1.90	12.99 (0.16)	1.28
TH-G3	Namurian	56.1590	-3.1360	-798	25±2	42	2779	2.06	1.47	28	0.0	30.36	147.1	7.4	110	12.00 (0.17)	1.79	13.31 (0.15)	1.20
CH-BH	Viséan	55.8370	-3.8750	-620	24±2	36	676	0.77	1.63	30	0.0	17.40	87.9	6.6	61	11.71 (0.19)	1.51	13.50 (0.13)	1.01
C6-BH	Viséan	55.9010	-2.9870	-460	23±2	12	500	1.49	1.74	36	0.0	20.4	147.4	18.6	94	11.22 (0.20)	1.96	13.16 (0.15)	1.35
DM-BH	Namurian	56.0790	-3.8110	-340	20±2	40	3367	3.33	1.69	39	0.0	51.81	149.3	10.4	120	11.62 (0.20)	2.13	13.57 (0.17)	1.31
KE-BH	Namurian	56.0580	-3.7050	-280	19±2	40	3441	1.96	1.71	27	0.0	22.91	186.1	9.3	120	11.08 (0.20)	2.16	13.12 (0.18)	1.45
GL-BH	Namurian	56.1140	-3.7050	-568	24±2	36	3306	3.43	1.65	33	0.0	35.01	206.3	12.7	120	10.80 (0.19)	2.13	13.08 (0.13)	1.34
MB3-G1	Namurian	56.1790	-3.1070	-1141	33±3	No Ap.													
ST-G1	Viséan	55.8710	-3.0190	-626	27±2	No Ap.													
LS-G1	Viséan	55.8020	-3.6510	-428	23±2	No Ap.													

Table 6-2: Midland Valley AFT borehole summary table. For superscript explanation see Table 6-3 figure caption.

6.2.3.3 Geotrack offshore borehole samples

Sample	Stratigraphic age	Lat. (°)	Long. (°)	Elevation /depth (m)	T (°C)	# of crystals	Ns[a]	Ps[b] (x10^6)	Dpar[c]	Diss.[d]	X^2 [e]	^{238}U[f]	Central age [g]	±1σ	# of lengths	M MTL[h] (µm) (±1σ)	SD[i]	P MTL[j] (µm) (±1σ)	SD[k]
GC397-49	Viséan	56.142	-2.913	-564-731	38	6	235	1.59	x	0	0.34	18.9	208.2	18.7	43	11.43 (0.30)	1.97	x	x
GC397-61	Viséan	56.142	-2.913	-1463·1637	62	5	243	1.54	x	0	0.09	11.98	268.9	25.2	66	12.09 (0.25)	2.02	x	x
GC397-68	Viséan	56.142	-2.913	-1859·1996	69	2	123	2.56	x	41	0.00	31.10	102.8	31.7	10	10.92 (0.48)	1.52	x	x
GC374-1	Triassic	56.713	-1.727	-370-440	23	20	1148	1.82	x	19	0.01	11.56	328.5	22.5	102	12.40 (0.17)	1.74	x	x
GC397-1	Rotliegend	56.713	-1.727	-1152-1157	45	4	198	0.69	x	23	0.07	8.87	383.1	43.3	3	11.50 (2.39)	4.13	x	x
GC374-2	Rotliegend	56.713	-1.727	-1160-1250	46	20	1339	1.97	x	13	0.05	16.87	257.0	10.9	111	11.17 (0.22)	2.32	x	x
GC374-3	Viséan	56.713	-1.727	-1450·1600	50	20	1660	2.21	x	22	0.00	22.16	251.1	16.7	132	10.63 (0.18)	2.09	x	x
GC397-3	Viséan	56.713	-1.727	-1490·1556	50	20	1942	2.24	x	16	0.00	22.1	215.8	12.1	103	11.97 (0.20)	2.06	x	x
GC374-4	Viséan	56.713	-1.727	-1850·2000	54	10	560	1.58	x	28	0.00	26.2	187.5	20.8	10	11.21 (0.39)	1.24	x	x
GC374-5	Viséan	56.713	-1.727	-2200·2300	58	20	1067	1.47	x	12	0.05	20.25	171.6	9.1	86	10.94 (0.20)	1.84	x	x
GC397-5	Rotliegend	56.565	-1.310	-1127	47	20	1316	1.73	x	28	0.00	20.05	235.2	8.3	106	11.12 (0.26)	2.73	x	x
GC397-7	L. Devonian	56.565	-1.310	-1141-1141	48	20	757	1.00	x	16	0.10	7.10	330.2	19.5	109	12.37 (0.20)	2.12	x	x
GC397-11	Silurian	56.565	-1.310	-1256	52	20	583	0.728	x	17	0.12	5.95	276.6	17.7	103	12.34 (0.21)	2.14	x	x
GC397-13	Cretaceous	56.947	-0.227	-792·806	76	20	515	1.11	x	10	0.18	7.09	369.2	26.3	60	12.51 (0.18)	1.43	x	x
GC397-14	Triassic	56.947	-0.227	-811·884	77	20	650	1.88	x	22	0.01	14.63	304.2	25.7	105	12.46 (0.16)	1.68	x	x
GC397-15	Rotliegend	56.947	-0.227	-1371-1400	83	20	640	1.42	x	0	0.41	12.86	252.9	14.0	119	11.93 (0.17)	1.89	x	x
GC397-16	L. Paleozoic	56.947	-0.227	-1381-1414	83	20	466	2.40	x	28	0.00	25.14	245.9	23.6	113	12.46 (0.14)	1.44	x	x
GC397-18	L. Paleozoic	56.947	-0.227	-1829-1920	89	20	455	1.52	x	9.3	0.40	12.66	252.7	16.1	84	12.66 (0.21)	1.95	x	x
GC397-19	L. Paleozoic	56.794	0.233	-1497	57	20	902	1.90	x	15	0.03	17.81	247.4	15.6	104	12.88 (0.17)	1.72	x	x
GC397-21	Devonian	56.713	0.431	-2250·2257	80	20	1864	3.00	x	19	0.00	27.55	246.4	14.9	107	12.63 (0.18)	1.84	x	x

Table 6-3: Geotrack Forth Approaches Basin borehole AFT summary table. a: Number of spontaneous tracks counted, b: spontaneous track density, c: etch pit diameter (Dpar) measurement used as resistance to annealing indicator, d: sample dispersion, e: p-value (0-1) of the chi-squared test age homogeneity test (Galbraith 2005), f: sample average ^{238}U concentration in ppm, g: central age calculated using radial plotter (Vermeesch 2009) with 1σ standard error, h: mean measured horizontal confined track lengths with 1σ standard error, i: standard deviation of mean measured horizontal confined lengths, j: mean c-axis projected horizontal confined track length measurement (Ketcham *et al.* 2007a), k: standard deviation of mean projected horizontal confined track length.

As mentioned above, AFT data from six offshore boreholes (Table 6-3) (Duddy *et al.* 1992) were used to compare the relationship between the thermal histories of the onshore Midland Valley and a neighbouring offshore region in the North Sea, to the east of the Midland Valley. The location of these boreholes is shown in Figure 6-4 and their age depth relationship is plotted alongside the Midland Valley data in Figure 6-5. These data help place the Midland Valley in context with the offshore region and will be discussed later in Chapter 8.

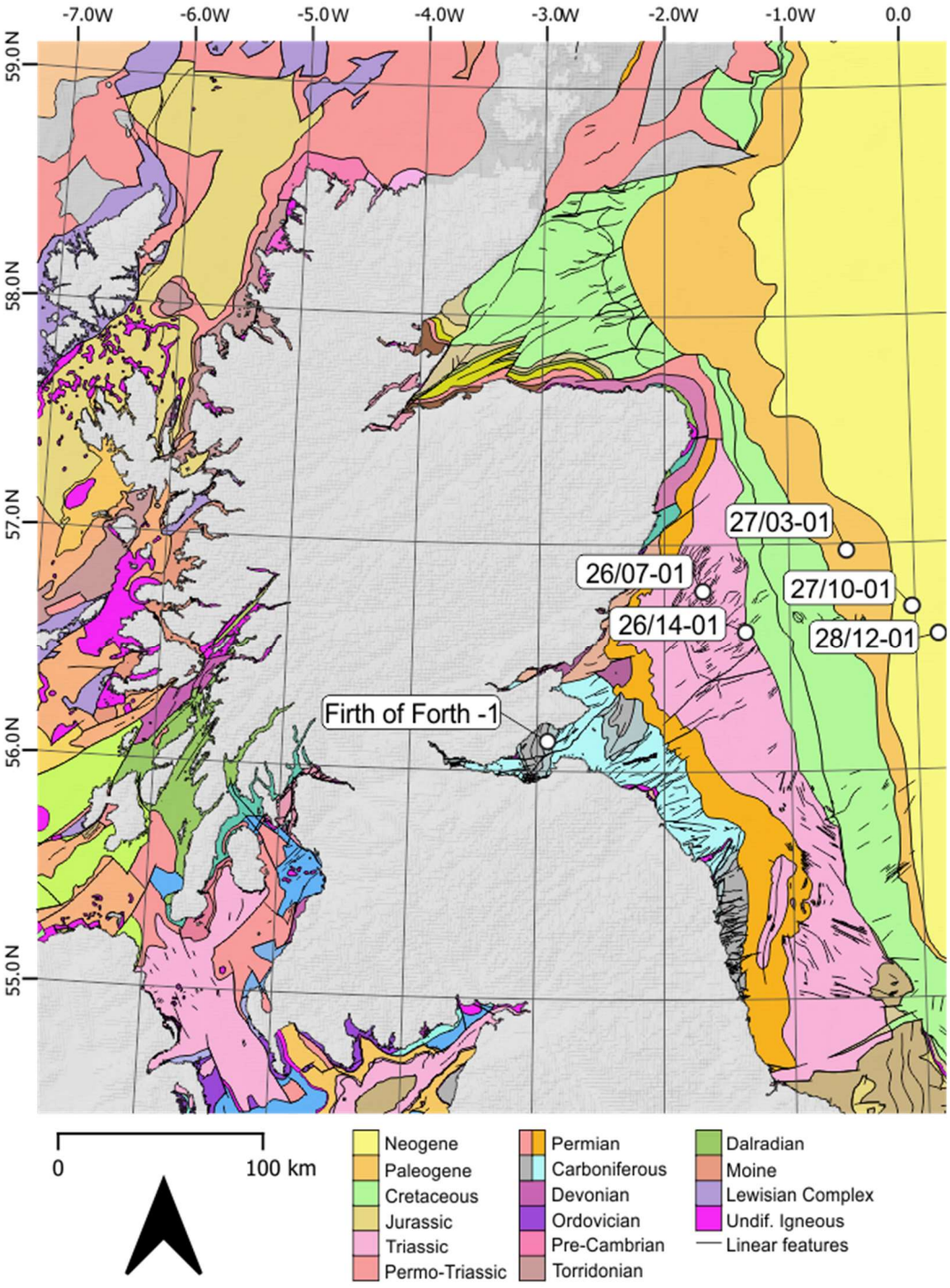

Figure 6-4:Offshore borehole locations. Data produced from these boreholes (Duddy *et al.* 1992) will be used to place the Midland Valley in a regional context later in this thesis.

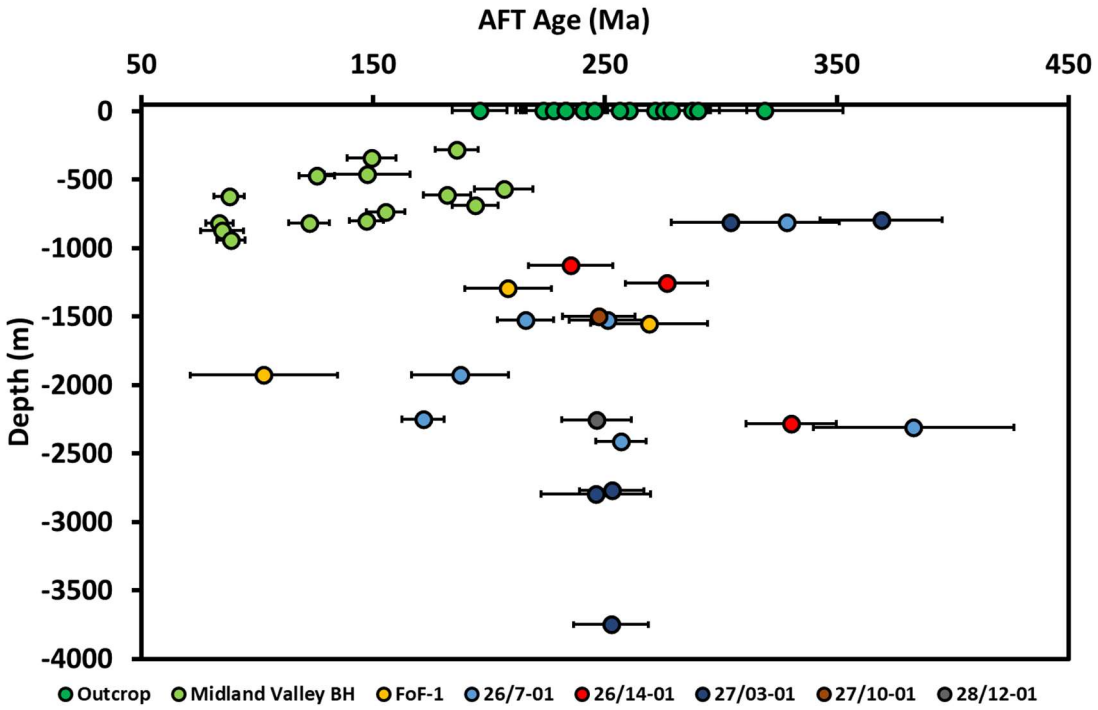

Figure 6-5: Midland Valley and Geotrack offshore well data. Sample AFT central ages and 1σ errors plotted against sample depth (Duddy *et al.* 1992). FoF-1, Firth of Forth-1.

6.2.4 Sample Dpar & ^{238}U concentration

Apatite chemistry, particularly chlorine concentration (Green *et al.* 1985) is believed to influence annealing resistance (Chapter 3 section 3.3.12). Although possible (Chew *et al.* 2014), measuring Cl concentration using a LA-ICP-MS can have large associated uncertainties; for this reason, the methodology was not applied to grains analysed in this investigation, instead the kinematic indicator Dpar was measured and used as an indication of annealing resistance. (Carlson *et al.* 1999; Barbarand *et al.* 2003). A minimum of four Dpar were measured in each grain and the average sample Dpar values (±1SD) range from 1.50 ±0.14-1.92 ±0.49 μm (Figure 6-6). Dpar variation exists between and within samples, evidenced by the large standard deviations (Figure 6-6); however, this is expected, due to the detrital nature of the samples and heterogenous lithological source region. All the sample Dpar values overlap within one SD with the Durango Dpar value range (pink bar in Figure 6-6), suggesting that the apatite analyses for this study are Fluorine rich, similar to the Durango standard used by Ketcham (2007b).

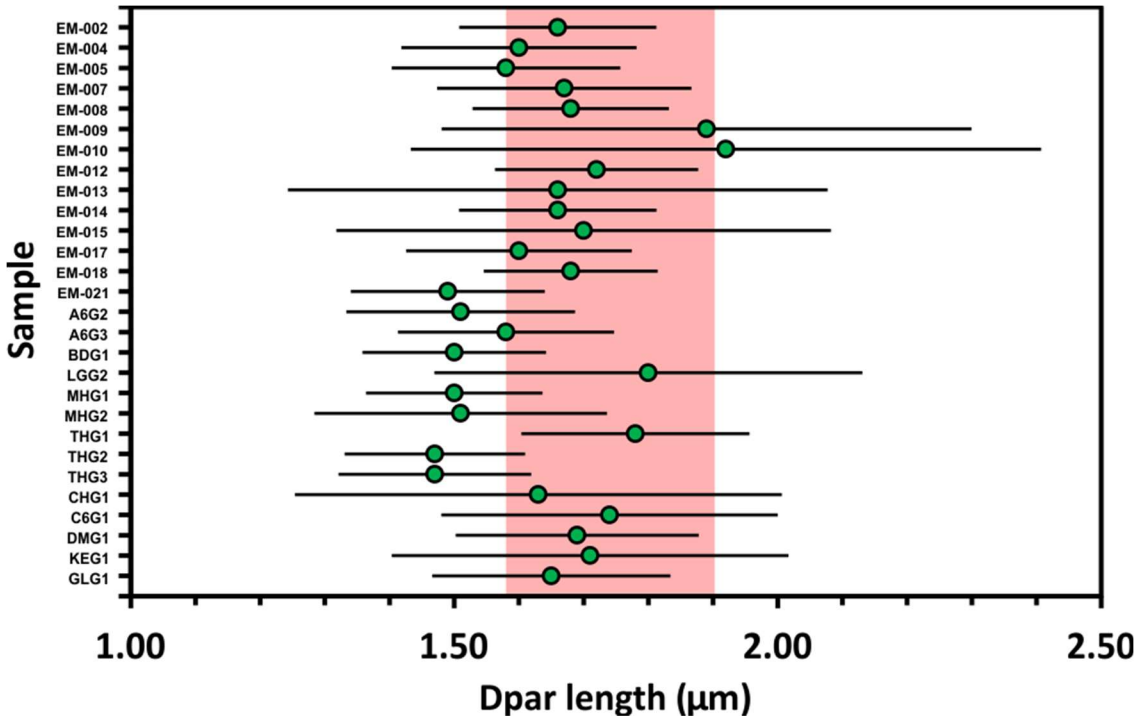

Figure 6-6: Average Dpar (µm) and standard deviation (1SD) for each sample. Pink bar represents average Durango Dpar value 1.75 ±0.17µm.

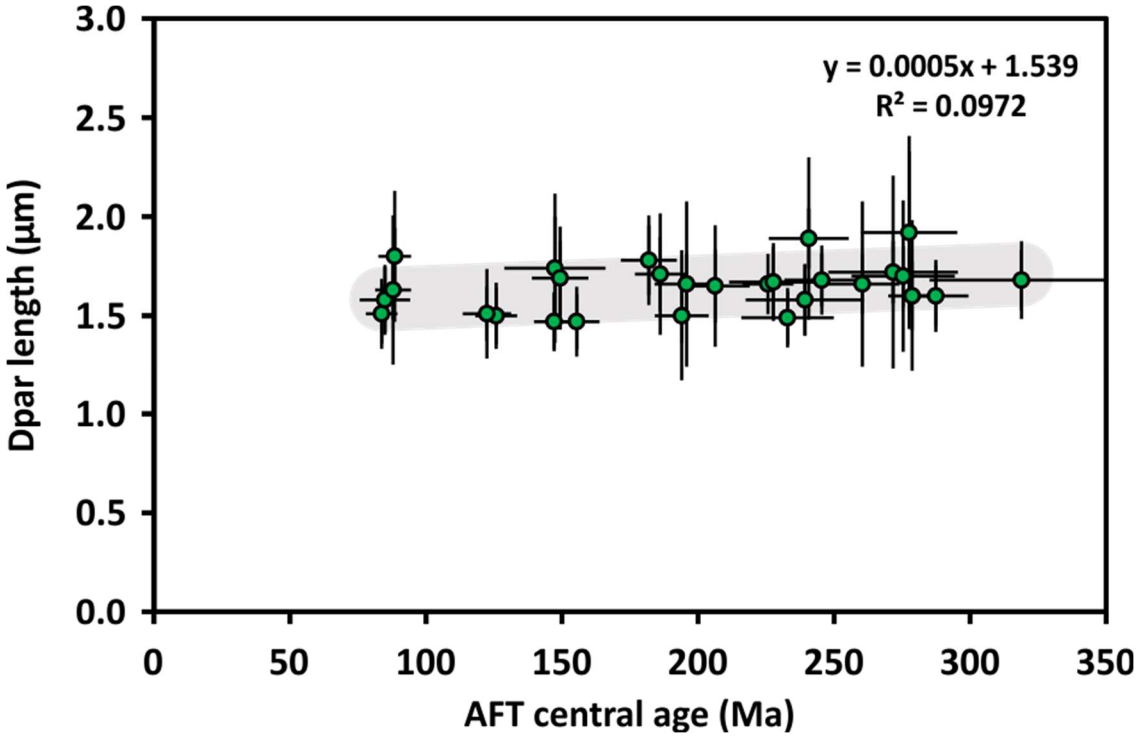

Figure 6-7: AFT central age (±1σ) vs Dpar (±1SD).

Sample Dpar values were plotted against their respective AFT central ages (Figure 6-7) to investigate the relationship between Dpar and annealing. If Dpar is an indicator of annealing resistance, then samples with larger Dpar would be expected to be older, due to their increased annealing resistance. In the Midland Valley, however, Dpar measurements between the samples does not vary greatly (1.50 ±0.15-1.92 ±0.49µm) (Figure 6-7) and therefore no relationship is found, as demonstrated by

the very low value of the R^2 (<0.1). This relationship is investigated further using radial plots in section 6.2.5.1.

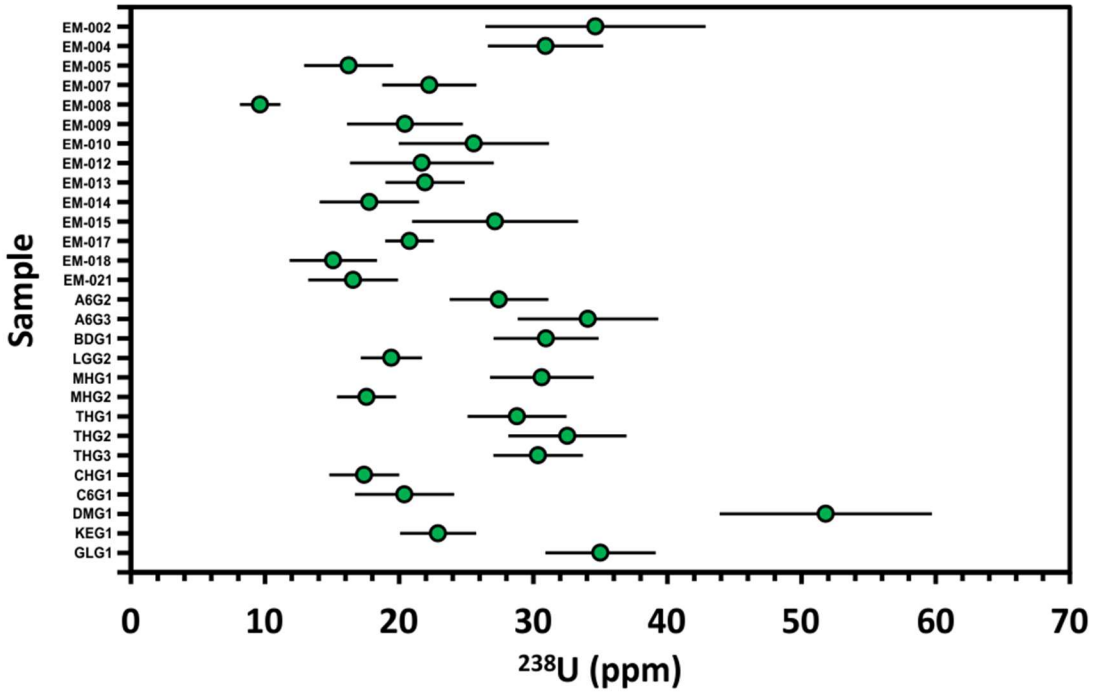

Figure 6-8: Average ^{238}U concentration and 1SD for samples from the Midland Valley.

As well as chlorine, other elemental substitutions have been suggested to exhibit a control on annealing (Barbarand *et al.* 2003) recently some authors have suggested that U concentration exerts some control on annealing, in particular on apatites that have a high concentration of U and/or have been accumulating fission tracks for a long time; this process has been called, radiation enhanced annealing (REA) (Hendriks and Redfield 2005; McDannell *et al.* 2019) and it is explained in Chapter 3 section 3.3.12.5. Samples used in this investigation have average ^{238}U concentrations ranging from 9.54 ±1.51–51.81 ±7.91 ppm (Figure 6-8). ^{238}U concentration, as a proxy for radiation damage, was plotted against AFT central age (Figure 6-7), to investigate whether a relationship between uranium concentration and AFT central age exists. The very low R^2 value (<0.1) clearly indicate that, in the samples analysed for this study, there is no correlation between average sample ^{238}U and AFT central ages. This relationship is investigated for single grain ages using radial plots (section 6.2.5.2).

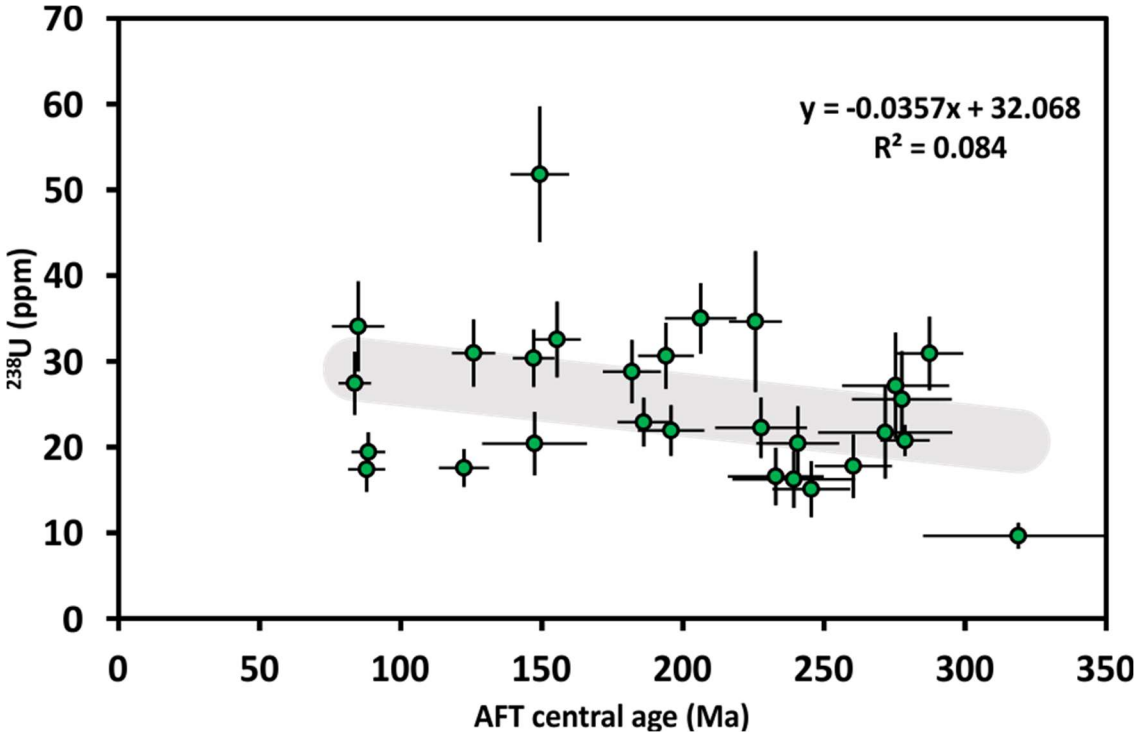

Figure 6-9: AFT central age (±1σ) plotted against ^{238}U (±1SD) concentration in parts per million (ppm).

6.2.5 Radial plots

Single grain apatite fission track ages are represented on radial plots (Chapter 3 Section 3.3.9.1) (Galbraith 1988; Galbraith 1990) using the Radial Plot software version 9.5 (Vermeesch 2009); these diagrams allow for quick examination of the single grain Dpar values (or U concentration in ppm), ages and their uncertainties, along with the sample central age (±1σ), Chi squared p-score ($P(\chi^2)$), and dispersion (%). Dpar values (or U concentration in ppm) of the single grains are identified by the colour scale. Radial plots reporting ^{238}U concentration to investigate REA are also reported with the stratigraphic age of the sample, indicated by the grey bar, allowing for a rapid assessment of the relationship between the single grain AFT ages and their depositional age. The albanico probability plot is also included. This KDE allows to assess whether the dispersion in single grain ages beyond the 2σ level, considered to be the analytical uncertainty, is due to the presence of more than one age component, or to other unknown factors e.g., variations in the apatite chemical composition. Multiple age components are typical of detrital apatites that have not been completely annealed; however, they are often not easy to separate from each other, as components may be discrete, continuous, or a combination of both (Vermeesch 2017). This was further investigated by allowing automatic mixture modelling of the samples to identify if multiple age components were present within a single sample; this procedure is briefly described in Chapter 3.

6.2.5.1 Dpar values on colour scale

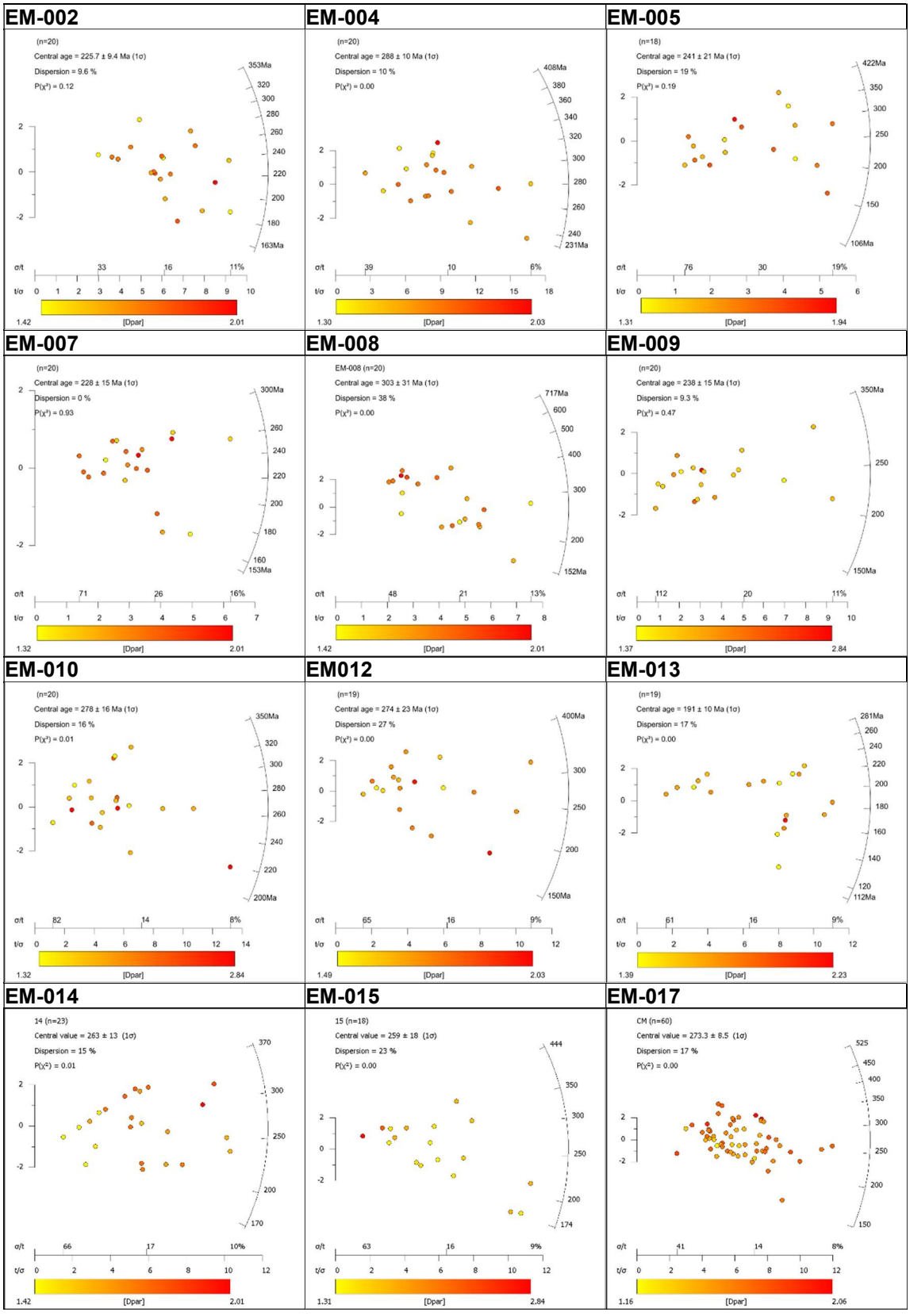

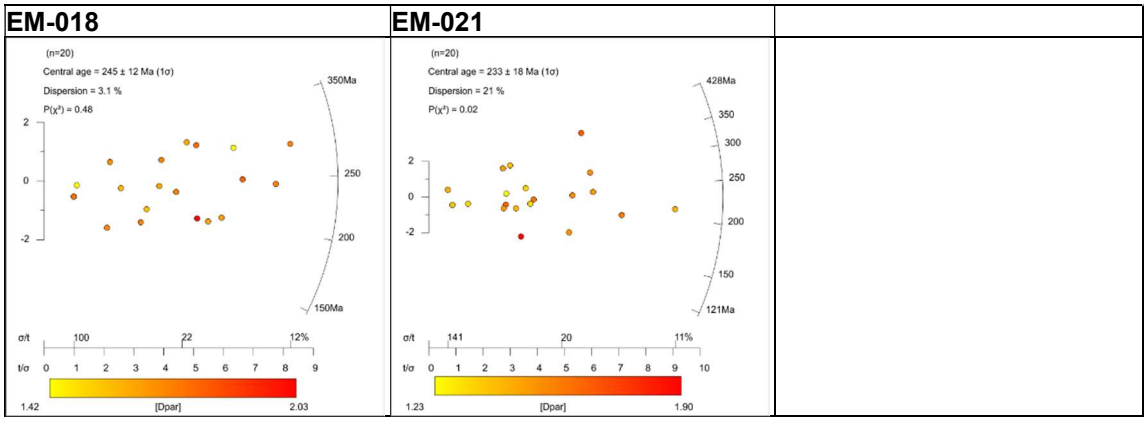

Figure 6-10: Outcrop radial plots (Dpar). The colour spectrum represents the Dpar measurement for each grain measured in µm, note values are relative to each sample. See text for discussion.

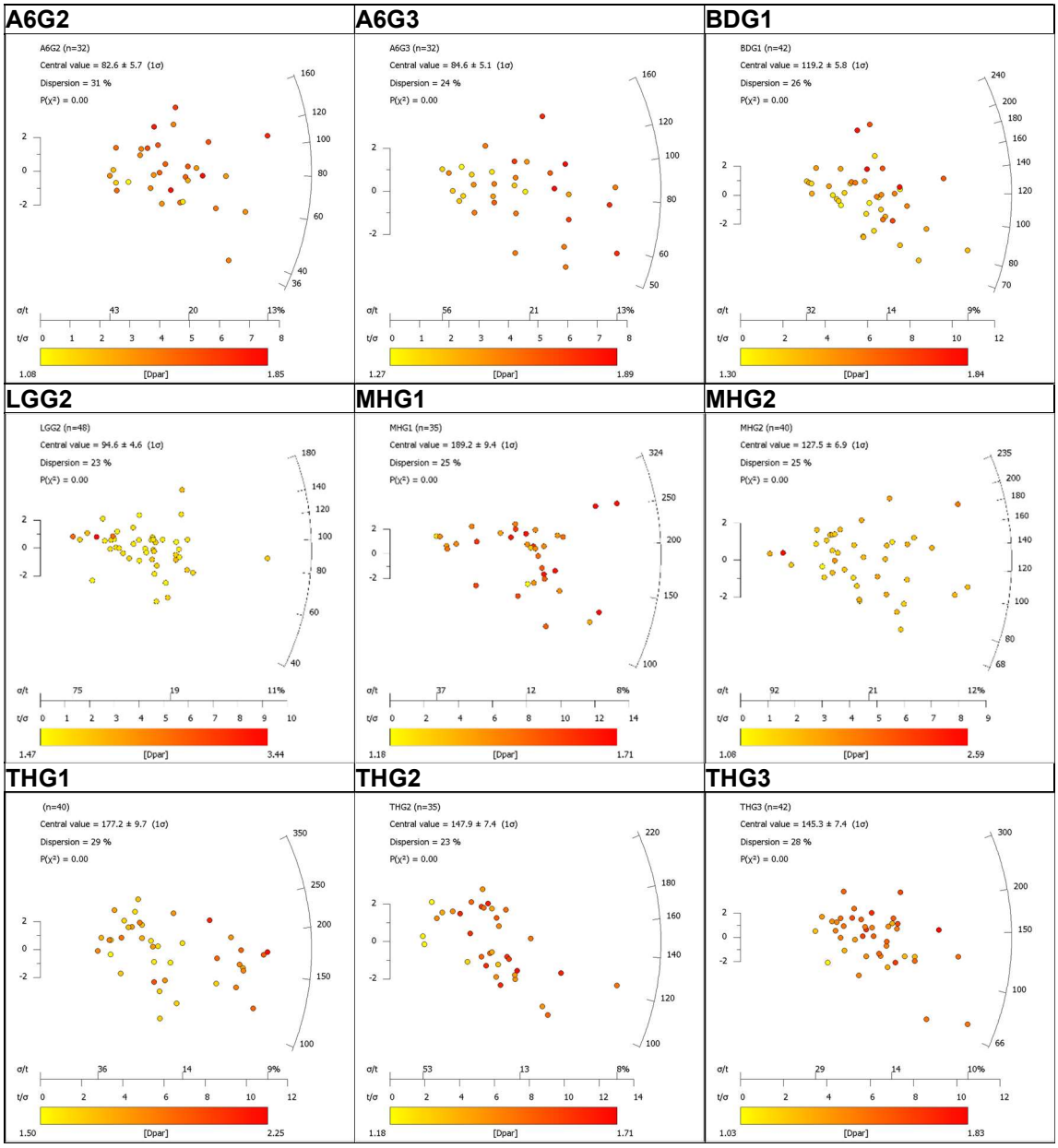

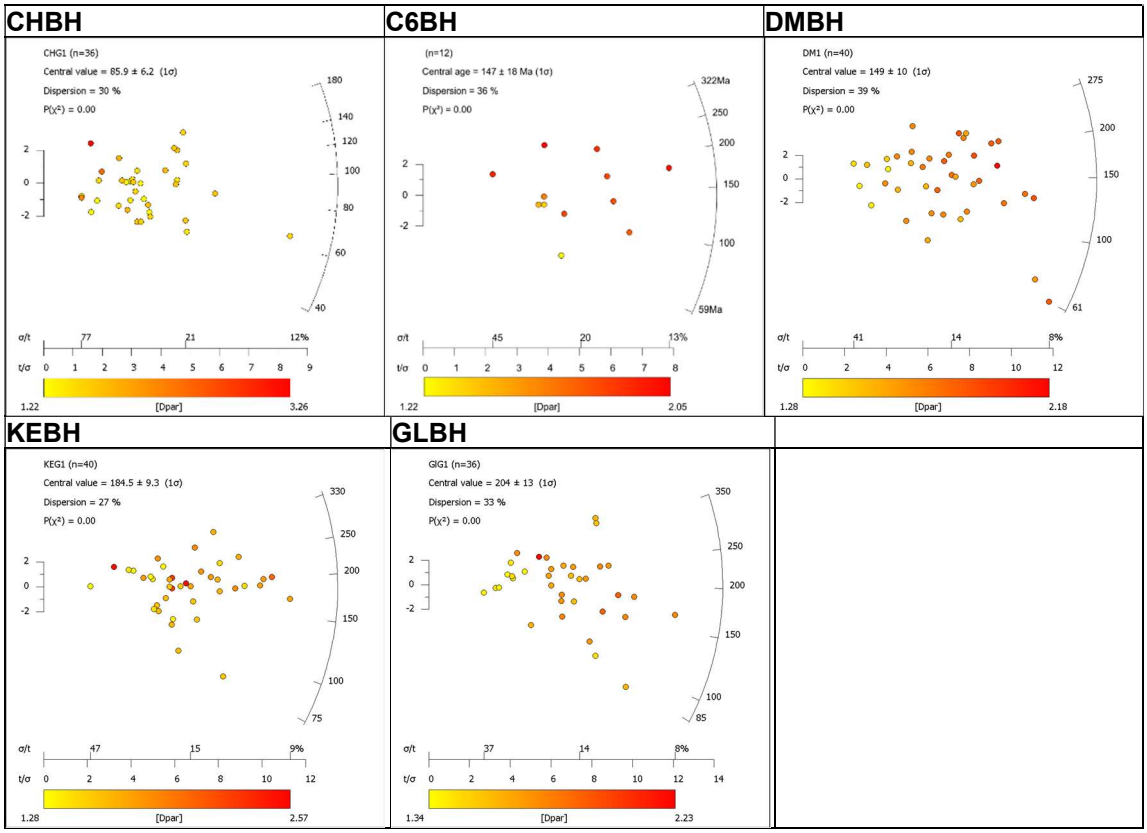

Figure 6-11: Borehole radial plots (Dpar). The colour spectrum represents the Dpar measurement for each grain measured in µm, note values are relative to each sample. See text for discussion.

6.2.5.2 ^{238}U values on colour scale and stratigraphic age

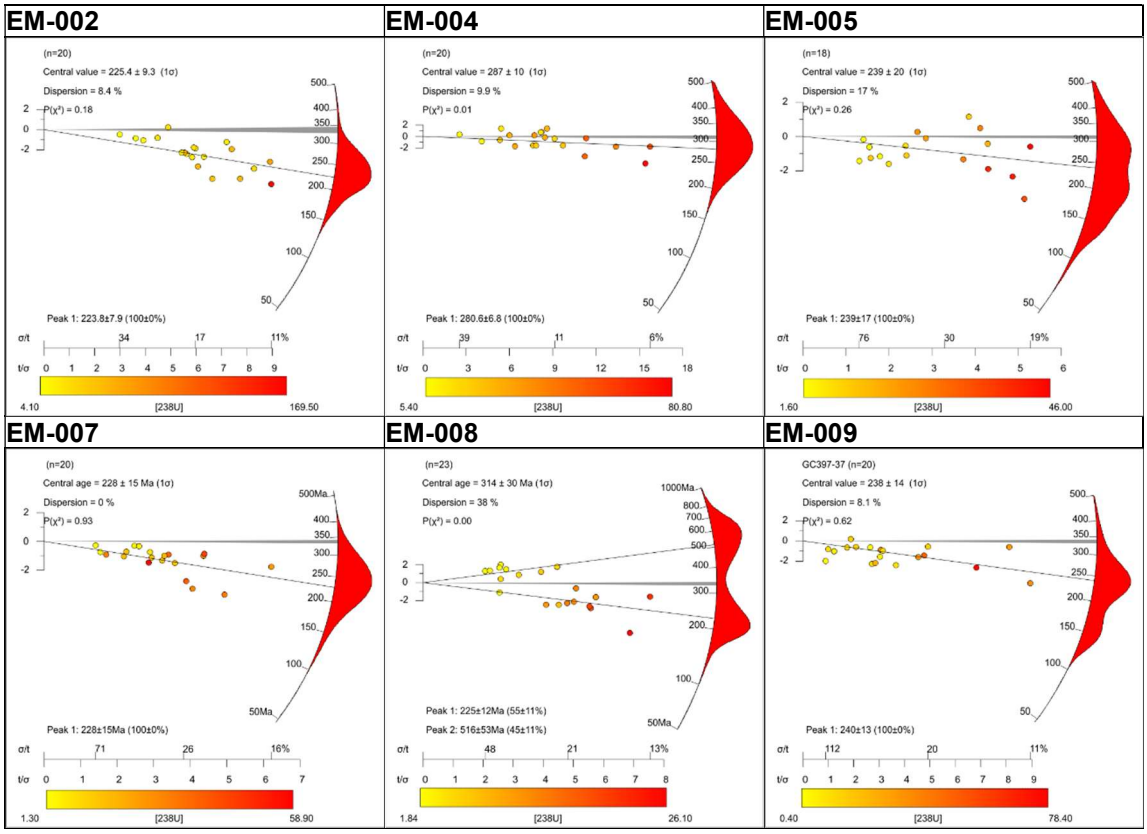

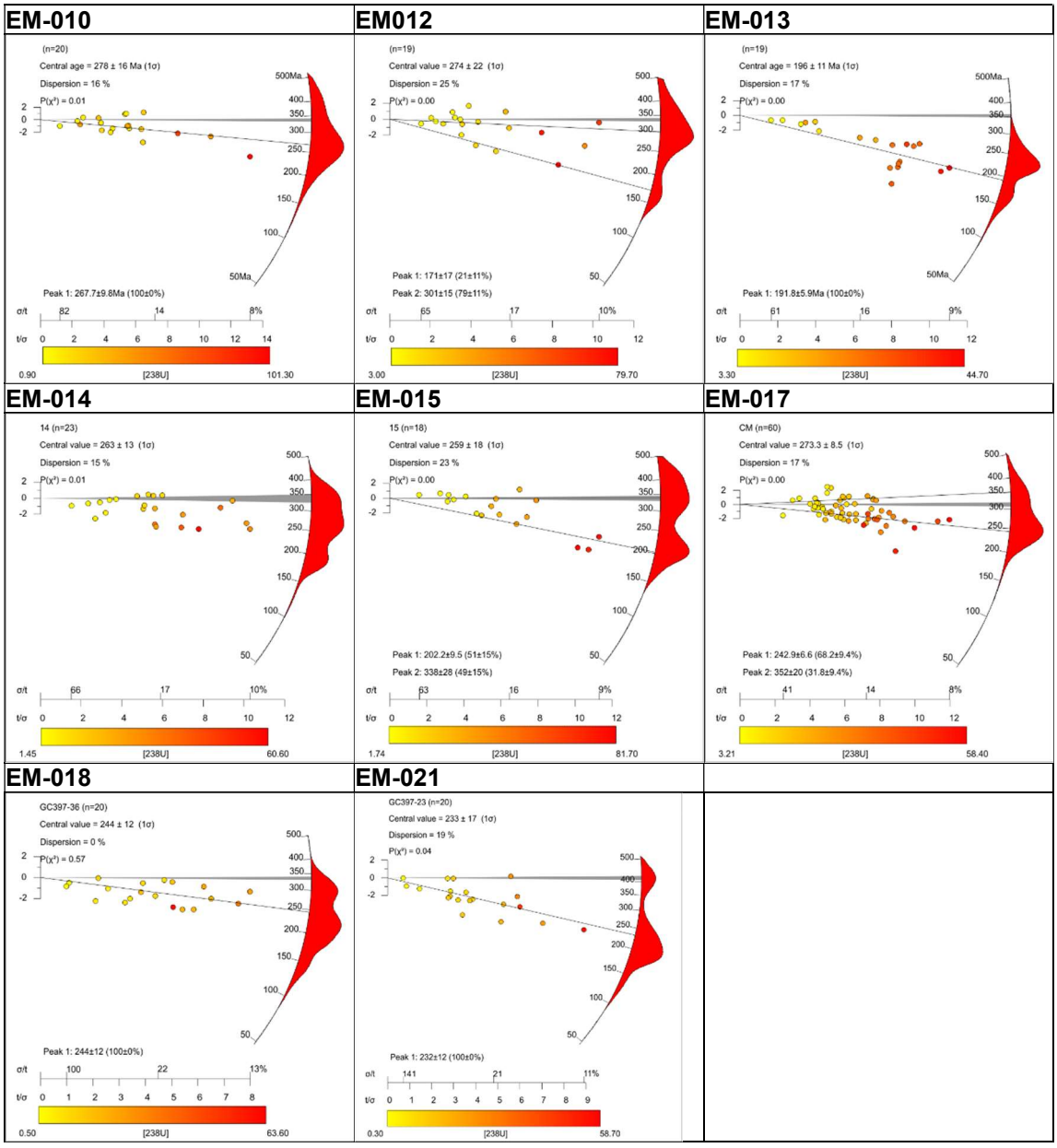

Figure 6-12: Outcrop radial plots (^{238}U). The colour spectrum represents the ^{238}U concentration measurement for each grain, measured in ppm, note values are relative to each sample. The albanico KDE probability plot is also included. See text for discussion.

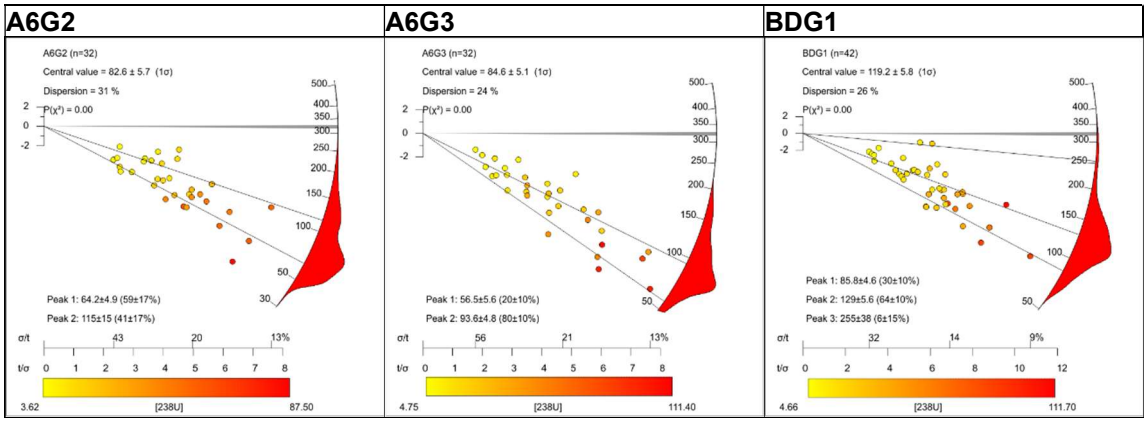

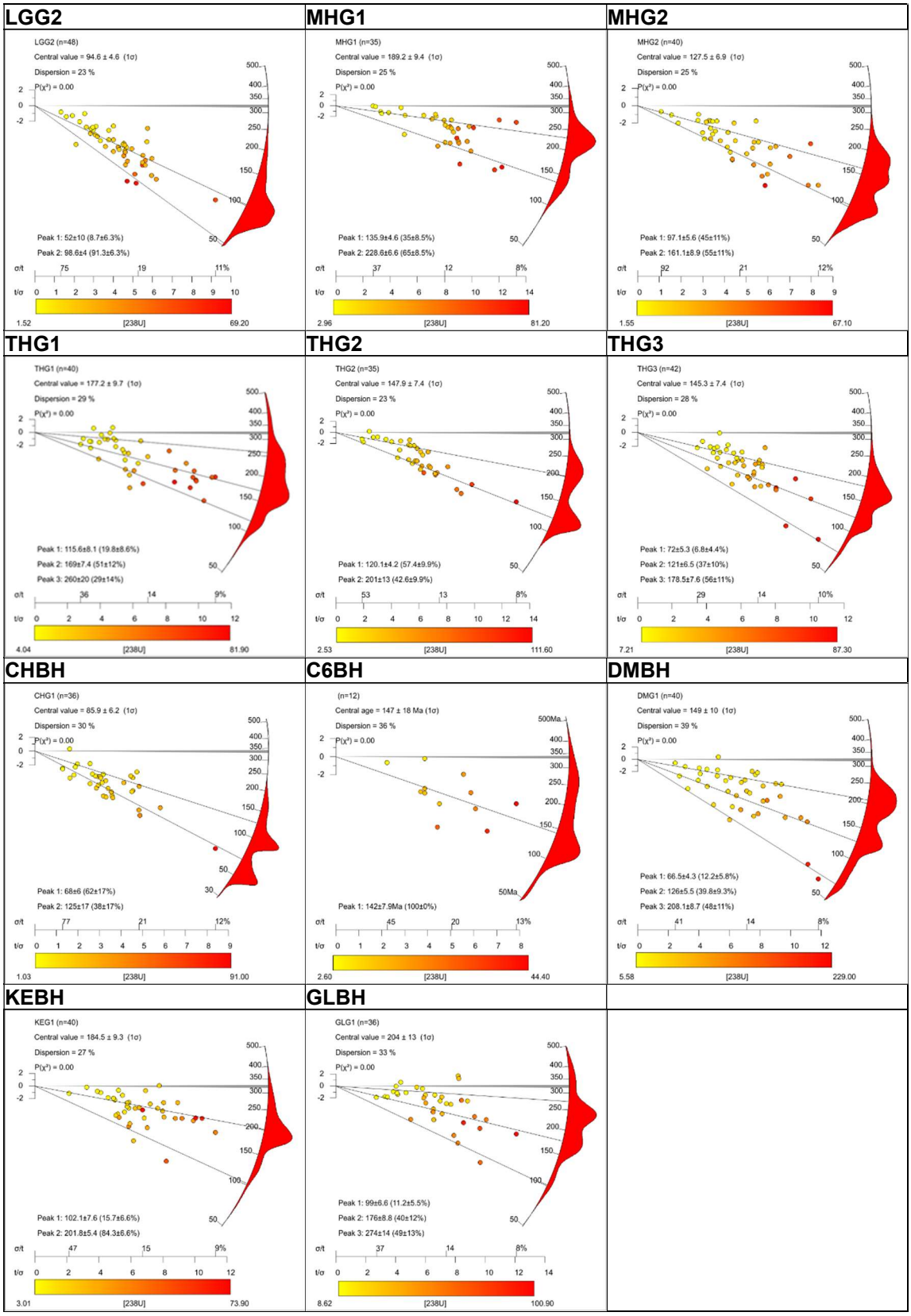

Figure 6-13: Borehole radial plots (^{238}U). The colour spectrum represents the ^{238}U concentration measurement for each grain, measured in ppm, note values are relative to each sample. The albanico KDE probability plot is also included. See text for discussion.

For outcrop samples, the number of single grains counted ranges between 18-60 (EM-05 - EM-17) with no clear relationship between Dpar and age. Single grain age dispersion ranges between <10% (EM-02) to 38% (EM-08) and of these samples, only five pass the χ^2 test. Central ages range

between 191.0 ±10 - 303.0 ±31 Ma (EM-13 - EM-08). Although all central ages are younger than the stratigraphic age, nine samples contain single grain ages that overlap or are older than their depositional age. This suggests that many of the outcrop samples have only been partially annealed by their post-depositional heating. When mixture modelling was applied to investigate the presence of multiple age populations, four outcrop samples indicate that there is the potential for two age populations (EM-08, EM-12, EM-17, and EM-15). however, the two populations cannot be separated clearly, suggesting that the spread in ages may be the result of the continuous spread in single grain ages caused by partially annealing the sample. The two populations in EM-08 fall into two groups defined by their ^{238}U concentration, with relatively low-medium concentration grain having older ages that grains with a higher concentration.

For borehole samples, the number of single grains counted ranges between 12-42 (C6BH – THG3) with no clear relationship between Dpar and age. Single grain age dispersion ranges between 23% to 39% (LGG2 - GLBH) and all of these samples fail the χ^2 test. Central ages range between 82.6 ±5.7 – 204.0 ±13 Ma (A6G3 - GLBH). Although all central ages are younger than their stratigraphic age, four samples contain single grain ages that overlap or are older than their depositional age (THG1, KEBH, GLBH, and DMBH). These samples are from the shallowest boreholes sampled in this thesis and suggests that they may have only been partially annealed by their post-depositional heating; however, it should be noted that no more than four single grain ages older than their stratigraphical age were dated in these samples, possibly indicating almost complete annealing. When mixture modelling was applied to borehole samples to investigate the presence of multiple age populations, all except one sample (C6BH) indicate that there is the potential for more than one age population. No clear divide can be seen within these age populations, suggesting this may be the result of the continuous spread in single grain ages caused by counting an increased number of single grains in these samples (Vermeesch 2019). Finally, it is worth noting that often the youngest single grain ages in many of these samples have the highest ^{238}U concentration, this relationship was highlighter in Chapter 3 and will be discussed later in Chapter 9.

6.3 Track lengths data

With the exception of EM-07, CHBH, C6BH, A6G2 at least 100 confined, horizontal tracks were measured in all samples (Table 6-1 & Table 6-2). Track length distributions (TLD) for each sample are displayed as measured length data and c-axis projected TLDs (Ketcham *et al.* 2007a) (Figure 6-17 & Figure 6-18). C-axis projection of measured track lengths leads to a narrowing of the TLD, reducing the SD, and an increase of the MTL of each sample. Unprojected mean track length measurement ranges between 9.13 ±2.5 and 12.58 ±1.57µm, with c-axis projected mean track lengths ranging between 12.27 ±1.32 and 14.10 ±1.01 µm (Figure 6-14). In general, for each sample, the standard deviation of the mean track length (MTL SD) decreases as the mean track length (MTL) increases, suggesting that, the more the track length distribution is dominated by long tracks, the more unimodal and narrow it becomes.

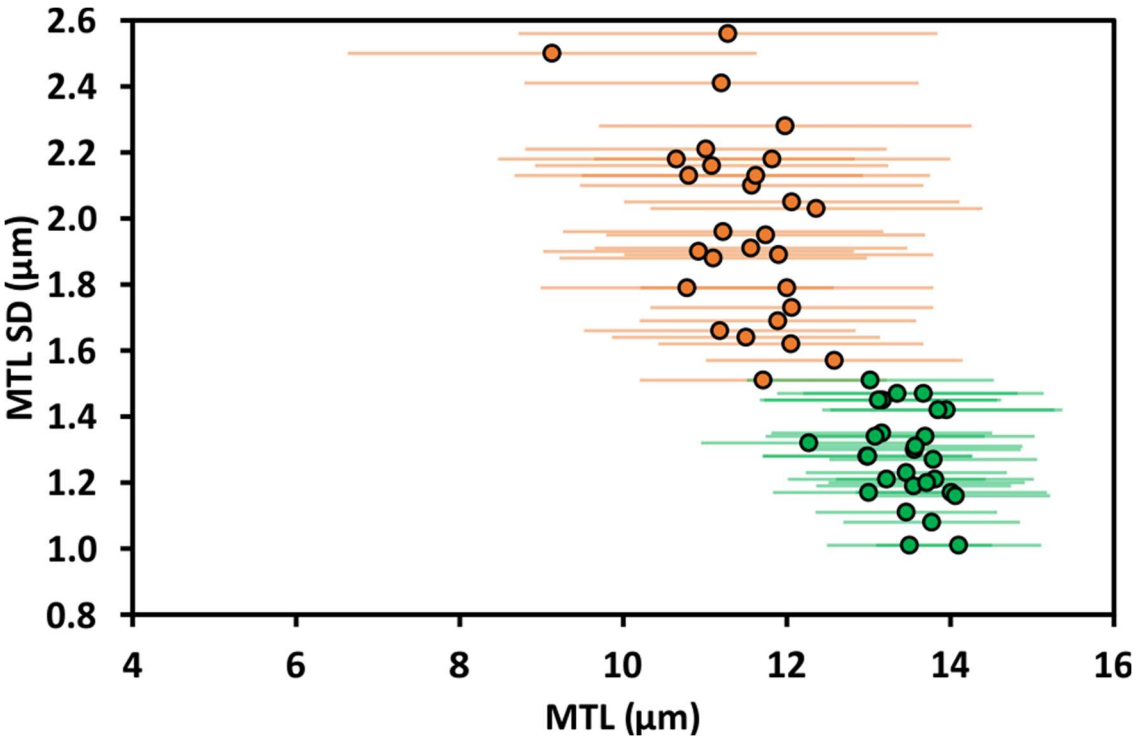

Figure 6-14: Measured mean track length (MTL) (orange) and projected MTL (green). Error bar represents ±1SD (standard deviation of the mean track length).

At the University of Melbourne, confined track lengths (TINTs) were measured as true 3D lengths using FastTracks after irradiation by ^{252}Cf and are corrected for a refractive index of 1.634 for apatite. At the University of Glasgow, confined tracks were measured in a digitising tablet, calibrated using a 1mm graticule, with an accuracy of 0.1µm. At both facilities, only horizontal confined tracks on grains polished parallel to their c-axis were measured to account for anisotropic annealing. Figure 6-15 shows the measured and projected MTL (±1SD) for outcrop sample, while Figure 6-16-- shows the

relationship between MTL (±1SD) and depth of sample; all values of MTL overlap at ±1SD, so they are indistinguishable from each other.

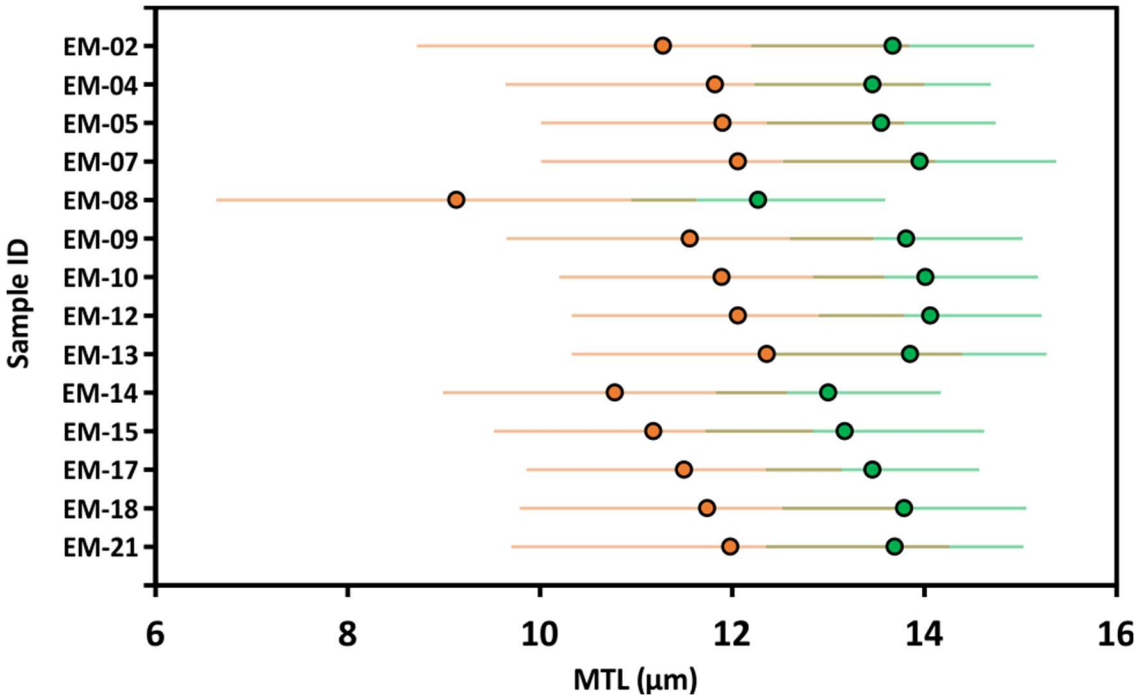

Figure 6-15: Outcrop measured (orange) and projected (green) MTL (±1SD).

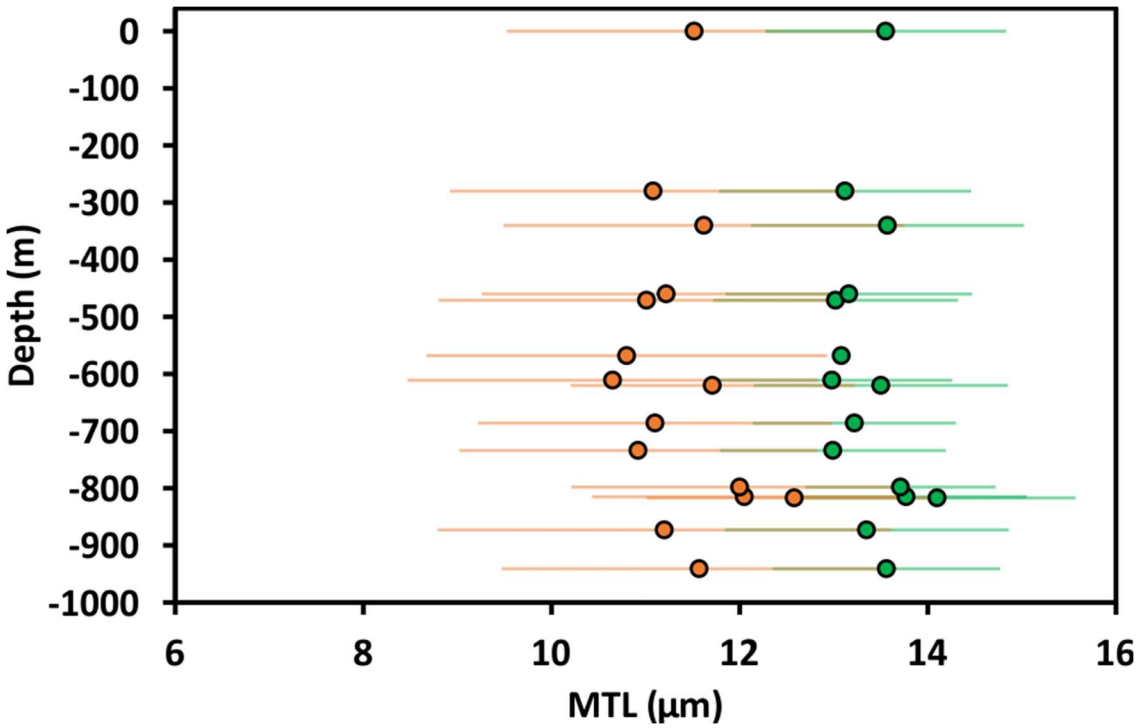

Figure 6-16: MTL(±1SD) vs Depth. Outcrop samples are presented in Figure 6-15 above.

6.3.1 Track length distributions

Outcrop samples (Figure 6-17) are dominated by asymmetrical, wide TLD with a moderate MTL and a tail of short track lengths. A small number of long, relatively unannealed track lengths are present in all samples. Borehole sample TLD (Figure 6-18) are more symmetrical and narrower than those of outcrop samples. Though a range of MTL are observed, they tend to be slightly longer, with a narrower SD, especially at greatest depth. Samples MHG1, THG1, THG2, KEG1 and GLG1 bear a resemblance to a bi-modal distribution, however the peaks are not well separated or defined. As with the outcrop samples, all TLD have a small number of relatively long unannealed track lengths. Unprojected TLD from the offshore samples have a broadly asymmetrical shape, with moderate MTL and a tail skewed towards shorter track lengths.

6.3.2 AFT Central age vs Mean Track Length

AFT age vs MTL plots, in a region that have experienced a broadly coeval thermal history with more than one thermal event, will form a concave up pattern, known as a 'boomerang plot' (Green 1986; Gallagher *et al.* 1998). The boomerang trend is defined by old AFT ages with relatively long MTL's, intermediate ages with the shortest MTL's, and young ages with relatively long MTL's. Old AFT ages with relatively long MTL's correspond to samples that have spent most of their thermal history above the PAZ and reflect cooling from the lowest maximum paleotemperatures. Intermediate ages with the shortest MTL's and large SD, correspond to samples that have spent most time within the PAZ and reflect a mixture of pre and post cooling track accumulation, with their latest cooling period occurring at a similar time to the youngest samples. Young samples should have the longest MTL's and small SD, as they have spent the least amount of time within the PAZ and reflect the rapid cooling from maximum paleotemperature in excess of 110 °C. AFT age vs MTL plots for the data in this study (Figure 6-19), display a partial boomerang style plot. AFT ages older than 225 Ma have generally long MTL's, >c.11.5 µm, whereas intermediate AFT ages, between 100-225Ma, have shorter MTL's (10.5-11.5 µm) and large SD. AFT ages younger than 100 Ma do have increased MTL's (>11 µm) and small SD, though there are few samples from this range. The relationship between the samples and their observed data will be discussed in greater detail in Chapter 8. The data from this investigation have been combined with previously published data from sedimentary and basement rocks from the rest of Scotland (Figure 6-20). This plot has aspects that resemble the boomerang trend in the sense that samples with long MTL's yield the youngest ages, suggesting that

the most recent rapid cooling event in Scotland occurred at around 60 Ma and affected the areas from which the samples with the longest and shortest mean track length were collected.

6.3.2.1 Outcrop

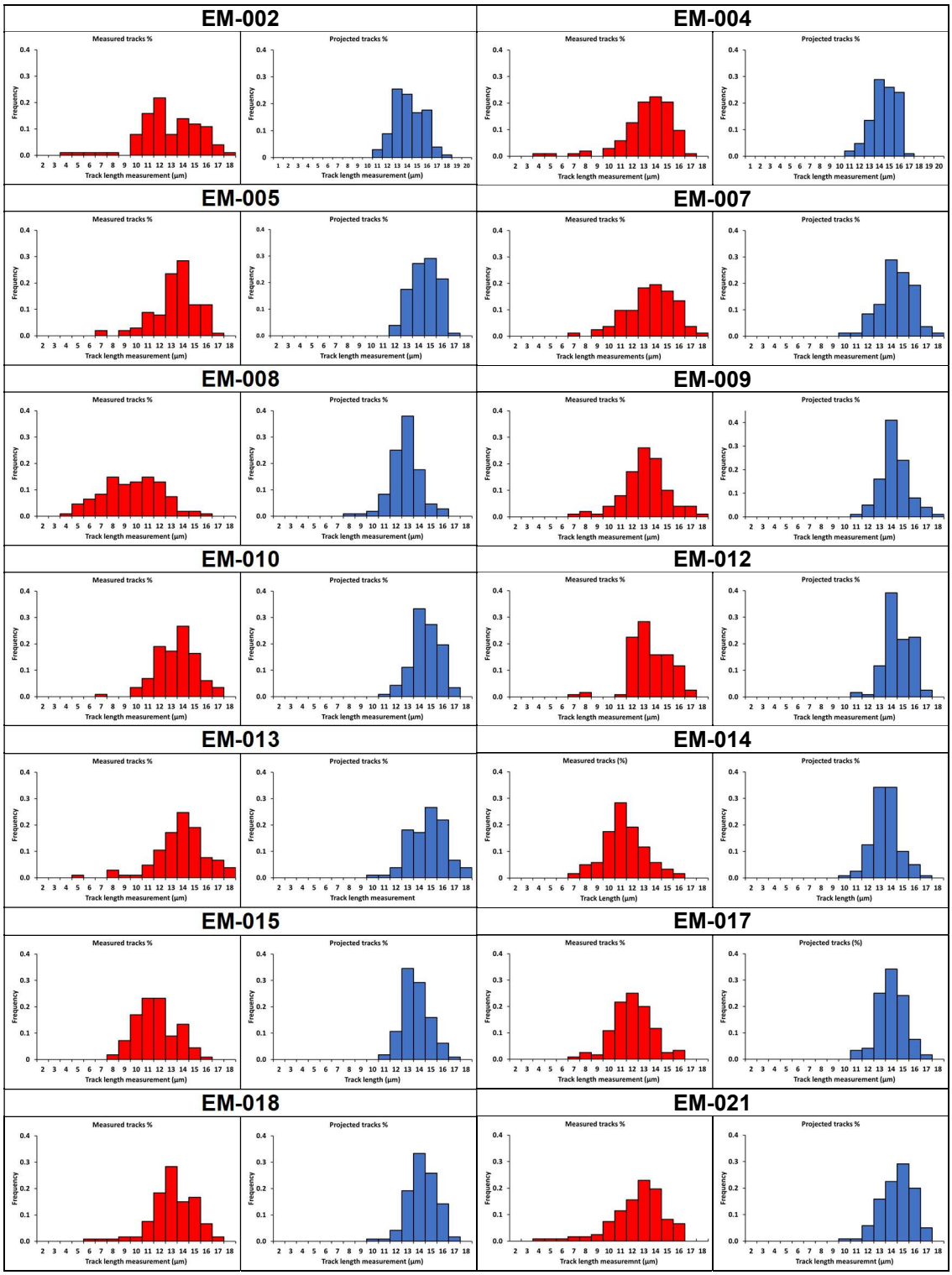

Figure 6-17: Track length distributions for outcrop samples. Measured (red) and c-axis orientation projected (blue) track length distributions for each sample.

6.3.2.2 Borehole

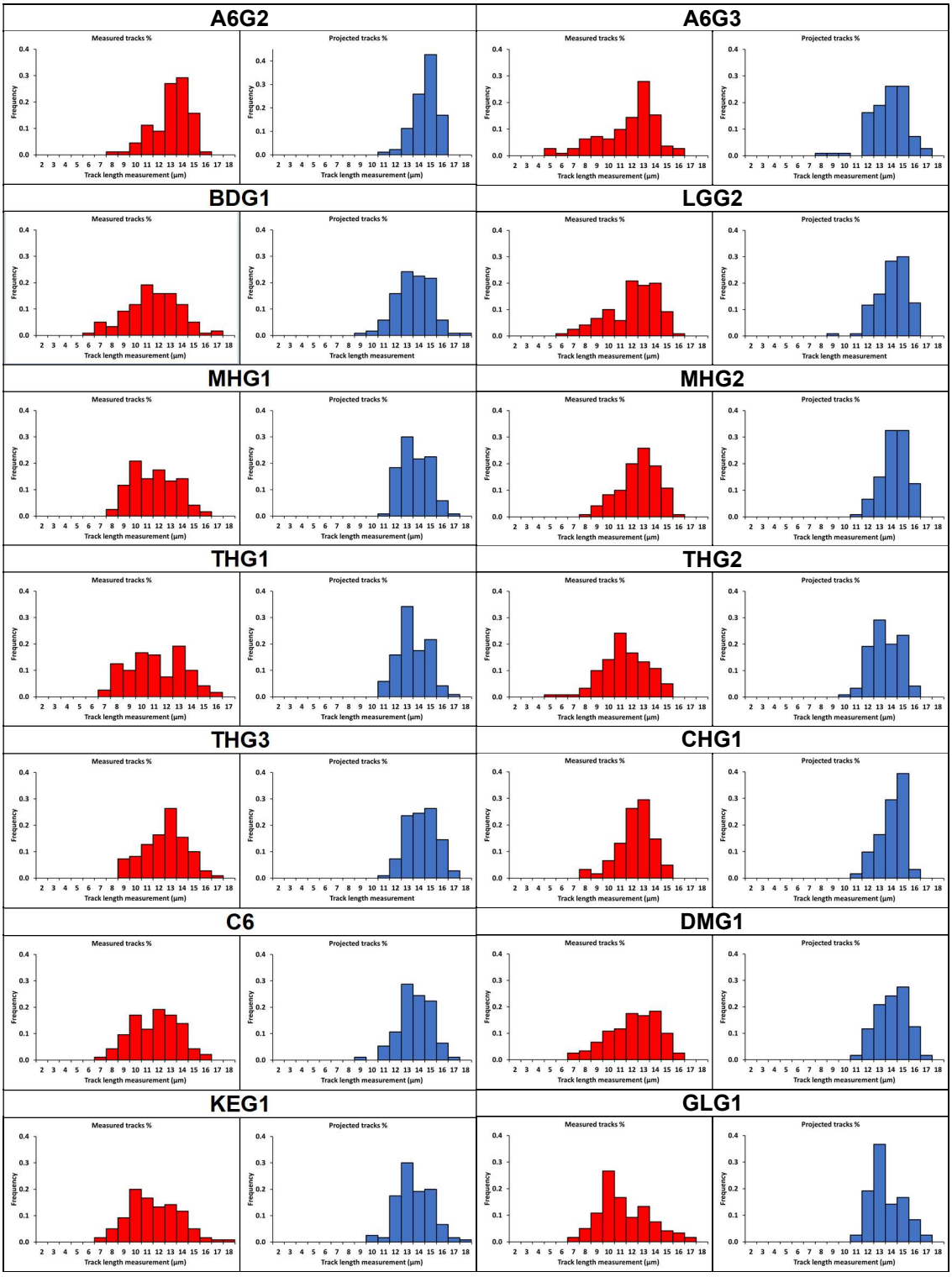

Figure 6-18: Track length distributions for borehole samples. Measured (red) and c-axis orientation projected (blue) track length distributions for each sample.

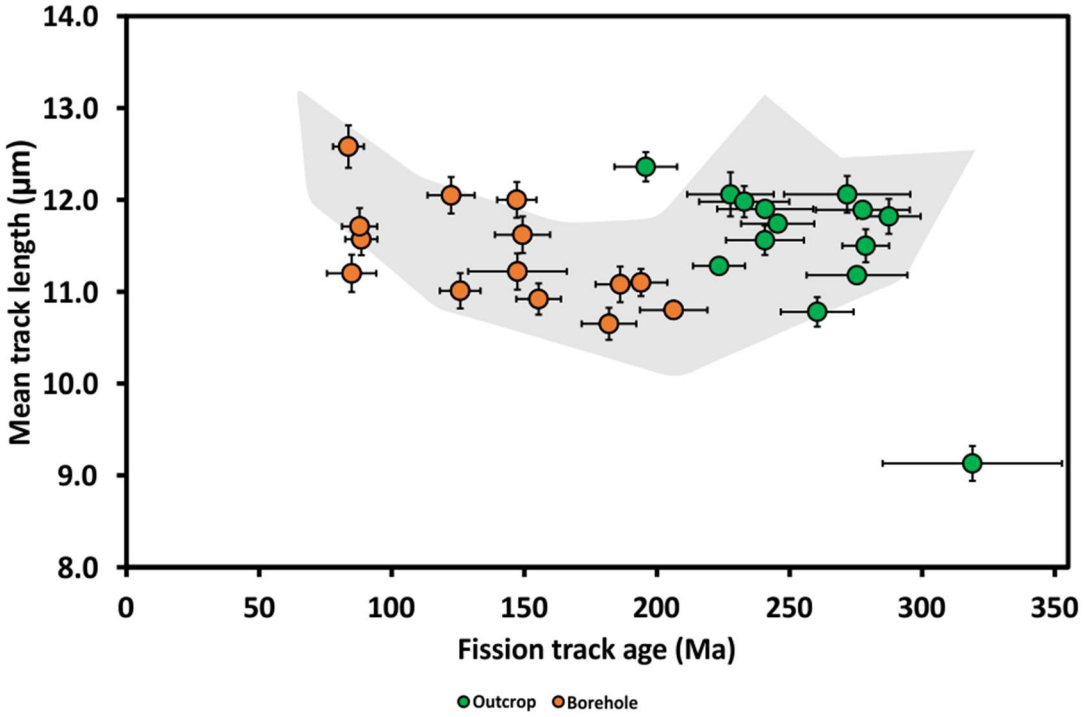

Figure 6-19: AFT age vs MTL's for data in this investigation. MTL's have not be corrected for their c-axis orientation (to make them comparable with the published data) and error bars represent 1SD for the MTL and the 1σ AFT central age.

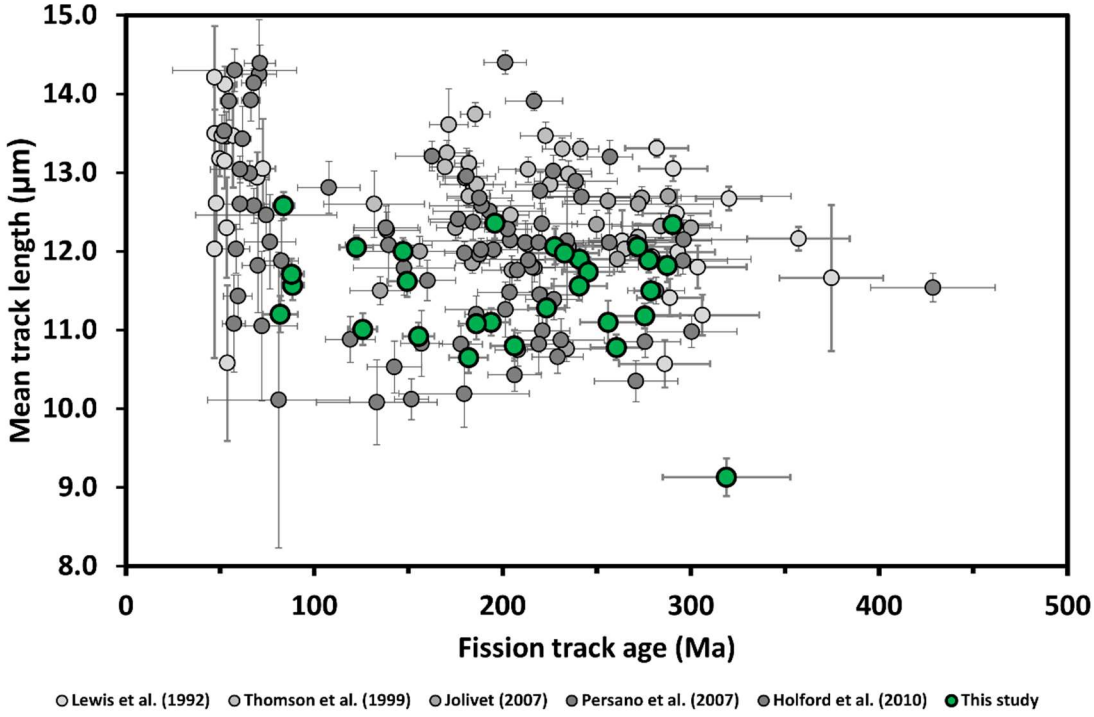

Figure 6-20: AFT central ages vs MTL's for data collected across all of Scotland. Both basement outcrop and sedimentary outcrop are included in this plot. Uncertainty of AFT central ages is at the 1σ level while uncertainty for length data varies between 1SD and 1SE depending on analyst.

6.4 Summary of AFT data

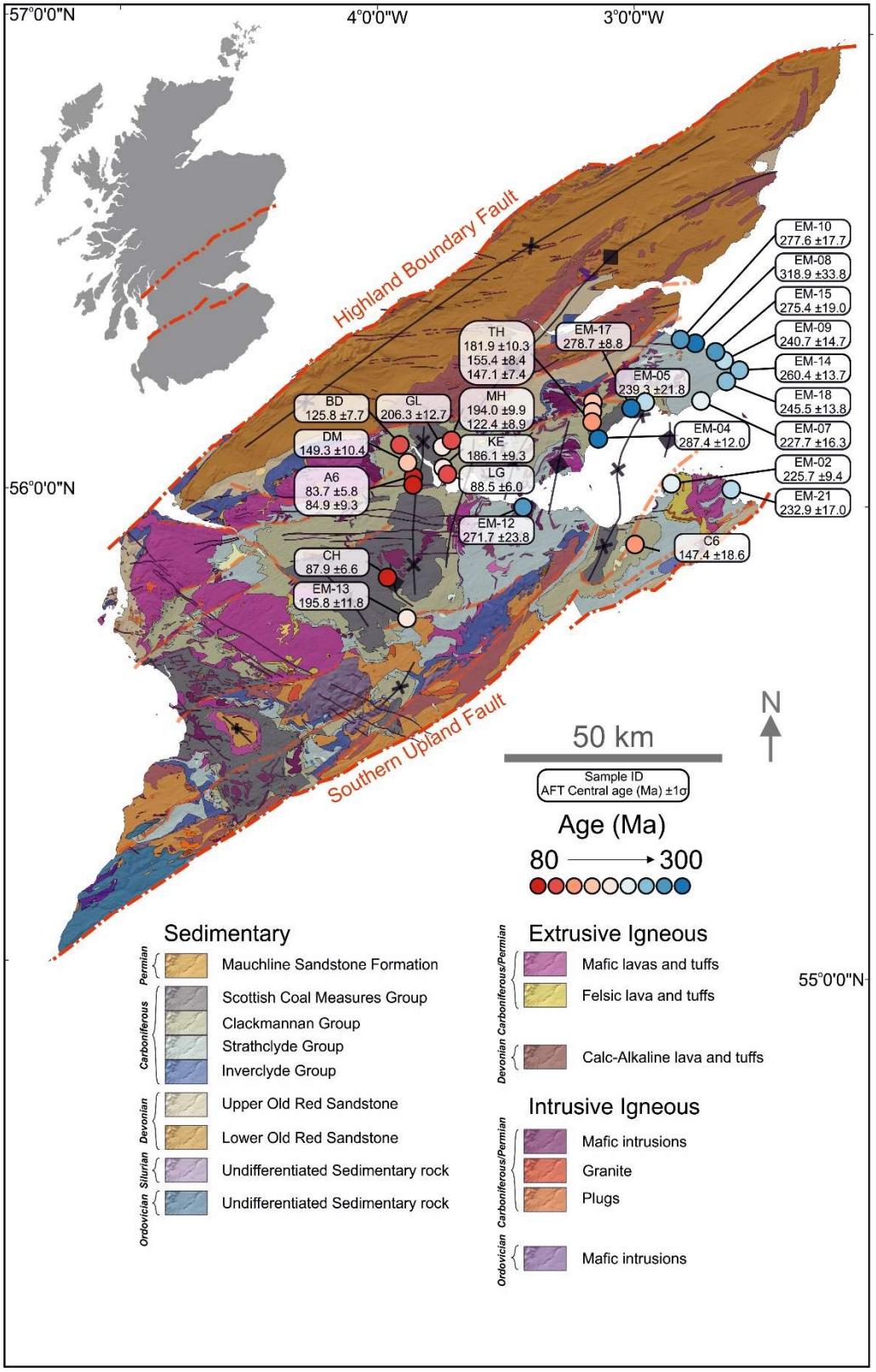

Figure 6-21: AFT data across the Midland Valley. The distribution of the AFT central ages across the region reflects its geological structure; the oldest, (>225 Ma) ages are found in Viséan samples in Fife, suggesting that post-Viséan deposition was never deep enough to reset the fission track ages, in agreement with the fact that no post Viséan outcrop occur at present. Conversely, the AFT central ages of Westphalian samples in the core of the Midlothian-Leven syncline, are all post depositional, suggesting complete reset. Drilled borehole samples are Namurian in age and their FT central ages are all younger that the outcrop ages and they display a younging with increasing depth.

AFT central ages for samples from Carboniferous sedimentary rocks from the Midland Valley of Scotland are younger than their stratigraphical age; however, a few single grains ages from some outcrops and shallow borehole samples are older or synchronous to the depositional age. This observation suggests that post burial heating of the samples occurred, though it may not have been of a magnitude for all samples to reach the total annealing zone, thus leaving some inherited AFT data in the sample. The possibility of inheritance of AFT data from the pre-burial history and its influence on the post-depositional thermal histories is investigated in the modelling section of this thesis. Radials plots show that Dpar or radiation damage, assessed through the determination of ^{238}U concentrations do not exert a primary control on the observed AFT ages, although often the youngest single grain ages in each sample has the highest ^{238}U concentration. A relationship of a similar nature was identified by Hendriks and Redfield (2005) and McDannell *et al.* (2019), who suggested that radiation enhanced annealing may be the reason why, in any FT age determination reported in the literature, old single grain ages are never associated with a high ^{238}U concentration. Although worth exploring further, it is also worth noting that high ^{238}U content increases the track density, potentially to a point where the sample is uncountable with an optical microscope; the bias, therefore, would reside with the analyst, simply not able to count with confidence the fission tracks in old, U-rich apatites. This issue has been identified in zircon fission track (ZFT) dating, where such high track density grains are counted on a scanning electron microscope (SEM), but it has never been attempted for apatite.

Sample dispersion ranges from 0-39% and most samples fail the Chi-squared test, suggesting that there is significant evidence to reject the common (pooled) age model (Galbraith 2005). However, inspection of the radial plots does not give a clear indication that discrete, multiple age populations are present within each sample. It is possible that there is a continuous mixture of ages through the sample caused by a range in chemical compositions and fission track inheritance from their pre-burial history the effects of which has been exaggerated by protracted cooling through the PAZ; this continuous spread in single grain ages may also be a result of counting large numbers of single grains per sample, much larger than usually done (Vermeesch 2019). The nature of the single grain age distributions indicates that the central age and its error are a good fit for the representation of the data in each sample and will be used in the modelling section of this thesis. The relationship between AFT central age and MTL in the boomerang plots (Figure 6-19 & Figure 6-20) indicates that heating of the samples occurred following burial in the Carboniferous. This heating was elevated

enough to reset outcrop central ages to post depositional ages and cause a reduction in MTL. Borehole samples experienced further elevated temperatures and they remained within or below PAZ until final cooling of the samples in the Cenozoic. Spatial and temporal variation of the heating and cooling across the basin and the number of episodes will be investigated using the Bayesian trans-dimensional approach, for individual samples and multi-sample profile modelling using the QTQt software as discussed in Chapter 3 section 3.4 (Gallagher 2012).

Chapter 7 AFT thermal histories

Thermal history models were constructed using the Bayesian Trans-dimensional Markov Chain Monte Carlo (MCMC) approach within the QTQt software (version 5.7.) (Gallagher 2012). The general theory behind this approach has been outlined in Chapter 3 section3.4.1. The software was applied in both forward and inverse modes. Forward modelling has been utilized to predict and generate synthetic AFT data for existing scenarios of the Midland Valley post-burial history (Chapter 1 section 1.3.3); the forward model generated data were then used in inversed mode to test the ability of QTQt to reproduce the same histories as those input in the forward model. This assesses the capacity of QTQt to investigate time-temperature space and identify all the possible thermal histories that fit the data, thus providing valuable insight on the robustness of the inverse modelling process performed by QTQt using the observed data. Secondly, the AFT data generated in this study were inverse modelled using the multi-kinetic fission track annealing model of Ketcham et al. (2007a), to produce time-temperature histories for samples across the Midland Valley.

7.1 Forward thermal history modelling

7.1.1 Approach

Highlighted in Chapter 1 section 1.3.3, several burial history models created for boreholes located within the Midland Valley exist. This section focuses on two such models (Duddy *et al.* 1992; Vincent *et al.* 2010) that show conflicting burial histories. Duddy et al. (1992) used VR data collected from drill cuttings from the Firth of Forth 1 borehole (Figure 7-1a) to create the burial history model seen in Figure 7-1b. Three AFT determinations accompany the VR data, with central ages calculated using only six, five and two single grain ages per sample; the number of track length is also low (43, 66, & 10 confined lengths respectively). It is not indicated how influential these AFT data were to produce the proposed burial history model. Vincent *et al.* (2010) used two modelling programmes on a selection of boreholes in the Midlothian-Leven syncline in the east of the Midland Valley to construct basin subsidence and thermal history models. One of these models, BasinMod, used stratigraphical and VR maturity data from three boreholes (Eskmouth, Firth of Forth Tower 1, and Milton of Balgonie 1) to reconstruct their individual burial histories. All three of the boreholes produced broadly similar results; the VR data for the Eskmouth borehole can be seen in Figure 7-1c, along with the resulting burial history model (Figure 7-1d).

The burial history models produced (Figure 7-1b & d) show conflicting predictions of the time, temperature, and burial evolution of the Midland Valley. Duddy et al (1992) suggest rapid burial and heating through the Carboniferous, with maximum paleo-temperatures reached just prior to the Permian. Following this, uplift and cooling continued at a steady rate through the Mesozoic until the end of the Paleogene, when recent sediments were deposited. The Vincent et al (2010) model also suggests rapid burial and heating for Carboniferous sediments, however, this was followed by uplift-driven rapid cooling during the late Carboniferous-early Permian, in association with the Variscan orogeny. This was followed by continuous burial and heating during the remaining Permian and throughout the Mesozoic, based on sedimentary unit compaction and the assumption that as deposits of this age are present offshore and in some nearby onshore localities they were also deposited at the well locations. In this model, maximum paleo-temperatures were reached during the Paleogene, just prior to rapid uplift and cooling in association with the emplacement of the proto-Icelandic plume (White 1988; Vincent *et al.* 2010).

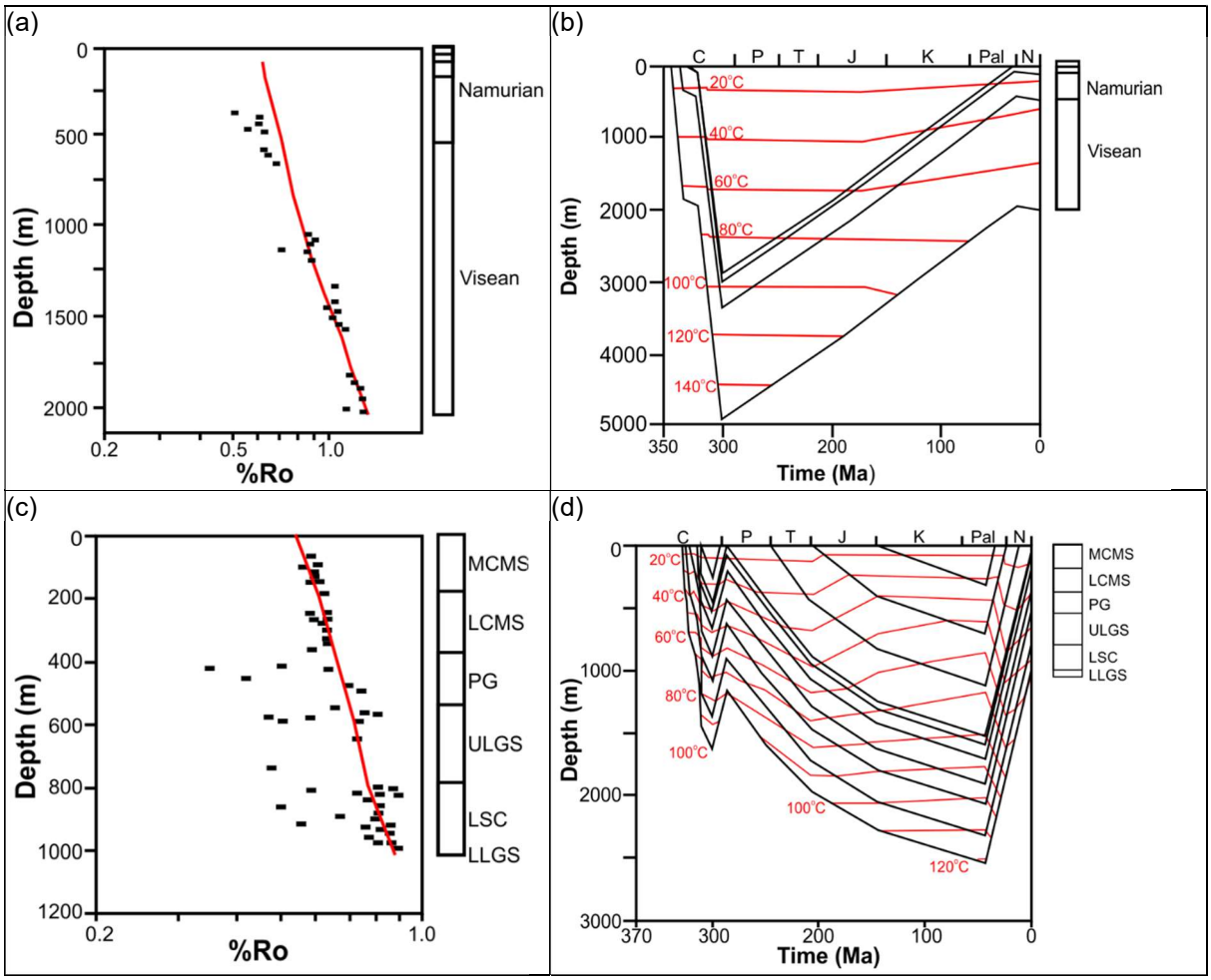

Figure 7-1: Existing burial history models for the Midland Valley. VR units displayed as %Ro. (a & b) VR data from and corresponding burial history from Duddy *et al.* (1992), (c &d) VR data and corresponding burial history from Vincent *et al.* (2010).

Time-temperature paths derived from these models were produced for specific horizons using the forward modelling function of QTQt. The forward modelling exercise generates synthetic observed AFT data (single grain ages, central age, and confined track length distributions – hereafter called 'synthetic observed AFT data') that are consistent with the input thermal histories. As the majority of borehole data produced in this study were derived from the Limestone Coal Formation and nearby outcrop samples e.g., the Scottish Coal Measures, the time-temperature paths tested in the forward models are from these stratigraphic levels. The forward models create synthetic AFT data for each of the two burial history scenarios which can be directly compared to the observed data from this study. The synthetic observed data was then inverse modelled to test QTQt's ability to reproduce the thermal histories initially input in the forward model.

7.1.2 Results

Results of the forward models, synthetic AFT data, and inverse modelling can be seen in Figure 7-2, Figure 7-3, Figure 7-4, & Figure 7-5 below. The synthetic observed AFT data for each sample contain 20 AFT single grain ages, the sample dispersion (%), χ^2 value, and the sample central age (1σ uncertainty), plotted on a radial plot, along with 100 confined track lengths forming the track length distribution (TLD) and mean track length (MTL) (see figures below for individual sample details). In both Duddy et al. (1992) and Vincent et al. (2010) scenarios, the synthetic central ages for the blue sample (representing the Scottish Coal Measures) is older and has a larger 1σ error than the underlying red sample (representing the Limestone Coal Formation). Both the blue and red samples of the Vincent et al. (2010) model are younger than the Duddy et al. (1992) model, most likely as a result of the more recent heating. Probably the most noteworthy difference between the synthetic data for each scenario is the TLD. In the Duddy et al. (1992) scenario, both the blue and red samples have unimodal peaks. The blue sample's TLD is asymmetrical, with a tail towards shorter lengths and MTL of 13.63 µm, while the red sample has a symmetrical form and a MTL of 12.45 µm. In the Vincent et al. (2010) scenario, the blue sample has a very distinct bimodal form, with a small wide peak centred around 15 µm and a taller narrow peak centred around 11 µm, and a MTL of 12.29 µm. The red sample's TLD is unimodal, asymmetrical with a tail towards shorter lengths, and has a MTL of 13.76 µm.

Results of the inverse modelling the synthetic observed data are shown in Figure 7-2, Figure 7-3, Figure 7-4, and Figure 7-5 below, which allows the comparison between the forward model, synthetic

observed data and the inverse model predicted data. To test the influence of various constraints on the output model, several models were run. Initially inverse models were performed without any constraint other than the stratigraphic age of the samples. Then the effect of post burial constraints on the inverse model were investigated. Firstly, in the Duddy et al. (1992) scenario, one burial constraint was added to represent maximum burial and heating during the late Carboniferous-early Permian. Then a second constraint was added to represent Neogene sediment re-burial. Following this, the VR values associated with these samples were added in each of the model, with zero, one or two constraints, as described above. In the Vincent et al. (2010) scenario, modelling was performed in a similar way, initially without constraint, then with the additional late Carboniferous-early Permian uplift associated with the Variscan orogeny. Finally, these models were re-run by adding the VR data.

All Duddy et al. (1992) inversion predictions (AFT central age, MTL, and TLD) show a good agreement (±10%) between the observed synthetic and the predicted data. The time-temperature pathway (t-T path) in the unconstrained model shows the largest uncertainty around the point of maximum paleo-temperature. The addition of the post burial constraints mentioned above, reduces the uncertainty around the point of maximum paleo-temperature and return t-T paths that are very similar to the forward model; the discrepancy between observed and predicted data, however, does not improve. The VR constrained inversion shows good agreement with the forward model, and the point of maximum paleo-temperature is replicated with less uncertainty than the unconstrained model. Like inverse models without the VR values, the addition of burial constraints improves the similarity between the t-T paths of the forward and inverse model produced, however no clear change in the predicted data is obvious, potentially with the exception of the VR plus multiple constraints model, where the predicted MTL and TLD are not reproduced as well as earlier models. This result may be caused by the fact that the Neogene burial event proposed by Duddy et al (1992) happened when the samples were already at temperatures cooler than the PAZ and, therefore, the AFT data are insensitive to this episode of re-heating.

In the Vincent et al. (2010) scenario, the unconstrained model reproduces the shape of the forward model t-T path well, however the predicted AFT central age for the blue sample is >±10% of the observed and the TLD is not reproduced well. The additional post burial constraints improve the predicted AFT central age to be within ±10% of the observed and the TLD is reproduced more accurately. The VR constrained inversion t-T path does not show good agreement with the forward

model, the predicted AFT central age of the blue sample is >±10% of the observed and the TLD has been poorly reproduced. The additional constraints based on those input into the original burial model, improve the similarity of the forward and inverse models t-T paths and predict an AFT central age within ±10% of the observed and reproduce the TLD accurately.

7.1.2.1 Conclusions

The forward models, synthetic observed AFT data and inverse modes produced here, allows for direct comparison between existing burial history models for the evolution of the Midland Valley and those produced in this thesis. The exercise of inverting the synthetic data shows that QTQt is capable of reproducing the thermal histories that were consistent with the input forward model, demonstrating that QTQt is capable of exploring time-Temperature space, to return known thermal histories. The synthetic data clearly show that the overall shape of the thermal histories is defined by the track length measurements, with unimodal distributions produced by thermal histories with one major heating event, followed by continuous cooling (Duddy *et al.* 1992), whereas two major events of heating/cooling produces bimodal distributions (Vincent *et al.* 2010). The models produced here also highlight the effects of adding constraints and complementary data, like the VR values, to increase the robustness of the derived thermal histories. For this reason, the inverse modelling of the AFT data produced in this investigation will be approached in the same manner; initially the stratigraphic age will be input as the sole constraint, then the literature-derived VR will be added (see VR data, Table 1-1), and finally any post burial constraints consistent with the geology of the basin will also be input in the model.

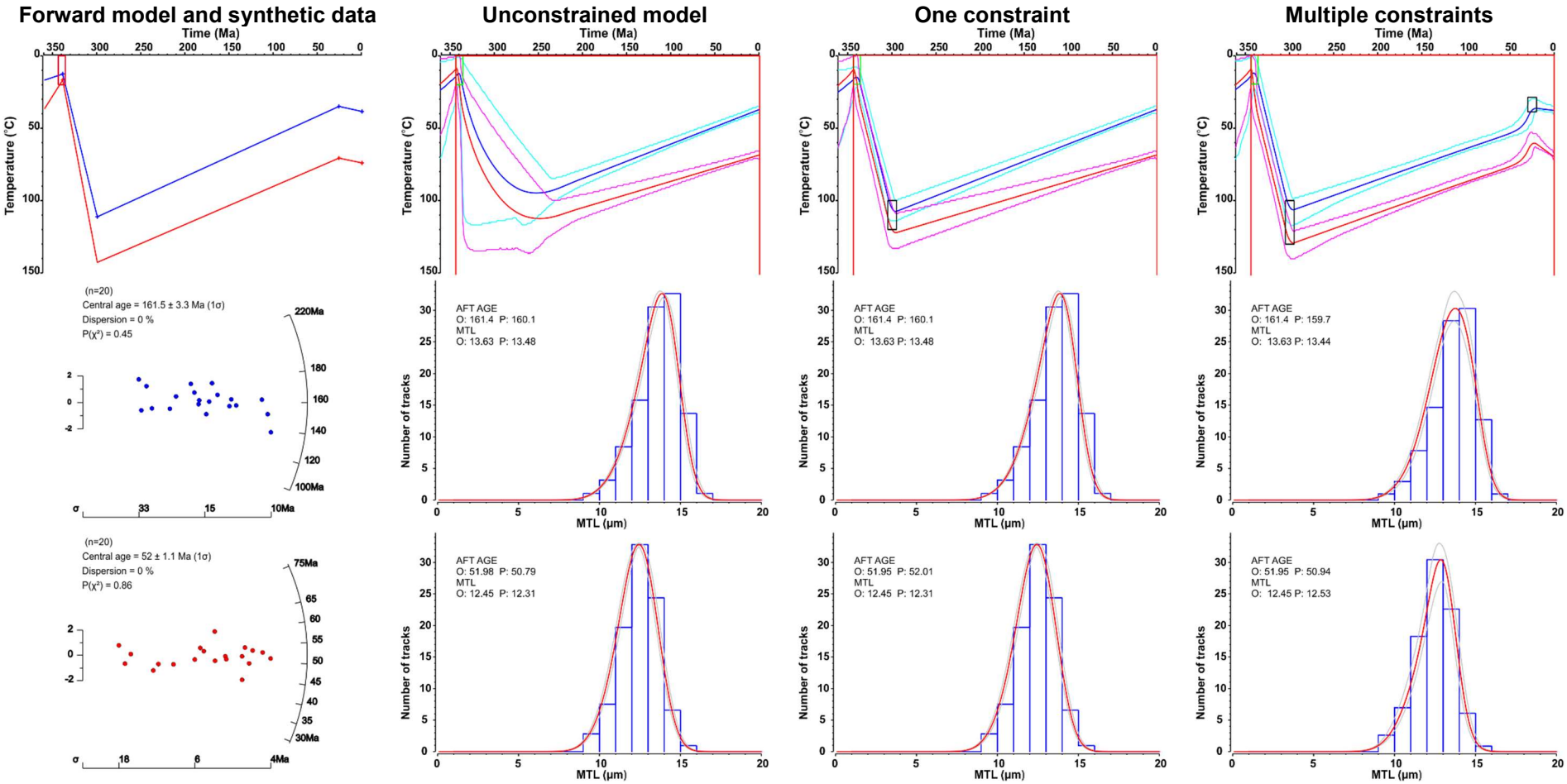

Figure 7-2: Forward model, synthetic data, and inversion of Duddy et al. (1992) scenario. Figure shows the forward model drawn from the time-temperature history taken from the literature and the synthetic observed data generated by QTQt (single grain ages plotted on a radial plot for ease of viewing) for two stratigraphic levels; blue representing the Scottish Coal Measures and red representing the Limestone Coal Formation. Stratigraphic constraint is represented by the green box with any post burial constraints are represented by a black box. Blue histograms represent synthetic TLD's while the inverse model TLD is represented by the red curve. O indicates observed data, P indicates inverse model predicated data.

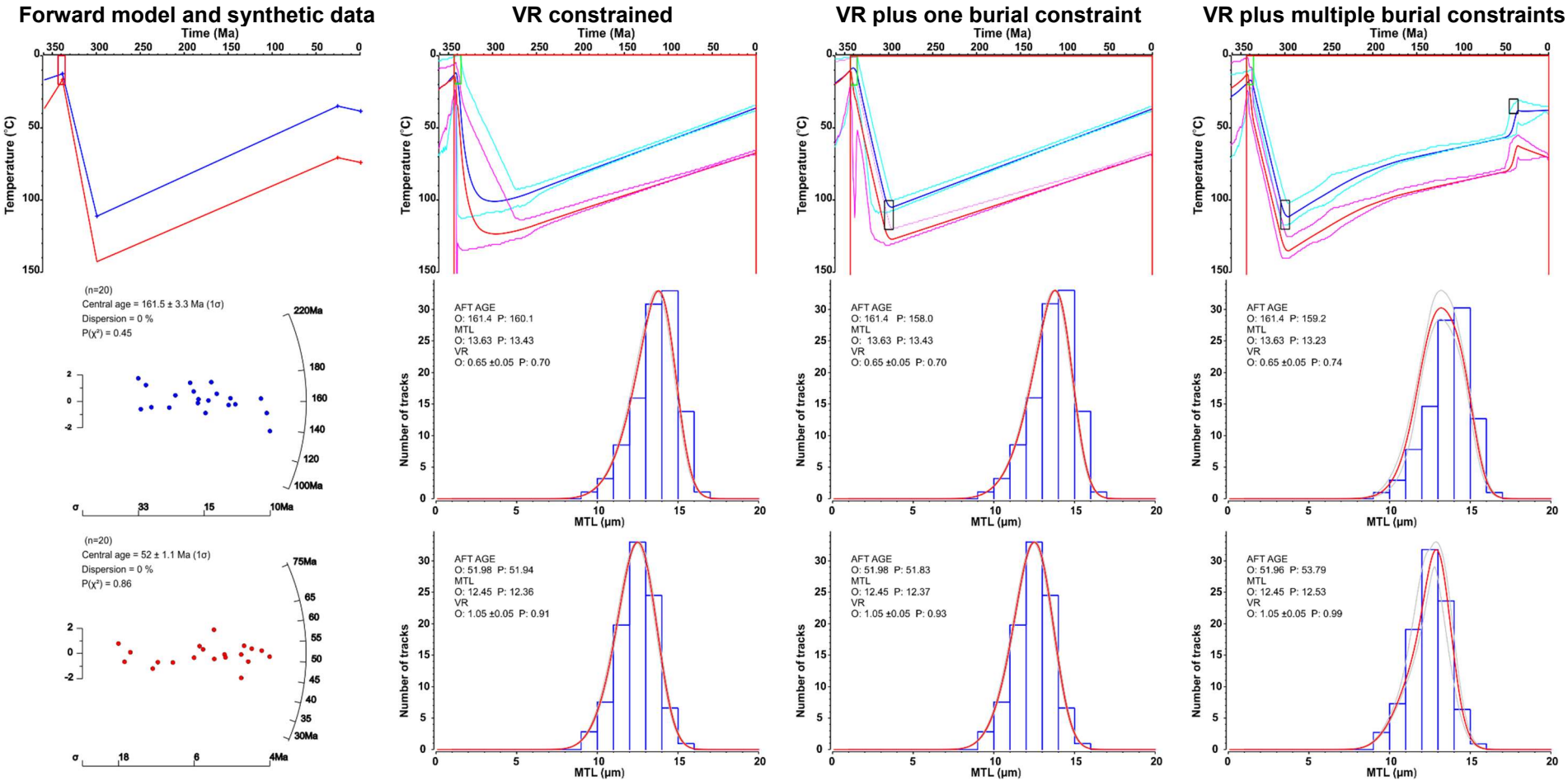

Figure 7-3: Forward model, synthetic data, and inversion including VR of Duddy et al. (1992) scenario. Figure shows the forward model drawn from the time-temperature history taken from the literature and the synthetic observed data generated by QTQt (single grain ages plotted on a radial plot for ease of viewing) for two stratigraphic levels; blue representing the Scottish Coal Measures and red representing the Limestone Coal Formation. Stratigraphic constraint is represented by the green box with any post burial constraints are represented by a black box. Blue histograms represent synthetic TLD's while the inverse model TLD is represented by the red curve. O indicates observed data, P indicates inverse model predicated data

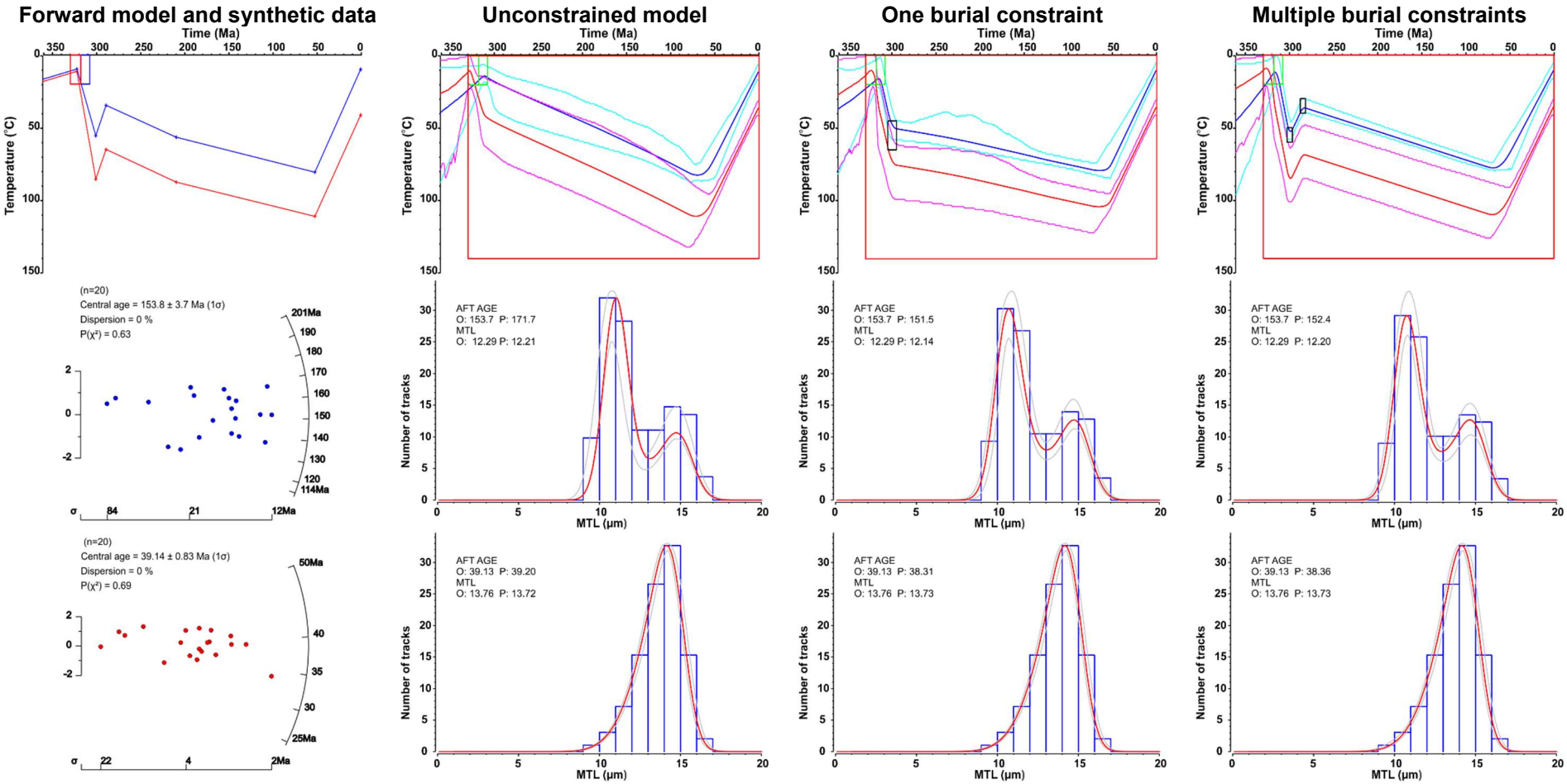

Figure 7-4: Forward model, synthetic data, and inversion of Vincent et al (2010) data. Figure shows the forward model drawn from the time-temperature history taken from the literature and the synthetic observed data generated by QTQt (single grain ages plotted on a radial plot for ease of viewing) for two stratigraphic levels; blue representing the Scottish Coal Measures and red representing the Limestone Coal Formation. Stratigraphic constraint is represented by the green box with any post burial constraints are represented by a black box. Blue histograms represent synthetic TLD's while the inverse model TLD is represented by the red curve. O indicates observed data, P indicates inverse model predicated data

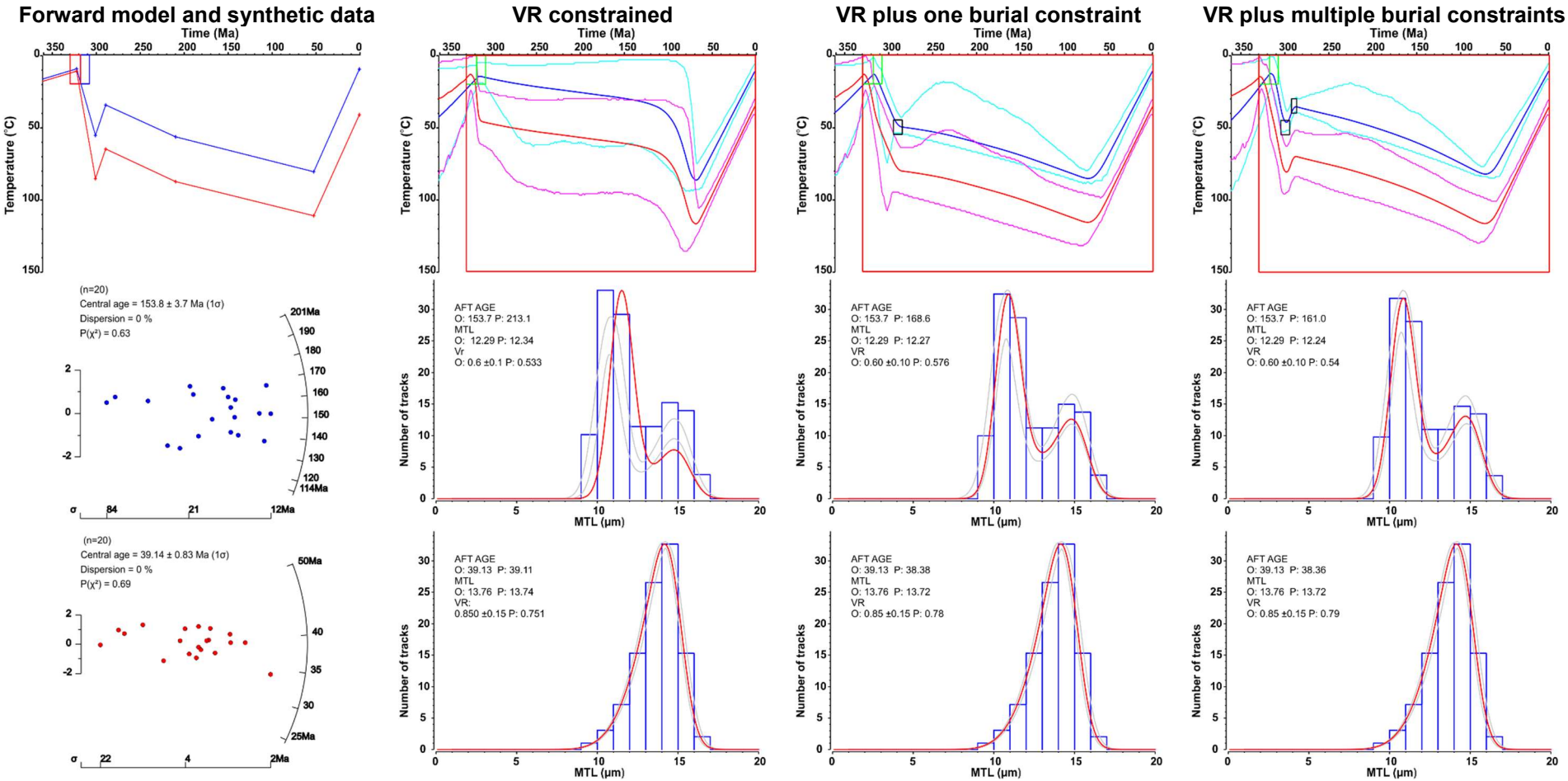

Figure 7-5: Forward model, synthetic data, and inversion including VR of Vincent et al (2010) data. Figure shows the forward model drawn from the time-temperature history taken from the literature and the synthetic observed data generated by QTQt (single grain ages plotted on a radial plot for ease of viewing) for two stratigraphic levels; blue representing the Scottish Coal Measures and red representing the Limestone Coal Formation. Stratigraphic constraint is represented by the green box with any post burial constraints are represented by a black box. Blue histograms represent synthetic TLD's while the inverse model TLD is represented by the red curve. O indicates observed data, P indicates inverse model predicated data.

7.2 Inverse thermal history modelling

7.2.1 Approach

The theoretical approach to inverse thermal history modelling used in this thesis was outlined in Chapter 3 section 3.4.1; the observed AFT data used to build individual QTQt file for each sample are reported in Chapter 6 and Appendix D & E. The general prior time-Temperature space (t-T space) was set using the samples stratigraphical age and a temperature range of 70°C ±70°C, to cover the temperature sensitivity of AFT thermochronology. The present-day temperature constraint for outcrop samples was set to 10°C ±10°C, whereas the present temperature of the borehole samples have been calculated from bottom-hole corrected temperatures with an uncertainty of ±5°C. Each sample's confined tracks were c-axis projected and the sample average Dpar value (± 1 standard deviation) was used as a proxy for annealing behaviour (Ketcham *et al.* 2007a). Outcrop and boreholes with a single sample were run individually, whereas boreholes that contained more than one sample (e.g. Thornton-1 borehole), were run together, as a profile, using the multi-sample approach of QTQt. Time-temperature steps and pre-depositional history (see section 7.2.2) were tuned using short 10,000 *burn-in*, 10,000 *post burn-in* iterations until optimised (QTQt acceptance rates between 0.2-0.6 (Gallagher 2012)). Following this step, a minimum of 200,000 *burn-in* and *post burn-in* iteration runs were performed for each sample or profile. Due to the success for the modelling approach taken for the inverse modelling of the synthetic data, the inverse modelling of the observed data collected in this study was approached in a similar way. Samples were initially modelled with only their stratigraphic age (unconstrained), then with a VR constraint (Table 1-1), and finally with any additional post burial constraints that are consistent with the geology of the area. The lack of geological evidence limits the position and certainty of any post-burial constraint box, these were therefore added speculatively to investigate their influence on the t-T path complexity and hypothesis testing.

7.2.2 Pre-depositional history

Given that the samples in this investigation are from a sedimentary basin, the potential for inherited pre-depositional thermal history data exists, especially if samples that have not been exposed to temperatures greater than the PAZ (c.120°C). Inheritance was investigated during the 'tuning phase' of modelling; as there are no available constraints on the AFT ages that apatite grains in the basin would have yielded at the time of their deposition, determining the effect of the pre-burial history of

the samples is key to appropriately determine the uncertainties associated with the derived thermal histories. The observed data were modelled in two ways, 1) without taking any pre-depositional history into account (i.e., the fission tracks formed prior deposition were completely annealed by burial) and 2) allowing for some record of the pre-depositional history to be preserved in the sample. In the latter case, another time-temperature point, older than the stratigraphic age, is added to the model as an input. Figure 7-6 shows the results of this approach for a representative sample selection, modelled without and with a pre-depositional history. When no pre-depositional history is allowed, the observed TLD and MTL are reproduced well, with the predicted value, within ±10% of the observed value. The predicted central age of the sample is reproduced less well and can be >±10% of the observed value, like in the case of EM-002 (Figure 7-6). However, there are some issues with the derived thermal histories. The time-temperature path of the expected model often does not begin in the stratigraphical age constraint box and, for any given sample, there is a strong disagreement between the Expected, Max. Likelihood, and Max. Posterior models. In the alternative scenario, where a pre-depositional history is allowed, the observed TLD and MTL are reproduced as well as before, however the central age is now also reproduced within ±10% of the observed age. The expected model now clearly passes through the stratigraphical age constraint box and there is a stronger agreement between the Expected, Max. Likelihood and Max. Posterior models, especially during the initial heating phase of the samples. The results shown in Figure 7-6 were similar to those of the other samples not displayed, borehole samples were less effected by the pre-depositional history, indicating they were likely to have been totally annealed after being deposited. Allowing the pre-depositional history to be sampled is not detrimental to any of the samples, as, in the case of complete post-burial annealing, it would be ignored; therefore, all samples modelled in this investigation were allowed to take pre-depositional history into account.

As there are no available constraints on the pre-burial history of the sediments that filled the Midland Valley basin, two contrasting scenarios were considered to investigate the influence of specific pre-depositional scenarios: 1) the sediments were eroded from a landscape characterised by rapid uplift, fast cooling setting or, 2) eroded from a landscape characterised by a stable craton, slowly cooled setting. Results are reported in Figure 7-7 and for this investigation the same samples reported in Figure 7-6 are displayed. The observed data are reproduced well in both scenarios (within ±10%), however allowing the pre-depositional point to be sampled randomly by QTQt (Figure 7-6, ‘with pre-depositional history’), taking into account all possible pre-deposition thermal histories reproduces the

observed data most accurately and removes the forced thermal history element for the modelling and the false confidence (narrow 95% credible interval) in the pre-depositional history. This investigation indicates that, when detrital apatites are not completely annealed, the pre-depositional time-Temperature space needs to be explored, when the data are inverse modelled. It is, however, important to notice that no information should be retrieved from the QTQt derived pre-burial thermal histories, as they represent the best-fitting, fictitious integration of all the possible cooling paths of the rocks from which the sediments were sourced. It has been shown that gathering more compositional information on the apatite used for both AFT age calculations and confined track length measurements, can help to unravel the pre-depositional thermal history of detrital apatite, allowing samples to be divided into sub-samples and inverse modelled together (Gallagher and Wildman 2020), however it was not possible to undertake this level of sample discrimination in this thesis. Given the considerations explained above, all samples were inversed modelled using QTQt, allowing the software to explore the pre-depositional time-temperature space; the results are reported below.

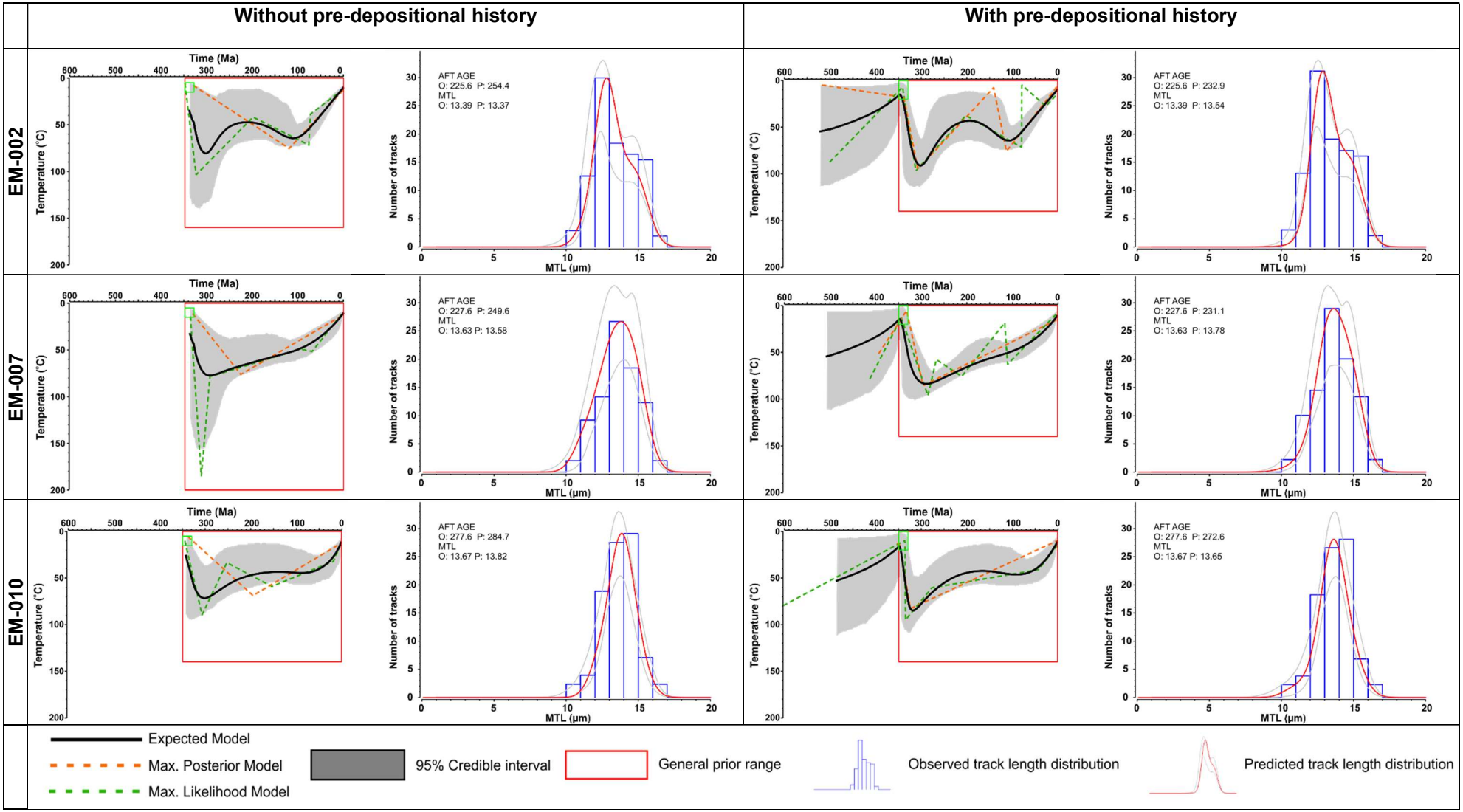

Figure 7-6: No pre-deposition vs pre-deposition point. See text for discussion.

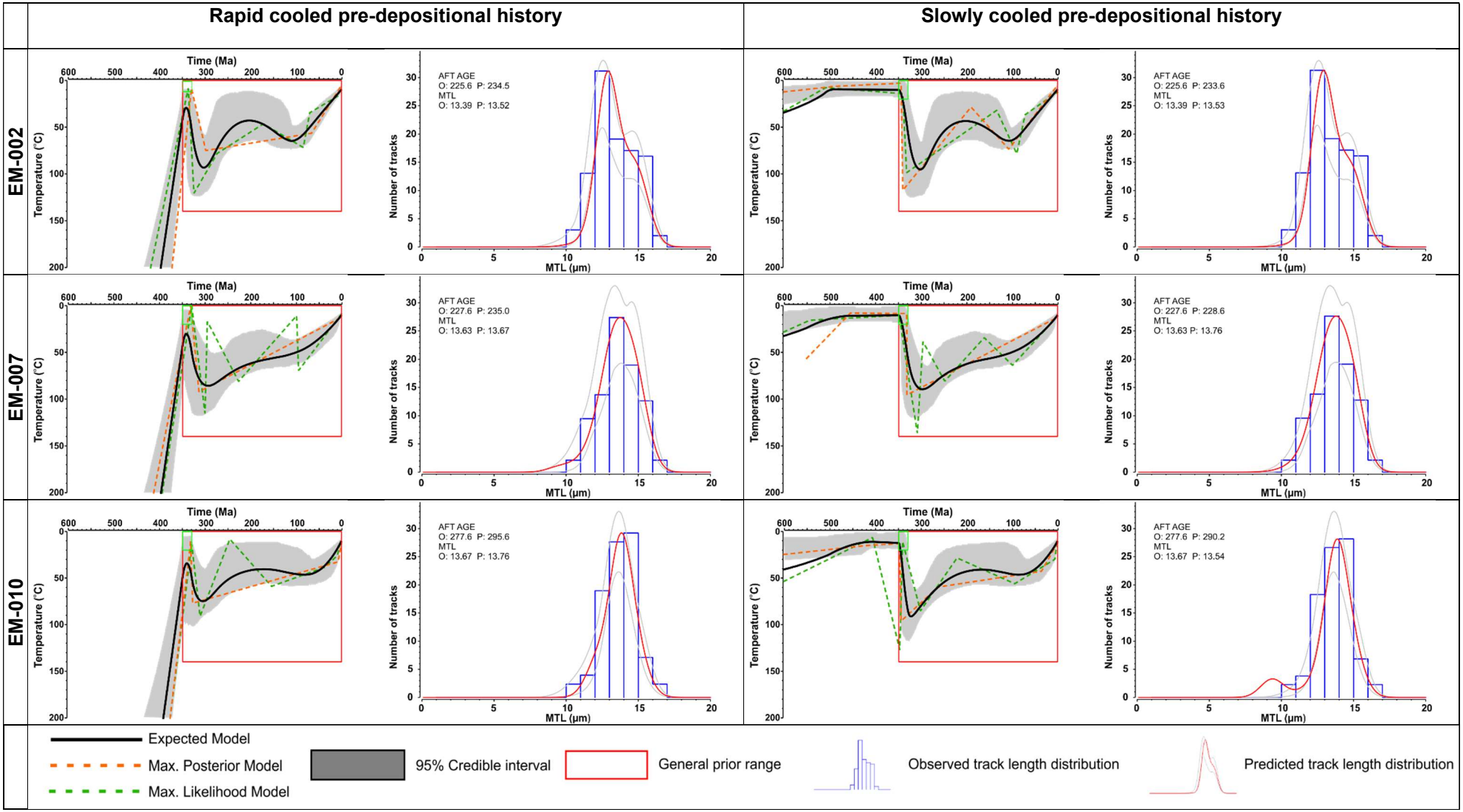

Figure 7-7: Rapid cooled vs slow cooled pre-depositional history. See text for discussion.

7.3 Results

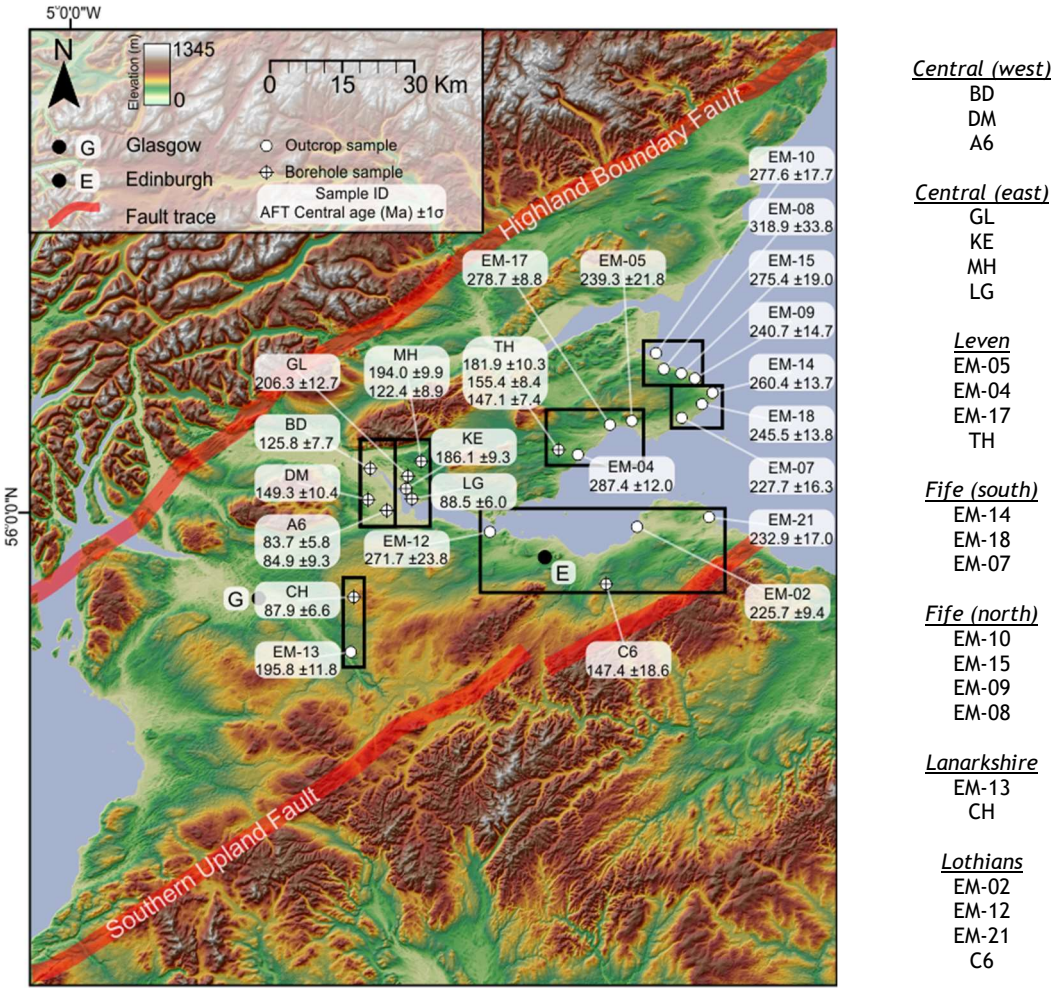

Figure 7-8: Map showing AFT sample locations and samples grouped into regions for modelling reporting.

Observed data from the 28 AFT outcrop and borehole samples were inverse modelled using the approach outlined in Chapter 3 section 3.4.1 and above. As highlighted above, the software (QTQt) sampled the pre-depositional thermal history for the inversion of the observed data; however, the time and temperature range for the output models reported below were set to 0-360 Ma and 0-150°C, to reflect the fact that the AFT data are able to provide information only on the post-depositional history of the sediments. For each sample there are three different thermal models; 1) the unconstrained model, with no constraints apart the stratigraphic age (the software is able to sample all the time-temperature space comprised between the stratigraphic age of the sample and the present, and between 0 and 150°C); 2) the additional VR data constrained model (the software is forced to investigate thermal histories that include the maximum temperature defined by the VR value for the same stratigraphic level from which the sample was collected), and, 3) when available, with an additional constraint that is derived from the geological history of the area and it is independent from the AFT data. Figure 7-9 reports the legend for all thermal

histories reported in this chapter. For the reporting of the inverse modelling, the Midland Valley was subdivided into regions; Central (west), Central (east), Leven, Fife (south), Fife (north), Lanarkshire, Lothians, (Figure 7-8). The regions were identified based on the similarity of the thermal histories; subsequently, AFT data from samples from the same region were combined, using a multi-sample modelling approach, as explained in section 7.5 below. For exact stratigraphical position of the samples, refer to Figure 1-3.

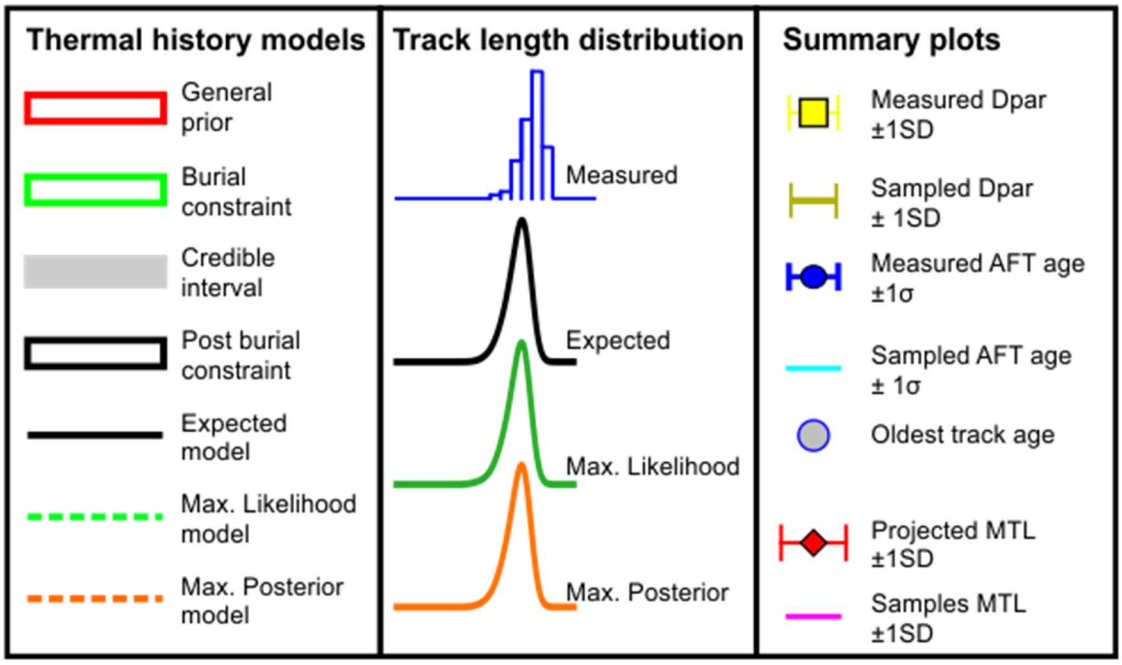

Figure 7-9: Key for all thermal history models, track length distribution (TLDs), and summary plots for multi-sample models.

7.3.1 Central region

7.3.1.1 West

The Central (west) region consists of four samples from Namurian sandstones (Limestone Coal Formation) from three boreholes, Bandeath-1, Dunmore Moss, and Airth 6 (Figure 7-10 & Figure 7-11). The AFT central ages are younger than their depositional age, and range between 80 and 150 Ma ±c.10 Ma (1σ); TLDs are unimodal with MTLs between 13.0 ±1.5 µm and 14.0 ±1.3 µm (Chapter 6, Table 6-2). In the unconstrained model, the Bandeath (BDBH) sample shows initial heating to c.100°C at c.200 Ma, followed by monotonic cooling to c.60°C; at 50 Ma a cooling pulse brought the rock to its present depth, at a rate of c.1°C/Myr. When the additional constraints are added, the timing of maximum paleo-temperature occurs at c. 300 Ma, synchronous with the thermal models of the other samples from this region. Also, the subsequent cooling is not monotonic, showing an increased rate of cooling from c.300 Ma to 250 Ma; afterwards, cooling

continues with rates and trends similar to those highlighted for the model with no constraints. The Dunmore Moss sample shows an initial period of heating to c.100°C at 200 Ma followed by protracted cooling at a rate of c.0.5°C/Myr. As above, the additional constraints align the timing of maximum paleo-temperature to that seen in other samples, c.300 Ma, followed by protracted cooling at c.0.3°C/Myr. The Airth-6 borehole contains two samples modelled as a profile. The unconstrained model shows heating until c.150 Ma followed by cooling at a rate of c.0.6°C/Myr. Additional VR and burial constraints were added, but the resulting models are associated with very large 95% credible intervals and thus are poorly constrained by the data.

7.3.1.2 East

The Central (east) region includes five samples from four boreholes, Gartlove-2, Kincardine East, Longannet-1, and Meadow Hill-1z (Figure 7-12, Figure 7-13, & Figure 7-14). All samples are from the Namurian, Limestone Coal Formation sandstones. The AFT central ages decrease with increasing depth and are all younger than their depositional age, ranging between 80 and 200 Ma ±c.10 Ma (1σ). Their TLD is unimodal with MTLs between 13.1 ±1.3 μm and 13.8 ±1.1 μm (Table 6-1 Table 6-2). Following deposition into the basin, the Gartlove-2 samples shows rapid heating to temperatures >100°C, which continues until c.280 Ma (c.2°C/Myr). The sample then cools out of the PAZ, at a rate of 1.7°C/Myr, reaching 60°C at c.250 Ma. The Expected, Max. Likelihood and Max. Posterior models show a re-heating of the sample by c.20°C between c.200 and 70 Ma, although the 95% confidence interval is very large in this segment of the thermal histories; an early Cenozoic rapid cooling pulse brought the rock to the to present temperatures, at a rate of 0.8°C/Myr. The Kincardine East and Meadow Hill borehole samples show a similar trend of rapid post burial heating followed by cooling out of the PAZ between c.250 and 200 Ma. This is followed by a possible period of re-heating that persists until c.80 Ma and c. 150 Ma, in the Kincardine East and in the Meadow Hill samples, respectively. Both samples then cool to present temperatures at rates of c.1°C/Myr (Kincardine East) and 0.6°C/Myr (Meadow Hill). The Longannet-1 borehole sample shows heating to c.100°C at 200 Ma followed by protracted cooling to present temperature at a rate of 1°C/Myr. It should be noted that this thermal history model has a very large 95% credible interval associated with it. A burial constraint was added, similar to that seen in other thermal histories, this changed the onset of cooling to be more in line with samples from the area and shows protracted cooling from c.300 Ma at a rate of c.0.4°C/Myr.

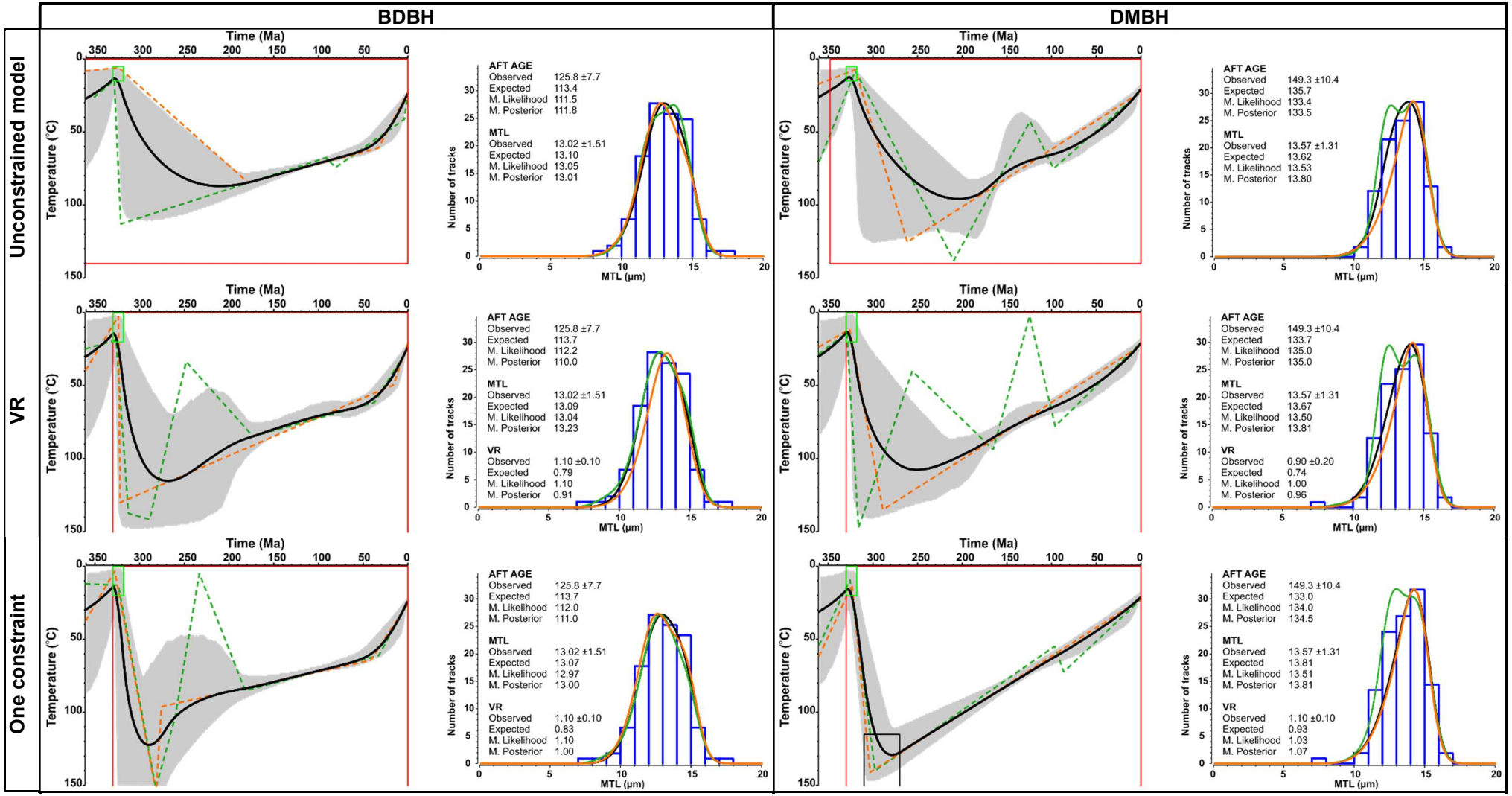

Figure 7-10: Thermal history modelling results from BDBH and DMBH samples from the Central (west) region. See Figure 7-9 for definitions of all features.

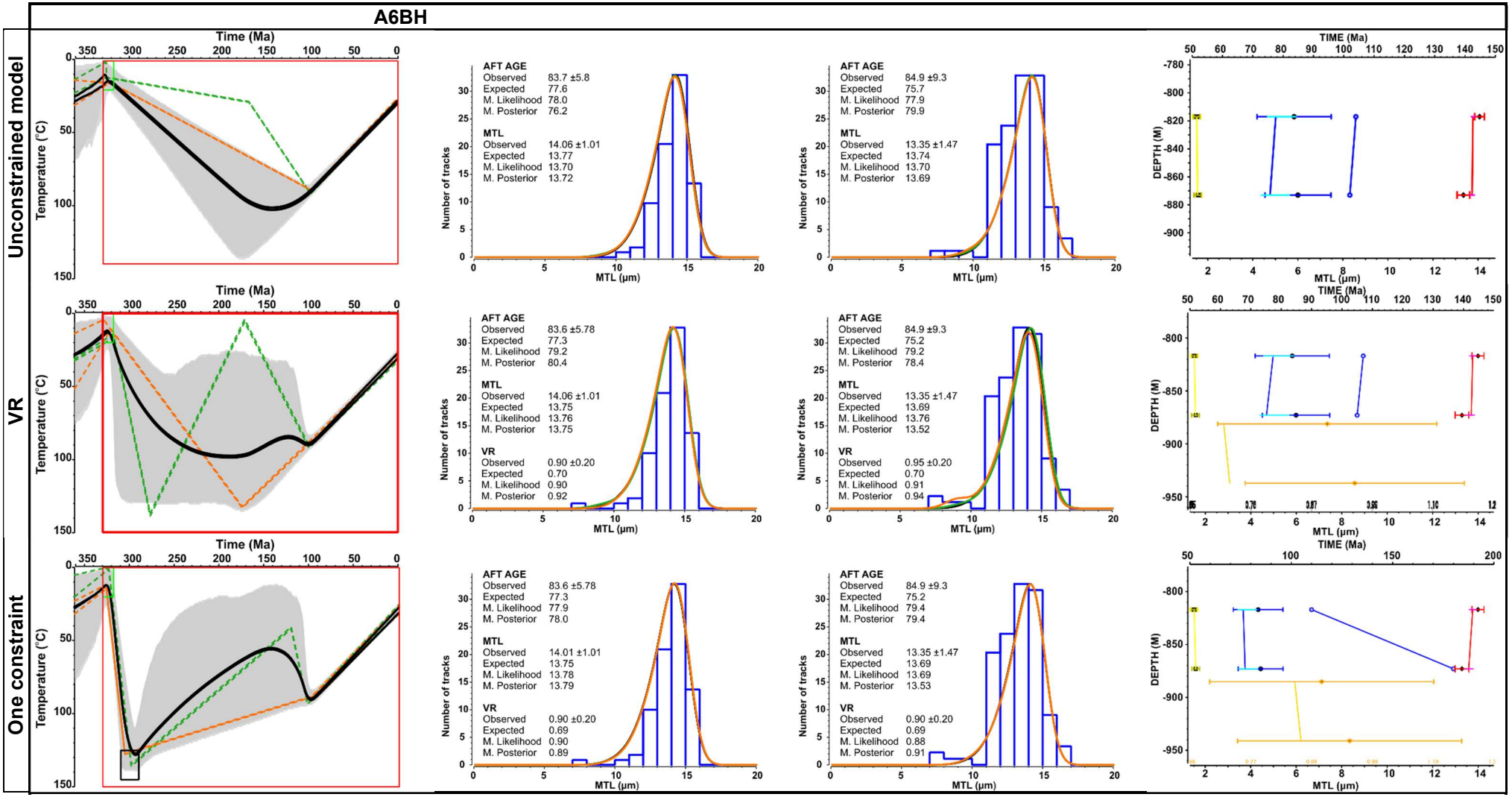

Figure 7-11: Thermal history modelling results from A6BH samples from the Central (west) region. See Figure 7-9 for definitions of all features.

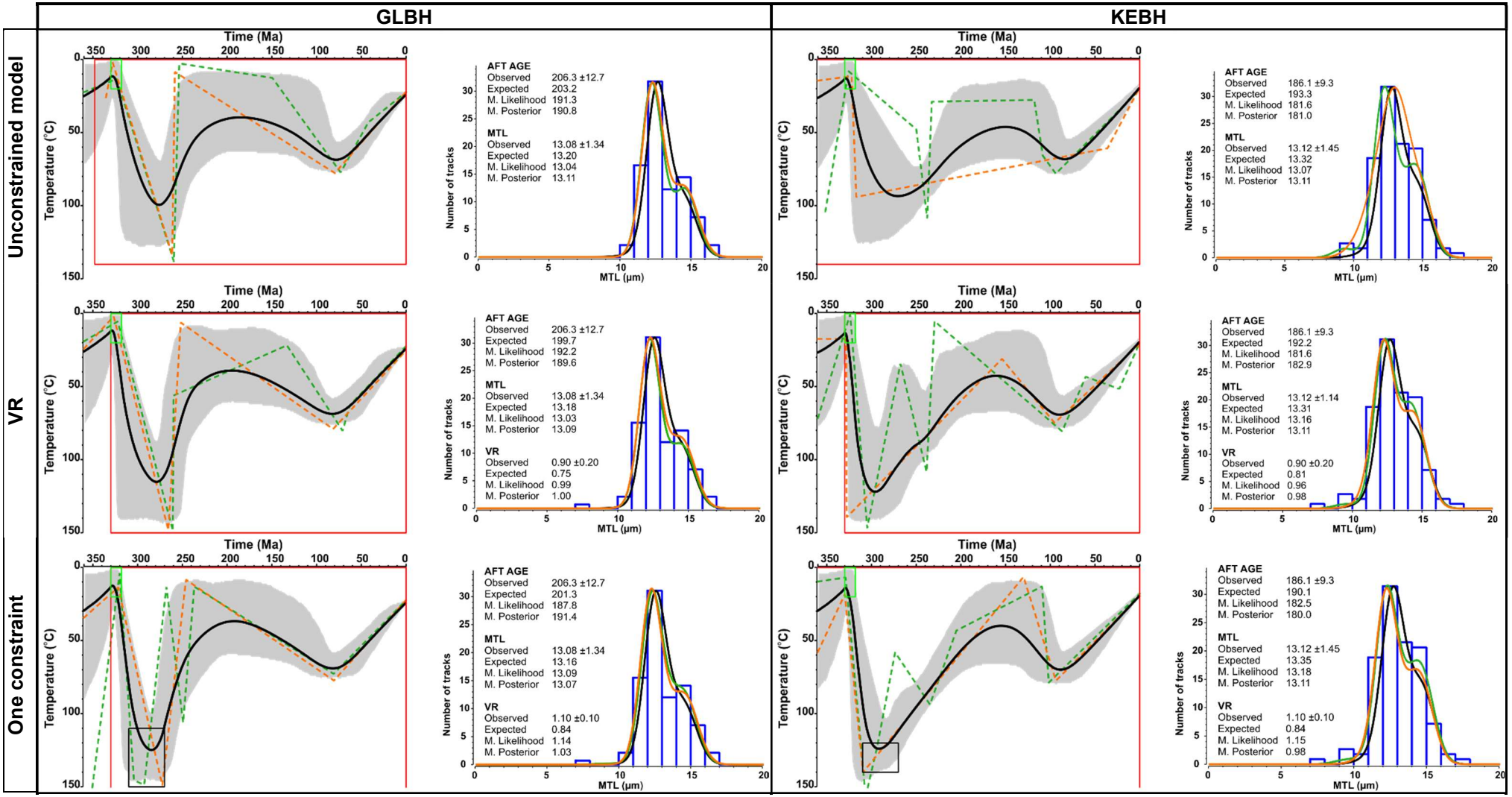

Figure 7-12: Thermal history modelling results from the GLBH and KEBH samples from the Central (east) region. See Figure 7-9 for definitions of all features.

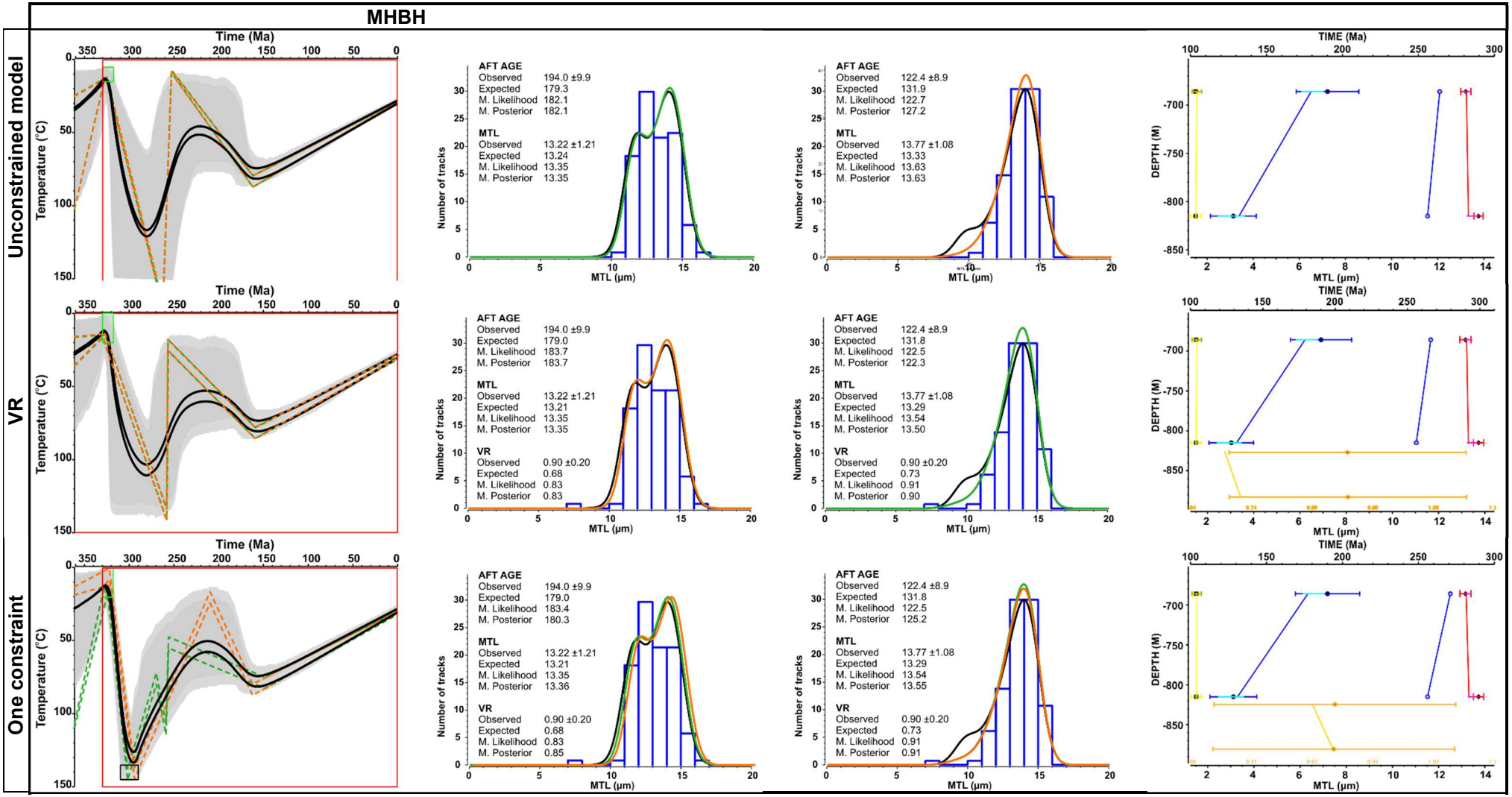

Figure 7-13: Thermal history modelling results from MHBH samples from the Central (east) region. See Figure 7-9 for definitions of all features.

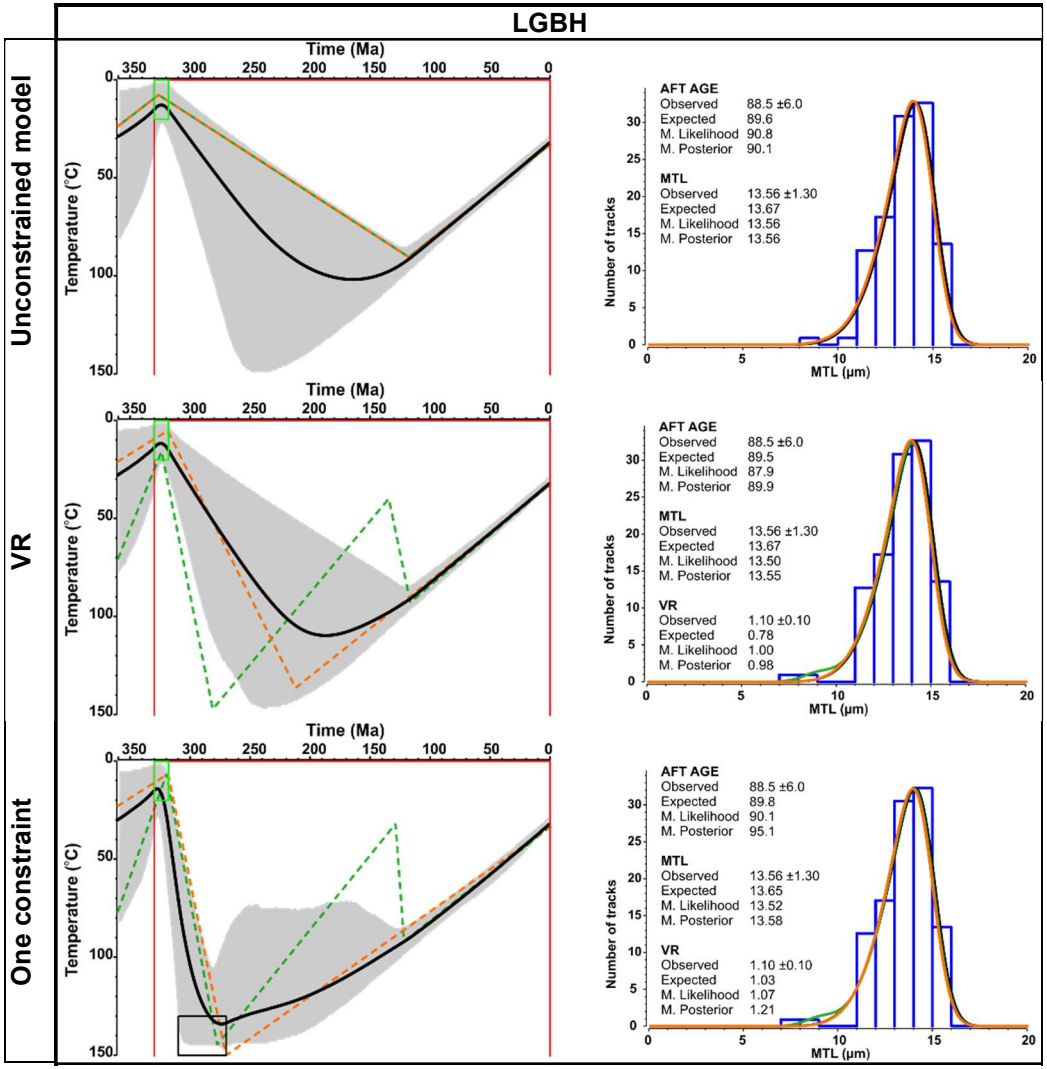

Figure 7-14: Thermal history modelling results from LGBH samples from the Central (east) region. See Figure 7-9 for definitions of all features.

7.3.2 Leven

The Leven region consists of six samples, three from Westphalian sandstone outcrops (EM-005, EM-004, & EM-017) and three from the Thornton-1 borehole (THG1, THG2, & THG3) from Namurian sandstones (Limestone Coal Formation) (Figure 7-15, Figure 7-16, & Figure 7-17). AFT central ages of the outcrop samples are younger that their depositional age and range between 240 and 290 Ma ±c.15 Ma (1σ). TLDs for these samples are unimodal with MTLs ranging between 13.5 ±1.1 μm to 13.7 ±1.2 μm (Table 6-1). Central ages from the Thornton-1 borehole are younger than the stratigraphical age of the samples and decrease with increasing depth; they vary between 180 and 155 Ma ±c.10 Ma (1σ). TLDs are unimodal with MTLs between 12.9 ±1.3 μm and 13.3 ±1.2 μm (Table 6-2). The thermal models accurately predict the observed data, with the exception of the central age in some outcrop samples (Figure 7-15 & Figure 7-16). Generally, the Expected models for the outcrops show good agreement through all modelling options, though the additional constraints do help to improve the QTQt predicted data. All outcrop samples show heating following deposition to c.60°C (c.1.5°C/Myr) until c.285 Ma; thereafter, the models differ in their t-T pathways. EM-005 remains at c.60°C until c.150 Ma, then cools to c.30°C by c.50 Ma (0.2°C/Ma), and finally it cools to present-day temperature at a rate of c.0.4°C/Ma. This sample has a very large 95% credible interval suggesting the thermal histories are poorly resolved by the data. The added additional constraints fail to improve the model predictions, probably because most of the post-burial history of the sample occurs at temperatures cooler than the PAZ. The unconstrained Expected model for EM-004 shows a more protracted cooling, from 285 Ma to the present, at a rate of 0.2°C/Myr. The additional constraints reduce the 95% confidence interval and identifies heating to c.60°C at 250 Ma (0.5°C/Myr), until the Paleogene, when the sample cooled at a rate of 0.7°C/Myr to present temperatures. This same t-T path is shared by EM-017, in particular when the VR value is added (Figure 7-16). Samples from the Thornton-1 borehole were modelled together in a profile (Figure 7-17). All modelling options (unconstrained, VR, & burial constrained) indicate that the samples were heated to their maximum paleo-temperatures following deposition at a rate of c.2°C/Myr. Post burial temperatures most likely exceeded the PAZ; thereafter, the cooling history of the profile varies between the modelling options. The unconstrained model shows cooling from 250-150 Ma, reaching a temperature of c.60°C (0.4°C/Myr), followed by c.50Ma of reheating to c.70°C. From here the samples cool to present day temperatures, at a rate of c.0.6°C/Myr. When the VR data is added to the model, the time of maximum paleo-temperature occur at c.280 Ma, which is

similar to the outcrop models in this region, however the predicted VR is much lower than the observed VR, implying that the samples experienced a higher temperature than predicted by the AFT data. The profile then cools monotonically to 50 Ma reaching a temperature of c.60°C, and from here the samples cool at a rate of c.1°C/Myr to present day conditions. A burial constraint was added to increase the maximum temperature attained to be more in line with the VR data. This model shows that the profile reached it max temperature (>120°C, outside the PAZ) at c.300Ma and then it cooled at a rate of 0.5°C/Myr until c.150 Ma, the profile then remains at the same temperatures until 100 Ma when it cools to surface conditions at c.0.55°C/Myr.

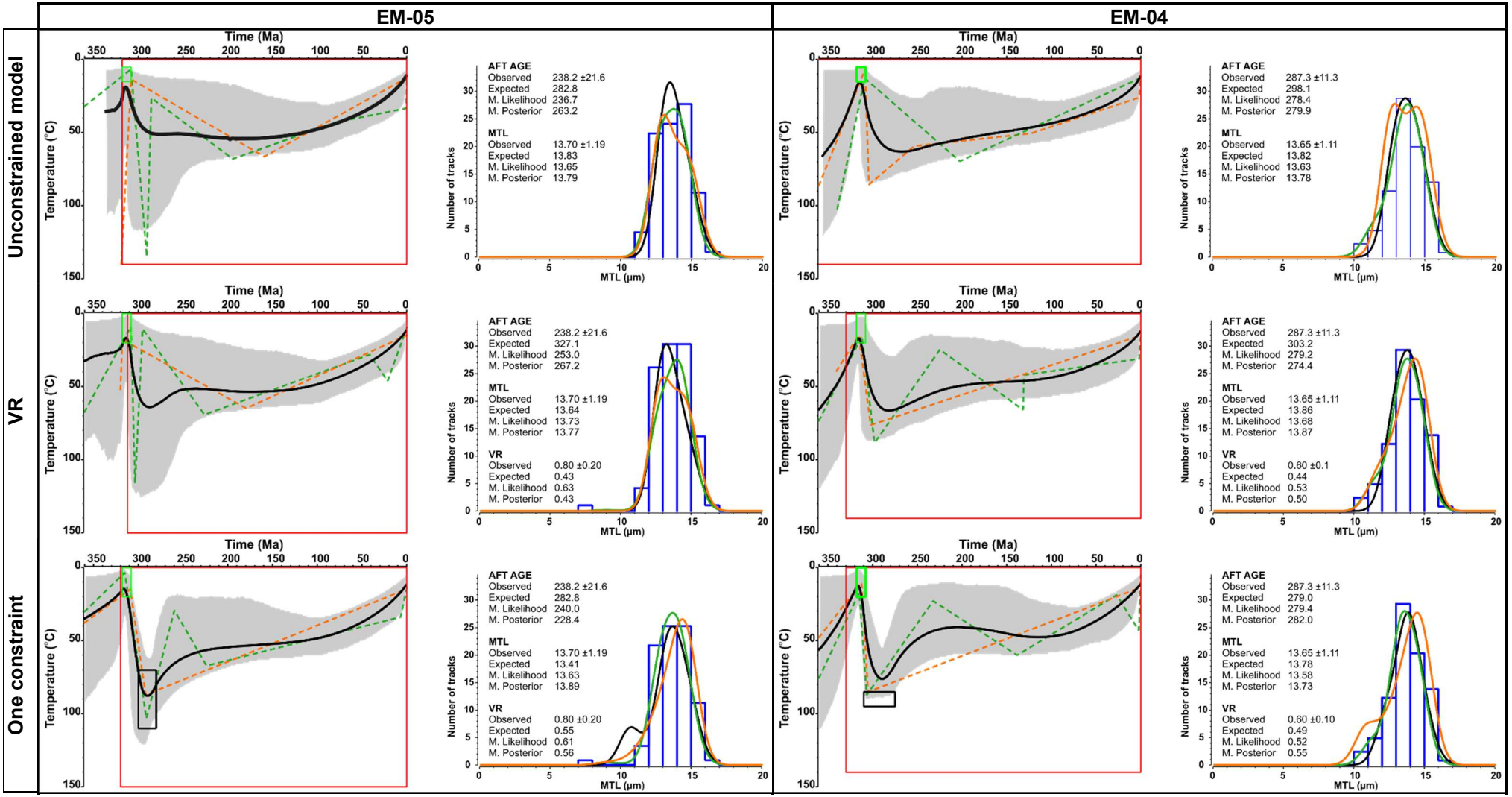

Figure 7-15: Thermal history modelling results from samples EM-04 and EM-05 from the Leven region. See Figure 7-9 for definitions of all features.

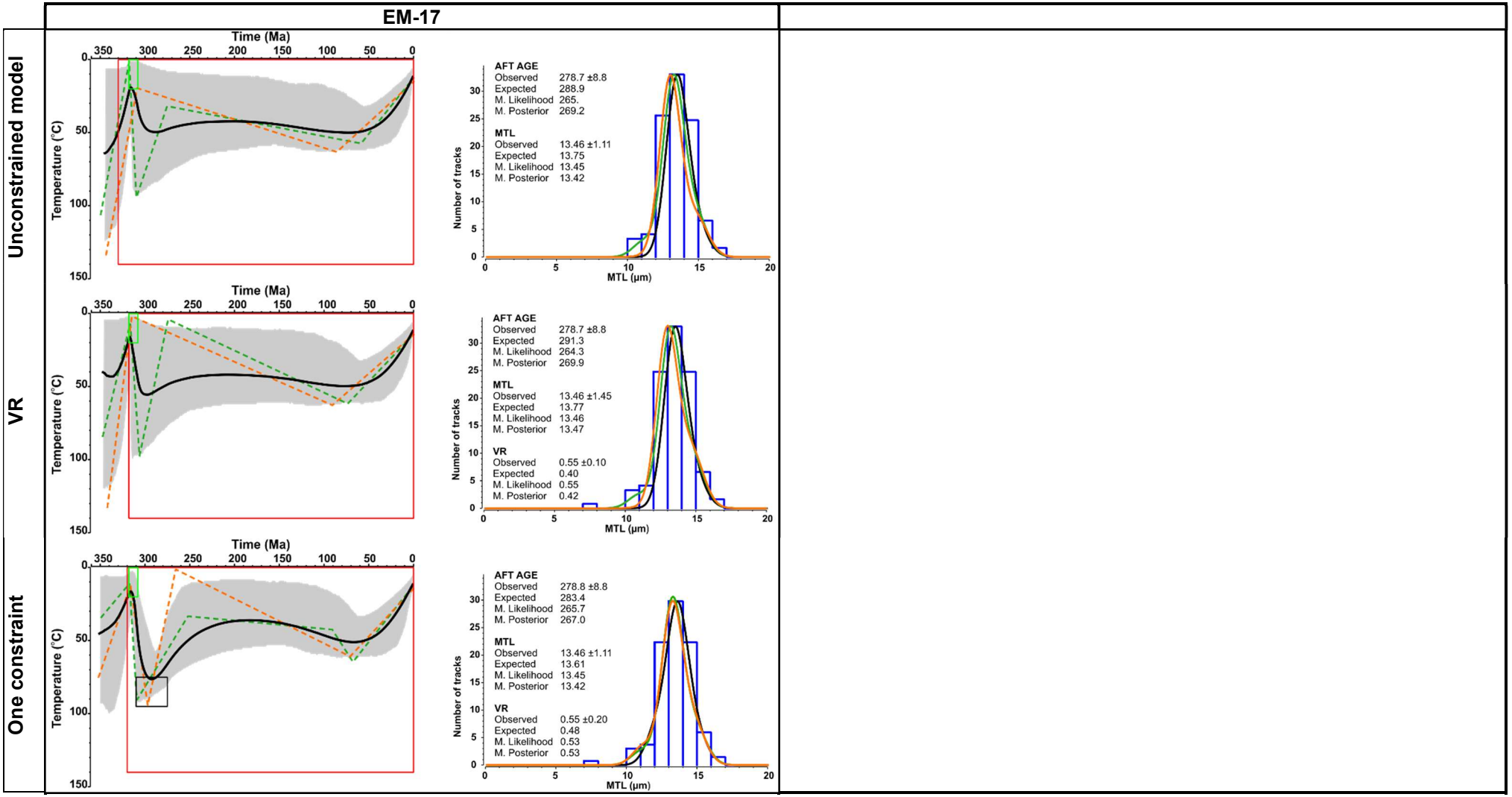

Figure 7-16: Thermal history modelling results from sample EM-17 from the Leven region. See Figure 7-9 for definitions of all features.

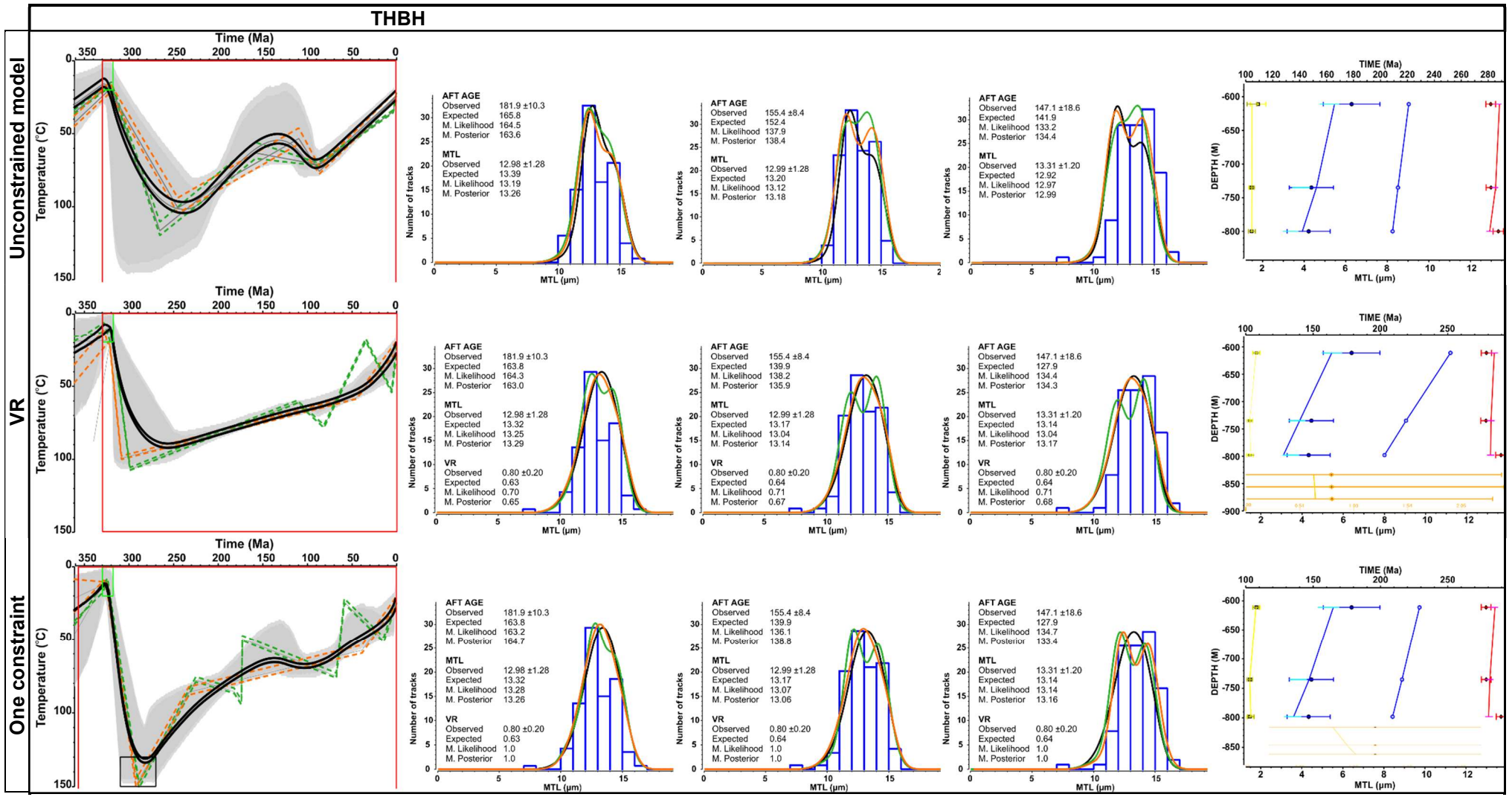

Figure 7-17: Thermal history modelling results from THBH samples from the Leven region. See Figure 7-9 for definitions of all features.Fife (south)

The Fife (south) region includes three samples, EM-014, EM-018, & EM-007 from the Fife Ness, Anstruther, and Pathhead Formations respectively. AFT central ages are younger than their Viséan depositional age and range between 227 to 260 Ma ±c.15 Ma (1σ). Their TLDs are unimodal and MTLs range between 13.0 ±1.2 μm and 13.8 ±1.3 μm (Table 6-1). The observed data have been predicted well by QTQt modelling, again with the exception of the central age in some cases. Generally, the Expected models show good agreement through all modelling options (unconstrained, VR, & burial constrained), though the additional constraints do influence the Max. Likelihood and Max. Posterior models (Figure 7-18 & Figure 7-19). Expected models for all three samples show rapid heating following deposition until c.310Ma (c.2.8°C/Myr) reaching temperatures around 80-90°C. Following this, the samples show subtle variations in their cooling histories. EM-014 cools by c.20°C from 310 Ma until c.200 Ma at a rate of 0.23°C/Myr, then exhibits reheating at a similar rate to c.60°C at c.50 Ma. The sample then cools to its present-day temperature at a rate of 1°C/Myr. EM-018 cools from its maximum paleo-temperature at 310 Ma to c.60°C (0.4°C/Myr) at c.250 Ma and then it remains at a constant temperature until c.60Ma, although there may be a minor reheating between 150-60 Ma. The final cooling pulse in the model is similar to EM-014, at c.60Ma where the sample cools to its present-day temperature at a rate of c.1°C/Myr. Following the maximum paleo-temperature reached at c.310 Ma, EM-007 cools to c.60°C at c.200 Ma (0.34°C/Myr) where it remains at a

constant temperature until c.100 Ma it then cools at a rate of 0.5°C/Myr to present-day conditions. In EM-014 and EM-018, the additional constraints bring the Max. Likelihood, the Max. Posterior and the Expected models closer to each other. In EM-007 the additional constraints produce a more protracted cooling history, from 270 Ma to present-day conditions, at a rate of c.0.26°C/Myr. The Palaegene cooling pulse occurs when these rocks were already at temperatures cooler than the sensitivity range of AFT analysis, thus the presence of this cooling pulse is uncertain.

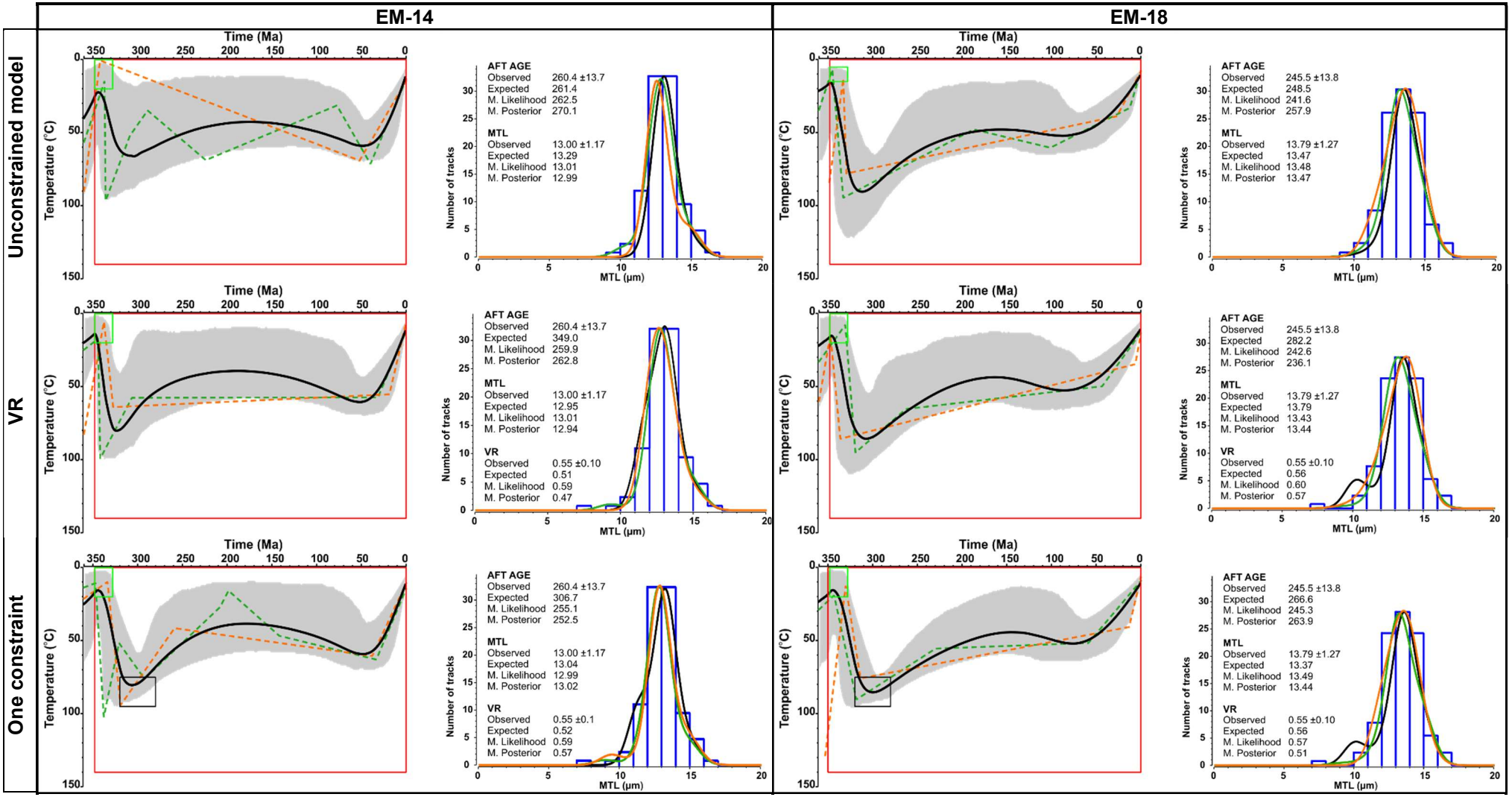

Figure 7-18: Thermal history modelling results from samples EM-14 and EM-18 from the Fife (south) region. See Figure 7-9 for definitions of all features.

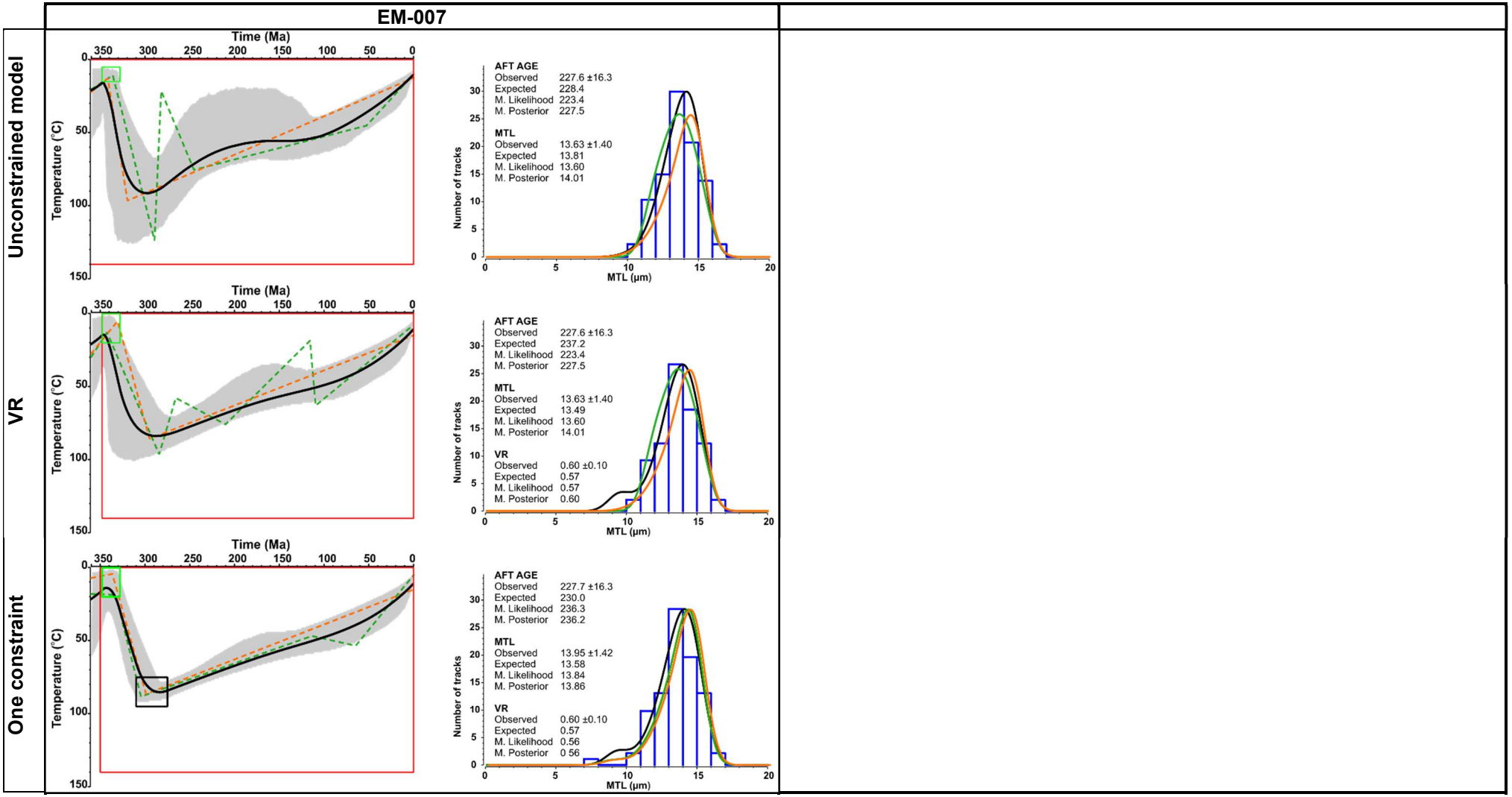

Figure 7-19: Thermal history modelling results from sample EM-07 from the Fife (south) region. See Figure 7-9 for definitions of all features.

7.3.4 Fife (north)

Samples in Fife (north) EM-010, EM-015, EM-008, EM-009 from the Sandy Craig, Anstruther, and Pittenweem Formations, are characterised by AFT central ages that are younger than their Viséan depositional age, ranging between 240 and 280 Ma ± c.20 Ma (1σ uncertainty). Their TLDs are unimodal with a MTLs between 13.2 ±1.4 μm and 14.0 ±1.2 μm (Table 6-1). The observed data is reproduced well by QTQt, (Figure 7-20 & Figure 7-21). Generally, the Expected models of individual samples show good agreement through all modelling options (unconstrained, VR, & burial constrained) and with each other; for these reasons, they are here described. Expected models for the region all show rapid heating following deposition until c.310Ma (c.2.7°C/Myr) where the maximum paleo-temperatures for all North Fife samples was reached, ranging between 80-90°C. The samples then cool moderately (0.4°C/Myr) until c.250Ma, reaching temperatures around 60°C. From 250Ma until c.150Ma the samples show a more subdued cooling rate and/or they resided at constant temperatures. After c.150Ma, the Expected models potentially indicate a period of reheating, on the scale of 5-10°C over 90Ma (c.0.08°C/Myr); this event, however, occurred when the rocks were already at temperatures colder than c.60°C, so it is very poorly constrained by the data. At c.60 Ma the models show a moderate cooling pulse from c.60°C to their present-day temperature, at a rate of 1°C/Myr. Again, as this cooling occurs below the temperature sensitivity range of AFT analysis, the true form of this cooling pulse is difficult to constrain from these data alone. The Max. Likelihood models for all samples are similar to each other; often they show a more complex path than the Expected models. The Max. Posterior models also produce a similar general thermal history however, none of these models require the reheating between 150-60Ma and the onset and magnitude of the latest cooling pulse shows more variability. A post burial constraint was added to firm up the late Carboniferous maximum paleo-temperature and to investigate how decreasing the uncertainty around this point altered the thermal history. The constraint, however, has no real quantifiable effects on the predicted thermal histories.

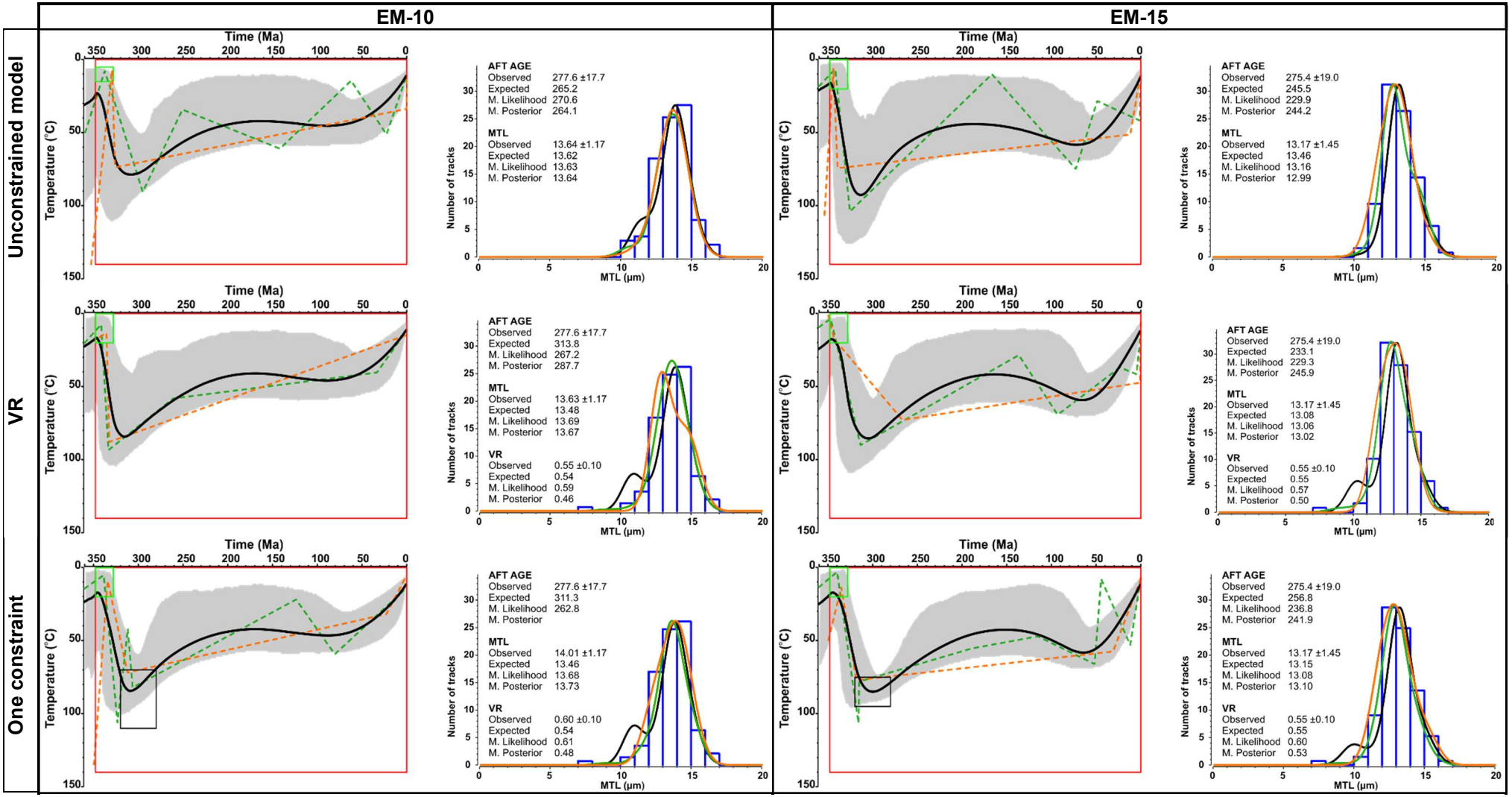

Figure 7-20: Thermal history modelling results from samples EM-10 and EM-15 from the Fife (north) region. See Figure 7-9 for definitions of all features.

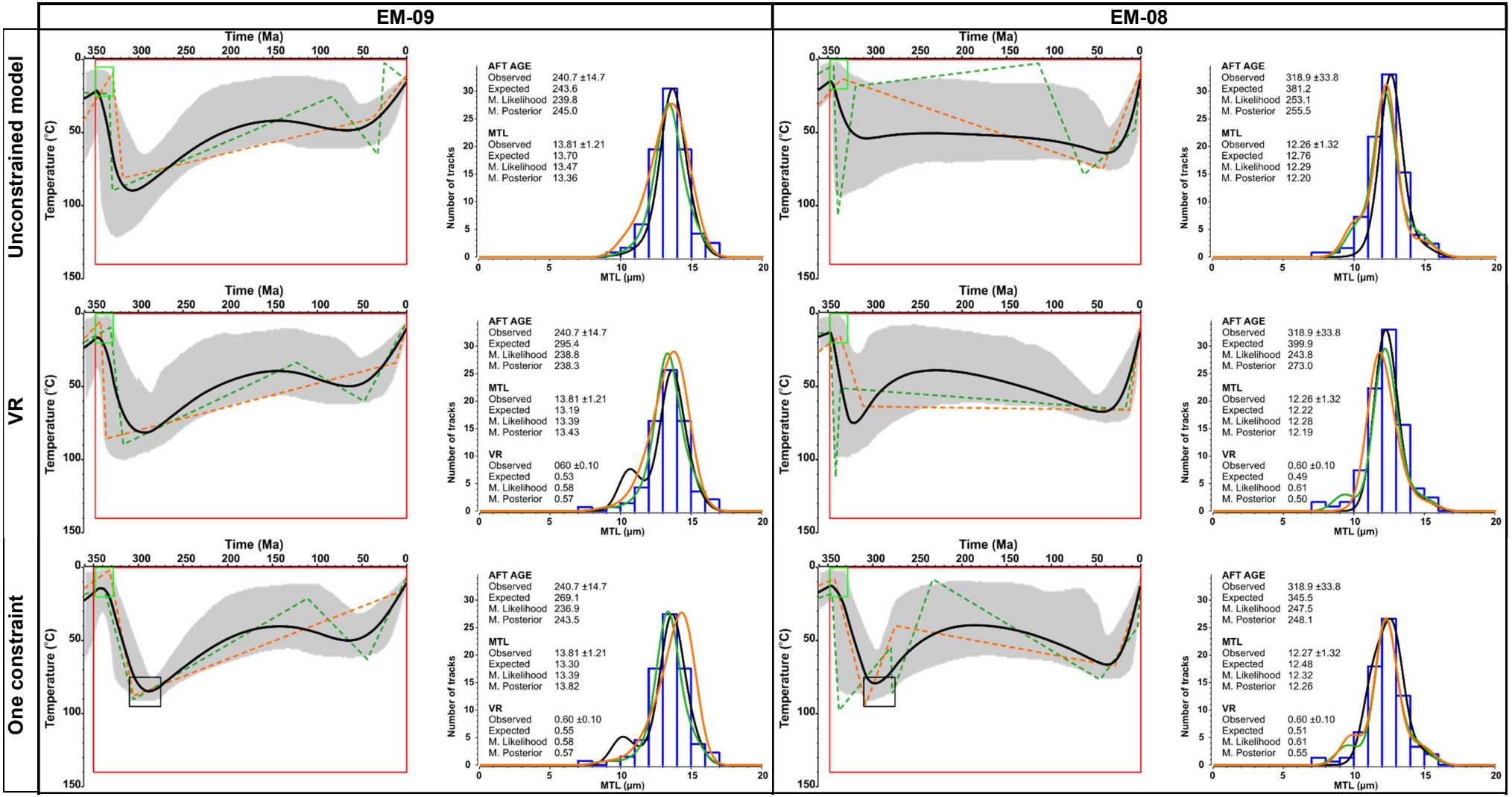

Figure 7-21: Thermal history modelling results from samples EM-09 and EM-08 from the Fife (north) region. See Figure 7-9 for definitions of all features.

7.3.5 Lanarkshire

The Lanarkshire region includes one outcrop sample (EM-013) of Viséan age and one borehole sample (Craighead-1) of Viséan age from the West Lothian Oil Shale Formation. The outcrop has an AFT central age of 195.8 Ma ±12 Ma (1σ), unimodal TLD and MTL of 13.7 ±1.3. The single sample from the borehole (CHG1) has a central age of c.90 ±7 Ma (1σ), a unimodal TLD and a MTL of 13.5 ±1.0 μm (Table 6-1 Table 6-2). All of the observed data are predicted within the analytical uncertainties and different models are in good agreement with each other (Figure 7-22), when a burial constraint is added to CHG1; however, the t-T are different than those obtained without the constraint. After being deposited, EM-013 shows heating to temperatures of c.100°C. The unconstrained Expected model suggests that the maximum palaeotemperature was reached at c.270 Ma; however, when the burial constraint is added, the fit between predicted and observed data improves and the max palaeotemperature is reached at c. 300 Ma. After burial, the sample shows a protracted cooling to present day temperatures, at a rate of 0.3°C/Myr. The CHG1 borehole sample shows heating to c.100°C until c.150 Ma, then a protracted cooling at 0.6°C/Myr. This model has a very large uncertainty, indicated by the large 95% credible interval until c.150 Ma. The additional constraints fail to improve the uncertainties.

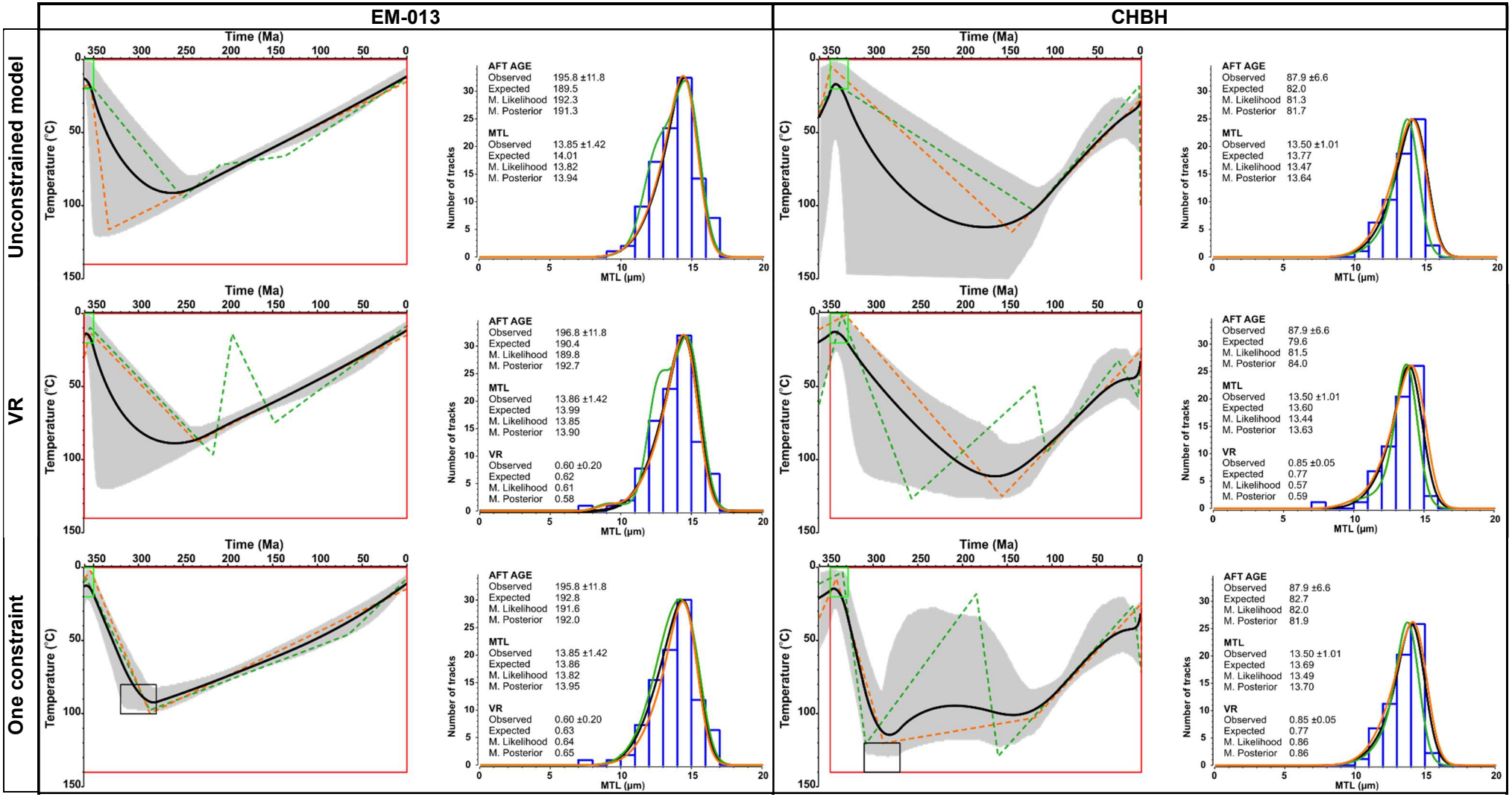

Figure 7-22: Thermal history modelling results from samples EM-13 and CHBH from the Lanarkshire region. See Figure 7-9 for definitions of all features.

7.3.6 Lothians

The Lothian region includes three outcrop samples (EM-002, EM-012, and EM-021) and one borehole sample (Cousland-6), all of Viséan age. The outcrops have AFT central ages between 225 and 270 ±c.20 Ma (1σ), unimodal TLDs and MTLs between 13.6 ±1.5 μm and 14.1 ±1.2 μm (Table 6-1 Table 6-2). From the borehole only one sample (C6BH) was retrieved; it has a central age of c.150 ±20 Ma (1σ), a unimodal TLD, with a MTL of 13.2 ±1.4 μm. The observed data have been predicted well by QTQt modelling, except for the central age in some outcrop samples. The Expected model of the outcrop samples show good agreement between predicted and observed FT data across the various modelling options (unconstrained, VR, & burial constrained) and with each other (Figure 7-23 & Figure 7-24). EM-002 and EM-012 show heating into the PAZ following deposition, reaching temperature between 70-100°C by 310 Ma (c.2-3°C/Myr), followed by cooling out of the PAZ by c.240 Ma. Both samples then remained at c.50°C until c.150 Ma; EM-002 then undergoes a period of reheating of c.10-15°C until 100 Ma then cools at a rate of c.0.55°C/Myr to present temperatures. EM-012 does not display this period of re-heating and cools from c.50°C at 100 Ma to present conditions. Following post depositional heating all models for EM-021 indicate a protracted cooling to surface temperatures at a rate of c.0.3°C/Ma. The unconstrained and VR Expected models for the borehole sample are virtually identical, showing burial until c.250 Ma to c.100°C, subsequent monotonic cooling at c.0.2°C/Myr until c.50 Ma, where the cooling rate increased to c.1°C/Myr. The additional burial constraint was added to increase the maximum temperature attained to be on par with the VR data, at a time similar to other models. The sample then cools from this higher temperature at c.0.4°C/Myr until c.250 Ma and then follows the cooling path seen in the unconstrained and VR models.

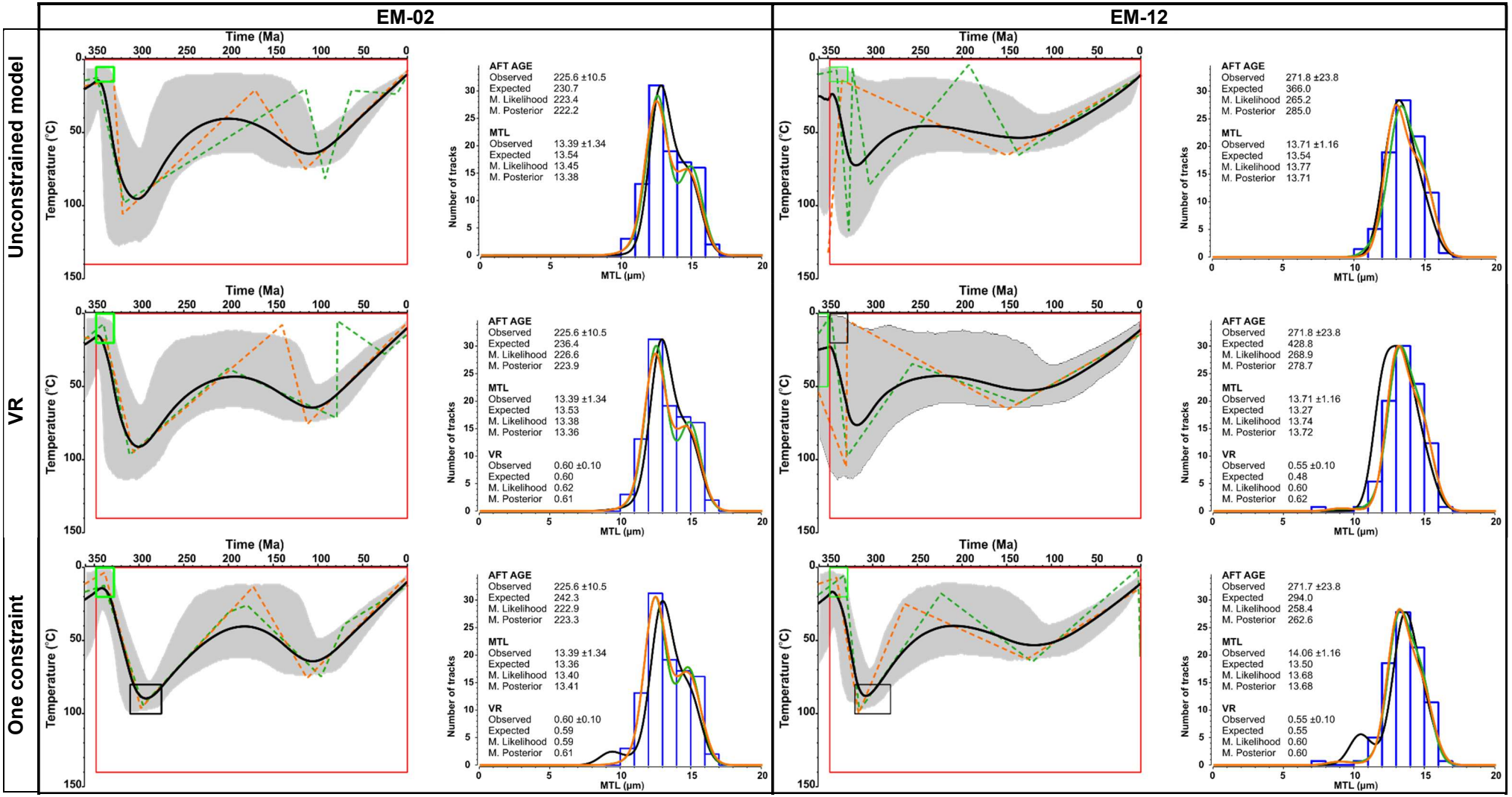

Figure 7-23: Thermal history modelling results from samples EM-02 and EM-12 from the Lothians region. See Figure 7-9 for definitions of all features.

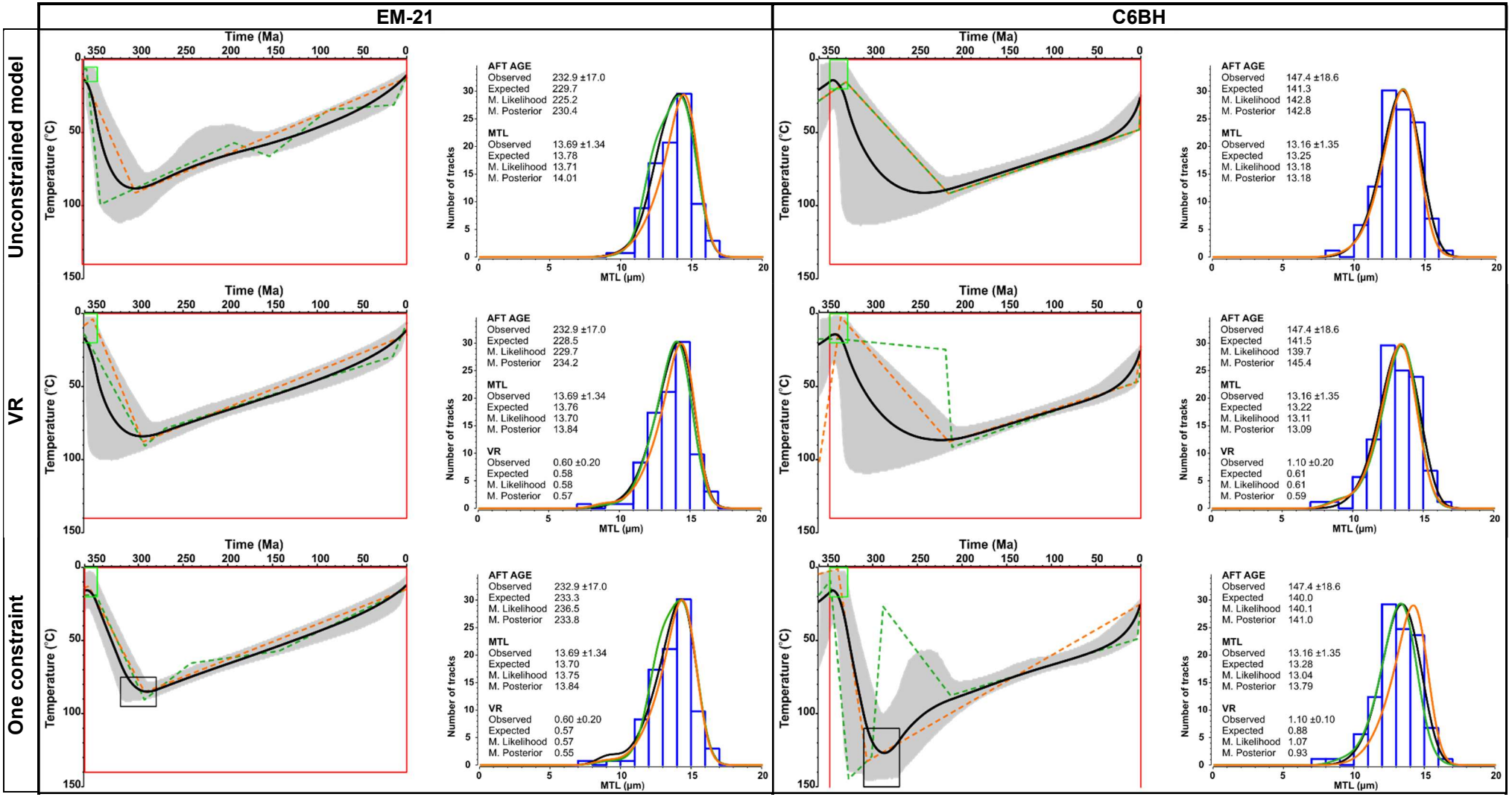

Figure 7-24: Thermal history modelling results from samples EM-21 and C6BH from the Lothians region. See Figure 7-9 for definitions of all features.

7.4 Regional summary of individual samples

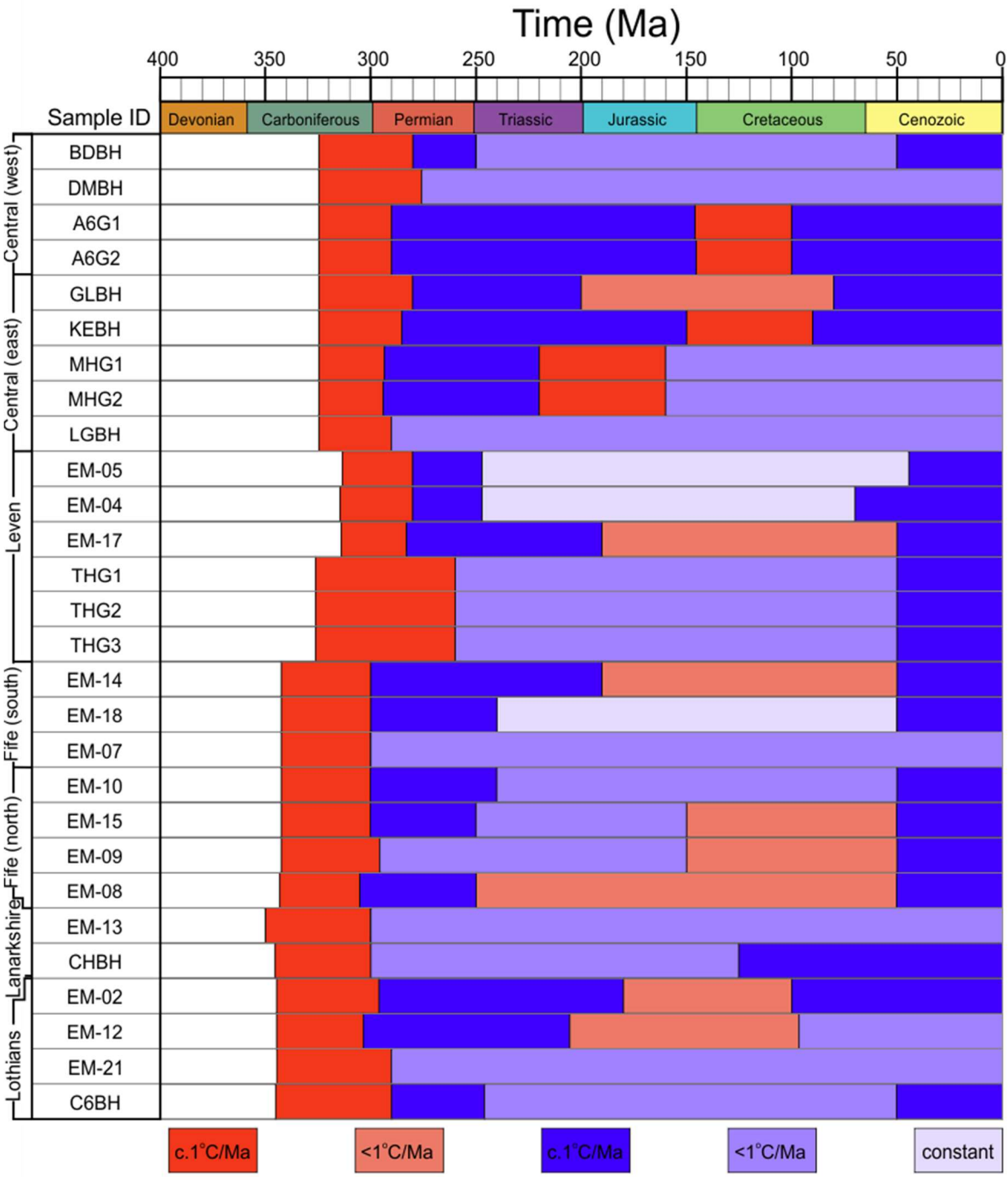

Figure 7-25: Regional summary of heating and cooling of Midland Valley samples. Individual samples arranged in the same order and regions as plotted throughout the modelling results chapter above. Dark red indicates when heating rate was in excess of c.1°C/Ma, light red indicates when heating rate was less than 1°C/Ma. Dark blue indicates when cooling rate was in excess of 1°C/Ma, light blue when cooling rate was less than 1°C/Ma. Pale blue indicates when temperature remained roughly constant.

The results of the thermal history modelling for outcrop and individual borehole samples are summarised in Figure 7-25. There are some features that are common to all or almost all samples; (i) a Carboniferous-Permian post-burial heating, (ii) a Permian-early Mesozoic rapid cooling, and (iii) an early Cenozoic rapid cooling. The first episode is present in all models and indicates that samples

experienced temperature within or hotter than the PAZ (c.60-120°C). The timing and extent of this episode vary between samples and they are influenced by the additional constraints added to the thermal histories. The second episode shows more variation between samples and although the regional trend is of cooling, the rate is variable, with some samples showing initial moderate rate of cooling followed by a slow rate or constant temperature (BDBH, EM-05), whereas others are characterised by monotonic cooling (EM-13). Some samples also show a Jurassic and/or Cretaceous reheating episode (GLBH, EM-17), though this often results in a small increase in temperature (<c.10°C), outside the temperature sensitivity of AFT analysis and is therefore poorly constrained by the data. Samples from the Meadow Hill borehole (MHG1, MHG2) show a heating event in the Triassic/Jurassic; however, the observed data are not reproduced well by the model suggesting that this heating event may not be accurate. The third episode, the rapid Cenozoic cooling, is present in all samples except DMBH, LGBH, EM-07, EM-13, and EM-21, which display a protracted cooling from their maximum palaeotemperature.

7.5 Multi-sample approach

When multiple samples are collected from a borehole (i.e., Thornton-1) they can be modelled together, producing a more robust thermal model due to their clear temporal, spatial, and temperature relationship. The combination of multi-sample data has the effect of lessening the influence of any outliers and returning a thermal history that is more consistent with the data, as a package. A great strength of the QTQt software is that multi-sample modelling is not restricted to vertical profiles collected from a borehole but can also be applied to a series of outcrop samples with a range of elevations, or by combining outcrop and borehole samples making a pseudo vertical profile. This technique can be applied providing the samples are collected in close proximity to each other (<c.10 km), not dissected by any major faults or other structural feature that would influence their thermal regime. Usually, this multi-sample approach is used when samples from a close-by region share similar thermal histories, like in this case study. A great strength of taking this approach, is that QTQt can allow the temperature offset between samples (geothermal gradient) to vary through time. By doing so, a wealth of information can be gathered about the pseudo-profile, including its paleo-geothermal gradient and how this varied through time. Geothermal gradients are a crucial parameter to estimate burial depth and exhumation (both rate and amount); however, their value is often assumed, depending on the geological setting, or a temporally and spatially constant average is applied. Given the variety of lithologies present in the Midland Valley and its complex geological

history, as highlighted in Chapter 2, it would be an over-simplistic assumption for the geothermal gradient to have remained constant through time; therefore, allowing this parameter to vary, gives an extremely valuable insight into the thermal history evolution of the region. Due to the increased amount of data used in the multi-sample approach the burn-in and post burn-in were adjusted to minimum values of 100,000 and 500,000 iterations; post burn-in iterations often exceeded 1,000,000.

7.5.1 Central region

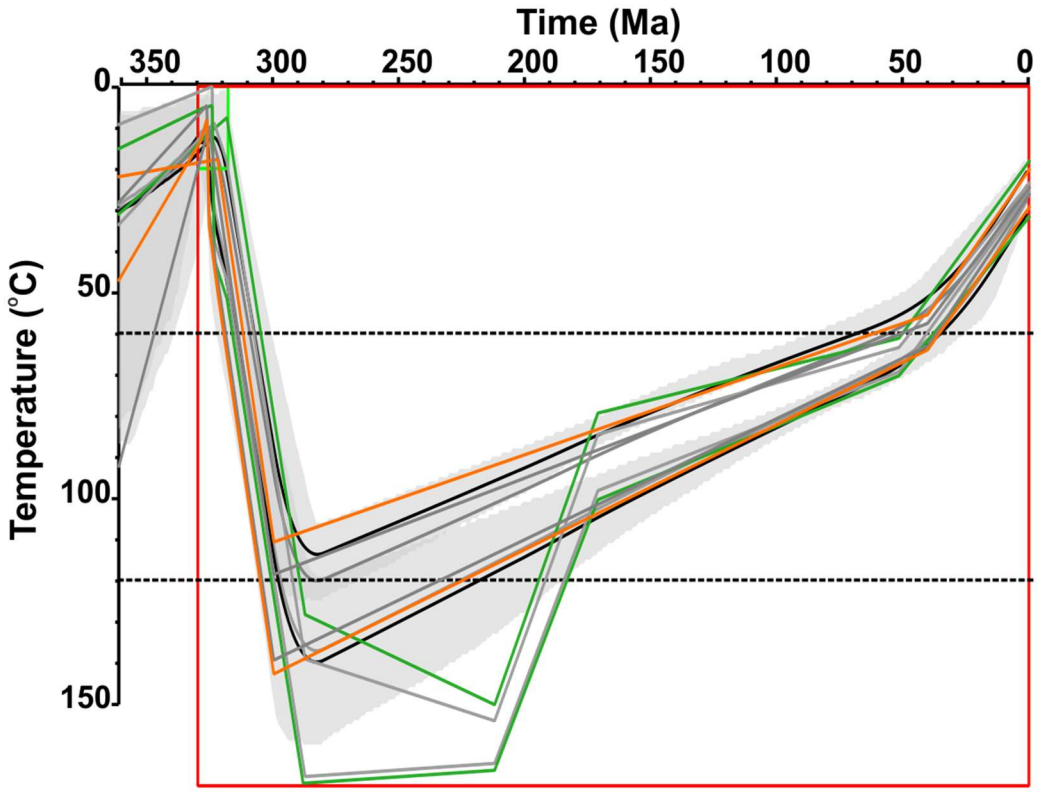

Figure 7-26: A multi-sample thermal history model for the Central region of the Midland Valley. This model was produced using samples from the Airth 6 (A6BH), Bandeath (BDBH), and Dunmore Moss (DMBH) boreholes. See Figure 7-9 for definitions of all features.

Figure 7-26 shows the resulting thermal histories for multi-sample modelling of the Central region. Samples used in this model are all from boreholes; they were selected on the bases of their location and depth, to cover the widest range possible. The models (Expected, Max. Likelihood, Max. Posterior, Figure 7-9) show good agreement among each other. They all indicate, irrespective of sample depth, an initial heating to maximum paleo-temperatures in excess of c.110°C at c.280Ma (c.3-5°C/Myr). Following the heating episode, the Expected and Max. Posterior models indicate cooling at a constant rate of c.0.3°C/Myr until c.50 Ma, followed by an increased rate (c.1°C/Myr) to the present day. The Max. Likelihood model shows a slight different scenario, and it suggests that the samples reached temperatures much greater than the sensitivity of AFT analysis. The post-

heating history of this region according to the Max Likelihood model was characterised by a period of rapid cooling at a rate of 1-2°C/Myr until c.200 Ma. From there, the model follows the same cooling path as the Expected and Max. Posterior models. It is worth noticing that the divergence among the models occurs at temperatures hotter than the sensitivity of the AFT thermochrometer and therefore it should be treated with caution.

7.5.2 Leven

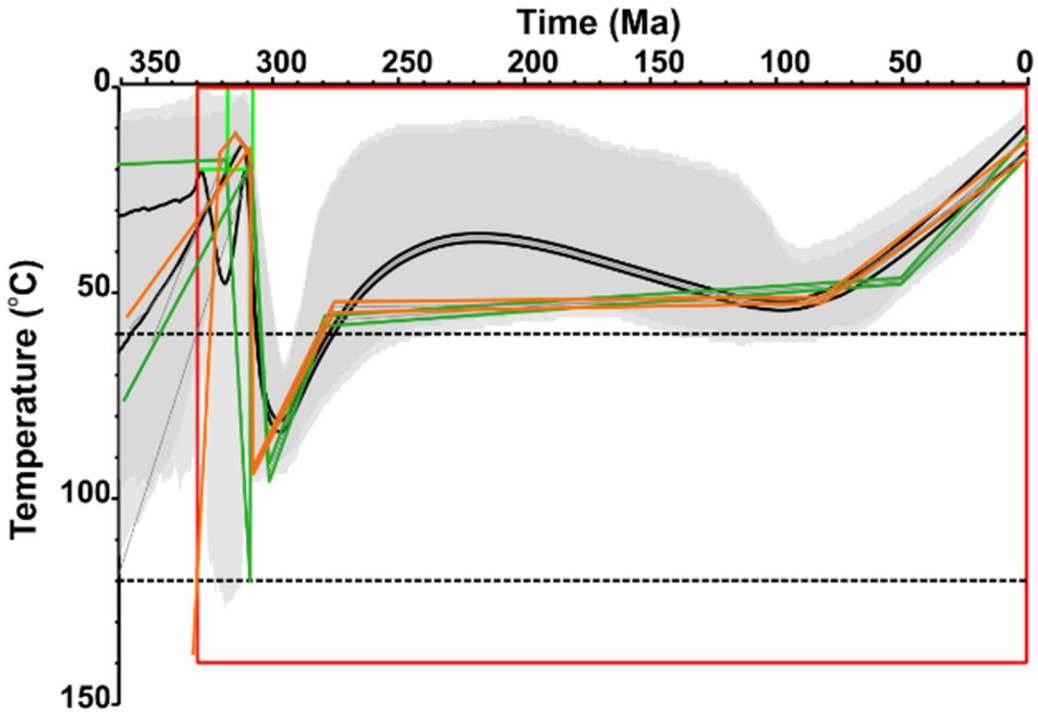

Figure 7-27: A multi-sample thermal history model for the Leven region. This model was produced using samples EM-005, EM-004, & EM-017; the only constraint used is the stratigraphic age of the samples. See Figure 7-9 for definitions of all features.

Samples collected in the Leven syncline region were modelled in two different ways, initially only the outcrop samples were considered together (Figure 7-27); subsequently, the vertical profile Thornton-1 was added (Figure 7-28). Figure 7-27 shows the results of the outcrop profile thermal history model, which has been produced without any additional confining constraints. Here, the Expected, Max. Likelihood, and Max. Posterior models of the outcrop samples show excellent agreement; the discrepancies occur above the PAZ, in a time-temperature space poorly constrained by the data. The models show rapid heating following deposition into the basin, reaching c.90°C at c.300 Ma (c.2.5°C/Myr). This was followed by a period of cooling, exiting the PAZ at c.270 Ma. From here, the expected model continues to cool to a temperature of c.40°C at 230 Ma then slowly reheats to 50°C at 90 Ma. This is followed by the final cooling pulse to present-day temperatures at a rate of c. 0.7°C/Myr. The Max. Likelihood and Max. Posterior display no evidence of the Mesozoic cooling and

re-heating seen in the expected model, instead they remain at a roughly constant temperature until the final cooling pulse, which occurs at c.80 Ma in the Max. Likelihood model and at c.50 Ma in the Max. Posterior model.

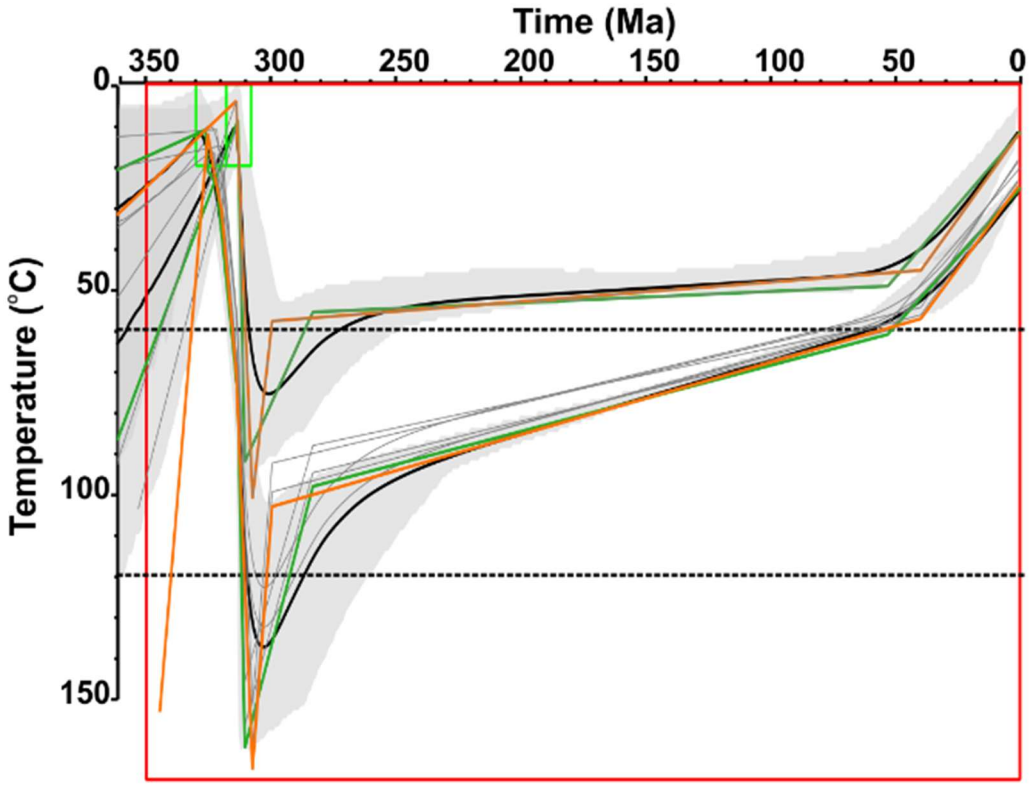

Figure 7-28: A multi-sample thermal model for the Leven region including Thornton-1 borehole samples. This model was produced using the outcrop samples highlighted above (Figure 7-27) along with those from the Thornton-1 borehole to increase the depth range covered by the samples. See Figure 7-9 for definitions of all features.

Figure 7-28 shows the thermal histories of the Leven syncline region with the addition of the Thornton-1 borehole samples; the models have no additional constraints, apart from the stratigraphic age of the samples. When the borehole is added, the Figure 7-27 the Expected model of the outcrop samples no longer requires Mesozoic cooling and reheating seen in Figure 7-27; all models concur in determining the onset of the latest cooling episode at c.60 Ma, with a cooling rate of c.1°C/Myr. The deeper, borehole samples show a similar cooling path with rapid heating through the PAZ at c.300 Ma at a rate of c.4.5°C/Myr. The samples then cool at a rate of c.1°C/Myr to 100°C at c.250 Ma. The samples then cool continuously through the Mesozoic reaching the low temperature limit of the PAZ at c.60 Ma. From here the samples cool at a rate of c.1°C/Myr to present-day temperatures. In the case of the Leven region, it is important to notice how the temperature interval between the outcrop and borehole samples vary with time, being the widest in the Carboniferous, when the rocks

reached their maximum palaeotemperatures, and the smallest in the Cenozoic. This variation suggests a change in palaeogeothermal gradient, which is discussed in section 7.7.

7.5.3 Fife (south)

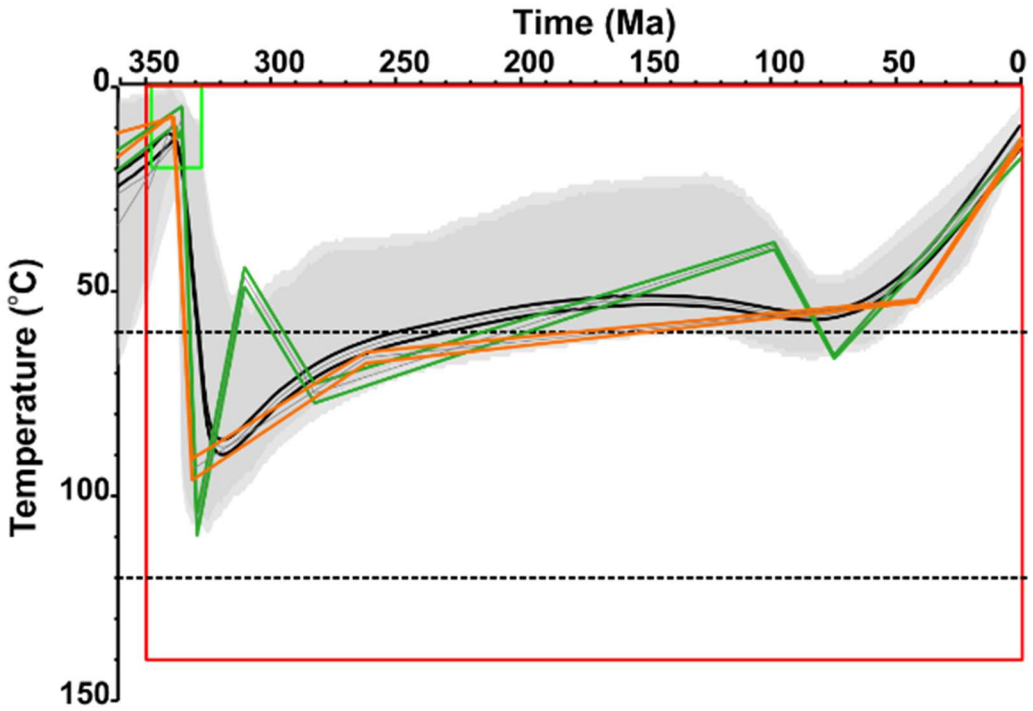

Figure 7-29: A multi-sample thermal history model for the Fife (south) region of the Midland Valley. This model was produced using samples EM-14, EM-18, and EM-07. See Figure 7-9 for definitions of all features. See Figure 7-9 for definitions of all features.

The thermal histories for the Fife (south) region have been produced using only outcrop samples, without any additional confining constraints. The Expected models suggest the samples were heated rapidly after deposition into the basin, reaching maximum paleo-temperatures of c.90°C at c.320 Ma (c.2.5°C/Myr); they were then cooled out of the PAZ at c.250 Ma (c.0.8°C/Myr). The models then remain at temperatures just cooler that the PAZ until c.60 Ma, when the most recent cooling pulse begins, bringing the samples to present day temperature at a rate of c.1°C/Myr. The Fife (south) thermal histories are similar to the individual models produced for the region, with narrower 95% credible intervals, indicating less uncertainty associated with the t-T paths. The Max. Posterior is very similar to the Expected model, whereas the Max. Likelihood shows a little more variability. This model suggests a period of rapid cooling and reheating occurred prior to the sample exiting the PAZ at c. 230 Ma and a period of reheating between c.100 and 70 Ma of c.20°C, which was followed by the Paleogene cooling pulse seen in other models (c.1°C/Myr).

7.5.4 Fife (north)

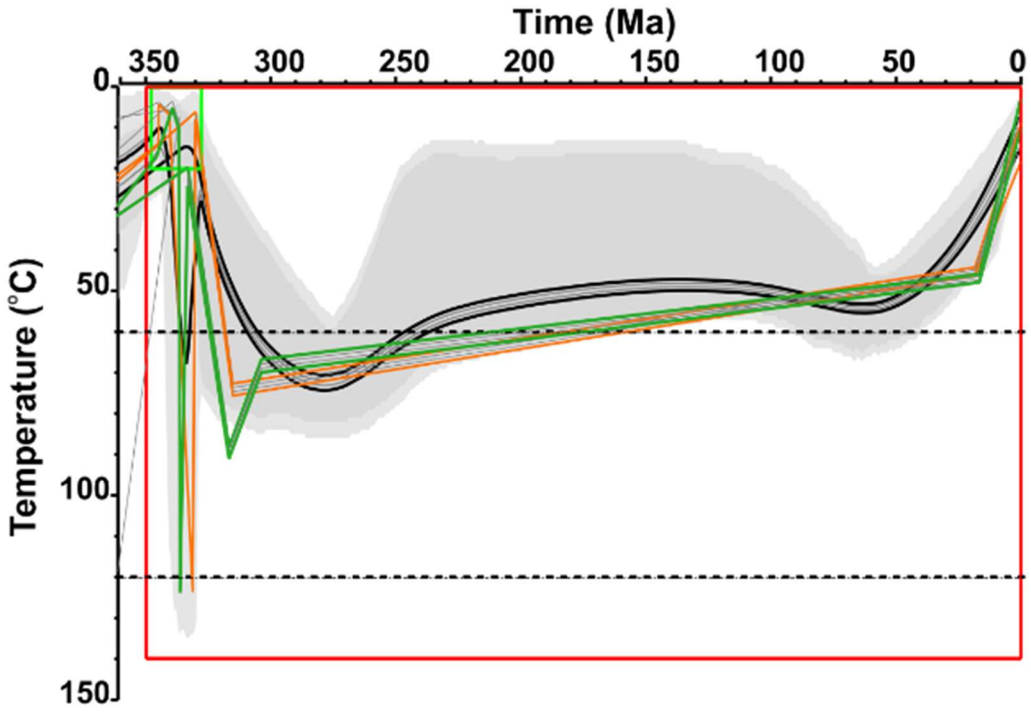

Figure 7-30: A multi-sample thermal history model for the Fife (north) region of the Midland Valley. This model was produced using samples EM-010, EM-015, and EM-009. See Figure 7-9 for definitions of all features.

Samples from Fife (north) have been modelled together without any additional confining constraints (VR or post burial constraint) to produce the thermal histories in Figure 7-30. The Expected models show post depositional heating at a rate of c.1.5°C/Myr. Maximum paleo-temperatures of 70-80°C were achieved at c.280 Ma; cooling out of the PAZ by c.250 Ma followed. The models then indicate a period of very slow cooling of only 10°C until 100 Ma. As in the individual models, the multi-sample Expected model suggests a period of very minor reheating in the Cretaceous, followed by a Paleogene cooling pulse from c.50°C to present day temperatures, at a rate of c.1°C/Myr. The combined sample model produces a similar thermal history to that of the individual models but with a greater degree of certainty, expressed by the narrower 95% credible interval envelope, especially around the initial heating and final cooling stages. The Max. Likelihood suggest that the maximum paleo-temperature achieved was greater, reaching c.90°C; this was followed by a period of rapid cooling to c.70°C at 300 Ma, with the samples exiting the PAZ around c.250 Ma. Slow cooling followed until the final pulse which in this model occurs at c.25 Ma. The Max. Posterior model follows the same cooling path; however a lower maximum paleo-temperature peak is suggested.

7.5.5 Lanarkshire

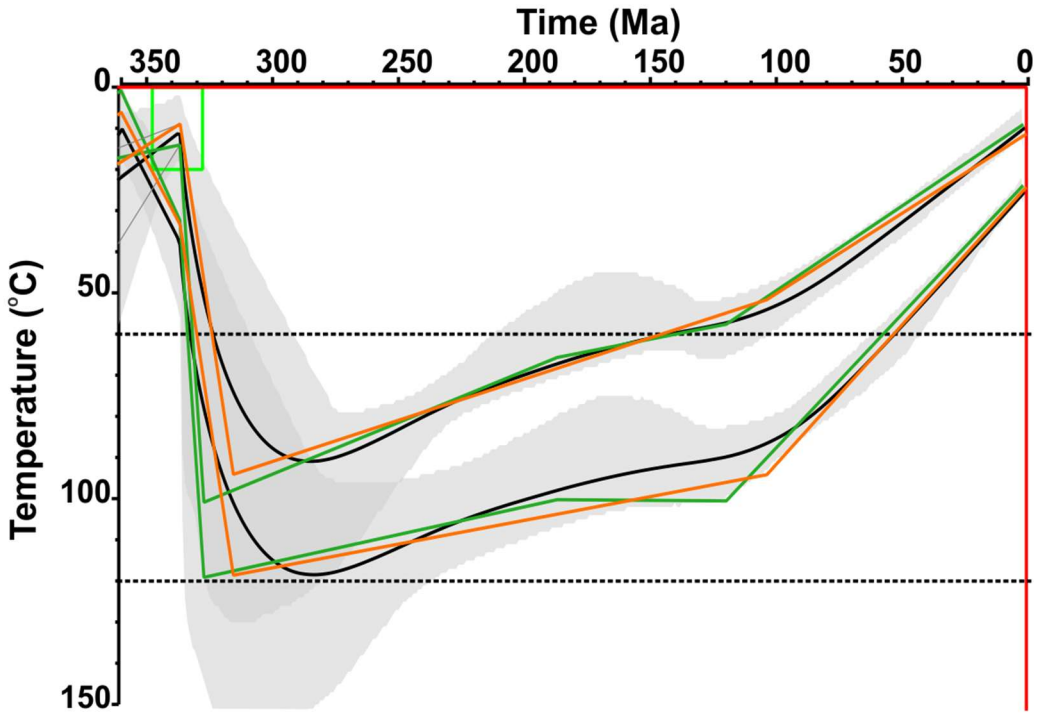

Figure 7-31: A multi-sample thermal history model for the Lanarkshire region of the Midland Valley. This model was produced using samples EM-013, EM-021, and the Craighead borehole (CHBH). See Figure 7-9 for definitions of all features.

The thermal histories for the Lanarkshire region (Figure 7-31) were created combining both outcrop and borehole samples without any additional constraints. The models show heating to maximum paleo-temperatures of c.90°C (outcrop) and c.120°C (borehole) at c.300Ma (c.2°C/Myr). This is followed by cooling to c.100 Ma at a rate of c.0.2°C/Ma, with the outcrop sample exiting the PAZ around c.140Ma. Following this, the rate of cooling increases to c.0.4°C/Ma to reach present day temperatures, with the borehole sample exiting the PAZ around 50 Ma. The thermal histories show good agreement between the Expected, Max. Likelihood, and Max. Posterior models. As in other multi-sample models, there is a reduction in the uncertainty expressed as a narrowed credible interval window, however uncertainty is still relatively large around the maximum palaeotemperature reached by the samples.

7.5.6 Lothians

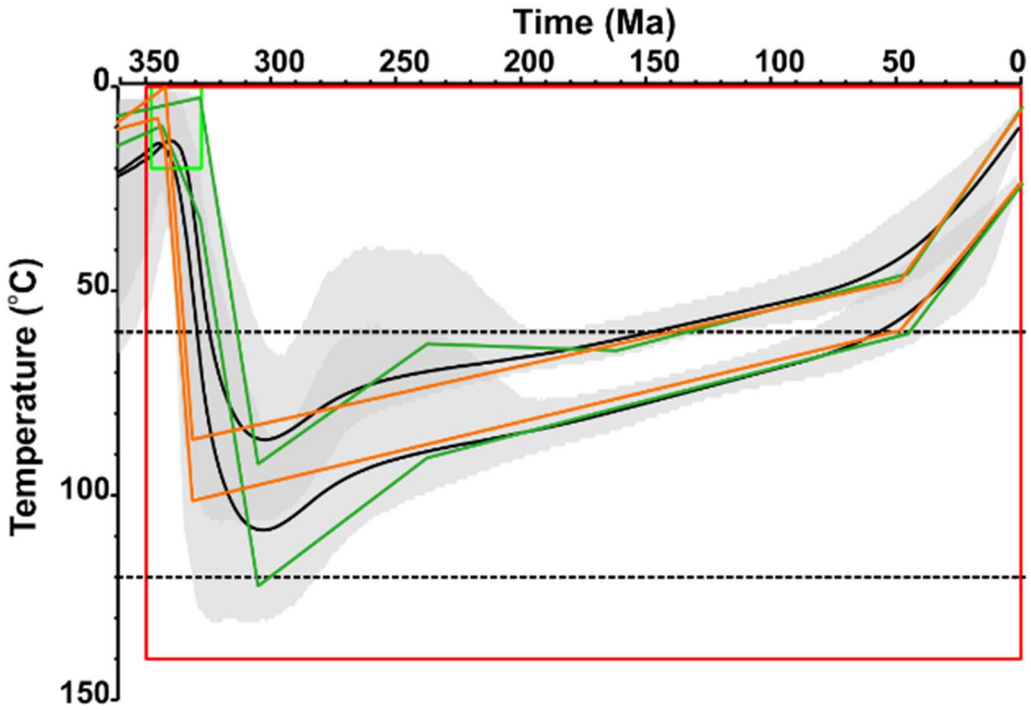

Figure 7-32: A multi-sample thermal history model for the Lothians region of the Midland Valley. This model was produced using samples C6BH and EM-02. See Figure 7-9 for definitions of all features.

Figure 7-32 shows the resulting thermal histories for the Lothian region, combining both outcrop and borehole samples without any additional constraints. The outcrop models (upper lines) show heating to maximum paleo-temperatures of c.90°C at c.300Ma (c.1-2°C/Myr). The Expected and Max. Likelihood models suggest this is followed by two periods of cooling, the first of which lasted until 270-250 Ma and proceeded at a rate of c. 0.5°C/Myr. The second period lasted until between 60-50 Ma and was at a more subdued rate (c.0.15°C/Myr). From here, the samples cooled at a rate of c.1°C/Myr to their present-day temperature. The borehole models (lower lines) show a similar t-T pathway to that described above, only at greater temperature and rate (c.3°C/Myr), as would be expected for deeper samples. The Expected thermal history produced for the borehole here has a strong similarity to the one produced when the sample was modelled individually with additional constraints, with the only subtle difference in the maximum paleo-temperature attained. The profile model above does have a wide 95% credible interval around the maximum paleo-temperature, indicating that the model would allow a greater maximum temperature than displayed by the Expected model, as indicated by the Max. Likelihood model.

7.6 Regional summary of combined samples

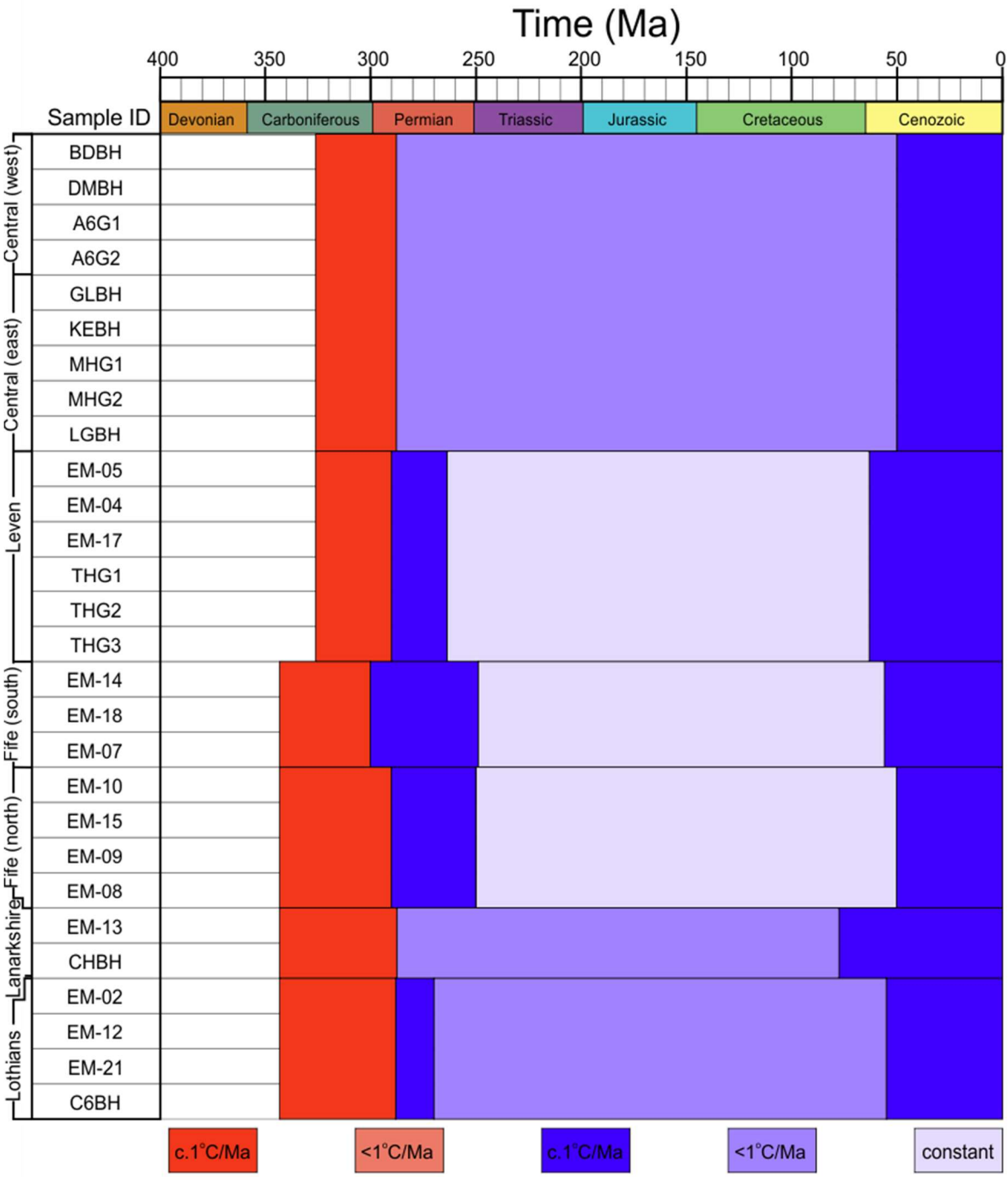

Figure 7-33: Regional summary of heating and cooling of combined Midland Valley samples (multi-samples approach). Arranged in the same order and regions as plotted throughout the modelling results chapter above. Dark red indicates when heating rate was in excess of c.1°C/Ma, light red indicates when rate was less than 1°C/Ma. Dark blue indicates when cooling rate was in excess of 1°C/Ma, light blue when cooling rate was less than 1°C/Ma. Pale blue indicates when temperature remained at a steady state.

Results for the thermal models produced using the multi-sample approach are shown in Figure 7-33. In general, there is a broad similarity between the multi- and individual sample results; the thermal histories still show three episodes, a Carboniferous-Permian post-burial heating, a Permian-Mesozoic cooling, and a Cenozoic more rapid cooling. Again, the first episode is present in all models

and indicates that samples entered and potentially exceeded the PAZ (c.60-120°C) following burial in the Midland Valley; all regions reached their maximum palaeotemperature in the Carboniferous. The second episode shows less variation between samples and regions than it did when modelling individually. The regional trend is still of cooling, but the rate is spatially and temporally variable (Figure 7-33). The Expected model from the outcrop only model from the Leven region still suggests the potential for reheating in the late Mesozoic, however the Max. Likelihood and Max. Posterior do not require this to fit the observed data; once combined with the borehole samples, this reheating is lost. Multiple sample models from the Fife region also indicate a slight reheat towards the end of the Mesozoic i.e., the Expected model from Fife (north) and the Max. Likelihood model from Fife (south), however these occur out with the sensitivity range of AFT analysis and thus are poorly defined. The third episode, the rapid Cenozoic cooling, is now present in all models though there is a slight variation in the onset timing of this between the regions.

7.7 Palaeogeothermal Gradient

An estimate of the geothermal gradient is necessary to constrain the amount of burial and exhumation that has occurred over time in a region of interest. This parameter is often assumed, based on either some prior knowledge, an estimate taken from a region with a similar geological history or, failing that, a 25°C/km assumption is often applied. An investigation into the geothermal potential within the Midland Valley by Browne *et al.* (1987) revealed the geothermal gradient ranged between c.20-30°C/Km with an average value of 22.5°C/Km. However geothermal gradients may vary over time, especially in area with a complex geological history such as the Midland Valley (highlighted in Chapter 1 and 2 in this thesis). Applying the multi-sample approach to thermal modelling allows for the evolution of the geothermal gradient to be calculated by QTQt. In practise, the variation of the geothermal gradient is investigated by allowing the offset temperature to vary between the samples combined to form a pseudo vertical profile. The geothermal histories resulting from the multi-sample thermal models produced above can be seen in Figure 7-34.

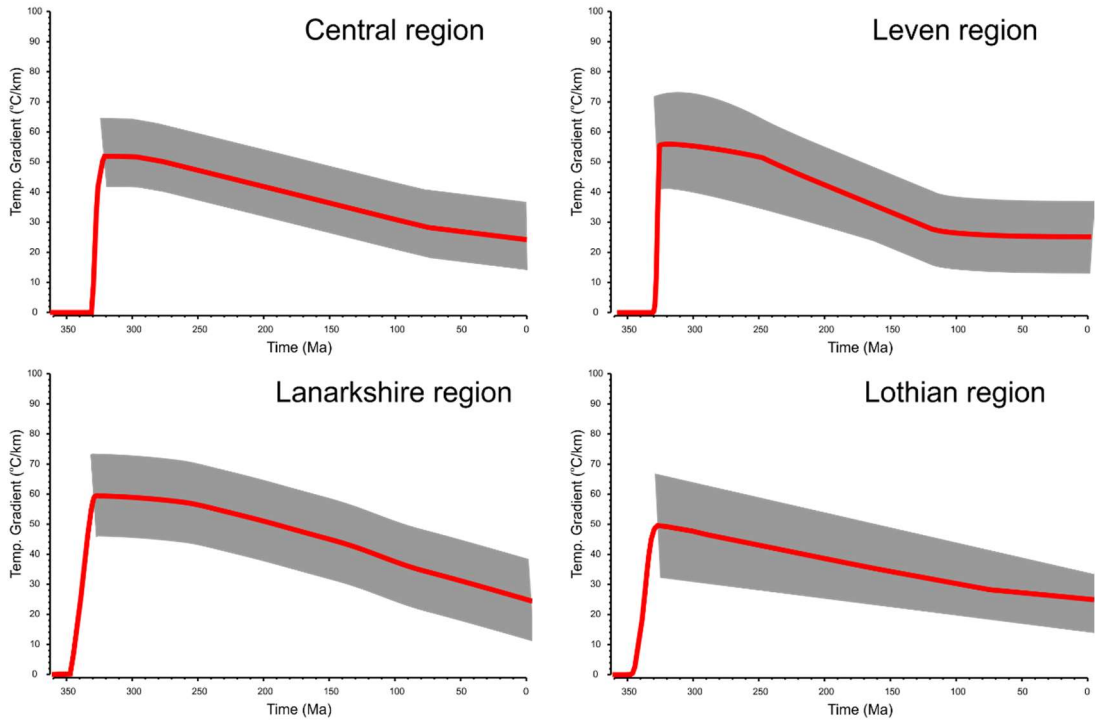

Figure 7-34: Geothermal gradients from multi-sample thermal models. QTQt modelled geothermal gradients (red line) and 95% credible interval uncertainty (grey) for four pseudo-vertical profiles across the Midland Valley.

The models show a general agreement between the four regions sampled across the Midland Valley, with all models requiring a higher geothermal gradient in the past that declines over time to one that is similar to that measured by Browne *et al.* (1987). A higher palaeogeothermal gradient has also been suggested for thermal history reconstructions in Carboniferous basins in England (Green *et al.* 1995; Hillis *et al.* 2008), potentially suggesting a regionally high geothermal gradient during this time. For all four regions, the highest geothermal gradient is estimated to have occurred at the time of deposition, in the Carboniferous, with a relaxation of the isotherms, thereafter. For the same time intervals, the values of the geothermal gradient are potentially spatially variable, with the Leven region maintaining a higher geothermal gradient into the early Mesozoic. However, as theses samples were not collected from single borehole vertical profiles, the palaeogeothermal gradients should be taken with caution as the uncertainty surrounding these modelled geothermal gradients (grey envelope) is c.±20°C.

Chapter 8 Burial and exhumation history of the Midland Valley

The AFT data collected from the Midland Valley of Scotland (Chapter 6) have been used to produce thermal histories, which reveal multiple episodes of heating and cooling, from the Carboniferous burial until recent times (Chapter 7). This chapter discusses the results obtained directly from AFT analysis and the derived thermal histories. Previous investigations have suggested differing evolutionary scenarios (Duddy *et al.* 1992; Vincent *et al.* 2010). The AFT data presented in this investigation offers an alternative burial and exhumation history for the Midland Valley, which has implications on the extent of burial under of Mesozoic successions and the petroleum prospectivity of the region.

8.1 Combining forward and inverse modelling

Previous thermal and burial history investigations in the Midland Valley used VR, limited AFT data and modelling software to construct time-temperature models, with contrasting results (Figure 7-1). The model of Duddy *et al.* (1992) for the Firth of Forth 1 well indicates rapid burial reaching maximum palaeotemperatures by the end of the Carboniferous, follow by protracted cooling to the present-day. For wells in the eastern onshore Midland Valley, Vincent *et al.* (2010) suggest a late Carboniferous uplift associated with the Variscan orogeny, followed by sedimentation from the Permian to Paleogene where maximum palaeotemperatures were reached; at this point, uplift associated with the proto-Icelandic plume (White 1988) brought the samples to or near their present positions. The thermal histories consistent with these two competing scenarios were forward modelled in QTQt to obtain synthetic observed AFT data that could be compared to those obtained in this study. The synthetic observed AFT ages and TLD were then used as input data in inverse mode, to compute thermal histories as shown in Figure 7-2, Figure 7-3, Figure 7-4, and Figure 7-5. This procedure, rarely performed or reported in other thermochronological investigations, has two main objectives; 1) to test the ability of QTQt to reproduce, in inverse mode, the thermal histories used as input in the forward model, with important implications in terms of the unicity of the thermal histories ‘found’ by QTQt on the bases of the AFT data; 2) to investigate the role of independent constraints added to the input data, to increase the accuracy of the thermal histories and/or reduce their associated uncertainties.

The results of this forward-inverse coupling exercise have brought important conclusions, both in terms of the specific question here investigated: are the scenarios proposed in the literature consistent with the AFT data presented in this thesis? and, in general, on the use of forward and inverse modelling in fission track thermochronology. Below, the main observations are summarized:

- The AFT data, in particular the TLD, are capable of distinguishing the two scenarios proposed in the literature for the post-depositional evolution of the Midland Valley basin (Duddy *et al.* 1992; Vincent *et al.* 2010) (Figure 7-1).
- The AFT data produced in this investigation are similar, for samples collected at comparable depths, to the synthetic AFT data derived from the forward model of the thermal histories proposed by Duddy *et al.* (1992) (Figure 7-2 and Figure 7-3).
- The thermal histories from borehole samples consistent with the evolutionary scenario proposed by Vincent *et al.* (2010) result in a clear bimodal track length distribution and in ~40 Ma AFT central ages, neither of which are found in the samples analysed during this project (red line in Figure 7-4 and Figure 7-5).
- The combination of forward and inverse modelling has indicated that QTQt is not biased in coupling AFT data with certain thermal histories, but it is capable of returning an accurate solution when synthetic data are modelled in inverse mode.
- Adding independent constraints to the AFT data when QTQt is used in inverse mode, can help to improve the accuracy and reduce the uncertainties of the obtained thermal histories. In cases where the true thermal histories are not known, it is highly recommended to explore the effects of adding constraints, following unconstrained inversions, to investigate their effect.

Modelling results produced in this investigation (Chapter 7) show that the thermal histories can be sub-divided into three episodes: 1) Carboniferous-Permian post-depositional heating, 2) Permian-Mesozoic cooling, 3) Cenozoic cooling. Although the AFT data from this investigation produce thermal models that are similar to those retrieved from Duddy *et al.* (1992), the exhumation history of the samples analysed in this study shows more variability than that predicted for the Firth of Forth 1 borehole. All thermal histories indicate that maximum palaeotemperatures were attained in late Carboniferous-early Permian concurring with Duddy *et al.* (1992). Also, when modelled individually, some samples display a post-Carboniferous monotonic cooling to their present position. However, other models show multiple cooling rates and, in some cases, episodes of re-heating. When modelled together, by region (section 7.5), all thermal histories show an early Cenozoic rapid cooling event that is not included in the thermal histories from Duddy *et al.* (1992).

The Permian-Mesozoic section in the Vincent *et al.* (2010) models display continuous sedimentation, which proceeded until the Paleogene where maximum palaeotemperatures were attained, prior to uplift (Vincent *et al.* 2010). Although the AFT data from this project show the opposite trend, indicating cooling, rather than heating, they are consistent with the accelerating early Cenozoic cooling rate.

The comparison above clearly indicates that the model presented here for the evolution of the Midland Valley basin is a third scenario, which shares characteristics with those in the existing literature, but it does not entirely agree with either.

8.2 Main thermal history episodes

As mentioned above, the thermal histories of the analysed samples in the Midland Valley can be subdivided into three episodes, spanning from Carboniferous burial to the present day: 1) Carboniferous-Permian heating; 2) Permian-Mesozoic cooling; 3) Cenozoic cooling. The regions highlighted in section 7.3 are here compared and contrasted to determine the overall thermal and exhumation history of the Carboniferous central and eastern Midland Valley. Figure 8-1 shows the result of regional profile thermal models created in this thesis and are discussed in the following sections.

Figure 8-1: Multi-sample profile thermal history models and their regional location (next page). Samples belonging to each region shown in black boxes (Chapter 7 section 7.3). Models include Expected model (black) and its 95% credible interval (grey), Max. Likelihood model (green), and Max. Posterior model (orange).

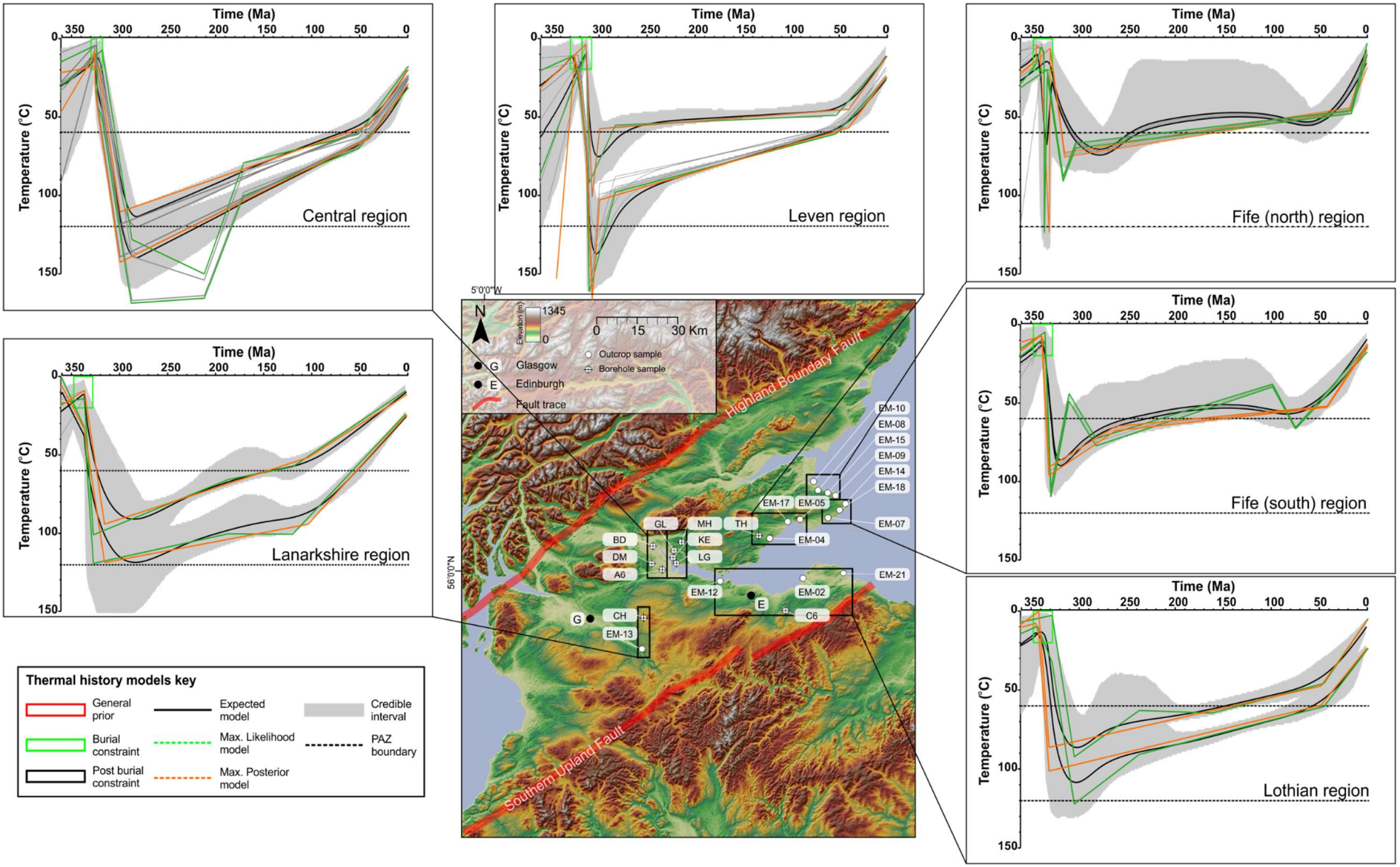
Time (Ma)
Temperature (°C)
Central region
Leven region
Fife (north) region
Lanarkshire region
Fife (south) region
Lothian region
Thermal history models key
General prior
Burial constraint
Post burial constraint
Expected model
Max. Likelihood model
Max. Posterior model
Credible interval
PAZ boundary
Glasgow
Edinburgh
Fault trace
Outcrop sample
Borehole sample
Highland Boundary Fault
Southern Upland Fault
GL
MH
TH
KE
LG
BD
DM
A6
CH
EM-13
EM-12
EM-17
EM-05
EM-04
EM-10
EM-08
EM-15
EM-09
EM-14
EM-18
EM-07
EM-21
EM-02
C6

8.2.1 Carboniferous-Permian heating

As highlighted in Chapter 7 section 7.2.2, the pre-depositional history of the samples analysed in this investigation cannot be unravelled from the AFT data alone; zircon and apatite U-Pb ages were used to provide such information (see Chapters 4 & 5). However, as demonstrated by the investigation into the effect of the pre-depositional history on the post-depositional thermal history (Chapter 7 section 7.2.2), the most important aspect in terms of modelling the data is that the pre-depositional T-t space is allowed to be sampled, whether its boundaries are known or not. This allows QTQt to include the possibility that some AFT data may be inherited from the pre-depositional history. The results from all models, both individual and profiles (Figure 8-1), indicate that all samples underwent heating immediately after deposition; it is during this first episode that they reached their maximum palaeotemperature. The timing and magnitude of this heating varies between samples and locations. When the data are modelled without any constraints, the maximum palaeotemperature is not well defined, in particular for DMBH, KEBH, and EM-12. However, the addition of post burial constraints helps to improve the fit of the observed and predicted data, providing a more robust thermal history. The most precise estimate of maximum palaeotemperatures is seen when the multi-sample approach is taken, both on profiles and across region (Figure 8-1). Using this approach, all thermal histories show that the samples may have experienced temperatures hotter than the PAZ, reaching their maximum palaeotemperature during the late Carboniferous–early Permian. Borehole samples show the highest rate of heating, with temperatures from the Central and Leven regions increasing by c.3-5°C/Myr, and c.2-3°C/Myr in Lanarkshire and Lothian regions. Outcrop samples heating rates are similar across all regions, at c.2°C/Myr, except for the Fife (north) region, where heating is slower, at c.1.5°C/Myr. Moving from Fife (north) to Fife (south), to Leven, the maximum palaeotemperatures increase, reaching the highest value in the Leven syncline. However, AFT central ages in the core of the Leven syncline are older than those collected from the syncline limbs and are close to depositional age of the sediments (Figure 6-21).

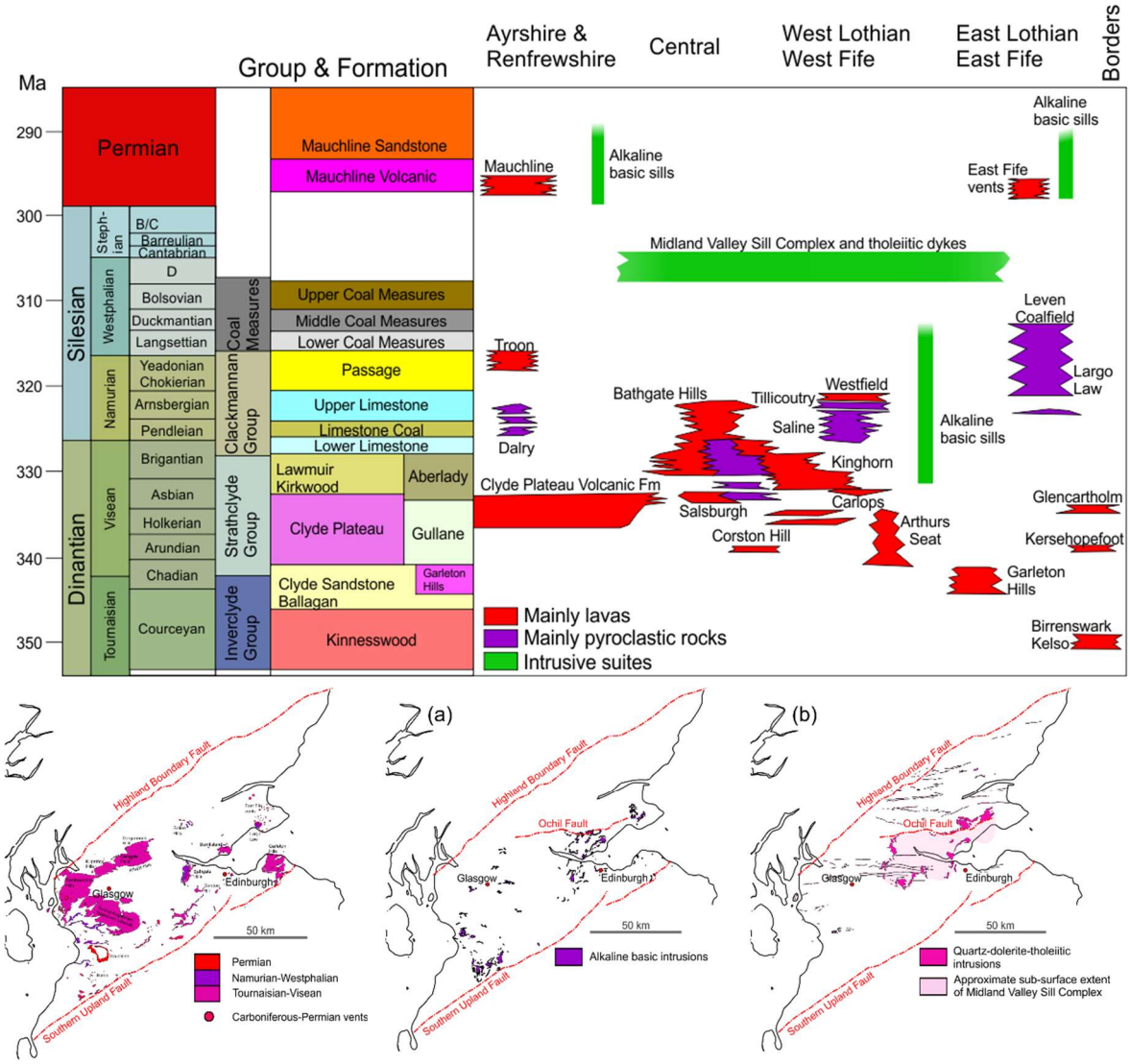

Figure 8-2: Summary for Carboniferous volcanic activity across the Midland Valley. These images were shown in Chapter 2 and are placed here again as a reminder of the timing and location of some of the main intrusive and extrusive igneous activity in the Midland Valley during the Carboniferous.

This post burial heating was most likely due to a combination of burial, as the region developed under transpressional-transtensional movement along the Highland Boundary and Southern Upland Faults, with subsidence, and late Carboniferous-early Permian extension (Coward 1993; Rippon *et al.* 1996; Ritchie *et al.* 2003; Underhill *et al.* 2008); and an elevated geothermal gradient, caused by a potentially high basal heat flow, of which the extensive Carboniferous volcanism may be an expression (Figure 8-2); heating may also have occurred via conduction if the samples were close to the igneous bodies and via the circulation of hot fluids.

Evidence for a Carboniferous elevated geothermal gradient of ~50°C/km at this time can be seen in Figure 7-34, as retrieved from the multi-sample profile models for each region. Using these elevated values and the estimated thicknesses of Carboniferous overburden (Figure 1-3), sedimentation rates

of ~0.22 m ka^{-1} would be required to reach the maximum palaeotemperatures during the late Carboniferous-early Permian, as recorded in the model thermal histories in this thesis. Estimated sedimentation rates for the Carboniferous Midland Valley are between 0.03-0.44 m ka^{-1} (BasinMod) and 0.2-0.6 m ka^{-1} (Hotpot) (Vincent *et al.* 2010), which agree with the findings of this thesis, although lower than those estimated for similar tectonic settings (Miall 2013). A high palaeo-geothermal gradient reconciles the relatively low sedimentation rates, and offer an explanation as to why a reduced overburden is sufficient to attain the value of organic maturity recorded in the Midland Valley (Raymond 1991).

To further highlight the synchronicity between the burial episode and magmatic activity, the phases of Carboniferous volcanism have been added to the thermal histories of the regions investigated in the Midland Valley (Figure 8-3 to Figure 8-8). These figures show how the continued volcanic activity across the Midland Valley would have supported the regional elevated geothermal gradient, while syn-depositional movement on bounding and internal faults allowed the continued growth and development of the major depocentres that accommodated the sediments.

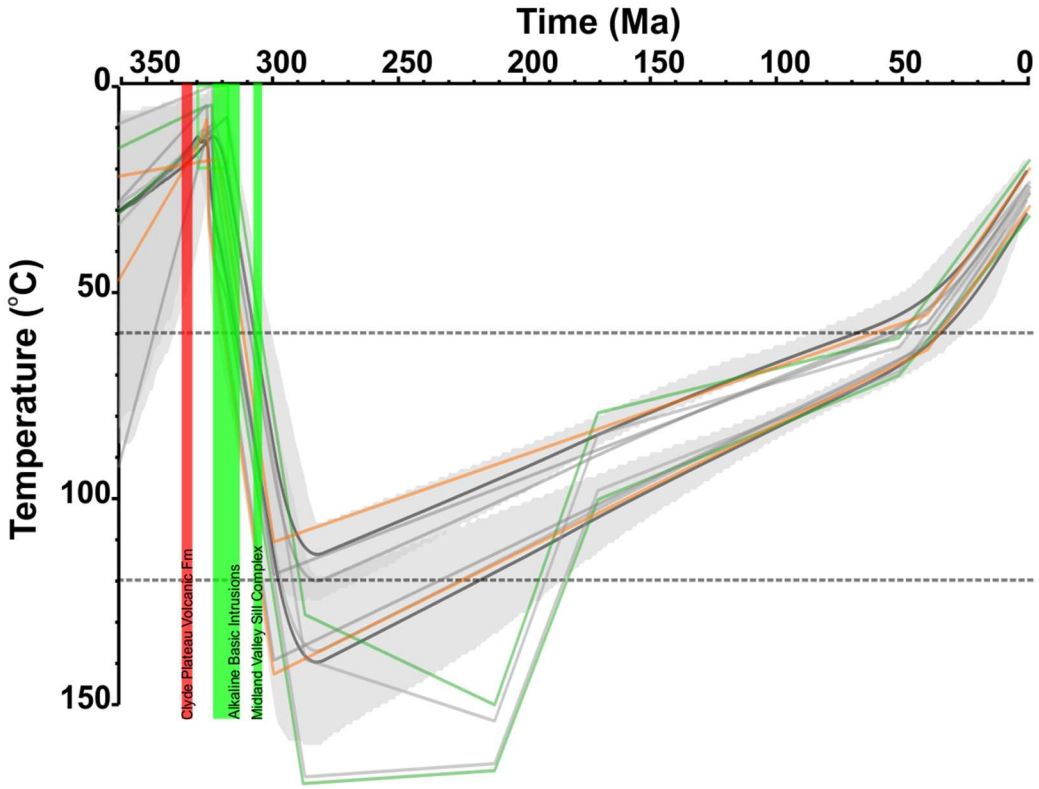

Figure 8-3: Multi-sample profile thermal model of the Central region combined with local igneous activity. Timing and location of igneous activity shown on Figure 8-2.

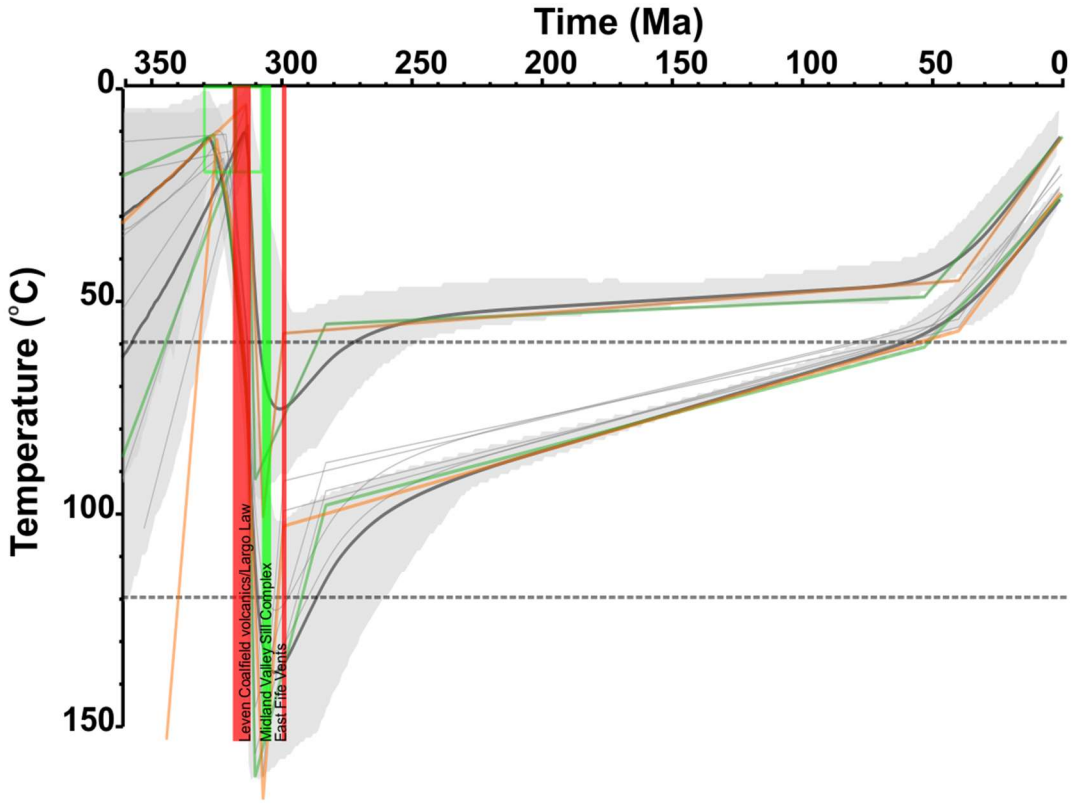

Figure 8-4: Multi-sample profile thermal model of the Leven region combined with local igneous activity. Timing and location of igneous activity shown on Figure 8-2.

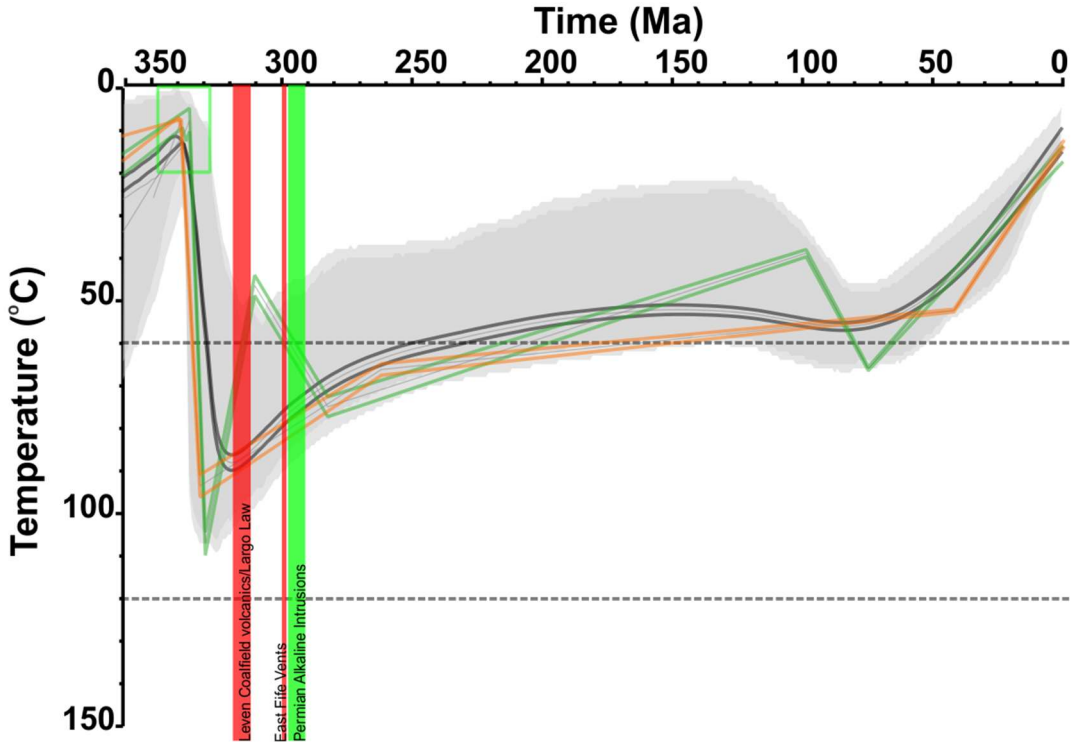

Figure 8-5: Multi-sample profile thermal model of the Fife (south) region combined with local igneous activity. Timing and location of igneous activity shown on Figure 8-2.

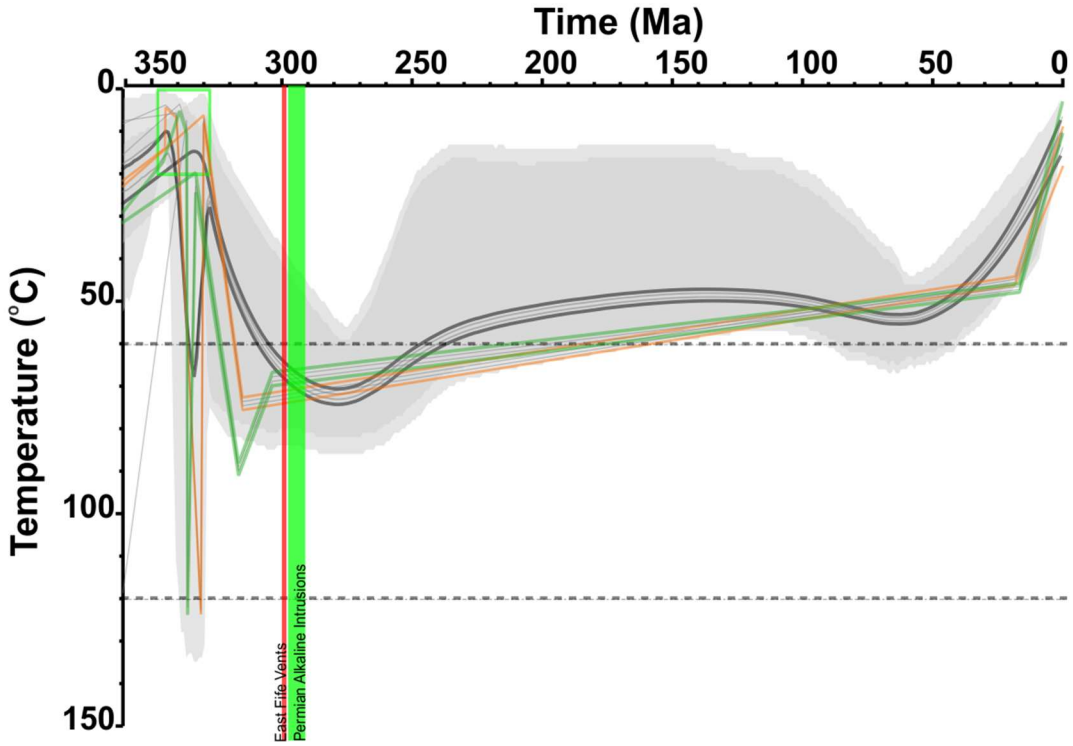

Figure 8-6: Multi-sample profile thermal model of the Fife (north) region combined with local igneous activity. Timing and location of igneous activity shown on Figure 8-2.

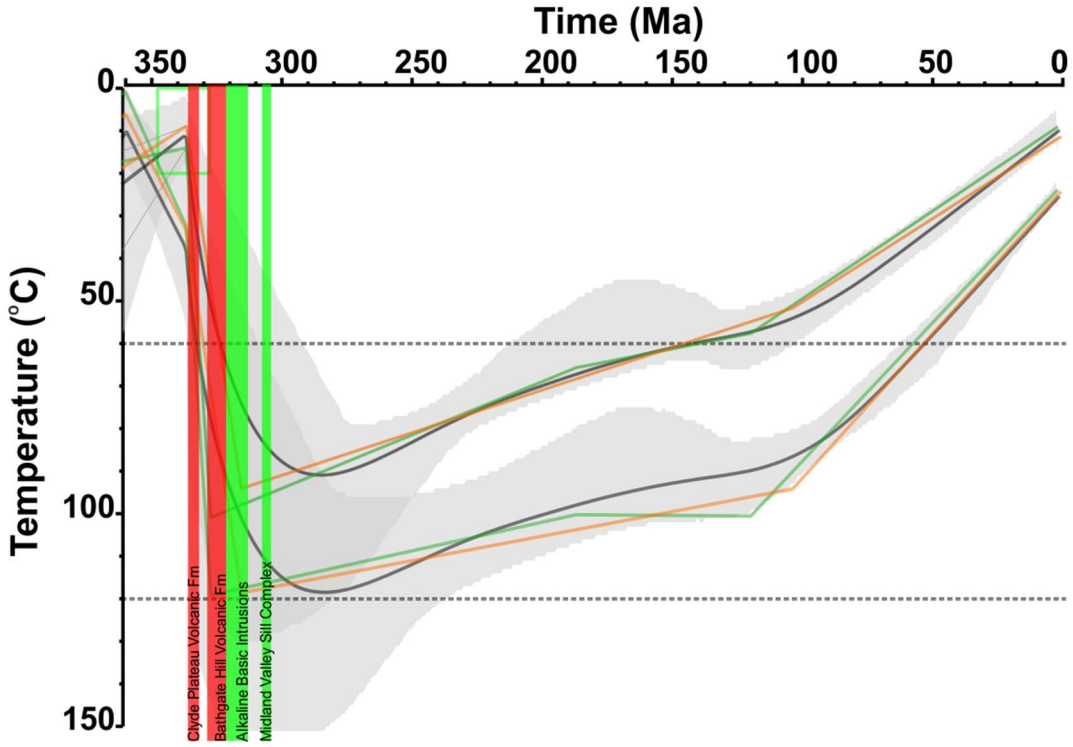

Figure 8-7: Multi-sample profile thermal model of the Lanarkshire region combined with local igneous activity. Timing and location of igneous activity shown on Figure 8-2.

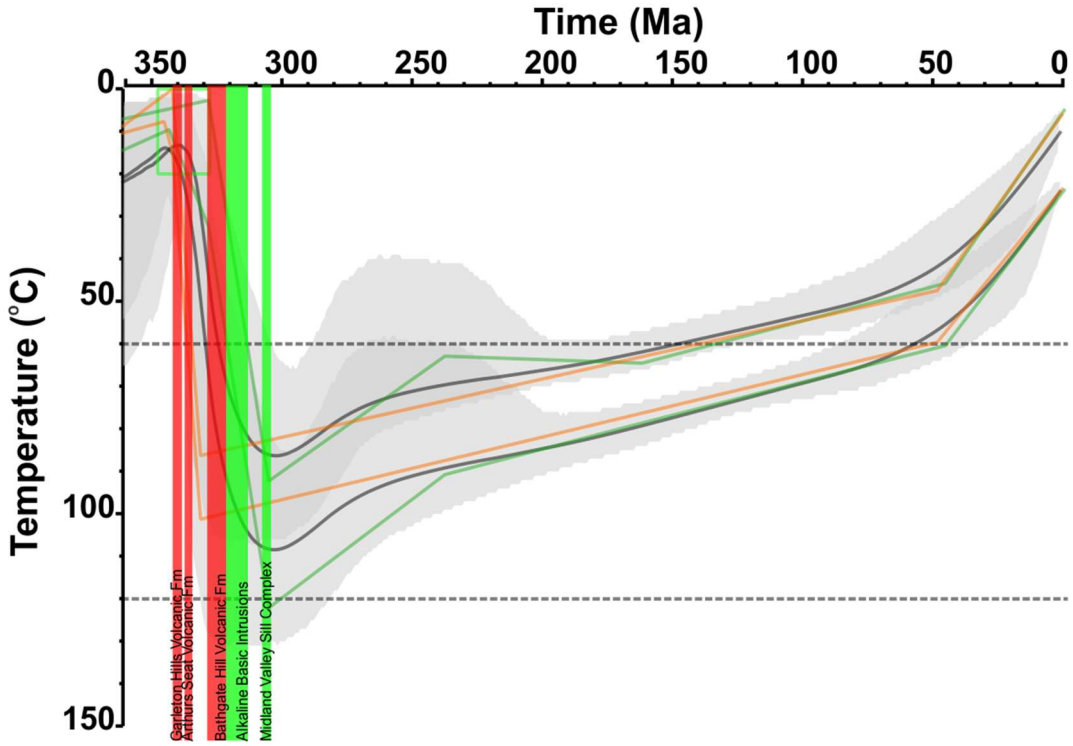

Figure 8-8: Multi-sample profile thermal model of the Lothians region combined with local igneous activity. Timing and location of igneous activity shown on Figure 8-2.

8.2.2 Permian-Mesozoic cooling

After reaching their maximum palaeotemperatures following Carboniferous-Permian burial, all samples from the Midland Valley display a general cooling trend. The cooling style varies between regions, from either monotonic or two stage cooling (fast then slow or slow to very slow). When modelled individually, some samples show the potential for a Jurassic-Cretaceous reheating; however, this event is poorly constrained by the AFT data as it occurs at a time when the rocks were already at temperatures cooler than the PAZ. Once the thermal histories from the individual samples are combined using the multi-sample approach, the reheating event is no longer present. However, the possibility of a late Mesozoic reheating episode is discussed further in below.

Individual sample thermal histories often show a disagreement between the Expected, Max. Likelihood, and Max. Posterior models, indicating they are not fitting the observed data well; The Max. Likelihood models are usually the most complex and the Expected models are accompanied by large 95% credible intervals, suggesting a degree of uncertainty in the thermal reconstructions. When the multi-samples approach is used (Figure 8-1), the agreement between the Expected, Max. Likelihood, and Max Posterior models improves, and 95% credible intervals become narrower, indicating that, by modelling a greater number of data together, the uncertainties decrease. For example, individual sample models from the Central region show some variation, with DMBH

displaying a protracted cooling through the Permian-Mesozoic and A6BH suggesting a potential reheating towards the end of the Mesozoic. The thermal history of the combined multi-sample profile for the region suggests a protracted cooling through the Permian-Mesozoic at c.0.3°C/Myr, with no late Mesozoic reheating event. The multi-samples approach reduces the uncertainties of the thermal histories in all regions. Time-temperature paths from the Leven, Fife (south), and Fife (north) regions (Figure 8-2) display a two-stage cooling history, with initially a cooling rate of c.1°C/Myr until c.260-270 Ma, followed by much slower cooling (c.0.2°C/Myr or lower) until the onset of the Cenozoic. The Lanarkshire profile displays a protracted cooling history, similar to Central region, with rates of c.0.2°C/Myr through the Permian-Mesozoic. The Lothian profile cools via a two-stage process, with the initial faster rate of c.0.5°C/Myr lasting until c.270 Ma, followed by a more subdued rate of c.0.15°C/Myr until the Cenozoic. When the thermal histories from the different regions are compared with each other (Figure 8-1), a clear east-west trend becomes visible; samples in the east display a two stage Mesozoic cooling path with an initial rate of c.1°C/Myr until c.260-270 Ma, followed a reduced rate of c.0.2°C/Myr; samples in the west display monotonic cooling rate of c.0.2-0.3°C/Myr.

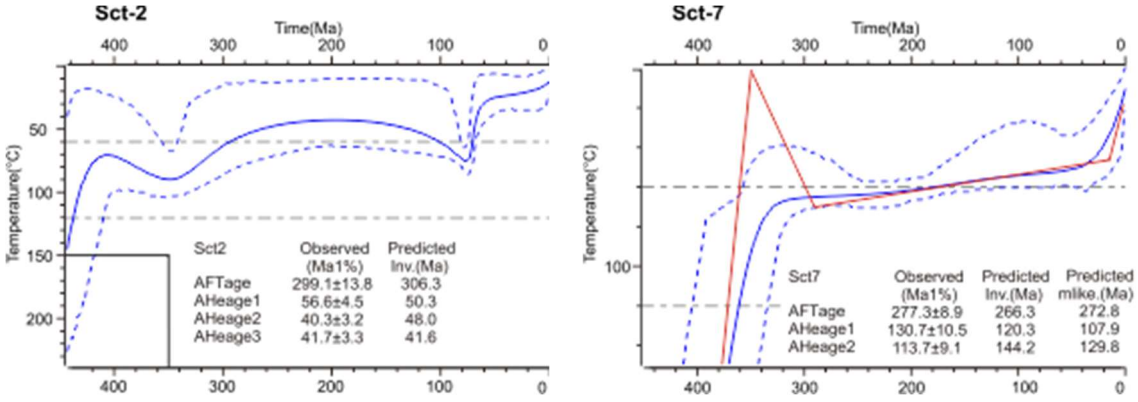

Figure 8-9: Thermal history models produced from Scotland. Models redrawn from Döpke (2017). Sample Sct-2 from a granitic intrusion at Distinkhorn (Lat. 55.59, Long. -4.22) and Sct-7 from a granitic intrusion from Glen Gairn (lat. 57.10, Long. -3.26).

Thermal histories of onshore Ireland, Britain and their offshore basins (Döpke 2017), and of the onshore Grampian terrane and Outer Hebrides of Scotland (Amin 2020), are similar to those reconstructed here for the Midland Valley. In particular, the evolutionary scenarios published by Döpke (2017) for onshore Scotland include a Permian-Mesozoic cooling, similar to those presented in this investigation (Figure 8-9). Early cooling (310-280 Ma) was attributed by Döpke (2017) to post-Variscan exhumation, while later cooling (c.280-65 Ma), more pronounced in Ireland and elsewhere in Britain, was associated with Pangea break-up and Mesozoic rifting (Cogné *et al.* 2014; Döpke

2017). In Scotland, this later phase is very subdued, with extremely low rates of cooling, similar to the trend seen here for the Midland Valley (Figure 8-9).

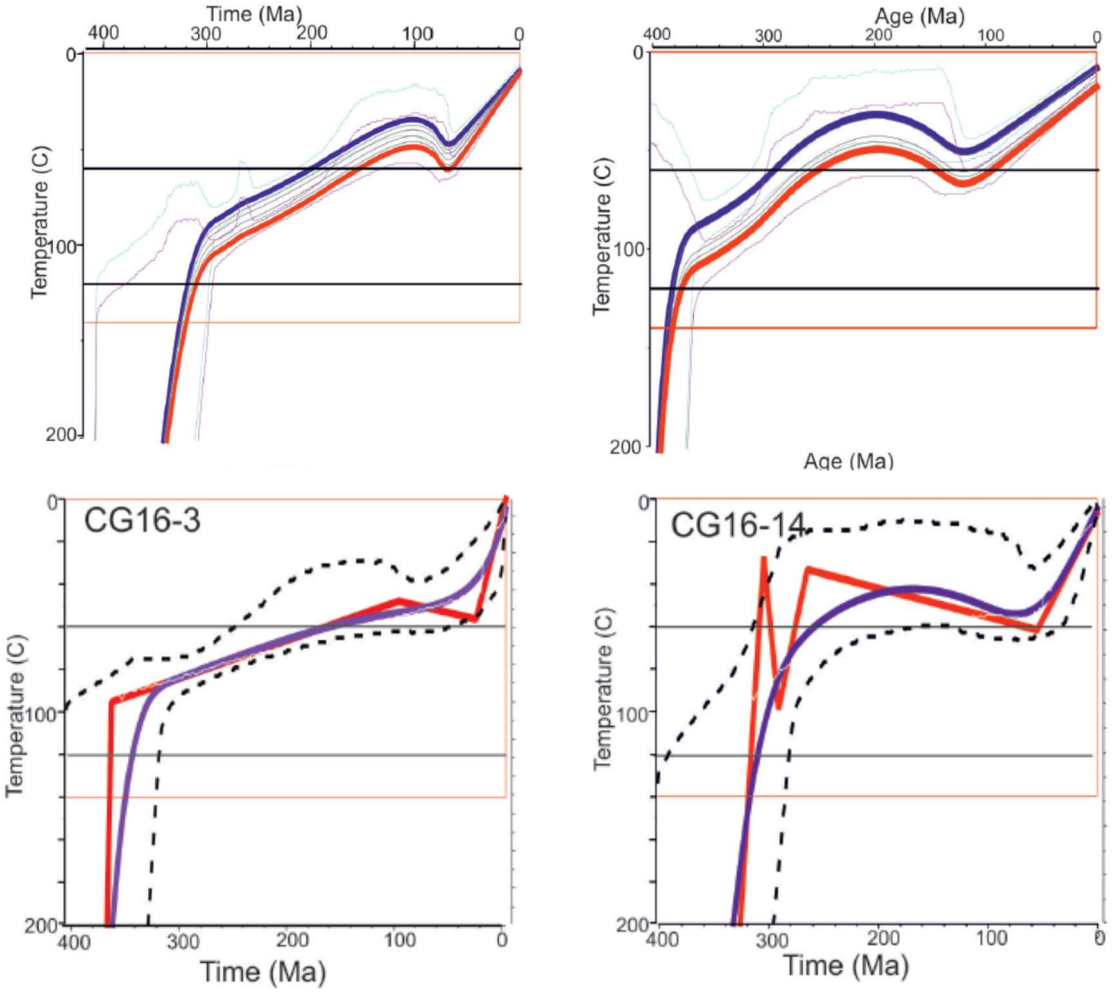

Figure 8-10: Thermal history models produced from samples from the Grampian terrane. Models redrawn from Amin (2020). Top left; multi-sample profile model from samples collected from Ben Nevis (Lat. 56.79, Long. -5.03). Top right; multi-sample profile model from samples collected from Lochnagar (G-rad-dam) (Lat. 56.95, Long. -3.22). Bottom left and right; individual sample models from the Cairngorms AFT data only (Lat. 57.04, Long. -3.12 & 57.25, -3.75 respectively).

Thermal histories produced for samples collected from the Grampian terrane Caledonian granites by Amin (2020) revealed a roughly monotonic cooling through the late Carboniferous to the early Cenozoic (Figure 8-10). Carboniferous-Triassic denudation was estimated at c.1.5-2.0 km, with cooling rates of c.1-2°C/Myr; uplift is associated with the Variscan orogeny, Pangea formation, and potentially magmatic underplating of which late Carboniferous quartz dolerite swarms and Permian Volcanic activity are considered the expression (Amin 2020). Mesozoic sediments are present in some localities onshore in western Scotland (e.g., Ardnamurchan, Skye, Raasay), this has led others to suggest that these sediments represent the remnants of once more expansive, thick deposits, consistent with the record offshore (Holford *et al.* 2005; Holford *et al.* 2009; Holford *et al.* 2010).

Holford *et al.* (2010) have suggested multiple post Caledonian exhumation events across onshore NW Scotland based on AFT data from onshore outcrop and offshore boreholes. However, little evidence to support this was found by Amin (2020) with the exception of a potential reheating event on isolated western onshore samples, suggesting that if these deposits existed, they were not of significant thickness or widespread. Holford *et al.* (2010) thermal history models are based on Max. Likelihood probability and suggest considerable thicknesses of Mesozoic sediments were deposited across the onshore Scottish Highlands, subsequently removed by regional scale erosion events during the early Cretaceous and mid- to late Cenozoic. These regional scale erosion events were attributed to exhumation caused by plate boundary reorganisation associated with North Atlantic Ocean ridge system and convergence of the Eurasian and African plates during Alpine collision leading to increased levels of intraplate stress, propagated from plate boundary interactions (Holford *et al.* 2010). Previous work has implied that offshore sediments once encroached onshore (Holford *et al.* 2010; Vincent *et al.* 2010) as thick successions of Permian and Mesozoic sediments. However, the results from this thesis and other work from onshore Scotland (Döpke 2017; Amin 2020) suggests that there are fundamental differences between the thermal histories of these two regions i.e., onshore vs offshore, indicating that the onshore region has not been buried under a sedimentary succession significant enough to leave a record in the thermochronological data.

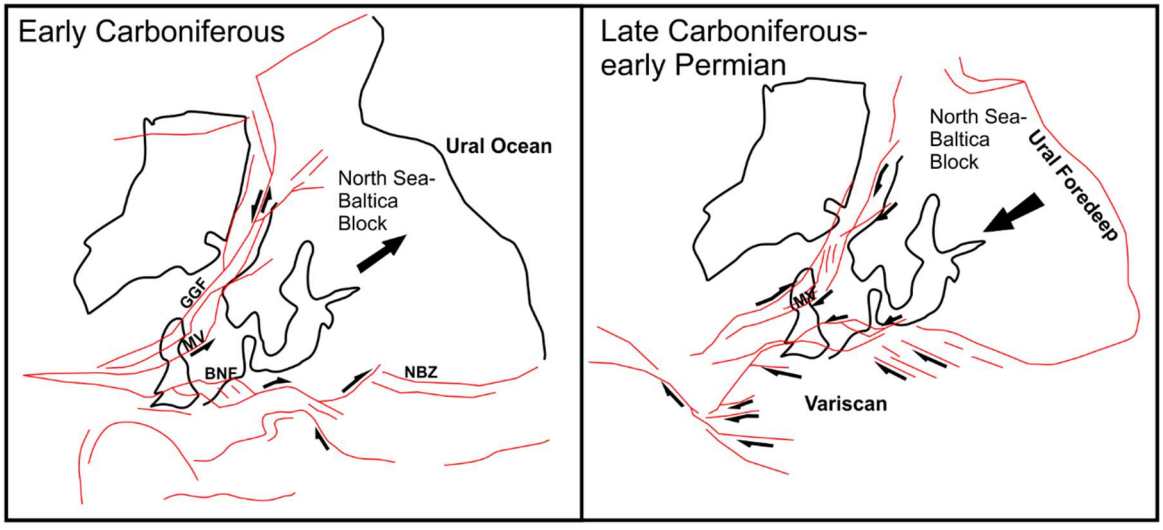

Figure 8-11: Tectonic model of Late Caledonian and Variscan continental escape tectonics. Redrawn from Coward (1993) the simplified maps show the lateral expulsion of the North Sea-Baltica block during the early Carboniferous, followed by its re-insertion during the late Carboniferous-early Permian involving the closure of the Ural Ocean and collision in the Urals. GGF, Great Glen Fault; MV, Midland Valley; BNF Brabant-North Sea fault system; NBZ, North Dobroagean Zone. Large arrow indicates direction of continent movement, small arrows indicate movement of faults.

Mechanisms for post Carboniferous cooling in the Midland Valley rely on the geological evolution of the area and its paleogeographic reconstructions and are similar to those evoked for samples north of the Highland Boundary Fault (Döpke 2017; Amin 2020) initially driven by Variscan uplift, followed by the Pangea breakup as Mesozoic rifting occurred. Evidence for Variscan deformation exists within the Midland Valley, with tightening of syn-sedimentary folds during the late Carboniferous, potentially caused by transpressional deformation that affected the entire Variscan foreland (S. Corfield *et al.* 1996; Underhill *et al.* 2008). The model of Coward (1993) highlighted in Chapter 2 (Figure 8-11) connects these local observations to the regional pattern of an early Carboniferous lateral expulsion of the North Sea-Baltic block, as it was squeezed out by the North American-Greenland and West Europe Variscan Block. In the late Carboniferous, inversion, growth folding, and erosion occurred due to a reversal in stress field and associated dextral strike-slip movement, caused by the re-insertion of the triangular block in association with the closure of the Ural Ocean (Figure 8-11). N-S tension replaced dextral strike-slip by the latest Carboniferous-early Permian, evidenced by E-W striking faults and igneous intrusions (Stephenson 2003; Monaghan and Parrish 2006). There is little evidence for continued differential subsidence in the Midland Valley synclinal depocentres, instead extensional faulting resulting from the N-S tensional regime, has been suggested to had led to the formation of the major Permian basins located offshore (Glennie 1995), and thus shifting the focus of deposition to the East. As well as the Variscan uplift and switching of tectonic regime, the volcanism that was prominent throughout the Carboniferous, was greatly reduced, with only the Alkaline igneous intrusions continuing through the Permian, leading to a thermal relaxation of the elevated geothermal gradient (Figure 8-2) (Monaghan and Parrish 2006). Reconstructions of the geothermal gradient based on multi-sample profile models (Figure 7-34) show evidence of this thermal relaxation and is particularly evident in eastern models which were close to numerous late Carboniferous volcanic centres and intrusions. During the remaining Mesozoic, thermal history models for the Midland Valley are again similar to those produced for Grampian terrane samples (Döpke 2017; Amin 2020). This shows further evidence that although areas surrounding Scotland experienced tectonic switching from a tensional regime to a compressional regime in the mid to late Mesozoic, leading to fault reactivation and significant volumes of sediment to accumulate in offshore basins (Holford *et al.* 2010), mainland Scotland remained relatively stable, remaining an uplifting positive structure supplying sediment to these offshore basins (Stoker *et al.* 2017).

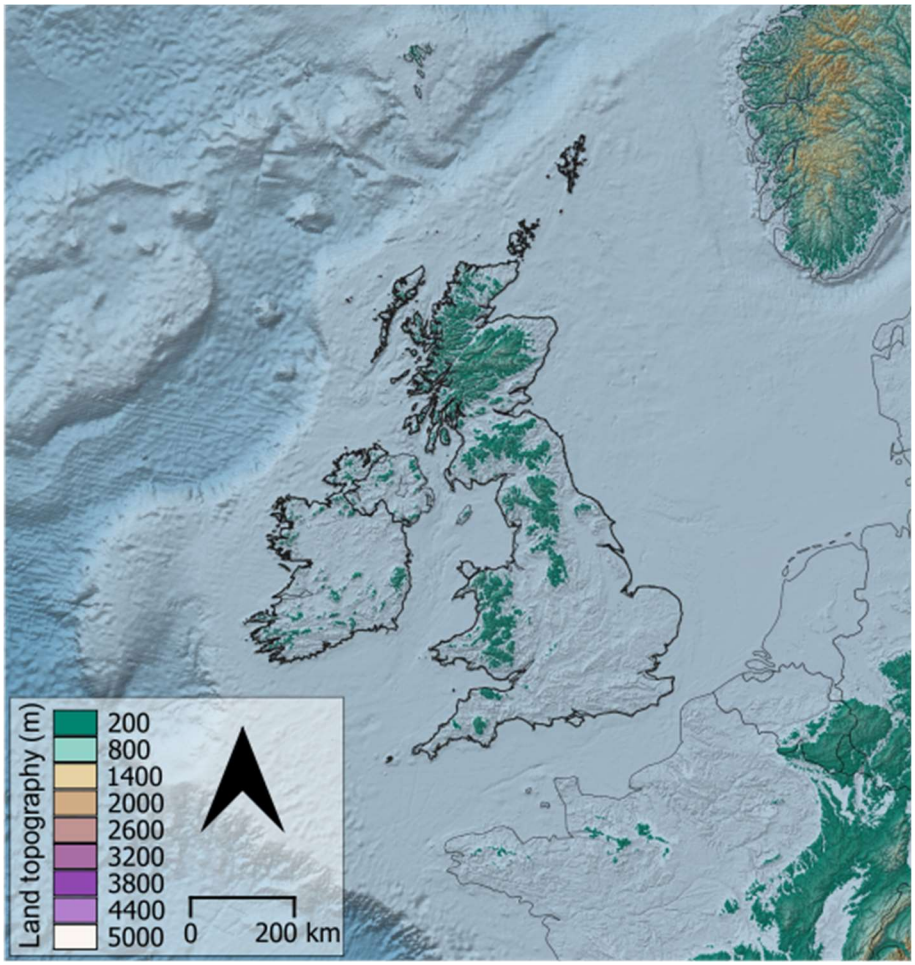

Figure 8-12: Palaeogeographical reconstruction for the Late Cretaceous. Reconstruction created using ETOPO1 Global relief model data and forcing an increased sea level by 200 m above present-day sea level.

As highlighted above, some individual sample thermal history models from the Midland Valley indicate the potential for reheating towards the late Mesozoic (Figure 7-25). Although this event is poorly constrained by the data and occurs out of the temperature sensitivity range of AFT analysis, similar features have been identified in other investigations (Holford *et al.* 2010; Łuszczak 2016; Döpke 2017; Amin 2020). This reheating event was attributed to the Late Cretaceous transgression leading to widespread burial of the region beneath sediment, (Ziegler 1988; Hancock 1989; Hall 1991). Figure 8-12 shows a palaeogeographical reconstruction for Britain and Ireland for the Late Cretaceous based on present-day topography with an increased sea level of c.200 m above present datum. The reconstruction is similar to those created by Hancock (1989) and Cope (2006) and shows how the Midland Valley would be susceptible to flooding with the sea-level changes proposed by these authors. The absence of the reheating event during this time in the multi-sample profile models suggests that, if the reheating event existed, it was not enough to significantly affect all of the fission track data. Thus, if sedimentary cover did exist across the Midland Valley during the late Mesozoic,

the results from the thermal history models produced in this investigation suggest it was not of a significant thickness.

8.2.2.1 Denudation estimate calculations

Existing estimates for denudation of the Midland Valley based on the maturation of organic material (VR) range between 2-3 km (Underhill *et al.* 2008; Vincent *et al.* 2010; Monaghan 2017). Denudation estimates were calculated using equation (8.1) from (Raab *et al.* 2002) and the input values from Table 8-1. Here the Expected profile models for each region was used to extract estimates of time and temperature for each of the regions. The Expected models of the top and bottom of the pseudo profiles were used, when available.

$$D_{t0-t1} = \frac{\Delta T_{t0-t1}}{G} \quad (8.1)$$

Region	t_0 (Ma)	t_1 (Ma)	Δt (Ma)	T_0 (°C)	T_1 (°C)	ΔT (°C)	(°C/km) 50	35	25
Central (Upper)	280	65	215	110	60	50	1.00	1.43	2.00
Central (Lower)	280	65	215	140	75	65	1.30	1.86	2.60
Leven (Upper)	300	65	235	70	40	30	0.60	0.86	1.20
Leven (Lower)	300	65	235	135	60	75	1.50	2.14	3.00
Fife (north)	280	65	215	65	50	15	0.30	0.43	0.60
Fife (south)	310	65	245	90	50	40	0.80	1.14	1.60
Lanarkshire (Upper)	290	100	190	90	50	40	0.80	1.14	1.60
Lanarkshire (Lower)	290	100	190	120	85	35	0.70	1.00	1.40
Lothians (Upper)	300	65	235	90	50	40	0.80	1.14	1.60
Lothians (Lower)	300	65	235	110	65	45	0.90	1.29	1.80

Table 8-1: Permian-Mesozoic denudation estimate input values. Values used in equation (8.1) for different values of geothermal gradient (50, 35 and 25 °C/km).

Where D is the denudation in km, t_0-t_1 is the beginning and end time interval respectively, ΔT_{t0-t1} is the change in temperature between the time interval, and G is the geothermal gradient in °C/km. This formula calculates the amount of denudation required to cool the sample from elevated temperatures in the past to more recent cooler temperatures, based on the geothermal gradient of the region. As the thermal histories in this thesis have indicated a complex geothermal gradient that was elevated in the past and declined with time, a range of geothermal gradients have been applied in attempt to capture the uncertainty of this calculation i.e., 50°C/km, 35°C/km, and 25°C/km, which represent the elevated palaeo-geothermal gradient, the present-day geothermal gradient, and an intermediate geothermal gradient (Table 8-1). The timing of the onset of cooling seen in the Expected models has been used for t_0 and 65 Ma has been used as t_1 except in the Lanarkshire region where 100 Ma has been used, based on the change in cooling rate. The magnitude of the denudation

(Figure 8-13) ranges between ~0.5-3.0 Km dependent of the geothermal gradient applied. Fife (north) shows the least amount of denudation with less than 1 km, while samples from Fife (south), Lanarkshire, and Lothians display similar denudation estimates ranging between ~0.8-1.6 km. Samples from the Central and Leven regions located in the syncline of the region show the most denudation, ranging between ~1-3 km.

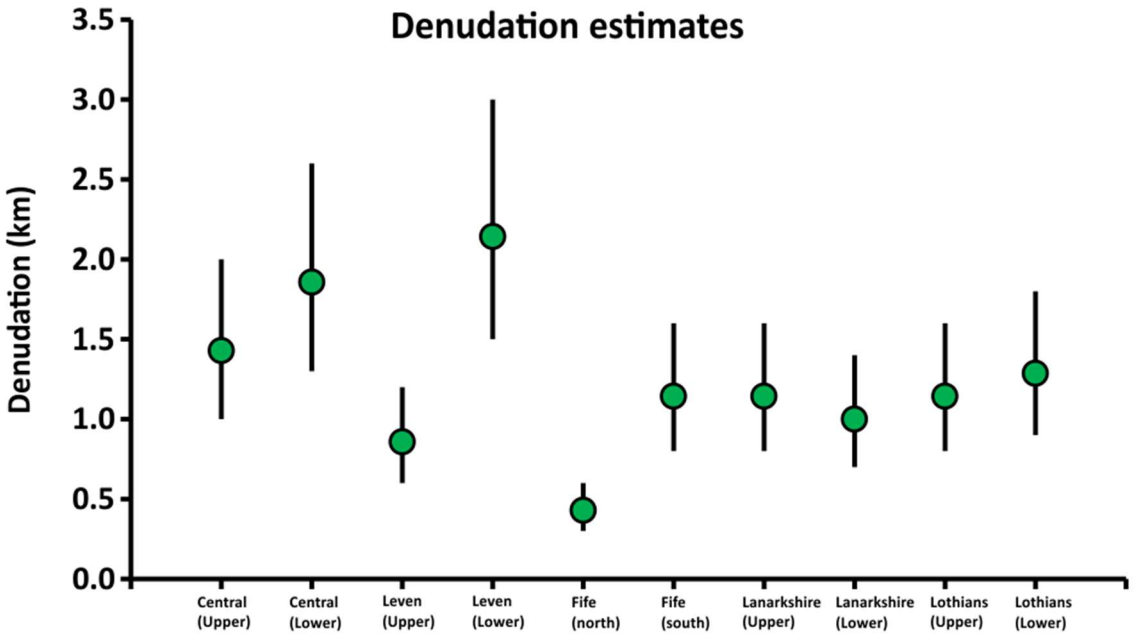

Figure 8-13: Estimated denudation in km for the regions of the Midland Valley.

However, the denudation values presented in Table 8-1 and Figure 8-13 using the equation (8.1) are highly uncertain. These values have been determined using the Expected model as a guide, which as highlighted in Chapter 3 section3.4.1 has an associated 95% credible interval uncertainty that has not been propagated through into this calculation. Also, although an attempt has been made to capture some on the uncertainties associated with the geothermal gradient by using a range of values, this does not capture the uncertainty associated with the thermal relaxation of the isotherms. This is explained in Figure 8-14, where in scenario (a) cooling of the sample is equal to exhumation as the thermal reference frame (Tc isotherm) remains stationary. However, in scenario (b) the thermal reference frame is not stationary and can move above (increasing geothermal gradient) or below the sample (decreasing geothermal gradient). In this case the heating and cooling of the sample is in relation to the complex evolution of the geothermal gradient and independent from exhumation.

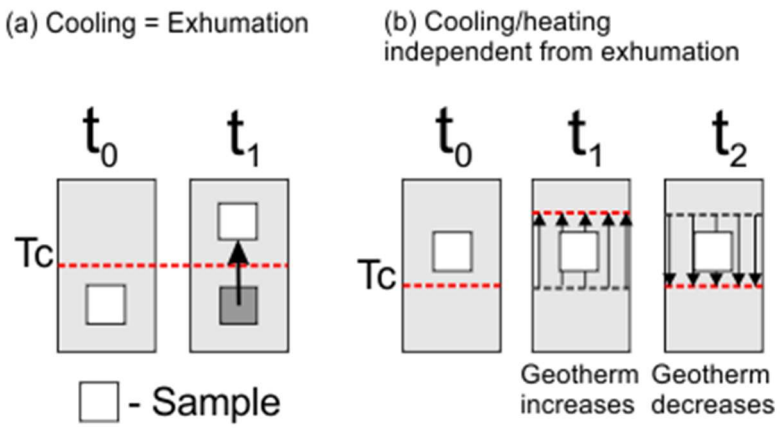

Figure 8-14: Scenarios of exhumation and movement of isotherms in relation to exhumation. Redrawn from Malusà and Fitzgerald (2019b).

In situations such as in the Midland Valley, cooling recorded by AFT data may be a complex interaction between both of these scenarios. The thermal histories have indicated a changing geothermal gradient with time and that volcanism may have influenced the heat flow on both a local and regional scale. This suggests that the cooling is both related to exhumation and the changing thermal structure of the crust, leaving the denudation values calculated above as estimates only.

8.2.3 Cenozoic cooling

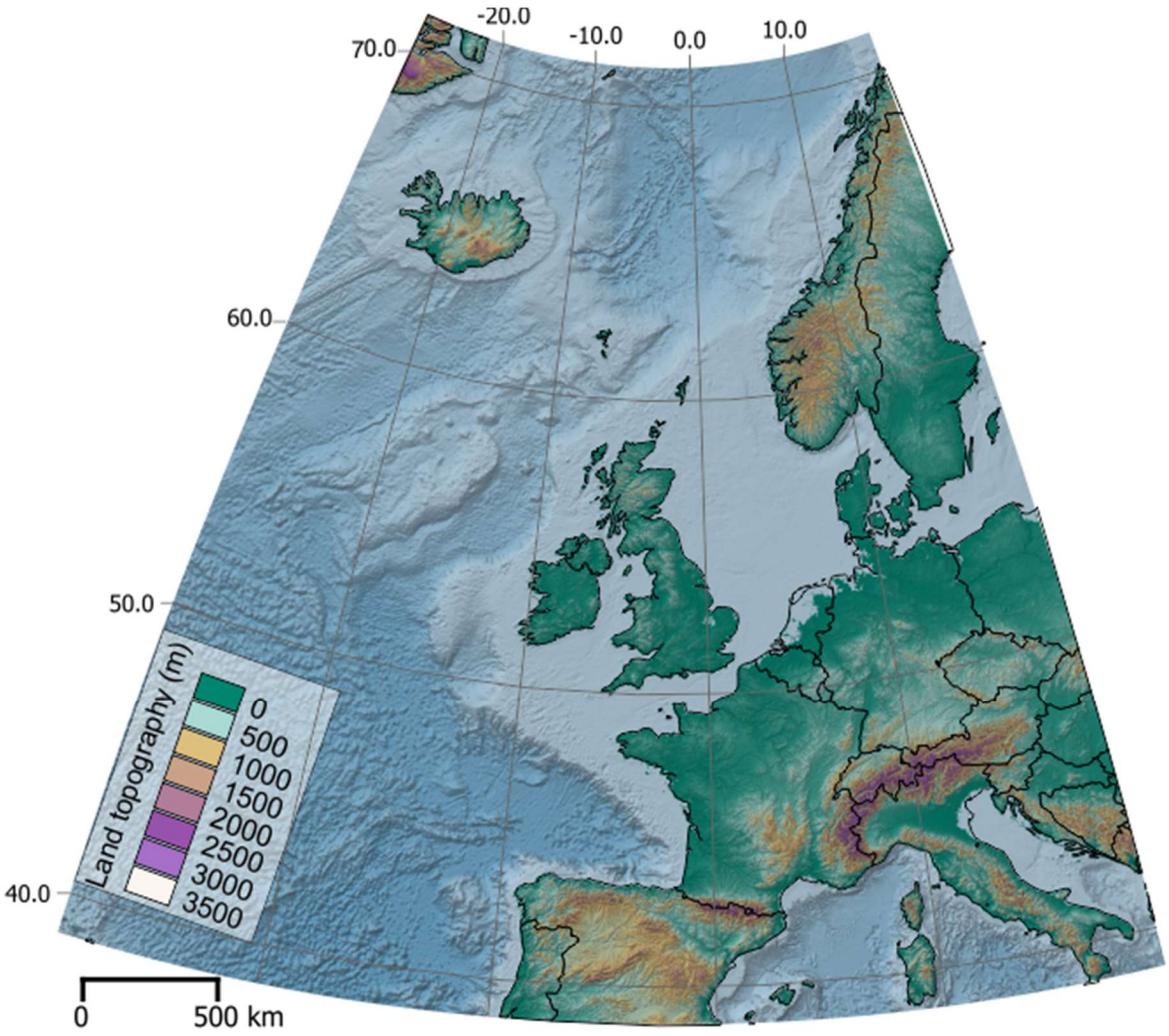

Figure 8-15: Digital elevation model of western Europe. Figure shows the present-day location of Iceland, Britain and Ireland, and the European Alps. Image adapted from the ETOPO1 global relief model data and processed using QGIS.

Though some samples when modelled individually continue to cool monotonically through the Cenozoic at the same rate they did through the Mesozoic (c.0.2°C/Myr) i.e., DMBH, and EM-13, many individual samples and all multi-sample profile thermal history models (Figure 8-1 & Figure 8-16) indicate an increased rate of cooling through the Cenozoic (c.1°C/Myr). This cooling rate is consistent through all regions, though the onset timing does show some variations, with the cooling beginning earlier in Lanarkshire, compared to other regions. This pattern of Cenozoic cooling has been reported in numerous thermal history investigations throughout Britain and Ireland (Green *et al.* 1995; Persano *et al.* 2007; Hillis *et al.* 2008; Holford *et al.* 2010; Łuszczak 2016; Döpke 2017; Amin 2020) and has been attributed to an exhumation pulse driven by two possible mechanisms; far field stress originating from the opening of the Atlantic Ocean and/or collision of the African and Eurasian plates (Lewis *et al.* 1992; Holford *et al.* 2005; Hillis *et al.* 2008; Holford *et al.* 2009), or the

proto-Icelandic plume emplacement and associated mantle driven processes such as magmatic underplating, lithospheric thinning and dynamically-supported uplift (White 1997; Jones *et al.* 2002; Al-Kindi *et al.* 2003; Jones and White 2003; Persano *et al.* 2007; Łuszczak 2016). For context, the present-day location of the Icelandic plume and the European Alps, created between the African and Eurasian plate collision are shown in Figure 8-15. Differentiating which of these processes was dominant across Britain and Ireland was the focus of Döpke (2017) who used a combination of AFT and apatite helium dating (AHe), which is sensitive to cooler temperatures than AFT thermochronology. The results of this investigation concluded that, based on the amount of Cenozoic exhumation experienced with an assumed geothermal gradient of 25°C/km, Britain and Ireland could be divided into zones (red, yellow, green, and white zones) with a focus of highest denudation around the Irish Sea and Southern Scotland (red zone) which deceased outwards (Figure 8-17). This pattern of exhumation was interpreted to support proto-Icelandic emplacement and mantle driven exhumation as the driving force for Cenozoic cooling and uplift across Britain and Ireland. The radiating pattern of exhumation agrees with previously published exhumation patterns and free-air gravity anomalies and seismic data (Jones *et al.* 2002; Arrowsmith *et al.* 2005; Tomlinson *et al.* 2006) (Figure 8-17). Employing a combination of AFT and AHe in NW Scotland Amin (2020) also concluded that the Cenozoic cooling pulse was spatially controlled, with samples in the eastern Grampian terrane recording no clear evidence for an early Cenozoic cooling pulse, while samples in the western Grampian terrane and Outer Hebrides recording cooling onset at 70-80 Ma and 60-70 Ma respectively, again favouring proto-Icelandic plume and mantle processes as the driving mechanism for exhumation.

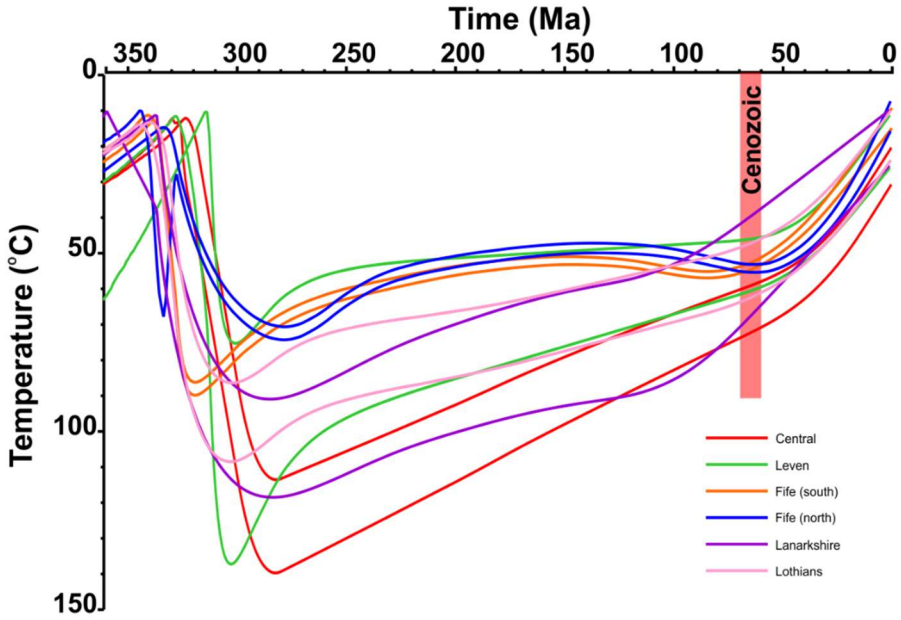

Figure 8-16: All Expected multi-sample profile thermal histories combined. Max. Likelihood, Max. Posterior, and 95% credible intervals removed from clarity. All expected models show an increased rate of cooling, initiating during the early Cenozoic (red), except for Lanarkshire models where onset of cooling begins earlier c. 100 Ma.

Unfortunately, although evidence for Cenozoic cooling is clear in the Midland Valley, due to the temperature sensitivity range of AFT it is difficult to discuss in too much detail the cause of the uplift mechanism. Nonetheless, using the pre-cooling pulse temperatures and a geothermal gradient of c.25°C/km (Figure 7-34) estimates of denudation experienced across the Midland Valley can be calculated. Estimates for the regions are; Central, c.1.4 km; Leven, 1.2 km; Fife (north and south) c.1.5 km; Lanarkshire c.2 km; Lothians c.1.3 km. These values are in agreement with the estimates of Döpke (2017) and Cogné *et al.* (2016) for Britain and Ireland Figure 8-17, and similar to those calculated for regions north of the Highland Boundary Fault (Persano *et al.* 2007; Amin 2020). Further evidence to support the proto-Icelandic plume effect on the Midland Valley is the presence of British and Irish Palaeogene Igneous Province (BIPIP) intrusions in the west of the Midland Valley, which are linked to opening of the North Atlantic Ocean and the initiation of the Icelandic mantle plume (White 1997; Ganerød *et al.* 2010). An increased rate of cooling was also revealed by the thermal modelling of Vincent *et al.* (2010) which was also associated with the opening of the North Atlantic Ocean and plume emplacement. However, the magnitude of denudation between Vincent *et al.* (2010) and that estimated in this investigation differ. Vincent *et al.* (2010) estimated cooling of c.60-70°C for samples now at the surface since the onset of Palaeogene uplift, suggesting c.2.4-2.8 km of denudation with a 25°C/km geothermal gradient.

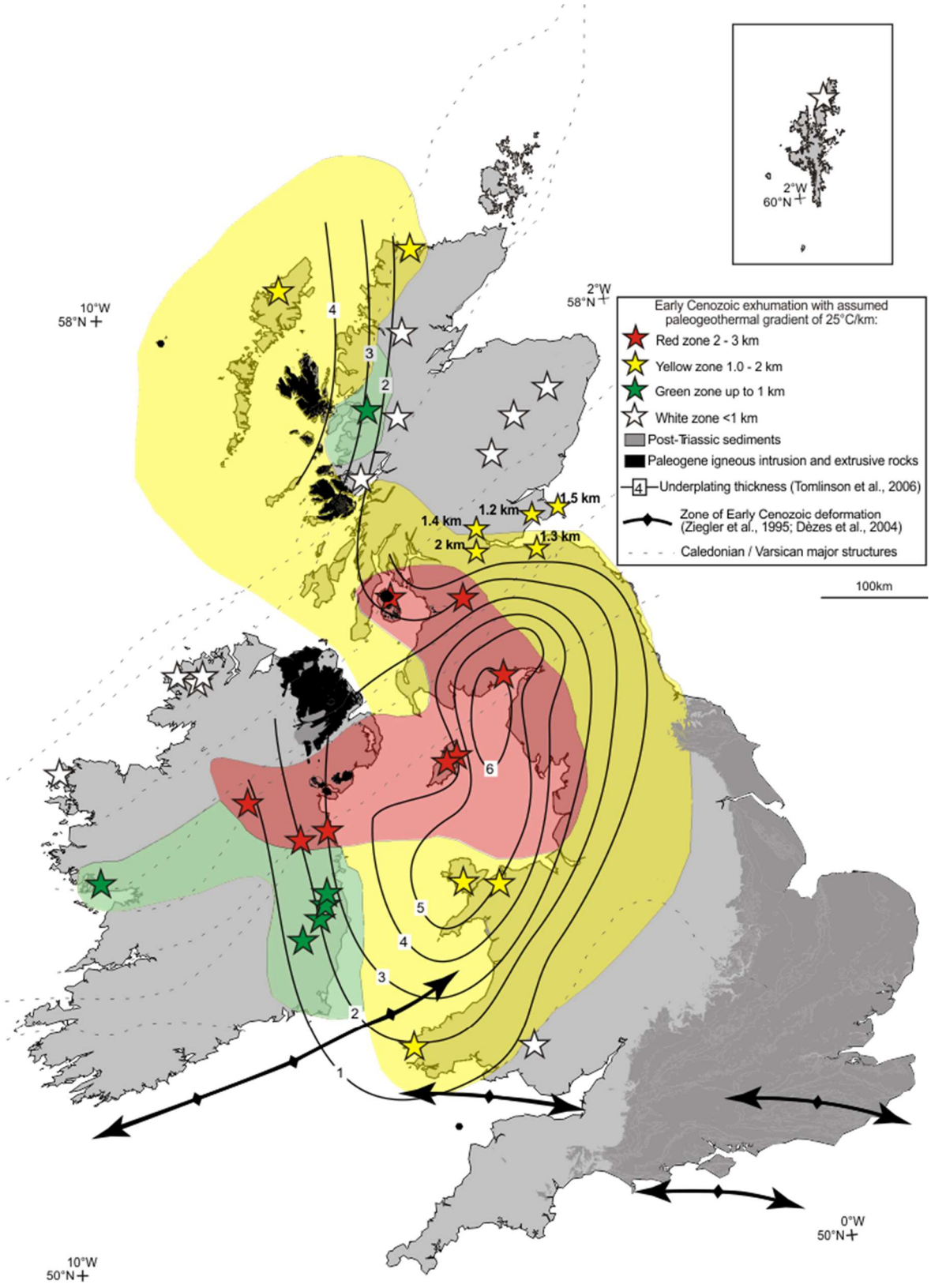

Figure 8-17: Map of Cenozoic exhumation across Britain and Ireland including new Midland Valley estimates. Redrawn from Döpke (2017), the map shows the inferred magnitude of Cenozoic exhumation centred around the Irish Sea. Also shown, the thickness of magmatic underplating after Tomlinson *et al.* (2006).

8.3 Conclusions

8.3.1 Burial and exhumation history of the Midland Valley

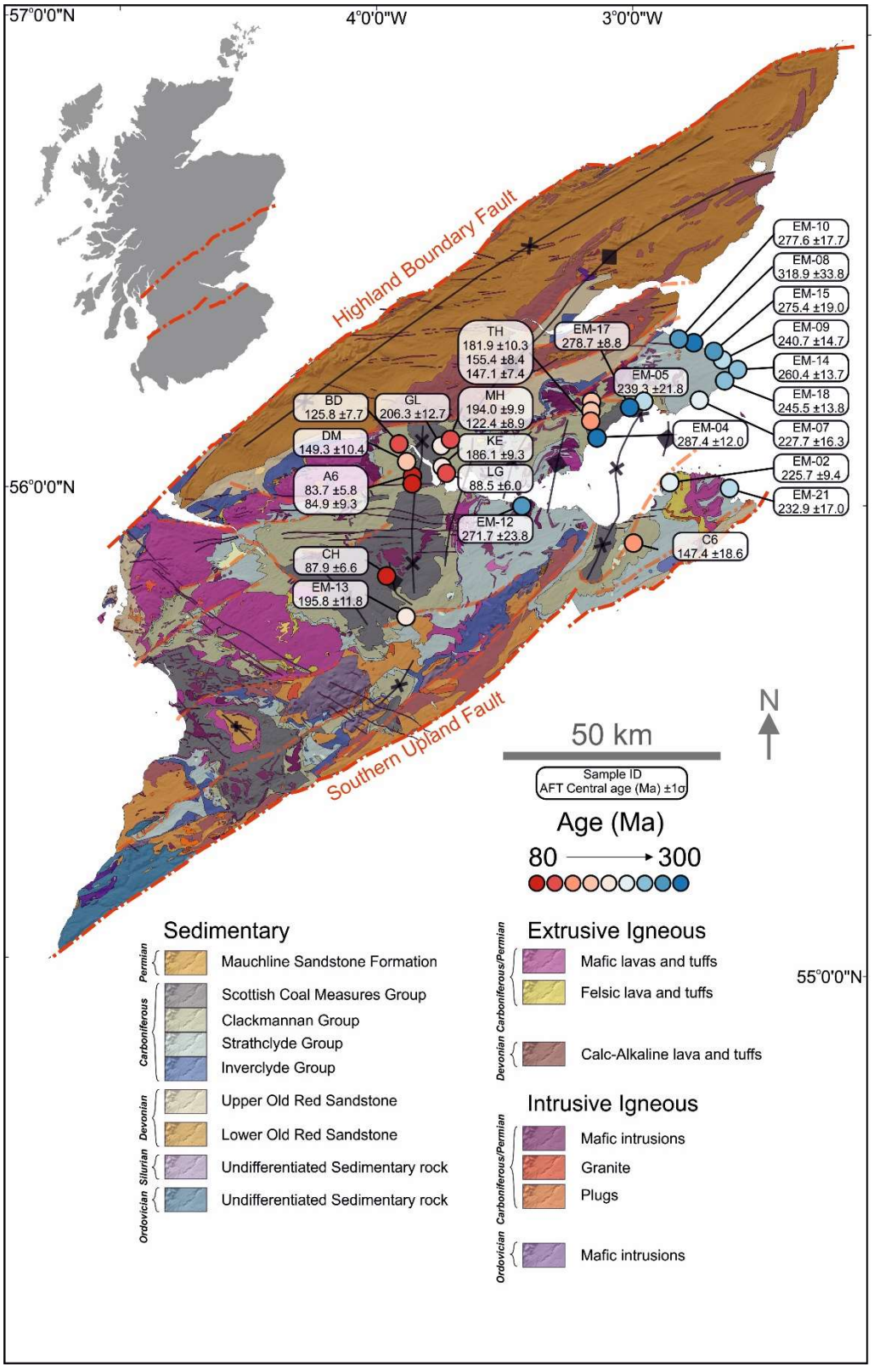

Figure 8-18: AFT central ages across the Midland Valley. Surface created using GMT modelling software (Wessel *et al.* 2019); the age distribution at the surface indicate that the AFT central ages are related to the Carboniferous basin structures (older in the anticlines and younger in the synclines), strongly suggesting that Mesozoic burial and heating, if present, was not enough the overprint these Carboniferous inherited ages.

The AFT data and thermal histories presented here offer an alternative to previous investigations that suggest either Carboniferous maximum palaeotemperature followed by protracted cooling or Mesozoic burial resulting in Cenozoic maximum palaeotemperatures followed by rapid exhumation related cooling (Duddy *et al.* 1992; Vincent *et al.* 2010). The trend of the AFT data generally reflects the Carboniferous structure of the region with older AFT ages found on anticlinal highs and younger ages found towards the synclinal limbs, partially reset AFT data are also found within synclinal cores, indicated by the similarity between the sample AFT central age and stratigraphic age (Figure 8-18). This age trend, along with the absence of bimodal TLD's suggest that a Cenozoic maximum palaeotemperature under Mesozoic successions is unlikely, though a recent period of accelerated cooling is supported. Though these observations on the AFT data provide an initial indication of the potential thermal history of the region, the best results are obtained by the combination of the observed AFT data with Bayesian trans-dimensional Markov Chain Monte Carlo (MCMC) data inversion thermal history modelling software (QTQt) (Chapter xx).

These results suggest that a more appropriate model for the burial and exhumation history for the Carboniferous Midland Valley begins with rapid heating following burial in the sedimentary basin. The influence of an elevated geothermal gradient, supported by the widespread Carboniferous volcanism, allowed the thermal maturation of organic matter without requiring the significant volumes of material necessary under normal geothermal gradients. Syn-sedimentary growth folding of major Carboniferous depocentres, the Midlothian-Leven and Clackmannan synclines, continued under a transtensional regime allowing the thermal resetting of AFT data of samples found within the synclines, while samples located on anticlinal and tectonic highs remained within the PAZ and thus were only partially reset. Folding proceeded into the Westphalian Scottish Coal Measures as either a continuation the transpressional-transtensional movement experienced during the Viséan-Namurian or as a result of Variscan exhumation and regional transpression (Coward 1993; Ritchie *et al.* 2003; Underhill *et al.* 2008). Dextral strike slip gave way to north-south extension in the latest Carboniferous-early Permian due to the opening of the Northern and Southern Permian basins in the North Sea, changing the focus of sedimentation and, hence, of the sedimentary routing system (Glennie and Underhill 2009). Thermal histories indicate that maximum palaeotemperatures were reached during the late Carboniferous-early Permian; however, due to the sensitivity of the AFT analysis it is not possible to decipher whether significant thicknesses of Permian deposits, like those seen in the Mauchline Basin and Arran once covered the entire Midland Valley or were limited to

their present-day locations. Volcanism within the Midland Valley ceased, following the intrusion of the Permian East Fife vents and Alkaline basic sills allowing the thermal relaxation of the elevated geothermal gradient. The initiation of cooling following Carboniferous-Permian heating is evident from all thermal histories with a slight variation seen in the eastern Midland Valley profile models, which suggest an initially higher rate of cooling until c.270 Ma followed by a similar rate seen in the western samples. Samples from the Central region suggest heating continued for longer here, or was to a greater extent, and took longer to return to the PAZ from elevated temperatures. The Fife (north) thermal histories suggest that the East Fife vents may have maintained elevated temperatures locally for longer than experienced elsewhere or that Permian sediments, present offshore may have encroached onto this region.

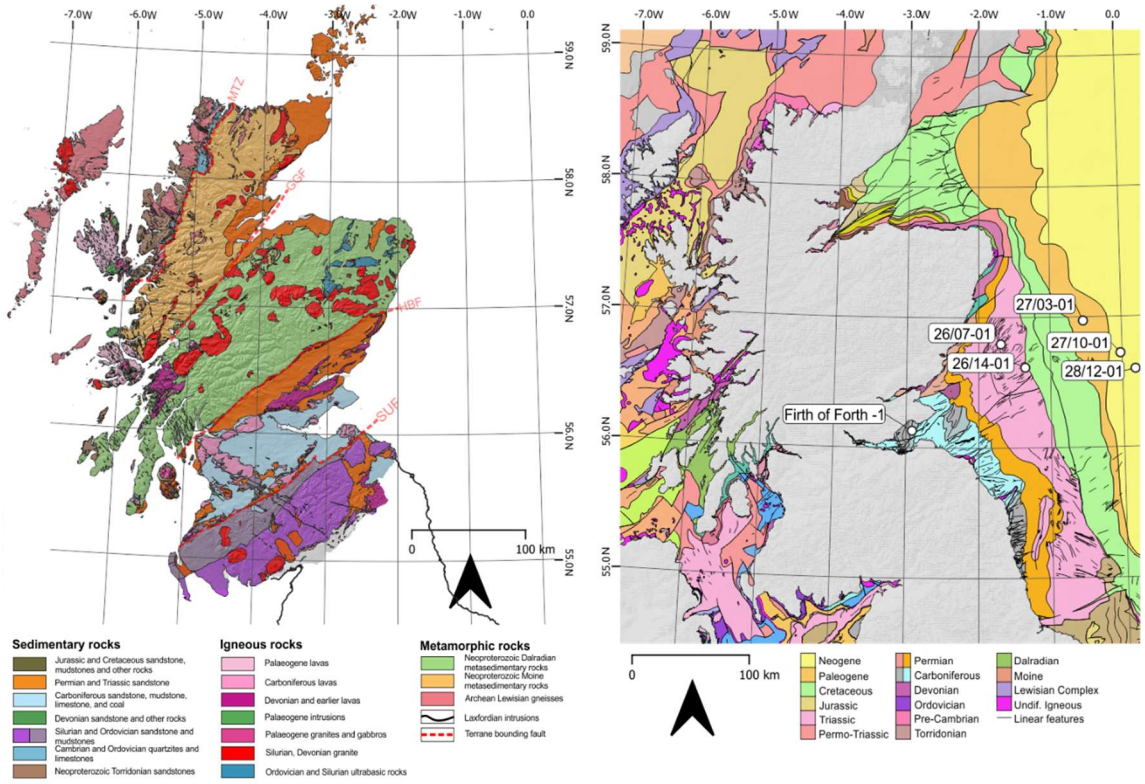

Figure 8-19: Relationship between the onshore and offshore geology of Scotland. Figure shows the comparison between the onshore geology of Scotland (left) and the offshore geology (right) with the position of offshore boreholes plotted in Chapter 6 Figure 5.

After maximum palaeotemperature was attained during the late Carboniferous-early Permian in the Midland Valley, the thermal histories produced in this thesis suggest that the cooling trend of the region was similar to that recorded in other thermal histories for onshore northern Scotland (Döpke 2017; Amin 2020). Further evidence for the disconnect between the post Carboniferous thermal histories of onshore Midland Valley and its offshore regions can been seen in Chapter 6 Figure 6-5, where the AFT data from offshore boreholes have a different age vs depth relationship in comparison

to onshore Midland Valley data. Many of these boreholes are positioned on the south side of the offshore extension of the Southern Upland Fault (Figure 8-19) and thus their depositional, structural, and thermal history may not be directly comparable. Regardless of this, the lack of overprinting/resetting of the AFT data by Mesozoic burial is clear (Figure 8-18) and thus the assumption that the sedimentary cover proven offshore may have extended onshore should be used with caution.

This cooling trend continued throughout the remaining Permian-Mesozoic without strong evidence of any thermally related events, although some individual thermal histories show of minor Late Cretaceous reheating, the occurrence of which is difficult to demonstrate given that the rocks were already at temperatures cooler than the PAZ. If this reheating event did exist, it was geographically restricted and it did not exceed ~1 km.

An increase in cooling rate approaching the beginning of the Cenozoic is most evident in the multi-sample profile thermal history models. This cooling pulse has been recorded frequently in thermal history investigations across Britain and Ireland and has been attributed to either far field stress originating from the opening of the Atlantic Ocean and/or collision of the African and Eurasian plates or proto-Icelandic plume emplacement and associated mantle driven processes such as magmatic underplating, lithospheric thinning and dynamically supported uplift. As the post Cenozoic cooling occurs out of the temperature sensitivity range of AFT analysis, it is difficult to differentiate between these two hypotheses, however the estimated exhumation calculated in this investigation conform to those calculated based on the proto-Icelandic plume emplacement and magmatic underplating model (Figure 8-17).

8.3.2 Implication for petroleum prospectivity

The Midland Valley, which has been a hydrocarbon producing province in the past with a rich history in exploration (Hallett *et al.* 1985) has received recent attention investigating its potential as a prospective source for both conventional and unconventional hydrocarbons (Underhill *et al.* 2008; Monaghan 2014). In these investigations the thermal maturation of organic material (VR) was used to estimate thermal history models for the region (Raymond 1991; Vincent *et al.* 2010; Monaghan 2014). Although this technique is well established and provides a robust estimate of maximum palaeotemperature attained by the samples, it cannot provide a quantitative constraint on the timing

of the thermal event/s causing the maturity. Integrating the new thermochronological data from this investigation with existing data provides important insights into the hydrocarbon potential of the Midland Valley. Previous investigations concluded that the Midland Valley contained the main elements required to make a successful petroleum play i.e. source rock, reservoir, seal, and structural traps (Figure 8-20) (Underhill *et al.* 2008). However, as well as these elements being present, the timing and mechanism for maturation and migration should be well understood in order to conclude the hydrocarbon preservation potential.

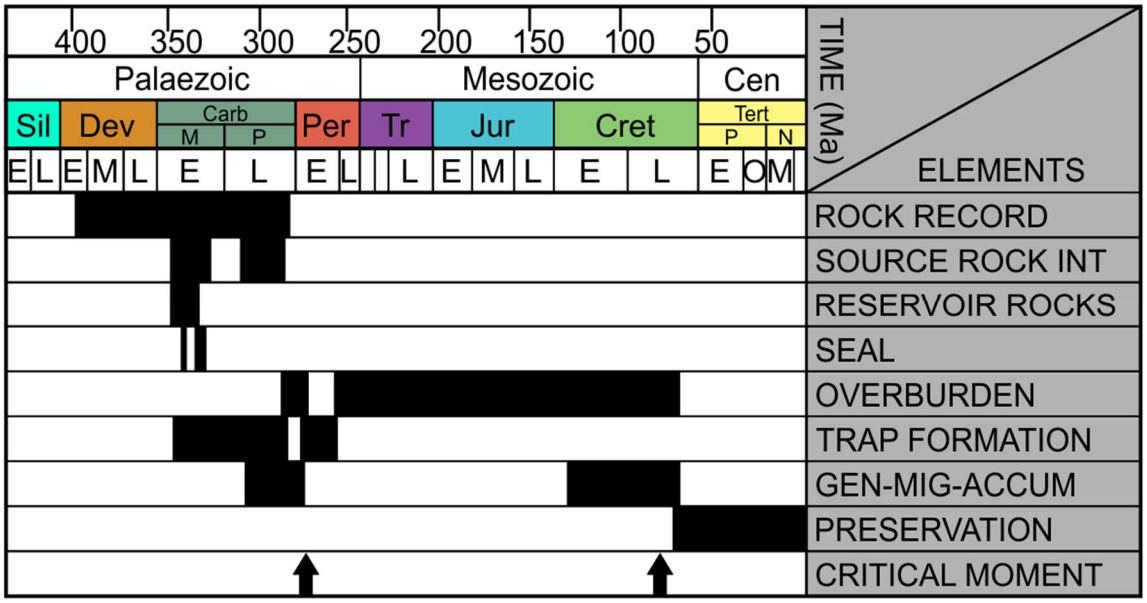

Figure 8-20: Petroleum elements table from the Midland Valley. Image shows the elements and timing of events estimated for the Midland Valley. In this model significant volumes of Mesozoic material are needed to reheat Carboniferous source rock, causing a second phase of generation, migration, and accumulation (GEN-MIG-ACCUM) during the late Mesozoic leading to the second critical moment in the play. Image adapted from Underhill *et al.* (2008).

The maturation of the organic matter at a regional scale has been considered as due to the effect of burial and the widespread nature of the igneous intrusions in the Midland Valley (Raymond and Murchison 1988a; Raymond and Murchison 1989). Using seismic data, however, Underhill *et al.* (2008) showed that source rocks in the centre of the Midlothian-Leven syncline, are at present depths of over 3 km, implying that burial alone is enough to explain the existence of the proven petroleum province. The thermal models of Underhill *et al.* (2008) and Vincent *et al.* (2010) suggest two phases of petroleum generation in the Midland Valley, an initial phase associated with Carboniferous burial prior to Variscan uplift, and a second during the late Mesozoic associated with the accumulation of Mesozoic deposits which were subsequently exhumed by Cenozoic uplift (Figure 8-20). In these reconstructions, it is the post-Variscan burial rather than the Carboniferous subsidence that controlled petroleum charge in the Midland Valley (Underhill *et al.* 2008). Though the findings from

this thesis agrees with late Carboniferous-early Permian maximum paleotemperatures and attainment of current levels of organic maturity (Underhill *et al.* 2008), there is little evidence to support continued and significant volumes of Mesozoic sediment across the Midland Valley as to generate a second phase of petroleum generation. The petroleum elements table from Figure 8-20 above has been modified to indicate the effects the lack of Mesozoic successions has on the evolution of the petroleum system (Figure 8-21).

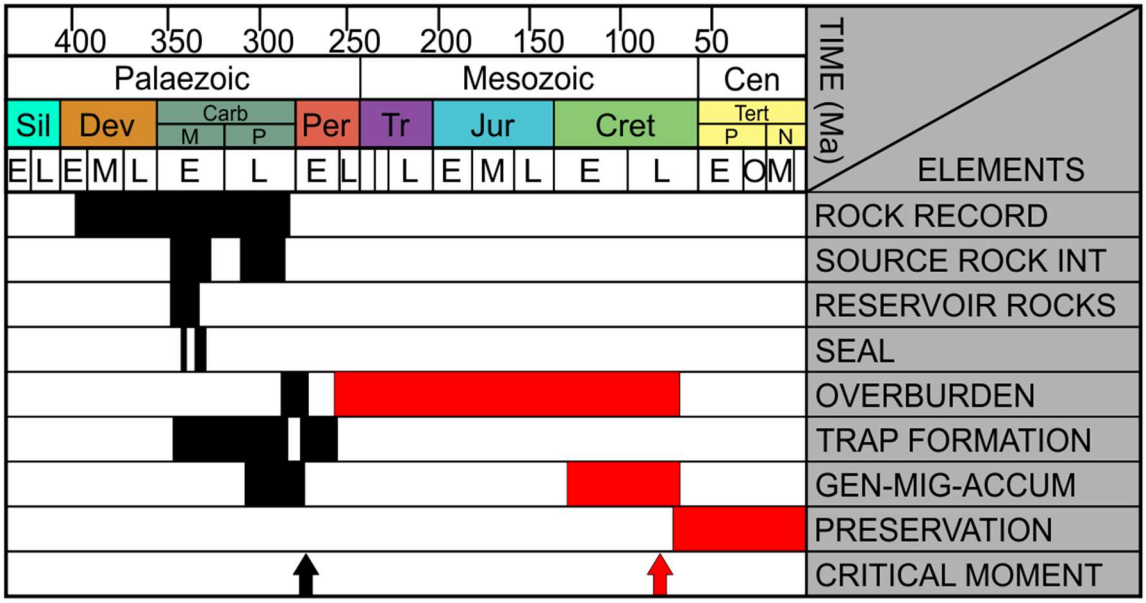

Figure 8-21: Modified petroleum elements table from the Midland Valley. Modified sections have been indicated as red. The lack of Mesozoic burial to cause the second phase of petroleum generation, migration, and accumulation means the second critical moments does not occur, thus prospectivity is greatly reduced.

The findings of this investigation have further implications of unconventional hydrocarbon exploration within the region. Unconventional hydrocarbon plays differ from conventional plays in that the source rock is also the reservoir and seal, requiring hydraulic stimulation to extract. Although the geological and geochemical criteria necessary for a successful unconventional play are widely met in regions of the Midland Valley (Monaghan 2014), the thermal histories produced in this investigation have implications for the remaining potential. If the province has been cooling since maximum palaeotemperatures were attained during the late Carboniferous-early Permian, then any hydrocarbons generated in the Paleozoic have since migrated, leaving any remaining source rocks, that may have been a target for unconventional exploration, depleted. Using the organic geochemistry parameter S2 value as a measure of the residual hydrocarbon available remaining in the sample, Monaghan (2014) found that the majority of the samples had relatively low S2 values. The highest S2 values were collected from outcrop samples, while low S2 values were from deeper

buried borehole samples, suggesting that hydrocarbons from more deeply buried samples may have already undergone maturation and migration.

Integration of the new thermochronological data for this investigation with existing information suggests that the effect of the igneous activity across the Midland Valley during the Carboniferous may have been more significant than previously estimated in the thermal maturation of organic material. Maximum palaeotemperatures would have been attained during the late Carboniferous-early Permian following burial under the elevated geothermal gradient. The cessation of volcanism and lack of significant Mesozoic successions, as indicated by the lack of overprinting the AFT data (Figure 8-18), suggests that the region maintained a general cooling trend during this time, although locally distributed, thin deposits cannot be ruled out. The lack of Mesozoic overburden burial eliminates the second critical moment in the petroleum generation play model (Figure 8-21) and indicates that the most significant generation, migration, and accumulation of hydrocarbons occurred during the late Carboniferous-early Permian. An increased Cenozoic cooling rate associated with exhumation by either the emplacement of the proto-Icelandic plume and magmatic underplating or far field stresses in relation to the opening of the Atlantic Ocean and/or collision of the African and Eurasian plates has exhumed the basin to its present-day level, thus continuing the trend of general cooling since the late Carboniferous-early Permian. The lack of a significant Mesozoic cover leaves the question of the origin of present-day proven oil and gas fields and seeps within the Midland Valley open, as it is unlikely that these are the result of Carboniferous-generated hydrocarbons still migrating. Thus, the source of this recent migration may be connected to the potential Late Cretaceous reheating, revealed by some thermal histories. Potential hydrocarbon source rocks are at present oil and gas mature at shallow depths, thus with relatively minor amounts of burial these source rocks may have generated the accumulations of hydrocarbons encountered in recent exploration ventures. Further analysis on the chemistry of the oil and gas in attempt to better constrain its provenance may be required, as well as attempting apatite helium thermochronology which can give insight into temperatures cooler than AFT analysis and better constrain any Late Cretaceous reheating.

Chapter 9 Conclusions and future work

As highlighted in Chapter 1, the main aims of this thesis were to provide a better understanding of the evolution of post-Caledonian sediment source(s) and pathways and to better constrain the post-Carboniferous thermal histories of the Midland Valley of Scotland, as the provenance of the sedimentary basin fill and the geological thermal history of the region were poorly constrained. Reducing the geological uncertainties associated with the region, which is vital for Scotland to meet its future low carbon geo-energy commitments, was achieved by quantifying the provenance of Carboniferous detrital material using a combination of multi-mineral, single grain U-Pb determinations, essential for discriminating between first cycle and poly-cycle sources. These data were used to construct a series of paleogeographical maps, which highlighted the evolution of the source areas and transport routes and compared these to existing models in published literature. The post-Carboniferous thermal histories of the Midland Valley were investigated using Apatite Fission Track Analysis; the combined data from both outcrops and boreholes, have provided quantitative and qualitative estimates on the timing, duration, and rate of the post-burial heating and cooling in the central and eastern Midland Valley. Reducing these uncertainties by constraining the provenance of the Carboniferous detrital material and the post-depositional thermal history of the region, is key to establishing the reservoir potentials, regardless of the stored medium (hydrocarbons, hydrogen, geothermal water), while constraining the magnitude and timing of post-Carboniferous heating, is vital for understanding the generation and migration of hydrocarbons from their source rock, and estimating the magnitude of burial and exhumation, essential for de-risking potential geo-energy options. The main conclusions of this thesis are summarised in the following sections along with suggestions of future work that could be undertaken.

9.1 Provenance

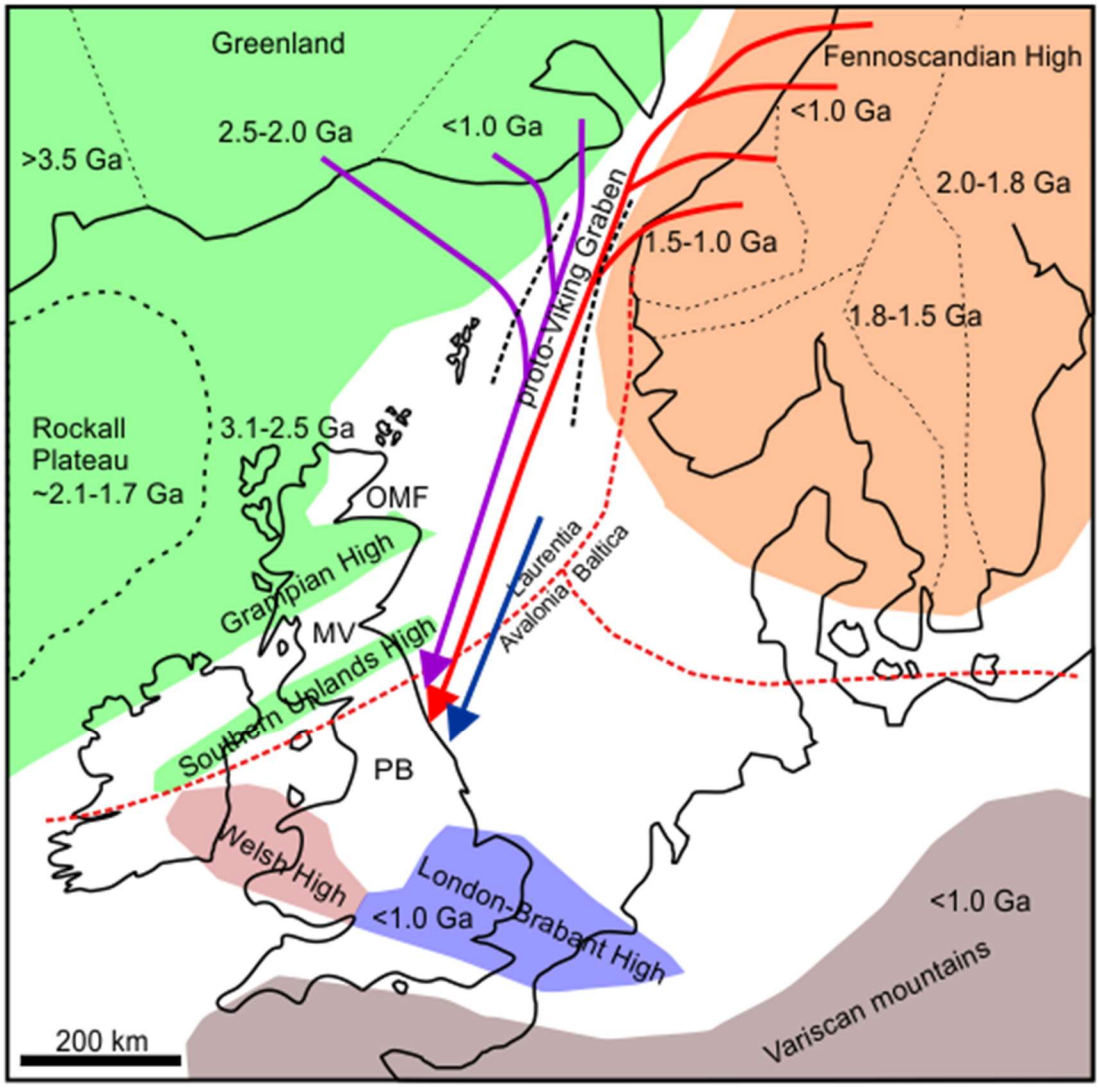

Figure 9-1: Palaeogeographical reconstruction indicating the suggested sediment provenance and pathways for previous studies during the late Devonian-Namurian. Arrows are redrawn from previous published literature. Blue arrow from Figure 10 of Hallsworth *et al.* (2000), indicating a derivation north of Scotland. Red arrow from Figure 8, Stuart *et al.* (2001), indicating a Scandian orogen related source. Purple arrow from Figure 1 and text description of Lancaster *et al.* (2017). While the provenance of the Lower Palaeozoic to Devonian sedimentary sequences within the Midland Valley has been studied in detail (Phillips *et al.* 1997; Phillips *et al.* 2004; Phillips *et al.* 2009; McKellar 2017), a modern provenance approach into investigating the source(s) of the Carboniferous clastic material had not been undertaken. In the past the source of the siliciclastic material has been attributed to have a derivation similar to that of Carboniferous strata in coeval basins across the British Isles (Figure 9-1) (Pennine, Southern North Sea, and Outer Moray Firth Basins) (Hallsworth *et al.* 2000; Morton *et al.* 2001; Morton and Whitham 2002; Lancaster *et al.* 2017; Heinemann *et al.* 2018). The conclusions of these previous studies were that the source of the Tayport Fm (Fammenian-Chadian) and the Firth Coal Fm (Brigantian) in the Outer Moray Firth and

the Millstone Grit Fm (Chokierian-Yeadonian) in the Pennine Basin lay to the north of Scotland, most likely East Greenland. This conclusion was largely based on the dominance of Palaeozoic age peaks in detrital U-Pb zircon spectra, which was attributed to first cycle material from the Caledonian orogeny related intrusions in East Greenland. Scotland was excluded as a major sediment contributor based on the lack of Proterozoic aged zircon, heavy mineral assemblages, and the greater availability of material to the north. Stuart *et al.* (2001) examined detrital muscovite $^{40}Ar/^{39}Ar$ from Fammenian-Westphalian sandstones across the British Isles, including one Holkerian ages sandstone from the eastern Midland Valley. The conclusion of this investigation attributed the source of the detrital material to unroofing of the Scandian nappes during the compressional phase of the Caledonian orogeny in Scandinavia along with post orogenic uplift of the Scandian orogeny (Stuart *et al.* 2001).

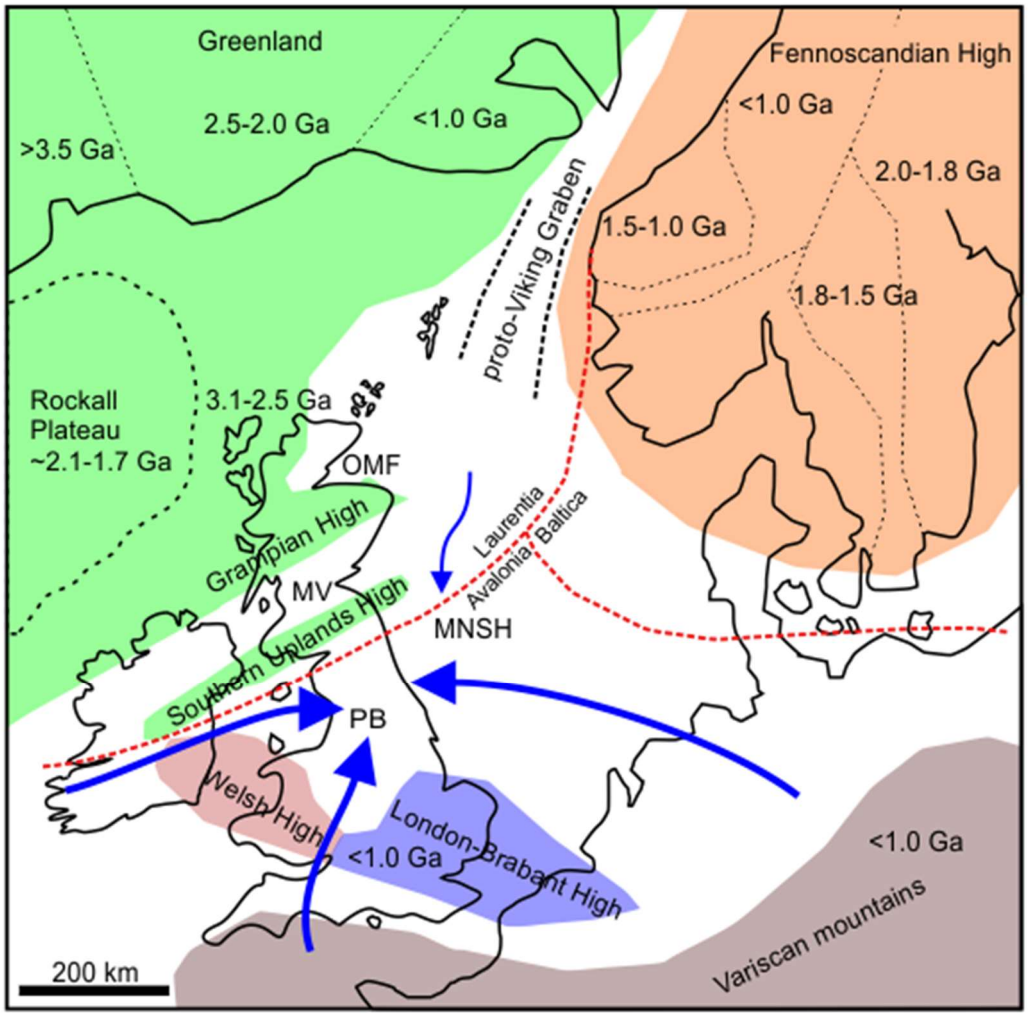

Figure 9-2: Palaeogeographical reconstruction indicating the suggested sediment provenance and pathways from previous studies during the Westphalian. Arrows are redrawn from Figure 10 of Hallsworth *et al.* (2000). Arrows indicate a wane of the northern source that dominated during the late Devonian-Namurian (Figure 9-1) and the appearance of material derived from eth east, west, and south.

Palaeocurrent indicators and detrital zircons from Westphalian samples from the Southern North Sea and onshore in the Pennine Basin (Hallsworth *et al.* 2000; Morton and Whitham 2002) suggest a decline in northerly sourced material with dominant sources now from the east, west, and south. The appearance of a younger Palaeozoic (c.330 Ma) and a 500-650 Ma populations in the zircon age spectra are attributed to Variscan and Cadomian sources to the south, while heavy mineral assemblages also indicating a westerly and easterly derivation (Figure 9-2) (Hallsworth *et al.* 2000; Morton and Whitham 2002).

The findings from this thesis indicate the sediment provenance of the Carboniferous Midland Valley show a greater affinity to material derived from the Scottish landmass and its nearby offshore regions, either through recycling of Devonian Old Red Sandstone, Grampian terrane metamorphic lithologies, and/or the Southern Upland terrane and first cycle material from Scottish Caledonian intrusions and associated volcanic material, compared to previous investigations (Hallsworth *et al.* 2000; Morton *et al.* 2001; Morton and Whitham 2002; Lancaster *et al.* 2017).

The multi-proxy provenance approach taken in this thesis allowed for the discrimination between first cycle and recycled material and indicates Arundian-Asbian sediments are dominated by Laurentian related recycled material with little first cycle input. This is evidenced by the wide range of Proterozoic zircon U-Pb ages sourced either directly from the Grampian High or from recycling Devonian Old Red Sandstone, located both onshore and offshore to the north-east Scotland and the scarcity of Palaeozoic U-Pb zircon ages. As well as sources to the north and northeast the Southern Uplands are also interpreted to have been a source, with the variations in the Proterozoic and Archean peaks taken as an indication that the sediments were not well homogenised prior to entering the Midland Valley.

Evidence of first cycle material entering the eastern Midland Valley from Scottish Caledonian intrusions occurs during the Brigantian, however local volcanic highs largely prevented this material from being deposited across the basin, thus western regions continued to receive sediment locally from the Southern Uplands and exposed volcanic highs. First cycle Caledonian material becomes the dominant source in the Midland Valley during the Pendleian-Arnsbergian, similar to that seen in the Outer Moray Forth and Pennine Basin, suggesting both a proximal Scottish and a distal East Greenland Caledonian sources were prevalent during this time. The Scottish Caledonian provenance continues to dominate the source in the Midland Valley during the Westphalian, contrary to the results

from the Pennine Basin, where the northerly derived influence is replaced by eastern, western, and southerly sources. This indicates the Southern Uplands remained a positive structure during the Westphalian, preventing material derived from other sources, that dominates the Pennine and Southern North Sea Basins, from entering the Midland Valley.

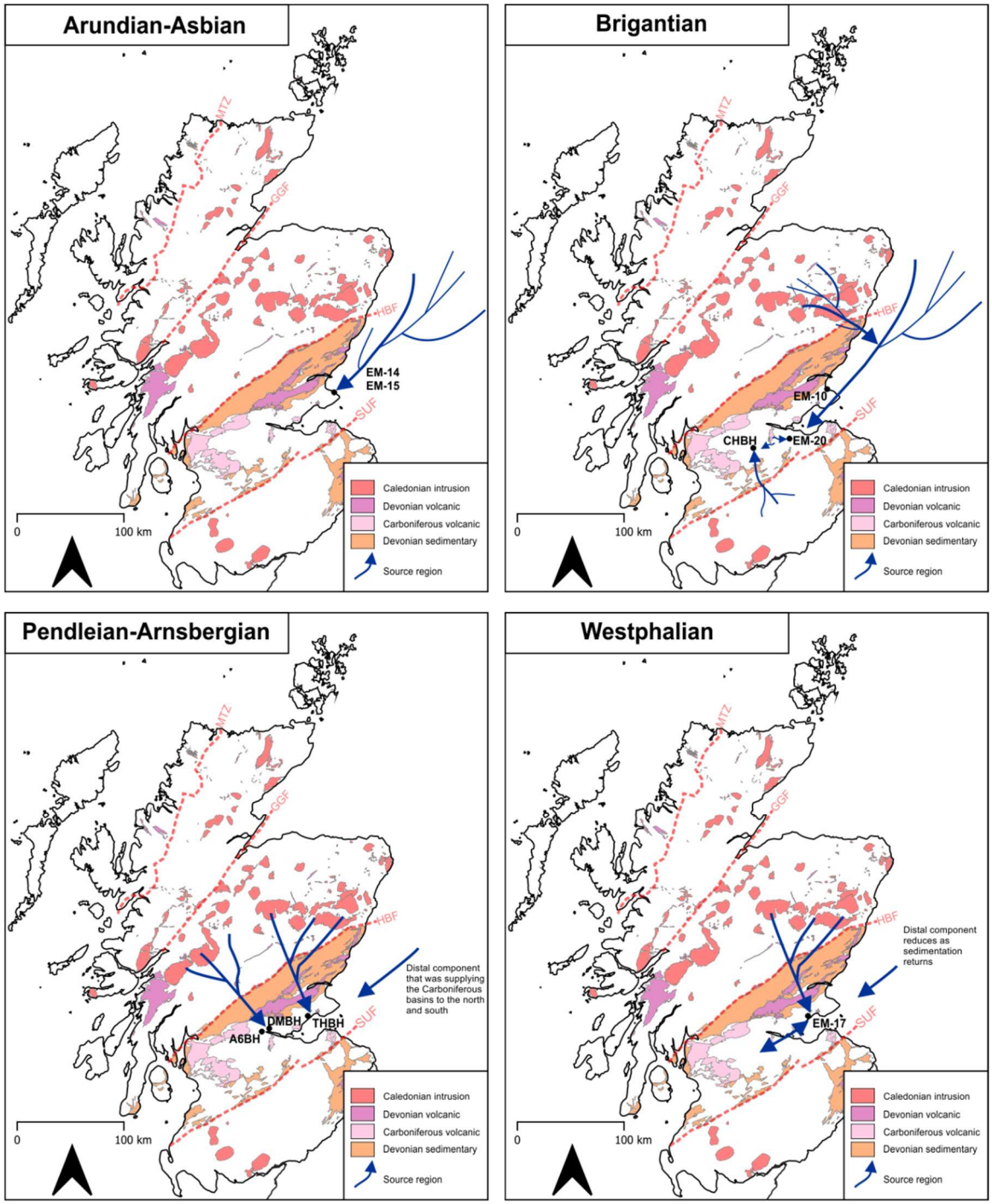

Figure 9-3: Palaeogeographical reconstruction indicating the suggested sediment provenance and pathways from this thesis during the Carboniferous.

The results from the provenance investigation undertaken in this thesis shows that the source of the sediment within the Carboniferous Midland Valley of Scotland changed through time. Although

similarities may exist between the Midland Valley and other Carboniferous depocentres in the British Isles, this temporal and spatial variability in a geologically complex area indicates, that assuming a constant similar provenance between these basins, may led to an erroneous reservoir characterisation. It has also shown that combining multi-proxy provenance approaches is essential to discriminate between first and polycyclic sources and that apatite may be able to survive recycling under the right conditions (limited exposure to acidic weathering, abundant in host sedimentary rock, relatively short residence time).

9.1.1 Future work

Recommended future work connected to this part of the thesis would be to include additional geochemical data from the detrital grains to better constrain their provenance. Trace element composition of apatite has received recent attention as a provenance indicator as trace element concentration is believed to be host specific (Glorie *et al.* 2017; Gillespie *et al.* 2018; O'Sullivan *et al.* 2020). Gathering this information for the detrital apatite in the Carboniferous Midland Valley and those found within Caledonian intrusions may help to pinpoint which region(s) the material was sourced from specifically. Some preliminary work of this nature was undertaken as a proof of concept at the University of Glasgow using the LA-ICP-MS methodology highlighted in Chapter 3.

9.2 Thermochronology

The AFT data and thermal histories presented in this thesis offer an alternative to previous investigations that suggest either Carboniferous maximum palaeotemperature followed by protracted cooling or Mesozoic burial resulting in Cenozoic maximum palaeotemperatures followed by rapid exhumation related cooling (Duddy *et al.* 1992; Vincent *et al.* 2010). The trend of the AFT data generally reflects the Carboniferous structure of the region with older AFT ages found on structural highs and younger ages found towards the synclinal limbs, partially reset AFT data are also found within synclinal cores, indicated by the similarity between the sample AFT central age and stratigraphic age. These results suggest that a more appropriate model for the burial and exhumation history for the Carboniferous Midland Valley can be subdivided into three episodes spanning from the Carboniferous to the present day: 1) Carboniferous-Permian heating; 2) Permian-Mesozoic cooling; 3) Cenozoic cooling.

9.2.1 Carboniferous-Permian heating

Rapid heating following burial in the sedimentary basin under the influence of an elevated geothermal gradient, supported by the widespread Carboniferous volcanism, allowed the thermal maturation of organic matter without requiring the significant volumes of material necessary under normal geothermal gradients. Syn-sedimentary growth folding of major Carboniferous depocentres, the Midlothian-Leven and Clackmannan synclines, continued under a transtensional regime allowing the thermal resetting of AFT data of samples found within the synclines, while samples located on anticlinal and tectonic highs remained within the PAZ and thus were only partially reset. Folding proceeded into the Westphalian Scottish Coal Measures as either a continuation the transpressional-transtensional movement experienced during the Viséan-Namurian, or as a result of Variscan exhumation and regional transpression (Coward 1993; Ritchie *et al.* 2003; Underhill *et al.* 2008). Dextral strike slip gave way to north-south extension in the latest Carboniferous-early Permian due to the opening of the Northern and Southern Permian basins in the North Sea, changing the focus of the sedimentary routing system (Glennie and Underhill 2009). Thermal histories indicate that maximum palaeotemperatures were reached during the late Carboniferous-early Permian; however, due to the sensitivity of the AFT analysis it is not possible to decipher whether significant thicknesses of Permian deposits, like those seen in the Mauchline Basin and Arran once covered the entire Midland Valley or were limited to their present-day locations. Volcanism within the Midland Valley ceased following the intrusion of the Permian East Fife vents and Alkaline basic sills allowing the thermal relaxation of the elevated geothermal gradient.

9.2.2 Permian-Mesozoic cooling

The initiation of cooling following Carboniferous-Permian heating is evident from all thermal histories with a slight variation seen in the eastern Midland Valley profile models, which suggest an initially higher rate of cooling until c.270 Ma, followed by a similar rate seen in the western samples. Samples from the Central region suggest heating continued for longer here, or was to a greater extent, and took longer to return to the PAZ from elevated temperatures. The Fife (north) thermal histories suggest that the East Fife vents may have maintained elevated temperatures locally for longer than experienced elsewhere or that Permian sediments, present offshore may have encroached onto this region. After maximum palaeotemperature was attained during the late Carboniferous-early Permian in the Midland Valley, the thermal histories produced in this thesis suggest that the cooling trend of

the region was similar to that recorded in other thermal histories for onshore northern Scotland (Döpke 2017; Amin 2020). Further evidence for the disconnect between the post Carboniferous thermal histories of onshore Midland Valley and its offshore regions can been seen in Chapter 6 Figure 6-5, where the AFT data from offshore boreholes have a different age vs depth relationship in comparison to onshore Midland Valley data.

9.2.3 Cenozoic cooling

An increase in cooling rate approaching the beginning of the Cenozoic is most evident in the multi-sample profile thermal history models. This cooling pulse has been recorded frequently in thermal history investigations across Britain and Ireland and has been attributed to either far field stress originating from the opening of the Atlantic Ocean and/or collision of the African and Eurasian plates or proto-Icelandic plume emplacement and associated mantle driven processes such as magmatic underplating, lithospheric thinning and dynamically supported uplift. As the post Cenozoic cooling occurs out of the temperature sensitivity range of AFT analysis, it is difficult to differentiate between these two hypotheses, however the estimated exhumation calculated in this investigation conform to those calculated based on the proto-Icelandic plume emplacement and magmatic underplating model.

9.2.4 Implication for petroleum prospectivity

As highlighted in Chapter 8 the findings of this thesis have implications of the petroleum prospectivity of the region. Previous work has suggested two phases of petroleum generation in the Midland Valley, an initial phase associated with Carboniferous burial prior to Variscan uplift, and a second during the late Mesozoic associated with the accumulation of Mesozoic deposits which was subsequently terminated by Cenozoic uplift (Underhill *et al.* 2008; Vincent *et al.* 2010). Though the findings from this thesis agrees with late Carboniferous-early Permian maximum paleotemperatures and attainment of current levels of organic maturity there is little evidence to support continued and significant volumes of Mesozoic sediment across the Midland Valley. However, the lack of a significant Mesozoic cover leaves the question of the origin of present-day proven oil and gas fields and seeps within the Midland Valley open, as it is unlikely that these are the result of Carboniferous generated hydrocarbons still migrating. One possible explanation for this could be that Mesozoic burial may not have been of the extent to have affected the AFT data in all samples and thus is lost when the multi-sample modelling approach. It has been noted that some individual models do

indicate a reheating event toward the end of the Mesozoic that could be connected to the Late Cretaceous transgression. This hypothesis would require further work to test. Also, in relation to unconventional prospects, whilst source rocks are present at the required rank in sampled locations, the high geothermal gradient experienced by these rocks post burial, may have driven off much of the potential resources by this early-stage heating and maturation.

9.2.5 Future work

Despite the success of this thermochronology study, there are still many questions left open, relating to both the Midland Valley study area and the applied methodology, that would require further work to investigate.

9.2.5.1 Midland Valley

To investigate the presence of late Mesozoic reheating prior to Cenozoic cooling, related to Late Cretaceous transgression and recent petroleum generation, low temperature thermochronology with a temperature sensitivity cooler that AFT could be applied. One such technique is apatite helium thermochronology (AHe), which is sensitive to temperatures between ~40-75°C (Farley 2000), although the validity of applying this technique to detrital samples has received recent attention (Fox *et al.* 2019). Application of the AHe technique may also help constrain the timing and magnitude of Cenozoic cooling and differentiate between its possible sources. Due to the availability of both outcrop and borehole samples, the scope of this thesis was limited to the central and eastern regions of the Midland Valley, however any additional samples collected from new boreholes drilled, particularly in the western area of the Midland Valley, would help in resolving the spatial variability and test the influence of the Clyde Plateau Volcanic Fm in this region of the basin which still remains poorly constrained.

9.2.5.2 Methods

There remains scope for methodological improvements to the AFT technique including improving annealing models (Ketcham 2019), increasing understanding around how radiation damage is affecting annealing (Kohn *et al.* 2009; McDannell *et al.* 2019), and the uncertainty around both producing and interpretating inverse models (Vermeesch and Tian 2014; Gallagher and Ketcham 2018). Although the LA-ICP-MS method for determining AFT ages has received recent attention

(Hasebe *et al.* 2004; Chew and Donelick 2012; Gleadow *et al.* 2015; Cogné *et al.* 2020; Ansberque *et al.* 2021) the approach between labs has yet to be standardised in the same way the EDM method has been, nor has a cross-laboratory comparison investigation been undertaken. This would be beneficial as the new method becomes increasingly adopted by more practicing thermochronology labs. The use of LA-ICP-MS for uranium concentration determinations also allows for the simultaneous acquisition of additional trace elements and REE data. This is not only useful for provenance determination, as discussed above, but identify the present of multi-kinetic AFT populations within single samples that would otherwise go unnoticed.

Chapter 10 Appendices

10.1 Appendix A - Sample details

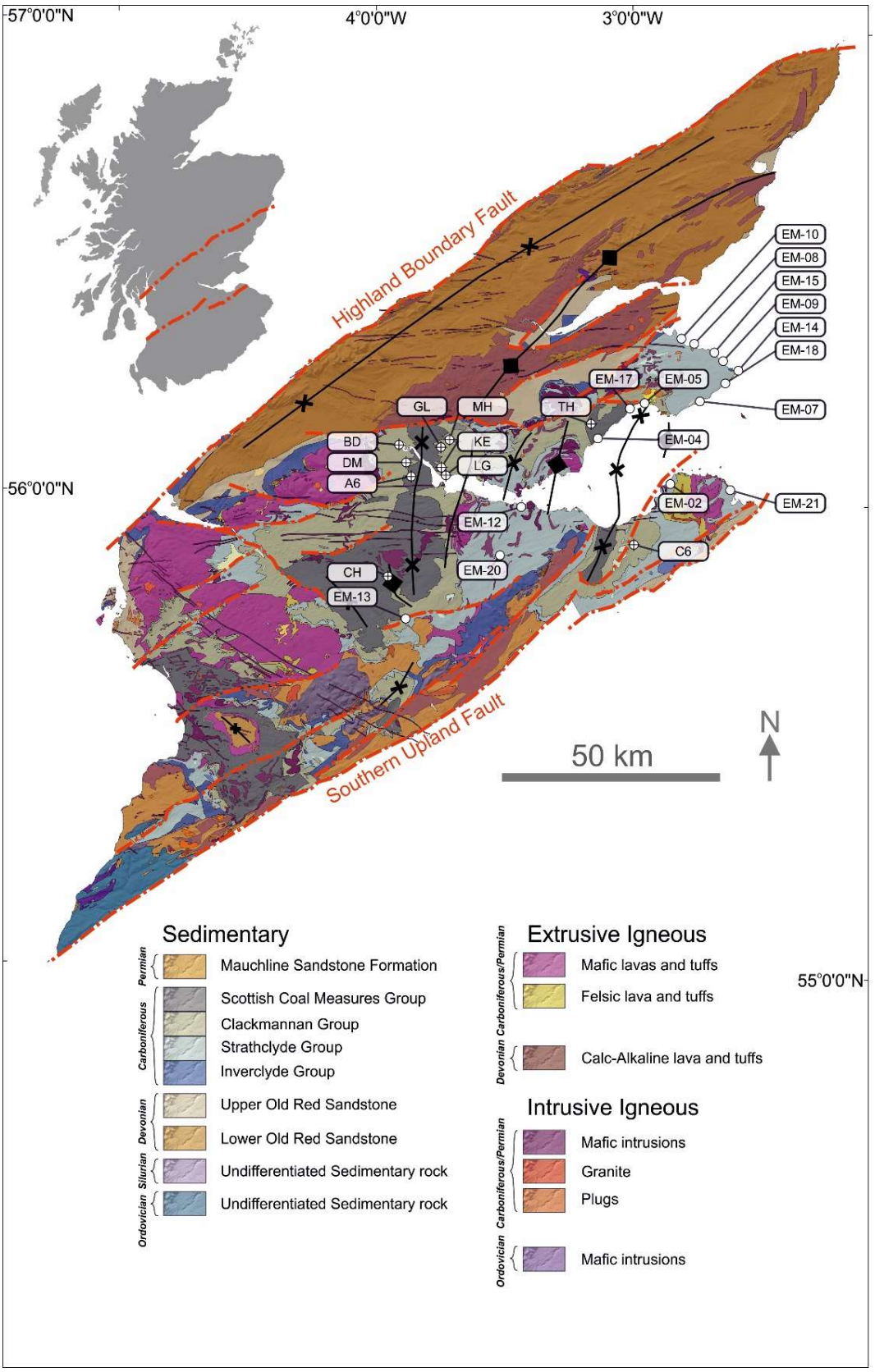

Figure 10-1: Sample locations and geology.

Table 10-1:Sample details.

Sample I.D.	Lat. (º)	Long. (º)	Grid Reference	Lithology	Depth (m)	Series	Formation	Analysis	VR Est.	Notes
Outcrop										
EM-001	56.0625	-2.8120	NT4953785815	Sandstone	Outcrop	Viséan	Gullane Fm	No apatite	N/A	Collected from near Archerfield Links golf course.
EM-002	56.0390	-2.8480	NT4726383226	Sandstone	Outcrop	Viséan	Gullane Fm	AFT	0.5-0.6*	Collected near Aberlady Bay.
EM-003	55.9730	-2.9400	NT4143175955	Sandstone	Outcrop	Namurian	ULGS	No apatite	N/A	Collect from coastal exposure near Prestonpans.
EM-004	56.1420	-3.0810	NT3292694892	Sandstone	Outcrop	Westphalian	MCMS	AFT	0.6-1.0*	Collected from West Wemyss.
EM-005	56.2110	-2.9450	NO4148202448	Sandstone	Outcrop	Westphalian	MCMS	AFT	0.6-1.0*	Collected from Lower Largo beach.
EM-006	56.2863	-2.6000	NO6295410589	Sandstone	Outcrop	Viséan	Clyde Sst Fm	No apatite	N/A	Collected from coastal exposure north of Crail.
EM-007	56.2100	-2.7390	NO5425802180	Sandstone	Outcrop	Viséan	Pathhead Fm	AFT	0.5-0.6*	Collected from St. Monans beach.
EM-008	56.3277	-2.7327	NO5478815277	Sandstone	Outcrop	Viséan	Pittenweem Fm	AFT	0.5-0.6*	Collected from coastal exposure along coast south of St. Andrews
EM-009	56.2930	-2.6259	NO6135811349	Sandstone	Outcrop	Viséan	Anstruther Fm	AFT	0.5-0.6*	Collected from coastal exposure south of Kingsbarns carpark.
EM-010	56.3320	-2.7750	NO5217815784	Sandstone	Outcrop	Viséan	Sandy Craig Fm	AFT	0.5-0.6*	Collected from St. Andrews, East Sands.
EM-011	56.2130	-2.7240	NO5519202504	Sandstone	Outcrop	Viséan	Pittenween Fm	No apatite	N/A	Collected from coastal exposure near Pittenween.
EM-012	55.9906	-3.3882	NT1349978385	Sandstone	Outcrop	Viséan	WLOS (H)	AFT	0.5-0.6*	Collected from South Queensferry, west of the railway bridge.
EM-013	55.7136	-3.8224	NS8560448190	Sandstone	Outcrop	Tournasian	Report	AFT	N/A	Collected from Braidwood
EM-014	56.2800	-2.5880	NO6369109881	Sandstone	Outcrop	Viséan	Fife Ness Fm	AFT & U-Pb	0.5-0.6*	Collected from Crail coastal exposure.
EM-015	56.3095	-2.6544	NO5961113202	Sandstone	Outcrop	Viséan	Anstrusther Fm	AFT & U-Pb	0.5-0.6*	Collected from coastal exposure north of Kingsbarns carpark.
EM-016	56.0294	-3.4690	NT0855182807	Sandstone	Outcrop	Viséan	Pathhead Fm	No apatite	N/A	Collect from coastal exposure near Rosyth Church, Limekilns.
EM-017	56.2099	-2.9582	NO4066102337	Sandstone	Outcrop	Westphalian	MCMS	AFT & U-Pb	0.6-1.0*	Collected from coastal exposure, south of Lundin Links golf course.
EM-018	56.2610	-2.6180	NO6181507783	Sandstone	Outcrop	Viséan	Anstruther Fm	AFT	0.5-0.6*	Collected from coastal exposure near Anstruther Village.
EM-019	56.1210	-3.1300	NT2984392604	Sandstone	Outcrop	Namurian	Passage Fm	No apatite	N/A	Collected from coastal exposure near Ravenscraig Park.
EM-020	55.8915	-3.4749	NT0785667468	Sandstone	Outcrop	Viséan	WLOS (H)	U-Pb	N/A	Collected from Calder Wood park, Mid Calder.
EM-021	56.0236	-2.5900	NT6332381345	Sandstone	Outcrop	Tournasian	Report	AFT	N/A	Collected from north of Belhaven Bay
Borehole										
A6-G1	56.049	-3.788	NS8872985457	Sandstone	-745	Namurian	LCF	AFT	0.8-0.9*	Collected from Airth 6 borehole, core sample. All samples from above the Black Metal Marine Band which is at a depth of 908.3 m. Other key horizons: Upper annockburn Coal 865.6 m, Lower Bannockburn Coal 879.3 m.
A6-G2	56.049	-3.788	NS8872985457	Sandstone	-817	Namurian	LCF	AFT	0.8-0.9*	
A6-G3	56.049	-3.788	NS8872985457	Sandstone	-873	Namurian	LCF	AFT & U-Pb	0.94**	

Sample I.D.	Lat. (º)	Long. (º)	Grid Reference	Lithology	Depth (m)	Series	Formation	Analysis	VR Est.	Notes
BD-G1	56.116	-3.842	NS8556593001	Sandstone	-471	Namurian	LCF	AFT	>1.0*	Collected from Bandeath borehole, core sample. Sample from above the Black Metals Marine Band at 545.5 m depth. Other key horizons: Hartley Coal 434.3 m., Upper Bannockburn Coal 493.8 m.
LG-G1	56.057	-3.704	NS9398386215	Sandstone	-810	Namurian	LCF	No apatite	N/A	Collected from Longannet 1 borehole, core sample. Samples collected from above the Black Metals Marine Band at 966.2 m depth.
LG-G2	56.057	-3.704	NS9398386215	Sandstone	-941	Namurian	LCF	AFT	>1.0*	
MH-G1	56.127	-3.672	NS9615293967	Sandstone	-686	Namurian	LCF	AFT	>1.0*	Collected from the Meadowhill 1z borehole, core samples. Samples collected from the Black Metals Marine Band at 875.0 m depth. Other key horizons: Cowdenbeath 7 Foot Coal 661 m, Lochgelly Splint Coal 813 m, Cowdenbeath 5 Foot Coal 981 m.
MH-G2	56.127	-3.672	NS9615293967	Sandstone	-815	Namurian	LCF	AFT	>1.0*	
TH-G1	56.159	-3.136	NT2954096839	Sandstone	-611	Namurian	LCF	AFT	0.6-1.0*	Collected from the Thornton 1 borehole, core samples. Samples THG1 and THG2 collected from above the Black Metals Marine Band at 735 m depth, sample THG3 collected below it. Other key horizons: Lochgelly Splint Coal 719 m, Cowdenbeath 5 Foot Coal 777.2 m.
TH-G2	56.159	-3.136	NT2954096839	Sandstone	-734	Namurian	LCF	AFT	0.6-1.0*	
TH-G3	56.159	-3.136	NT2954096839	Sandstone	-798	Namurian	LCF	AFT & U-Pb	0.6-1.0*	
CH-G1	55.837	-3.875	NS8267162010	Sandstone	-720	Viséan	WLOS (H)	AFT & U-Pb	0.8-0.9**	Collected from Craighead borehole, core sample. Sample collected from above the Burdiehouse Limestone, not penetrated by bore and above the Raeburn Shale at a depth of 720 m.
C6-G2	55.901	-2.987	NT3838367983	Sandstone	-460	Viséan	WLOS (C)	AFT & U-Pb	0.6-0.8**	Collected from the Cousland 6 borehole, core sample. Sample collected from below the Burdiehouse Limestone at a depth of 325 m. Other key horizons: Top of the Gullane Fm 500 m.
DM-G1	56.079	-3.811	NS8738588833	Sandstone	-340	Namurian	ULGS	AFT & U-Pb	>1.0*	Collected from the Dunmore Moss borehole, core sample. Sample collected from beneath the Castlecary Limestone at a depth of 296 m. Other Key horizons: Plean No. 1 Limestone 396 m, Upper Hirst 486 m.
KE-G1	56.058	-3.705	NS9392386328	Sandstone	-280	Namurian	ULGS	AFT	>1.0*	Collected from the Kincardine East Longannet Col. Borehole, core sample. Sample collected from beneath the Castlecary Limestone at a depth of 260 m. Other key horizons Plean No. 1 Limestone Coal 350, Calmy Limestone 460 m, Upper Hirst 500m.
GL-G1	56.114	-3.705	NS9407792560	Sandstone	-568	Namurian	ULGS	AFT & U-Pb	0.6-0.7*	Collected from the Gartlove borehole, core sample. Sample collected from beneath the Castlecary Limestone at a depth of 229 m. Other key horizons Plean No. 1 Limestone 340 m.
MB3-G1	56.179	-3.107	NT3137699036	Sandstone	-1141	Namurian	LLGS	No apatite	N/A	Collected from Milton of Balgonie 3 borehole, core sample.
ST-G1	55.871	-3.019	NT3633364673	Sandstone	-626	Viséan	Gullane Fm	No apatite	N/A	Collected from Stewart 1 borehole, core sample.
LS-G1	55.802	-3.651	NS9660657758	Sandstone	-428	Viséan	WLOS (H)	No apatite	N/A	Collected from Leven Seat 1 borehole, core samples

10.2 Appendix B - Sample preparation

The following appendix details the practical approach adopted for sample preparation and uranium concentrations determinations by LA-ICP-MS in this thesis.

10.2.1 Mineral separation

Apatite and zircon crystals used in this study were separated from their host rock and processed using a series of techniques i.e. crushing, sieving, washing, density liquid and magnetic separation.

Sedimentary samples were collected from outcrop and drilled boreholes across the Midland Valley of Scotland. Samples were disaggregated using a jaw crusher and sieved to extract the 63-500µm fraction, with the >500µm fraction reprocessed, until all fractions were smaller than 500 microns. A disk mill was not used in the separation process to avoid unnecessary crystal fragmentation. The 63-500µm fraction was then washed and separated on the bases of density using a Gemini shaking table, which advantageously removes clay and light material, while concentrating dense minerals. The total sample was then dried in a low temperature (~40°C) oven to avoid exposing the sample to any excess heating. As apatite (c.3.2 g/cm^3) and zircon (c.4.7 g/cm^3) are denser than the minerals that comprise the bulk of sedimentary rocks (i.e. quartz c.2.65 g/cm^3 and feldspar c.2.70 g/cm^3), the dense fraction separated by the Gemini table was selected for further processing, while the light fraction was preserved. The 'heavy' fraction was then passed through a vertical Frantz Magnetic separator (@ 1.0–2.0 A) for the removal of strongly magnetic minerals (apatite and zircon are non-magnetic or with a very low magnetic susceptibility). Further density separation of the non-magnetic fraction was undertaken using the heavy liquid, lithium hetropolytungstate (LST) which has a density of 2.80 g/cm^3. The sample fraction is immersed in the liquid, and stirred for a few minutes, to ensure a good mix and then left to rest. After a period of time, usually 15 to 20 minutes, minerals of density >2.80 g/cm^3 (including apatite and zircon) will sink and become concentrated at the bottom of a separation flask and can then be easily tapped off. Following this separation, all fractions were washed in de-ionized water and dried, while the LST was recovered for further use. Once dried, the heavy fraction was passed through a horizontal Frantz magnetic separator with a range of inclinations (5°-20°) and forward slopes (10°-20°) and increasing the current through the magnet with each pass (0.3, 0.5, 1.0, &1.5 A). Each separated fraction was checked under binocular microscope to ensure there was a satisfactory separation and concentration of the target minerals

(apatite & zircon) in the non-magnetic fraction. Separation of the apatite and zircon fraction was achieved by using a second density liquid Di-iodomethane (DiM) which has a density of 3.3 g/cm^3. The float (apatite) and sink (zircon) fractions of this separation were then washed with acetone and dried under an extraction hood.

10.2.2 Mounting

A small quantity of dry apatite separate was mounted in epoxy resin, which was contained using a nylon washer with an internal diameter of 25mm, lying on a glass slide coated in releasing agent. The mounts were allowed to cure and harden at room temperature for 48 hours as per manufacture instructions.

10.2.3 Polishing

Once hardened, the washer was cut out and the sample mounts detached from the glass. The mounts were ground and polished using a polishing machine. Internal surfaces were revealed using #1200 resin bonded diamond lap. Further polishing of grain internal surfaces was achieved using 6μm, 3μm, and 1μm diamond paste. The amount of time spent at each stage varied between samples and regular checks of the polished surface are necessary to ensure the satisfactory finish has been achieved before moving to the next stage.

10.2.4 Etching

In order to observe fission tracks under an optical microscope, the polished apatite mounts are etched in acid. All samples used in this investigation were etched for 20 seconds in 5.5 Molar nitric acid (HNO_3) kept at a constant temperature of 20℃ ±1℃. This allows all tracks intersecting the polished surface of the mineral to be enlarged, so they can be viewed under an optical microscope and counted. Following etching the samples are immediately submerged in clean water to stop the etching process.

10.2.5 Microscope Methodology for AFT analysis

Fission track analysis for this investigation was undertaken in two locations, 1) The University of Glasgow, Scotland. 2) the University of Melbourne, Australia.

10.2.6 The University of Glasgow

Fission tracks and track length measurements were counted using a Zeiss Axioplan microscope at a magnification of x1250. Mount referencing, grain location, and track length measurements were recorded using the FT Stage 4.04 software (Dumitru 1993). Each mount was systematically scanned for grains that intersected the polished surface parallel to the minerals c-axis. Such grains can be identified by the uniform alignment of etch figures (parameter Dpar). Grains with a poorly polished surface, fracture network, visible zonation, and inclusions were not considered for counting, as these would be detrimental to accurate analysis. The area of interest was defined using a measuring grid and spontaneous fission tracks were then counted on a minimum of 20 grains per sample. The long axis of the etch figure, parallel to the c-axis, parameter Dpar, was also measured using this setup and a minimum of four measurements were taken per grain, with the average of these measurements reported.

Track length measurements were also recorded using the equipment highlighted above, which had been previously calibrated by the analyst using a microscope 1mm graticule with an accuracy of 1µm. Only confined tracks on grain which intersected the polished surface parallel to their c-axis were measured. The total length of the confined track, its angle to the crystal c-axis and a minimum of four Dpar measurements were recorded for each track length measurement. If possible, a minimum of 100 tracks lengths were measured per sample, however in cases of low track density this was not always achievable.

10.2.7 The University of Melbourne

Fission tracks and track lengths were measured on a Zeiss AxioImager at a magnification of x1000. This was connected to the Autoscan system software, Trackworks. Grain mount referencing and coordination was undertaken by recording the location of 3 copper target TEM grids. Once the reference system had been setup, the mount was then systematically scanned for grains that intersected the polished surface parallel to the crystals c-axis. Similar to the University of Glasgow method, these grains were screened for zonation, inclusions, and any other defect that would be detrimental to quality analysis. Target regions for possible counting are selected using the following criteria: appropriate grains (i.e. no mineral inclusions, fractures or deep polishing scratches); uniform track density (no parent zonation), countable area of at least 50 microns in diameter, large enough to contain a laser ablation pit, and contained within a minimum of 10µm from the grain edge or

penetrating fracture. The use of this setup allows for a series of high-resolution stacked images to be taken in transmitted and reflected light. This permanent record is a major advantage because laser ablation is a destructive technique and thus removes the physical evidence of the area of interest and, with it, the spontaneous tracks. Analyses were captured by TrackWorks using a 3.2MP AVT Oscar F-320C camera mounted on a Zeiss AxioImager microscope with a 1000x total magnification and a 100x dry objective (calibration = 0.07 µm by 0.07 µm per pixel). Track counts were obtained by automated counting in FastTracks using the 'coincidence mapping' technique of Gleadow et al. (2009); however, each track count area was also manually inspected for both spontaneous tracks and Dpar measurements.

The same procedure was used to measure the lengths of the horizontal, confined tracks, and high-quality images of each track length are permanently stored and can be revisited at any time. A target of at least 100 track lengths was set for each sample and this was often surpassed. Samples with particularly low spontaneous track densities were exposed to ^{252}Cf-irradiation at the University of Melbourne. This technique greatly increases the number of fission track lengths available for track length measurement. In this case, another mount was prepared. mount was exposed to a ^{252}Cf fission source in a vacuum chamber to enhance the number of confined track intersections below the surface. Isotopic concentrations for analysis were measured by LA-ICP-MS using the analytical equipment and parameters highlighted in Chapter 3, 4, and 6.

10.3 Appendix C - U-Pb data tables

10.3.1.1 EM-17 (Zircon)

Grain I.D.	238U (ppm)	238/206 ratio	206/238 1SE	207/235 ratio	207/235 1SE	207/206 ratio	207/206 1SE	238/206 Age (Ma)	2σ	207/235 Age (Ma)	2σ	207/206 Age (Ma)	2σ	Disc. (%)	preferred Age (Ma)	preferred Err. (2σ)
17Z-01	112.4	3.995	0.020	3.231	0.018	0.0937	0.0002	1440.0	13.0	1464.6	8.8	1500.4	9.1	4	1500.4	9.1
17Z-02	15.5	1.912	0.012	13.589	0.096	0.1885	0.0006	2712.3	28.1	2721.5	13.9	2728.4	10.5	1	2728.4	10.5
17Z-03	48.4	3.690	0.025	3.628	0.027	0.0971	0.0003	1545.9	18.3	1555.6	12.0	1568.9	12.4	1	1568.9	12.4
17Z-04	161.1	3.877	0.021	3.336	0.020	0.0939	0.0002	1479.1	14.4	1489.5	9.5	1504.2	9.3	2	1504.2	9.3
17Z-05	326.0	4.822	0.033	2.384	0.017	0.0834	0.0002	1215.0	15.0	1237.7	10.6	1277.5	10.8	5	1277.5	10.8
17Z-06	152.0	3.429	0.012	4.149	0.018	0.1032	0.0003	1649.5	10.1	1664.0	7.4	1682.3	9.7	2	1682.3	9.7
17Z-07	28.9	3.552	0.026	5.990	0.050	0.1544	0.0007	1598.9	20.7	1974.4	14.9	2394.5	14.3	33		
17Z-08	219.4	3.492	0.028	4.271	0.036	0.1082	0.0002	1623.5	23.1	1687.7	13.9	1768.5	8.3	8	1768.5	8.3
17Z-09	82.8	1.939	0.015	14.084	0.115	0.1982	0.0004	2680.5	34.6	2755.4	15.9	2810.7	7.4	5	2810.7	7.4
17Z-10	327.6	5.233	0.033	2.128	0.014	0.0808	0.0002	1127.3	13.0	1158.0	9.5	1215.9	10.0	7	1127.3	13.0
17Z-11	303.3	14.567	0.097	0.531	0.004	0.0561	0.0002	428.0	5.5	432.6	5.3	456.9	15.0	6	428.0	5.5
17Z-12	62.8	6.184	0.054	1.593	0.015	0.0715	0.0003	966.2	15.6	967.4	11.8	970.0	14.6	0	966.2	15.6
17Z-13	195.0	3.566	0.033	3.945	0.038	0.1021	0.0003	1593.4	26.2	1623.0	15.9	1661.6	10.7	4	1661.6	10.7
17Z-14	237.2	2.902	0.021	6.008	0.045	0.1265	0.0003	1908.8	23.6	1977.0	13.3	2049.2	8.5	7	2049.2	8.5
17Z-15	349.0	14.767	0.077	0.518	0.003	0.0555	0.0002	422.4	4.3	423.6	4.3	429.8	14.5	2	422.4	4.3
17Z-16	117.2	14.815	0.143	0.506	0.006	0.0544	0.0003	421.1	7.9	416.0	7.9	387.9	28.5	-9	421.1	7.9
17Z-17	228.3	3.765	0.028	3.704	0.029	0.1012	0.0003	1518.4	19.9	1572.2	12.6	1645.2	9.6	8	1645.2	9.6
17Z-18	44.3	1.934	0.021	13.325	0.146	0.1870	0.0005	2686.4	46.8	2702.9	21.0	2715.3	8.3	1	2715.3	8.3
17Z-19	231.0	5.970	0.089	1.930	0.030	0.0836	0.0003	998.3	27.6	1091.6	20.5	1282.6	13.3	22	998.3	27.6
17Z-20	208.0	2.061	0.019	13.161	0.128	0.1968	0.0005	2549.9	39.6	2691.3	18.7	2799.3	8.3	9	2799.3	8.3
17Z-21	530.0	6.969	0.146	1.612	0.035	0.0815	0.0005	864.4	33.8	974.7	27.3	1232.4	24.1	30	864.4	33.8
17Z-22	167.7	5.992	0.047	1.696	0.014	0.0737	0.0002	995.0	14.4	1006.9	10.7	1032.9	11.8	4	995.0	14.4
17Z-23	474.1	7.800	0.064	1.268	0.011	0.0718	0.0002	777.6	12.0	831.5	10.1	978.5	13.9	21	777.6	12.0
17Z-24	272.0	14.948	0.123	0.512	0.005	0.0556	0.0002	417.5	6.7	419.9	6.2	433.4	16.1	4	417.5	6.7
17Z-25	26.1	2.096	0.011	12.115	0.073	0.1843	0.0005	2514.2	22.4	2613.4	11.8	2691.1	9.0	7	2691.1	9.0
17Z-26	47.3	1.950	0.013	13.368	0.091	0.1891	0.0004	2669.0	28.3	2706.0	13.4	2733.7	7.6	2	2733.7	7.6
17Z-27	604.6	15.328	0.083	0.501	0.003	0.0557	0.0002	407.4	4.3	412.4	4.2	440.6	12.8	8	407.4	4.3
17Z-28	1042.0	15.129	0.126	0.511	0.004	0.0561	0.0002	412.6	6.7	419.3	6.0	456.1	11.9	10	412.6	6.7
17Z-29	72.2	4.193	0.037	2.941	0.027	0.0895	0.0003	1378.9	21.9	1392.4	14.3	1413.2	11.8	2	1413.2	11.8
17Z-30	109.4	4.405	0.038	2.741	0.025	0.0876	0.0002	1318.8	20.5	1339.5	13.6	1372.9	10.8	4	1372.9	10.8
17Z-31	247.0	5.886	0.052	1.732	0.016	0.0740	0.0002	1011.6	16.6	1020.6	11.9	1040.0	10.7	3	1011.6	16.6
17Z-32	279.0	14.641	0.107	0.519	0.004	0.0551	0.0002	425.9	6.1	424.3	5.9	415.3	18.7	-3	425.9	6.1
17Z-33	131.2	1.989	0.013	14.052	0.101	0.2028	0.0005	2625.8	29.3	2753.2	14.1	2848.1	7.8	8	2848.1	7.8
17Z-34	61.7	14.771	0.142	0.517	0.006	0.0554	0.0004	422.3	7.9	423.0	8.6	426.6	34.6	1	422.3	7.9
17Z-35	113.3	14.635	0.100	0.512	0.004	0.0544	0.0003	426.1	5.6	420.1	5.7	387.5	21.1	-10	426.1	5.6
17Z-36	124.9	13.459	0.127	0.572	0.006	0.0558	0.0002	462.0	8.4	459.1	7.7	444.6	19.5	-4	462.0	8.4
17Z-37	156.4	4.388	0.033	2.869	0.023	0.0914	0.0003	1323.5	17.9	1373.9	12.3	1453.1	11.9	9	1453.1	11.9
17Z-38	45.5	2.057	0.017	12.301	0.107	0.1836	0.0006	2553.8	34.4	2627.6	16.7	2685.0	9.9	5	2685.0	9.9
17Z-39	469.9	14.793	0.120	0.516	0.004	0.0554	0.0002	421.7	6.7	422.8	6.0	428.6	13.3	2	421.7	6.7
17Z-40	388.0	8.696	0.605	1.230	0.099	0.0776	0.0031	701.7	92.5	814.3	89.9	1135.8	159.0	38	701.7	92.5
17Z-41	341.0	8.425	0.071	1.133	0.010	0.0693	0.0002	723.1	11.6	769.2	9.8	905.6	13.1	20	723.1	11.6
17Z-42	244.9	6.489	0.046	1.498	0.012	0.0705	0.0002	923.9	12.3	929.6	9.4	943.2	11.6	2	923.9	12.3
17Z-43	69.1	1.850	0.016	14.866	0.131	0.1996	0.0004	2785.1	38.6	2806.7	17.2	2822.2	7.2	1	2822.2	7.2
17Z-44	57.1	1.834	0.016	15.137	0.137	0.2015	0.0004	2805.2	40.2	2823.9	17.6	2837.3	6.7	1	2837.3	6.7
17Z-45	19.2	2.008	0.019	12.749	0.127	0.1858	0.0006	2605.2	40.5	2661.3	19.1	2704.2	10.7	4	2704.2	10.7
17Z-46	710.0	15.773	0.249	0.516	0.010	0.0590	0.0006	396.3	12.1	422.2	13.0	566.1	44.3	30	396.3	12.1
17Z-47	216.0	14.577	0.138	0.527	0.005	0.0558	0.0002	427.7	7.9	430.1	7.2	442.6	17.6	3	427.7	7.9
17Z-48	52.5	14.556	0.138	0.519	0.006	0.0548	0.0004	428.3	7.9	424.5	8.5	403.9	34.3	-6	428.3	7.9
17Z-49	258.0	3.935	0.030	3.310	0.026	0.0945	0.0002	1459.6	20.1	1483.3	12.6	1517.5	8.0	4	1517.5	8.0
17Z-50	157.0	4.662	0.033	2.434	0.018	0.0823	0.0002	1252.7	16.0	1252.7	10.9	1252.5	10.2	0	1252.5	10.2
17Z-51	154.7	14.306	0.102	0.530	0.004	0.0550	0.0002	435.6	6.0	431.6	5.9	410.4	19.5	-6	435.6	6.0
17Z-52	375.0	4.746	0.037	2.514	0.021	0.0866	0.0002	1232.5	17.6	1276.0	12.1	1349.8	9.6	9	1349.8	9.6
17Z-53	235.1	3.081	0.018	5.417	0.033	0.1211	0.0003	1812.2	18.1	1887.5	10.9	1971.4	8.3	8	1971.4	8.3

Grain I.D.	238U (ppm)	238/206 ratio	206/238 1SE	207/235 ratio	207/235 1SE	207/206 ratio	207/206 1SE	238/206 Age (Ma)	2σ	207/235 Age (Ma)	2σ	207/206 Age (Ma)	2σ	Disc. (%)	preferred Age (Ma)	preferred Err. (2σ)
17Z-54	181.4	3.219	0.032	4.972	0.051	0.1161	0.0002	1744.2	30.6	1814.5	17.4	1896.4	7.6	8	1896.4	7.6
17Z-55	454.0	13.193	0.165	0.789	0.024	0.0755	0.0021	471.0	11.4	590.4	27.3	1080.9	111.6	56		
17Z-56	532.8	15.015	0.124	0.512	0.004	0.0557	0.0001	415.6	6.7	419.5	6.0	441.0	11.2	6	415.6	6.7
17Z-57	474.0	7.391	0.063	1.360	0.012	0.0729	0.0002	818.0	13.1	871.9	10.4	1011.4	10.3	19	818.0	13.1
17Z-58	45.6	5.754	0.053	1.773	0.018	0.0740	0.0003	1033.0	17.6	1035.4	13.0	1040.6	15.6	1	1033.0	17.6
17Z-59	54.2	1.900	0.018	13.961	0.137	0.1925	0.0006	2725.8	41.9	2747.0	19.0	2762.6	9.4	1	2762.6	9.4
17Z-60	456.0	14.767	0.098	0.517	0.004	0.0554	0.0002	422.4	5.5	423.2	5.0	427.4	12.5	1	422.4	5.5
17Z-61	96.6	3.162	0.025	4.826	0.040	0.1107	0.0003	1771.6	24.6	1789.5	14.1	1810.4	8.9	2	1810.4	8.9
17Z-62	58.4	16.207	0.144	0.465	0.005	0.0547	0.0004	386.0	6.7	387.5	7.2	396.9	30.0	3	386.0	6.7
17Z-63	372.3	14.769	0.105	0.519	0.004	0.0556	0.0002	422.3	5.8	424.3	5.5	435.0	14.8	3	422.3	5.8
17Z-64	242.0	3.386	0.017	4.397	0.024	0.1081	0.0003	1668.0	14.5	1711.8	9.3	1766.0	8.5	6	1766.0	8.5
17Z-65	81.2	5.333	0.082	2.221	0.036	0.0860	0.0004	1107.8	31.5	1187.7	22.5	1336.2	16.0	17	1336.2	16.0
17Z-66	126.6	3.440	0.036	4.352	0.047	0.1086	0.0003	1645.0	30.5	1703.2	18.1	1775.6	10.1	7	1775.6	10.1
17Z-67	360.8	14.970	0.146	0.509	0.005	0.0553	0.0002	416.8	7.9	417.7	7.1	422.6	15.0	1	416.8	7.9
17Z-68	351.0	4.843	0.040	2.599	0.023	0.0913	0.0003	1210.1	18.2	1300.4	13.1	1452.6	12.5	17	1452.6	12.5
17Z-69	731.0	14.104	0.109	0.553	0.005	0.0566	0.0001	441.6	6.6	447.3	5.9	476.5	11.3	7	441.6	6.6
17Z-70	291.6	5.903	0.042	1.732	0.013	0.0742	0.0002	1008.8	13.3	1020.5	9.8	1045.7	10.4	4	1008.8	13.3
17Z-71	103.2	5.163	0.041	2.033	0.017	0.0762	0.0002	1141.4	16.8	1126.7	11.8	1098.6	12.4	-4	1141.4	16.8
17Z-72	176.0	14.881	0.122	0.508	0.005	0.0548	0.0002	419.3	6.7	417.0	6.3	404.7	19.2	-4	419.3	6.7
17Z-73	171.0	14.286	0.112	0.531	0.005	0.0551	0.0003	436.2	6.6	432.7	6.5	414.5	21.1	-5	436.2	6.6
17Z-74	117.7	14.789	0.092	0.508	0.004	0.0546	0.0002	421.8	5.1	417.4	5.3	393.2	20.2	-7	421.8	5.1
17Z-75	405.5	14.995	0.069	0.509	0.003	0.0554	0.0002	416.2	3.7	417.9	3.7	427.4	12.5	3	416.2	3.7
17Z-76	78.3	3.375	0.019	4.305	0.027	0.1054	0.0003	1672.9	16.5	1694.3	10.6	1720.8	10.6	3	1720.8	10.6
17Z-77	132.1	3.047	0.017	5.138	0.032	0.1136	0.0003	1829.7	17.6	1842.4	10.8	1856.8	10.2	1	1856.8	10.2
17Z-78	129.7	15.088	0.079	0.499	0.004	0.0546	0.0003	413.7	4.2	411.0	5.1	395.7	24.6	-5	413.7	4.2
17Z-79	202.2	5.556	0.029	1.884	0.011	0.0759	0.0002	1067.0	10.4	1075.3	8.2	1092.3	12.2	2	1067.0	10.4
17Z-80	72.2	1.894	0.011	14.362	0.089	0.1973	0.0005	2733.4	25.5	2773.9	12.3	2803.5	7.9	2	2803.5	7.9
17Z-81	171.5	14.641	0.107	0.517	0.004	0.0550	0.0002	425.9	6.1	423.4	5.8	410.0	17.5	-4	425.9	6.1
17Z-82	371.0	6.143	0.032	1.726	0.010	0.0769	0.0002	972.3	9.5	1018.1	7.6	1118.0	10.4	13	972.3	9.5
17Z-83	165.1	4.320	0.031	2.812	0.022	0.0881	0.0002	1342.4	17.3	1358.7	11.6	1384.5	10.7	3	1384.5	10.7
17Z-84	43.6	3.431	0.019	4.102	0.026	0.1021	0.0003	1649.0	16.1	1654.7	10.6	1662.0	11.8	1	1662.0	11.8
17Z-85	116.0	6.341	0.157	1.986	0.052	0.0914	0.0009	944.0	43.4	1110.9	35.7	1454.1	35.4	35	944.0	43.4
17Z-86	291.0	4.515	0.050	2.996	0.035	0.0981	0.0004	1289.8	25.9	1406.5	18.1	1588.0	15.4	19	1588.0	15.4
17Z-87	45.1	2.131	0.019	10.854	0.101	0.1679	0.0004	2480.1	37.0	2510.7	17.6	2535.6	8.4	2	2535.6	8.4
17Z-88	143.1	14.599	0.128	0.529	0.005	0.0560	0.0003	427.1	7.3	431.0	7.0	451.8	21.0	5	427.1	7.3
17Z-89	213.9	5.682	0.058	2.020	0.022	0.0833	0.0003	1045.1	19.8	1122.1	14.7	1274.4	12.7	18	1045.1	19.8
17Z-90	404.1	15.473	0.113	0.520	0.004	0.0584	0.0002	403.7	5.7	425.2	5.6	543.1	14.2	26	403.7	5.7
17Z-91	180.9	3.555	0.020	3.966	0.024	0.1023	0.0003	1597.9	15.7	1627.2	10.3	1665.3	10.3	4	1665.3	10.3
17Z-92	248.2	3.654	0.027	3.888	0.031	0.1031	0.0003	1559.6	20.8	1611.2	13.0	1679.3	9.9	7	1679.3	9.9
17Z-93	134.9	4.496	0.031	2.612	0.019	0.0852	0.0002	1294.5	16.4	1304.1	11.1	1319.9	10.0	2	1319.9	10.0
17Z-94	188.4	4.706	0.093	3.672	0.074	0.1254	0.0004	1242.1	44.7	1565.2	32.1	2033.2	11.9	39		
17Z-95	214.3	2.969	0.037	5.796	0.073	0.1249	0.0003	1871.3	40.1	1945.8	21.9	2026.0	8.7	8	2026.0	8.7
17Z-96	349.0	14.605	0.078	0.519	0.003	0.0550	0.0002	426.9	4.4	424.4	4.3	410.8	13.4	-4	426.9	4.4
17Z-97	140.2	5.222	0.027	2.046	0.012	0.0775	0.0002	1129.5	10.9	1130.8	8.2	1133.4	10.8	0	1129.5	10.9
17Z-98	29.2	3.628	0.020	3.635	0.025	0.0957	0.0004	1569.2	15.3	1557.1	11.0	1540.8	15.3	-2	1540.8	15.3
17Z-99	411.3	5.984	0.038	1.718	0.012	0.0746	0.0002	996.1	11.6	1015.4	8.9	1057.4	11.1	6	996.1	11.6
17Z-100	173.0	14.658	0.101	0.521	0.004	0.0555	0.0003	425.4	5.7	426.1	5.9	429.8	21.3	1	425.4	5.7
17Z-101	130.1	14.839	0.086	0.512	0.004	0.0552	0.0003	420.4	4.7	420.0	5.2	417.7	21.5	-1	420.4	4.7
17Z-102	259.9	5.992	0.052	1.724	0.016	0.0750	0.0002	995.0	16.1	1017.6	11.7	1066.5	9.9	7	995.0	16.1
17Z-103	1001.0	15.026	0.068	0.519	0.003	0.0566	0.0002	415.3	3.7	424.3	3.8	473.0	13.3	12	415.3	3.7
17Z-104	73.3	1.940	0.007	13.509	0.058	0.1902	0.0004	2679.6	16.8	2715.9	9.0	2743.1	6.9	2	2743.1	6.9
17Z-105	285.0	13.947	0.107	0.558	0.006	0.0565	0.0004	446.4	6.6	450.4	7.4	470.7	29.0	5	446.4	6.6
17Z-106	236.0	14.168	0.057	0.538	0.003	0.0553	0.0002	439.6	3.5	436.8	4.0	421.8	17.4	-4	439.6	3.5
17Z-107	134.2	1.888	0.010	14.906	0.083	0.2042	0.0004	2740.6	23.4	2809.3	11.3	2858.9	6.7	4	2858.9	6.7
17Z-108	212.0	14.654	0.072	0.517	0.003	0.0550	0.0002	425.5	4.1	423.4	4.3	411.6	17.1	-3	425.5	4.1
17Z-109	132.8	3.503	0.018	4.005	0.023	0.1018	0.0003	1619.0	15.1	1635.2	9.8	1656.0	9.5	2	1656.0	9.5
17Z-110	736.0	14.883	0.078	0.517	0.003	0.0558	0.0002	419.2	4.3	423.1	4.3	444.6	14.8	6	419.2	4.3

Grain I.D.	238U (ppm)	238/206 ratio	206/238 1SE	207/235 ratio	207/235 1SE	207/206 ratio	207/206 1SE	238/206 Age (Ma)	2σ	207/235 Age (Ma)	2σ	207/206 Age (Ma)	2σ	Disc. (%)	preferred Age (Ma)	preferred Err. (2σ)
17Z-111	80.7	5.181	0.031	2.015	0.014	0.0757	0.0003	1137.6	12.5	1120.4	9.4	1087.3	13.2	-5	1137.6	12.5
17Z-112	81.6	14.932	0.070	0.501	0.003	0.0543	0.0003	417.9	3.8	412.3	4.5	381.3	21.1	-10	417.9	3.8
17Z-113	176.1	7.148	0.041	1.331	0.009	0.0690	0.0002	844.1	9.1	859.2	7.6	898.4	12.6	6	844.1	9.1
17Z-114	145.9	5.804	0.040	1.745	0.013	0.0735	0.0002	1024.8	13.2	1025.2	10.0	1026.0	13.2	0	1024.8	13.2
17Z-115	379.0	14.890	0.100	0.519	0.004	0.0560	0.0002	419.0	5.5	424.2	5.5	452.6	19.0	7	419.0	5.5
17Z-116	32.7	5.192	0.024	2.020	0.014	0.0761	0.0004	1135.4	9.8	1122.3	9.3	1096.8	19.7	-4	1135.4	9.8
17Z-117	141.2	11.038	0.073	0.780	0.006	0.0625	0.0003	559.1	7.1	585.5	7.0	689.3	18.1	19	559.1	7.1
17Z-118	35.1	4.798	0.046	2.381	0.027	0.0829	0.0005	1220.3	21.4	1236.8	16.1	1265.7	22.4	4	1265.7	22.4
17Z-119	114.5	3.971	0.023	3.216	0.021	0.0927	0.0003	1447.8	15.0	1461.1	10.1	1480.5	10.7	2	1480.5	10.7
17Z-120	228.6	13.576	0.085	0.568	0.004	0.0560	0.0002	458.2	5.5	457.0	5.4	451.0	16.7	-2	458.2	5.5
17Z-121	709.0	14.813	0.078	0.519	0.003	0.0558	0.0002	421.1	4.3	424.5	4.2	442.6	12.4	5	421.1	4.3
17Z-122	45.7	5.650	0.034	1.819	0.013	0.0746	0.0003	1050.6	11.6	1052.3	9.4	1055.8	15.7	0	1050.6	11.6
17Z-123	106.6	1.976	0.009	13.244	0.066	0.1899	0.0004	2639.5	19.9	2697.2	10.2	2740.6	7.0	4	2740.6	7.0

10.3.1.2 DMBH (Zircon)

Grain I.D.	238U (ppm)	238/206 ratio	238/206 1SE	207/235 ratio	207/235 1SE	207/206 ratio	207/206 1SE	238/206 Age (Ma)	2σ	207/235 Age (Ma)	2σ	207/206 Age (Ma)	2σ	Disc. (%)	preferred Age (Ma)	preferred Err. (2σ)
DMZ-01	36.6	6.920	0.175	1.356	0.037	0.0681	0.0007	870.1	41.1	870.2	31.6	870.7	39.9	0%	870.1	41.1
DMZ-02	29.4	5.935	0.157	1.707	0.048	0.0735	0.0007	1003.8	49.1	1011.1	35.7	1026.9	36.1	2%	1003.8	49.1
DMZ-03	285.1	3.788	0.100	3.571	0.096	0.0981	0.0005	1510.3	71.4	1543.0	42.8	1588.2	18.4	5%	1588.2	18.4
DMZ-04	38.5	3.774	0.078	3.473	0.075	0.0951	0.0006	1515.4	56.1	1521.2	34.3	1529.2	24.4	1%	1529.2	24.4
DMZ-05	142.7	13.774	0.285	0.567	0.013	0.0567	0.0005	451.8	18.0	456.3	16.4	479.3	37.7	6%	451.8	18.0
DMZ-06	79.6	7.018	0.165	1.413	0.035	0.0719	0.0005	858.8	37.8	894.3	29.2	983.0	28.7	13%	858.8	37.8
DMZ-07	59.5	7.225	0.206	1.347	0.040	0.0706	0.0006	835.6	44.7	866.1	34.7	944.9	35.2	12%	835.6	44.7
DMZ-08	117.5	5.741	0.117	1.724	0.037	0.0718	0.0005	1035.2	39.0	1017.5	27.5	979.6	27.1	-6%	1035.2	39.0
DMZ-09	58.8	3.333	0.089	4.185	0.114	0.1012	0.0006	1691.3	79.4	1671.0	44.7	1645.6	20.9	-3%	1645.6	20.9
DMZ-10	77.5	5.540	0.123	1.930	0.047	0.0776	0.0008	1069.7	43.7	1091.7	32.4	1135.8	38.8	6%	1069.7	43.7
DMZ-11	300.7	14.368	0.310	0.530	0.012	0.0553	0.0003	433.7	18.1	432.0	15.7	423.0	25.4	-3%	433.7	18.1
DMZ-12	126.1	3.046	0.042	7.090	0.104	0.1567	0.0008	1830.1	44.2	2122.8	26.3	2419.7	17.5	24%	2419.7	17.5
DMZ-13	110.7	4.695	0.121	2.544	0.067	0.0867	0.0004	1244.8	58.5	1284.6	38.4	1351.9	20.3	8%	1351.9	20.3
DMZ-14	107.4	14.903	0.366	0.511	0.014	0.0553	0.0006	418.7	19.9	419.4	18.2	423.4	44.6	1%	418.7	19.9
DMZ-15	95.4	14.577	0.244	0.532	0.010	0.0563	0.0006	427.7	13.9	433.3	13.7	463.2	43.5	8%	427.7	13.9
DMZ-16	515.0	15.106	0.194	0.512	0.007	0.0561	0.0004	413.2	10.3	419.6	9.9	454.9	29.2	9%	413.2	10.3
DMZ-17	348.3	14.280	0.133	0.536	0.006	0.0555	0.0004	436.3	7.8	435.6	8.0	431.4	28.5	-1%	436.3	7.8
DMZ-18	273.0	4.600	0.062	2.698	0.039	0.0900	0.0004	1268.1	31.3	1327.8	21.3	1425.5	18.4	11%	1425.5	18.4
DMZ-19	257.9	4.615	0.065	2.548	0.038	0.0853	0.0004	1264.4	32.3	1285.8	21.8	1321.7	19.4	4%	1321.7	19.4
DMZ-20	64.4	5.141	0.083	2.121	0.037	0.0791	0.0006	1145.7	34.0	1155.7	24.4	1174.5	28.0	2%	1145.7	34.0
DMZ-21	70.5	5.305	0.080	2.033	0.034	0.0782	0.0006	1113.2	30.9	1126.5	22.7	1152.1	28.4	3%	1113.2	30.9
DMZ-22	56.1	2.968	0.041	5.405	0.082	0.1164	0.0007	1871.7	45.4	1885.6	26.2	1900.8	22.4	2%	1900.8	22.4
DMZ-23	53.6	5.402	0.095	1.969	0.039	0.0772	0.0007	1094.8	35.4	1105.1	26.7	1125.5	36.5	3%	1094.8	35.4
DMZ-24	169.7	2.732	0.052	6.306	0.124	0.1250	0.0006	2010.6	66.1	2019.3	34.5	2028.3	16.7	1%	2028.3	16.7
DMZ-25	179.5	2.770	0.054	6.241	0.124	0.1255	0.0006	1986.9	66.3	2010.3	34.9	2034.4	16.6	2%	2034.4	16.6
DMZ-26	118.3	14.388	0.331	0.525	0.013	0.0548	0.0005	433.1	19.3	428.6	17.3	404.3	41.1	-7%	433.1	19.3
DMZ-27	101.0	4.062	0.050	3.213	0.043	0.0947	0.0005	1418.8	31.6	1460.3	21.0	1521.1	20.7	7%	1521.1	20.7
DMZ-28	225.8	2.088	0.024	13.122	0.160	0.1988	0.0008	2522.5	48.0	2688.5	23.3	2815.8	14.9	10%	2815.8	14.9
DMZ-29	112.7	3.322	0.042	4.435	0.059	0.1069	0.0005	1696.3	37.7	1719.0	22.3	1746.7	17.4	3%	1746.7	17.4
DMZ-30	33.0	5.565	0.094	1.858	0.034	0.0750	0.0005	1065.3	33.4	1066.3	23.9	1068.1	25.7	0%	1065.3	33.4
DMZ-31	156.4	14.793	0.350	0.523	0.013	0.0561	0.0006	421.7	19.3	427.0	17.9	456.1	43.7	8%	421.7	19.3
DMZ-32	174.5	3.689	0.050	3.809	0.055	0.1020	0.0005	1546.4	37.1	1594.7	23.2	1659.1	19.0	7%	1659.1	19.0
DMZ-33	210.9	1.745	0.061	17.491	0.615	0.2215	0.0009	2920.1	164.0	2962.2	67.6	2990.8	14.9	2%	2990.8	14.9
DMZ-34	169.9	5.141	0.096	2.075	0.043	0.0774	0.0007	1145.7	39.4	1140.5	28.2	1130.6	33.8	-1%	1145.7	39.4
DMZ-35	107.6	6.143	0.147	1.614	0.040	0.0720	0.0004	972.3	43.3	975.8	30.8	983.6	22.6	1%	972.3	43.3
DMZ-36	44.0	4.184	0.131	2.879	0.093	0.0874	0.0007	1381.5	78.1	1376.4	48.8	1368.5	31.3	-1%	1368.5	31.3
DMZ-37	176.6	3.716	0.040	3.745	0.044	0.1010	0.0005	1536.2	29.5	1581.1	19.1	1641.4	19.2	6%	1641.4	19.2
DMZ-38	80.8	13.928	0.349	0.545	0.015	0.0551	0.0007	447.0	21.7	441.9	20.1	415.3	57.0	-8%	447.0	21.7
DMZ-39	72.4	4.442	0.067	2.849	0.046	0.0918	0.0005	1308.8	35.8	1368.5	24.2	1463.0	21.4	11%	1463.0	21.4
DMZ-40	202.3	5.889	0.055	1.758	0.019	0.0751	0.0004	1011.0	17.7	1030.0	14.2	1070.5	22.8	6%	1011.0	17.7
DMZ-41	71.5	5.568	0.104	1.892	0.038	0.0765	0.0006	1064.8	36.6	1078.4	26.6	1106.0	29.2	4%	1064.8	36.6
DMZ-42	52.2	5.821	0.097	1.781	0.033	0.0752	0.0007	1022.0	31.4	1038.4	24.4	1072.9	35.1	5%	1022.0	31.4
DMZ-43	119.5	4.838	0.092	2.554	0.051	0.0897	0.0005	1211.2	42.2	1287.7	29.1	1417.7	22.0	15%	1417.7	22.0
DMZ-44	108.7	4.378	0.051	2.791	0.037	0.0887	0.0006	1326.1	27.8	1353.2	20.2	1396.4	26.5	5%	1396.4	26.5
DMZ-45	62.9	4.527	0.046	2.673	0.033	0.0878	0.0006	1286.6	23.8	1321.0	18.2	1377.2	26.8	7%	1377.2	26.8
DMZ-46	376.0	3.956	0.049	3.476	0.045	0.0998	0.0005	1452.9	31.9	1521.9	20.7	1619.1	17.9	10%	1619.1	17.9
DMZ-47	136.7	3.648	0.038	3.853	0.044	0.1020	0.0005	1561.6	28.9	1603.8	18.7	1659.8	19.0	6%	1659.8	19.0
DMZ-48	156.8	15.504	0.180	0.488	0.007	0.0549	0.0004	402.9	9.1	403.3	9.2	405.1	33.0	1%	402.9	9.1
DMZ-49	121.7	3.918	0.044	3.508	0.044	0.0998	0.0006	1465.2	29.3	1529.1	19.8	1618.6	21.3	9%	1618.6	21.3
DMZ-50	53.9	5.316	0.052	1.952	0.024	0.0753	0.0006	1111.1	20.1	1099.2	16.5	1075.6	29.8	-3%	1111.1	20.1
DMZ-51	139.9	3.129	0.034	4.864	0.059	0.1104	0.0006	1787.8	34.2	1796.0	20.4	1805.5	19.0	1%	1805.5	19.0
DMZ-52	91.4	5.659	0.061	1.785	0.025	0.0733	0.0007	1048.9	20.8	1040.0	18.2	1021.3	36.2	-3%	1048.9	20.8

Grain I.D.	238U (ppm)	238/206 ratio	238/206 1SE	207/235 ratio	207/235 1SE	207/206 ratio	207/206 1SE	238/206 Age (Ma)	2σ	207/235 Age (Ma)	2σ	207/206 Age (Ma)	2σ	Disc. (%)	preferred Age (Ma)	preferred Err. (2σ)
DMZ-53	188.0	4.342	0.070	2.765	0.047	0.0871	0.0005	1336.1	38.8	1346.1	25.4	1362.1	22.1	2%	1362.1	22.1
DMZ-54	452.0	4.671	0.049	2.786	0.033	0.0944	0.0006	1250.6	23.9	1351.9	18.0	1515.9	22.6	17%	1515.9	22.6
DMZ-55	296.1	14.205	0.232	0.549	0.010	0.0566	0.0004	438.6	13.9	444.6	12.6	476.2	28.5	8%	438.6	13.9
DMZ-56	168.4	3.368	0.040	4.139	0.054	0.1012	0.0006	1675.9	35.3	1662.0	21.6	1644.5	20.9	-2%	1644.5	20.9
DMZ-57	184.0	3.448	0.083	4.076	0.100	0.1020	0.0005	1641.5	70.0	1649.6	40.2	1659.8	18.3	1%	1659.8	18.3
DMZ-58	176.2	3.477	0.032	3.972	0.043	0.1002	0.0006	1629.5	26.6	1628.5	17.5	1627.1	21.2	0%	1627.1	21.2
DMZ-59	56.3	5.721	0.072	1.843	0.026	0.0765	0.0005	1038.5	24.2	1061.0	18.6	1107.5	25.8	6%	1038.5	24.2
DMZ-60	59.4	15.129	0.217	0.504	0.010	0.0553	0.0007	412.6	11.5	414.3	13.0	423.4	56.7	3%	412.6	11.5
DMZ-61	660.0	14.065	0.178	0.552	0.008	0.0563	0.0003	442.8	10.8	446.4	9.9	464.8	23.3	5%	442.8	10.8
DMZ-62	189.9	3.141	0.039	4.728	0.063	0.1078	0.0005	1781.9	38.7	1772.3	22.3	1760.9	17.9	-1%	1760.9	17.9
DMZ-63	402.0	5.869	0.077	2.283	0.033	0.0972	0.0006	1014.3	24.8	1207.0	20.4	1570.4	21.9	35%	1570.4	21.9
DMZ-64	614.9	13.661	0.159	0.600	0.009	0.0595	0.0005	455.4	10.2	477.4	10.9	584.5	36.8	22%	455.4	10.2
DMZ-65	150.6	5.682	0.060	1.786	0.023	0.0736	0.0006	1045.1	20.3	1040.4	16.8	1030.7	30.6	-1%	1045.1	20.3
DMZ-66	142.6	5.149	0.068	2.108	0.030	0.0788	0.0005	1144.1	27.6	1151.4	19.9	1165.2	24.0	2%	1144.1	27.6
DMZ-67	154.6	4.008	0.048	3.227	0.042	0.0939	0.0005	1435.9	31.0	1463.8	20.3	1504.4	19.7	5%	1504.4	19.7
DMZ-68	211.3	6.120	0.103	1.692	0.031	0.0751	0.0005	975.6	30.5	1005.4	23.1	1070.8	26.7	9%	975.6	30.5
DMZ-69	56.3	15.291	0.210	0.513	0.011	0.0569	0.0010	408.4	10.9	420.4	14.9	486.7	73.8	16%	408.4	10.9
DMZ-70	143.7	15.053	0.147	0.509	0.007	0.0556	0.0006	414.6	7.9	417.8	10.0	435.4	48.3	5%	414.6	7.9
DMZ-71	473.0	5.033	0.051	2.170	0.024	0.0793	0.0004	1168.3	21.5	1171.6	15.4	1177.7	18.2	1%	1168.3	21.5
DMZ-72	384.3	4.963	0.069	2.436	0.036	0.0877	0.0004	1183.4	30.1	1253.4	21.2	1375.7	18.7	14%	1375.7	18.7
DMZ-73	172.6	3.619	0.049	3.817	0.055	0.1002	0.0005	1572.7	37.9	1596.3	23.4	1627.5	19.4	3%	1627.5	19.4
DMZ-74	368.0	15.974	0.255	0.477	0.008	0.0553	0.0004	391.4	12.1	396.1	11.4	423.4	30.2	8%	391.4	12.1
DMZ-75	42.3	5.666	0.096	1.939	0.037	0.0797	0.0007	1047.8	32.9	1094.5	25.3	1188.7	32.6	12%	1047.8	32.9
DMZ-76	481.0	14.925	0.167	0.512	0.006	0.0555	0.0003	418.1	9.1	419.9	8.7	430.2	26.5	3%	418.1	9.1
DMZ-77	175.1	14.771	0.327	0.515	0.012	0.0552	0.0005	422.3	18.1	422.0	16.5	420.5	40.7	0%	422.3	18.1
DMZ-78	121.4	4.405	0.136	2.769	0.087	0.0885	0.0006	1318.8	73.6	1347.1	47.0	1392.5	24.4	5%	1392.5	24.4
DMZ-79	649.0	14.347	0.226	0.537	0.009	0.0559	0.0003	434.3	13.3	436.5	11.8	447.8	24.3	3%	434.3	13.3
DMZ-80	177.7	3.925	0.058	3.282	0.051	0.0935	0.0004	1463.2	38.6	1476.9	24.0	1496.6	17.9	2%	1496.6	17.9
DMZ-81	375.0	15.198	0.185	0.500	0.007	0.0552	0.0004	410.8	9.7	412.0	9.5	418.9	31.1	2%	410.8	9.7
DMZ-82	60.6	1.949	0.025	13.358	0.182	0.1889	0.0010	2669.9	55.5	2705.3	26.0	2731.9	17.9	2%	2731.9	17.9
DMZ-83	121.7	2.024	0.035	11.466	0.204	0.1684	0.0008	2588.0	73.4	2561.8	33.4	2541.2	16.3	-2%	2541.2	16.3
DMZ-84	76.4	4.325	0.052	2.772	0.039	0.0870	0.0007	1340.8	29.4	1348.1	21.3	1359.6	29.3	1%	1359.6	29.3
DMZ-85	142.3	4.427	0.085	2.740	0.055	0.0880	0.0005	1313.0	45.8	1339.5	29.7	1382.1	20.4	5%	1382.1	20.4
DMZ-86	143.3	5.838	0.104	1.743	0.033	0.0738	0.0004	1019.3	33.6	1024.6	24.2	1035.9	23.8	2%	1019.3	33.6
DMZ-87	132.1	5.302	0.124	1.935	0.047	0.0745	0.0006	1113.8	47.7	1093.4	32.8	1053.1	30.2	-6%	1113.8	47.7
DMZ-88	198.4	4.100	0.067	3.037	0.052	0.0903	0.0004	1406.9	41.5	1416.9	26.2	1431.9	19.6	2%	1431.9	19.6
DMZ-89	472.0	6.557	0.185	1.472	0.042	0.0700	0.0003	915.0	48.1	918.9	34.6	928.3	20.0	1%	915.0	48.1
DMZ-90	243.0	3.704	0.117	3.414	0.109	0.0917	0.0005	1540.8	86.3	1507.6	50.2	1461.2	21.4	-5%	1461.2	21.4
DMZ-91	666.0	4.968	0.080	2.235	0.038	0.0806	0.0005	1182.3	34.9	1192.2	24.0	1210.1	22.6	2%	1182.3	34.9
DMZ-92	63.6	6.274	0.150	1.582	0.041	0.0720	0.0008	953.4	42.3	963.0	32.4	985.0	42.7	3%	953.4	42.3
DMZ-93	82.6	6.645	0.161	1.535	0.040	0.0740	0.0007	903.8	40.9	944.5	31.7	1040.6	35.8	13%	903.8	40.9
DMZ-94	106.2	5.631	0.073	1.847	0.027	0.0755	0.0006	1053.8	25.2	1062.4	19.6	1079.9	29.7	2%	1053.8	25.2
DMZ-95	115.1	5.200	0.126	2.121	0.053	0.0800	0.0005	1133.8	50.3	1155.7	34.4	1197.1	23.7	5%	1133.8	50.3
DMZ-96	47.4	5.760	0.108	1.979	0.043	0.0827	0.0009	1031.9	35.7	1108.2	29.3	1261.3	42.9	18%	1031.9	35.7
DMZ-97	70.4	5.450	0.148	1.894	0.054	0.0749	0.0006	1086.1	54.5	1079.1	37.8	1064.9	32.6	-2%	1086.1	54.5
DMZ-98	794.0	4.219	0.107	3.092	0.079	0.0947	0.0004	1371.1	62.6	1430.8	39.4	1520.7	16.3	10%	1520.7	16.3
DMZ-99	105.0	5.316	0.090	1.959	0.035	0.0756	0.0004	1111.1	34.7	1101.6	24.2	1082.8	23.4	-3%	1111.1	34.7
DMZ-100	116.8	3.333	0.072	4.177	0.093	0.1010	0.0005	1691.3	64.5	1669.5	36.5	1642.1	19.2	-3%	1642.1	19.2
DMZ-101	272.0	3.472	0.090	4.169	0.110	0.1050	0.0005	1631.5	75.1	1667.9	43.3	1714.0	16.9	5%	1714.0	16.9
DMZ-102	286.4	3.436	0.083	4.066	0.099	0.1014	0.0004	1646.5	69.9	1647.6	39.9	1648.9	17.2	0%	1648.9	17.2
DMZ-103	493.0	14.225	0.344	0.535	0.013	0.0552	0.0004	438.0	20.5	435.2	17.8	420.5	31.1	-4%	438.0	20.5
DMZ-104	140.6	3.289	0.092	4.239	0.120	0.1012	0.0005	1711.1	84.1	1681.6	46.7	1645.0	19.2	-4%	1645.0	19.2
DMZ-105	147.2	13.550	0.349	0.565	0.016	0.0555	0.0006	459.0	22.8	454.6	20.2	432.2	44.4	-6%	459.0	22.8
DMZ-106	508.0	4.202	0.132	2.861	0.091	0.0872	0.0004	1376.3	78.1	1371.6	47.9	1364.3	16.8	-1%	1364.3	16.8
DMZ-107	211.3	14.265	0.163	0.539	0.008	0.0558	0.0005	436.8	9.6	437.5	10.1	441.4	38.2	1%	436.8	9.6
DMZ-108	510.7	3.779	0.056	3.655	0.057	0.1002	0.0006	1513.3	39.8	1561.6	25.2	1627.5	21.2	7%	1627.5	21.2
DMZ-109	114.6	15.198	0.162	0.511	0.008	0.0564	0.0006	410.8	8.5	419.4	10.4	467.2	47.3	12%	410.8	8.5

Grain I.D.	238U (ppm)	238/206 ratio	238/206 1SE	207/235 ratio	207/235 1SE	207/206 ratio	207/206 1SE	238/206 Age (Ma)	2σ	207/235 Age (Ma)	2σ	207/206 Age (Ma)	2σ	Disc. (%)	preferred Age (Ma)	preferred Err. (2σ)
DMZ-110	118.0	4.719	0.059	2.522	0.035	0.0864	0.0005	1238.9	28.2	1278.4	20.1	1345.4	23.0	8%	1345.4	23.0
DMZ-111	910.0	5.999	0.133	1.708	0.039	0.0743	0.0003	993.9	40.9	1011.5	29.0	1049.8	18.6	5%	993.9	40.9
DMZ-112	222.9	5.935	0.088	1.704	0.027	0.0734	0.0004	1003.8	27.6	1009.9	20.5	1023.0	24.8	2%	1003.8	27.6
DMZ-113	542.0	16.234	0.277	0.503	0.010	0.0593	0.0006	385.3	12.8	414.0	13.2	577.2	40.6	33%	385.3	12.8
DMZ-114	114.8	5.531	0.067	1.896	0.027	0.0761	0.0006	1071.3	24.0	1079.7	18.9	1096.5	29.4	2%	1071.3	24.0
DMZ-115	554.0	4.310	0.130	5.090	0.158	0.1592	0.0011	1345.0	73.3	1834.5	52.6	2446.4	24.3	45%	2446.4	24.3
DMZ-116	97.9	5.173	0.056	2.062	0.028	0.0774	0.0006	1139.2	22.7	1136.3	18.3	1130.6	31.3	-1%	1139.2	22.7
DMZ-117	26.0	4.049	0.090	3.053	0.075	0.0897	0.0009	1423.0	56.9	1421.1	37.4	1418.3	38.7	0%	1418.3	38.7
DMZ-118	349.0	14.045	0.316	0.541	0.013	0.0552	0.0004	443.4	19.3	439.3	16.7	417.7	29.5	-6%	443.4	19.3
DMZ-119	39.6	9.285	0.345	0.886	0.035	0.0597	0.0008	659.4	46.6	644.3	37.7	591.7	58.3	-11%	659.4	46.6
DMZ-120	146.0	1.938	0.062	14.116	0.456	0.1985	0.0009	2682.2	140.4	2757.5	61.4	2813.2	16.4	5%	2813.2	16.4
DMZ-121	208.8	14.451	0.428	0.531	0.016	0.0556	0.0004	431.3	24.7	432.2	21.5	437.0	31.9	1%	431.3	24.7
DMZ-122	273.3	5.774	0.085	1.763	0.027	0.0739	0.0004	1029.7	28.0	1031.9	20.2	1036.5	20.6	1%	1029.7	28.0
DMZ-123	149.4	5.705	0.067	1.816	0.023	0.0752	0.0004	1041.2	22.5	1051.4	16.9	1072.4	22.2	3%	1041.2	22.5
DMZ-124	149.1	3.300	0.052	4.469	0.074	0.1070	0.0006	1706.2	47.5	1725.2	27.7	1748.5	19.7	2%	1748.5	19.7
DMZ-125	111.3	2.880	0.026	5.770	0.060	0.1206	0.0007	1921.2	29.7	1941.9	18.2	1964.0	20.1	2%	1964.0	20.1
DMZ-126	99.8	1.911	0.022	14.004	0.173	0.1942	0.0009	2713.2	50.9	2750.0	23.7	2777.1	16.7	2%	2777.1	16.7
DMZ-127	149.1	4.686	0.046	2.461	0.028	0.0837	0.0005	1246.9	22.4	1260.7	16.7	1284.2	23.6	3%	1284.2	23.6
DMZ-128	54.6	5.417	0.134	1.900	0.050	0.0747	0.0007	1092.1	49.5	1081.2	34.8	1059.5	35.4	-3%	1092.1	49.5
DMZ-129	127.5	3.415	0.058	4.072	0.073	0.1009	0.0006	1655.5	49.9	1648.8	29.3	1640.3	21.0	-1%	1640.3	21.0
DMZ-130	90.0	5.385	0.103	1.945	0.040	0.0760	0.0006	1098.0	38.6	1096.7	27.8	1093.9	32.0	0%	1098.0	38.6
DMZ-131	183.4	13.661	0.261	0.566	0.012	0.0561	0.0006	455.4	16.8	455.5	15.8	455.7	43.7	0%	455.4	16.8
DMZ-132	253.0	3.876	0.098	3.244	0.084	0.0912	0.0006	1479.6	66.6	1467.7	40.5	1450.6	25.6	-2%	1450.6	25.6
DMZ-133	92.3	3.012	0.082	5.027	0.142	0.1099	0.0009	1848.1	87.1	1823.9	47.8	1796.4	28.7	-3%	1796.4	28.7
DMZ-134	281.0	5.875	0.119	1.723	0.037	0.0735	0.0006	1013.2	38.0	1017.3	27.8	1026.0	30.7	1%	1013.2	38.0
DMZ-135	184.9	5.587	0.172	1.821	0.058	0.0738	0.0006	1061.5	60.2	1052.9	41.5	1035.1	30.5	-3%	1061.5	60.2
DMZ-136	259.2	5.737	0.120	1.818	0.040	0.0757	0.0005	1035.8	40.1	1052.0	28.8	1086.0	27.0	5%	1035.8	40.1
DMZ-137	179.9	3.086	0.081	4.732	0.129	0.1060	0.0008	1809.2	82.8	1772.9	45.6	1730.4	26.6	-5%	1730.4	26.6
DMZ-138	92.1	1.799	0.032	14.327	0.275	0.1870	0.0013	2850.1	82.9	2771.6	36.6	2714.9	23.1	-5%	2714.9	23.1
DMZ-139	82.6	13.755	0.331	0.544	0.015	0.0543	0.0008	452.4	21.0	441.1	19.9	382.5	62.2	-18%	452.4	21.0
DMZ-140	63.6	13.459	0.317	0.688	0.036	0.0672	0.0031	462.0	21.0	531.7	42.9	843.0	192.1	45%	462.0	21.0
DMZ-141	180.0	3.268	0.069	4.262	0.095	0.1011	0.0007	1721.0	64.2	1686.0	36.6	1642.8	24.5	-5%	1642.8	24.5
DMZ-142	256.0	6.998	0.218	1.559	0.050	0.0792	0.0006	861.0	50.2	954.0	39.7	1175.0	30.4	27%	861.0	50.2
DMZ-143	128.2	13.774	0.304	0.551	0.014	0.0550	0.0006	451.8	19.2	445.4	17.7	412.4	49.0	-10%	451.8	19.2
DMZ-144	31.8	3.300	0.071	4.159	0.101	0.0996	0.0012	1706.2	64.3	1666.0	39.9	1615.8	43.4	-6%	1615.8	43.4
DMZ-145	154.0	4.082	0.125	2.943	0.093	0.0872	0.0007	1412.6	77.7	1393.0	47.8	1362.9	29.2	-4%	1362.9	29.2
DMZ-146	169.2	4.189	0.088	2.829	0.062	0.0860	0.0006	1379.9	52.1	1363.3	33.2	1337.3	27.5	-3%	1337.3	27.5
DMZ-147	129.6	4.950	0.135	2.109	0.059	0.0758	0.0006	1186.1	59.0	1151.7	38.8	1087.6	29.5	-9%	1186.1	59.0
DMZ-148	146.0	3.704	0.117	3.679	0.119	0.0989	0.0007	1540.8	86.3	1566.9	51.6	1602.3	27.0	4%	1602.3	27.0
DMZ-149	120.5	5.848	0.205	1.727	0.063	0.0733	0.0007	1017.6	66.1	1018.7	46.6	1021.1	36.3	0%	1017.6	66.1
DMZ-150	218.0	12.706	0.428	0.609	0.021	0.0561	0.0006	488.4	31.7	482.9	27.0	456.9	43.7	-7%	488.4	31.7
DMZ-151	66.1	5.587	0.187	1.835	0.064	0.0744	0.0007	1061.5	65.6	1058.0	45.6	1050.9	35.6	-1%	1061.5	65.6
DMZ-152	43.5	13.986	0.401	0.546	0.019	0.0554	0.0011	445.2	24.7	442.3	24.7	427.4	84.6	-4%	445.2	24.7
DMZ-153	70.6	3.257	0.085	4.286	0.116	0.1013	0.0008	1725.9	78.9	1690.7	44.7	1647.2	28.0	-5%	1647.2	28.0
DMZ-154	261.0	4.184	0.131	4.589	0.148	0.1393	0.0010	1381.5	78.1	1747.3	53.7	2218.0	25.7	38%	2218.0	25.7
DMZ-155	258.0	4.329	0.122	2.695	0.079	0.0847	0.0007	1339.7	68.1	1327.1	43.5	1306.9	32.5	-3%	1306.9	32.5
DMZ-156	130.0	13.123	0.353	0.584	0.017	0.0556	0.0006	473.4	24.6	467.2	21.7	436.6	48.2	-8%	473.4	24.6
DMZ-157	98.1	14.184	0.463	0.547	0.019	0.0563	0.0006	439.2	27.7	443.0	24.7	463.2	47.5	5%	439.2	27.7
DMZ-158	75.5	14.184	0.453	0.545	0.019	0.0561	0.0007	439.2	27.1	441.8	24.6	455.3	55.6	4%	439.2	27.1
DMZ-159	239.0	3.731	0.118	3.433	0.111	0.0929	0.0006	1530.6	86.4	1511.9	50.9	1485.8	25.1	-3%	1485.8	25.1

10.3.1.3 A6BH (Zircon)

Grain I.D.	238U (ppm)	238/206 ratio	238/206 1SE	207/235 ratio	207/235 1SE	207/206 ratio	207/206 1SE	238/206 Age (Ma)	2σ	207/235 Age (Ma)	2σ	207/206 Age (Ma)	2σ	Disc. (%)	preferred Age (Ma)	preferred Err. (2σ)
A6Z-01	180.5	14.318	0.101	0.528	0.004	0.0548	0.0002	435.2	6.0	430.2	5.8	403.5	18.4	-8	435.2	6.0
A6Z-02	102.2	5.322	0.052	1.932	0.020	0.0746	0.0002	1110.0	20.1	1092.1	13.9	1056.6	12.7	-5	1110.0	20.1
A6Z-03	64.2	4.968	0.033	2.182	0.016	0.0787	0.0003	1182.3	14.5	1175.3	10.5	1162.4	13.1	-2	1182.3	14.5
A6Z-04	23.4	3.300	0.023	4.182	0.034	0.1001	0.0004	1706.2	20.9	1670.4	13.4	1625.8	15.2	-5	1625.8	15.2
A6Z-05	96.4	1.762	0.012	15.122	0.108	0.1934	0.0004	2897.1	31.8	2822.9	14.1	2770.4	7.1	-5	2770.4	7.1
A6Z-06	297.0	14.124	0.140	0.533	0.006	0.0546	0.0002	441.0	8.4	433.8	7.4	396.1	15.2	-11	441.0	8.4
A6Z-07	367.0	10.352	0.220	0.875	0.022	0.0657	0.0010	594.5	24.1	638.1	24.3	795.9	60.6	25	594.5	24.1
A6Z-08	235.5	3.093	0.022	4.760	0.036	0.1068	0.0003	1805.8	23.0	1777.9	13.1	1745.4	8.8	-3	1745.4	8.8
A6Z-09	192.4	2.989	0.026	5.136	0.047	0.1114	0.0003	1860.6	28.6	1842.1	15.7	1821.2	8.8	-2	1821.2	8.8
A6Z-10	99.5	3.333	0.023	4.162	0.031	0.1007	0.0003	1691.3	20.4	1666.5	12.4	1635.5	10.7	-3	1635.5	10.7
A6Z-11	25.4	3.346	0.031	4.062	0.041	0.0986	0.0004	1685.9	27.9	1646.7	16.7	1597.0	14.4	-6	1597.0	14.4
A6Z-12	119.4	13.831	0.115	0.547	0.005	0.0549	0.0003	450.0	7.2	443.2	6.9	408.4	21.2	-10	450.0	7.2
A6Z-13	9.0	2.546	0.031	5.662	0.074	0.1046	0.0005	2135.3	44.0	1925.5	22.6	1706.6	17.6	-25	1706.6	17.6
A6Z-14	66.8	6.024	0.045	1.582	0.014	0.0691	0.0003	990.0	13.9	963.0	11.1	901.7	19.1	-10	990.0	13.9
A6Z-15	242.4	3.755	0.025	3.449	0.024	0.0940	0.0002	1522.0	17.9	1515.7	11.3	1506.9	9.7	-1	1506.9	9.7
A6Z-16	373.0	13.980	0.076	0.544	0.003	0.0552	0.0002	445.4	4.7	440.8	4.5	417.3	13.8	-7	445.4	4.7
A6Z-17	98.0	13.600	0.091	0.549	0.005	0.0542	0.0003	457.4	5.9	444.2	6.0	376.3	22.0	-22	457.4	5.9
A6Z-18	163.0	5.222	0.055	1.983	0.021	0.0751	0.0002	1129.5	21.7	1109.7	14.6	1071.1	11.0	-5	1129.5	21.7
A6Z-19	395.0	6.592	0.043	1.551	0.011	0.0742	0.0002	910.5	11.2	950.8	8.8	1045.2	10.1	13	910.5	11.2
A6Z-20	136.1	1.905	0.015	13.655	0.113	0.1887	0.0004	2720.4	35.6	2726.1	16.1	2730.3	7.3	0	2730.3	7.3
A6Z-21	379.2	3.566	0.029	4.351	0.041	0.1126	0.0005	1593.4	23.2	1703.0	15.6	1840.7	16.1	13	1840.7	16.1
A6Z-22	19.5	11.062	0.226	0.677	0.015	0.0543	0.0005	557.9	21.9	524.7	18.3	382.9	39.3	-46	557.9	21.9
A6Z-23	225.4	4.950	0.043	2.154	0.020	0.0774	0.0002	1186.1	18.8	1166.2	12.7	1129.6	10.6	-5	1186.1	18.8
A6Z-24	223.0	13.850	0.192	0.547	0.008	0.0549	0.0002	449.4	12.0	442.8	10.3	408.8	16.7	-10	449.4	12.0
A6Z-25	294.9	14.088	0.091	0.538	0.004	0.0550	0.0002	442.1	5.6	437.2	5.4	411.6	17.5	-7	442.1	5.6
A6Z-26	53.6	5.249	0.030	2.023	0.016	0.0770	0.0004	1124.1	12.0	1123.1	10.8	1121.3	21.5	0	1124.1	12.0
A6Z-27	154.4	4.073	0.024	2.974	0.019	0.0879	0.0002	1415.2	15.1	1400.9	9.9	1379.2	9.6	-3	1379.2	9.6
A6Z-28	653.0	14.395	0.098	0.529	0.004	0.0553	0.0002	433.0	5.7	431.3	5.3	422.2	13.3	-3	433.0	5.7
A6Z-29	34.7	1.889	0.014	13.401	0.104	0.1837	0.0005	2738.5	32.6	2708.3	15.1	2685.9	8.7	-2	2685.9	8.7
A6Z-30	96.0	13.510	0.100	0.561	0.005	0.0550	0.0002	460.3	6.6	452.3	6.3	411.6	18.7	-12	460.3	6.6
A6Z-31	101.4	4.953	0.028	0.337	0.004	0.0567	0.0004	272.0	4.9	294.7	5.9	479.3	30.4	43	272.0	4.9
A6Z-32	90.0	3.852	0.030	2.138	0.015	0.0768	0.0003	1185.5	12.4	1161.0	9.8	1115.6	16.4	-6	1185.5	12.4
A6Z-33	398.0	3.810	0.024	3.401	0.029	0.0951	0.0003	1487.8	21.0	1504.5	13.4	1528.2	11.3	3	1528.2	11.3
A6Z-34	343.0	3.179	0.050	3.410	0.023	0.0943	0.0002	1502.6	16.9	1506.6	10.8	1512.3	9.0	1	1512.3	9.0
A6Z-35	200.0	1.941	0.016	4.945	0.079	0.1141	0.0003	1763.3	48.6	1810.0	27.0	1864.1	9.0	5	1864.1	9.0
A6Z-36	111.0	1.866	0.026	13.021	0.114	0.1834	0.0005	2678.8	36.7	2681.2	16.9	2683.0	8.9	0	2683.0	8.9
A6Z-37	55.3	1.748	0.017	13.682	0.194	0.1852	0.0005	2766.7	63.0	2727.9	27.1	2699.3	8.2	-2	2699.3	8.2
A6Z-38	102.9	4.876	0.031	15.230	0.151	0.1932	0.0005	2916.0	45.2	2829.7	19.3	2768.8	8.0	-5	2768.8	8.0
A6Z-39	168.5	13.774	0.123	2.243	0.016	0.0794	0.0002	1202.7	14.0	1194.7	9.9	1180.2	11.2	-2	1202.7	14.0
A6Z-40	356.0	13.812	0.134	0.559	0.005	0.0558	0.0002	451.8	7.8	450.7	7.0	445.0	14.7	-2	451.8	7.8
A6Z-41	359.0	3.418	0.023	0.552	0.006	0.0553	0.0002	450.6	8.4	446.4	7.4	425.0	13.7	-6	450.6	8.4
A6Z-42	101.7	3.339	0.023	3.963	0.029	0.0983	0.0003	1654.5	20.0	1626.6	12.1	1590.7	10.1	-4	1590.7	10.1
A6Z-43	134.4	1.929	0.016	4.136	0.030	0.1002	0.0002	1688.8	20.4	1661.5	12.1	1627.1	8.9	-4	1627.1	8.9
A6Z-44	53.2	4.105	0.021	13.047	0.111	0.1826	0.0005	2692.8	35.8	2683.1	16.4	2675.7	8.3	-1	2675.7	8.3
A6Z-45	114.7	4.742	0.031	2.914	0.017	0.0868	0.0002	1405.4	13.0	1385.5	8.9	1355.0	10.2	-4	1355.0	10.2
A6Z-46	95.4	4.405	0.033	2.342	0.017	0.0806	0.0003	1233.6	15.0	1225.3	10.7	1210.6	13.0	-2	1210.6	13.0
A6Z-47	62.2	5.010	0.041	2.628	0.022	0.0840	0.0003	1318.8	17.9	1308.6	12.2	1291.9	13.2	-2	1291.9	13.2
A6Z-48	243.8	1.648	0.009	2.155	0.019	0.0784	0.0002	1173.2	17.8	1166.8	12.1	1154.9	9.6	-2	1173.2	17.8
A6Z-49	71.4	1.734	0.012	18.377	0.109	0.2198	0.0006	3056.8	26.3	3009.7	12.1	2978.4	8.1	-3	2978.4	8.1
A6Z-50	60.3	5.467	0.037	15.993	0.120	0.2012	0.0005	2935.3	33.7	2876.4	14.9	2835.4	7.9	-4	2835.4	7.9
A6Z-51	66.7	4.205	0.034	1.848	0.015	0.0733	0.0003	1082.8	13.7	1062.7	10.5	1021.6	15.8	-6	1082.8	13.7
A6Z-52	108.4	5.252	0.032	2.784	0.023	0.0849	0.0002	1375.2	19.8	1351.2	12.7	1313.3	10.3	-5	1313.3	10.3
A6Z-53	161.9	16.639	0.208	1.967	0.013	0.0750	0.0002	1123.5	12.5	1104.2	9.1	1066.3	11.6	-5	1123.5	12.5

Grain I.D.	238U (ppm)	238/206 ratio	238/206 1SE	207/235 ratio	207/235 1SE	207/206 ratio	207/206 1SE	238/206 Age (Ma)	2σ	207/235 Age (Ma)	2σ	207/206 Age (Ma)	2σ	Disc. (%)	preferred Age (Ma)	preferred Err. (2σ)
A6Z-54	822.0	14.037	0.080	0.460	0.006	0.0555	0.0002	376.2	9.1	384.3	8.3	433.0	14.1	13	376.2	9.1
A6Z-55	113.2	1.785	0.008	0.539	0.004	0.0549	0.0002	443.6	4.9	437.8	5.2	407.1	20.0	-9	443.6	4.9
A6Z-56	76.6	13.096	0.081	15.135	0.077	0.1960	0.0005	2867.9	21.3	2823.8	10.4	2792.4	7.5	-3	2792.4	7.5
A6Z-57	178.0	3.076	0.021	0.579	0.004	0.0550	0.0002	474.4	5.7	463.6	5.5	410.8	17.5	-15	474.4	5.7
A6Z-58	65.8	1.841	0.014	4.911	0.037	0.1096	0.0003	1814.6	22.0	1804.2	13.0	1792.1	11.1	-1	1792.1	11.1
A6Z-59	137.7	13.515	0.086	15.646	0.148	0.2090	0.0012	2796.8	34.4	2855.4	18.5	2897.1	18.6	3	2897.1	18.6
A6Z-60	169.4	13.908	0.082	0.560	0.004	0.0549	0.0002	460.1	5.7	451.6	5.4	408.4	17.1	-13	460.1	5.7
A6Z-61	98.8	3.187	0.022	0.550	0.004	0.0555	0.0003	447.6	5.1	445.2	5.6	432.6	22.1	-3	447.6	5.1
A6Z-62	148.3	5.056	0.035	4.408	0.032	0.1019	0.0002	1759.4	21.2	1713.8	12.2	1658.5	8.9	-6	1658.5	8.9
A6Z-63	208.3	13.961	0.081	2.078	0.015	0.0762	0.0002	1163.5	14.6	1141.7	10.1	1100.5	10.3	-6	1163.5	14.6
A6Z-64	442.2	5.200	0.031	0.543	0.004	0.0551	0.0002	446.0	5.0	440.7	4.7	413.2	13.8	-8	446.0	5.0
A6Z-65	229.5	1.439	0.016	1.982	0.013	0.0748	0.0002	1133.8	12.5	1109.4	9.0	1062.0	10.8	-7	1133.8	12.5
A6Z-66	11.0	1.888	0.011	63.093	0.701	0.6587	0.0018	3401.7	57.2	4224.3	22.9	4642.5	7.7	27		
A6Z-67	93.3	13.637	0.074	13.738	0.089	0.1882	0.0006	2740.6	25.9	2731.8	12.8	2725.3	9.6	-1	2725.3	9.6
A6Z-68	260.6	13.604	0.102	0.554	0.004	0.0549	0.0002	456.2	4.8	447.8	4.8	405.1	16.3	-13	456.2	4.8
A6Z-69	93.9	13.600	0.071	0.547	0.005	0.0540	0.0003	457.3	6.6	443.1	6.7	370.5	24.6	-23	457.3	6.6
A6Z-70	76.9	13.699	0.082	0.560	0.004	0.0553	0.0003	457.4	4.6	451.9	5.6	423.8	25.0	-8	457.4	4.6
A6Z-71	91.4	14.386	0.084	0.552	0.004	0.0549	0.0002	454.2	5.2	446.2	5.4	405.1	20.0	-12	454.2	5.2
A6Z-72	386.8	13.791	0.074	0.527	0.004	0.0550	0.0002	433.2	4.9	429.6	4.7	410.4	14.7	-6	433.2	4.9
A6Z-73	247.0	5.931	0.040	0.552	0.004	0.0553	0.0002	451.3	4.7	446.6	5.1	422.6	19.8	-7	451.3	4.7
A6Z-74	53.4	3.713	0.022	1.623	0.013	0.0698	0.0003	1004.4	12.7	979.1	10.5	922.7	19.4	-9	1004.4	12.7
A6Z-75	53.8	1.734	0.011	3.367	0.023	0.0907	0.0003	1537.2	16.3	1496.8	11.1	1440.1	13.7	-7	1440.1	13.7
A6Z-76	76.9	4.068	0.027	15.872	0.104	0.1997	0.0005	2935.7	29.2	2869.1	13.1	2822.7	7.5	-4	2822.7	7.5
A6Z-77	98.8	1.872	0.013	2.838	0.021	0.0838	0.0002	1416.8	17.1	1365.7	11.1	1286.6	11.2	-10	1286.6	11.2
A6Z-78	78.3	1.888	0.011	13.921	0.101	0.1891	0.0005	2759.5	30.8	2744.3	14.3	2733.2	8.3	-1	2733.2	8.3
A6Z-79	108.4	13.495	0.100	14.150	0.088	0.1939	0.0005	2739.8	25.9	2759.8	12.4	2774.5	7.7	1	2774.5	7.7
A6Z-80	228.0	1.804	0.012	0.566	0.005	0.0554	0.0002	460.8	6.6	455.2	6.0	427.0	14.1	-8	460.8	6.6
A6Z-81	147.9	1.780	0.012	14.423	0.099	0.1888	0.0004	2842.6	30.0	2777.9	13.6	2731.3	7.3	-4	2731.3	7.3
A6Z-82	106.1	13.382	0.072	14.606	0.104	0.1886	0.0005	2874.1	31.1	2789.9	14.1	2729.6	8.4	-5	2729.6	8.4
A6Z-83	393.2	13.742	0.063	0.565	0.003	0.0549	0.0002	464.6	4.8	454.9	4.6	406.3	13.9	-14	464.6	4.8
A6Z-84	335.4	14.265	0.153	0.552	0.003	0.0550	0.0002	452.8	4.1	446.3	4.0	412.8	13.0	-10	452.8	4.1
A6Z-85	264.0	4.883	0.039	0.532	0.006	0.0551	0.0002	436.8	9.0	433.4	8.0	415.3	16.6	-5	436.8	9.0
A6Z-86	92.0	1.752	0.014	2.160	0.019	0.0765	0.0003	1201.1	17.7	1168.3	12.6	1108.1	15.9	-8	1201.1	17.7
A6Z-87	124.0	12.739	0.170	15.808	0.127	0.2010	0.0004	2910.7	36.3	2865.3	15.8	2833.5	7.2	-3	2833.5	7.2
A6Z-88	46.1	1.998	0.019	0.595	0.009	0.0550	0.0004	487.2	12.6	474.1	11.5	411.2	31.3	-18	487.2	12.6
A6Z-89	10.6	7.628	0.172	11.095	0.110	0.1608	0.0006	2616.4	40.0	2531.1	18.8	2463.4	11.6	-6	2463.4	11.6
A6Z-90	358.0	3.586	0.055	1.565	0.039	0.0866	0.0009	794.1	33.6	956.3	30.7	1350.7	40.1	41	794.1	33.6
A6Z-91	136.0	5.288	0.034	3.592	0.055	0.0935	0.0002	1585.8	42.9	1547.8	24.6	1496.2	9.1	-6	1496.2	9.1
A6Z-92	81.4	13.831	0.163	1.940	0.014	0.0744	0.0002	1116.5	13.1	1094.9	9.5	1052.2	12.2	-6	1116.5	13.1
A6Z-93	570.0	3.349	0.025	0.554	0.007	0.0556	0.0002	450.0	10.2	447.8	8.8	436.6	13.6	-3	450.0	10.2
A6Z-94	89.2	3.441	0.024	4.383	0.036	0.1065	0.0003	1684.4	22.4	1709.2	13.7	1739.7	11.7	3	1739.7	11.7
A6Z-95	136.3	3.377	0.024	3.938	0.030	0.0983	0.0003	1644.5	20.6	1621.5	12.5	1591.9	10.7	-3	1591.9	10.7
A6Z-96	103.7	1.859	0.013	4.060	0.031	0.0995	0.0003	1671.9	21.0	1646.2	12.5	1613.5	9.4	-4	1613.5	9.4
A6Z-97	52.6	1.816	0.014	13.841	0.101	0.1867	0.0004	2774.7	31.2	2738.9	14.3	2712.6	7.8	-2	2712.6	7.8
A6Z-98	160.7	3.945	0.029	15.266	0.123	0.2011	0.0004	2828.1	35.5	2832.0	15.8	2834.7	7.2	0	2834.7	7.2
A6Z-99	41.4	4.575	0.051	3.115	0.025	0.0892	0.0003	1456.5	19.1	1436.3	12.5	1406.5	12.9	-4	1406.5	12.9
A6Z-100	161.3	13.477	0.109	2.418	0.028	0.0803	0.0002	1274.5	26.0	1248.0	16.6	1202.7	10.1	-6	1202.7	10.1
A6Z-101	236.5	1.815	0.015	0.564	0.005	0.0551	0.0002	461.4	7.2	454.0	6.4	416.5	15.0	-11	461.4	7.2
A6Z-102	26.5	5.476	0.037	14.023	0.124	0.1847	0.0006	2828.9	38.4	2751.3	17.2	2694.8	9.9	-5	2694.8	9.9
A6Z-103	188.2	13.423	0.117	1.846	0.013	0.0733	0.0002	1081.2	13.7	1061.9	9.7	1022.5	10.2	-6	1081.2	13.7
A6Z-104	317.0	1.866	0.021	0.565	0.006	0.0550	0.0002	463.2	7.8	454.9	7.2	412.8	19.9	-12	463.2	7.8
A6Z-105	81.4	5.482	0.044	13.454	0.154	0.1821	0.0004	2766.7	50.4	2712.1	22.0	2671.6	8.1	-4	2671.6	8.1
A6Z-106	135.0	13.316	0.098	1.824	0.016	0.0725	0.0002	1080.1	15.9	1053.9	11.3	1000.2	12.9	-8	1080.1	15.9
A6Z-107	133.3	4.505	0.026	0.569	0.005	0.0550	0.0003	466.8	6.6	457.7	6.5	412.0	21.1	-13	466.8	6.6
A6Z-108	56.7	14.493	0.116	2.453	0.017	0.0802	0.0003	1292.4	13.8	1258.4	10.0	1200.5	14.0	-8	1200.5	14.0
A6Z-109	70.4	13.504	0.077	0.513	0.007	0.0539	0.0006	430.1	6.6	420.2	8.9	365.9	46.0	-18	430.1	6.6
A6Z-110	283.9	4.153	0.018	0.563	0.004	0.0551	0.0002	460.5	5.1	453.3	5.1	416.9	18.2	-10	460.5	5.1

Grain I.D.	238U (ppm)	238/206 ratio	238/206 1SE	207/235 ratio	207/235 1SE	207/206 ratio	207/206 1SE	238/206 Age (Ma)	2σ	207/235 Age (Ma)	2σ	207/206 Age (Ma)	2σ	Disc. (%)	preferred Age (Ma)	preferred Err. (2σ)
A6Z-111	22.5	2.480	0.015	2.768	0.016	0.0834	0.0003	1390.9	11.0	1346.9	8.9	1277.7	15.0	-9	1277.7	15.0
A6Z-112	90.2	3.499	0.017	7.175	0.047	0.1291	0.0003	2184.2	22.6	2133.4	12.1	2084.8	9.0	-5	2084.8	9.0
A6Z-113	261.4	3.306	0.015	4.088	0.026	0.1038	0.0004	1620.5	13.6	1651.9	10.6	1692.0	15.6	4	1692.0	15.6
A6Z-114	209.9	12.950	0.083	4.195	0.022	0.1006	0.0002	1703.7	14.0	1673.1	8.9	1634.9	9.1	-4	1634.9	9.1
A6Z-115	253.0	12.531	0.165	0.589	0.004	0.0553	0.0002	479.5	5.9	470.1	5.6	424.6	16.5	-13	479.5	5.9
A6Z-116	505.0	1.804	0.010	0.646	0.011	0.0587	0.0006	494.9	12.5	505.8	13.3	555.0	44.6	11	494.9	12.5
A6Z-117	83.3	13.523	0.084	14.379	0.090	0.1882	0.0005	2843.4	26.3	2775.0	12.5	2725.7	8.8	-4	2725.7	8.8
A6Z-118	158.0	6.223	0.046	0.563	0.004	0.0552	0.0002	459.9	5.5	453.4	5.5	420.5	18.6	-9	459.9	5.5
A6Z-119	746.0	4.585	0.024	1.581	0.012	0.0714	0.0002	960.7	13.4	962.8	9.9	967.7	10.0	1	960.7	13.4
A6Z-120	108.8	5.519	0.032	2.363	0.015	0.0786	0.0003	1271.8	12.2	1231.5	9.3	1161.4	14.4	-10	1161.4	14.4
A6Z-121	56.9	4.655	0.028	1.797	0.013	0.0720	0.0003	1073.5	11.5	1044.4	9.3	983.9	16.1	-9	1073.5	11.5
A6Z-122	60.5	13.546	0.085	2.319	0.017	0.0783	0.0003	1254.3	13.9	1218.1	10.2	1154.4	15.0	-9	1154.4	15.0
A6Z-123	118.9	7.364	0.133	0.562	0.005	0.0552	0.0004	459.1	5.6	452.7	6.6	420.1	28.3	-9	459.1	5.6
A6Z-124	280.0	13.965	0.095	1.447	0.027	0.0773	0.0004	820.9	27.8	908.4	22.5	1127.8	19.6	27	820.9	27.8
A6Z-125	173.4	5.705	0.072	0.539	0.004	0.0546	0.0002	445.8	5.9	437.5	5.7	393.6	18.9	-13	445.8	5.9
A6Z-126	105.0	4.158	0.032	1.724	0.022	0.0714	0.0003	1041.2	24.2	1017.5	16.8	966.8	14.6	-8	1041.2	24.2
A6Z-127	139.1	10.428	0.103	2.816	0.023	0.0850	0.0003	1389.3	19.3	1359.7	12.5	1313.5	11.4	-6	1313.5	11.4
A6Z-128	13.1	13.351	0.152	0.775	0.013	0.0586	0.0008	590.3	11.2	582.3	15.0	551.3	59.6	-7	590.3	11.2
A6Z-129	118.5	3.244	0.032	0.568	0.007	0.0550	0.0003	465.6	10.2	456.4	9.2	410.4	23.6	-13	465.6	10.2
A6Z-130	113.1	5.322	0.047	4.258	0.044	0.1002	0.0003	1732.3	30.1	1685.3	17.2	1627.1	11.1	-6	1627.1	11.1
A6Z-131	75.7	13.889	0.135	1.877	0.018	0.0725	0.0003	1110.0	17.9	1073.2	12.7	999.1	15.1	-11	1110.0	17.9
A6Z-132	36.2	13.966	0.156	0.542	0.007	0.0546	0.0005	448.2	8.4	439.5	9.5	394.0	41.1	-14	448.2	8.4
A6Z-133	137.3	7.299	0.426	0.534	0.007	0.0541	0.0003	445.8	9.6	434.2	8.7	373.0	22.5	-20	445.8	9.6
A6Z-134	109.2	4.587	0.045	1.339	0.083	0.0709	0.0015	827.7	90.7	862.7	72.2	953.6	86.5	13	827.7	90.7
A6Z-135	281.0	3.317	0.032	2.529	0.026	0.0842	0.0003	1271.3	22.8	1280.5	15.2	1296.1	12.5	2	1296.1	12.5

10.3.1.4 THBH (Zircon)

Grain I.D.	238U (ppm)	238/206 ratio	238/206 1SE	207/235 ratio	207/235 1SE	207/206 ratio	207/206 1SE	238/206 Age (Ma)	2σ	207/235 Age (Ma)	2σ	207/206 Age (Ma)	2σ	Disc. (%)	preferred Age (Ma)	preferred Err. (2σ)
THZ-01	342.0	4.577	0.077	3.057	0.055	0.1015	0.001	1273.9	39.2	1422.1	27.5	1651.4	22.6	23%		
THZ-02	389.0	3.186	0.047	4.641	0.071	0.1073	0.000	1759.9	45.7	1756.7	25.7	1752.9	15.3	0%	1752.9	15.3
THZ-03	371.0	3.811	0.071	3.433	0.066	0.0949	0.000	1502.1	50.1	1511.9	30.2	1525.6	17.0	2%	1525.6	17.0
THZ-04	150.7	6.983	0.102	1.555	0.025	0.0788	0.001	862.7	23.7	952.3	20.1	1165.5	28.1	26%		
THZ-05	323.0	3.030	0.027	5.876	0.146	0.1292	0.003	1838.4	28.2	1957.7	43.2	2086.3	81.9	12%	2086.3	81.9
THZ-06	79.9	5.208	0.095	2.538	0.064	0.0959	0.002	1132.2	37.9	1282.9	36.6	1545.0	64.9	27%		
THZ-07	181.0	3.058	0.075	5.218	0.129	0.1158	0.000	1823.8	77.8	1855.5	42.3	1891.2	15.9	4%	1891.2	15.9
THZ-08	314.0	3.003	0.059	5.211	0.104	0.1136	0.001	1852.9	62.9	1854.4	34.2	1856.2	16.9	0%	1856.2	16.9
THZ-09	264.8	3.247	0.084	4.654	0.122	0.1096	0.000	1730.9	78.9	1758.9	44.0	1792.5	15.1	3%	1792.5	15.1
THZ-10	119.4	3.195	0.051	4.723	0.079	0.1095	0.001	1755.5	49.1	1771.3	28.2	1790.1	19.2	2%	1790.1	19.2
THZ-11	235.0	3.390	0.063	4.232	0.083	0.1041	0.001	1666.5	54.8	1680.3	32.4	1697.6	23.7	2%	1697.6	23.7
THZ-12	417.0	1.908	0.073	13.492	0.517	0.1868	0.001	2716.1	169.2	2714.7	72.6	2713.6	14.1	0%	2713.6	14.1
THZ-13	884.0	6.734	0.132	1.444	0.029	0.0705	0.000	892.5	32.6	907.2	24.1	943.2	18.9	5%	892.5	32.6
THZ-14	64.9	3.257	0.074	6.528	0.154	0.1543	0.001	1725.9	69.1	2049.7	41.7	2393.4	21.9	28%		
THZ-15	273.7	3.896	0.075	3.509	0.071	0.0992	0.001	1472.9	50.8	1529.4	32.0	1608.3	23.2	8%	1608.3	23.2
THZ-16	240.1	4.651	0.141	2.782	0.085	0.0939	0.000	1255.4	69.0	1350.8	45.9	1505.3	20.7	17%	1505.3	20.7
THZ-17	748.0	5.319	0.113	2.101	0.046	0.0811	0.000	1110.5	43.4	1149.1	30.0	1222.5	18.7	9%	1110.5	43.4
THZ-18	159.3	3.610	0.085	3.850	0.092	0.1009	0.000	1576.2	65.6	1603.3	38.6	1639.2	18.0	4%	1639.2	18.0
THZ-19	349.0	15.723	0.457	0.570	0.017	0.0650	0.000	397.5	22.4	457.7	22.1	772.7	30.5	49%		
THZ-20	535.0	14.837	0.253	0.520	0.009	0.0559	0.000	420.5	13.9	424.9	12.6	449.0	27.0	6%	420.5	13.9
THZ-21	909.0	16.367	0.429	0.478	0.013	0.0568	0.000	382.3	19.4	397.0	17.5	483.6	22.2	21%	382.3	19.4
THZ-22	102.4	1.957	0.034	12.507	0.227	0.1776	0.001	2660.9	76.8	2643.3	34.4	2629.8	16.4	-1%	2629.8	16.4
THZ-23	179.9	1.927	0.030	12.737	0.202	0.1781	0.001	2694.9	68.0	2660.4	30.0	2634.2	13.9	-2%	2634.2	13.9
THZ-24	194.9	5.893	0.141	1.823	0.045	0.0779	0.000	1010.5	44.7	1053.7	32.4	1144.5	25.5	12%	1010.5	44.7
THZ-25	286.0	5.420	0.141	1.946	0.052	0.0765	0.000	1091.5	52.3	1097.0	35.7	1107.8	22.0	1%	1091.5	52.3
THZ-26	111.9	3.597	0.084	3.870	0.092	0.1010	0.000	1581.3	65.6	1607.4	38.5	1641.7	18.3	4%	1641.7	18.3
THZ-27	582.0	13.569	0.267	0.628	0.013	0.0618	0.000	458.4	17.4	494.9	16.0	667.3	22.7	31%		
THZ-28	210.3	3.840	0.074	3.630	0.072	0.1011	0.001	1491.9	51.2	1556.1	31.8	1644.3	20.9	9%	1644.3	20.9
THZ-29	293.9	14.706	0.216	0.520	0.009	0.0555	0.000	424.1	12.1	425.4	11.4	432.6	32.0	2%	424.1	12.1
THZ-30	360.0	14.306	0.184	0.540	0.008	0.0560	0.000	435.6	10.9	438.2	10.4	452.2	31.2	4%	435.6	10.9
THZ-31	362.0	3.623	0.079	3.892	0.086	0.1023	0.000	1571.2	60.6	1611.9	35.8	1665.6	16.0	6%	1665.6	16.0
THZ-32	159.0	5.510	0.062	2.021	0.025	0.0808	0.000	1075.2	22.4	1122.7	17.1	1215.9	21.8	12%	1075.2	22.4
THZ-33	240.7	3.584	0.077	3.904	0.086	0.1015	0.000	1586.3	60.5	1614.5	35.6	1651.4	18.2	4%	1651.4	18.2
THZ-34	703.0	15.060	0.284	0.523	0.010	0.0572	0.000	414.4	15.1	427.1	13.5	496.3	21.3	17%	414.4	15.1
THZ-35	268.3	14.815	0.362	0.512	0.013	0.0550	0.000	421.1	19.9	419.6	17.7	411.2	36.1	-2%	421.1	19.9
THZ-36	38.8	4.787	0.091	2.410	0.052	0.0837	0.001	1223.0	42.1	1245.5	30.9	1284.7	39.9	5%	1284.7	39.9
THZ-37	391.0	3.571	0.077	3.926	0.086	0.1018	0.000	1591.4	60.5	1619.1	35.4	1655.5	16.1	4%	1655.5	16.1
THZ-38	218.0	2.342	0.036	9.202	0.144	0.1564	0.001	2292.2	58.8	2358.3	28.9	2415.9	14.5	5%	2415.9	14.5
THZ-39	791.0	14.514	0.295	0.535	0.011	0.0563	0.000	429.5	16.9	435.1	14.9	464.8	24.8	8%	429.5	16.9
THZ-40	756.0	15.152	0.241	0.594	0.010	0.0653	0.001	412.0	12.7	473.6	13.4	784.0	32.5	47%		
THZ-41	580.0	3.953	0.227	6.943	0.399	0.1991	0.001	1453.9	149.2	2104.2	102.0	2818.3	14.1	48%		
THZ-42	285.0	1.942	0.043	14.361	0.325	0.2023	0.001	2677.9	97.9	2773.9	43.1	2844.4	13.9	6%	2844.4	13.9
THZ-43	33.6	3.484	0.079	3.912	0.094	0.0989	0.001	1626.5	65.1	1616.1	39.0	1602.6	30.7	-1%	1602.6	30.7
THZ-44	344.0	3.425	0.088	4.128	0.108	0.1026	0.000	1651.5	74.9	1659.8	42.6	1670.3	17.0	1%	1670.3	17.0
THZ-45	251.0	4.132	0.102	2.943	0.074	0.0882	0.000	1397.1	62.3	1393.0	38.4	1386.9	19.7	-1%	1386.9	19.7
THZ-46	285.0	3.546	0.088	4.001	0.101	0.1030	0.000	1601.4	70.4	1634.4	41.0	1677.1	16.8	5%	1677.1	16.8
THZ-47	147.7	3.298	0.040	4.326	0.057	0.1035	0.001	1707.2	36.7	1698.4	21.8	1687.5	18.7	-1%	1687.5	18.7
THZ-48	183.2	2.008	0.046	12.999	0.304	0.1894	0.001	2605.2	99.0	2679.6	44.2	2736.2	14.0	5%	2736.2	14.0
THZ-49	76.0	3.487	0.042	4.051	0.056	0.1025	0.001	1625.5	34.6	1644.6	22.6	1669.0	25.9	3%	1669.0	25.9
THZ-50	398.4	3.512	0.056	4.029	0.066	0.1027	0.000	1615.0	45.7	1640.0	26.9	1672.3	16.0	3%	1672.3	16.0
THZ-51	1114.0	4.132	0.222	4.736	0.256	0.1420	0.001	1397.1	135.0	1773.6	90.6	2251.0	20.4	38%		
THZ-52	189.6	1.934	0.021	13.917	0.157	0.1953	0.001	2686.4	46.8	2744.1	21.8	2786.7	14.3	4%	2786.7	14.3

Grain I.D.	238U (ppm)	238/206 ratio	238/206 1SE	207/235 ratio	207/235 1SE	207/206 ratio	207/206 1SE	238/206 Age (Ma)	2σ	207/235 Age (Ma)	2σ	207/206 Age (Ma)	2σ	Disc. (%)	preferred Age (Ma)	preferred Err. (2σ)
THZ-53	100.2	4.755	0.068	2.484	0.044	0.0857	0.001	1230.4	32.0	1267.3	25.7	1330.6	41.0	8%	1330.6	41.0
THZ-54	99.9	3.954	0.076	3.925	0.079	0.1126	0.001	1453.4	49.9	1618.8	32.5	1841.0	21.7	21%		
THZ-55	156.1	4.132	0.145	3.003	0.107	0.0900	0.001	1397.1	88.2	1408.4	54.3	1425.5	23.9	2%	1425.5	23.9
THZ-56	946.0	15.385	0.249	0.506	0.009	0.0565	0.000	406.0	12.7	415.8	11.7	470.7	25.1	14%	406.0	12.7
THZ-57	410.0	14.771	0.164	0.542	0.010	0.0581	0.001	422.3	9.1	439.8	13.1	532.6	64.2	21%	422.3	9.1
THZ-58	908.0	14.993	0.214	0.522	0.008	0.0568	0.000	416.2	11.5	426.5	10.8	482.4	27.2	14%	416.2	11.5
THZ-59	83.6	11.062	0.104	2.294	0.031	0.1841	0.002	557.9	10.1	1210.3	19.0	2689.4	32.1	79%		
THZ-60	83.3	13.477	0.127	0.588	0.009	0.0575	0.001	461.4	8.4	469.6	11.6	509.8	53.7	9%	461.4	8.4
THZ-61	659.0	3.295	0.035	7.546	0.088	0.1804	0.001	1708.6	31.7	2178.4	21.1	2655.8	17.9	36%		
THZ-62	456.0	14.706	0.238	0.528	0.009	0.0563	0.000	424.1	13.3	430.5	12.6	464.8	34.9	9%	424.1	13.3
THZ-63	668.0	14.771	0.316	0.542	0.012	0.0581	0.000	422.3	17.5	439.9	15.9	533.3	26.8	21%	422.3	17.5
THZ-64	76.0	5.485	0.122	2.138	0.051	0.0851	0.001	1079.5	44.2	1161.2	32.8	1316.9	32.3	18%		
THZ-65	177.9	2.008	0.034	13.283	0.232	0.1935	0.001	2605.2	73.2	2699.9	33.3	2771.7	14.5	6%	2771.7	14.5
THZ-66	285.9	3.623	0.079	3.792	0.084	0.0997	0.000	1571.2	60.6	1591.0	35.8	1617.5	18.8	3%	1617.5	18.8
THZ-67	173.7	3.942	0.076	3.530	0.071	0.1010	0.001	1457.5	50.4	1533.9	31.8	1640.8	21.0	11%	1640.8	21.0
THZ-68	77.8	4.032	0.089	5.369	0.124	0.1571	0.001	1428.2	56.8	1880.0	39.6	2423.9	22.5	41%		
THZ-69	408.0	4.978	0.123	2.348	0.059	0.0848	0.000	1180.2	53.2	1227.0	35.7	1310.3	18.0	10%	1310.3	18.0
THZ-70	333.0	14.620	0.331	0.519	0.013	0.0550	0.000	426.5	18.7	424.3	16.8	412.4	37.6	-3%	426.5	18.7
THZ-71	290.0	14.184	0.382	0.577	0.016	0.0594	0.001	439.2	22.9	462.6	21.2	580.8	40.5	24%		
THZ-72	190.2	1.949	0.057	13.434	0.396	0.1900	0.001	2669.4	127.9	2710.6	55.9	2741.5	14.7	3%	2741.5	14.7
THZ-73	271.9	2.982	0.043	5.448	0.082	0.1179	0.000	1864.0	46.9	1892.5	25.8	1923.8	15.0	3%	1923.8	15.0
THZ-74	360.0	2.747	0.075	13.720	0.381	0.2735	0.001	2001.1	94.5	2730.6	52.7	3325.5	15.2	40%		
THZ-75	79.3	2.110	0.062	12.164	0.364	0.1862	0.001	2501.1	122.5	2617.1	56.3	2708.1	17.3	8%	2708.1	17.3
THZ-76	356.0	14.205	0.313	0.651	0.015	0.0671	0.001	438.6	18.7	509.1	19.0	839.9	37.5	48%		
THZ-77	292.0	13.495	0.337	0.766	0.020	0.0750	0.001	460.8	22.2	577.4	23.3	1067.6	35.2	57%		
THZ-78	65.0	5.488	0.098	2.521	0.051	0.1004	0.001	1079.0	35.5	1278.1	29.4	1630.7	35.6	34%		
THZ-79	52.0	4.606	0.090	2.483	0.057	0.0830	0.001	1266.5	45.0	1267.2	33.3	1268.3	47.3	0%	1268.3	47.3
THZ-80	565.0	14.749	0.305	0.520	0.011	0.0557	0.000	422.9	16.9	425.3	15.2	438.6	32.7	4%	422.9	16.9
THZ-81	793.0	15.015	0.316	0.557	0.012	0.0607	0.000	415.6	16.9	449.4	15.9	626.2	26.7	34%		
THZ-82	360.0	5.504	0.108	1.908	0.038	0.0762	0.000	1076.3	38.7	1083.9	26.9	1099.2	20.3	2%	1076.3	38.7
THZ-83	139.6	14.925	0.245	0.502	0.010	0.0544	0.001	418.1	13.3	413.3	13.4	386.6	49.7	-8%	418.1	13.3
THZ-84	139.6	14.925	0.245	0.502	0.010	0.0544	0.001	418.1	13.3	413.3	13.4	386.6	49.7	-8%	418.1	13.3
THZ-85	43.4	3.37	0.063	4.355	0.090	0.1066	0.0010	1673.4	54.7	1703.8	34.1	1741.3	33.2	4%	1741.3	33.2
THZ-86	36.1	3.17	0.071	5.005	0.126	0.1153	0.0014	1765.3	68.7	1820.2	42.6	1883.8	42.6	6%	1883.8	42.6
THZ-87	155.9	14.73	0.249	0.535	0.011	0.0572	0.0006	423.5	13.9	435.2	14.1	497.9	46.4	15%	423.5	13.9
THZ-88	316	15.46	0.263	0.510	0.010	0.0572	0.0005	404.1	13.3	418.2	13.0	496.3	37.3	19%	404.1	13.3
THZ-89	141.7	2.84	0.048	5.846	0.109	0.1206	0.0009	1943.2	57.3	1953.3	32.4	1964.0	27.3	1%	1964.0	27.3
THZ-90	161	13.62	0.223	0.571	0.011	0.0564	0.0007	456.6	14.4	458.4	14.8	467.2	51.2	2%	456.6	14.4
THZ-91	146.8	14.16	0.201	0.547	0.010	0.0562	0.0007	439.8	12.1	442.9	13.1	459.3	51.5	4%	439.8	12.1
THZ-92	227	5.24	0.122	2.041	0.050	0.0776	0.0006	1126.2	48.2	1129.4	33.2	1135.5	28.7	1%	1126.2	48.2
THZ-93	134.2	5.59	0.172	1.876	0.060	0.0761	0.0006	1061.5	60.2	1072.7	42.0	1095.5	32.0	3%	1061.5	60.2
THZ-94	72	6.02	0.094	2.252	0.085	0.0983	0.0034	991.1	28.8	1197.3	53.4	1591.3	129.3	38%	1591.3	129.3
THZ-95	183.4	5.32	0.136	2.419	0.065	0.0934	0.0008	1110.5	52.1	1248.4	38.5	1494.8	30.9	26%	1494.8	30.9
THZ-96	343	3.33	0.066	4.419	0.094	0.1067	0.0008	1693.3	59.5	1715.9	35.1	1743.7	26.4	3%	1743.7	26.4
THZ-97	62.6	4.81	0.103	2.284	0.054	0.0798	0.0008	1216.6	47.5	1207.4	33.5	1191.2	39.9	-2%	1191.2	39.9
THZ-98	888	21.74	0.425	0.411	0.009	0.0649	0.0007	289.9	11.1	349.9	13.0	770.1	42.4	62%	289.9	11.1
THZ-99	94	3.87	0.065	3.343	0.062	0.0938	0.0007	1482.2	44.6	1491.1	28.8	1503.8	28.7	1%	1503.8	28.7
THZ-100	275.7	3.38	0.056	4.164	0.074	0.1022	0.0007	1669.0	48.8	1666.9	29.2	1664.3	24.2	0%	1664.3	24.2
THZ-101	198.4	4.88	0.058	2.241	0.031	0.0794	0.0006	1201.6	26.2	1194.1	19.5	1180.5	27.9	-2%	1201.6	26.2
THZ-102	187.5	1.86	0.031	14.141	0.254	0.1911	0.0013	2770.9	75.6	2759.2	34.3	2750.7	22.6	-1%	2750.7	22.6
THZ-103	156.7	1.86	0.036	14.329	0.295	0.1936	0.0013	2770.9	88.1	2771.8	39.3	2772.4	22.3	0%	2772.4	22.3
THZ-104	43.9	1.51	0.022	22.377	0.365	0.2449	0.0019	3278.8	73.7	3200.3	32.0	3151.4	25.7	-4%	3151.4	25.7
THZ-105	399	3.21	0.062	4.555	0.093	0.1059	0.0007	1750.5	59.0	1741.1	33.9	1729.9	24.9	-1%	1729.9	24.9
THZ-106	58.4	3.10	0.058	6.944	0.148	0.1560	0.0017	1804.4	58.5	2104.3	38.1	2412.0	36.5	25%	2412.0	36.5
THZ-107	118.2	4.10	0.064	3.034	0.052	0.0901	0.0007	1408.5	39.4	1416.1	26.3	1427.6	28.1	1%	1427.6	28.1
THZ-108	88.1	4.22	0.125	2.887	0.088	0.0884	0.0007	1371.1	73.0	1378.5	46.2	1389.9	30.9	1%	1389.9	30.9
THZ-109	880	13.68	0.262	0.566	0.012	0.0562	0.0004	454.8	16.8	455.3	15.1	458.1	33.1	1%	454.8	16.8

Grain I.D.	238U (ppm)	238/206 ratio	238/206 1SE	207/235 ratio	207/235 1SE	207/206 ratio	207/206 1SE	238/206 Age (Ma)	2σ	207/235 Age (Ma)	2σ	207/206 Age (Ma)	2σ	Disc. (%)	preferred Age (Ma)	preferred Err. (2σ)
THZ-110	383	5.29	0.112	2.046	0.046	0.0785	0.0006	1116.5	43.4	1130.8	30.4	1158.4	28.3	4%	1116.5	43.4
THZ-111	311	5.28	0.127	2.045	0.051	0.0784	0.0006	1117.6	49.3	1130.7	34.2	1155.9	28.3	3%	1117.6	49.3
THZ-112	374	4.05	0.090	3.137	0.073	0.0921	0.0006	1423.0	56.9	1441.7	35.8	1469.4	25.3	3%	1469.4	25.3
THZ-113	263	13.89	0.444	0.553	0.018	0.0557	0.0006	448.2	27.7	446.9	24.2	440.2	44.2	-2%	448.2	27.7
THZ-114	623	3.56	0.076	4.028	0.090	0.1040	0.0007	1596.4	60.4	1639.9	36.5	1696.0	25.4	6%	1696.0	25.4
THZ-115	95.5	1.22	0.024	40.472	0.833	0.3590	0.0023	3853.3	113.5	3782.3	41.1	3744.9	21.1	-3%	3744.9	21.1
THZ-116	867	11.03	0.322	0.957	0.029	0.0766	0.0006	559.7	31.3	681.9	29.9	1109.4	29.1	50%	559.7	31.3
THZ-117	578	14.06	0.257	0.567	0.011	0.0579	0.0004	442.8	15.7	456.1	14.6	523.9	34.0	15%	442.8	15.7
THZ-118	114.6	3.34	0.046	4.570	0.075	0.1108	0.0010	1687.8	41.2	1743.9	27.3	1811.8	31.7	7%	1811.8	31.7
THZ-119	63.9	13.91	0.222	0.520	0.011	0.0525	0.0008	447.6	13.8	425.3	15.4	306.2	69.6	-46%	447.6	13.8
THZ-120	275	3.23	0.057	4.931	0.094	0.1155	0.0008	1739.2	54.2	1807.5	32.3	1887.2	25.6	8%	1887.2	25.6
THZ-121	151.6	13.87	0.240	0.582	0.012	0.0586	0.0007	448.8	15.0	465.9	15.7	551.3	52.4	19%	448.8	15.0
THZ-122	193.6	5.72	0.079	1.767	0.028	0.0734	0.0006	1038.0	26.4	1033.2	20.3	1023.3	30.7	-1%	1038.0	26.4
THZ-123	161.1	5.74	0.109	1.758	0.036	0.0732	0.0006	1035.8	36.2	1030.2	26.4	1018.3	30.8	-2%	1035.8	36.2
THZ-124	98.5	6.54	0.184	1.459	0.043	0.0692	0.0006	917.8	48.1	913.4	35.5	902.9	36.1	-2%	917.8	48.1
THZ-125	265.8	6.18	0.122	1.562	0.033	0.0700	0.0006	966.8	35.5	955.2	26.4	928.6	32.6	-4%	966.8	35.5
THZ-126	140.6	4.70	0.071	2.396	0.039	0.0817	0.0006	1243.7	34.0	1241.3	23.7	1237.2	26.9	-1%	1237.2	26.9
THZ-127	170.6	14.18	0.241	0.839	0.041	0.0863	0.0040	439.2	14.5	618.3	45.2	1344.0	176.9	67%	439.2	14.5
THZ-128	58.4	1.88	0.028	13.669	0.225	0.1861	0.0013	2754.1	67.3	2727.0	31.3	2707.1	23.2	-2%	2707.1	23.2
THZ-129	86	2.35	0.042	9.284	0.176	0.1585	0.0011	2283.1	67.9	2366.4	34.9	2439.0	24.4	6%	2439.0	24.4
THZ-130	58.5	5.51	0.100	1.865	0.038	0.0745	0.0007	1075.7	36.0	1068.6	27.1	1054.1	38.2	-2%	1075.7	36.0
THZ-131	78.7	1.77	0.028	14.881	0.258	0.1914	0.0013	2883.1	74.3	2807.6	33.2	2753.8	23.3	-5%	2753.8	23.3
THZ-84	96	3.02	0.059	5.071	0.107	0.111	0.001	1843.2	63.0	1831.2	35.8	1817.7	28.4	-1%	1817.7	28.4
THZ-85	139.6	14.925	0.245	0.502	0.010	0.0544	0.001	418.1	13.3	413.3	13.4	386.6	49.7	-8%	418.1	13.3
THZ-86	43.4	3.37	0.063	4.355	0.090	0.1066	0.0010	1673.4	54.7	1703.8	34.1	1741.3	33.2	4%	1741.3	33.2
THZ-87	36.1	3.17	0.071	5.005	0.126	0.1153	0.0014	1765.3	68.7	1820.2	42.6	1883.8	42.6	6%	1883.8	42.6
THZ-88	155.9	14.73	0.249	0.535	0.011	0.0572	0.0006	423.5	13.9	435.2	14.1	497.9	46.4	15%	423.5	13.9
THZ-89	316	15.46	0.263	0.510	0.010	0.0572	0.0005	404.1	13.3	418.2	13.0	496.3	37.3	19%	404.1	13.3
THZ-90	141.7	2.84	0.048	5.846	0.109	0.1206	0.0009	1943.2	57.3	1953.3	32.4	1964.0	27.3	1%	1964.0	27.3
THZ-91	161	13.62	0.223	0.571	0.011	0.0564	0.0007	456.6	14.4	458.4	14.8	467.2	51.2	2%	456.6	14.4
THZ-92	146.8	14.16	0.201	0.547	0.010	0.0562	0.0007	439.8	12.1	442.9	13.1	459.3	51.5	4%	439.8	12.1
THZ-93	227	5.24	0.122	2.041	0.050	0.0776	0.0006	1126.2	48.2	1129.4	33.2	1135.5	28.7	1%	1126.2	48.2
THZ-94	134.2	5.59	0.172	1.876	0.060	0.0761	0.0006	1061.5	60.2	1072.7	42.0	1095.5	32.0	3%	1061.5	60.2
THZ-95	72	6.02	0.094	2.252	0.085	0.0983	0.0034	991.1	28.8	1197.3	53.4	1591.3	129.3	38%	1591.3	129.3
THZ-96	183.4	5.32	0.136	2.419	0.065	0.0934	0.0008	1110.5	52.1	1248.4	38.5	1494.8	30.9	26%	1494.8	30.9
THZ-97	343	3.33	0.066	4.419	0.094	0.1067	0.0008	1693.3	59.5	1715.9	35.1	1743.7	26.4	3%	1743.7	26.4
THZ-98	62.6	4.81	0.103	2.284	0.054	0.0798	0.0008	1216.6	47.5	1207.4	33.5	1191.2	39.9	-2%	1191.2	39.9
THZ-99	888	21.74	0.425	0.411	0.009	0.0649	0.0007	289.9	11.1	349.9	13.0	770.1	42.4	62%	289.9	11.1
THZ-100	94	3.87	0.065	3.343	0.062	0.0938	0.0007	1482.2	44.6	1491.1	28.8	1503.8	28.7	1%	1503.8	28.7
THZ-101	275.7	3.38	0.056	4.164	0.074	0.1022	0.0007	1669.0	48.8	1666.9	29.2	1664.3	24.2	0%	1664.3	24.2
THZ-102	198.4	4.88	0.058	2.241	0.031	0.0794	0.0006	1201.6	26.2	1194.1	19.5	1180.5	27.9	-2%	1201.6	26.2
THZ-103	187.5	1.86	0.031	14.141	0.254	0.1911	0.0013	2770.9	75.6	2759.2	34.3	2750.7	22.6	-1%	2750.7	22.6
THZ-104	156.7	1.86	0.036	14.329	0.295	0.1936	0.0013	2770.9	88.1	2771.8	39.3	2772.4	22.3	0%	2772.4	22.3
THZ-105	43.9	1.51	0.022	22.377	0.365	0.2449	0.0019	3278.8	73.7	3200.3	32.0	3151.4	25.7	-4%	3151.4	25.7
THZ-106	399	3.21	0.062	4.555	0.093	0.1059	0.0007	1750.5	59.0	1741.1	33.9	1729.9	24.9	-1%	1729.9	24.9
THZ-107	58.4	3.10	0.058	6.944	0.148	0.1560	0.0017	1804.4	58.5	2104.3	38.1	2412.0	36.5	25%	2412.0	36.5
THZ-108	118.2	4.10	0.064	3.034	0.052	0.0901	0.0007	1408.5	39.4	1416.1	26.3	1427.6	28.1	1%	1427.6	28.1
THZ-109	88.1	4.22	0.125	2.887	0.088	0.0884	0.0007	1371.1	73.0	1378.5	46.2	1389.9	30.9	1%	1389.9	30.9
THZ-110	880	13.68	0.262	0.566	0.012	0.0562	0.0004	454.8	16.8	455.3	15.1	458.1	33.1	1%	454.8	16.8
THZ-111	383	5.29	0.112	2.046	0.046	0.0785	0.0006	1116.5	43.4	1130.8	30.4	1158.4	28.3	4%	1116.5	43.4
THZ-112	311	5.28	0.127	2.045	0.051	0.0784	0.0006	1117.6	49.3	1130.7	34.2	1155.9	28.3	3%	1117.6	49.3
THZ-113	374	4.05	0.090	3.137	0.073	0.0921	0.0006	1423.0	56.9	1441.7	35.8	1469.4	25.3	3%	1469.4	25.3
THZ-114	263	13.89	0.444	0.553	0.018	0.0557	0.0006	448.2	27.7	446.9	24.2	440.2	44.2	-2%	448.2	27.7
THZ-115	623	3.56	0.076	4.028	0.090	0.1040	0.0007	1596.4	60.4	1639.9	36.5	1696.0	25.4	6%	1696.0	25.4
THZ-116	95.5	1.22	0.024	40.472	0.833	0.3590	0.0023	3853.3	113.5	3782.3	41.1	3744.9	21.1	-3%	3744.9	21.1
THZ-117	867	11.03	0.322	0.957	0.029	0.0766	0.0006	559.7	31.3	681.9	29.9	1109.4	29.1	50%	559.7	31.3
THZ-118	578	14.06	0.257	0.567	0.011	0.0579	0.0004	442.8	15.7	456.1	14.6	523.9	34.0	15%	442.8	15.7

Grain I.D.	238U (ppm)	238/206 ratio	238/206 1SE	207/235 ratio	207/235 1SE	207/206 ratio	207/206 1SE	238/206 Age (Ma)	2σ	207/235 Age (Ma)	2σ	207/206 Age (Ma)	2σ	Disc. (%)	preferred Age (Ma)	preferred Err. (2σ)
THZ-119	114.6	3.34	0.046	4.570	0.075	0.1108	0.0010	1687.8	41.2	1743.9	27.3	1811.8	31.7	7%	1811.8	31.7
THZ-120	63.9	13.91	0.222	0.520	0.011	0.0525	0.0008	447.6	13.8	425.3	15.4	306.2	69.6	-46%	447.6	13.8
THZ-121	275	3.23	0.057	4.931	0.094	0.1155	0.0008	1739.2	54.2	1807.5	32.3	1887.2	25.6	8%	1887.2	25.6
THZ-122	151.6	13.87	0.240	0.582	0.012	0.0586	0.0007	448.8	15.0	465.9	15.7	551.3	52.4	19%	448.8	15.0
THZ-123	193.6	5.72	0.079	1.767	0.028	0.0734	0.0006	1038.0	26.4	1033.2	20.3	1023.3	30.7	-1%	1038.0	26.4
THZ-124	161.1	5.74	0.109	1.758	0.036	0.0732	0.0006	1035.8	36.2	1030.2	26.4	1018.3	30.8	-2%	1035.8	36.2
THZ-125	98.5	6.54	0.184	1.459	0.043	0.0692	0.0006	917.8	48.1	913.4	35.5	902.9	36.1	-2%	917.8	48.1
THZ-126	265.8	6.18	0.122	1.562	0.033	0.0700	0.0006	966.8	35.5	955.2	26.4	928.6	32.6	-4%	966.8	35.5
THZ-127	140.6	4.70	0.071	2.396	0.039	0.0817	0.0006	1243.7	34.0	1241.3	23.7	1237.2	26.9	-1%	1237.2	26.9
THZ-128	170.6	14.18	0.241	0.839	0.041	0.0863	0.0040	439.2	14.5	618.3	45.2	1344.0	176.9	67%	439.2	14.5
THZ-129	58.4	1.88	0.028	13.669	0.225	0.1861	0.0013	2754.1	67.3	2727.0	31.3	2707.1	23.2	-2%	2707.1	23.2
THZ-130	86	2.35	0.042	9.284	0.176	0.1585	0.0011	2283.1	67.9	2366.4	34.9	2439.0	24.4	6%	2439.0	24.4
THZ-131	58.5	5.51	0.100	1.865	0.038	0.0745	0.0007	1075.7	36.0	1068.6	27.1	1054.1	38.2	-2%	1075.7	36.0

10.3.1.5 CHBH (Zircon)

Grain I.D.	238U (ppm)	238/206 ratio	238/206 1SE	207/235 ratio	207/235 1SE	207/206 ratio	207/206 1SE	238/206 Age (Ma)	2σ	207/235 Age (Ma)	2σ	207/206 Age (Ma)	2σ	Disc. (%)	preferred Age (Ma)	preferred Err. (2σ)
CHZ-01	331.8	3.479	0.051	4.044	0.075	0.1021	0.0012	1628.5	42.1	1643.1	30.1	1661.8	42.1	2%	1661.8	42.1
CHZ-02	220.7	4.191	0.058	2.949	0.053	0.0897	0.0011	1379.4	34.4	1394.6	27.5	1417.9	45.1	3%	1417.9	45.1
CHZ-03	277.1	3.147	0.043	4.828	0.086	0.1102	0.0013	1779.0	42.6	1789.9	30.0	1802.5	41.6	1%	1802.5	41.6
CHZ-04	111.0	3.690	0.102	3.290	0.106	0.0881	0.0015	1545.9	76.1	1478.8	50.2	1383.8	63.5	-12%	1383.8	63.5
CHZ-05	265.9	3.550	0.052	3.892	0.072	0.1003	0.0012	1599.9	41.3	1612.0	30.0	1627.9	43.0	2%	1627.9	43.0
CHZ-06	245.5	2.916	0.042	5.563	0.102	0.1177	0.0014	1900.6	47.1	1910.4	31.6	1921.1	41.5	1%	1921.1	41.5
CHZ-07	152.5	3.472	0.053	3.988	0.077	0.1005	0.0012	1631.5	44.1	1631.8	31.6	1632.1	44.7	0%	1632.1	44.7
CHZ-08	278.3	3.060	0.056	4.994	0.108	0.1109	0.0013	1822.9	58.3	1818.3	36.5	1813.1	41.4	-1%	1813.1	41.4
CHZ-09	341.0	3.353	0.049	4.395	0.081	0.1069	0.0012	1682.4	43.7	1711.3	30.8	1746.9	41.5	4%	1746.9	41.5
CHZ-10	214.1	3.475	0.049	4.082	0.075	0.1029	0.0012	1630.5	41.1	1650.8	30.1	1676.6	43.5	3%	1676.6	43.5
CHZ-11	364.1	3.906	0.060	3.303	0.063	0.0936	0.0011	1469.3	40.6	1481.8	29.8	1499.6	42.8	2%	1499.6	42.8
CHZ-12	293.6	2.951	0.044	5.562	0.103	0.1191	0.0014	1881.4	48.2	1910.2	32.1	1941.7	41.0	3%	1941.7	41.0
CHZ-13	115.2	3.658	0.054	3.721	0.070	0.0988	0.0012	1558.0	41.0	1575.9	30.2	1600.0	43.8	3%	1600.0	43.8
CHZ-14	69.6	5.238	0.082	2.024	0.040	0.0769	0.0010	1126.2	32.5	1123.6	27.2	1118.5	49.5	-1%	1126.2	32.5
CHZ-15	364.0	3.297	0.048	4.468	0.082	0.1069	0.0012	1707.7	43.6	1725.0	30.5	1746.1	41.5	2%	1746.1	41.5
CHZ-16	108.5	3.420	0.050	4.024	0.076	0.0999	0.0012	1653.5	42.9	1639.0	31.0	1620.5	45.1	-2%	1620.5	45.1
CHZ-17	300.6	3.596	0.060	3.914	0.079	0.1021	0.0012	1581.8	46.9	1616.5	32.7	1662.0	42.1	5%	1662.0	42.1
CHZ-18	182.1	3.549	0.059	3.832	0.077	0.0987	0.0012	1600.4	46.8	1599.4	32.6	1598.1	43.9	0%	1598.1	43.9
CHZ-19	215.0	7.616	0.133	1.598	0.032	0.0883	0.0009	795.3	26.2	969.4	25.3	1388.2	39.5	43%	795.3	26.2
CHZ-20	145.0	2.204	0.034	10.028	0.165	0.1604	0.0009	2411.7	62.1	2437.3	30.5	2458.8	20.1	2%	2458.8	20.1
CHZ-21	319.0	18.553	0.310	0.436	0.011	0.0586	0.0012	338.4	11.0	367.1	15.9	552.4	85.7	39%	338.4	11.0
CHZ-22	126.9	14.605	0.224	0.521	0.009	0.0552	0.0004	426.9	12.7	426.0	11.9	420.9	33.8	-1%	426.9	12.7
CHZ-23	81.0	14.347	0.237	0.546	0.011	0.0568	0.0006	434.3	13.9	442.1	14.1	482.8	46.9	10%	434.3	13.9
CHZ-24	198.0	3.364	0.057	4.371	0.078	0.1067	0.0006	1677.9	49.7	1706.9	29.4	1742.6	21.4	4%	1742.6	21.4
CHZ-25	542.0	3.520	0.056	3.996	0.067	0.1021	0.0006	1612.0	45.2	1633.5	27.3	1661.3	20.7	3%	1661.3	20.7
CHZ-26	126.2	3.536	0.062	3.871	0.072	0.0993	0.0006	1605.4	49.8	1607.6	30.0	1610.4	23.2	0%	1610.4	23.2
CHZ-27	115.7	3.413	0.076	4.240	0.098	0.1050	0.0007	1656.5	64.8	1681.7	38.1	1713.3	25.2	3%	1713.3	25.2
CHZ-28	130.4	3.498	0.067	3.959	0.080	0.1005	0.0007	1621.0	55.2	1625.8	33.0	1632.0	24.7	1%	1632.0	24.7
CHZ-29	416.0	4.630	0.150	3.046	0.101	0.1023	0.0007	1260.7	74.2	1419.2	50.5	1665.8	24.2	24%	1665.8	24.2
CHZ-30	98.6	4.202	0.087	2.983	0.065	0.0909	0.0006	1376.3	51.6	1403.2	33.2	1444.3	25.7	5%	1444.3	25.7
CHZ-31	122.2	3.494	0.067	3.998	0.081	0.1014	0.0007	1622.5	55.2	1633.7	33.0	1648.2	24.4	2%	1648.2	24.4
CHZ-32	94.0	5.631	0.114	1.844	0.040	0.0754	0.0006	1053.8	39.4	1061.4	28.7	1077.0	32.4	2%	1053.8	39.4
CHZ-33	222.3	3.164	0.065	4.824	0.103	0.1107	0.0007	1770.7	63.7	1789.1	36.1	1810.6	22.1	2%	1810.6	22.1
CHZ-34	106.5	5.208	0.087	2.015	0.037	0.0762	0.0006	1132.2	34.6	1120.7	24.7	1098.4	29.3	-3%	1132.2	34.6
CHZ-35	50.8	1.967	0.033	12.187	0.218	0.1739	0.0011	2650.2	72.7	2618.9	33.7	2594.8	22.1	-2%	2594.8	22.1
CHZ-36	286.1	3.224	0.052	4.602	0.078	0.1077	0.0006	1741.7	49.2	1749.7	28.6	1759.2	21.2	1%	1759.2	21.2
CHZ-37	240.0	4.686	0.080	2.434	0.044	0.0828	0.0005	1246.9	38.8	1252.8	26.1	1262.9	23.3	1%	1262.9	23.3
CHZ-38	170.4	3.479	0.058	3.974	0.071	0.1003	0.0006	1628.5	48.1	1629.0	28.9	1629.6	22.9	0%	1629.6	22.9
CHZ-39	168.4	1.420	0.023	30.727	0.533	0.3167	0.0019	3435.8	87.1	3510.4	34.5	3553.2	19.6	3%	3553.2	19.6
CHZ-40	103.3	3.411	0.058	4.154	0.076	0.1028	0.0008	1657.5	49.4	1665.0	30.2	1674.5	27.5	1%	1674.5	27.5
CHZ-41	365.0	3.386	0.057	4.156	0.074	0.1021	0.0006	1668.0	49.8	1665.4	29.4	1662.2	22.5	0%	1662.2	22.5
CHZ-42	309.9	3.358	0.052	4.167	0.069	0.1015	0.0006	1680.4	45.7	1667.6	27.2	1651.4	22.6	-2%	1651.4	22.6
CHZ-43	95.6	2.938	0.047	5.325	0.096	0.1135	0.0009	1888.6	52.9	1872.8	30.9	1855.4	29.2	-2%	1855.4	29.2
CHZ-44	76.2	3.327	0.053	4.194	0.074	0.1012	0.0008	1694.3	47.6	1672.8	29.0	1646.0	28.1	-3%	1646.0	28.1
CHZ-45	266.0	3.269	0.069	4.258	0.095	0.1010	0.0007	1720.5	64.2	1685.4	36.6	1641.9	24.5	-5%	1641.9	24.5
CHZ-46	112.5	5.266	0.092	1.971	0.039	0.0753	0.0007	1120.8	35.8	1105.6	26.6	1075.6	37.7	-4%	1120.8	35.8
CHZ-47	400.0	7.698	0.213	1.393	0.040	0.0778	0.0006	787.3	41.1	886.1	34.0	1141.6	31.1	31%	787.3	41.1
CHZ-48	139.9	5.184	0.099	2.246	0.046	0.0845	0.0007	1137.1	40.0	1195.4	29.1	1302.5	30.4	13%	1302.5	30.4
CHZ-49	24.8	1.745	0.037	16.118	0.354	0.2041	0.0014	2920.1	98.4	2883.8	42.2	2858.5	22.6	-2%	2858.5	22.6
CHZ-50	35.6	5.757	0.111	1.788	0.039	0.0747	0.0008	1032.5	36.8	1041.2	28.4	1059.5	40.7	3%	1032.5	36.8
CHZ-51	124.3	2.718	0.048	7.038	0.151	0.1388	0.0017	2019.5	61.3	2116.2	38.3	2211.5	42.9	9%	2211.5	42.9
CHZ-52	86.0	3.634	0.079	4.059	0.092	0.1070	0.0007	1567.1	60.7	1646.0	37.2	1748.3	24.6	10%	1748.3	24.6

Grain I.D.	238U (ppm)	238/206 ratio	238/206 1SE	207/235 ratio	207/235 1SE	207/206 ratio	207/206 1SE	238/206 Age (Ma)	2σ	207/235 Age (Ma)	2σ	207/206 Age (Ma)	2σ	Disc. (%)	preferred Age (Ma)	preferred Err. (2σ)
CHZ-53	193.0	3.448	0.083	4.452	0.111	0.1114	0.0007	1641.5	70.0	1722.1	41.4	1821.4	23.5	10%	1821.4	23.5
CHZ-54	161.0	5.879	0.143	2.029	0.051	0.0866	0.0006	1012.7	45.7	1125.4	34.5	1350.1	27.3	25%	1012.7	45.7
CHZ-55	83.7	3.679	0.068	3.787	0.074	0.1011	0.0007	1549.9	50.7	1589.9	31.4	1643.4	24.5	6%	1643.4	24.5
CHZ-56	127.0	1.935	0.034	14.377	0.267	0.2019	0.0013	2685.2	76.6	2774.9	35.5	2840.9	22.1	5%	2840.9	22.1
CHZ-57	272.5	5.747	0.099	1.734	0.033	0.0723	0.0006	1034.1	33.0	1021.2	24.3	993.5	31.3	-4%	1034.1	33.0
CHZ-58	155.0	3.914	0.070	3.398	0.064	0.0965	0.0006	1466.8	47.3	1503.9	29.7	1556.7	22.1	6%	1556.7	22.1
CHZ-59	105.5	4.323	0.073	2.794	0.052	0.0877	0.0007	1341.3	40.9	1353.9	28.0	1374.0	31.2	2%	1374.0	31.2
CHZ-60	101.1	4.024	0.062	3.164	0.055	0.0924	0.0008	1430.7	39.8	1448.5	27.1	1474.8	31.3	3%	1474.8	31.3
CHZ-61	90.8	1.873	0.039	15.006	0.321	0.2039	0.0012	2758.3	92.5	2815.6	41.0	2856.9	20.4	3%	2856.9	20.4
CHZ-62	66.2	3.842	0.074	4.043	0.083	0.1127	0.0009	1491.4	51.2	1642.9	33.7	1842.6	27.9	19%	1842.6	27.9
CHZ-63	78.2	3.667	0.074	3.788	0.082	0.1008	0.0008	1554.5	55.7	1590.3	34.9	1638.1	30.0	5%	1638.1	30.0
CHZ-64	161.5	5.935	0.113	1.731	0.036	0.0745	0.0007	1003.8	35.3	1019.9	26.9	1054.7	35.5	5%	1003.8	35.3
CHZ-65	82.1	3.923	0.085	3.279	0.074	0.0933	0.0007	1463.7	56.5	1476.1	35.3	1493.9	26.9	2%	1493.9	26.9
CHZ-66	89.7	1.845	0.034	14.581	0.284	0.1952	0.0012	2791.8	83.7	2788.3	37.2	2785.7	21.3	0%	2785.7	21.3
CHZ-67	192.6	3.510	0.068	3.926	0.079	0.1000	0.0006	1616.0	55.2	1619.0	32.8	1622.9	23.0	0%	1622.9	23.0
CHZ-68	244.7	5.995	0.119	1.724	0.036	0.0750	0.0005	994.5	36.5	1017.5	26.8	1067.3	26.8	7%	994.5	36.5
CHZ-69	165.7	3.124	0.063	4.841	0.102	0.1097	0.0007	1790.2	63.5	1792.0	35.7	1794.1	22.3	0%	1794.1	22.3
CHZ-70	132.1	3.299	0.054	4.432	0.078	0.1061	0.0007	1706.7	49.5	1718.4	29.3	1732.6	23.2	1%	1732.6	23.2
CHZ-71	266.7	5.076	0.089	2.677	0.064	0.0986	0.0016	1159.2	37.2	1322.1	35.3	1597.0	60.8	27%	1597.0	60.8
CHZ-72	199.2	3.981	0.069	3.215	0.059	0.0929	0.0006	1444.7	44.9	1460.9	28.4	1484.6	23.1	3%	1484.6	23.1
CHZ-73	71.3	3.978	0.062	3.243	0.055	0.0936	0.0007	1445.7	40.2	1467.6	26.5	1499.4	26.8	4%	1499.4	26.8
CHZ-74	193.6	2.950	0.070	5.444	0.132	0.1165	0.0007	1881.9	77.1	1891.8	41.7	1902.7	20.9	1%	1902.7	20.9
CHZ-75	116.7	3.432	0.077	4.133	0.096	0.1029	0.0007	1648.5	64.9	1660.9	38.0	1676.6	24.0	2%	1676.6	24.0
CHZ-76	63.1	5.708	0.099	1.862	0.036	0.0771	0.0007	1040.7	33.5	1067.6	25.6	1122.9	34.0	7%	1040.7	33.5
CHZ-77	175.3	4.148	0.081	3.148	0.065	0.0948	0.0006	1392.4	48.8	1444.6	31.7	1522.3	24.5	9%	1522.3	24.5
CHZ-78	99.9	3.415	0.058	4.099	0.075	0.1016	0.0007	1655.5	49.4	1654.1	29.9	1652.4	26.2	0%	1652.4	26.2
CHZ-79	189.1	5.862	0.091	1.734	0.030	0.0738	0.0006	1015.4	29.2	1021.4	22.2	1034.3	30.5	2%	1015.4	29.2
CHZ-80	81.4	3.495	0.056	3.860	0.068	0.0979	0.0007	1622.0	46.1	1605.3	28.5	1583.5	27.3	-2%	1583.5	27.3
CHZ-81	341.0	4.914	0.074	2.292	0.037	0.0817	0.0005	1194.1	32.7	1210.0	22.9	1238.4	24.5	4%	1238.4	24.5
CHZ-82	281.3	3.445	0.052	4.083	0.066	0.1021	0.0006	1643.0	44.0	1651.0	26.6	1661.1	22.5	1%	1661.1	22.5
CHZ-83	121.3	5.571	0.088	1.851	0.033	0.0748	0.0006	1064.2	31.2	1063.8	23.5	1062.8	32.7	0%	1064.2	31.2
CHZ-84	419.0	3.525	0.054	3.984	0.065	0.1019	0.0006	1610.0	43.7	1631.0	26.8	1658.2	22.5	3%	1658.2	22.5
CHZ-85	181.8	4.545	0.079	2.535	0.047	0.0836	0.0006	1281.9	40.2	1282.2	27.3	1282.9	28.4	0%	1282.9	28.4
CHZ-86	229.5	3.511	0.052	3.947	0.063	0.1006	0.0006	1615.5	42.2	1623.4	25.9	1633.6	22.9	1%	1633.6	22.9
CHZ-87	240.3	5.225	0.082	2.636	0.045	0.0999	0.0007	1129.0	32.5	1310.7	25.0	1621.8	24.8	30%	1621.8	24.8
CHZ-88	102.2	1.962	0.031	13.463	0.225	0.1917	0.0011	2655.3	68.4	2712.7	31.8	2755.6	20.1	4%	2755.6	20.1
CHZ-89	343.0	2.962	0.044	5.377	0.085	0.1156	0.0007	1875.1	48.2	1881.2	27.2	1887.8	21.1	1%	1887.8	21.1
CHZ-90	496.0	6.562	0.101	1.499	0.025	0.0714	0.0004	914.4	26.3	930.1	20.3	967.4	25.6	5%	914.4	26.3
CHZ-91	266.0	2.378	0.037	9.596	0.159	0.1656	0.0010	2262.7	59.0	2396.8	30.7	2512.8	21.3	10%	2512.8	21.3
CHZ-92	314.0	4.156	0.086	3.460	0.074	0.1044	0.0006	1389.8	51.5	1518.2	33.7	1702.1	21.9	18%	1702.1	21.9
CHZ-93	188.0	3.834	0.057	3.352	0.055	0.0933	0.0006	1493.9	39.9	1493.2	25.5	1492.1	25.0	0%	1492.1	25.0
CHZ-94	331.9	4.511	0.070	2.741	0.046	0.0897	0.0006	1290.9	36.4	1339.7	25.0	1418.7	24.0	9%	1418.7	24.0
CHZ-95	287.7	4.303	0.066	2.736	0.045	0.0854	0.0005	1347.1	37.2	1338.4	24.4	1324.4	23.3	-2%	1324.4	23.3
CHZ-96	219.2	5.679	0.084	1.808	0.029	0.0745	0.0005	1045.6	28.5	1048.5	21.3	1054.4	27.5	1%	1045.6	28.5
CHZ-97	114.5	3.418	0.058	4.090	0.075	0.1014	0.0007	1654.5	49.9	1652.3	29.9	1649.4	24.4	0%	1649.4	24.4
CHZ-98	101.1	3.153	0.048	4.799	0.080	0.1098	0.0008	1776.0	47.5	1784.7	28.2	1794.9	25.5	1%	1794.9	25.5
CHZ-99	487.6	13.831	0.230	0.607	0.014	0.0609	0.0010	450.0	14.4	481.6	17.5	634.7	67.3	29%	450.0	14.4
CHZ-100	392.0	3.377	0.057	4.815	0.091	0.1180	0.0010	1671.9	49.8	1787.6	31.9	1925.3	30.9	13%	1925.3	30.9
CHZ-101	136.9	5.141	0.095	2.084	0.042	0.0778	0.0007	1145.7	38.9	1143.6	27.9	1139.6	33.6	-1%	1145.7	38.9
CHZ-102	89.1	5.200	0.082	2.059	0.037	0.0777	0.0007	1133.8	33.0	1135.4	24.6	1138.3	33.7	0%	1133.8	33.0
CHZ-103	208.5	3.278	0.049	4.542	0.074	0.1080	0.0007	1716.5	45.5	1738.6	27.1	1765.3	22.7	3%	1765.3	22.7
CHZ-104	295.0	3.729	0.067	3.787	0.071	0.1025	0.0006	1531.7	48.8	1590.0	30.3	1668.3	22.4	8%	1668.3	22.4
CHZ-105	70.0	4.114	0.093	3.059	0.074	0.0913	0.0008	1402.8	57.1	1422.5	36.9	1452.0	31.7	3%	1452.0	31.7
CHZ-106	72.6	5.956	0.105	1.696	0.034	0.0733	0.0008	1000.5	32.6	1007.1	26.0	1021.3	41.7	2%	1000.5	32.6
CHZ-107	38.6	4.539	0.077	2.590	0.051	0.0853	0.0009	1283.5	39.6	1297.8	29.0	1321.5	39.0	3%	1321.5	39.0
CHZ-108	299.0	5.105	0.103	2.104	0.044	0.0779	0.0005	1153.3	42.6	1150.0	29.1	1143.9	25.0	-1%	1153.3	42.6
CHZ-109	82.1	1.898	0.036	13.479	0.268	0.1856	0.0011	2728.8	84.5	2713.8	37.8	2702.6	20.7	-1%	2702.6	20.7

Grain I.D.	238U (ppm)	238/206 ratio	238/206 1SE	207/235 ratio	207/235 1SE	207/206 ratio	207/206 1SE	238/206 Age (Ma)	2σ	207/235 Age (Ma)	2σ	207/206 Age (Ma)	2σ	Disc. (%)	preferred Age (Ma)	preferred Err. (2σ)
CHZ-110	230.2	3.922	0.066	3.330	0.059	0.0948	0.0006	1464.2	44.2	1488.1	27.9	1522.3	22.6	4%	1522.3	22.6
CHZ-111	113.4	1.855	0.033	14.300	0.265	0.1925	0.0011	2779.3	79.6	2769.8	35.4	2763.0	20.0	-1%	2763.0	20.0
CHZ-112	286.7	3.357	0.062	4.169	0.081	0.1016	0.0006	1680.9	54.7	1668.0	31.8	1651.8	22.6	-2%	1651.8	22.6
CHZ-113	32.4	4.303	0.086	3.123	0.069	0.0975	0.0010	1347.1	48.7	1438.3	34.3	1576.0	36.9	15%	1576.0	36.9
CHZ-114	108.9	5.537	0.101	1.864	0.037	0.0749	0.0006	1070.3	36.1	1068.5	26.4	1064.9	32.6	-1%	1070.3	36.1
CHZ-115	32.1	2.519	0.048	7.047	0.142	0.1288	0.0009	2155.2	69.3	2117.4	35.9	2080.9	25.3	-4%	2080.9	25.3
CHZ-116	166.0	4.058	0.063	2.989	0.050	0.0880	0.0006	1419.9	39.9	1404.8	25.7	1382.1	24.6	-3%	1382.1	24.6
CHZ-117	135.2	3.213	0.062	4.631	0.094	0.1080	0.0007	1746.6	59.0	1754.8	34.1	1764.6	24.4	1%	1764.6	24.4
CHZ-118	131.2	3.429	0.058	4.095	0.074	0.1019	0.0007	1649.5	48.9	1653.3	29.7	1658.0	26.1	1%	1658.0	26.1
CHZ-119	421.0	3.154	0.049	4.709	0.078	0.1078	0.0006	1775.6	48.5	1768.9	27.9	1761.1	21.1	-1%	1761.1	21.1
CHZ-120	191.0	3.134	0.047	4.707	0.076	0.1070	0.0007	1785.3	47.0	1768.5	27.3	1748.6	23.0	-2%	1748.6	23.0
CHZ-121	90.0	3.339	0.054	4.211	0.074	0.1020	0.0007	1688.8	48.2	1676.1	29.0	1660.2	26.0	-2%	1660.2	26.0
CHZ-122	121.4	5.914	0.098	1.681	0.031	0.0721	0.0006	1007.2	30.9	1001.3	23.6	988.4	34.2	-2%	1007.2	30.9
CHZ-123	546.0	3.570	0.059	3.882	0.067	0.1006	0.0006	1591.9	46.4	1609.9	28.0	1633.6	21.1	3%	1633.6	21.1
CHZ-124	74.8	3.546	0.058	3.867	0.069	0.0995	0.0008	1601.4	46.3	1606.8	29.1	1613.9	28.6	1%	1613.9	28.6
CHZ-125	73.4	5.747	0.102	1.837	0.036	0.0766	0.0007	1034.1	34.1	1058.7	26.0	1109.9	34.3	7%	1034.1	34.1
CHZ-126	303.0	3.830	0.061	3.414	0.058	0.0949	0.0006	1495.5	42.5	1507.6	26.7	1524.6	22.5	2%	1524.6	22.5
CHZ-127	88.0	3.573	0.077	3.830	0.086	0.0993	0.0007	1590.9	60.5	1599.0	36.2	1609.8	25.0	1%	1609.8	25.0
CHZ-128	264.0	3.621	0.058	3.891	0.067	0.1022	0.0007	1572.2	44.5	1611.7	27.8	1663.8	24.2	6%	1663.8	24.2
CHZ-129	139.7	2.984	0.045	5.142	0.082	0.1114	0.0007	1863.1	48.3	1843.1	27.4	1820.8	22.0	-2%	1820.8	22.0
CHZ-130	115.0	4.243	0.072	2.792	0.051	0.0859	0.0006	1364.3	41.8	1353.3	27.5	1336.0	27.5	-2%	1336.0	27.5
CHZ-131	82.6	4.938	0.077	2.233	0.039	0.0800	0.0007	1188.7	33.8	1191.5	24.7	1196.6	32.5	1%	1188.7	33.8
CHZ-132	234.9	3.215	0.049	4.597	0.075	0.1073	0.0006	1745.6	46.8	1748.7	27.2	1752.4	21.3	0%	1752.4	21.3
CHZ-133	199.2	3.423	0.050	4.061	0.064	0.1009	0.0006	1652.0	42.9	1646.6	26.0	1639.7	22.8	-1%	1639.7	22.8

10.3.1.6 EM-10 (Zircon)

Grain I.D.	238U (ppm)	238/206 ratio	238/206 1SE	207/235 ratio	207/235 1SE	207/206 ratio	207/206 1SE	238/206 Age (Ma)	2σ	207/235 Age (Ma)	2σ	207/206 Age (Ma)	2σ	Disc. (%)	preferred Age (Ma)	preferred Err. (2σ)
SCF-01	93.1	12.005	0.519	1.250	0.180	0.1060	0.0130	515.0	21.0	748.0	72.0	1280.0	230.0	93	515.0	21.0
SCF-02	185.9	15.432	0.333	0.481	0.042	0.0543	0.0049	404.3	8.2	383.0	29.0	240.0	160.0	118	404.3	8.2
SCF-03	463.0	5.136	0.055	2.033	0.065	0.0757	0.0024	1148.0	12.0	1120.0	23.0	1043.0	65.0	-32	1148.0	12.0
SCF-04	231.0	5.659	0.080	1.735	0.081	0.0715	0.0035	1050.0	13.0	1007.0	32.0	870.0	100.0	-17	1050.0	13.0
SCF-05	98.0	8.032	0.619	1.740	0.240	0.1070	0.0100	747.0	55.0	964.0	93.0	1370.0	200.0	84	747.0	55.0
SCF-06	471.0	3.818	0.061	3.771	0.086	0.1040	0.0022	1498.0	22.0	1585.0	19.0	1692.0	41.0	9	1498.0	22.0
SCF-07	103.3	13.495	0.382	0.532	0.065	0.0541	0.0070	462.0	13.0	414.0	45.0	160.0	210.0	101	462.0	13.0
SCF-08	68.4	4.523	0.098	2.700	0.180	0.0888	0.0060	1286.0	25.0	1294.0	50.0	1230.0	140.0	67	1286.0	25.0
SCF-09	42.6	5.814	0.179	1.660	0.180	0.0712	0.0078	1021.0	29.0	906.0	73.0	630.0	210.0	58	1021.0	29.0
SCF-10	144.0	14.388	0.435	0.790	0.095	0.0796	0.0091	433.0	13.0	546.0	47.0	910.0	220.0	93	433.0	13.0
SCF-11	93.2	4.819	0.088	2.440	0.150	0.0848	0.0052	1214.0	20.0	1216.0	45.0	1140.0	130.0	21	1214.0	20.0
SCF-12	256.0	3.979	0.044	3.116	0.097	0.0894	0.0026	1444.0	14.0	1425.0	24.0	1385.0	57.0	-16	1444.0	14.0
SCF-13	143.0	14.771	0.371	0.735	0.084	0.0793	0.0088	422.0	10.0	531.0	46.0	810.0	200.0	104	422.0	10.0
SCF-14	146.8	3.476	0.048	3.900	0.150	0.0983	0.0039	1629.0	20.0	1598.0	33.0	1521.0	83.0	-28	1629.0	20.0
SCF-15	537.0	2.113	0.019	10.900	0.150	0.1661	0.0020	2496.0	18.0	2513.0	13.0	2513.0	20.0	1	2496.0	18.0
SCF-16	162.3	6.180	0.118	1.613	0.085	0.0733	0.0040	966.0	17.0	962.0	34.0	900.0	110.0	61	966.0	17.0
SCF-17	146.7	3.663	0.058	3.900	0.150	0.1035	0.0042	1554.0	22.0	1593.0	33.0	1622.0	78.0	-8	1554.0	22.0
SCF-18	89.2	5.774	0.127	1.760	0.120	0.0744	0.0051	1028.0	21.0	1002.0	45.0	860.0	150.0	86	1028.0	21.0
SCF-19	75.2	4.492	0.097	2.540	0.180	0.0845	0.0062	1294.0	25.0	1245.0	52.0	1090.0	150.0	38	1294.0	25.0
SCF-20	190.4	13.793	0.304	0.581	0.039	0.0598	0.0042	450.7	9.6	458.0	27.0	450.0	140.0	94	450.7	9.6
SCF-21	54.3	5.811	0.149	2.000	0.150	0.0847	0.0063	1022.0	24.0	1082.0	54.0	1090.0	160.0	30	1022.0	24.0
SCF-22	71.7	4.660	0.117	2.540	0.150	0.0859	0.0050	1251.0	29.0	1250.0	46.0	1190.0	130.0	49	1251.0	29.0
SCF-23	78.5	18.248	0.633	0.420	0.064	0.0565	0.0087	344.0	11.0	323.0	45.0	100.0	250.0	104	344.0	11.0
SCF-24	107.8	5.663	0.099	1.740	0.100	0.0719	0.0044	1047.0	17.0	998.0	41.0	840.0	130.0	110	1047.0	17.0
SCF-25	258.0	3.811	0.042	3.283	0.097	0.0911	0.0028	1501.0	15.0	1469.0	23.0	1413.0	58.0	-15	1501.0	15.0
SCF-26	244.0	3.157	0.036	4.590	0.120	0.1050	0.0028	1773.0	17.0	1740.0	21.0	1690.0	48.0	-8	1773.0	17.0
SCF-27	360.0	6.398	0.184	1.627	0.079	0.0764	0.0031	935.0	25.0	970.0	31.0	1063.0	77.0	5	935.0	25.0
SCF-28	217.2	14.793	0.284	0.531	0.046	0.0575	0.0050	421.6	7.7	414.0	30.0	330.0	160.0	84	421.6	7.7
SCF-29	21.7	1.942	0.057	12.100	0.660	0.1740	0.0110	2668.0	62.0	2580.0	52.0	2490.0	100.0	-16	2668.0	62.0
SCF-30	48.5	5.754	0.162	1.860	0.160	0.0783	0.0073	1031.0	27.0	1012.0	64.0	880.0	190.0	88	1031.0	27.0
SCF-31	25.5	4.139	0.142	4.300	0.400	0.1300	0.0120	1389.0	43.0	1612.0	77.0	1750.0	190.0	-40	1389.0	43.0
SCF-32	291.0	3.964	0.047	3.194	0.093	0.0917	0.0027	1449.0	15.0	1449.0	22.0	1440.0	57.0	-14	1449.0	15.0
SCF-33	144.0	5.063	0.133	2.010	0.170	0.0762	0.0066	1160.0	28.0	1065.0	63.0	840.0	170.0	14	1160.0	28.0
SCF-34	351.0	14.728	0.282	0.524	0.033	0.0564	0.0037	423.4	7.6	421.0	23.0	380.0	130.0	97	423.4	7.6
SCF-35	198.9	3.917	0.087	3.450	0.140	0.0974	0.0035	1463.0	29.0	1494.0	33.0	1543.0	70.0	-9	1463.0	29.0
SCF-36	488.0	8.251	0.095	1.184	0.046	0.0710	0.0029	737.4	8.3	784.0	22.0	880.0	89.0	29	737.4	8.3
SCF-37	176.7	9.560	0.548	1.269	0.095	0.0914	0.0062	642.0	36.0	803.0	43.0	1260.0	140.0	57	642.0	36.0
SCF-38	22.3	4.824	0.207	2.180	0.270	0.0840	0.0110	1213.0	48.0	1030.0	110.0	750.0	260.0	64	1213.0	48.0
SCF-39	0.0			no value	NAN	no value	NAN	no value	NAN	no value	NAN	no value	NAN	no value	no value	NAN
SCF-40	95.6	5.666	0.122	1.790	0.120	0.0742	0.0051	1047.0	21.0	1012.0	46.0	860.0	140.0	10	1047.0	21.0
SCF-41	327.0	3.145	0.034	4.720	0.130	0.1078	0.0028	1779.0	16.0	1761.0	23.0	1733.0	48.0	-5	1779.0	16.0
SCF-42	188.9	3.743	0.050	3.490	0.130	0.0952	0.0035	1525.0	18.0	1510.0	29.0	1467.0	72.0	-15	1525.0	18.0
SCF-43	575.0	5.724	0.069	1.749	0.056	0.0734	0.0022	1038.0	11.0	1023.0	21.0	974.0	66.0	-26	1038.0	11.0
SCF-44	457.0	13.263	0.299	0.598	0.047	0.0570	0.0042	468.0	10.0	462.0	30.0	390.0	140.0	98	468.0	10.0
SCF-45	111.5	3.385	0.061	4.010	0.180	0.0993	0.0044	1667.0	26.0	1609.0	38.0	1532.0	89.0	-34	1667.0	26.0
SCF-46	78.8	6.477	0.168	1.560	0.140	0.0723	0.0064	924.0	22.0	897.0	56.0	770.0	180.0	65	924.0	22.0
SCF-47	383.0	5.470	0.063	1.871	0.062	0.0740	0.0024	1082.0	12.0	1067.0	22.0	1007.0	73.0	-24	1082.0	12.0
SCF-48	83.5	5.356	0.129	1.940	0.150	0.0769	0.0060	1102.0	24.0	1054.0	53.0	880.0	160.0	58	1102.0	24.0
SCF-49	146.3	5.669	0.112	1.642	0.095	0.0682	0.0041	1046.0	19.0	971.0	35.0	750.0	120.0	66	1046.0	19.0
SCF-50	237.0	5.543	0.095	2.070	0.110	0.0822	0.0044	1068.0	17.0	1112.0	36.0	1150.0	110.0	21	1068.0	17.0
SCF-51	667.0	3.286	0.052	4.490	0.100	0.1072	0.0023	1711.0	24.0	1724.0	19.0	1739.0	40.0	-1	1711.0	24.0
SCF-52	378.0	5.546	0.062	1.882	0.067	0.0760	0.0028	1068.0	11.0	1073.0	23.0	1058.0	74.0	-28	1068.0	11.0

Grain I.D.	238U (ppm)	238/206 ratio	238/206 1SE	207/235 ratio	207/235 1SE	207/206 ratio	207/206 1SE	238/206 Age (Ma)	2σ	207/235 Age (Ma)	2σ	207/206 Age (Ma)	2σ	Disc. (%)	preferred Age (Ma)	preferred Err. (2σ)
SCF-53	59.5	4.205	0.127	3.020	0.210	0.0926	0.0065	1371.0	37.0	1398.0	52.0	1380.0	140.0	0	1371.0	37.0
SCF-54	80.2	4.669	0.102	2.400	0.170	0.0821	0.0061	1252.0	25.0	1199.0	51.0	1030.0	150.0	39	1252.0	25.0
SCF-55	191.9	4.357	0.063	2.770	0.120	0.0878	0.0039	1333.0	18.0	1330.0	33.0	1307.0	84.0	-13	1333.0	18.0
SCF-56	243.0	5.711	0.082	1.792	0.085	0.0747	0.0036	1040.0	14.0	1027.0	32.0	960.0	100.0	-13	1040.0	14.0
SCF-57	57.2	5.397	0.163	1.760	0.160	0.0715	0.0068	1097.0	31.0	970.0	62.0	680.0	180.0	56	1097.0	31.0
SCF-58	268.0	5.695	0.107	1.723	0.087	0.0716	0.0037	1042.0	18.0	1004.0	33.0	880.0	110.0	-3	1042.0	18.0
SCF-59	146.6	4.486	0.068	2.650	0.130	0.0864	0.0044	1296.0	18.0	1298.0	36.0	1260.0	100.0	7	1296.0	18.0
SCF-60	367.0	16.447	0.325	0.708	0.052	0.0854	0.0064	380.4	7.2	537.0	32.0	1170.0	150.0	85	380.4	7.2
SCF-61	117.7	2.922	0.051	5.450	0.220	0.1172	0.0054	1895.0	29.0	1872.0	36.0	1831.0	86.0	-15	1895.0	29.0
SCF-62	88.7	12.300	0.484	1.470	0.180	0.1370	0.0150	503.0	19.0	848.0	73.0	1660.0	240.0	78	503.0	19.0
SCF-63	129.7	6.523	0.132	1.540	0.110	0.0732	0.0053	919.0	17.0	917.0	46.0	820.0	150.0	24	919.0	17.0
SCF-64	106.7	5.501	0.112	1.850	0.130	0.0736	0.0054	1078.0	19.0	1030.0	47.0	830.0	150.0	60	1078.0	19.0
SCF-65	308.0	4.978	0.069	2.049	0.093	0.0739	0.0036	1180.0	15.0	1121.0	33.0	950.0	100.0	30	1180.0	15.0
SCF-66	419.0	3.821	0.042	3.352	0.095	0.0928	0.0025	1498.0	15.0	1484.0	22.0	1449.0	52.0	-7	1498.0	15.0
SCF-67	162.2	5.414	0.100	2.000	0.110	0.0787	0.0042	1092.0	18.0	1089.0	37.0	1030.0	110.0	16	1092.0	18.0
SCF-68	580.0	5.435	0.071	1.933	0.066	0.0755	0.0026	1088.0	13.0	1082.0	23.0	1035.0	73.0	-26	1088.0	13.0
SCF-69	430.9	14.970	0.224	0.512	0.034	0.0555	0.0038	416.5	6.3	412.0	23.0	340.0	130.0	116	416.5	6.3
SCF-70	34.6	3.103	0.089	4.670	0.400	0.1056	0.0091	1795.0	45.0	1713.0	73.0	1430.0	180.0	16	1795.0	45.0
SCF-71	147.3	5.682	0.110	1.850	0.130	0.0766	0.0053	1044.0	19.0	1028.0	47.0	910.0	150.0	100	1044.0	19.0
SCF-72	335.0	14.793	0.306	0.490	0.034	0.0533	0.0038	421.6	8.4	400.0	24.0	260.0	130.0	89	421.6	8.4
SCF-73	278.0	6.460	0.113	1.477	0.079	0.0692	0.0037	927.0	15.0	908.0	34.0	800.0	110.0	180	927.0	15.0
SCF-74	49.1	5.862	0.210	1.360	0.180	0.0592	0.0080	1012.0	33.0	766.0	85.0	280.0	240.0	96	1012.0	33.0
SCF-75	73.3	5.214	0.125	2.100	0.160	0.0805	0.0062	1129.0	25.0	1113.0	54.0	970.0	160.0	0	1129.0	25.0
SCF-76	621.0	5.311	0.062	2.000	0.064	0.0763	0.0024	1112.0	12.0	1109.0	21.0	1066.0	64.0	-14	1112.0	12.0
SCF-77	320.0	5.152	0.069	2.100	0.090	0.0780	0.0033	1143.0	14.0	1136.0	29.0	1069.0	87.0	13	1143.0	14.0
SCF-78	153.8	5.198	0.089	1.990	0.110	0.0754	0.0045	1133.0	18.0	1093.0	39.0	930.0	130.0	47	1133.0	18.0
SCF-79	348.1	4.151	0.047	3.567	0.092	0.1070	0.0030	1391.0	14.0	1536.0	21.0	1714.0	52.0	16	1391.0	14.0
SCF-80	136.3	5.862	0.110	1.870	0.110	0.0791	0.0049	1014.0	18.0	1037.0	42.0	1000.0	130.0	8	1014.0	18.0
SCF-81	259.0	4.058	0.053	3.320	0.120	0.0978	0.0037	1421.0	16.0	1478.0	28.0	1523.0	74.0	-4	1421.0	16.0
SCF-82	94.5	6.180	0.153	1.730	0.150	0.0768	0.0067	965.0	22.0	967.0	59.0	840.0	180.0	100	965.0	22.0
SCF-83	138.5	6.452	0.133	1.480	0.110	0.0685	0.0052	928.0	18.0	882.0	50.0	690.0	160.0	100	928.0	18.0
SCF-84	136.1	5.302	0.112	2.150	0.140	0.0825	0.0056	1113.0	21.0	1131.0	49.0	1080.0	140.0	100	1113.0	21.0
SCF-85	95.8	3.818	0.076	3.400	0.190	0.0933	0.0055	1497.0	27.0	1469.0	47.0	1330.0	130.0	8	1497.0	27.0
SCF-86	200.0	13.624	0.390	0.536	0.052	0.0538	0.0055	456.0	12.0	418.0	35.0	220.0	180.0	94	456.0	12.0
SCF-87	47.6	4.600	0.129	2.470	0.220	0.0832	0.0082	1265.0	32.0	1176.0	74.0	940.0	200.0	101	1265.0	32.0
SCF-88	129.9	4.078	0.078	3.170	0.170	0.0933	0.0047	1412.0	24.0	1420.0	42.0	1360.0	110.0	-50	1412.0	24.0
SCF-89	231.0	5.855	0.099	1.792	0.096	0.0759	0.0044	1016.0	16.0	1025.0	34.0	960.0	110.0	20	1016.0	16.0
SCF-90	269.0	13.986	0.293	0.524	0.043	0.0537	0.0044	445.1	9.2	416.0	29.0	230.0	150.0	105	445.1	9.2
SCF-91	120.1	3.726	0.064	3.820	0.180	0.1034	0.0050	1531.0	24.0	1570.0	38.0	1583.0	97.0	-10	1531.0	24.0
SCF-92	230.0	5.171	0.080	2.137	0.095	0.0797	0.0040	1139.0	16.0	1142.0	32.0	1080.0	100.0	33	1139.0	16.0
SCF-93	69.9	5.528	0.150	2.100	0.160	0.0858	0.0069	1070.0	27.0	1116.0	54.0	1060.0	170.0	-33	1070.0	27.0
SCF-94	68.7	3.103	0.065	4.890	0.240	0.1094	0.0056	1798.0	33.0	1775.0	42.0	1710.0	100.0	-43	1798.0	33.0
SCF-95	465.0	4.299	0.046	2.841	0.074	0.0882	0.0026	1348.0	13.0	1362.0	19.0	1354.0	56.0	-10	1348.0	13.0
SCF-96	100.1	6.510	0.153	1.560	0.120	0.0753	0.0060	920.0	20.0	912.0	52.0	830.0	160.0	82	920.0	20.0
SCF-97	738.0	5.236	0.049	2.029	0.050	0.0763	0.0019	1126.7	9.9	1120.0	16.0	1071.0	49.0	-14	1126.7	9.9
SCF-98	151.1	13.210	0.314	0.662	0.061	0.0636	0.0061	470.0	11.0	488.0	38.0	480.0	180.0	99	470.0	11.0
SCF-99	286.0	3.568	0.043	3.930	0.110	0.1008	0.0027	1592.0	17.0	1613.0	22.0	1616.0	53.0	-3	1592.0	17.0
SCF-100	32.8	6.124	0.214	1.510	0.220	0.0657	0.0095	972.0	32.0	802.0	97.0	430.0	260.0	60	972.0	32.0
SCF-101	376.0	13.038	0.187	0.725	0.042	0.0677	0.0040	477.4	7.0	542.0	25.0	740.0	120.0	74	477.4	7.0
SCF-102	119.2	3.406	0.057	4.170	0.190	0.1030	0.0046	1658.0	25.0	1660.0	37.0	1623.0	89.0	-16	1658.0	25.0
SCF-103	133.7	4.805	0.115	2.260	0.130	0.0793	0.0048	1216.0	27.0	1182.0	40.0	1060.0	120.0	34	1216.0	27.0
SCF-104	243.0	3.289	0.062	4.340	0.140	0.1036	0.0032	1712.0	29.0	1695.0	27.0	1662.0	56.0	-9	1712.0	29.0
SCF-105	89.3	3.570	0.064	4.010	0.210	0.1033	0.0054	1590.0	25.0	1600.0	43.0	1570.0	100.0	-9	1590.0	25.0
SCF-106	124.0	5.227	0.096	2.100	0.110	0.0803	0.0045	1127.0	19.0	1128.0	39.0	1070.0	120.0	4	1127.0	19.0
SCF-107	192.5	9.872	0.195	1.055	0.073	0.0756	0.0055	622.0	12.0	711.0	35.0	890.0	150.0	4	622.0	12.0
SCF-108	165.3	1.843	0.024	14.830	0.310	0.1982	0.0041	2792.0	29.0	2804.0	20.0	2805.0	33.0	0	2792.0	29.0
SCF-109	474.0	4.237	0.119	3.070	0.120	0.0946	0.0030	1362.0	34.0	1410.0	31.0	1480.0	62.0	-3	1362.0	34.0

Grain I.D.	238U (ppm)	238/206 ratio	238/206 1SE	207/235 ratio	207/235 1SE	207/206 ratio	207/206 1SE	238/206 Age (Ma)	2σ	207/235 Age (Ma)	2σ	207/206 Age (Ma)	2σ	Disc. (%)	preferred Age (Ma)	preferred Err. (2σ)
SCF-110	86.8	3.090	0.055	4.850	0.220	0.1100	0.0053	1805.0	28.0	1772.0	39.0	1697.0	96.0	-25	1805.0	28.0
SCF-111	745.0	10.753	2.428	3.300	2.300	0.0800	0.0190	514.0	84.0	540.0	100.0	760.0	200.0	20	514.0	84.0
SCF-112	340.0	5.131	0.058	2.067	0.074	0.0768	0.0027	1147.0	12.0	1135.0	24.0	1079.0	73.0	-10	1147.0	12.0
SCF-113	100.9	2.517	0.041	7.550	0.280	0.1373	0.0049	2158.0	29.0	2165.0	33.0	2146.0	66.0	-4	2158.0	29.0
SCF-114	338.0	4.577	0.050	2.583	0.089	0.0855	0.0030	1273.0	13.0	1283.0	25.0	1272.0	73.0	-19	1273.0	13.0
SCF-115	314.0	15.244	0.349	0.569	0.062	0.0623	0.0066	409.6	9.0	432.0	40.0	460.0	200.0	98	409.6	9.0
SCF-116	269.0	4.912	0.070	2.224	0.086	0.0789	0.0031	1194.0	15.0	1178.0	26.0	1114.0	81.0	-34	1194.0	15.0
SCF-117	278.2	6.321	0.088	1.497	0.069	0.0688	0.0032	946.0	12.0	918.0	28.0	801.0	97.0	61	946.0	12.0
SCF-118	58.0	6.158	0.174	1.630	0.150	0.0749	0.0073	968.0	26.0	922.0	65.0	760.0	200.0	59	968.0	26.0
SCF-119	111.1	6.079	0.133	1.650	0.120	0.0734	0.0055	980.0	20.0	970.0	44.0	840.0	150.0	61	980.0	20.0
SCF-120	384.0	2.120	0.030	11.810	0.230	0.1821	0.0033	2488.0	30.0	2585.0	18.0	2665.0	29.0	6	2488.0	30.0
SCF-121	363.0	6.974	0.097	1.450	0.059	0.0737	0.0032	863.0	11.0	901.0	25.0	951.0	89.0	13	863.0	11.0
SCF-122	223.0	3.887	0.059	3.430	0.130	0.0963	0.0036	1477.0	20.0	1496.0	32.0	1530.0	73.0	-12	1477.0	20.0
SCF-123	486.0	13.624	0.223	0.594	0.035	0.0592	0.0035	456.4	7.3	467.0	22.0	480.0	120.0	100	456.4	7.3
SCF-124	801.0	3.188	0.037	4.740	0.100	0.1097	0.0021	1758.0	18.0	1768.0	18.0	1778.0	35.0	0	1758.0	18.0
SCF-125	280.7	6.680	0.103	1.464	0.076	0.0713	0.0037	899.0	13.0	896.0	32.0	840.0	110.0	27	899.0	13.0
SCF-126	304.0	14.859	0.265	0.531	0.044	0.0564	0.0045	419.6	7.0	416.0	29.0	340.0	150.0	102	419.6	7.0
SCF-127	226.0	3.044	0.044	4.980	0.150	0.1102	0.0035	1830.0	23.0	1804.0	26.0	1765.0	59.0	-7	1830.0	23.0
SCF-128	276.0	5.731	0.079	1.732	0.079	0.0720	0.0033	1036.0	13.0	1015.0	29.0	919.0	98.0	-46	1036.0	13.0
SCF-129	90.3	5.705	0.133	1.720	0.140	0.0718	0.0062	1040.0	22.0	959.0	55.0	720.0	170.0	-20	1040.0	22.0
SCF-130	150.7	13.193	0.348	0.643	0.069	0.0603	0.0063	470.0	12.0	470.0	42.0	390.0	200.0	96	470.0	12.0
SCF-131	71.3	1.927	0.037	13.110	0.510	0.1856	0.0080	2688.0	42.0	2671.0	37.0	2652.0	71.0	-5	2688.0	42.0
SCF-132	518.0	4.838	0.061	2.338	0.075	0.0819	0.0027	1211.0	14.0	1213.0	24.0	1203.0	68.0	-31	1211.0	14.0
SCF-133	217.2	5.453	0.098	2.050	0.100	0.0823	0.0043	1084.0	18.0	1112.0	34.0	1120.0	110.0	-2	1084.0	18.0
SCF-134	738.0	14.025	0.236	0.541	0.031	0.0546	0.0030	443.5	7.4	431.0	21.0	330.0	110.0	106	443.5	7.4
SCF-135	48.6	12.034	0.478	0.770	0.130	0.0690	0.0120	514.0	20.0	477.0	72.0	250.0	290.0	83	514.0	20.0
SCF-136	146.0	4.968	0.111	2.650	0.140	0.0962	0.0051	1180.0	24.0	1284.0	41.0	1410.0	110.0	23	1180.0	24.0
SCF-137	104.6	5.470	0.132	1.980	0.150	0.0804	0.0065	1081.0	24.0	1068.0	53.0	940.0	160.0	-10	1081.0	24.0
SCF-138	436.0	15.504	0.312	0.528	0.040	0.0592	0.0046	402.9	7.6	417.0	26.0	430.0	150.0	84	402.9	7.6
SCF-139	189.1	1.955	0.023	13.370	0.310	0.1885	0.0044	2661.0	25.0	2697.0	22.0	2713.0	40.0	1	2661.0	25.0
SCF-140	254.0	5.522	0.091	1.834	0.097	0.0735	0.0038	1072.0	16.0	1038.0	35.0	910.0	110.0	20	1072.0	16.0
SCF-141	8.4	6.944	0.772	2.040	0.610	0.1190	0.0360	859.0	86.0	900.0	220.0	850.0	600.0	75	859.0	86.0

10.3.1.7 EM-14 (Zircon)

Grain I.D.	238U (ppm)	238/206 ratio	238/206 1SE	207/235 ratio	207/235 1SE	207/206 ratio	207/206 1SE	238/206 Age (Ma)	2σ	207/235 Age (Ma)	2σ	207/206 Age (Ma)	2σ	Disc. (%)	preferred Age (Ma)	preferred Err. (2σ)
14Z-01	159.1	3.568	0.038	4.164	0.047	0.1078	0.0004	1592.9	30.3	1666.9	18.5	1761.4	12.6	10	1761.4	12.6
14Z-02	174	3.389	0.024	4.114	0.032	0.1012	0.0003	1667.0	21.0	1657.0	13.1	1644.5	12.5	-1	1644.5	12.5
14Z-03	74.9	3.021	0.027	4.978	0.048	0.1091	0.0004	1843.2	28.6	1815.6	16.4	1784.1	12.7	-3	1784.1	12.7
14Z-04	89.2	4.975	0.035	2.151	0.017	0.0776	0.0003	1180.7	15.1	1165.3	11.2	1136.8	15.9	-4	1180.7	15.1
14Z-05	346.2	12.853	0.099	0.599	0.005	0.0559	0.0002	483.0	7.2	476.8	6.6	447.0	17.5	-8	483.0	7.2
14Z-06	55.9	5.464	0.036	1.843	0.016	0.0731	0.0004	1083.3	13.1	1060.8	11.5	1014.7	23.0	-7	1083.3	13.1
14Z-07	35.7	4.907	0.028	2.218	0.017	0.0790	0.0004	1195.7	12.4	1186.8	11.1	1170.7	21.6	-2	1195.7	12.4
14Z-08	173.3	6.116	0.041	1.575	0.012	0.0699	0.0003	976.2	12.2	960.3	9.6	924.2	15.0	-6	976.2	12.2
14Z-09	363	5.432	0.052	1.937	0.020	0.0764	0.0003	1089.3	19.1	1094.0	13.7	1103.4	14.7	1	1089.3	19.1
14Z-10	147.5	3.981	0.022	3.028	0.020	0.0875	0.0003	1444.7	14.5	1414.8	10.2	1370.0	13.2	-5	1370.0	13.2
14Z-11	171.4	3.326	0.024	4.179	0.033	0.1008	0.0003	1694.8	21.4	1669.8	13.1	1638.6	12.2	-3	1638.6	12.2
14Z-12	155.7	3.366	0.022	4.137	0.030	0.1010	0.0003	1676.9	19.5	1661.7	12.1	1642.5	11.6	-2	1642.5	11.6
14Z-13	17.52	5.171	0.056	1.978	0.027	0.0742	0.0006	1139.8	22.7	1107.9	18.3	1046.0	32.6	-9	1139.8	22.7
14Z-14	155.8	5.498	0.038	1.841	0.015	0.0735	0.0003	1077.3	13.7	1060.3	10.5	1025.5	16.0	-5	1077.3	13.7
14Z-15	114.7	5.297	0.035	1.941	0.015	0.0746	0.0003	1114.9	13.6	1095.3	10.4	1056.6	15.4	-6	1114.9	13.6
14Z-16	219.9	3.455	0.021	4.047	0.028	0.1015	0.0003	1638.5	18.1	1643.8	11.5	1650.5	11.3	1	1650.5	11.3
14Z-17	42.17	6.010	0.045	1.644	0.015	0.0717	0.0004	992.2	13.9	987.3	11.8	976.2	22.2	-2	992.2	13.9
14Z-18	423	4.907	0.042	2.204	0.020	0.0785	0.0002	1195.7	18.8	1182.4	12.9	1158.2	12.4	-3	1195.7	18.8
14Z-19	80.5	3.532	0.025	3.780	0.031	0.0969	0.0004	1607.0	20.2	1588.4	13.3	1563.9	15.5	-3	1563.9	15.5
14Z-20	34.7	5.379	0.062	1.857	0.024	0.0725	0.0004	1099.1	23.4	1065.9	16.9	998.5	21.6	-10	1099.1	23.4
14Z-21	150.4	3.098	0.024	4.814	0.040	0.1082	0.0003	1803.4	24.4	1787.3	14.3	1768.5	11.7	-2	1768.5	11.7
14Z-22	56.98	6.127	0.032	1.572	0.012	0.0699	0.0004	974.5	9.5	959.2	9.3	924.2	21.8	-5	974.5	9.5
14Z-23	47.4	1.639	0.012	17.969	0.139	0.2137	0.0007	3070.8	35.0	2988.1	15.5	2932.9	9.9	-5	2932.9	9.9
14Z-24	129.7	3.125	0.032	4.722	0.051	0.1071	0.0004	1789.7	31.8	1771.1	18.3	1749.1	13.9	-2	1749.1	13.9
14Z-25	132.7	5.647	0.026	1.833	0.011	0.0751	0.0003	1051.1	8.8	1057.4	7.7	1070.3	14.2	2	1051.1	8.8
14Z-26	191.9	3.027	0.017	5.059	0.033	0.1111	0.0004	1840.3	18.5	1829.3	11.4	1816.8	11.6	-1	1816.8	11.6
14Z-27	140.7	3.279	0.020	4.447	0.047	0.1058	0.0009	1716.1	18.9	1721.2	17.6	1727.4	31.2	1	1727.4	31.2
14Z-28	381.3	3.527	0.021	3.934	0.027	0.1007	0.0003	1609.0	17.2	1620.6	11.2	1635.8	12.0	2	1635.8	12.0
14Z-29	66.6	3.319	0.018	4.268	0.029	0.1028	0.0004	1697.8	16.4	1687.3	11.2	1674.3	14.2	-1	1674.3	14.2
14Z-30	241.2	5.740	0.023	1.767	0.009	0.0736	0.0003	1035.3	7.8	1033.5	7.0	1029.9	14.0	-1	1035.3	7.8
14Z-31	291.4	3.765	0.018	3.451	0.020	0.0943	0.0003	1518.4	13.3	1516.2	9.4	1513.1	12.0	0	1513.1	12.0
14Z-32	29.19	5.385	0.026	1.920	0.016	0.0750	0.0005	1098.0	9.9	1088.2	11.0	1068.7	26.5	-3	1098.0	9.9
14Z-33	103	5.456	0.030	1.895	0.013	0.0750	0.0003	1085.0	11.0	1079.2	9.5	1067.6	18.0	-2	1085.0	11.0
14Z-34	110.9	1.972	0.010	12.276	0.071	0.1757	0.0006	2643.8	21.2	2625.7	11.4	2611.9	10.4	-1	2611.9	10.4
14Z-35	107.6	4.968	0.026	2.141	0.014	0.0772	0.0003	1182.3	11.3	1162.2	9.0	1124.9	15.0	-5	1182.3	11.3
14Z-36	59.5	2.992	0.013	5.136	0.030	0.1115	0.0004	1858.7	14.2	1842.0	10.2	1823.2	14.2	-2	1823.2	14.2
14Z-37	207.2	5.450	0.028	1.892	0.012	0.0748	0.0002	1086.1	10.4	1078.4	8.3	1063.0	13.2	-2	1086.1	10.4
14Z-38	150.5	5.159	0.021	2.075	0.011	0.0777	0.0003	1142.1	8.7	1140.5	7.6	1137.3	13.8	0	1142.1	8.7
14Z-39	113.7	1.935	0.009	13.422	0.071	0.1885	0.0006	2685.6	19.8	2709.8	10.7	2727.9	9.6	2	2727.9	9.6
14Z-40	311.6	4.144	0.016	2.952	0.015	0.0888	0.0003	1393.5	10.0	1395.3	7.7	1398.1	11.5	0	1398.1	11.5
14Z-41	140.2	5.420	0.029	1.882	0.013	0.0740	0.0003	1091.5	10.9	1074.8	9.0	1041.1	16.1	-5	1091.5	10.9
14Z-42	43.23	3.328	0.019	4.369	0.039	0.1055	0.0007	1693.8	17.4	1706.5	14.8	1722.2	24.4	2	1722.2	24.4
14Z-43	139.4	5.336	0.028	1.935	0.013	0.0749	0.0003	1107.3	10.9	1093.2	8.8	1065.2	14.8	-4	1107.3	10.9
14Z-44	80.7	1.820	0.013	14.235	0.111	0.1880	0.0006	2822.3	32.6	2765.5	15.2	2724.4	10.5	-4	2724.4	10.5
14Z-45	166.1	3.121	0.020	4.714	0.035	0.1068	0.0004	1791.7	20.6	1769.7	12.5	1743.8	12.2	-3	1743.8	12.2
14Z-46	139	14.426	0.104	0.525	0.005	0.0550	0.0003	432.1	6.0	428.5	6.4	409.6	24.4	-5	432.1	6.0
14Z-47	117.9	5.005	0.033	2.145	0.016	0.0779	0.0003	1174.2	14.0	1163.5	10.7	1143.4	15.8	-3	1174.2	14.0
14Z-48	61.8	13.824	0.091	0.550	0.005	0.0552	0.0004	450.2	5.7	444.9	7.0	417.3	32.0	-8	450.2	5.7
14Z-49	255.5	5.435	0.038	1.904	0.015	0.0751	0.0003	1088.8	14.2	1082.5	10.6	1070.0	14.2	-2	1088.8	14.2
14Z-50	373.8	5.102	0.040	2.172	0.019	0.0804	0.0003	1153.8	16.8	1172.2	12.0	1206.4	13.0	4	1153.8	16.8
14Z-51	38.31	5.721	0.033	1.741	0.013	0.0723	0.0003	1038.5	11.0	1023.8	9.6	992.6	18.9	-5	1038.5	11.0
14Z-52	191.9	4.198	0.024	2.935	0.020	0.0894	0.0003	1377.3	14.1	1390.9	10.3	1411.7	13.5	2	1411.7	13.5

Grain I.D.	238U (ppm)	238/206 ratio	238/206 1SE	207/235 ratio	207/235 1SE	207/206 ratio	207/206 1SE	238/206 Age (Ma)	2σ	207/235 Age (Ma)	2σ	207/206 Age (Ma)	2σ	Disc. (%)	preferred Age (Ma)	preferred Err. (2σ)
14Z-53	84.81	3.509	0.017	3.896	0.024	0.0992	0.0004	1616.5	14.2	1612.9	10.3	1608.1	14.1	-1	1608.1	14.1
14Z-54	711.1	5.688	0.032	1.875	0.012	0.0774	0.0003	1044.0	11.0	1072.4	8.8	1130.6	13.1	8	1044.0	11.0
14Z-55	78	5.590	0.036	1.818	0.014	0.0737	0.0003	1061.0	12.6	1051.8	10.1	1032.9	16.7	-3	1061.0	12.6
14Z-56	446.1	13.362	0.098	0.578	0.005	0.0561	0.0002	465.2	6.6	463.3	6.1	453.7	16.3	-3	465.2	6.6
14Z-57	86.8	3.483	0.024	3.787	0.029	0.0957	0.0004	1627.0	19.6	1590.0	12.7	1541.2	14.2	-6	1541.2	14.2
14Z-58	33.55	5.473	0.033	1.828	0.015	0.0726	0.0004	1081.7	12.0	1055.6	11.1	1001.9	23.5	-8	1081.7	12.0
14Z-59	38.06	3.306	0.026	4.178	0.037	0.1002	0.0004	1703.7	23.3	1669.7	14.8	1627.1	16.3	-5	1627.1	16.3
14Z-60	150.9	5.435	0.034	1.866	0.014	0.0736	0.0003	1088.8	12.6	1069.3	9.7	1029.6	14.8	-6	1088.8	12.6
14Z-61	161.8	4.160	0.029	2.875	0.023	0.0868	0.0003	1388.8	17.7	1375.5	12.0	1355.0	13.6	-2	1355.0	13.6
14Z-62	195.8	1.820	0.015	15.142	0.132	0.1999	0.0007	2823.1	37.1	2824.2	17.1	2825.0	10.6	0	2825.0	10.6
14Z-63	29.86	5.356	0.033	1.930	0.017	0.0750	0.0005	1103.5	12.5	1091.4	11.8	1067.3	24.9	-3	1103.5	12.5
14Z-64	54.3	1.597	0.012	19.129	0.157	0.2217	0.0007	3133.8	37.8	3048.3	16.4	2992.5	10.2	-5	2992.5	10.2
14Z-65	459	3.862	0.034	3.305	0.031	0.0926	0.0003	1484.2	23.6	1482.2	14.9	1479.3	12.1	0	1479.3	12.1
14Z-66	12.17	4.755	0.046	2.281	0.029	0.0787	0.0007	1230.4	21.9	1206.4	18.1	1163.7	32.7	-6	1230.4	21.9
14Z-67	111.8	5.546	0.031	1.821	0.012	0.0733	0.0003	1068.6	11.0	1053.0	8.9	1020.8	15.2	-5	1068.6	11.0
14Z-68	140.8	3.108	0.020	4.713	0.034	0.1063	0.0004	1798.5	20.1	1769.5	12.4	1735.4	12.8	-4	1735.4	12.8
14Z-69	70.5	3.719	0.024	3.458	0.026	0.0933	0.0004	1535.2	17.4	1517.6	11.9	1493.1	14.8	-3	1493.1	14.8
14Z-70	116.9	2.957	0.020	5.115	0.038	0.1097	0.0004	1878.0	21.8	1838.6	12.8	1794.3	11.8	-5	1794.3	11.8
14Z-71	337	5.513	0.036	1.853	0.014	0.0741	0.0003	1074.6	13.1	1064.6	9.9	1044.1	13.6	-3	1074.6	13.1
14Z-72	211.3	5.583	0.028	1.806	0.011	0.0732	0.0003	1062.1	9.9	1047.5	8.2	1017.2	14.7	-4	1062.1	9.9
14Z-73	70.4	6.189	0.027	1.548	0.010	0.0695	0.0004	965.6	7.8	949.7	8.4	913.0	21.0	-6	965.6	7.8
14Z-74	29.51	5.453	0.048	1.894	0.021	0.0749	0.0005	1085.5	17.5	1079.0	14.7	1065.7	26.8	-2	1085.5	17.5
14Z-75	196	3.083	0.019	4.807	0.034	0.1075	0.0004	1811.2	19.6	1786.1	12.2	1757.0	12.8	-3	1757.0	12.8
14Z-76	103.9	1.805	0.015	15.549	0.138	0.2037	0.0006	2841.4	38.7	2849.5	17.4	2855.3	9.6	0	2855.3	9.6
14Z-77	147.9	5.525	0.038	1.821	0.014	0.0730	0.0003	1072.4	13.7	1053.0	10.5	1012.8	15.8	-6	1072.4	13.7
14Z-78	97.7	3.690	0.024	3.856	0.029	0.1032	0.0004	1545.9	17.8	1604.4	12.1	1682.2	13.4	8	1682.2	13.4
14Z-79	33.84	4.585	0.022	2.561	0.017	0.0852	0.0004	1271.8	11.2	1289.6	9.9	1319.2	18.0	4	1319.2	18.0
14Z-80	227	14.436	0.092	0.520	0.004	0.0544	0.0002	431.8	5.3	424.8	5.3	387.5	18.2	-11	431.8	5.3
14Z-81	198.2	3.027	0.019	5.051	0.036	0.1109	0.0003	1840.3	20.4	1828.0	12.3	1813.9	11.3	-1	1813.9	11.3
14Z-82	405	3.297	0.018	4.539	0.028	0.1086	0.0003	1707.7	16.4	1738.2	10.7	1775.1	11.4	4	1775.1	11.4
14Z-83	131.8	3.359	0.022	4.151	0.031	0.1012	0.0004	1679.9	19.5	1664.4	12.3	1644.9	12.9	-2	1644.9	12.9
14Z-84	13.75	5.371	0.039	1.886	0.023	0.0735	0.0007	1100.8	14.7	1076.2	16.0	1026.9	38.5	-7	1100.8	14.7
14Z-85	89.2	10.854	0.052	0.739	0.006	0.0582	0.0004	568.1	5.2	562.0	6.8	537.1	27.1	-6	568.1	5.2
14Z-86	85.64	4.396	0.021	2.777	0.017	0.0886	0.0003	1321.4	11.6	1349.3	9.4	1393.8	14.7	5	1393.8	14.7
14Z-87	138.7	5.821	0.025	1.728	0.009	0.0730	0.0002	1022.0	8.3	1018.9	7.1	1012.2	13.1	-1	1022.0	8.3
14Z-88	46.1	4.789	0.024	2.290	0.015	0.0796	0.0003	1222.4	11.3	1209.3	9.2	1186.0	15.6	-3	1186.0	15.6
14Z-89	65.3	3.308	0.022	4.175	0.030	0.1002	0.0003	1702.7	19.9	1669.0	12.1	1627.0	11.2	-5	1627.0	11.2
14Z-90	147.3	13.396	0.081	0.563	0.004	0.0547	0.0002	464.1	5.4	453.4	5.2	399.4	16.4	-16	464.1	5.4
14Z-91	353.8	3.140	0.022	4.803	0.036	0.1094	0.0003	1782.4	22.1	1785.3	12.9	1788.8	9.5	0	1788.8	9.5
14Z-92	195	4.235	0.026	2.827	0.019	0.0869	0.0002	1366.4	15.2	1362.6	10.2	1356.7	10.0	-1	1356.7	10.0
14Z-93	46.9	5.438	0.025	1.879	0.011	0.0741	0.0003	1088.2	9.3	1073.7	8.0	1044.4	15.3	-4	1088.2	9.3
14Z-94	28.78	1.785	0.008	14.306	0.080	0.1853	0.0006	2867.9	22.1	2770.2	11.2	2699.9	9.8	-6	2699.9	9.8
14Z-95	324.1	5.368	0.035	1.933	0.013	0.0753	0.0002	1101.3	13.1	1092.6	9.4	1075.4	10.2	-2	1101.3	13.1
14Z-96	192	3.964	0.026	3.043	0.021	0.0875	0.0002	1450.3	17.1	1418.4	10.9	1370.9	9.7	-6	1370.9	9.7
14Z-97	108.1	5.208	0.022	1.965	0.010	0.0743	0.0002	1132.2	8.7	1103.5	6.9	1047.4	11.4	-8	1132.2	8.7
14Z-98	336.4	12.590	0.063	0.612	0.004	0.0559	0.0002	492.7	4.8	485.1	4.6	449.0	13.9	-10	492.7	4.8
14Z-99	241.2	3.209	0.017	4.569	0.027	0.1064	0.0003	1748.6	16.3	1743.6	10.0	1737.6	9.0	-1	1737.6	9.0
14Z-100	429	4.141	0.020	2.969	0.016	0.0892	0.0002	1394.5	12.0	1399.6	8.4	1407.4	9.5	1	1407.4	9.5
14Z-101	37.6	3.013	0.019	4.959	0.035	0.1084	0.0004	1847.6	19.9	1812.4	12.1	1772.2	12.3	-4	1772.2	12.3
14Z-102	163.6	3.377	0.017	4.122	0.023	0.1010	0.0002	1671.9	15.0	1658.7	9.5	1641.9	9.0	-2	1641.9	9.0
14Z-103	95.6	3.258	0.019	4.363	0.027	0.1032	0.0003	1725.4	17.4	1705.4	10.6	1680.9	9.5	-3	1680.9	9.5
14Z-104	17.03	6.031	0.036	1.626	0.015	0.0712	0.0005	988.9	11.1	980.2	11.7	960.8	28.7	-3	988.9	11.1
14Z-105	145.3	3.177	0.016	4.634	0.026	0.1068	0.0003	1764.3	15.8	1755.3	9.7	1744.7	8.9	-1	1744.7	8.9
14Z-106	252.2	4.329	0.022	2.840	0.018	0.0892	0.0003	1339.7	12.6	1366.3	9.5	1408.0	13.1	5	1408.0	13.1
14Z-107	85.9	5.672	0.039	1.755	0.013	0.0723	0.0003	1046.7	13.2	1029.2	10.0	992.1	14.4	-6	1046.7	13.2
14Z-108	169.1	5.543	0.032	1.834	0.012	0.0738	0.0002	1069.2	11.5	1057.7	8.5	1034.3	10.4	-3	1069.2	11.5
14Z-109	175.4	5.051	0.031	2.106	0.014	0.0772	0.0002	1164.6	13.0	1150.9	9.3	1125.2	11.1	-3	1164.6	13.0

Grain I.D.	238U (ppm)	238/206 ratio	238/206 1SE	207/235 ratio	207/235 1SE	207/206 ratio	207/206 1SE	238/206 Age (Ma)	2σ	207/235 Age (Ma)	2σ	207/206 Age (Ma)	2σ	Disc. (%)	preferred Age (Ma)	preferred Err. (2σ)
14Z-110	161.9	5.705	0.042	1.752	0.014	0.0725	0.0002	1041.2	14.3	1028.0	10.3	999.9	11.2	-4	1041.2	14.3
14Z-111	361	14.205	0.111	0.536	0.005	0.0553	0.0002	438.6	6.6	436.0	6.0	422.6	14.1	-4	438.6	6.6
14Z-112	41.84	1.737	0.014	15.561	0.131	0.1961	0.0005	2931.2	38.2	2850.2	16.5	2793.4	7.8	-5	2793.4	7.8
14Z-113	74.3	5.834	0.037	1.688	0.013	0.0715	0.0003	1019.8	12.2	1004.1	9.6	970.0	15.7	-5	1019.8	12.2
14Z-114	56.3	4.627	0.029	2.461	0.018	0.0826	0.0003	1261.2	14.4	1260.7	10.8	1259.8	15.1	0	1259.8	15.1
14Z-115	292.8	3.026	0.020	5.070	0.036	0.1113	0.0003	1840.8	21.4	1831.2	12.2	1820.3	8.3	-1	1820.3	8.3
14Z-116	95.5	4.861	0.043	2.171	0.021	0.0766	0.0003	1205.9	19.3	1171.8	13.2	1109.4	14.4	-9	1205.9	19.3
14Z-117	267.1	6.215	0.118	2.007	0.062	0.0905	0.0022	961.8	33.9	1117.8	41.8	1435.2	92.7	33	961.8	33.9
14Z-118	180.9	1.919	0.013	13.389	0.094	0.1864	0.0004	2703.8	29.4	2707.5	13.7	2710.2	7.4	0	2710.2	7.4
14Z-119	108.1	5.236	0.045	1.970	0.018	0.0748	0.0002	1126.8	17.9	1105.2	12.4	1063.0	11.8	-6	1126.8	17.9
14Z-120	280.5	3.113	0.023	4.921	0.038	0.1112	0.0003	1795.6	23.0	1805.8	13.2	1817.7	8.8	1	1817.7	8.8
14Z-121	113.9	3.274	0.020	4.234	0.028	0.1006	0.0003	1718.0	18.9	1680.7	11.2	1634.4	9.3	-5	1634.4	9.3
14Z-122	52.16	5.319	0.030	1.924	0.013	0.0743	0.0003	1110.5	11.5	1089.4	9.1	1047.4	15.0	-6	1110.5	11.5
14Z-123	125.5	5.476	0.051	1.832	0.018	0.0728	0.0002	1081.2	18.6	1057.0	13.1	1007.5	13.4	-7	1081.2	18.6
14Z-124	192.9	3.704	0.030	3.488	0.030	0.0937	0.0002	1540.8	22.4	1524.5	13.6	1502.0	9.1	-3	1502.0	9.1
14Z-125	40.9	2.034	0.019	11.031	0.110	0.1628	0.0005	2578.0	40.3	2525.8	18.8	2484.1	10.4	-4	2484.1	10.4
14Z-126	234.7	5.513	0.033	1.855	0.012	0.0742	0.0002	1074.6	12.1	1065.1	8.9	1045.7	11.2	-3	1074.6	12.1
14Z-127	133.4	1.733	0.017	15.586	0.159	0.1960	0.0007	2936.5	45.1	2851.8	19.8	2792.4	11.7	-5	2792.4	11.7
14Z-128	46.56	6.562	0.047	1.619	0.014	0.0771	0.0004	914.4	12.3	977.5	11.3	1122.1	21.0	19	914.4	12.3
14Z-129	63.5	5.907	0.035	1.643	0.011	0.0704	0.0002	1008.3	11.1	986.9	8.8	939.7	14.3	-7	1008.3	11.1
14Z-130	170	13.430	0.088	0.564	0.004	0.0550	0.0002	463.0	5.9	454.2	5.5	410.0	15.9	-13	463.0	5.9
14Z-131	177.5	6.270	0.051	1.541	0.013	0.0701	0.0002	954.0	14.5	946.9	10.7	930.4	12.0	-3	954.0	14.5
14Z-132	466.8	5.596	0.039	1.872	0.014	0.0760	0.0002	1059.9	13.7	1071.3	10.0	1094.7	10.3	3	1059.9	13.7
14Z-133	274.6	4.577	0.040	2.592	0.023	0.0861	0.0002	1273.9	20.1	1298.4	13.4	1339.1	9.9	5	1339.1	9.9
14Z-134	307.7	3.460	0.028	4.120	0.035	0.1034	0.0002	1636.5	23.6	1658.2	13.9	1685.7	8.1	3	1685.7	8.1
14Z-135	37.9	2.024	0.023	11.018	0.126	0.1618	0.0004	2588.0	47.5	2524.7	21.6	2474.2	9.1	-5	2474.2	9.1
14Z-136	87.7	2.953	0.018	5.195	0.034	0.1113	0.0003	1879.9	19.8	1851.8	11.4	1820.4	9.1	-3	1820.4	9.1
14Z-137	85.1	5.405	0.044	1.887	0.016	0.0740	0.0002	1094.2	16.4	1076.4	11.7	1040.6	12.8	-5	1094.2	16.4
14Z-138	220.5	13.793	0.124	0.568	0.006	0.0568	0.0002	451.2	7.8	456.5	7.3	483.2	18.7	7	451.2	7.8
14Z-139	25.49	1.669	0.011	17.036	0.130	0.2063	0.0007	3026.6	33.2	2936.9	15.2	2876.0	11.0	-5	2876.0	11.0

10.3.1.8 EM-15 (Zircon)

Grain I.D.	238U (ppm)	238/206 ratio	206/238 1SE	207/235 ratio	207/235 1SE	207/206 ratio	207/206 1SE	238/206 Age (Ma)	2σ	207/235 Age (Ma)	2σ	207/206 Age (Ma)	2σ	Disc. (%)	preferred Age (Ma)	preferred Err. (2σ)
15Z-01	29.3	5.780	0.043	1.745	0.022	0.0732	0.0008	1028.6	14.3	1025.4	16.5	1018.6	41.8	-1%	1028.6	14.3
15Z-02	70.9	3.493	0.016	3.972	0.029	0.1007	0.0006	1623.0	13.6	1628.5	11.9	1635.7	21.1	1%	1635.7	21.1
15Z-03	32.0	3.479	0.025	4.008	0.038	0.1012	0.0006	1628.5	21.1	1635.9	15.5	1645.4	22.7	1%	1645.4	22.7
15Z-04	268.8	3.601	0.012	3.782	0.018	0.0988	0.0003	1579.8	9.2	1588.9	7.8	1601.1	13.6	1%	1601.1	13.6
15Z-05	14.4	5.126	0.091	2.159	0.048	0.0803	0.0011	1148.9	37.2	1168.0	31.1	1203.5	54.2	5%	1148.9	37.2
15Z-06	29.2	4.983	0.041	2.169	0.027	0.0784	0.0008	1179.1	17.8	1171.0	17.6	1156.1	38.3	-2%	1179.1	17.8
15Z-07	256.2	14.611	0.059	0.529	0.004	0.0561	0.0004	426.8	3.3	431.3	5.5	455.7	30.0	6%	426.8	3.3
15Z-08	21.2	2.008	0.030	14.701	0.241	0.2142	0.0014	2605.2	64.6	2796.1	31.4	2936.9	22.3	11%	2936.9	22.3
15Z-09	127.8	4.500	0.026	2.539	0.019	0.0829	0.0004	1293.5	13.8	1283.2	11.2	1266.0	19.6	-2%	1266.0	19.6
15Z-10	84.6	3.589	0.021	3.812	0.029	0.0993	0.0005	1584.3	16.7	1595.3	12.6	1609.8	19.2	2%	1609.8	19.2
15Z-11	71.3	5.438	0.028	1.919	0.016	0.0757	0.0005	1088.2	10.4	1087.8	11.3	1086.8	27.0	0%	1088.2	10.4
15Z-12	246.0	5.459	0.027	1.903	0.012	0.0754	0.0003	1084.4	9.9	1082.1	8.5	1077.5	16.8	-1%	1084.4	9.9
15Z-13	132.0	2.203	0.065	12.345	0.375	0.1973	0.0012	2413.0	119.7	2631.0	57.1	2803.3	21.1	14%	2803.3	21.1
15Z-14	1035.0	16.658	0.050	0.492	0.003	0.0595	0.0003	375.8	2.2	406.6	3.5	585.2	18.8	36%		
15Z-15	238.1	14.211	0.060	0.539	0.005	0.0556	0.0004	438.4	3.6	438.0	6.2	435.8	34.3	-1%	438.4	3.6
15Z-16	42.2	2.035	0.011	11.378	0.082	0.1680	0.0008	2576.7	23.1	2554.6	13.9	2537.1	17.3	-2%	2537.1	17.3
15Z-17	172.7	1.885	0.009	14.448	0.084	0.1976	0.0007	2743.6	21.7	2779.6	11.7	2805.9	12.8	2%	2805.9	12.8
15Z-18	67.1	1.786	0.009	15.820	0.101	0.2050	0.0008	2866.6	24.6	2866.0	12.9	2865.5	13.8	0%	2865.5	13.8
15Z-19	93.2	1.920	0.011	13.602	0.090	0.1895	0.0007	2702.6	25.2	2722.4	13.1	2737.2	13.2	1%	2737.2	13.2
15Z-20	168.3	3.569	0.015	3.841	0.022	0.0995	0.0004	1592.4	11.7	1601.3	9.4	1613.2	15.6	1%	1613.2	15.6
15Z-21	165.2	3.463	0.017	4.047	0.027	0.1017	0.0005	1635.5	14.6	1643.7	11.2	1654.2	17.5	1%	1654.2	17.5
15Z-22	28.8	4.352	0.039	2.746	0.033	0.0867	0.0007	1333.5	21.5	1341.0	18.0	1353.0	31.6	1%	1353.0	31.6
15Z-23	52.0	4.228	0.023	2.813	0.022	0.0863	0.0005	1368.5	13.6	1359.0	12.1	1344.0	23.0	-2%	1344.0	23.0
15Z-24	21.7	6.061	0.062	1.628	0.026	0.0716	0.0009	984.5	18.8	981.2	19.8	973.7	48.7	-1%	984.5	18.8
15Z-25	417.3	5.274	0.019	2.046	0.010	0.0783	0.0003	1119.2	7.7	1130.9	6.9	1153.3	13.9	3%	1119.2	7.7
15Z-26	127.2	4.331	0.027	2.747	0.022	0.0863	0.0004	1339.2	15.3	1341.2	12.1	1344.3	20.0	0%	1344.3	20.0
15Z-27	36.2	1.801	0.014	15.270	0.140	0.1996	0.0009	2846.3	37.0	2832.2	17.9	2822.2	16.3	-1%	2822.2	16.3
15Z-28	226.9	2.475	0.058	12.391	0.294	0.2225	0.0008	2187.4	87.3	2634.5	44.8	2998.4	13.0	27%		
15Z-29	41.0	5.627	0.038	1.798	0.019	0.0734	0.0006	1054.4	13.2	1044.6	13.9	1024.1	33.5	-3%	1054.4	13.2
15Z-30	197.3	3.719	0.010	3.555	0.017	0.0959	0.0004	1535.2	7.8	1539.7	7.8	1545.8	15.3	1%	1545.8	15.3
15Z-31	90.1	3.357	0.019	4.184	0.031	0.1019	0.0005	1680.9	17.0	1671.0	12.2	1658.5	18.0	-1%	1658.5	18.0
15Z-32	122.0	3.047	0.014	5.006	0.030	0.1107	0.0004	1829.7	14.7	1820.3	10.5	1809.6	15.3	-1%	1809.6	15.3
15Z-33	207.0	5.311	0.042	2.116	0.019	0.0815	0.0004	1112.2	16.3	1153.9	12.8	1233.1	18.8	10%	1112.2	16.3
15Z-34	341.7	3.415	0.017	4.166	0.025	0.1032	0.0003	1655.5	14.6	1667.3	9.9	1682.2	13.1	2%	1682.2	13.1
15Z-35	145.3	1.846	0.009	14.721	0.089	0.1972	0.0007	2790.6	23.2	2797.4	12.1	2802.3	12.8	0%	2802.3	12.8
15Z-36	17.9	3.427	0.037	4.046	0.055	0.1006	0.0009	1650.5	31.5	1643.4	22.4	1634.4	31.9	-1%	1634.4	31.9
15Z-37	26.0	3.044	0.030	4.917	0.058	0.1086	0.0007	1831.1	31.6	1805.1	20.1	1775.2	24.2	-3%	1775.2	24.2
15Z-38	76.6	4.294	0.020	2.791	0.021	0.0870	0.0005	1349.7	11.6	1353.2	11.1	1358.7	22.4	1%	1358.7	22.4
15Z-39	162.7	3.226	0.015	4.570	0.029	0.1070	0.0005	1740.7	14.4	1743.8	10.8	1747.4	16.8	0%	1747.4	16.8
15Z-40	170.9	3.181	0.012	4.671	0.024	0.1078	0.0004	1762.3	11.9	1762.0	9.0	1761.6	13.9	0%	1761.6	13.9
15Z-41	67.6	3.222	0.027	4.988	0.053	0.1166	0.0008	1742.7	25.6	1817.3	18.0	1903.9	23.8	8%	1903.9	23.8
15Z-42	100.5	3.570	0.018	3.799	0.026	0.0984	0.0004	1591.9	14.7	1592.4	11.3	1593.2	17.8	0%	1593.2	17.8
15Z-43	103.8	2.901	0.014	5.533	0.034	0.1165	0.0005	1909.2	16.0	1905.7	10.9	1901.9	15.2	0%	1901.9	15.2
15Z-44	43.1	3.391	0.022	4.125	0.037	0.1015	0.0006	1666.0	19.5	1659.3	14.7	1650.9	22.6	-1%	1650.9	22.6
15Z-45	24.2	1.875	0.017	13.749	0.136	0.1871	0.0009	2754.9	39.6	2732.6	19.1	2716.1	16.5	-1%	2716.1	16.5
15Z-46														0%		
15Z-47	195.0	3.928	0.032	3.254	0.029	0.0928	0.0004	1462.2	21.1	1470.2	14.2	1481.9	16.6	1%	1481.9	16.6
15Z-48	54.9	5.322	0.045	1.973	0.023	0.0762	0.0006	1110.0	17.4	1106.4	15.7	1099.4	31.9	-1%	1110.0	17.4
15Z-49	158.6	4.098	0.037	3.026	0.031	0.0900	0.0004	1407.5	22.9	1414.3	15.7	1424.7	19.2	1%	1424.7	19.2
15Z-50	343.0	4.119	0.039	3.059	0.032	0.0914	0.0004	1401.2	23.9	1422.4	16.0	1454.3	17.1	4%	1454.3	17.1
15Z-51	30.6	1.518	0.011	22.753	0.185	0.2506	0.0011	3262.5	35.9	3216.4	16.4	3187.8	15.2	-2%	3187.8	15.2
15Z-52	90.2	3.375	0.025	4.109	0.036	0.1006	0.0005	1672.9	22.0	1656.1	14.3	1634.7	17.5	-2%	1634.7	17.5

Grain I.D.	238U (ppm)	238/206 ratio	206/238 1SE	207/235 ratio	207/235 1SE	207/206 ratio	207/206 1SE	238/206 Age (Ma)	2σ	207/235 Age (Ma)	2σ	207/206 Age (Ma)	2σ	Disc. (%)	preferred Age (Ma)	preferred Err. (2σ)
15Z-53	81.0	4.188	0.034	2.877	0.027	0.0874	0.0004	1380.5	20.3	1376.0	14.5	1369.1	19.7	-1%	1369.1	19.7
15Z-54	40.8	3.175	0.025	4.644	0.042	0.1070	0.0005	1765.3	24.1	1757.3	15.3	1747.8	18.0	-1%	1747.8	18.0
15Z-55	144.7	3.223	0.025	4.601	0.041	0.1076	0.0004	1742.2	24.2	1749.5	14.9	1758.2	15.4	1%	1758.2	15.4
15Z-56	246.1	2.908	0.023	5.649	0.050	0.1192	0.0004	1905.4	26.5	1923.5	15.4	1943.2	14.5	2%	1943.2	14.5
15Z-57	407.0	4.284	0.039	2.802	0.028	0.0871	0.0003	1352.3	22.5	1356.1	15.0	1362.1	15.3	1%	1362.1	15.3
15Z-58	99.1	3.578	0.047	4.045	0.060	0.1050	0.0008	1588.8	36.8	1643.2	24.3	1713.5	26.9	7%	1713.5	26.9
15Z-59	137.2	3.433	0.025	4.070	0.034	0.1014	0.0004	1648.0	21.5	1648.2	13.7	1648.5	15.2	0%	1648.5	15.2
15Z-60	184.7	3.404	0.025	4.139	0.034	0.1022	0.0004	1660.5	21.5	1662.0	13.6	1663.8	14.9	0%	1663.8	14.9
15Z-61	233.5	4.132	0.030	2.984	0.025	0.0895	0.0004	1397.1	18.2	1403.5	12.8	1413.4	16.7	1%	1413.4	16.7
15Z-62	565.0	14.388	0.186	0.547	0.007	0.0571	0.0003	433.1	10.9	443.0	9.9	494.4	20.2	12%	433.1	10.9
15Z-63	298.3	3.465	0.027	4.130	0.036	0.1038	0.0004	1634.5	22.6	1660.2	14.3	1692.9	15.0	3%	1692.9	15.0
15Z-64	152.1	3.426	0.026	4.144	0.035	0.1030	0.0004	1651.0	22.0	1663.0	14.2	1678.2	15.9	2%	1678.2	15.9
15Z-65	437.0	3.890	0.032	3.436	0.031	0.0970	0.0004	1475.0	21.6	1512.7	14.3	1566.0	15.2	6%	1566.0	15.2
15Z-66	126.7	4.259	0.034	2.787	0.026	0.0861	0.0004	1359.6	19.9	1352.0	13.8	1340.0	17.4	-1%	1340.0	17.4
15Z-67	15.4	4.464	0.059	2.525	0.042	0.0818	0.0009	1303.0	31.1	1279.3	24.5	1239.9	41.1	-5%	1239.9	41.1
15Z-68	255.9	1.958	0.017	13.477	0.128	0.1915	0.0008	2659.6	37.7	2713.7	18.3	2754.2	14.6	3%	2754.2	14.6
15Z-69	690.0	3.165	0.125	5.191	0.208	0.1192	0.0008	1770.2	122.5	1851.2	68.4	1943.5	24.7	9%	1943.5	24.7
15Z-70	523.1	5.470	0.046	1.961	0.018	0.0778	0.0003	1082.3	16.9	1102.1	12.7	1141.4	16.4	5%	1082.3	16.9
15Z-71	300.4	12.882	0.091	0.606	0.005	0.0567	0.0003	482.0	6.6	481.2	6.7	477.7	23.1	-1%	482.0	6.6
15Z-72	249.7	4.125	0.028	2.989	0.023	0.0895	0.0003	1399.2	17.2	1404.8	12.0	1413.4	15.5	1%	1413.4	15.5
15Z-73	612.0	3.525	0.038	4.146	0.047	0.1060	0.0004	1610.0	30.7	1663.4	18.8	1731.4	15.3	7%	1731.4	15.3
15Z-74	75.9	1.785	0.012	15.588	0.127	0.2019	0.0009	2867.5	32.4	2851.9	16.0	2840.9	15.4	-1%	2840.9	15.4
15Z-75	124.8	4.581	0.042	2.395	0.025	0.0796	0.0004	1272.9	21.2	1241.1	14.8	1186.2	19.1	-7%	1186.2	19.1
15Z-76	221.0	3.413	0.041	4.174	0.053	0.1034	0.0004	1656.5	34.9	1668.9	20.8	1684.5	15.9	2%	1684.5	15.9
15Z-77	118.0	3.056	0.023	5.007	0.043	0.1110	0.0005	1824.8	23.9	1820.5	14.8	1815.5	16.6	-1%	1815.5	16.6
15Z-78	390.0	4.266	0.076	3.495	0.064	0.1082	0.0005	1357.5	43.4	1526.2	28.8	1768.5	16.4	23%		
15Z-79	184.1	3.207	0.019	4.657	0.032	0.1084	0.0004	1749.6	17.8	1759.6	11.7	1771.5	14.8	1%	1771.5	14.8
15Z-80	114.2	3.444	0.025	4.346	0.041	0.1086	0.0007	1643.5	21.6	1702.2	15.9	1775.2	22.6	7%	1775.2	22.6
15Z-81	265.0	3.282	0.032	4.385	0.047	0.1044	0.0005	1714.6	29.2	1709.4	17.9	1703.1	17.9	-1%	1703.1	17.9
15Z-82	299.0	3.144	0.020	4.899	0.037	0.1117	0.0004	1780.4	20.1	1802.0	12.9	1827.1	15.3	3%	1827.1	15.3
15Z-83	224.7	6.234	0.043	1.694	0.014	0.0766	0.0003	959.0	12.3	1006.3	10.4	1110.9	17.9	14%	959.0	12.3
15Z-84	177.9	4.277	0.026	2.770	0.020	0.0860	0.0003	1354.4	14.7	1347.5	10.9	1336.6	16.4	-1%	1336.6	16.4
15Z-85	208.6	3.670	0.030	3.871	0.036	0.1031	0.0004	1553.5	22.9	1607.7	15.2	1679.5	16.7	8%	1679.5	16.7
15Z-86	226.0	3.845	0.040	3.648	0.041	0.1018	0.0005	1490.4	27.7	1560.2	18.1	1656.0	17.3	10%	1656.0	17.3
15Z-87	74.4	4.859	0.032	2.262	0.019	0.0797	0.0004	1206.4	14.5	1200.4	11.6	1189.7	20.0	-1%	1206.4	14.5
15Z-88	54.6	5.020	0.034	2.158	0.020	0.0786	0.0005	1171.0	14.6	1167.7	12.7	1161.4	24.5	-1%	1171.0	14.6
15Z-89	183.8	3.862	0.025	3.345	0.026	0.0938	0.0004	1484.2	17.5	1491.7	12.1	1502.4	15.9	1%	1502.4	15.9
15Z-90	135.3	5.718	0.038	1.894	0.016	0.0786	0.0004	1039.1	12.7	1079.0	11.6	1160.7	22.8	10%	1039.1	12.7
15Z-91	29.9	5.814	0.042	1.719	0.019	0.0725	0.0006	1023.1	13.8	1015.5	14.2	999.1	34.0	-2%	1023.1	13.8
15Z-92	71.4	3.169	0.022	4.657	0.038	0.1071	0.0005	1768.2	21.6	1759.5	14.0	1749.1	17.2	-1%	1749.1	17.2
15Z-93	164.9	3.234	0.022	4.579	0.036	0.1075	0.0004	1736.8	20.8	1745.5	13.2	1756.0	15.1	1%	1756.0	15.1
15Z-94	61.0	5.015	0.038	2.310	0.022	0.0841	0.0005	1172.1	16.2	1215.5	13.7	1293.3	23.7	9%	1293.3	23.7
15Z-95	171.1	3.506	0.020	3.937	0.028	0.1002	0.0004	1617.5	16.6	1621.3	11.6	1626.2	16.0	1%	1626.2	16.0
15Z-96	42.9	3.598	0.026	3.842	0.033	0.1003	0.0005	1580.8	20.2	1601.6	14.0	1629.0	18.3	3%	1629.0	18.3
15Z-97	663.2	4.243	0.028	2.988	0.022	0.0920	0.0003	1364.3	16.2	1404.4	11.6	1465.9	14.7	7%	1465.9	14.7
15Z-98																
15Z-99	83.9	1.882	0.014	14.175	0.116	0.1936	0.0007	2746.9	33.0	2761.5	16.0	2772.2	13.7	1%	2772.2	13.7
15Z-100	83.3	1.874	0.013	14.286	0.111	0.1942	0.0008	2757.0	30.4	2768.9	15.2	2777.6	14.4	1%	2777.6	14.4
15Z-101	140.5	1.914	0.020	13.703	0.154	0.1903	0.0008	2710.2	46.7	2729.4	21.6	2743.6	14.7	1%	2743.6	14.7
15Z-102	131.7	1.900	0.017	13.793	0.131	0.1902	0.0007	2725.8	39.0	2735.6	18.3	2742.8	13.9	1%	2742.8	13.9
15Z-103	257.5	4.468	0.031	2.912	0.023	0.0944	0.0004	1301.9	16.4	1385.1	12.3	1515.7	16.1	14%	1515.7	16.1
15Z-104	123.9	3.383	0.024	4.126	0.034	0.1013	0.0004	1669.5	21.0	1659.4	13.6	1646.7	16.2	-1%	1646.7	16.2
15Z-105	114.2	3.317	0.025	4.220	0.036	0.1016	0.0004	1698.7	22.4	1677.8	14.3	1651.8	16.7	-3%	1651.8	16.7
15Z-106	222.7	4.778	0.038	2.323	0.021	0.0805	0.0003	1225.1	17.6	1219.3	12.7	1209.1	16.9	-1%	1209.1	16.9
15Z-107	165.0	6.477	0.191	1.628	0.049	0.0765	0.0004	925.6	50.8	980.9	37.7	1107.0	22.8	16%		
15Z-108	99.1	3.304	0.027	4.257	0.039	0.1021	0.0004	1704.7	24.8	1685.1	15.4	1660.9	16.4	-3%	1660.9	16.4
15Z-109	180.4	4.131	0.029	2.981	0.025	0.0894	0.0004	1397.6	17.7	1402.8	12.8	1410.8	18.0	1%	1410.8	18.0

Grain I.D.	238U (ppm)	238/206 ratio	206/238 1SE	207/235 ratio	207/235 1SE	207/206 ratio	207/206 1SE	238/206 Age (Ma)	2σ	207/235 Age (Ma)	2σ	207/206 Age (Ma)	2σ	Disc. (%)	preferred Age (Ma)	preferred Err. (2σ)
15Z-110	48.0	4.973	0.043	2.230	0.025	0.0805	0.0006	1181.2	18.8	1190.6	15.6	1207.6	27.4	2%	1181.2	18.8
15Z-111	71.6	5.084	0.043	2.121	0.022	0.0782	0.0005	1157.6	17.8	1155.6	14.3	1151.8	24.1	0%	1157.6	17.8
15Z-112	238.3	3.438	0.024	4.117	0.033	0.1027	0.0004	1646.0	20.5	1657.8	13.3	1672.7	15.1	2%	1672.7	15.1
15Z-113	190.4	2.111	0.014	12.002	0.093	0.1838	0.0007	2499.8	28.6	2604.6	14.9	2687.1	13.5	7%	2687.1	13.5
15Z-114	45.9	1.988	0.014	12.697	0.103	0.1832	0.0008	2626.7	30.2	2657.4	15.6	2680.9	15.1	2%	2680.9	15.1
15Z-115	550.0	8.251	0.095	2.435	0.030	0.1458	0.0007	737.5	16.1	1253.1	18.1	2296.5	17.7	68%		
15Z-116	398.3	3.102	0.025	4.968	0.045	0.1118	0.0005	1801.4	25.9	1814.0	15.7	1828.4	15.7	1%	1828.4	15.7
15Z-117	229.2	3.973	0.026	3.155	0.024	0.0910	0.0003	1447.2	17.1	1446.3	11.8	1444.9	15.4	0%	1444.9	15.4
15Z-118	102.6	4.602	0.032	2.490	0.021	0.0832	0.0004	1267.6	15.9	1269.3	12.6	1272.1	20.8	0%	1272.1	20.8
15Z-119	229.9	3.990	0.029	3.283	0.027	0.0951	0.0004	1441.6	18.6	1477.1	13.0	1528.6	16.2	6%	1528.6	16.2
15Z-120	103.5	4.794	0.043	2.270	0.023	0.0790	0.0004	1221.4	19.8	1203.0	14.1	1170.2	18.5	-4%	1221.4	19.8
15Z-121	357.0	5.219	0.045	2.152	0.021	0.0815	0.0004	1130.0	17.9	1165.7	13.5	1232.6	18.1	8%	1130.0	17.9
15Z-122	90.8	3.299	0.023	4.197	0.035	0.1005	0.0005	1706.7	21.4	1673.4	13.9	1632.0	17.6	-5%	1632.0	17.6
15Z-123	163.4	3.390	0.021	4.123	0.030	0.1014	0.0004	1666.5	18.0	1658.8	12.1	1649.1	15.8	-1%	1649.1	15.8
15Z-124	786.0	7.220	0.096	3.130	0.047	0.1640	0.0012	836.2	21.0	1440.2	23.3	2496.6	24.5	67%		
15Z-125	308.4	2.618	0.025	9.231	0.096	0.1753	0.0007	2085.6	34.1	2361.2	19.2	2608.5	14.9	20%		
15Z-126	101.9	1.894	0.014	13.508	0.112	0.1856	0.0007	2733.0	33.0	2715.8	16.1	2703.1	14.2	-1%	2703.1	14.2
15Z-127	479.0	2.506	0.047	10.607	0.208	0.1929	0.0011	2164.4	69.2	2489.4	36.6	2766.3	19.9	22%		
15Z-128	308.0	1.900	0.016	14.398	0.132	0.1985	0.0008	2726.3	37.3	2776.3	17.8	2812.8	14.2	3%	2812.8	14.2
15Z-129	501.7	4.606	0.033	2.600	0.021	0.0869	0.0003	1266.5	16.5	1300.6	12.1	1357.2	16.0	7%	1357.2	16.0
15Z-130	97.5	1.878	0.013	13.800	0.105	0.1880	0.0007	2752.4	30.0	2736.0	14.9	2724.0	14.0	-1%	2724.0	14.0
15Z-131	331.9	4.148	0.026	3.026	0.022	0.0911	0.0004	1392.4	15.7	1414.1	11.5	1447.0	16.4	4%	1447.0	16.4
15Z-132	295.3	3.133	0.034	4.862	0.056	0.1105	0.0004	1785.8	34.3	1795.7	19.6	1807.2	14.7	1%	1807.2	14.7
15Z-133	150.6	12.796	0.090	0.605	0.006	0.0562	0.0004	485.1	6.6	480.5	7.3	458.9	28.8	-6%	485.1	6.6
15Z-134	216.0	3.469	0.027	4.026	0.035	0.1013	0.0004	1633.0	22.6	1639.4	14.2	1647.6	14.7	1%	1647.6	14.7
15Z-135	137.4	3.400	0.024	4.095	0.034	0.1010	0.0004	1662.0	21.0	1653.2	13.8	1642.1	16.8	-1%	1642.1	16.8
15Z-136	611.0	3.690	0.075	4.116	0.086	0.1102	0.0006	1545.9	55.8	1657.4	34.2	1801.9	19.1	14%	1801.9	19.1
15Z-137	397.0	9.225	0.094	1.308	0.015	0.0876	0.0004	663.4	12.8	849.4	12.9	1372.4	18.6	52%		
15Z-138	177.3	5.438	0.043	1.983	0.017	0.0782	0.0003	1088.2	15.8	1109.7	11.9	1152.1	16.1	6%	1088.2	15.8
15Z-139	255.2	2.960	0.022	5.509	0.046	0.1183	0.0004	1876.1	24.7	1902.0	14.6	1930.4	14.2	3%	1930.4	14.2
15Z-140	160.5	2.890	0.021	5.557	0.045	0.1165	0.0004	1915.5	24.0	1909.4	14.2	1902.9	14.5	-1%	1902.9	14.5
15Z-141	257.3	3.172	0.023	4.669	0.038	0.1075	0.0004	1766.7	22.6	1761.7	13.8	1755.8	14.1	-1%	1755.8	14.1
15Z-142	430.7	4.838	0.035	2.343	0.019	0.0823	0.0003	1211.2	16.1	1225.5	11.8	1250.8	16.1	3%	1250.8	16.1
15Z-143	208.1	2.952	0.022	5.404	0.045	0.1158	0.0004	1880.4	24.2	1885.6	14.4	1891.2	14.7	1%	1891.2	14.7
15Z-144	159.6	4.608	0.037	2.432	0.022	0.0813	0.0004	1266.0	18.6	1252.1	13.4	1228.3	18.4	-3%	1228.3	18.4
15Z-145	172.4	3.510	0.031	3.946	0.039	0.1005	0.0004	1616.0	25.6	1623.2	16.0	1632.5	15.8	1%	1632.5	15.8
15Z-146	224.3	5.618	0.041	1.820	0.015	0.0742	0.0003	1056.0	14.3	1052.8	11.0	1046.0	16.8	-1%	1056.0	14.3
15Z-147	48.0	5.126	0.035	2.023	0.019	0.0752	0.0005	1148.9	14.6	1123.3	12.8	1074.0	25.9	-7%	1148.9	14.6
15Z-148	122.3	6.266	0.041	1.541	0.012	0.0700	0.0003	954.6	11.7	946.7	10.0	928.6	20.0	-3%	954.6	11.7
15Z-149	196.0	6.262	0.039	1.545	0.012	0.0702	0.0003	955.1	11.2	948.4	9.6	933.0	19.1	-2%	955.1	11.2
15Z-150	153.9	5.099	0.035	2.099	0.017	0.0777	0.0003	1154.3	14.6	1148.4	11.2	1137.3	17.4	-1%	1154.3	14.6
15Z-151	83.6	5.013	0.039	2.129	0.020	0.0774	0.0004	1172.6	16.7	1158.2	13.0	1131.4	21.4	-4%	1172.6	16.7
15Z-152	135.5	13.831	0.115	0.609	0.007	0.0611	0.0004	450.0	7.2	482.6	8.5	640.7	31.3	30%		
15Z-153	230.5	14.438	0.098	0.529	0.005	0.0554	0.0003	431.7	5.7	430.8	6.2	426.2	25.0	-1%	431.7	5.7
15Z-154	223.6	5.992	0.043	1.664	0.014	0.0724	0.0003	995.0	13.3	995.0	10.8	994.9	18.9	0%	995.0	13.3
15Z-155	202.1	2.910	0.021	5.563	0.045	0.1175	0.0004	1904.0	24.1	1910.4	14.2	1917.4	14.3	1%	1917.4	14.3
15Z-156	211.0	2.876	0.031	5.678	0.065	0.1185	0.0005	1923.6	35.9	1928.1	20.0	1932.9	15.2	0%	1932.9	15.2
15Z-157	203.2	4.139	0.056	3.874	0.056	0.1164	0.0006	1395.0	33.8	1608.3	23.4	1900.1	19.4	27%		
15Z-158	54.1	3.463	0.023	3.966	0.033	0.0997	0.0005	1635.5	19.1	1627.3	13.6	1616.7	19.5	-1%	1616.7	19.5
15Z-159														0%		
15Z-160	63.7	3.397	0.030	4.095	0.039	0.1009	0.0004	1663.5	26.0	1653.2	15.8	1640.3	15.1	-1%	1640.3	15.1
15Z-161	140.1	5.013	0.043	2.155	0.020	0.0784	0.0003	1172.6	18.3	1166.7	13.0	1155.6	15.8	-1%	1172.6	18.3
15Z-162	268.4	5.184	0.054	2.107	0.023	0.0793	0.0003	1137.1	21.7	1151.1	15.0	1177.5	13.5	3%	1137.1	21.7
15Z-163	227.0	2.012	0.028	14.648	0.212	0.2139	0.0007	2600.9	60.4	2792.6	27.7	2934.2	12.7	11%	2934.2	12.7
15Z-164	302.6	2.388	0.025	9.837	0.110	0.1704	0.0007	2255.0	39.6	2419.7	20.9	2561.2	15.3	12%	2561.2	15.3
15Z-165	292.0	3.423	0.039	4.443	0.053	0.1104	0.0004	1652.0	33.5	1720.3	19.9	1804.5	13.2	8%	1804.5	13.2
15Z-166	212.0	1.908	0.017	14.578	0.135	0.2018	0.0007	2717.0	38.6	2788.1	18.0	2840.0	12.6	4%	2840.0	12.6

Grain I.D.	238U (ppm)	238/206 ratio	206/238 1SE	207/235 ratio	207/235 1SE	207/206 ratio	207/206 1SE	238/206 Age (Ma)	2σ	207/235 Age (Ma)	2σ	207/206 Age (Ma)	2σ	Disc. (%)	preferred Age (Ma)	preferred Err. (2σ)
15Z-167	248.4	4.394	0.046	2.756	0.031	0.0879	0.0003	1321.9	25.2	1343.7	16.6	1378.6	14.4	4%	1378.6	14.4
15Z-168	283.1	5.187	0.058	2.147	0.025	0.0808	0.0003	1136.5	23.3	1164.1	16.4	1215.7	15.5	7%	1136.5	23.3
15Z-169	219.0	2.315	0.054	13.663	0.319	0.2295	0.0007	2314.7	90.1	2726.6	44.3	3047.7	12.2	24%		
15Z-170	203.0	1.914	0.018	14.558	0.151	0.2022	0.0008	2709.4	42.4	2786.8	20.0	2843.3	14.7	5%	2843.3	14.7
15Z-171	129.6	3.488	0.032	3.985	0.039	0.1009	0.0004	1625.0	26.1	1631.1	16.0	1639.0	14.4	1%	1639.0	14.4
15Z-172	134.7	3.535	0.028	4.277	0.059	0.1097	0.0013	1606.0	22.7	1689.0	23.0	1793.6	41.9	10%	1793.6	41.9
15Z-173	208.2	5.695	0.045	1.806	0.016	0.0746	0.0003	1042.9	15.4	1047.5	11.6	1057.1	15.7	1%	1042.9	15.4
15Z-174	420.0	3.310	0.039	4.741	0.059	0.1139	0.0004	1701.7	35.7	1774.4	20.9	1861.1	13.5	9%	1861.1	13.5
15Z-175	455.0	3.535	0.034	4.172	0.043	0.1070	0.0004	1606.0	27.7	1668.6	17.2	1748.3	14.8	8%	1748.3	14.8
15Z-176	170.6	3.253	0.031	4.623	0.046	0.1091	0.0004	1727.9	28.7	1753.4	17.0	1784.0	13.9	3%	1784.0	13.9
15Z-177	200.7	4.558	0.039	2.557	0.024	0.0846	0.0003	1278.7	20.1	1288.3	13.7	1304.4	14.1	2%	1304.4	14.1
15Z-178	141.4	3.765	0.031	3.759	0.034	0.1027	0.0004	1518.4	22.5	1584.1	14.6	1672.7	14.3	9%	1672.7	14.3
15Z-179	218.6	3.438	0.037	4.310	0.049	0.1075	0.0003	1646.0	31.5	1695.2	18.8	1756.6	13.1	6%	1756.6	13.1
15Z-180	156.8	3.427	0.031	4.157	0.040	0.1034	0.0004	1650.5	26.0	1665.7	15.9	1684.8	14.4	2%	1684.8	14.4
15Z-181	125.7	1.970	0.019	13.469	0.139	0.1925	0.0006	2646.8	42.9	2713.1	19.9	2762.9	12.3	4%	2762.9	12.3
15Z-182	65.3	1.935	0.016	13.788	0.122	0.1936	0.0006	2685.6	36.7	2735.3	17.2	2772.2	12.3	3%	2772.2	12.3
15Z-183	80.6	4.382	0.037	2.719	0.025	0.0865	0.0003	1325.1	20.5	1333.8	14.0	1347.8	15.5	2%	1347.8	15.5
15Z-184	382.0	3.561	0.030	4.066	0.037	0.1051	0.0003	1595.4	23.7	1647.5	14.8	1714.7	13.3	7%	1714.7	13.3
15Z-185	90.2	3.299	0.032	4.300	0.045	0.1030	0.0004	1706.7	29.2	1693.5	17.4	1677.1	15.4	-2%	1677.1	15.4
15Z-186	88.2	3.400	0.034	4.112	0.044	0.1015	0.0004	1662.0	29.4	1656.7	17.6	1650.0	15.0	-1%	1650.0	15.0
15Z-187	265.0	2.315	0.021	11.278	0.106	0.1894	0.0006	2314.7	34.8	2546.4	17.8	2736.5	11.8	15%	2736.5	11.8
15Z-188	190.3	2.217	0.029	12.487	0.171	0.2009	0.0007	2399.7	53.4	2641.8	26.0	2832.8	12.6	15%	2832.8	12.6
15Z-189	66.6	3.571	0.033	3.747	0.038	0.0971	0.0004	1591.4	26.2	1581.6	16.2	1568.5	15.3	-1%	1568.5	15.3
15Z-190	144.3	3.177	0.031	4.790	0.049	0.1104	0.0004	1764.3	30.0	1783.1	17.4	1805.2	13.8	2%	1805.2	13.8
15Z-191	584.0	6.566	0.106	2.241	0.037	0.1068	0.0005	913.8	27.4	1194.1	23.5	1744.5	17.3	48%		
15Z-192	57.4	5.618	0.057	1.809	0.020	0.0738	0.0004	1056.0	19.7	1048.8	14.7	1033.7	20.1	-2%	1056.0	19.7
15Z-193	151.2	3.422	0.034	4.121	0.043	0.1023	0.0003	1652.5	29.0	1658.5	17.2	1666.0	13.0	1%	1666.0	13.0
15Z-194	470.0	4.411	0.085	6.232	0.122	0.1995	0.0007	1317.2	45.7	2009.0	34.2	2821.1	13.4	53%		
15Z-195	138.7	1.921	0.018	13.860	0.139	0.1932	0.0006	2701.3	42.1	2740.2	19.3	2768.9	12.3	2%	2768.9	12.3
15Z-196	135.8	3.521	0.032	3.973	0.038	0.1015	0.0004	1611.5	25.7	1628.7	15.8	1651.1	14.1	2%	1651.1	14.1
15Z-197	146.3	3.146	0.031	4.783	0.050	0.1092	0.0004	1779.5	30.9	1781.8	17.7	1784.6	13.5	0%	1784.6	13.5
15Z-198	738.0	5.233	0.047	2.162	0.021	0.0821	0.0003	1127.3	18.4	1168.9	13.6	1246.8	16.1	10%	1127.3	18.4
15Z-199	173.0	2.052	0.023	12.945	0.153	0.1927	0.0007	2559.4	47.8	2675.6	22.6	2764.7	13.8	7%	2764.7	13.8
15Z-200	112.8	1.918	0.016	13.727	0.124	0.1911	0.0006	2704.7	37.4	2731.1	17.4	2750.7	12.4	2%	2750.7	12.4
15Z-201	34.4	5.045	0.053	2.193	0.026	0.0803	0.0004	1165.6	22.6	1178.8	16.4	1203.0	20.5	3%	1165.6	22.6
15Z-202	177.5	5.714	0.049	1.794	0.017	0.0744	0.0003	1039.6	16.5	1043.2	12.1	1050.6	14.7	1%	1039.6	16.5
15Z-203	220.2	4.163	0.050	2.989	0.038	0.0903	0.0004	1387.7	30.2	1404.7	19.4	1430.6	15.7	3%	1430.6	15.7
15Z-204	128.0	1.901	0.022	15.012	0.179	0.2071	0.0007	2724.6	50.8	2816.0	23.0	2882.2	13.0	5%	2882.2	13.0
15Z-205	205.5	1.961	0.019	14.421	0.149	0.2052	0.0007	2656.6	42.8	2777.8	19.9	2867.0	12.5	7%	2867.0	12.5
15Z-206	321.0	2.165	0.030	12.824	0.187	0.2014	0.0008	2448.4	57.4	2666.8	27.8	2836.8	14.7	14%	2836.8	14.7
15Z-207	20.7	1.804	0.020	14.909	0.182	0.1952	0.0011	2842.6	49.9	2809.5	23.5	2785.7	19.7	-2%	2785.7	19.7
15Z-208	72.7	3.362	0.031	4.154	0.041	0.1014	0.0004	1678.4	27.4	1665.0	16.3	1648.2	14.1	-2%	1648.2	14.1
15Z-209	277.0	3.467	0.029	4.156	0.038	0.1046	0.0004	1633.5	24.6	1665.5	15.1	1705.9	13.6	4%	1705.9	13.6
15Z-210	59.7	3.511	0.033	3.872	0.039	0.0987	0.0004	1615.5	26.6	1607.9	16.3	1597.9	14.9	-1%	1597.9	14.9
15Z-211	158.6	3.161	0.033	4.780	0.052	0.1096	0.0004	1772.1	32.4	1781.3	18.5	1792.1	13.0	1%	1792.1	13.0
15Z-212	394.0	10.173	0.223	1.113	0.025	0.0822	0.0004	604.4	25.2	759.6	24.1	1248.5	21.4	52%		
15Z-213	93.4	12.350	0.107	0.863	0.013	0.0773	0.0010	501.9	8.4	631.5	14.2	1128.0	49.2	56%		
15Z-214	187.1	5.086	0.043	2.189	0.020	0.0808	0.0003	1157.0	17.8	1177.5	12.7	1215.5	14.4	5%	1157.0	17.8
15Z-215	36.0	2.023	0.023	11.371	0.133	0.1669	0.0006	2589.7	47.5	2554.0	22.1	2525.8	13.8	-3%	2525.8	13.8
15Z-216	107.5	1.784	0.018	15.513	0.160	0.2009	0.0007	2868.3	45.5	2847.3	20.1	2832.5	12.6	-1%	2832.5	12.6
15Z-217	486.0	4.082	0.042	3.283	0.036	0.0972	0.0004	1412.6	25.9	1477.1	17.0	1571.0	14.9	10%	1571.0	14.9
15Z-218	95.8	4.316	0.038	2.740	0.026	0.0858	0.0003	1343.4	21.5	1339.5	14.2	1333.3	14.3	-1%	1333.3	14.3

10.3.1.9 EM-20 (Zircon)

Grain I.D.	238U (ppm)	238/206 ratio	238/206 1SE	207/235 ratio	207/235 1SE	207/206 ratio	207/206 1SE	238/206 Age (Ma)	2σ	207/235 Age (Ma)	2σ	207/206 Age (Ma)	2σ	Disc. (%)	preferred Age (Ma)	preferred Err. (2σ)
20Z-01	54.4	3.068	0.019	5.036	0.034	0.1121	0.0003	1818.5	19.5	1825.4	11.9	1833.4	11.0	1	1833.4	11.0
20Z-02	29.1	5.631	0.049	1.809	0.019	0.0739	0.0004	1053.8	17.0	1048.8	13.6	1038.4	22.7	-1	1053.8	17.0
20Z-03	402.0	6.519	0.042	1.557	0.011	0.0736	0.0002	920.0	11.2	953.1	8.8	1030.4	11.0	11	920.0	11.2
20Z-04	103.8	2.044	0.010	12.570	0.070	0.1864	0.0004	2567.2	21.8	2648.0	11.1	2710.3	7.5	5	2710.3	7.5
20Z-05	198.2	14.656	0.103	0.512	0.004	0.0545	0.0002	425.5	5.8	419.9	5.7	389.5	19.4	-9	425.5	5.8
20Z-06	109.4	13.075	0.077	0.588	0.005	0.0558	0.0003	475.1	5.4	469.8	5.9	443.8	23.1	-7	475.1	5.4
20Z-07	158.4	5.804	0.032	1.737	0.011	0.0731	0.0002	1024.8	10.5	1022.3	8.2	1016.9	12.2	-1	1024.8	10.5
20Z-08	264.5	13.137	0.053	0.593	0.003	0.0565	0.0002	472.9	3.7	472.9	3.9	472.6	13.7	0	472.9	3.7
20Z-09	130.9	5.488	0.038	1.876	0.014	0.0747	0.0002	1079.0	13.7	1072.6	10.0	1059.5	11.6	-2	1079.0	13.7
20Z-10	23.8	6.035	0.031	1.612	0.014	0.0706	0.0005	988.4	9.5	975.0	11.0	944.9	29.0	-5	988.4	9.5
20Z-11	202.8	5.015	0.021	2.198	0.011	0.0800	0.0002	1172.1	9.2	1180.4	7.3	1195.6	11.1	2	1172.1	9.2
20Z-12	130.2	6.485	0.038	1.482	0.010	0.0697	0.0002	924.5	10.1	923.0	8.1	919.5	12.4	-1	924.5	10.1
20Z-13	348.5	14.706	0.119	0.515	0.005	0.0550	0.0002	424.1	6.7	422.0	6.1	410.8	15.9	-3	424.1	6.7
20Z-14	161.8	13.576	0.070	0.567	0.004	0.0559	0.0002	458.2	4.6	456.1	4.9	445.8	18.3	-3	458.2	4.6
20Z-15	25.2	4.760	0.046	2.385	0.026	0.0824	0.0004	1229.4	21.9	1238.1	15.5	1253.4	18.1	2	1253.4	18.1
20Z-16	155.0	5.118	0.030	2.136	0.014	0.0793	0.0002	1150.6	12.5	1160.5	9.2	1179.0	11.5	2	1150.6	12.5
20Z-17	71.5	5.931	0.040	1.695	0.013	0.0730	0.0002	1004.4	12.7	1006.8	9.8	1011.9	13.6	1	1004.4	12.7
20Z-18	90.2	5.308	0.030	2.017	0.013	0.0777	0.0002	1112.7	11.5	1121.2	8.8	1137.8	12.6	2	1112.7	11.5
20Z-19	150.7	13.405	0.099	0.578	0.005	0.0562	0.0002	463.8	6.6	463.1	6.3	459.7	17.8	-1	463.8	6.6
20Z-20	91.3	2.027	0.013	12.233	0.083	0.1799	0.0004	2584.9	27.3	2622.4	13.3	2651.5	7.9	3	2651.5	7.9
20Z-21	407.3	6.215	0.033	1.627	0.010	0.0734	0.0002	961.8	9.5	980.8	7.6	1023.6	10.8	6	961.8	9.5
20Z-22	618.0	13.799	0.087	0.567	0.004	0.0567	0.0002	451.0	5.5	455.7	5.0	479.7	11.7	6	451.0	5.5
20Z-23	83.2	5.959	0.041	1.687	0.013	0.0730	0.0003	1000.0	12.7	1003.6	10.1	1011.7	15.3	1	1000.0	12.7
20Z-24	95.4	1.995	0.015	12.807	0.100	0.1854	0.0004	2619.4	32.3	2665.5	15.1	2700.8	7.1	3	2700.8	7.1
20Z-25	298.0	13.446	0.064	0.574	0.003	0.0560	0.0002	462.4	4.3	460.5	4.5	451.0	15.9	-3	462.4	4.3
20Z-26	69.3	19.227	0.144	0.378	0.004	0.0527	0.0004	326.9	4.8	325.2	6.3	313.6	38.5	-4	326.9	4.8
20Z-27	87.6	1.948	0.008	13.384	0.061	0.1892	0.0004	2671.1	17.7	2707.1	9.3	2734.1	7.2	2	2734.1	7.2
20Z-28	59.1	3.011	0.026	5.186	0.047	0.1133	0.0003	1848.6	27.7	1850.3	15.5	1852.4	9.9	0	1852.4	9.9
20Z-29	49.7	5.043	0.039	2.155	0.019	0.0789	0.0004	1166.2	16.7	1166.6	12.6	1167.5	17.6	0	1166.2	16.7
20Z-30	519.0	5.189	0.044	2.141	0.019	0.0806	0.0002	1136.0	17.9	1162.2	12.5	1211.3	10.3	6	1136.0	17.9
20Z-31	47.9	13.495	0.091	0.567	0.005	0.0555	0.0003	460.8	6.0	455.9	6.8	431.4	27.7	-7	460.8	6.0
20Z-32	66.9	18.961	0.117	0.383	0.003	0.0526	0.0003	331.3	4.0	329.0	4.8	312.3	26.4	-6	331.3	4.0
20Z-33	102.0	5.879	0.041	1.701	0.013	0.0726	0.0002	1012.7	13.3	1008.8	10.0	1000.5	13.2	-1	1012.7	13.3
20Z-34	47.5	1.966	0.013	12.934	0.090	0.1845	0.0005	2651.1	28.3	2674.9	13.6	2692.9	8.3	2	2692.9	8.3
20Z-35	384.0	13.532	0.101	0.576	0.005	0.0566	0.0002	459.6	6.6	462.1	6.1	474.6	14.5	3	459.6	6.6
20Z-36	81.9	3.004	0.021	5.272	0.039	0.1149	0.0003	1852.4	22.3	1864.3	12.7	1877.5	8.6	1	1877.5	8.6
20Z-37	261.1	18.529	0.142	0.392	0.003	0.0527	0.0002	338.8	5.1	336.0	4.8	316.6	15.5	-7	338.8	5.1
20Z-38	137.7	3.036	0.025	5.174	0.045	0.1140	0.0003	1835.5	26.7	1848.4	15.1	1863.0	9.2	1	1863.0	9.2
20Z-39	36.4	6.064	0.046	1.643	0.014	0.0723	0.0003	984.0	13.9	986.9	11.1	993.5	17.4	1	984.0	13.9
20Z-40	43.1	4.239	0.032	2.888	0.024	0.0888	0.0003	1365.3	18.8	1378.8	12.7	1399.6	12.7	2	1399.6	12.7
20Z-41	27.7	5.025	0.035	2.173	0.019	0.0792	0.0004	1169.9	15.1	1172.3	12.2	1176.7	20.2	1	1169.9	15.1
20Z-42	63.5	4.815	0.032	2.342	0.017	0.0818	0.0003	1216.6	15.0	1225.2	10.7	1240.6	12.2	2	1240.6	12.2
20Z-43	166.5	5.797	0.040	1.769	0.013	0.0744	0.0002	1025.9	13.2	1034.2	9.8	1052.0	10.8	2	1025.9	13.2
20Z-44	145.5	15.432	0.119	0.490	0.004	0.0549	0.0002	404.8	6.1	404.8	5.9	405.1	19.6	0	404.8	6.1
20Z-45	259.9	3.729	0.021	3.774	0.023	0.1021	0.0002	1531.7	15.3	1587.3	9.9	1662.0	8.5	8	1662.0	8.5
20Z-46	62.1	10.309	0.058	0.807	0.007	0.0604	0.0004	596.8	6.5	600.7	7.6	615.5	26.1	3	596.8	6.5
20Z-47	121.4	2.178	0.017	11.585	0.095	0.1831	0.0005	2436.0	31.5	2571.4	15.7	2680.0	8.9	9	2680.0	8.9
20Z-48	63.4	5.770	0.035	1.777	0.012	0.0744	0.0002	1030.3	11.6	1037.0	9.0	1051.2	13.0	2	1030.3	11.6
20Z-49	236.0	4.810	0.036	2.367	0.019	0.0826	0.0002	1217.6	16.6	1232.8	11.5	1259.4	10.9	3	1259.4	10.9
20Z-50	105.7	5.222	0.027	2.048	0.013	0.0776	0.0003	1129.5	10.9	1131.7	8.5	1136.0	12.8	1	1129.5	10.9
20Z-51	31.3	1.938	0.012	13.418	0.090	0.1887	0.0006	2682.6	26.5	2709.5	13.1	2729.7	9.6	2	2729.7	9.6
20Z-52	321.9	5.252	0.037	2.049	0.015	0.0781	0.0002	1123.5	14.7	1132.0	10.4	1148.3	10.4	2	1123.5	14.7

Grain I.D.	238U (ppm)	238/206 ratio	238/206 1SE	207/235 ratio	207/235 1SE	207/206 ratio	207/206 1SE	238/206 Age (Ma)	2σ	207/235 Age (Ma)	2σ	207/206 Age (Ma)	2σ	Disc. (%)	preferred Age (Ma)	preferred Err. (2σ)
20Z-53	52.1	4.281	0.035	2.791	0.024	0.0867	0.0003	1353.3	19.9	1353.2	13.2	1353.0	12.3	0	1353.0	12.3
20Z-54	88.5	4.207	0.034	2.858	0.024	0.0872	0.0003	1374.7	19.8	1370.9	13.0	1364.9	11.7	-1	1364.9	11.7
20Z-55	107.7	3.855	0.025	3.328	0.023	0.0931	0.0003	1486.8	17.0	1487.7	11.1	1489.1	11.0	0	1489.1	11.0
20Z-56	18.2	5.774	0.038	1.751	0.015	0.0733	0.0004	1029.7	12.7	1027.4	11.4	1022.5	23.2	-1	1029.7	12.7
20Z-57	55.9	4.308	0.019	2.757	0.014	0.0862	0.0003	1345.5	10.6	1344.0	8.0	1341.6	11.4	0	1341.6	11.4
20Z-58	19.9	4.682	0.025	2.420	0.020	0.0822	0.0005	1248.0	12.3	1248.5	11.8	1249.4	23.8	0	1249.4	23.8
20Z-59	133.8	5.974	0.020	1.680	0.008	0.0728	0.0002	997.8	6.2	1001.2	6.0	1008.6	13.1	1	997.8	6.2
20Z-60	275.0	4.494	0.016	2.640	0.011	0.0861	0.0002	1295.1	8.6	1311.7	6.5	1339.1	8.6	3	1339.1	8.6
20Z-61	163.3	4.794	0.021	2.343	0.012	0.0815	0.0002	1221.4	9.7	1225.4	7.4	1232.4	10.6	1	1232.4	10.6
20Z-62	52.4	5.187	0.022	2.062	0.012	0.0776	0.0003	1136.5	8.7	1136.3	8.0	1135.8	15.9	0	1136.5	8.7
20Z-63	48.7	1.916	0.011	13.541	0.088	0.1882	0.0005	2707.7	26.4	2718.2	12.8	2726.0	8.8	1	2726.0	8.8
20Z-64	49.3	5.479	0.030	1.858	0.013	0.0739	0.0003	1080.6	11.0	1066.2	9.1	1036.7	16.4	-4	1080.6	11.0
20Z-65	128.0	4.373	0.019	2.781	0.014	0.0882	0.0003	1327.7	10.6	1350.3	8.0	1386.4	10.9	4	1386.4	10.9
20Z-66	82.6	3.206	0.020	4.690	0.032	0.1091	0.0003	1750.0	19.3	1765.5	11.6	1783.8	9.5	2	1783.8	9.5
20Z-67	326.0	5.157	0.027	2.118	0.012	0.0793	0.0002	1142.5	10.9	1154.8	8.2	1178.0	11.0	3	1142.5	10.9
20Z-68	89.6	5.734	0.028	1.784	0.011	0.0742	0.0003	1036.3	9.4	1039.6	7.8	1046.5	13.6	1	1036.3	9.4
20Z-69	76.3	19.198	0.140	0.380	0.004	0.0529	0.0004	327.3	4.7	326.7	6.0	322.2	36.1	-2	327.3	4.7
20Z-70	40.2	5.612	0.031	1.819	0.014	0.0741	0.0004	1057.1	11.0	1052.3	9.8	1042.2	19.6	-1	1057.1	11.0
20Z-71	153.8	3.067	0.020	5.198	0.037	0.1157	0.0003	1819.5	21.0	1852.4	12.3	1889.5	9.0	4	1889.5	9.0
20Z-72	230.9	5.333	0.037	2.026	0.015	0.0784	0.0002	1107.8	14.2	1124.2	10.1	1155.9	9.9	4	1107.8	14.2
20Z-73	64.4	5.382	0.032	1.990	0.013	0.0777	0.0002	1098.6	12.0	1112.3	9.1	1139.1	11.8	4	1098.6	12.0
20Z-74	278.8	3.146	0.011	4.989	0.021	0.1139	0.0002	1779.5	11.4	1817.5	7.5	1861.4	7.8	4	1861.4	7.8
20Z-75	78.8	5.504	0.026	1.873	0.011	0.0748	0.0003	1076.3	9.3	1071.5	8.2	1062.0	15.6	-1	1076.3	9.3
20Z-76	89.8	5.362	0.030	1.939	0.013	0.0754	0.0003	1102.4	11.5	1094.7	9.0	1079.3	14.1	-2	1102.4	11.5
20Z-77	206.1	14.954	0.073	0.506	0.003	0.0549	0.0002	417.3	4.0	415.9	4.0	408.4	13.9	-2	417.3	4.0
20Z-78	141.2	5.269	0.024	2.057	0.011	0.0786	0.0002	1120.3	9.3	1134.5	7.2	1161.7	10.4	4	1120.3	9.3
20Z-79	92.8	5.869	0.029	1.719	0.011	0.0732	0.0003	1014.3	9.4	1015.6	8.2	1018.3	15.5	0	1014.3	9.4
20Z-80	243.9	13.784	0.080	0.559	0.004	0.0559	0.0002	451.5	5.1	451.0	4.9	448.2	14.7	-1	451.5	5.1
20Z-81	53.0	13.583	0.086	0.616	0.009	0.0607	0.0008	457.9	5.6	487.3	11.3	627.7	56.8	27	457.9	5.6
20Z-82	189.1	16.085	0.076	0.475	0.003	0.0555	0.0003	388.8	3.6	394.8	4.8	430.2	24.9	10	388.8	3.6
20Z-83	191.5	6.010	0.027	1.690	0.009	0.0737	0.0002	992.2	8.4	1004.7	6.9	1032.1	11.5	4	992.2	8.4
20Z-84	96.2	13.978	0.072	0.546	0.004	0.0554	0.0003	445.4	4.5	442.6	5.2	428.2	22.5	-4	445.4	4.5
20Z-85	245.3	3.416	0.019	4.309	0.025	0.1068	0.0002	1655.0	16.1	1695.2	10.0	1745.2	8.1	5	1745.2	8.1
20Z-86	79.9	13.535	0.063	0.571	0.004	0.0561	0.0003	459.5	4.2	458.5	5.3	453.4	23.8	-1	459.5	4.2
20Z-87	170.2	3.332	0.015	4.493	0.022	0.1086	0.0002	1691.8	13.5	1729.7	8.6	1775.9	7.6	5	1775.9	7.6
20Z-88	145.8	6.031	0.031	1.672	0.010	0.0732	0.0002	988.9	9.5	997.8	7.4	1017.5	10.0	3	988.9	9.5
20Z-89	34.9	2.230	0.011	9.944	0.057	0.1609	0.0004	2388.1	20.6	2429.6	11.1	2464.6	8.7	3	2464.6	8.7
20Z-90	67.6	13.930	0.080	0.550	0.004	0.0556	0.0003	446.9	5.0	444.9	5.9	434.2	26.1	-3	446.9	5.0
20Z-91	80.3	4.617	0.018	2.562	0.013	0.0858	0.0003	1263.9	9.1	1289.9	7.5	1333.5	11.7	5	1333.5	11.7
20Z-92	66.9	5.824	0.031	1.753	0.012	0.0741	0.0003	1021.5	10.0	1028.2	8.7	1042.5	16.4	2	1021.5	10.0
20Z-93	78.9	14.112	0.069	0.549	0.005	0.0562	0.0004	441.3	4.2	444.4	6.0	460.5	29.6	4	441.3	4.2
20Z-94	207.1	3.786	0.019	3.673	0.020	0.1009	0.0002	1510.8	13.4	1565.4	9.0	1639.9	9.0	8	1639.9	9.0
20Z-95	408.0	5.981	0.025	1.730	0.008	0.0751	0.0002	996.7	7.8	1019.6	6.4	1069.2	9.7	7	996.7	7.8
20Z-96	61.4	4.122	0.028	2.960	0.022	0.0885	0.0003	1400.2	17.2	1397.5	11.5	1393.4	11.7	0	1393.4	11.7
20Z-97	85.7	2.146	0.012	11.989	0.074	0.1867	0.0004	2465.6	23.9	2603.6	12.1	2712.7	6.9	9	2712.7	6.9
20Z-98	81.8	6.105	0.026	1.661	0.010	0.0736	0.0003	977.9	7.8	993.6	7.4	1028.5	15.4	5	977.9	7.8
20Z-99	49.5	3.555	0.020	3.984	0.024	0.1028	0.0003	1597.9	15.7	1631.0	10.2	1673.9	9.7	5	1673.9	9.7
20Z-100	136.4	6.192	0.033	1.625	0.010	0.0730	0.0002	965.1	9.5	980.0	7.9	1013.6	13.3	5	965.1	9.5
20Z-101	114.9	14.762	0.096	0.510	0.004	0.0547	0.0003	422.5	5.3	418.6	5.7	396.9	22.6	-6	422.5	5.3
20Z-102	232.0	3.431	0.014	4.318	0.021	0.1075	0.0003	1649.0	12.1	1696.9	8.2	1756.5	8.9	6	1756.5	8.9
20Z-103	139.2	5.669	0.027	1.807	0.010	0.0743	0.0002	1047.3	9.4	1047.8	7.5	1049.0	11.7	0	1047.3	9.4
20Z-104	174.1	2.870	0.011	5.836	0.025	0.1215	0.0003	1927.0	12.6	1951.7	7.9	1978.2	7.8	3	1978.2	7.8
20Z-105	158.9	5.992	0.038	1.701	0.012	0.0740	0.0002	995.0	11.6	1009.1	8.8	1039.7	10.7	4	995.0	11.6
20Z-106	84.6	5.744	0.043	1.782	0.015	0.0743	0.0003	1034.7	14.3	1038.8	10.9	1047.6	14.7	1	1034.7	14.3
20Z-107	30.9	6.502	0.036	1.484	0.012	0.0700	0.0004	922.2	9.5	923.8	9.9	927.4	24.4	1	922.2	9.5
20Z-108	86.0	4.706	0.035	2.426	0.021	0.0828	0.0004	1242.1	17.1	1250.4	12.7	1264.6	17.2	2	1264.6	17.2
20Z-109	89.7	3.750	0.020	3.624	0.022	0.0986	0.0003	1524.0	14.8	1554.8	10.0	1597.0	10.8	5	1597.0	10.8

Grain I.D.	238U (ppm)	238/206 ratio	238/206 1SE	207/235 ratio	207/235 1SE	207/206 ratio	207/206 1SE	238/206 Age (Ma)	2σ	207/235 Age (Ma)	2σ	207/206 Age (Ma)	2σ	Disc. (%)	preferred Age (Ma)	preferred Err. (2σ)
20Z-110	110.8	3.065	0.023	5.071	0.040	0.1128	0.0003	1820.4	23.9	1831.3	13.7	1843.7	9.2	1	1843.7	9.2
20Z-111	31.7	1.346	0.011	34.386	0.291	0.3358	0.0009	3581.7	44.5	3621.2	17.4	3643.1	7.8	2	3643.1	7.8
20Z-112	224.0	4.829	0.036	2.374	0.019	0.0832	0.0002	1213.3	16.6	1234.7	11.4	1272.1	9.6	5	1272.1	9.6
20Z-113	70.5	5.615	0.039	1.833	0.015	0.0747	0.0003	1056.6	13.7	1057.5	10.7	1059.3	15.9	0	1056.6	13.7
20Z-114	66.2	4.527	0.029	2.597	0.019	0.0853	0.0003	1286.6	14.8	1299.9	10.6	1322.0	12.7	3	1322.0	12.7
20Z-115	206.6	5.414	0.048	1.980	0.018	0.0778	0.0002	1092.6	18.0	1108.9	12.6	1140.9	10.0	4	1092.6	18.0
20Z-116	122.5	14.514	0.126	0.517	0.005	0.0545	0.0003	429.5	7.3	423.4	7.1	389.9	23.5	-10	429.5	7.3
20Z-117	124.6	5.252	0.041	2.037	0.017	0.0776	0.0002	1123.5	16.3	1128.1	11.5	1136.8	11.6	1	1123.5	16.3
20Z-118	13.6	5.405	0.056	1.922	0.024	0.0754	0.0005	1094.2	20.7	1088.9	16.4	1078.3	26.6	-1	1094.2	20.7
20Z-119	127.6	3.178	0.026	4.766	0.040	0.1099	0.0003	1763.8	25.1	1778.9	14.4	1796.6	8.8	2	1796.6	8.8
20Z-120	29.3	5.770	0.042	1.708	0.014	0.0715	0.0003	1030.3	13.8	1011.4	10.9	970.8	18.0	-6	1030.3	13.8
20Z-121	160.2	1.976	0.012	12.988	0.085	0.1862	0.0004	2640.0	26.7	2678.8	12.9	2708.2	7.7	3	2708.2	7.7
20Z-122	15.7	13.055	0.094	0.593	0.007	0.0562	0.0005	475.8	6.6	473.0	8.7	459.3	39.5	-4	475.8	6.6
20Z-123	294.4	18.622	0.191	0.391	0.004	0.0529	0.0002	337.2	6.7	335.3	6.3	322.2	18.1	-5	337.2	6.7
20Z-124	64.3	5.587	0.042	1.839	0.016	0.0746	0.0004	1061.5	14.8	1059.6	11.9	1055.8	19.5	-1	1061.5	14.8
20Z-125	264.1	13.626	0.092	0.568	0.004	0.0562	0.0002	456.5	6.0	456.9	5.6	458.9	15.0	1	456.5	6.0
20Z-126	54.6	5.734	0.048	1.801	0.017	0.0749	0.0003	1036.3	16.0	1045.8	12.3	1065.7	17.5	3	1036.3	16.0
20Z-127	31.3	5.790	0.047	1.753	0.017	0.0737	0.0004	1027.0	15.4	1028.4	12.3	1031.5	19.8	0	1027.0	15.4
20Z-128	351.1	13.620	0.091	0.568	0.004	0.0561	0.0002	456.7	5.9	456.8	5.4	456.9	13.1	0	456.7	5.9
20Z-129	127.0	6.013	0.036	1.677	0.011	0.0732	0.0002	991.7	11.1	999.8	8.8	1017.5	13.0	3	991.7	11.1
20Z-130	25.6	4.602	0.038	2.510	0.024	0.0838	0.0004	1267.6	19.1	1275.0	13.9	1287.5	18.1	2	1287.5	18.1
20Z-131	144.3	4.398	0.030	2.744	0.020	0.0876	0.0002	1320.9	16.3	1340.6	10.9	1372.2	9.0	4	1372.2	9.0
20Z-132	172.6	5.734	0.043	1.811	0.014	0.0754	0.0002	1036.3	14.3	1049.6	10.5	1077.2	10.9	4	1036.3	14.3
20Z-133	19.0	2.342	0.033	9.781	0.163	0.1662	0.0015	2292.2	54.3	2414.3	30.9	2519.0	30.3	9	2519.0	30.3
20Z-134	129.2	6.345	0.044	1.574	0.012	0.0725	0.0002	943.4	12.3	960.0	9.5	998.3	12.1	5	943.4	12.3
20Z-135	60.2	5.549	0.035	1.847	0.014	0.0744	0.0003	1068.1	12.6	1062.4	10.1	1050.9	16.5	-2	1068.1	12.6
20Z-136	179.2	13.289	0.074	0.577	0.004	0.0557	0.0002	467.7	5.1	462.8	4.9	438.2	14.8	-7	467.7	5.1
20Z-137	58.4	1.888	0.009	14.097	0.074	0.1931	0.0005	2739.8	21.3	2756.3	10.7	2768.3	7.7	1	2768.3	7.7
20Z-138	97.1	19.153	0.121	0.378	0.003	0.0525	0.0003	328.1	4.1	325.4	5.0	306.2	29.1	-7	328.1	4.1
20Z-139	189.2	5.817	0.041	1.736	0.013	0.0733	0.0002	1022.6	13.2	1022.0	9.7	1020.8	10.2	0	1022.6	13.2
20Z-140	142.7	3.233	0.017	4.674	0.027	0.1097	0.0002	1737.3	16.4	1762.7	10.0	1792.9	8.2	3	1792.9	8.2
20Z-141	103.2	6.662	0.027	1.432	0.008	0.0692	0.0003	901.5	6.8	902.2	6.9	903.8	16.7	0	901.5	6.8

10.3.1.10 EM-17 (Apatite)

rain I.D.	238U (ppm)	238/206 ratio	238/206 1SE	207/235 ratio	207/235 1SE	207/206 ratio	207/206 1SE	238/206 Age (Ma)	2σ	207/235 Age (Ma)	2σ	207/206 Age (Ma)	2σ	Disc. (%)	preferred Age (Ma)	preferred Err. (2σ)
17A-01	23.4	8.537	0.077	5.678	0.288	0.3517	0.0176	714.1	12.2	1928.1	87.8	3713.8	152.5	81	435.6	3.7
17A-02	2.8	4.452	0.085	17.681	0.946	0.5712	0.0286	1306.2	45.0	2972.6	102.9	4435.7	146.1	71	417.3	7.2
17A-03	5.0	5.771	0.064	12.002	0.615	0.5026	0.0251	1030.1	21.0	2604.5	96.0	4248.1	147.6	76	422.8	4.4
17A-04	16.5	7.430	0.037	7.362	0.370	0.3969	0.0198	814.0	7.6	2156.4	89.9	3896.7	150.7	79	448.6	2.1
17A-05	0.3	1.704	7.381	66.313	287.312	0.8197	0.0410	2977.1	20659.5	4274.1	8667.9	4955.8	142.5	40		
17A-06	12.6	9.576	0.080	3.999	0.203	0.2779	0.0139	640.3	10.1	1634.0	82.4	3350.3	156.5	81	453.4	3.6
17A-07	4.5	4.356	0.054	18.435	0.950	0.5827	0.0291	1332.2	29.9	3012.7	99.3	4464.8	145.9	70	404.3	4.7
17A-08	1.4	0.976	0.029	75.116	4.374	0.5317	0.0266	4548.7	194.8	4398.9	116.8	4330.9	146.9	-5		
17A-09	3.0	2.730	0.038	33.954	1.763	0.6726	0.0336	2011.9	48.4	3608.7	102.5	4672.7	144.4	57	365.9	4.8
17A-10	16.7	8.166	0.074	6.197	0.315	0.3672	0.0184	744.7	12.8	2004.1	88.9	3779.4	151.8	80	439.2	3.8
17A-11	23.3	8.291	0.124	5.884	0.307	0.3540	0.0177	734.1	20.7	1958.9	90.6	3723.4	152.4	80	446.0	6.2
17A-12	19.4	8.510	0.109	5.542	0.286	0.3422	0.0171	716.2	17.5	1907.2	88.9	3672.0	152.9	80	446.2	5.4
17A-13	18.4	8.009	0.080	6.247	0.319	0.3631	0.0182	758.5	14.4	2011.1	89.3	3762.0	152.0	80	452.0	4.3
17A-14	22.5	8.849	0.059	5.077	0.256	0.3260	0.0163	690.2	8.7	1832.2	85.6	3597.5	153.7	81	444.8	2.8
17A-15	35.1	9.732	0.064	4.086	0.206	0.2885	0.0144	630.5	7.9	1651.4	82.3	3408.9	155.8	82	437.2	2.7
17A-16	11.5	6.853	0.062	8.965	0.456	0.4458	0.0223	878.1	14.9	2334.5	92.9	4070.5	149.1	78	426.4	3.7
17A-17	19.5	7.573	0.066	7.457	0.379	0.4097	0.0205	799.6	13.2	2167.9	90.9	3944.5	150.3	80	426.2	3.6
17A-18	45.9	12.506	0.101	1.543	0.078	0.1400	0.0070	495.9	7.7	947.8	62.4	2226.8	173.3	78	440.9	3.4
17A-19	0.0	4.515	14.588	31.126	100.582	1.0197	0.0510	1289.7	7553.7	3523.0	6358.1	5264.1	140.7	75		
17A-20	17.2	10.286	0.099	3.505	0.178	0.2616	0.0131	598.1	11.0	1528.3	80.5	3255.5	157.6	82	435.9	4.0
17A-21	8.3	6.888	0.092	8.958	0.464	0.4477	0.0224	873.9	21.8	2333.7	94.6	4076.9	149.1	79	421.9	5.3
17A-22	39.7	9.980	0.086	3.590	0.182	0.2599	0.0130	615.6	10.2	1547.2	80.6	3245.7	157.7	81	450.3	3.7
17A-23	100.0	11.851	0.282	2.301	0.127	0.1979	0.0099	522.2	23.9	1212.7	78.4	2808.3	163.6	81	424.1	8.8
17A-24	9.9	1.825	0.019	16.485	0.842	0.2183	0.0109	2816.2	47.3	2905.4	97.8	2967.8	161.3	5		
17A-25	13.4	6.953	0.037	8.561	0.430	0.4319	0.0216	866.3	8.7	2292.4	91.5	4023.3	149.5	78	437.0	2.2
17A-26	13.3	7.651	0.104	6.637	0.344	0.3685	0.0184	791.8	20.3	2064.3	91.5	3784.5	151.8	79	466.8	5.9
17A-27	8.5	4.373	0.061	17.655	0.917	0.5602	0.0280	1327.5	33.7	2971.1	99.9	4407.4	146.3	70	445.6	5.8
17A-28	0.6	6.487	1.358	10.999	2.367	0.5178	0.0259	924.2	360.4	2523.1	400.6	4291.9	147.3	78		
17A-29	59.2	10.134	0.084	3.549	0.180	0.2609	0.0130	606.7	9.6	1538.2	80.3	3251.7	157.7	81	442.8	3.5
17A-30	1.5	3.340	0.069	26.746	1.448	0.6483	0.0324	1688.1	61.6	3374.2	106.1	4619.5	144.8	63	361.2	6.7
17A-31	37.5	9.312	0.101	4.337	0.222	0.2931	0.0147	657.5	13.6	1700.4	84.5	3433.2	155.5	81	452.4	4.6
17A-32	0.0	0.898	0.620	124.279	86.076	0.8099	0.0405	4823.9	4692.2	4904.8	1395.3	4938.6	142.7	2		
17A-33	39.3	9.623	0.070	3.981	0.201	0.2779	0.0139	637.3	8.9	1630.3	82.0	3350.7	156.5	81	451.2	3.1
17A-34	2.9	2.814	0.055	32.290	1.734	0.6592	0.0330	1960.4	66.3	3559.2	105.9	4643.6	144.6	58	395.1	7.0
17A-35	35.1	9.848	0.089	4.000	0.203	0.2858	0.0143	623.5	10.8	1634.2	82.6	3394.3	156.0	82	434.4	3.8
17A-36	15.1	8.670	0.098	5.691	0.292	0.3580	0.0179	703.7	15.1	1930.0	88.6	3740.8	152.2	81	423.0	4.5
17A-37	37.6	10.626	0.083	2.989	0.151	0.2304	0.0115	579.8	8.7	1404.8	77.0	3054.4	160.2	81	446.6	3.3
17A-38	3.6	3.466	0.044	24.973	1.289	0.6280	0.0314	1634.2	36.9	3307.2	100.9	4573.5	145.1	64	397.3	4.8
17A-39	18.5	7.522	0.059	7.217	0.365	0.3939	0.0197	804.6	11.8	2138.6	90.3	3885.3	150.8	79	446.6	3.3
17A-40	33.9	10.135	0.079	3.503	0.177	0.2576	0.0129	606.6	9.0	1528.0	80.0	3231.6	157.9	81	445.5	3.3
17A-41	18.3	7.102	0.046	8.323	0.420	0.4289	0.0214	849.2	10.3	2266.9	91.5	4013.0	149.6	79	431.5	2.7
17A-42	28.4	9.519	0.114	4.457	0.229	0.3078	0.0154	643.9	14.7	1723.0	85.3	3509.5	154.7	82	429.9	4.8
17A-43	3.8	5.676	0.077	9.228	0.478	0.3801	0.0190	1046.1	26.1	2360.9	94.9	3831.3	151.3	73		
17A-44	6.2	5.282	0.067	15.461	0.798	0.5925	0.0296	1117.7	26.1	2844.1	98.5	4489.2	145.7	75	318.9	3.8
17A-45	0.0	1.885	1.396	60.160	44.646	0.8228	0.0411	2743.7	3309.1	4176.8	1482.5	4961.1	142.5	45		
17A-46	4.9	3.678	0.057	24.428	1.279	0.6519	0.0326	1550.3	43.0	3285.6	102.3	4627.6	144.7	66	320.1	4.7
17A-47	1.8	1.965	0.052	48.444	2.744	0.6908	0.0345	2651.8	115.8	3960.8	112.8	4711.0	144.1	44	428.6	9.7
17A-48	3.7	1.974	0.026	22.281	1.151	0.3191	0.0160	2642.4	56.3	3196.0	100.5	3564.7	154.1	26		
17A-49	16.4	8.622	0.139	6.351	0.334	0.3973	0.0199	707.4	21.6	2025.5	92.2	3898.2	150.7	82	387.3	5.8
17A-50	63.8	12.258	0.066	1.717	0.086	0.1527	0.0076	505.5	5.2	1014.9	64.5	2375.6	170.6	79	441.0	2.3
17A-51	7.5	6.429	0.070	9.975	0.510	0.4653	0.0233	932.0	18.8	2432.4	94.5	4134.2	148.6	77	428.7	4.4
17A-52	0.8	0.994	0.052	105.067	7.615	0.7575	0.0379	4489.0	339.3	4735.8	145.9	4843.2	143.3	7	279.6	9.9

rain I.D.	238U (ppm)	238/206 ratio	238/206 1SE	207/235 ratio	207/235 1SE	207/206 ratio	207/206 1SE	238/206 Age (Ma)	2σ	207/235 Age (Ma)	2σ	207/206 Age (Ma)	2σ	Disc. (%)	preferred Age (Ma)	preferred Err. (2σ)
17A-53	11.1	7.261	0.073	7.786	0.397	0.4102	0.0205	831.8	15.7	2206.5	91.8	3946.1	150.2	79	443.7	4.2
17A-54	25.8	10.122	0.064	3.741	0.189	0.2748	0.0137	607.3	7.3	1580.2	80.8	3332.8	156.7	82	431.9	2.6
17A-55	14.6	8.259	0.056	5.887	0.297	0.3528	0.0176	736.8	9.5	1959.4	87.6	3718.4	152.4	80	448.9	2.9
17A-56	27.9	10.804	0.067	2.834	0.143	0.2222	0.0111	570.7	6.8	1364.6	75.7	2995.7	161.0	81	445.7	2.7
17A-57	264.7	7.496	0.076	1.387	0.071	0.0755	0.0038	807.2	15.3	883.6	60.2	1080.1	200.7	25		
17A-58	8.7	4.720	0.074	16.010	0.839	0.5483	0.0274	1238.8	35.3	2877.4	100.2	4375.9	146.6	72	434.5	6.3
17A-59	42.9	11.834	0.112	2.151	0.109	0.1847	0.0092	523.0	9.5	1165.4	70.6	2694.7	165.3	81	434.0	3.9
17A-60	28.8	8.447	0.077	5.795	0.295	0.3552	0.0178	721.3	12.5	1945.6	88.1	3728.6	152.3	81	436.7	3.8
17A-61	18.3	6.321	0.041	10.555	0.532	0.4841	0.0242	946.8	11.3	2484.8	93.6	4192.8	148.1	77	411.1	2.5
17A-62	0.0	3.184	6.036	34.587	65.588	0.7990	0.0400	1760.7	5841.5	3626.9	3742.8	4919.4	142.8	64		
17A-63	18.4	8.010	0.087	6.772	0.347	0.3936	0.0197	758.4	15.7	2082.1	90.6	3884.2	150.8	80	420.1	4.3
17A-64	27.5	9.162	0.179	4.718	0.253	0.3137	0.0157	667.8	24.9	1770.5	90.0	3538.3	154.3	81	441.0	7.8
17A-65	33.0	9.990	0.086	4.185	0.212	0.3034	0.0152	615.0	10.2	1671.2	83.2	3486.9	154.9	82	413.7	3.4
17A-66	36.3	9.432	0.083	4.583	0.233	0.3136	0.0157	649.6	10.9	1746.1	84.7	3538.2	154.3	82	428.6	3.6
17A-67	10.5	4.648	0.052	16.329	0.837	0.5507	0.0275	1256.3	25.7	2896.3	98.1	4382.3	146.5	71	436.9	4.6
17A-68	10.0	10.527	0.144	3.666	0.190	0.2800	0.0140	585.0	15.3	1563.9	82.7	3362.2	156.3	83	411.5	5.3
17A-69	20.3	7.507	0.061	6.970	0.353	0.3796	0.0190	806.2	12.3	2107.6	90.0	3829.6	151.3	79	463.3	3.6
17A-70	28.1	9.153	0.062	4.154	0.210	0.2759	0.0138	668.4	8.7	1665.1	82.6	3339.1	156.6	80	475.7	3.1
17A-71	3.5	3.852	0.099	21.178	1.191	0.5920	0.0296	1487.7	68.5	3146.8	109.2	4487.7	145.7	67	436.2	9.7
17A-72	28.2	9.250	0.068	4.197	0.212	0.2817	0.0141	661.7	9.3	1673.4	82.9	3371.6	156.2	80	465.6	3.3
17A-73	12.0	5.809	0.045	11.586	0.586	0.4883	0.0244	1024.0	14.7	2571.6	94.6	4205.7	148.0	76	440.6	3.3
17A-74	0.0	2.772	2.288	37.427	30.943	0.7528	0.0376	1985.7	2820.7	3704.9	1635.3	4834.3	143.3	59		
17A-75	3.3	2.995	0.094	29.442	1.740	0.6399	0.0320	1857.0	101.7	3468.4	116.2	4600.6	144.9	60	425.4	11.0
17A-76	17.2	7.147	0.077	7.867	0.402	0.4080	0.0204	844.2	17.2	2215.9	92.2	3938.1	150.3	79	453.2	4.6
17A-77	37.4	8.875	0.073	4.920	0.249	0.3168	0.0158	688.3	10.8	1805.6	85.6	3553.7	154.2	81	452.1	3.6
17A-78	28.1	8.668	0.086	5.136	0.262	0.3230	0.0162	703.9	13.2	1842.1	86.7	3583.5	153.9	80	456.7	4.3
17A-79	9.9	6.543	0.077	9.574	0.492	0.4545	0.0227	916.9	20.2	2394.6	94.5	4099.3	148.9	78	435.1	4.8
17A-80	1.6	1.361	0.050	77.936	4.826	0.7699	0.0385	3550.3	199.5	4435.8	124.3	4866.3	143.1	27	127.4	3.7
17A-81	22.7	8.222	0.082	5.704	0.291	0.3403	0.0170	739.9	14.0	1932.0	88.1	3663.5	153.0	80	463.5	4.4
17A-82	0.2	37.553	230.268	2.569	15.754	0.7000	0.0350	169.4	2050.6	1291.9	8963.7	4730.1	144.0	96		
17A-83	14.7	8.520	0.095	5.290	0.271	0.3270	0.0164	715.4	15.1	1867.2	87.5	3602.4	153.7	80	460.6	4.8
17A-84	11.5	7.453	0.065	6.803	0.345	0.3679	0.0184	811.6	13.4	2086.1	89.9	3782.2	151.8	79	479.6	4.0
17A-85	3.8	3.757	0.060	21.877	1.148	0.5964	0.0298	1521.3	43.4	3178.3	102.0	4498.5	145.7	66	437.3	6.4
17A-86	11.4	7.131	0.102	7.714	0.401	0.3991	0.0200	846.0	22.7	2198.2	93.6	3905.2	150.6	78	464.5	6.2
17A-87	8.0	4.170	0.092	18.942	1.036	0.5732	0.0287	1385.6	55.2	3038.9	105.5	4440.8	146.1	69	441.0	8.6
17A-88	8.5	5.516	0.074	11.706	0.606	0.4685	0.0234	1074.0	26.7	2581.2	97.0	4144.5	148.5	74	493.2	6.2
17A-89	5.8	4.196	0.051	18.948	0.975	0.5769	0.0288	1377.9	30.3	3039.2	99.4	4450.3	146.0	69	430.9	4.9
17A-90	34.4	9.020	0.068	4.538	0.229	0.2970	0.0149	677.7	9.7	1737.9	84.2	3454.0	155.3	80	463.2	3.3
17A-91	25.0	9.220	0.066	5.138	0.260	0.3437	0.0172	663.8	9.1	1842.4	85.9	3678.8	152.9	82	411.1	2.8
17A-92	18.6	9.065	0.104	4.728	0.243	0.3110	0.0155	674.6	14.8	1772.3	86.0	3525.2	154.5	81	448.1	4.9
17A-93	7.6	5.619	0.062	12.018	0.615	0.4900	0.0245	1055.8	21.5	2605.8	96.1	4210.7	147.9	75	452.7	4.7
17A-94	5.7	4.748	0.068	15.249	0.793	0.5253	0.0263	1232.1	32.2	2830.9	99.2	4313.2	147.1	71	472.2	6.3
17A-95	24.4	9.569	0.132	3.821	0.198	0.2653	0.0133	640.8	16.9	1597.2	83.5	3277.8	157.3	80	464.6	6.0
17A-96	17.8	7.602	0.056	6.390	0.323	0.3524	0.0176	796.7	11.1	2030.8	88.8	3716.9	152.5	79	487.3	3.4
17A-97	68.5	8.958	0.066	3.901	0.197	0.2536	0.0127	682.2	9.6	1613.9	81.7	3206.6	158.2	79	506.5	3.6
17A-98	34.3	11.284	0.109	2.442	0.124	0.1999	0.0100	547.4	10.2	1255.1	73.4	2825.0	163.4	81	443.5	4.1
17A-99	12.9	7.965	0.076	7.056	0.359	0.4078	0.0204	762.4	13.7	2118.5	90.6	3937.4	150.3	81	407.6	3.7
17A-100	13.3	6.686	0.065	9.200	0.469	0.4463	0.0223	898.6	16.3	2358.1	93.3	4072.2	149.1	78	436.2	4.0
17A-101	1.8	1.744	0.059	56.109	3.393	0.7100	0.0355	2921.8	159.8	4107.2	120.8	4750.5	143.9	38	389.9	10.6
17A-102	11.6	7.627	0.085	7.136	0.366	0.3949	0.0197	794.2	16.7	2128.5	91.3	3889.1	150.8	80	439.5	4.6
17A-103	40.7	13.288	0.198	1.864	0.097	0.1797	0.0090	467.7	13.5	1068.3	69.0	2649.3	166.0	82	390.5	5.4
17A-104	18.0	7.760	0.077	6.700	0.341	0.3773	0.0189	781.4	14.6	2072.6	90.1	3820.1	151.4	80	451.0	4.2
17A-105	16.1	8.256	0.069	6.268	0.318	0.3755	0.0188	737.1	11.7	2014.0	88.8	3812.9	151.5	81	426.2	3.4
17A-106	5.0	2.643	0.036	33.845	1.753	0.6491	0.0325	2068.5	47.8	3605.5	102.3	4621.3	144.8	55	451.9	5.7
17A-107	0.1	10.214	7.331	10.920	7.857	0.8093	0.0405	602.1	825.2	2516.4	1338.5	4937.6	142.7	88		
17A-108	0.1	10.211	20.078	11.024	21.684	0.8168	0.0408	602.3	2261.3	2525.2	3662.2	4950.6	142.6	88		
17A-109	4.4	1.450	0.020	29.452	1.529	0.3098	0.0155	3381.8	73.8	3468.7	102.1	3519.3	154.5	4		

rain I.D.	238U (ppm)	238/206 ratio	238/206 1SE	207/235 ratio	207/235 1SE	207/206 ratio	207/206 1SE	238/206 Age (Ma)	2σ	207/235 Age (Ma)	2σ	207/206 Age (Ma)	2σ	Disc. (%)	preferred Age (Ma)	preferred Err. (2σ)
17A-110	23.4	8.648	0.105	5.266	0.271	0.3304	0.0165	705.4	16.3	1863.3	87.9	3618.4	153.5	81	450.6	5.2
17A-111	0.2	6.789	11.567	14.171	24.152	0.6981	0.0349	885.8	2819.9	2761.2	3233.0	4726.1	144.0	81		
17A-112	6.5	4.604	0.057	16.615	0.856	0.5550	0.0278	1267.1	28.5	2912.9	98.7	4393.8	146.4	71	433.1	5.0
17A-113	37.1	12.259	0.105	1.727	0.088	0.1536	0.0077	505.5	8.3	1018.7	65.3	2385.9	170.4	79	440.4	3.6
17A-114	214.6	13.194	0.120	1.112	0.056	0.1064	0.0053	470.9	8.3	759.0	54.3	1738.3	183.4	73	439.5	3.8
17A-115	6.9	6.107	0.280	10.983	0.745	0.4866	0.0243	977.6	83.3	2521.7	126.4	4200.6	148.0	77	421.7	13.7
17A-116	11.7	6.172	0.081	10.250	0.530	0.4591	0.0230	967.9	23.6	2457.6	95.7	4114.2	148.7	76	454.5	5.6
17A-117	43.6	9.554	0.090	3.915	0.199	0.2714	0.0136	641.7	11.5	1616.8	82.3	3313.6	156.9	81	460.0	4.1
17A-118	1.8	2.446	0.077	27.155	1.606	0.4819	0.0241	2209.7	118.3	3389.1	116.0	4186.2	148.1	47		
17A-119	33.2	9.887	0.126	3.086	0.159	0.2214	0.0111	621.1	15.1	1429.2	79.2	2990.1	161.0	79	486.9	5.8
17A-120	13.7	7.557	0.083	7.707	0.395	0.4226	0.0211	801.2	16.6	2197.5	92.1	3990.8	149.8	80	412.9	4.3
17A-121	14.0	7.358	0.056	7.293	0.369	0.3893	0.0195	821.5	11.7	2147.9	90.4	3867.8	151.0	79	461.5	3.3
17A-122	5.0	3.902	0.054	20.823	1.080	0.5895	0.0295	1470.9	36.3	3130.4	100.6	4481.7	145.8	67	436.0	5.6
17A-123	5.1	7.943	0.152	6.948	0.372	0.4004	0.0200	764.5	27.5	2104.8	95.1	3910.0	150.6	80	416.5	7.2
17A-124	6.6	4.830	0.061	14.875	0.767	0.5214	0.0261	1212.9	28.0	2807.3	98.2	4302.1	147.2	72	471.1	5.6

10.3.1.11 DMBH (Apatite)

Grain I.D.	238U (ppm)	238/206 ratio	238/206 1SE	207/235 ratio	207/235 1SE	207/206 ratio	207/206 1SE	238/206 Age (Ma)	2σ	207/235 Age (Ma)	2σ	207/206 Age (Ma)	2σ	Disc. (%)	preferred Age (Ma)	preferred Err. (2σ)
DMA-01	91.9	13.202	0.106	1.350	0.068	0.1293	0.0065	470.7	7.3	867.64	59.10	2088.3	176.0	426.32	3.27	DMA-01
DMA-02	8.1	2.874	0.208	30.399	2.678	0.6339	0.0317	1924.9	241.4	3499.81	173.26	4587.0	145.0	515.3	20.3	DMA-02
DMA-03	4.1	5.149	0.071	13.930	0.723	0.5204	0.0260	1144.2	29.1	2744.98	98.39	4299.4	147.2	468.79	6.04	DMA-03
DMA-04	22.2	7.686	0.043	7.388	0.372	0.4120	0.0206	788.5	8.4	2159.55	90.04	3952.8	150.2	430.34	2.32	DMA-04
DMA-05	4.6	3.526	0.043	25.028	1.289	0.6403	0.0320	1609.5	35.1	3309.29	100.66	4601.6	144.9	407.02	4.72	DMA-05
DMA-06	5.1	3.927	0.046	21.653	1.112	0.6169	0.0308	1462.5	30.7	3168.28	99.78	4547.7	145.3	414.28	4.58	DMA-06
DMA-07	9.1	6.605	0.129	10.883	0.584	0.5216	0.0261	908.8	33.1	2513.19	99.88	4302.7	147.2	365.71	6.45	DMA-07
DMA-08	2.8	2.236	0.055	43.786	2.439	0.7105	0.0355	2382.5	97.8	3860.37	110.72	4751.6	143.9	384.13	8.21	DMA-08
DMA-09	13.7	6.498	0.052	10.106	0.512	0.4765	0.0238	922.7	13.9	2444.54	93.65	4169.5	148.3	427.58	3.3	DMA-09
DMA-10	26.3	6.976	0.189	8.971	0.510	0.4541	0.0227	863.6	43.8	2335.06	103.93	4097.9	148.9	424.75	9.76	DMA-10
DMA-11	4.4	3.694	0.046	23.458	1.208	0.6288	0.0314	1544.3	34.0	3246.13	100.42	4575.4	145.1	413.97	4.81	DMA-11
DMA-12	3.3	2.252	0.039	43.063	2.277	0.7037	0.0352	2368.7	68.2	3843.85	105.06	4737.6	144.0	406.08	6.4	DMA-12
DMA-13	9.8	5.209	0.044	14.632	0.742	0.5530	0.0276	1132.1	17.6	2791.60	96.47	4388.4	146.5	413.18	3.34	DMA-13
DMA-14	6.5	4.361	0.071	18.811	0.990	0.5953	0.0298	1330.8	39.3	3032.19	101.52	4495.8	145.7	413.83	6.23	DMA-14
DMA-15	37.4	10.435	0.072	3.563	0.180	0.2698	0.0135	589.9	7.8	1541.35	80.06	3304.1	157.0	428.83	2.82	DMA-15
DMA-16	1.5	1.309	0.042	81.141	4.817	0.7707	0.0385	3658.8	178.7	4476.25	119.24	4867.8	143.1	280.03	7.38	DMA-16
DMA-17	7.2	3.603	0.049	23.887	1.238	0.6244	0.0312	1579.1	38.4	3263.81	101.15	4565.3	145.2	434.03	5.55	DMA-17
DMA-18	2.8	2.343	0.078	41.032	2.466	0.6977	0.0349	2290.9	128.6	3795.95	119.26	4725.4	144.0	411.1	11	DMA-18
DMA-19	4.2	4.675	0.101	17.251	0.939	0.5851	0.0293	1249.7	48.9	2948.89	104.57	4470.8	145.9	404.07	7.74	DMA-19
DMA-20	2.7	1.614	0.032	62.750	3.382	0.7347	0.0367	3108.8	99.3	4218.89	107.89	4799.5	143.5	408.83	7.39	DMA-20
DMA-21	11.6	7.872	0.088	7.018	0.360	0.4009	0.0200	770.9	16.4	2113.66	91.14	3911.6	150.6	431.74	4.58	DMA-21
DMA-22	11.4	6.466	0.049	10.257	0.519	0.4812	0.0241	927.1	13.2	2458.26	93.64	4184.0	148.1	423.82	3.09	DMA-22
DMA-23	6.6	5.885	0.053	11.649	0.592	0.4974	0.0249	1011.7	16.8	2576.65	95.06	4232.9	147.7	442.68	3.77	DMA-23
DMA-24	13.4	5.885	0.144	12.986	0.723	0.5545	0.0277	1011.7	46.0	2678.65	105.08	4392.5	146.5	364.35	7.79	DMA-24
DMA-25	491.9	19.908	0.206	0.384	0.020	0.0554	0.0028	315.9	6.4	329.78	28.76	428.6	223.0			DMA-25
DMA-26	98.1	13.056	0.070	1.396	0.070	0.1323	0.0066	475.7	4.9	887.28	59.51	2127.4	175.2	429.19	2.21	DMA-26
DMA-27	10.2	4.378	0.048	18.133	0.928	0.5759	0.0288	1326.3	26.3	2996.79	98.59	4447.8	146.0	447.84	4.62	DMA-27
DMA-28	1.9	1.349	0.042	76.498	4.497	0.7487	0.0374	3575.8	169.7	4417.18	117.99	4826.4	143.4	404.2	10.3	DMA-28
DMA-29	16.6	5.937	0.048	11.695	0.592	0.5038	0.0252	1003.4	15.2	2580.30	94.84	4251.8	147.6	430.11	3.34	DMA-29
DMA-30	2.4	2.498	0.056	37.658	2.062	0.6827	0.0341	2170.2	82.4	3710.97	108.46	4694.0	144.3	434.6	8.57	DMA-30
DMA-31	13.3	4.710	0.063	16.607	0.859	0.5675	0.0284	1241.2	30.1	2912.44	99.19	4426.4	146.2	431.18	5.37	DMA-31
DMA-32	9.7	4.580	0.050	17.450	0.893	0.5799	0.0290	1273.0	25.1	2959.89	98.34	4457.9	146.0	421.35	4.32	DMA-32
DMA-33	42.7	10.004	0.062	4.002	0.202	0.2905	0.0145	614.2	7.3	1634.54	81.90	3419.5	155.7	430.31	2.58	DMA-33
DMA-34	12.3	6.610	0.049	9.754	0.493	0.4678	0.0234	908.2	12.5	2411.84	93.15	4142.2	148.5	431.05	3.04	DMA-34
DMA-35	38.0	9.198	0.072	4.897	0.248	0.3268	0.0163	665.3	9.9	1801.72	85.38	3601.6	153.7	435.49	3.25	DMA-35
DMA-36	124.7	13.277	0.064	1.336	0.067	0.1287	0.0064	468.1	4.4	861.53	58.36	2079.7	176.1	424.34	1.98	DMA-36
DMA-37	15.0	6.382	0.054	10.502	0.533	0.4863	0.0243	938.4	14.9	2480.10	94.10	4199.5	148.0	422.89	3.42	DMA-37
DMA-38	12.3	7.463	0.063	8.065	0.409	0.4368	0.0218	810.6	13.0	2238.37	91.69	4040.0	149.4	416.23	3.38	DMA-38
DMA-39	18.9	6.448	0.074	10.273	0.527	0.4807	0.0240	929.4	19.9	2459.67	95.01	4182.3	148.2	425.62	4.61	DMA-39
DMA-40	28.4	7.730	0.081	5.753	0.294	0.3227	0.0161	784.2	15.5	1939.32	88.41	3581.9	153.9			DMA-40
DMA-41	20.3	7.815	0.084	7.164	0.366	0.4062	0.0203	776.2	15.7	2132.01	91.17	3931.6	150.4	429.33	4.35	DMA-41
DMA-42	8.2	5.452	0.045	13.560	0.687	0.5364	0.0268	1085.6	16.7	2719.49	95.94	4344.0	146.8	419.52	3.34	DMA-42
DMA-43	8.6	6.425	0.067	10.391	0.531	0.4844	0.0242	932.5	18.2	2470.27	94.68	4193.9	148.1	422.39	4.18	DMA-43
DMA-44	23.0	6.696	0.060	9.438	0.480	0.4586	0.0229	897.2	15.2	2381.54	93.35	4112.6	148.8	436.72	3.75	DMA-44
DMA-45	0.2	6.881	13.080	15.541	29.551	0.7760	0.0388	874.7	3109.5	2849.02	3628.03	4877.7	143.0			DMA-45
DMA-46	11.2	5.125	0.050	15.111	0.770	0.5619	0.0281	1149.0	20.4	2822.26	97.08	4411.9	146.3	405.7	3.73	DMA-46
DMA-47	17.4	6.903	0.143	8.915	0.482	0.4465	0.0223	872.1	33.7	2329.29	98.82	4073.0	149.1	437.9	8.06	DMA-47
DMA-48	9.4	4.870	0.044	16.082	0.817	0.5683	0.0284	1204.0	19.9	2881.68	97.22	4428.2	146.2	416.1	3.58	DMA-48
DMA-49	12.1	5.411	0.042	13.663	0.691	0.5365	0.0268	1093.1	15.6	2726.64	95.81	4344.0	146.8	422.61	3.12	DMA-49
DMA-50	21.8	2.207	0.021	11.861	0.604	0.1900	0.0095	2408.7	38.6	2593.47	95.41	2741.1	164.6	2318.9	17.6	DMA-50
DMA-51	3.2	3.087	0.063	29.451	1.591	0.6596	0.0330	1809.1	64.5	3468.68	106.19	4644.5	144.6	413.47	7.57	DMA-51
DMA-52	48.5	9.954	0.169	3.977	0.210	0.2872	0.0144	617.1	20.0	1629.45	85.72	3401.8	155.9	435.1	6.75	DMA-52

Grain I.D.	238U (ppm)	238/206 ratio	238/206 1SE	207/235 ratio	207/235 1SE	207/206 ratio	207/206 1SE	238/206 Age (Ma)	2σ	207/235 Age (Ma)	2σ	207/206 Age (Ma)	2σ	Disc. (%)	preferred Age (Ma)	preferred Err. (2σ)
DMA-53	3.4	2.226	0.029	43.416	2.245	0.7013	0.0351	2391.8	52.7	3851.95	102.77	4732.7	144.0	419.51	5.17	DMA-53
DMA-54	29.7	7.663	0.065	7.388	0.375	0.4108	0.0205	790.7	12.6	2159.51	90.75	3948.3	150.2	432.88	3.49	DMA-54
DMA-55	6.3	2.270	0.069	43.300	2.529	0.7132	0.0357	2353.1	119.0	3849.31	116.04	4756.8	143.8	369.27	9.27	DMA-55
DMA-56	0.7	1.343	0.163	95.109	12.465	0.9265	0.0463	3588.4	666.8	4635.72	263.46	5129.3	141.5			DMA-56
DMA-57	4.5	4.043	0.059	20.742	1.081	0.6085	0.0304	1424.8	37.5	3126.63	101.03	4527.7	145.4	419.45	5.71	DMA-57
DMA-58	3.9	3.299	0.038	31.634	1.623	0.7572	0.0379	1706.9	34.4	3538.96	101.09	4842.6	143.3			DMA-58
DMA-59	5.7	3.467	0.042	25.288	1.301	0.6361	0.0318	1633.7	34.9	3319.38	100.59	4592.1	145.0	423.57	4.81	DMA-59
DMA-60	30.6	8.237	0.067	6.189	0.313	0.3699	0.0185	738.6	11.3	2002.85	88.59	3790.3	151.7	443.24	3.42	DMA-60
DMA-61	2.1	1.835	0.059	54.428	3.232	0.7248	0.0362	2803.9	145.7	4076.84	118.55	4780.0	143.7	403.9	10.6	DMA-61
DMA-62	40.4	10.406	0.069	3.600	0.182	0.2718	0.0136	591.5	7.5	1549.47	80.18	3315.8	156.9	428.45	2.71	DMA-62
DMA-63	2.5	1.579	0.029	64.275	3.428	0.7366	0.0368	3162.1	92.8	4242.90	106.81	4803.2	143.5	407.86	6.88	DMA-63
DMA-64	32.7	7.062	0.048	8.300	0.419	0.4253	0.0213	853.7	10.9	2264.29	91.51	4000.4	149.7	452.41	2.94	DMA-64
DMA-65	2.2	1.511	0.039	67.036	3.776	0.7350	0.0367	3274.2	133.2	4284.96	112.86	4800.0	143.5	434.66	9.67	DMA-65
DMA-66	17.8	8.064	0.151	6.934	0.370	0.4058	0.0203	753.6	26.7	2103.07	94.81	3929.9	150.4	416.77	7.07	DMA-66
DMA-67	12.3	4.473	0.073	17.475	0.919	0.5672	0.0284	1300.6	38.6	2961.28	101.15	4425.5	146.2	454.14	6.82	DMA-67
DMA-68	57.9	10.867	0.067	2.989	0.151	0.2357	0.0118	567.5	6.7	1404.75	76.68	3090.2	159.7	437.4	2.59	DMA-68
DMA-69	3.0	2.148	0.039	45.387	2.412	0.7075	0.0354	2463.6	73.8	3896.05	105.73	4745.5	143.9	410.9	6.74	DMA-69
DMA-70	2.2	1.693	0.039	73.477	4.042	0.9024	0.0451	2992.8	109.8	4376.80	110.36	5092.0	141.7			DMA-70
DMA-71	18.8	7.584	0.099	7.734	0.400	0.4256	0.0213	798.4	19.5	2200.56	92.95	4001.4	149.7	421.54	5.13	DMA-71
DMA-72	16.2	7.764	0.059	7.339	0.371	0.4134	0.0207	781.1	11.2	2153.56	90.44	3957.9	150.1	424.64	3.09	DMA-72
DMA-73	5.2	4.418	0.051	18.034	0.925	0.5782	0.0289	1315.2	27.5	2991.57	98.81	4453.4	146.0	439.75	4.77	DMA-73
DMA-74	27.0	7.312	0.046	7.841	0.395	0.4160	0.0208	826.3	9.7	2212.96	90.80	3967.3	150.0	447.49	2.68	DMA-74
DMA-75	2.5	1.833	0.031	31.694	1.674	0.4216	0.0211	2806.5	77.3	3540.85	104.06	3987.1	149.9	2081.4	27.9	DMA-75
DMA-76	1.3	1.652	0.063	61.057	3.834	0.7319	0.0366	3051.2	184.7	4191.55	125.58	4794.0	143.6	413.1	12.1	DMA-76
DMA-77	11.3	6.671	0.066	10.037	0.512	0.4858	0.0243	900.4	16.6	2438.18	94.18	4198.1	148.0	405.47	3.8	DMA-77
DMA-78	50.3	9.923	0.074	4.285	0.217	0.3085	0.0154	619.0	8.8	1690.43	83.27	3512.7	154.6	419.16	3	DMA-78
DMA-79	7.8	3.230	0.049	28.665	1.497	0.6719	0.0336	1738.6	45.9	3442.10	102.58	4671.0	144.4	364.8	5.11	DMA-79
DMA-80	2.1	1.305	0.030	79.291	4.355	0.7506	0.0375	3668.1	127.3	4453.12	110.33	4830.1	143.3	405.84	8.14	DMA-80
DMA-81	34.5	7.453	0.057	7.445	0.377	0.4026	0.0201	811.7	11.7	2166.36	90.60	3918.1	150.5	453.7	3.31	DMA-81
DMA-82	21.1	7.251	0.063	8.106	0.411	0.4265	0.0213	832.9	13.7	2242.90	91.80	4004.4	149.7	439.62	3.65	DMA-82
DMA-83	5.7	5.521	0.078	13.766	0.715	0.5515	0.0276	1073.1	27.9	2733.74	98.43	4384.5	146.5	392.36	5.17	DMA-83
DMA-84	4.9	3.945	0.050	21.045	1.086	0.6025	0.0301	1456.3	33.4	3140.64	100.15	4513.3	145.5	441.9	5.29	DMA-84
DMA-85	6.0	3.395	0.103	26.025	1.523	0.6412	0.0321	1664.1	89.2	3347.48	114.54	4603.5	144.9	420.4	10.6	DMA-85
DMA-86	18.5	7.553	0.092	7.381	0.380	0.4045	0.0202	801.5	18.5	2158.69	92.11	3925.3	150.4	445.72	5.12	DMA-86
DMA-87	2.7	2.773	0.058	33.690	1.827	0.6780	0.0339	1984.8	71.7	3601.01	107.04	4684.1	144.3	405.93	7.6	DMA-87
DMA-88	3.3	4.168	0.086	20.662	1.117	0.6248	0.0312	1386.4	51.4	3122.87	104.83	4566.1	145.2	375.49	6.94	DMA-88
DMA-89	10.2	6.680	0.077	9.721	0.499	0.4712	0.0236	899.3	19.5	2408.67	94.56	4152.8	148.4	422.57	4.61	DMA-89
DMA-90	16.3	1.678	0.015	18.296	0.929	0.2228	0.0111	3013.1	43.0	3005.41	97.88	3000.3	160.9	3021	19.6	DMA-90
DMA-91	3.0	2.150	0.063	47.503	2.758	0.7412	0.0371	2461.7	120.7	3941.35	115.59	4812.2	143.5	283.49	7.04	DMA-91
DMA-92	34.6	9.794	0.116	4.203	0.216	0.2987	0.0149	626.7	14.2	1674.61	84.34	3462.7	155.2	432.62	4.83	DMA-92
DMA-93	11.8	4.895	0.053	15.129	0.774	0.5374	0.0269	1198.3	23.6	2823.37	97.50	4346.4	146.8	464.78	4.72	DMA-93
DMA-94	71.5	12.182	0.066	2.113	0.106	0.1867	0.0093	508.6	5.4	1152.97	69.34	2712.9	165.1	423.42	2.22	DMA-94
DMA-95	24.0	8.526	0.069	6.057	0.307	0.3747	0.0187	714.9	10.9	1984.05	88.32	3809.8	151.5	423.97	3.27	DMA-95
DMA-96	6.9	2.152	0.032	45.836	2.392	0.7156	0.0358	2460.5	61.2	3905.84	103.85	4761.8	143.8	379.91	5.28	DMA-96
DMA-97	13.4	5.487	0.069	12.945	0.667	0.5154	0.0258	1079.2	25.0	2675.68	97.24	4285.3	147.3	447.7	5.26	DMA-97
DMA-98	19.8	6.776	0.050	9.127	0.461	0.4488	0.0224	887.3	12.3	2350.80	92.56	4080.4	149.0	443.3	3.13	DMA-98
DMA-99	3.2	4.397	0.078	19.773	1.048	0.6309	0.0315	1321.0	42.2	3080.32	102.58	4580.1	145.1	345.09	5.59	DMA-99
DMA-100	13.6	5.271	0.041	14.005	0.709	0.5357	0.0268	1119.8	16.0	2750.07	95.98	4341.9	146.9	434.79	3.22	DMA-100
DMA-101	55.4	2.072	0.019	11.862	0.603	0.1784	0.0089	2538.5	38.3	2593.59	95.25	2636.9	166.2	2508.9	17.6	DMA-101
DMA-102	9.5	7.574	0.161	8.057	0.438	0.4428	0.0221	799.5	31.9	2237.39	98.17	4060.4	149.2	403.87	7.63	DMA-102
DMA-103	27.0	9.718	0.113	4.268	0.219	0.3010	0.0150	631.4	14.1	1687.24	84.51	3474.5	155.0	434.05	4.77	DMA-103
DMA-104	6.0	4.030	0.047	20.398	1.047	0.5964	0.0298	1428.9	29.9	3110.44	99.48	4498.7	145.7	444.83	4.88	DMA-104
DMA-105	51.9	11.681	0.088	2.299	0.116	0.1948	0.0097	529.5	7.6	1211.91	71.57	2782.7	164.0	435.62	3.12	DMA-105
DMA-106	17.5	5.672	0.055	12.570	0.640	0.5173	0.0259	1046.7	18.9	2647.98	95.90	4290.7	147.3	430.71	4	DMA-106
DMA-107	0.6	8.219	16.810	11.984	24.519	0.7147	0.0357	740.2	2860.5	2603.18	3834.77	4759.9	143.8			DMA-107
DMA-108	12.2	5.534	0.049	13.103	0.665	0.5261	0.0263	1070.9	17.7	2687.07	95.90	4315.4	147.1	428.53	3.64	DMA-108
DMA-109	12.0	6.062	0.047	11.402	0.577	0.5015	0.0251	984.3	14.1	2556.58	94.52	4245.0	147.6	424.57	3.13	DMA-109

Grain I.D.	238U (ppm)	238/206 ratio	238/206 1SE	207/235 ratio	207/235 1SE	207/206 ratio	207/206 1SE	238/206 Age (Ma)	2σ	207/235 Age (Ma)	2σ	207/206 Age (Ma)	2σ	Disc. (%)	preferred Age (Ma)	preferred Err. (2σ)
DMA-110	3.1	3.268	0.054	27.424	1.444	0.6502	0.0325	1721.1	49.8	3398.73	103.24	4623.8	144.7	414.16	6.27	DMA-110
DMA-111	6.1	5.318	0.050	13.980	0.711	0.5395	0.0270	1110.8	19.3	2748.38	96.50	4352.1	146.8	425.36	3.82	DMA-111
DMA-112	3.6	2.926	0.040	32.128	1.664	0.6820	0.0341	1895.4	44.4	3554.21	102.12	4692.6	144.3	374.13	4.74	DMA-112
DMA-113	80.7	11.105	0.067	2.751	0.139	0.2217	0.0111	555.8	6.5	1342.45	75.04	2992.3	161.0	438.33	2.55	DMA-113
DMA-114	7.5	6.757	0.062	9.235	0.469	0.4528	0.0226	889.7	15.2	2361.56	93.20	4093.7	148.9	439.74	3.83	DMA-114
DMA-115	4.7	4.129	0.061	20.286	1.058	0.6077	0.0304	1398.2	37.3	3105.09	101.02	4525.9	145.5	412.38	5.68	DMA-115
DMA-116	6.2	3.947	0.043	21.009	1.075	0.6017	0.0301	1455.8	28.5	3138.98	99.31	4511.3	145.6	443.37	4.58	DMA-116
DMA-117	41.7	10.697	0.095	3.165	0.161	0.2456	0.0123	576.1	9.8	1448.65	78.38	3156.2	158.9	436.72	3.67	DMA-117
DMA-118	77.0	12.453	0.087	1.814	0.092	0.1639	0.0082	497.9	6.7	1050.42	66.10	2495.3	168.5	429.16	2.85	DMA-118
DMA-119	8.5	4.476	0.101	17.837	0.979	0.5794	0.0290	1299.8	53.2	2980.98	105.58	4456.4	146.0	432.02	8.59	DMA-119
DMA-120	19.4	8.475	0.064	6.045	0.306	0.3717	0.0186	719.0	10.3	1982.29	88.15	3797.7	151.7	429.29	3.1	DMA-120
DMA-121	33.6	10.205	0.042	4.080	0.205	0.3021	0.0151	602.6	4.7	1650.27	81.85	3480.2	155.0	412.85	1.62	DMA-121
DMA-122	2.3	3.832	0.132	21.855	1.326	0.6076	0.0304	1494.9	91.8	3177.29	117.93	4525.6	145.5	444	12.1	DMA-122
DMA-123	9.0	3.762	0.031	22.333	1.131	0.6096	0.0305	1519.6	22.1	3198.31	98.57	4530.3	145.4	447.82	3.48	DMA-123
DMA-124	8.7	4.986	0.063	15.247	0.786	0.5516	0.0276	1178.4	27.3	2830.77	98.37	4384.7	146.5	433.59	5.14	DMA-124
DMA-125	30.2	10.165	0.106	3.806	0.194	0.2808	0.0140	604.9	12.1	1594.11	82.17	3366.4	156.3	431.32	4.26	DMA-125
DMA-126	8.0	5.120	0.063	14.856	0.765	0.5519	0.0276	1150.1	25.9	2806.06	98.04	4385.6	146.5	421.87	4.87	DMA-126
DMA-127	6.2	4.434	0.062	18.323	0.952	0.5895	0.0295	1311.0	33.4	3006.83	100.10	4481.7	145.8	417.63	5.47	DMA-127
DMA-128	26.9	10.141	0.071	3.843	0.194	0.2828	0.0141	606.3	8.1	1601.90	81.38	3377.8	156.1	430.73	2.87	DMA-128
DMA-129	25.5	11.749	0.062	2.308	0.116	0.1968	0.0098	526.6	5.4	1214.90	71.26	2799.1	163.8	431.81	2.19	DMA-129
DMA-130	1.6	4.031	0.167	20.899	1.356	0.6112	0.0306	1428.7	105.9	3133.92	125.79	4534.3	145.4	415.2	12.8	DMA-130
DMA-131	12.2	7.383	0.078	8.063	0.412	0.4319	0.0216	818.9	16.2	2238.11	92.37	4023.5	149.5	425.93	4.25	DMA-131
DMA-132	12.4	6.602	0.051	9.621	0.487	0.4609	0.0230	909.2	13.3	2399.20	93.15	4120.0	148.7	440.08	3.28	DMA-132
DMA-133	12.7	7.336	0.098	7.851	0.406	0.4179	0.0209	823.8	20.7	2214.05	93.28	3974.0	150.0	444.01	5.54	DMA-133
DMA-134	39.7	11.137	0.102	2.749	0.140	0.2222	0.0111	554.3	9.8	1341.88	75.72	2995.8	161.0	436.74	3.8	DMA-134
DMA-135	11.6	7.159	0.199	8.307	0.475	0.4315	0.0216	842.9	43.9	2265.05	103.72	4021.9	149.5	439.5	10.3	DMA-135
DMA-136	31.3	9.712	0.057	4.328	0.218	0.3050	0.0152	631.8	7.2	1698.76	83.09	3495.1	154.8	430.99	2.45	DMA-136
DMA-137	1.8	0.888	0.045	119.844	8.523	0.7723	0.0386	4861.8	345.3	4868.25	143.38	4870.9	143.1	394.8	13.6	DMA-137
DMA-138	2.6	3.013	0.122	29.372	1.890	0.6420	0.0321	1847.8	130.2	3466.04	126.46	4605.5	144.9	470.3	14.2	DMA-138
DMA-139	24.0	8.619	0.072	5.521	0.280	0.3453	0.0173	707.6	11.3	1903.93	87.21	3685.7	152.8	446.94	3.58	DMA-139
DMA-140	1.2	1.378	0.063	77.079	5.231	0.7708	0.0385	3517.0	248.8	4424.75	136.19	4868.0	143.1	265.4	8.79	DMA-140
DMA-141	180.4	13.287	0.079	1.372	0.069	0.1323	0.0066	467.8	5.4	877.08	59.16	2127.7	175.2	421.88	2.41	DMA-141
DMA-142	5.5	3.172	0.058	27.728	1.476	0.6382	0.0319	1766.5	56.6	3409.51	104.47	4596.8	144.9	456.95	7.58	DMA-142
DMA-143	4.2	4.573	0.093	17.713	0.956	0.5878	0.0294	1274.9	47.1	2974.29	103.85	4477.4	145.8	408.24	7.45	DMA-143
DMA-144	23.3	9.031	0.095	5.351	0.273	0.3507	0.0175	677.0	13.6	1877.10	87.47	3709.1	152.5	422.17	4.21	DMA-144
DMA-145	66.1	10.580	0.093	3.238	0.164	0.2486	0.0124	582.2	9.8	1466.24	78.79	3174.9	158.6	439.23	3.66	DMA-145
DMA-146	2.4	2.060	0.061	46.998	2.731	0.7025	0.0351	2550.9	124.8	3930.71	115.68	4735.2	144.0	447.9	11	DMA-146
DMA-147	7.6	5.463	0.068	13.192	0.680	0.5229	0.0261	1083.7	25.0	2693.51	97.36	4306.5	147.1	438.68	5.14	DMA-147
DMA-148	8.2	1.453	0.040	34.550	1.970	0.3643	0.0182	3375.2	144.1	3625.87	112.65	3767.4	152.0	2901.6	45.8	DMA-148
DMA-149	15.4	7.281	0.075	7.915	0.404	0.4181	0.0209	829.7	16.0	2221.34	92.08	3974.9	150.0	447.05	4.34	DMA-149
DMA-150	12.3	6.546	0.083	9.550	0.493	0.4536	0.0227	916.4	21.8	2392.35	94.90	4096.4	148.9	452.64	5.38	DMA-150
DMA-151	23.7	7.763	0.083	6.700	0.343	0.3774	0.0189	781.1	15.7	2072.62	90.38	3820.7	151.4	461.98	4.65	DMA-151
DMA-152	68.6	11.380	0.087	2.410	0.122	0.1990	0.0100	543.0	8.0	1245.61	72.61	2817.3	163.5	443.99	3.23	DMA-152
DMA-153	2.3	3.138	0.095	28.704	1.678	0.6536	0.0327	1783.2	94.4	3443.46	114.82	4631.3	144.7	422.3	10.6	DMA-153
DMA-154	12.4	5.054	0.043	14.786	0.750	0.5422	0.0271	1163.8	18.1	2801.56	96.53	4359.7	146.7	442.67	3.57	DMA-154
DMA-155	15.3	8.727	0.069	5.630	0.285	0.3565	0.0178	699.4	10.5	1920.66	87.33	3734.2	152.3	431.21	3.25	DMA-155
DMA-156	0.1	5.837	6.031	18.180	18.806	0.7699	0.0385	1019.4	1948.5	2999.30	1991.16	4866.5	143.1			DMA-156
DMA-157	1.7	2.269	0.084	42.716	2.661	0.7034	0.0352	2353.4	146.5	3835.84	123.70	4737.1	144.0	404	11.7	DMA-157
DMA-158	12.0	4.631	0.042	16.543	0.841	0.5559	0.0278	1260.3	20.8	2908.75	97.39	4396.1	146.4	458.57	3.95	DMA-158
DMA-159	15.3	7.790	0.125	6.728	0.353	0.3803	0.0190	778.5	23.6	2076.28	92.89	3832.3	151.3	457.41	6.74	DMA-159
DMA-160	21.5	9.089	0.103	5.342	0.274	0.3523	0.0176	672.9	14.5	1875.63	87.74	3716.3	152.5	418.08	4.48	DMA-160
DMA-161	17.5	6.503	0.042	9.536	0.481	0.4500	0.0225	922.1	11.2	2391.01	92.73	4084.4	149.0	460.1	2.86	DMA-161
DMA-162	3.4	5.899	0.113	11.549	0.618	0.4943	0.0247	1009.5	35.8	2568.56	100.12	4223.6	147.8	445.92	7.69	DMA-162
DMA-163	2.0	2.222	0.061	42.883	2.449	0.6913	0.0346	2395.8	110.5	3839.69	113.46	4712.0	144.1	456.6	10.6	DMA-163
DMA-164	15.1	8.891	0.062	5.195	0.262	0.3352	0.0168	687.1	9.1	1851.84	86.00	3640.1	153.3	442.7	2.95	DMA-164
DMA-165	7.1	6.045	0.090	11.866	0.619	0.5205	0.0260	986.9	27.3	2593.85	97.79	4299.5	147.2	400.46	5.55	DMA-165
DMA-166	60.7	10.324	0.072	3.202	0.162	0.2398	0.0120	596.0	8.0	1457.55	78.16	3118.2	159.3	456.68	3.06	DMA-166

10.3.1.12 A6BH (Apatite)

Grain I.D.	238U (ppm)	238/206 ratio	238/206 1SE	207/235 ratio	207/235 1SE	207/206 ratio	207/206 1SE	238/206 Age (Ma)	2σ	207/235 Age (Ma)	2σ	207/206 Age (Ma)	2σ	Disc. (%)	preferred Age (Ma)	preferred Err. (2σ)
A6A-1	4.8	4.87	0.05	16.10	0.82	0.569	0.028	1203.5	24.7	2882.5	98.1	4430.1	146.2	72.8	397.6	4.2
A6A-2	32.5	7.46	0.04	8.29	0.42	0.448	0.022	811.3	9.0	2262.7	91.3	4078.8	149.0	80.1	395.6	2.3
A6A-3	8.7	6.73	0.06	9.03	0.46	0.441	0.022	892.7	15.6	2340.6	93.0	4054.2	149.3	78.0	446.2	4.0
A6A-4	21.9	10.77	0.06	3.60	0.18	0.281	0.014	572.6	6.5	1550.1	80.1	3370.1	156.2	83.0	403.8	2.3
A6A-5	3.7	3.10	0.03	29.26	1.49	0.658	0.033	1803.1	29.5	3462.3	100.0	4640.5	144.6	61.1	385.1	3.4
A6A-6	8.4	4.55	0.03	17.49	0.88	0.577	0.029	1281.0	17.7	2962.3	97.2	4451.6	146.0	71.2	410.0	3.0
A6A-7	5.0	5.56	0.05	13.44	0.68	0.542	0.027	1066.3	17.8	2711.3	96.1	4359.8	146.7	75.5	388.8	3.4
A6A-8	25.8	9.97	0.05	4.17	0.21	0.302	0.015	616.1	6.4	1667.7	82.4	3477.4	155.0	82.3	418.8	2.2
A6A-9	16.9	11.18	0.08	3.58	0.18	0.290	0.015	552.1	7.6	1544.2	80.2	3417.7	155.7	83.8	382.6	2.6
A6A-10	22.6	10.50	0.14	4.45	0.23	0.339	0.017	586.7	14.6	1721.6	85.7	3656.9	153.1	84.0	368.9	4.5
A6A-11	16.3	8.16	0.06	6.81	0.34	0.403	0.020	745.5	10.0	2087.6	89.5	3920.7	150.5	81.0	407.6	2.8
A6A-12	50.0	11.17	0.09	3.61	0.18	0.293	0.015	552.5	9.0	1552.3	80.7	3432.4	155.5	83.9	380.8	3.1
A6A-13	6.3	4.97	0.04	15.44	0.78	0.557	0.028	1181.6	17.7	2843.1	96.7	4399.2	146.4	73.1	409.5	3.2
A6A-14	19.4	9.03	0.04	5.44	0.27	0.356	0.018	677.3	6.0	1890.8	86.2	3732.9	152.3	81.9	412.0	1.8
A6A-15	6.0	6.47	0.08	10.39	0.53	0.488	0.024	926.5	20.3	2469.8	95.2	4203.5	148.0	78.0	404.7	4.5
A6A-16	32.6	10.64	0.06	3.64	0.18	0.281	0.014	579.3	6.2	1558.2	80.2	3367.0	156.3	82.8	409.1	2.2
A6A-17	24.7	10.32	0.10	3.96	0.20	0.297	0.015	596.0	10.7	1625.9	82.5	3451.7	155.3	82.7	408.7	3.7
A6A-18	15.2	10.44	0.06	3.48	0.18	0.264	0.013	589.8	6.1	1523.0	79.4	3268.0	157.5	82.0	430.2	2.2
A6A-19	4.8	3.57	0.03	24.82	1.26	0.644	0.032	1590.2	24.9	3301.2	99.2	4609.2	144.8	65.5	367.2	3.1
A6A-20	10.3	5.01	0.03	15.36	0.77	0.559	0.028	1172.8	14.2	2837.9	96.2	4403.2	146.4	73.4	403.8	2.6
A6A-21	8.5	6.53	0.06	10.25	0.52	0.486	0.024	918.1	15.5	2458.0	94.1	4198.9	148.0	78.1	402.8	3.5
A6A-22	8.3	7.43	0.05	8.25	0.42	0.445	0.022	814.1	9.7	2259.1	91.3	4067.4	149.1	80.0	400.8	2.4
A6A-23	9.4	5.82	0.08	12.24	0.63	0.517	0.026	1022.0	25.8	2622.8	97.3	4289.3	147.3	76.2	407.7	5.2
A6A-24	4.3	4.24	0.07	18.59	0.97	0.573	0.029	1363.7	37.8	3020.7	100.9	4439.1	146.1	69.3	448.3	6.4
A6A-25	39.7	11.84	0.06	2.93	0.15	0.252	0.013	522.9	5.1	1390.4	76.1	3195.8	158.4	83.6	388.5	1.9
A6A-26	33.6	9.29	0.07	5.22	0.26	0.352	0.018	659.3	9.8	1855.6	86.3	3713.3	152.5	82.2	404.8	3.0
A6A-27	0.1	5.84	5.72	17.19	16.88	0.728	0.036	1019.5	1849.3	2945.6	1884.3	4786.5	143.6	78.7		
A6A-28	25.0	9.91	0.07	4.11	0.21	0.296	0.015	620.0	8.5	1656.9	82.6	3446.8	155.4	82.0	426.4	2.9
A6A-29	6.1	4.07	0.04	20.60	1.05	0.609	0.030	1415.4	23.5	3119.9	98.6	4528.2	145.4	68.7	393.9	3.5
A6A-30	2.8	3.99	0.09	21.81	1.19	0.632	0.032	1440.9	56.7	3175.5	106.1	4582.7	145.0	68.6	353.6	6.9
A6A-31	57.6	12.04	0.07	2.60	0.13	0.228	0.011	514.3	5.4	1301.9	73.8	3034.3	160.4	83.1	398.6	2.1
A6A-32	11.6	4.01	0.02	21.17	1.06	0.615	0.031	1436.8	14.1	3146.6	97.6	4544.0	145.3	68.4	386.8	2.0
A6A-33	16.7	9.06	0.06	5.41	0.27	0.355	0.018	675.1	8.2	1886.1	86.4	3729.5	152.3	81.9	411.4	2.5
A6A-34	29.9	10.91	0.07	3.66	0.18	0.290	0.015	565.2	6.6	1563.8	80.4	3418.0	155.7	83.5	391.8	2.3
A6A-35	40.2	11.75	0.09	2.70	0.14	0.230	0.011	526.6	7.6	1327.4	74.9	3050.2	160.2	82.7	406.8	2.9
A6A-36	3.8	3.50	0.05	25.32	1.31	0.643	0.032	1620.3	40.0	3320.6	101.5	4607.5	144.9	64.8	376.7	4.9
A6A-37	13.1	6.02	0.04	11.67	0.59	0.510	0.025	990.6	12.4	2578.3	94.4	4269.0	147.4	76.8	404.1	2.6
A6A-38	3.3	9.21	0.10	5.06	0.26	0.338	0.017	664.5	14.3	1829.0	86.9	3652.9	153.1	81.8	420.3	4.5
A6A-39	48.0	11.60	0.08	2.82	0.14	0.237	0.012	533.0	7.0	1360.2	75.7	3100.5	159.6	82.8	406.6	2.7
A6A-40	38.3	12.10	0.07	3.00	0.15	0.263	0.013	512.0	5.8	1407.5	76.7	3265.8	157.5	84.3	372.4	2.1
A6A-41	16.8	10.25	0.10	4.43	0.23	0.329	0.016	600.3	10.7	1717.5	84.3	3612.6	153.5	83.4	385.5	3.4
A6A-42	11.0	6.42	0.06	10.97	0.56	0.511	0.026	933.2	16.2	2520.3	94.7	4272.1	147.4	78.2	378.0	3.4
A6A-43	21.4	10.68	0.09	3.67	0.19	0.285	0.014	576.8	9.7	1565.7	81.1	3388.6	156.0	83.0	404.3	3.4
A6A-44	5.4	4.38	0.04	18.97	0.96	0.603	0.030	1325.8	21.0	3040.0	98.0	4513.8	145.5	70.6	378.2	3.2
A6A-45	16.0	9.66	0.07	5.09	0.26	0.356	0.018	635.1	8.4	1833.8	85.7	3734.2	152.3	83.0	385.2	2.6
A6A-46	10.6	7.05	0.10	9.40	0.49	0.481	0.024	855.6	21.7	2377.8	95.1	4181.9	148.2	79.5	380.5	4.8
A6A-47	4.0	3.38	0.08	26.37	1.45	0.647	0.032	1669.4	67.8	3360.2	107.8	4617.1	144.8	63.8	379.0	7.7
A6A-48	57.8	11.53	0.06	3.03	0.15	0.253	0.013	536.1	5.6	1414.5	76.8	3204.8	158.2	83.3	397.5	2.1
A6A-49	13.0	8.69	0.08	6.12	0.31	0.386	0.019	702.3	12.0	1992.9	88.7	3853.6	151.1	81.8	399.8	3.4
A6A-50	18.1	6.85	0.05	9.69	0.49	0.481	0.024	879.0	10.9	2405.6	92.9	4184.1	148.1	79.0	390.6	2.5
A6A-51	14.6	5.79	0.04	12.49	0.63	0.525	0.026	1026.4	12.2	2641.7	94.8	4312.1	147.1	76.2	398.1	2.5
A6A-52	17.8	6.49	0.04	10.14	0.51	0.478	0.024	923.4	11.4	2447.3	93.3	4172.9	148.2	77.9	416.0	2.6

Grain I.D.	238U (ppm)	238/206 ratio	238/206 1SE	207/235 ratio	207/235 1SE	207/206 ratio	207/206 1SE	238/206 Age (Ma)	2σ	207/235 Age (Ma)	2σ	207/206 Age (Ma)	2σ	Disc. (%)	preferred Age (Ma)	preferred Err. (2σ)
A6A-53	2.0	3.18	0.07	28.23	1.55	0.650	0.033	1764.6	71.1	3427.0	108.1	4624.4	144.7	61.8	394.8	8.0
A6A-54	14.3	7.00	0.05	9.06	0.46	0.460	0.023	861.2	11.8	2344.6	92.5	4117.9	148.7	79.1	407.0	2.8
A6A-55	5.4	4.37	0.05	17.93	0.92	0.569	0.028	1327.8	28.0	2985.8	98.8	4429.3	146.2	70.0	442.7	4.9
A6A-56	22.9	8.59	0.05	6.16	0.31	0.384	0.019	709.7	8.2	1999.5	88.0	3848.2	151.2	81.6	405.5	2.4
A6A-57	10.1	6.19	0.04	10.31	0.52	0.463	0.023	966.0	12.1	2462.7	93.5	4125.7	148.6	76.6	456.1	2.9
A6A-58	6.6	4.90	0.06	15.60	0.81	0.555	0.028	1197.4	28.2	2852.7	98.6	4392.7	146.5	72.7	419.6	5.1
A6A-59	9.7	6.54	0.06	9.69	0.49	0.459	0.023	917.6	14.7	2405.4	93.4	4115.3	148.7	77.7	436.1	3.6
A6A-60	5.7	5.59	0.05	12.89	0.66	0.523	0.026	1060.9	19.2	2671.8	96.1	4306.6	147.1	75.4	415.2	3.9
A6A-61	7.2	4.80	0.04	16.04	0.81	0.559	0.028	1219.9	19.7	2879.0	97.1	4403.1	146.4	72.3	421.3	3.6
A6A-62	45.7	11.72	0.06	2.26	0.11	0.192	0.010	527.7	4.8	1198.7	70.7	2757.9	164.4	80.9	434.2	2.0
A6A-63	9.9	5.23	0.13	14.53	0.81	0.551	0.028	1128.2	49.6	2785.0	105.4	4383.9	146.5	74.3	398.8	8.3
A6A-64	6.1	4.42	0.05	20.94	1.07	0.672	0.034	1314.6	26.8	3135.8	99.4	4670.6	144.4	71.9	245.2	2.6
A6A-65	3.5	3.42	0.06	25.56	1.35	0.634	0.032	1654.4	48.4	3329.7	103.0	4586.8	145.0	63.9	407.6	6.2
A6A-66	13.9	7.71	0.04	7.12	0.36	0.398	0.020	786.1	8.7	2126.1	89.7	3901.3	150.7	79.8	436.3	2.4
A6A-67	20.5	6.89	0.04	8.21	0.41	0.410	0.021	873.8	9.6	2254.5	91.2	3946.9	150.2	77.9	472.6	2.6
A6A-68	5.6	4.75	0.04	16.46	0.83	0.567	0.028	1232.4	18.9	2903.9	97.1	4424.7	146.2	72.1	411.5	3.3
A6A-69	13.0	6.27	0.05	10.54	0.53	0.479	0.024	953.9	13.0	2483.1	93.8	4178.3	148.2	77.2	428.2	3.0
A6A-70	5.5	4.29	0.10	18.74	1.03	0.583	0.029	1351.9	54.5	3028.6	105.6	4465.1	145.9	69.7	424.4	8.4
A6A-71	11.4	6.74	0.04	9.20	0.46	0.450	0.022	891.6	9.4	2357.8	92.2	4084.2	149.0	78.2	434.7	2.3
A6A-72	4.9	5.34	0.05	13.83	0.70	0.535	0.027	1107.4	18.3	2738.1	96.3	4341.1	146.9	74.5	415.5	3.6
A6A-73	12.6	5.88	0.19	11.09	0.66	0.473	0.024	1012.1	60.3	2530.9	110.8	4159.9	148.3	75.7	464.1	12.1
A6A-74	22.5	9.68	0.10	4.23	0.22	0.297	0.015	633.5	12.0	1679.7	83.7	3454.8	155.3	81.7	434.7	4.1
A6A-75	44.2	10.42	0.06	3.49	0.18	0.264	0.013	590.8	6.8	1524.8	79.5	3268.8	157.4	81.9	430.9	2.5
A6A-76	3.5	4.57	0.06	17.19	0.89	0.569	0.028	1276.8	30.8	2945.5	99.4	4431.3	146.2	71.2	422.9	5.3
A6A-77	78.3	11.66	0.10	2.68	0.14	0.227	0.011	530.3	8.4	1323.2	75.0	3029.5	160.5	82.5	411.7	3.2
A6A-78	12.4	5.95	0.04	11.72	0.59	0.506	0.025	1001.8	12.4	2582.5	94.4	4257.9	147.5	76.5	414.2	2.6
A6A-79	21.7	8.37	0.05	6.28	0.32	0.381	0.019	727.9	8.8	2015.5	88.3	3835.7	151.3	81.0	419.4	2.6
A6A-80	45.2	11.96	0.05	2.99	0.15	0.259	0.013	517.7	3.9	1404.1	76.3	3240.7	157.8	84.0	379.5	1.4
A6A-81	29.4	10.66	0.04	3.84	0.19	0.297	0.015	578.1	4.3	1601.1	80.8	3453.7	155.3	83.3	395.8	1.5
A6A-82	3.7	3.94	0.06	21.47	1.12	0.613	0.031	1459.6	38.2	3160.0	101.2	4538.6	145.4	67.8	398.3	5.4
A6A-83	4.7	4.08	0.05	20.89	1.07	0.619	0.031	1412.1	28.7	3133.3	99.4	4552.1	145.3	69.0	372.5	4.0
A6A-84	17.8	11.31	0.04	3.17	0.16	0.260	0.013	546.0	3.8	1450.1	77.4	3247.8	157.7	83.2	400.0	1.4
A6A-85	13.3	8.06	0.04	7.02	0.35	0.411	0.021	753.8	7.3	2114.5	89.4	3948.7	150.2	80.9	404.6	2.0
A6A-86	2.6	2.60	0.07	36.25	2.08	0.684	0.034	2096.6	100.8	3673.4	113.5	4697.7	144.2	55.4	372.9	8.9
A6A-87	7.5	5.80	0.05	12.45	0.63	0.524	0.026	1025.7	15.5	2638.8	95.3	4308.6	147.1	76.2	399.6	3.1
A6A-88	6.2	3.80	0.06	22.52	1.17	0.621	0.031	1505.8	39.2	3206.6	101.4	4557.5	145.2	67.0	394.8	5.4
A6A-89	12.3	6.56	0.14	9.83	0.54	0.468	0.023	914.1	37.2	2419.3	100.6	4143.9	148.5	77.9	423.2	8.2
A6A-90	28.9	13.18	0.09	1.88	0.09	0.180	0.009	471.5	6.2	1074.6	66.9	2651.3	166.0	82.2	394.6	2.6
A6A-91	0.4	6.75	1.11	17.46	2.99	0.855	0.043	890.2	272.7	2960.3	329.4	5016.3	142.2	82.3		
A6A-92	10.9	7.03	0.06	8.97	0.45	0.457	0.023	857.8	13.3	2334.5	92.6	4107.7	148.8	79.1	409.0	3.2
A6A-93	7.1	2.62	0.09	35.45	2.12	0.673	0.034	2087.2	116.1	3651.2	117.9	4672.9	144.4	55.3	407.8	10.8
A6A-94	53.1	11.57	0.07	2.53	0.13	0.212	0.011	534.6	6.1	1280.7	73.3	2922.5	162.0	81.7	425.6	2.4
A6A-95	16.3	7.14	0.05	8.61	0.44	0.447	0.022	844.5	11.9	2298.1	92.1	4073.2	149.1	79.3	414.5	3.0
A6A-96	31.7	10.51	0.06	3.54	0.18	0.270	0.014	585.9	6.0	1536.7	79.7	3306.1	157.0	82.3	422.3	2.2
A6A-97	40.6	11.91	0.08	2.39	0.12	0.207	0.010	519.9	7.0	1241.0	72.3	2880.6	162.6	82.0	417.3	2.8
A6A-98	23.5	9.71	0.07	4.61	0.23	0.325	0.016	632.1	8.5	1751.7	84.3	3592.4	153.8	82.4	410.2	2.8
A6A-99	14.6	6.72	0.05	9.69	0.49	0.472	0.024	894.8	13.5	2405.8	93.3	4156.1	148.4	78.5	409.0	3.2
A6A-100	3.2	3.67	0.05	23.56	1.22	0.627	0.031	1554.6	35.1	3250.2	100.6	4570.5	145.1	66.0	396.4	4.7
A6A-101	61.8	12.06	0.05	2.10	0.11	0.183	0.009	513.5	3.9	1147.7	69.0	2683.7	165.5	80.9	428.1	1.6
A6A-102	12.5	7.20	0.04	8.55	0.43	0.447	0.022	838.0	9.4	2291.3	91.6	4074.2	149.1	79.4	410.8	2.4
A6A-103	10.1	4.65	0.02	16.88	0.85	0.570	0.028	1254.9	12.1	2928.1	96.5	4432.6	146.2	71.7	414.3	2.1
A6A-104	2.9	5.68	0.08	14.45	0.75	0.595	0.030	1045.9	28.7	2779.5	99.1	4495.4	145.7	76.7	304.0	4.2
A6A-105	33.2	10.57	0.07	3.90	0.20	0.299	0.015	582.9	7.2	1614.1	81.5	3465.3	155.1	83.2	397.4	2.5
A6A-106	77.2	14.00	0.07	1.71	0.09	0.174	0.009	444.8	4.4	1014.0	64.5	2597.0	166.9	82.9	375.3	1.8
A6A-107	13.2	6.83	0.04	9.55	0.48	0.474	0.024	880.4	8.9	2392.8	92.5	4160.8	148.3	78.8	400.3	2.1
A6A-108	1.9	1.32	0.03	78.72	4.42	0.756	0.038	3628.5	142.2	4445.9	112.8	4840.1	143.3	25.0	281.1	6.3
A6A-109	22.3	9.69	0.05	4.92	0.25	0.346	0.017	633.2	6.1	1806.4	84.9	3689.6	152.7	82.8	392.8	1.9

Grain I.D.	238U (ppm)	238/206 ratio	238/206 1SE	207/235 ratio	207/235 1SE	207/206 ratio	207/206 1SE	238/206 Age (Ma)	2σ	207/235 Age (Ma)	2σ	207/206 Age (Ma)	2σ	Disc. (%)	preferred Age (Ma)	preferred Err. (2σ)
A6A-110	5.2	4.86	0.08	16.06	0.85	0.567	0.028	1205.4	38.4	2880.2	101.3	4424.1	146.2	72.8	402.2	6.4
A6A-111	6.4	4.84	0.04	16.56	0.84	0.582	0.029	1209.7	19.5	2909.8	97.3	4463.5	145.9	72.9	377.4	3.2
A6A-112	34.7	11.27	0.04	3.46	0.17	0.283	0.014	548.0	3.7	1517.0	79.0	3376.5	156.2	83.8	385.2	1.3
A6A-113	23.7	10.84	0.11	3.66	0.19	0.288	0.014	568.6	10.7	1563.7	81.3	3408.0	155.8	83.3	395.7	3.7
A6A-114	145.1	12.45	0.04	2.52	0.13	0.228	0.011	497.9	2.8	1278.4	72.9	3036.5	160.4	83.6	385.4	1.1
A6A-115	7.5	6.63	0.12	10.05	0.54	0.484	0.024	905.2	31.6	2439.6	98.7	4192.0	148.1	78.4	399.7	6.8
A6A-116	81.2	12.59	0.03	2.28	0.11	0.209	0.010	492.7	2.4	1206.8	70.7	2893.2	162.4	83.0	394.0	0.9
A6A-117	33.2	10.96	0.05	3.22	0.16	0.256	0.013	563.0	5.1	1461.8	77.8	3221.3	158.0	82.5	416.0	1.9
A6A-118	3.1	1.47	0.09	68.46	5.40	0.731	0.037	3341.5	318.3	4306.0	158.0	4792.9	143.6	30.3	391.3	14.7
A6A-119	21.5	7.35	0.08	8.43	0.43	0.450	0.022	822.1	15.9	2278.6	92.7	4083.8	149.0	79.9	399.4	3.9
A6A-120	2.8	3.16	0.06	34.15	1.83	0.782	0.039	1774.1	60.0	3614.3	105.9	4888.9	143.0	63.7		
A6A-121	11.4	7.21	0.05	8.90	0.45	0.465	0.023	837.7	11.4	2328.0	92.3	4134.7	148.6	79.7	389.4	2.7
A6A-122	14.2	5.67	0.03	12.80	0.64	0.526	0.026	1047.6	11.5	2664.8	94.9	4315.7	147.1	75.7	405.0	2.3
A6A-123	2.9	2.78	0.08	33.79	1.93	0.681	0.034	1983.1	94.3	3603.8	112.8	4689.7	144.3	57.7	361.2	8.5
A6A-124	47.7	11.05	0.09	3.20	0.16	0.256	0.013	558.5	9.0	1456.7	78.4	3223.9	158.0	82.7	412.3	3.3
A6A-125	8.2	6.90	0.05	9.14	0.46	0.458	0.023	872.5	12.4	2352.1	92.6	4109.4	148.8	78.8	415.8	3.0
A6A-126	29.4	11.11	0.06	3.22	0.16	0.260	0.013	555.7	5.6	1463.1	78.0	3245.3	157.7	82.9	407.6	2.1
A6A-127	59.0	12.33	0.06	2.35	0.12	0.210	0.011	502.6	4.9	1228.2	71.6	2908.4	162.2	82.7	400.8	1.9
A6A-128	22.4	9.23	0.04	5.32	0.27	0.356	0.018	662.8	5.3	1872.1	85.8	3734.3	152.3	82.3	402.6	1.6
A6A-129	5.1	4.90	0.06	16.48	0.85	0.586	0.029	1196.9	27.9	2905.1	98.9	4473.4	145.8	73.2	366.4	4.4
A6A-130	3.9	1.36	0.02	76.41	3.97	0.753	0.038	3558.6	76.9	4416.0	104.3	4833.8	143.3	26.4	294.6	3.9
A6A-131	39.9	11.25	0.04	3.06	0.15	0.250	0.012	549.0	3.7	1423.2	76.8	3183.4	158.5	82.8	409.8	1.4
A6A-132	10.9	6.92	0.05	9.24	0.47	0.464	0.023	870.4	10.9	2361.9	92.5	4129.1	148.6	78.9	407.4	2.6
A6A-133	19.6	9.27	0.03	5.24	0.26	0.352	0.018	660.4	4.6	1859.1	85.5	3716.9	152.5	82.2	404.7	1.4
A6A-134	38.9	14.18	0.25	2.40	0.13	0.247	0.012	439.3	14.7	1241.6	75.8	3162.2	158.8	86.1		
A6A-135	10.6	6.62	0.05	9.93	0.50	0.477	0.024	906.6	11.9	2428.4	93.2	4171.5	148.2	78.3	408.6	2.7
A6A-136	8.2	6.18	0.09	10.95	0.57	0.491	0.025	967.1	25.8	2519.0	96.9	4213.5	147.9	77.0	419.1	5.6
A6A-137	30.1	8.79	0.29	5.22	0.31	0.333	0.017	694.6	44.1	1856.0	102.6	3630.1	153.4	80.9		
A6A-138	36.6	10.45	0.04	3.76	0.19	0.285	0.014	589.1	3.9	1584.3	80.4	3390.4	156.0	82.6	412.9	1.4
A6A-139	73.1	13.37	0.05	1.24	0.06	0.120	0.006	464.9	3.4	819.2	56.4	1961.1	178.5	76.3	425.6	1.5
A6A-140	3.7	4.15	0.07	20.33	1.08	0.612	0.031	1391.6	44.7	3107.2	102.9	4536.6	145.4	69.3	379.8	6.2
A6A-141	6.6	6.03	0.07	11.84	0.61	0.519	0.026	988.5	21.0	2592.2	96.1	4294.3	147.2	77.0	391.1	4.2
A6A-142	42.0	10.66	0.20	3.24	0.17	0.251	0.013	578.1	21.2	1466.7	83.1	3187.5	158.5	81.9	431.6	7.4
A6A-143	51.8	11.52	0.04	2.86	0.14	0.239	0.012	536.5	3.3	1370.7	75.4	3111.8	159.4	82.8	408.1	1.2
A6A-144	15.8	6.95	0.05	8.95	0.45	0.452	0.023	866.4	12.1	2333.2	92.4	4089.8	148.9	78.8	419.8	3.0
A6A-145	17.5	6.91	0.05	9.44	0.48	0.473	0.024	871.5	12.1	2382.0	92.9	4159.5	148.3	79.0	396.6	2.8
A6A-146	12.6	7.41	0.05	8.16	0.41	0.438	0.022	816.3	10.5	2248.5	91.3	4045.7	149.3	79.8	409.1	2.7
A6A-147	6.1	4.28	0.04	19.31	0.98	0.600	0.030	1353.6	23.5	3057.7	98.4	4506.9	145.6	70.0	392.3	3.6
A6A-148	6.8	5.40	0.05	16.74	0.85	0.656	0.033	1095.8	19.5	2920.2	97.7	4635.7	144.7	76.4		
A6A-149	8.8	5.69	0.05	13.24	0.67	0.546	0.027	1044.1	17.7	2696.8	96.1	4370.8	146.6	76.1	374.3	3.3
A6A-150	34.4	10.46	0.05	4.11	0.21	0.312	0.016	588.4	5.0	1656.9	82.0	3531.5	154.4	83.3	391.0	1.7
A6A-151	8.6	5.61	0.05	12.97	0.66	0.528	0.026	1057.1	18.7	2677.3	96.0	4320.8	147.0	75.5	406.2	3.7
A6A-152	8.5	1.82	0.02	20.22	1.03	0.267	0.013	2825.8	38.8	3102.0	98.2	3286.0	157.2	14.0		
A6A-153	16.6	8.26	0.03	6.74	0.34	0.404	0.020	736.8	5.5	2078.2	88.7	3923.4	150.5	81.2	402.0	1.5

10.3.1.13 THBH (Apatite)

Grain I.D.	238U (ppm)	238/206 ratio	238/206 1SE	207/235 ratio	207/235 1SE	207/206 ratio	207/206 1SE	238/206 Age (Ma)	2σ	207/235 Age (Ma)	2σ	207/206 Age (Ma)	2σ	Disc. (%)	preferred Age (Ma)	preferred Err. (2σ)
THA-01	25.1	10.521	0.080	4.153	0.210	0.3170	0.0159	585.3	8.6	1664.8	82.8	3554.7	154.2		388.6	2.9
THA-02	1.9	1.982	0.033	50.807	2.680	0.7308	0.0365	2632.7	72.7	4008.2	105.2	4792.0	143.6		341.7	5.3
THA-03	8.1	6.897	0.067	9.738	0.496	0.4873	0.0244	872.9	16.0	2410.3	93.9	4202.5	148.0		389.2	3.6
THA-04	20.9	7.271	0.056	9.675	0.490	0.5104	0.0255	830.7	12.1	2404.4	93.2	4270.9	147.4		343.7	2.6
THA-05	11.4	6.170	0.062	11.582	0.591	0.5185	0.0259	968.3	18.1	2571.2	95.4	4294.1	147.2		393.2	3.8
THA-06	10.9	4.251	0.039	19.657	0.999	0.6064	0.0303	1361.8	22.4	3074.6	98.3	4522.7	145.5		400.2	3.5
THA-07	0.9	1.252	0.048	84.048	5.300	0.7634	0.0382	3785.0	220.1	4511.6	126.7	4854.3	143.2		326.4	9.7
THA-08	18.5	9.812	0.061	4.862	0.245	0.3461	0.0173	625.6	7.5	1795.7	84.9	3689.4	152.7		392.2	2.4
THA-09	18.3	8.934	0.065	5.844	0.295	0.3788	0.0189	684.0	9.4	1953.0	87.6	3826.4	151.4		400.4	2.8
THA-10	8.7	4.001	0.033	21.452	1.087	0.6228	0.0311	1438.1	21.3	3159.2	98.4	4561.4	145.2		391.6	3.1
THA-11	4.1	3.217	0.040	28.768	1.483	0.6716	0.0336	1744.7	38.5	3445.6	101.3	4670.5	144.4		362.4	4.3
THA-12	16.5	7.061	0.067	9.294	0.473	0.4761	0.0238	853.9	15.1	2367.4	93.4	4168.3	148.3		393.1	3.5
THA-13	30.6	9.507	0.061	5.193	0.262	0.3582	0.0179	644.7	7.9	1851.4	85.9	3741.6	152.2		394.2	2.4
THA-14	15.5	6.158	0.047	11.470	0.580	0.5125	0.0256	970.0	13.7	2562.1	94.5	4276.9	147.4		401.9	2.9
THA-15	9.3	6.134	0.060	11.760	0.599	0.5234	0.0262	973.5	17.8	2585.5	95.4	4308.0	147.1		389.0	3.7
THA-16	6.2	5.337	0.062	14.742	0.757	0.5709	0.0285	1107.2	23.5	2798.7	97.7	4434.9	146.1		374.1	4.1
THA-17	40.6	11.719	0.079	3.196	0.161	0.2718	0.0136	527.9	6.9	1456.2	78.1	3315.6	156.9		380.9	2.5
THA-18	68.1	11.424	0.079	3.044	0.154	0.2523	0.0126	541.0	7.2	1418.7	77.2	3198.6	158.3		404.3	2.7
THA-19	13.5	6.801	0.055	9.498	0.481	0.4687	0.0234	884.3	13.5	2387.4	93.1	4145.0	148.5		416.7	3.2
THA-20	26.7	9.044	0.092	5.654	0.289	0.3710	0.0186	676.1	13.1	1924.4	88.1	3795.0	151.7		402.6	3.9
THA-21	2.4	3.146	0.071	29.473	1.616	0.6727	0.0336	1779.5	70.1	3469.4	107.8	4672.8	144.4		367.7	7.3
THA-22	34.5	10.333	0.076	4.253	0.215	0.3189	0.0159	595.5	8.4	1684.4	83.1	3563.9	154.1		394.1	2.8
THA-23	73.4	11.897	0.071	2.830	0.143	0.2443	0.0122	520.3	6.0	1363.5	75.6	3147.3	159.0		394.0	2.3
THA-24	13.1	7.438	0.064	8.880	0.451	0.4792	0.0240	813.2	13.3	2325.8	92.7	4177.9	148.2		370.2	3.1
THA-25	7.5	5.543	0.058	13.747	0.702	0.5529	0.0276	1069.1	20.8	2732.5	96.8	4388.3	146.5		386.6	3.9
THA-26	14.8	7.992	0.098	7.376	0.380	0.4278	0.0214	760.0	17.6	2158.1	92.1	4009.0	149.7		397.2	4.6
THA-27	8.1	3.157	0.033	28.485	1.455	0.6525	0.0326	1773.8	32.7	3435.9	100.4	4628.9	144.7		418.1	4.2
THA-28	3.5	3.516	0.042	24.999	1.285	0.6378	0.0319	1613.4	34.0	3308.2	100.5	4596.0	144.9		410.0	4.6
THA-29	20.5	8.088	0.056	6.905	0.349	0.4052	0.0203	751.5	9.9	2099.3	89.6	3928.0	150.4		415.1	2.8
THA-30	16.9	7.191	0.050	8.638	0.436	0.4507	0.0225	839.3	11.0	2300.5	91.9	4086.9	149.0		414.7	2.8
THA-31	26.9	7.323	0.073	8.541	0.436	0.4539	0.0227	825.1	15.5	2290.3	92.7	4097.3	148.9		403.9	3.8
THA-32	6.7	7.371	0.071	8.014	0.408	0.4286	0.0214	820.2	14.9	2232.6	92.0	4011.9	149.6		429.1	3.9
THA-33	4.3	4.825	0.068	16.030	0.833	0.5612	0.0281	1214.2	31.2	2878.6	99.4	4410.0	146.3		429.2	5.6
THA-34	5.2	4.617	0.056	17.449	0.898	0.5846	0.0292	1263.8	27.7	2959.9	98.9	4469.5	145.9		407.3	4.6
THA-35	17.7	7.578	0.049	8.053	0.406	0.4428	0.0221	799.0	9.7	2237.0	91.1	4060.6	149.2		402.4	2.5
THA-36	9.8	5.259	0.050	13.815	0.703	0.5271	0.0264	1122.3	19.6	2737.1	96.4	4318.3	147.0		446.8	4.0
THA-37	4.7	3.777	0.032	25.250	1.281	0.6919	0.0346	1514.3	23.2	3317.9	99.2	4713.4	144.1		265.5	2.2
THA-38	12.4	9.984	0.062	4.326	0.218	0.3134	0.0157	615.3	7.3	1698.3	83.1	3536.9	154.4		412.1	2.5
THA-39	1.8	1.213	0.034	87.665	5.010	0.7713	0.0386	3876.9	161.4	4553.9	114.9	4869.0	143.1		283.6	6.7
THA-40	7.1	4.547	0.025	17.403	0.875	0.5741	0.0287	1281.5	12.8	2957.3	96.7	4443.2	146.1		432.0	2.3
THA-41	21.3	8.083	0.030	6.844	0.343	0.4014	0.0201	751.9	5.4	2091.4	88.9	3913.5	150.5		419.2	1.5
THA-42	43.5	10.786	0.052	3.298	0.166	0.2581	0.0129	571.6	5.3	1480.6	78.3	3234.6	157.9		423.4	2.0
THA-43	14.0	8.123	0.039	6.619	0.332	0.3901	0.0195	748.5	6.9	2061.9	88.7	3870.7	150.9		428.4	2.0
THA-44	21.9	7.421	0.031	7.926	0.398	0.4268	0.0213	814.9	6.5	2222.6	90.5	4005.6	149.7		428.2	1.7
THA-45	3.4	3.353	0.034	26.675	1.361	0.6489	0.0324	1682.7	30.2	3371.6	100.0	4620.9	144.8		402.8	3.9
THA-46	60.7	10.002	0.046	3.875	0.195	0.2812	0.0141	614.3	5.4	1608.4	81.1	3369.0	156.3		437.3	1.9
THA-47	36.6	11.842	0.060	2.781	0.140	0.2389	0.0119	522.6	5.1	1350.3	75.1	3112.1	159.4		399.5	2.0
THA-48	53.0	11.587	0.040	2.908	0.146	0.2445	0.0122	533.6	3.6	1383.9	75.8	3148.6	158.9		404.2	1.4
THA-49	15.0	8.063	0.052	6.860	0.346	0.4013	0.0201	753.7	9.1	2093.5	89.4	3913.5	150.5		420.2	2.6
THA-50	27.0	10.097	0.046	4.026	0.202	0.2950	0.0147	608.8	5.3	1639.4	81.7	3443.2	155.4		422.3	1.8
THA-51	14.3	5.972	0.028	11.526	0.579	0.4994	0.0250	998.1	8.9	2566.7	93.9	4238.9	147.7		431.9	2.0
THA-52	5.2	5.464	0.061	13.737	0.704	0.5446	0.0272	1083.4	22.3	2731.8	97.1	4366.2	146.7		404.4	4.3

Grain I.D.	238U (ppm)	238/206 ratio	238/206 1SE	207/235 ratio	207/235 1SE	207/206 ratio	207/206 1SE	238/206 Age (Ma)	2σ	207/235 Age (Ma)	2σ	207/206 Age (Ma)	2σ	Disc. (%)	preferred Age (Ma)	preferred Err. (2σ)
THA-53	20.4	8.978	0.036	5.641	0.283	0.3675	0.0184	680.8	5.2	1922.3	86.6	3780.3	151.8		408.7	1.6
THA-54	60.0	11.099	0.052	3.350	0.168	0.2698	0.0135	556.1	5.1	1492.8	78.6	3304.1	157.0		403.2	1.8
THA-55	9.4	7.258	0.044	8.585	0.432	0.4521	0.0226	832.1	9.5	2295.0	91.7	4091.5	148.9		409.5	2.4
THA-56	14.7	4.860	0.026	15.049	0.757	0.5307	0.0265	1206.1	12.0	2818.4	95.8	4328.3	147.0		476.7	2.5
THA-57	31.7	8.829	0.029	5.464	0.274	0.3500	0.0175	691.7	4.4	1894.9	86.1	3706.4	152.6		431.4	1.4
THA-58	76.7	13.468	0.086	1.641	0.083	0.1603	0.0080	461.7	5.7	985.9	63.6	2458.2	169.2		399.4	2.5
THA-59	84.6	12.878	0.038	1.669	0.084	0.1559	0.0078	482.1	2.8	996.6	63.6	2411.0	170.0		420.1	1.2
THA-60	8.3	3.082	0.014	29.797	1.496	0.6663	0.0333	1811.6	14.3	3480.1	98.7	4659.1	144.5		391.9	1.7
THA-61	49.4	11.407	0.054	2.994	0.150	0.2478	0.0124	541.7	4.9	1406.2	76.5	3170.3	158.7		408.1	1.9
THA-62	9.1	4.090	0.026	20.255	1.021	0.6011	0.0301	1409.9	16.4	3103.6	97.7	4510.1	145.6		426.0	2.6
THA-63	9.2	6.486	0.051	10.559	0.534	0.4969	0.0248	924.4	13.6	2485.1	94.0	4231.3	147.7		401.5	3.0
THA-64	53.1	11.755	0.089	2.732	0.138	0.2330	0.0116	526.3	7.7	1337.1	75.2	3072.0	159.9		406.5	3.0
THA-65	1.6	1.171	0.032	90.069	5.127	0.7655	0.0383	3978.9	161.7	4581.0	114.5	4858.2	143.2		334.1	7.8
THA-66	4.7	3.382	0.042	25.985	1.338	0.6376	0.0319	1669.9	36.2	3346.0	100.8	4595.6	144.9		426.4	4.9
THA-67	4.5	3.450	0.028	25.645	1.299	0.6420	0.0321	1640.7	23.5	3333.1	99.1	4605.5	144.9		407.8	3.2
THA-68	13.1	6.570	0.073	9.569	0.490	0.4562	0.0228	913.3	19.0	2394.2	94.2	4104.9	148.8		446.4	4.7
THA-69	4.2	4.059	0.050	20.045	1.032	0.5904	0.0295	1419.6	31.2	3093.5	99.7	4483.9	145.8		450.5	5.2
THA-70	4.4	3.286	0.044	27.656	1.432	0.6594	0.0330	1712.8	40.3	3407.0	101.6	4643.9	144.6		385.2	4.8
THA-71	3.7	4.346	0.071	19.406	1.021	0.6120	0.0306	1334.9	39.5	3062.2	101.7	4536.1	145.4		381.1	5.8
THA-72	15.6	1.841	0.014	17.293	0.874	0.2310	0.0116	2796.4	34.1	2951.2	97.1	3058.5	160.1			
THA-73	14.9	10.253	0.078	4.087	0.207	0.3041	0.0152	599.9	8.8	1651.7	82.5	3490.3	154.9		408.8	3.0
THA-74	85.1	13.374	0.085	1.433	0.072	0.1390	0.0070	464.8	5.7	902.8	60.3	2214.6	173.5		415.0	2.5
THA-75	59.2	11.422	0.072	2.894	0.146	0.2398	0.0120	541.1	6.5	1380.4	76.1	3118.2	159.3		413.2	2.5
THA-76	29.8	10.305	0.066	3.960	0.200	0.2961	0.0148	597.0	7.4	1626.1	81.8	3449.4	155.3		413.0	2.6
THA-77	3.0	1.947	0.030	54.296	2.840	0.7672	0.0384	2671.8	67.3	4074.4	104.5	4861.3	143.1		195.1	2.8
THA-78	14.2	7.442	0.057	8.107	0.410	0.4378	0.0219	812.8	11.7	2243.1	91.5	4043.5	149.4		415.1	3.0
THA-79	18.5	7.325	0.066	8.962	0.455	0.4763	0.0238	824.9	14.0	2334.1	92.9	4168.9	148.3		379.0	3.3
THA-80	10.5	4.018	0.035	21.125	1.072	0.6159	0.0308	1432.6	22.4	3144.4	98.5	4545.4	145.3		403.8	3.4
THA-81	6.2	5.038	0.047	15.405	0.783	0.5631	0.0282	1167.2	19.7	2840.6	97.0	4415.0	146.3		408.4	3.6
THA-82	19.6	8.140	0.059	7.131	0.360	0.4212	0.0211	747.0	10.3	2128.0	90.0	3985.8	149.9		396.6	2.8
THA-83	9.9	5.836	0.056	12.386	0.630	0.5245	0.0262	1019.6	18.0	2634.1	95.7	4310.8	147.1		407.1	3.7
THA-84	20.0	8.230	0.059	6.701	0.338	0.4002	0.0200	739.2	10.0	2072.8	89.3	3909.1	150.6		413.0	2.8
THA-85	4.2	3.934	0.055	22.218	1.154	0.6342	0.0317	1460.0	36.8	3193.3	101.0	4587.8	145.0		374.6	4.9
THA-86	28.0	10.660	0.093	3.603	0.183	0.2787	0.0139	578.0	9.6	1550.3	80.7	3355.0	156.4		412.7	3.4
THA-87	13.9	6.989	0.054	8.881	0.449	0.4504	0.0225	862.1	12.5	2325.8	92.4	4085.7	149.0		426.9	3.2
THA-88	45.1	11.188	0.108	3.072	0.156	0.2493	0.0125	551.9	10.3	1425.6	78.0	3179.9	158.5		414.8	3.8
THA-89	28.9	10.992	0.099	3.235	0.164	0.2580	0.0129	561.3	9.7	1465.6	78.8	3233.9	157.9		415.7	3.6
THA-90	15.2	7.430	0.069	8.319	0.423	0.4485	0.0224	814.0	14.3	2266.3	92.3	4079.5	149.0		404.1	3.6
THA-91	47.8	11.148	0.074	3.238	0.163	0.2619	0.0131	553.8	7.1	1466.3	78.3	3257.6	157.6		407.2	2.6
THA-92	102.0	12.904	0.122	1.878	0.096	0.1758	0.0088	481.1	8.8	1073.3	67.4	2613.1	166.6		406.8	3.7
THA-93	7.4	5.836	0.083	12.879	0.669	0.5453	0.0273	1019.6	26.8	2670.8	98.0	4368.1	146.6		378.1	5.0
THA-94	59.0	12.956	0.122	1.973	0.100	0.1855	0.0093	479.3	8.7	1106.4	68.6	2702.0	165.2		399.1	3.6
THA-95	28.6	9.616	0.073	5.158	0.261	0.3599	0.0180	637.8	9.2	1845.6	86.0	3748.6	152.1		388.5	2.8
THA-96	6.7	10.481	0.093	3.705	0.188	0.2817	0.0141	587.5	9.9	1572.4	81.2	3371.9	156.2		417.3	3.5
THA-97	7.3	4.764	0.058	17.012	0.876	0.5881	0.0294	1228.2	27.4	2935.5	98.8	4478.3	145.8		388.9	4.5
THA-98	30.3	9.794	0.071	4.829	0.244	0.3431	0.0172	626.7	8.7	1789.9	85.0	3676.1	152.9		395.4	2.8
THA-99	9.7	5.923	0.169	11.879	0.684	0.5106	0.0255	1005.6	53.2	2594.9	107.9	4271.4	147.4		420.2	10.1
THA-100	76.7	12.065	0.064	2.703	0.136	0.2366	0.0118	513.3	5.3	1329.2	74.6	3096.4	159.6		393.8	2.0
THA-101	35.0	11.019	0.078	3.386	0.171	0.2708	0.0135	560.0	7.6	1501.3	79.2	3309.7	157.0		405.4	2.7
THA-102	19.8	9.599	0.073	4.932	0.249	0.3435	0.0172	638.8	9.2	1807.8	85.4	3677.9	152.9		402.9	2.9
THA-103	26.8	10.184	0.064	3.829	0.193	0.2829	0.0141	603.8	7.2	1598.9	81.2	3378.5	156.1		428.3	2.6
THA-104	17.3	10.728	0.098	3.817	0.194	0.2971	0.0149	574.5	10.0	1596.4	81.8	3454.6	155.3		396.3	3.4
THA-105	9.0	6.736	0.052	9.801	0.496	0.4790	0.0240	892.3	12.9	2416.2	93.3	4177.3	148.2		408.3	3.0
THA-106	17.8	7.222	0.110	8.613	0.450	0.4513	0.0226	836.0	23.9	2297.9	95.1	4089.0	149.0		412.3	5.8
THA-107	36.2	12.499	0.086	2.130	0.107	0.1932	0.0097	496.2	6.6	1158.5	69.8	2768.4	164.2		408.5	2.7
THA-108	8.8	5.836	0.035	12.339	0.621	0.5225	0.0261	1019.5	11.5	2630.6	94.7	4305.4	147.1		409.8	2.4
THA-109	6.7	4.440	0.044	18.376	0.937	0.5919	0.0296	1309.6	23.4	3009.6	98.2	4487.7	145.7		409.9	3.8

Grain I.D.	238U (ppm)	238/206 ratio	238/206 1SE	207/235 ratio	207/235 1SE	207/206 ratio	207/206 1SE	238/206 Age (Ma)	2σ	207/235 Age (Ma)	2σ	207/206 Age (Ma)	2σ	Disc. (%)	preferred Age (Ma)	preferred Err. (2σ)
THA-110	2.9	2.356	0.042	40.650	2.159	0.6950	0.0347	2280.4	69.0	3786.7	105.4	4719.7	144.1		411.9	6.7
THA-111	10.9	6.078	0.062	11.555	0.590	0.5096	0.0255	981.9	18.7	2569.0	95.5	4268.5	147.4		411.0	4.0
THA-112	8.7	4.802	0.042	16.256	0.825	0.5664	0.0283	1219.4	19.3	2892.0	97.2	4423.5	146.2		422.4	3.5
THA-113	59.9	12.607	0.090	1.979	0.100	0.1810	0.0091	492.1	6.8	1108.4	68.2	2661.6	165.8		412.8	2.8
THA-114	58.2	13.607	0.087	1.675	0.084	0.1654	0.0083	457.2	5.7	999.0	64.1	2510.4	168.3		392.3	2.4
THA-115	18.1	9.065	0.072	5.261	0.266	0.3461	0.0173	674.5	10.2	1862.6	86.4	3689.1	152.7		423.9	3.2
THA-116	20.4	10.280	0.052	2.043	0.103	0.1524	0.0076	598.4	5.8	1129.9	68.5	2371.9	170.7			
THA-117	75.4	11.628	0.104	2.616	0.133	0.2208	0.0110	531.8	9.2	1305.3	74.7	2985.5	161.1		419.3	3.6
THA-118	16.6	8.740	0.083	6.436	0.327	0.4081	0.0204	698.4	12.5	2037.1	89.5	3938.5	150.3		382.0	3.4
THA-119	28.7	7.972	0.076	7.191	0.366	0.4160	0.0208	761.8	13.8	2135.4	90.8	3967.1	150.0		410.1	3.7
THA-120	32.3	10.889	0.065	3.165	0.159	0.2500	0.0125	566.4	6.5	1448.6	77.7	3184.2	158.5		425.5	2.5
THA-121	18.1	7.597	0.046	8.070	0.407	0.4448	0.0222	797.2	9.2	2238.9	91.1	4067.4	149.1		399.3	2.4
THA-122	7.2	8.229	0.079	7.324	0.373	0.4374	0.0219	739.3	13.5	2151.8	91.0	4042.1	149.4		376.5	3.5
THA-123	3.7	2.646	0.041	35.891	1.881	0.6891	0.0345	2066.5	55.5	3663.5	103.6	4707.6	144.2		385.5	5.6
THA-124	20.0	4.516	0.031	17.732	0.895	0.5810	0.0290	1289.6	16.0	2975.3	97.1	4460.5	145.9		422.7	2.8
THA-125	72.0	13.357	0.069	2.049	0.103	0.1986	0.0099	465.4	4.7	1131.8	68.6	2813.6	163.5		379.4	1.9
THA-126	14.6	7.193	0.056	8.618	0.436	0.4498	0.0225	839.2	12.4	2298.5	92.1	4083.8	149.0		415.7	3.1
THA-127	34.0	10.341	0.067	4.152	0.209	0.3115	0.0156	595.0	7.4	1664.5	82.6	3527.8	154.5		399.6	2.5
THA-128	49.2	11.265	0.063	3.104	0.156	0.2537	0.0127	548.3	6.0	1433.6	77.3	3207.2	158.2		409.0	2.2
THA-129	49.4	10.661	0.099	3.681	0.187	0.2847	0.0142	578.0	10.2	1567.2	81.2	3388.4	156.0		408.1	3.6
THA-130	52.7	12.858	0.068	1.830	0.092	0.1707	0.0085	482.8	4.9	1056.1	66.0	2563.7	167.4		411.4	2.1
THA-131	7.9	5.250	0.055	14.572	0.744	0.5551	0.0278	1124.0	21.6	2787.7	97.2	4393.9	146.4		404.6	4.0
THA-132	24.8	7.815	0.041	7.632	0.384	0.4328	0.0216	776.2	7.8	2188.6	90.3	4026.3	149.5		400.8	2.0
THA-133	17.5	5.299	0.081	13.882	0.726	0.5337	0.0267	1114.4	31.2	2741.7	99.1	4336.5	146.9		433.4	6.1
THA-134	21.8	9.374	0.051	5.406	0.272	0.3677	0.0184	653.4	6.8	1885.7	86.2	3781.2	151.8		391.6	2.1
THA-135	8.2	4.182	0.036	20.094	1.020	0.6097	0.0305	1382.2	21.7	3095.9	98.3	4530.7	145.4		400.3	3.3
THA-136	18.3	7.228	0.043	8.651	0.436	0.4537	0.0227	835.4	9.3	2301.9	91.7	4096.6	148.9		409.4	2.3
THA-137	54.7	12.687	0.117	1.888	0.096	0.1738	0.0087	489.1	8.7	1077.0	67.5	2594.2	166.9		414.8	3.7
THA-138	12.8	6.512	0.055	10.496	0.532	0.4960	0.0248	920.9	14.6	2479.6	94.1	4228.6	147.8		401.0	3.3
THA-139	10.4	3.647	0.033	24.284	1.234	0.6426	0.0321	1562.2	25.2	3279.8	99.2	4606.7	144.9		385.0	3.3
THA-140	24.5	10.029	0.053	4.229	0.213	0.3078	0.0154	612.7	6.2	1679.7	82.6	3509.1	154.7		414.8	2.1
THA-141	49.2	11.492	0.100	3.028	0.154	0.2525	0.0126	537.9	9.0	1414.8	77.5	3200.0	158.3		401.8	3.3
THA-142	17.7	9.316	0.073	5.277	0.267	0.3567	0.0178	657.3	9.8	1865.1	86.4	3735.2	152.3		403.5	3.0
THA-143	1.8	1.635	0.052	62.239	3.683	0.7384	0.0369	3076.3	154.9	4210.7	118.4	4806.7	143.5		375.3	9.8
THA-144	33.4	4.714	0.024	16.493	0.829	0.5642	0.0282	1240.1	11.4	2905.8	96.3	4417.7	146.3		434.0	2.1
THA-145	0.5	1.162	0.199	110.546	19.752	0.9322	0.0466	4002.2	1022.9	4787.0	359.7	5137.8	141.5			
THA-146	150.9	13.752	0.070	1.311	0.066	0.1309	0.0065	452.5	4.5	850.8	57.9	2108.7	175.6		408.6	2.0
THA-147	76.7	12.711	0.110	2.008	0.102	0.1852	0.0093	488.2	8.2	1118.2	68.8	2699.2	165.3		406.9	3.4
THA-148	36.2	8.686	0.067	5.971	0.302	0.3763	0.0188	702.4	10.3	1971.6	88.0	3816.3	151.5		413.9	3.1
THA-149	51.0	11.531	0.085	2.961	0.150	0.2477	0.0124	536.1	7.6	1397.6	76.8	3169.6	158.7		403.9	2.9
THA-150	40.4	10.691	0.049	3.523	0.177	0.2733	0.0137	576.4	5.1	1532.4	79.4	3324.4	156.8		415.6	1.8
THA-151	4.6	3.409	0.042	26.403	1.360	0.6531	0.0327	1658.3	36.3	3361.6	100.9	4630.1	144.7		386.5	4.5
THA-152	76.8	11.065	0.060	3.364	0.169	0.2701	0.0135	557.7	5.8	1496.0	78.7	3305.7	157.0		404.2	2.1
THA-153	17.4	8.107	0.055	7.058	0.356	0.4152	0.0208	749.8	9.7	2118.8	89.8	3964.4	150.1		404.2	2.7
THA-154	7.9	5.108	0.089	15.719	0.832	0.5827	0.0291	1152.5	36.8	2859.9	101.2	4464.7	145.9		371.8	5.9
THA-155	6.0	4.292	0.045	19.484	0.995	0.6068	0.0303	1350.1	25.6	3066.1	98.8	4523.8	145.5		395.6	3.9
THA-156	14.8	5.905	0.060	12.456	0.636	0.5337	0.0267	1008.5	19.1	2639.4	96.0	4336.4	146.9		389.8	3.8
THA-157	25.4	8.271	0.036	6.870	0.345	0.4123	0.0206	735.8	6.1	2094.8	89.0	3954.0	150.2		399.1	1.7
THA-158	2.7	3.083	0.076	29.339	1.635	0.6563	0.0328	1811.0	77.7	3464.9	109.5	4637.3	144.7		418.0	8.9
THA-159	4.2	3.938	0.052	22.322	1.155	0.6379	0.0319	1458.6	34.6	3197.8	100.6	4596.1	144.9		366.6	4.6
THA-160	33.0	10.078	0.063	4.505	0.227	0.3295	0.0165	609.9	7.3	1732.0	83.8	3613.9	153.5		395.4	2.4
THA-161	12.2	8.000	0.049	7.470	0.376	0.4336	0.0217	759.3	8.8	2169.4	90.3	4029.3	149.5		390.9	2.3
THA-162	56.2	14.408	0.156	1.277	0.065	0.1335	0.0067	432.6	9.1	835.6	58.3	2144.0	174.9		388.8	4.0
THA-163	38.8	9.513	0.057	5.355	0.270	0.3696	0.0185	644.4	7.4	1877.7	86.2	3789.2	151.7		384.3	2.2
THA-164	6.1	4.689	0.050	17.444	0.892	0.5935	0.0297	1246.2	24.2	2959.6	98.3	4491.5	145.7		385.7	3.9
THA-165	21.0	8.153	0.092	7.266	0.372	0.4298	0.0215	745.8	15.9	2144.7	91.5	4016.2	149.6		387.4	4.1
THA-166	28.9	9.596	0.056	5.158	0.260	0.3591	0.0180	639.1	7.1	1845.7	85.7	3745.4	152.2		389.9	2.2

Grain I.D.	238U (ppm)	238/206 ratio	238/206 1SE	207/235 ratio	207/235 1SE	207/206 ratio	207/206 1SE	238/206 Age (Ma)	2σ	207/235 Age (Ma)	2σ	207/206 Age (Ma)	2σ	Disc. (%)	preferred Age (Ma)	preferred Err. (2σ)
THA-167	32.9	11.542	0.159	3.155	0.164	0.2642	0.0132	535.6	14.2	1446.3	80.0	3271.5	157.4		391.9	5.1
THA-168	35.5	8.046	0.048	7.122	0.359	0.4158	0.0208	755.2	8.6	2126.8	89.7	3966.5	150.1		406.6	2.4
THA-169	46.6	10.982	0.074	3.679	0.186	0.2932	0.0147	561.8	7.2	1566.8	80.6	3433.7	155.5		390.2	2.5
THA-170	49.9	10.971	0.129	3.487	0.179	0.2776	0.0139	562.3	12.6	1524.3	81.1	3348.6	156.5		402.1	4.4
THA-171	21.9	8.928	0.100	5.924	0.304	0.3838	0.0192	684.4	14.6	1964.8	89.1	3845.9	151.2		396.2	4.2
THA-172	47.6	10.735	0.090	3.733	0.189	0.2908	0.0145	574.2	9.2	1578.5	81.2	3421.1	155.6		400.8	3.2
THA-173	14.2	7.872	0.065	7.386	0.374	0.4218	0.0211	771.0	12.0	2159.2	90.7	3988.1	149.9		409.2	3.2

10.3.1.14 CHBH (Apatite)

Grain I.D.	238U (ppm)	238/206 ratio	238/206 1SE	207/235 ratio	207/235 1SE	207/206 ratio	207/206 1SE	238/206 Age (Ma)	2σ	207/235 Age (Ma)	2σ	207/206 Age (Ma)	2σ	Disc. (%)	preferred Age (Ma)	preferred Err. (2σ)
CHG1-01	14.05	6.17	0.135	12.06	0.72	0.527	0.009	986	41	2592	57	4292	51	0.714921	459	23
CHG1-02	9.29	2.026	0.0275	19.39	0.76	0.2856	0.005	2581	66	3056	38	3384	54	0.491706	2278	62
CHG1-03	2.75	3.06	0.165	36.2	6.6	0.804	0.0165	1900	160	3720	120	-	43	0.559621	410	72
CHG1-04	14.65	6.48	0.08	10.54	0.38	0.493	0.007	925	18	2485	36	4211		0.576251	458	10
CHG1-05	11.13	1.761	0.0155	21.24	0.56	0.2724	0.00395	2906	40	3152	28	3311	46	0.313064	2729	39
CHG1-06	66.6	10.88	0.105	3.51	0.13	0.274	0.0055	569	10	1527	29	3319	60	0.241769	420.2	7.6
CHG1-07	5.68	3.18	0.13	33.4	2.4	0.774	0.0175	1760	110	3611	88			0.915497	381	47
CHG1-08	10.73	2.373	0.022	13.48	0.49	0.2312	0.0038	2273	35	2708	34	3049	53	0.403362	2073	33
CHG1-09	14.09	3.951	0.0475	22.19	0.49	0.635	0.0085	1462	30	3190	21	4489	34	0.272627	538	15
CHG1-10	23.6	7.72	0.085	8.17	0.26	0.452	0.0075	789	16	2246	29	4082	50	0.119739	422.1	9.8
CHG1-11	4.59	1.651	0.022	28.1	1.2	0.336	0.006	3051	71	3424	38	3634	58	0.514814	2727	68
CHG1-12	11.58	8.15	0.15	5.95	0.32	0.35	0.0085	752	27	1961	47	3690	77	0.48089	480	18
CHG1-13	4.69	1.666	0.0215	27	1	0.327	0.006	3032	69	3376	37	3590	56	0.432242	2729	66
CHG1-14	3.83	4.91	0.195	17.8	1.8	0.602	0.0175	1257	96	2960	100	4320	93	0.786854	494	50
CHG1-15	12.04	2.346	0.0265	13.65	0.43	0.2333	0.00345	2298	43	2729	34	3066	48	0.580905	2096	41
CHG1-16	27.69	7.47	0.09	7.29	0.28	0.398	0.0075	815	19	2141	35	3888	57	0.581027	492	12
CHG1-17	34.08	6.7	0.06	10.35	0.24	0.502	0.006	899	14	2464	22	4243	35	0.176319	432.8	7.9
CHG1-18	20.47	3.89	0.065	20.09	0.38	0.565	0.0085	1488	45	3094	19	4391	42	0.449853	681	26
CHG1-19	0.745	0.493	0.013	237	17	0.838	0.0165	7160	220	5551	64			0.780708		
CHG1-20	16.62	2.102	0.017	15.04	0.52	0.2295	0.00315	2505	38	2812	32	3040	44	0.595832	2345	36
CHG1-21	2.19	1.262	0.0425	91.7	4.6	0.838	0.02	3790	190	4590	49			0.73368	1365	79
CHG1-22	40.7	2.077	0.0115	14.44	0.28	0.2181	0.00205	2536	24	2778	18	2963	30	0.143528	2414	24
CHG1-23	1.357	1.059	0.0245	98.6	4.5	0.768	0.0175	4300	160	4661	47	4503	37	0.635557	1856	67
CHG1-24	10.6	2.08	0.05	18.5	1.1	0.276	0.007	2560	100	3005	60	3325	82	0.539894	2240	100
CHG1-25	4.73	2.561	0.0435	39.7	1.8	0.732	0.0135	2141	61	3755	44	4537	23	0.604248		

10.3.1.15 EM-14 (Apatite)

Grain I.D.	238U (ppm)	238/206 ratio	238/206 1SE	207/235 ratio	207/235 1SE	207/206 ratio	207/206 1SE	238/206 Age (Ma)	2σ	207/235 Age (Ma)	2σ	207/206 Age (Ma)	2σ	Disc. (%)	preferred Age (Ma)	preferred Err. (2σ)
14A-01	62.6	6.718	0.151	4.136	0.227	0.2016	0.0101	894.49	37.7	1661.5	89.7	2838.7	163.2	68		
14A-02	69.0	4.687	0.453	13.703	1.492	0.4660	0.0233	1246.76	219.2	2729.4	206.1	4136.4	148.5	70		
14A-03	36.8	12.005	0.089	2.373	0.120	0.2067	0.0103	515.78	7.3	1234.6	72.2	2879.3	162.6	82	416.1	2.9
14A-04	21.3	6.765	0.061	9.665	0.491	0.4744	0.0237	888.71	15.1	2403.4	93.6	4163.1	148.3	79	413.1	3.6
14A-05	9.7	3.021	0.034	24.655	1.263	0.5405	0.0270	1843.25	35.6	3294.6	100.1	4354.9	146.8	58		
14A-06	9.7	4.967	0.052	15.326	0.783	0.5524	0.0276	1182.46	22.5	2835.7	97.4	4386.8	146.5	73	433.4	4.3
14A-07	3.5	4.113	0.100	20.877	1.160	0.6231	0.0312	1402.83	61.2	3132.9	107.8	4562.2	145.2	69	383.0	8.1
14A-08	4.2	6.184	0.169	12.814	0.731	0.5750	0.0287	966.31	49.2	2666.1	107.5	4445.3	146.1	78		
14A-09	7.8	4.924	0.060	15.709	0.808	0.5613	0.0281	1191.81	26.5	2859.2	98.3	4410.2	146.3	73	422.5	4.8
14A-10	153.6	12.841	0.070	1.776	0.089	0.1655	0.0083	483.44	5.1	1036.9	65.4	2511.9	168.3	81	415.4	2.2
14A-11	67.3	11.236	0.082	3.087	0.156	0.2517	0.0126	549.64	7.7	1429.5	77.5	3194.6	158.4	83	411.8	2.9
14A-12	5.6	5.130	0.086	3.052	0.161	0.1136	0.0057	1148.11	35.3	1420.7	80.7	1856.7	180.8	38	1105.7	15.5
14A-13	4.1	3.313	0.051	29.695	1.553	0.7139	0.0357	1700.35	46.0	3476.8	102.9	4758.2	143.8	64		
14A-14	25.8	8.634	0.162	5.534	0.295	0.3467	0.0173	706.45	25.0	1905.8	91.9	3691.8	152.7	81	444.7	7.5
14A-15	3.7	1.110	0.020	98.294	5.221	0.7920	0.0396	4139.46	109.6	4668.8	107.0	4906.8	142.9	16	168.6	2.8
14A-16	5.7	3.959	0.073	21.291	1.135	0.6116	0.0306	1451.90	48.2	3151.9	103.5	4535.1	145.4	68	421.2	7.1
14A-17	104.1	12.462	0.112	1.642	0.083	0.1485	0.0074	497.57	8.7	986.5	64.1	2327.7	171.4	79	438.8	3.8
14A-18	139.1	3.730	0.024	4.180	0.211	0.1131	0.0057	1531.00	17.8	1670.1	82.7	1849.8	180.9	17	1501.7	8.6
14A-19	11.3	4.592	0.052	17.425	0.893	0.5807	0.0290	1269.96	26.0	2958.6	98.5	4459.7	145.9	72	418.4	4.5
14A-20	1.1	0.881	0.062	126.141	10.846	0.8066	0.0403	4888.44	479.4	4919.8	173.4	4932.8	142.7	1		
14A-21	2.8	3.135	0.125	15.287	0.979	0.3477	0.0174	1784.94	124.7	2833.3	122.1	3696.2	152.7	52	1321.4	35.3
14A-22	9.8	3.155	0.031	23.370	1.191	0.5351	0.0268	1774.67	30.4	3242.5	99.3	4340.2	146.9	59		
14A-23	14.2	10.692	0.109	3.795	0.194	0.2944	0.0147	576.37	11.3	1591.7	82.1	3440.5	155.4	83	400.0	3.9
14A-24	24.0	1.991	0.016	14.543	0.736	0.2101	0.0105	2623.25	34.8	2785.8	96.3	2905.7	162.2	10	2505.4	15.9
14A-25	22.4	7.320	0.103	7.753	0.403	0.4118	0.0206	825.45	21.9	2202.8	93.5	3952.1	150.2	79	451.3	5.9
14A-26	4.2	3.546	0.068	6.880	0.369	0.1770	0.0089	1601.44	54.8	2096.0	95.1	2624.3	166.4	39	1467.3	22.5
14A-27	7.3	4.119	0.207	20.272	1.438	0.6059	0.0303	1401.16	126.7	3104.4	137.3	4521.4	145.5	69	416.3	14.2
14A-28	10.3	4.121	0.041	19.784	1.008	0.5916	0.0296	1400.49	25.0	3080.8	98.6	4486.8	145.7	69	444.0	4.2
14A-29	21.1	2.796	0.024	8.662	0.439	0.1757	0.0088	1970.97	29.2	2303.1	92.4	2612.4	166.6	25	1850.0	13.3
14A-30	21.0	11.291	0.145	3.709	0.191	0.3039	0.0152	547.07	13.5	1573.3	82.6	3489.3	154.9	84	372.4	4.5
14A-31	2.9	6.869	0.195	8.968	0.516	0.4470	0.0223	876.15	46.5	2334.8	105.1	4074.5	149.1	78		
14A-32	3.5	0.973	0.314	102.967	33.668	0.7268	0.0363	4557.92	2111.8	4715.5	657.7	4783.9	143.6	5	1764.6	61.2
14A-33	10.5	3.820	0.046	7.168	0.369	0.1987	0.0099	1499.06	32.0	2132.6	91.7	2814.6	163.5	47	1331.7	13.8
14A-34	14.5	4.586	0.053	17.345	0.890	0.5772	0.0289	1271.63	26.7	2954.1	98.6	4450.9	146.0	71	425.2	4.6
14A-35	11.5	3.656	0.023	15.612	0.787	0.4141	0.0207	1558.77	17.3	2853.3	96.2	3960.4	150.1	61	1028.6	5.9
14A-36	3.2	2.631	0.065	36.029	2.012	0.6878	0.0344	2076.82	88.4	3667.3	110.5	4704.7	144.2	56	396.3	8.6
14A-37	4.0	4.017	0.074	20.963	1.117	0.6110	0.0305	1433.09	47.5	3136.9	103.4	4533.7	145.4	68	416.4	7.0
14A-38	31.8	8.444	0.088	5.873	0.300	0.3598	0.0180	721.51	14.3	1957.2	88.7	3748.4	152.1	81	442.0	4.4
14A-39	3.2	2.728	0.074	31.479	1.793	0.6232	0.0312	2013.00	94.3	3534.1	112.2	4562.3	145.2	56	572.3	13.1
14A-40	22.3	3.748	0.032	4.964	0.252	0.1350	0.0068	1524.54	23.3	1813.3	85.8	2163.4	174.5	30	1459.4	10.9
14A-41	0.8	0.846	0.089	125.476	14.559	0.7702	0.0385	5029.90	731.3	4914.5	233.9	4867.0	143.1	-3	429.8	18.7
14A-42	56.4	12.623	0.113	1.749	0.089	0.1602	0.0080	491.46	8.5	1026.9	65.6	2457.3	169.2	80	425.8	3.6
14A-43	10.4	1.513	0.052	66.772	4.055	0.7329	0.0366	3271.46	176.9	4281.0	121.6	4795.9	143.6	32	443.1	12.1
14A-44	10.3	5.583	0.070	13.762	0.710	0.5575	0.0279	1062.09	24.7	2733.5	97.7	4400.3	146.4	76	378.9	4.5
14A-45	22.4	3.158	0.045	6.395	0.332	0.1465	0.0073	1773.34	44.2	2031.5	91.3	2305.1	171.8	23	1699.7	19.4
14A-46	0.8	2.372	0.598	47.261	12.157	0.8133	0.0407	2268.03	964.9	3936.2	511.6	4944.5	142.6	54		
14A-47	1.3	4.072	0.614	15.351	2.438	0.4536	0.0227	1415.54	383.2	2837.2	302.9	4096.3	148.9	65		
14A-48	22.0	5.728	0.036	12.394	0.625	0.5151	0.0258	1037.32	12.2	2634.7	94.8	4284.4	147.3	76	429.3	2.6
14A-49	1.4	2.001	0.113	47.430	3.573	0.6888	0.0344	2612.28	242.1	3939.8	149.9	4706.8	144.2	45		
14A-50	1.0	1.244	0.147	73.247	9.388	0.6611	0.0331	3803.04	678.1	4373.7	256.8	4647.8	144.6	18	1712.9	62.5
14A-51	11.8	3.890	0.062	21.382	1.123	0.6035	0.0302	1474.89	42.2	3156.1	101.9	4515.8	145.5	67	445.2	6.6
14A-52	3.6	3.215	0.161	12.640	0.893	0.2949	0.0147	1745.63	152.8	2653.2	133.1	3442.9	155.4	49	1389.5	39.7

Grain I.D.	238U (ppm)	238/206 ratio	238/206 1SE	207/235 ratio	207/235 1SE	207/206 ratio	207/206 1SE	238/206 Age (Ma)	2σ	207/235 Age (Ma)	2σ	207/206 Age (Ma)	2σ	Disc. (%)	preferred Age (Ma)	preferred Err. (2σ)
14A-53	44.5	10.528	0.096	2.852	0.145	0.2179	0.0109	584.93	10.2	1369.3	76.4	2964.3	161.4	80	464.7	4.0
14A-54	36.4	7.665	0.055	7.105	0.359	0.3952	0.0198	790.52	10.7	2124.7	90.0	3890.1	150.8	80	448.9	3.1
14A-55	22.4	8.638	0.078	5.480	0.278	0.3435	0.0172	706.19	12.1	1897.5	87.3	3677.6	152.9	81	447.5	3.8
14A-56	5.6	3.123	0.051	28.197	1.483	0.6389	0.0319	1790.88	51.2	3426.0	103.3	4598.4	144.9	61	461.2	6.9
14A-57	5.6	1.547	0.020	33.717	1.741	0.3786	0.0189	3213.37	65.4	3601.8	102.0	3825.5	151.4	16	2539.3	25.4
14A-58	0.3	1.022	1.167	116.364	132.943	0.8631	0.0432	4397.86	7276.9	4838.6	2300.3	5029.0	142.1	13		
14A-59	318.2	7.391	0.044	1.373	0.069	0.0737	0.0037	818.04	9.3	877.6	59.2	1031.1	202.2	21		
14A-60	11.5	6.728	0.085	9.155	0.472	0.4469	0.0223	893.34	21.2	2353.6	94.5	4074.2	149.1	78	448.4	5.3
14A-61	7.6	4.670	0.149	18.460	1.094	0.6255	0.0313	1250.75	72.4	3014.0	114.3	4567.8	145.1	73		
14A-62	45.6	9.945	0.058	3.697	0.186	0.2668	0.0133	617.66	6.9	1570.7	80.5	3286.5	157.2	81	451.9	2.5
14A-63	2.7	1.084	0.104	99.820	10.775	0.7848	0.0392	4214.79	592.0	4684.3	217.1	4893.8	142.9	14		
14A-64	11.1	3.250	0.135	10.440	0.678	0.2462	0.0123	1729.49	125.8	2474.6	120.4	3159.6	158.8	45	1466.6	37.3
14A-65	10.9	8.267	0.093	5.725	0.293	0.3434	0.0172	736.08	15.6	1935.2	88.6	3677.5	152.9	80	467.2	4.9
14A-66	12.1	6.998	0.069	7.944	0.405	0.4034	0.0202	861.04	15.8	2224.7	92.0	3921.0	150.5	78	481.4	4.5
14A-67	22.3	9.303	0.059	4.711	0.237	0.3180	0.0159	658.19	8.0	1769.1	84.5	3559.3	154.1	82	438.2	2.7
14A-68	1.8	6.828	0.247	7.412	0.457	0.3672	0.0184	881.02	59.5	2162.4	110.4	3779.3	151.8	77	535.4	14.9
14A-69	20.5	5.563	0.064	13.009	0.668	0.5251	0.0263	1065.59	22.8	2680.3	96.9	4312.7	147.1	75	427.2	4.7
14A-70	6.7	2.708	0.046	12.474	0.658	0.2451	0.0123	2026.27	58.9	2640.8	99.3	3152.5	158.9	36	1752.1	23.7
14A-71	1.8	1.626	0.075	44.403	3.013	0.5238	0.0262	3090.49	225.3	3874.3	134.9	4308.9	147.1	28	1838.7	50.8
14A-72	13.5	3.193	0.041	6.497	0.335	0.1505	0.0075	1756.45	39.4	2045.5	90.9	2351.0	171.0	25	1674.1	17.6
14A-73	106.4	9.838	0.566	4.681	0.357	0.3342	0.0167	624.04	68.5	1763.9	127.6	3635.6	153.3	83	401.5	14.5
14A-74	77.6	12.886	0.083	2.065	0.104	0.1931	0.0097	481.81	6.0	1137.3	69.0	2767.8	164.2	83	396.7	2.5
14A-75	2.1	1.904	0.064	52.857	3.178	0.7301	0.0365	2721.77	148.2	4047.6	119.9	4790.4	143.6	43		
14A-76	133.4	5.057	0.033	2.316	0.117	0.0850	0.0042	1163.27	14.0	1217.3	71.5	1314.3	194.0	11	1155.6	6.8
14A-77	3.4	3.601	0.061	22.678	1.198	0.5925	0.0296	1579.91	47.7	3213.2	102.8	4489.1	145.7	65	504.7	7.8
14A-78	24.1	11.148	0.057	2.940	0.148	0.2378	0.0119	553.78	5.5	1392.2	76.2	3104.6	159.5	82	425.0	2.1
14A-79	1.6	2.272	0.100	47.830	3.189	0.7883	0.0394	2351.70	173.9	3948.2	132.7	4900.2	142.9	52		
14A-80	18.5	2.706	0.015	9.128	0.459	0.1792	0.0090	2027.22	19.2	2350.9	92.1	2645.0	166.1	23	1902.5	8.9
14A-81	8.1	3.858	0.040	22.018	1.124	0.6163	0.0308	1485.88	27.6	3184.5	99.3	4546.3	145.3	67	422.1	4.2
14A-82	1.1	1.172	0.081	87.193	7.446	0.7417	0.0371	3976.16	410.9	4548.4	171.6	4813.1	143.5	17	508.2	19.8
14A-83	40.1	11.389	0.102	3.335	0.169	0.2756	0.0138	542.53	9.3	1489.3	79.4	3337.6	156.6	84	389.3	3.3
14A-84	0.4	4.301	1.793	4.323	1.815	0.1349	0.0067	1347.56	1013.6	1697.8	692.3	2162.3	174.5	38	1278.9	14.8
14A-85	553.7	17.720	0.161	0.478	0.024	0.0614	0.0031	353.90	6.3	396.4	33.4	652.6	214.7	46		
14A-86	19.3	8.853	0.081	5.330	0.271	0.3424	0.0171	689.86	12.0	1873.7	87.0	3672.9	152.9	81	437.8	3.8
14A-87	1.9	3.035	0.140	12.296	0.837	0.2708	0.0135	1835.92	147.6	2627.3	127.9	3309.8	157.0	45	1517.1	40.4
14A-88	2.1	1.506	0.043	62.631	3.597	0.6845	0.0342	3282.36	145.4	4217.0	114.9	4697.8	144.2	30		
14A-89	42.0	9.759	0.097	4.605	0.235	0.3261	0.0163	628.85	12.0	1750.3	85.1	3598.3	153.7	83	411.3	3.9
14A-90	15.5	7.878	0.052	7.401	0.373	0.4231	0.0212	770.39	9.6	2161.1	90.3	3992.4	149.8	81	408.5	2.6
14A-91	16.6	6.443	0.070	10.003	0.512	0.4676	0.0234	930.07	19.0	2435.0	94.5	4141.6	148.5	78	441.9	4.6
14A-92	4.4	3.365	0.056	10.552	0.556	0.2576	0.0129	1677.51	49.3	2484.5	97.8	3231.4	157.9	48	1397.8	19.5
14A-93	5.0	4.987	0.083	17.101	0.901	0.6187	0.0309	1178.22	35.7	2940.5	101.1	4552.0	145.3	74		
14A-94	10.1	5.341	0.049	13.644	0.694	0.5287	0.0264	1106.43	18.8	2725.3	96.3	4322.7	147.0	74	439.3	3.9
14A-95	21.0	8.143	0.058	5.911	0.299	0.3493	0.0175	746.72	10.1	1962.9	87.8	3703.1	152.6	80	468.4	3.2
14A-96	1.0	1.119	0.067	100.023	7.815	0.8121	0.0406	4116.28	365.4	4686.3	157.2	4942.4	142.6	17	18.2	0.7
14A-97	4.0	3.586	0.069	24.055	1.288	0.6259	0.0313	1585.63	53.8	3270.6	104.5	4568.7	145.1	65	431.9	7.5
14A-98	6.8	3.777	0.090	22.350	1.239	0.6124	0.0306	1514.30	64.7	3199.1	107.8	4537.1	145.4	67	439.2	9.2
14A-99	20.1	10.413	0.119	4.083	0.209	0.3085	0.0154	591.10	13.0	1650.9	83.7	3512.9	154.6	83	399.6	4.3
14A-100	131.3	12.909	0.152	1.370	0.070	0.1283	0.0064	480.97	10.9	876.2	60.3	2074.5	176.2	77	436.4	4.8
14A-101	39.2	3.263	0.021	6.109	0.308	0.1446	0.0072	1723.37	19.6	1991.5	88.0	2282.6	172.3	24	1650.3	9.2
14A-102	12.1	4.733	0.167	16.479	1.009	0.5659	0.0283	1235.76	79.6	2905.0	117.3	4422.1	146.2	72	431.4	12.0
14A-103	6.3	1.720	0.026	54.037	2.821	0.6743	0.0337	2954.61	71.3	4069.7	104.2	4676.3	144.4	37	662.6	9.1
14A-104	5.5	3.298	0.080	25.402	1.411	0.6079	0.0304	1707.17	72.6	3323.8	108.6	4526.4	145.4	62	512.6	10.7
14A-105	6.2	2.773	0.042	20.383	1.066	0.4101	0.0205	1985.29	52.3	3109.7	101.3	3945.8	150.2	50	1349.8	17.7
14A-106	3.4	1.692	0.032	62.851	3.359	0.7715	0.0386	2993.85	90.4	4220.5	107.0	4869.4	143.1	39	210.8	3.7
14A-107	20.8	11.279	0.109	2.971	0.151	0.2431	0.0122	547.60	10.1	1400.1	77.4	3139.8	159.1	83	416.3	3.8
14A-108	16.8	8.017	0.128	6.477	0.340	0.3768	0.0188	757.77	22.8	2042.8	92.3	3818.2	151.5	80	448.1	6.6
14A-109	5.6	2.149	0.029	23.711	1.229	0.3697	0.0185	2463.29	55.8	3256.6	101.1	3789.4	151.7	35	1841.1	20.7

Grain I.D.	238U (ppm)	238/206 ratio	238/206 1SE	207/235 ratio	207/235 1SE	207/206 ratio	207/206 1SE	238/206 Age (Ma)	2σ	207/235 Age (Ma)	2σ	207/206 Age (Ma)	2σ	Disc. (%)	preferred Age (Ma)	preferred Err. (2σ)
14A-110	7.6	4.704	0.081	16.533	0.874	0.5643	0.0282	1242.67	38.9	2908.1	101.3	4417.9	146.3	72	436.8	6.9
14A-111	4.6	4.492	0.079	17.963	0.951	0.5855	0.0293	1295.69	41.1	2987.7	102.0	4471.7	145.9	71	418.9	6.7
14A-112	3.6	3.372	0.068	29.986	1.617	0.7337	0.0367	1674.10	59.7	3486.4	106.1	4797.6	143.6	65	198.9	3.7
14A-113	185.0	13.177	0.117	1.651	0.084	0.1578	0.0079	471.53	8.1	989.8	64.2	2431.8	169.6	81	409.7	3.5
14A-114	2.3	2.119	0.072	26.684	1.612	0.4103	0.0205	2491.69	140.0	3371.9	118.3	3946.7	150.2	37	1748.5	40.6
14A-115	2.8	4.554	0.206	19.058	1.285	0.6298	0.0315	1279.58	105.0	3044.7	130.2	4577.6	145.1	72		
14A-116	21.2	7.564	0.634	7.722	0.754	0.4239	0.0212	800.38	126.2	2199.2	175.5	3995.3	149.8	80	424.2	17.3
14A-117	2.8	4.413	0.100	19.732	1.083	0.6318	0.0316	1316.66	53.8	3078.3	106.1	4582.3	145.0	71	341.4	6.8
14A-118	0.4	3.445	9.063	34.371	90.442	0.8592	0.0430	1642.91	7631.0	3620.7	5192.6	5022.5	142.1	67		
14A-119	0.5	1.075	0.357	102.816	34.529	0.8021	0.0401	4239.06	2063.3	4714.0	675.5	4924.8	142.7	14		
14A-120	0.4	2.267	1.288	47.332	27.009	0.7785	0.0389	2355.91	2243.5	3937.8	1134.8	4882.2	143.0	52		
14A-121	7.8	2.871	0.107	13.835	0.862	0.2882	0.0144	1926.78	124.0	2738.5	118.1	3407.1	155.8	43	1564.0	37.9
14A-122	4.3	2.618	0.050	37.640	2.014	0.7151	0.0358	2085.21	67.8	3710.5	105.9	4760.8	143.8	56		
14A-123	7.0	2.783	0.055	35.341	1.902	0.7137	0.0357	1978.90	67.9	3648.2	106.4	4757.9	143.8	58	299.3	5.4
14A-124	2.4	2.812	0.083	32.544	1.890	0.6640	0.0332	1961.46	99.9	3566.9	114.5	4654.0	144.5	58	439.4	10.8
14A-125	5.4	7.045	0.150	9.554	0.519	0.4884	0.0244	855.60	34.1	2392.7	99.9	4205.9	148.0	80	381.0	7.2
14A-126	11.5	3.355	0.062	28.193	1.503	0.6862	0.0343	1681.89	54.7	3425.8	104.6	4701.5	144.2	64	315.7	5.3
14A-127	7.4	4.753	0.063	16.816	0.869	0.5799	0.0290	1231.02	29.5	2924.4	99.2	4457.7	146.0	72	405.9	5.0
14A-128	125.2	3.857	0.029	3.897	0.197	0.1091	0.0055	1485.96	19.9	1613.0	81.7	1783.1	182.4	17	1460.6	9.5
14A-129	12.4	8.614	0.193	6.082	0.333	0.3802	0.0190	708.03	30.1	1987.7	95.6	3831.7	151.3	82		
14A-130	0.1	1.098	2.848	110.499	286.644	0.8805	0.0440	4173.49	15937.1	4786.5	5220.8	5057.2	141.9	17		
14A-131	1.6	2.822	0.172	17.694	1.394	0.3623	0.0181	1955.27	205.3	2973.2	151.4	3758.9	152.0	48	1430.1	44.5
14A-132	25.1	3.686	0.026	14.412	0.728	0.3855	0.0193	1547.23	19.7	2777.2	96.0	3852.7	151.1	60	1068.2	6.9
14A-133	12.0	6.986	0.114	9.146	0.481	0.4636	0.0232	862.46	26.3	2352.7	96.3	4128.7	148.6	79	412.9	6.2
14A-134	26.5	8.413	0.071	6.065	0.308	0.3702	0.0185	724.03	11.6	1985.2	88.4	3791.6	151.7	81	433.7	3.5
14A-135	1.5	1.363	0.055	85.222	5.470	0.8426	0.0421	3547.99	219.6	4525.5	129.0	4994.8	142.3	29	4977.2	28.7
14A-136	9.3	7.761	0.104	8.545	0.442	0.4812	0.0241	781.28	19.7	2290.7	94.1	4183.9	148.1	81	354.0	4.4
14A-137	2.6	1.372	0.054	72.560	4.608	0.7225	0.0361	3528.55	212.8	4364.2	127.4	4775.5	143.7	26	547.6	16.2
14A-138	3.7	4.462	0.134	19.560	1.140	0.6333	0.0317	1303.50	70.7	3069.9	112.7	4585.7	145.0	72	334.9	8.4
14A-139	24.2	12.321	0.200	2.533	0.133	0.2264	0.0113	503.06	15.7	1281.4	76.5	3026.1	160.6	83	392.7	5.9
14A-140	34.9	8.913	0.094	5.963	0.305	0.3856	0.0193	685.51	13.8	1970.4	88.9	3853.2	151.1	82	395.8	4.0
14A-141	3.5	4.108	0.170	20.481	1.329	0.6105	0.0305	1404.49	104.4	3114.4	125.7	4532.5	145.4	69	408.3	12.6
14A-142	9.3	6.457	0.069	10.551	0.539	0.4943	0.0247	928.26	18.5	2484.4	94.9	4223.6	147.8	78	407.7	4.1
14A-143	34.2	7.408	0.048	8.087	0.408	0.4347	0.0217	816.28	10.0	2240.8	91.2	4032.9	149.5	80	421.3	2.6
14A-144	2.7	2.383	0.057	17.322	0.959	0.2995	0.0150	2258.96	90.7	2952.9	106.4	3466.9	155.1	35	1845.0	32.5
14A-145	40.6	3.570	0.048	5.242	0.272	0.1358	0.0068	1591.77	38.1	1859.5	88.4	2173.7	174.3	27	1527.9	17.0
14A-146	2.3	2.369	0.089	28.811	1.803	0.4951	0.0248	2270.49	144.0	3447.1	122.9	4226.1	147.8	46	1352.2	35.7
14A-147	33.5	10.786	0.121	2.902	0.149	0.2271	0.0114	571.58	12.3	1382.4	77.4	3031.1	160.5	81	446.9	4.7
14A-148	21.6	6.021	0.100	11.495	0.605	0.5022	0.0251	990.57	30.4	2564.2	98.5	4246.9	147.6	77	426.1	6.5
14A-149	31.6	9.343	0.126	4.725	0.245	0.3203	0.0160	655.49	16.8	1771.6	86.8	3570.5	154.0	82	434.3	5.5
14A-150	2.3	2.251	0.058	45.116	2.537	0.7370	0.0368	2369.39	102.1	3890.1	111.8	4803.9	143.5	51	284.8	6.4
14A-151	11.6	7.000	0.105	9.318	0.487	0.4732	0.0237	860.83	24.3	2369.8	95.8	4159.3	148.3	79	400.9	5.6
14A-152	13.4	3.335	0.151	29.721	2.006	0.7191	0.0360	1690.75	134.9	3477.6	132.7	4768.7	143.7	65	237.1	7.8
14A-153	1.6	2.286	0.098	45.051	2.968	0.7472	0.0374	2339.36	168.4	3888.7	131.0	4823.6	143.4	52	243.9	7.8
14A-154	71.9	13.612	0.095	1.166	0.059	0.1151	0.0058	457.01	6.2	784.5	55.2	1880.8	180.2	76	422.1	2.8
14A-155	13.2	8.223	0.153	6.653	0.355	0.3970	0.0198	739.80	26.0	2066.4	94.2	3897.0	150.7	81	417.2	7.0
14A-156	26.6	9.280	0.097	4.958	0.253	0.3338	0.0167	659.74	13.1	1812.1	86.4	3634.0	153.3	82	425.5	4.2
14A-157	3.0	1.144	0.022	95.575	5.131	0.7936	0.0397	4048.49	117.6	4640.6	108.1	4909.6	142.8	18	152.3	2.7
14A-158	2.1	1.143	0.041	92.743	5.685	0.7695	0.0385	4050.63	213.3	4610.4	123.3	4865.6	143.1	17		
14A-159	15.3	3.883	0.060	22.268	1.165	0.6274	0.0314	1477.14	40.8	3195.5	101.8	4572.2	145.1	68	396.2	5.7
14A-160	1.7	0.905	0.046	114.874	8.229	0.7540	0.0377	4799.67	347.3	4825.6	144.4	4836.6	143.3	1	546.6	18.7

10.3.1.16 EM-15 (Apatite)

Grain I.D.	238U (ppm)	238/206 ratio	238/206 1SE	207/235 ratio	207/235 1SE	207/206 ratio	207/206 1SE	238/206 Age (Ma)	2σ	207/235 Age (Ma)	2σ	207/206 Age (Ma)	2σ	Disc. (%)	preferred Age (Ma)	preferred Err. (2σ)
15A-01	67.7	12.995	0.119	1.759	0.089	0.1658	0.0083	477.9	8.4	1030.3	65.8	2515.2	168.2		412.2	3.6
15A-02	1.9	10.008	0.243	3.497	0.194	0.2540	0.0127	614.0	28.5	1526.6	87.8	3209.0	158.2		463.6	9.7
15A-03	11.5	3.212	0.038	16.747	0.861	0.3903	0.0195	1747.3	36.6	2920.4	98.6	3871.4	150.9		1209.9	12.7
15A-04	27.8	10.225	0.076	3.888	0.196	0.2884	0.0144	601.5	8.5	1611.1	81.7	3408.5	155.8		427.6	3.0
15A-05	17.0	2.738	0.022	10.180	0.516	0.2022	0.0101	2007.1	28.0	2451.3	93.7	2843.5	163.1		1829.2	12.6
15A-06	2.0	2.303	0.051	42.143	2.305	0.7043	0.0352	2324.6	86.6	3822.4	108.6	4738.8	144.0		454.0	8.9
15A-07	1.2	1.247	0.077	85.520	6.817	0.7741	0.0387	3795.0	356.2	4529.0	160.1	4874.1	143.1		392.5	14.8
15A-08	1.7	1.392	0.034	74.988	4.168	0.7577	0.0379	3489.1	130.8	4397.2	111.5	4843.5	143.3		444.8	9.4
15A-09	0.3	0.935	0.235	117.213	30.019	0.7951	0.0398	4688.8	1673.7	4845.9	515.7	4912.4	142.8		343.9	16.4
15A-10	7.1	2.072	0.029	30.067	1.560	0.4521	0.0226	2538.2	58.0	3489.0	102.1	4091.5	148.9		1663.8	19.3
15A-11	17.5	2.028	0.015	14.392	0.728	0.2118	0.0106	2584.1	32.4	2775.9	96.1	2918.5	162.0		2450.5	14.9
15A-12	3.7	3.310	0.104	28.395	1.678	0.6819	0.0341	1701.9	94.3	3432.8	116.0	4692.4	144.3		371.3	9.6
15A-13	38.5	2.315	0.021	12.557	0.638	0.2109	0.0105	2314.9	35.8	2647.0	95.7	2911.6	162.1		2137.9	16.0
15A-14	8.0	5.301	0.067	14.462	0.746	0.5563	0.0278	1114.0	26.0	2780.5	98.0	4397.0	146.4		420.9	5.0
15A-15	9.0	1.850	0.019	20.547	1.049	0.2759	0.0138	2785.1	46.2	3117.5	98.9	3339.1	156.6		2468.5	19.9
15A-16	13.8	1.970	0.022	14.634	0.749	0.2092	0.0105	2646.5	48.0	2791.7	97.4	2898.4	162.3		2538.6	21.2
15A-17	18.1	8.716	0.079	6.061	0.308	0.3833	0.0192	700.2	12.1	1984.7	88.6	3844.3	151.2		414.8	3.6
15A-18	9.3	1.664	0.016	21.462	1.092	0.2591	0.0130	3034.2	45.9	3159.7	98.8	3240.4	157.8		2868.5	20.4
15A-19	12.5	2.321	0.019	13.081	0.663	0.2203	0.0110	2309.6	31.6	2685.5	95.6	2982.1	161.2		2106.3	14.1
15A-20	6.5	5.021	0.079	16.517	0.865	0.6017	0.0301	1170.9	33.6	2907.2	100.4	4511.5	145.6		372.8	5.4
15A-21	1.0	0.864	0.064	124.192	11.121	0.7784	0.0389	4957.3	513.9	4904.1	180.5	4882.2	143.0		523.0	20.8
15A-22	17.8	3.464	0.044	24.997	1.290	0.6284	0.0314	1634.8	36.8	3308.1	100.8	4574.4	145.1		476.3	5.7
15A-23	16.3	1.921	0.021	15.217	0.779	0.2121	0.0106	2701.6	48.0	2828.9	97.6	2921.0	162.0		2600.1	21.2
15A-24	11.2	2.922	0.027	9.541	0.485	0.2023	0.0101	1897.3	30.8	2391.5	93.6	2844.1	163.1		1716.4	13.6
15A-25	5.3	2.788	0.064	33.822	1.860	0.6842	0.0342	1975.9	77.9	3604.9	108.6	4697.2	144.2		433.0	8.7
15A-26	3.4	3.032	0.068	30.595	1.676	0.6732	0.0337	1837.4	71.7	3506.1	107.9	4673.8	144.4		427.3	8.5
15A-27	0.3	1.338	1.067	78.677	62.864	0.7638	0.0382	3598.1	4397.7	4445.3	1602.3	4855.0	143.2			
15A-28	1.4	1.434	0.041	71.794	4.131	0.7469	0.0373	3410.9	150.9	4353.6	115.4	4823.1	143.4		490.9	11.7
15A-29	3.8	1.934	0.033	19.196	1.013	0.2694	0.0135	2686.8	74.4	3051.7	102.0	3301.6	157.1		2377.3	29.6
15A-30	30.1	1.997	0.021	13.382	0.684	0.1939	0.0097	2616.8	44.9	2707.0	96.6	2775.1	164.1		2553.6	20.1
15A-31	2.9	1.598	0.034	32.258	1.755	0.3740	0.0187	3133.0	106.4	3558.2	107.3	3807.0	151.6		2471.5	37.5
15A-32	3.8	6.238	0.122	11.199	0.601	0.5069	0.0253	958.5	34.8	2539.9	100.1	4260.8	147.5		420.9	7.4
15A-33	7.7	5.282	0.050	14.270	0.726	0.5469	0.0273	1117.8	19.6	2767.8	96.7	4372.1	146.6		436.3	4.0
15A-34	4.0	1.534	0.047	31.938	1.874	0.3555	0.0178	3235.5	156.4	3548.4	115.7	3730.0	152.3		2672.7	47.5
15A-35	2.8	1.079	0.016	101.672	5.294	0.7958	0.0398	4228.8	90.2	4702.8	104.9	4913.5	142.8		294.1	4.0
15A-36	1.4	1.221	0.057	85.835	5.860	0.7607	0.0380	3855.8	269.8	4532.7	137.2	4849.3	143.2		486.2	15.9
15A-37	-0.1	8.192	72.927	15.911	141.651	0.9457	0.0473	742.5	12487.1	2871.5	17010.1	5158.2	141.3			
15A-38	4.7	3.384	0.051	30.686	1.603	0.7534	0.0377	1669.1	44.7	3509.0	102.9	4835.5	143.3		195.4	2.8
15A-39	21.6	2.780	0.030	9.730	0.498	0.1963	0.0098	1980.5	37.3	2409.5	94.3	2794.9	163.8		1770.8	16.1
15A-40	6.2	2.445	0.034	11.485	0.597	0.2037	0.0102	2210.6	52.7	2563.4	97.1	2855.6	162.9		1994.1	22.1
15A-41	10.1	7.085	0.080	10.399	0.533	0.5346	0.0267	851.1	18.0	2470.9	95.0	4338.8	146.9		340.7	3.7
15A-42	3.1	4.028	0.086	21.303	1.159	0.6226	0.0311	1429.6	54.9	3152.5	105.6	4561.0	145.2		422.2	8.0
15A-43	0.2	0.889	0.807	140.252	127.473	0.9047	0.0452	4858.7	6193.9	5026.7	1832.7	5095.6	141.7			
15A-44	3.4	2.593	0.046	9.213	0.488	0.1734	0.0087	2102.4	63.3	2359.4	97.2	2589.6	167.0		1969.4	25.9
15A-45	11.1	7.254	0.062	8.360	0.424	0.4400	0.0220	832.6	13.4	2270.9	92.1	4051.2	149.3		435.4	3.6
15A-46	20.7	7.867	0.097	7.310	0.377	0.4173	0.0209	771.4	18.0	2150.1	92.1	3971.8	150.0		424.8	4.9
15A-47	2.9	3.208	0.059	30.999	1.651	0.7215	0.0361	1749.3	56.2	3519.0	104.9	4773.5	143.7		285.4	4.8
15A-48	1.9	7.072	0.156	8.620	0.471	0.4423	0.0221	852.6	35.3	2298.7	99.5	4059.0	149.2		443.8	8.7
15A-49	6.1	1.758	0.025	20.481	1.064	0.2612	0.0131	2903.1	65.9	3114.3	100.7	3253.5	157.6		2673.5	27.3
15A-50	2.5	5.869	0.133	11.827	0.649	0.5037	0.0252	1014.2	42.6	2590.8	102.9	4251.3	147.6		451.1	9.0
15A-51	17.1	1.905	0.016	16.062	0.815	0.2220	0.0111	2720.3	38.2	2880.5	97.1	2994.5	161.0		2588.0	17.3
15A-52	13.7	9.861	0.065	4.135	0.209	0.2959	0.0148	622.7	7.9	1661.3	82.5	3448.0	155.3		437.1	2.8

Grain I.D.	238U (ppm)	238/206 ratio	238/206 1SE	207/235 ratio	207/235 1SE	207/206 ratio	207/206 1SE	238/206 Age (Ma)	2σ	207/235 Age (Ma)	2σ	207/206 Age (Ma)	2σ	Disc. (%)	preferred Age (Ma)	preferred Err. (2σ)
15A-53	0.7	1.113	0.217	112.241	22.570	0.9061	0.0453	4133.6	1188.7	4802.3	404.8	5097.8	141.7			
15A-54	35.1	10.235	0.083	3.750	0.190	0.2785	0.0139	601.0	9.3	1582.1	81.2	3353.8	156.4		434.8	3.4
15A-55	6.6	3.260	0.068	28.737	1.557	0.6797	0.0340	1724.7	63.2	3444.6	106.4	4687.8	144.3		382.1	7.2
15A-56	2.0	1.392	0.030	75.172	4.087	0.7594	0.0380	3489.6	115.1	4399.7	109.1	4846.7	143.2		435.3	8.3
15A-57	3.0	2.683	0.047	35.091	1.858	0.6832	0.0342	2042.0	61.0	3641.2	104.7	4695.2	144.2		452.4	7.2
15A-58	13.2	1.818	0.012	17.962	0.906	0.2369	0.0118	2825.5	31.4	2987.7	97.2	3098.8	159.6		2669.8	14.4
15A-59	12.9	10.835	0.104	3.138	0.160	0.2467	0.0123	569.1	10.5	1442.1	78.4	3163.1	158.8		434.1	4.0
15A-60	1.5	0.982	0.039	108.996	6.979	0.7766	0.0388	4527.4	260.3	4772.7	129.0	4878.7	143.0		476.4	14.3
15A-61	7.5	3.031	0.030	30.589	1.559	0.6727	0.0336	1838.1	31.9	3505.9	100.4	4672.8	144.4		428.7	4.0
15A-62	1.0	0.896	0.248	150.013	42.145	0.9750	0.0487	4833.1	1880.2	5094.6	566.8	5201.1	141.1			
15A-63	8.6	1.998	0.022	17.220	0.882	0.2497	0.0125	2615.7	48.3	2947.2	98.4	3182.0	158.5		2361.9	20.8
15A-64	2.8	3.395	0.065	26.186	1.403	0.6450	0.0323	1664.3	56.6	3353.5	104.9	4612.2	144.8		447.5	7.8
15A-65	13.7	1.789	0.016	18.476	0.939	0.2398	0.0120	2862.5	42.7	3014.9	98.0	3118.1	159.3		2708.5	19.1
15A-66	9.2	4.682	0.066	17.511	0.909	0.5949	0.0297	1247.8	31.9	2963.3	99.9	4495.0	145.7		410.6	5.4
15A-67	4.2	2.125	0.034	23.601	1.240	0.3640	0.0182	2485.8	66.6	3252.1	102.5	3765.8	152.0		1708.8	22.7
15A-68	0.8	1.690	0.239	69.983	10.491	0.8581	0.0429	2996.5	677.4	4328.0	300.2	5020.7	142.1			
15A-69	2.0	1.507	0.032	41.280	2.239	0.4512	0.0226	3281.8	108.1	3801.9	107.7	4088.6	149.0		2288.0	35.8
15A-70	1.8	1.096	0.034	97.956	5.776	0.7792	0.0390	4178.7	192.3	4665.4	118.7	4883.6	143.0		408.5	10.5
15A-71	22.0	2.147	0.020	11.316	0.576	0.1763	0.0088	2464.5	39.1	2549.6	95.0	2617.9	166.5		2415.8	17.9
15A-72	1.6	1.606	0.059	45.636	2.832	0.5318	0.0266	3120.3	181.9	3901.5	123.4	4331.3	146.9		1829.7	45.2
15A-73	35.5	10.784	0.102	3.175	0.162	0.2485	0.0124	571.6	10.3	1451.2	78.6	3174.3	158.6		434.9	3.9
15A-74	7.5	1.990	0.019	17.448	0.888	0.2519	0.0126	2624.7	41.6	2959.8	97.9	3196.2	158.3		2364.8	18.2
15A-75	3.1	3.421	0.150	24.979	1.662	0.6201	0.0310	1653.0	128.1	3307.4	130.0	4555.1	145.2		501.1	15.9
15A-76	29.6	1.910	0.022	14.699	0.755	0.2038	0.0102	2713.8	51.7	2795.9	97.7	2855.7	162.9		2648.2	22.6
15A-77	1.5	1.341	0.049	78.048	4.830	0.7594	0.0380	3591.7	200.9	4437.3	124.2	4846.8	143.2		451.4	12.8
15A-78	4.1	2.028	0.044	49.208	2.681	0.7241	0.0362	2584.2	92.2	3976.4	108.6	4778.6	143.7		438.0	8.4
15A-79	3.8	6.893	0.109	8.820	0.463	0.4411	0.0221	873.3	25.9	2319.5	95.7	4054.9	149.3		456.5	6.7
15A-80	3.7	8.211	0.147	6.045	0.321	0.3601	0.0180	740.9	25.1	1982.3	92.6	3749.8	152.1		461.9	7.5
15A-81	2.5	2.583	0.048	19.721	1.053	0.3696	0.0185	2109.7	67.6	3077.8	103.3	3789.1	151.7		1394.2	21.7
15A-82	13.5	6.359	0.060	11.897	0.605	0.5489	0.0274	941.5	16.5	2596.3	95.4	4377.7	146.6		361.1	3.2
15A-83	10.5	1.786	0.021	18.566	0.953	0.2407	0.0120	2865.7	53.3	3019.5	98.9	3123.6	159.3		2709.3	23.1
15A-84	22.6	2.781	0.036	9.431	0.487	0.1903	0.0095	1979.9	44.3	2380.8	94.9	2744.3	164.6		1786.7	19.0
15A-85	24.5	2.672	0.019	8.939	0.451	0.1733	0.0087	2049.1	24.9	2331.8	92.3	2589.3	167.0		1909.9	11.4
15A-86	10.7	2.074	0.024	14.672	0.754	0.2208	0.0110	2536.5	49.5	2794.2	97.7	2985.8	161.1		2363.2	21.5
15A-87	9.1	5.011	0.050	15.433	0.787	0.5611	0.0281	1173.0	21.5	2842.4	97.3	4409.8	146.3		437.1	4.1
15A-88	10.2	2.166	0.030	47.158	2.447	0.7413	0.0371	2446.6	56.5	3934.1	103.3	4812.3	143.5		347.9	4.5
15A-89	7.2	0.936	0.086	91.226	9.516	0.6195	0.0310	4685.6	609.7	4593.8	209.6	4553.7	145.2			
15A-90	25.6	8.824	0.087	5.575	0.284	0.3569	0.0178	692.1	13.0	1912.3	87.8	3736.2	152.3		433.3	4.1
15A-91	16.6	2.840	0.040	11.687	0.607	0.2408	0.0120	1944.6	46.8	2579.6	97.2	3124.8	159.3		1613.8	18.7
15A-92	2.5	8.998	0.182	4.670	0.252	0.3049	0.0152	679.3	26.1	1761.8	90.3	3494.5	154.8		470.3	8.5
15A-93	31.7	4.995	0.038	6.645	0.336	0.2408	0.0120	1176.4	16.4	2065.4	89.3	3124.8	159.3			
15A-94	2.8	1.665	0.031	61.183	3.259	0.7393	0.0370	3031.7	88.9	4193.6	106.6	4808.5	143.5		459.6	7.7
15A-95	2.7	2.193	0.182	32.595	3.164	0.5187	0.0259	2421.9	336.0	3568.5	191.3	4294.5	147.2		1123.6	42.2
15A-96	7.5	1.657	0.023	22.713	1.179	0.2731	0.0137	3043.6	68.0	3214.7	101.1	3323.3	156.8		2814.0	28.0
15A-97	8.6	1.990	0.021	14.994	0.767	0.2165	0.0108	2624.9	46.6	2814.9	97.5	2953.9	161.5		2485.5	20.6
15A-98	6.7	2.718	0.020	9.639	0.487	0.1901	0.0095	2019.5	25.4	2400.9	93.0	2742.4	164.6		1829.2	11.4
15A-99	13.2	2.180	0.020	25.476	1.295	0.4030	0.0201	2433.8	37.5	3326.6	99.5	3919.6	150.5		1530.1	12.3
15A-100	2.5	2.664	0.082	35.554	2.090	0.6873	0.0344	2054.5	108.7	3654.1	116.2	4703.7	144.2		443.6	11.3
15A-101	15.8	1.879	0.015	16.491	0.835	0.2249	0.0112	2750.4	36.1	2905.7	97.0	3015.1	160.7		2616.9	16.5
15A-102	8.8	1.978	0.024	15.060	0.775	0.2162	0.0108	2637.3	52.9	2819.0	98.1	2951.7	161.6		2502.2	23.0
15A-103	31.4	2.171	0.017	10.694	0.541	0.1684	0.0084	2442.5	31.6	2496.9	94.0	2541.5	167.8		2412.6	14.8
15A-104	2.8	1.281	0.026	82.031	4.433	0.7622	0.0381	3720.4	116.0	4487.2	108.6	4852.0	143.2		455.3	8.3
15A-105	2.5	4.746	0.134	16.678	0.958	0.5743	0.0287	1232.6	63.6	2916.5	110.2	4443.7	146.1		439.3	10.4
15A-106	2.7	1.316	0.032	81.282	4.511	0.7764	0.0388	3642.8	134.1	4478.0	111.5	4878.4	143.0		358.2	7.6
15A-107	3.5	2.493	0.063	38.949	2.185	0.7045	0.0352	2174.3	93.8	3744.3	111.2	4739.3	143.9		419.3	9.2
15A-108	2.0	3.087	0.120	28.342	1.795	0.6348	0.0317	1809.1	122.7	3431.0	124.4	4589.1	145.0		517.0	15.2
15A-109	3.5	3.556	0.056	24.450	1.281	0.6309	0.0315	1597.4	44.5	3286.5	102.3	4580.2	145.1		458.6	6.6

Grain I.D.	238U (ppm)	238/206 ratio	238/206 1SE	207/235 ratio	207/235 1SE	207/206 ratio	207/206 1SE	238/206 Age (Ma)	2σ	207/235 Age (Ma)	2σ	207/206 Age (Ma)	2σ	Disc. (%)	preferred Age (Ma)	preferred Err. (2σ)
15A-110	1.9	1.387	0.065	71.608	4.895	0.7205	0.0360	3500.5	251.8	4351.0	137.0	4771.4	143.7		655.0	21.2
15A-111	5.6	1.830	0.030	18.594	0.979	0.2470	0.0123	2809.8	75.4	3021.0	101.6	3164.7	158.7		2609.1	30.1

10.3.1.17 EM-20 (Apatite)

Grain I.D.	238U (ppm)	238/206 ratio	238/206 1SE	207/235 ratio	207/235 1SE	207/206 ratio	207/206 1SE	238/206 Age (Ma)	2σ	207/235 Age (Ma)	2σ	207/206 Age (Ma)	2σ	Disc. (%)	preferred Age (Ma)	preferred Err. (2σ)
20A-01	2.2	7.174	0.190	7.844	0.444	0.4083	0.0204	841.2	41.7	2213.3	101.9	3939.3	150.3	79	479.2	10.8
20A-02	4.0	2.620	0.037	16.728	0.870	0.3180	0.0159	2084.3	50.8	2919.4	99.7	3559.3	154.1	41	1639.3	19.5
20A-03	0.4	0.923	0.187	115.968	24.157	0.7763	0.0388	4733.3	1356.1	4835.1	419.5	4878.2	143.0	3	578.6	26.7
20A-04	2.9	4.150	0.079	19.851	1.062	0.5978	0.0299	1391.6	47.7	3084.1	103.5	4502.0	145.6	69	468.5	8.0
20A-05	12.3	1.847	0.016	54.464	2.763	0.7301	0.0365	2788.8	39.0	4077.5	101.3	4790.5	143.6	42	487.2	4.0
20A-06	4.5	2.426	0.030	39.445	2.032	0.6944	0.0347	2224.9	46.7	3756.9	102.1	4718.5	144.1	53	487.0	5.6
20A-07	44.2	4.259	0.024	3.253	0.164	0.1005	0.0050	1359.6	14.1	1469.9	78.2	1633.0	185.9	17	1340.3	6.8
20A-08	7.8	7.624	0.076	7.944	0.405	0.4395	0.0220	794.5	14.9	2224.7	92.0	4049.3	149.3	80	419.8	4.0
20A-09	8.8	6.118	0.048	11.802	0.597	0.5239	0.0262	975.9	14.3	2588.8	94.8	4309.3	147.1	77	414.1	3.1
20A-10	46.4	7.711	0.042	7.349	0.370	0.4112	0.0206	786.1	8.0	2154.8	89.9	3949.8	150.2	80	443.6	2.3
20A-11	35.7	8.882	0.172	6.383	0.342	0.4114	0.0206	687.7	25.2	2029.9	94.2	3950.4	150.2	83	386.0	6.7
20A-12	5.0	2.713	0.030	14.650	0.750	0.2884	0.0144	2022.9	38.2	2792.8	97.4	3408.2	155.8	41	1651.3	15.5
20A-13	7.9	11.575	0.236	4.233	0.229	0.3555	0.0178	534.2	20.9	1680.5	88.7	3730.2	152.3	86	336.7	6.2
20A-14	12.8	5.219	0.043	14.017	0.710	0.5308	0.0265	1130.1	17.2	2750.9	96.1	4328.5	147.0	74	473.7	3.7
20A-15	7.5	4.513	0.045	17.448	0.889	0.5714	0.0286	1290.2	23.2	2959.8	98.0	4436.1	146.1	71	476.9	4.5
20A-16	87.0	3.475	0.030	5.000	0.254	0.1261	0.0063	1630.4	25.3	1819.4	85.9	2043.2	176.9	20	1585.4	11.9
20A-17	3.1	11.879	0.275	3.498	0.193	0.3015	0.0151	521.0	23.2	1526.8	87.0	3477.4	155.0	85	363.4	7.4
20A-18	2.7	13.209	0.339	2.704	0.152	0.2592	0.0130	470.4	23.3	1329.6	83.3	3240.9	157.8	85	352.3	7.8
20A-19	9.0	6.770	0.069	8.536	0.436	0.4193	0.0210	888.2	16.9	2289.8	92.8	3979.1	149.9	78	494.7	4.7
20A-20	24.6	5.422	0.105	13.433	0.720	0.5285	0.0264	1091.2	38.9	2710.6	101.4	4322.0	147.0	75	459.7	8.0
20A-21	10.2	5.438	0.114	13.562	0.735	0.5351	0.0268	1088.2	41.8	2719.6	102.6	4340.3	146.9	75	448.9	8.4
20A-22	4.7	4.023	0.049	20.426	1.051	0.5963	0.0298	1431.0	31.4	3111.8	99.7	4498.3	145.7	68	485.9	5.6
20A-23	27.2	10.858	0.082	2.381	0.120	0.1876	0.0094	567.9	8.2	1237.0	72.3	2720.7	164.9	79	476.9	3.4
20A-24	4.2	2.660	0.037	35.105	1.821	0.6776	0.0339	2057.1	48.8	3641.6	102.6	4683.4	144.3	56	493.6	6.3
20A-25	7.0	2.593	0.027	15.005	0.766	0.2823	0.0141	2103.0	37.3	2815.6	97.3	3374.8	156.2	38	1740.0	15.3
20A-26	5.7	1.690	0.014	26.190	1.328	0.3211	0.0161	2996.8	40.8	3353.7	99.3	3574.4	153.9	16	2540.9	17.2
20A-27	0.8	1.673	0.112	63.211	5.276	0.7672	0.0384	3021.2	322.4	4226.2	167.0	4861.3	143.1	38	365.6	14.2
20A-28	9.1	8.040	0.088	6.228	0.319	0.3634	0.0182	755.7	15.7	2008.4	89.6	3763.3	152.0	80	471.8	4.9
20A-29	114.2	5.630	0.093	3.283	0.173	0.1341	0.0067	1054.0	32.3	1477.0	82.0	2151.6	174.7	51	988.8	14.1
20A-30	22.9	8.242	0.065	6.512	0.330	0.3895	0.0195	738.2	11.0	2047.6	89.1	3868.3	151.0	81	436.0	3.3
20A-31	1.4	0.976	0.368	115.272	43.839	0.8166	0.0408	4545.9	2459.4	4829.1	765.7	4950.4	142.6	8	226.1	11.0
20A-32	13.7	2.555	0.025	13.535	0.690	0.2510	0.0125	2129.0	36.2	2717.8	96.5	3190.2	158.4	33	1839.7	15.4
20A-33	47.7	9.155	0.065	4.633	0.234	0.3078	0.0154	668.3	9.0	1755.2	84.4	3509.0	154.7	81	462.5	3.1
20A-34	32.3	10.528	0.091	3.819	0.194	0.2918	0.0146	585.0	9.7	1596.8	81.7	3426.3	155.6	83	415.1	3.4
20A-35	11.3	16.790	0.173	1.073	0.055	0.1307	0.0065	372.9	7.5	740.1	53.7	2106.5	175.6	82	337.6	3.3
20A-36	14.1	5.425	0.035	13.435	0.677	0.5289	0.0264	1090.5	13.0	2710.7	95.4	4323.1	147.0	75	458.8	2.8
20A-37	4.2	14.164	0.143	2.111	0.108	0.2170	0.0108	439.8	8.6	1152.4	70.3	2957.6	161.5	85	352.0	3.4
20A-38	41.6	9.174	0.098	5.088	0.260	0.3387	0.0169	667.0	13.6	1834.2	86.8	3656.2	153.1	82	435.4	4.4
20A-39	3.9	4.328	0.080	15.719	0.838	0.4936	0.0247	1340.0	44.8	2859.9	101.9	4221.7	147.8	68	634.4	10.5
20A-40	14.4	8.135	0.061	5.958	0.301	0.3517	0.0176	747.4	10.6	1969.7	88.0	3713.5	152.5	80	477.5	3.4
20A-41	8.2	9.570	0.073	3.536	0.179	0.2456	0.0123	640.7	9.3	1535.4	80.1	3155.6	158.9	80	493.0	3.6
20A-42	4.2	3.505	0.056	24.804	1.302	0.6308	0.0315	1618.2	45.8	3300.5	102.6	4579.8	145.1	65	480.4	7.0
20A-43	4.7	1.481	0.022	68.579	3.577	0.7370	0.0369	3325.8	77.4	4307.7	104.6	4804.0	143.5	31	568.9	7.8
20A-44	13.3	7.893	0.044	6.550	0.330	0.3751	0.0188	769.0	8.1	2052.7	88.7	3811.6	151.5	80	468.9	2.5
20A-45	17.3	6.314	0.052	10.501	0.532	0.4811	0.0241	947.8	14.4	2480.0	94.0	4183.6	148.1	77	454.1	3.5
20A-46	9.5	5.184	0.068	13.906	0.719	0.5230	0.0262	1137.2	27.5	2743.3	98.0	4306.8	147.1	74	488.5	6.0
20A-47	13.3	6.253	0.031	11.664	0.586	0.5292	0.0265	956.3	8.8	2577.8	94.0	4324.1	147.0	78	398.8	1.9
20A-48	31.8	9.980	0.070	4.243	0.214	0.3072	0.0154	615.6	8.2	1682.3	83.0	3506.3	154.7	82	425.4	2.9
20A-49	20.2	1.448	0.009	72.236	3.642	0.7590	0.0379	3384.8	34.5	4359.7	101.2	4846.0	143.2	30	464.8	2.9
20A-50	8.2	6.073	0.061	11.425	0.583	0.5035	0.0252	982.6	18.3	2558.5	95.3	4250.8	147.6	77	443.2	4.2
20A-51	85.4	12.350	0.054	1.102	0.055	0.0987	0.0049	501.9	4.2	754.3	53.4	1599.7	186.7	69	476.1	2.0
20A-52	5.6	5.736	0.066	12.659	0.649	0.5269	0.0263	1035.9	21.9	2654.7	96.6	4317.7	147.0	76	437.1	4.7

Grain I.D.	238U (ppm)	238/206 ratio	238/206 1SE	207/235 ratio	207/235 1SE	207/206 ratio	207/206 1SE	238/206 Age (Ma)	2σ	207/235 Age (Ma)	2σ	207/206 Age (Ma)	2σ	Disc. (%)	preferred Age (Ma)	preferred Err. (2σ)
20A-53	2.5	12.143	0.245	3.429	0.185	0.3021	0.0151	510.2	19.8	1511.0	84.8	3480.2	155.0	85	355.3	6.5
20A-54	5.0	2.326	0.030	24.080	1.242	0.4063	0.0203	2305.8	49.3	3271.7	100.7	3932.0	150.4	41	1608.5	17.4
20A-55	3.9	13.321	0.182	2.656	0.138	0.2567	0.0128	466.6	12.3	1316.3	76.5	3225.9	158.0	86	350.8	4.5
20A-56	5.7	2.335	0.025	35.180	1.799	0.5959	0.0298	2298.2	41.5	3643.7	101.1	4497.5	145.7	49		
20A-57	6.7	15.630	0.157	1.509	0.077	0.1711	0.0086	399.8	7.8	933.9	62.3	2567.6	167.3	84	342.2	3.3
20A-58	6.6	7.510	0.074	7.975	0.406	0.4346	0.0217	805.8	14.9	2228.3	92.0	4032.8	149.5	80	431.0	4.0
20A-59	2.2	2.083	0.049	45.609	2.521	0.6893	0.0345	2527.6	98.6	3900.9	110.0	4708.0	144.2	46	583.8	11.9
20A-60	7.4	2.486	0.023	17.565	0.894	0.3168	0.0158	2179.6	34.8	2966.2	97.8	3553.8	154.2	39	1727.7	13.9
20A-61	24.4	9.930	0.053	3.402	0.171	0.2451	0.0123	618.5	6.3	1504.9	78.9	3152.9	158.9	80	475.8	2.4
20A-62	16.6	9.995	0.088	4.284	0.218	0.3107	0.0155	614.7	10.4	1690.3	83.6	3523.7	154.5	83	422.1	3.6
20A-63	7.6	15.428	0.109	1.829	0.092	0.2048	0.0102	404.9	5.5	1056.1	66.3	2864.1	162.8	86	329.7	2.2
20A-64	8.5	13.860	0.105	2.426	0.123	0.2440	0.0122	449.1	6.6	1250.5	72.7	3145.6	159.0	86	344.5	2.5
20A-65	2.6	2.789	0.065	33.334	1.838	0.6745	0.0337	1975.5	79.2	3590.5	108.8	4676.7	144.4	58	480.0	9.8
20A-66	54.8	12.254	0.383	4.655	0.274	0.4139	0.0207	505.7	30.4	1759.2	98.6	3959.7	150.1	87	281.3	7.3
20A-67	5.3	7.696	0.066	6.783	0.344	0.3787	0.0189	787.6	12.7	2083.5	89.8	3826.0	151.4	79	477.1	3.9
20A-68	0.0	6.694	31.813	16.822	79.948	0.8171	0.0409	897.5	7963.5	2924.7	9110.1	4951.1	142.6	82		
20A-69	39.4	5.964	0.113	11.803	0.631	0.5108	0.0255	999.3	35.0	2588.9	100.1	4272.0	147.4	77	441.7	7.5
20A-70	6.4	3.493	0.031	24.983	1.269	0.6331	0.0317	1623.1	25.8	3307.6	99.3	4585.3	145.0	65	476.8	4.1
20A-71	3.0	2.457	0.065	42.264	2.393	0.7536	0.0377	2200.9	99.1	3825.3	112.4	4835.9	143.3	54	293.5	6.7
20A-72	32.4	10.700	0.034	2.380	0.119	0.1848	0.0092	575.9	3.5	1236.7	71.7	2695.8	165.3	79	485.8	1.5
20A-73	7.9	6.121	0.057	10.566	0.537	0.4693	0.0235	975.5	16.9	2485.7	94.4	4146.8	148.5	76	483.0	4.3
20A-74	2.1	10.973	0.323	4.156	0.241	0.3309	0.0165	562.2	31.7	1665.3	95.0	3620.5	153.5	84	372.2	9.1
20A-75	0.6	1.076	0.163	96.803	15.468	0.7557	0.0378	4236.9	942.6	4653.5	321.2	4839.8	143.3	12	644.6	28.9
20A-76	13.7	3.605	0.035	6.563	0.334	0.1717	0.0086	1578.2	27.5	2054.4	89.8	2573.4	167.2	39	1453.2	12.3
20A-77	29.0	9.129	0.230	5.357	0.300	0.3548	0.0177	670.1	32.0	1878.0	95.8	3727.2	152.4	82	423.8	9.2
20A-78	1.4	9.622	0.397	5.259	0.341	0.3672	0.0184	637.4	50.1	1862.3	110.7	3779.2	151.8	83	392.5	12.0
20A-79	12.4	7.673	0.083	7.855	0.402	0.4373	0.0219	789.8	16.2	2214.5	92.2	4041.9	149.4	80	419.4	4.3
20A-80	76.8	3.731	0.025	4.319	0.218	0.1169	0.0058	1530.9	18.0	1697.0	83.2	1908.7	179.7	20	1495.5	8.6
20A-81	6.2	13.383	0.150	2.738	0.140	0.2659	0.0133	464.6	10.1	1338.8	76.3	3281.1	157.3	86	343.9	3.7
20A-82	29.3	11.778	0.078	1.755	0.089	0.1500	0.0075	525.3	6.7	1028.9	65.3	2344.7	171.1	78	465.1	3.0
20A-83	7.9	4.548	0.047	17.163	0.876	0.5663	0.0283	1281.3	23.9	2944.0	98.0	4423.3	146.2	71	481.8	4.7
20A-84	2.4	4.279	0.094	18.014	0.983	0.5592	0.0280	1354.0	53.4	2990.5	105.1	4404.8	146.4	69	524.3	10.1
20A-85	3.4	6.266	0.104	10.350	0.545	0.4706	0.0235	954.5	29.4	2466.5	97.6	4150.8	148.4	77	470.5	7.1
20A-86	6.7	4.361	0.124	18.146	1.043	0.5742	0.0287	1330.9	68.2	2997.5	110.7	4443.3	146.1	70	488.3	11.6
20A-87	4.4	12.878	0.158	2.919	0.150	0.2727	0.0136	482.1	11.4	1386.8	77.9	3321.2	156.8	85	353.0	4.1
20A-88	5.9	3.799	0.042	24.196	1.239	0.6670	0.0334	1506.2	29.6	3276.3	99.9	4660.6	144.5	68	369.8	3.9
20A-89	39.1	11.324	0.094	3.075	0.156	0.2527	0.0126	545.5	8.7	1426.6	77.7	3201.0	158.3	83	413.2	3.3
20A-90	1.7	11.604	0.308	4.012	0.227	0.3378	0.0169	532.9	27.1	1636.6	92.0	3652.1	153.1	85	347.7	7.9
20A-91	5.2	3.453	0.071	25.147	1.360	0.6300	0.0315	1639.6	59.7	3313.9	105.7	4578.2	145.1	64	489.1	9.0
20A-92	14.3	2.756	0.026	10.937	0.557	0.2187	0.0109	1995.4	32.7	2517.8	94.8	2970.7	161.3	33	1780.4	14.3
20A-93	6.4	14.180	0.192	2.059	0.107	0.2118	0.0106	439.3	11.5	1135.2	70.8	2918.7	162.0	85	354.4	4.5
20A-94	65.5	12.266	0.043	1.391	0.070	0.1238	0.0062	505.2	3.4	885.0	59.2	2010.7	177.5	75	463.5	1.6
20A-95	3.9	3.105	0.040	29.038	1.500	0.6542	0.0327	1799.9	40.9	3454.8	101.5	4632.5	144.7	61	482.8	5.9
20A-96	4.2	2.659	0.032	35.796	1.840	0.6906	0.0345	2058.1	42.0	3660.9	101.7	4710.6	144.1	56	456.3	5.1
20A-97	6.4	12.884	0.144	2.777	0.142	0.2596	0.0130	481.9	10.4	1349.3	76.5	3243.5	157.8	85	360.7	3.8
20A-98	2.4	1.983	0.071	52.548	3.230	0.7562	0.0378	2632.0	154.5	4041.8	122.6	4840.7	143.3	46	352.6	10.0
20A-99	4.4	1.932	0.086	41.785	2.800	0.5856	0.0293	2689.4	196.3	3814.0	133.0	4472.1	145.9	40		
20A-100	1.1	1.371	0.083	72.260	5.687	0.7188	0.0359	3531.2	330.6	4360.1	157.8	4768.2	143.8	26		
20A-101	7.9	10.217	0.102	3.162	0.161	0.2344	0.0117	602.0	11.5	1447.9	78.7	3081.7	159.8	80	470.8	4.4
20A-102	12.4	4.247	0.020	19.277	0.968	0.5940	0.0297	1363.1	11.9	3055.8	97.1	4492.8	145.7	70	465.0	2.1
20A-103	6.5	2.077	0.032	25.692	1.344	0.3871	0.0194	2534.0	64.5	3334.9	102.4	3859.2	151.1	34	1852.1	23.3
20A-104	10.2	2.071	0.017	15.935	0.807	0.2394	0.0120	2540.0	33.8	2872.9	96.8	3115.4	159.4	18	2307.9	15.1
20A-105	15.3	6.920	0.056	8.206	0.416	0.4121	0.0206	870.1	13.2	2254.0	91.7	3953.0	150.2	78	492.2	3.8
20A-106	2.9	1.982	0.043	49.282	2.687	0.7086	0.0354	2633.6	94.1	3977.9	108.7	4747.7	143.9	45	538.3	10.3
20A-107	26.4	9.447	0.180	4.848	0.259	0.3323	0.0166	648.6	23.5	1793.2	90.1	3627.0	153.4	82	428.3	7.4
20A-108	6.2	2.592	0.044	36.350	1.919	0.6836	0.0342	2103.6	60.7	3676.0	104.4	4695.9	144.2	55	488.8	7.5
20A-109	17.1	9.256	0.116	4.329	0.223	0.2907	0.0145	661.3	15.8	1698.9	85.1	3420.9	155.7	81	471.7	5.5

Grain I.D.	238U (ppm)	238/206 ratio	238/206 1SE	207/235 ratio	207/235 1SE	207/206 ratio	207/206 1SE	238/206 Age (Ma)	2σ	207/235 Age (Ma)	2σ	207/206 Age (Ma)	2σ	Disc. (%)	preferred Age (Ma)	preferred Err. (2σ)
20A-110	3.4	1.746	0.027	40.294	2.106	0.5104	0.0255	2919.5	71.6	3778.0	103.7	4270.8	147.4	32	1762.2	22.3
20A-111	6.1	13.827	0.199	2.574	0.134	0.2582	0.0129	450.1	12.5	1293.2	76.1	3235.1	157.9	86	337.3	4.5
20A-112	41.1	12.962	0.068	1.143	0.057	0.1075	0.0054	479.1	4.9	773.9	54.5	1756.7	183.0	73	448.8	2.3
20A-113	27.8	16.539	0.160	1.495	0.076	0.1794	0.0090	378.4	7.1	928.4	62.0	2646.8	166.1	86	319.8	3.0
20A-114	5.4	13.822	0.124	2.543	0.129	0.2550	0.0127	450.3	7.8	1284.3	74.1	3215.3	158.1	86	339.2	2.9
20A-115	3.9	14.435	0.201	2.192	0.114	0.2296	0.0115	431.8	11.6	1178.6	72.4	3048.7	160.3	86	338.7	4.4
20A-116	3.3	12.861	0.193	2.994	0.156	0.2794	0.0140	482.7	14.0	1406.2	79.5	3359.0	156.4	86	349.4	4.9
20A-117	28.2	6.586	0.066	9.587	0.489	0.4581	0.0229	911.3	17.0	2396.0	93.8	4111.2	148.8	78	462.7	4.4
20A-118	5.4	3.855	0.083	21.983	1.197	0.6149	0.0307	1486.7	57.2	3183.0	105.8	4543.1	145.3	67	469.3	9.0
20A-119	5.8	2.975	0.063	20.977	1.139	0.4528	0.0226	1868.0	68.8	3137.5	105.4	4093.8	148.9	54	1173.8	20.8
20A-120	6.6	12.626	0.177	3.234	0.168	0.2963	0.0148	491.3	13.3	1465.4	80.6	3450.4	155.3	86	345.5	4.5
20A-121	4.5	2.440	0.162	32.210	2.680	0.5702	0.0285	2214.4	249.3	3556.7	164.0	4433.2	146.1	50	871.4	32.0
20A-122	13.3	3.346	0.024	27.167	1.372	0.6595	0.0330	1685.8	21.1	3389.5	99.0	4644.3	144.6	64	436.4	3.0
20A-123	31.0	5.200	0.040	7.921	0.401	0.2988	0.0149	1134.0	15.9	2222.1	91.3	3463.5	155.2	67		
20A-124	9.8	4.258	0.100	18.967	1.047	0.5860	0.0293	1359.9	57.5	3040.2	106.6	4473.0	145.8	70	478.3	9.8
20A-125	7.5	5.880	0.089	12.035	0.629	0.5134	0.0257	1012.5	28.4	2607.1	98.0	4279.6	147.4	76	444.4	6.2
20A-126	8.3	12.341	0.091	3.370	0.170	0.3017	0.0151	502.3	7.2	1497.4	79.2	3478.5	155.0	86	349.9	2.5
20A-127	12.5	4.119	0.049	19.920	1.024	0.5953	0.0298	1401.2	30.1	3087.5	99.5	4496.0	145.7	69		

10.4 Appendix D - AFT sample data sheets - Outcrop

10.4.1.1 EM-002

Sample details

Grid reference	NT4726383226	Pooled age	223.4 ±9.8 Ma
Elevation (m)	5	Central age	225.7±9.4 Ma
Lithology	Sandstone	P(chi squared)	0.12
Age	Viséan	Age dispersion	9.6%
Depositional constraint	338 ±10Ma	Length Data	101
N_S	1549	Measured (SD)	11.28 (2.56)
P_S	1.37 x10^6	Projected (SD)	13.67 (1.47)

Apatite fission track data

Grain I.D.	Ns	Ni	Area (um^2)	Track density	Average Dpar (µm)	se (µm)	^{238}U (ppm)	se (ppm)	AFT Age (Ma)	se (Ma)
1	54	64	4.30E-05	5.86E+06	1.77	0.22	55.4	1.1	224.3	40.4
2	40	37	2.50E-05	2.85E+06	1.73	0.22	21.2	0.4	283.7	63.2
3	52	61	4.10E-05	1.82E+06	1.64	0.21	17.2	0.3	222.7	41.0
4	70	84	5.60E-05	1.51E+06	1.74	0.22	14.5	0.3	220.8	35.0
5	106	107	7.20E-05	6.09E+06	1.75	0.22	49.5	0.9	260.0	35.1
6	59	73	4.90E-05	2.03E+06	1.65	0.21	20.3	0.4	212.3	36.3
7	134	192	1.30E-04	1.45E+07	1.43	0.18	166.1	3.2	185.5	20.7
8	25	24	1.60E-05	6.13E+05	1.74	0.22	4.8	0.1	267.5	73.9
9	121	151	1.00E-04	2.62E+06	2.01	0.25	26.3	0.5	212.1	25.6
10	66	71	4.70E-05	1.14E+06	1.45	0.18	9.8	0.2	247.7	41.4
11	65	69	4.60E-05	3.13E+06	1.79	0.22	26.5	0.5	250.9	42.4
12	68	111	7.40E-05	3.27E+06	1.84	0.23	42.7	0.8	162.9	24.5
13	148	165	1.10E-04	7.11E+06	1.56	0.2	63.7	1.2	236.2	26.5
14	53	39	2.60E-05	3.84E+06	1.47	0.18	22.8	0.4	353.3	72.2
15	17	16	1.10E-05	8.39E+05	1.42	0.18	6.2	0.1	287.4	96.3
16	105	97	6.50E-05	2.26E+06	1.65	0.21	16.8	0.3	284.7	39.5
17	55	66	4.40E-05	1.49E+06	1.8	0.23	14.2	0.3	221.6	39.4
18	98	143	9.60E-05	4.21E+06	1.6	0.2	49.5	0.9	180.9	23.4
19	29	29	2.00E-05	4.93E+05	1.73	0.22	4.0	0.1	257.8	65.8
20	60	86	5.70E-05	4.13E+06	1.6	0.2	47.4	0.9	185.2	30.5

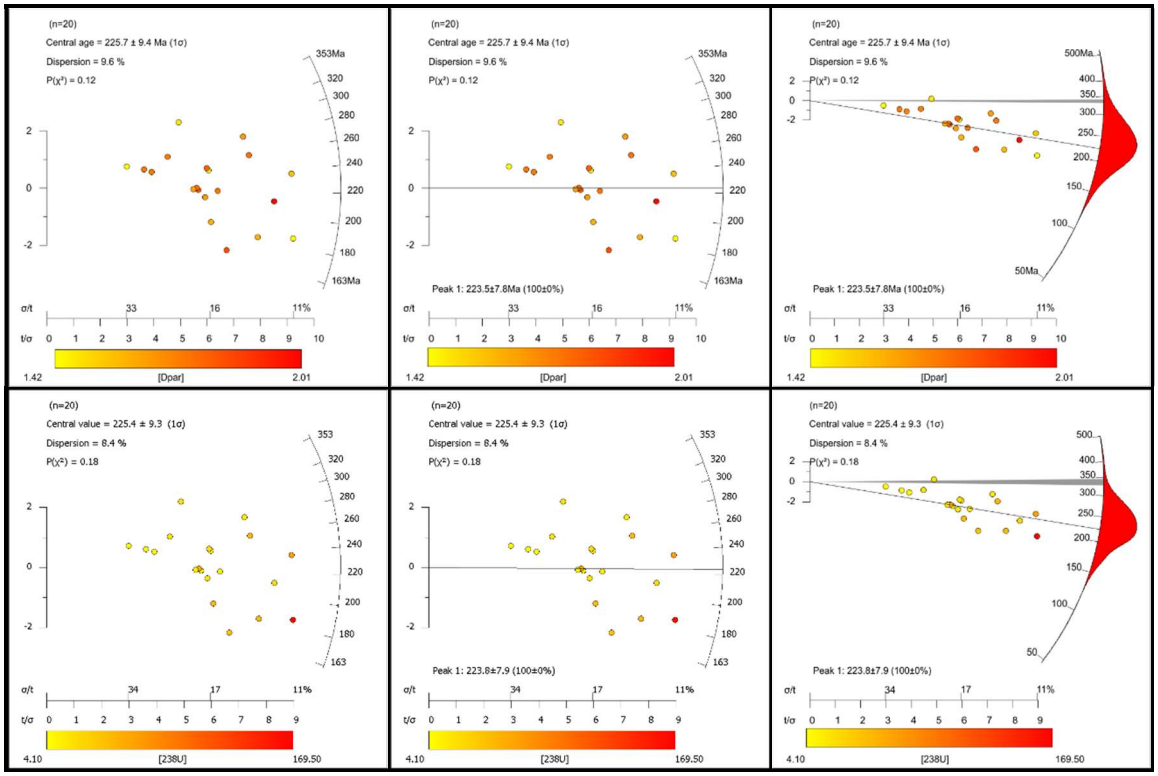

10.4.1.2 EM-004

Sample details

Grid reference	NT3292694892	Pooled age	279.3 ±8.9 Ma
Elevation (m)	<5	Central age	287.4 ±12.0 Ma
Lithology	Sandstone	P(chi squared)	0.0
Age	Westphalian	Age dispersion	10%
Depositional constraint	313 ±5 Ma	Length Data	103
N_S	3057	Measured (SD)	11.83µm (2.18)
P_S	4.02 x10^6	Projected (SD)	13.46 µm (1.23)

Apatite fission track data

Grain I.D.	Ns	Ni	Area (um^2)	Track density	Average Dpar (µm)	se (µm)	^{238}U (ppm)	se (ppm)	AFT Age (Ma)	se (Ma)
1	118	166	3.10E-05	4.15E+06	1.73	0.26	29.9	0.6	307.4	36.3
2	111	186	6.30E-05	5.10E+06	1.79	0.27	41.2	0.8	274.7	20.5
3	60	108	1.90E-05	3.44E+06	1.71	0.26	31.7	0.6	241.5	37.8
4	190	358	3.80E-05	5.46E+06	1.52	0.23	52.4	1.0	231.2	20.6
5	216	307	3.10E-05	7.47E+06	1.57	0.24	54.0	1.0	305.5	27.0
6	94	159	4.40E-05	2.32E+06	1.69	0.25	20.0	0.4	257.6	32.8
7	44	69	1.80E-05	2.72E+06	1.76	0.26	21.6	0.4	280.1	52.4
8	25	42	4.40E-05	6.13E+05	1.42	0.21	5.3	0.1	256.1	62.6
9	136	196	6.30E-05	2.35E+06	1.73	0.26	17.2	0.3	301.2	33.0
10	148	241	6.30E-05	2.56E+06	1.73	0.26	21.2	0.4	268.2	27.6
11	115	146	6.30E-05	1.99E+06	1.46	0.22	12.8	0.2	341.9	41.8
12	99	133	2.00E-05	5.36E+06	1.66	0.25	36.7	0.7	322.9	41.8
13	88	150	3.80E-05	2.54E+06	1.64	0.25	22.1	0.4	256.1	33.5
14	132	156	3.10E-05	4.58E+06	2.03	0.30	27.4	0.5	367.0	42.6
15	106	157	5.00E-05	8.24E+06	1.57	0.24	79.2	1.5	231.4	15.0
16	11	13	1.30E-05	9.53E+05	1.57	0.24	5.8	0.1	362.8	142.9
17	117	146	2.80E-05	4.49E+06	1.31	0.20	28.4	0.5	347.2	42.2
18	54	57	2.50E-05	2.34E+06	1.30	0.20	12.6	0.2	407.9	75.0
19	60	101	6.30E-05	7.39E+06	1.47	0.22	58.4	1.1	280.2	17.8
20	60	80	1.60E-05	4.13E+06	1.37	0.21	28.1	0.5	324.6	54.0

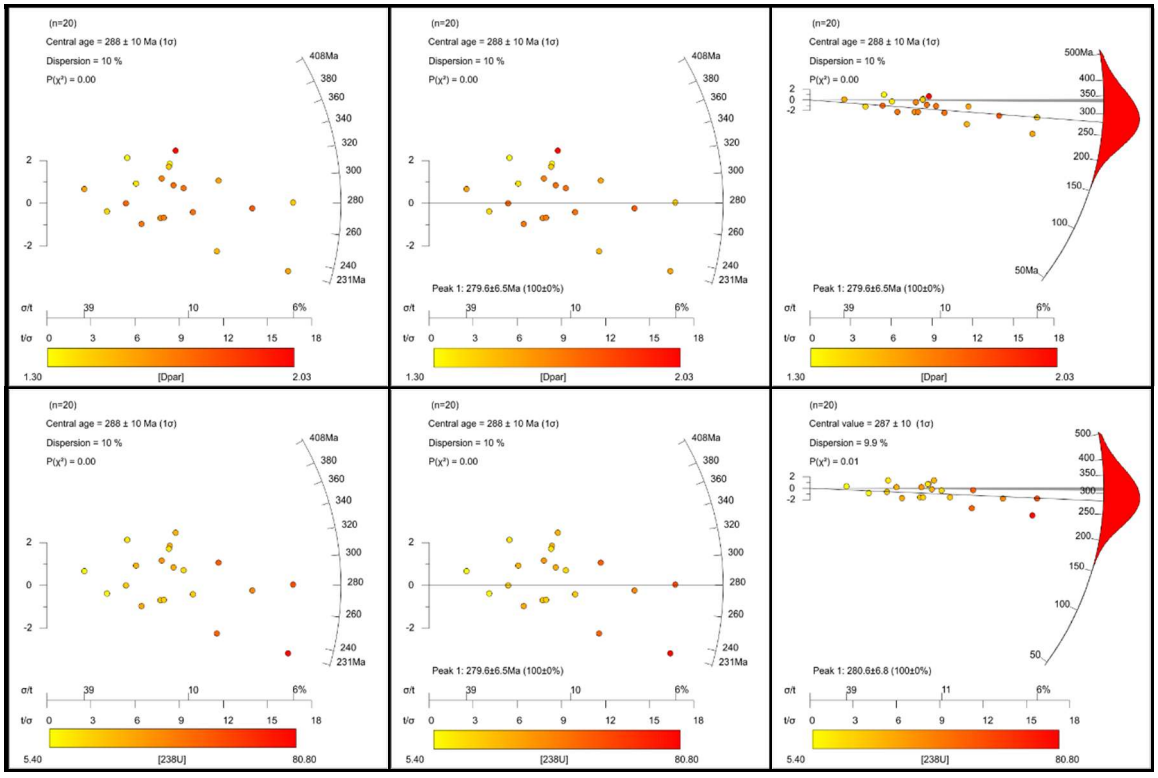

10.4.1.3 EM-005

Sample details

Grid reference	NO4148202448	Pooled age	240.8 ± 18.1 Ma
Elevation (m)	<5	Central age	239.3 ± 21.8 Ma
Lithology	Sandstone	P(chi squared)	0.19
Age	Westphalian	Age dispersion	19%
Depositional constraint	313 ±5Ma	Length Data	102
N_S	578	Measured (SD)	11.9 (1.89) µm
P_S	1.49x10^6	Projected (SD)	13.55 (1.19)µm

Apatite fission track data

Grain I.D.	Ns	Ni	Area (um^2)	Track density	Average Dpar (µm)	se (µm)	^{238}U (ppm)	se (ppm)	AFT Age (Ma)	se (Ma)
1	6	6	3.80E-05	1.85E+05	1.49	0.19	2.5	0.1	164.7	91.8
2	7	8	1.90E-05	4.24E+05	1.76	0.22	6.7	0.1	141.5	70.9
3	13	9	1.60E-05	8.90E+05	1.46	0.18	10.1	0.2	197.2	81.9
4	42	30	1.30E-05	3.66E+06	1.31	0.16	40.3	0.8	202.4	47.0
5	3	4	3.10E-05	9.73E+04	1.47	0.18	2.1	0.0	106.4	81.3
6	52	49	2.50E-05	2.26E+06	1.73	0.22	32.7	0.6	154.9	30.1
7	56	23	1.60E-05	3.88E+06	1.33	0.17	24.1	0.5	353.7	85.9
8	15	8	2.20E-05	7.26E+05	1.37	0.17	6.5	0.1	249.4	104.2
9	33	22	1.50E-05	2.38E+06	1.71	0.21	24.1	0.5	220.1	59.1
10	79	40	1.50E-05	5.69E+06	1.67	0.21	45.1	0.9	279.9	53.0
11	5	5	7.60E-06	6.62E+05	1.69	0.21	10.5	0.2	141.5	89.6
12	23	9	7.60E-06	3.31E+06	1.94	0.24	21.0	0.4	348.0	130.6
13	52	26	3.10E-05	1.85E+06	1.52	0.19	14.4	0.3	284.8	66.3
14	53	39	1.60E-05	3.69E+06	1.64	0.21	42.2	0.8	194.6	39.9
15	24	11	1.00E-05	2.58E+06	1.73	0.22	18.8	0.4	302.7	106.0
16	56	19	3.10E-05	1.94E+06	1.49	0.19	10.1	0.2	422.1	109.5
17	6	3	3.00E-05	1.99E+05	1.67	0.21	1.6	0.0	279.9	198.1
18	6	4	2.20E-05	2.72E+05	1.52	0.19	2.8	0.1	211.1	136.4

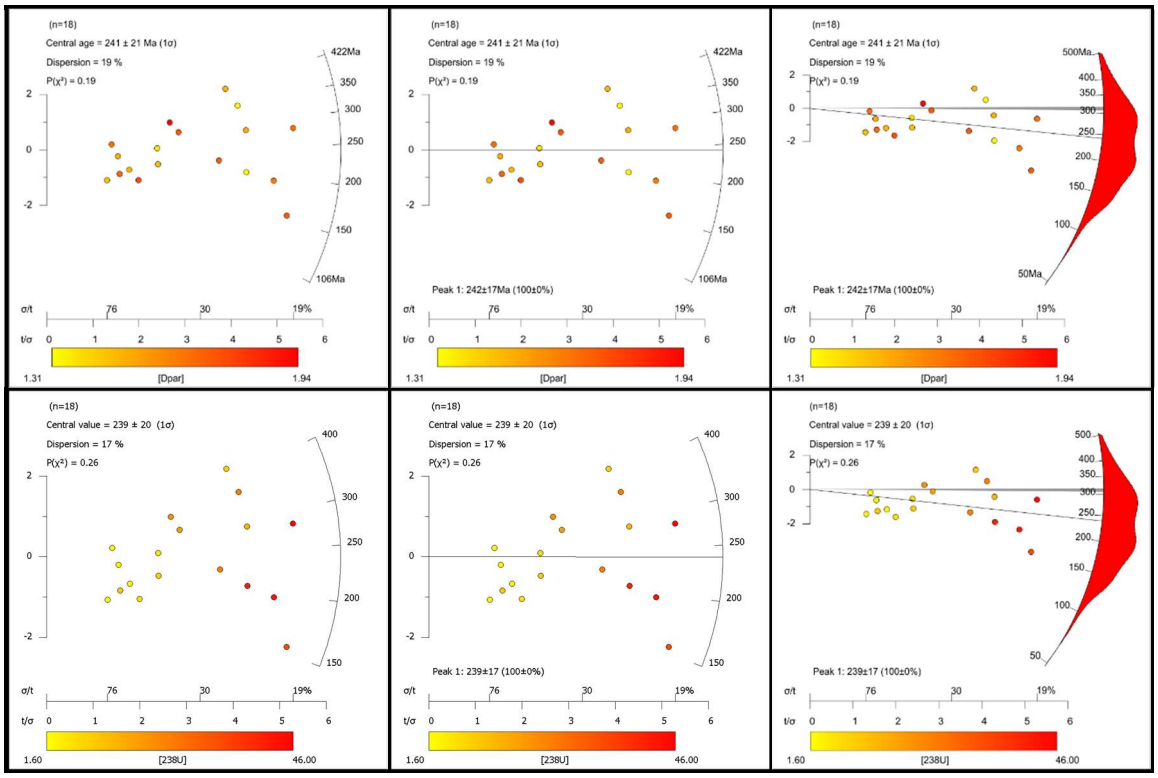

10.4.1.4 EM-007

Sample details

Grid reference	NO5425802180	Pooled age	227.7 ±16.3 Ma
Elevation (m)	<5	Central age	227.7 ±16.4 Ma
Lithology	Sandstone	P(chi squared)	0.93
Age	Viséan	Age dispersion	0%
Depositional constraint	338 ±10Ma	Length Data	82
N_S	614	Measured (SD)	12.05 (2.05) µm
P_S	$1.62x10^6$	Projected (SD)	13.95 (1.42) µm

Apatite fission track data

Grain I.D.	Ns	Ni	Area (um^2)	Track density	Average Dpar (µm)	se (µm)	^{238}U (ppm)	se (ppm)	AFT Age (Ma)	se (Ma)
1	30	26	1.10E-05	2.91E+06	1.77	0.22	38.5	0.7	169.0	43.7
2	31	30	1.70E-05	2.00E+06	1.58	0.20	29.3	0.6	152.6	37.9
3	51	27	1.60E-05	3.50E+06	2.01	0.25	28.7	0.6	269.9	62.5
4	18	13	3.80E-06	5.30E+06	1.45	0.18	57.7	1.1	204.3	71.5
5	52	27	1.00E-05	5.66E+06	1.45	0.18	44.9	0.9	279.5	64.3
6	48	43	2.30E-05	2.30E+06	1.34	0.17	31.7	0.6	162.2	33.2
7	13	8	7.60E-06	1.85E+06	1.32	0.17	16.5	0.3	249.4	110.8
8	22	12	3.10E-05	7.63E+05	1.74	0.22	6.5	0.1	262.8	90.9
9	6	4	1.80E-05	3.41E+05	1.75	0.22	3.5	0.1	214.4	138.5
10	99	56	3.80E-05	2.86E+06	1.43	0.18	24.8	0.5	256.4	42.0
11	6	3	3.80E-05	1.59E+05	1.73	0.22	1.3	0.0	284.3	201.2
12	17	8	3.80E-05	5.03E+05	1.76	0.22	3.7	0.1	299.7	121.6
13	19	9	3.80E-05	5.56E+05	1.45	0.18	4.1	0.1	298.2	114.9
14	30	20	2.30E-05	1.46E+06	1.79	0.22	14.4	0.3	224.4	63.0
15	30	17	7.60E-06	4.37E+06	1.64	0.21	37.1	0.7	261.1	76.9
16	6	5	2.50E-06	2.78E+06	1.74	0.22	31.0	0.6	200.3	117.4
17	11	8	7.60E-06	1.59E+06	1.74	0.22	16.5	0.3	214.4	98.1
18	21	13	1.50E-05	1.52E+06	1.65	0.21	14.4	0.3	234.4	79.8
19	25	16	1.90E-05	1.43E+06	1.75	0.22	14.0	0.3	226.8	70.5
20	28	16	1.50E-05	1.99E+06	2.01	0.25	17.5	0.3	251.5	76.7

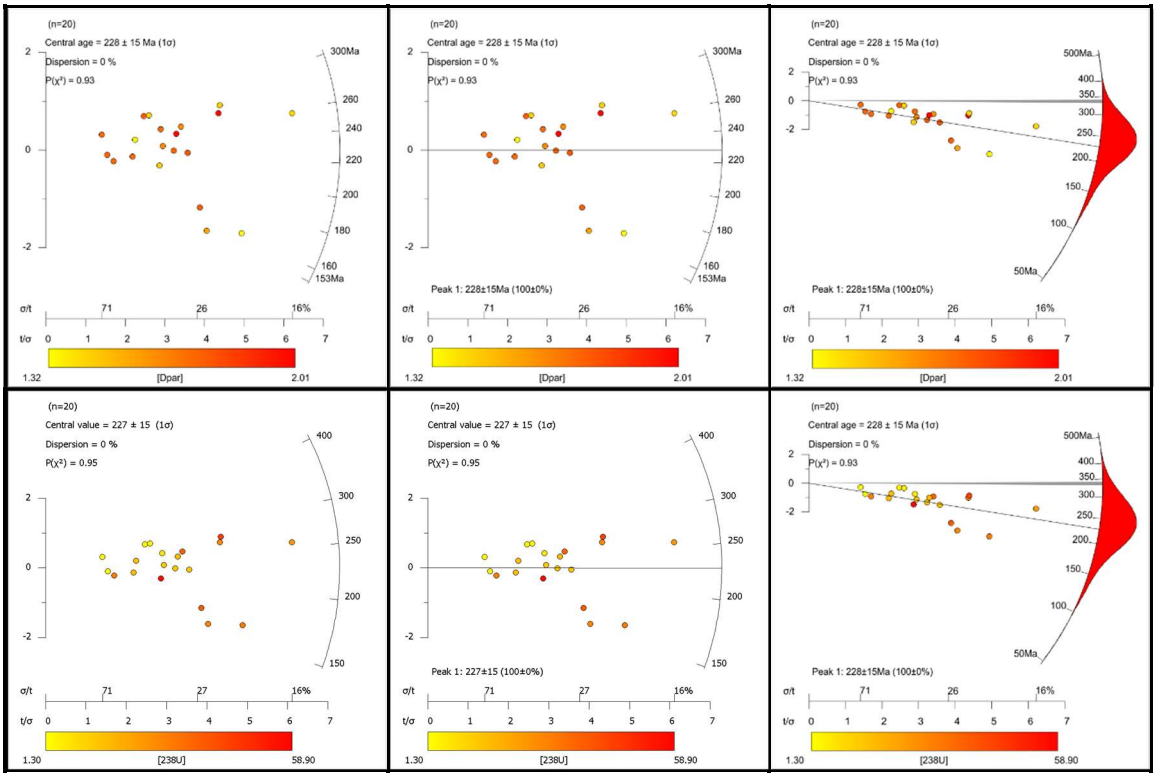

10.4.1.5 EM-008

Sample details

Grid reference	NO5478815277	Pooled age	
Elevation (m)	<5	Central age	314 ±30Ma
Lithology	Sandstone	P(chi squared)	0.0
Age	Viséan	Age dispersion	38%
Depositional constraint	338 ±10Ma	Length Data	108
N_S	996	Measured (SD)	9.13 (2.5) µm
P_S	$1.46x10^6$	Projected (SD)	12.27 (1.32)µm

Apatite fission track data

Grain I.D.	Ns	Ni	Area (um^2)	Track density	Average Dpar (µm)	se (µm)	^{238}U (ppm)	se (ppm)	AFT Age (Ma)	se (Ma)
G1-FT	25	11	2.50E-05	1.00E+06	1.84	0.06	3.28	0.41	563.4	132.9
G9-FT	59	30	4.20E-05	1.40E+06	1.65	0.05	5.32	0.33	490.7	70.8
G12-FT	66	66	4.20E-05	1.57E+06	1.80	0.18	11.5	1.10	258.6	40.3
G19-FT	29	40	2.50E-05	1.16E+06	1.65	0.09	11.74	0.88	188.0	37.7
G20-FT	42	51	2.50E-05	1.68E+06	1.43	0.15	14.9	1.00	214.1	36.0
G25-FT	28	16	2.00E-05	1.40E+06	1.74	0.16	5.94	0.74	439.8	99.5
G29-FT	15	6	2.50E-05	6.00E+05	1.73	0.12	1.84	0.26	600.8	176.8
G32-FT	26	9	2.50E-05	1.04E+06	1.74	0.22	2.51	0.30	754.2	173.2
G34-FT	17	7	2.50E-05	6.80E+05	1.75	0.12	1.95	0.26	640.5	177.3
F2-G1-FT	23	9	2.50E-05	9.20E+05	2.01	0.11	2.79	0.50	607.2	167.0
F2-G2-FT	12	14	3.60E-05	3.33E+05	1.45	0.13	2.91	0.29	217.5	66.4
F2-G4-FT	36	47	4.20E-05	8.57E+05	1.79	0.13	8.18	0.56	199.2	35.9
F2-G7-FT	17	11	1.60E-05	1.06E+06	1.47	0.09	5.27	0.37	378.0	95.4
F2-G8-FT	118	110	3.60E-05	3.28E+06	1.42	0.03	22.5	1.30	275.3	29.9
F2-G9-FT	75	128	3.60E-05	2.08E+06	1.60	0.15	26.1	1.60	152.3	19.9
F2-G11-FT	56	70	2.50E-05	2.24E+06	1.60	0.15	20.6	1.20	206.6	30.1
F2-G13-FT	56	68	2.50E-05	2.24E+06	1.73	0.17	19.9	1.00	213.8	30.5
F2-G16-FT	56	48	2.50E-05	2.24E+06	1.61	0.09	14.1	1.10	299.7	46.4
F2-G19-FT	43	24	2.50E-05	1.72E+06	1.78	0.15	7.01	0.88	457.2	90.3
F2-G21-FT	47	54	3.00E-05	1.57E+06	1.61	0.09	13.29	0.91	223.7	36.0
G1-FT	25	11	2.50E-05	1.00E+06	1.84	0.06	3.28	0.41	563.4	132.9
G9-FT	59	30	4.20E-05	1.40E+06	1.65	0.05	5.32	0.33	490.7	70.8
G12-FT	66	66	4.20E-05	1.57E+06	1.80	0.18	11.5	1.10	258.6	40.3

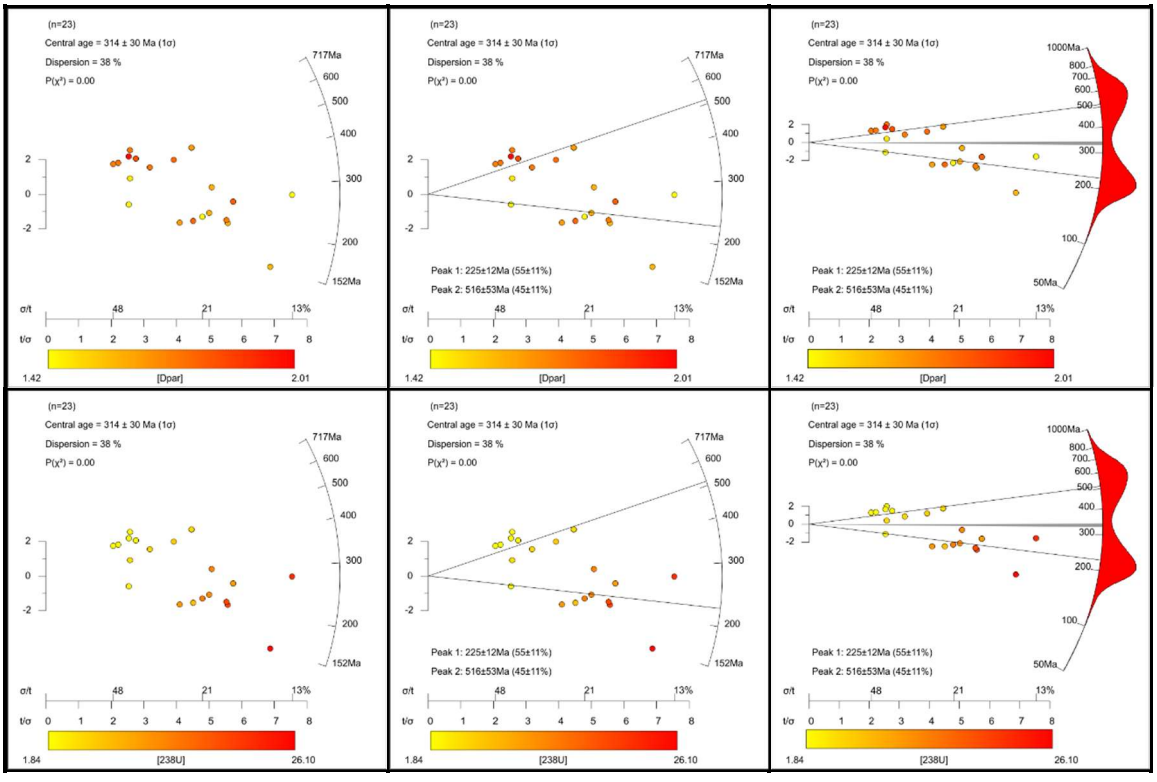

10.4.1.6 EM-009

Sample details

Grid reference	NO6135811349	Pooled age	240.7 ±14.6 Ma
Elevation (m)	<5	Central age	238.0 ±14.4 Ma
Lithology	Sandstone	P(chi squared)	0.47
Age	Viséan	Age dispersion	9.3%
Depositional constraint	338 ±10Ma	Length Data	100
N_S	949	Measured (SD)	11.56 (1.91) µm
P_S	$1.98x10^6$	Projected (SD)	13.81 (1.21) µm

Apatite fission track data

Grain I.D.	Ns	Ni	Area (um^2)	Track density	Average Dpar (µm)	se (µm)	^{238}U (ppm)	se (ppm)	AFT Age (Ma)	se (Ma)
1	1	4	6.30E-05	1.59E+04	1.79	0.22	1.0	0.0	37.4	41.8
2	18	10	3.10E-05	6.36E+05	1.71	0.21	0.4	0.0	266.9	100.5
3	20	15	4.40E-05	4.99E+05	1.71	0.21	5.5	0.1	202.9	66.9
4	58	35	1.10E-05	5.56E+06	1.64	0.21	49.3	1.0	250.3	52.4
5	16	15	1.00E-05	1.69E+06	1.64	0.21	24.0	0.5	157.3	55.0
6	2	2	2.50E-06	7.95E+05	1.57	0.20	12.0	0.2	148.2	148.2
7	7	5	5.70E-06	1.41E+06	2.03	0.25	13.3	0.3	235.5	134.4
8	25	15	2.00E-05	1.34E+06	1.74	0.22	12.0	0.2	248.1	78.6
9	70	35	3.80E-05	2.01E+06	1.69	0.21	14.8	0.3	300.8	61.0
10	3	3	1.00E-05	2.98E+05	1.57	0.20	4.5	0.1	148.2	121.1
11	51	32	1.60E-05	3.50E+09	1.70	0.21	32.6	0.6	238.0	52.4
12	14	14	1.90E-05	7.95E+05	2.31	0.29	12.0	0.2	148.2	54.3
13	24	14	6.30E-06	4.13E+06	2.84	0.36	36.0	0.7	254.7	82.9
14	115	75	1.60E-05	7.95E+06	1.37	0.17	76.8	1.5	230.0	33.7
15	12	5	5.00E-06	2.58E+06	2.03	0.25	15.0	0.3	378.4	199.5
16	193	137	6.30E-05	3.34E+06	1.75	0.22	35.1	0.7	212.1	23.7
17	28	24	4.40E-05	6.81E+05	2.01	0.25	8.5	0.2	177.4	48.3
18	11	7	7.60E-06	1.59E+06	1.45	0.18	14.0	0.3	252.0	120.1
19	111	97	5.00E-05	4.39E+06	1.73	0.22	30.9	0.6	313.8	38.6
20	3	3	1.60E-05	1.91E+05	2.31	0.29	2.8	0.1	148.2	121.1

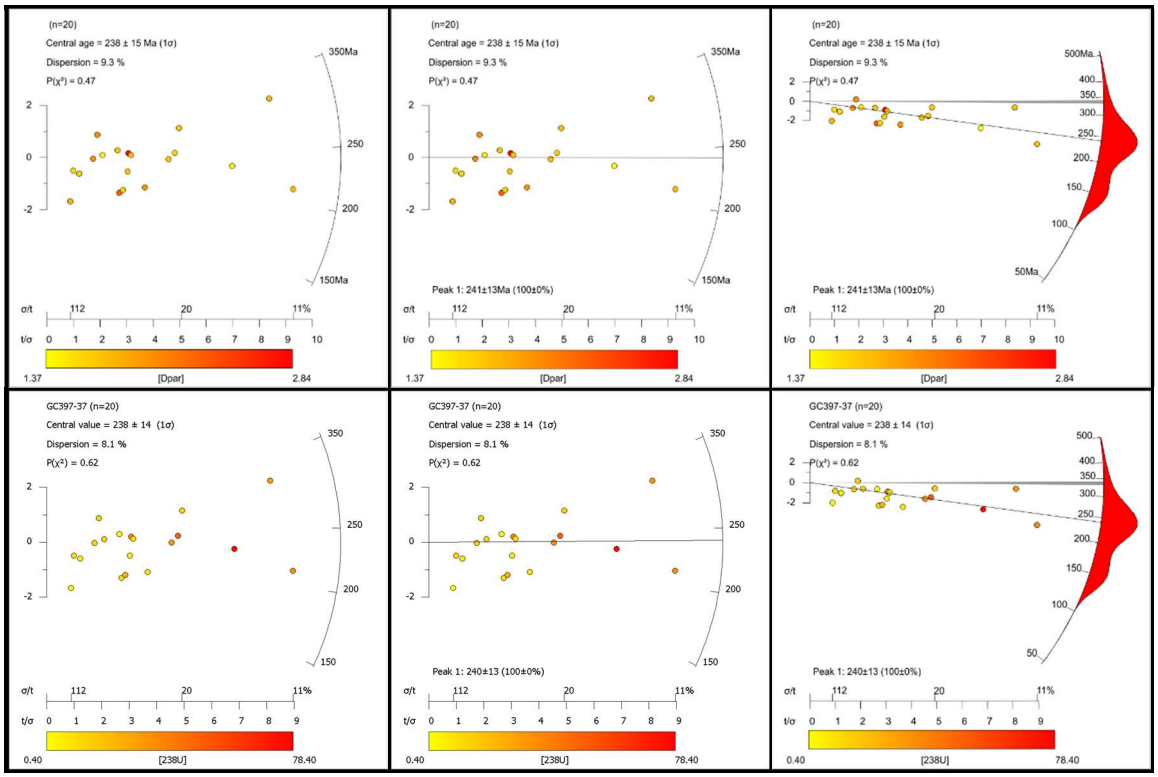

10.4.1.7 EM-010

Sample details

Grid reference	NO5217815784	Pooled age	267.5 ± 12.7 Ma
Elevation (m)	<5	Central age	277.6 ±15 Ma
Lithology	Sandstone	P(chi squared)	0.01
Age	Dinantian	Age dispersion	16%
Depositional constraint	338 ±10Ma	Length Data	116
N_S	2100	Measured (SD)	11.89 (1.69) µm
P_S	2.78 x10^6	Projected (SD)	14.01 (1.17) µm

Apatite fission track data

Grain I.D.	Ns	Ni	Area (um^2)	Track density	Average Dpar (µm)	se (µm)	^{238}U (ppm)	se (ppm)	AFT Age (Ma)	se (Ma)
1	16	9	3.80E-06	4.50E+06	2.84	0.36	39.4	0.8	253.6	101.4
2	34	24	2.30E-05	1.63E+06	2.31	0.29	16.5	0.3	221.4	57.7
3	105	59	3.80E-05	3.02E+06	1.44	0.18	24.8	0.5	269.6	43.1
4	16	8	1.60E-05	1.08E+06	1.65	0.21	7.5	0.1	315.5	135.6
5	3	3	5.00E-05	5.96E+04	1.43	0.18	0.9	0.0	150.4	122.9
6	98	37	6.30E-05	1.68E+06	2.31	0.29	9.2	0.2	400.9	76.1
7	101	38	6.30E-05	1.75E+06	1.37	0.17	9.4	0.2	405.5	75.9
8	24	9	1.90E-05	1.38E+06	1.32	0.17	7.8	0.2	384.0	143.4
9	80	43	1.90E-05	4.61E+06	1.75	0.22	36.3	0.7	281.6	52.0
10	43	18	1.10E-05	4.15E+06	1.73	0.22	25.0	0.5	365.9	100.1
11	110	169	6.30E-05	5.09E+06	1.77	0.22	42.5	0.8	265.0	26.0
12	52	31	5.00E-05	1.11E+06	1.64	0.21	9.8	0.2	253.2	56.1
13	44	31	4.40E-05	1.09E+06	1.76	0.22	11.2	0.2	217.6	49.7
14	118	276	4.40E-05	9.72E+06	2.84	0.36	99.3	1.9	217.8	17.8
15	99	110	2.30E-05	9.18E+06	1.74	0.22	76.8	1.5	265.0	31.7
16	88	70	6.30E-05	1.53E+06	1.77	0.22	17.5	0.3	194.5	30.7
17	80	46	6.30E-05	1.38E+06	2.84	0.36	11.6	0.2	264.7	48.0
18	84	44	3.10E-05	2.89E+06	2.31	0.29	22.2	0.4	288.1	52.5
19	99	55	3.80E-05	4.19E+06	1.76	0.22	22.8	0.4	401.8	62.9
20	40	21	3.10E-05	1.43E+06	1.73	0.22	10.6	0.2	297.4	78.2

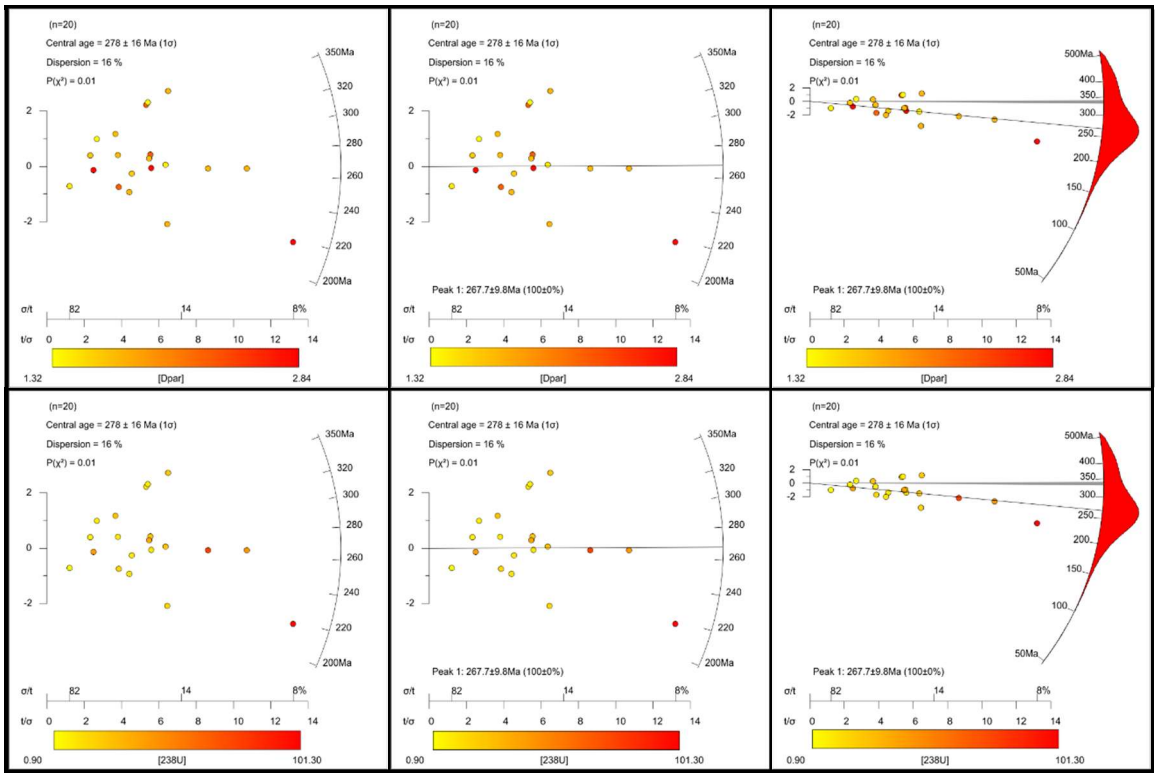

10.4.1.8 EM-012

Sample details

Grid reference	NT1349978385	Pooled age	
Elevation (m)	<5	Central age	274 ±22Ma
Lithology	Sandstone	P(chi squared)	0.0
Age	Dinantian	Age dispersion	27%
Depositional constraint	338 ±10Ma	Length Data	121
N_S	1576	Measured (SD)	12.06 (1.73) µm
P_S	2.65 x10^6	Projected (SD)	14.06 (1.16) µm

Apatite fission track data

Grain I.D.	Ns	Ni	Area (um^2)	Track density	Average Dpar (µm)	se (µm)	^{238}U (ppm)	se (ppm)	AFT Age (Ma)	se (Ma)
1	26	22	3.80E-05	7.42E+05	1.76	0.22	8.4	0.2	196.2	55.5
2	14	8	3.80E-05	3.97E+05	1.49	0.19	2.9	0.1	299.7	131.5
3	102	133	2.50E-05	6.00E+06	2.03	0.26	78.1	1.5	171.7	20.7
4	146	88	1.80E-05	9.02E+06	1.77	0.22	73.8	1.4	271.0	36.2
5	34	12	2.80E-05	1.31E+06	1.73	0.22	6.4	0.1	449.6	145.6
6	100	158	6.30E-05	3.99E+06	1.73	0.22	36.9	0.7	239.9	25.0
7	91	53	3.80E-05	2.62E+06	1.49	0.19	20.5	0.4	282.9	48.1
8	33	19	2.00E-05	1.79E+06	1.74	0.22	13.7	0.3	288.0	80.8
9	52	27	3.00E-05	1.89E+06	2.01	0.26	13.3	0.3	313.8	72.2
10	107	165	3.80E-05	9.43E+06	1.71	0.22	64.1	1.2	324.5	31.5
11	6	4	1.90E-05	3.18E+05	1.64	0.21	2.9	0.1	240.9	155.6
12	33	35	3.10E-05	1.14E+06	1.77	0.22	16.3	0.3	157.3	37.1
13	31	14	3.80E-05	9.01E+05	1.69	0.21	5.5	0.1	360.6	112.3
14	17	10	1.30E-05	1.51E+06	1.57	0.20	12.1	0.2	276.6	105.1
15	109	44	2.50E-05	4.69E+06	1.58	0.20	25.9	0.5	398.2	69.7
16	52	54	5.10E-05	1.10E+06	1.75	0.22	15.5	0.3	158.8	30.3
17	35	17	3.10E-05	1.21E+06	1.64	0.21	7.9	0.2	336.5	96.8
18	61	19	2.50E-05	2.62E+06	1.73	0.22	11.0	0.2	518.5	133.3
19	13	6	1.00E-05	1.39E+06	1.79	0.23	8.2	0.2	370.9	181.3

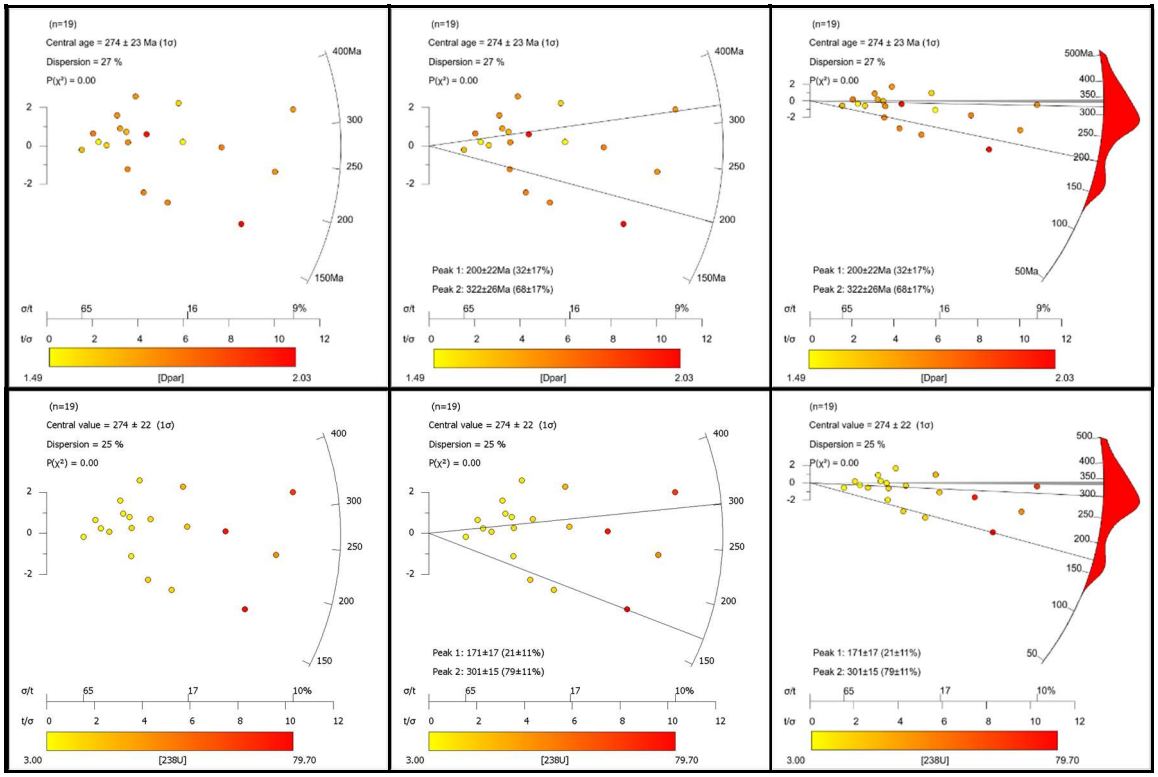

10.4.1.9 EM-013

Sample details

Grid reference	NS8560448190	Pooled age	
Elevation (m)	<5	Central age	196 ±11Ma
Lithology	Sandstone	P(chi squared)	0.0
Age	Tournasian	Age dispersion	17%
Depositional constraint	356 ±6Ma	Length Data	105
N_S	2039	Measured (SD)	12.36 (2.03) µm
P_S	$2.07x10^6$	Projected (SD)	13.85 (1.42) µm

Apatite fission track data

Grain I.D.	Ns	Ni	Area (um^2)	Track density	Average Dpar (µm)	se (µm)	^{238}U (ppm)	se (ppm)	AFT Age (Ma)	se (Ma)
1	72	150	6.30E-05	2.83E+06	1.75	0.24	27.4	0.5	228.9	25.7
2	112	151	6.30E-05	1.94E+06	1.77	0.24	27.6	0.5	156.8	19.3
3	26	20	1.10E-05	2.47E+06	1.65	0.23	20.0	0.4	273.4	79.3
4	77	72	4.40E-05	1.91E+06	1.72	0.24	18.9	0.4	224.6	36.0
5	97	138	4.40E-05	3.75E+06	1.40	0.19	36.1	0.7	231.0	26.9
6	92	169	6.30E-05	1.59E+06	1.39	0.19	30.9	0.6	115.3	14.7
7	124	240	6.30E-05	3.73E+06	1.75	0.24	43.8	0.8	190.2	18.0
8	33	32	5.00E-05	7.15E+05	1.77	0.24	7.3	0.1	218.1	52.5
9	117	149	6.30E-05	2.02E+06	2.23	0.31	27.1	0.5	166.2	20.3
10	99	92	6.30E-05	1.72E+06	1.76	0.24	16.9	0.3	226.8	32.2
11	6	5	1.30E-05	4.77E+05	1.72	0.24	4.3	0.1	246.6	149.5
12	35	25	2.50E-05	1.51E+06	1.62	0.22	11.6	0.2	288.3	73.0
13	121	148	6.30E-05	2.08E+06	1.70	0.23	27.0	0.5	172.5	20.9
14	100	229	6.30E-05	3.32E+06	1.70	0.23	41.9	0.8	177.0	17.4
15	123	118	5.00E-05	2.66E+06	1.42	0.19	27.0	0.5	219.0	27.8
16	11	8	2.60E-05	4.54E+05	1.67	0.23	3.7	0.1	273.4	120.8
17	99	142	6.30E-05	1.72E+06	1.42	0.19	26.0	0.5	148.1	19.1
18	179	157	6.30E-05	3.10E+06	1.58	0.22	28.7	0.6	240.1	26.1
19	21	18	6.30E-05	3.66E+05	1.43	0.20	3.2	0.1	248.7	77.4

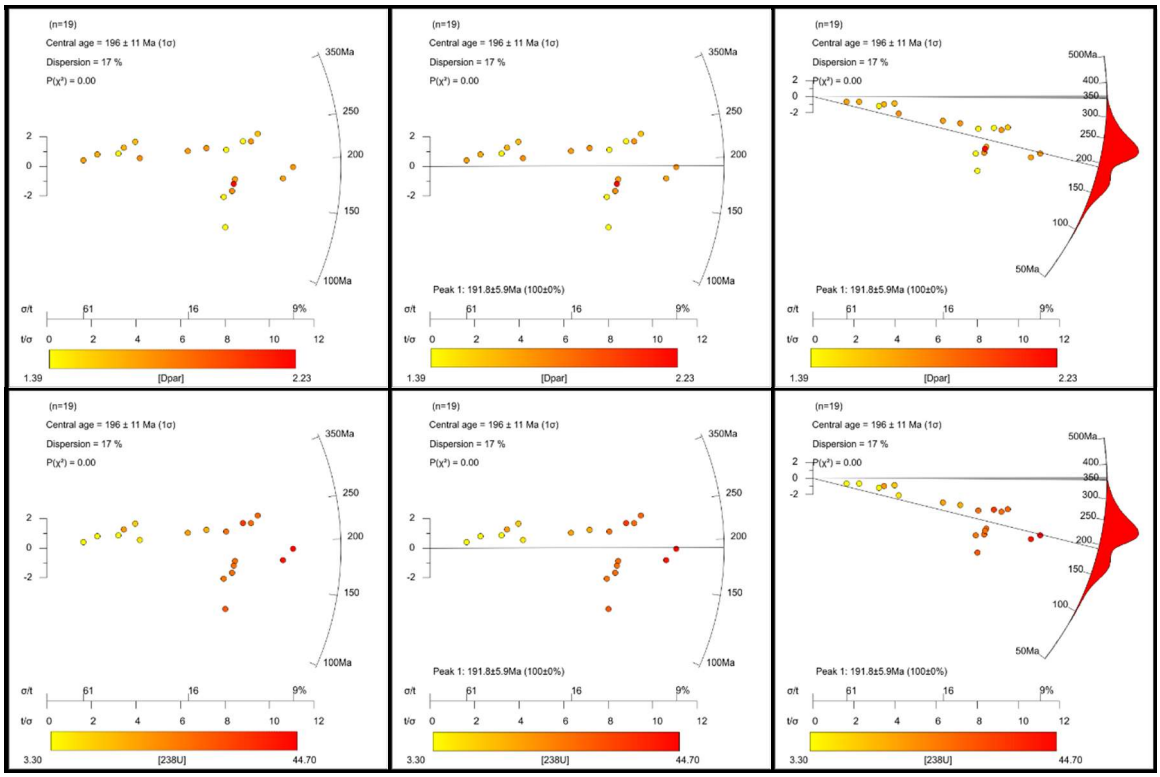

10.4.1.10 EM-014

Sample details

Grid reference	NO6369109881	Pooled age	
Elevation (m)	<5	Central age	263 ±13Ma
Lithology	Sandstone	P(chi squared)	0.01
Age	Visean	Age dispersion	15%
Depositional constraint	338 ±10Ma	Length Data	120
N_S	1808	Measured (SD)	10.78 (1.79) µm
P_S	$2.27x10^6$	Projected (SD)	13.00 (1.17) µm

Apatite fission track data

Grain I.D.	Ns	Ni	Area (um^2)	Track density	Average Dpar (µm)	se (µm)	^{238}U (ppm)	se (ppm)	AFT Age (Ma)	se (Ma)
Grain03	213	167	5.92E-05	3.60E+06	1.84	0.06	20.7	1.2	327.0	24.3
Grain04	66	63	2.21E-05	2.99E+06	1.56	0.06	21.0	1.3	269.4	34.2
Grain05	75	54	3.20E-05	2.34E+06	1.65	0.05	12.3	0.9	357.3	43.1
Grain08	70	48	3.84E-05	1.82E+06	1.80	0.18	9.3	0.6	369.8	45.5
Grain09	100	102	2.93E-05	3.41E+06	1.65	0.09	25.5	1.4	253.1	26.3
Grain10	11	22	2.89E-05	3.81E+05	1.43	0.15	5.5	0.8	132.4	41.0
Grain12	113	141	1.71E-05	4.95E+06	1.74	0.16	60.6	4.9	207.1	21.2
Grain13	56	76	1.67E-05	3.36E+06	1.77	0.21	33.5	1.9	191.0	26.1
Grain14	56	80	2.31E-05	2.43E+06	1.73	0.12	25.4	1.6	181.9	25.0
Grain15	87	112	1.99E-05	4.38E+06	1.64	0.14	41.4	2.5	201.3	22.4
Grain17	32	25	4.27E-05	7.50E+05	1.74	0.22	4.3	0.4	328.2	59.5
Grain18	52	51	2.92E-05	1.78E+06	1.75	0.12	12.9	0.7	261.0	36.9
Grain19	176	153	3.11E-05	5.66E+06	2.01	0.11	36.1	2.7	295.9	24.9
Grain21	26	21	4.90E-05	5.31E+05	1.45	0.13	3.1	0.6	319.2	69.9
Grain24	55	39	2.73E-05	2.01E+06	1.79	0.13	10.6	0.7	357.1	49.7
Grain25	18	24	3.78E-05	4.76E+05	1.47	0.09	4.7	0.4	193.7	46.4
Grain26	4	6	2.81E-05	1.42E+05	1.42	0.03	1.5	0.2	186.8	94.4
Grain27	212	219	6.22E-05	3.41E+06	1.60	0.15	25.9	1.4	249.2	18.4
Grain27b	213	235	6.04E-05	3.53E+06	1.60	0.15	28.6	1.5	233.7	17.1
Grain28	56	50	3.85E-05	1.46E+06	1.73	0.17	9.6	0.6	285.5	39.3
Grain29	18	16	3.18E-05	5.66E+05	1.61	0.09	3.7	0.4	285.8	68.9
Grain30	11	11	2.43E-05	4.52E+05	1.43	0.20	3.3	0.3	257.1	78.4
Grain31	88	62	4.88E-05	1.77E+06	1.78	0.15	9.4	0.7	360.3	40.4

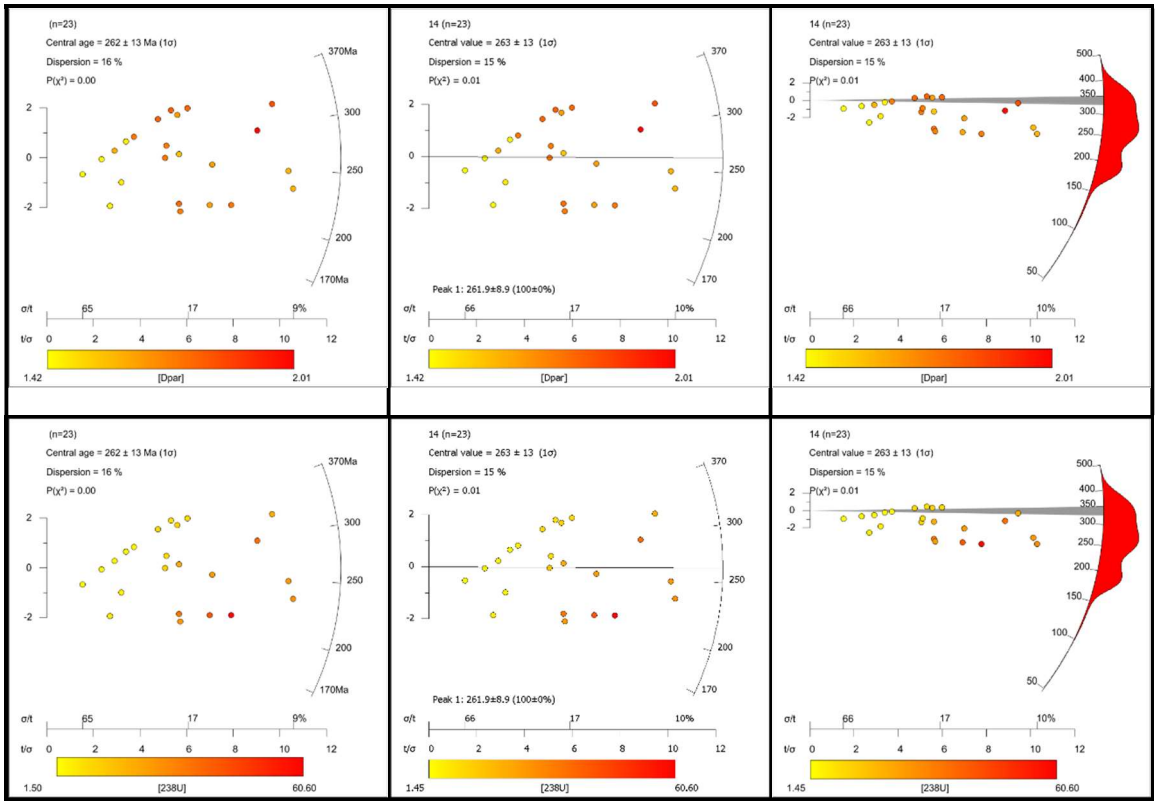

10.4.1.11 EM-015

Sample details

Grid reference	NO5961113202	Pooled age	
Elevation (m)	<5	Central age	259±18Ma
Lithology	Sandstone	P(chi squared)	0.0
Age	Visean	Age dispersion	23%
Depositional constraint	338 ±10Ma	Length Data	112
N_S	1545	Measured (SD)	11.18 (1.67) µm
P_S	$3.17x10^6$	Projected (SD)	13.17 (1.45) µm

Apatite fission track data

Grain I.D.	Ns	Ni	Area (um^2)	Track density	Average Dpar (µm)	se (µm)	^{238}U (ppm)	se (ppm)	AFT Age (Ma)	se (Ma)
Grain02	7	4	1.69E-05	4.14E+05	2.84	0.19	1.74	0.17	444.0	169.2
Grain03	20	12	2.78E-05	7.19E+05	2.31	0.10	3.14	0.28	427.9	97.6
Grain06	77	59	1.57E-05	4.90E+06	1.45	0.07	27.50	1.50	334.9	39.2
Grain08	64	59	1.52E-05	4.22E+06	1.34	0.11	28.50	1.50	279.5	35.7
Grain16	109	117	2.65E-05	4.12E+06	1.58	0.17	32.50	2.00	240.0	24.1
Grain18	181	269	2.42E-05	7.49E+06	1.76	0.15	81.70	4.80	174.5	13.9
Grain20	68	76	2.38E-05	2.86E+06	1.32	0.09	23.40	1.80	231.7	29.5
Grain22	130	83	2.46E-05	5.24E+06	1.75	0.12	24.50	1.50	400.1	37.3
Grain24	26	17	4.36E-05	5.97E+05	1.44	0.06	2.86	0.28	390.9	79.0
Grain26	250	302	2.81E-05	8.82E+06	1.77	0.18	78.50	4.90	213.4	15.1
Grain27	147	115	2.28E-05	6.45E+06	1.68	0.08	37.20	2.20	326.4	28.6
Grain32	206	301	2.98E-05	6.91E+06	1.42	0.14	74.40	4.60	177.0	13.5
Grain35	45	55	2.06E-05	2.18E+06	1.51	0.08	19.70	1.20	210.4	32.0
Grain36	85	109	2.62E-05	3.25E+06	1.46	0.23	30.50	1.90	202.3	22.8
Grain37	27	21	4.39E-05	6.16E+05	1.80	0.18	3.60	0.28	322.0	63.2
Grain40	41	49	4.01E-05	7.98E+05	1.48	0.06	6.99	0.53	216.7	39.2
Grain41	41	29	3.47E-05	1.18E+06	1.83	0.17	6.17	0.62	359.8	59.0
Grain42	21	18	2.29E-05	9.19E+05	1.31	0.13	5.86	0.38	295.8	65.3

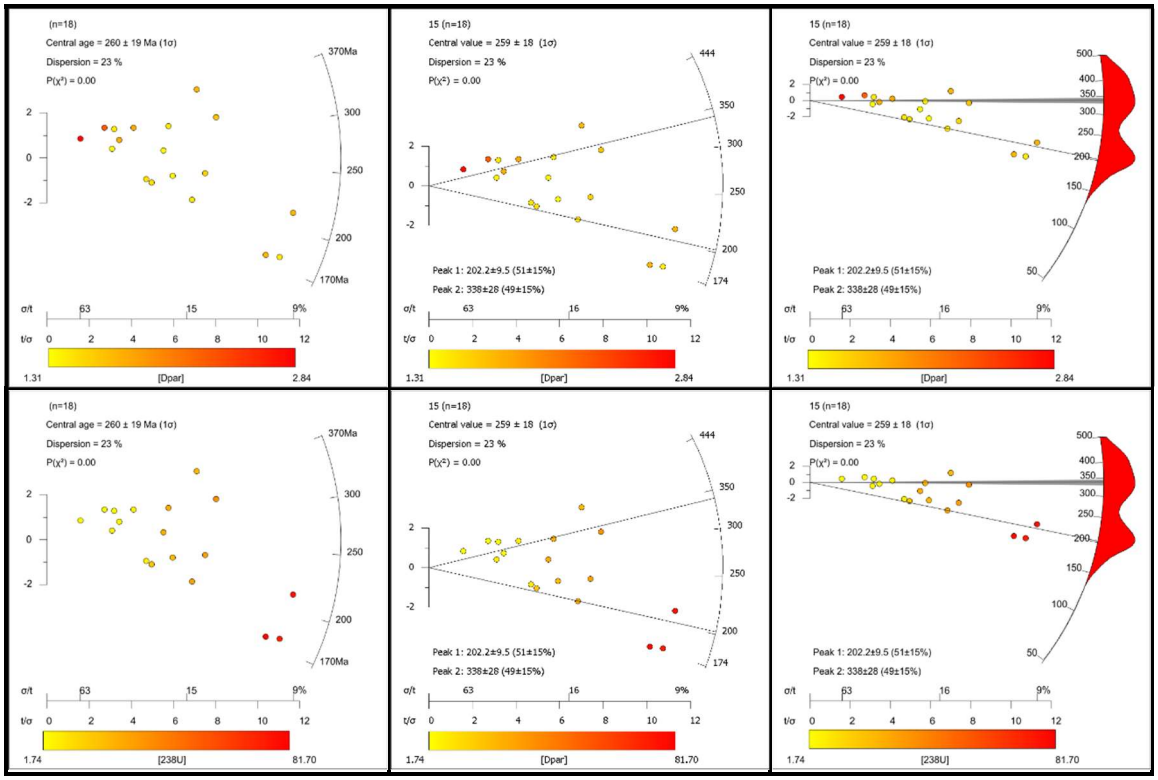

10.4.1.12 EM-017

Sample details

Grid reference	NO4066102337	Pooled age	
Elevation (m)	<5	Central age	273.3 ± 8.5 Ma
Lithology	Sandstone	P(chi squared)	0.0
Age	Westphalian	Age dispersion	17%
Depositional constraint	3113 ±5Ma	Length Data	120
N_S	5538	Measured (SD)	11.50 (1.64) µm
P_S	$2.79x10^6$	Projected (SD)	13.46 (1.11) µm

Apatite fission track data

Grain I.D.	Ns	Ni	Area (um^2)	Track density	Average Dpar (µm)	se (µm)	^{238}U (ppm)	se (ppm)	AFT Age (Ma)	se (Ma)
Grain01	82	42	2.80E-05	2.93E+06	1.73	0.40	10.95	0.82	497.3	58.0
Grain02	271	275	4.36E-05	6.21E+06	1.66	0.24	46.40	3.50	253.4	18.1
Grain03	134	92	2.67E-05	5.02E+06	2.06	0.23	25.40	1.80	371.1	34.6
Grain04	23	15	2.19E-05	1.05E+06	1.34	0.07	5.11	0.45	385.1	82.1
Grain05	78	37	3.96E-05	1.97E+06	1.73	0.10	6.97	0.55	524.2	62.9
Grain06	107	116	2.67E-05	4.00E+06	1.69	0.09	31.80	1.50	238.6	23.7
Grain07	84	97	4.06E-05	2.07E+06	1.49	0.07	17.60	1.00	223.4	25.2
Grain07b	66	78	3.75E-05	1.76E+06	1.49	0.07	15.21	0.89	219.7	27.8
Grain08	69	70	3.39E-05	2.04E+06	1.33	0.05	15.20	1.20	253.7	32.1
Grain09	37	29	2.44E-05	1.51E+06	1.67	0.13	8.79	0.69	324.3	54.8
Grain09b	59	67	3.86E-05	1.53E+06	1.67	0.13	12.75	0.92	227.5	30.7
Grain10	47	31	2.65E-05	1.77E+06	1.94	0.19	8.66	0.67	383.4	57.9
Grain11	48	42	2.89E-05	1.66E+06	1.52	0.14	10.74	0.79	292.3	43.5
Grain11b	46	35	2.97E-05	1.55E+06	1.52	0.14	8.57	0.65	340.1	51.8
Grain12	46	36	4.57E-05	1.01E+06	1.76	0.22	5.81	0.46	326.3	49.8
Grain13	79	81	3.19E-05	2.48E+06	1.31	0.08	18.70	1.20	250.9	29.3
Grain14	72	64	2.49E-05	2.90E+06	1.47	0.08	19.00	1.30	287.9	35.3
Grain15	72	86	2.56E-05	2.81E+06	1.46	0.08	24.70	1.70	216.0	26.5
Grain16	47	44	3.79E-05	1.24E+06	1.37	0.11	8.54	0.58	274.4	41.1
Grain17	197	226	2.85E-05	6.91E+06	1.73	0.16	58.40	3.80	224.7	17.6
Grain18	56	56	3.59E-05	1.56E+06	1.79	0.14	11.41	0.86	258.6	35.9
Grain19	128	133	3.83E-05	3.35E+06	1.71	0.05	25.50	1.70	248.4	23.5
Grain20	45	35	2.87E-05	1.57E+06	1.64	0.11	8.88	0.76	332.8	51.6
Grain21	142	104	4.76E-05	2.98E+06	2.03	0.10	16.00	1.10	350.3	31.8
Grain22	118	127	2.49E-05	4.75E+06	1.57	0.10	37.60	2.00	239.4	22.9
Grain23	123	133	2.32E-05	5.31E+06	1.69	0.14	42.30	2.30	238.1	22.4
Grain24	133	158	3.48E-05	3.82E+06	1.57	0.15	33.40	2.70	217.2	20.8
Grain24b	159	159	3.81E-05	4.18E+06	1.57	0.15	30.70	2.00	257.4	22.1
Grain25	42	38	3.34E-05	1.26E+06	1.42	0.05	8.41	0.64	282.1	44.8
Grain26	310	306	3.89E-05	7.97E+06	1.73	0.05	57.80	3.80	260.9	17.1
Grain27	39	44	4.28E-05	9.12E+05	1.73	0.05	7.58	0.63	228.3	37.8
Grain01	157	147	3.25E-05	4.83E+06	1.66	0.14	33.30	1.80	274.2	23.1
Grain02	98	117	4.29E-05	2.29E+06	1.30	0.12	20.10	1.30	216.1	22.9
Grain03	142	130	3.68E-05	3.86E+06	1.81	0.24	26.00	1.50	280.8	24.9
Grain04	53	54	1.91E-05	2.77E+06	1.49	0.18	20.80	1.30	252.1	35.5
Grain05	43	55	2.21E-05	1.94E+06	1.47	0.11	18.33	0.97	201.5	31.2
Grain06	67	56	2.03E-05	3.30E+06	1.59	0.20	20.30	1.40	306.7	38.9
Grain07	181	192	4.24E-05	4.27E+06	1.79	0.13	33.30	2.00	243.0	19.5
Grain08	90	91	3.56E-05	2.53E+06	1.54	0.21	18.70	1.30	255.7	28.4
Grain09	117	157	3.93E-05	2.98E+06	1.68	0.14	29.40	1.90	192.5	18.9
Grain10	111	109	1.72E-05	6.44E+06	1.51	0.15	46.70	3.10	260.9	26.2
Grain11	140	104	3.30E-05	4.25E+06	1.58	0.15	23.20	1.30	344.0	30.6
Grain11b	145	110	3.25E-05	4.46E+06	1.58	0.15	24.80	1.70	338.0	30.4
Grain12	48	50	2.13E-05	2.26E+06	1.16	0.06	17.40	1.00	245.7	36.2
Grain13	130	228	3.12E-05	4.17E+06	1.64	0.11	53.80	3.40	147.8	13.8
Grain14	85	69	5.68E-05	1.50E+06	1.43	0.12	8.90	0.62	316.8	36.1
Grain14b	124	110	5.68E-05	2.19E+06	1.43	0.12	14.28	0.94	288.9	27.6
Grain15	10	16	3.58E-05	2.79E+05	1.85	0.10	3.21	0.29	165.9	53.0
Grain16	99	80	3.45E-05	2.87E+06	1.40	0.08	17.00	1.10	317.6	33.5
Grain17	88	61	2.23E-05	3.95E+06	1.73	0.21	20.10	1.40	369.0	41.4
Grain18	30	19	3.16E-05	9.50E+05	1.78	0.08	4.37	0.41	406.8	76.7
Grain19	63	72	3.98E-05	1.58E+06	1.51	0.09	13.30	1.00	225.9	29.7
Grain20	79	58	2.90E-05	2.72E+06	1.68	0.15	14.70	1.10	348.0	41.3
Grain21	37	35	2.97E-05	1.24E+06	1.41	0.15	8.64	0.68	272.2	46.0
Grain22	40	35	3.10E-05	1.29E+06	1.72	0.14	8.24	0.63	295.3	48.0
Grain23	54	57	2.25E-05	2.40E+06	1.65	0.16	18.70	1.00	243.4	33.8
Grain24	92	116	1.56E-05	5.91E+06	1.53	0.08	54.60	2.90	205.7	22.1
Grain25	99	66	3.40E-05	2.91E+06	1.62	0.12	14.38	0.97	379.6	40.2
Grain26	88	59	2.61E-05	3.37E+06	1.62	0.09	16.60	1.10	380.7	42.5
Grain27	69	40	6.35E-05	1.09E+06	1.69	0.20	4.61	0.32	440.1	55.1

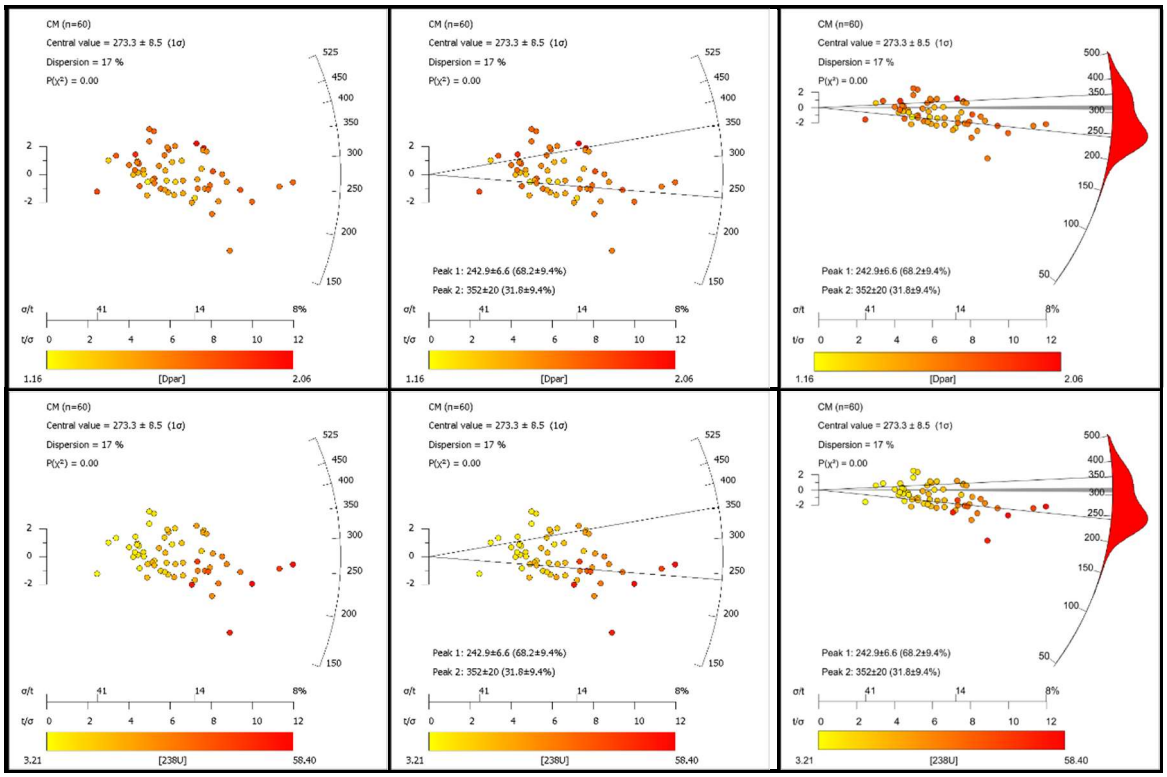
CM (n=60)
Central value = 273.3 ± 8.5 (1σ)
Dispersion = 17 %
P(χ²) = 0.00
Peak 1: 242.9±6.6 (68.2±9.4%)
Peak 2: 352±20 (31.8±9.4%)
α/t
t/σ
[Dpar]
[238U]

10.4.1.13 EM-018

Sample details

Grid reference	NO6181507783	Pooled age	245.5 ± 13.8 Ma
Elevation (m)	<5	Central age	244.7 ± 14.2 Ma
Lithology	Sandstone	P(chi squared)	0.48
Age	Viséan	Age dispersion	3%
Depositional constraint	338 ±10Ma	Length Data	122
N_S	1209	Measured (SD)	11.74 (1.95) µm
P_S	$1.46x10^6$	Projected (SD)	13.00 (1.17) µm

Apatite fission track data

Grain I.D.	Ns	Ni	Area (um^2)	Track density	Average Dpar (µm)	se (µm)	^{238}U (ppm)	se (ppm)	AFT Age (Ma)	se (Ma)
1	68	31	6.30E-05	1.18E+06	1.64	0.19	8.0	0.2	322.8	68.3
2	25	20	5.10E-05	5.30E+05	1.57	0.18	6.3	0.1	187.0	54.7
3	75	36	3.80E-05	2.17E+06	1.79	0.21	15.5	0.3	310.9	61.7
4	20	19	4.00E-05	5.46E+05	1.74	0.20	7.6	0.1	160.4	49.8
5	2	2	6.30E-05	3.18E+04	1.77	0.21	0.5	0.0	145.9	146.0
6	77	57	5.00E-05	1.67E+06	1.65	0.19	18.6	0.4	200.1	34.2
7	56	43	1.10E-05	5.39E+06	2.03	0.24	62.3	1.2	192.8	38.1
8	7	9	2.60E-05	3.03E+05	1.71	0.20	5.8	0.1	117.0	55.6
9	46	30	5.00E-05	9.93E+05	1.73	0.20	9.7	0.2	226.6	51.8
10	2	2	2.30E-05	8.83E+04	1.57	0.18	1.4	0.0	145.9	146.0
11	3	2	3.00E-05	9.93E+04	1.42	0.16	1.0	0.0	217.7	198.8
12	16	10	6.30E-05	2.70E+05	1.57	0.18	2.6	0.1	224.2	87.0
13	15	7	8.80E-06	1.82E+06	1.69	0.20	12.2	0.2	328.8	149.4
14	43	22	3.80E-05	1.25E+06	1.73	0.20	9.3	0.2	294.8	75.5
15	64	50	4.40E-05	1.59E+06	1.64	0.19	18.4	0.4	192.1	35.5
16	148	90	4.40E-05	3.66E+06	1.73	0.20	33.4	0.6	242.9	32.2
17	94	96	6.30E-05	3.21E+06	1.73	0.20	24.9	0.5	285.9	35.8
18	112	56	3.80E-05	3.23E+06	1.43	0.17	24.4	0.5	293.4	47.1
19	36	23	2.20E-05	1.77E+06	1.65	0.19	16.8	0.3	235.5	61.5
20	110	66	6.30E-05	1.91E+06	1.80	0.21	17.1	0.3	248.2	38.1

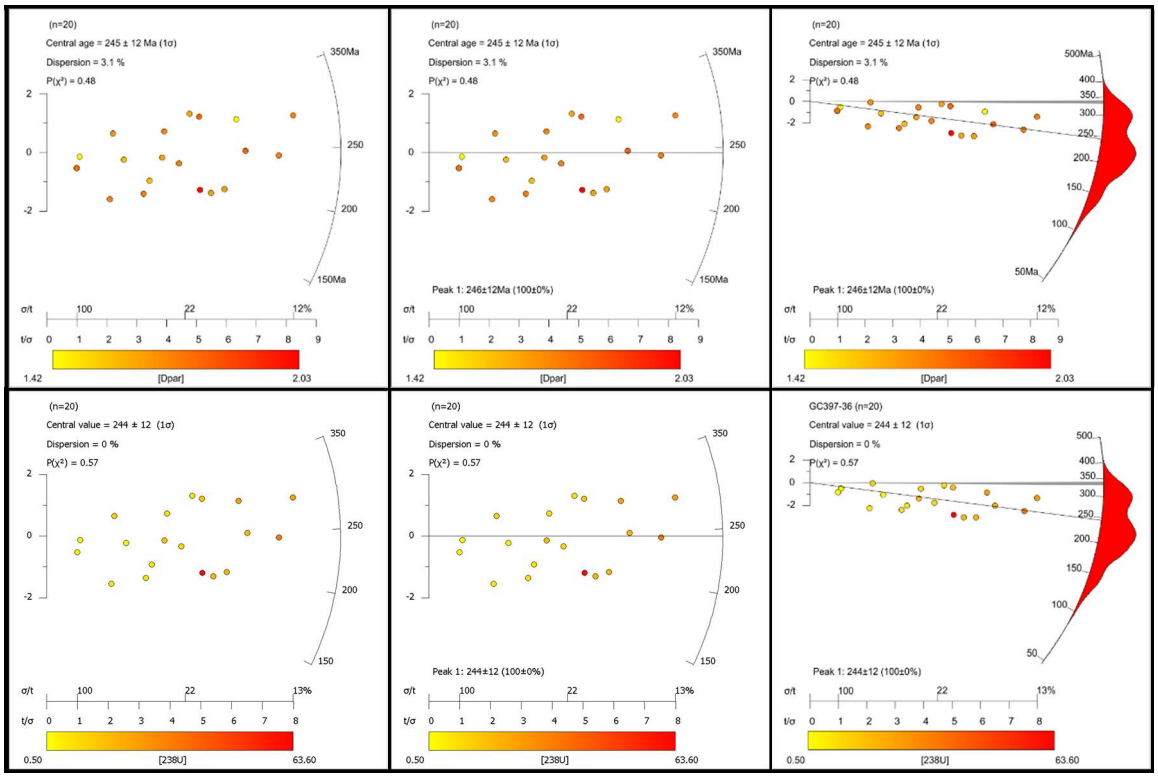

10.4.1.14 EM-021

Sample details

Grid reference	NT6332381345	Pooled age	230.0 ± 12.4 Ma
Elevation (m)	<5	Central age	232.9 ± 17 Ma
Lithology	Sandstone	P(chi squared)	0.02
Age	Tournasian	Age dispersion	21%
Depositional constraint	356 ±6Ma	Length Data	122
N_S	633	Measured (SD)	11.98 (2.28) µm
P_S	$1.71x10^6$	Projected (SD)	13.69 (1.34) µm

Apatite fission track data

Grain I.D.	Ns	Ni	Area (um^2)	Track density	Average Dpar (µm)	se (µm)	^{238}U (ppm)	se (ppm)	AFT Age (Ma)	se (Ma)
1	53	94	1.10E-05	5.12E+06	1.49	0.19	47.3	0.9	240.5	40.0
2	55	81	1.60E-05	3.81E+06	1.52	0.19	29.3	0.6	288.2	48.9
3	11	24	1.00E-05	1.19E+06	1.64	0.21	13.3	0.3	199.6	70.2
4	10	24	1.10E-05	9.71E+05	1.51	0.19	11.9	0.2	183.2	66.4
5	3	7	1.70E-05	1.77E+05	1.33	0.17	2.3	0.0	178.5	123.3
6	12	21	3.10E-05	4.22E+05	1.23	0.16	3.8	0.1	244.9	85.8
7	19	39	1.80E-05	1.19E+06	1.33	0.17	12.7	0.3	207.8	55.7
8	1	3	1.30E-05	7.95E+04	1.38	0.18	1.3	0.0	139.3	160.9
9	115	228	2.30E-05	5.52E+06	1.43	0.18	57.5	1.1	213.7	24.0
10	14	49	2.30E-05	6.62E+05	1.90	0.24	12.3	0.2	120.7	35.5
11	60	58	1.30E-05	4.92E+06	1.67	0.21	25.2	0.5	428.3	76.6
12	17	17	7.60E-06	2.38E+06	1.40	0.18	12.7	0.3	409.1	136.7
13	40	73	2.30E-05	1.94E+06	1.54	0.20	18.4	0.4	234.0	44.4
14	14	14	1.30E-05	1.19E+06	1.50	0.19	6.4	0.1	409.1	149.7
15	69	147	3.50E-05	2.13E+09	1.59	0.20	23.7	0.5	199.9	28.4
16	21	40	2.30E-05	1.02E+06	1.61	0.21	10.2	0.2	222.1	57.6
17	34	92	3.10E-05	1.18E+06	1.52	0.19	16.7	0.3	157.5	30.6
18	14	31	1.90E-05	7.95E+05	1.43	0.18	9.4	0.2	189.2	59.1
19	19	31	1.80E-05	1.19E+06	1.35	0.17	10.0	0.2	263.4	73.7
20	5	5	1.60E-05	6.36E+04	1.45	0.19	1.3	0.0	409.1	578.7

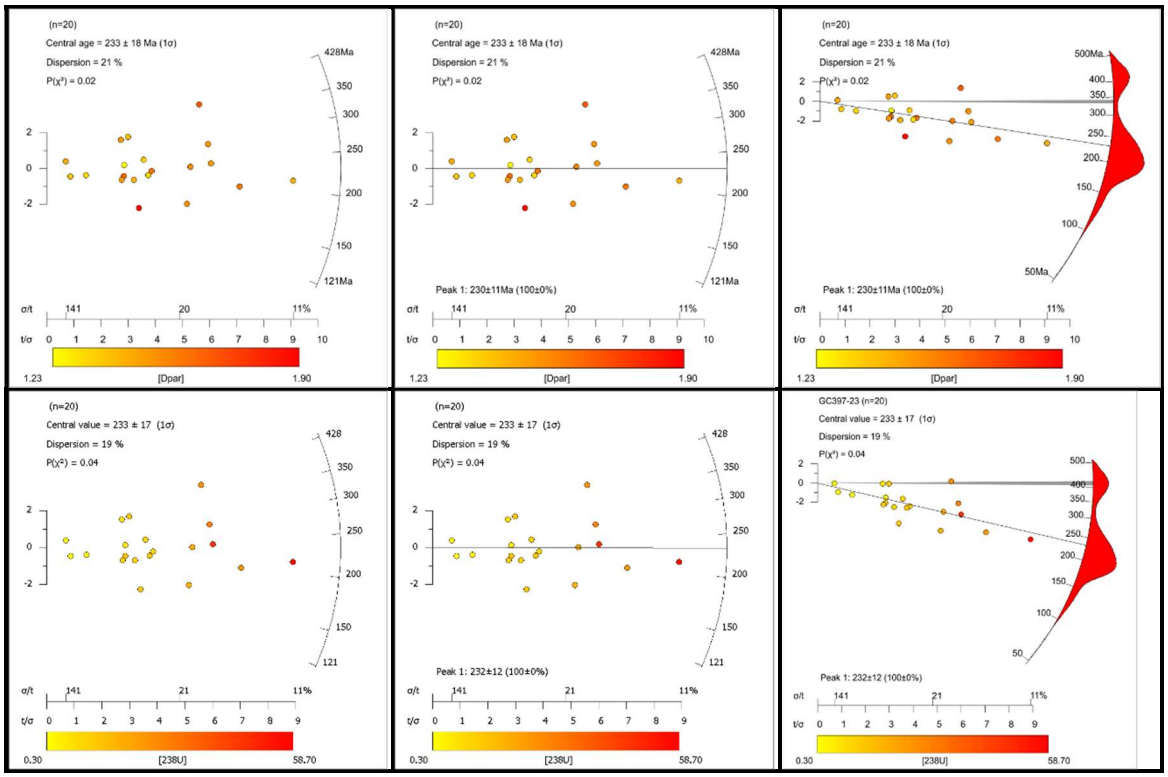

10.5 Appendix E - AFT sample data sheets - Borehole

10.5.1.1 Airth 6 G2

Sample details

Grid reference	NS8872985457	Pooled age	
Elevation (m)	-817	Central age	83.6 ±5.7 Ma
Lithology	Sandstone	P(chi squared)	0.0
Age	Namurian	Age dispersion	31 %
Depositional constraint	324± 6Ma	Length Data	89
N_S	901	Measured (SD)	12.58 (1.57) µm
P_S	$1.04x10^6$	Projected (SD)	14.10 (1.00) µm

Apatite fission track data

Grain I.D.	Ns	Ni	Area (um^2)	Track density	Average Dpar (µm)	se (µm)	^{238}U (ppm)	se (ppm)	AFT Age (Ma)	se (Ma)
Grain01	7	25	2.07E-05	3.39E+05	1.45	0.15	8.77	0.84	74.2	28.3
Grain02	8	33	1.55E-05	5.18E+05	1.23	0.17	15.70	1.00	63.4	22.5
Grain03	20	101	1.64E-05	1.22E+06	1.42	0.04	45.30	3.40	51.8	11.8
Grain04	27	127	1.56E-05	1.73E+06	1.52	0.16	59.70	6.30	55.7	11.1
Grain05	37	112	2.01E-05	1.85E+06	1.40	0.14	41.20	2.70	85.9	14.4
Grain06	51	169	2.59E-05	1.97E+06	1.40	0.18	47.90	3.80	79.0	11.5
Grain07	19	41	2.42E-05	7.87E+05	1.65	0.07	12.40	1.00	121.4	28.3
Grain08	28	129	2.60E-05	1.08E+06	1.17	0.11	36.50	2.70	56.8	10.9
Grain09	39	129	1.88E-05	2.08E+06	1.85	0.35	50.50	3.80	78.9	13.0
Grain10	84	201	2.62E-05	3.21E+06	1.76	0.13	56.40	5.00	108.8	12.8
Grain11	47	342	2.88E-05	1.63E+06	1.48	0.15	87.50	7.20	36.0	5.5
Grain12	11	43	2.65E-05	4.15E+05	1.08	0.00	11.94	0.90	66.7	20.3
Grain13	21	68	2.75E-05	7.64E+05	1.58	0.11	18.10	1.10	81.0	17.9
Grain14	10	18	3.68E-05	2.71E+05	1.54	0.14	3.62	0.39	143.2	45.9
Grain15	8	24	2.77E-05	2.89E+05	1.29	0.10	6.44	0.71	86.0	30.8
Grain16	32	54	2.94E-05	1.09E+06	1.48	0.13	13.51	0.85	154.0	27.7
Grain17	17	36	3.14E-05	5.42E+05	1.48	0.00	8.47	0.69	122.3	30.1
Grain18	46	106	2.95E-05	1.56E+06	1.62	0.09	26.50	1.70	112.6	17.0
Grain19	16	38	2.85E-05	5.62E+05	1.45	0.08	9.77	0.81	110.1	27.9
Grain20	24	38	2.89E-05	8.31E+05	1.79	0.18	9.63	0.80	164.5	34.3
Grain21	24	98	2.96E-05	8.12E+05	1.82	0.29	24.30	2.00	64.2	13.4
Grain22	59	264	3.33E-05	1.77E+06	1.43	0.14	58.40	4.50	58.4	7.9
Grain23	23	49	2.15E-05	1.07E+06	1.61	0.15	16.65	0.90	122.7	25.8
Grain24	8	39	3.65E-05	2.19E+05	1.55	0.02	7.91	0.66	53.2	19.0
Grain25	31	105	4.37E-05	7.10E+05	1.58	0.20	17.60	1.10	77.4	14.1
Grain26	32	113	1.98E-05	1.62E+06	1.36	0.03	41.90	2.40	74.2	13.3
Grain27	17	70	2.80E-05	6.08E+05	1.46	0.05	18.50	1.30	63.2	15.5
Grain28	33	98	2.63E-05	1.26E+06	1.61	0.06	27.50	1.60	87.6	15.5
Grain29	24	68	4.19E-05	5.73E+05	1.59	0.13	12.01	0.80	91.5	18.9
Grain30	19	63	3.28E-05	5.79E+05	1.42	0.02	14.17	0.94	78.4	18.2
Grain31	43	197	2.65E-05	1.62E+06	1.51	0.09	54.70	2.90	57.0	8.8
Grain32	36	49	2.44E-05	1.48E+06	1.70	0.10	14.75	0.90	190.5	32.3

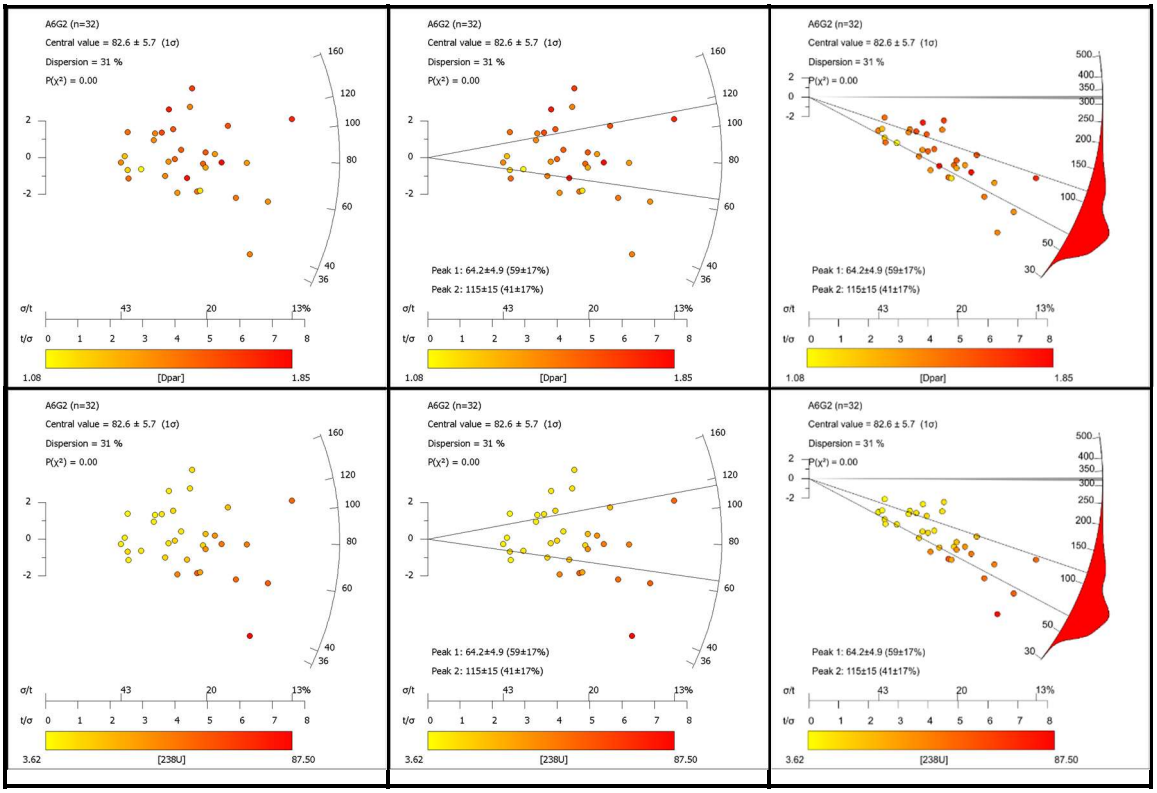

10.5.1.2 Airth 6 G3

Sample details

Grid reference	NS8872985457	Pooled age	
Elevation (m)	-873.5	Central age	84.9 ± 5.4 Ma
Lithology	Sandstone	P(chi squared)	0.0
Age	Namurian	Age dispersion	24 %
Depositional constraint	324 ±6Ma	Length Data	120
N_S	3014	Measured (SD)	11.20 (2.41) µm
P_S	$4.36x10^6$	Projected (SD)	13.35 (1.47) µm

Apatite fission track data

Grain I.D.	Ns	Ni	Area (um^2)	Track density	Average Dpar (µm)	se (µm)	^{238}U (ppm)	se (ppm)	AFT Age (Ma)	se (Ma)
Grain01	49	155	5.08E-05	9.66E+05	1.51	0.06	22.40	1.30	82.7	12.1
Grain02	11	25	2.87E-05	3.83E+05	1.38	0.13	6.52	0.42	112.6	34.1
Grain03	26	57	2.46E-05	1.06E+06	1.78	0.19	17.10	1.20	118.2	23.6
Grain04	17	40	1.09E-05	1.57E+06	1.33	0.03	27.20	1.50	110.2	26.9
Grain05	11	30	1.52E-05	7.24E+05	1.56	0.20	14.70	1.10	94.4	28.7
Grain06	10	44	2.07E-05	4.84E+05	1.61	0.33	15.54	0.96	59.9	19.0
Grain07	17	27	2.59E-05	6.57E+05	1.61	0.12	7.70	0.85	162.8	40.5
Grain07b	80	241	3.99E-05	2.01E+06	1.61	0.12	44.40	2.70	86.7	10.1
Grain08	24	69	3.23E-05	7.44E+05	1.42	0.20	15.81	0.90	90.3	18.6
Grain08b	7	26	1.72E-05	4.07E+05	1.42	0.20	11.14	0.70	70.1	26.6
Grain09	9	17	8.64E-06	1.04E+06	1.27	0.14	14.71	0.91	135.3	45.3
Grain10	6	12	1.04E-05	5.76E+05	1.58	0.30	8.47	0.62	130.1	53.3
Grain11	5	9	1.24E-05	4.02E+05	1.39	0.25	5.08	0.37	151.0	67.8
Grain12	6	18	2.82E-05	2.13E+05	1.42	0.18	4.75	0.38	85.9	35.2
Grain13	42	234	1.70E-05	2.48E+06	1.61	0.11	101.60	5.70	46.9	7.4
Grain13b	21	127	1.79E-05	1.18E+06	1.61	0.11	52.30	2.60	43.2	9.5
Grain14	28	86	2.51E-05	1.11E+06	1.32	0.04	25.30	1.60	84.5	16.2
Grain15	47	180	1.19E-05	3.96E+06	1.75	0.06	111.40	5.70	68.3	10.1
Grain16	8	27	1.83E-05	4.36E+05	1.39	0.05	10.76	0.62	77.8	27.6
Grain18	73	328	2.36E-05	3.09E+06	1.80	0.18	102.10	5.10	58.2	7.0
Grain18b	73	245	2.10E-05	3.47E+06	1.80	0.18	85.60	4.50	77.8	9.3
Grain19	16	53	1.65E-05	9.70E+05	1.52	0.13	23.50	1.30	79.2	19.9
Grain20	44	69	3.87E-05	1.14E+06	1.81	0.17	13.05	0.73	166.3	25.5
Grain21	23	90	2.54E-05	9.07E+05	1.62	0.10	26.10	1.40	66.8	14.0
Grain22	43	206	2.64E-05	1.63E+06	1.61	0.15	57.20	3.20	54.7	8.5
Grain23	31	71	2.34E-05	1.33E+06	1.53	0.15	22.20	1.20	114.2	20.7
Grain25	50	124	2.11E-05	2.37E+06	1.89	0.15	43.40	2.00	104.8	15.0
Grain25b	42	126	1.60E-05	2.63E+06	1.89	0.15	58.10	2.40	86.7	13.5
Grain26	17	47	8.64E-06	1.97E+06	1.60	0.05	40.40	2.60	93.4	22.8
Grain26b	25	66	1.45E-05	1.72E+06	1.60	0.05	33.50	2.20	98.5	20.0
Grain28b	16	57	9.96E-06	1.61E+06	1.68	0.16	42.10	2.10	73.3	18.4
Grain29	41	108	3.02E-05	1.36E+06	1.68	0.17	26.30	1.30	99.1	15.7

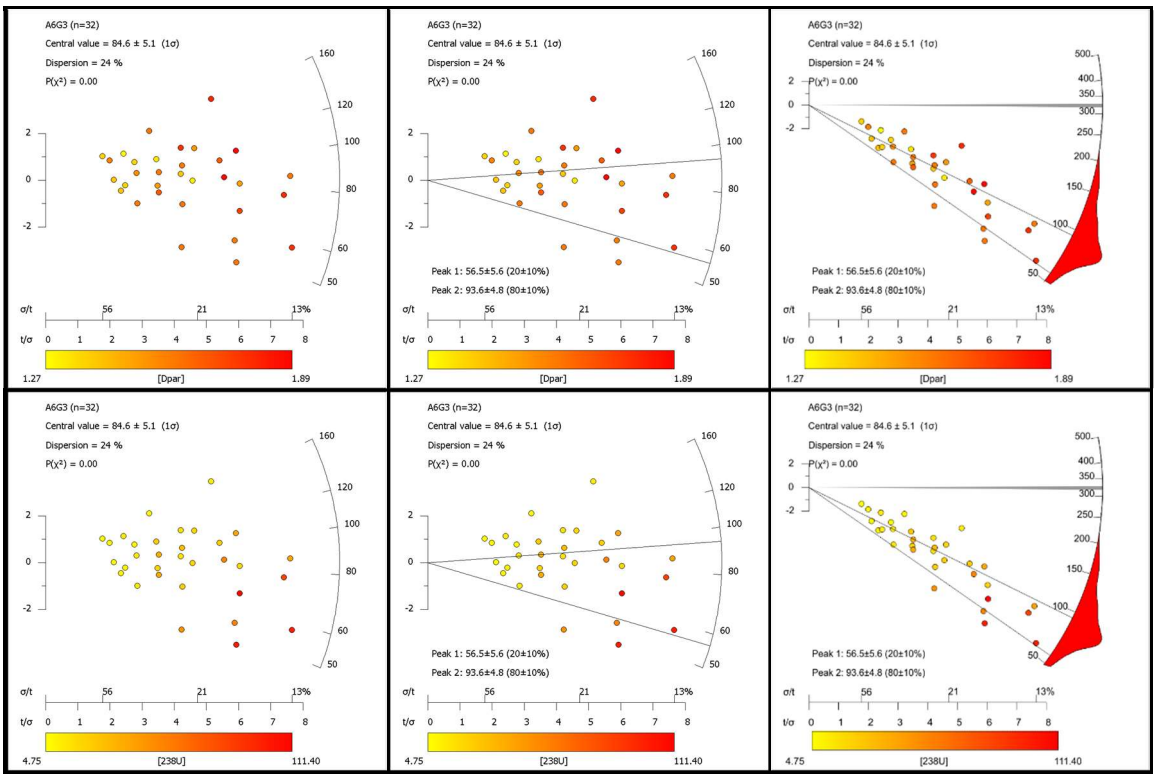

10.5.1.3 Bandeath 1

Sample details

Grid reference	NS8556593001	Pooled age	
Elevation (m)	-471.5	Central age	120.7 ± 5.95 Ma
Lithology	Sandstone	P(chi squared)	0.0
Age	Namurian	Age dispersion	26 %
Depositional constraint	324 ±6 Ma	Length Data	120
N_S	2467	Measured (SD)	11.01 (2.21) µm
P_S	1.61 x10^6	Projected (SD)	13.02 (1.51) µm

Apatite fission track data

Grain I.D.	Ns	Ni	Area (um^2)	Track density	Average Dpar (µm)	se (µm)	^{238}U (ppm)	se (ppm)	AFT Age (Ma)	se (Ma)
Grain01	87	180	3.70E-05	2.35E+06	1.30	0.12	35.70	2.10	125.9	14.0
Grain01b	63	141	3.10E-05	2.03E+06	1.30	0.12	33.40	1.60	116.3	14.9
Grain02	42	78	3.12E-05	1.35E+06	1.40	0.06	18.40	1.00	139.7	21.9
Grain03	16	25	3.52E-05	4.55E+05	1.41	0.33	5.32	0.44	163.0	41.3
Grain04	66	178	1.51E-05	4.38E+06	1.50	0.20	87.10	5.30	96.4	12.2
Grain05	17	36	4.34E-05	3.92E+05	1.49	0.19	6.09	0.40	123.1	30.1
Grain05b	17	28	4.49E-05	3.79E+05	1.49	0.19	4.66	0.41	155.1	38.2
Grain06	44	157	4.88E-05	9.02E+05	1.36	0.19	23.70	1.20	73.1	11.2
Grain06b	28	61	2.43E-05	1.15E+06	1.36	0.19	18.40	1.10	119.6	22.9
Grain07	63	159	2.92E-05	2.16E+06	1.43	0.08	40.10	2.00	103.0	13.2
Grain08	30	69	5.18E-05	5.79E+05	1.41	0.22	9.86	0.79	112.4	21.0
Grain09	109	311	3.54E-05	3.08E+06	1.50	0.12	64.60	3.30	91.4	9.1
Grain10	72	201	2.34E-05	3.08E+06	1.71	0.14	63.10	2.80	93.4	11.2
Grain11	49	133	2.45E-05	2.00E+06	1.39	0.17	39.90	2.20	96.3	14.0
Grain12	44	158	3.94E-05	1.12E+06	1.46	0.12	29.50	2.70	72.7	11.5
Grain13	38	56	3.20E-05	1.19E+06	1.51	0.17	12.90	0.77	175.2	28.9
Grain13b	27	51	2.99E-05	9.03E+05	1.51	0.17	12.44	0.84	138.6	27.1
Grain14	36	76	3.41E-05	1.06E+06	1.40	0.04	16.40	1.00	123.3	20.9
Grain15	66	143	4.45E-05	1.48E+06	1.56	0.59	23.70	1.30	119.8	15.1
Grain16	53	171	4.70E-05	1.13E+06	1.38	0.15	26.80	1.50	80.7	11.3
Grain17	23	30	4.52E-05	5.09E+05	1.52	0.18	4.80	0.35	201.5	42.7
Grain18	77	75	2.24E-05	3.44E+06	1.69	0.09	24.50	1.60	265.4	31.5
Grain19	59	95	2.07E-05	2.85E+06	1.84	0.08	33.70	2.30	161.3	21.7
Grain20	146	282	1.86E-05	7.85E+06	1.68	0.13	111.70	6.80	134.3	11.8
Grain21	70	99	5.19E-05	1.35E+06	1.38	0.14	14.06	0.96	182.7	22.7
Grain22	31	74	3.20E-05	9.68E+05	1.41	0.05	16.90	1.00	109.7	20.0
Grain23	87	176	3.01E-05	2.89E+06	1.83	0.10	43.00	2.60	128.6	14.3
Grain24	74	122	4.34E-05	1.71E+06	1.68	0.08	20.70	1.30	157.2	18.9
Grain25	61	135	5.20E-05	1.17E+06	1.59	0.20	19.10	1.30	117.6	15.6
Grain25b	43	79	4.53E-05	9.50E+05	1.59	0.20	12.76	0.91	142.1	22.3
Grain26	46	85	3.02E-05	1.52E+06	1.60	0.05	20.80	1.80	139.9	21.5
Grain27	76	263	4.70E-05	1.62E+06	1.45	0.16	41.20	2.10	75.4	8.9
Grain27b	160	499	4.21E-05	3.80E+06	1.45	0.16	87.30	4.60	83.6	7.0
Grain28	54	100	3.88E-05	1.39E+06	1.49	0.10	18.90	1.40	140.8	19.9
Grain29	54	129	5.78E-05	9.35E+05	1.32	0.14	16.40	1.00	109.1	15.2
Grain29b	32	81	3.69E-05	8.67E+05	1.32	0.14	16.10	1.00	103.1	18.5
Grain30	63	177	5.61E-05	1.12E+06	1.62	0.11	23.20	1.50	92.9	12.1
Grain31	63	61	3.54E-05	1.78E+06	1.82	0.14	12.56	0.78	267.7	34.7
Grain32	18	31	3.09E-05	5.83E+05	1.39	0.16	7.33	0.54	151.8	36.2
Grain33	93	348	2.93E-05	3.18E+06	1.44	0.17	87.40	4.90	69.8	7.5
Grain34	80	172	2.94E-05	2.72E+06	1.59	0.17	43.10	2.40	120.9	13.9
Grain35	90	216	3.03E-05	2.97E+06	1.57	0.11	52.50	3.10	108.5	11.9

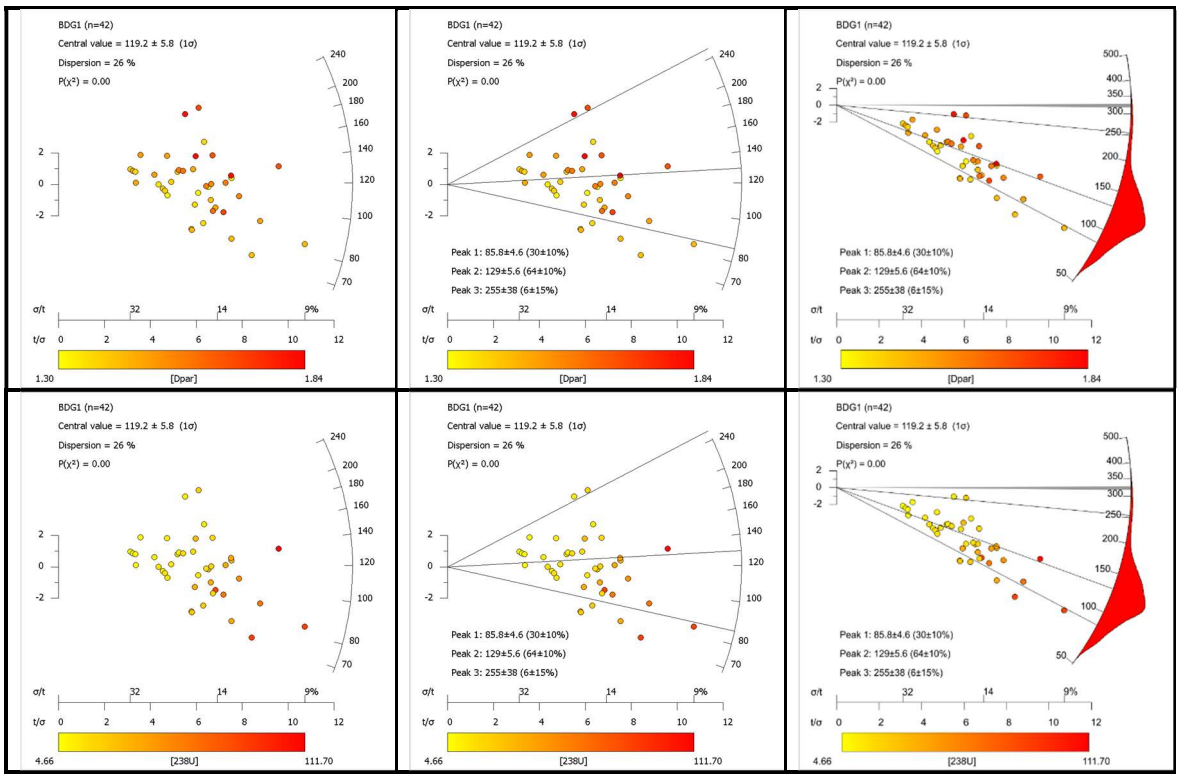

10.5.1.4 Longannet G2

Sample details

Grid reference	NS9398386215	Pooled age	
Elevation (m)	-941	Central age	94.6 ± 4.65 Ma
Lithology	Sandstone	P(chi squared)	0.0
Age	Namurian	Age dispersion	23 %
Depositional constraint	324 ±6 Ma	Length Data	120
N_S	1337	Measured (SD)	11.57 (2.10) µm
P_S	$0.84x10^6$	Projected (SD)	13.56 (1.30) µm

Apatite fission track data

Grain I.D.	Ns	Ni	Area (um^2)	Track density	Average Dpar (µm)	se (µm)	^{238}U (ppm)	se (ppm)	AFT Age (Ma)	se (Ma)
Grain01	6	9	3.40E-05	1.76E+05	1.98	0.10	2.01	0.26	167.2	71.7
Grain02	27	111	3.63E-05	7.44E+05	1.64	0.16	22.50	1.30	63.5	12.8
Grain03	29	105	2.72E-05	1.07E+06	1.83	0.16	28.30	2.20	72.4	14.6
Grain04	27	89	2.10E-05	1.28E+06	1.91	0.19	31.00	2.20	79.4	16.3
Grain05	59	78	2.61E-05	2.26E+06	1.98	0.13	21.90	1.30	196.5	28.1
Grain06	40	128	1.70E-05	2.36E+06	2.02	0.21	55.60	3.50	81.3	13.8
Grain07	5	42	2.80E-05	1.79E+05	1.54	0.07	10.95	0.76	31.4	14.2
Grain08	12	14	2.49E-05	4.82E+05	1.67	0.07	4.19	0.27	218.4	64.6
Grain09	27	41	3.61E-05	7.47E+05	1.54	0.19	8.32	0.58	171.1	35.1
Grain10	50	183	4.76E-05	1.05E+06	1.79	0.27	28.30	1.70	71.2	11.0
Grain11	30	72	5.13E-05	5.85E+05	1.61	0.11	10.30	1.40	108.8	24.7
Grain12	21	72	2.63E-05	7.99E+05	1.61	0.05	20.20	1.30	75.9	17.3
Grain13	44	123	2.61E-05	1.69E+06	1.59	0.19	34.60	1.70	93.5	14.8
Grain13b	35	85	2.87E-05	1.22E+06	1.59	0.19	21.80	1.60	107.1	19.7
Grain14	20	51	3.20E-05	6.25E+05	1.69	0.15	11.64	0.69	102.8	23.8
Grain15	13	29	4.37E-05	2.98E+05	1.60	0.07	4.86	0.40	117.2	33.9
Grain16	41	123	4.44E-05	9.23E+05	1.84	0.06	20.40	1.40	86.8	14.8
Grain17	15	28	3.33E-05	4.50E+05	1.56	0.08	6.18	0.38	139.1	37.0
Grain18	13	35	2.35E-05	5.53E+05	1.72	0.11	10.95	0.81	96.7	27.8
Grain19	26	162	1.73E-05	1.51E+06	1.69	0.18	69.20	3.60	41.9	8.5
Grain20	30	69	3.18E-05	9.43E+05	1.80	0.15	16.00	1.20	112.8	22.3
Grain01	43	109	3.77E-05	1.14E+06	1.47	0.10	21.30	1.30	102.7	16.9
Grain02	32	144	2.41E-05	1.33E+06	1.58	0.18	43.90	2.80	58.1	10.9
Grain02b	25	69	2.03E-05	1.23E+06	1.58	0.18	25.10	1.40	94.1	19.5
Grain03	43	133	4.20E-05	1.02E+06	1.60	0.14	23.20	1.20	84.6	13.6
Grain03b	10	22	1.81E-05	5.54E+05	1.60	0.14	9.16	0.79	115.7	37.8
Grain04	3	4	1.16E-05	2.59E+05	2.66	0.06	2.74	0.28	180.0	105.4
Grain05	46	165	5.05E-05	9.11E+05	1.89	0.17	24.10	1.40	72.6	11.5
Grain05b	31	78	4.59E-05	6.75E+05	1.89	0.17	12.45	0.94	103.9	20.2
Grain06	14	38	1.77E-05	7.93E+05	1.70	0.09	16.00	1.10	95.0	26.2
Grain07	29	70	4.18E-05	6.93E+05	1.73	0.17	12.30	0.66	108.0	20.9
Grain07b	52	93	5.35E-05	9.71E+05	1.73	0.17	12.82	0.93	144.7	22.7
Grain08	25	74	3.70E-05	6.76E+05	1.57	0.15	14.70	1.20	88.2	19.0
Grain09	4	7	3.63E-05	1.10E+05	1.79	0.11	1.52	0.23	138.6	72.4
Grain10	15	46	4.41E-05	3.40E+05	1.79	0.18	7.67	0.72	85.1	23.4
Grain11	51	126	3.96E-05	1.29E+06	1.68	0.09	23.50	1.90	105.0	17.0
Grain11b	30	72	3.24E-05	9.27E+05	1.68	0.09	16.40	1.50	108.2	22.1
Grain12	12	27	3.82E-05	3.14E+05	1.79	0.17	5.15	0.47	116.8	35.3
Grain13	8	15	5.08E-05	1.58E+05	3.44	0.27	2.24	0.26	134.4	50.0
Grain14	29	82	4.43E-05	6.55E+05	1.84	0.08	13.60	1.00	92.3	18.4
Grain15	17	57	2.69E-05	6.32E+05	1.79	0.08	15.72	0.98	77.2	19.3
Grain16	23	55	2.67E-05	8.61E+05	1.65	0.14	15.02	0.99	109.8	24.0
Grain17	11	31	1.44E-05	7.63E+05	1.72	0.11	15.65	0.84	93.4	28.7
Grain18	32	176	1.92E-05	1.67E+06	1.84	0.25	67.40	4.10	47.6	8.9
Grain18b	29	84	2.35E-05	1.23E+06	1.84	0.25	26.30	1.60	90.0	17.6
Grain19	118	352	4.87E-05	2.42E+06	1.89	0.14	53.10	3.30	87.5	9.7
Grain20	13	27	4.63E-05	2.81E+05	2.62	0.19	4.23	0.48	126.9	38.0
Grain21	22	41	3.81E-05	5.78E+05	1.76	0.17	7.83	0.56	140.9	31.7

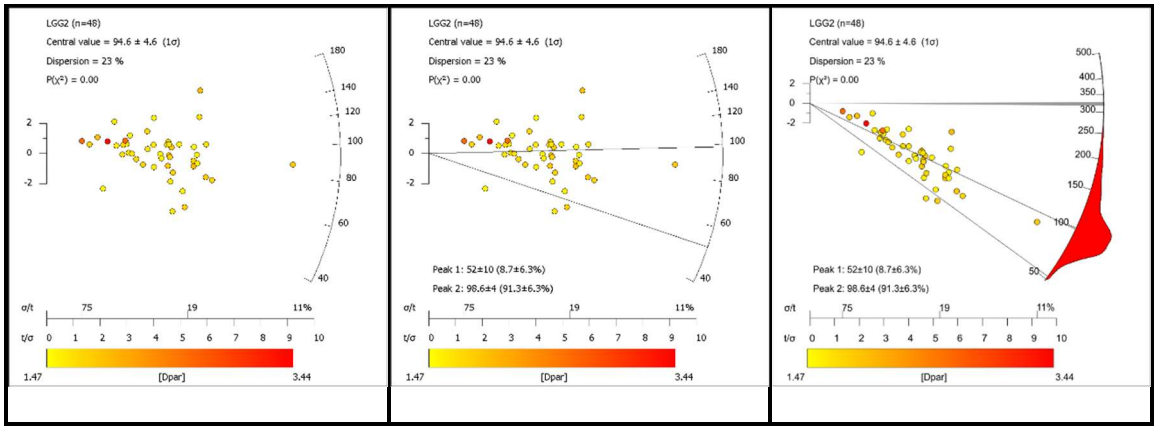

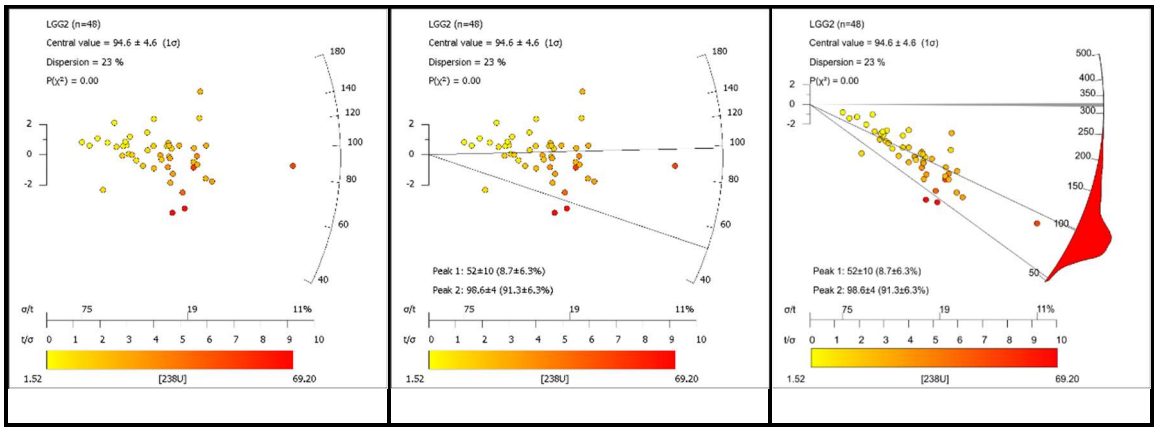
LGG2 (n=48)
Central value = 94.6 ± 4.6 (1σ)
Dispersion = 23 %
P(χ²) = 0.00
σ/t
t/σ
1.52
[238U]
69.20
Peak 1: 52±10 (8.7±6.3%)
Peak 2: 98.6±4 (91.3±6.3%)

10.5.1.5 Meadowhill G1

Sample details

Grid reference	NS9615293967	Pooled age	
Elevation (m)	-568	Central age	193.98 ± 9.91 Ma
Lithology	Sandstone	P(chi squared)	0.0
Age	Namurian	Age dispersion	25 %
Depositional constraint	324 ±6 Ma	Length Data	120
N_S	4411	Measured (SD)	10.80 (2.13) µm
P_S	2.72 x10^6	Projected (SD)	13.08 (1.34) µm

Apatite fission track data

Grain I.D.	Ns	Ni	Area (um^2)	Track density	Average Dpar (µm)	se (µm)	^{238}U (ppm)	se (ppm)	AFT Age (Ma)	se (Ma)
Grain01	85	184	3.98E-05	2.14E+06	1.57	0.10	34.00	1.90	120.1	13.5
Grain02	97	109	3.55E-05	2.73E+06	1.68	0.12	22.60	1.60	229.5	24.7
Grain03	103	191	5.52E-05	1.87E+06	1.18	0.10	25.40	1.60	140.3	14.5
Grain04	200	238	2.54E-05	7.88E+06	1.50	0.19	68.90	3.90	217.1	16.5
Grain05	50	56	3.81E-05	1.31E+06	1.62	0.21	10.80	0.73	230.7	33.5
Grain05b	131	166	2.56E-05	5.11E+06	1.62	0.21	47.50	3.10	204.4	19.1
Grain06	17	13	1.83E-05	9.30E+05	1.24	0.24	5.41	0.41	323.8	79.5
Grain07	125	160	5.22E-05	2.39E+06	1.30	0.12	22.60	1.50	201.3	19.2
Grain08	241	487	4.41E-05	5.46E+06	1.71	0.10	81.20	4.60	128.6	9.1
Grain09	151	192	3.07E-05	4.91E+06	1.43	0.18	46.00	2.20	203.0	17.2
Grain10	134	174	5.30E-05	2.53E+06	1.43	0.18	24.10	1.40	199.5	18.2
Grain11	212	466	5.00E-05	4.24E+06	1.36	0.06	68.60	2.60	118.2	8.4
Grain12	84	88	4.90E-05	1.72E+06	1.37	0.18	13.19	0.89	246.4	28.1
Grain13	188	219	5.77E-05	3.26E+06	1.41	0.13	28.00	1.50	221.1	17.2
Grain14	135	188	5.94E-05	2.27E+06	1.50	0.11	23.30	1.20	185.7	16.7
Grain15	19	16	3.01E-05	6.32E+05	1.43	0.16	3.85	0.37	309.2	72.5
Grain16	21	23	5.78E-05	3.63E+05	1.39	0.20	2.96	0.30	232.8	52.2
Grain17	21	25	5.52E-05	3.81E+05	1.48	0.21	3.37	0.35	214.4	48.1
Grain19	136	224	5.87E-05	2.32E+06	1.68	0.22	28.00	1.40	157.8	14.1
Grain20	125	139	5.52E-05	2.27E+06	1.69	0.18	18.50	1.10	232.3	21.9
Grain20b	161	253	5.19E-05	3.10E+06	1.69	0.18	35.90	2.20	164.6	13.9
Grain21	29	32	3.95E-05	7.34E+05	1.43	0.16	5.95	0.50	233.9	44.5
Grain22	136	233	4.51E-05	3.01E+06	1.53	0.13	38.00	1.90	151.3	13.5
Grain22b	121	316	3.21E-05	3.77E+06	1.53	0.13	72.40	3.30	99.7	9.4
Grain23	110	114	6.16E-05	1.79E+06	1.60	0.12	13.60	1.00	248.6	25.4
Grain24	137	213	2.23E-05	6.14E+06	1.54	0.10	70.10	3.80	166.8	15
Grain25	115	208	4.80E-05	2.39E+06	1.42	0.23	31.90	1.90	143.3	14
Grain25b	160	296	6.14E-05	2.61E+06	1.42	0.23	35.50	2.20	140.2	11.9
Grain26	112	109	5.23E-05	2.14E+06	1.46	0.19	15.40	1.20	263.1	26.9
Grain27	145	157	7.27E-05	2.00E+06	1.42	0.10	15.91	0.83	237.8	20.7
Grain27b	121	149	6.25E-05	1.94E+06	1.42	0.10	17.60	1.00	209.2	19.9
Grain28	386	385	4.51E-05	8.56E+06	1.70	0.17	62.80	3.60	257.8	15.1
Grain28b	315	310	3.74E-05	8.42E+06	1.70	0.17	61.00	3.20	261.3	16.2
Grain29	37	84	6.03E-05	6.14E+05	1.59	0.09	10.30	0.75	114.1	19.2
Grain30	51	43	4.13E-05	1.24E+06	1.45	0.11	7.71	0.64	302.3	44.2

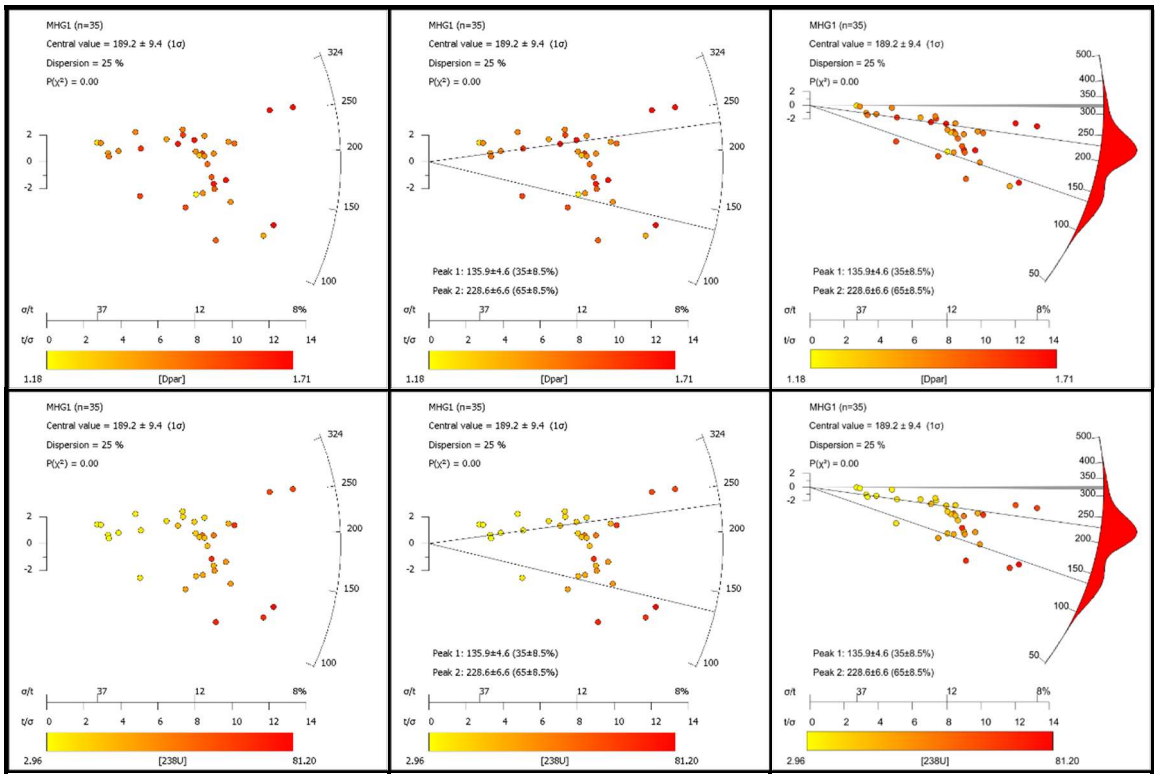

10.5.1.6 Meadowhill G2

Sample details

Grid reference	NS9615293967	Pooled age	
Elevation (m)	-815	Central age	127.5 ± 6.9 Ma
Lithology	Sandstone	P(chi squared)	0.0.
Age	Namurian	Age dispersion	25 %
Depositional constraint	324 ±6 Ma	Length Data	120
N_S	1423	Measured (SD)	12.05 (1.62) µm
P_S	1.09 x10^6	Projected (SD)	13.78 (1.08) µm

Apatite fission track data

Grain I.D.	Ns	Ni	Area (um^2)	Track density	Average Dpar (µm)	se (µm)	^{238}U (ppm)	se (ppm)	AFT Age (Ma)	se (Ma)
Grain01	36	88	4.38E-05	8.22E+05	1.64	0.17	14.70	1.10	107.0	18.3
Grain02	31	61	3.46E-05	8.95E+05	1.51	0.15	12.90	0.93	132.6	24.3
Grain03	13	36	4.39E-05	2.96E+05	1.38	0.08	6.00	0.53	94.6	26.6
Grain04	54	131	3.91E-05	1.38E+06	1.43	0.07	24.60	1.30	107.5	14.9
Grain05	5	12	2.20E-05	2.28E+05	1.40	0.12	3.90	0.35	111.8	50.3
Grain06	18	31	3.37E-05	5.34E+05	1.35	0.23	6.84	0.55	149.0	35.6
Grain07	15	17	2.14E-05	7.00E+05	1.45	0.17	5.80	0.49	229.0	59.9
Grain08	39	112	2.61E-05	1.50E+06	1.61	0.14	31.70	1.70	90.5	14.7
Grain09	46	81	3.20E-05	1.44E+06	1.52	0.12	18.50	1.30	148.2	22.5
Grain10	16	40	1.54E-05	1.04E+06	1.52	0.16	19.10	1.20	104.5	26.3
Grain11	113	157	2.31E-05	4.90E+06	1.90	0.19	50.00	2.90	186.5	18.4
Grain12	58	64	5.19E-05	1.12E+06	1.67	0.13	9.01	0.76	235.1	32.4
Grain13	44	146	3.00E-05	1.47E+06	1.50	0.08	35.80	2.60	78.7	12.2
Grain14	43	87	3.56E-05	1.21E+06	1.49	0.10	17.90	1.80	129.1	20.7
Grain15	25	84	2.45E-05	1.02E+06	1.33	0.09	25.30	1.60	77.4	15.7
Grain16	13	19	2.29E-05	5.67E+05	1.33	0.17	6.13	0.46	176.1	49.3
Grain17	50	85	5.20E-05	9.62E+05	1.23	0.12	12.03	0.79	152.5	22.1
Grain18	78	144	2.65E-05	2.94E+06	1.54	0.16	40.00	2.40	140.3	16.4
Grain19	2	3	7.50E-06	2.67E+05	1.59	0.19	2.87	0.31	177.0	125.5
Grain20	21	49	2.31E-05	9.09E+05	1.43	0.12	15.50	1.10	112.3	24.8
Grain21	102	247	6.71E-05	1.52E+06	1.50	0.18	27.10	1.80	107.4	11.2
Grain21b	88	228	4.42E-05	1.99E+06	1.50	0.18	37.90	2.60	100.6	11.3
Grain22	28	47	3.09E-05	9.07E+05	1.46	0.18	11.16	0.86	155.1	29.9
Grain23	19	25	1.27E-05	1.50E+06	1.43	0.14	14.80	1.40	193.0	45.2
Grain24	20	27	2.22E-05	9.01E+05	1.50	0.14	8.89	0.57	192.9	43.6
Grain25	36	45	2.85E-05	1.26E+06	1.60	0.20	11.59	0.70	207.2	35.1
Grain26	17	24	1.40E-05	1.22E+06	1.39	0.10	12.88	0.85	180.0	44.1
Grain27	66	111	3.51E-05	1.88E+06	1.47	0.07	23.20	1.50	154.7	19.7
Grain28	21	28	3.92E-05	5.36E+05	1.40	0.21	5.30	0.41	192.4	42.6
Grain29	13	30	2.55E-05	5.09E+05	1.08	0.08	8.52	0.67	114.3	32.0
Grain30	18	37	4.99E-05	3.61E+05	1.73	0.18	5.44	0.58	126.8	30.7
Grain31	24	61	4.01E-05	5.98E+05	1.29	0.16	11.25	0.72	101.8	21.0
Grain32	4	6	2.99E-05	1.34E+05	2.59	0.31	1.55	0.23	164.7	83.2
Grain33	25	71	4.82E-05	5.19E+05	1.39	0.14	10.77	0.94	92.4	18.9
Grain34	24	31	4.87E-05	4.93E+05	1.51	0.20	4.68	0.45	200.4	42.0
Grain35	44	170	1.86E-05	2.36E+06	1.38	0.11	67.10	4.80	67.6	10.5
Grain36	25	83	2.03E-05	1.23E+06	1.56	0.12	30.20	1.80	78.5	15.9
Grain37	20	36	2.92E-05	6.86E+05	1.40	0.16	9.18	0.81	142.7	32.5
Grain38	60	106	4.12E-05	1.46E+06	1.60	0.11	18.90	1.10	147.0	19.4
Grain39	49	148	4.58E-05	1.07E+06	1.35	0.18	23.80	1.40	86.3	12.6

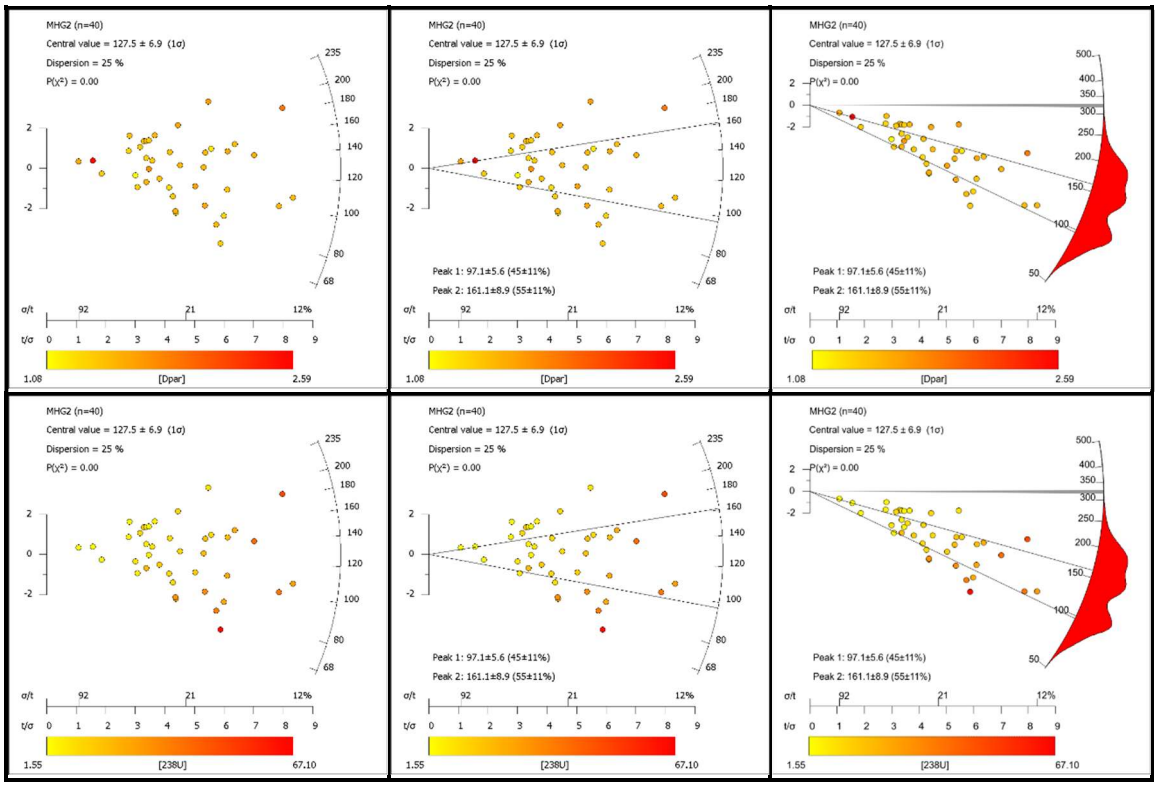

10.5.1.7 Thornton G1

Sample details

Grid reference	NT2954096839	Pooled age	
Elevation (m)	-611	Central age	177.2 ± 9.7 Ma
Lithology	Sandstone	P(chi squared)	0.0
Age	Namurian	Age dispersion	29 %
Depositional constraint	324 ±6 Ma	Length Data	120
N_S	3147	Measured (SD)	10.65 (2.18) µm
P_S	2.37 x10^6	Projected (SD)	12.98 (1.27) µm

Apatite fission track data

Grain I.D.	Ns	Ni	Area (um^2)	Track density	Average Dpar (µm)	se (µm)	^{238}U (ppm)	se (ppm)	AFT Age (Ma)	se (Ma)
Grain01	22	50	1.57E-05	1.40E+06	1.68	0.09	23.60	1.30	113.9	24.5
Grain02	17	19	2.27E-05	7.50E+05	1.74	0.16	6.02	0.52	236.2	58.2
Grain03	132	148	2.08E-05	6.36E+06	2.17	0.13	52.60	2.90	229.3	20.9
Grain04	48	38	2.11E-05	2.28E+06	1.60	0.06	13.42	0.86	320.0	47.3
Grain05	114	222	2.00E-05	5.71E+06	1.65	0.17	81.90	4.20	133.3	12.9
Grain05b	62	164	1.97E-05	3.14E+06	1.65	0.17	61.00	4.00	98.7	12.9
Grain06	57	80	2.72E-05	2.10E+06	1.61	0.18	21.60	1.40	184.6	25.2
Grain07	33	22	3.14E-05	1.05E+06	1.79	0.15	5.05	0.42	389.6	69.7
Grain08	163	273	3.41E-05	4.77E+06	1.75	0.15	58.90	3.60	154.7	13.0
Grain09	48	118	3.79E-05	1.27E+06	1.65	0.14	23.00	1.20	105.5	15.5
Grain09b	44	152	3.44E-05	1.28E+06	1.65	0.14	32.50	1.40	75.5	11.5
Grain10	45	56	3.49E-05	1.29E+06	1.75	0.09	11.71	0.76	209.0	31.9
Grain11	52	73	3.75E-05	1.39E+06	1.80	0.10	14.33	0.90	184.4	26.2
Grain12	52	68	4.07E-05	1.28E+06	1.58	0.14	12.21	0.74	198.8	28.2
Grain13	22	26	3.39E-05	6.49E+05	1.54	0.18	5.68	0.49	217.0	47.2
Grain14	165	364	4.69E-05	3.52E+06	1.98	0.13	57.20	2.60	117.8	9.6
Grain15	158	210	3.95E-05	4.00E+06	1.83	0.14	39.10	2.00	194.6	16.3
Grain16	216	321	3.37E-05	6.41E+06	2.25	0.04	70.10	3.70	174.3	12.7
Grain17	162	277	3.28E-05	4.94E+06	1.88	0.09	62.00	2.90	151.9	12.5
Grain17b	158	258	3.16E-05	5.00E+06	1.88	0.09	60.10	3.50	158.6	13.4
Grain18	45	101	2.56E-05	1.76E+06	2.05	0.23	28.90	1.20	116.2	17.5
Grain19	55	116	2.20E-05	2.50E+06	1.84	0.06	38.80	2.00	123.1	16.9
Grain20	40	40	1.69E-05	2.38E+06	1.80	0.15	17.57	0.98	255.8	41.1
Grain21	21	25	2.12E-05	9.89E+05	1.88	0.24	8.61	0.62	218.0	48.2
Grain22	167	245	3.43E-05	4.87E+06	1.98	0.27	52.60	2.70	176.5	14.4
Grain23	85	116	3.92E-05	2.17E+06	1.60	0.20	21.80	1.10	189.4	21.1
Grain24	142	277	2.84E-05	5.01E+06	1.90	0.16	72.00	3.30	133.0	11.6
Grain25	29	34	3.06E-05	9.49E+05	1.93	0.16	8.18	0.61	220.3	41.7
Grain26	36	31	4.52E-05	7.96E+05	1.63	0.19	5.08	0.46	295.9	51.1
Grain27	13	20	3.59E-05	3.62E+05	1.86	0.13	4.04	0.41	170.8	48.2
Grain28	49	50	4.31E-05	1.14E+06	1.69	0.21	8.49	0.57	253.4	37.2
Grain28b	57	38	4.13E-05	1.38E+06	1.69	0.21	6.84	0.56	378.1	52.4
Grain29	48	46	3.10E-05	1.55E+06	1.92	0.12	11.01	0.90	265.9	39.9
Grain30	87	84	4.05E-05	2.15E+06	1.83	0.14	15.29	0.95	265.5	29.6
Grain31	37	37	3.17E-05	1.17E+06	1.71	0.10	8.53	0.71	258.7	43.9
Grain32	65	110	5.92E-05	1.10E+06	1.56	0.27	13.70	1.00	152.9	19.8
Grain32b	49	84	5.14E-05	9.53E+05	1.56	0.27	12.06	0.83	150.9	22.2
Grain33	207	313	4.57E-05	4.53E+06	2.02	0.10	50.40	3.40	171.3	13.2
Grain34	126	198	2.92E-05	4.32E+06	1.97	0.11	49.90	2.50	164.9	15.3
Grain35	19	31	3.96E-05	4.80E+05	1.50	0.07	5.70	0.51	160.7	37.6

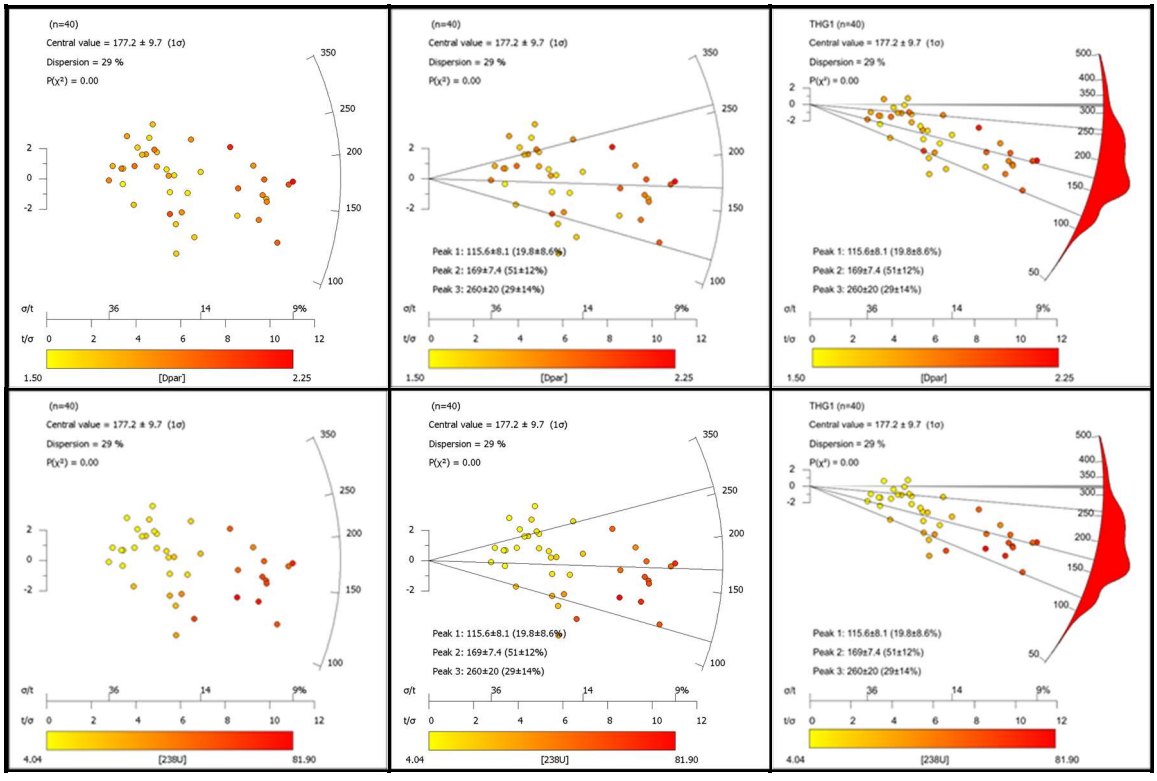

10.5.1.8 Thornton G2

Sample details

Grid reference	NT2954096839	Pooled age	
Elevation (m)	-734	Central age	147.9 ± 7.4 Ma
Lithology	Sandstone	P(chi squared)	0.0
Age	Namurian	Age dispersion	23 %
Depositional constraint	324 ±6 Ma	Length Data	120
N_S	2206	Measured (SD)	10.92 (1.90) µm
P_S	2.37 x10^6	Projected (SD)	12.99 (1.28) µm

Apatite fission track data

Grain I.D.	Ns	Ni	Area (um^2)	Track density	Average Dpar (µm)	se (µm)	^{238}U (ppm)	se (ppm)	AFT Age (Ma)	se (Ma)
Grain01	57	144	1.30E-05	4.39E+06	1.64	0.04	81.8	4.1	102.8	13.9
Grain02	14	15	2.13E-05	6.59E+05	1.43	0.08	5.28	0.49	236.4	64.1
Grain03	6	11	1.30E-05	4.61E+05	1.18	0.27	6.41	0.55	137.5	56.4
Grain04	14	10	1.77E-05	7.91E+05	1.18	0.17	4.15	0.42	358.1	97.4
Grain07	51	100	2.28E-05	2.24E+06	1.51	0.10	32.2	1.7	132.8	18.9
Grain08	65	92	2.35E-05	2.76E+06	1.54	0.09	28.8	1.7	182.5	23.3
Grain09	18	19	1.98E-05	9.09E+05	1.37	0.18	6.93	0.59	248.3	59.5
Grain10	62	80	1.89E-05	3.28E+06	1.37	0.21	31.2	1.9	199.9	26.1
Grain11	30	36	3.48E-05	8.63E+05	1.66	0.09	7.63	0.61	214.7	40.1
Grain12	51	62	2.79E-05	1.83E+06	1.59	0.17	16.4	1.2	211.4	30.6
Grain13	70	139	2.88E-05	2.43E+06	1.62	0.11	35.4	2.3	131.3	16.3
Grain14	276	580	3.82E-05	7.22E+06	1.49	0.15	111.6	5.6	123.7	8.1
Grain15	42	46	2.11E-05	2.00E+06	1.5	0.22	16.24	0.82	232.9	36.4
Grain16	80	174	2.97E-05	2.69E+06	1.71	0.15	43	2	119.9	13.7
Grain17	58	124	2.23E-05	2.60E+06	1.32	0.12	40.8	2.2	121.8	16.3
Grain18	42	86	2.54E-05	1.65E+06	1.5	0.10	24.8	1.9	127.3	20.2
Grain19	116	315	3.37E-05	3.44E+06	1.52	0.10	68.7	3.2	96.0	9.2
Grain20	72	145	2.84E-05	2.54E+06	1.6	0.17	37.5	2.2	129.2	15.7
Grain21	35	56	2.63E-05	1.33E+06	1.63	0.23	15.58	0.92	162.6	27.9
Grain22	59	72	2.66E-05	2.22E+06	1.67	0.14	19.8	1.2	212.8	28.4
Grain24	57	59	1.81E-05	3.15E+06	1.41	0.05	23.8	1.3	250.6	33.9
Grain25	79	107	2.23E-05	3.54E+06	1.49	0.17	35.2	1.9	191.3	22.1
Grain26	107	184	2.62E-05	4.08E+06	1.48	0.18	51.5	3	151.2	15.3
Grain27	66	101	3.43E-05	1.93E+06	1.45	0.10	21.7	1.3	169.2	21.4
Grain28	25	28	3.30E-05	7.58E+05	1.43	0.04	6.21	0.51	231.4	47.3
Grain29	54	129	3.48E-05	1.55E+06	1.42	0.14	27.4	1.9	108.6	15.3
Grain30	76	176	2.04E-05	3.72E+06	1.42	0.04	63.6	3.5	112.1	13.2
Grain31	111	290	3.29E-05	3.37E+06	1.41	0.12	64.8	3.1	99.7	9.8
Grain32	29	65	3.69E-05	7.86E+05	1.27	0.08	12.93	0.68	116.3	21.8
Grain33	53	102	2.16E-05	2.45E+06	1.37	0.08	34.7	1.7	134.9	18.8
Grain34	53	66	2.65E-05	2.00E+06	1.5	0.21	18.3	1.3	207.4	29.4
Grain35	76	171	3.92E-05	1.94E+06	1.41	0.10	32.2	2.1	115.4	13.8
Grain38	6	9	2.60E-05	2.31E+05	1.22	0.10	2.53	0.27	173.9	71.6
Grain39	45	100	3.83E-05	1.17E+06	1.64	0.17	19.1	1.1	117.6	17.9
Grain40	151	314	2.55E-05	5.93E+06	1.66	0.21	90.9	5.1	124.8	10.7

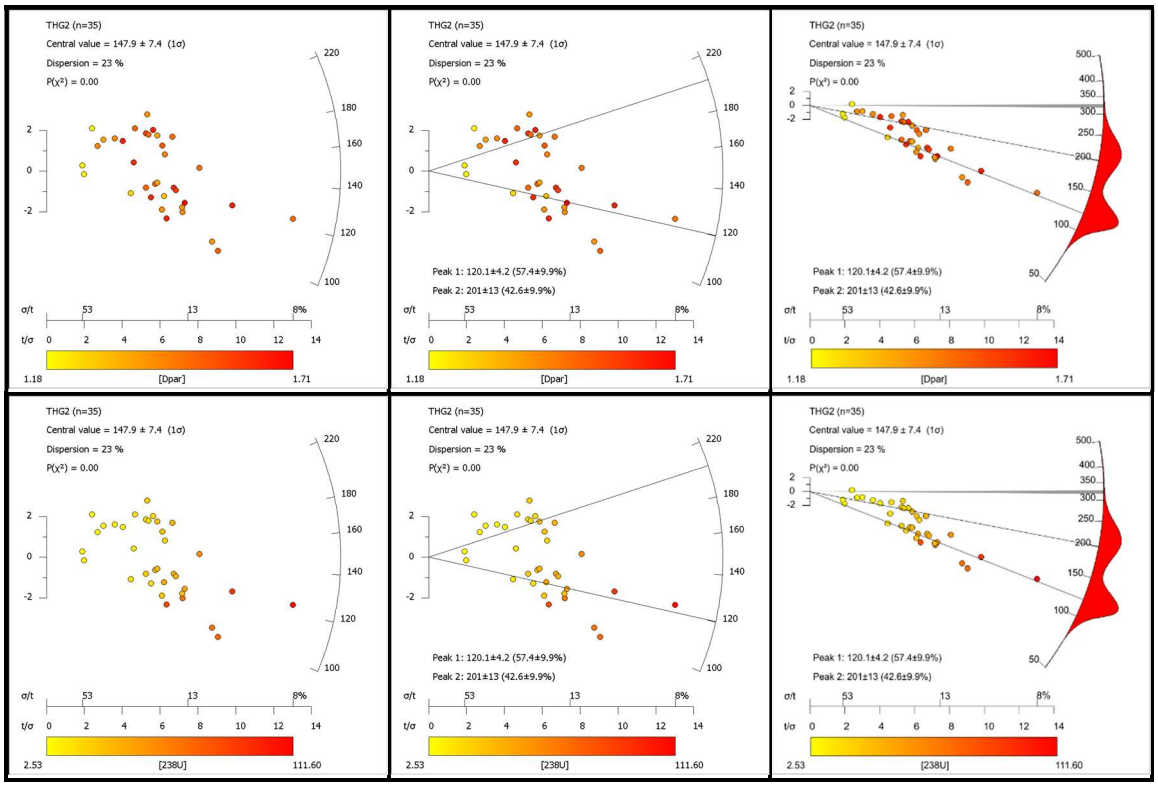

10.5.1.9 Thornton G3

Sample details

Grid reference	NT2954096839	Pooled age	
Elevation (m)	-798.35	Central age	145.3 ± 7.4 Ma
Lithology	Sandstone	P(chi squared)	0.0
Age	Namurian	Age dispersion	28 %
Depositional constraint	324 ±6 Ma	Length Data	110
N_S	2779	Measured (SD)	12.00 (1.79) µm
P_S	2.06 x10^6	Projected (SD)	13.71 (1.20) µm

Apatite fission track data

Grain I.D.	Ns	Ni	Area (um^2)	Track density	Average Dpar (µm)	se (µm)	^{238}U (ppm)	se (ppm)	AFT Age (Ma)	se (Ma)
Grain01	67	85	3.80E-05	1.76E+06	1.72	0.17	16.52	0.97	202.9	25.5
Grain02	141	236	2.15E-05	6.57E+06	1.83	0.08	80.80	5.20	155.2	14.0
Grain03	27	30	2.31E-05	1.17E+06	1.37	0.27	9.66	0.71	229.2	44.9
Grain04	109	117	2.50E-05	4.36E+06	1.63	0.23	34.40	1.80	240.0	23.8
Grain05	66	170	3.16E-05	2.09E+06	1.30	0.16	39.50	2.60	101.4	12.9
Grain05b	84	127	3.53E-05	2.38E+06	1.30	0.16	26.40	1.70	171.9	19.6
Grain06	62	140	3.00E-05	2.07E+06	1.42	0.35	34.40	1.90	114.9	14.9
Grain07	62	97	2.78E-05	2.23E+06	1.44	0.17	25.60	1.40	166.1	21.6
Grain08	159	334	3.31E-05	4.81E+06	1.50	0.13	74.20	4.30	123.9	10.5
Grain09	87	191	2.93E-05	2.97E+06	1.27	0.26	47.90	3.40	118.6	13.4
Grain09b	98	214	2.06E-05	4.76E+06	1.27	0.26	76.30	4.40	119.3	12.5
Grain10	34	76	2.49E-05	1.37E+06	1.28	0.12	22.50	1.40	116.2	20.3
Grain11	40	127	3.95E-05	1.01E+06	1.43	0.20	23.60	2.00	82.3	13.5
Grain12	79	123	2.34E-05	3.38E+06	1.40	0.13	38.90	3.20	165.8	19.9
Grain13	32	50	3.77E-05	8.50E+05	1.46	0.16	9.80	0.69	165.2	29.8
Grain14	53	60	4.58E-05	1.16E+06	1.50	0.16	9.59	0.80	228.9	32.9
Grain14b	39	57	3.22E-05	1.21E+06	1.50	0.16	13.04	0.86	177.1	29.0
Grain15	20	30	3.11E-05	6.44E+05	1.24	0.17	7.21	0.81	170.1	39.2
Grain16	61	135	2.51E-05	2.43E+06	1.55	0.16	39.40	2.40	117.9	15.5
Grain16b	61	107	2.60E-05	2.35E+06	1.55	0.16	30.30	2.10	148.0	19.6
Grain17	48	62	3.19E-05	1.51E+06	1.61	0.11	14.40	1.20	198.9	29.9
Grain18	22	66	2.03E-05	1.08E+06	1.03	0.15	23.80	1.80	87.3	18.9
Grain19	32	42	3.32E-05	9.63E+05	1.42	0.11	9.19	0.73	199.3	36.1
Grain20	70	139	2.41E-05	2.91E+06	1.45	0.13	42.40	3.10	130.9	16.4
Grain21	34	61	3.25E-05	1.05E+06	1.46	0.19	13.80	1.10	144.8	25.5
Grain22	44	81	2.90E-05	1.52E+06	1.35	0.15	20.60	1.50	140.9	21.9
Grain23	49	115	3.40E-05	1.44E+06	1.39	0.14	24.90	1.70	111.0	16.3
Grain24	72	135	3.26E-05	2.21E+06	1.55	0.18	30.50	2.90	138.3	17.6
Grain25	96	218	3.06E-05	3.13E+06	1.52	0.13	52.40	4.10	114.4	12.5
Grain26	56	89	2.77E-05	2.03E+06	1.70	0.15	23.70	2.00	162.9	22.8
Grain27	88	125	3.77E-05	2.33E+06	1.56	0.18	24.40	2.50	182.0	21.5
Grain28	35	47	3.36E-05	1.04E+06	1.43	0.16	10.24	0.85	193.7	33.7
Grain29	51	89	2.71E-05	1.88E+06	1.64	0.23	24.20	2.40	148.3	22.0
Grain29b	90	137	3.19E-05	2.82E+06	1.64	0.23	31.60	3.00	170.0	19.7
Grain30	75	179	4.68E-05	1.60E+06	1.69	0.52	28.20	2.70	108.9	13.6
Grain31	150	532	4.49E-05	3.34E+06	1.48	0.05	87.30	6.40	73.5	6.6
Grain31b	97	382	3.41E-05	2.84E+06	1.48	0.05	82.30	7.30	66.3	7.4
Grain32	39	49	2.71E-05	1.44E+06	1.51	0.10	13.37	0.81	204.7	33.4
Grain33	87	140	5.04E-05	1.73E+06	1.46	0.14	20.50	1.30	160.7	18.0
Grain34	52	41	3.35E-05	1.55E+06	1.55	0.16	9.10	0.71	321.1	46.3
Grain34b	55	75	3.77E-05	1.46E+06	1.55	0.16	14.68	0.96	189.4	26.3
Grain35	56	86	4.63E-05	1.21E+06	1.46	0.20	13.60	1.10	169.5	23.7

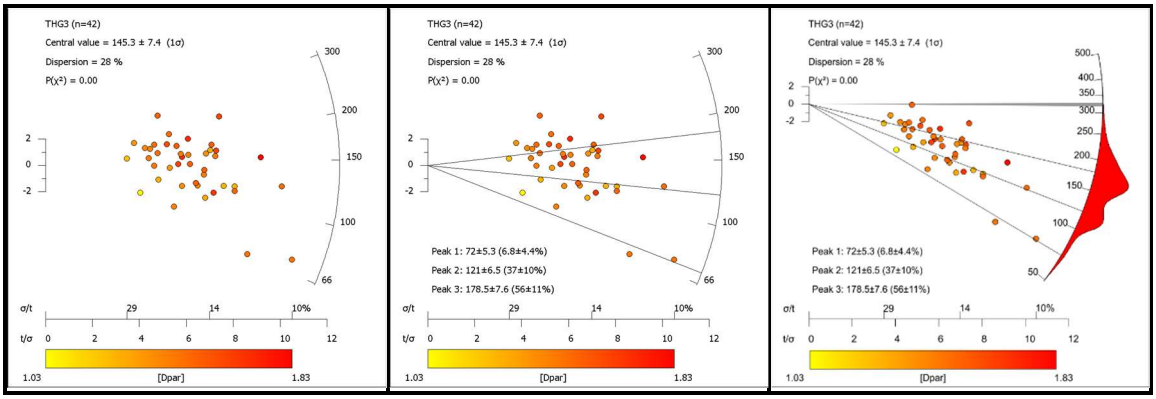

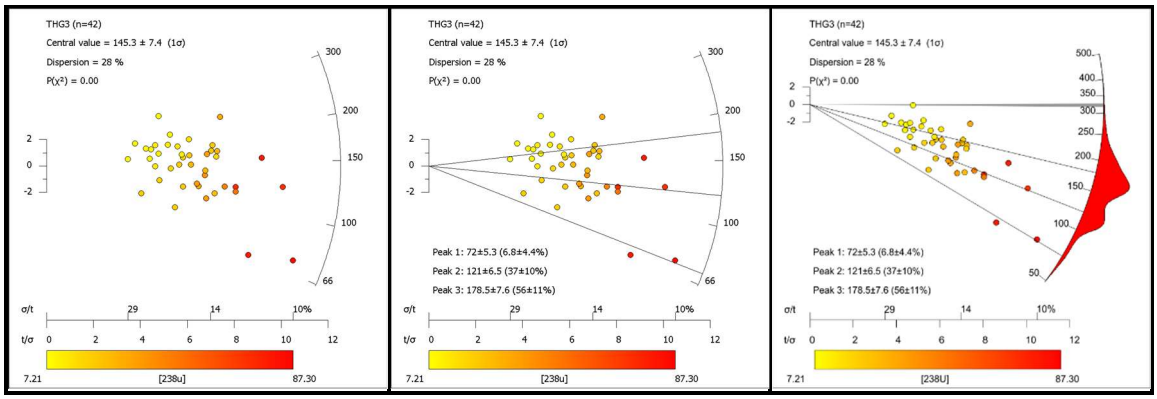
THG3 (n=42)
Central value = 145.3 ± 7.4 (1σ)
Dispersion = 28 %
P(χ²) = 0.00
300
200
150
100
66
2
0
-2
σ/t
29
14
10%
t/σ
0 2 4 6 8 10 12
7.21
[238u]
87.30
THG3 (n=42)
Central value = 145.3 ± 7.4 (1σ)
Dispersion = 28 %
P(χ²) = 0.00
Peak 1: 72±5.3 (6.8±4.4%)
Peak 2: 121±6.5 (37±10%)
Peak 3: 178.5±7.6 (56±11%)
THG3 (n=42)
Central value = 145.3 ± 7.4 (1σ)
Dispersion = 28 %
P(χ²) = 0.00
Peak 1: 72±5.3 (6.8±4.4%)
Peak 2: 121±6.5 (37±10%)
Peak 3: 178.5±7.6 (56±11%)
500
400
350
300
250
200
150
100
50
[238U]

10.5.1.10 Craighead

Sample details

Grid reference	NS8267162010	Pooled age	
Elevation (m)	-620	Central age	87.87 ± 6.62 Ma
Lithology	Sandstone	P(chi squared)	0.0
Age	Viséan	Age dispersion	30 %
Depositional constraint	338 ±10 Ma	Length Data	61
N_S	676	Measured (SD)	11.71 (1.51) µm
P_S	0.77 x10^6	Projected (SD)	13.50 (1.01) µm

Apatite fission track data

Grain I.D.	Ns	Ni	Area (um^2)	Track density	Average Dpar (µm)	se (µm)	^{238}U (ppm)	se (ppm)	AFT Age (Ma)	se (Ma)
Grain01	6	11	2.59E-05	2.32E+05	2.45	0.09	3.25	0.35	136.2	56.1
Grain02	16	72	3.19E-05	5.01E+05	1.26	0.14	16.50	1.30	58.4	14.8
Grain03	35	75	1.83E-05	1.92E+06	1.58	0.23	30.20	2.10	121.4	21.0
Grain04	2	10	2.24E-05	8.94E+04	1.36	0.09	3.28	0.44	52.4	37.3
Grain05	12	68	3.12E-05	3.84E+05	1.73	0.18	16.10	1.60	45.9	13.5
Grain06	29	76	3.28E-05	8.84E+05	1.42	0.16	17.10	1.30	99.0	18.8
Grain07	12	32	1.85E-05	6.50E+05	1.38	0.15	12.60	1.10	98.9	28.9
Grain08	4	20	2.52E-05	1.59E+05	1.22	0.10	5.73	0.67	53.4	26.9
Grain09	15	32	2.36E-05	6.36E+05	1.51	0.09	10.10	0.80	120.5	31.5
Grain10	8	38	2.38E-05	3.36E+05	1.51	0.13	11.60	0.94	55.7	19.8
Grain11	7	4	3.00E-05	2.34E+05	3.26	0.60	1.03	0.18	423.6	164.4
Grain12	33	58	2.88E-05	1.15E+06	1.70	0.10	14.80	1.00	147.6	26.2
Grain13	39	56	3.03E-05	1.29E+06	1.57	0.17	13.50	1.40	181.7	30.6
Grain14	15	41	1.90E-05	7.89E+05	1.30	0.09	15.90	1.30	95.1	24.9
Grain15	10	48	2.07E-05	4.82E+05	1.81	0.39	17.10	1.20	54.2	17.3
Grain16	28	78	3.82E-05	7.34E+05	1.70	0.32	15.00	1.00	93.8	18.0
Grain17	2	11	1.97E-05	1.02E+05	2.21	0.02	4.00	0.34	48.9	34.7
Grain18	11	17	1.82E-05	6.06E+05	1.85	0.14	6.70	0.61	172.3	52.5
Grain20	25	57	1.67E-05	1.50E+06	1.79	0.22	25.00	1.70	114.9	23.3
Grain21	32	54	2.31E-05	1.38E+06	1.67	0.20	17.20	1.20	153.5	27.7
Grain23	11	43	2.48E-05	4.44E+05	1.42	0.08	12.76	0.88	66.8	20.3
Grain24	13	33	1.86E-05	6.98E+05	1.46	0.32	12.92	0.85	103.4	28.9
Grain25	15	54	2.34E-05	6.42E+05	1.23	0.09	17.10	1.20	72.1	18.8
Grain26	11	30	2.22E-05	4.96E+05	1.33	0.19	9.79	0.72	97.1	29.5
Grain27	10	26	2.26E-05	4.42E+05	1.74	0.16	8.34	0.71	101.6	32.4
Grain28	3	24	2.03E-05	1.48E+05	1.27	0.06	8.73	0.73	32.6	18.9
Grain29	5	12	1.54E-05	3.25E+05	1.57	0.06	5.97	0.51	104.2	46.8
Grain31	46	141	3.06E-05	1.50E+06	1.68	0.26	33.80	2.50	85.3	13.0
Grain32	13	35	1.60E-05	8.14E+05	1.64	0.08	16.00	1.10	97.5	27.3
Grain33	16	63	2.07E-05	7.75E+05	1.73	0.14	22.60	1.40	65.9	16.6
Grain35	16	77	2.47E-05	6.47E+05	1.60	0.17	22.80	1.80	54.5	13.8
Grain36	29	127	2.94E-05	9.86E+05	1.65	0.20	31.80	2.50	59.6	11.3
Grain37	29	146	2.43E-05	1.20E+06	1.42	0.18	44.40	3.30	51.8	9.8
Grain39	13	42	2.72E-05	4.78E+05	1.61	0.04	11.29	0.98	81.2	22.8
Grain40	13	72	2.60E-05	5.00E+05	1.60	0.09	20.40	1.70	47.1	13.2
Grain41	92	372	3.00E-05	3.06E+06	1.54	0.13	91.00	12.00	64.7	8.0

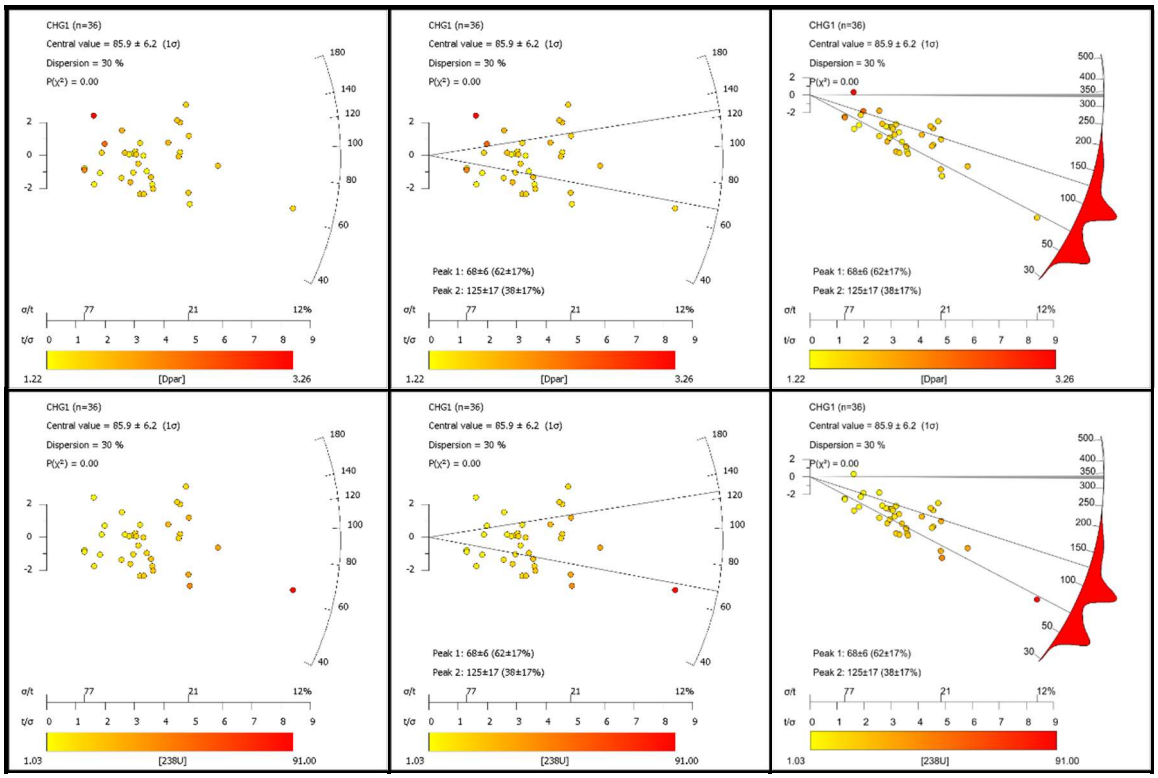

10.5.1.11 Cousland 6

Sample details

Grid reference	NT3838367983	Pooled age	
Elevation (m)	-460	Central age	147 ±18 Ma
Lithology	Sandstone	P(chi squared)	0.0
Age	Visean	Age dispersion	36 %
Depositional constraint	338 ±10 Ma	Length Data	94
N_S	500	Measured (SD)	11.22 (1.96) µm
P_S	1.49 x10^6	Projected (SD)	13.16 (1.35) µm

Apatite fission track data

Grain I.D.	Ns	Ni	Area (um^2)	Track density	Average Dpar (µm)	se (µm)	^{238}U (ppm)	se (ppm)	AFT Age (Ma)	se (Ma)
Grain05	24	106	2.62E-05	9.16E+05	1.22	0.06	29.90	2.20	58.9	12.8
Grain08	56	109	3.38E-05	1.66E+06	1.81	0.17	23.70	1.70	133.6	20.3
Grain13	29	69	4.21E-05	6.90E+05	1.85	0.04	12.03	0.83	109.8	21.7
Grain15	20	43	2.19E-05	9.14E+05	1.47	0.12	14.50	1.20	120.6	28.8
Grain16	22	47	2.61E-05	8.45E+05	1.38	0.20	13.22	0.94	122.2	27.5
Grain19	104	152	2.52E-05	4.12E+06	2.01	0.16	44.40	2.60	176.9	20.2
Grain26	60	158	2.86E-05	2.10E+06	1.76	0.11	40.70	2.50	98.8	14.1
Grain27	34	27	2.97E-05	1.15E+06	2.05	0.25	6.61	0.63	326.6	64.1
Grain29	10	10	2.85E-05	3.50E+05	1.97	0.04	2.60	0.32	255.1	86.6
Grain30	60	64	2.29E-05	2.62E+06	1.93	0.15	20.40	1.20	243.1	34.5
Grain32	58	86	2.72E-05	2.14E+06	1.83	0.25	23.40	1.40	173.9	25.1
Grain34	23	43	2.36E-05	9.74E+05	1.65	0.06	13.33	0.95	139.6	30.8

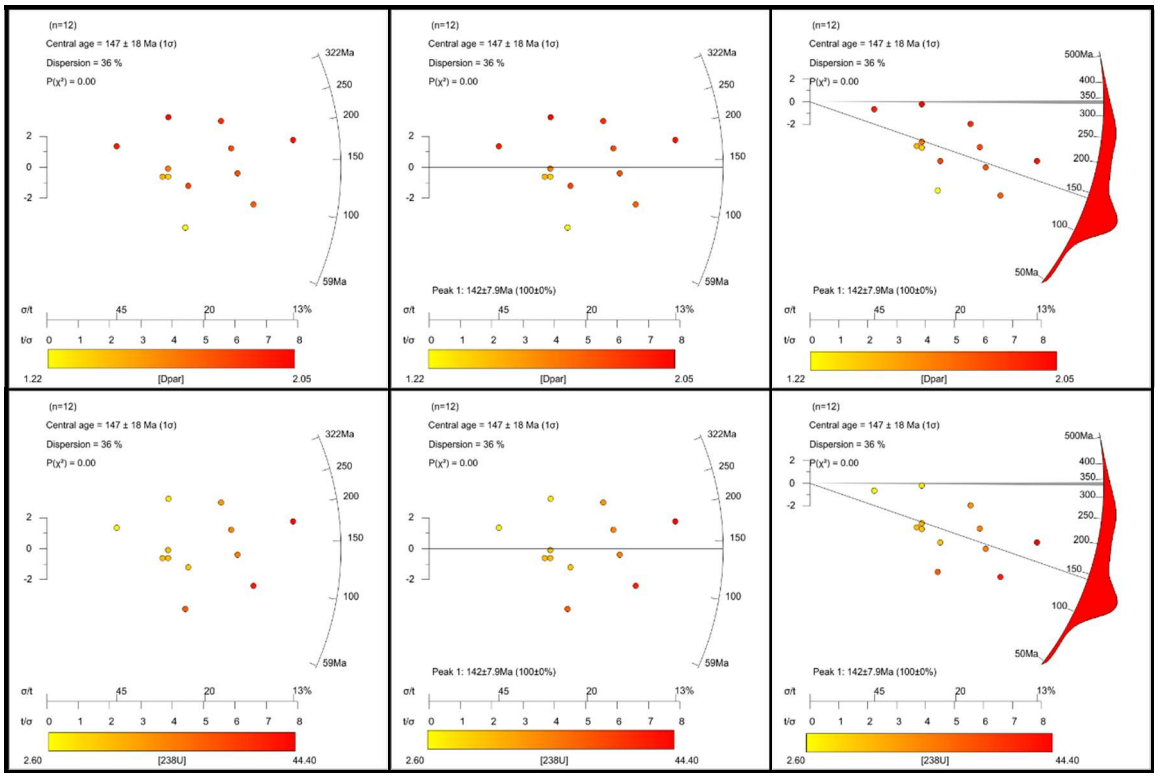

10.5.1.12 Dunmore Moss

Sample details

Grid reference	NS8738588833	Pooled age	
Elevation (m)	-340	Central age	149.9 ±10.1 Ma
Lithology	Sandstone	P(chi squared)	0.0
Age	Namurian	Age dispersion	39 %
Depositional constraint	324 ±6 Ma	Length Data	120
N_S	3367	Measured (SD)	11.62 (2.13) µm
P_S	3.33 x10^6	Projected (SD)	13.57 (1.31) µm

Apatite fission track data

Grain I.D.	Ns	Ni	Area (um^2)	Track density	Average Dpar (µm)	se (µm)	^{238}U (ppm)	se (ppm)	AFT Age (Ma)	se (Ma)
Grain01	90	116	2.25E-05	4.00E+06	1.77	0.16	37.90	2.40	200.7	22.1
Grain01b	57	83	2.56E-05	2.23E+06	1.77	0.16	23.80	1.60	178.1	24.3
Grain02	54	104	2.58E-05	2.09E+06	1.54	0.20	29.80	2.20	134.3	18.9
Grain02b	31	66	1.94E-05	1.60E+06	1.54	0.20	24.90	1.80	122.7	22.5
Grain03	67	49	1.71E-05	3.92E+06	1.72	0.12	21.00	1.40	351.2	44.5
Grain04	117	128	3.82E-05	3.06E+06	1.72	0.12	24.70	1.20	235.1	22.5
Grain04b	53	59	2.75E-05	1.93E+06	1.72	0.12	15.70	1.10	233.2	33.1
Grain05	48	64	2.13E-05	2.26E+06	1.56	0.09	22.20	1.20	193.5	28.4
Grain06	117	207	1.16E-05	1.01E+07	1.85	0.06	131.00	6.70	146.5	14.1
Grain07	63	173	1.36E-05	4.64E+06	1.72	0.22	93.70	6.10	95.0	12.4
Grain08	12	12	1.11E-05	1.08E+06	1.40	0.12	8.03	0.67	255.5	74.5
Grain09	64	129	1.43E-05	4.47E+06	1.84	0.31	66.40	3.70	128.6	16.5
Grain10	107	197	2.21E-05	4.84E+06	1.67	0.18	65.50	3.30	141.1	14.1
Grain11	11	24	1.76E-05	6.26E+05	1.31	0.05	9.88	0.81	121.2	36.9
Grain12	14	48	2.82E-05	4.97E+05	1.32	0.27	12.65	0.79	75.4	20.3
Grain13	81	112	2.26E-05	3.59E+06	1.87	0.20	36.50	2.10	187.1	21.5
Grain14	39	44	2.76E-05	1.42E+06	1.72	0.16	11.77	0.82	228.1	37.4
Grain15	143	308	2.63E-05	5.45E+06	1.80	0.12	86.30	5.10	120.7	10.7
Grain16	81	223	2.87E-05	2.82E+06	1.52	0.08	57.00	3.30	94.8	10.9
Grain17	182	775	2.49E-05	7.32E+06	1.88	0.08	229.00	11.00	61.4	4.8
Grain18	18	21	2.76E-05	6.51E+05	1.51	0.10	5.58	0.60	221.5	53.6
Grain19	154	190	2.78E-05	5.54E+06	1.87	0.12	50.40	2.30	208.9	17.5
Grain20	114	117	2.01E-05	5.69E+06	1.92	0.21	42.90	3.10	251.0	25.2
Grain21	89	221	1.66E-05	5.37E+06	1.71	0.19	98.20	5.40	104.7	11.5
Grain22	32	114	2.14E-05	1.49E+06	1.70	0.06	39.30	2.00	73.0	13
Grain23	197	398	2.72E-05	7.24E+06	1.91	0.21	107.60	6.50	128.7	10
Grain24	24	46	4.56E-05	5.26E+05	1.69	0.19	7.42	0.52	135.6	28.1
Grain24b	53	149	3.64E-05	1.46E+06	1.69	0.19	30.10	2.10	92.8	13.2
Grain25	67	87	2.19E-05	3.06E+06	1.72	0.20	29.20	2.00	199.0	25.3
Grain26	84	139	1.97E-05	4.26E+06	1.80	0.17	52.00	2.90	156.4	17.6
Grain27	46	192	2.49E-05	1.85E+06	1.59	0.09	56.80	2.80	62.5	9.4
Grain28	150	230	2.03E-05	7.40E+06	2.18	0.28	83.60	4.60	168.8	14.5
Grain29	167	205	4.73E-05	3.53E+06	1.88	0.07	31.90	1.90	210.5	17.5
Grain30	29	41	2.61E-05	1.11E+06	1.28	0.13	11.49	0.73	183.9	34.6
Grain31	182	358	2.69E-05	6.77E+06	1.80	0.20	97.80	5.30	132.3	10.4
Grain32	31	35	3.26E-05	9.52E+05	1.46	0.27	7.88	0.70	229.2	42.4
Grain33	124	130	3.82E-05	3.25E+06	1.60	0.16	25.10	1.50	245.3	23.2
Grain33b	88	149	3.73E-05	2.36E+06	1.60	0.16	29.40	1.80	153.3	17
Grain34	166	628	2.21E-05	7.51E+06	1.66	0.23	208.80	9.20	69.1	5.6
Grain35	121	164	2.46E-05	4.92E+06	1.93	0.22	49.10	2.80	190.6	18.2

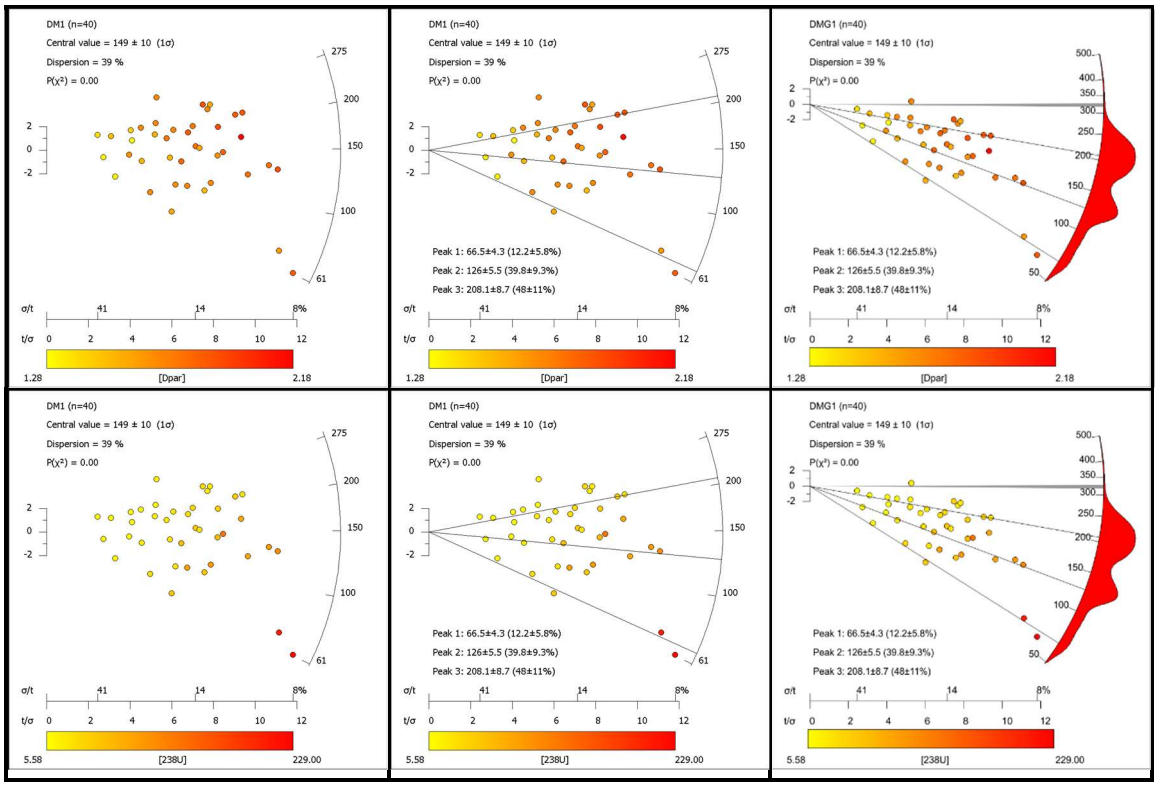

10.5.1.13 Kincardine East

Sample details

Grid reference	NS9392386328	Pooled age	
Elevation (m)	-280	Central age	186.12 ± 9.26 Ma
Lithology	Sandstone	P(chi squared)	0.0
Age	Namurian	Age dispersion	27 %
Depositional constraint	324 ±6 Ma	Length Data	120
N_S	3441	Measured (SD)	11.08 (2.16) µm
P_S	1.96 x10^6	Projected (SD)	13.20 (1.45) µm

Apatite fission track data

Grain I.D.	Ns	Ni	Area (um^2)	Track density	Average Dpar (µm)	se (µm)	^{238}U (ppm)	se (ppm)	AFT Age (Ma)	se (Ma)
Grain01	42	78	4.18E-05	1.01E+06	1.63	0.10	13.73	0.84	140.0	22.0
Grain02	80	111	1.11E-05	7.21E+06	1.76	0.14	73.50	3.90	186.6	21.4
Grain03	116	150	5.01E-05	2.32E+06	1.65	0.04	22.10	1.70	199.4	20.0
Grain03b	113	165	5.10E-05	2.22E+06	1.65	0.04	23.80	1.40	177.4	17.5
Grain04	51	84	5.81E-05	8.78E+05	1.63	0.25	10.62	0.70	157.7	22.7
Grain04b	51	165	5.74E-05	8.89E+05	1.63	0.25	21.10	1.30	80.8	11.6
Grain05	225	342	6.37E-05	3.53E+06	1.76	0.17	39.50	2.60	170.3	12.7
Grain05b	178	246	5.76E-05	3.09E+06	1.76	0.17	31.40	2.30	187.3	15.6
Grain06	59	53	7.30E-05	8.08E+05	1.85	0.06	5.31	0.49	287.4	39.7
Grain07	189	248	2.47E-05	7.67E+06	1.81	0.09	73.90	6.60	197.2	16.8
Grain08	39	46	4.00E-05	9.75E+05	1.80	0.12	8.51	0.71	217.6	36.0
Grain09	64	79	5.68E-05	1.13E+06	2.29	0.09	10.20	0.73	210.0	27.3
Grain09b	60	85	7.13E-05	8.41E+05	2.29	0.09	8.81	0.69	181.8	24.5
Grain10	23	19	3.42E-05	6.72E+05	2.57	0.09	4.15	0.34	305.5	64.9
Grain11	46	57	3.95E-05	1.16E+06	1.43	0.11	10.52	0.64	210.1	31.6
Grain12	69	96	3.51E-05	1.97E+06	1.58	0.17	20.10	1.20	186.4	23.1
Grain13	77	128	6.89E-05	1.12E+06	1.58	0.14	13.67	0.93	156.0	18.6
Grain13b	58	81	4.93E-05	1.18E+06	1.58	0.14	12.03	0.69	186.1	25.0
Grain14	34	34	4.24E-05	8.03E+05	1.32	0.15	5.97	0.45	254.5	44.7
Grain15	61	77	3.72E-05	1.64E+06	1.73	0.09	15.20	1.10	205.1	27.3
Grain16	90	304	4.21E-05	2.14E+06	1.58	0.15	53.20	3.70	77.2	8.6
Grain16b	75	153	4.01E-05	1.87E+06	1.58	0.15	28.00	1.60	127.7	15.2
Grain17	205	265	2.88E-05	7.11E+06	2.09	0.21	67.70	4.10	199.7	15.2
Grain18	50	117	2.25E-05	2.22E+06	1.66	0.12	38.30	2.40	111.0	16.1
Grain18b	42	85	1.98E-05	2.13E+06	1.66	0.12	31.80	1.80	127.8	20.1
Grain19	105	92	4.09E-05	2.57E+06	1.88	0.14	16.60	1.10	292.0	30.1
Grain20	52	113	3.99E-05	1.30E+06	1.34	0.18	20.80	1.20	119.8	17.0
Grain21	60	62	4.94E-05	1.22E+06	1.31	0.06	9.20	0.65	250.1	33.5
Grain21b	45	53	4.12E-05	1.09E+06	1.31	0.06	9.47	0.61	218.9	33.4
Grain22	137	194	4.33E-05	3.17E+06	1.86	0.21	33.00	2.10	182.6	16.7
Grain23	152	211	3.88E-05	3.92E+06	1.47	0.13	39.90	2.40	186.8	16.2
Grain23b	128	140	4.59E-05	2.79E+06	1.47	0.13	22.50	1.40	235.2	22.0
Grain24	8	11	2.65E-05	3.02E+05	1.28	0.04	3.01	0.31	190.8	68.2
Grain25	31	30	2.64E-05	1.18E+06	1.42	0.11	8.46	0.56	262.7	48.0
Grain26	142	111	4.99E-05	2.85E+06	1.69	0.13	16.40	1.00	326.8	29.2
Grain26b	161	171	5.40E-05	2.98E+06	1.69	0.13	23.30	1.40	242.7	20.5
Grain27	39	78	3.91E-05	9.98E+05	1.43	0.09	14.60	1.00	130.6	21.4
Grain28	76	102	3.13E-05	2.43E+06	2.56	0.25	23.90	1.40	193.3	22.9
Grain29	109	137	6.34E-05	1.72E+06	1.82	0.17	15.90	1.10	205.5	20.9
Grain29b	99	116	5.32E-05	1.86E+06	1.82	0.17	16.10	1.00	219.4	23.1

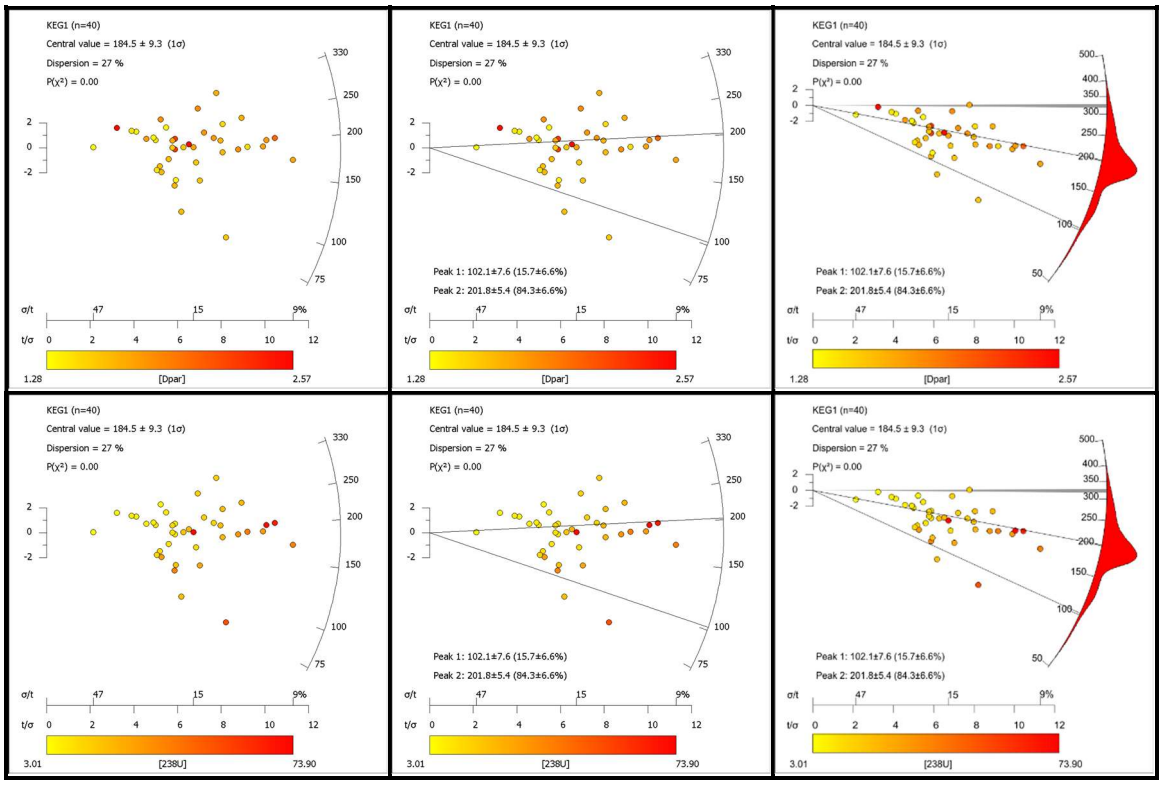

10.5.1.14 Gartlove 2

Sample details

Grid reference	NS9407792560	Pooled age	
Elevation (m)	-568	Central age	206.3 ± 12.7 Ma
Lithology	Sandstone	P(chi squared)	0.0
Age	Namurian	Age dispersion	33 %
Depositional constraint	324 ±6 Ma	Length Data	120
N_S	3306	Measured (SD)	10.80 (2.13) µm
P_S	3.43 x10^6	Projected (SD)	13.08 (1.34) µm

Apatite fission track data

Grain I.D.	Ns	Ni	Area (um^2)	Track density	Average Dpar (µm)	se (µm)	^{238}U (ppm)	se (ppm)	AFT Age (Ma)	se (Ma)
Grain01	90	89	4.40E-05	2.05E+06	1.65	0.11	14.90	1.10	260.1	29.1
Grain02	157	166	4.95E-05	3.17E+06	1.72	0.15	24.60	1.50	244.2	20.9
Grain02b	113	133	4.14E-05	2.73E+06	1.72	0.15	23.70	1.40	218.7	21.6
Grain03	36	88	1.23E-05	2.92E+06	1.62	0.22	52.60	2.80	106.3	17.9
Grain04	33	36	2.00E-05	1.65E+06	1.42	0.11	13.36	0.84	234.5	41.5
Grain05	66	84	1.39E-05	4.74E+06	1.67	0.04	44.30	2.20	203.3	25.5
Grain06	74	63	3.62E-05	2.05E+06	1.77	0.11	12.83	0.98	301.0	36.8
Grain08	19	26	2.00E-05	9.49E+05	1.42	0.08	9.45	0.65	191.1	44.3
Grain09	86	132	2.82E-05	3.05E+06	1.58	0.10	34.40	2.30	168.8	19.1
Grain10	12	19	1.35E-05	8.89E+05	1.40	0.00	10.44	0.74	162.4	47.2
Grain11	184	257	3.37E-05	5.45E+06	1.76	0.08	56.00	2.80	185.4	14.4
Grain11b	157	262	2.51E-05	6.26E+06	1.76	0.08	76.80	4.50	155.4	13.2
Grain12	21	28	2.21E-05	9.50E+05	1.39	0.18	9.37	0.77	192.9	42.8
Grain13	47	32	1.91E-05	2.47E+06	1.75	0.10	12.33	0.69	374.9	55.7
Grain14	37	29	1.75E-05	2.12E+06	1.43	0.09	12.36	0.96	322.5	54.5
Grain15	74	106	2.19E-05	3.37E+06	1.75	0.12	35.50	2.40	180.9	21.9
Grain16	102	104	2.76E-05	3.69E+06	1.70	0.16	27.80	1.50	251.6	25.8
Grain16b	73	74	2.23E-05	3.28E+06	1.70	0.16	24.40	1.20	254.2	30.4
Grain17	257	400	2.91E-05	8.82E+06	1.77	0.04	100.90	4.00	166.7	10.9
Grain19	66	54	1.83E-05	3.60E+06	2.23	0.18	21.70	1.50	312.5	40.0
Grain20	96	249	3.34E-05	2.88E+06	1.45	0.10	54.80	2.50	100.6	10.5
Grain21	143	150	1.74E-05	8.23E+06	1.77	0.12	63.60	3.40	245.0	21.5
Grain22	30	30	2.57E-05	1.17E+06	1.34	0.09	8.62	0.67	256.0	47.8
Grain23	129	391	4.34E-05	2.98E+06	1.60	0.26	66.30	4.00	86.1	8.0
Grain23b	178	113	3.10E-05	5.74E+06	1.60	0.26	26.90	1.60	399.3	32.2
Grain24	174	117	2.87E-05	6.06E+06	1.56	0.21	30.00	1.50	378.5	30.2
Grain27	156	216	2.59E-05	6.02E+06	1.92	0.13	61.30	3.10	186.9	15.7
Grain28	122	200	1.55E-05	7.86E+06	1.91	0.20	94.90	4.30	158.0	14.8
Grain29	45	45	3.09E-05	1.46E+06	1.34	0.10	10.66	0.72	258.7	39.5
Grain30	93	213	2.95E-05	3.16E+06	1.73	0.22	53.10	2.80	113.8	12.2
Grain31	67	126	2.97E-05	2.25E+06	1.78	0.12	31.30	1.70	137.6	17.2
Grain32	33	35	2.50E-05	1.32E+06	1.47	0.13	10.26	0.74	244.2	43.4
Grain33	71	110	1.60E-05	4.44E+06	1.73	0.12	50.80	2.40	166.7	20.2
Grain34	67	74	1.40E-05	4.78E+06	1.68	0.27	39.00	2.00	232.5	29.0
Grain35	104	123	4.41E-05	2.36E+06	1.58	0.19	20.50	1.00	218.4	22.1
Grain35b	94	107	3.79E-05	2.48E+06	1.58	0.19	20.70	1.40	227.6	24.7

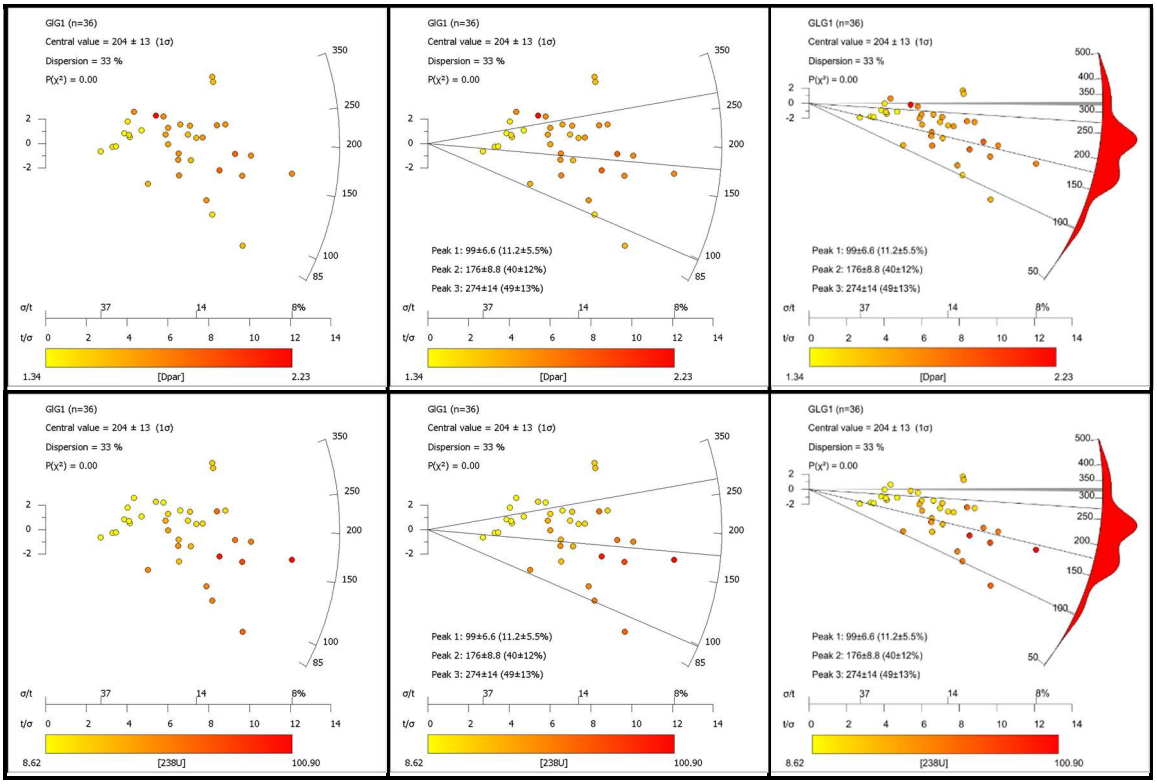

10.5.1.15 Geotrack borehole radial plots and TLDs

GC397-49	GC397-61	GC397-68
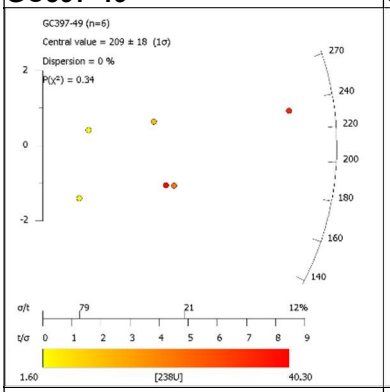	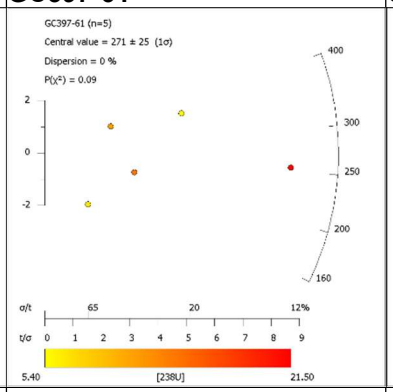	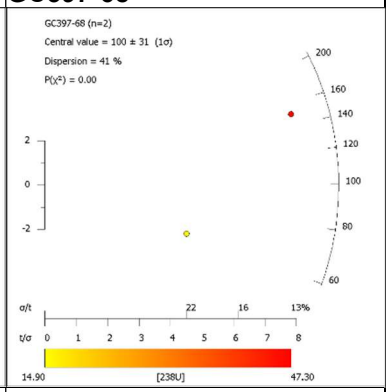
GC374-1	**GC397-1**	**GC374-2**
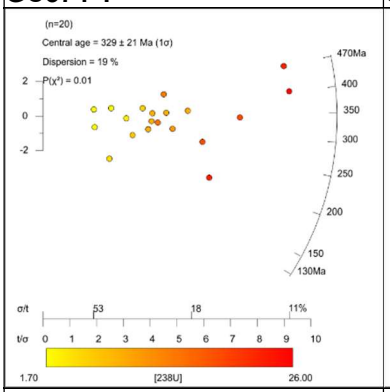	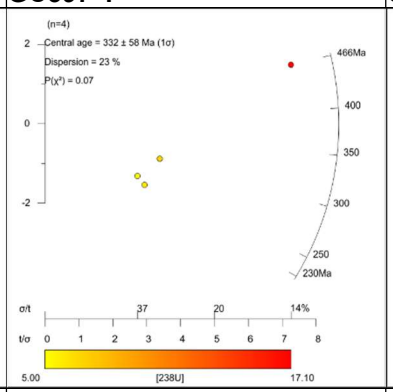	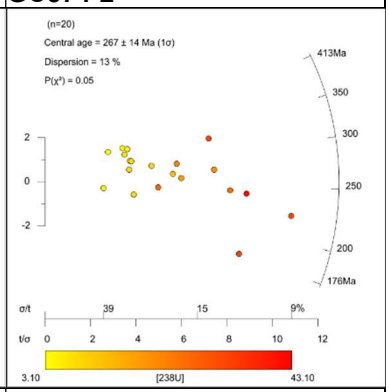
GC374-3	**GC397-3**	**GC374-4**
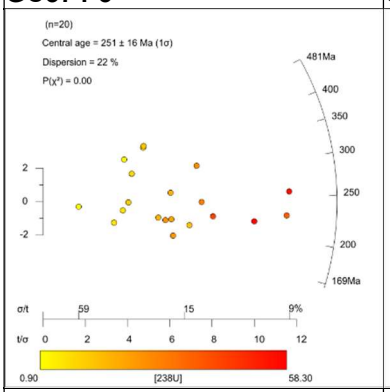	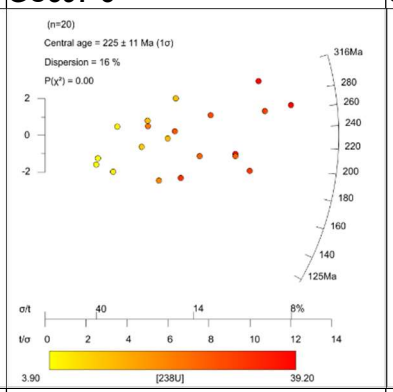	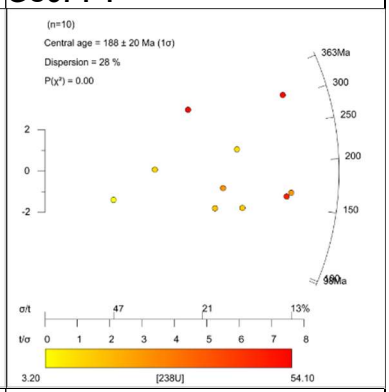
GC374-5	**GC397-5**	**GC397-7**
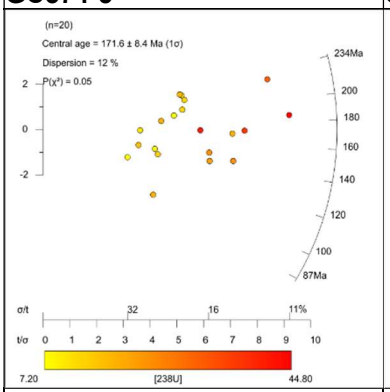	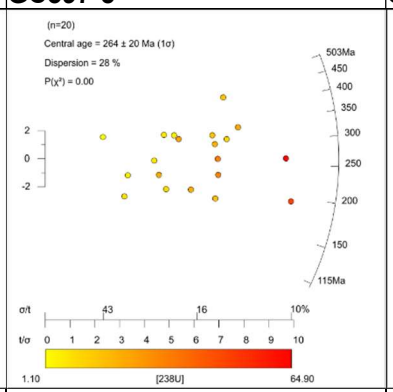	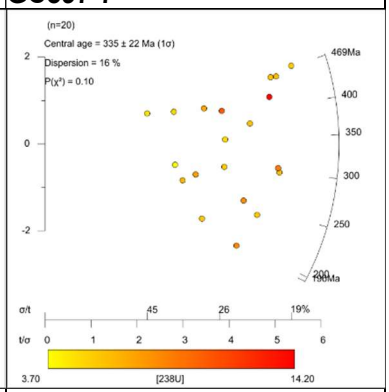
GC397-11	**GC397-13**	**GC397-14**

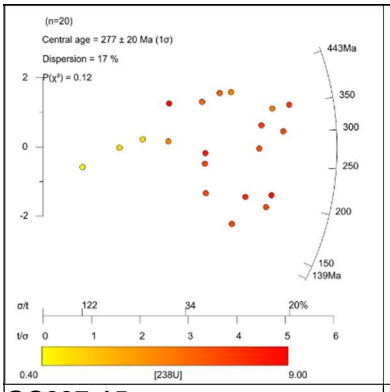

GC397-15

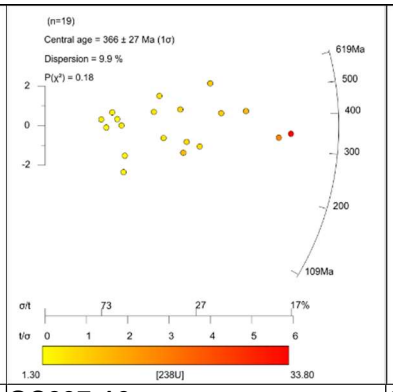

GC397-16

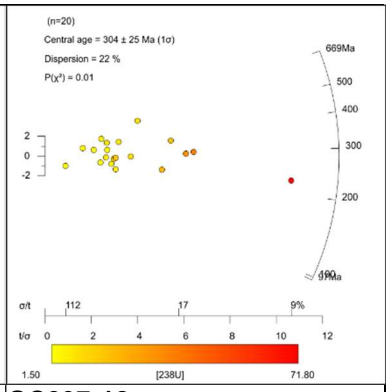

GC397-18

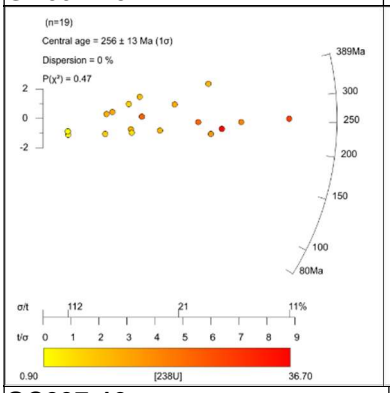

GC397-19

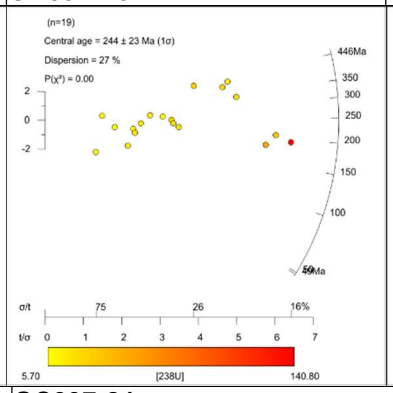

GC397-21

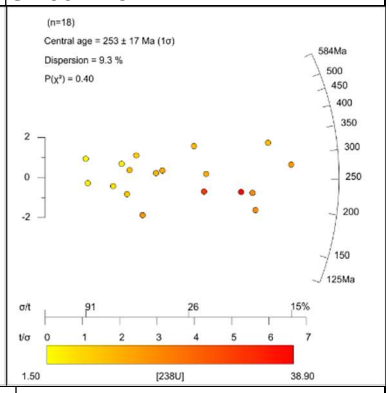

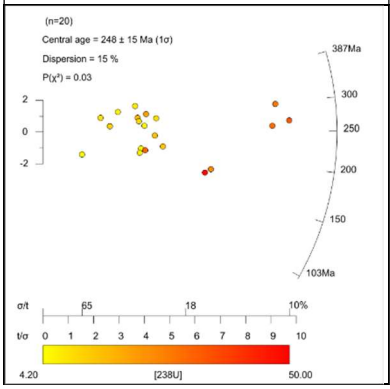

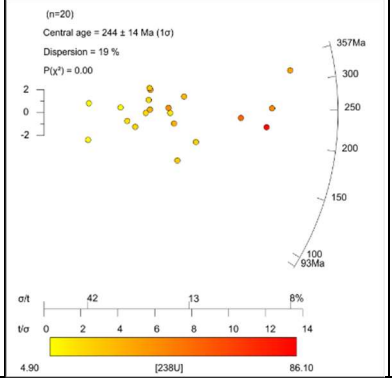

10.5.1.16 Geotrack samples- no projected lengths

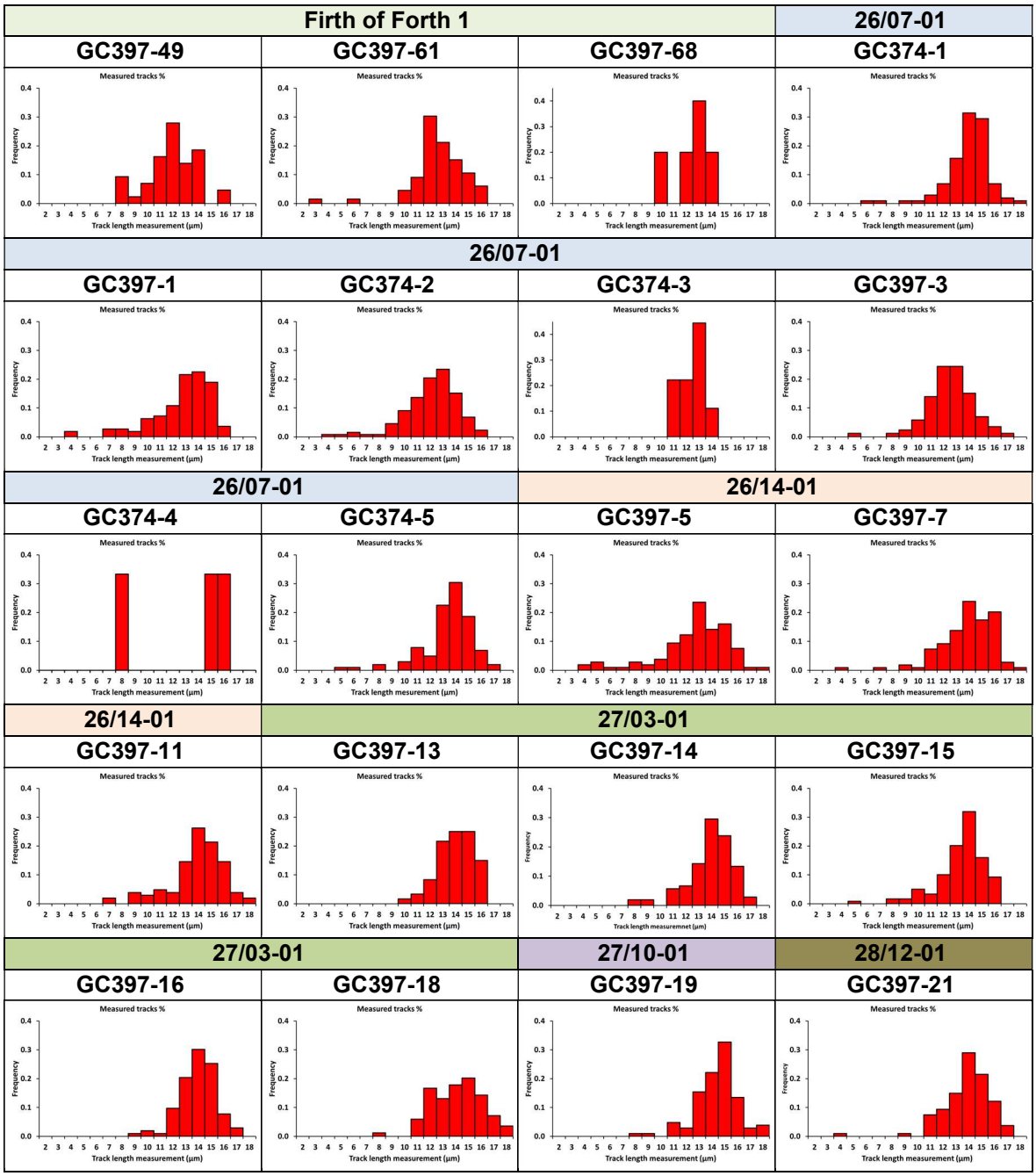

List of References

Al-Kindi, S., White, N., Sinha, M., England, R. and Tiley, R. (2003) 'Crustal trace of a hot convective sheet', *Geology*, 31(3), 207-210.

Allen, P.A. (2009) *Earth surface processes*, John Wiley & Sons.

Amin, A. (2020) *A study of the tectonic and geomorphic history of Scotland using a joint apatite fission track and (U-Th-Sm)/He analysis approach*, unpublished thesis, University of Glasgow.

Andersen, C. and Hinthorne, J. (1972) 'Ion microprobe mass analyzer', *Science*, 175(4024), 853-860.

Andersen, T. (2002) 'Correction of common lead in U–Pb analyses that do not report 204Pb', *Chemical Geology*, 192(1-2), 59-79.

Andersen, T., Kristoffersen, M. and Elburg, M.A. (2016) 'How far can we trust provenance and crustal evolution information from detrital zircons? A South African case study', *Gondwana Research*, 34, 129-148.

Andrews, J.E., Turner, M.S., Nabi, G. and Spiro, B. (1991) 'The anatomy of an early Dinantian terraced floodplain: palaeo-environment and early diagenesis', *Sedimentology*, 38(2), 271-287.

Ansberque, C., Chew, D.M. and Drost, K. (2021) 'Apatite fission-track dating by LA-Q-ICP-MS imaging', *Chemical Geology*, 560, 119977.

ARMSTRONG, H.A. and OWEN, A.W. (2001) 'Terrane evolution of the paratectonic Caledonides of northern Britain', *Journal of the Geological Society*, 158(3), 475-486.

Arrowsmith, S.J., Kendall, M., White, N., VanDecar, J.C. and Booth, D.C. (2005) 'Seismic imaging of a hot upwelling beneath the British Isles', *Geology*, 33(5), 345-348.

Arthaud, F. and Matte, P. (1977) 'Late Paleozoic strike-slip faulting in southern Europe and northern Africa: Result of a right-lateral shear zone between the Appalachians and the Urals', *Geological Society of America Bulletin*, 88(9), 1305-1320.

Bamford, D. (1979) 'Seismic constraints on the deep geology of the Caledonides of northern Britain', *Geological Society, London, Special Publications*, 8(1), 93-96.

Barbarand, J., Carter, A., Wood, I. and Hurford, T. (2003) 'Compositional and structural control of fission-track annealing in apatite', *Chemical Geology*, 198(1-2), 107-137.

Beerling, D.J., Lake, J.A., Berner, R.A., Hickey, L.J., Taylor, D.W. and Royer, D.L. (2002) 'Carbon isotope evidence implying high O2/CO2 ratios in the Permo-Carboniferous atmosphere', *Geochimica et Cosmochimica Acta*, **66**(21), pp.3757-3767.

Bell, B., Williamson, I. and Trewin, N. (2002) 'Tertiary igneous activity', *The Geology of Scotland*, 4, 371-407.

Bertagnolli, E., Keil, R. and Pahl, M. (1983) 'Thermal history and length distribution of fission tracks in apatite: Part I', *Nuclear Tracks and Radiation Measurements (1982)*, 7(4), 163-177.

BGS-Geoindex (2020) *GeoIndex (onshore)*, available: https://www.bgs.ac.uk/map-viewers/geoindex-onshore/ [accessed 28/03].

Bluck, B. (1983) 'Role of the Midland Valley of Scotland in the Caledonian orogeny', *Transactions of the Royal Society of Edinburgh: Earth Sciences*, **74**(03), pp.119-136.

Bluck, B. (1984) 'Pre-carboniferous history of the Midland Valley of Scotland', *Earth and Environmental Science Transactions of The Royal Society of Edinburgh*, 75(2), 275-295.

Bluck, B. (1987) 'British regional geology: The midland valley of Scotland (3rd edition)British Geological Survey', *Geological Journal*, **22**(1), pp.64-64.

Bluck, B. (2013) 'Geotectonic evolution of Midland Scotland from Cambrian to Silurian: a review', *SCOTTISH JOURNAL OF GEOLOGY*, **49**(2), pp.105-116.

Bluck, B., Ingham, J., Curry, G. and Williams, A. (1984) 'Stratigraphy and tectonic setting of the Highland Border Complex', *Trans. R. Soc. Edinb. Earth Sci*, 75, 124-33.

Bluck, B., Ingham, J., Lawson, J. and Weedon, D. (1992) 'Geological excursions around Glasgow and Girvan'.

Bluck, B.J. (2000) 'Old Red Sandstone basins and alluvial systems of Midland Scotland', *Geological Society, London, Special Publications*, **180**(1), pp.417-437.

Bonfiglioli, G., Ferro, A. and Mojoni, A. (1961) 'Electron microscope investigation on the nature of tracks of fission products in mica', *Journal of Applied Physics*, 32(12), 2499-2503.

Boulton, G., Peacock, J. and Sutherland, D. (1991) 'Quaternary', *Geology of Scotland*, 3, 503-543.

Brand, P., Armstrong, M. and Wilson, R.B. (1980) 'The Carboniferous strata at the Westfield Opencast Site, Fife, Scotland'.

Braun, J., Van Der Beek, P. and Batt, G. (2006) *Quantitative thermochronology: numerical methods for the interpretation of thermochronological data*, Cambridge University Press.

Browne, M. (1980) *The Upper Devonian and Lower Carboniferous (Dinantian) of the Firth of Tay, Scotland*, HMSO.

Browne, M., Hargreaves, R. and Smith, I. (1985) *Investigation of the Geothermal Potential of the UK: The Upper Palaeozoic Basins of the Midland Valley of Scotland*, British Geological Survey Geothermal Resources Programme.

Browne, M.A., Robins, N., Evans, R., Monro, S. and Robson, P. (1987) 'Upper Devonian and Carboniferous sandstones of the Midland Valley of Scotland. Investigation of the geothermal potential of the UK'.

Browne, M.A.E., Dean, M.T., Hall, I.H.S., McAdam, A.D., Monro, S.K. and Chisholm, J.I. (1999) 'A lithostratigraphical framework for the Carboniferous rocks of the Midland Valley of Scotland. Version 2', *British Geological Survey Research Report*, **RR/99/07**.

Bue, E.P. and Andresen, A. (2014) 'Constraining depositional models in the Barents Sea region using detrital zircon U–Pb data from Mesozoic sediments in Svalbard', *Geological Society, London, Special Publications*, 386(1), 261-279.

Caldwell, W. and Young, G. (2013) 'Structural controls in the western offshore Midland Valley of Scotland: implications for Late Palaeozoic regional tectonics', *Geological Magazine*, 150(4), 673-698.

Cameron, I.B. and Stephenson, D. (1985) *British Regional Geology: The Midland Valley of Scotland, thrid ed.*, 3rd ed., London for the British Geological survey, London: H.M.S.O.

Carlson, W.D., Donelick, R.A. and Ketcham, R.A. (1999) 'Variability of apatite fission-track annealing kinetics; I, Experimental results', *American Mineralogist*, **84**(9), pp. 1213-1223.

Cartwright, J., Stewart, S. and Clark, J. (2001) 'Salt dissolution and salt-related deformation of the Forth Approaches Basin, UK North Sea', *Marine and Petroleum Geology*, **18**(6), pp.757-778.

Cavosie, A.J., Valley, J.W. and Wilde, S.A. (2007) 'The Oldest Terrestrial Mineral Record: A Review of 4400 to 4000 Ma Detrital Zircons from Jack Hills, Western Australia', *Developments in Precambrian Geology*, 15, 91-111.

Cawood, P.A., Nemchin, A.A., Smith, M. and Loewy, S. (2003) 'Source of the Dalradian Supergroup constrained by U–Pb dating of detrital zircon and implications for the East Laurentian margin', *Journal of the Geological Society*, 160(2), 231-246.

Cawood, P.A., Nemchin, A.A., Strachan, R., Prave, T. and Krabbendam, M. (2007) 'Sedimentary basin and detrital zircon record along East Laurentia and Baltica during assembly and breakup of Rodinia', *Journal of the Geological Society*, 164(2), 257-275.

Chadderton, L. and Montagu-Pollock, H. (1963) 'Fission fragment damage to crystal lattices: heat-sensitive crystals', *Proceedings of the Royal Society of London. Series A. Mathematical and Physical Sciences*, 274(1357), 239-252.

Chadderton, L.T. (2003) 'Nuclear tracks in solids: registration physics and the compound spike', *Radiation Measurements*, 36(1), 13-34.

Chakoumakos, B.C., Murakami, T., Lumpkin, G.R. and Ewing, R.C. (1987) 'Alpha-decay—Induced fracturing in zircon: The transition from the crystalline to the metamict state', *Science*, 236(4808), 1556-1559.

Cherniak, D. and Watson, E. (2001) 'Pb diffusion in zircon', *Chemical Geology*, 172(1-2), 5-24.

Chew, D.M. and Donelick, R.A. (2012) 'Combined apatite fission track and U-Pb dating by LA-ICP-MS and its application in apatite provenance analysis', *Quantitative mineralogy and microanalysis of sediments and sedimentary rocks: Mineralogical Association of Canada Short Course*, **42**, pp. 219-247.

Chew, D.M., Donelick, R.A., Donelick, M.B., Kamber, B.S. and Stock, M.J. (2014) 'Apatite chlorine concentration measurements by LA-ICP-MS', *Geostandards and Geoanalytical Research*, 38(1), 23-35.

Chew, D.M. and Spikings, R.A. (2015) 'Geochronology and thermochronology using apatite: time and temperature, lower crust to surface', *Elements*, **11**(3), pp. 189-194.

Chew, D.M. and Strachan, R.A. (2014) 'The Laurentian Caledonides of Scotland and Ireland', *Geological Society, London, Special Publications*, 390(1), 45-91.

Chisholm, J. and Dean, J. (1974) 'The Upper Old Red Sandstone of Fife and Kinross: a fluviatile sequence with evidence of marine incursion', *SCOTTISH JOURNAL OF GEOLOGY*, 10(1), 1-30.

Clarkson, E.N.K., Harper, D.A.T. and Höey, A.N. (1998) 'Basal Wenlock biofacies from the Girvan district, SW Scotland', *SCOTTISH JOURNAL OF GEOLOGY*, 34(1), 61-71.

Clayburn, J., Harmon, R., Pankhurst, R. and Brown, J. (1983) 'Sr, O, and Pb isotope evidence for origin and evolution of Etive igneous complex, Scotland', *Nature*, 303(5917), 492-497.

Clemmensen, L.B. and Abrahamsen, K. (1983) 'Aeolian stratification and facies association in desert sediments, Arran basin (Permian), Scotland', *Sedimentology*, 30(3), 311-339.

Cliff, R., Drewery, S. and Leeder, M. (1991) 'Sourcelands for the Carboniferous Pennine river system: constraints from sedimentary evidence and U-Pb geochronology using zircon and monazite', *Geological Society, London, Special Publications*, 57(1), 137-159.

Cochrane, R., Spikings, R.A., Chew, D., Wotzlaw, J.-F., Chiaradia, M., Tyrrell, S., Schaltegger, U. and Van der Lelij, R. (2014) 'High temperature (> 350 C) thermochronology and mechanisms of Pb loss in apatite', *Geochimica et Cosmochimica Acta*, 127, 39-56.

Cocks, L.R.M. and Toghill, P. (1973) 'The biostratigraphy of the Silurian rocks of the Girvan District, Scotland', *Journal of the Geological Society*, 129(3), 209-243.

Cogné, N., Chew, D. and Stuart, F.M. (2014) 'The thermal history of the western Irish onshore', *Journal of the Geological Society*, 171(6), 779-792.

Cogné, N., Chew, D.M., Donelick, R.A. and Ansberque, C. (2020) 'LA-ICP-MS apatite fission track dating: A practical zeta-based approach', *Chemical Geology*, 531, 119302.

Cogné, N., Doepke, D., Chew, D., Stuart, F.M. and Mark, C. (2016) 'Measuring plume-related exhumation of the British Isles in Early Cenozoic times', *Earth and Planetary Science Letters*, 456, 1-15.

Comerford, A., Fraser-Harris, A., Johnson, G. and McDermott, C. (2018) 'Controls on geothermal heat recovery from a hot sedimentary aquifer in Guardbridge, Scotland: Field measurements, modelling and long term sustainability', *Geothermics*, 76, 125-140.

Cope, J.C. (2006) 'Upper Cretaceous palaeogeography of the British Isles and adjacent areas', *Proceedings of the Geologists' Association*, 117(2), 129-143.

Cope, J.C.W., Ingham, J.K., Rawson, P.F. and London, G.S.o. (1992) *Atlas of Palaeogeography and Lithofacies*, Geological Society.

Corfield, S., Gawthorpe, R., Gage, M., Fraser, A. and Besly, B. (1996) 'Inversion tectonics of the Variscan foreland of the British Isles', *Journal of the Geological Society*, 153(1), 17-32.

Corfield, S.M., Gawthorpe, R.L., Gage, M., Fraser, A.J. and Besly, B.M. (1996) 'Inversion tectonics of the Variscan foreland of the British Isles', *Journal of the Geological Society*, 153(1), pp.17-32.

Corfu, F., Hanchar, J., Hoskin, P. and Kinny, P. (2003) 'Zircon: Reviews in Mineralogy and Geochemistry'.

Coward, M.P. (1993) 'The effect of Late Caledonian and Variscan continental escape tectonics on basement structure, Paleozoic basin kinematics and subsequent Mesozoic basin development in NW Europe', *Petroleum Geology of Northwest Europe. The Geological Society, London*, **4**, pp. 1095-1108.

Dempster, A. (1918) 'A new method of positive ray analysis', *Physical Review*, 11(4), 316.

Dempster, T. (1985) 'Uplift patterns and orogenic evolution in the Scottish Dalradian', *Journal of the Geological Society*, 142(1), 111-128.

Dempster, T., Hudson, N. and Rogers, G. (1995) 'Metamorphism and cooling of the NE Dalradian', *Journal of the Geological Society*, 152(2), 383-390.

Dempster, T., Rogers, G., Tanner, P., Bluck, B., Muir, R., Redwood, S., Ireland, T. and Paterson, B. (2002) 'Timing of deposition, orogenesis and glaciation within the Dalradian rocks of Scotland: constraints from U–Pb zircon ages', *Journal of the Geological Society*, 159(1), 83-94.

Dentith, M. and Hall, J. (1989) 'Mavis—an upper crustal seismic refraction experiment in the Midland Valley of Scotland', *Geophysical Journal International*, 99(3), 627-643.

Dewey, J.F. (1982) 'Plate tectonics and the evolution of the British Isles: Thirty-fifth William Smith Lecture', *Journal of the Geological Society*, **139**(4), pp. 371-412.

Dickin, A.P. (2018) *Radiogenic isotope geology*, Cambridge university press.

Dickinson, W.R. (2008) 'Impact of differential zircon fertility of granitoid basement rocks in North America on age populations of detrital zircons and implications for granite petrogenesis', *Earth and Planetary Science Letters*, 275(1-2), 80-92.

DiGRock250k (2013) *[SHAPE geospatial data]*, available: https://digimap.edina.ac.uk [accessed 03-14].

Dobson, K.J., Stuart, F.M. and Dempster, T.J. (2010) 'Constraining the post-emplacement evolution of the Hebridean Igneous Province (HIP) using low-temperature thermochronology: how long has the HIP been cool?', *Journal of the Geological Society*, 167(5), 973-984.

Dodson, M.H. (1973) 'Closure temperature in cooling geochronological and petrological systems', *Contributions to Mineralogy and Petrology*, 40(3), 259-274.

Donelick, R.A. (1991) 'Crystallographic orientation dependence of mean etchable fission track length in apatite; an empirical model and experimental observations', *American Mineralogist*, **76**(1-2), pp. 83-91.

Donelick, R.A. (2005) 'Apatite Fission-Track Analysis', *Reviews in Mineralogy and Geochemistry*, 58(1), 49-94.

Donelick, R.A., Ketcham, R.A. and Carlson, W.D. (1999) 'Variability of apatite fission-track annealing kinetics; II, Crystallographic orientation effects', *American Mineralogist*, **84**(9), pp. 1224-1234.

Donelick, R.A. and Miller, D.S. (1991) 'Enhanced TINT fission track densities in low spontaneous track density apatites using 252Cf-derived fission fragment tracks: A model and experimental observations', *International Journal of Radiation Applications and Instrumentation. Part D. Nuclear Tracks and Radiation Measurements*, 18(3), 301-307.

Döpke, D. (2017) *Modelling the Thermal History of Onshore Ireland, Britain and Its Offshore Basins Using Low-temperature Thermochronology*, unpublished thesis, Trinity College Dublin.

Duddy, I.R., Arne, D.C., O'Sullivan, P. and Green, P.F. (1992) *Forth approaches basin report #397*: Geotrack International Pty. Ltd.

Dumitru, T.A. (1993) 'A new computer-automated microscope stage system for fission-track analysis', *Nuclear Tracks and Radiation Measurements*, 21(4), 575-580.

Durrani, S. and Bull, R. (1987) *Solid state nuclear track detection (Principles , Methods and Applications)* Pergamon Press: New York p. 318.

Farley, K. (2000) 'Helium diffusion from apatite: General behavior as illustrated by Durango fluorapatite', *Journal of Geophysical Research: Solid Earth*, 105(B2), 2903-2914.

Faure, G. (1977) 'Principles of isotope geology'.

Fedo, C.M., Sircombe, K.N. and Rainbird, R.H. (2003) 'Detrital zircon analysis of the sedimentary record', *Reviews in Mineralogy and Geochemistry*, 53(1), 277-303.

Finch, R.J. and Hanchar, J.M. (2003) 'Structure and chemistry of zircon and zircon-group minerals', *Reviews in Mineralogy and Geochemistry*, 53(1), 1-25.

Fleischer, R., Price, P. and Walker, R. (1965a) 'Effects of temperature, pressure, and ionization of the formation and stability of fission tracks in minerals and glasses', *Journal of Geophysical Research*, 70(6), 1497-1502.

Fleischer, R., Price, P. and Walker, R. (1965b) 'Ion explosion spike mechanism for formation of charged-particle tracks in solids', *Journal of Applied Physics*, 36(11), 3645-3652.

Fleischer, R.L., Price, P.B. and Walker, R.M. (1975) *Nuclear Tracks in Solids:Principals and Applications. University of California Press, Berkeley. p. 605*.

Forsyth, I.H., Hall, I.H.S. and McMillan, A.A. (1996) *Geology of the Airdrie district: memoir for 1: 50 000 geological sheet 31W (Scotland)*, HMSO.

Fox, M., Dai, J.G. and Carter, A. (2019) 'Badly behaved detrital (U-Th)/He ages: Problems with He diffusion models or geological models?', *Geochemistry, Geophysics, Geosystems*, 20(5), 2418-2432.

Friend, C. and Kinny, P. (2001) 'A reappraisal of the Lewisian Gneiss Complex: geochronological evidence for its tectonic assembly from disparate terranes in the Proterozoic', *Contributions to Mineralogy and Petrology*, 142(2), 198-218.

Friend, C., Strachan, R., Kinny, P. and Watt, G. (2003) 'Provenance of the Moine Supergroup of NW Scotland: evidence from geochronology of detrital and inherited zircons from (meta) sedimentary rocks, granites and migmatites', *Journal of the Geological Society*, 160(2), 247-257.

Gain, S.E., Gréau, Y., Henry, H., Belousova, E., Dainis, I., Griffin, W.L. and O'reilly, S.Y. (2019) 'Mud Tank Zircon: Long-term evaluation of a reference material for U-Pb dating, Hf-isotope analysis and trace element analysis', *Geostandards and Geoanalytical Research*, 43(3), 339-354.

Galbraith, R.F. (1990) 'The radial plot: graphical assessment of spread in ages', *International Journal of Radiation Applications and Instrumentation. Part D. Nuclear Tracks and Radiation Measurements*, 17(3), 207-214.

Galbraith, R.F. (2005) *Statistics for fission track analysis*, Chapman and Hall/CRC.

Galbraith, R.F. and Laslett, G.M. (1993) 'Statistical models for mixed fission track ages', *Nuclear Tracks and Radiation Measurements*, 21(4), 459-470.

Gallagher, K. (2012) 'Transdimensional inverse thermal history modeling for quantitative thermochronology', *Journal of Geophysical Research: Solid Earth*, 117(B2).

Gallagher, K., Brown, R. and Johnson, C. (1998) 'FISSION TRACK ANALYSIS AND ITS APPLICATIONS TO GEOLOGICAL PROBLEMS', *Annual Review of Earth and Planetary Sciences*, 26(1), 519-572.

Gallagher, K., Charvin, K., Nielsen, S., Sambridge, M. and Stephenson, J. (2009) 'Markov chain Monte Carlo (MCMC) sampling methods to determine optimal models, model resolution and model choice for Earth Science problems', *Marine and Petroleum Geology*, 26(4), 525-535.

Gallagher, K. and Ketcham, R.A. (2018) 'Comment on “Thermal history modelling: HeFTy vs. QTQt” by Vermeesch and Tian, Earth-Science Reviews (2014), 139, 279–290', *Earth-Science Reviews*, 176, 387-394.

Gallagher, K. and Wildman, M. (2020) 'From sink to source: extracting onshore erosion signals preserved in offshore thermochronometric data', in *European Geosciences Union General Assembly*, EGU2020-6696.

Ganerød, M., Smethurst, M., Torsvik, T., Prestvik, T., Rousse, S., McKenna, C., Van Hinsbergen, D. and Hendriks, B. (2010) 'The North Atlantic Igneous Province reconstructed and its relation to the plume generation zone: the Antrim Lava Group revisited', *Geophysical Journal International*, 182(1), 183-202.

Gehrels, C.B. (2012) 'G.(2011) Detrital zircon U-Pb geochronology: current methods and new opportunities', *Tectonics of Sedimentary Basins: Recent Advances (Ed. by C. Busby, A. Azor)*, 47-62.

George, T.N. (1960) 'VI.—The Stratigraphical Evolution of the Midland Valley', *Transactions of the Geological Society of Glasgow*, 24(1), 32-107.

Gillespie, J., Glorie, S., Khudoley, A. and Collins, A. (2018) 'Detrital apatite U-Pb and trace element analysis as a provenance tool: Insights from the Yenisey Ridge (Siberia)', *Lithos*, 314, 140-155.

Gillespie, M., Crane, E. and Barron, H. (2013) 'Study into the Potential for Deep Geothermal Energy in Scotland. Volume 2 of 2. Scottish Government Project'.

Gleadow, A., Duddy, I., Green, P.F. and Lovering, J. (1986) 'Confined fission track lengths in apatite: a diagnostic tool for thermal history analysis', *Contributions to Mineralogy and Petrology*, 94(4), 405-415.

Gleadow, A., Duddy, I. and Lovering, J. (1983) 'Fission track analysis: a new tool for the evaluation of thermal histories and hydrocarbon potential', *The APPEA Journal*, **23**(1), pp. 93-102.

Gleadow, A., Harrison, M., Kohn, B., Lugo-Zazueta, R. and Phillips, D. (2015) 'The Fish Canyon Tuff: A new look at an old low-temperature thermochronology standard', *Earth and Planetary Science Letters*, 424, 95-108.

Gleadow, A., Kohn, B. and Seiler, C. (2019) 'The future of fission-track thermochronology' in *Fission-Track Thermochronology and its Application to Geology* Springer, 77-92.

Gleadow, A.J., Gleadow, S.J., Belton, D.X., Kohn, B.P., Krochmal, M.S. and Brown, R.W. (2009) 'Coincidence mapping-a key strategy for the automatic counting of fission tracks in natural minerals', *Geological Society, London, Special Publications*, 324(1), 25-36.

Gleadow, A.J.W. and Duddy, I.R. (1981) 'A natural long-term track annealing experiment for apatite', *Nuclear Tracks*, **5**(1), pp. 169-174.

Glennie, K. (1995) 'Permian and Triassic rifting in northwest Europe', *Geological Society, London, Special Publications*, 91(1), 1-5.

Glennie, K.W. and Underhill, J.R. (2009) 'Origin, Development and Evolution of Structural Styles' in *Petroleum Geology of the North Sea* Blackwell Science Ltd, 42-84.

Glorie, S., Alexandrov, I., Nixon, A., Jepson, G., Gillespie, J. and Jahn, B.-M. (2017) 'Thermal and exhumation history of Sakhalin Island (Russia) constrained by apatite U-Pb and fission track thermochronology', *Journal of Asian Earth Sciences*, 143, 326-342.

Gower, C.F. (1996) 'The evolution of the Grenville Province in eastern Labrador, Canada', *Geological Society, London, Special Publications*, 112(1), 197-218.

Graham, A.M. and Upton, B.G.J. (1978) 'Gneisses in diatremes, Scottish Midland Valley: petrology and tectonic implications', *Journal of the Geological Society*, 135(2), 219-228.

Green, P., Duddy, I., Laslett, G., Hegarty, K., Gleadow, A.W. and Lovering, J. (1989) 'Thermal annealing of fission tracks in apatite 4. Quantitative modelling techniques and extension to geological timescales', *Chemical Geology: Isotope Geoscience section*, 79(2), 155-182.

Green, P.F. (1986) 'On the thermo-tectonic evolution of Northern England: evidence from fission track analysis', *Geological Magazine*, **123**(5), pp. 493-506.

Green, P.F., Duddy, I.R. and Bray, R.J. (1995) 'Applications of thermal history reconstruction in inverted basins', *Geological Society, London, Special Publications*, 88(1), 149-165.

Green, P.F., Duddy, I.R., Gleadow, A.J.W., Tingate, P.R. and Laslett, G.M. (1985) 'Fission-track annealing in apatite: Track length measurements and the form of the Arrhenius plot', *Nuclear Tracks and Radiation Measurements*, **10**(3), pp. 323-328.

Green, P.F., Duddy, I.R., Gleadow, A.J.W., Tingate, P.R. and Laslett, G.M. (1986) 'Thermal annealing of fission tracks in apatite 1. A qualitative description', *Chemical Geology*, **59**(4), pp. 237-253.

Guirdham, C. (1998) *Regional stratigraphy, lithofacies, diagenesis and dolomitisation of microbial carbonates in the Lower Carbonifereous, West Lothian Oil-Shale Formation*, unpublished thesis, University of East Anglia.

Hall, A. (1991) 'Pre-Quaternary landscape evolution in the Scottish Highlands', *Transactions of the Royal Society of Edinburgh: Earth Sciences*, 82(1), 1-26.

Hallett, D., Durant, G. and Farrow, G. (1985) 'Oil exploration and production in Scotland', *SCOTTISH JOURNAL OF GEOLOGY*, 21(4), 547-570.

Hallsworth, C., Morton, A., Claoué-Long, J. and Fanning, C. (2000) 'Carboniferous sand provenance in the Pennine Basin, UK: constraints from heavy mineral and detrital zircon age data', *Sedimentary Geology*, 137(3-4), 147-185.

Hamilton, P., Bluck, B. and Halliday, A. (1984) 'Sm—Nd ages from the Ballantrae complex, SW Scotland', *Earth and Environmental Science Transactions of The Royal Society of Edinburgh*, 75(2), 183-187.

Hanchar, J.M. (2013) *Zircon*, Springer.

Hancock, J.M. (1989) 'Sea-level changes in the British region during the Late Cretaceous', *Proceedings of the Geologists' Association*, 100(4), 565-IN1.

Harker, S. (2002) 'Cretaceous', *The Geology of Scotland. 4th edn. Geological Society, London*, 351, 360.

Hasebe, N., Barbarand, J., Jarvis, K., Carter, A. and Hurford, A.J. (2004) 'Apatite fission-track chronometry using laser ablation ICP-MS', *Chemical Geology*, 207(3), 135-145.

Haszeldine, R. (1988) 'Crustal lineaments in the British Isles: their relationship to Carboniferous basins', *Sedimentation in a synorogenic basin complex—The Upper Carboniferous of northwest Europe: Glasgow, Blackie*, 53-68.

Haughton, P. and Bluck, B. (1988) 'Diverse alluvial sequences from the Lower Old Red Sandstone of the Strathmore region, Scotland—implications for the relationship between Late Caledonian tectonics and sedimentation'.

Haughton, P.D.W. (1988) 'A cryptic Caledonian flysch terrane in Scotland', *Journal of the Geological Society*, 145(4), 685-703.

Heinemann, N., Alcalde, J., Johnson, G., Roberts, J., McCay, A. and Booth, M. (2019) 'Low-carbon GeoEnergy resource options in the Midland Valley of Scotland, UK', *SCOTTISH JOURNAL OF GEOLOGY*, 55(2), 93-106.

Heinemann, N., Booth, M., Haszeldine, R.S., Wilkinson, M., Scafidi, J. and Edlmann, K. (2018) 'Hydrogen storage in porous geological formations–onshore play opportunities in the midland valley (Scotland, UK)', *International Journal of Hydrogen Energy*, 43(45), 20861-20874.

Hendriks, B. and Redfield, T. (2005) 'Apatite fission track and (U-Th)/He data from Fennoscandia: An example of underestimation of fission track annealing in apatite', *Earth and Planetary Science Letters*, 236(1-2), 443-458.

Henrichs, I.A., O'Sullivan, G., Chew, D.M., Mark, C., Babechuk, M.G., McKenna, C. and Emo, R. (2018) 'The trace element and U-Pb systematics of metamorphic apatite', *Chemical Geology*, 483, 218-238.

Hiess, J., Condon, D.J., McLean, N. and Noble, S.R. (2012) '238U/235U systematics in terrestrial uranium-bearing minerals', *Science*, 335(6076), 1610-1614.

Hillis, R.R., Holford, S.P., Green, P.F., Doré, A.G., Gatliff, R.W., Stoker, M.S., Thomson, K., Turner, J.P., Underhill, J.R. and Williams, G.A. (2008) 'Cenozoic exhumation of the southern British Isles', *Geology*, 36(5), 371-374.

Hillis, R.R., Thomson, K. and Underhill, J.R. (1994) 'Quantification of Tertiary erosion in the Inner Moray Firth using sonic velocity data from the Chalk and the Kimmeridge Clay', *Marine and Petroleum Geology*, 11(3), 283-293.

Holford, S., Turner, J. and Green, P. (2005) 'Reconstructing the Mesozoic–Cenozoic exhumation history of the Irish Sea basin system using apatite fission track analysis and vitrinite reflectance data', in *Geological Society, London, Petroleum Geology Conference series*, Geological Society of London, 1095-1107.

Holford, S.P., Green, P.F., Duddy, I.R., Turner, J.P., Hillis, R.R. and Stoker, M.S. (2009) 'Regional intraplate exhumation episodes related to plate-boundary deformation', *Geological Society of America Bulletin*, 121(11-12), 1611-1628.

Holford, S.P., Green, P.F., Hillis, R.R., Underhill, J.R., Stoker, M.S. and Duddy, I.R. (2010) 'Multiple post-Caledonian exhumation episodes across NW Scotland revealed by apatite fission-track analysis', *Journal of the Geological Society*, 167(4), 675-694.

Horstwood, M.S., Nesbitt, R.W., Noble, S.R. and Wilson, J.F. (1999) 'U-Pb zircon evidence for an extensive early Archean craton in Zimbabwe: A reassessment of the timing of craton formation, stabilization, and growth', *Geology*, 27(8), 707-710.

Hudson, J. and Trewin, N.H. (2002) 'Jurassic' in *The Geology of Scotland 4th Edition (ed. Trewin, NH)* The Geological Society, 323-350.

Hurford, A.J. (1977) 'A preliminary fission track dating survey of Caledonian “newer and last granites” from the Highlands of Scotland', *SCOTTISH JOURNAL OF GEOLOGY*, 13(4), 271-284.

Hurford, A.J. and Green, P.F. (1982) 'A users' guide to fission track dating calibration', *Earth and Planetary Science Letters*, **59**(2), pp. 343-354.

Hurford, A.J. and Green, P.F. (1983) 'The zeta age calibration of fission-track dating', *Chemical Geology*, 41, 285-317.

Hurst, A. and Morton, A. (2014) 'Provenance models: the role of sandstone mineral–chemical stratigraphy', *Geological Society, London, Special Publications*, 386(1), 7-26.

Hurter, S. and Schellschmidt, R. (2003) 'Atlas of geothermal resources in Europe', *Geothermics*, 32(4-6), 779-787.

Hutchison, A. and Oliver, G. (1998) 'Garnet provenance studies, juxtaposition of Laurentian marginal terranes and timing of the Grampian Orogeny in Scotland', *Journal of the Geological Society*, 155(3), 541-550.

Ince, D. (1984) 'Sedimentation and tectonism in the Middle Ordovician of the Girvan district, SW Scotland', *Transactions of the Royal Society of Edinburgh: Earth Sciences*, **75**(02), pp. 225-237.

Jaffey, A., Flynn, K., Glendenin, L., Bentley, W.t. and Essling, A. (1971) 'Precision measurement of half-lives and specific activities of U 235 and U 238', *Physical review C*, 4(5), 1889.

Japsen, P., Green, P.F., Nielsen, L.H., Rasmussen, E.S. and Bidstrup, T. (2007) 'Mesozoic–Cenozoic exhumation events in the eastern North Sea Basin: a multi-disciplinary study based on palaeothermal, palaeoburial, stratigraphic and seismic data', *Basin Research*, 19(4), 451-490.

Jarvie, D., Claxton, B., Henk, F. and Breyer, J. (2001) 'Oil and Shale Gas from the Barnett Shale, Ft. Worth Basin, Texas. Talk presented at the AAPG National Convention, June 3–6, 2001, Denver, CO', *American Association of Petroleum Geologists Bulletin A*, 100.

Jarvis, G.T. and Mckenzie, D.P. (1980) 'Sedimentary basin formation with finite extension rates', *Earth and Planetary Science Letters*, 48(1), 42-52.

Jennings, E.S., Marschall, H., Hawkesworth, C. and Storey, C. (2011) 'Characterization of magma from inclusions in zircon: Apatite and biotite work well, feldspar less so', *Geology*, 39(9), 863-866.

Jin, M., Pickup, G., Mackay, E., Todd, A., Sohrabi, M., Monaghan, A. and Naylor, M. (2012) 'Static and dynamic estimates of CO2-storage capacity in two saline formations in the UK', *SPE Journal*, 17(04), 1108-1118.

Jolivet, M. (2007) 'Denudation history of the Loch Ness corridor (Scotland): differential vertical movements along the Great Glen Fault', *Comptes Rendus Géoscience*, 339(2), 121-131.

Jolivet, M., Dempster, T. and Cox, R. (2003) 'Répartition de l'uranium et du thorium dans les apatites: implications pour la thermochronologie U・Th/He', *Comptes Rendus Géoscience*, 335(12), 899-906.

Jonckheere, R. (2003) 'On the densities of etchable fission tracks in a mineral and co-irradiated external detector with reference to fission-track dating of minerals', *Chemical Geology*, 200(1-2), 41-58.

Jones, S.M. and White, N. (2003) 'Shape and size of the starting Iceland plume swell', *Earth and Planetary Science Letters*, 216(3), 271-282.

Jones, S.M., White, N., Clarke, B.J., Rowley, E. and Gallagher, K. (2002) 'Present and past influence of the Iceland Plume on sedimentation', *Geological Society, London, Special Publications*, 196(1), 13-25.

Kalsbeek, F., Thrane, K., Nutman, A.P. and Jepsen, H.F. (2000) 'Late Mesoproterozoic to early Neoproterozoic history of the East Greenland Caledonides: evidence for Grenvillian orogenesis?', *Journal of the Geological Society*, 157(6), 1215-1225.

Kelly, S. (1992) 'Milankovitch cyclicity recorded from Devonian non-marine sediments', *Terra Nova*, 4(5), 578-584.

Ketcham, R. (2005) 'HeFTy: Forward and inverse modeling thermochronometer systems', *Computational Tools for Low-Temperature Thermocronometer Interpretation. Mineralogical Society of America, Chantilly, VA*.

Ketcham, R.A. (2019) 'Fission-track annealing: From geologic observations to thermal history modeling' in *Fission-Track Thermochronology and its Application to Geology* Springer, 49-75.

Ketcham, R.A., Carter, A., Donelick, R.A., Barbarand, J. and Hurford, A.J. (2007a) 'Improved measurement of fission-track annealing in apatite using c-axis projection', *American Mineralogist*, 92(5-6), 789-798.

Ketcham, R.A., Carter, A., Donelick, R.A., Barbarand, J. and Hurford, A.J. (2007b) 'Improved modeling of fission-track annealing in apatite', *American Mineralogist*, 92(5-6), 799-810.

Ketcham, R.A., Carter, A. and Hurford, A.J. (2015) 'Inter-laboratory comparison of fission track confined length and etch figure measurements in apatite', *American Mineralogist*, 100(7), 1452-1468.

Kirkland, C., Yakymchuk, C., Szilas, K., Evans, N., Hollis, J., McDonald, B. and Gardiner, N. (2018) 'Apatite: a U-Pb thermochronometer or geochronometer?', *Lithos*, 318, 143-157.

Kirkland, C.L., Stephen Daly, J. and Whitehouse, M.J. (2007) 'Provenance and terrane evolution of the Kalak Nappe Complex, Norwegian Caledonides: implications for Neoproterozoic paleogeography and tectonics', *The Journal of Geology*, 115(1), 21-41.

Kneller, B. and Aftalion, M. (1987) 'The isotopic and structural age of the Aberdeen Granite', *Journal of the Geological Society*, 144(5), 717-721.

Kohn, B., Chung, L. and Gleadow, A. (2019) 'Fission-track analysis: field collection, sample preparation and data acquisition' in *Fission-track thermochronology and its application to geology* Springer, 25-48.

Kohn, B.P., Lorencak, M., Gleadow, A.J., Kohlmann, F., Raza, A., Osadetz, K.G. and Sorjonen-Ward, P. (2009) 'A reappraisal of low-temperature thermochronology of the eastern Fennoscandia Shield and radiation-enhanced apatite fission-track annealing', *Geological Society, London, Special Publications*, 324(1), 193-216.

Košler, J. (2007) 'Laser ablation ICP—MS—a new dating tool in Earth science', *Proceedings of the Geologists' Association*, 118(1), 19-24.

Košler, J. and Sylvester, P.J. (2003) 'Present trends and the future of zircon in geochronology: laser ablation ICPMS', *Reviews in Mineralogy and Geochemistry*, 53(1), 243-275.

Lancaster, P.J., Daly, J.S., Storey, C.D. and Morton, A.C. (2017) 'Interrogating the provenance of large river systems: multi-proxy in situ analyses in the Millstone Grit, Yorkshire', *Journal of the Geological Society*, 174(1), 75-87.

Lancaster, P.J., Storey, C.D., Hawkesworth, C.J. and Dhuime, B. (2011) 'Understanding the roles of crustal growth and preservation in the detrital zircon record', *Earth and Planetary Science Letters*, 305(3-4), 405-412.

Larson, S.Å., Cederbom, C.E., Tullborg, E.-L. and Stiberg, J.-P. (2006) 'Comment on “Apatite fission track and (U–Th)/He data from Fennoscandia: An example of underestimation of fission track annealing in apatite” by Hendriks and Redfield [Earth Planet. Sci. Lett. 236 (443–458)]', *Earth and Planetary Science Letters*, 248(1-2), 561-568.

Laslett, G., Green, P.F., Duddy, I. and Gleadow, A. (1987) 'Thermal annealing of fission tracks in apatite 2. A quantitative analysis', *Chemical Geology: Isotope Geoscience section*, 65(1), 1-13.

Laslett, G.M., Green, P.F., Duddy, I.R. and Gleadow, A.J.W. (1987) 'Thermal annealing of fission tracks in apatite 2. A quantitative analysis', *Chemical Geology*, **65**(1), pp. 1-13.

Leeder, M. and McMahon, A. (1988) *Upper Carboniferous (Silesian) basin subsidence in northern Britain. In: Sedimentation in a Synorogenic Basin Complex: the Upper Carboniferous of Northwest Europe.* , Glasgow: Blackie.

Leeder, M.R. (1982) 'Upper Palaeozoic basins of the British Isles--Caledonide inheritance versus Hercynian plate margin processes', *Journal of the Geological Society*, 139(4), 479-491.

Leeder, M.R. (1988) 'Devono-Carboniferous river systems and sediment dispersal from the orogenic belts and cratons of NW Europe', *Geological Society, London, Special Publications*, 38(1), 549-558.

Leggett, J.K. (1980) 'The sedimentological evolution of a Lower Palaeozoic accretionary fore-arc in the Southern Uplands of Scotland', *Sedimentology*, 27(4), 401-417.

Lewis, C.L., Carter, A. and Hurford, A.J. (1992) 'Low-temperature effects of the Skye Tertiary intrusions on Mesozoic sediments in the Sea of Hebrides Basin', *Geological Society, London, Special Publications*, 62(1), 175-188.

Lisker, F., Ventura, B. and Glasmacher, U.A. (2009) 'Apatite thermochronology in modern geology', *Geological Society, London, Special Publications*, 324(1), 1-23.

Loftus, G. and Greensmith, J. (1988) 'The lacustrine Burdiehouse Limestone Formation—a key to the deposition of the Dinantian Oil Shales of Scotland', *Geological Society, London, Special Publications*, 40(1), 219-234.

Longman, C.D. (1980) *Age and affinity of granitic detritus in Lower Palaeozoic conglomerates, SW Scotland: implications for Caledonian evolution*, unpublished thesis, University of Glasgow.

Lowden, B., Braley, S., Hurst, A. and Lewis, J. (1992) 'Sedimentological studies of the Cretaceous Lochaline Sandstone, NW Scotland', *Geological Society, London, Special Publications*, 62(1), 159-162.

Lundmark, A.M., Bue, E.P., Gabrielsen, R.H., Flaat, K., Strand, T. and Ohm, S.E. (2014) 'Provenance of late Palaeozoic terrestrial sediments on the northern flank of the Mid North Sea High: Detrital zircon geochronology and rutile geochemical constraints', *Geological Society, London, Special Publications*, 386(1), 243-259.

Łuszczak, K. (2016) *Quantifying uplift and denudation of a thermally heterogeneous crust: a detailed multi-thermochronometeric study of central west Britain*, unpublished thesis, University of Glasgow.

Macdonald, R., Fettes, D.J. and Bagiński, B. (2015) 'The Mull Paleocene dykes: some insights into the nature of major dyke swarms', *SCOTTISH JOURNAL OF GEOLOGY*, 51(2), 116-124.

Mackay, L., Turner, J., Jones, S. and White, N. (2005) 'Cenozoic vertical motions in the Moray Firth Basin associated with initiation of the Iceland Plume', *Tectonics*, 24(5).

Maddox, S.J. and Andrews, J.E. (1987) 'Lithofacies and stratigraphy of a Dinantian non-marine dolostone from the Lower Oil-Shale Group of Fife and West Lothian', *SCOTTISH JOURNAL OF GEOLOGY*, 23(2), 129-147.

Malusà, M.G. and Fitzgerald, P.G. (2019a) *Fission-track thermochronology and its application to geology*, Springer.

Malusà, M.G. and Fitzgerald, P.G. (2019b) 'From cooling to exhumation: setting the reference frame for the interpretation of thermochronologic data' in *Fission-track thermochronology and its application to geology* Springer, 147-164.

Mark, C., Cogné, N. and Chew, D. (2016) 'Tracking exhumation and drainage divide migration of the Western Alps: A test of the apatite U-Pb thermochronometer as a detrital provenance tool', *Bulletin*, 128(9-10), 1439-1460.

Masson, O. (1921) 'XXIV. The constitution of atoms', *The London, Edinburgh, and Dublin Philosophical Magazine and Journal of Science*, 41(242), 281-285.

McDannell, K.T., Issler, D.R. and O'Sullivan, P.B. (2019) 'Radiation-enhanced fission track annealing revisited and consequences for apatite thermochronometry', *Geochimica et Cosmochimica Acta*, 252, 213-239.

McDowell, F.W., McIntosh, W.C. and Farley, K.A. (2005) 'A precise 40Ar–39Ar reference age for the Durango apatite (U–Th)/He and fission-track dating standard', *Chemical Geology*, 214(3-4), 249-263.

McGiven, A. (1968) *Sedimentation and provenance of post-Valentian conglomerates up to and including the basal conglomerate of the lower old red sandstone in the southern part of the midland valley of Scotland*, unpublished thesis (Dissertation/Thesis).

McKellar, Z. (2017) *Sedimentology of the Lower Old Red Sandstone of the northern Midland Valley and Grampian outliers, Scotland: implications for post-orogenic basin development*, unpublished thesis, University of Aberdeen.

McKellar, Z., Hartley, A.J., Morton, A. and Frei, D. (2020) 'A multidisciplinary approach to sediment provenance analysis of the late Silurian–Devonian Lower Old Red Sandstone succession, northern Midland Valley Basin, Scotland', *Journal of the Geological Society*, 177(2), 297-314.

McKenzie, D. (1978) 'Some remarks on the development of sedimentary basins', *Earth and Planetary Science Letters*, 40(1), 25-32.

McKerrow, W., Dewey, J. and Scotese, C. (1991) 'The Ordovician and Silurian development of the Iapetus ocean', *Special Papers in Palaeontology*, 44, 165-178.

McKerrow, W., Mac Niocaill, C. and Dewey, J. (2000) 'The Caledonian orogeny redefined', *Journal of the Geological Society*, 157(6), 1149-1154.

McKerrow, W. and Soper, N. (1989) 'The Iapetus suture in the British Isles', *Geological Magazine*, 126(1), 1-8.

Miall, A.D. (2013) *Principles of sedimentary basin analysis*, Springer Science & Business Media.

Mitchell, G.H. and Mykura, W. (1962) *The geology of the neighbourhood of Edinburgh*, HM Stationery Office.

Moecher, D.P. and Samson, S.D. (2006) 'Differential zircon fertility of source terranes and natural bias in the detrital zircon record: Implications for sedimentary provenance analysis', *Earth and Planetary Science Letters*, 247(3-4), 252-266.

Monaghan, A., Starcher, V., O Dochartaigh, B., Shorter, K. and Burkin, J. (2018) 'UK Geoenergy Observatories: Glasgow Geothermal Energy Research Field Site: science infrastructure'.

Monaghan, A.A. (2014) 'The Carboniferous shales of the Midland Valley of Scotland: geology and resource estimation', *British Geological Survey for Department of Energy and Climate Change, London, UK.*

Monaghan, A.A. (2017) 'Unconventional energy resources in a crowded subsurface: reducing uncertainty and developing a separation zone concept for resource estimation and deep 3D subsurface planning using legacy mining data', *Science of the Total Environment*, 601, 45-56.

Monaghan, A.A., Browne, M.A.E. and Barfod, D.N. (2014) 'An improved chronology for the Arthur's Seat volcano and Carboniferous magmatism of the Midland Valley of Scotland', *SCOTTISH JOURNAL OF GEOLOGY*, **50**, pp. 156-172.

Monaghan, A.A. and Parrish, R.R. (2006) 'Geochronology of Carboniferous-Permian magmatism in the Midland Valley of Scotland: implications for regional tectonomagmatic evolution and the numerical time scale', *Journal of the Geological Society*, **163**(1), pp. 15-28.

Monaghan, A.A. and Pringle, M.S. (2004) '40Ar/39Ar geochronology of Carboniferous-Permian volcanism in the Midland Valley, Scotland', *Geological Society, London, Special Publications*, **223**(1), pp. 219-242.

Monro, S.K. (1982) 'Sedimentation, stratigraphy and tectonics in the Dalry Basin, Ayrshire'.

Morton, A.C., Claoué-Long, J. and Hallsworth, C. (2001) 'Zircon age and heavy mineral constraints on provenance of North Sea Carboniferous sandstones', *Marine and Petroleum Geology*, 18(3), 319-337.

Morton, A.C. and Hallsworth, C.R. (1999) 'Processes controlling the composition of heavy mineral assemblages in sandstones', *Sedimentary Geology*, 124(1-4), 3-29.

Morton, A.C. and Whitham, A.G. (2002) 'The Millstone Grit of northern England: a response to tectonic evolution of a northern sourceland', *Proceedings of the Yorkshire Geological Society*, 54(1), 47-56.

Muir, R.O. (1963) 'Petrography and provenance of the Millstone Grit of Central Scotland', *Transactions of the Edinburgh Geological Society*, 19(4), 439-485.

Murchison, D.G. and Raymond, A.C. (1989) 'Igneous activity and organic maturation in the Midland Valley of Scotland', *International Journal of Coal Geology*, 14(1-2), 47-82.

Mykura, W., Calver, M. and Wilson, R. (1967) 'The Upper Carboniferous rocks of south-west Ayrshire', *Bulletin of the Geological Survey of Great Britain*, **26**, pp. 23-98.

Naeser, C.W. (1981) 'The fading of fission tracks in the geologic environment— Data from deep drill holes', *Nuclear Tracks*, **5**(1), pp. 248-250.

Naing, T.T., Bussien, D., Winkler, W., Nold, M. and Von Quadt, A. (2014) 'Provenance study on Eocene–Miocene sandstones of the Rakhine coastal belt, Indo-Burman Ranges of Myanmar: Geodynamic implications', *Geological Society, London, Special Publications*, 386(1), 195-216.

Nance, R.D., Murphy, J.B., Strachan, R.A., Keppie, J.D., Gutiérrez-Alonso, G., Fernández-Suárez, J., Quesada, C., Linnemann, U., D'lemos, R. and Pisarevsky, S.A. (2008) 'Neoproterozoic-early Palaeozoic tectonostratigraphy

and palaeogeography of the peri-Gondwanan terranes: Amazonian v. West African connections', *Geological Society, London, Special Publications*, 297(1), 345-383.

Neves, R., Gueinn, K.J., Clayton, G., Ioannides, N.S., Neville, R.S. and Kruszewska, K. (1973) '2.—Palynological Correlations within the Lower Carboniferous of Scotland and Northern England', *Earth and Environmental Science Transactions of The Royal Society of Edinburgh*, 69(2), 23-70.

Nielsen, S., Clausen, O.R. and McGregor, E. (2017) 'Basin% Ro: a vitrinite reflectance model derived from basin and laboratory data', *Basin Research*, 29, 515-536.

O'Sullivan, G., Chew, D., Kenny, G., Henrichs, I. and Mulligan, D. (2020) 'The trace element composition of apatite and its application to detrital provenance studies', *Earth-Science Reviews*, 201, 103044.

Oliver, G., Chen, F., Buchwaldt, R. and Hegner, E. (2000) 'Fast tectonometamorphism and exhumation in the type area of the Barrovian and Buchan zones', *Geology*, 28(5), 459-462.

Oliver, G., Stone, P., Bluck, B. and Trewin, N. (2002) 'The Ballantrae Complex and Southern Uplands terrane', *The Geology of Scotland. Geological Society, London*, 167, 200.

Oliver, G.J., Wilde, S.A. and Wan, Y. (2008) 'Geochronology and geodynamics of Scottish granitoids from the late Neoproterozoic break-up of Rodinia to Palaeozoic collision', *Journal of the Geological Society*, 165(3), 661-674.

Owens, B., McLEAN, D., Simpson, K.R., Shell, P.M. and Robinson, R. (2005) 'Reappraisal of the Mississippian palynostratigraphy of the east Fife coast, Scotland, United Kingdom', *Palynology*, 29(1), 23-47.

Park, R., Stewart, A., Wright, D. and Trewin, N. (2002) 'The Hebridean terrane', *The Geology of Scotland. Geological Society, London*, 45, 80.

Parker, J. (1993) *Petroleum geology of northwest Europe*, Geological Society.

Parrish, R.R., Parrish, R.R. and Noble, S.R. (2003) 'Zircon U-Th-Pb Geochronology by Isotope Dilution — Thermal Ionization Mass Spectrometry (ID-TIMS)', *Reviews in Mineralogy and Geochemistry*, 53(1), 183-213.

Paterson, I.B. and Hall, I.H.S. (1986) *Lithostratigraphy of the late Devonian and early Carboniferous rocks in the Midland Valley of Scotland*, London: HMSO.

Paterson, S.R. and Fowler Jr, T.K. (1993) 'Re-examining pluton emplacement processes', *Journal of Structural Geology*, 15(2), 191-206.

Paton, C., Hellstrom, J., Paul, B., Woodhead, J. and Hergt, J. (2011) 'Iolite: Freeware for the visualisation and processing of mass spectrometric data', *Journal of Analytical Atomic Spectrometry*, 26(12), 2508-2518.

Pearce, N.J., Perkins, W.T., Westgate, J.A., Gorton, M.P., Jackson, S.E., Neal, C.R. and Chenery, S.P. (1997) 'A compilation of new and published major and trace element data for NIST SRM 610 and NIST SRM 612 glass reference materials', *Geostandards newsletter*, 21(1), 115-144.

Penn, I., Holliday, D., Kirby, G., Kubala, M., Sobey, R., Mitchell, W., Harrison, R. and Beckinsale, R. (1983) 'The Larne No. 2 Borehole: discovery of a new Permian volcanic centre', *SCOTTISH JOURNAL OF GEOLOGY*, 19(3), 333-346.

Persano, C., Barfod, D.N., Stuart, F.M. and Bishop, P. (2007) 'Constraints on early Cenozoic underplating-driven uplift and denudation of western Scotland from low temperature thermochronometry', *Earth and Planetary Science Letters*, 263(3-4), 404-419.

Petrus, J.A. and Kamber, B.S. (2012) 'VizualAge: A novel approach to laser ablation ICP-MS U-Pb geochronology data reduction', *Geostandards and Geoanalytical Research*, 36(3), 247-270.

Phillips, E., Barron, H., Smith, R. and Arkley, S. (2004) 'Composition and provenance of the Silurian to Devonian sandstone sequences of the southern Midland Valley', *SCOTTISH JOURNAL OF GEOLOGY*, 40(1), 23-42.

Phillips, E., Smith, R. and Carroll, S. (1997) 'Strike-slip, terrane accretion and the pre-Carboniferous evolution of the Midland Valley of Scotland'.

Phillips, E.R., Smith, R.A., Stone, P., Pashley, V. and Horstwood, M. (2009) 'Zircon age constraints on the provenance of Llandovery to Wenlock sandstones from the Midland Valley terrane of the Scottish Caledonides', *SCOTTISH JOURNAL OF GEOLOGY*, **45**(2), pp. 131-146.

Powell, J.W., Schneider, D.A. and Issler, D.R. (2018) 'Application of multi-kinetic apatite fission track and (U-Th)/He thermochronology to source rock thermal history: a case study from the Mackenzie Plain, NWT, Canada', *Basin Research*, 30, 497-512.

Price, P.B. and Walker, R.M. (1962) 'Chemical Etching of Charged-Particle Tracks in Solids', *Journal of Applied Physics*, 33(12), 3407-3412.

Price, P.B. and Walker, R.M. (1963) 'Fossil tracks of charged particles in mica and the age of minerals', *Journal of Geophysical Research*, 68(16), 4847-4862.

Raab, M.J., Brown, R.W., Gallagher, K., Carter, A. and Weber, K. (2002) 'Late Cretaceous reactivation of major crustal shear zones in northern Namibia: constraints from apatite fission track analysis', *Tectonophysics*, 349(1-4), 75-92.

Rainbird, R.H., Hamilton, M.A. and Young, G.M. (2001) 'Detrital zircon geochronology and provenance of the Torridonian, NW Scotland', *Journal of the Geological Society*, 158(1), 15-27.

Raymond, A.C. (1991) 'Carboniferous rocks of the eastern and central Midland Valley of Scotland: organic petrology, organic geochemistry and effects of igneous activity. Unpublished Ph.D Thesis, University of Newcastle Upon Tyne'.

Raymond, A.C. and Murchison, D.G. (1988a) 'Development of organic maturation in the thermal aureoles of sills and its relation to sediment compaction', *Fuel*, 67(12), 1599-1608.

Raymond, A.C. and Murchison, D.G. (1988b) 'Effect of volcanic activity on level of organic maturation in Carboniferous rocks of East Fife, Midland Valley of Scotland', *Fuel*, 67(8), 1164-1166.

Raymond, A.C. and Murchison, D.G. (1989) 'Organic maturation and its timing in a Carboniferous sequence in the central Midland Valley of Scotland: comparisons with northern England', *Fuel*, 68(3), 328-334.

Read, H.H. (1961) 'Aspects of Caledonian magmatism in Britain', *Geological Journal*, 2(4), 653-683.

Read, W. (1994) 'The frequencies of Scottish Pendleian allocycles', *SCOTTISH JOURNAL OF GEOLOGY*, 30(1), 91-93.

Read, W. and Forsyth, I. (1991) 'Allocycles in the upper part of the limestone coal group (pendleian, E1) of the glasgow-stirling region viewed in the light of sequence stratigraphy', *Geological Journal*, 26(1), 85-89.

Read, W.A. (1988) *Controls on Sedimentation in the Midland Valley of Scotland. In. Besly, B.M. & Kelling, G. (eds.) Sedimentation in a synorogenic basin complex: the Upper Carboniferous of northwest Europe*, London;Glasgow;New York, NY;: Blackie.

Read, W.A., Browne, M.A.E., Stephenson, D. and Upton, B.G.J. (2002) 'Carboniferous. In: Trewin, N.H. (Ed.) The Geology of Scotland', *Geological Society, London, fourth ed.*, pp.251-300.

Reiners, P.W. and Ehlers, T.A. (2005) *Low-temperature thermochronology: techniques, interpretations, and applications*, Chantilly, Va: Mineralogical Society of America, Geochemical Society.

Reiners, P.W., Ehlers, T.A. and Zeitler, P.K. (2005) 'Past, Present, and Future of Thermochronology', *Reviews in Mineralogy and Geochemistry*, 58(1), 1-18.

Renne, P.R., Swisher, C.C., Deino, A.L., Karner, D.B., Owens, T.L. and DePaolo, D.J. (1998) 'Intercalibration of standards, absolute ages and uncertainties in 40Ar/39Ar dating', *Chemical Geology*, 145(1-2), 117-152.

Rippon, J. (1998) 'The identification of syn-depositionally-active structures in the coal-bearing Upper Carboniferous of Great Britain', *Proceedings of the Yorkshire Geological Society*, 52(1), 73-93.

Rippon, J., Read, W.A. and Park, R.G. (1996) 'The Ochil Fault and the Kincardine basin: key structures in the tectonic evolution of the Midland Valley of Scotland', *Journal of the Geological Society*, **153**(4), pp. 573-587.

Ritchie, J.D., Johnson, H., Browne, M.A.E. and Monaghan, A.A. (2003) 'Late Devonian-Carboniferous tectonic evolution within the Firth of Forth, Midland Valley; as revealed from 2D seismic reflection data', *SCOTTISH JOURNAL OF GEOLOGY*, **39**(2), pp. 121-134.

Rutherford, E. (1920) 'Nuclear constitution of atoms'.

Rutherford, E. and Soddy, F. (1902) 'XLI. The cause and nature of radioactivity.—Part I', *The London, Edinburgh, and Dublin Philosophical Magazine and Journal of Science*, 4(21), 370-396.

Sambridge, M., Gallagher, K., Jackson, A. and Rickwood, P. (2006) 'Trans-dimensional inverse problems, model comparison and the evidence', *Geophysical Journal International*, 167(2), 528-542.

Saunders, A., Fitton, J., Kerr, A.C., Norry, M. and Kent, R. (1997) 'The north Atlantic igneous province', *GEOPHYSICAL MONOGRAPH-AMERICAN GEOPHYSICAL UNION*, 100, 45-94.

Schneider, D.A. and Issler, D.R. (2019) 'Application of low-temperature thermochronology to hydrocarbon exploration' in *Fission-Track Thermochronology and its Application to Geology* Springer, 315-333.

Schoene, B. and Bowring, S.A. (2006) 'U–Pb systematics of the McClure Mountain syenite: thermochronological constraints on the age of the 40 Ar/39 Ar standard MMhb', *Contributions to Mineralogy and Petrology*, 151(5), 615.

Schoene, B. and Bowring, S.A. (2007) 'Determining accurate temperature–time paths from U–Pb thermochronology: An example from the Kaapvaal craton, southern Africa', *Geochimica et Cosmochimica Acta*, 71(1), 165-185.

Scott, A.C. (2001) 'Roasted alive in the Carboniferous', *Geoscientist*, **11**(3), pp. 4-7.

Seitz, F. (1949) 'On the disordering of solids by action of fast massive particles', *Discussions of the Faraday Society*, 5, 271-282.

Silk, E.C.H. and Barnes, R.S. (1959) 'Examination of fission fragment tracks with an electron microscope', *Philosophical Magazine*, 4(44), 970-972.

Sláma, J., Košler, J., Condon, D.J., Crowley, J.L., Gerdes, A., Hanchar, J.M., Horstwood, M.S., Morris, G.A., Nasdala, L. and Norberg, N. (2008) 'Plešovice zircon—a new natural reference material for U–Pb and Hf isotopic microanalysis', *Chemical Geology*, 249(1-2), 1-35.

Small, D., Parrish, R.R., Austin, W.E., Cawood, P.A. and Rinterknecht, V. (2013) 'Provenance of North Atlantic ice-rafted debris during the last deglaciation—A new application of U-Pb rutile and zircon geochronology', *Geology*, 41(2), 155-158.

Smellie, J. and Stone, P. (2000) 'Geochemical characteristics and geotectonic setting of early Ordovician basalt lavas in the Ballantrae Complex ophiolite, SW Scotland', *Earth and Environmental Science Transactions of The Royal Society of Edinburgh*, 91(3-4), 539-555.

Smith, R.A. (1995) 'The Siluro-Devonian evolution of the southern Midland Valley of Scotland', *Geological Magazine*, **132**(5), pp. 503-513.

Sobel, E.R. and Seward, D. (2010) 'Influence of etching conditions on apatite fission-track etch pit diameter', *Chemical Geology*, **271**(1), pp. 59-69.

Soddy, F. (1913) 'Intra-atomic Charge', *Nature*, 92(2301), 399-400.

Spencer, C.J., Cawood, P.A., Hawkesworth, C.J., Prave, A.R., Roberts, N.M., Horstwood, M.S. and Whitehouse, M.J. (2015) 'Generation and preservation of continental crust in the Grenville Orogeny', *Geoscience Frontiers*, 6(3), 357-372.

Spiegel, C., Kohn, B., Raza, A., Rainer, T. and Gleadow, A. (2007) 'The effect of long-term low-temperature exposure on apatite fission track stability: A natural annealing experiment in the deep ocean', *Geochimica et Cosmochimica Acta*, **71**(18), pp. 4512-4537.

Stedman, C., Besly, B. and Kelling, G. (1988) 'Namurian E1 tectonics and sedimentation in the Midland Valley of Scotland: rifting versus strike-slip influence', *Sedimentation in a synorogenic basin complex: the Upper Carboniferous of northwest Europe*, 242-254.

Stephens, W. and Halliday, A. (1979) 'Compositional variation in the Galloway plutons' in *Origin of Granite Batholiths* Springer, 9-17.

Stephenson, D. (2003) *Carboniferous and Permian igneous rocks of Great Britain, north of the Variscan Front*, Peterborough: Joint Nature Conservation Committee.

Stoker, M.S., Stewart, M.A., Shannon, P.M., Bjerager, M., Nielsen, T., Blischke, A., Hjelstuen, B., Gaina, C., McDermott, K. and Ólavsdóttir, J. (2017) 'An overview of the Upper Palaeozoic–Mesozoic stratigraphy of the NE Atlantic region', *Geological Society, London, Special Publications*, 447(1), 11-68.

Stone, P. and Evans, J. (2000) 'Silurian provenance variation in the Southern Uplands terrane, Scotland, assessed using neodymium isotopes and linked with regional tectonic evolution', *Earth and Environmental Science Transactions of The Royal Society of Edinburgh*, 91(3-4), 447-455.

Strachan, R., Smith, M., Harris, A., Fettes, D. and Trewin, N. (2002) 'The northern Highland and Grampian terranes', *The Geology of Scotland. Geological Society, London*, 81, 147.

Stuart, F.M., Bluck, B.J. and Pringle, M.S. (2001) 'Detrital muscovite 40Ar/39Ar ages from Carboniferous sandstones of the British Isles: Provenance and implications for the uplift history of orogenic belts', *Tectonics*, 20(2), 255-267.

Sweeney, J.J. and Burnham, A.K. (1990) 'Evaluation of a simple model of vitrinite reflectance based on chemical kinetics', *AAPG bulletin*, 74(10), 1559-1570.

Syba, E. (1989) *The sedimentation and provenance of the Lower Old Red Sandstone Greywacke Conglomerate, southern Midland Valley, Scotland*, unpublished thesis (Dissertation/Thesis).

Sylvester, P.J. (2001) *Laser-ablation-ICPMS in the Earth Sciences: Principles and Applications*, Mineralogical Association of Canada.

Tagami, T. (2019) 'Application of fission-track thermochronology to understand fault zones' in *Fission-Track Thermochronology and its Application to Geology* Springer, 221-233.

Tagami, T. and O'Sullivan, P.B. (2005) 'Fundamentals of Fission-Track Thermochronology', *Reviews in Mineralogy and Geochemistry*, 58(1), 19-47.

Tera, F. and Wasserburg, G. (1972) 'U-Th-Pb systematics in lunar highland samples from the Luna 20 and Apollo 16 missions', *Earth and Planetary Science Letters*, 17(1), 36-51.

Thigpen, J., Law, R., Loehn, C., Strachan, R., Tracy, R., Lloyd, G., Roth, B. and Brown, S. (2013) 'Thermal structure and tectonic evolution of the Scandian orogenic wedge, S cottish Caledonides: integrating geothermometry, deformation temperatures and conceptual kinematic-thermal models', *Journal of Metamorphic Geology*, 31(8), 813-842.

Thirlwall, M. (1983) 'Isotope geochemistry and origin of calc-alkaline lavas from a Caledonian continental margin volcanic arc', *Journal of Volcanology and Geothermal Research*, 18(1-4), 589-631.

Thirlwall, M. (1988) 'Geochronology of Late Caledonian magmatism in northern Britain', *Journal of the Geological Society*, 145(6), 951-967.

Thomas, W.A. (2011) 'Detrital-zircon geochronology and sedimentary provenance', *Lithosphere*, 3(4), 304-308.

Thomson, K., Underhill, J.R., Green, P., Bray, R. and Gibson, H. (1999) 'Evidence from apatite fission track analysis for the post-Devonian burial and exhumation history of the northern Highlands, Scotland', *Marine and Petroleum Geology*, 16(1), 27-39.

Thomson, S.N., Gehrels, G.E., Ruiz, J. and Buchwaldt, R. (2012) 'Routine low-damage apatite U-Pb dating using laser ablation–multicollector–ICPMS', *Geochemistry, Geophysics, Geosystems*, 13(2).

Tomlinson, J., Denton, P., Maguire, P. and Booth, D. (2006) 'Analysis of the crustal velocity structure of the British Isles using teleseismic receiver functions', *Geophysical Journal International*, 167(1), 223-237.

Trewin, N.H. (2002) *The geology of Scotland*, London: The Geological Society.

Trewin, N.H. and Thirlwall, M.F. (2002) *Old Red Sandstone. In: Trewin, N.H. (Ed.), The Geology of Scotland*, London: The Geological Society.

Underhill, J.R., Monaghan, A.A. and Browne, M.A.E. (2008) 'Controls on structural styles, basin development and petroleum prospectivity in the Midland Valley of Scotland', *Marine and Petroleum Geology*, 25(10), 1000-1022.

Upton, B.G., Aspen, P. and Hunter, R.H. (1984) 'Xenoliths and their implications for the deep geology of the Midland Valley of Scotland and adjacent region', *Earth and Environmental Science Transactions of The Royal Society of Edinburgh*, 75(2), 65-70.

Upton, B.G.J., Aspen, P., Graham, A. and Chapman, N.A. (1976) 'Pre-Palaeozoic basement of the Scottish Midland Valley', *Nature*, 260, 517.

Upton, B.G.J., Stephenson, D., Smedley, P.M., Wallis, S.M. and Fitton, J.G. (2004) 'Carboniferous and Permian magmatism in Scotland', *Geological Society, London, Special Publications*, **223**(1), pp. 195-218.

USGS (2021) *Earth Explorer*, available: https://earthexplorer.usgs.gov/ [accessed 06/02].

Vermeesch, P. (2004) 'How many grains are needed for a provenance study?', *Earth and Planetary Science Letters*, 224(3-4), 441-451.

Vermeesch, P. (2009) 'RadialPlotter: A Java application for fission track, luminescence and other radial plots', *Radiation Measurements*, 44(4), 409-410.

Vermeesch, P. (2012) 'On the visualisation of detrital age distributions', *Chemical Geology*, 312, 190-194.

Vermeesch, P. (2017) 'Statistics for LA-ICP-MS based fission track dating', *Chemical Geology*, 456, 19-27.

Vermeesch, P. (2018) 'IsoplotR: A free and open toolbox for geochronology', *Geoscience Frontiers*, 9(5), 1479-1493.

Vermeesch, P. (2019) 'Statistics for fission-track thermochronology' in *Fission-Track Thermochronology and its Application to Geology* Springer, 109-122.

Vermeesch, P. and Tian, Y. (2014) 'Thermal history modelling: HeFTy vs. QTQt', *Earth-Science Reviews*, 139, 279-290.

Vincent, C.J., Rowley, W.J. and Monaghan, A.A. (2010) 'Thermal and burial history modelling in the Midlothian-Leven syncline in the Midland Valley of Scotland using BasinMod and HotPot', *SCOTTISH JOURNAL OF GEOLOGY*, **46**(2), pp. 125-142.

Vineyard, G.H. (1976) 'Thermal spikes and activated processes', *Radiation Effects*, 29(4), 245-248.

Wagner, G. (1968) 'Fission track dating of apatites', *Earth and Planetary Science Letters*, 4(5), 411-415.

Waldron, J.W., Floyd, J.D., Simonetti, A. and Heaman, L.M. (2008) 'Ancient Laurentian detrital zircon in the closing Iapetus ocean, Southern Uplands terrane, Scotland', *Geology*, 36(7), 527-530.

Warren, C.J., Hanke, F. and Kelley, S.P. (2012) 'When can muscovite 40Ar/39Ar dating constrain the timing of metamorphic exhumation?', *Chemical Geology*, 291, 79-86.

Waters, C., Browne, M., Jones, N. and Somerville, I. (2011) 'Midland valley of Scotland', in Geological Society of London.

Webster, D.M. (2018) *The fragment effect: an innovative new approach to apatite (U-Th)/He thermochronology*, unpublished thesis, University of Glasgow.

Weedon, G. and Read, W. (1995) 'Orbital-climatic forcing of Namurian cyclic sedimentation from spectral analysis of the Limestone Coal Formation, Central Scotland', *Geological Society, London, Special Publications*, 85(1), 51-66.

Wessel, P., Luis, J., Uieda, L., Scharroo, R., Wobbe, F., Smith, W. and Tian, D. (2019) 'The generic mapping tools version 6', *Geochemistry, Geophysics, Geosystems*, 20(11), 5556-5564.

Wetherill, G.W. (1956) 'An interpretation of the Rhodesia and Witwatersrand age patterns', *Geochimica et Cosmochimica Acta*, 9(5), 290-292.

White, R. (1988) 'A hot-spot model for early Tertiary volcanism in the N Atlantic', *Geological Society, London, Special Publications*, 39(1), 3-13.

White, R.S. (1997) 'Rift–plume interaction in the North Atlantic', *Philosophical Transactions of the Royal Society of London. Series A: Mathematical, Physical and Engineering Sciences*, 355(1723), 319-339.

Whitehouse, M., Claesson, S., Sunde, T. and Vestin, J. (1997) 'Ion microprobe U‐Pb zircon geochronology and correlation of Archaean gneisses from the Lewisian Complex of Gruinard Bay, northwestern Scotland', *Geochimica et Cosmochimica Acta*, 61(20), 4429-4438.

Wiedenbeck, M., Alle, P., Corfu, F., Griffin, W., Meier, M., Oberli, F.v., Quadt, A.v., Roddick, J. and Spiegel, W. (1995) 'Three natural zircon standards for U-Th-Pb, Lu-Hf, trace element and REE analyses', *Geostandards newsletter*, 19(1), 1-23.

Wildman, M., Brown, R., Persano, C., Beucher, R., Stuart, F.M., Mackintosh, V., Gallagher, K., Schwanethal, J. and Carter, A. (2017) 'Contrasting Mesozoic evolution across the boundary between on and off craton regions of the South African plateau inferred from apatite fission track and (U-Th-Sm)/He thermochronology', *Journal of Geophysical Research: Solid Earth*, 122(2), 1517-1547.

Williams, A. (1962) *The Barr and lower Ardmillan series (Caradoc) of the Girvan district, South-West Ayrshire: with descriptions of the Brachiopoda*, Geological Society.

Williams, D.M. and Harper, D.A.T. (1988) 'A basin model for the Silurian of the Midland Valley of Scotland and Ireland', *Journal of the Geological Society*, 145(5), 741-748.

Williams, D.M. and Harper, D.A.T. (1991) 'End-Silurian modifications of Ordovician terranes in western Ireland', *Journal of the Geological Society*, 148(1), 165-171.

Wilson, A.C. (1980) 'The Devonian sedimentation and tectonism of a rapidly subsiding, semi-arid fluvial basin in the Midland Valley of Scotland', *SCOTTISH JOURNAL OF GEOLOGY*, **16**(4), pp. 291-313.

Wilson, R. (1989) 'A study of the Dinantian marine macrofossils of central Scotland', *Earth and Environmental Science Transactions of The Royal Society of Edinburgh*, 80(2), 91-126.

Witzke, B. and Heckel, P. (1988) 'Paleoclimatic indicators and inferred Devonian paleolatitudes of Euramerica'.

Woodcock, N. (2003) *The Geology of Scotland* 4th ed., Cambridge: Cambridge University Press.

Woodcock, N.H., Strachan, R.A. and Dawson, B. (2012a) *Geological history of Britain and Ireland*, Chichester, West Sussex: Wiley-Blackwell.

Woodcock, N.H., Strachan, R.A. and Dawson, B. (2012b) *Geological history of Britain and Ireland*, Second ed., Chichester, West Sussex: Wiley-Blackwell.

Ziegler, P. and Dèzes, P. (2006) 'Crustal evolution of western and central Europe', *Geological Society, London, Memoirs*, 32(1), 43-56.

Ziegler, P.A. (1988) 'Evolution of the Arctic-North Atlantic and the Western Tethys: A visual presentation of a series of Paleogeographic-Paleotectonic maps', *AAPG memoir*, 43, 164-196.